UNIVERSITY OF ZULULAND

Proceedings of SAIP2013:

the 58th annual conference of the
South African Institute of Physics

Edited by:
Roelf Botha and Thulani Jili

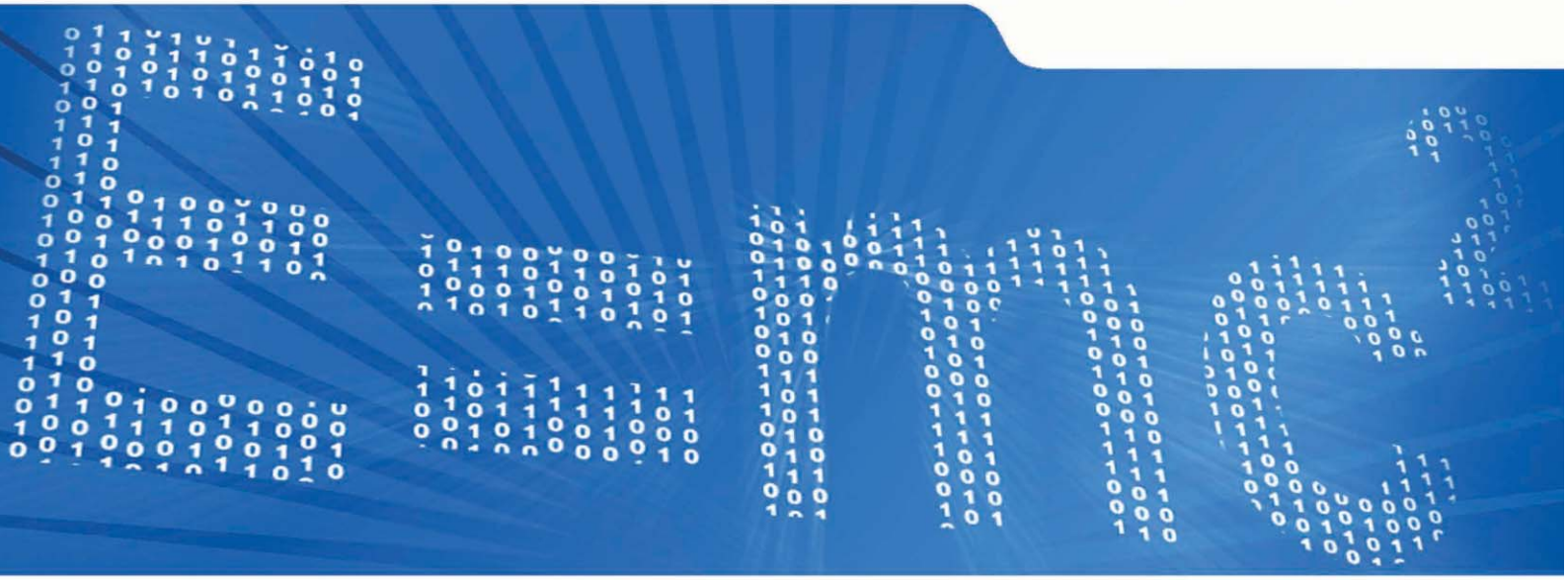

8-12 July 2013

RICHARDS BAY CAMPUS, UNIVERSITY OF ZULULAND

www.unizulu.ac.za · www.saip.org.za

RESTRUCTURED FOR RELEVANCE

PUBLISHER: The South African Institute of Physics (SAIP), http://www.saip.org.za

COVER DESIGNER: Thulani Jili

The Proceedings of SAIP2013, the 58th annual conference of the South African Institute of Physics (SAIP) will only be available electronically on compact disk (CD) and on the SAIP website www.saip.org.za.

ISBN: 978-0-620-62819-8

SAIP2013

Proceedings of SAIP2013: the 58th annual conference of the South African Institute of Physics (SAIP)

Hosted by the University of Zululand

8 - 12 July 2013
Richards Bay Campus
University of Zululand
Richards Bay
South Africa

Edited by
Roelf Botha and Thulani Jili

SA Institute of Physics 2013 ISBN: 978-0-620-62819-8

Table of Contents

Message from the Conference Chair and Co-Chair *xi*

Message from the SAIP2013 Review Committee *xiii*

Conference Chairs and Committees *xiv*

List of Reviewers *xv*

Full Research Papers

Division A - Division for Condensed Matter Physics and Materials

Effect of Ag nanoparticles on the luminescence of Tb doped sol-gel silica 2
A E Abbass, H C Swart and R E Kroon

Parameterization and validation of Pd and Pd nanoclusters using SCC-DFTB 8
M H Chuma, H R Chauke, G Jones and P E Ngoepe

Energy transfer and photoluminescence properties of Ce^{3+} or/and Tb^{3+}-doped PbS nanorods 13
B F Dejene and L F Koao

The effect of EWG and EDG on the HOMO and LUMO of Alq_3. 19
M M Duvenhage, O M Ntwaeaborwa, H G Visser, P J Swarts, J C Swarts and H C Swart

Magnetic Phase Diagram of Cr_{100-x} Os_x alloys 25
P R Fernando, A R E Prinsloo, C J Sheppard and J A L Lodya

YVO_4:Eu phosphor thin films prepared by PLD 31
K E Foka, B F Dejene, H C Swart and K Roro

Influence of magnetic field on the transition temperature of the $(Cr_{84}Re_{16})_{89.6}$ $V_{10.4}$ alloy 37
B S Jacobs, C J Sheppard and A R E Prinsloo

Luminescence properties of Bi^{3+} in Y_2 O_3 43
R M Jafer, A Yousif, E Coetsee and H C Swart

Effect of synthesis temperature on the structure, morphology and optical properties of PbS nanostructures prepared by chemical bath deposition method 49
L F Koao, F B Dejene and H C Swart

Raman spectral analysis of an organometallic composite film synthesized by electrochemical route 55
V Kumar, Y Ali, V Kumar, R G Sonkawade, A S Dhaliwal and H C Swart

Synthesis of zinc oxide based nanophosphors by solution combustion method 61
V Kumar, H C Swart and O M Ntwaeaborwa

Structural, electronic and mechanical stability of olivine $LiMPO_4$ (M: Mn, Fe, Co) 67
N L Lethole, H R Chauke and P E Ngoepe

AES and TOF-SIMS measurements of In segregation in a polycrystalline Cu crystal 73
M J Madito, H C Swart and J J Terblans

The elastic properties and the phonon dispersions of TiPtCo shape memory alloy using the supercell approach 79
R Mahlangu, H R Chauke and P E Ngoepe

Characterisation of carbon microspheres using electron paramagnetic resonance spin-concentration techniques 85
V D Marsicano, W P Wright, J M Keartland, R M Erasmus, S Dube and N J Coville

Efficiency degradation of organic solar cells with solution processed ZnO nanoparticles 91
P S Mbule, H C Swart and O M Ntwaeaborwa

Computational studies of the bulk cobalt pentlandite (Co_9S_8): Validation of the potential model 98
M A Mehlape, P E Ngoepe and S C Parker

Luminescent properties of $Ca_5(PO_4)_3OH:Gd^{3+}$, Pr^{3+} phosphor powder 104
P P Mokoena, I M Nagpure, V Kumar, H C Swart and O M Ntwaeaborwa

Magnetic properties of the $(Cr_{100-x}Al_x)_{99}V_1$ alloy system 110
B Muchono, C J Sheppard, A R E Prinsloo and H L Alberts

Low-energy electronic structure of the itinerant metamagnet $Sr_3Ru_2O_7$ 116
A S Ngankeu, E Carleschi and B P Doyle

Effects of different TiO_2 phases on the luminescence of $CaTiO_3:Pr^{3+}$ 121
L L Noto, S S Pitale, O M Ntwaeaborwa, J J Terblans, M Y A Yagoub and H C Swart

Structural and magnetic properties of $Mg_xSr_xMn_xCo_{1-3x}Fe_2O_4$ nanoparticle ferrites 128
N S E Osman, T Moyo and H M I Abdallah

Magnetic properties of epitaxial $Cr/Cr_{99.65}Ru_{0.35}$ heterostructures 134
A R E Prinsloo, C J Sheppard, A M Venter, E E Fullerton, B S Jacobs and K C Rule

White cathodoluminescence from $Zn_{0.3}Mg_{0.7}Al_2O_4:Tb^{3+},Eu^{3+}$. 140
S K K Shaat, H C Swart and O M Ntwaeaborwa

Characterization of epitaxial Cr thin films 146
C J Sheppard, A R E Prinsloo, P R Fernando, Z P Mudau, A M Venter and E E Fullerton

Spectrally selective doped zinc and aluminium oxide thin films prepared by spray pyrolysis for solar energy applications 152
P C Simpemba, K Chinyama, J Simfukwe and N R Mlyuka

Synthesis and Characterization of $CaB_4O_7:Eu^{3+}$ nano phosphors prepared using Solution - Combustion Method 158
T M Sithole, B F Dejene and L F Koao

The effect of chemical pressure on the ferromagnetic ordering of CeTX compounds 163
B M Sondezi, T Nemakhavhani and A M Strydom

The determination of critical behaviour of ferromagnetic CeCuGe using magnetocaloric effect 169
B M Sondezi, J L Snyman and A M Strydom

Blue luminescence from Bi doped $MgAl_2O_4$ prepared by the combustion method 175
W A I Tabaza, H C Swart and R E Kroon

Photoluminescent properties of $Sr_2SiO_4:Tb^{3+},Eu^{3+}$ phosphor 181
M A Tshabalala, H C Swart and O M Ntwaeaborwa

Effect of annealing on undoped and Ce, Dy, Eu, Ni-doped ZnO properties synthesized by sol-gel method. 187
J Ungula and F B Dejene

A preliminary study of Thermoluminescence of beta-irradiated $SrAl_2O_4:Eu^{2+}$, Dy^{3+} phosphors 193
A H Wako, B F Dejene and H C Swart

The electrical transport properties of bulk nitrogen doped carbon microspheres 199
W P Wright, V D Marsicano, J M Keartland, R M Erasmus, S Dube and N J Coville

Luminescent properties of Pr^{3+} doped SrF_2 prepared by different synthesis techniques 205
M Y A Yagoub, H C Swart, L L Noto and E Coetsee

Effect of annealing on the structure of $Y_3(Al,Ga)_5O_{12}$:Tb thinfilms grown by PLD 211
A Yousif, H C Swart and O M Ntwaeaborwa

Division B - Nuclear, Particle and Radiation Physics

Investigations beyond the standard model 218
G Amar

Challenges in the simulations of the iThemba LABS segmented clover detector 224
T D Bucher, S P Noncolela, E A Lawrie, O Shirinda and J L Easton

Lifetime measurements in the transitional nucleus ^{150}Sm 230
S P Bvumbi, S H Connell, J F Sharpey-Scafer, S M Mullins, R A Bark, E A Lawrie, J J Lawrie, P L Masiteng, S S Ntshangase and O Shirinda

Using the Higgs as a portal to the "hidden sector" 237
E Castaneda-Miranda

Re-mobilization of uranium and thorium from sediments contaminated by naturally occurring radioactive material (NORM) through leaching by acid mine drainage (AMD). 243
A Faanhof, N S Shongwe and S H Connell

Cytogenetic analysis of ^{60}Co gamma-radiation-induced chromosome damage and simulations using the Geant4 Monte Carlo toolkit 248
H Fourie, R T Newman, J P Slabbert and P Beukes

Research progress of the inclusion of tau-leptons in the Higgs to four lepton decay channel with the ATLAS detector 254
G N Hamity

Validation of a passive beam Monte Carlo model for measuring prompt gamma rays during proton radiotherapy 260
J Jeyasugiththan, S Peterson, J N Camero and J Symons
Aspects of the structure of heavy carbon isotopes 267
S Karataglidis, K Amos, J P Svenne, L Canton, P R Fraser and D van der Knijff
Determination of ^{235}U in the context of interference with ^{226}Ra for the study of the disequilibrium in the ^{238}U decay series 272
T N Khumalo, J Watterson, A Kwelilanga and S Connell
Developing gamma-ray tracking with a segmented Ge detector 278
E A Lawrie, T D Bucher, J L Easton, S P Noncolela and O Shirinda
^{194}Tl as the first example revealing chiral symmetry breaking in a pair of four-quasiparticle bands 283
P L Masiteng, E A Lawrie, T M Ramashidzha, R A Bark, B G Carlsson, J J Lawrie, R Lindsay, F Komati, J Kau, P Maine, S M Maliage, I Matamba, S M Mullins, S H T Murray, K P Mutshena, A A Pasternak, I Ragnarsson, D G Roux, J F Sharpey-Schafer, O Shirinda and P A Vymers
The Discovery of a Higgs Boson at the LHC 288
B Mellado
Search for invisible anomalous Higgs boson decay with the ATLAS detector at the LHC 294
G C Montoya and I Molefi
Search for chirality in ^{193}Tl 302
J Ndayishimye, E A Lawrie, J L Easton, R A Bark, S B Bvumbi, T S Dinoko, P M Jones, A Kamblawe, E Khaleel, N Y Kheswa, J J Lawrie, S N T Majola, P L Masiteng, D Negi, J N Orce, P Papka, A A Pasternak, J F Sharpey-Schafer, O Shirinda, M A Stankiewicz, M Wiedeking and S M Wyngaardt
Emissions of Trace Elements from Motor Vehicles Monitored by Active Biomonitoring: a tunnel study in the Western Cape, South Africa using ICP-MS and neutron activation 307
N B Ndlovu, M V Frontasyeva, R T Newman and P P Maleka
Measuring the performance of the iThemba LABS segmented clover detector 313
O Shirinda, J L Easton, E A Lawrie, T D Bucher and S P Noncolela

Division C - Photonics

The Impact of Low Intensity Laser Irradiation on Lung Cancer Stem Cell Viability and Proliferation 321
A Crous and H Abrahamse
Cold atoms at the University of KwaZulu-Natal 325
M Gumede, S Dlamini, M J Morrissey and F Petruccione
Low Intensity Laser Irradiation (LILI) in Combination with Growth Factors in a Co-culture System Supports the Differentiation of Mesenchymal Stem Cells 332
B Mvula and H Abrahamse
Design and evaluation of a low-cost Photovoltaic system with semi-diffuse structured aluminium reflectors 337
J Simfukwe, K G Chinyama, P Simpemba and S Hatwaambo

Division D1 - Astrophysics

Dust in the Radio Galaxy and Merger Remnant NGC 1316 (Fornax A) 344
B D Asabere, C Horellou, H Winkler, T Jarrett and L Leeuw

Implementation of an o set-dipole magnetic field in a pulsar modelling code 350
M Breed, C Venter, A K Harding and T J Johnson

Investigating Brightest Cluster Galaxies: kinematics with SALT 356
S I Loubser

Recent Results on the Spatially Resolved Molecular Gas Star Formation Law from CARMA Survey Toward Infrared-bright Nearby Galaxies (STING) 362
N Rahman, A D Bolatto, and the STING Collaboration

SDSS J120011-020452: Unusual I Zw 1 object or a nearby BAL Seyfert? 368
N Rahman† and H Winkler

Galaxy peculiar velocities in the Zone of Avoidance 374
K Said, R C Kraan-Korteweg and T H Jarrett

Modelling the gamma-ray and radio light curves of the double pulsar system 380
A S Seyffert, C Venter, A K Harding and T J Johnson

Modelling the light curves of *Fermi* LAT millisecond pulsars 385
C Venter, T J Johnson, A K Harding and J E Grove

Line, LINER, linest - from micro-AGN to ultra-luminous LINERs. One and the same? 391
H Winkler

Division D2 - Space Science

Evaluation of the NeQuick model in Southern mid-latitudes using South African co-located GPS and Ionosonde data 398
S M Ahoua, P J Cilliers, O K Obrou and J B Habarulema

Extraction of surface impedance from magnetotelluric data 404
S Khanyile and P Cilliers

Methods of measuring and modelling geomagnetically induced currents (GIC) in a power line. 410
E Matandirotya, P J Cilliers and R R van Zyl

Tomographic imaging of the ionospheric structure and disturbances in the East-Central Africa region 416
M Mutale, P Sibanda

Study of the geomagnetic field over southern Africa applying harmonic splines technique on CHAMP satellite data 422
E Nahayo, P B Kotze and H McCreadie

Inversion of geomagnetic fields to derive ionospheric currents that drive geomagnetically induced currents. 428
J S de Villiers and P J Cilliers

Division E - Physics Education

University students' performance in different types of exam questions informs on their problem solving skills as well as studying ability 435
C Albers, D Clerk and D Naidoo

Correlation between mathematics proficiency and performance in a first-year physics course 441
E Carleschi and B S Jacobs

Physics foundation program: Implications for second year mainstream physics module. 446
P Molefe and B M Sondezi

Is there a gap between the high school curriculum and first year university experience? 452
B M Sondezi and P Molefe

Division F - Applied Physics

Digital Signal Processing Algorithm for Signal Analysis and Performance Monitoring in an Optical Communication Link 460
T V Chabata, R R G Gamatham, H Y S Kourouma, E K Rotich Kipnoo, A W R Leitch and T B Gibbon

Advancement of quantum communication through entanglement 464
Y Ismail, A Mirza, A Forbes and F Petruccione

Open-Source electronics for quantum key distribution 470
M Mariola, A Mirza and F Petruccione

An assessment of wind energy potential of the Amatole district in the Eastern Cape Province of South Africa 476
P Masukume, G Makaka and D Tinarwo

Analyses of the spatial and spectral neutron distribution of various conceptual core designs with the aim of optimizing the SAFARI-1 research reactor 483
O Oluwaleye, R H Prinsloo, B A Adetula and S H Connell

Chromatic Dispersion Compensation for VCSEL Transmission for Applications such as Square Kilometre Array South Africa 490
E K Rotich Kipnoo, H Y S Kourouma, R R G Gamatham, A W R Leitch and T B Gibbon

Modelling and real time simulation of the instantaneous performance of residential air source heat pump water heater. 496
S L Tangwe, M Simon and E L Meyer

Elemental analysis of Kimberlite and associated Country Rock 502
M Tchonang, M Cook, F Bornman, S Connell and S Ballestrero

Pulse Delay Chromatic Dispersion Measurements in Single Mode Fibre 507
S Wassin, E K Rotich Kipnoo, R R G Gamatham, A W R Leitch and T B Gibbon

South African night sky brightness during high aerosol epochs 513
H Winkler, F van Wyk and F Marang

Division G - Theoretical and Computational Physics

A Review of Generalized and Unsharp Measurements 520
H Bassa and T Konrad

Heavy Baryons with Strangeness 525
J P Blanckenberg and H Weigel

Quantum measurements along accelerated world-lines 531
J M Hartman, S H Connell and F Petruccione

Concavity of energy surfaces 537
S Karataglidis and B G Giraud

Tsallis entropy and quantum uncertainty in information measurement 542
M Mafu and F Petruccione

Finite-size key in QKD protocols for Renyi entropies 548
M Mafu, K Garapo and F Petruccione

Message from the Conference Chair and Co-Chair

In 2013 the Physics and Engineering Department of the University of Zululand (UNIZULU) successfully hosted the 58th Annual Conference of the South African Institute of Physics (SAIP) hosted for the first time in the Institution's history. We are extremely excited and proud that, for the first time, the Physics and Engineering Department at UNIZULU, in collaboration with the South African Institute of Physics, presents to you the peer-reviewed Proceedings of the SAIP 2013. We would like to take this opportunity to convey our heartfelt appreciation to the authors and especially to the reviewers who did excellent work in getting reviews done. The proceedings present a superb platform for the Masters and Doctoral students, as well as regular experienced researchers, to showcase their new findings. The proceedings are electronically available through the SAIP official website www.saip.org.za

We truly appreciate the participation from those within our borders, those from several African countries, as well as those who were coming from abroad. The Winter School was on The Applications of Synchrotron Radiation, High Energy Physics and Biophysics. A special word of appreciation goes to the Italian Scientists, Dr Cinzia Cepek and Dr Marco Lazarino, both of Consiglio Nazionale delle Ricerche (CNR) located in Basovizza , Dr Andrea Goldoni and Dr Elena Magnano, both of Sincrotrone Trieste, who all presented work related to the applications of synchrotrons. The immense contribution of the local and international speakers during the Winter School is much appreciated. The participation of Masters and Doctoral students and the entire Physics community during the Winter School is truly appreciated. We still hold the record of twelve international and national plenary speakers. The plenary sessions were of immense benefit not only to the students and the Physics community at large, but more specifically to the country itself.

We are very proud to have introduced for the first time, the mace, which symbolizes our unconditional commitment to the objectives of the South African Institute of Physics and the strengthening of physics research in our beloved country. This tradition of handing over the mace from the outgoing SAIP President to the incoming SAIP President and from the outgoing Conference Chair to the incoming Conference Chair, will definitely inspire future Physicists, and we believe they will be proud and appreciate the foundation, sacrifices and unity we are building today.

We salute and thank all the delegates of the SAIP2013 who allowed us to put our University on the world map. The immense support we received from the SAIP Council led by the energetic outgoing SAIP President Prof Simon Connell is very much appreciated. We also welcome the new SAIP President Dr Igle Gledhill and thank her for her brilliant ideas and advice given to the Local Organizing Committee (LOC). We would be doing injustice if we did not thank the SAIP CEO, Mr Brian Masara and Mrs Linette White for ensuring that our Conference was a success. The support we received from the management of the University of Zululand, led by the Vice-Chancellor Prof N.M. Mazibuko and the Deputy Vice-Chancellor, Prof R. Midgley, is truly appreciated. Mr Roelf Botha deserves to be mentioned because of the pivotal role he played as far as the success of proceedings is concerned.

We sincerely thank the Mayor of the City of Mhlathuze, the Honourable Councillor, Mr Elphas Mbatha for gracing the opening of the conference. We also thank the Speaker of Mhlathuze, Honourable Mr Mvuseni Mnqayi, who graced the conference banquet.

We thank all the staff of the Physics and Engineering Department together with the staff from Communication and Marketing Division for their excellent commitment before and after the conference.

OM Ndwandwe

SAIP2014 Conference Chair

TP Jili

SAIP2014 Conference Co-Chair

Message from the SAIP2013 Review Committee

The SAIP2013 review committee considered 116 contributions towards the proceedings, and subjected 114 of these to peer-review. For each contribution, the review committee selected at least two independent reviewers that could provide impartial expert opinions. Each paper received two or more independent reviews from reviewers who had no conflicts of interest for the paper (declarations were made by all reviewers to indicate possible conflicts of interests that may have been overlooked by the review committee). At least one additional independent review was solicited in cases where reviewers' reports were in conflict. A total number of 94 subject specialists assisted with this review process, all of whom hold at least a PhD in Physics or in a related field. The review panel consisted of 6 members, 3 with at least a PhD in Physics. The final selection of papers was made by the Editors, based on the outcome of the peer-review process. A total of 91 contributions were finally accepted (78%), with each paper reporting on original research which has not been published previously.

The review committee appreciates the diligence of the reviewers. The quality of feedback which was received contributed to the quality and overall high standard of the research reported in these proceedings. The committee would like to thank all the authors who submitted papers to SAIP2013, as well as the reviewers who generously gave of their time and expertise to ensure that each contribution received a proper peer review.

Roelf Botha

On behalf of the SAIP2013 Review Committee

Conference Chairs and Committees

SAIP2013 Conference Chair
Muzi Ndwandwe, Department of Physics, University of Zululand

SAIP2013 Programme Chair
Thulani Jili, Department of Physics, University of Zululand

SAIP Division Chairs
Division A: Japie Engelbrecht (Nelson Mandela Metropolitan University)
Division B: Simon Mullins (iThemba LABS)
Division C: Erich Rohwer (University of Stellenbosch)
Division D: Illani Loubser (University of North West)
Division E: Sam Ramaila (University of Johannesburg)
Division F: Freddie Vorster (Nelson Mandela Metropolitan University)
Division G: Frederik Scholtz (National Institute for Theoretical Physics)

Finance Chair
Brian Masara, SAIP Office, CSIR, Pretoria, South Africa

Proceedings Editorial Team
Editor: Roelf Botha (SAIP and HartRAO)
Co-Editor: Thulani Jili (University of Zululand)
Ilsa Basson (UNISA)
Administration and PDF Compilation: Juan Grey

Proceedings Review Panel
Thulani Jili (University of Zululand)
Roelf Botha (SAIP and HartRAO)
Betty Kibirige (University of Zululand)
Sifiso Ntshangase (University of Zululand)
Thembinkosi Nyawo (University of Zululand)

List of Reviewers

Dr.	ACQUAVIVA, Giovanni	University of Zululand
Dr.	AKHALWAYA, Ismail	University of Johannesburg
Dr.	ALBERS, Claudia	University of the Witwatersrand
Dr.	BARWAY, Sudhansu	South African Astronomical Observatory
Prof.	BHARUTH-RAM, Krish	University of Kwazulu-Natal and iThemba Labs
Dr.	BIETENHOLZ, Michael	Hartebeeshoek Radio Astonomy Observatory
Prof.	BLUMENTHAL, Mark	University of Cape Town
Dr.	BOTTCHER, Markus	North West University
Prof.	BRAUN, Moritz	University of South Africa
Dr.	BUCHER, T Daphney	iThemba Labs
Prof.	BUFFLER, Andy	University of Cape Town
Dr.	BVUMBI, Suzan P	University of Johannesburg
Dr.	CHIGUVARE,Zivai	Polytechnic of Namibia and University of the Witwatersrand
Dr.	CHIRWA, Max	Walter Sisulu University
Prof.	CHITHAMBO, Makaiko	Rhodes University
Dr.	CILLIERS, Pierre	South African National Space Agency
Prof.	CLEYMANS, Jean	University of Cape Town
Dr.	CLUVER, Michelle	University of Cape Town
Dr.	COETZEE, Annaretha	Tshwane University of Technology
Prof.	CONNELL, Simon H	University of Johannesburg
Dr.	CRAWFORD, Steven	South African Astronomical Observatory
Prof.	DE MELLO KOCH, Robert	University of the Witwatersrand
Prof.	ENGELBRECHT, Japie A A	Nelson Mandela Metropolitan University
Prof.	FAANHOF, Arnaud	South African Nuclear Energy Corporation (Necsa)
Dr.	FORBES, Andrew	Council for Scientific and Industrial Research
Dr.	FRESCURA, Fabio	University of the Witwatersrand
Dr.	GAYLARD, Mike	Hartebeeshoek Radio Astonomy Observatory
Dr.	GILBANK, David	South African Astronomical Observatory
Dr.	HAMILTON, Andrew	University of Cape Town
Dr.	HEARNE, Giovanne	University of Johannesburg
Dr.	KARSTEN, Aletta	Council for Scientific and Industrial Research and NLC
Dr.	KEARTLAND, Jonathan	University of the Witwatersrand
Dr.	KILKENNY, David	University of the Western Cape
Prof.	KOK, Schalk	University of Pretoria
Prof.	KONRAD, Thomas	University of Kwazulu-Natal
Dr.	KORTE, Monika	GeoForschungsZentrum (GFZ)
Dr.	KROON, Ted	University of the Free State
Dr.	LAWRIE, Elena	iThemba Labs
Prof.	LINDSAY, Robert	University of Cape Town
Dr.	LITVIN, Igor	Council for Scientific and Industrial Research and NLC
Dr.	LOUBSER, Ilani	University of South Africa
Dr.	MADHUKU, Morgan	iThemba Labs
Dr.	MAFUSIRE, Cosmas	Council for Scientific and Industrial Research and NLC
Prof.	MALHERBE, Johan	University of Pretoria
Dr.	MAMPHWELI, Sampson	University of Fort Hare
Dr.	MANYALA, Reccab O	University of Zambia
Dr.	MAPASHA, Edwin	University of Pretoria
Dr.	MASITENG, Paulus	University of Johannesburg
Dr.	MATHE, Bhekumusa	University of the Witwatersrand
Dr.	MBULE, Pontsho S	University of South Africa
Prof.	MELLADO, Bruce	University of Wisconsin - Madison, USA
Dr.	MISHRA, Yogendra K	University of Kiel, Germany
Dr.	MOTHUDI, Bakang M	University of the Free State
Dr.	MOYO, Thomas	University of Kwazulu-Natal
Dr.	MSIMANGA, Mandla	Tshwane University of Technology
Prof.	MURONGA, Azwindini	University of Johannesburg
Dr.	NAICKER, Vishnu	North West University

Dr.	NAIDOO, Deena	University of the Witwatersrand
Dr.	NEETHLING, Pieter H	Stellenbosch University
Dr.	NEMRAOUI, Ouassini	University of Zululand and iThemba Labs
Prof.	NETSHISAULU, Tom	University of Limpopo
Dr.	NGWIRA, Chigomezyo	National Aeronautics and Space Administration, USA
Prof.	NTWAEABORWA, Odireleng	University of the Free State
Dr.	ORCE, Nico	University of the Western Cape
Prof.	OYEYEMI, Elijah O	University of Lagos, Nigeria
Dr.	PETERSON, Steve	University of Cape Town
Prof.	PETRUCCIONE, Francesco	University of Kwazulu-Natal
Dr.	PHASHA, Maje	Council for Scientific and Industrial Research
Dr.	REDDY, Leelakrishna	University of Johannesburg
Dr.	ROMERO-COLMANERO, Encarni	South African Astronomical Observatory
Prof.	ROOS, Wiets D	University of the Free State
Dr.	ROUX, David	Rhodes University
Dr.	ROUX, Stef	Council for Scientific and Industrial Research
Prof.	SCHOLTZ, Frederik G	Stellenbosch University and NITheP
Dr.	SCHROEDER, Anja	South African Astronomical Observatory
Dr.	SHARMA, Kashma	University of Biotechnology and Management Sciences
Prof.	SHARPEY-SCHAFER, John F	University of the Western Cape
Dr.	SINAYSKIY, Ilya	University of Kwazulu-Natal and NITheP
Prof.	SMITS, Derck	University of South Africa
Dr.	STEENKAMP, Christine M	Stellenbosch University
Dr.	STEYN, Deon	iThemba Labs
Prof.	STRYDOM, Andre	University of Johannesburg
Prof.	SWART, Hendrik C	University of the Free State
Prof.	TCHOULA TCHOKONTE, Moise Bertin	University of the Western Cape
Dr.	TIBANE, Malebo	University of South Africa
Dr.	VENTER, Christo	North West University
Dr.	VORSTER, Frederick J	Nelson Mandela Metropolitan University
Dr.	WAMWANGI, Daniel	University of the Witwatersrand
Prof.	WATTERSON, John	University of the Witwatersrand
Dr.	WHEATON, Spencer	University of Cape Town
Dr.	WILKE, D Nico	University of Pretoria
Dr.	YACOOB, Sahal	University of Kwazulu-Natal
Dr.	ZAMONSKY RIMOLDI, Oscar M	South African Nuclear Energy Corporation (Necsa)
Dr.	ZHANG, Jiangfeng	University of Pretoria

Division A – Division for Condensed Matter Physics and Materials

Effect of Ag nanoparticles on the luminescence of Tb doped sol-gel silica

Abad Ellateef Abbass[1,2], HC Swart[2] and RE Kroon[2]

[1]Department of Physics, Sudan University of Science and Technology, Sudan
[2]Department of Physics, University of the Free State, Bloemfontein, South Africa

E-mail: KroonRE@ufs.ac.za

Abstract: Tb doped silica has been synthesized using the sol-gel method and emits green light of wavelength 544 nm. X-ray diffraction (XRD) results show that these samples remain amorphous even after annealing at 1000˚C. In other samples, silver nitrate was added during the synthesis. The presence of Ag nanoparticles (NPs) in the silica matrix was confirmed by XRD and transmission electron microscopy (TEM) analysis and the average crystallite size was found to be 20-30 nm. The TEM results showed that the shape of NPs was changed by thermal treatment and the average NPs size of Ag increased by increasing the temperature in the thermal treatment process. Photoluminescence showed that in the presence of 1 mol% Ag there was a great enhancement in the emission from the Tb ions when excited by a wavelength of 325 nm. The effect of the concentration of the Ag NPs on the excitation and emission of the Tb ions was systematically studied.

1. Introduction

Nanomaterials are of importance for science and technology, due to their small size and large surface areas. Noble metal nanoparticles (NPs) are particularly interesting due to their plasmonic effects [1-2]. The study of the interaction of lanthanide ions with metal NPs has been paid much attention [3-9] because of their unique luminescent behaviours and potential applications. The interaction between Ag NPs and lanthanide ions, both dispersed in a host material, can result in enhanced luminescence from the lanthanide ions. This occurs when the excitation or emission wavelength of the lanthanide ions are close to the LSPR wavelength of the NPs [7]. Ag is known to give more pronounced near-field effects than Au due to less pronounced resonance damping by interband electron transitions, as it is known to have a higher energy separation between localized surface plasmon resonance (LSPR) and interband absorption [10]. Ag NPs can be incorporated into silica using a sol-gel process [11], which is attractive due to its low cost, low temperature operation and environmental friendliness.

Among the lanthanides, the green luminescence of Tb ions finds many uses for light emitting devices and display applications. However, Tb ions have a small absorption cross section due to parity forbidden f-f transitions, which mean that they cannot be efficiently excited directly by long wavelength ultraviolet (UV) light longer than 300 nm. Researchers have used different approaches, particularly exciting the strong f-d transitions of Tb at shorter wavelengths or employing energy transfer from a sensitizer such as Ce, to enhance the excitation efficiency of Tb ions. In the present work, Ag NPs have been incorporated together with Tb ions in silica, with the aim to enhance the f-f absorption of Tb ions due to the strong electric field associated with the LSPR of the metal NPs. The effect of the Ag NPs on the luminescent properties of the Tb ions in amorphous silica is reported.

2. Experimental

All the chemicals were purchased from Sigma Aldrich and used without further purification. The reagents for the sol-gel process to make silica were tetraethoxysilane (TEOS) (99.0%), ethanol (99.7%) and water [12]. The molar ratio of the starting solution was taken as 1:5:10 for TEOS: ethanol: water. For all samples the TEOS was dissolved in the ethanol and stirred for 30 min. Dilute HNO_3 (0.15 M) was then added to the solution instead of the water, to catalyse the reaction, followed by stirring for a further 30 min. To dope the silica samples, $Tb(NO_3)_3$ (99.999%) and/or $AgNO_3$ (99.9%) were dissolved ultrasonically in a small amount of ethanol and added to the mixture, which was stirred for another 5 h. All solutions were then stored in closed containers in a water bath at 50˚C until a gel was formed. For drying, gels were placed in open containers in air for 22 h, ground to fine powder and transferred to a drying oven at 50˚C for a further 20 h. Each sample was divided into two parts, one annealed at 500˚C and the other annealed at 1000˚C for 2 h. Samples were analysed at room temperature. X-ray diffraction (XRD) patterns were recorded with a Bruker D8 diffractometer. Morphology and size of the Ag NPs were obtained from transmission electron microscope (TEM) images recorded with a Philips CM 100. Diffuse reflection spectra were obtained using a PerkinElmer Lambda 950 UV-vis spectrophotometer with spectralon as a standard, while phosphorescence emission and excitation spectra were measured using a Cary Eclipse fluorescence spectrophotometer.

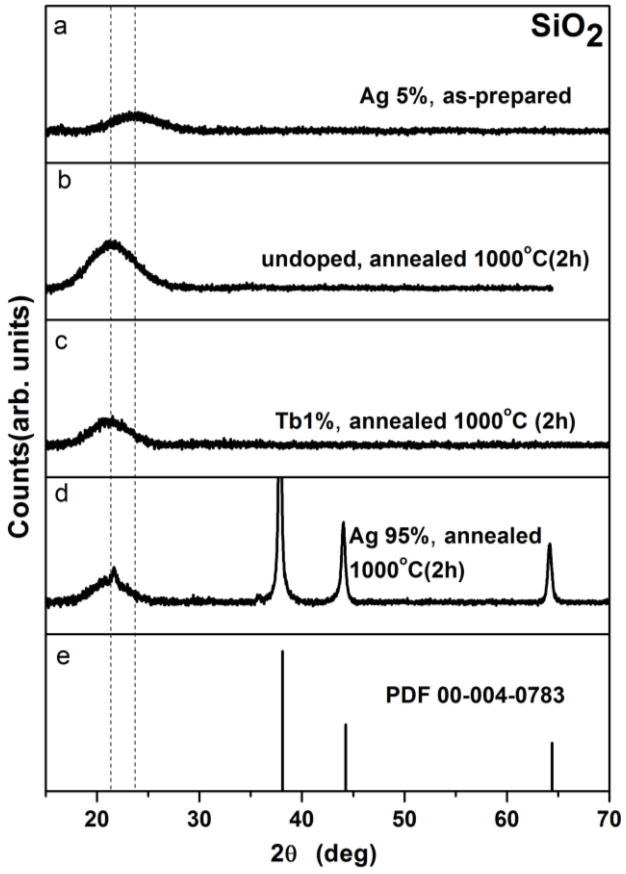

Figure 1. XRD patterns of (a) as-prepared silica with 5 mol% Ag, (b) pure silica annealed at 1000˚C (2h), (c) silica with 1 mol% Tb annealed at 1000˚C (2 h), (d) silica with 5 mol% Ag annealed at 1000˚C (2 h) and (e) PDF 00-004-0783 file for Ag.

3. Results and discussion

3.1 Structural and morphological characterization

Figure 1 shows the XRD patterns of several samples prepared during the study. The as-prepared samples (before annealing) showed only a broad amorphous diffraction band centred at 2θ ~ 23˚, even when doped with 5 mol% Ag (figure 1(a)). In the undoped sample annealed at 1000˚C for 2 h (figure 1(b)) this peak shifted to 2θ ~ 21˚, corresponding to an increase in the structural order of the amorphous silica towards the cristobalite phase, which is one of the crystalline forms of silica [11]. The addition of 1 mol% Tb did not produce any additional peaks in the XRD pattern, even after annealing (figure 1(c)), but when the sample containing 5 mol% Ag was annealed (figure 1(d)) peaks corresponding to crystalline Ag appeared, as confirmed by comparison with the Powder Diffraction File (PDF 00-004-0783, figure 1(e)). In addition, a small peak on the amorphous silica band near 2θ ~ 21˚ indicates that some of the amorphous silica converts to the crystalline phase due to the Ag doping. The average size of Ag NPs was calculated by Scherrer's equation $D = 0.9\lambda/(\beta \cos\theta)$ where β is the full width at half maximum of a diffraction peak in radians, θ is the corresponding Bragg angle and λ is the wavelength of the x-rays (154 pm). The average diameter of the NPs obtained using the different Ag diffraction peaks was in the range of 20-30 nm.

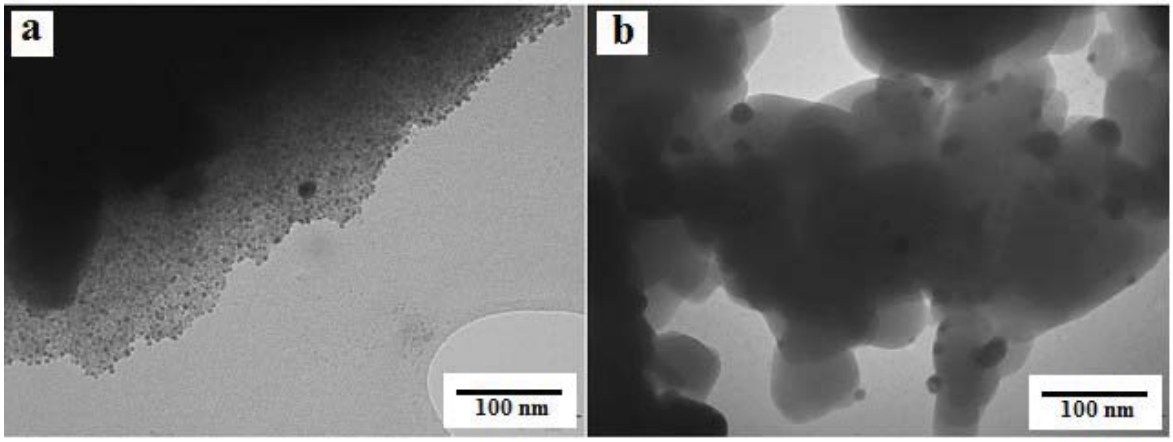

Figure 2. TEM results for two silica samples doped with 5 mol% Ag (a) annealed at 500ºC for 2 h, (b) annealed at 1000ºC for 2 h.

Figure 2 shows TEM images of silica doped with 5 mol% Ag annealed at (a) 500˚C and (b) 1000˚C for 2 h. The sample annealed at 500˚C shows a fine distribution of a large number of Ag NPs in the silica matrix, which appear spherical in shape and about 5-10 nm in diameter. In the sample annealed at 1000˚C the Ag NP density was much lower and the NPs were much larger in size (20-33 nm in diameter, in agreement with the mean size calculated by Scherrer's equation) and not perfectly spherical in shape. This is attributed to aggregation of the Ag NPs during the high temperature treatment. This means that the thermal treatment can affect the size and shape of the Ag NPs. The phenomenon of aggregation is controlled by the Gibbs–Thomson effect, where the chemical potential is inversely proportional to the particle size [13].

3.2 Optical characterization

Figure 3 shows diffuse reflectance spectra of two silica samples annealed at 1000 ºC for 2 h of (a) pure silica (b) 0.1 mol% Ag doped silica. The broad absorption peak in the doped sample near 405 nm

corresponds to the LSPR peak of Ag NPs and confirms the formation of Ag NPs in the silica matrix, in agreement with the XRD and TEM measurements.

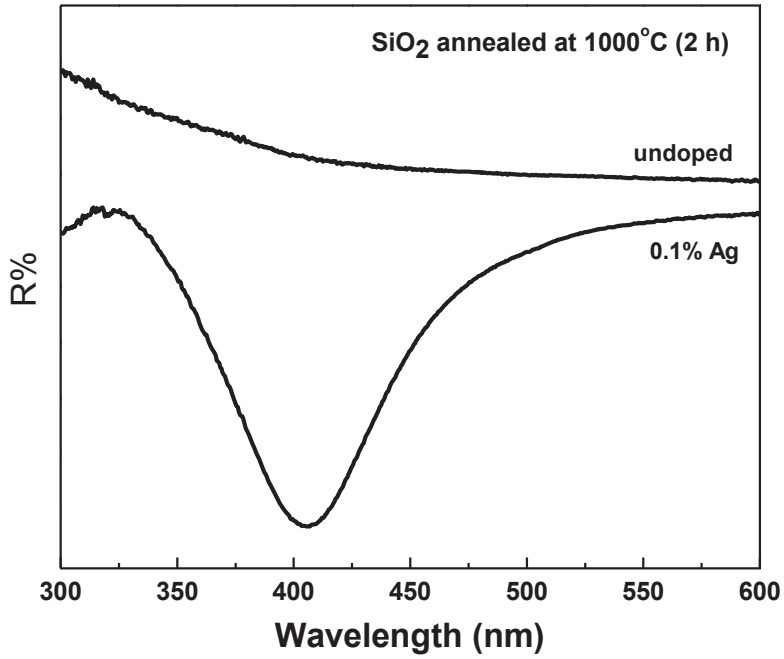

Figure 3. UV–vis diffuse reflectance spectra of (a) pure silica (b) silica doped with 0.1 mol % Ag, both annealed at 1000ºC for 2 h.

For silica samples doped only with Tb, the green emission from the Tb^{3+} ions at 544 nm increased in intensity with the doping concentration up to 7 mol%, which was the highest concentration considered. However, due to the high cost of terbium nitrate it was decided to work with further samples doped with 5 mol% Tb. Figure 4(a) shows the excitation spectra for the 544 nm emission of Tb for sol-gel silica samples with 5 mol% Tb in the presence of different amounts of Ag, where the samples have been annealed at 500˚C for 2 h. For the sample with no Ag added, we observed six peaks at 485, 377, 369, 351, 340, and 318 nm and assigned them to the electronic transitions of Tb^{3+} ions from the ground state $^7F_6$ to the $^5D_4$, $^5D_3$, $^5L_{10}$, $^5D_2$, $^5G_4$, and $^5D_1$ excited states, respectively. As the amount of Ag increased, the excitation peaks below 400 nm become less distinct, although the $^7F_6$ to $^5D_4$ transition near 485 nm is little affected. It is clear that the shorter wavelength f-f transitions are highly affected by the addition of Ag. Depending on the excitation wavelength, there can be considerable enhancement of the Tb emission. The emission intensity of all samples at 544 nm excited by 325 nm as the function of Ag load is shown in Figure 4(b). The intensity increases with increasing Ag load from 0 to 1 mol%, whereas further increasing of Ag concentration decreases the intensity. The inset shows the relation between Ag load and enhancement factor (the Tb emission intensity relative to the sample without Ag) and it can be seen that the maximum enhancement factor is 8.8. This enhancement factor is particularly high because the wavelength of 325 nm does not correspond to one of the Tb f-f transition wavelengths. However, even for those wavelengths some enhancement does occur, e.g. for the $^7F_6$ to $^5D_3$ transition near 377 nm the peak height is increased by the addition of some Ag and the maximum occurs for a Ag load of 0.3 mol%. For simple plasmonic enhancement of the Tb f-f levels, it was expected that the excitation bands would retain their positions and that the peaks closest to the LSPR of the Ag NPs would increase in height. Clearly the experimental results are different to this, with the f-f excitation bands becoming less distinct. Stark splitting of the energy

levels could be the reason for this, but is not considered to be the case since the 4f levels are well shielded and stark splitting would also result in a broadening of the emission bands, which is not observed. So although we have achieved some enhancement of the green Tb emission by the addition of Ag, the mechanism does not appear to be simple plasmonic enhancement, but is unclear and requires further study. One possibility is the interaction of Tb ions with Ag ions, instead of Ag NPs, and energy transfer from the Ag ions instead of a plasmonic enhancement [14].

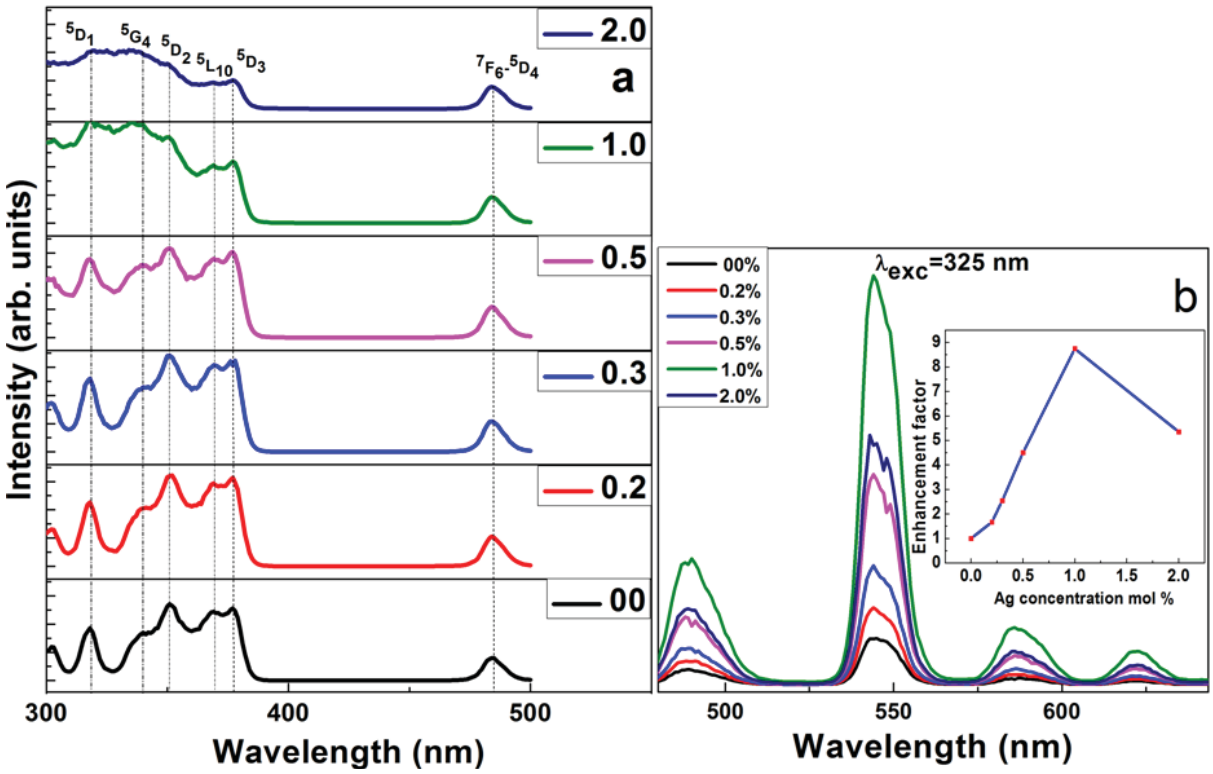

Figure 4. Luminescence spectra of silica samples doped with 5 mol% Tb and various concentrations of Ag (a) excitation (λ_{em} = 544 nm) (b) emission (λ_{exc} = 325 nm), after annealing at 500˚C for 2 h.

4. Conclusion

Tb and Ag co-doped silica samples have been successfully synthesized using the sol-gel method. XRD, TEM and UV-vis diffuse reflectance results confirmed the formation of Ag NPs in the silica matrix. The results showed that the annealing temperature can be used as mechanism to control the shape and size of the Ag NPs in amorphous silica. For an excitation wavelength of 325 nm, the highest intensity of the green emission of Tb ions at 544 nm is obtained when the doping concentration of Ag was 1 mol %. The change in the Tb f-f excitation spectrum is not merely an increase in the f-f excitation peaks closest to the LSPR wavelength of the Ag NPs, as expected for simple plasmonic enhancement, but instead the peaks merge into a broad excitation band. This may be evidence that energy transfer from Ag ions also plays a role in the luminescence enhancement.

Acknowledgements
The authors thank Prof. van Wyk at the University of the Free State Centre for Microscopy for assisting with TEM measurements. This work is based on the research supported by the South African Research Chairs Initiative of the Department of Science and Technology and National Research Foundation of South Africa. The University of the Free State Cluster programme is acknowledged for financial support.

References

[1] Willets K A and Van Duyne R P 2007 *Annu. Rev. Phys. Chem.* **58** 267–297
[2] Hayashi S and Okamoto T 2012 *J. Phys. D: Appl. Phys.* **45** 433001 (24 pages)
[3] Malta O L, Santa-Cruz P A, De Sá G F and Auzel F 1985 *J. Lumin.* **33** 261–272
[4] Malta O L and Couto dos Santos M A 1990 *Chem. Phys. Lett.* **174** 13–18
[5] Lipowska B and Kłonkowski A M 2008 *J. Non-Cryst. Solids* **354** 4383–4387
[6] Piasecki P, Piasecki A, Pan Z, Mu R and Morgan S H 2010 *J. Nanophotonics* **4** 043522 (9 pages)
[7] Pan Z, Ueda A, Aga R, Burger A, Mu R and Morgan S H 2010 *J. Non-Cryst. Solids* **356** 1097–1101
[8] Verma R K, Kumar K and Rai S B 2010 *Solid State Commun.* **150** 1947–1950
[9] Zhang D, Hu X, Ji R, Zhan S, Gao J, Yan Z, Liu E, Fan J and Hou X 2012 *J. Non-Cryst. Solids* **358** 2788–2792
[10] Drozdowicz-Tomsia K and Goldys E M 2011 Gold and silver nanowires for fluorescence enhancement, in *Nanowires - Fundamental Research* ed A Hashim (InTech) ch. 14 p. 315
[11] Duhan S, Kishore N, Aghamkar P and Devi S 2010 *J. Alloys Compd.* **507** 101–104
[12] Seed Ahmed H A A, Ntwaeaborwa O M and Kroon R E 2013 *J. Lumin.* **135** 15–17
[13] De Marchi G, Mattei G, Mazzoldi P, Sada C and Miotello A 2002 *J. Appl. Phys.* **92** 4249–4254
[14] Eichelbaum M and Rademann K 2009 *Adv. Funct. Mater.* **19** 2045–2052

Parameterization and validation of Pd and Pd nanoclusters using SCC-DFTB

M H Chuma[1], H R Chauke[1], G Jones [2, 3] and P E Ngoepe[1]

[1]Materials Modelling Centre, University of Limpopo, Private Bag x1106, Sovenga, 0727, South Africa
[2]Johnson Matthey Technology Centre - Pretoria, Building 22 CSIR, Meiring Naude Road, Brummeria, South Africa
[3]Department of Chemistry, University College London, 20 Gordon Street, London, WC1H OAJ, Unite Kingdom

E-mail: moyahaboc@gmail.com

Abstract. The self-consistent-charge density functional tight binding (SCC-DFTB) approach has been used to describe large scale Pd systems with accuracy and precision than the density functional theory method [1]. DFTB+ has been used to develop a set of SCC-DFTB parameters for Pd-Pd atomic pairs of elements. The SCC-DFTB parameterization has been performed to describe bulk Pd structure and nanoclusters. It was found that the predicted equilibrium lattice parameters using the recently developed set of SCC-DFTB parameters are in good agreement with the experimental data. The Pd-Pd interaction in the Pd_n (n = 2 – 6 atoms) nanoclusters gives better prediction of bond length with DFTB+ than the conventional DFT [2, 3]. Furthermore, their calculated bond lengths lie within 0.1% with the available literature data [4].

1. Introduction

Noble metals such as silver and gold, together with the platinum group metals (PGMs) namely: platinum, palladium, ruthenium, rhodium, iridium and osmium have been extensively studied recently, and are regarded as good catalysts for chemical and electrochemical reactions [5, 6]. These metals are mostly used as catalysts in fuel cells and emissions control technology. Unfortunately, due to their excessive production cost and poor durability, fuel cells including direct methanol (DM) and proton exchange membrane (PEM) fuel cells are finding it difficult to reach the desired markets [5].

In recent years, metal nanoparticles have been of interest in several areas including physics and material sciences for application in heterogeneous catalysis, fuel cells and chemosensors. The properties of these nanoparticles were found to differ from those of bulk materials [7]. It has also been reported that metal atoms in small clusters exhibit particular electronic, structural and chemical properties that relate to their catalytic activities [8, 9].

The catalyst that is commonly used in proton exchange membrane fuel cells (PEMFC) is the platinum-based catalyst, however, because of the high cost [10] and limited resources of platinum, further developments become more challenging and costly, thus other materials are now being taken into consideration. For example, palladium nanoclusters because of their similar electronic

configurations, lattice constants and cheaper than platinum [4], and ability of high methanol-tolerant, are considered a promising future catalyst.

In the current paper, we use DFTB+ code to develop a set of SCC-DFTB parameters for Pd-Pd atomic pairs of elements. The set of parameters has been developed to describe Pd structure and Pd_n (n = 2 – 6 atoms) nanoclusters. The optimised parameters were validated by performing a geometry optimization on bulk Pd structure and the dependence on bond length of the Pd_n nanoclusters are also evaluated.

2. Computational methodology

2.1. SCC-DFTB method

The self-consistent density functional tight-binding (SCC-DFTB) method is used to improve the description of the Pd-Pd bonds for Pd bulk and nanoclusters, when the balance of charges between pairs of atoms is small. It is an approximate method derived from DFT and is based on the second order expansion of the Khohn-Sham total energy with respect to charge density fluctuations [11-14], given by

$$E_{tot} = E_{BS} + E_{rep} + E_2(n, \Delta n), \quad (1)$$

where the total energy E_{tot} includes the electrostatic-interaction term $E_2(n, \Delta n)$ to the standard tight-binding E_{BS} and the short range repulsive E_{rep} term. The electrostatic-interaction accounting for the charge fluctuations is written as

$$E_2(n, \Delta n) = \frac{1}{2}\sum_{x,y}^{M} \gamma_{xy} \Delta q_x \Delta q_y. \quad (2)$$

This term is represented by the Mulliken charges based atomic charge fluctuation Δq_x and Δq_y together with the analytical interpolating function, γ_{xy}.

2.2. SCC-DFTB calculations

The SCC-DFTB parameterization of bulk Pd and nanoclusters was carried out using DFTB+ code [15], and geometry optimizations calculations were performed with all parameters allowed to relax. Thus the major properties such as bond length and electronic aspects of the Pd system are produced with agreement to the experimental results. The GGA-PBE and LDA-PWC exchange-correlation function coupled with DND basis set was used. Mankhorst-Pack grids [16] for k-points sampling of 6x6x6 was used for the bulk palladium structure. The smart algorithm was applied with a maximum force of 0.5 Kcal/mol/Å. During geometry optimization, thermal smearing was varied from 0.005 to 0.3 Ha.

3. Results and discussion

The developed SCC-DFTB set of parameters for Pd-Pd pair of elements for describing Pd system was validated by performing a geometry optimization on the bulk Pd structure. Two sets of parameters were developed using different exchange-correlation fuctionals namely GGA and LDA. The obtained structural properties were compared with the experimental results to validate the developed set of parameter as shown in Table 1. We notice that, as the thermal smearing was increased, the lattice parameters of bulk Pd structure for both set of parameters decreases. More importantly, a thermal smearing of 0.2 and 0.3 Ha for the set of parameters using LDA and GGA, respectively, was sufficient to adjust the lattice parameters to 3.891 Å, in good agreement with the experimental results. It was also observed that LDA gives better structural lattice, than the set of parameters using GGA exchange-

correlation functional. Moreover, the GGA is found to overestimate the lattice constants while LDA underestimates, as expected. We also note that the smearing of 0.2 Ha correspond to the energy of -48.735 eV/atom using LDA, which is in reasonable energy change as the smearing is increased from 0.005 Ha compared to GGA.

Table 1. Comparison of the structural properties of bulk Pd with experimental data.

Properties	SCC-DFTB						Experimental[a]
	GGA			LDA			
Smearing (Ha)	0.005	0.200	0.300	0.005	0.200	0.300	-
a (Å)	4.075	3.991	3.891	3.896	3.891	3.683	3.891
Volume (Å^3)	67.692	63.555	58.896	59.144	58.896	49.975	58.896
Energy (eV/atom)	-45.795	-44.708	-40.133	-48.922	-48.735	-45.187	-

[a] The lattice and volume were taken from ref [4]

The various palladium nanoclusters were constructed starting from the optimized bulk Pd. The structures (a) and (b) represent the planar structures while (c), (d) and (e) represent the three dimensional structures namely, triangular pyramid, triangular bipyramid and tetragonal bipyramid, respectively, as shown in Fig. 1.

The planar structure in (a) is a Pd_2 and (b) representing Pd_3 nanocluster, is a line style structure with 90˚ angle between atoms 1 and 3. The triangular pyramid is made up of an isosceles triangle as a base with three scalene triangles above. The triangular bipyramid is made up of an isosceles triangle in the middle with three unequal sided taper on both sides. The tetragonal bipyramid used for these calculations has a square in the middle and four isosceles sides both below and above.

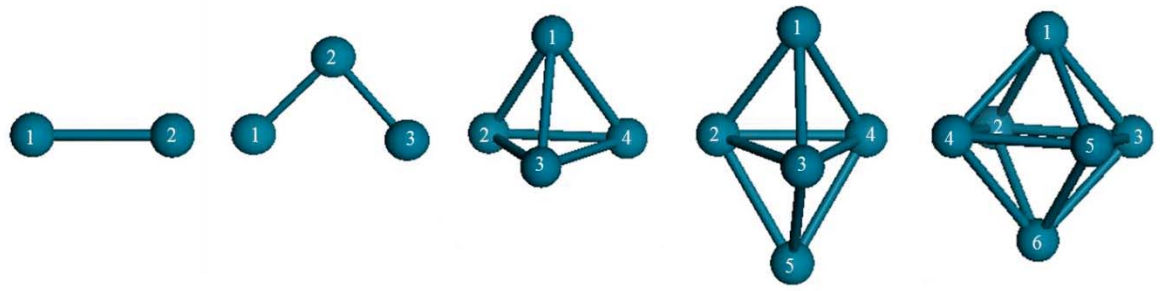

Figure 1. The structures of Pd_n nanoclusters (a) Pd_2, (b) Pd_3, (c) Pd_4, (d) Pd_5 and (e) Pd_6.

The Pd_n nanoclusters were optimized using the developed set of parameters with LDA exchange correlation functional and applied a thermal smearing of 0.2 Ha. The possible Pd-Pd bonds in Pd_n (n = 2 – 6 atoms) were calculated and are shown in Table 2. The average Pd_n bond length increased with an increase in the size of the nanoclusters. The calculated bond lengths and the values obtained from the literature have a difference of 0.1 Å.

Table 2.comparism of Pd-Pd average bond lengths with literature and total energies per atom (E_T) of Pd_2 to Pd_6 nanoclusters.

Nanocluster	Bond Length (Å)		E_T (eV/atom)
	SCC-DFTB	Literature	
Pd_2	2,679	2.480[a]	-39,0645
Pd_3	2,684	-	-39,941
Pd_4	2,686	2.580[b]	-42,039
	2,686	2.840 [b]	
	2,686	2.580 [b]	
	2,686	2.580 [b]	
	2,686	-	
Pd_5	2,692	-	-42,774
Pd_6	2,694	-	-43,425

[a] The literature bond length was found from ref. [2] and the similar value was also obtained in ref. [3].
[b] The experimental values were obtained from ref [17].

4. Conclusions

The SCC-DFTB sets of parameters for Pd-Pd atomic pair of elements were successfully developed. The lattice parameters for bulk Pd structure obtained using LDA are in better agreement with the experimental results compare to GGA. In addition, less smearing was required to adjust the lattice parameters to the experimental value of 3.891 Å when using LDA. For Pd_n nanocluster, the Pd – Pd bond lengths were found to be within 0.1% with the available literature. The total energy per atom trend suggests that the Pd_6 is more favourable since it has the lowerst energy value, thus the energy is lowered with size of the nanocluster.

Acknowledgements

The computations were performed at the Materials Modelling Centre (MMC), University of Limpopo. We also acknowledge the support of National Research Foundation and Johnson Matthey Technology Centre.

References

[1] Hohenberg P and Kohn W 1964 *Phys. Rev. B* **136** 864
[2] Schultz N E, Gherman B F, Cramer C J and Truhlar D G 2006 *J. Phys. Chem. B* **110** 24030
[3] Tang C -M, Wang H, Zhu W -H, Liu M -Y, Zhang A -M, Gong J -F, Zou H and Guo W 2013 *J. At. Mol. Sci.* **4** 49
[4] Stevens K J, Ingham B, Toney M F, Brown S A and Lassesson A 2008 *Curr. Appl. Phys.* **8** 443
[5] Sharma Y C, Singh B and Korstad J 2011 *Fuel* **90** 1309
[6] Marafi M and Stanislaus A 2008 *Resour. Conserv. Recycl.* **52** 859
[7] Wu B, Kuang Y, Zhang X and Chen J 2011 *Nano Today* **6** 75
[8] Piccolo L and Henry C R 2000 *Surf. Sci.***452** 198
[9] Thomann A L, Rozenbaum J P, Brault P, Andreazza-Vignolle C and Andreazza P 2000 *Appl.*

Surf. Sci. **158** 172
[10] Hermann P, Tardy B, Simon D, Guigner J M, Bigot B and Bertolini J C 1994 *Surf. Sci.* **309** 422
[11] Dolgonos G, Aradi B, Moreira N H and Frauenheim T 2010 *J. Chem. Theory Comput.***6** 266
[12] Elstner M, Porezag D, Jungnickel G, Elsner J, Haugk M, Frauenheim T, Suhai S and Seifert G 1998 *Phys. Rev. B* **58** 7260
[13] Elstner M, Frauenheim T and Suhai S 2003 *J. Mol. Struct.* **632** 29
[14] Elstner M 2007 *J. Phys. Chem. A* **111** 5614
[15] Aradi B, Hourahine B and Frauenheim T 2007 *J. Phys. Chem. A* **111** 5678
[16] Monkhorst H J and Pack J D 1976 *Phys. Rev. B* **13** 5188
[17] Prasomsri T, Shi D and Resasco D E 2010 *Chem. Phys. Lett*. **497** 103

Energy transfer and photoluminescence properties of Ce^{3+} or/and Tb^{3+}-doped PbS nanorods

Dejene BF, Koao LF

Department of Physics, University of the Free State (Qwaqwa), Private Bag x 13, Phuthaditjhaba, 9866

dejenebf@qwa.ufs.ac.za

Abstract. A series of luminescent PbS:Ce^{3+};Tb^{3+} material phosphors have been synthesized by low temperature chemical bath deposition (CBD) method. The X-ray diffraction (XRD) spectra of the PbS nanorods correspond to the various planes of a single cubic PbS phase. The PL spectrum monitored at 452 nm exhibits two overlapping excitation bands at 276 and 282 nm, which is assigned to the 4d-5f transitions of Ce^{3+}. Under excitation (λ_{Exc}= 282 nm), the PL spectrum exhibits two luminescence bands with the maximum wavelengths at 452 and 486 nm in the visible region. The two transitions ascribed to a direct band to band and the sulphur vacancies transitions in the nanocrystalline PbS. Upon the excitation at 276 nm, the PbS:Ce^{3+};Tb^{3+} phosphor shows intense UV emissions located at 334 and 380 nm assigned to the transitions from the lowest $5d_1$ crystal field component ($^2D_{3/2}$) to the two compounds ($^2F_{5/2}$ and $^2F_{7/2}$) of the 4f ground state, and weak emissions at around 700 nm due to the transitions of PbS deep levels defects. The photoluminescence (PL) intensity of Ce^{3+} increases with an increasing Tb^{3+} concentration up to an optimum value of Tb^{2+}:Ce^{3+} of 2, indicating the effective energy transfer (ET) occurred from Tb^{3+} to Ce^{3+} in PbS:Ce^{3+};Tb^{3+}.

1. Introduction

PbS belong to a class of IV-VI nanocrystals with narrow energy gaps of relevance for optical applications in the near-IR region of the electromagnetic spectrum such as long wavelength (1.3 and 1.55 μm) telecommunications [1], photovoltaics [2] and bio-imaging in the spectroscopic window of low absorption of biological systems (1-1.2 μm) [3]. Bulk lead sulfide (PbS) has a small hole mass, which is almost equal to the mass of the electron. This leads to a large exciton Bohr radius R_{ex} ~20 nm. Owing to these properties, electrons and holes, and hence the exciton, can be strongly confined. This is not always feasible in other semiconductors because of the different electron and hole effective masses [4]. Thus this system provides an ideal platform to investigate the exciton in the strong confinement regime. The ability to tune the photon emission of PbS nanostructures in the near infrared region of the electromagnetic spectrum makes this type of nanostructures suitable for several applications. The investigation of materials at the nano-scale has gained a great deal of interest as it fills the gap between bulk and atoms or molecules, thus improving our understanding of fundamental properties and providing new physical effects. This has been one of the hottest areas of research in the last twenty years [1, 5], fueled by the shrinking approach in device fabrication for optoelectronics and electronics. Up to date, due to a joint effort of physicists, chemists, biologists and material scientists, many achievements have been reported in this field. By controlling their size/shape and/or their chemical compositions, the electronic and optical properties of semiconductor nanostructures, can be manipulated [1, 6]. In particular, the confinement of the electron and hole in all spatial directions is responsible for atomic-like energy levels and physical properties. Nanostructures can be produced by different synthesis methods. Wet chemistry process provides an attractive method of synthesizing high

quality nanocrystals. Being not attached to any surface, nanostructures are promising candidates to be used as building blocks for ordered structures [6, 7]. In this study we present an experimental investigation of the structural and optical properties of undoped, singly and doubly doped PbS nanostructure synthesized in aqueous solution with different do-pants. The photoluminescence emission and the effect of Tb^{3+} or/and Ce^{3+} doping concentration are investigated in detail.

2. Experimental

The preparation of PbS powders were carried out using the following procedure: The PbS precursors were prepared by dissolving 0.13 M of lead acetate, 0.18 M of thiourea and 98.8 mL of ammonia in 400 mL of deionised water, separately. The chemical bath solution was prepared as follows: 60 mL of a lead acetate, thiourea and ammonia solutions as a complexing agent were mixed. The amount of solutions of lead acetate, thiourea and ammonia was held constant at ratio of 1:1:1. The amounts of do-pants and/or co-dopants were varied from 0 to 2.0. Each mixture was continuous stirred for 10 minutes while the synthesis temperature was maintained at 65 ºC. The PbS particles were washed with 60 mL of acetone and ethanol in that order. The precipitates formed were left overnight and then filtered. The obtained particles were dried at ambient conditions for a weeek and ready to be characterized. The particle size, phase and crystallinity were investigated by powder X-ray diffraction (XRD) using a Bruker D8 (Bruker Co., Germany) X-ray diffractometer with CuK_α (λ= 1.5406 Å). The PL excitation and emission spectra was measured using a Cary Eclipse fluorescence spectrophotometer equipped with a monochromatic xenon lamp.

3. Results and discussion

3.1 Structure properties

Figure 1 shows XRD profiles of PbS, $Pb_{0.99}S{:}Ce_{0.01}$, $Pb_{0.99}S{:}Tb_{0.01}$ and $Pb_{0.98}S{:}Ce_{0.01}Tb_{0.01}$ samples. All the peaks observed in the diffractogram at around 2θ = 25.99, 30.11, 43.09 and 51.03º for these four samples belonging to cubic phase of PbS matched well with the standard JCPDS card no. (05-0592, a= 5.936 Å). According to XRD profiles for $Pb_{1-x-y}S;Ce_x;Tb_y$ samples with various Ce^{3+} and Tb^{3+} concentrations (not shown), single phase with cubic-type structure is obtained in the ranges of $0 \leq x \leq 0.20$ and $0 \leq y \leq 0.20$. The estimated average value of the cell constant a is 5.934 Å which match perfectly with the standard data.

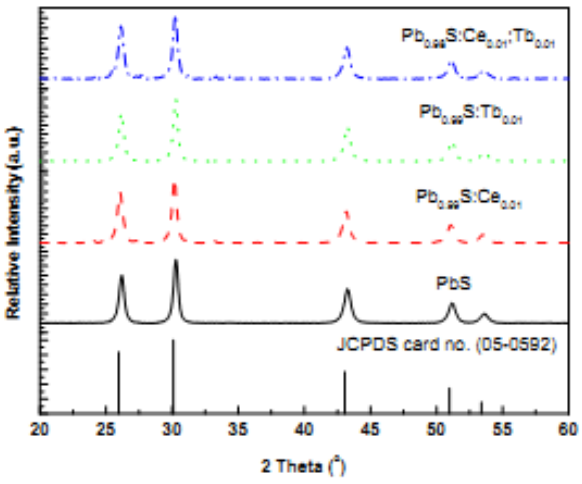

Figure 1: XRD patterns of undoped, Ce-doped, Tb-doped and Ce;Tb co-doped PbS nanostructures depict cubic structure.

No significant changes were observed for lattice parameter with the type of dopants. However, the widths of the diffraction lines are broadened because of the small size of the crystallites. The average crystalline size of the prepared PbS nanostructures calculated from the Scherer equation is between 25 and 40 nm. It was observed that low doping concentration have no significant effect on the size of the nanostructures.

3.2 Photoluminescence characteristics

In order to study the energy transfer between host, Ce^{3+} and Tb^{3+} ions, the emission spectra of PbS:Ce^{3+}/Tb^{3+} nanocrystals were measured under different excitation wavelengths. The PL emission spectra were measured at the excitation wavelengths of 276 and 282 nm. Fig. 2(a) shows the room-temperature photoluminescence emission spectra of undoped, doped and co-doped PbS nanostructures after drying in air at 60 ^{o}C for 2hr measured under 282 nm excitation wavelengths. The spectrum in Fig. 2(a) shows that the two broad luminescence peaks in visible and IR region ascribed to the nanocrystalline PbS nanostructutes sample are not symmetrical, but has a tail towards longer wavelengths. To investigate this, the spectrum excited at 280 nm was fitted with multiple Gaussian profiles.

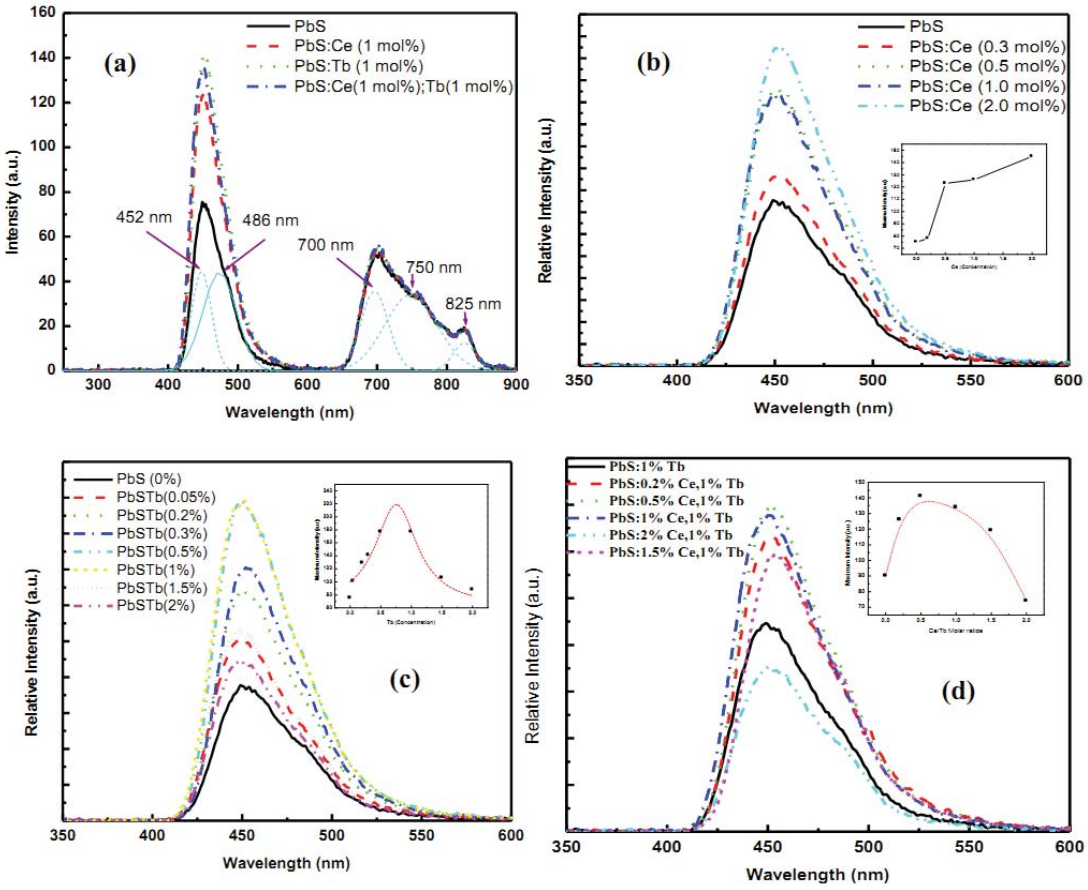

Figure 2: The effects of (a) types of dopants (b) the concentration of Ce^{3+} ions (c) the concentration of Tb^{3+} ions and (d) the molar ratios of Tb^{3+}:Ce^{3+} on the emission spectra of PbS nanostructures under 282 nm excitation wavelengths.

Fig. 2(a) shows that five Gaussian peaks are necessary to provide an acceptable fit, with peak wavelengths of 452 nm, 486 nm in the visible region and broad band with peak intensities at 700, 750 and 825 nm in the IR region. From the first two wavelengths, the shorter wavelength 452 nm is ascribed to a direct band to band transition of nanocrystalline PbS and the second peak centered at 486 nm is attributed to the presence of sulphur vacancies in the lattice [9]. This emission results from the recombination of photo generated charge carriers in shallow traps [10, 11]. The remaining three peaks centred at longer wavelengths 700, 750 and 825 nm are due to the deep level transitions in nanocrystalline PbS. The shorter wavelength emission is ascribed to a direct recombination and the longer wavelength to a recombination through shallow surface states [12 - 15]. The PL emission spectra from PbS:Ce^{3+} is very similar to that of undoped PbS but with enhanced luminescence in the visible region without any significant shift in peak positions while no changes are observed in IR region emission. Increase in Ce concentration increases the intensity of PbS emissions in the visible regions. This implies that there is the possibility of the absorbing centre Ce^{3+} transfers energy to the host PbS in contrast. The dependence of the luminescence spectra of PbS: Ce on the Ce concentration is illustrated in the inset to Fig. 2(b). The emission intensity is related to the concentration of the Ce^{3+} activator ions. With the increase of the concentration of the activator ion, the energy transferring centres increases and the emission intensity is enhanced for the range of Ce dopants investigated. Accordingly, we can find substantial emission differences between Tb^{3+} or Ce^{3+} singly doped samples. For Tb^{3+}-doped samples, with the increase of the concentration of the rare earth ion, the energy transfer centers increases and the emission intensity is enhanced. The highest luminescent intensity yield of the samples was obtained at a terbium concentration of 0.8% and lower or higher terbium content results in a substantial decrease in emission intensity in contrast to Ce doping. In order to further investigate the energy transfer process between the host, Ce^{3+} and Tb^{3+} ions in the PbS lattice, a series of co-doped samples were prepared. The concentration of Tb^{3+} was fixed at the optimal value x = 0.01 and the content of Ce^{3+} was varied in the range of 0 − 0.2.

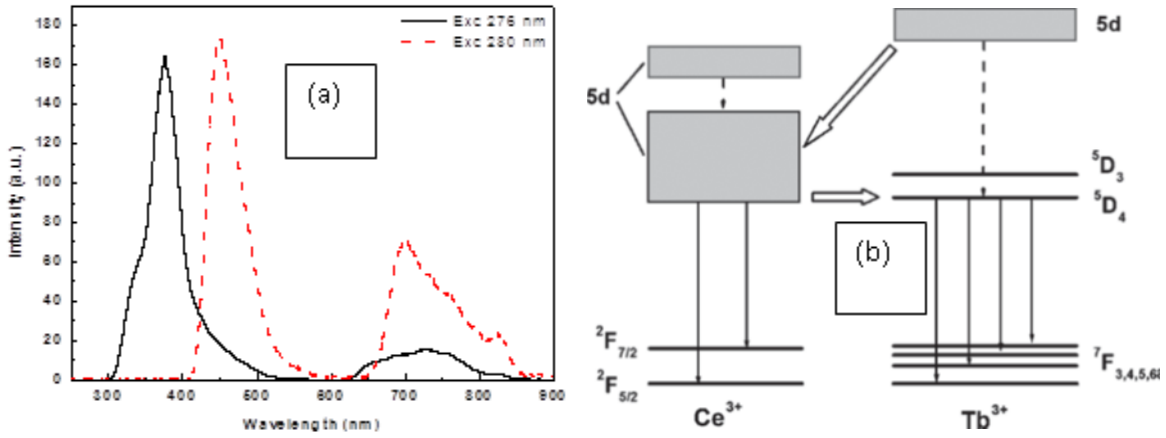

Figure 3: (a) Emission spectra of TbS:Ce^{3+}(1%)/Tb^{3+}(1%) nanostructures under different excitation wavelengths and (b) Schematic for the energy transfer and luminescence processes in Ce^{3+}/Tb^{3+}-codoped PbS nanocrystals [19].

The highest luminescent intensity yield of the particles was obtained at Tb^{3+}: Ce^{3+} molar ratio of 2.0 and lower or higher molar ratios results in a substantial decrease in emission intensity. The PL

emission spectra of PbS:Ce^{3+}(1%)/Tb^{3+}(1%) nanostructures under 276 nm excitation show peaks at 334 and 380 nm possibly be due to transition in and Ce^{3+} emitting centres. A broad peak is also observed in the IR region, but with lower intensity and blue shifted to lower wavelengths. This implies that there is the possibility of host PbS/Tb^{3+} transfers energy to the emitting centre Ce^{3+} just like in the commercially used ZnS:Ag^{+}, in which the sulphide host transfers energy to Ag^{+}. The existence of several peaks in the visible can be attributed to the non-equivalence of the Ce ions (e.g. coordination number changing with the surrounding ligands from one side to another). These luminescence bands are characteristic emissions of $4f^1 \rightarrow 5d^1$ transitions of triply charged cerium ions [16, 17, 18], commonly in either in the ultraviolet or visible region (blue) spectral region and it consists typically of two bands, which corresponds to the transitions from the lowest $5d_1$ crystal field component ($^2D_{3/2}$) to the two compounds ($^2F_{5/2}$ and $^2F_{7/2}$) of the 4f ground state [20]. When excited at 276 nm the spectra exhibit the emissions of Ce^{3+}, indicating that energy transfer could only take place from Tb^{3+} to Ce^{3+} ions but not Ce^{3+} to Tb^{3+}. The emissions from Ce^{3+} are dominant under 276 nm excitation, while the emission from PbS is dominant under 280 nm excitation. The schematics of the energy transfer and luminescent processes in PbS:Ce^{3+}/Tb^{3+} nanocrystals are shown in Fig. 3(b). In luminescent materials, energy transfer mechanisms between ions of the same or different types and between the host and the activator are well known [20, 21, 22, 23, 24]. They are either due to resonance or exchange interactions or multipolar interactions between the ions of the same or different types and depend on the critical energy transfer distance (*R*c) between the absorbing groups in the crystal lattice [21, 22]. In addition, the lifetime of the excited state of the sensitizer ion also plays a major role, and both radiative and nonradiative processes of energy transfer can occur.

4. Conclusion

In summary, we have synthesized single crystalline PbS nanostructures by a chemical bath deposition method using easily available reactants. The product also showed a photoluminescence peak at 452, 486, 700, 750 and 825 nm due to radiative recombination from the surface states. These PbS crystals may find potential applications in fundamental studies of nanostructure as well as for the fabrication of semiconductor devices based on these structures.

Acknowledgment

The authors send gratitude to the National Research Foundation (NRF) for funding the project and the University of Free State Physics (Physics department) for the research techniques used in this study.

References

[1] Rogach A L, Eychmuller A, Hickey S G, and Kershaw S V Small **3**(4), 536–557 (2007).

[2] McDonald S A, Konstantatos G, Zhang S G, Cyr P W, Klem E J D, Levina L, Sargent E H Nature Materials **4**(2), 138–U14 (2005).

[3] Hyun B-R, Chen H, Rey D A, Wise F W, Batt C A Journal of Physical Chemistry B **111**(20), 5726–5730 (2007).

[4] Zhao X S, Gorelikov I, Musikhin S, Cauchi S, Sukhovatkin V, Sargent E H, Kumacheva E Langmuir **21**(3), 1086–1090 (2005).

[5] Alivisatos A P Science 271(5251), 933–937 (1996).

[6] Hollingsworth J, Klimov V Semiconductor and Metal Nanocrystals: synthesis and Electronic and Optical properties, chapter 'Soft' Chemical Synthesis and Manipulation of Semiconductor Nanocrystals, 1–64. New York: Marcel Dekker, Inc. (2004).

[7] Zrenner A Journal of Chemical Physics **112**(18), 7790–7798 (2000).

[8] Dhas N A, Zaban N A, Gedanken A, Chem. mater **11**, 806 (1999).

[9] Sooklal K, Cullum B S, Angel S M, Mur C J J. Phys. Chem.**100**, 4551 (1996).

[10] Becker W G, Bard A J, J. Phys. Chem **87**, 4888 (1983).
[11] Fernee M J, Watt A, Warner J, Cooper S, Heckenberg N Rubinsztein-Dunlop H, Nanotechnology **14**(9), 991–997 (2004).
[12] Fernee M J, Watt A, Warner J, Cooper S, Heckenberg N Rubinsztein-Dunlop H Nanotechnology **15**(9), 1328–1337 (2004).
[13] Capoena B, Martuccib A, Turrellb S Bouazaoui M, J. Mol. Struct. **651**, 467–473 (2003).
[14] Fernee M J, Watt A, Warner J, Heckenberg N Rubinsztein-Dunlop H Nanotechnology **15**(9), 1351–1355 (2004).
[15] Patra A, Ganguli D, J. Non-Cryst. Solids **144**, 111 (1992).
[16] Turos-Matysiak R, Gryk W, Grinberg M, Lin Y S, Liu R S J. Phys. Condens. Matter. **18**, 10531(2006).
[17] Reisfeld R, Patra A, Panczer G, et al., Opt. Mater. **13**, 81 (1999).
[18]Wang G, Qin W, Zhang D, Wei G, Zheng K, Wang L, Ding F, J. Nanosci. Nanotechnol **10**, 1939–1942, 2010
[19] Blasse G, Grabmaier E C Luminescent Materials, Springer-Verlag, Berlin (1994).
[20] Smets B M J, Mater. Chem. Phys., **16**, 283 (1987).
[21] Fouassier C, Curr. Opin. Solid State Mater. Sci., **2**, 231 (1997).
[22] Ronda C R, Justel T, Nikol H J. Alloys Compd., **275-277**, 669 (1998).
[23] Ronda C, Angew. Chem. Int. Ed. 37, 3084 (1998).
[24] Shea L E, Datta R K, Brown J J Jr. J. Electrochem. Soc., **141**, 1950 (1994).

The effect of EWG and EDG on the HOMO and LUMO of Alq_3.

M M Duvenhage[1], O M Ntwaeaborwa[1], HG Visser[2], PJ Swarts[2], JC Swarts[2] and H C Swart[1,3]

[1]Department of Physics, University of the Free State, P.O. Box 339, Bloemfontein, 9300, South Africa
[2] Department of Chemistry, University of the Free State, Bloemfontein, 9300, South Africa

[3]Email: swarthc@ufs.ac.za

Abstract Tris-(8-hydroxyquinoline) aluminium (Alq_3) is used as both the emission and electron transporting layer in organic light emitting diodes. One way to tune the emissive colour of Alq_3 is to introduce electron-withdrawing or electron-donating groups (EWG and EDG) onto the hydroxyquinoline ligands. These groups will have an effect on the energy gap between the highest occupied molecular orbital and the lowest unoccupied molecular orbital. In this study Alq_3 powders were synthesized with an EDG ($-CH_3$) substituted at position 5 and 7 ((5,7-dimethyl-8-hydroxyquinoline) aluminium) and EWG (-Cl) at position 5 ((5-chloro-8-hydroxyquinoline) aluminium). Optical absorption and cyclic voltammetry measurements were done on the samples. The optical band gap was determined from these measurements. The band gap does not vary with more than 0.2 eV from the theoretical value of Alq_3.

1. Introduction

Organic materials such as small molecules and polymers have unique properties that open up new approaches for the fabrication of plastic electronic devices rather than conventional inorganic materials, such as Si and Ge devices. Organic light emitting diodes (OLEDs) are a promising energy alternative for the future and are therefore one of the most interesting organic devices. It can be used for potential low cost lighting as well as flexible devices. The first step in the fabrication of these devices is the selection of the emissive layer, which forms the heart of the OLED device and generates the desired photons when a current is applied. In the preparation of OLEDs, emissive layers are needed that fit in the band diagram to fulfil the energy requirements to generate photons [1]. The optical band gap (E_g) is a necessary parameter to be considered. The value of E_g defines the fundamental light absorption edge. Light with enough energy can promote electrons from the highest occupied molecular orbital (HOMO) to the lowest unoccupied molecular orbital (LUMO). Therefore tuning the optical band gap into the desired value for applications is of great importance.

In OLED devices the matching of the HOMO and LUMO energy levels of the emissive materials with the work functions of the electrodes as well as their optical, chemical and electrical stabilities are of utmost importance. The electronic energy levels (HOMOs and LUMOs) of the materials determine the OLED device structure and selection of electrodes and charge transfer materials [2].

By introducing substituents to the Alq_3 molecule, the optical properties of the material will change, because these substituents take part in the formation of the HOMO and LUMO levels [3]. An accurate way of determining the HOMO and LUMO levels of these new materials is needed in order to see if

they are suitable replacements for the emissive layer in OLED devices. Generally the ionization potential (I_p) of the organic molecules is measured by ultraviolet photoelectron spectroscopy (UPS), while the electron affinity (E_a) is determined from the difference of the ionization potential and the optical band gap, from optical absorption spectra [2]. But this is not a direct measurement technique to determine the position of the HOMO and LUMO energy levels.

The electrochemical processes are similar to the charge injection and transport in the OLED devices. Cyclic Voltammetry (CV) has therefore been recognized as an easy and effective approach to evaluate the position of both the HOMO and LUMO energy levels and the optical band gap of the organic materials. It has also been used to determine the reversibility, reproducibility and stability of organic films on the electrodes [2].

In this paper CV measurements were done on Alq_3, as well as Alq_3 substituted with chloride in the 5 position (5Cl-Alq_3) or methyl groups in the 5 and 7 positions (5,7Me-Alq_3) in dichloromethane (DCM). Optical absorption was also done on these 3 samples in DCM. The I_p, E_a (HOMO and LUMO energy levels) and E_g were determined from the CV and absorption measurements.

2. Experimental details

The HOMO and LUMO energy levels of the emissive layers in OLEDs can be estimated by cyclic voltammetry. CV gives direct information of the reduction and oxidation potentials of the materials. The oxidation process corresponds to the removal of electrons from the HOMO energy level and the reduction process corresponds to electron addition in the LUMO energy level of the materials [2]. The current will arise from the transfer of electrons between the energy level of the working electrode and the molecular energy levels of the materials under study.

The onset potentials of oxidation and reduction of a material can be correlated to the ionization potential (I_p) and electron affinity (E_a) according to the empirical relationship proposed by Bredas et al [4] on the basis of a detailed comparison between valence effective Hamiltonian calculations and experimental electrochemical measurements. The correlation can be expressed as:

$$I_p = -\left(E_{ox} + 4.4\right)eV \tag{1}$$

$$E_a = -\left(E_{red} + 4.4\right)eV \tag{2}$$

$$\text{and } E_g = I_p - E_a \tag{3}$$

where E_{ox} and E_{red} are the onset potentials of oxidation and reduction, respectively, while E_g is the optical band gap of the material. The 4.4 eV constant in the relation between Ip, Ea and the redox potentials arises from the difference in gas-phase ionization potentials and electrochemical oxidation potentials of solid films and the solid-state polarization energy [5]. The onset potentials are determined from the intersection of the two tangents drawn at the rising current and baseline charging current of the CV traces.

Cyclic voltammograms of the samples were recorded with a PARSTAT 2273 model potentiostat utilising a three-electrode electrochemical cell at a constant scan rate of 100 mV/s. The samples were dissolved in DCM (0.5 mM) and 0.2M of $[^n Bu_4N][B(C_6F_5)_4]$ was used as the electrolyte because this solvent-electrolyte combination is known to minimize substrate-solvent and substrate-electrolyte interactions after generating charged species during oxidation or reduction [6], [7]. Glassy carbon (3.14 mm^2) was used as the working electrode and Pt was used as both the auxiliary and pseudo reference electrode. Free ferrocene with redox potential for the FcH/FcH^+ coupled assigned as 0.00 V was used as internal reference standard. The experiment was done in a glove box under Ar atmosphere at 25 °C.

Optical absorption spectroscopy was used to determine the optical band gap of the three Alq_3 derivatives. The E_g of the samples were estimated from the optical absorption edge and using the Tauc relation [8]:

$$\alpha h\nu = \left(h\nu - E_g\right)^n \tag{4}$$

where α is the absorbance, E_g is the band gap corresponding to a particular absorption of photon energy at $h\nu$ and n is 1/2 for allowed direct, 3/2 for forbidden direct, 2 for allowed indirect and 3 for forbidden indirect transitions in the materials [2]. The direct band gap were obtained from extrapolation of the straight line portion of their $(\alpha h\nu)^2$ versus $h\nu$ plots to $\alpha = 0$.

The absorption spectra of the samples were recorded with a Perkin Elmer Lambda 950 UV-VIS spectrophotometer. The optical absorption spectroscopy studies of the samples were carried out in DCM solutions so that they can be directly compared to the results obtained from the CV measurements.

2.1 Synthesis

A methanol solution (20 ml) of the preferred 8-hydroxyquinoline (8-hydroxyquinoline, 5-chloro-8-hydroxyquinoline or 5,7-dimethyl-8-hydroxyquinoline (purchased from Sigma Aldrich and used without further purification)) (1.36 mmol) was slowly added to a water solution (20 ml) of aluminium trichloride (0.1 g, 0.45 mmol) with stirring at room temperature. Stirring was continued overnight and a yellow precipitate was filtered out and washed with cold methanol to remove excess 8-hydroxyquinoline. The filtrate was recrystalized in a water/methanol mixture (10:90 %) by slow evaporation at room temperature. Yellow crystalline powder was obtained after one week of drying at room temperature. Yield: 0.228 g (87 % based on Al).

3. Results and discussion

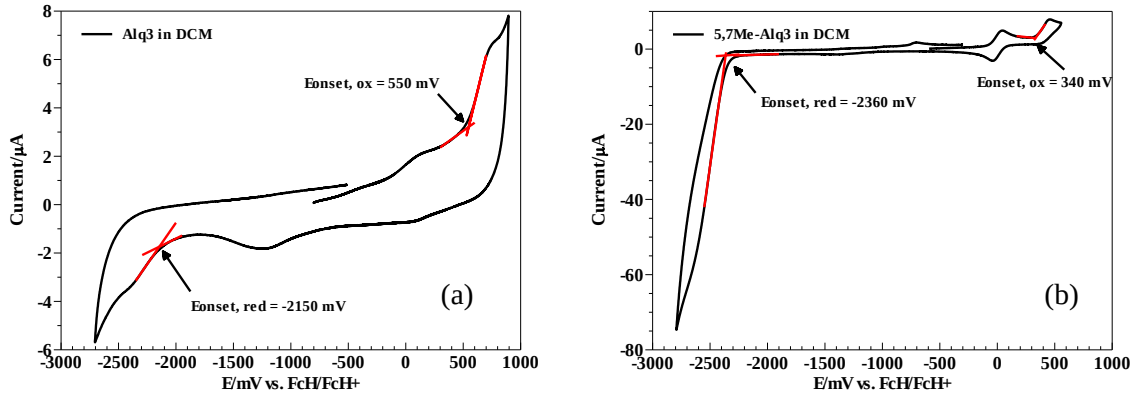

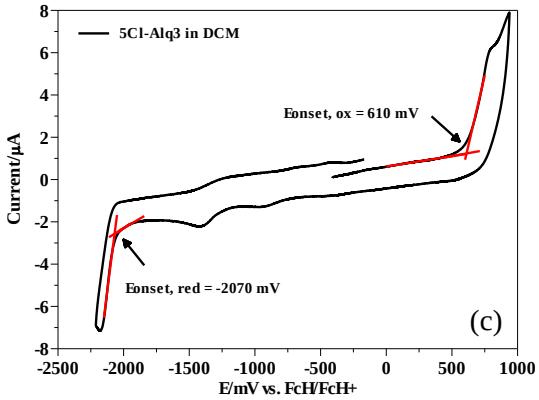

Figure 1: Cyclic voltammograms of (a) Alq_3 (b) 5,7Me-Alq_3 and (c) 5Cl-Alq_3 in DCM.

Figure 1 shows the cyclic voltammograms for the 3 synthesized samples. The onset potentials for oxidation of the samples were observed at 550, 340 and 610 mV, while reduction potentials were -2150, -2630 and -2070 mV for Alq_3, 5,7Me-Alq_3 and 5Cl-Alq_3 respectively. The electronic band gaps for the samples were determined using equation 3 and are listed in table 1.

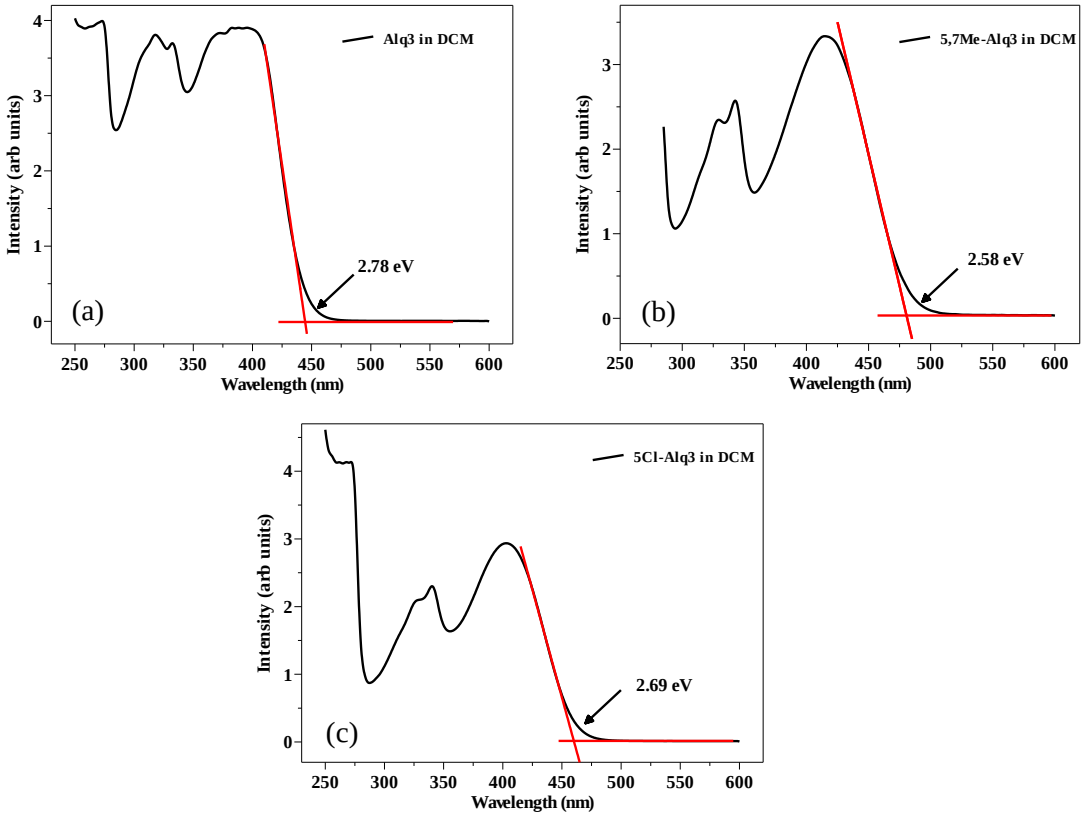

Figure 2: The absorption spectra of (a) Alq_3 (b) 5,7Me-Alq_3 and (c) 5Cl-Alq_3 in DCM. The energy gap is determined from the absorption edges.

Figure 2 shows the absorption spectra for the three Alq_3 samples dissolved in DCM. The spectrum of Alq_3 is dominated by an intense absorption band at ~380 nm. In addition to this intense band, there are 2 weak absorption bands at ~320 and ~330 nm. The broad band at 380 nm is reported to be a ligand centered electronic transitions [9]. The two bands at 320 and 330 nm are assigned to the vibronic progression due to the ring deformation mode of an electronic transition at 346 nm [9]. The same bands are observed for the 5,7Me-Alq_3 and 5Cl-Alq_3 samples, but are red shifted. The corrected base line of the absorption spectra is drawn horizontally. In order to determine the absorption edge a straight line was fitted to the right hand side of the maximum peak (located at ~380 nm for Alq_3) and its intersection with the corrected baseline was determined [10]. In the case of Alq_3, the intersection was found to be at ~445 nm, which corresponds to an optical gap of 2.78 eV. For 5,7Me-Alq_3 and 5Cl-Alq_3 the band gap is 2.58 and 2.69 eV respectively.

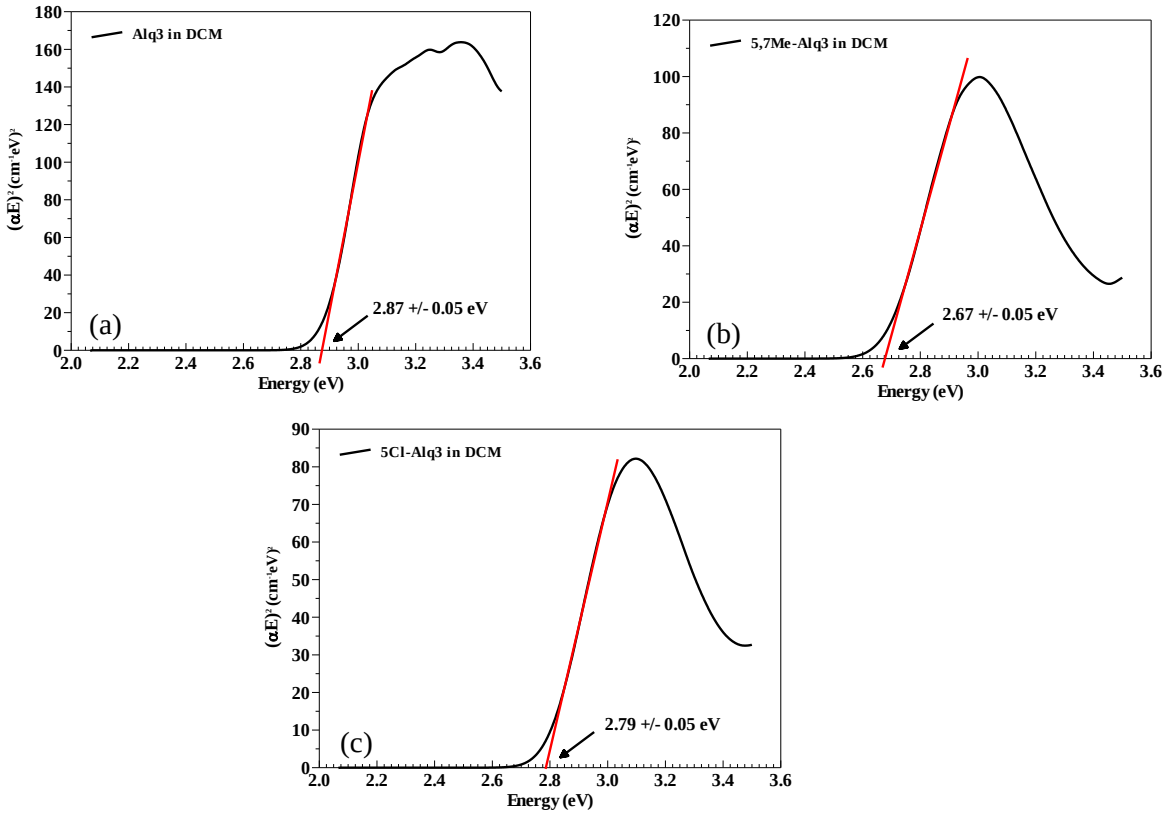

Figure 3: Plot of $(\alpha E)^2$ versus photon energy (E) for (a) Alq_3 (b) 5,7Me-Alq_3 and (c) 5Cl-Alq_3 in DCM.

The direct allowed band gap was determined for the three samples and the plots are shown in figure 3. The obtained values are recorded in table 1.

Table 1: Comparison of the optical band gap of the three samples obtained from CV and optical absorption measurements.

	CV	Absorption edge	Tauc
Alq_3	2.70 eV	2.78 eV	2.87 eV
5,7Me-Alq_3	2.70 eV	2.58 eV	2.67 eV
5Cl- Alq_3	2.68 eV	2.69 eV	2.79 eV

Table 1 summarizes the results obtained for the optical band gap of Alq_3, 5,7Me-Alq_3 and 5Cl-Alq_3 respectively, by using CV and optical absorption measurements. The theoretical value of the optical band gap of solid state Alq_3 is 2.80 eV [11]. The value obtained from CV measurements is 0.1 eV lower, while the values obtained from the optical absorption are 0.02 eV lower and 0.07 eV higher respectively. These values differ from the theoretical value because the band gap was determined from a DCM solution and it is known that solvents play a role on the value of the band gap [12]. The band gap obtained from the CV measurements should be more meaningful [2] as it corresponds directly to an electron being excited from the HOMO to the LUMO level. The EWG and EDG do not have a big influence on the band gap and it does not vary by more than 0.2 eV from the theoretical value of Alq_3. It is therefore suitable to use in OLED devices with the same device architecture as that of Alq_3 devices. This, however, explains the red shift that was observed in the absorption spectra.

4. Conclusion:

Alq_3 molecules with Cl and methyl substituents were successfully synthesized. The absorption spectra of Alq_3 show a broad band at 380 nm and two weak bands at 320 and 330 nm. The main peak of 5Cl-Alq_3 and 5,7Me- Alq_3 is red shifted. The optical band gap for the three samples were determined from the CV and optical absorption measurements and was found to vary by no more than 0.2 eV from the theoretical value of Alq_3. Samples with EWG and EDG are thus suitable to use as the emissive layer in OLED devices.

Acknowledgments
The authors gratefully thank the NRF, the Research Fund of the University of the Free State, SASOL, NECSA, Advanced Metals Initiative (AMI) and the Department of Science and Technology (DST) of South Africa. This work is based on the research supported by the South African Research Chairs Initiative of the Department of Science and Technology and the National Research Foundation of South Africa.

5. References

[1] Shafiee A, Salleh M M and Yahaya M 2011 *Sains Malaysiana* **40** 173.
[2] Misra A, Kumar P, Srivastava R, Dhawan S K, Kamalasanan M N and Chandra S 2005 **43** *Indian J. Pure Ap. Phy.* 921 .
[3] Shi Y W, Shi M M, Haung J C, Chen H Z, Wang M, Liu X D, Ma Y G, Xu H and Yang B 2006 *Chem. Commun.* 1941.
[4] Bradas J L, Silbey R, Boudreux D X and Chance R R 1983 *J. Am. Chem. Soc.* **105** 6555.
[5] Yang C J and Jenekhe S A 1995 *Macromolecules* **28** 1180.
[6] Kemp K C, Fourie E, Conradie J and Swarts J C 2008 *Organomet*. **27** 353.
[7] Cook M J, Chambrier I, White G F, Fourie E and Swarts J C 2009 *Dalton Trans.* 1136.
[8] Tauc J, Grigorovici R and Vancu A 1966 *Phys. Status Sol.* **15** 627.
[9] Ravi Kishore V V N, Aziz A, Narasimhan K L, Periasamy N, Meenakshi P S and Wategaonkar S 2002 *Synth. Met.* **126** 199.
[10] Schlaf R, Schroeder P G, Nelson M W, Parkinson B A, Merritt C D, Crisafulli L A Murata H and Kafafi Z H 2000 *Surf. Sci.* **450** 142.
[11] Dalasinski P, Lukasiak Z, Wojdyla M, Rebarz M and Bala W 2006 *Opt. Mater.* **28** 98
[12] Su B, Xhang M, Shao Y and Girault H H 2006 *J. Phys. Chem.* **110** 21460.

Magnetic Phase Diagram of $Cr_{100-x}Os_x$ alloys

PR Fernando[1], ARE Prinsloo[1], CJ Sheppard[1] and JAL Lodya[2]

[1]Department of Physics, University of Johannesburg, PO Box 524, Auckland Park, 2006, South Africa
[2]Sasol Technology, Research & Development, 1, Klasie Havenga Road, Sasolburg, 1947, South Africa

Author e-mail address: alettap@uj.ac.za

Abstract: The magnetic phase diagram of $Cr_{100-x}Os_x$ exhibits a triple point at 315 K and for a concentration $x = x_L = 0.14$, where the incommensurate (I) spin-density-wave (SDW), commensurate (C) SDW and paramagnetic (P) phases coexist. Previous studies focused on measurements around the triple point and concentrations up to $x = 2$. The possible merits of an investigation into the magnetic phase diagram of Cr-Os specifically at high diluent concentrations should be considered against the background of other Cr alloys with group-8 diluents, such as those of Cr-Re and Cr-Ru. These alloys show interesting features for $x >> x_L$, such as superconducting properties and quantum critical behaviour. Thus, in order to initiate similar studies a polycrystalline $Cr_{100-x}Os_x$ alloy series with $2 < x < 22$ were prepared and characterized using scanning electron microscopy, electron microprobe analysis and X-ray diffraction. Electrical resistivity (ρ) and magnetization (M) measurements as a function of temperature (T) were performed in the temperature range of 2 K < T < 1100 K. These results were used to obtain the Néel transition temperatures (T_N) of the various alloys and to map out the magnetic phase diagram of the $Cr_{100-x}Os_x$ alloy system for $x > 2$.

1. Introduction

The magnetic phase diagram of $Cr_{100-x}Os_x$ exhibits a triple point at 315 K and for a concentration $x = x_L = 0.14$, where the incommensurate (I) spin-density-wave (SDW), commensurate (C) SDW and paramagnetic (P) phases coexist [1, 2]. Previous studies on the physical properties of Cr-Os included heat capacity (C_p) [2], electrical resistivity (ρ) [2, 3, 4], thermal expansion [2, 4] and magnetic susceptibility (χ) [5, 6]. These studies focused on measurements around the triple point and concentrations up to $x = 2$, leaving the phase diagram of Cr-Os incomplete for $x \gg x_L$.

It is surprising that the Cr-Os magnetic phase diagram has not been fully explored and is still unknown for concentrations $x > 2$ [1-6], as the magnetic phase diagrams of many Cr alloys with group-8 metals, such as Cr with Re and Ru have very interesting properties for $x \gg x_L$ [1]. These properties include possible superconducting behaviour existing together with antiferromagnetism [1], as well as quantum critical behaviour [7, 8]. These properties are strongly associated with current interests as is revealed in recent literature [7-12]. Superconducting properties in Cr-Os alloys with very high concentrations of Os have been previously reported [13, 14, 15]. Alloys containing 25, 28 and 33 at.% Os show superconducting transition temperature (T_s) at 2.4 and 2.75, 4.03 and 1.03 K, respectively [13, 14, 15]. This is in agreement with results obtained for other alloys with group-8 diluents such as in the case of Cr-Ir, Cr-Ru and Cr-Rh [14, 16].

In order to extend the investigations of the unique properties of Cr alloys with group-8 diluents and to be ultimately inclusive of all Cr alloys with group-8 metals, the present investigation focusses on

the properties of the $Cr_{100-x}Os_x$ alloys with $2 \leq x \leq 22$. This study utilizes electrical resistivity (ρ) and magnetization (M) measurements in order to complete the phase diagram of $Cr_{100-x}Os_x$, from which further investigations can follow.

2. Experimental

Polycrystalline binary $Cr_{100-x}Os_x$ alloys with $2 \leq x \leq 22$ were prepared by arc melting in a purified low pressure argon atmosphere from Cr and Os of mass fractional purities of 99.999% and 99.99% respectively. The constituent metals were melted fifteen times in total, turning it upside down between melts with two crushes after every five melts in order to improve the homogeneity. Powder X-ray diffraction (XRD) analyses, using Cu-K_α was used to characterize the samples structurally and confirm whether the samples were single or multi-phase. The actual elemental composition and homogeneity were determined using electron microprobe analyses. Electrical resistivities (ρ) were measured in the range $2 \leq T \leq 380$ K, using the Quantum Design Physical Properties Measurement System (PPMS) incorporating the appropriate measurement option. Resistivity measurements for the temperature range 273 K to 1100 K were performed under high vacuum using the standard dc-four probe method with Keithley instrumentation. In order to eliminate the thermal EMF the sample current was reversed for each set of readings [17]. For samples with transitions in a range 300 K $\leq T \leq$ 700 K the PPMS with the vibrating sample magnetometer (VSM) oven option were used to measure the magnetization (M) on heating in an applied magnetic field of 20 kOe. The Quantum Design Magnetic Property Measurement System (MPMS) was used to measure the magnetization for samples with transitions in the temperature range 2 K $\leq T \leq$ 390 K. These samples were zero field cooled (ZFC) to 2 K and measurements were taken on heating in an applied magnetic field of 50 Oe.

3. Results and discussion

Figure 1(a) and (b) show the X-ray diffraction (XRD) spectra of the as-cast $Cr_{98}Os_2$ and $Cr_{87}Os_{13}$ in grey, while the XRD spectrum for pure Cr is shown in black. The XRD spectra were compared to that in the Joint Council of Powder Diffraction Database (JCPDD) for pure body centred cubic (bcc) Cr (reference number: 04-008-5987). Comparing the relative peak positions, obtained from the JCPDD data base to the current XRD spectra of $Cr_{98}Os_2$ and $Cr_{87}Os_{13}$, it is observed that only the primary reflections [110], [200], [211] and [220] were obtained. The absence of any other reflections, which might be observed for other Cr-Os binary alloys, indicates that the current alloys were in single phase. Since annealing of the samples created additional phases it was decided to only use as-cast samples in the present study.

It is also observed in Figure 1(a) and (b) that for the Cr-Os alloys the primary reflections are slightly shifted to lower 2θ values, relative to the primary peak positions of pure Cr. This displacement is more apparent for $Cr_{87}Os_{13}$ than for $Cr_{98}Os_2$ though, i.e. it increases with increasing

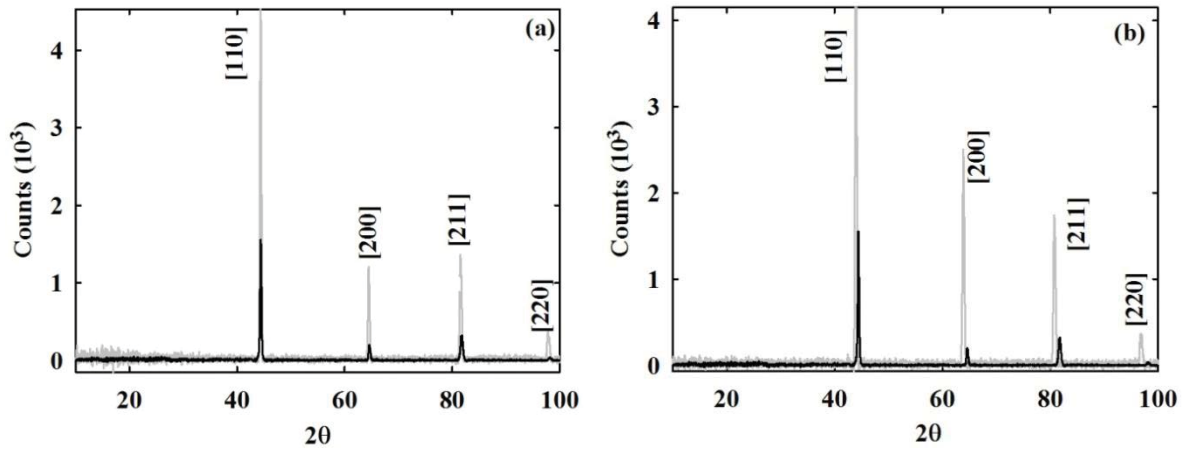

Figure 1. XRD patterns for (a) $Cr_{98}Os_2$ and (b) $Cr_{87}Os_{13}$ alloys are shown in grey, together with the pattern expected for pure Cr shown in black. The (*hkl*) Miller indices of the various reflections obtained from the JCPDD expected for the profile of bcc Cr are indicated (reference number: 04-008-5987).

Os concentration. It is believed that the shift is caused by a distortion in the lattice parameter due to the addition of the large Os atoms. The lattice parameters (a) as function of x for $Cr_{100-x}Os_x$ alloys, as calculated from the XRD results, are represented by solid circles Figure 2. The lattice parameter increased linearly from the value of 0.28800 nm obtained for pure Cr to 0.29108 nm for the $Cr_{78}Os_{22}$ alloy. Following the work of Vegard [18] the theoretically expected lattice parameters were calculated using:

$$a_{\text{alloy}} = (1 - x)a_{\text{Cr}} + xa_{\text{Os}}, \quad (1)$$

where a_{Cr} and a_{Os} refer to the lattice parameters of Cr and Os at room temperature, respectively, and a_{alloy} is the calculated value for the lattice parameter for the specific $Cr_{100-x}Os_x$ alloy. The values obtained using equation (1) is represented by the open triangles in Figure 2, these correspond well with those calculated from XRD results. A linear fit, $a = bx + c$, to the data in the investigated concentration range gives $b = (1.4\times10^{-3} \pm 2.5\times10^{-5})$ Å/at.% Os and $c = (2.9 \pm 3.2\times10^{-4})$ Å.

Electron microprobe analyses of the Cr-Os alloys indicate that all the samples are homogeneous in composition and that the actual concentrations of the Os vary by less than 1 at.% from the nominal concentrations. The relatively small deviation in the actual and nominal concentrations can be attributed to mass losses during the manufacturing process of Cr alloys, due to the evaporation and diffusion of tiny mass particles during melting and/or to the mass losses during crushing process.

Representative $\rho(T)$ curves for $Cr_{100-x}Os_x$ alloys with $2 \leq x \leq 22$ are shown in Figures 3(a) and (b). Well defined anomalies appear in the form of clear minima followed by prominent domes in all the $\rho(T)$ curves for alloys with $x \leq 13$. This behaviour is associated with the formation of the SDW on entering the antiferromagnetic phase on cooling through the Néel temperature (T_N) [1]. The sudden increase in resistivity on cooling through T_N finds its origin in the nesting of electron and hole Fermi surfaces [1]. This leads to a reduction in the charge carriers available for conduction resulting in an increase in resistivity just below T_N [1]. The anomalies become more pronounced on increasing the Os concentration up to $x = 4$, as the electron and hole Fermi surfaces become increasingly similar in size. Greater parts of the Fermi surfaces are thus being affected, causing an increase in the resistivity anomalies as the SDW becomes more commensurate [3, 19] with the lattice. However, for alloys with $x \geq 6$ it is observed that the relative size of the magnetic anomalies, as well as the values of T_N, decreases.

The Néel temperature for Cr alloys can be defined either as the temperature of the minimum in $\rho(T)$ accompanying the magnetic phase transition or the inflection point in $\rho(T)$ curve; determined by considering the temperature associated with the minimum in $d\rho/dT$ versus T curve [1]. Considering all the results obtained it was decided to implement the first definition of T_N for the present study regarding the magnetic phase transitions in the $Cr_{100-x}Os_x$ alloy system.

Figure 4 shows representative reduced magnetization, $M_r(T)$, curves for $Cr_{100-x}Os_x$ alloys. For measurements in the temperature range 300 K < T < 700 K M_r is defined as M/M_{300K}, while for measurements in the range 2 K < T < 300 K, $M_r = M/M_{2K}$. The dashed lines in Figure 4(a) and the inset of Figure 4(b) represents a back extrapolation from the paramagnetic phase at $T > T_N$. The T_N

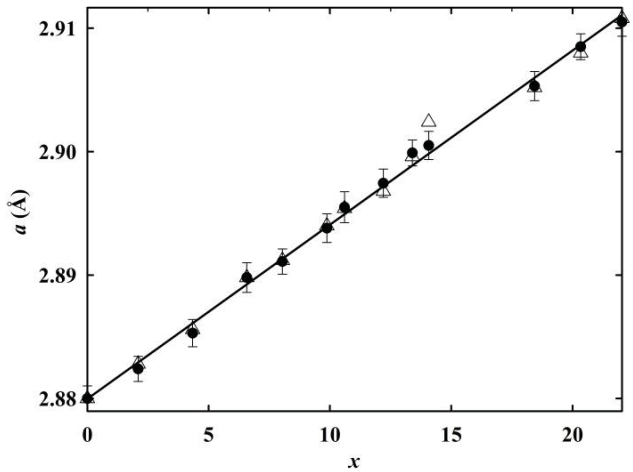

Figure 2. The lattice constant (a) as function of x for various $Cr_{100-x}Os_x$ alloys. The values obtained from the XRD measurements are represented by the solid circles (•) with error bars. Open triangles (△) represent the values obtained using $a_{\text{alloy}} = (1 - x)a_{\text{Cr}} + xa_{\text{Os}}$, where a_{Cr} and a_{Os} refer to the lattice parameters of Cr and Os at room temperature, respectively, and a_{alloy} is the calculated value of the lattice parameter for each specific $Cr_{100-x}Os_x$ alloy [18]. The line is a linear fit to the experimental data.

values indicated by arrows were obtained from the point where the $M_r(T)$ curve deviates from the dashed line. Anomalies, in the form of a downturn on cooling, are observed in the vicinity of T_N for the alloys with $x < 13$, similar to the behaviour normally observed for Cr alloys below T_N [1]. The downturn in $M_r(T)$ on cooling through T_N is ascribed to a decrease in the density of states at the Fermi surface when the nested parts of the electron and hole Fermi sheets are annihilated. The decrease in the density of states is accompanied by a decrease in the itinerant electron concentration responsible for magnetism [1]. It is again noted that the anomalies become more pronounced for Cr-Os alloys approaching the concentration $x = 4$, after which a further increase in Os content results in an increasingly weaker anomaly in the $M_r(T)$ curves at T_N. As an example of this, consider the $M_r(T)$ curve of the $x = 12$ alloy shown in Figure 4(b). A relatively weak anomaly at T_N for this alloy (at approximately 150 K) is hardly visible in the full scale curve, it is however clearly seen on an enlarged scale on the inset shown in Figure 4(b). The results of the $x = 12$ alloy show a slight increase in M_r when cooling from $T > T_N$, followed by the expected downturn for $T < T_N$, resulting in a weak

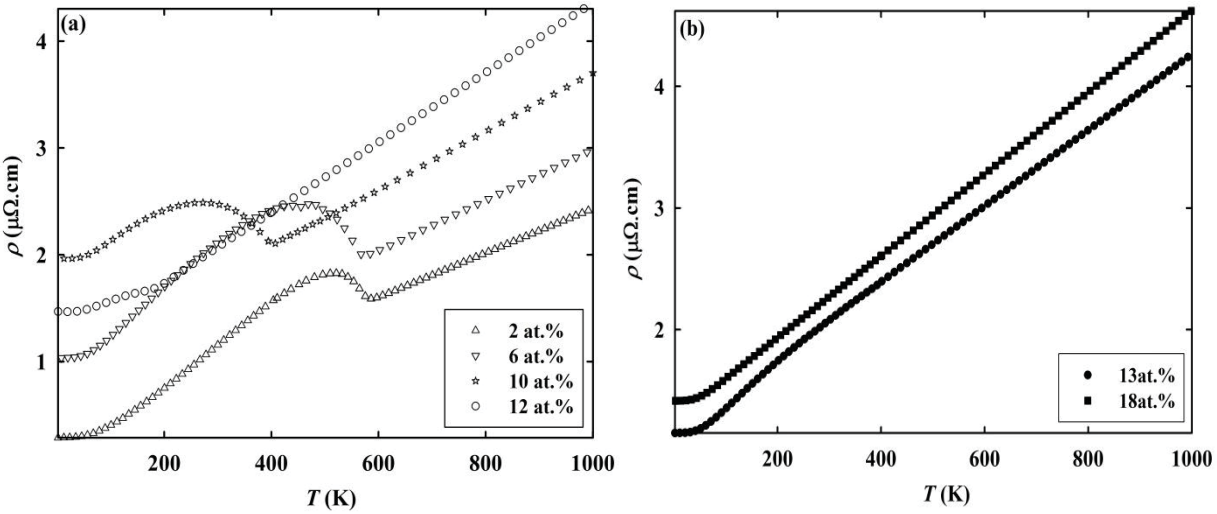

Figure 3 (a) and (b). The electrical resistivity, ρ, of selected $Cr_{100-x}Os_x$ alloys in the temperature range $2 \leq T \leq 1000$ K, with (a) $x = 2$ (△), 6 (▽), 10 (☆) and 12 (○) and, (b) $x = 13$ (•) and 18 (■).The experimental error in the absolute value of ρ is approximately 3% and originates mainly from errors in the determination of the sample dimensions.

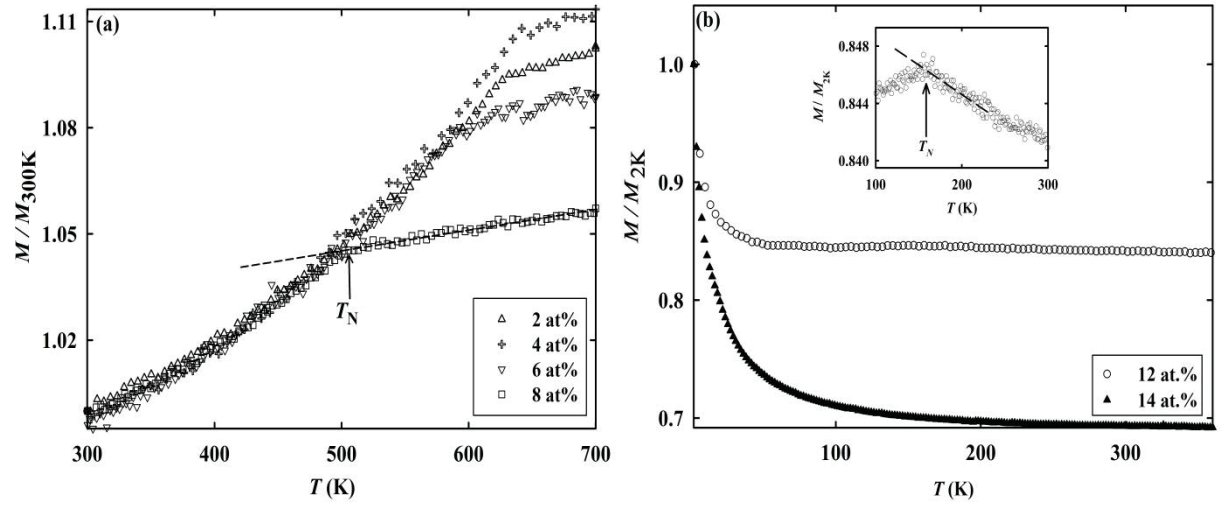

Figure 4. The temperature dependence of the magnetization, $M_r(T)$, of the $Cr_{100-x}Os_x$ alloy system with (a) $x = 2$ (△), 4 (+), 6 (▽) and 8 (□) in the temperature range 300 to 700 K and, (b) $x = 12$ (○) and 14 (▲) in the temperature range 2 to 390 K. The inset in (b) shows $M_r(T)$ curve for $x = 12$ on an enlarged scale. The dashed lines are discussed in the text.

peak in $M_r(T)$ at T_N. Alloys with $x > 13$ did not show anomalous behaviour associated with a magnetic transition in their $M_r(T)$ curves in the temperature range 2 to 390 K – see for example the $M_r(T)$ curve for the $x = 14$ alloy shown in Figure 4(b). These samples were taken to be paramagnetic at all temperatures down to 2 K.

In Figure 5 the magnetic phase diagram for the Cr-Os alloys is shown, constructed from the T_N values obtained from the current $\rho(T)$ and $M(T)$ results, together with those determined in previous studies [2-6]. It is evident that the T_N values obtained from the current $\rho(T)$ results correspond well with those found in previous studies on this alloy system for $x = 2$. However, discrepancies are observed in the T_N values obtained from the $\rho(T)$ and $M(T)$ results for samples with $x = 2$, 4, 6, 8, 10 and 12. Resistivity measurements are known to be extremely sensitive to anomalies at T_N and are normally the first type of measurements to be considered in determining the magnetic transition temperatures [1]. As mentioned earlier, the $M(T)$ results for these samples were obtained using the VSM option of PPMS that could be used for measurements in the temperature range 300 to 700 K, while $M(T)$ results for the samples with $x > 8$ was obtained from magnetization measurements utilizing the MPMS in a temperature range 2 to 400 K. From Figure 5 it is clear that the T_N values obtained from the $M(T)$ results using the VSM option of the PPMS differ to a larger extend from those determined from the $\rho(T)$ results, when compared to those T_N values obtained from the $M(T)$ results obtained using the MPMS. It is speculated that these discrepancies can possibly be related to the differences in heating rates (0.6 K/min for the MPMS versus 5 K/min for the PPMS) or the differences in the applied magnetic fields (50 Oe for the MPMS versus 20 kOe for the PPMS, i.e. relatively high applied magnetic fields were required to effect magnetic transitions with the VSM oven option). On the other hand it is also important to remember that the MPMS is equipped with a more sensitive SQUID sensor, thus enabling extremely accurate magnetic measurements, two orders of magnitude better than the magnetization values obtained using a VSM option of the PPMS [20, 21]. However, the reasons for the observed discrepancies still warrant further investigation.

The present study extends the magnetic phase diagram of this alloy system to much higher Os diluent concentrations than what were previously determined [2-6]. The magnetic phase diagram obtained for $Cr_{100-x}Os_x$ alloy system resembles the typical behaviour of Cr alloys with group-8 metals. The initial increase in T_N with increasing Os concentration can be understood by Fedders and Martin's theory [3, 5, 17, 19, 22-24]. According to this theory, addition of metals to the right of Cr in the periodic table increases the electron to atom ratio (e/a) and the size of the electron Fermi sheet of pure Cr. This leads to an increase in the contact area between the electron and hole sheets which correspond to an increase in T_N [24]. Applied to the current alloy system this implies that the Os increases the electron concentration and enlarges the interaction area of the electron-hole Fermi

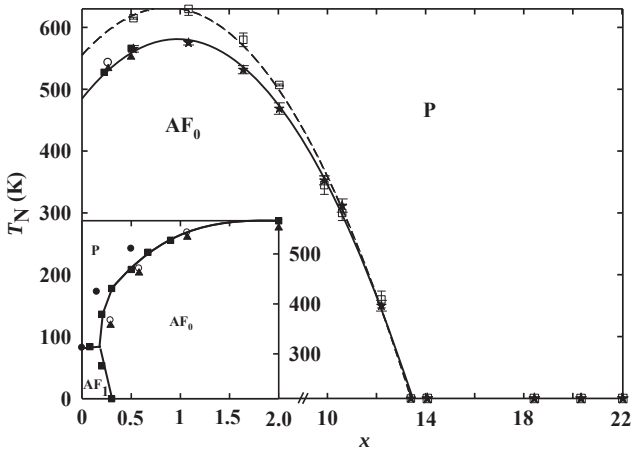

Figure 5. The magnetic phase diagram for the $Cr_{100-x}Os_x$ alloy system as function of Os concentration, showing T_N (K) values obtained from electrical resistivity (★) and magnetization (□) in the present study. Data points from previous studies are also shown in the Figure: Arajs *et al.* [3] (●), Butylenko *et al.* [1, 2, 4] (▲,■) and Hedman *et al.* [5] (○). P refers to the paramagnetic phase, while AF_1 and AF_0 refer to the incommensurate and commensurate SDW phases, respectively. The solid and dashed lines are guides to the eye.

surfaces. This effect improves the nesting and stabilises the SDW. As x is increased, the CSDW phase forms at $x = x_L$. On addition of Os concentration above triple point concentration, T_N rises rapidly and reaches saturation at approximately 4 at.% Os, where perfect nesting occurs, when the size of electron sheet becomes nearly equal to the hole sheet. Further addition of Os leads to Fermi surface mismatch again and the electron sheet becomes bigger than the hole sheet. This effect destabilizes the structure and reduces the T_N. According to the current results, the antiferromagnetic order is completely suppressed for Cr-Os alloys with $x > 13$ and samples with $x > 13$ remain paramagnetic for all $T > 2$ K.

4. Conclusion

The magnetic phase diagram of $Cr_{100-x}Os_x$ alloy system was, for the first time, as could be ascertained, determined for concentrations as high as $x = 22$. The general behaviour is similar to that observed for other Cr alloys with group-8 non-magnetic transition metals such as Cr-Ru and Cr-Re [1]. It is important to note that the present $\rho(T)$ results fit well in with those obtained from previous studies [2-6] on this system for $x < 2$ and shows that the antiferromagnetism in this system appears to be fully suppressed for $x = 13$. However, discrepancies is observed in the T_N values obtained from the $\rho(T)$ and $M(T)$ results for samples with $x = 2$, 4, 6, 8, 10 and 12 – this needs to be clarified through further investigation. No indication of superconductivity was found in the $\rho(T)$ measurements of the alloys investigated, in the temperature range $T > 2$ K.

This project has addressed certain fundamental questions regarding the behaviour of the Cr-Os magnetic phase diagram at relatively high diluent concentrations. This is a first step from where investigations into possible quantum criticalities in this alloy system can follow.

Acknowledgments Financial support from the South African NRF (Grant numbers 80928 and 80626) and the Faculty of Science from the University of Johannesburg is acknowledged.

References

[1] Fawcett E, Alberts H L, Galkin V Y, Noakes D R and Yakhmi J V 1994 *Rev. Mod. Phys.* **66** 25.
[2] Butylenko A K and Nevadcha V V 1982 *Sov. Phys. Tech. Phys.* **27**(1) 102.
[3] Arajs S, De Young F. Tice and Andreson E E 1970 *J. Appl. Phys*. **41**(3) 1426.
[4] Butylenko A K 1985 *Sov. Phys. Tech. Phys*. **30** (8) 942.
[5] Moyer C A, Kelly J R, Arajs S, Kote G and Garbe K 1981 *J. Appl .Phys*. **52**(3) 1643.
[6] Booth J G 1964 *Phys. Stat. Sol.* **7** K157.
[7] Jacobs B S, Prinsloo A R E, Sheppard C J and Strydom A M 2013 *J. Appl. Phys*. **113** 17E126.
[8] Reddy L, Alberts H L, Strydom A M, Prinsloo A R E and Venter A M 2008 *J. Appl. Phys.* **103** 07C903.
[9] Yeh A, Soh Y-A, J Brooke J, Aeppli G, Rosenbaum T F and Hayden S M 2002 *Nature* **419** 459.
[10] Lee M, Husmann A, Rosenbaum T F and Aeppli G 2004 *Phys. Rev. Lett*. **92**(18) 187201.
[11] Jaramillo R, Feng Y, Wang J and Rosenbaum T F 2010 Proc. Nat. Acad. of Sci. USA (PNAS) **107**(9) 09E116.
[12] Sheppard C J, Prinsloo A R E, Alberts H L and Strydom A M 2011 *J. Appl. Phys*. **109**(7) 07E104.
[13] Venkatraman M and Neumann J P 1990 *Bulletin of Alloy Phase Diagrams*. **11**(1) 8.
[14] Blakgher R D, Hein R E, Cox J E and Waterstrat R M 1969 *J. Low. Temp. Phys.* **1** (6) 539.
[15] Fluliger R, Paoli A and Muller J 1974 *Solid State Commun.* **14** 443.
[16] Matthias B T, Geballe T H, Compton V B, Corenzwit E and Hull G W 1962 *Phys. Rev.* **128**(2) 588.
[17] Gopalakrishnan I K,Yakhmi J V and Iyer R M 1984 *J. Magn. Magn. Mat*. **46** 207.
[18] Denton A R and Ashcroft N W 1991 *Phys. Rev. A*. **43**(6) 3161.
[19] De Young T F, Arajs S and Anderson E E 1971 *Amer. Inst. Phys. Conf. Proc. Magn and Magn. Mat*. **5** 517.
[20] PPMS MultiVu Application User's Manual 2008 Rev.A2.
[21] MPMS MultiVu Application User's Manual 1999 Rev.A2.
[22] Fukamichi K and Siato H 1975 *J. Less Common Met.* **40** 357.
[23] Fedders P A and Martin P C 1966 *Phys. Rev*. **143**(1) 245.
[24] Yakhmi J V, Gopalakrishnan I K and Iyer R M 1983 *J. Less Common Met*. **91** 327.

YVO_4:Eu phosphor thin films prepared by PLD

Foka KE[1], Dejene BF[1], Swart HC[2], R Kittesa[3]

[1]Department of Physics, University of the Free State (Qwaqwa), Private Bag x 13, Phuthaditjhaba, 9866

[2]Department of Physics, University of the Free State, P.O. Box 339, Bloemfontein, 9300

[3]CSIR National Laser Centre, P.O. Box 395, Pretoria 0001, South Africa

fokake@qwa.ufs.ac.za

Abstract. Yttrium vanadate doped europium (YVO_4:Eu) phosphor thin films were deposited on silicon substrates using the pulse laser deposition technique. The films were deposited at room temperature at different O_2 pressures of 20, 100 and 200 mTorr. The X-ray diffraction patterns of the films deposited at 100 mTorr exhibits a strong preferential orientation in the (200) direction. The thin films showed a rough surface and large number of spherical particles at higher O_2 pressure than that at the lower O_2 pressure. Luminescence of the YVO_4:Eu showed a strong red emission peak at 618 nm due to the $^5D_0$-$^7F_2$ transition.

1. Introduction

Oxide thin film phosphors have been given attention because of their high resolution and high efficiency planar display. The oxide based phosphors appeared to be a potential choice for red field emission display (FED). The luminescence efficiency of most phosphor materials is affected by the concentration of the activator. YVO_4:Eu^{3+} thin film phosphors are one of the most promising oxide-based red phosphors with application in high pressure mercury lamps but mostly in plasma display panels [1, 2]. YVO_4 has a body-centered tetragonal structure that consists of four formula units in a unit Cell with lattice parameters of α=0.71192 and c=0.62898 nm [3]. Thin films have been prepared by many other deposition techniques, such as spray pyrolysis, chemical vapor deposition (CVD), Molecular beam epitaxy (MBE) or vacuum deposition [4]. These methods showed a lack of crystallographic orientation control or an enrich nonstoichiometric phase [5]. Thin films of YVO_4:Eu^{3+} have been prepared by pulse laser deposition (PLD). PLD is known as a unique process that provides stoichiometric transfer of target materials. This technique allows deposition of good quality thin films at low temperatures. The factors that can influence the brightness of the thin film phosphors can be crystallinity, morphology and surface roughness [6]. PLD is an attractive method for growing high-quality crystalline films because it is cheap, simple and a reliable technique. In this work the structural characteristics and photoluminescence (PL) properties of YVO_4:Eu films prepared by PLD were investigated.

2. Experimental

The Commercial YVO_4:Eu phosphor powder was purchased from phosphor technology. Targets for PLD were prepared from YVO_4:Eu powder by cold-pressing followed by sintering for 2 hours at 800 ^oC in air. YVO_4:Eu thin films were deposited on Si substrate with typical size of 25 x 25 mm^2 at room temperature using a frequency tripled Nd:YAG Laser. A laser pulse of 10 Hz was focused onto the rotating target and the laser energy was approximately 47 J/cm^2. The distance between the target and the substrate was kept constant at 45 mm during the deposition of each film. The films were deposited at different oxygen background pressures of 20 mTorr, 100 mTorr and 200 mTorr at room temperature.

The characterization of the films structure and phase identification was carried out with x-ray diffraction (XRD). Morphologies of the films were obtained using a scanning electron microscope (SEM) and Atomic force microscopy (AFM) micrographs were obtained with the Shimadzu SPM – 96 model. PL data were recorded with a Cary Eclipse Fluorescence spectrophotometer.

3. Results and discussion

3.1. Structure and morphology

Figure 1 shows the XRD patterns of the YVO_4:Eu powder and thin films deposited on Si substrate at room temperature at different O_2 pressures of 20 mTorr, 100 mTorr and 200 mTorr. All the peaks of the powder are matched well with the tetragonal phase (JCPS Card 17-341) and no secondary phase was observed. Compared with XRD pattern of polycrystalline YVO_4:Eu phosphor powder used as a target, most peaks in all films are broadened most probably due to small particle size but still could be indexed on tetragonal YVO_4:Eu phase. And again XRD thin films show that the diffraction peaks emerges with an increase with O_2 pressure. It was observed that crystallization improves with increase in oxygen deposition pressure. Films deposited at low pressure of 20 mTorr display a single peak along the (200) direction. The films grown at O_2 pressure of 100 mTorr depict high intensity peak at (200) and a second low intensity one along (400) showing relativity well-preferred orientation of (200) plane. When the growth O_2 pressure increased to 200 mTorr the film showed diffraction peaks at (200) and (112). There is also a small diffraction peak at (400), indicating that there is no predominantly preferential growing orientation at the present films condition.

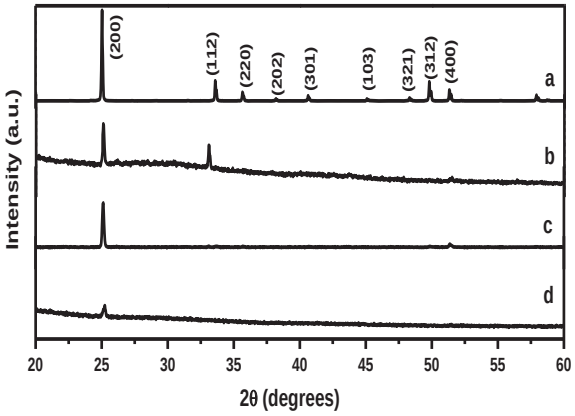

.

Figure 1. XRD patterns of YVO_4:Eu (a) powder, and thin films deposited at (b) 200m Torr (c) 100 mTorr (d) 20mTorr at room temperature

AFM images of YVO_4:Eu thin films deposited at room temperature at varying O_2 Pressure in the range of 20 – 200 mTorr are shown in figure 2. It can be observed from the results that different morphologies were obtained by changing the O_2 pressure during deposition. It is clear that the particle sizes of the films deposited at higher O_2 pressure were much larger than those of the films deposited at lower O_2 pressure of 20 mTorr. But is appears that the particles deposited at 200 mTorr are more but

not lager than those of 100 mTorr, suggesting that the growth rate of deposited particles was much faster at higher O_2 pressure. The increase in crystallite size possibly results from the enhancement of the film surface atomic mobility with abundance of oxygen species, which enables the thermodynamically favored grains to grow. The films deposited at lower O_2 pressure of 20 mTorr had smoother surfaces than the film deposited at higher O_2 pressure. The surface topography changed from smooth to nodular with an increase in O_2 pressure. Increasing the O_2 pressure to 100 mTorr yielded a complete development of nodular surface with well defined grain boundaries. Further increase of the oxygen pressure to 200 mTorr resulted into a well-developed nodule surface with slightly less rough surface but well defined edges are obtained as compared to the films deposited at O_2 pressure of 100 mTorr.

Figure 3 shows the SEM micrographs of YVO_4:Eu films grown on Si substrate at room temperature during 27000 pulses. SEM pictures confirm that the surface roughness of the films increases as oxygen pressure increases. The thin film deposited at 20 mTorr O_2 pressure has smooth surface with small nearly spherical particles, and the bigger particles at some regions are due to spitting. Film deposited at O_2 pressure of 100 mTorr had a rougher surface also with larger spherical particles as shown in figure 3(b) but with no developed edges. The results shows that the film deposited in higher oxygen pressure of 200 mTorr had also rougher surface packed with nearly spherical particles with well developed straight edges. The SEM pictures shows that increasing oxygen pressure increases surface roughness and this maybe due to the enhanced particulate formation in plume, which is characteristic of high pressure ablation [7].

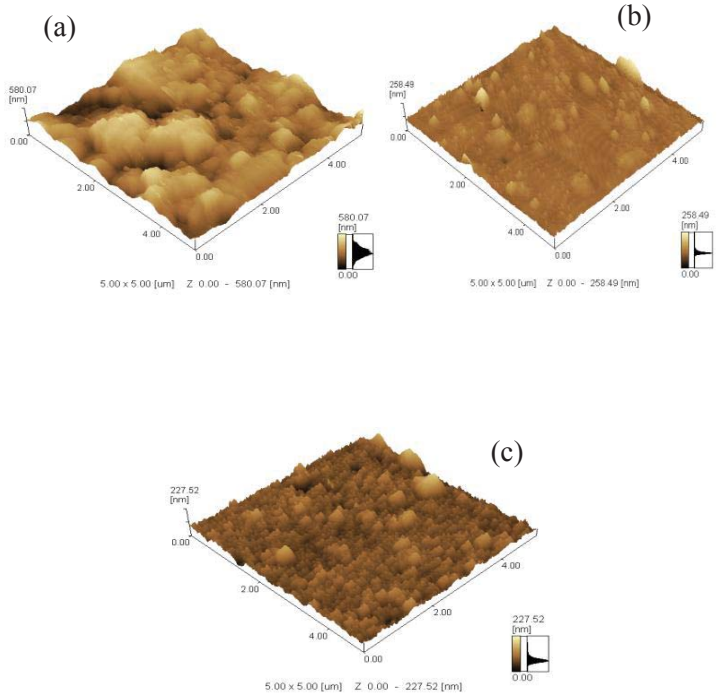

Figure 2. AFM images of YVO_4:Eu thin films deposited on Si substrates at O_2 pressures of (a) 20 mTorr (b) 100 mTorr and (c) 200 mTorr

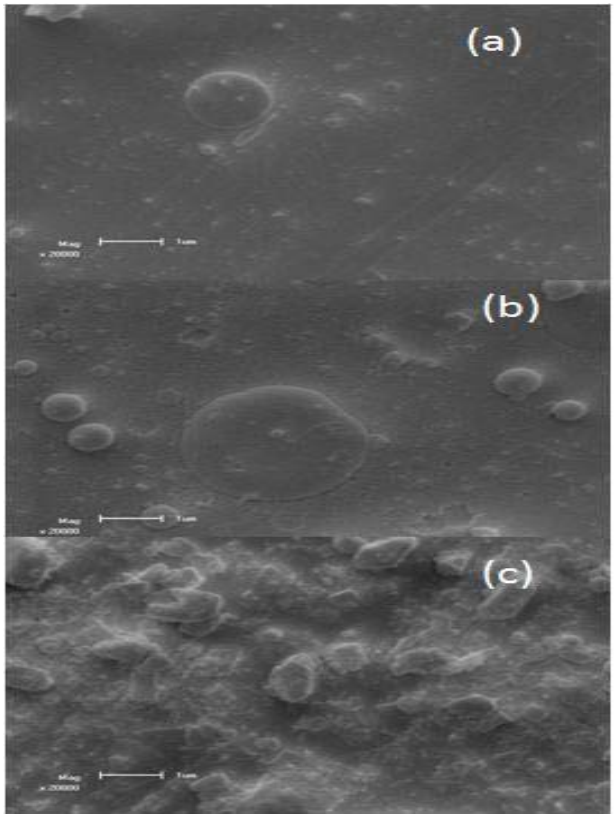

Figure 3. SEM images of Eu:YVO_4 thin films deposited on Si substrate at (a) 20 mTorr, (b) 100 mTorr and (c) 200 mTorr O_2 pressure.

3.2. Photoluminescence characteristics

Figure 4 shows the excitation spectra of YVO_4:Eu thin films deposited at room temperature at different O_2 pressures as well as the phosphor powder. The excitation spectra monitored with 618 nm emission of Eu^{3+} ($^5D_0$-$^7F_2$) consists of a strong absorption band from 200 nm to 340 nm with a median maximum at 275 nm due to the VO_4^{3-} ion. Obviously, this band is ascribed to a charge transfer from the oxygen ligands to the central vanadium atom within the VO_4^{3-} group ions [7]. From the viewpoint of molecular orbital theory, it corresponds to transitions from the $^1A_2$ ($^1T_1$) ground state to $^1A_1$ (^1E) and ^1E ($^1T_2$) excited states of VO_4^{3-} ion [8]. The general f-f transition lines of Eu^{3+} in the longer wavelength region have not been observed due to their weak intensity relative to that of the VO_4^{3-}. This indicates that the excitation of Eu^{3+} is mainly through the VO_4^{3-} ions, i.e., by energy transfer from VO_4^{3-} to Eu^{3+} [9]. The excitation intensity of the films increases with increase in O_2 pressure. This means that the energy transfer from host YVO_4 to Eu^{3+} is gradually enhanced. The PL emission spectra of YVO_4:Eu phosphor in figure 5 show a considerable number of lines between 575 and 725 nm, representing the transitions $^5D_0$-$^7F_{0\text{-}4}$ between the first excited states and the ground states of the Eu^{3+}. YVO_4:Eu showed a strong red emission peak at 618 nm assigned to $^5D_0$-$^7F_2$ transition. Other peaks at 594 nm, 650 nm and 699 nm represent the transitions $^5D_0$-$^7F_1$, $^5D_0$-$^7F_3$ and $^5D_0$-$^7F_4$, respectively. No emission from the VO_4^{3-} group is observed, suggesting that the energy transfer from VO_4^{3-} to Eu^{3+} is very efficient. The PL spectra of films show some differences with oxygen pressure, and the intensity of PL in films is relatively weak compared with the powder. As the O_2 pressure increased from 20m Torr to 100 mTorr the PL intensity did not show much difference but increased significantly as the O_2 pressure increased to 200 mTorr (Fig. 4(c)). The $^5D_0$-^7F_J emission is very suitable to survey the environmental effects on the sites of Eu^{3+} ion in a host lattice without inversion symmetry such as

YVO_4 [10]. While the $^5D_0$-$^7F_4$ transition is sensitive to long range environmental effects, the $^5D_0$-$^7F_2$ transition, which originates from interactions with neighbours, is hypersensitive to, especially short-range, environmental effects. However, the $^5D_0$-$^7F_1$, the allowed magnetic-dipole transition, is not affected by the Eu^{3+} ion so that it is usually utilized as an internal standard. The similar intensity ratios of $^5D_0$-$^7F_2$ and $^5D_0$-$^7F_4$ transitions to $^5D_0$-$^7F_1$ transition in PL spectrum of YVO_4:Eu show that Eu^{3+} ions are occupied in yttrium sites of YVO_4 lattice and the long-range environments of Eu^{3+} ions in the film are not much different from powder. This indicates that YVO_4:Eu film deposited by PLD is well crystallized even without any post-annealing. The dependence of PL emission on the deposition O_2 pressure is shown in insertion graph in Figure 5.

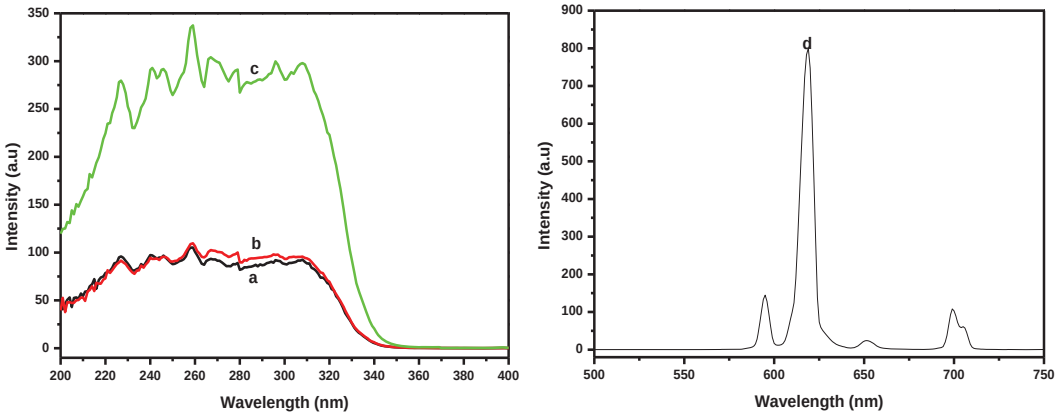

Figure 4. PL excitation spectra of Eu:YVO_4 thin films deposited on Si substrate at (a) 20 mTorr, (b) 100 mTorr and (c) 200 mTorr and powder (d).

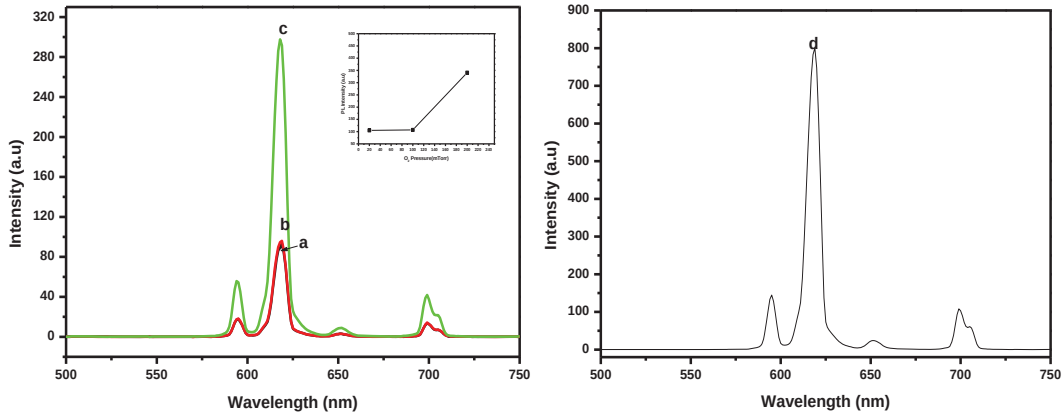

Figure 5. PL emission spectra of YVO_4:Eu thin films deposited on Si substrate at (a) 20 mTorr, (b) 100 mTorr and (c) 200 mTorr and (d)Powder

4. Conclusion

YVO_4:Eu thin film phosphors have been deposited on Si substrates using PLD. AFM results show that the surface roughness of the films highly depends on oxygen pressure. The films deposited at lower O_2 pressure of 20 mTorr had smoother surfaces than the film deposited at higher O_2 pressure. The SEM images confirm that the surfaces of the films prepared at higher O_2 pressure are much rougher and packed with nearly spherical particles than that deposited at low O_2 pressure. The XRD patterns of phosphor powder showed the tetragonal single phase. Thin films peaks are broadened, most probably due to small particle size but still could be indexed on tetragonal YVO_4:Eu phase. The thin films diffraction peaks emerge and increases with an increase in O_2 pressure. PL emission spectra showed a

red emission peak at 618 nm which was assigned to $^5D_0$-$^7F_2$ transition. The PL intensity increased when the O_2 pressure increased to 200 mTorr.

Acknowledgement
The authors send gratitude to the National Research Foundation (NRF) for funding the project and the University of Free State (Physics department) for the research techniques used in this study.

References

[1] Kim D, Kang W, 2004 *Bull. Korean Chem. Soc* **25** 1859–1862.
[2] Xiao X, Lu G, Shen S, Mao D, Guo Y, Wang Y, 2011 *Material Science and Engineering* 176 72- 78.
[3] Hyun K Y, Kyoo S S, Byung K M, Jung H J, Soung S S, Jung H K, 2008 *Thin Solid Films* **516** 5577–5581.
[4] Milev D R, Atanasov P A, Dikovska A O G, Dimitrov I G, Petrov K P, Avdeev K P, 2007 *Applied Science* **253** 8250–8253.
[5] Kang W, Park J, Kim D, Suh K, 2001 *Bull. Korean Chem. Soc*. **22** 921–924.
[6] Klausch A, Althues H, Freudenberg T, Kaskel S, 2012 *Thin Solid Films* **520** 4297–4301.
[7] Coetsee E, Swart H C, Terblans J J , Ntwaeaborwa O M, Hillie K T, Jordaan W A, Buttnerk U, 2007 *opt. Mater*. **29** 1338–1343.
[8] Hsu C, Powell RC, 1975 J. Lumin **10** 273–293.
[9] Yi S, Bae J S, Choi B C, Shim K S, Yang H K, Moon B K, Jeon J H, Kim J H, 2006 *Optical Materials* **28** 703–708.
[10] Carlos L D, Videira A L L, 1994 *Phys. Rev.* **49** 11721–11728.

Influence of magnetic field on the transition temperature of the $(Cr_{84}Re_{16})_{89.6}V_{10.4}$ alloy

BS Jacobs, CJ Sheppard and ARE Prinsloo

Department of Physics, University of Johannesburg, PO Box 524, Auckland Park, 2006

E-mail address: sjacobs@uj.ac.za

Abstract. In this study, the variation of the Néel transition temperature of the $(Cr_{84}Re_{16})_{89.6}V_{10.4}$ alloy is investigated through the application of magnetic field. Magnetic susceptibility (χ) was measured as a function of temperature (T) in the temperature range 2 K ≤ T ≤ 200 K. The sample was cooled to 2 K in zero field, followed by measurements being collected upon warming the sample in static applied fields (H) in the range 0.01 T ≤ H ≤ 6.5 T. The $\chi(T)$ curves obtained for the various applied fields show a clear peak and the temperature associated with the peak was taken as the Néel temperature, T_N. Results indicate that the sharpness of the peak improves on increasing H, with an accompanying suppression of T_N. The $T_N(H)$ curve varies exponentially with applied field up to 6.5 T, the highest applied field used in the present study. This is linked to previously reported quantum critical behaviour in Cr.

1. Introduction

Long range spin-density-wave (SDW) antiferromagnetic ordering occurs in chromium below 311 K, its Néel temperature (T_N) [1]. The characteristic changes in the transport properties observed in the vicinity of T_N can be attributed to gap formation in portions of the Fermi surface as itinerant electron antiferromagnetism is established in this material [1].

Studies on the possible tuning of pure Cr and certain of its alloys through a quantum critical point (QCP) have intensified in recent years, as is reflected in the literature [2, 3, 4]. Charge density wave (CDW) and SDW systems appear to be good candidates for investigations into quantum critical behaviour (QCB), in which quantum fluctuations cause a disruption in electron pairing and results in the restoration of the metallic Fermi surface (FS) [5, 6, 7]. In CDW and SDW systems the interaction strengths are considered relatively weak, therefore allowing relatively easy experimental access to the quantum critical point in comparison to strongly correlated systems [7].

A quantum critical point (QCP) occurs when the phase transition temperature is driven to zero by the application of a tuning parameter such as magnetic field, pressure or by doping [2]. No thermal fluctuations exist at absolute zero; instead, quantum fluctuations drive the transitions in accordance with Heisenberg's uncertainty principle [8]. A state of constant agitation is adopted at the QCP, even when thermal motion ceases, in order to abide by the uncertainty principle [9].

Doping a particular alloy in order to drive it to a QCP is regularly used by experimentalists, however fine doping of the alloy close to the QCP is difficult and it also induces disorder in the system [10]. Another control parameter used is applied pressure. Although fine tuning of this control parameter is possible close to the QCP, there are other associated difficulties that are introduced by the

pressure cell itself [10]. Hence, magnetic field has recently been used more frequently to probe and understand critical behaviour [10, 11].

According to Fischer and Rosch [10], the magnetic field has two main effects. Firstly, it suppresses or induces magnetic order and secondly, it causes a precession of the magnetic moments perpendicular to the magnetic field and therefore modifies the dynamics of the order parameter. Fischer and Rosch [10] also argue that the susceptibility, $\chi = \partial \mathrm{M}/\partial B$, is the thermodynamic quantity that will show the most substantial change upon approaching the QCP.

With the discovery of QCB in Cr and its alloys, not much work has been reported on investigations into QCB induced by the application of magnetic field in these alloys. However, extensive work on pressure induced QCB in Cr has been reported by Jaramillo *et al.* [12, 13]. It was found that the order parameter varied exponentially with the tuning parameter at low pressures of less than 7 GPa. This is referred to as the Bardeen-Cooper-Schrieffer (BCS) regime and in this pressure range, Cr is modelled by a BCS-like weak coupling theory. However, at pressures above 7 GPa and low temperatures, this exponentially tuned ground state is destabilized and at 10 GPa the SDW is terminated by a quantum phase transition [12].

Signatures of QCB have previously been reported [2, 3, 4] in electrical resistivity (ρ), magnetic susceptibility (χ), Hall coefficient (R_H) and Sommerfeld coefficient of specific heat (γ) measurements of Cr and its alloys. Even though the QCP occurs at absolute zero, its influence and the corresponding signatures occur at low, finite temperatures in the quantum critical regime. Considering these results, possible quantum critical behaviour in the $(Cr_{84}Re_{16})_{100-y}V_y$ alloy system has been previously investigated utilizing ρ, χ, R_H and γ [14]. A putative QCP was reported at a critical concentration of $y_c \approx 10.5$ in this alloy system. The $\chi(T)$ results on the $(Cr_{84}Re_{16})_{100-y}V_y$ alloy system showed weak anomalies at the phase transition temperatures that become more pronounced with increase in the V concentration. This corresponds to observations by Yeh *et al*. [3] that investigated the QCB in the $Cr_{1-x}V_x$ alloy system through χ measurements. This system shows antiferromagnetic ordering below the critical concentration (x_c) of 0.035. In their results, a reduction in χ is observed on entering the ordered state for $x < x_c$ as is expected for Cr and its alloys [1]. This is explained in terms of the band theory and the reduction of the density of states at the Fermi level on SDW formation [3].

Extending the quantum criticality studies on the $(Cr_{84}Re_{16})_{100-y}V_y$ alloy system, the present study reports the results of the effect of magnetic field on the magnetic susceptibility of the $(Cr_{84}Re_{16})_{89.6}V_{10.4}$ antiferromagnetic alloy by studying $\chi(T)$ at different constant applied magnetic fields. The selected alloy has V concentration very close to the previously reported critical concentration of the $(Cr_{84}Re_{16})_{100-y}V_y$ system [14] and the vision is to explore possible QCB in this sample by considering a new tuning parameter, namely magnetic field.

2. Experimental

The polycrystalline $(Cr_{84}Re_{16})_{89.6}V_{10.4}$ alloy was prepared from the constituent metals Cr, Re and V of mass fractional purities of 99.99%, 99.99% and 99.8%, respectively, by repeated arc melting in purified argon atmosphere. The sample was sealed in a quartz ampoule filled with pure argon gas at low pressure and annealed at 1343 K for seven days followed by quenching in iced water. Powder X-ray diffraction (XRD) analyses confirmed the expected body centred cubic (bcc) crystal structure. Electron microprobe analyses were used to determine the homogeneity and elemental compositions of Cr, Re and V in the sample. A portion of the sample in the form of a disc was prepared from the alloy ingot using spark erosion technique. Magnetic susceptibility (χ) as a function of temperature (T) was measured, on this disc, in the temperature range 1.9 K $\leq T \leq$ 200 K using the Quantum Design Magnetic Property Measurement System (MPMS). The sample was cooled to 1.9 K in the absence of a field, followed by the measurements being collected upon warming the sample in static applied fields (H) in the range 0.01 T to 6.5 T.

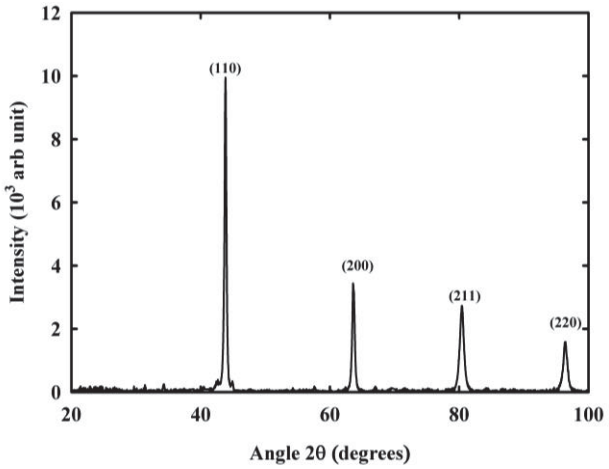

Figure 1: The XRD pattern for the $(Cr_{84}Re_{16})_{89.6}V_{10.4}$ sample with (*hkl*) Miller indices of the various reflections expected for the profile of bcc Cr indicated.

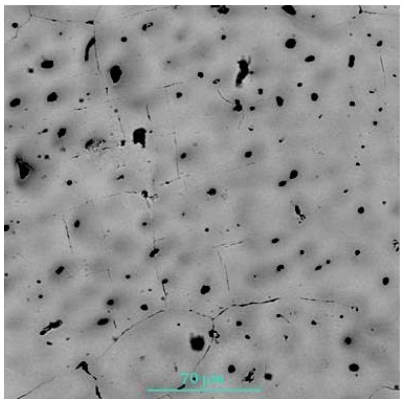

Figure 2: The backscattered-electron image for the $(Cr_{84}Re_{16})_{89.6}V_{10.4}$ sample.

Table 1: Elemental concentrations obtained from electron microprobe analyses on the $(Cr_{84}Re_{16})_{89.6}V_{10.4}$ sample. The dark and the light regions refer to backscattered-electron image shown in Figure 2.

	at.% Cr	at.% Re	at.% V
Actual Average Elemental Compositions	85.0 ± 1.3	15.0 ± 1.2	10.4 ± 0.2
Dark regions in back scattered image	85.0 ± 0.8	15.0 ± 0.7	9.6 ± 0.2
Light regions in back scattered image	81.9 ± 0.5	18.1 ± 0.3	10.2 ± 0.2

3. Results and discussion

Figure 1 shows the XRD pattern for the $(Cr_{84}Re_{16})_{89.6}V_{10.4}$ sample. The entire profile in the $(Cr_{84}Re_{16})_{89.6}V_{10.4}$ pattern is well fitted to the XRD pattern of pure bcc Cr by adjusting the lattice parameter of pure Cr (0.28839 nm) to 0.2926 nm for this alloy. No additional peaks are detected to within instrumental resolution indicating that the alloy formed in the bcc phase of pure Cr.

Electron microprobe analyses of the samples showed good homogeneity of the alloy and the average actual elemental compositions of Cr, Re and V are listed in Table 1. Figure 2 shows the backscattered-electron image obtained on this sample. The light and the dark regions observed in the image differ slightly in concentration as is summarized in Table 1. Also clear in this image are black spots. The spots were also analysed and found to be either empty pores or in certain cases the wavelength dispersive X-ray spectra analyses showed the presence of oxygen within these dark inclusions. Further analyses showed that these were inclusions of predominantly Cr_2O_3 and V_2O_3. These inclusions cover approximately 2% of the image having a surface area of about 61500 μm^2. Considering that $\chi(T)$ measured at 0.01 T, $\rho(T)$ and $S(T)$ measurements all give similar T_N-values [14], it is however not expected that, at this low concentration levels, these inclusions will have a substantial influence on the Néel temperatures determined from $\chi(T)$ and that effects of these inclusions may be neglected in the present study.

The $\chi(T)$ data for a series of $(Cr_{84}Re_{16})_{100-y}V_y$ alloys were previously reported [14]. Weak anomalies are seen in the $\chi(T)$ curves at the phase transition temperatures, becoming more pronounced as the V concentration is increased [14]. For samples with $y < 10.4$, χ decreases almost linearly on cooling for $T > T_N$, followed by an anomalous sharper downturn in χ on cooling through T_N, similar to the $\chi(T)$-behaviour behaviour usually observed in Cr and certain of its alloys in the vicinity of T_N [1].

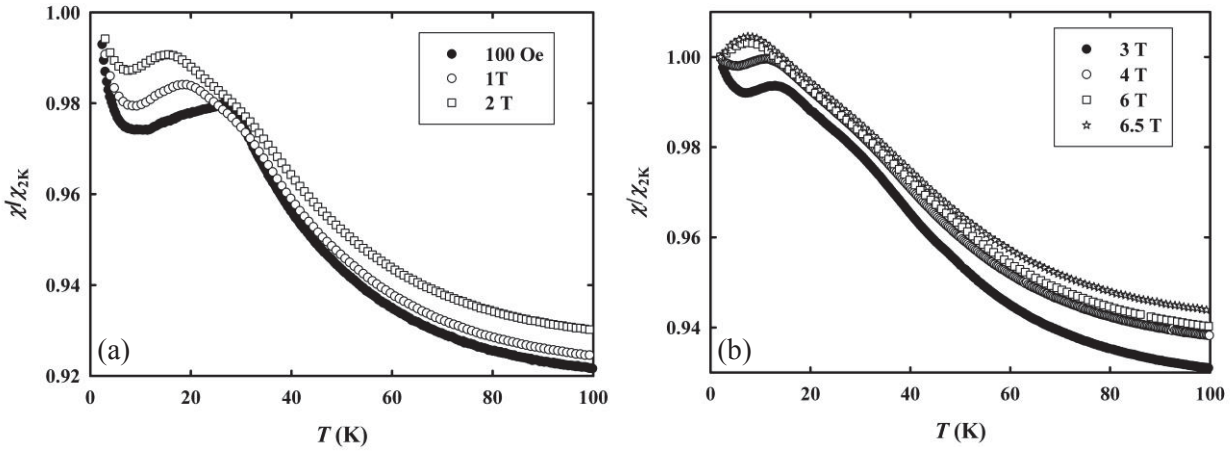

Figure 3 (a) and (b): Temperature dependence of χ/χ_{2K} at various static fields. The experimental error associated with absolute values of χ is approximately 0.1% and originates from the measurements of the masses of the samples.

The anomalous downturn in the $\chi(T)$ curves below T_N is ascribed to a decrease in the density of electron states at the Fermi energy, $N(E_F)$, when the nested parts of the electron and hole Fermi sheets these alloys are annihilated on SDW formation below [1]. On cooling the $(Cr_{84}Re_{16})_{89.6}V_{10.4}$ alloy from the paramagnetic phase down through T_N, nesting of the electron and hole FS sheets should also result in a reduction in the density of states due to the appearance of the SDW energy gap, thus explaining the reduction in $\chi(T)$ observed for this alloy for $T < T_N$. However, a different behaviour is observed in the region $T > T_N$. For this sample, the linear decrease in $\chi(T)$ on cooling from $T > T_N$ is not seen. Instead, a clear increase is observed in this temperature range on cooling, ending in a maximum value for χ at T_N, followed by the expected decrease on further cooling, resulting in a clear peak at T_N. This might be indicative of the presence local magnetic moments in the paramagnetic phase. A similar behaviour was observed by Sousa *et al*. [15] in the $Cr_{100-x}Al_x$ alloy system for the commensurate (C) SDW alloys with x = 2.23 and 2.83. De Oliveira *et al*. [16] also observed similar peaks at T_N in the $Cr_{100-y}V_y$ alloy system for incommensurate (I) SDW alloys with $y \leq 0.67$. They attributed the peaks in χ at T_N to a local SDW that is formed around the V atoms, resulting in Curie-Weiss paramagnetism above T_N [16]. This might then also be of importance to consider in the present $(Cr_{84}Re_{16})_{89.6}V_{10.4}$ alloy.

Against this background, we can now consider the temperature dependence of χ/χ_{2K} in various applied static fields (H) for the $(Cr_{84}Re_{16})_{89.6}V_{10.4}$ alloy. These results are shown in Figure 3(a) and (b). Each curve shows a well-defined anomaly in the form of a clear peak and for this alloy, the temperature associated with the peak was taken as T_N. The T_N value obtained in this way for the 0.01 T field corresponds well with T_N values obtained for the same sample through $\rho(T)$ (considering $d\rho(T)/dT$) and $S(T)$ measurements reported in a previous study [14]. It is also important to note that the T_N-anomaly observed in the $\chi(T)$ measurements at 0.01 T for this sample is better defined than those observed in the $\rho(T)$ and $S(T)$ curves [14], emphasizing the fact that the susceptibility measurement is a sensitive tool for probing the magnetic transition in this specific alloy. The slight low temperature upturn observed in the curves shown in Figure 3 for measurements with $H \leq 4$ T may be attributed to a Curie tail arising from oxide impurities, that were identified in the backscattered-electron image shown in Figure 2. Considering the results shown in Figure 3 (a) and (b), it is evident that the sharpness of peaks observed at T_N improves with field. Furthermore, the application of the field suppresses T_N.

The field dependence of T_N obtained from the curves in Figure 3 (a) and (b) is shown in Figure 4. T_N varies exponentially with applied field, as is indicated by the exponential fit to the data (see the broken line in Figure 4). The broken line indicates an exponential decay fit of the form

$y = Ae^{(-x/t)} + y_0$ to the data, where A = (20.1 ± 1.2) K, t = (2.8 ± 0.4) T and y_0 = (5.8 ± 1.2) K are the fitting parameters and x is the applied static field.

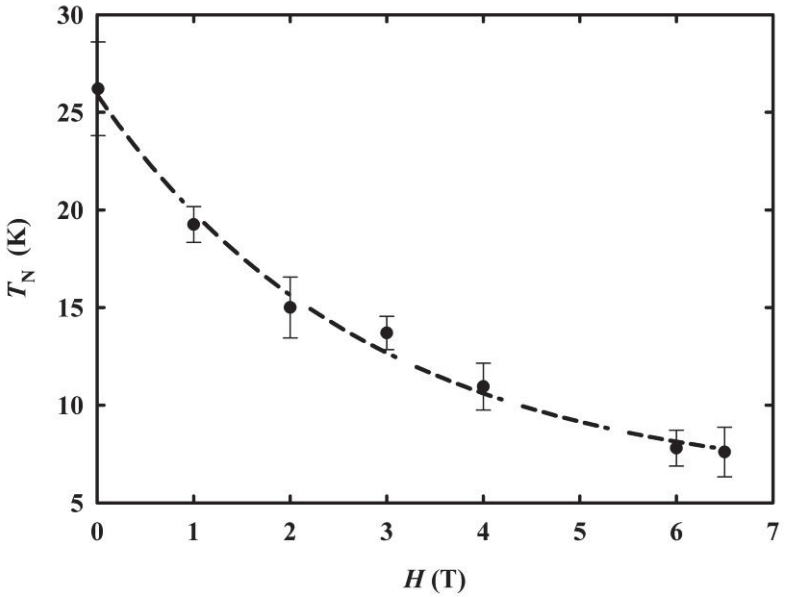

Figure 4: The field dependence of T_N obtained from the $\chi(T)$ curves shown in Figure 3. The broken line indicates an exponential decay fit of the form $= Ae^{(-x/t)} + y_0$ where A = (20.1 ± 1.2) K, t = (2.8 ± 0.4) T and y_0 = (5.8 ± 1.2) K are the fitting parameters and x is the applied static field.

The exponentially decaying behaviour in the ordering temperature with respect to the tuning parameter is reminiscent of the work by Jaramilo *et al.* [12, 13] on a pressure induced quantum criticality in pure Cr. The Néel temperature, T_N, investigated varied exponentially at low pressures of less than 7 GPa. However, at high pressures and low temperatures this exponentially tuned ground state is destabilized and the spin density wave (SDW) is terminated by a quantum phase transition [12]. It is therefore hypothesized that the $(Cr_{84}Re_{16})_{89.6}V_{10.4}$ alloy presently investigated is still in the BCS-regime up to the maximum applied field we could attain and that at higher magnetic fields and low temperatures this exponentially tuned ground state can be destabilized and the SDW might be terminated by a quantum phase transition.

4. Conclusion

The results presented here on the antiferromagnetic $(Cr_{84}Re_{16})_{89.6}V_{10.4}$ alloy provide an overview on this sample's behaviour in the presence of magnetic fields. Measurements need to be extended to include $\chi(T)$ measurements in higher applied fields. This might result, at high applied magnetic fields and low temperatures, in the destabilization of this exponentially tuned ground state and the termination of the SDW by a quantum phase transition.

Acknowledgments

Financial support from the South African NRF (Grant numbers 80631, 80928 and 80626) is acknowledged.

References

[1] Fawcett E, Alberts H L, Galkin V Y, Noakes D R and Yakhmi J V 1994 *Rev. Mod. Phys.* **66** 25

[2] Lee M, Hussman A, Rosenbaum T F and Aeppli G 2004 *Phys. Rev. Lett* **92** 187201

[3] Yeh A, Soh Y A, J Brooke J, Aeppli G, Rosenbaum T F and Hayden S M 2002 *Nature* **419** 459
[4] Takeuchi J, Sasakura H and Masuda Y 1980 *J. Phys. Soc. Japan* **49** 508
[5] Altshuler B L, Ioffe L B and Millis A J 1995 *Phys. Rev. B* **52** 5563
[6] Metlitski M A and Sachdev S 2010 *Phys. Rev. B* **82** 075128
[7] Feng Y, Wang J, Jaramillo R, van Wezel J, Haravifard S, Srajer G, Liu Y, Xu Z-A, Littlewood P B and Rosenbaum T F 2012 *PNAS.* **109**(19) 7229
[8] Sachdev S and Keimer B 2011 *Physics Today* 29
[9] Coleman P and Schofield A J 2005 *Nature* **433**226
[10] Fischer I and Rosch A 2005 *Phys. Rev. B* **71** 184429
[11] Carretta P, Giovannini M, Graf M J, Papinutto N, Rigamonti A and Sullivan K 2006 *Physica B* **378-380** 84-86
[12] Jaramillo R, Feng Y and Rosenbaum T F 2010 *J. Appl. Phys*. **107** 09E116
[13] Jaramillo R, Feng Y, Wang J and Rosenbaum T F 2010 *PNAS.* **107** 13631
[14] Jacobs B S, Prinsloo A R E, Sheppard C J and Strydom A M 2013 *J. Appl. Phys* **113** 17E126
[15] Sousa J B, Amado M M, Pinto R P, Pinheiro M F, Braga M E, Moreira J M, Hedman L E, Åström H U, Khlaif L, Walker P, Garton G and Hukin D 1980 *J .Phys. F: Metal Phys.* 10 2535
[16] De Oliveira A J A, Ortiz W A, de Lima, O F and de Camargo P C 1997 *J. Appl. Phys*. 81 4209

Luminescence properties of Bi^{3+} in Y_2O_3

R M Jafer[1,2] , A Yousif [1,2], E Coetsee[1] and HC Swart[1]

[1] Department of Physics, University of the Free State, P.O. Box 339, Bloemfontein, ZA 9300, South Africa.

[2]Department of Physics, Faculty of Education, University of Khartoum, P.O. Box 321, Postal Code 11115, Omdurman, Sudan.

Corresponding Author Email address: coetseeE@ufs.ac.za

Abstract. The luminescent properties of $Y_{2-x}O_3$:$Bi_{x=0.002}$ were investigated and the fluorescence spectra show that the luminescence was produced by the emission from two types of centers. These two types of centers were associated with the substitution of the Y^{3+} ion with the Bi^{3+} ion in two different sites in the crystal lattice of Y_2O_3 (with point symmetries C_2 and S_6). The emission of Bi^{3+} in the S_6 site caused blue luminescence with maxima at 360 nm and 407 nm, and in the C_2 site it gave green luminescence with the maximaum at 495 nm. Both these emissions are related to the $^3P_1$-$^1S_0$ transition in Bi^{3+}. The diffuse reflectance was measured for Y_2O_3 and Y_2O_3:Bi. No change in the band gap, when 0.2 mol% of Bi was doped in the Y_2O_3 host, was observed.

1. Introduction

Metal ions with outer ns^2 configuration are of great importance in the luminescence field. The luminescence of Bi^{3+} in oxides, phosphates, aluminates, and borates [1, 2] has been extensively studied since 1960. The Bi^{3+} ion with a $6s^2$ electronic configuration shows strong optical absorption in the near ultraviolet region (300 - 400 nm) due to the s^2-sp transition [3,4]. The $6s^2$ electronic configuration splits into one level for the ground state (singlet $^1S_0$) and four levels for the excited 6s6p state (triplet ($^3P_0$, $^3P_1$ and $^3P_2$) and singlet ($^1P_1$)). The transitions from $^1S_0$ to $^3P_0$ and $^3P_2$ are strongly forbidden due to the Δj selection rule, while the transitions from $^1S_0$ to $^3P_1$ and $^1P_1$ are allowed due to the $^3P_1$ and $^1P_1$ spin – orbital coupling [5,7,11]. In this research we only consider the transition $^1S_0 \rightarrow {}^3P_1$, due to absorption occurring in the range of 300 - 400 nm for the Bi^{3+} ion while the transition $^1S_0 \rightarrow {}^1P_1$ usually is located at higher energies [1,4,11]. Furthermore, it is well known that the level $^3P_1$ split into sublevels due to the crystal field effect, corresponding to the position of the Bi^{3+} in the host [5,8,9].

Y_2O_3 is known as an excellent phosphor material and it is widely used in high-temperature-resistant windows, lighting and display applications, host materials for solid state lasers or scintillators etc. [18]. The crystallographic structure of Y_2O_3 has a C-type cubic structure with each unit cell containing 32 cationic sites. Eight are centrosymmetric with a S_6 symmetry and 24 are non centrosymmetric with a C_2 symmetry [7,11,12]. These two sites have an impact on the excitation and emission spectra of the Y_2O_3 phosphor material [12,19].

In this study the Y_2O_3:Bi phosphor was synthesized by the combustion method and characterized by X-ray diffraction (XRD), photoluminescence (PL) and UV-Vis spectroscopy. PL and UV-Vis spectroscopy were also used to obtain the luminescent mechanism.

2. Experimental

Powder samples of $Y_{2-X}O_3$: $Bi^{3+}{}_{X=0.002}$ were prepared by urea-nitrate solution combustion synthesis. $Y(NO_3)_3.4H_2O$, CH_4N_2O and $Bi(NO_3)_3.5H_2O$ were used as the starting materials, which dissolved in diluted water under stirring and heating to obtain a mixed aqueous homogenous precursor solution. The solution was placed in a furnace preheated at 550^o C. After the combustion process was completed, the obtained solid precursors were then ground and fired at 700 ^{o}C for 1 h in air to produce the final samples. The crystal structure was determined by using a Bruker D8 diffractometer, the

diffuse reflectance spectra were recorded using a Lambda 950 UV-Vis spectrophotometer, PL was measured with a Cary eclipse spectrophotometer and the 325 nm He-Cd laser PL system.

3. Results and discussion

3.1 Structural analysis

The XRD results for the Y_2O_3:Bi powder and the profile of the ICSD reference data file are shown in Figure 1. The results indicated that the single phase cubic crystal structure with Ia-3 space group was formed [10], which is in agreement with the ICSD reference data file no. 16394. The main peak of the cubic structure corresponds well with that for the {222} crystalline plane centred at 29.16°.

In this structure every unit cell has 32 cationic sites with a coordination number of 6. These sites can be substituted by rare earth ions where eight will have the S_6 symmetry and the other 24 will have the C_2 symmetry. The sites with S_6 symmetry are where two oxygen vacancies are located on a cube and the sites with C_2 symmetry are where the vacancies are located on a face diagonal, see Figure 2(a) and (b) [7,11,12].

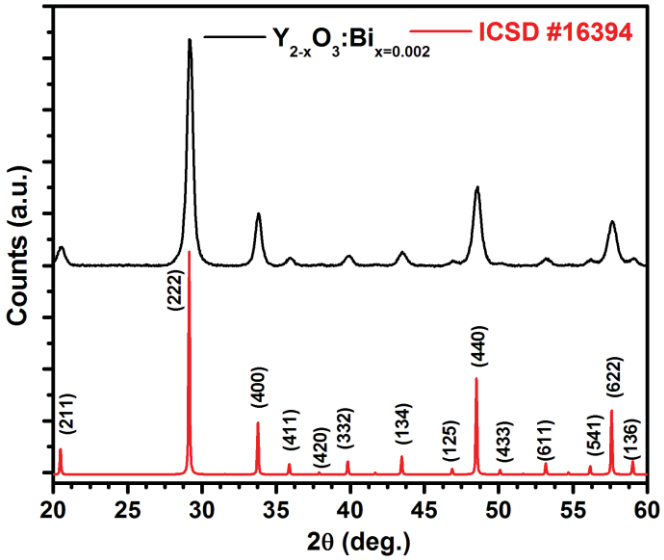

Figure 1: XRD pattern of $Y_{2-x}O_3$:$Bi_{x=0.002}$ phosphor powder and the reference spectrum from the ICSD data base.

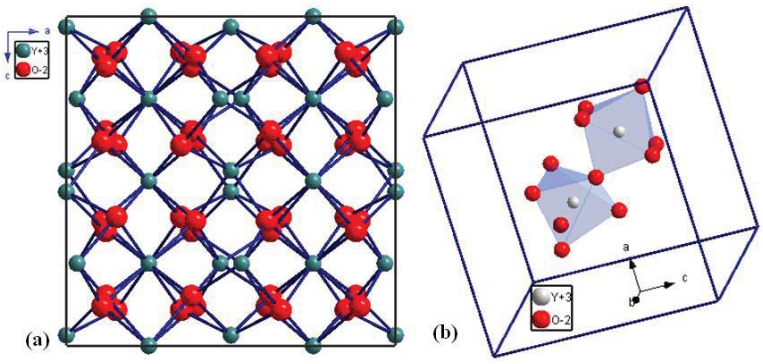

Figure 2: (a) The unit cell (ICSD-16394) and (b) schematic representation of the two different symmetry sites (S_6 and C_2) for the Y_2O_3 host.

3.2 Diffuse reflection spectra (DR) and band gap calculations

Figure (3) shows the diffuse reflectance measurements for Y_2O_3 and Y_2O_3:Bi samples against a reference standard ($BaSO_4$ compound). The band around 219 nm was observed for both the Y_2O_3 and Y_2O_3:Bi samples, which is attributed to the band gap as shown in Figure 3. The weak band around 280 nm was observed for the un-doped sample which is probably due to defect formation. The absorbance increased in the case of the Bi-doped sample and there are three bands, located around 255, 330 and 372 nm. These bands are due to the O^{2-}- Bi^{3+} charge transfer (CT) absorption to the different sites (C_2 and S_6 respectively).

The DR spectra for both the Y_2O_3 and Y_2O_3:Bi samples were used to calculate the band gap by using Kubelka-Munk and Tauc relation (1) [10], if the material scatters in a perfectly diffused manner.

$$F(R_\infty)^2 = C_1(h\nu - E_g) \qquad (1)$$

$R_\infty = R_{sample}/R_{reference}$ is the ratio of the light scattered from a thick layer of the sample and an ideal non-absorbing reference sample and it is measured as a function of the wavelength λ. E_g is the band gap, hυ is the photon energy and C_1 is a proportionality constant.

Plotting relation (1) as a function of $h\nu$, gives the value of the E_g by extrapolating the linear fitted regions to $[F(R_\infty)h\nu]^2 = 0$. The curve (as an inset in Figure 3) exhibits non-linear and linear portions, which are the characteristic of a direct allowed transition. The nonlinear portion corresponds to a residual absorption involving impurity states and the linear portion characterizes the fundamental absorption [10]. The calculated band gap was found to be almost 5.65 ± 0.1 eV for both Y_2O_3 and Y_2O_3:Bi samples which means that there is no change in the band gap when the Y_2O_3 host is doped with 0.2 mol % of Bi. Our results are in agreement with what Som et al. [10] have found. Their band gap was around 5.6 eV for Y_2O_3.

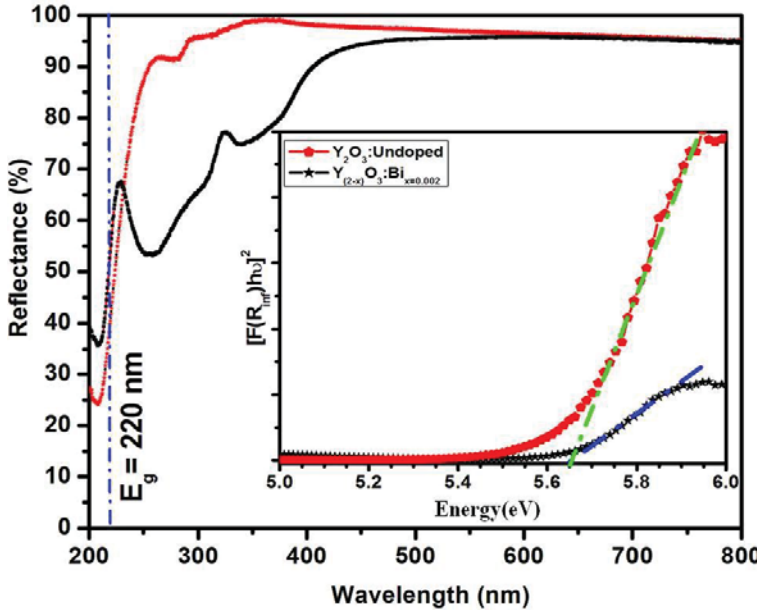

Figure 3: Diffuse reflection spectra measurements for Y_2O_3 and Y_2O_3:Bi samples.

3.3 Luminescence properties

Figure 4(a) shows the emission spectrum when the sample was excited with the 325 nm He-Cd laser. The phosphor has three emission bands, two bands centred at 360 nm and 407 nm (blue emission) and the other band is centred at 495 nm (green emission). Figure 4(b) shows the excitation and emission spectra of $Y_{2-x}O_3$:$Bi_{x=0.002}$ at room temperature. For emission at 495 nm (green emission) two excitation bands were observed in the 300 - 400 nm range, with maxima at 330 nm and 345 nm. For

emission at 407 nm (blue emission) two excitation bands were also observed in the 300 – 400 nm range but with maxima at 338 and 372 nm. For emission at 360 nm one excitation band centered at 345 nm were observed. When excited by 330 nm the same broad green emission with the two extra shoulders from the blue site was recorded. When excited by 372 nm the emission spectrum only showed a strong blue emission (407 nm) without any contribution from the green (495 nm) site [3,7,13-15]. The band centred at 330 nm is a result of the excitation of the Bi^{3+} ion in the C_2 site, where the band centered at 372 nm are a result of the excitation of the Bi^{3+} ion in the S_6 site [1,11,17]. There is a partial overlap between the 330, 338 and 345 nm excitation bands for the two different sites (C_2 and S_6) and this result in the two extra shoulders in the emission spectrum when excited by 330 nm radiation. If the phosphor is excited with 338 nm there is a slight increase in the blue emission bands (360 and 407 nm) and a slight decrease in the green emission band at 495 nm if compared to the emission spectra when excited by 330 nm. If the phosphor is excited with 345 nm there is an increase in 360 nm emission band and a decrease in the 407 and 495 nm emission bands.

The fact that the 325 nm HeCd laser and the excitation in the Cary Eclips Xe lamp between 300 to 400 nm show the same broad green emission spectrum indicates that the emission spectrum is not influenced by the excitation source. Figure 5 shows a schematic diagram of the energy levels in the free Bi^{3+} ion and of the Bi^{3+} ion in the C_2 and S_6 sites. The $^3P_1$ level is splitting into two (^3A_u and ^3E_u) and three (^3A, ^3B and ^3B) sub levels in the S_6 and C_2 symmetry sites respectively [11,16]. All the excitation bands are assigned to the $^1S_0 \rightarrow {}^3P_1$ transitions of the Bi^{3+} ion, in the multiple independent crystallographic cation sites, S_6 and C_2[1,7].

Figure 6 represent the chromaticity co-ordinates of the PL spectra for Y_2O_3:Bi, which were determined using the Commission Internationale de I'Eclairage (CIE) coordinates system. The algorithm is based on such intuitive color characteristics as tint, shade and tone. The coordinate system is cylindrical, and the colors are defined inside a hexcone. The algorithm also shows the position of the co-ordinates in the chromaticity diagram and the expected color of the material [17]. The calculated chromaticity coordinates for Bi^{3+} in the blue site (S_6) and the green site (C_2) are (0.16, 0.09) and (0.197, 0.320) respectively. It can be concluded that, two different chromaticity coordinates can be achieved from one luminescence center under different excitation bands.

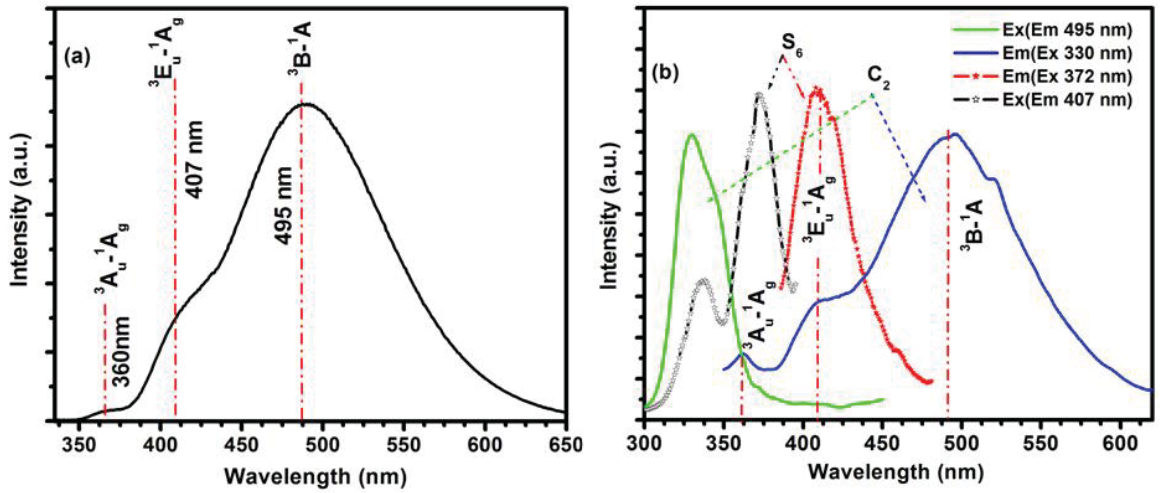

Figure 4: PL spectra of $Y_{2-x}O_3$:$Bi_{x=0.002}$ measured with (a) a 325 nm He-Cd laser and (b) with the Cary Eclipse Xe lamp.

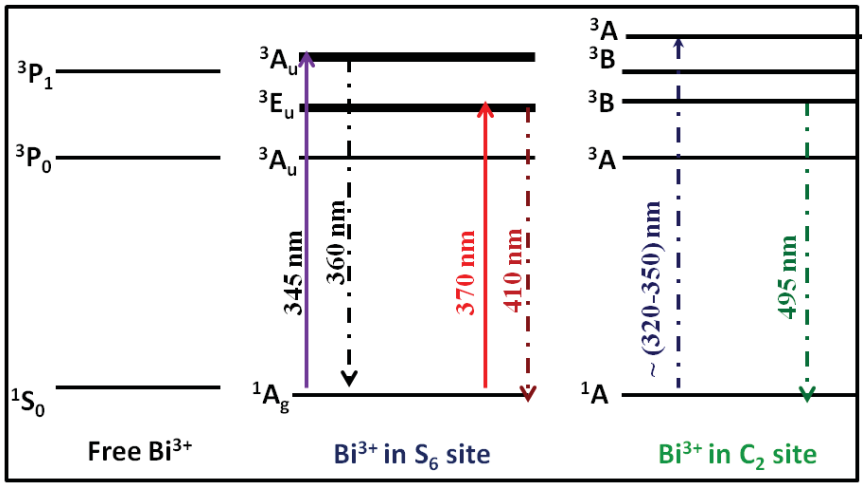

Figure 5: Schematic diagram of the energy levels of the Bi^{3+} ion [11].

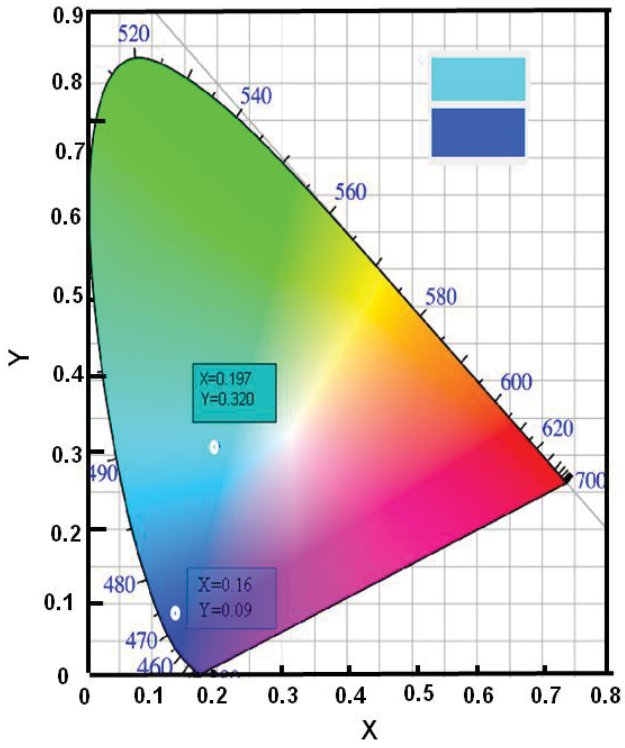

Figure 6: The calculated chromaticity coordinates for Bi^{3+} in the two different sites (S_6 and C_2)

4. Conclusion

The XRD results showed that the sample was successfully prepared by the combustion method and that the single cubic crystal structure phase with Ia-3 space group was formed. The DR spectra for the doped sample showed three bands located around 255, 330 and 372 nm. These bands are attributed to the O^{2-}- Bi^{3+} charge transfer (CT) absorption to the different sites (C_2 and S_6 respectively). The calculated band gap that was found to be almost 5.65 ± 0.1 eV for both the host and the doped sample indicated that the band gap is not affected by doping the host with Bi. The PL results showed that the phosphor have two emission bands centered at 360 and 407 nm for blue emission and a third band

centered at 495 nm for green emission. The excitation spectra showed 4 bands that corresponds to the $^1S_0 \rightarrow {}^3P_1$ transitions in the Bi^{3+} ion in the two different sites (S_6 and C_2). Excitation with the two main peaks at 330 and 372 nm result in broad green emission for the C_2 site and only blue emission for the S_6 site. Further investigations will be done with X-ray photo-electron spectroscopy to proof the two different sites that will contribute to the luminescent mechanism.

5. Acknowledgment

This work is based on the research supported by the South African Research Chairs Initiative of the Department of Science and Technology and National Research Foundation of South Africa. The University of the Free State Cluster program for financial support. We would like to thank Dr. R.E. Kroon for helping in the 325 nm He-Cd laser PL system.

References

[1] Huang X Y, Ji X H, Zhang Q Y 2011*American Ceramic Society* **94** 833
[2] Gorbenko V, krasnikov A, Mihokova E, Nikl M, Zazubovich S, Zorenko Yu 2013 ***J.****Luminescence* **134** 469
[3] Bordun O M, 2002 *Applied Spectroscopy* **69** 1
[4] Ju G, Hu Y, Chen L, Wang X, Mu Z, Wu H, Kang F 2011 *Electrochemical Society* **158** 294
[5] Huang X Y, Ji X H, Zhang Q Y 2011 *The American Ceramic Society* **94** 833
[6] Kumar V, Kumar R, Lochab S P, Singh N 2007 *Science Direct* **262** 194
[7] Jacobsohn L G, Blair M W, Tornga S C, Brown L O, Bennett B L 2008 *J. Applied Physics* **104** 124303.
[8] Schamps J, Flament J P, Real F, Noiret I 2003 *Optical Materials* **24** 221
[9] Babin V, Gorbenko V, Krasnikov A, Makhov A 2009 *J. Physics:Condensed Matter* **21** 415502
[10] Som S, Sharma S K 2012 *J. Physics D: Appied Physics.* **45** 415102
[11] Ju G, Hu Y,. Chen L, Wang X, Mu Z, Wu H, Kang F 2011 *J. The Electrochemical Society*. **158** 294
[12] Real F, Ordejon B, Vallet V, Flament J P, Schamps J 2009 *J. Chemical Physics* **131** 194501
[13] Chi L S, Liu R S, Lee B J 2005 *J. The Electrochemical Society* **152** 93
[14] Bordun O M 2002 *J. Applied Spectroscopy* **69**1
[15] Craats A M V D, Blasse G 1995 *Chemical Physics Letter* **234** 559
[16] Ju G, Hu Y, Chen L, Wang X, Mu Z,Wu H, Kang F 2012 *J. luminescence* **132** 1859
[17] Yousif A, Swart H C, Ntwaeaborwa O M 2013 *J. Luminescence* **143** 201
[18] Huang Z, Guo W, Liu Y, Huang Q, Tang F, Cao Y 2011 *Materials Chemistry and Physics* **128** 44
[19] Toma S Z,.Palumbo D T 1969 *J. Electrochemical Society*: Solid State Science**116** 2

Effect of synthesis temperature on the structure, morphology and optical properties of PbS nanostructures prepared by chemical bath deposition method

LF Koao[1], FB Dejene[1*] and HC Swart[2]

[1]Department of Physics, University of the Free State (Qwaqwa Campus), Private Bag X13, Phuthaditjhaba, 9866, South Africa
[2]Department of Physics, University of the Free State, P.O. Box 339, Bloemfontein, 9300, South Africa.

*Corresponding author: Tel: +27 58 718 5307; Fax: +27 58 718 5444; E-mail: dejenebf@ufs.ac.za

Abstract. Lead sulfide (PbS) powders were prepared by chemical bath deposition (CBD) method by varying the synthesis temperatures. The influence of the synthesis temperature on the structure, morphology and optical properties of PbS nanostructures were investigated. The X-ray diffraction (XRD) patterns of the PbS nanostructures correspond to the various planes of a single phase cubic PbS. It was observed that a decrease in the synthesis temperature resulted into additional diffraction peaks due to the presence of impurity phases. It was observed that the estimated average grain sizes from XRD analysis increased slightly with an increase in the synthesis temperature. The crystallinity of the cubic PbS improved significantly with an increase in synthesis temperature. The surface morphology study revealed nanorod structures at low synthesis temperatures but a cubic structure at the high synthesis temperatures. The reflectance spectra showed a partially increase in percentage reflectance and shift of the absorption edge to a higher wavelength with an increase in the synthesis temperature. An additional absorption band in the visible region (647 nm) emerged with an increase in the synthesis temperature. The band gap energy of PbS was found to decrease with an increase in the synthesis temperature. The maximum luminescence intensity was found at a synthesis temperature of 55 ºC.

1. Introduction

In recent years, interest in the development of the semiconductor nanostructured materials has grown rapidly owing to their unique physical and chemical properties [1]. This is due to their potential application in the area of solar cells, optoelectronic devices, photoconductors, sensor and infrared detector devices. Their attractiveness arises from their low synthetic cost, their solution processing ability and the dependence of their optoelectronic properties as a function of size, shape, doping and surface chemistry [2-3]. PbS nanocrystals are attractive for infrared-related applications because the energy of their first excitonic transition can be easily tuned from the visible to the infrared [4]. As its large exciton Bohr radius (18 nm) [5-6], the effects of strong quantum confinement can be achieved even for relatively large structures [7]. The band gap energy of PbS can changed from 0.39 to the values up to 5.2 eV by varying the shape and size from the bulk materials to nanocrystal structures [8].The preparation of PbS has been explored by a number of methods including sonochemical [5], liquid phase synthesis [9], chemical bath deposition [10] and gas phase synthesis [11]. We have selected chemical bath deposition method owing to its many advantages such as low cost, large area production and simplicity in instrumental operation. The aim of this paper is to investigate the effect of synthesis temperature on the structure, morphology and optical properties of PbS nanoparticles prepared by chemical bath deposition method.

2. Experimental

The preparation of PbS powders were carried out using the following procedure: The PbS precursors were prepared by dissolving 0.13 M of lead acetate, 0.18 M of thiourea and 98.8 mL of ammonia in 400 mL of deionised water, separately. During the preparation of the nano-powders, ammonia was used as a complexing agent. The chemical bath solution was prepared as follows: 60 mL of a lead acetate, thiourea and ammonia solutions were mixed. The amount of solutions of lead acetate, thiourea and ammonia was held constant at ratio of 1:1:1. Each mixture was continuously stirred for 10 minutes whilst varying the synthesizing temperature at 55, 65, 70 and 80ºC, respectively. The PbS particles were washed with 60 mL of acetone and ethanol in that order. The precipitates formed were left overnight and then filtered. The obtained particles were dried at ambient conditions for 5 days and ready to be characterized using various characterization technique. The particle size and morphology and the structural and luminescent properties of the as-synthesized phosphors were examined by means of scanning electron microscopy (SEM), X-ray diffraction (XRD), Uv-vis spectroscopy and Photoluminescence (PL).

3. Results and Discussion

3.1 Structural analysis and Composition analysis

Figure 1(a) shows XRD patterns of PbS powders synthesized at various bath temperatures such as 55, 65, 70 and 80 ºC. All XRD patterns show four maximum peaks observed in the diffractogram at around 2θ= 25.99, 30.11, 43.09 and 51.03º. All these peaks corresponding to the cubic phase of PbS matched well with the standard JCPDS card no. (05-0592, a= 5.936 Å). The estimated average value of the cell constant a is 5.934 Å which match perfectly with the standard data. No significant changes were observed for lattice parameter with the variations of the synthesis temperature.

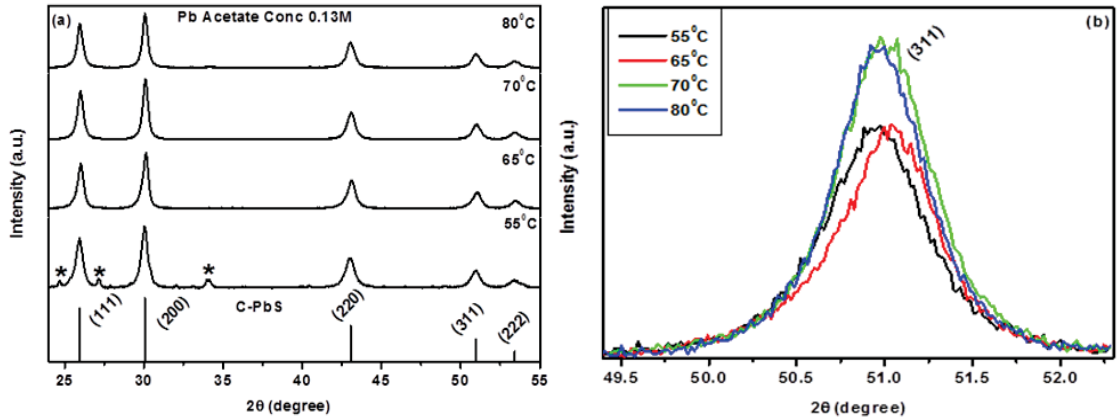

Figure 1. X-ray powder diffraction patterns of PbS (a) prepared at different synthesis temperatures and (b) X-ray powder diffraction patterns of the (111) planes of the PbS powders prepared by the CBD method.

The PbS powder prepared at 55 ºC shows extra peaks which are marked with a star (*) and are due to unreacted lead acetate oxide hydrate due to the low synthesizing temperature. This is confirmed by the JCPDS card no: 18-1740. However, as the bath temperature was increased from 65 to 80 ºC the extra peaks disappear and the intensity of the peaks attributed to PbS improved as shown in Fig. 1(b). This improved intensity with well-defined sharper peaks indicates a high crystallinity of the prepared material. This means that the grain sizes of the PbS powders increases with an increase in the

synthesise temperature. The increase in grain size with an increase in synthesis temperature is due to the "Ostwald ripening process" [12]. The average grain size of the as-prepared nanocrystals can be calculated from the Full Width Half Maximum (FWHM) of the diffraction peaks using the Debye-Scherrer formula [13]. All major diffraction peaks for all samples were chosen to estimate the average size of the nano grains by the least square method. From Fig. 2 it is clear that the estimated average particle size increased slightly with an increase in synthesis temperature.

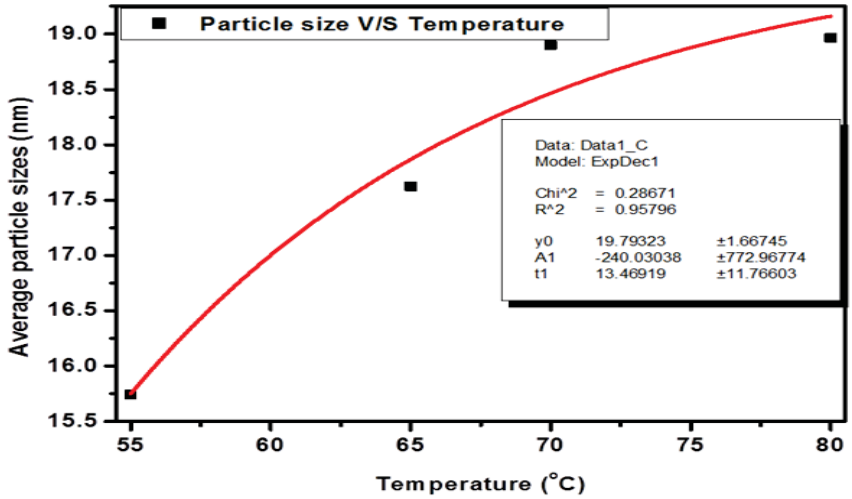

Figure 2. The dependence of average grain sizes of the PbS on the the synthesis temperature of the CBD.

3.2 Surface morphological analysis

Figure 3 (a), (b), (c) and (d) show surface morphologies of the PbS powders synthesized at various temperatures ranging from 55 to 80 ºC. All the samples were taken at 10 keV with a 0.05 nm field of view. The surfaces aspects of the SEM images of the PbS powders are composed of uniform nanorods structures for the synthesis temperature of 55 to 70 ºC, however, the grain size have slightly increased in size with an increase in the synthesis temperature.

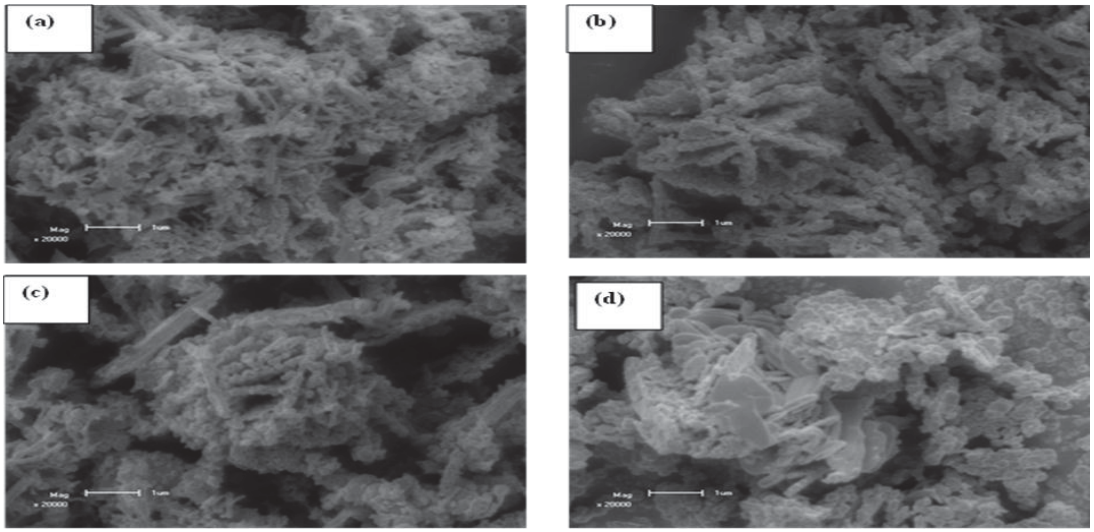

Figure 3: The SEM micrograph of PbS powders synthesized at the various temperatures: (a) 55 ºC, (b) 65 ºC, (c) 70 ºC and (d) 80 ºC.

With further increase in the synthesis temperature to 80 ºC, the nanorods structure broke up in mixed structures with the emergence of spherical nanoparticle and plates-like shapes.

3.3 Optical properties

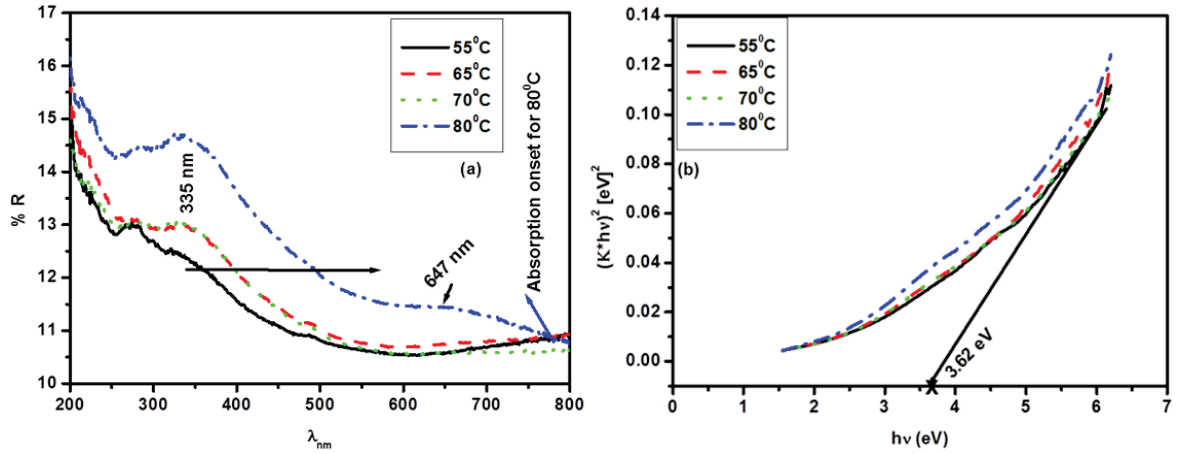

Figure 4. (a) The absorbance spectra and (b) plot to determine the band gap energy of PbS powders prepared at various temperature by the CBD method. The Eg value is marked with a cross.

The UV-visible reflectance spectra of the as prepared samples are illustrated in Figure 4(a). The optical spectra of the samples prepared at 55, 65 and 70 ºC have an absorption onset at about 550 nm, meanwhile in the spectra of the sample prepared at 80 ºC, the onset is observed at about 780 nm. The absorption edge is strongly shifted to higher wavelengths. In addition, the three optical spectra at temperature between 55 and 70 ºC display one well-defined absorption band with a maximum at about 335 nm. At synthesis temperature of 80 ºC an extra absorption band emerges with a maximum at around 647 nm. We can ascribe the origin of the absorption bands at 335 and 647 nm to $1s_e$-$1s_h$ and $1p_e$-$1p_h$ transitions in PbS nanoparticles, respectively [14-15].
Figure 4(b) shows the plot of the band gap energy synthesized at various temperatures estimated using the Kubelka-Munk function remission function [16] for direct transitions. The results reveal that the band gap energy decreased slightly when the synthesis temperature was increased. The value of Eg was determined by plotting tangent line (black solid line) to the curves. The obtained Eg values were found to be 3.63, 3.57, 3.12 and 2.87 eV as synthesis temperature was increased from 55, 65, 70 to 80 ºC, respectively. Their average error analysis is ± 0.35 eV. The decrease in band gap energy and the shift of absorption edges to higher wavelengths can be attributed to the increase in grain size with an increase in synthesis temperature. This result correlates well with the data obtained from the XRD and SEM analysis. The estimated band gap energies are larger than the theoretical band gap (0.39 eV) [17].

3.4 Photoluminescence
Figure 5 depicts the room temperature excitation spectrum of the PbS nanostructures. It can be seen that the excitation spectrum consists of a broad band with a maximum peak at 277 nm whose intensity decreases with the increase in synthesizing temperature. The absorption band may correspond to the $1d_h \rightarrow 1d_e$ transition of PbS **[18-20]**. Figure 6 and 7 shows the PL emission spectra of the PbS nanostructures excited at 277 nm. The emission spectra depict the peaks at around 338, 378 and a less intense broad peak at around 726 nm with a shoulder at around 825 nm. The peaks are associated to the electronic transitions from the $1p_e \rightarrow 1p_h$ (345 nm) and $1s_e \rightarrow 1p_h$ (376 nm) energy levels [18, 21 - 22]. The emissions at 338 nm which arises from the recombination of excitons and/or shallowly

trapped electron-hole pairs. The emissions at around 725 and 825 nm are deep level defects. It is clear that the emission bands of the PbS nanostructures did not change, only the emission intensity changed as the synthesis temperature increased. The relative decrease of the PL intensity with the increase in the synthesis temperature, suggested the depletion of the grains which plays a major role in decreasing the defect densities. In other words, their gradual decrease of PL emission intensities reveals a significant decrease in the surface/volume ratio for high temperature grown samples. In this work it was very interesting to find that the grain sizes, morphology, optical and luminescence properties of PbS nanostructures depend on the synthesis temperatures.

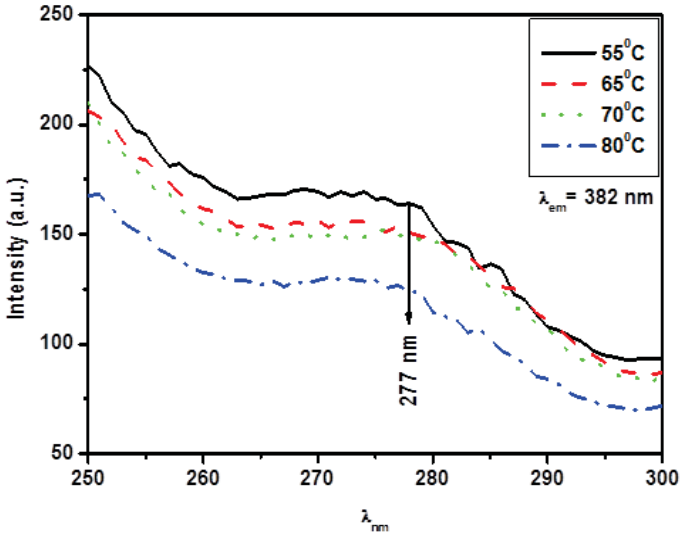

Figure 5. PL excitation spectra of PbS nanostructures prepared at various synthesis temperature emitted at λ_{em} = 382 nm.

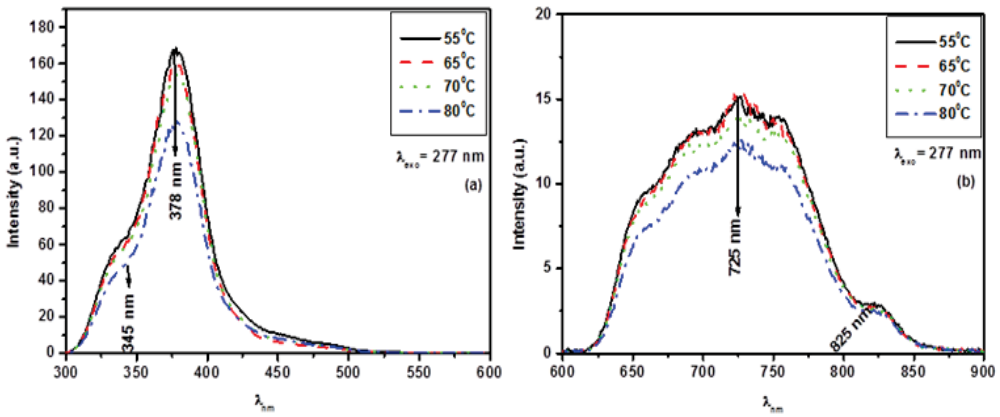

Figure 6. PL emission spectra of PbS nanostructures (a) in visible region and (b) for infrared region synthesized at various synthesis temperatures.

4.1 **Conclusion**

The PbS nanostructures have been successfully synthesized by the chemical bath deposition technique at 55, 65, 70 and 80°C. XRD showed that the structure of the material obtained is cubic PbS. UV spectroscopy showed that the band gap energy of the PbS nanostructures decreased with an increase in the synthesizing temperature. PL showed that the emission intensity of the nanostructures depends on the synthesizing temperatures.

Acknowledgement
The author would like to acknowledge the National Research Foundation, Department of science and technology and the University of the Free State for financial support.

Reference
[1] Xia Y N, Yang P D, Sun Y G, Wu Y Y, Mayers B, Gates B, Yin Y D, Kim F, Yan Y Q, 2003 A*dv. Mater*. **15** 353-389.
[2] Alivisatos A P, 1996 *J. Phys. Chem*. **100** 13226-13239.
[3] Erwin S C, Zu L, Haftel M I, Efros A L, Kennedy T A, Norris D J, 2005 *Nature*. **436** 91-94.
[4] McDonald S A, Konstantatos G, Zhang S, Cyr P W, E. Klem J D, Levina L, Sargent E H, 2005 *Nat. Mater*. **4** 138-142.
[5] Zhou S M, Zhang X H, Meng X M, Fan X, Lee S T, Wu S K, 2005 *J. Solid State Chem*. **178** 399–403.
[6] Zhu J, Liu S, Palchik O, Koltypin Y, Gedanken A, 2000 *J. Solid State Chem*. **153** 342-348.
[7] Dutta A K, Ho T, Zhang L, Stroeve P, 2000 *Chem. Mater.* **12** 1042-1048.
[8] Kumar D, Agarwal G, Tripathi B, Vyas D, Kulshrestha V, 2009 *J. of Alloys and Comp.* **484** 463-466.
[9] Wang C, Zhang W X, Qian X F, Zhang X M, Xie Y, Qian Y T, 1999 *Mater. Lett.* **40** 255-304.
[10] Koao L F, Dejene F B, Swart H C, SAIP'2011 Proceedings, the 56th Annual Conference of the South African Institute of Physics, edited by I. Basson and A.E. Botha (University of South Africa, Pretoria, 2011), p 151-155. ISBN: 978-1-86888-688-3.
[11] Kaito C, Saito Y, Fujita K, 1987 *Jpn. J. Appl. Phys*. **26** 1973-1975.
[12] Krichershy O, Stavan J, 1993 *Phys. Rev. Lett*. **70** 1473-1471.
[13] Cullity B D, 1956 *Elements of X-ray Diffraction (2nd Ed)*, (Addison Wesley) 285-284.
[14] Ai X, Guo L, Zou Y, Li Q, Zhu H, 1999 *Mater. Lett.* **38** 131-135.
[15] Babu K S, Vijayan C, Haridoss P, 2007 *Mater. Sci. Eng C*. **27** 922-927.
[16] RangaRao G, RanjanSahu H, 2001 *Proc. Indian Acad. Sci. (Chem. Sci)*. **113** 651-658.
[17] Z. Wang, B. Zhao, F. Zhang, W.Mao, G. Qian, X. Fan, Mater Lett. 61(2007) 3733–3735.
[18] Ai X, Guo L, Zou Y, Li Q, Zhu H, 1999 *Mater. Lett.* **38** 131-135.
[19] Babu K S, Vijayan C, Haridoss P, 2007 *Mater. Sci. Eng C*. **27** 922-927.
[20] Lu S, Sohling U, Krajewski T, Menning M, Schmidt H, 1998 *J. Mater. Sci. Lett.* **17** 2071-2073.
[21] Wang Z S, Yang S, 1999 *Chem.Mater.* **11** 3365-3369.
[22] Li L S, Qu L, Wang L, Lu R, Peng X, Zhao Y, Li T J, 1997 *Langmuir*, **13** 6183-6187.

Raman spectral analysis of an organometallic composite film synthesized by electrochemical route

Vijay Kumar[1, 2#], Y Ali[2], Vinod Kumar[1], R G Sonkawade[3], A S Dhaliwal[2] and H C Swart[1]

[1]Department of Physics, University of the Free State, P.O Box 339, Bloemfontein, ZA 9300, South Africa

[2]Department of Physics, Sant Longowal Institute of Engineering and Technology, Longowal Distt. Sangrur (Pb.)-148106, India

[3]School of Physical Sciences, BBA University (A Central University), Lucknow-226025, India

[#]Email: vj.physics@gmail.com

Abstract. The fabrication and characterization of Au-polyaniline (Au-PANI) composite films using electrochemical synthesis are presented. The PANI film is prepared by the chronopotentiometery technique on a Pt substrate. The as deposited PANI film was modified with Au nanoparticles using cyclic voltammetery. X-ray diffraction (XRD), Raman spectroscopy and Scanning electron microscopy (SEM) techniques were used to establish the structural-morphological properties of the Au–PANI composite. XRD spectra revealed (100) and (200) planes in the composite. A SEM image of PANI shows a rough and porous morphology, whereas Au-PANI composite exhibit a mesh type structure with uniform dispersion of the Au nanoparticles. It is observed that the Au-PANI composite showed enhanced Raman characteristics (due to the Surface Enhanced Raman Spectroscopy effect of the Au nanoparticles) in comparison to the pure PANI film. The analysis revealed that the Au-PANI composite can be used for highly sensitive and selective chemical and biological sensing applications.

1. Introduction

Organometallic composites offer a great opportunity to be exploited in sensing devices, catalysis materials, super capacitors, batteries, EMI, solar cells, etc. [1-4] The insertion of metal particles on the surface of polymers projects new ways and means to enhance the electrochemical, optical and electro catalytic performance thereof. It also broadens their applications in other diverse domains [5-7]. Various synthetic methods such as chemical, electrochemical, co-sputtering, sol-gel, self-assembly and radiolysis are adopted for the fabrication of organometallic composites [8-11]. In order to improve the functional properties of the Au-PANI composite a facile technique is reported by modifying the surface of the PANI films by Au-metal particles in an acidic solution. Recent studies confirm that metal conducting polymer composites are useful substrates for SERS (Surface Enhanced Raman Spectroscopy) [12-13]. These substrates are highly sensitive and cost effective.

Polynailine (PANI) is a conjugated polymer whose chain contains two types of nitrogen atoms: amine (–NH–) and imine (=N–). The chemical structure of PANI may be presented as follows:

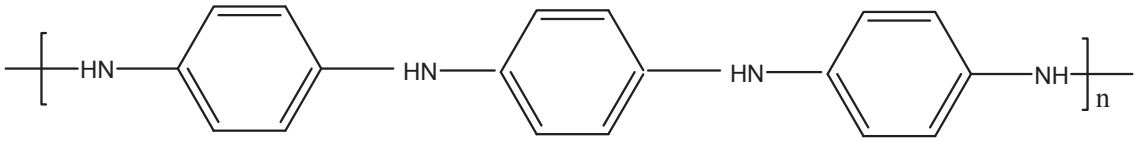

The ratio of imino nitrogen to amino nitrogen determines the conductive state of PANI. Nitrogen atoms present in the structure of PANI offers potential sites for PANI-metal complexes interaction and are responsible for the strong affinity towards the metal ions for modifying the functional properties in the organometallic composites.

In this study the electrochemical route is applied for the synthesis of rough surface PANI films. The surface is modified by Au particles to enhance its surface sensitivity.. In this synthesis process the nitrogen atoms are used as sites for a selective doping process and are responsible for the strong affinity with the Au^{2+} cations for modifying the functional properties in the composites. This work is related to the surface modification of PANI films by making the co-ordination between imine sties of PANI with the Au^{2+} cations. Chronopotentiometery is used for the fabrication of PANI films and later the synthesized surface of the films is modified by the Au-particles using cyclic voltammetry (CV) which shows strong redox reactivity occurring during synthesis. It should be noted that the system selected for the present studies are of practical importance due to their potential to improve the functional properties in chemical and biochemical sensing. This study shows the systematic interaction between metal and organic compounds.

2. Experimental

2.1. Material

Aniline monomer (Merck, 99.5% purity), pTS (Merck, 99%) and HNO_3 were used as starting materials in the present study. All the reagents were of analytical grade and used without further purifications. All the experiments were carried out with double-distilled water.

Electrochemical synthesis was carried out using a CHI 660D electrochemical workstation. The standard three electrode setup was employed in a one compartment electrochemical cell. A rectangular conducting indium tin oxide (ITO) sheet of size 20 × 10 × 0.7 mm^3 was used as a working electrode whereas a Pl sheet of size 20 × 40 × 0.25 mm^3 was used as a counter electrode. The reference electrode was an Ag/AgCl electrode. The first step involves the aqueous electro polymerization of aniline containing a 80 ml aqueous solution onto an ITO substrate using a chronopotentiometery technique. The electrolyte solution was composed of 0.15 M aniline monomer and 0.60 M pTS. The surface modification of the synthesized PANI film was conducted in an aqueous solution of 80 ml containing 0.0002 M $HAuCl_4$ and 0.005 M HNO_3 using CV between potential windows of 0.0 to 1.0 V at a scan rate of 30 mV s^{-1}. The surface of the PANI film was uniformly decorated with Au nanoparticles by controlling the scan rate and applied potential during the synthesis process. The thickness of the synthesized composite film was 20 ± 2 μm.

Scanning electron microscopy (SEM) images were obtained using a JSM-6490LV Joel at 25 keV after covered with a thin layer (~15 nm) of sputtered gold. The micro-RAMAN investigation was carried out using a Renishaw InVia Raman micro-scope. The Ar ion laser excitation at 514 nm at a very low power (<1 mW, 20× objective) was used to avoid any heating effects. X-ray diffraction (XRD) patterns of the Au-PANI composite film was recorded on a Phillips X-ray diffractometer with Cu-Kα radiation (1.54°A) for a wide range of Bragg's angle 2θ ($20^0 < \theta < 50^0$) at a scanning rate of 1^0 per min. The operating voltage and current for the X-ray gun were 40 kV and 40 mA, respectively.

3. Results and discussion

The electrochemical synthesis of PANI on ITO substrates using chronopotentiometery was investigated as a function of various reaction parameters that seem to influence the formation of the PANI films (Fig. 1). A porous film with a rough surface was obtained at a low polymerization potential during the first step of the electrochemical synthesis (see SEM images in the next section). The prepared film was immersed in an acidic solution of 0.005 M HNO_3 containing 0.0002 M $HAuCl_4$ for the surface modification of the PANI film using CV (Fig. 1). The scan rate was kept at 30 mV/s for less sweep segments in a potential range 0.0 V to 1 V during CV. The redox process is initiated with the dissociation of $HAuCl_4$ into cations and anions followed by further oxidation of the NO_3^- at the anode. The formation of Au ions and the subsequent reduction at the working electrode is well established as shown in Fig. 2. The cathodic peak indicates the reduction of Au-particles on the surface of the PANI film and the oxidation peak clearly represents the formation of imine nitrogen for reducing more Au-particles.

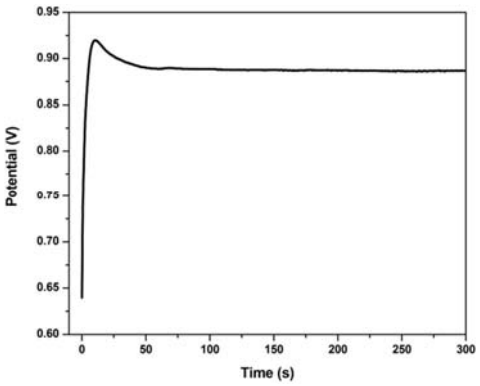

Fig. 1 Chronopotentiogram recorded during the synthesis of the PANI film.

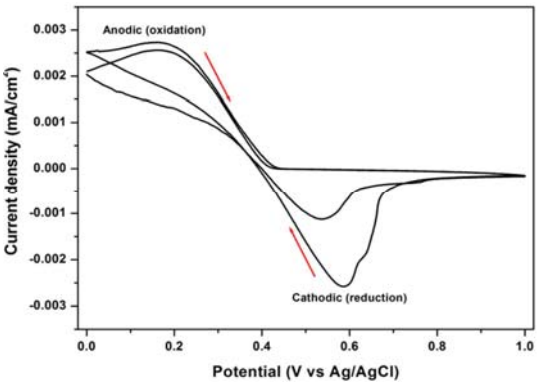

Fig. 2 The CV of the Au-PANI film between potential windows of 0.0 V to 1.0 V in a solution of $HAuCl_4$+HNO_3 in a ratio 0.0002:0.005, respectively with scan rate of 30 mV s^{-1}.

3.1. SEM results

SEM is carried out to provide confirmation of the PANI film and decoration of the film with Au nanoparticles on the surface of the PANI film. Fig. 3(a)-(b) shows the SEM images of the PANI and the Au-PANI composite films.

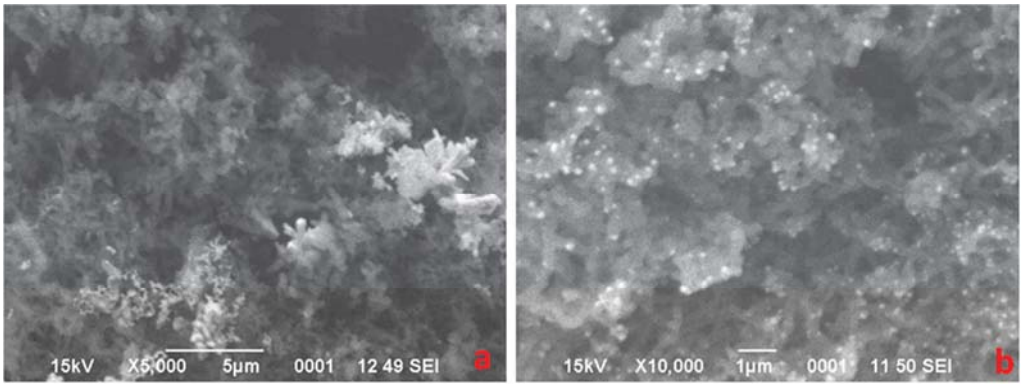

Fig. 3 SEM images of (a) PANI and (b) Au-PANI composite film

From Fig. 3(a), it is clear that the PANI film shows micro rods with a rough surface morphology. Moreover, the PANI film shows a fibrous network with porous structures.

Fig. 3(b) shows that Au particles were uniformly dispersed on the PANI surface indicate the coupling of the Au particles with the surface of the PANI film. The Au particles appear as white spots on the PANI film. Moreover, the image shows homogeneous distribution of the Au particles on the rough surface of the PANI film, which indicates their reliability in using as a SERS substrate [14-16].

3.2. X-ray diffraction analysis

The structural characteristics of the Au-PANI composite have been analysed by XRD and are shown in Fig. 4. The peaks between 2θ = 21.36°, 25.12 and 27.26° is the characteristic peaks of PANI [17]. The prominent peaks corresponding to 2θ = 38.12° and 44.28° are due to (111) and (200) planes of Au and indicate the presence of Au particles in the Au-PANI composite. Furthermore, it confirmed the Au particles retained its structure. Hence it is reasonable to accept that Au in the Au-PANI composite is accountable for the SERS and other properties.

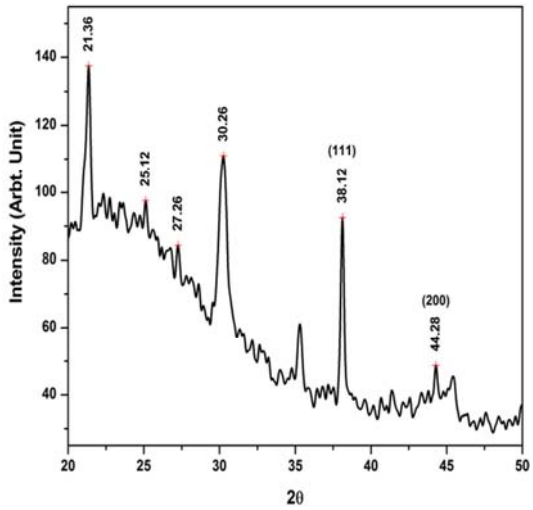

Fig. 4 XRD pattern of the Au-PANI composite film.

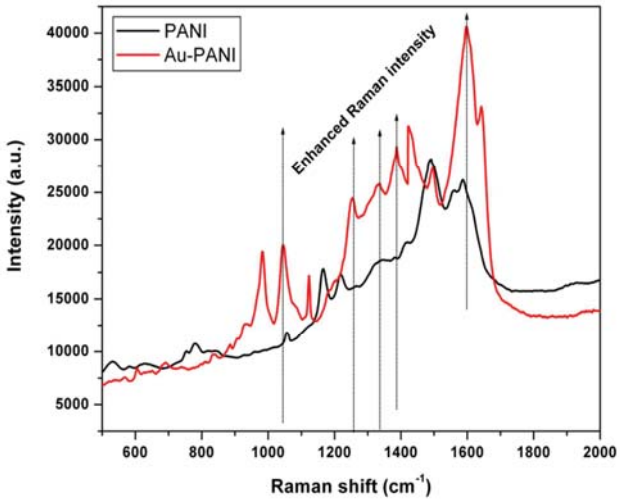

Fig. 5 Raman spectra of the PANI and Au-PANI composite films.

3.3. Raman studies of the Au-polyaniline composite film

The Raman spectra of PANI and Au-PANI composite films are shown in Fig. 5. The bands in the wavenumber range of 1100 to 1700 cm^{-1} corresponds to the stretching modes of different bonds. The benzene C–H bending deformation mode lies at 1140 to 1190 cm^{-1} for the reduced semiquinone and quinoid ring structure. The different C–N stretching mode (amines, imines, and polarons) lies between 1210 and 1520 cm^{-1}. The Raman band at 1586 cm^{-1} is attributed to the C–C stretching vibration of a benzene ring [18]. The band at 1254 cm^{-1} can be assigned to the C–N stretching mode of the polaronic units. The band at 1336 cm^{-1} corresponds to the $C–N^{\bullet+}$ stretching modes of the delocalized polaronic charge carriers [19]. A low intensity band at 1495 cm^{-1} corresponds to the bending deformation of the $N^{\bullet+}–H$ unit. The bands at 1320, 1340, 1478 and 1495 cm^{-1} are assigned to C-N, protonated C-N+, C=N and protonated $C=N^{+}$ according to literature [20]. The band at 1165 cm^{-1} represents the C-H bending vibration in the aromatic ring [21]. The observed Raman bands for PANI film are in good agreement with the literature [22].

It is interesting to compare the spectra of PANI with the Au-PANI composite. The Raman shifts and relative intensity observed in the PANI and Au-PANI spectra are listed in Table 1. The Raman spectrum of Au-PANI shows a doublet with bands at 1387 and 1421 cm^{-1} coupled with the $C–N^{\bullet+}$ polarons [23]. This doublet is consistent with the Raman spectrum of metallic PANI [24]. Here, remarkable increases in the intensity of the Au-PANI composite bands were observed with respect to pure PANI bands (Table 1). This remarkable increase in the Raman intensity may be due to the SERS

effect of Au-particles on the surface of PANI. This shows the strong interaction of Au ions with the imines sites of PANI after the reduction of Au ions on the nitrogen atom hence alteration of quinoid units into benzoid in the PANI backbone [25-26].

Baibarac et al. [14-16] investigated the SERS spectra of PANI thin films on rough Au, Ag and Cu substrates. They further suggested that SERS spectra of PANI depend on the oxidizing properties of the metallic surface which reflect that chemical reactions take place at the PANI/metal interface. Barnard and Goff [27] reported a significant enhancement in the band at 1350 cm^{-1} for PANI with Au particles. According to them this band is related to vibrations due to C-N segments. Saheb and Seo [25] reported that the enhancement at 1350 cm^{-1} is more significant when the PANI was electro polymerized in the presence of gold nanoparticles. This clearly shows the enhanced Raman scattering in Au-PANI composites. This suggests that surface decoration of PANI films with Au particles enhances the Raman intensity [26].

Table 1 Band position and Raman intensity for PANI and Au-PANI composite

Polyaniline		**Au-polyaniline**	
Band position (cm^{-1})	Intensity (a.u.)	Band position (cm^{-1})	Intensity (a.u.)
1586	26178	1597	40629
1491	28137	1495	27329
1218	17304	1421	31271
1165	17826	1387	29324
1056	11790	1254	24448
778	10763	1123	17196
531	9044	1044	20055
		983	19412
		690	8948
		604	8413

4. Conclusion

Au-PANI composite films have been synthesized successfully with a two steps electrochemical technique. XRD patterns confirmed the presence of Au particles in the composite. Interestingly, the Raman spectrum of the Au-PANI composite shows significant enhancement in the Raman intensity. SEM image shows porous and rough surface morphology of the PANI film reflecting better substrates for SERS activity. This enhancement in the Raman intensity in the Au-PANI composite film indicates their possible use in the chemical and biochemical sensing applications.

Acknowledgment

The research is supported by the South African Research Chairs Initiative of the Department of Science and Technology and National Research Foundation of South Africa. The University of the Free State Cluster program for financial support.

References

[1] Manners I 2001 *Science* **294** 1664
[2] Lee H S, Choi J, Jin J, Chun J, Lee S M, Kim H J and Son S U 2012 *Chem. Commun.* **48**, 94
[3] Cao H, Sun X, Zhang Y and Jia N 2012 *Anal. Biochem.* **15** 111
[4] Avasthi D K, Mishra Y K, Kabiraj D, Lalla N P and Pivin J C 2007 *Nanotechnol.* **18** 125604

[5] Muzalev P A, Kosobudskii I D, Kul'batskii D M and Ushakov N M 2012 *Inorganic Mater.: Appl. Res.* **3** 40
[6] Giesfeldt K S, Connatser R M, De Jesús M A, Lavrik N V, Dutta P, and Sepaniak M J 2003 *Appl. Spectroscopy* **57** 1346
[7] Takele H, Schürmann U, Greve H, Paretkar D, Zaporojtchenkoa V and Faupel F, 2006 *Eur. Phys. J. Appl. Phys*.**33** 83
[8] Nesher G, Marom G and Avnir D 2008 *Chem. Mater.* **20** 4425
[9] Ali Y, Sharma K, Kumar V, Sonkawade R G and Dhaliwal A S 2013 *Appl. Surf. Sci.* **280** 950
[10] Mishra Y K, Chakravadhanula V S K, Schumann U, Kumar H, Kabiraj D, Ghosh S, Zaporojtchenko V, Avasthi D K and Faupel F 2008 *Nucl. Instrum. Meth. Phys. Res. B* **266** 1804
[11] Mishra Y K, Mohapatra S, Chakravadhanula V S K, Lalla N P, Zaporojtchenko V, Avasthi D K, and Faupel F 2010 *J. Nanosci. Nanotechnol.* **10** 2833
[12] Mack N H, Bailey J A, Doorn S K, Chien-An Chen, Gau H M, Xu P, Williams D J, Akhadov E A and Wang H L 2011 *Langmuir* **27** 4979
[13] Biswas A, Bayer I S, Dahanayaka D H, Bumm L A, Li Z, Watanabe F, Sharma R, Xu Y, Biris A S, Norton M G and Suhir E 2009 *Nanotechnol.* **20** 325705 (7pp)
[14] Baibarac M, Cochet M, Lapkowski M, Mihut L, Lefrant S and Baltog I 1998 *Synth. Met.* **96** 63
[15] Baibarac M, Mihut L, Louarn G, Lefrant S and Baltog I 2000 *J. Polym. Sci. Part B* **38** 2599
[16] Baibarac M, Mihut L, Louarn G, Mevellec J Y, Wery J, Lefrant S and Baltog I 1999 *J. Raman Spectrosc.* **30** 1105
[17] Mallick K, Witcomb M, Scurrell M and Strydom A 2009 *J. Phys. D: Appl. Phys.* **42** 095409 (9pp)
[18] Liu C, Zhang J, Shi G and Chen F 2004 *J. Appl. Polym. Sci.* **92** 171
[19] Tseng R J, Baker C O, Shedd B, Huang J, Kaner R B, Ouyang J and Yang Y 2007 *Appl. Phys. Lett.* **90** 053101
[20] Bernard M C and Goff A H L 1997 *Synth. Met.* **85** 1145
[21] Gniadek M, Bak E, Stojek Z, Donten M 2010 *J. Solid State Electrochem.* **14** 1303
[22] Mazeikiene R, Statino A, Kuodis Z, Niaura G, Malinauskas A 2006 *Electrochem. Commun.* **8** 1082
[23] Ciric-Marjanovic G, Trchova M and Stejskal J 2008 *J. Raman Spectrosc.* **39** 1375
[24] Engert C, Umapathy S, Kiefer W and Hamaguchi H 1994 *Chem. Phys. Lett.* **218** 87
[25] Saheb A H and Seo S S 2011 *Analyt. Lett.* **44** 1206
[26] Ali Y, Kumar V, Sonkawade R G, Shisrat M D, Dhaliwal A S 2013 *Vacuum* **93** 79
[27] Bernard M C and Hugot-Le Goff A 2006 *Electrochimica Acta* **52** 728

Synthesis of zinc oxide based nanophosphors by solution-combustion method

Vinod Kumar, H. C. Swart and O. M. Ntwaeaborwa
Department of Physics, University of the Free State,
Bloemfontein, ZA9300, South Africa
Email- vinod.phy@gmail.com, swarthc@ufs.ac.za
Tel. +27-514012926

Abstract.
Undoped and doped ZnO nanophosphors (NPr) were synthesized by solution-combustion method. Hexagonal wurtzite structures of ZnO were confirmed by the X-rays diffraction patterns. A broad band orange-red emission from 500 to 850 nm was obtained from the ZnO NPr prepared with the nitrate precursor which may be attributed to oxygen related defects. Terbium doped ZnO (ZnO:Tb) NPr has shown red-green coupled emission. The intensity of the luminescence decreased at higher concentration of Tb due to the formation of Tb_2O_3.

1. Introduction

The optical properties of ZnO studied using photoluminescence (PL), photoconductivity and absorption, reflect the intrinsic direct bandgap, a strongly bound exciton state and gap states due to the point defects [1, 2]. The PL spectra show ultra violet (UV) near band edge emission around 380 nm and defect related deep level emission (DLE), which depends upon the preparation methods and growth conditions. The visible emission is a result of DLE bands present in ZnO [3, 4]. It is important to understand the origin of these emissions for the development of highly efficient optoelectronic devices. A large number of studies on the luminescence properties of ZnO have been investigated and suggested that, the green and red emissions originated from oxygen vacancies (V_o) and zinc interstitials (Zn_i) [5–7]. Other authors have attributed the green emission to both V_o and zinc vacancies (V_{Zn}) [8, 9]. The violet-blue and blue emissions were attributed to Zn_i and V_{Zn}, respectively, in the DLE [10, 11]. The origin of the red emission peaks are attributed to deep level defects such as vacancies and oxygen interstitials, usually observed in the oxygen rich system [12, 13]. Rare-earth (RE) ions like Tb^{3+} are very attractive luminescent centers owing to the high color purity and luminescence efficiency [13].

In this paper, undoped and Tb doped ZnO nano-phosphors (NPr) were synthesized. The PL of undoped and Tb doped are studied and discussed.

2. Experimental details

ZnO NPr were synthesized using the combustion method. Both Zinc acetate dehydrate (ZA) and zinc nitrate tetra hydrates (ZN) were used as precursors, respectively. Zinc precursors and urea were mixed and dissolved in distilled water. A homogeneous solution was obtained after stirring for 20 min. The solution was transferred to a preheated muffle furnace maintained at a temperature of 450°C. All the liquid evaporated and a large amount of heat released resulted in a flame that decomposed there agents further and released more gases. The flame lasted for 60 s and the combustion process was completed within 5 min. These NPr were cooled down to room temperature and were ground gently using a pestle and mortar. Terbium nitrate pentahydrate was used as a dopant source for terbium (Tb). Dopant is used with varying doping concentration from 0.0 to 6.0 mol%.

The crystalline structure of the phosphor was analyzed using a Bruker D8 Advanced powder diffractometer. For chemical states and surface examination, X-ray photoelectron spectroscopy (XPS) using a PHI 5000 Versa probe equipped with monochromatic Al-K_α radiation (hν=1253.6 eV) was conducted. The photoluminescence data was recorded using a He-Cd laser excitation wavelength of 325 nm. The reflectance spectra were collected using a Perkin Elmer Lambda 950 UV-Vis spectrophotometer.

3. Results and discussion

XRD patterns of both the ZN and ZA ZnO NPr are shown in Figure 1. The intensity of the XRD peaks shows that the NPr are highly crystalline. The strong diffraction peaks at 31.71, 34.31 and 36.21° correspond to the (100), (002) and (101) planes of the hexagonal wurtzite structure of ZnO. The preferred orientation corresponding to the plane (101) is the most prominent peak [14].

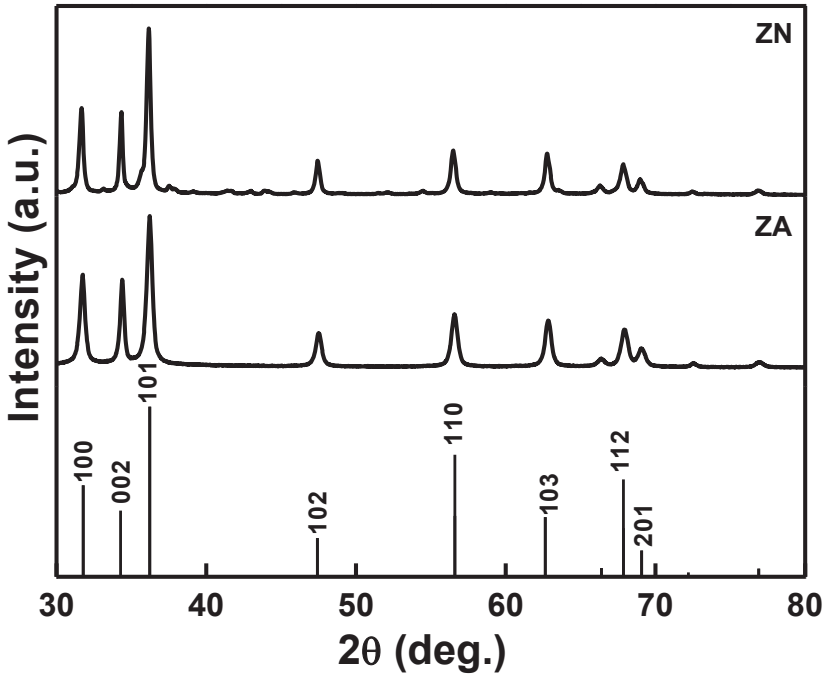

Figure1. XRD spectra of ZnO NPr.

Figure 2(a) displays the optical reflectance spectra of both the ZnO NPr. The ZA sample has less optical reflectance with respect to the ZN sample. It's due to a higher concentration of the defects (V_o) in the sample and provided luminescence killers. The optical bandgap of ZnO NPr is estimated by the extrapolation of the linear portion of the $(\alpha h\nu)^2$ versus $h\nu$ plots. The bandgap is calculated by Tauc's plot method [15]

$$(\alpha h\nu)^2 = A(h\nu - E_g) \quad (4)$$

Where, A is a constant, E_g is optical bandgap, h is plank constant and α is the absorption coefficient. The plot of $(\alpha h\nu)^2$ versus hν for different ZnO NPr is shown in Figure2(b). The bandgap of ZnO NPr was observed at 3.16 eV for both sample.

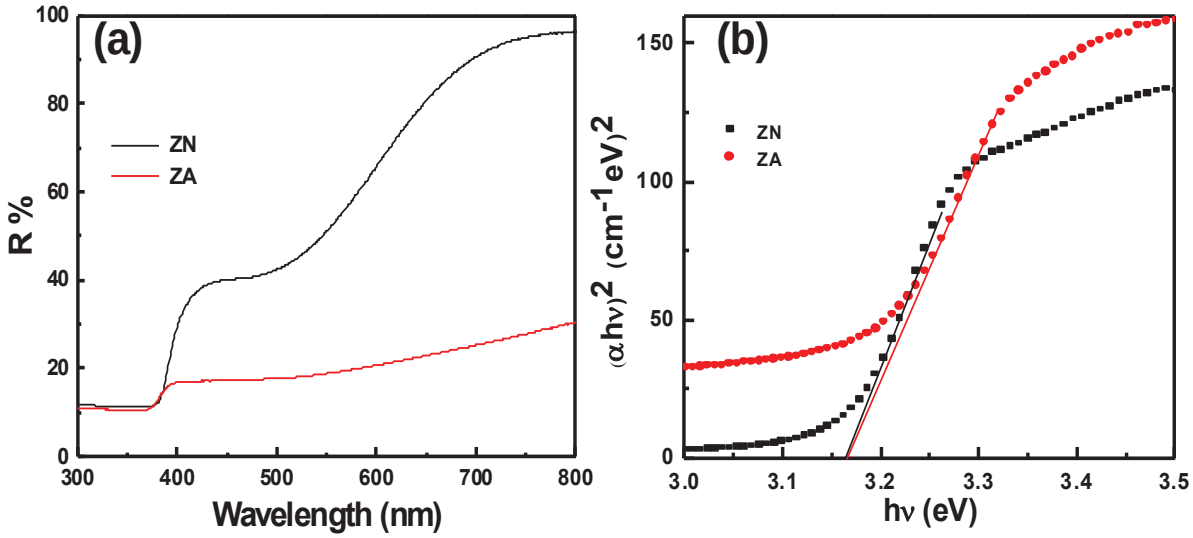

Figure 2. (a) Reflectance curve of ZnO NPr **(b)** band gap by tauc's plots.

Figure 3(a) and (b) shows the de-convoluted oxygen O 1s peaks. The component on the low binding energy side (O1 peak) on spectrum at 530.3±0.3 eV is attributed to O^{2-} ions on the wurtzite structure of a hexagonal Zn^{2-} ion array, surrounded by Zn atoms with their full complement of nearest neighbour O^{2-} ions [16]. In other words, the intensity of this component is a measure of the number of oxygen atoms in a fully oxidised stoichiometric surrounding. The medium binding energy (O2 peak) component centred at 531.2±0.3 eV is associated with O^{2-} ions that are in oxygen deficient regions with in the matrix of ZnO [17, 18] and/or Zn-OH groups [18, 19]. Therefore, changes in the intensity of this component may be partly connected to the variation in the concentration of oxygen defects (V_o or/and oxygen interstitial (Oi)). The higher binding energy (O3 peak) at 532.6±0.3 eV is usually attributed to chemisorbed species (such as CO_3, adsorbed H_2O or O_2) on the surface of the ZnO [18]. The intensity of the O3 peak has decreased after sputtered cleaning due to the removal of surface contaminants. After sputtering, the relative intensity of the O2 peak is much higher for the ZN with respect to the ZA sample, meaning that the concentration of oxygen defect is higher in the case of the ZN. Figure3(c) shows the XPS spectrum of Zn 2p. It contained a doublet, whose binding energies were at 1021.3 and 1044.4 eV, indicating that the Zn atoms were in the Zn 2p oxidation state.

Emission behaviour of ZnO NPr is shown in Figure 3(d). The main features of PL spectra of ZnO can be divided into two categories: near band edge emission and DLE. For the ZA sample, the emission band is composed of a strong UV band around 378 nm, an orange band around 614 nm and a red band around 753 nm. The UV emission band must be explained by a near band-edge transition, namely the free exciton recombination through an excition-excition collision process [20]. An orange-red band had also been observed and it is attributed to defects (O_i and V_o) in ZnO [21-23]. For the ZN sample, the UV band around 392 nm is very weak compared to the orange-red emission. The relative area of the XPS peaks compared to the PL fitted peaks suggests that the orange-red emission intensity and wavelength is definitely affected by the related defects.

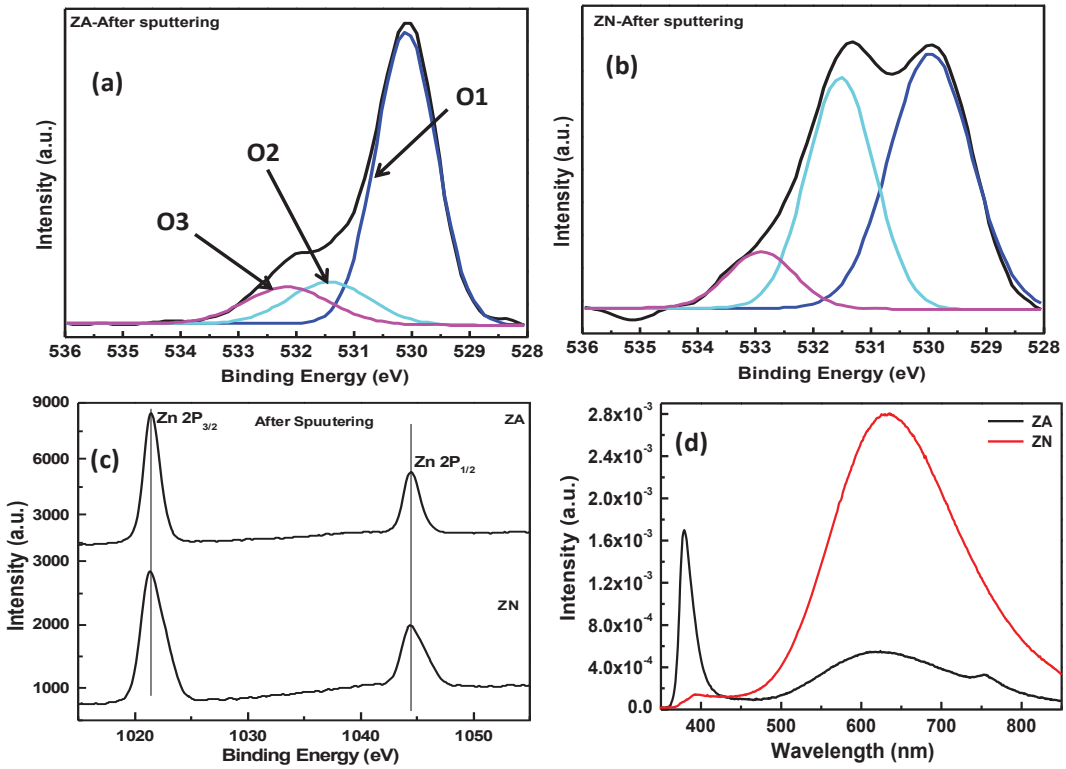

Figure 3. (a) XPS of ZA sample **(b)** XPS of ZN sample **(c)** XPS of Zn peaks **(d)** PL spectra of ZA and ZN.

The XRD spectra of ZnO:Tb with different Tb concentration is shown in Figure 4(a). The strong diffraction peaks at 31.71, 34.31 and 36.21° correspond to the (100), (002) and (101) planes of the hexagonal wurtzite structure of ZnO. At higher doping concentration some other peak is shown. It is due to the formation of Tb_2O_3.

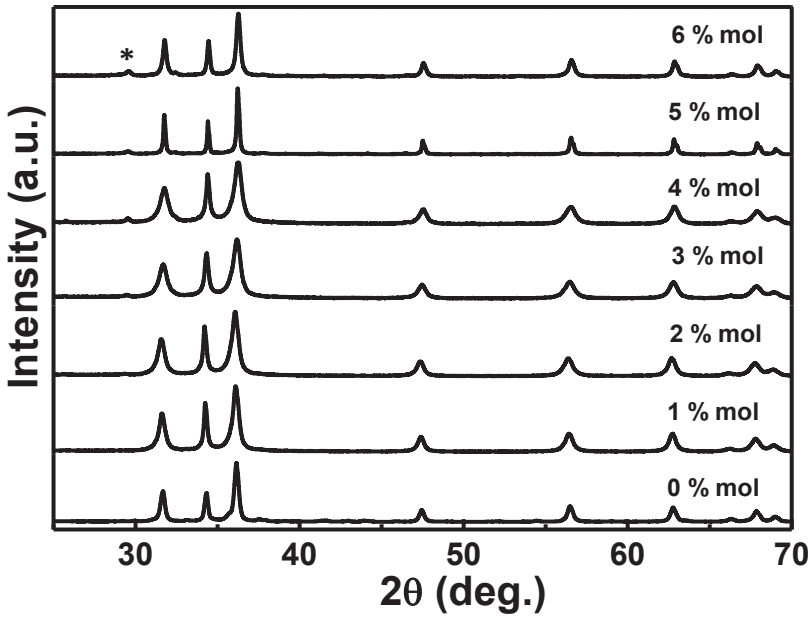

Figure 4. XRD curve of ZnO:Tb with different doping concentration of Tb.

XPS data of oxygen O1s peak ZnO:Tb is shown in Figure 5. In Figure 5 (a), the component on the O1, O2 and O3 peaks on the spectrum is attributed to the contributions discussed above. T higher doping concentration (6 mol%), Tb2O3 peak is also observed. It is attributed to the formation of terbium oxide.

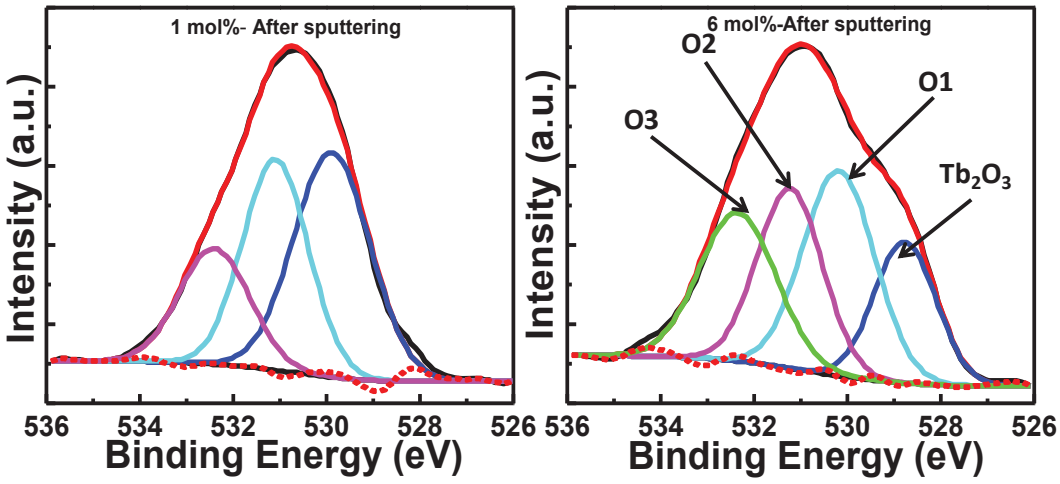

Figure 5. XPS of oxygen peak of ZnO:Tb after 30 sec of Ar sputtering for 1 and 6 mol% Tb.

Figure 6 (a) and (b) shows the PL spectra of ZnO:Tb with different doping concentration of Tb from 0 to 6 mol%. ZnO:Tb shows a green-red coupled emission of the ZN sample. The process of the energy transfer from the ZnO host to Tb through defect states may be described as follows. Firstly, a large amount of electrons are excited from the valence band to the conduction band of the ZnO host. Then non-radiative transition between the conduction band and the surface defects occurs, so the excited electrons may be trapped in the defects and the excitation energy of the ZnO host can be temporarily stored in the defect centers. Because of the short life span of these excited electrons, the energy rapidly transfers from the defects to the dopant ions, and then the higher excited states relax to the main emitting level, so the characteristic emission peaks of dopant ions are observed. As the electrons relax to the defect states of ZnO and recombine with the holes in the valence band, a broad luminescence was observed. The intensity of the $^5D_4$-$^7F_5$ peak has increased with the doping concentration up to 5 mol% of Tb after that it's decreased due to the formation of Tb_2O_3.

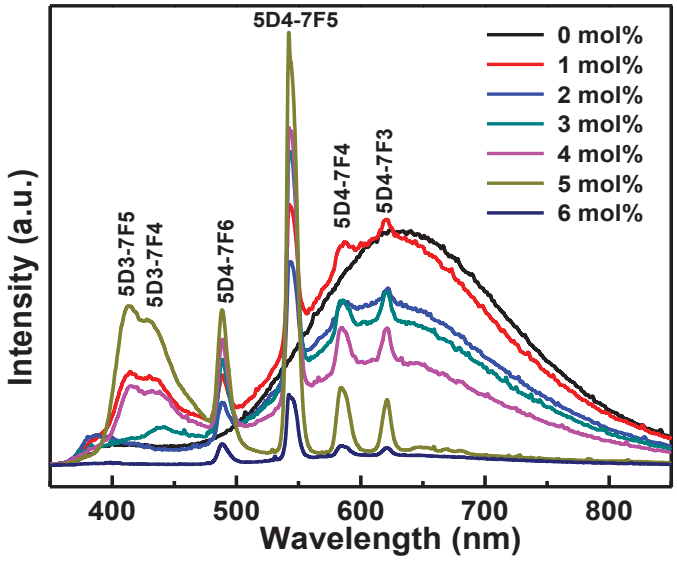

Figure 6. PL spectra of ZnO:Tb with different doping concentration of Tb.

4. Conclusion

Highly crystalline undoped and doped ZnO NPr were synthesized using the solution combustion method. The observed broad PL emission from 500-850 nm is attributed to a coupled emission of orange-red from ZnO. The red emission in ZnO NPr was observed due to the oxygen rich system. Zinc nitrate has shown a good red emission with respect to the zinc acetate based NPr. Orange-red coupled emission is observed in ZnO NPr due to the interstitial and vacancies of oxygen as confirmed by XPS O 1S data. ZnO;Tb NPr has shown green-red coupled emission.

Acknowledgments

This work is based on the research supported by the South African Research Chairs Initiative of the Department of Science and Technology and National Research Foundation of South Africa. The financial support from the Cluster program of the University of the Free State is highly recognised

References

[1] Gutowski J, Presser N, Broser I 1988 *Phys Rev B* **38**, 9746.
[2] Bethke S, Pan H, Wessels BW 1988 *Appl Phys Lett* **52,** 138.
[3] Gong Y, Andelman T, Neumark G, O'Brien S, Kuskovsky I 2007 *Nanoscale Res Lett* **2,** 297
[4] Look DC 2001 *Mater Sci Eng B* **80**, 383.
[5] Yang LL, Zhao QX, Willander M, Yang JH, Ivanov I 2009 *J Appl Phys* **105,** 053503.
[6] Djurisic AB, Leung YH, Tam KH, Hsu YF, Ding L, Ge WK, et al. 2007 *Nanotechnology* **18**,095702
[7] Djurisic AB, Leung YH, Tam KH, Ding L, Ge WK, Chen HY, et al. 2006 *Appl Phys Lett* **88**, 103107
[8] Zhao QX, Klason P, Willander M, Zhong HM, Lu W, Yang JH 2005 *Appl Phys Lett* **87,** 211912
[9] Yamauchi S, Goto Y, Hariu T 2004 *J Cryst Grow* **260,** 1
[10] Cao B, Cai W, Zeng H 2006 *Appl Phys Lett* **88,**161101
[11] Zeng H, Li Z, Cai W, Liu P 2007 *J Appl Phys* **102**, 104307.
[12] Wu L, Wu Y, Pan X, Kong F 2006 *Opt Mater* **28**, 418.
[13] Kumar Vinod, Swart HC, Ntwaeaborwa OM, Kroon RE, Terblans JJ, Shaat SKK, Yousif A Duvenhage MM 2013 *Materials Letters* **101**, 57.
[13] Devi SKL, Sudarsana Kumar K, Balakrishnan A. 2011 *Materials Letters* **65,** 35.
[14] Singh N, Mehra R. M., Kapoor Avinashi, Soga T 2012 *J. Renewable Sustain Energy* **4,** 013110.
[15] Kumar V, Singh RG, Singh F, Purohit LP 2012 *J. Alloys & Comp.* **544** 120.
[16] Chen M, Wang X, Yu YH, Pei ZL, Bai XD, Sun C 2000 *Appl Surf Sci* **158**, 134.
[17] Al-Gaashani R, Radiman S, Daud AR, Tabet N, Al-Douri Y 2013 *Ceram Int* **39**, 2283.
[18] Islam MN, Ghosh TB, Chopra KL, Acharya HN 1996 *Thin Solid Films* **280**, 20.
[19] Kim YS, Tai WP, Shu SJ 2005 *Thin Solid Films* **491,** 153.
[20] Ahn CH, Kim YY, Kim DC, Mohanta SK, Choa HK 2009 *J. Appl. Phys.* **105**, 013502.
[21] Kong YC, Yu DP, Zhang B, Fang W, Feng SQ 2007 *Appl Phys Lett* **78,** 407.
[22] Pierce BJ, Hengehold RL 1976 *J Appl Phys* **47,** 644.
[23] Studenikinm SA, Golegu N, Cocivera M 1998 *J Appl Phys* **84,** 2287.

Structural, electronic and mechanical stability of olivine $LiMPO_4$ (M: Mn, Fe, Co)

NL Lethole, HR Chauke and PE Ngoepe
Materials Modeling Centre, University of Limpopo, Private Bag X1106, Sovenga, 0727, South Africa

E-mail: Lesley.lethole@ul.ac.za

Abstract. First-principles calculations used to investigate the structural, thermodynamic, electronic and mechanical stabilities of $LiMPO_4$ crystal structures have been performed. The structural lattice parameters are in good agreement with the available experimental data to within 3 %. The independent elastic constants suggested mechanical stability of $LiMPO_4$ crystal structures. Lastly, the electronic density of states suggested that considered $LiMPO_4$ systems are metallic.

1. Introduction

Previous studies have shown that olivine lithium iron phosphate, $LiFePO_4$ is a promising cathode material for new generation of lithium rechargeable batteries. The following characteristics: low cost, non-toxicity, remarkable thermal stability, good electrochemical properties and environmental benign make this material a competitive candidate [1, 2]. Consequently, attention has also been shifted to the other olivine lithium transition metal phosphates such as $LiMnPO_4$ and $LiCoPO_4$. It is known that $LiFePO_4$ has an operating voltage of 3.45 V which is twice more than that of standard AA alkaline battery. Moreover, its theoretical capacity is relatively high (170 mAh/g) [2]. On the other hand $LiMnPO_4$ and $LiCoPO_4$ show operating voltages of 4.1 V and 4.5 V, and theoretical capacities of 171 mAh/g and 70 mAh/g, respectively [3, 4, 5].

$LiMPO_4$ (M: Mn, Fe, Co) is an ordered olivine orthorhombic system with space group *Pnma* where M and P atoms occupy half of the octahedral sites and quota of the tetrahedral sites in a hexagonal close-packed array of oxygen atoms, respectively (Figure 1). In this work, we present first-principles stability study on $LiMPO_4$ structures, particularly the thermodynamic, electronic and mechanical stability. The equilibrium lattice parameters, heats of formation, densities of states, phonon dispersion curves and elastic properties will be investigated to mimic the stability trend between $LiMPO_4$ structures.

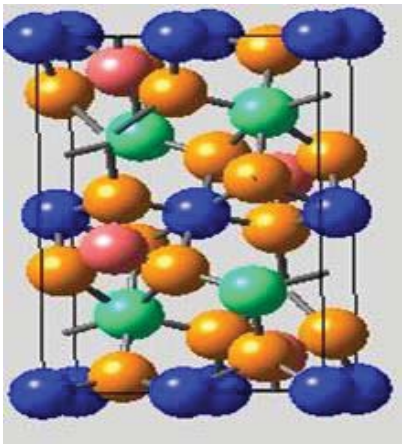

Figure 1: Schematic representation of olivine $LiMPO_4$ structure.

2. Methodology

First-principles calculations were performed using the density functional theory (DFT) method as implemented in the Vienna ab initio simulation package (VASP) [6]. The projector augmented wave (PAW) potential sets were used with the exchange and correlation energies approximation in the local density approximation with the Hubbard parameter correction (LDA+*U*) following the rotationally invariant. A plane wave basis set cut-off of 500 eV and k-mash of 4x6x6 were chosen since they were found to be sufficient to converge the total energy of the systems. Optimisation of structural parameters was achieved by minimisation of forces and stress tensors. Finally, the densities of states (DOS) were calculated using a smearing width of 0.05 eV using a Methfessel-Paxton smearing approach [7].

3. Results and discussion

Table 1. Structural lattice parameters, cell volumes, heats of formation, elastic constants andmoduli of $LiMPO_4$ polymorphs; the experimental data are in parenthesis.

Structure	$LiMnPO_4$	$LiFePO_4$	$LiCoPO_4$
a (Å)	10.52 (10.40)[a]	10.38 (10.30)[b]	10.42 (10.20)[c]
b (Å)	6.12 (6.09)[a]	6.06 (5.99)[b]	5.89 (5.92)[c]
c (Å)	4.78 (4.74)[a]	4.71 (4.69)[b]	4.73 (4.69)[c]
V ($Å^3$)	307.74 (300.21)[a]	296.27 (289.36)[b]	290.29 (283.20)[c]
Hf (kJ/mol)	-1340.45	-1184.49	-1097.25
C_{11}	167.61	209.56	152.17
C_{12}	82.33	117.29	68.83
C_{13}	79.07	99.83	61.75
C_{22}	199.84	270.49	192.50
C_{23}	63.41	80.53	51.42
C_{33}	200.78	249.58	199.33
C_{44}	49.99	56.89	47.67
C_{55}	62.56	72.27	59.67
C_{66}	54.79	62.10	58.33
B_H	113.00	146.80	100.53
G_H	55.77	65.97	56.53
E_H	143.67	172.13	142.83

[8][a] [9][b] [10][c]

3.1. Structural and thermodynamic properties

Presented in Table 1 are the structural lattice parameters, cell volumes, formation energies and elastic properties which have been calculated by performing full geometric optimization and are presented in table 1. We note that our calculated lattice parameters and cell volumes are in good agreement with the experimental values to within 3% which is reasonable for DFT transition metal phosphates calculations [11]. It is also observed that our calculated values slightly overestimate the experimental data except for the $LiCoPO_4$ lattice parameter b; however, the volume is overestimated as expected from DFT+*U* calculations. The heats of formation were calculated using expression 1.

$$\Delta H_f(LiMPO_4) = {}^{1}\!/_{N}[E - (E_{Li} + E_M + E_P + 4E_O)] \quad (1)$$

According to this expression, it was found that the $LiMPO_4$ structures show relatively low formation energy values, with the $LiMnPO_4$ (-1340.45 kJ/mol) displaying the lowest value. This suggests that the structure is the most stable over $LiFePO_4$ (-1184.49 kJ/mol) and $LiCoPO_4$ (-1097.25 kJ/mol), respectively.

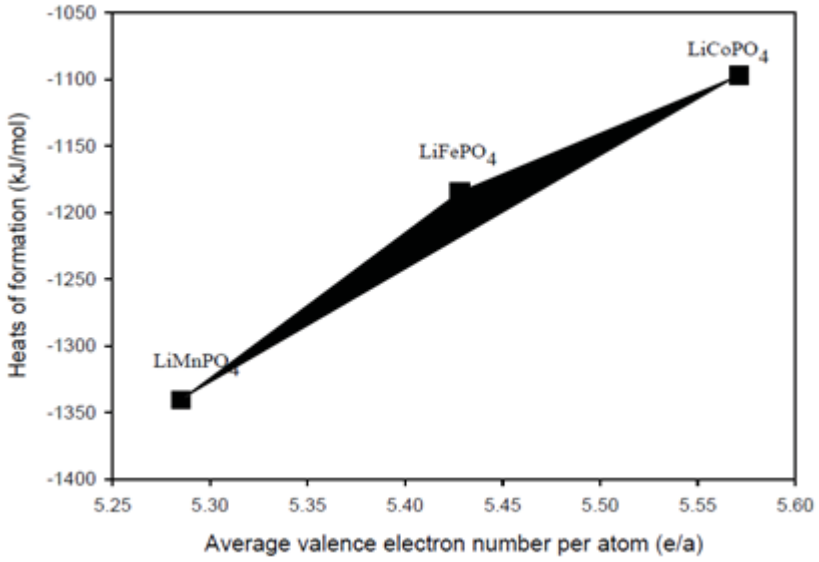

Figure 2 Heats of formation for $LiMPO_4$ structures as a function of the average number of valence electrons per atom (*e*/*a*).

The heat of formation for $LiMPO_4$ structures as a function of the average number of valence electrons per atom (*e*/*a*) is shown in Figure 2. It is clear from this figure that $LiMnPO_4$ has the lowest heat of formation as compared to $LiFePO_4$ and $LiCoPO_4$. This indicates highest stability for $LiMnPO_4$ structure over $LiFePO_4$ and $LiCoPO_4$, respectively. The observed linear trend predicts that the average number of valence electrons per atom increases with the heats of formation across the transition metal element (Mn, Fe and Co).

3.2. Electronic properties

The total densities of states of $LiMPO_4$ structures were calculated using the spin polarised DFT+*U* approach and presented in Figure 3.

$$N(E) = \int_E^{\Delta E} g(E)dE \quad (2)$$

Thus $g(E)dE$ represents the number of states between E and dE.

It was observed that all structures show relatively wide band gaps around the Fermi level. However, the Fermi level falls with the 3*d* M band suggesting the metallic behaviour characteristic of the $LiMPO_4$ systems, particularly for $LiMnPO_4$ and $LiFePO_4$. On the other hand the partial densities of states show that states around the Fermi level are mainly due to contribution from transition metal, M 3*d* electrons.

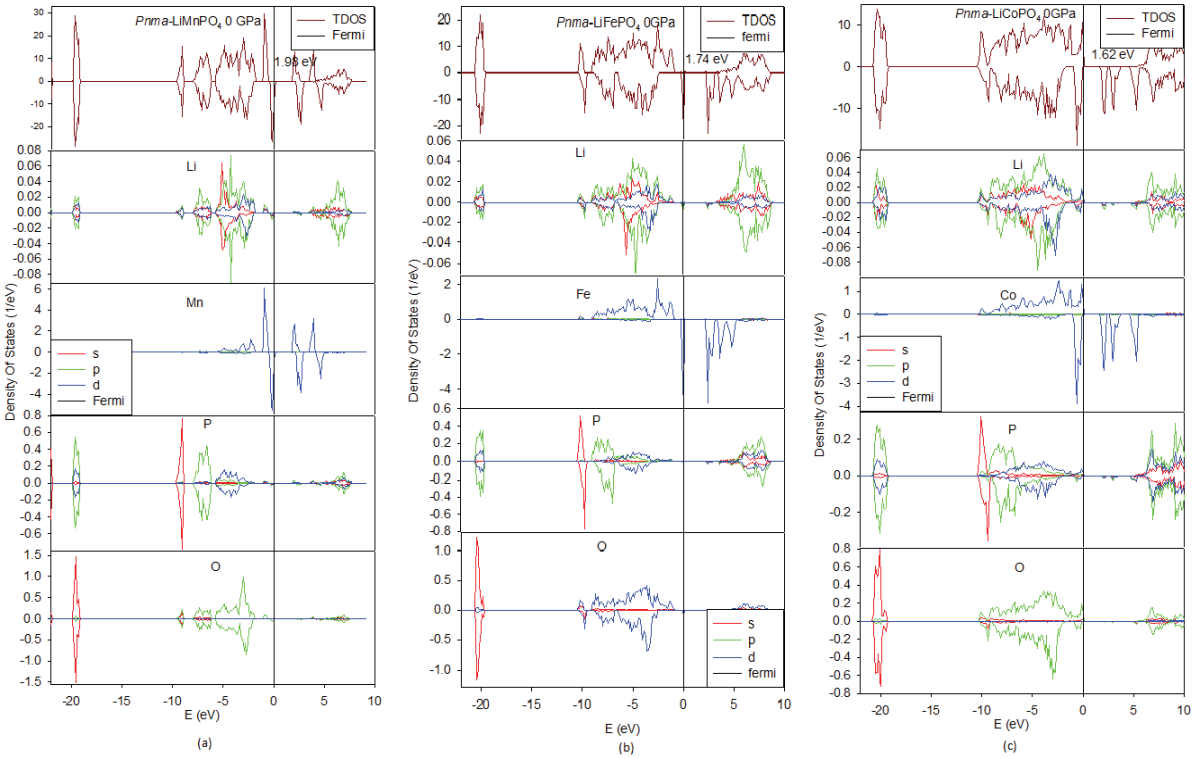

Figure 3. Total and partial densities of states of $LiMPO_4$ structures: (a) $LiMnPO_4$, (b) $LiFePO_4$ and (c) $LiCoPO_4$

3.3. Elastic properties

Elastic constants were calculated by means of Taylor expansion of the total energy as follows:

$$U(V,\varepsilon) = U(V_0,0) + V_0\left[\sum_i \tau_i\zeta_i\delta_i + \frac{1}{2}\sum_{ij} C_{ij}\zeta_i\delta_i\zeta_j\delta_j\right] \qquad (3)$$

where $U(V_0,0)$ is the unstrained system energy, V0 is the equilibrium volume while τ_i and ζ_i are elements in the stress tensor and factor to take of Voigt index, respectively. The orthorhombic $LiMPO_4$ crystals have nine (C_{11}, C_{12}, C_{13}, C_{22}, C_{23}, C_{33}, C_{44}, C_{55}, C_{66}) independent elastic constants [12] as listed in Table 1. The necessary mechanical stability conditions for orthorhombic systems are given as follows:

$(C_{11}+C_{22}-2C_{12})>0$, $(C_{11}+C_{33}-2C_{13})>0$, $(C22+C33-2C23)>0$,

$(C_{11}+C_{22}+C_{33}+2C_{12}+2C_{13}+2C_{23})>0$, $C_{11}>0$, $C_{22}>0$, $C_{33}>0$, $C_{44}>0$, $C_{55}>0$, $C_{66}>0$

It is clear from Table 1 that all the independent elastic moduli (Cij) are positive satisfying all the stability conditions; this suggests that all LiMPO4 structures are elastically stable. Their resultant bulk modulus B, shear modulus G and Young's modulus E were also obtained from the calculated elastic constants using the Hill method [13].

$$B_H = \frac{1}{2}(B_R + B_V) \quad (4)$$

$$G_H = \frac{1}{2}(G_R + G_V) \quad (5)$$

$$E_H = \frac{9B_H G_H}{G_H + 3B_H} \quad (6)$$

where V (upper limit), R (lower limit) and H (average) are Voigt, Reus and Hill, respectively.

The highest values of B, G and E are obtained for $LiFePO_4$, while $LiMnPO_4$ and $LiCoPO_4$ are comparable. The B and E values suggest hardness and Stiffness, respectively of materials. Furthermore, we note that G is less than B for all structures, implying that the Shear modulus is the limiting parameter for stability [14].

4. Conclusion

First-principles calculations on thermodynamic, structural, electronic and mechanical properties of $LiMPO_4$ crystals have been performed using DFT+*U* approach. From the calculated properties, the stability trend within $LiMnPO_4$, $LiFePO_4$ and $LiCoPO_4$ has also been determined. The calculated structural lattice parameters and equilibrium cell volume are in good agreement with the experimental data to within 3 %. The predicted heats of formation suggest that $LiMnPO_4$ is the most stable structure over $LiFePO_4$ and $LiCoPO_4$, respectively. Moreover, the independent elastic properties have shown that $LiMPO_4$ crystals are mechanically stable. There is a good agreement between the heats of formation and the electronic densities of states which are consistent with elastic stability.

Acknowledgements

This work has been done at the Materials Modelling Centre, University of Limpopo, supported by the National Research Foundation.

5. References

[1] Amine K, Yashuda H and Yamachi M 2000 *Electrochem. and Solid-State Lett.* **3** 178

[2] Padhi AK, Nanjundaswamy K and Goodenough JB 1997 *J. Electrochem. Soc*. **144** 1188

[3] Zhang Y, Sun C.S and Zhou Z 2009 *Electrochem. Commun.* **11** 1183

[4] Nakayama M, Goto S, Uchimoto Y, Wakihara M and Kitajima Y 2004 *Chem. Mat.* **16** 3399

[5] Wang L, Sun W, He X, Li J and Jiang C 2011 *Int. J. Electrochem. Sci.* **6** 2022

[6] Kresse G and Furthmüller J 1996 *Phys. Rev. B* **54** 1169

[7] Methfessel M and Paxton A 1989 *Phys. Rev. B* **40** 616

[8] Osorio-Guille´n JM, Holma B, Ahuja R and Johansson B 2004 *Solid State Ionics* **167** 221

[9] Sanchez MAE, Brito GES, Fantini MCA, Goya GF and Matos JR 2006 *Solid State Ionics* **177** 497

[10] Kubel F 1994 *Zeitschrift fuer Kristallographi* **209** 755

[11] Li G, Azuma H and Tohda M 2002 *Electrochem. Solid-State Lett.* **5** A135

[12] Patil SKZ, Khare SV, Tuttle BR, Bording JK and Kodambaka S 2006 Phys. Rev. B **73** 104118

[13] Hill R 1952 *Proc. Phys. Soc. A* **65** 349

[14] Shein IR and Ivanovskii AL 2008 *J. Phys. Conden. Mat.* **20** 415218

AES and TOF-SIMS measurements of In segregation in a polycrystalline Cu crystal

MJ Madito, HC Swart and JJ Terblans[1]

Department of Physics, University of the Free State, P O Box 339, Bloemfontein, 9300, South Africa.

E-mail: terblansjj@ufs.ac.za

Abstract. The bulk-to-surface segregation of In impurity in a polycrystalline Cu crystal was measured using Auger Electron Spectroscopy (AES) and time-of-flight secondary ion mass spectrometry (TOF-SIMS) coupled with a programmable heater. AES segregation measurements were carried out using constant temperatures in the temperature range 733 K to 853 K. The measured AES data showed that In segregate to the surface and it has reached a relative high surface concentration on the Cu surface. The AES In segregation data was fitted with the semi-infinite model of Fick's equation to obtain the In bulk diffusion parameters ($D_0 = 1.1 \times 10^{-5}$ m^2 s^{-1}, Q = 191.9 kJ mol^{-1}). In a polycrystalline Cu crystal, segregation measurements could be affected by the surface orientation of the different grains. The effect that the surface orientation of the grains has on the In segregation was obtained with TOF-SIMS measurements (carried out using the linear temperatures method). The TOF-SIMS In segregation data from two twin grains showed equal segregation rates, which is expected since the twin grains have the same surface orientation. However, segregation data from two different grains showed different segregation rates which confirm the effect surface orientation has on segregation.

1. Introduction

The Cu-In system receives attention particularly for applications in solar cells, thin-film transistor liquid-crystal display, ultra-large-scale integrated devices [1–3]. In surface and interface science, the properties of a surface layer of a crystal can be modified such that they differ significantly from that of the bulk layers especially in elemental composition. Similarly, a grain boundary composition can be modified such that it differs significantly from that of the grain/bulk layers. Such modification in surface and grain boundary composition could be attained through a diffusion and segregation process (that results from a heat treatment of a crystal). A crystal containing active impurities (with a negligible bulk concentration), if is heat treated at a relatively high temperature the impurities accumulates on the surface and grain boundaries of a crystal as a result of the segregation process [4]. In some of these crystals, not only segregation of impurities occurs during heat treatment but also twinning (i.e. twin boundaries) that also occurs during crystal deformation [5]. In a polycrystalline crystal, a single grain without twinning has identical surface orientation of atoms arrangements (Figure

[1] To whom any correspondence should be addressed.

1). However, for adjoining grains the surface orientation differs from grain to grain. For a single grain with twin boundaries the surface orientation for twin grains is identical, what is observed is a special mirror image misorientation of the initial lattice structure (see figure 1) [5]. It has been shown in literature that segregation kinetics depends on the grain/surface orientation of the crystal [6, 7]. In support of literature, segregation kinetics measurements on different grains with probably different surface orientations are fascinating aspects to investigate.

In this study, the focus is on measuring the bulk-to-surface segregation of In impurity in a polycrystalline Cu crystal using Auger Electron Spectroscopy (AES) and time-of-flight secondary ion mass spectrometry (TOF-SIMS) coupled with a programmable heater. Note that studies on In segregating from the bulk to the surface and grain boundaries of a Cu crystal are lacking in literature. The AES In segregation data (carried out using the constant temperatures) was fitted with the semi-infinite model of Fick to obtain the In bulk diffusion parameters, namely the pre-exponential factor (D_0) and the activation energy (Q). The effect that the surface orientation of the grains has on the In segregation was also obtained with TOF-SIMS measurements (carried out using the linear temperatures method).

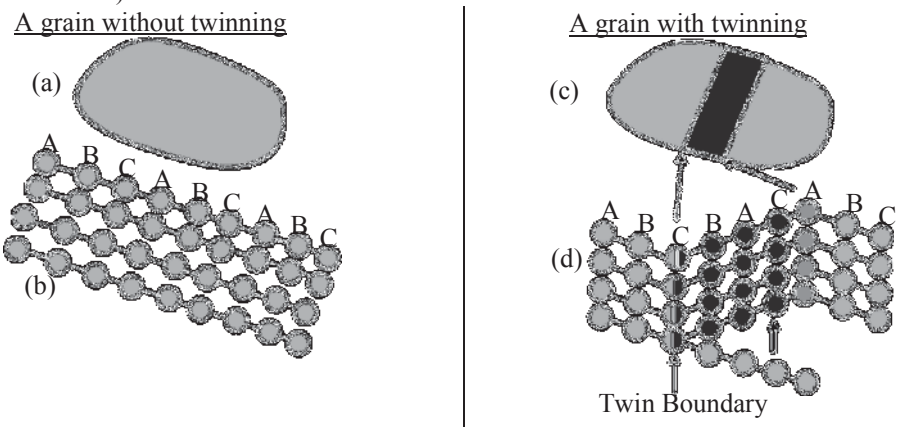

Figure 1. The schematic diagrams of (a) a grain without twin boundaries ((b) has identical surface orientation of atoms arrangements); (c) for a grain divided into twin grains by twin boundary ((d) a special mirror image misorientation of the initial lattice structure is observed [5]).

2. Experimental details

Cu crystals (0.70 mm thick and 10 mm diameter) with a S bulk concentration of 0.0008 at% (8 ppm) were obtained from a high purity (99.99 %) polycrystalline Cu. The Cu crystals were doped with a low concentration of In of 0.06 at%. The detailed Cu(0.06 at% In) alloy preparation procedure is published elsewhere [8].

An In doped Cu crystal was mounted on a heater inside the AES ultra high vacuum chamber. AES was used to monitor the polished surface (mechanically polished to 0.05 μm using a diamond suspension solution) of the crystal during constant heating of the crystal. AES constant temperature measurements were recorded for Cu (922 eV), S (153 eV) and In (405 eV) for temperatures 733 K; 763 K; 793 K; 823 K and 853 K. For each temperature, a crystal was heated for 1 h to establish a thermal equilibrium then sputtered over a 2000 × 2000 μm^2 area for 30 s. The Auger spectra of the crystal were obtained and showed only the segregation of In and S.

Furthermore, an In doped Cu crystal was mounted on a programmable heater inside the TOF-SIMS ultra high vacuum chamber. TOF-SIMS measurements were recorded (from a crystal polished surface) for In impurity segregation from a Cu crystal using a 30 keV Bi_1^+ Ion beam and linear temperature ramp at a heating rate of 0.05 K/s. Measurements were performed in a positive polarity. Before each segregation measurement the crystal surface was sputtered over a 700 × 700 μm^2 area using a 2 keV O_2^+ Ion beam.

3. Results and Discussion

The AES segregation measurements were performed in the middle of a grain on the surface as shown (with a marker A) in the insert of figure 2. Figure 2, shows the surface enrichment of In and S from an In doped polycrystalline Cu crystal, which was obtained from the constant temperature measurements at 733 K. In figure 2, two distinctive regions (looking at In data) are shown: In region A (kinetic region), it can be seen that initially In segregated to the surface at a higher segregation rate. However, in region B the segregation rate of In decreased significantly. From the measured AES segregation data, S (a common Cu impurity) was also observed to segregate with In. A high segregation rate of In could be as a result of a higher In bulk concentration (0.06 at%) and the bulk diffusion coefficient (D). Since, the segregation rate is limited by the change in the chemical potential ($\Delta\mu$) (i.e. a function of the impurities bulk concentration) and the bulk diffusion coefficient is characterized by inherent activation energy (that could be lower to give a higher diffusion coefficient) and the pre-exponential factor. The effects of the bulk concentration (X^B) and the bulk diffusion coefficient (D) on segregation kinetics are brought together by the semi-infinite model of Fick that best describe the kinetics of segregation.

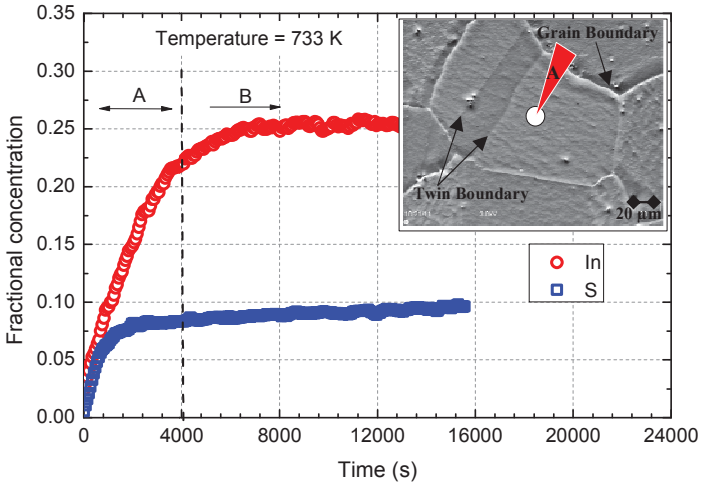

Figure 2. AES In and S segregation data measured at a constant temperature of 733 K. The insert is the secondary electron detector micro image of a polycrystalline Cu crystal surface that demonstrates a spot A used for the segregation measurements.

The semi-infinite model of Fick for surface concentration (X^{ϕ}) of segregating impurities with time (t) (also adapted to account for the sputter depletion after sputtering for time (t_0) is given by the following expression [9−10]:

$$X^{\phi} = X_0^{\phi} + X^B\left[1+\frac{2}{d}\left(\frac{D(t+t_0)}{\pi}\right)^{1/2}\right] - X^B\left[\frac{2}{d}\left(\frac{Dt_0}{\pi}\right)^{1/2}\right] \quad (1)$$

where X_0^{ϕ} is the number of segregated impurities that were not sputtered, X^B is the impurity bulk concentration, d is the thickness of the segregated layer and $D = D_0 \exp(-Q/RT)$ is a diffusion coefficient with activation energy Q and pre-exponential factor D_0 at a constant temperature T.

The data points of the kinetics of segregation (region A in figure 2) of In measured from a In doped polycrystalline Cu crystal at constant temperatures of 733 K; 763 K; 793 K; 823 K and 853 K were fitted with equation 1 adjusting a parameter D as shown in figure 3(a). Fitted D values were plotted as

shown in figure 3(b) and from a plot the pre-exponential factor and the activation energy ($D_0 = 1.1 \times 10^{-5}$ m^2 s^{-1}, $Q = 191.9$ kJ mol^{-1}) were extracted for In bulk diffusion in the Cu crystal.

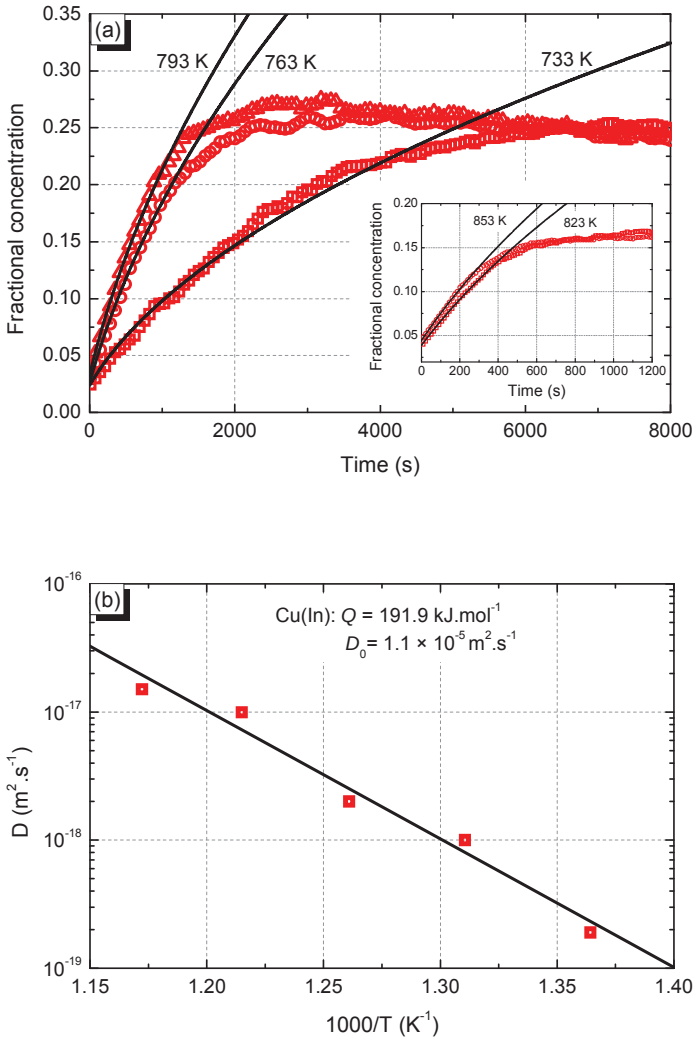

Figure 3. (a) In segregation data measured from a In doped polycrystalline Cu crystal at a constant temperatures of 733 K; 763 K; 793 K; 823 K and 853 K. The solid lines are the best fits of the semi-infinite model of Fick. (b) Arrhenius plot of fitted D values.

The bulk diffusion parameters ($D_0 = 1.1 \times 10^{-5}$ m^2 s^{-1}, $Q = 191.9$ kJ mol^{-1}) of In segregation in Cu crystal obtained from this study using the constant temperature method compare well with those obtained from the same crystal using the linear temperature method ($D_0 = 1.8 \times 10^{-5}$ m^2 s^{-1}, $Q = 184.3$ kJ mol^{-1}) [12].

The In bulk diffusion parameters obtained in this study could be affected by the surface orientation of the different grains, since they were extracted from the segregations kinetics. It is known in literature that segregation kinetics depends on the grain/surface orientation of the crystal [6, 7]. The effect that the surface orientation of the grains has on the In segregation

was obtained with TOF-SIMS measurements (see figure 4). From the insert of figure 4, it can be seen from the elemental map that the In segregated from the bulk to the grain boundaries and grain surfaces. The TOF-SIMS In segregation data from two twin grains (indicated with a marker A and B in figure 4(a) insert) showed equal segregation rates (from low crystal temperatures up to 520 K as shown in figure 4(a)), which is expected since the twin grains have the same surface orientation. However, segregation data from two different main grains showed different segregation rates (see figure 4(b)) which confirm the effect surface orientation has on segregation kinetics. Clearly, these suggest that the In bulk diffusion parameters obtained in this study will differ significantly between grains with different surface orientations. However, the parameters could be comparable.

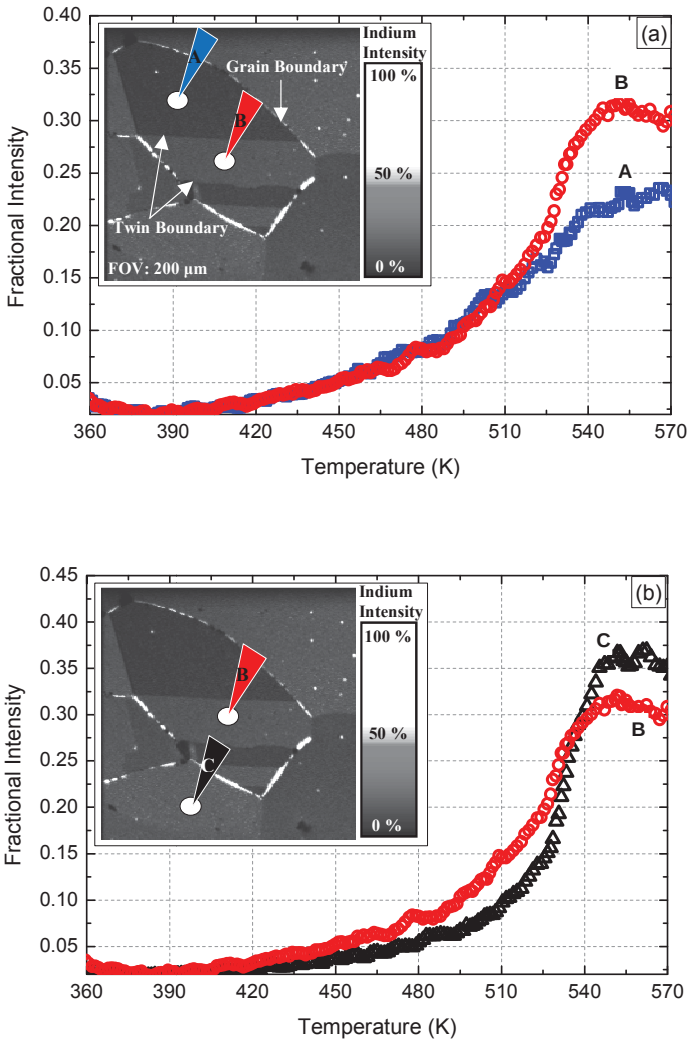

Figure 4. TOF-SIMS In segregation data of a linear heat run measured at different positions (A–C) on the Cu surface. The insert is a TOF-SIMS elemental map of the In segregation on the surface of the Cu crystal after annealing.

It should be mentioned that in TOF-SIMS measurements the segregation of other impurity such as K was measured at higher temperatures (> 520 K), and as its concentration increased on the surface it strongly interacted with In on the surface causing In desegregation.

The large difference as seen in the maximum surface intensities from the two twin grains (Figure 4(a)) could be related to the impurities interaction energies according to the Guttmann model (that relates the maximum surface concentrations to the impurities segregation and interaction energies) [13]. Nevertheless, such a large difference in the intensities could not be related to impurities interaction energies (because the twin grains have the same surface orientation and the same impurities were measured from either grain). A high intensity in figure 4(a) suggested that there is more of In impurity in the twin grain marked B in figure 4(a) (as compared to the adjacent twin grain).

4. Conclusion

In this study, the bulk-to-surface segregation of In impurity in a polycrystalline Cu crystal was measured using AES and TOF-SIMS coupled with a programmable heater. From the measured AES data the In bulk diffusion parameters ($D_0 = 1.1 \times 10^{-5}$ m^2 s^{-1}, Q = 191.9 kJ mol^{-1}) were obtained. The In bulk diffusion parameters obtained in this study compare well with those obtained from the same crystal using the linear temperature method ($D_0 = 1.8 \times 10^{-5}$ m^2 s^{-1}, Q = 184.3 kJ mol^{-1}) [12]. Since measurements were carried out from a polycrystalline crystal, the effect that the surface orientation of the grains has on the In segregation was obtained with TOF-SIMS measurements. The TOF-SIMS segregation data from two twin grains showed equal segregation rates, which is expected since the twin grains have the same surface orientation. The TOF-SIMS segregation data from two different grains showed different segregation rates which confirm the effect surface orientation has on segregation data. Therefore, In bulk diffusion parameters obtained in this study could be expected to differ significantly if measured on a different grain with a different surface orientation.

Acknowledgments

This work is based on the research supported by the South African Research Chairs Initiative of the Department of Science and Technology and National Research Foundation of South Africa. The University of the Free State Cluster program is acknowledged for financial support.

References

[1] Hsu CS, Hsieh HY, Fang JS 2008 *Journal of Electronic Materials* **37** 6
[2] Wronkowska AA, Wronkowski A, Skowroński Ł 2009 *Journal of Alloys and Compounds* **479** 583
[3] Fang JS, Hsieh HY 2007 *Journal of Electronic Materials* **36** 129
[4] 1990 *Surface Segregation Phenomena*, ed PA Dowben and A Miller (Florida: CRC Press, Inc.)
[5] 1996 *The Science and Engineering of Materials* 3rd edition, ed DR Askeland (United Kingdom: Nelson Thornes Ltd) chapter 4 p 101
[6] Terblans JJ and van Wyk GN 2003 *Surface and Interface Analysis* **35** 779
[7] Terblans JJ and van Wyk GN 2004 *Surface and Interface Analysis* **36** 935
[8] Madito MJ, Swart HC and Terblans JJ 2013 *Thin Solid Films* 10.1016/j.tsf.2013.05.143
[9] Terblans JJ, Swart HC 2009 *e-Journal of Surface Science and Nanotechnology* **7** 480
[10] Viljoen EC and du Plessis J 1995 *Surface and Interface Analysis* **23** 110
[11] Du Plessis J, Viljoen PE, Van Wyk GN 1991 *Surface Science* **244** 277
[12] Madito MJ, Swart HC and Terblans JJ 2013 *Surface and Interface Analysis* **45** 1020
[13] Swart HC, Roos WD, Terblans JJ 2004 *Surface and Interface Analysis* **36** 285

The elastic properties and the phonon dispersions of TiPtCo shape memory alloy using the supercell approach

R. Mahlangu, H.R. Chauke and P.E. Ngoepe

Materials Modelling Centre, School of Physical and Mineral Sciences, University of Limpopo, Private Bag X1106, Sovenga, South Africa

Rosinah.mahlangu@ul.ac.za

Abstract. Shape memory alloys (SMAs) are classified as a group of metallic materials that has the ability to retain or remember their original shape or size when subjected to the appropriate thermal deformation processes. In general, these materials can easily be elastically or plastically deformed at some relatively low temperature, and upon exposure to some higher temperature can return to their original shape. The effect of substituting Pt with Co as the third element in the TiPt shape memory alloy system using the supercell approach has been investigated. The elastic properties and phonon dispersions of the TiPtCo were investigated using the *ab initio* approach employed in VASP.

1. Introduction

Shape memory alloys (SMAs) are classified as group of metallic materials that has the ability to retain or remember their original shape or size when subjected to the appropriate thermal deformation processes. This unique behaviour is due to the shape memory effect (SME) and superelasticity. Some of the known SMAs include nickel titanium (NiTi), nickel titanium copper (NiTiCu), copper aluminium nickel (CuAlNi) and many other metallic alloy systems [1]. Although they have been around for over half a century, new applications continue to be developed for SMAs [2]. Titanium based SMAs have been widely used in the fields of engineering and medicine due to their shape memory effect and super-plasticity which are displayed in martensitic transformations [3]. Some of the applications include actuators and medical stents [3, 4, 5, 6].

Relatively a wide range of alloys are known to exhibit the shape memory effect (SME), however only those that can recover substantial amounts of strain or that generate significant force upon changing shape are of commercial importance [2]. Many aspects of the transformation are still not well understood [7, 8] even though many theoretical and experimental studies have been devoted to these extraordinary phenomena. There is a growing need of SMAs that can be used at high temperatures and only a limited number of such alloys have the potential to be high temperature shape memory alloys (HTSMAs). Some of them include Ti(Ni,Pt) [9, 10, 11] and Ti(Ni,Pd) [12, 13, 14, 15, 16, 17]. However, the T_m of TiPt is much higher, at approximately 1000 °C [18] and this is considered to be of potential technological interest for elevated temperature SMA applications. It also undergoes a B2-B19 martensite phase transformation with a transition temperature of approximately 1050 °C [18]

and this can be observed on the Ti-Pt phase diagran shown in Figure 1 [19]. In this work we look at the effect of substituting some of the Pt with Co in the B2 TiPt alloy *i.e.* $Ti_{50}Pt_{50-x}$ Co_x using the supercell of 16 atoms of TiPt.

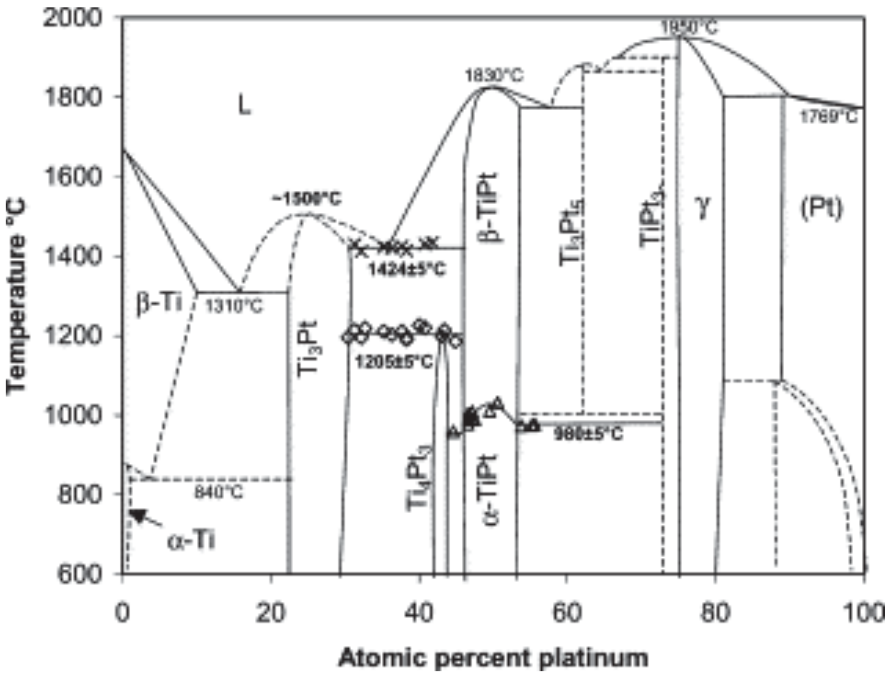

Figure 1. The phase diagram of of the Ti-Pt alloys. The area of interest is at the 50 at. % Pt where the low temperature α-TiPt also known as B19 and the high temperature phase β-TiPt known as B2 exists [19].

2. Methodology

The calculations were carried out using *ab initio* density functional theory (DFT) formalism as implemented in the Vienna *ab initio* Simulation Package (VASP) [20] with the projector augmented wave (PAW) [21]. An energy cutoff of 500 eV was used as it was sufficient to converge the total energy of the TiPt alloys. For the exchange-correlation functional, the generalized gradient approximation of Perdew and Wang (GGA-PBE) [22] was chosen. The Brillouin zone integrations were performed for suitably large sets of *k*-points according to Monkhorst and Pack [23]. A 2x2x2 supercell of TiPt with 16 atoms was used to substitute some of the Pt with Co. The phonon dispersion spectra were evaluated using PHONON code [24] as implemented in Materials Design within MedeA software of VASP code. A *k*-point mesh of 3x3x3 was used. The phonon dispersions and phonon densities of states for the structures were calculated in the framework of the direct method, for which the force constants were derived by a supercell approach.

3. Results and discussion

In table1 we show the calculated lattice parameters and elastic properties of the $Ti_{50}Pt_{50-x}Co_x$ (x = 6.25, 18.75, 25). The calculated results show that as we increase the Co concentration in the system the lattice parameter decreases. The calculated elastic constants are all positive indicating the mechanical stability of the structures. It is argued that higher anisotropy *A* is a sufficient condition for B2-B19

martensitic transformation. However, smaller *A* indicates that there is a stronger correlation between C_{44} and C′. The origin of B19′ phase is a result of the coupling between C_{44} and C′ just as proposed by Ren and Otsuka [25]. The C_{44} can be understood that is related to resistance to {001}[100] shear for cubic crystals which is just the non-basal monoclinic shear required by B19′ martensite. Therefore, C_{44} is crucial for the formation of B19′ martensite and controls the transformation temperature of B2 to B19′ transformation [26]. The C′ at x = 6.25 is rather smaller as compared to the other concentrations which results in a larger *A*, this indicates that at this concentration B2 to B19 martensitic transformation occurs. The *A* at x = 18.75 and 25 becomes smaller as we increase the Co content indicating a good correlation between the C_{44} and C′. At this (x = 18.75 and 25) concentrations there is a B2 to B19' transformation. The C' shear of the B2 TiPt was found to be negative in the previous study and the addition of Co indicates that the C' of the calculated concentrations is positive. It can be inferred from this findings that the addition of Co reduces the martensitic transformation temperature of the cubic TiPt phase since our study suggest more stable phases of $Ti_{50}Pt_{50-x}Co_x$.

Table 1. Elastic properties (GPa) of $Ti_{50}Pt_{50-x}Co_x$ ternaries and their anisotropy *A* using the supercell approach.

Structures	Lattice parameters	C_{11}	C_{12}	C_{44}		C'	*A*
^{27}TiPt	3.19	145		210	45	-32	
$Ti_{50}Pt_{43.75}Co_{6.25}$	3.15	200		184	35	8	4.37
$Ti_{50}Pt_{31.25}Co_{18.75}$	3.11	212		172	51	20	2.55
$Ti_{50}Pt_{25}Co_{25}$	3.07	260		155	55	52	1.05

The analyses of the vibrational properties of the structures with respect to the phonon dispersion and phonon densities of states were also calculated and are shown in figure 2. At first, the B2 TiPt phonon dispersion curve was calculated and the soft modes with frequencies less than zero were observed. These imaginary frequencies indicate the instability of the phase at room temperature which is consistent with the elastic instability (negative C′) [27]. In the case of ternary alloying with Co, there are also soft modes observed on the phonon curves suggesting the instability of the phases with respect to the vibrations of the atoms. The results suggest that substituting Pt with Co reduces the negative frequencies of the TiPt. In figure 2(b), the frequency of $Ti_{50}Pt_{43.75}Co_{6.25}$ is found to be -6.00 THz at the gamma point and as the Co concentration is increased to x = 18.5, the frequency is approximately -3.31 THz. The phonons of $Ti_{50}Pt_{25}Co_{25}$ are also shown in figure 2(c) and the frequency of -3.11THz is observed at gamma which is more stable than the other concentrations.

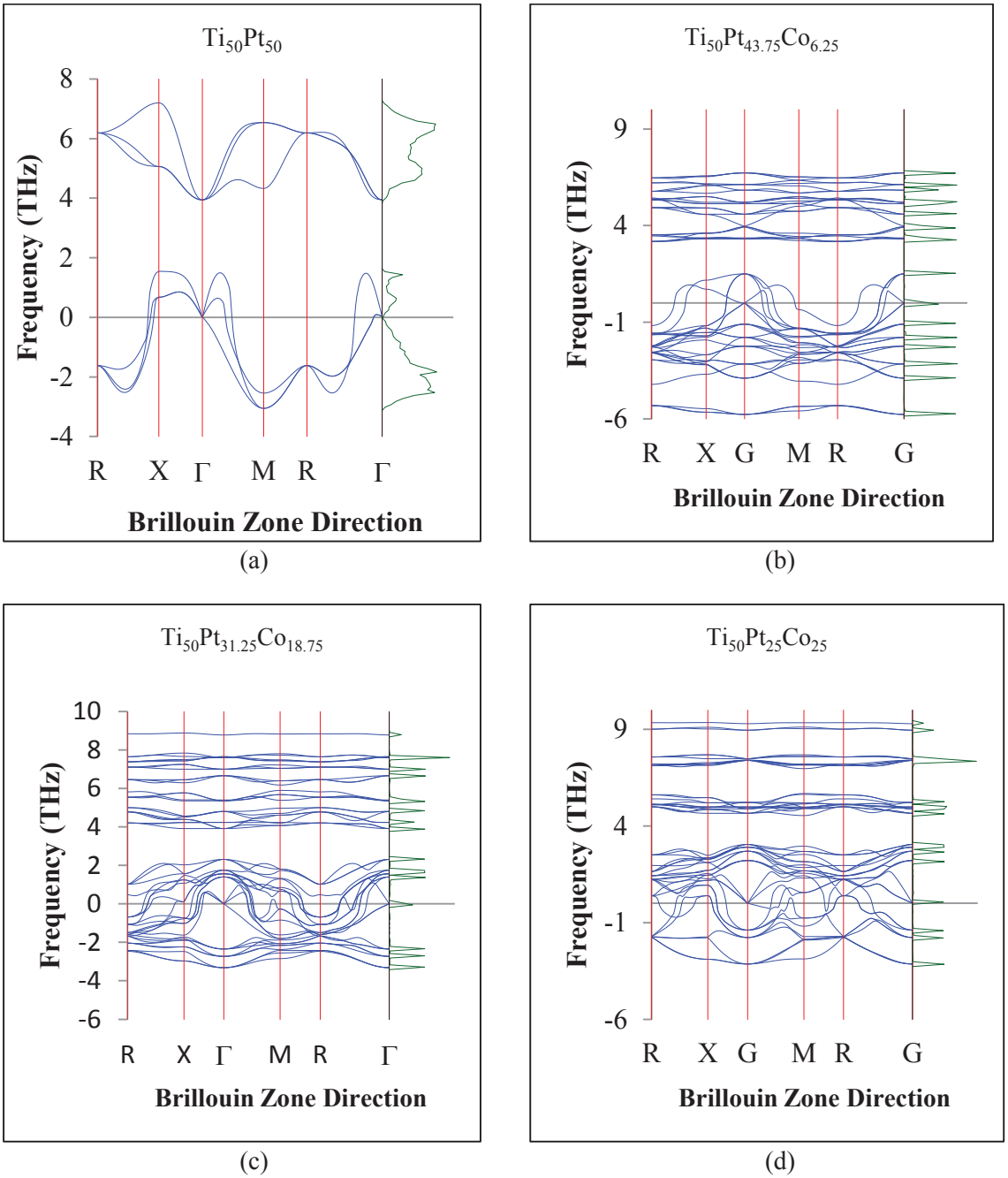

Figure 2. Phonon dispersion curves of the (a) binary TiPt and (b) $Ti_{50}Pt_{43.75}Co_{6.25}$, (c) $Ti_{50}Pt_{43.75}Co_{18.75}$, (d) $Ti_{50}Pt_{25}Co_{25}$ ternaries

4. Conclusion

The supercell approach method was used to investigate the addition of the third element in the TiPt alloy. As the Co concentration is increased in the system, the lattice parameter decreases. The calculated elastic properties were found to be mechanically stable as opposed to the binary TiPt which has a negative C′. It is evident from our results that the addition of Co reduces the martensitic transformation temperature and this is due to the higher values of C′. The phonon dispersion curves were also calculated and suggest that the addition of Co stabilises the TiPt since it reduces its vibrational soft modes, in particular 25 at.% Co.

Acknowledgements

The authors acknowledge the CSIR and NRF for their financial support. The support of the South African Research Chair Initiative of the Department of Science and Technology and the National Research Foundation is highly recognised.

References

[1] Otsuka K and Wayman C M 1998 *Shape Memory Materials*, (Cambridge: Cambirdge University Press) 220-239
[2] Duerig T, Melton K, Stockel D, 1990 *Engineering Aspects of Shape Memory Alloys* Eds Wayman C (London: Butterworth-Heinemann) 89-95
[3] Wu M H and Schetky L M, California: Pacific Grove, 2000 *SMST* 171-182
[4] Otsuka K and Kakeshita T 2002 *MRS Bull*. **27** 91-100
[5] Van Humbeeck J 1999 *Mater. Sci. Eng*. A **273–275** 134-148
[6] Duerig T, Pelton A and Stockel D 1999 *Mater. Sci. Eng*. A **273–275** 149-160
[7] Otsuka K and Ren X 2005 Prog. Mater. Sci. **50** 511-678
[8] Cai J, Wang D S, Liu S J, Duan S Q, Ma B K 1999 *Phys. Rev.* B **60** 15691-15698
[9] Hosoda H, Tsuji M, Mimura M, Takahashi Y, Wakashima K and Yamabe-Mitarai Y 2003 *MRS Bull*. **753** BB5-51-1–BB5-51-6
[10] Takahashi Y, Inamura T, Sakurai J, Hosoda H, Wakashima K and Miyazaki S 2004, *Trans. MRS-J*. **29** 3005–3008
[11] Inamura T, Takahashi Y, Hosoda H, Wakashima K, Nagase T, Nakano T, Umakoshi Y and Miyazaki S 2004 *MRS Bull*. **842** 347–352
[12] Otsuka K, Oda K, Ueno Y, Piao M, Ueki T and Horikawa H 1993 *Scr. Metal* **29** 1355–1359
[13] Golberg D, Xu Y, Murakami Y, Morito S, Otsuka K, Ueki T and Horikawa H 1994 *Scr. Metal.* **30** 1349–1354
[14] Xu Y, Otsuka K, Furubayashi E, Ueki T and Mitose K Mater. 1997 *Mater. Lett*. **30** 189–197
[15] Xu Y, Shimizu S, Suzuki Y, Otsuka K, Ueki T and Mitose K 1997 *Acta Mater*. **45** 1503–1511
[16] Suzuki Y, Xu Y, Morito S, Otsuka K and Mitose K 1998 *Mater. Lett*. **36** 85–94
[17] Shimizu S, Xu Y, Okunishi E, Tanaka S, Otsuka K and Mitose K 1998 *Mater. Lett*. **34** 23–29
[18] Donkersloot H C and Van Vucht J H N 1970 *J. Less-Common Met*. **20** 8391
[19] Biggs T, Cornish L A, Witcomb M J and Cortie M B 2004 *J. Alloys Compd*. **375** 120-127
[20] Kresse G and Hafner J 1993 *Phys. Rev.* B **47** 558-561
[21] Blöchl P E 1994 *Phys. Rev.* B **50** 17953-17979
[22] Perdew J P and Wang Y 1992 *Phys. Rev.* B **45** 13244-13249
[23] Monkhorst H J and Pack J D 1976 *Phys. Rev.* B **13** 5188-5192
[24] Parlinski K and Li Z Q, Kawazoe Y 1997 *Phys. Rev. Lett*. **78** 4063
[25] Ren X, Miura N, Taniwaki L, Otsuka K, Suzuki T, Tanaka K, Chumlyakov Y I and Asai M 1999 *Mater. Sci. Eng*. A **273-275** 190-194
[26] Ren X, Miura N, Zhang J, Otsuka K, Tanaka K, Koiwa M, Suzuki T, Chumlyakov Y I and Asai

M 2001 *Mater. Sci. Eng.* A **312** 196
[27] Mahlangu R, Phasha M J, Chauke H R, Ngoepe P E 2013 *Intermetallics* **33** 27-32

Characterisation of carbon microspheres using electron paramagnetic resonance spin-concentration techniques

V D Marsicano[1,2], W P Wright[1,2], J M Keartland[1,2], R M Erasmus[1,2], S Dube[2,3] and N J Coville[2,3]

1 School of Physics, University of the Witwatersrand, P.O. Wits, 2050 Johannesburg, South Africa

2 DST/NRF Centre of Excellence in Strong Materials, P.O. Wits, 2050 Johannesburg, South Africa

3 Molecular Sciences Institute and School of Chemistry, University of the Witwatersrand, P.O. Wits, 2050 Johannesburg, South Africa

E-mail: keartland@psi.wits.ac.za

Abstract. A new technique to accurately determine the nitrogen concentration of doped carbon microspheres was developed using electron paramagnetic resonance (EPR) techniques. Samples of carbon microspheres of varying nitrogen concentrations were synthesised in a horizontal chemical vapour deposition reactor. The spin concentrations of samples of known nitrogen concentration were determined using a Bruker ESP 300E and used to calibrate the device. Samples of unknown nitrogen doping were then analysed to determine their concentration. Raman spectroscopy was also used to confirm the effect the nitrogen incorporation has on the structure of the microspheres.

1. Introduction

In recent years many allotropes of carbon have been studied extensively [1,2,3] because of their many applications. One of these allotropes, the carbon microsphere (CMS), has recently been the subject of new attention due to its applicability to lubricants, electronic devices and lithium ion batteries [1,4]. The level of nitrogen doped in to the spheres can affect many of its properties hence a non-destructive technique to determine dopant levels will prove useful. With refinement, electron paramagnetic resonance (EPR) spectroscopy could determine small nitrogen concentrations, beyond what is currently possible with other elementary analysis techniques, without consuming the sample.

Samples were prepared using the popular chemical vapour deposition (CVD) technique [5,6] in a horizontal reactor. The advantage of CVD reactors is their ability to produce spheres without a catalyst. [7] Synthesis was conducted using varying reactor parameters to create spheres of with different characteristics.

EPR and Raman spectroscopy have successfully been used to study the structure of CMS [8]. These techniques can give an indication of the effect of nitrogen incorporation Each nitrogen introduced in to the graphitic lattice creates a paramagnetic centre which adds to the EPR spectrometer signal. By normalising the signal magnitude to the mass of the sample the spin concentration, and therefore the nitrogen concentration, of the samples can be determined. A calibration curve for a specific spectrometer under a specific set of conditions can be created allowing for the characterisation of samples of unknown nitrogen content. Other experiments can confirm the relative levels of nitrogen concentration, such as sample g value or Raman spectrum. Dopant introduction in to any carbon structure adds disorder which can be detected in the Raman spectra [9,10]. Similarly the presence of nitrogen changes the spin-orbit coupling of electrons in the spheres, which changes the g values [11]. While these techniques can indicate a relative difference in nitrogen concentration if absolute nitrogen concentration is needed then the number of free spins per gram of sample must be determined.

2. Synthesis

Synthesis of the CMS was conducted inside a horizontal CVD reactor using acetylene as the primary reagent. The acetylene is introduced via a carrier gas, in this case argon, at a flow rate of 100ml/min. The source of nitrogen dopant was acetonitrile, introduced into the gas stream during the reaction. The flow of gas was initiated when the reactor had stabilized at the desired reaction temperature. Reactor parameters were varied to create the different samples. The temperature was set to 850^{o}C or 900^{o}C and the reaction ran for either 1.5 or 2 hours. The reactor has a quartz tube placed in the center where the majority of the spheres are collected however some samples were collected from the quartz boat, an excess collection area, to observe the difference in the spheres based on final location in the reactor.

Table 1. Samples investigated.

Sample	Concentration	Sample	Synthesis Detail
SDA	0%	SD1	Reaction of 1.5 hours
SDB	0.4%	SD2	Reaction of 2 hours
SDC	2.5%	SD3	From quartz tube
SDD	5%	SD4	From quartz boat

3. Characterisation

3.1. Electron Paramagnetic Resonance

The EPR experiments were conducted using a Bruker ESP 300E spectrometer in continuous wave mode. Spin-concentration measurements represent a particularly challenging experiment due the number of parameters which can affect the results [11]. The spectrometer settings were kept identical throughout all the spin-concentration measurements to ensure signal magnitudes could be meaningfully compared. Further parameters which affect the results include the mass of the samples, sample geometry as well as conductive shielding therefore the samples were packed in identical quartz tubes and their masses carefully measured.

The CMS samples all display a single, strong paramagnetic resonance signal characteristic of carbon materials [12] which is slightly Dysonian in character. Dysonian lineshapes are indicative of conduction electrons [13] which we expect to see introduced with the nitrogen. The spin-concentration can be determined by double integration of signal however great care must be taken to ensure the baseline for the integration is corrected for, [11] therefore the spectrometer was set to a wide sweep of both the low-field and high-field sides of the spectrum. Figure 1 shows the results from the samples of known nitrogen concentration. The regression curve has a R^2 value of 0.86 and represents the calibration curve for the spectrometer. The samples do not fit the expected straight line especially well, this may be due to errors in the determination of nitrogen concentration. The spectrometer detects only paramagnetic nitrogen bonded in to the lattice structure, other techniques, such as mass spectrometry, detect the total number of nitrogen atoms present. The unknown samples were then measured and placed along the curve to determine the concentration of paramagnetic nitrogen. Their concentrations are displayed in Table 2.

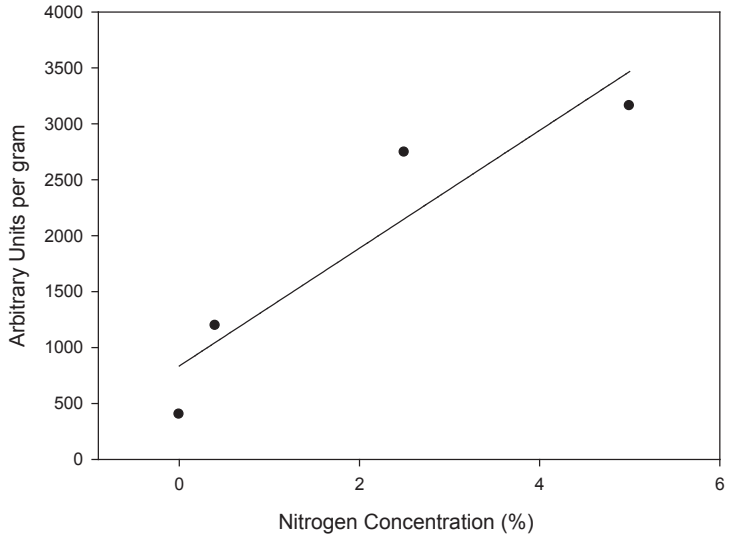

Figure 1. Calibration curve of the Bruker ESP 300E spectrometer

Table 2. Nitrogen Concentrations of unknown samples determined by spin-concentration EPR experiment.

Sample	Concentration	Error
SD1	1.7%	0.5%
SD2	3.3%	0.9%
SD3	3.4%	1.0%
SD4	1.7%	0.5%

The g value of the samples was investigated using a deconvolution technique. The samples were placed in standard EPR quartz tubes with a smaller tube containing DPPH placed within the larger one. The DPPH is used as a standard marker in EPR experiments because it has a well defined resonance peak. This is then used to mark a particular magnetic field value to the well known g-value of DPPH. By measuring the difference between the peak of the DPPH signal and the peak of the microspheres a relatively accurate determination of the sample's g-value can be obtained. The results for the known samples are shown in Figure 2. It shows the g value of the spheres tends away from the free electron g-value. This implies that spin-orbit coupling increases as nitrogen is introduced in to the lattice.

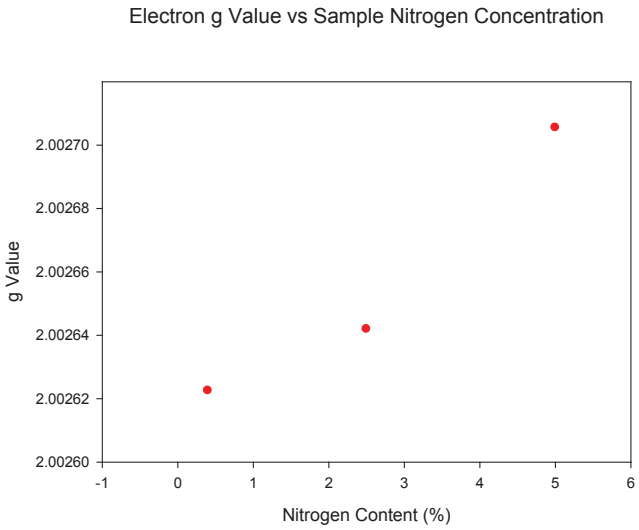

Figure 2. Effective g value of sample with increasing nitrogen content.

The unknown sample's g values were also investigated with the same technique. SD1 and SD2 have similar nitrogen doping levels however the SD1 has a larger g value. This indicates that a longer time spent in the reactor seems to increase the coupling the free electron has with the lattice. This may be due to annealing, which appears to be confirmed by Raman spectroscopy. SD4 has a much larger g value than SD3 which indicates that depending on where in the reactor a sample is collected has a large effect on the chemistry of the bonds seen by the free electron. This may be due to the spheres collected in the boat experiencing a varying temperature on the periphery of the pyrolisis, creating a different bond structure.

3.2 Raman Spectroscopy

Raman spectroscopy was used to confirm the EPR data by observing the effect of the nitrogen on the structure of the CMS. The CMS samples were studied at 514 nm and 647 nm laser wavelengths. Major peaks were observed at 1381cm^{-1} and 1595cm^{-1} with a minor peak at approximately 1200cm- The two dominant spectral lines, namely the D and G bands, indicate the presence of a graphitic carbon structure [14]. The G peak is indicative of a doubly degenerate E_{2g} phonon mode characteristic of sp2 hybridised carbon networks, while the D peak is induced by defects in the carbon structure [15]. The peaks studied are very broad which makes curve fitting difficult, and reduces the resolution for detecting the peak centres.

The intensity ratio, R, is given by

$$R = \frac{I_D}{I_G}$$

where I_D and I_G are the intensities of the D and G bands respectively.

I_D is proportional to the number of ordered rings in the sample and is reduced as the introduction of the nitrogen causes bond bending disorder in the structure. Sp3 hybridized bonds can also be formed during the introduction of the nitrogen, further reducing the intensity of the D peak [16,17]. The it is found that R of the known samples decreases for the 514 nm laser indicating the presence of bond bending disorder introduced in to the structure with the nitrogen. The 647 nm laser does not show this trend and has a relatively unchanged intensity ratio. Resonance of the D band at this laser wavelength can occur and completely overshadow the smaller effect of the increased bond disorder. An anomaly can be seen in both laser wavelengths for the SDB sample. This seems to indicate an error in the reactor conditions when this sample was produced. The anomaly is shown on the graph as a triangle.

Figure 3. Intensity ratio change with nitrogen incorporation.

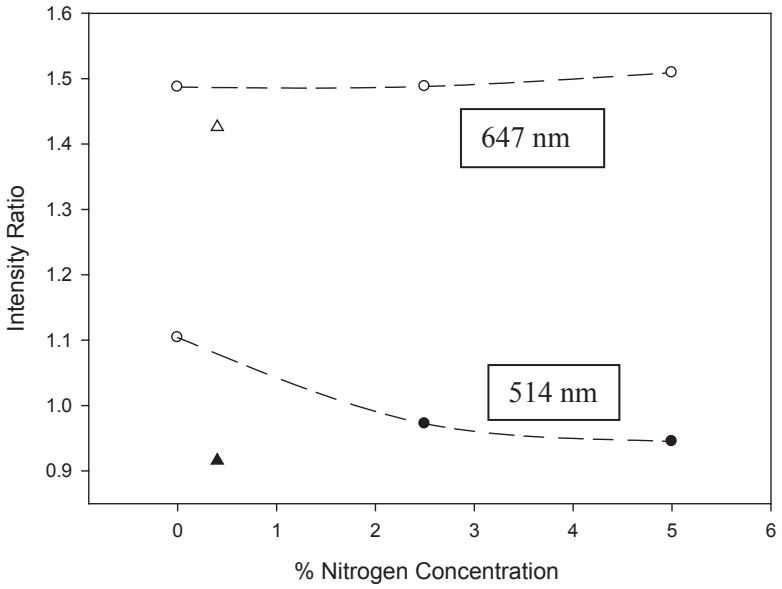

The centre of the G line shifts towards a higher frequency as the nitrogen is introduced in to the sample at both laser wavelengths explored. A blue shift in the G peak is expected when a sample changes from nanocrystaline structure to a less ordered (amorphous) structure as the disorder in the sample increases [18]. A red shift in the spectra of carbon microspheres doped with boron has been associated with increases in average CMS size [6,19]. It is important to note that the red shift was not indicative of a particular sphere diameter, but rather of a trend towards larger spheres being produced on average in the presence of boron dopant [19]. It is possible in this case that the spheres have a slightly smaller diameter when nitrogen is introduced, if unlikely. Further TEM investigations are required to confirm this possibility. The G shift in either case is caused by the reduction of the characteristic length L_a of the lattice, [20] either by shrinking sphere size or introduced disorder.

Table 3. Raman spectra data of known nitrogen concentration samples.

		514 nm Laser Wavelength			617 nm Laser Wavelength		
Sample	Nitrogen Content	R	G band width	G band centre	R	G band width	G band centre
SDA	0%	1.104	107	1600.2	1.487	81	1590.8
SDB	0.4%	0.916	95	1599.8	1.426	78	1589.8
SDC	2.5%	0.972	96	1592.0	1.488	80	1585.6
SDD	5%	0.945	91	1592.4	1.509	84	1584.5

The ratio R and the G peak blue shift are signs that the sample is becoming increasingly amorphous as defects are introduced in to the graphitic structure. Ferrari *et al* [9,18] describe this as the second stage of their 3 stage model of carbon Raman spectra. Reduction of the G peak width for the green laser wavelength can also be observed. Previous research has detected the formation of a D' peak around 1620cm^{-1} with increasing sample disorder and, while not clearly visible in the spectra as a separate line, it is the likely contributing to thinning the G peak [20,21].

4. Conclusion

The CVD technique employed synthesized CMS. A rudimentary calibration curve was successfully created for the EPR spectrometer and the nitrogen content of unknown samples was determined. Measurements of the g value of the samples and the Raman spectra confirm that trends in these values are directly related to nitrogen dopant level. This confirms that spin concentration, with complementary experiments, can determine the nitrogen concentration of CMS samples.

References

[1] Nieto-Márquez A, Romero R, Romero A and Valverde J L 2011 *Journal of Materials Chemistry* **21** 1664

[2] Molitor F, Güttinger J, Stampfer C, Dröscher S, Jacobsen A, Ihn T and Ensslin K 2011 *Journal of physics Condensed matter an Institute of Physics journal* **23** 243201

[3] Shiraishi M and Ata M 2002 **128** 235–9

[4] Sharon M, Mukhopadhyay K, Yase K, Iijima S, Ando Y and Zhao X 1998 *Carbon* **36** 507–11

[5] Serp P, Feurer R, Kalck P and Kihn Y 2001 *Letters to the editor* **39** 621–6

[6] Miao J-Y, Hwang D W, Narasimhulu K V, Lin P-I, Chen Y-T, Lin S-H and Hwang L-P 2004 *Carbon* **42** 813–22

[7] Poinern G and Brundavanam S 2012 *Nanotechnology, …* 49–59

[8] Pol V G, Motiei M, Gedanken A, Calderon-Moreno J and Yoshimura M 2004 *Carbon* **42** 111–6

[9] Ferrari A C, Meyer J C, Scardaci V, Casiraghi C, Lazzeri M, Mauri F, Piscanec S, Jiang D, Novoselov K S, Roth S and Geim A K 2006 *Physical Review Letters* **97** 187401

[10] Mondal K C, Strydom A M, Erasmus R M, Keartland J M and Coville N J 2008 *Materials Chemistry and Physics* **111** 386–90

[11] Weil J A and Bolton J R 2007 *Electron Paramagnetic Resonance, Elementary Theory and Practical Applications* (New York, USA: Wiley)

[12] Mrozowski S 1979 ESR of carbons in the transition range—I *Carbon* **17** 227–36

[13] Dyson F J 1958 *Physical Review* **98** 349–59

[14] Tuinstra F 1970 Raman Spectrum of Graphite *The Journal of Chemical Physics* **53** 1126

[15] Pimenta M A, Dresselhaus G, Dresselhaus M S, Cançado L G, Jorio A and Saito R 2007 *Physical chemistry chemical physics : PCCP* **9** 1276–91

[16] Köhler T, Frauenheim T and Jungnickel G 1995 *Physical Review B* **52** 837–44

[17] Beeman D, Silverman J, Lynds R and Anderson M 1984 *Physical Review B* **52**

[18] Ferrari A and Robertson J 2000 *Physical Review B* **61** 14095–107

[19] Mondal K C, Strydom A M, Tetana Z, Mhlanga S D, Witcomb M J, Havel J, Erasmus R M and Coville N J 2009 *Materials Chemistry and Physics* **114** 973–7

[20] Matthews M, Pimenta M, Dresselhaus G, Dresselhaus M and Endo M 1999 *Physical Review B* **59** R6585–R6588

[21] Loa I and Möschel C 2001 *Physica Status Solidi (b)* **293** 293–8

Efficiency degradation of organic solar cells with solution processed ZnO nanoparticles

P.S. Mbule[1], H.C. Swart[1] and O.M. Ntwaeaborwa[1]
Department of Physics, University of the Free State, Bloemfontein, ZA9300, South Africa

E-mail: mbuleps@gmail.com

Abstract: In this study we investigated the performance of organic solar cells (OSCs) with ZnO nanoparticles used as electron extraction layer (EEL). The device was fabricated by spin-coating poly(3,4-ethylenedioxythiophene) poly(styrenesulfonate) (PEDOT:PSS) polymer on a glass substrates pre-coated with a layer of transparent indium-tin-oxide (ITO) followed consecutively by layers of a blend of poly(3-hexylthiopene) (P3HT) and [6,6] –phenyl C_{61}-butyric acid methyl ester (PCBM), ZnO nanoparticles and evaporation of aluminium metal as cathode electrode. The power conversion efficiency (PCE) of 2.37 % was recorded from the OSC device incorporating a concentration of 0.5 mg/ml ZnO nanoparticles EEL and the PCE of 0.20 % was recorded from the same device after 10 days of storage in ambient laboratory conditions. The mechanisms of degradation of the OSC devices are discussed.

1. Introduction

Organic photovoltaic devices have drawn a lot of attention as means for the renewable energy conversion due to the remarkable combination of prospective low cost of manufacturing and rapid improvement of performance promising to approach the traditional silicon solar cells [1]. By introducing metal oxides in organic photovoltaics, the organic solar cells show great potential in terms of device performance with high exciton dissociation, the favourable charge transport ability and the air stability [2]. One of the key solar cell parameters affecting the cell power conversion efficiency (PCE) is the series resistance or internal resistance, R_s. The series resistance represents the total resistance of the cell and is a composite of (i) the active and interfacial layer resistances, (ii) electrode resistances and (iii) the various contacts and interconnect resistances [3]. Normal geometry of bulk heterojunction (BHJ) organic solar cells can suffer degradation of the top electrode, which is normally made of a low-work function metal (Al) that is reactive and oxidize easily in air. The exposure of Al cathode can cause oxidation and degradation of the active layer due to the diffusion of oxygen and moisture through pinholes and grain boundaries [4].

[1] Mbule P.S, Email: mbuleps@gmail.com

2. Experimental

2.1. ZnO nanoparticles synthesis

ZnO nanoparticles were synthesized by hydroxylation of zinc acetate dihydrate ($ZnAc.2H_2O$) by tetramethylammonium hydroxide (TMAH). In a typical preparation, TMAH dissolved in 30 ml of ethanol was added dropwise to 0.1M zinc acetate dihydrate dissolved in 30 ml of dimethylsulfoxide (DMSO). The nanoparticles were precipitated by adding ethyl acetate and then washed at least 3 times with heptane. Then nanoparticles were dried at 110 ^{o}C in an oven or re-dispersed in methanol. Figure 1 shows the schematic diagram of the ZnO synthesis.

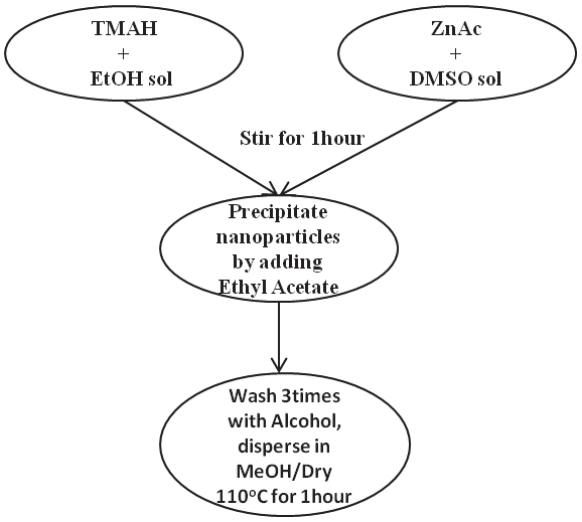

Figure 1: Schematic diagram of ZnO nanoparticles synthesis

2.2. Device Fabricaion

The organic solar cell device consisting of successive layers PEDOT:PSS (hole extraction layer), P3HT:PCBM (photo-active layer), ZnO nanoparticles (electron extraction layer) and Al cathode spin-coated on a glass substrate pre-coated with a layer of transparent indium-tin-oxide or ITO (anode) was fabricated. The glass substrate was first cleaned ultrasonically using isopropanol followed by drying at ~80 ^{o}C for 20 min and was finally treated in an ultraviolet ozone generator for 20 min. A thin layer of poly(3,4-PEDOT:PSS (CLEVIOS™ AI 4083) was spin-coated on the cleaned ITO pre-coated glass substrate at the speed of 4000 rpm for 35 s followed by drying in an oven/hot plate at 110 ^{o}C for 10 min. The active layer of P3HT:PCBM blend with a weight ratio of 1:0.6, dissolved in chlorobenzene, was spin-coated at the speed of 1000 rpm for 15 s. This was followed by the deposition of the layer of methanol solution of 0.5 mg/ml ZnO nanoparticles at 4000 rpm for 35 s. The top Al metal electrode (~100 nm) was thermally evaporated at ~ 1 x 10^{-6} Torr pressure through a shadow mask and the device area was 0.12 cm^2.

ZnO nanoparticles film structure was analyzed by X-ray diffractometer (XRD). The morphology of nanoparticles was determined by Field emission scanning electron microscopy (FE-SEM). The current density-voltage (J-V) curves of the device was measured in air using a Keithley 2400 source meter and an Oriel xenon lamp (150 W) coupled with an AM1.5 filter to simulate sunlight. The light intensity was calibrated with a silicon reference cell with a KG2 filter following standard solar cell testing procedures. All J-V measurements were conducted at the light intensity of 100 mW/cm^2. And finally SIMS depth profiling was performed by iontof TOF-SIMS^5 using two depth profiling ion beams operating in dual beam mode (Cs^+ ions for sputtering and Bi^{3++} for analyzing) to analyse the interface of different layers in the device.

3. Results and discussion

XRD patterns of ZnO nanoparticles are shown in figure 2. The diffraction peaks at scattering angles of 31.8 °, 34.4 °, 36.3 °, 47.5 °, 56.5 °, 62.7 °, 66.3 °, 67.9 ° and 69.0 ° correspond to the reflection from (100), (002), (101), (102), (110), (103), (200), (112) and (210) crystal planes, respectively, and they match well with the standard JCPDS data, card number 80-0075. Furthermore, the XRD data indicate that ZnO nanostructures exhibit the hexagonal wurtzite structure and the Debye-Scherrer equation [5] was used to estimate the crystallite size which was found to be ~ 5 ± 0.2 nm. FE-SEM images of spherical ZnO nanoparticles were observed and nanoparticles are evenly distributed on the surface. This is shown in figure 3.

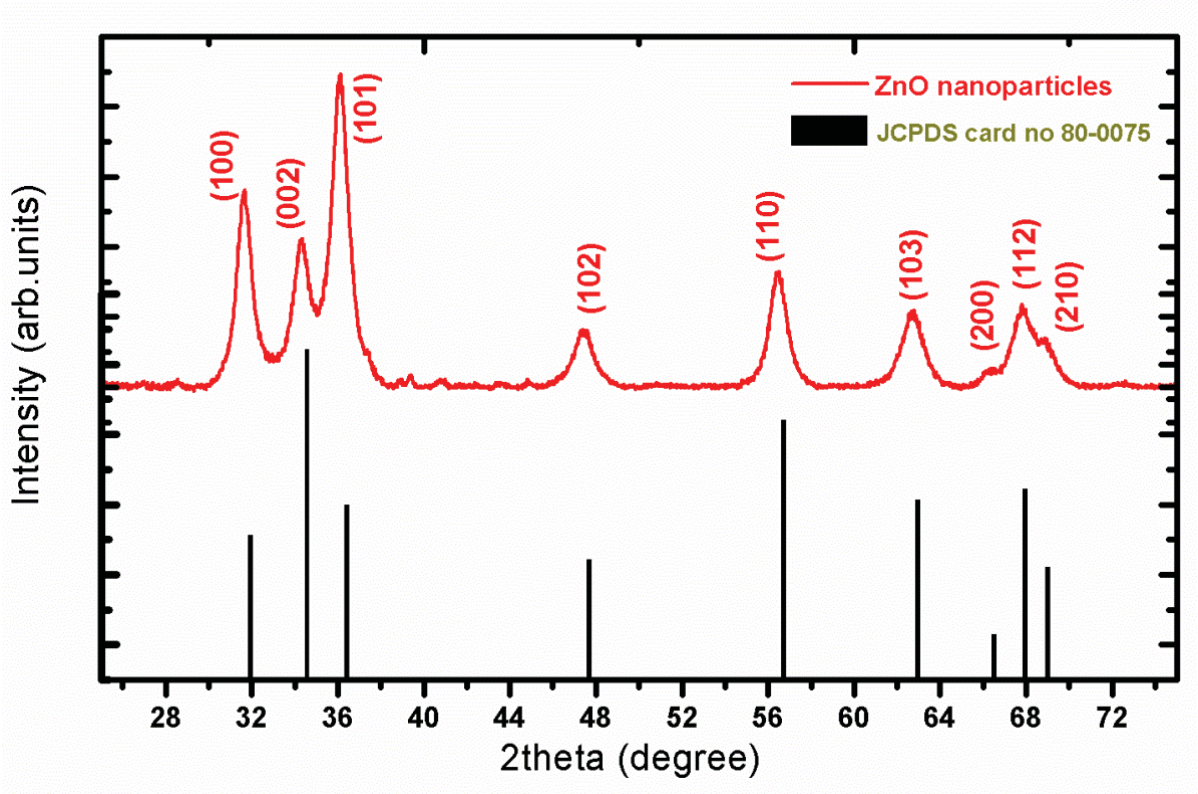

Figure 2: XRD patttern of ZnO nanoparticles.

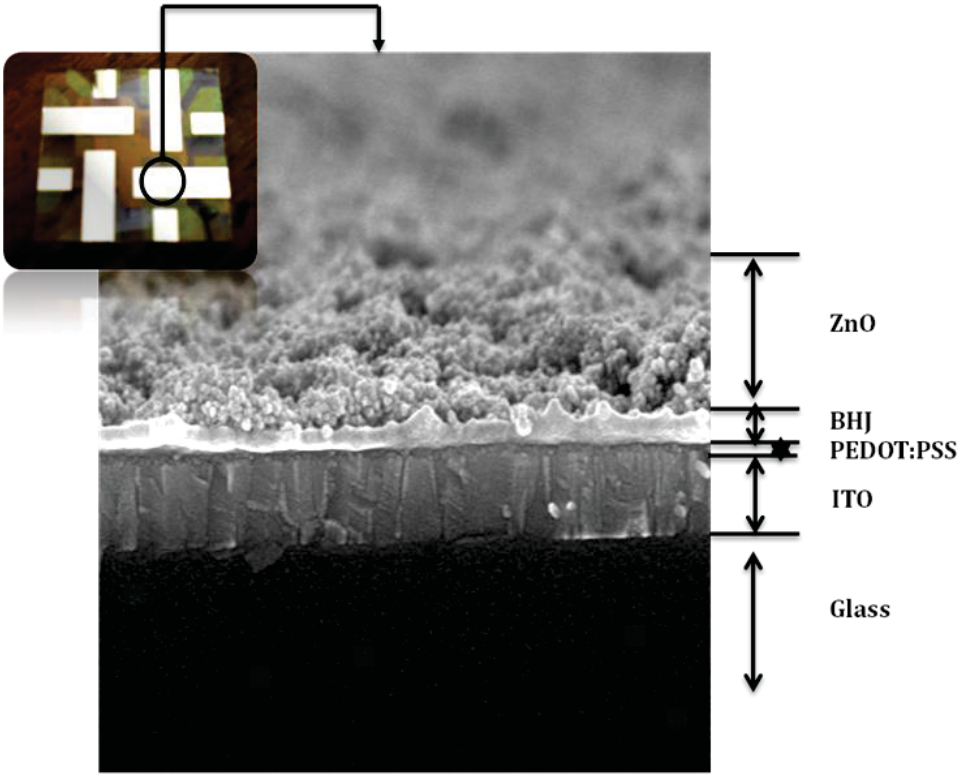

Figure 3: An image of a complete conventional organic solar cell and the FE-SEM cross-sectional view showing the different components of the device.

The Photovoltaic (PV) response curves of the device are illustrated in figure 4 with the summary of the PV characteristics presented in table 1. The initial device characteristics under solar irradiation in air yielded a power conversion efficiency of 2.37 %. The device significantly degraded after 10 days of storage with encapsulation in ambient laboratory conditions resulting in an efficiency of 0.20 %. The reduction of efficiency results primarily from a decrease in the short circuit current density and the degradation of active layer materials. There are different factors that can cause degradation of the OSC device and these factors can be classified as physical and/ or chemical. Generally, large serial resistances due to degradation of the bulk of a material or the quality of the metal electrode reduce the performance of the device. As observed in figure 4, after 10 days of storage the device suffers large series resistance, significantly increasing from 217 to 13 552 Ωcm^2. This is due to the deterioration of charge transport in the layers. The reduced fill factor (FF) from 49.50% to 37.18 % could be due to the reduced interfacial charge transfer efficiency between different layers [6]. Additionally, the degradation can be localized in the electrode layer itself or at the electrode/ZnO layer/active layer interfaces. In this last case, the degradation mechanism generally leads to a decrease of the interface quality between the active layer/ZnO layer and the electrode, therefore leading to a reduction of the charge transfer and extraction. This reduction of electrode/active layer interface can be due to physical loss of contact between the layers due to delamination [7], creation of voids or the formation of electrically insulating patches at the interface due to change of chemical reactions at the surface of the metal electrode [8]. Moreover, Positive secondary ion polarity, SIMS depth profiling of the device is presented in figure 5. Signals arising from different layers of the device components are clearly identified and the diffusion of tin (^{120}Sn) and indium (^{115}In) into the active layer has been recognized as one of the main factors that are detrimental to the life time of organic solar cells [9]. Different causes of device degradation are reported elsewhere [10].

Table 1: Photovoltaic comparison of the device

Device after fabrication				
J_{sc}(mA/cm^2)	V_{oc}(V)	FF(%)	PCE (%)	R_s (Ω.cm^2)
7.18	0.67	49.5	2.37	217
Device after 10 days of storage				
J_{sc}(mA/cm^2)	V_{oc}(V)	FF(%)	PCE (%)	R_s (Ω.cm^2)
0.91	0.59	37.18	0.20	13 552

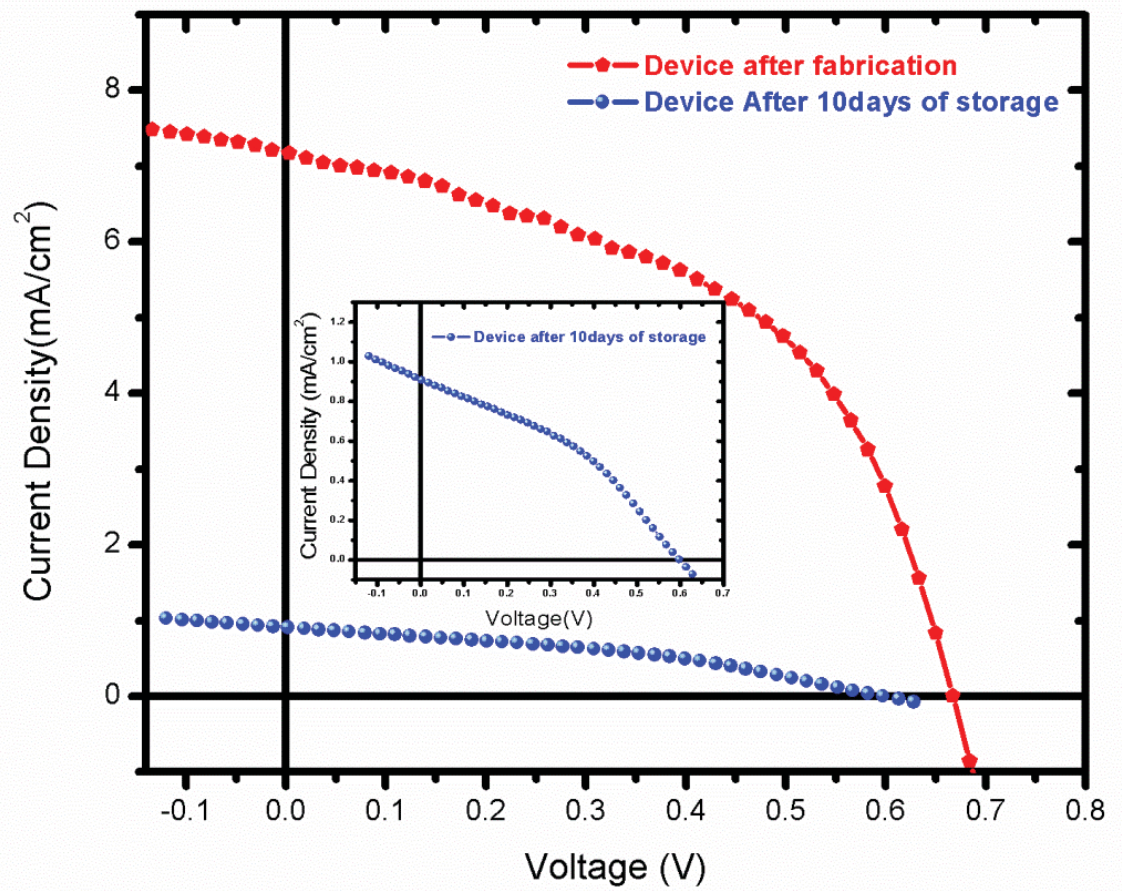

Figure 4: J-V curves of the device after fabrication and 10 days after storage

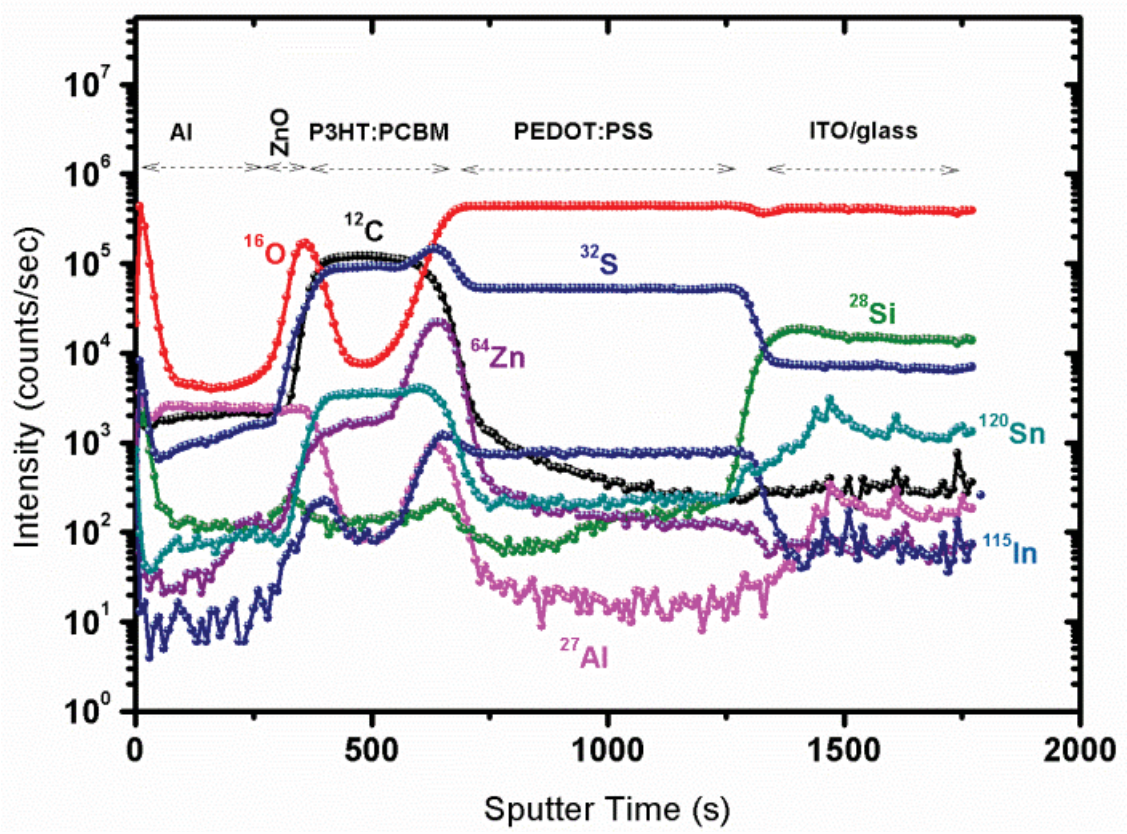

Figure 5: SIMS depth profiles of organic solar cell.

4. Conclusion

In conclusion, deterioration of charge collection in organic solar cell is reported. This is due to chemical degradation or oxidation of the compounds of the photoactive layer caused by atmospheric moisture or oxygen. Furthermore, atoms or molecules resulting from chemical degradation of the electrode can migrate through the other layers of the organic solar cell which may be damaging to the performance of the device. Chemical, physical and interfacial stability in organic devices remain a critical matter since polymeric materials are known to be less durable over a period of time.

5. Acknowledgement

The authors would like to thank the University of the Free State (UFS), South African National Research Foundation (NRF), the South African national laser centre (NLC) and Photonic Initiative of South Africa (PISA) for financial support. This research was partially supported by the KRCF (Korea Research Council of Fundamental Science and Technology) and the KIST (Korea Institute of Science and Technology) for ‘‘NAP (National Agenda Project) program’. The authors would like to thank Dr.-BongSoo Kim and Mr. Taehee Kim at KIST for their help with data collection and discussions.

References

[1] Ma W, Yang C, Gong X, Lee K and Heeger A.J, 2005 Adv. Funct. Mater. **15** 1617-1622
[2] Sekine N, Chou C.-H, Kwan W.-L and Yang Y, 2009 Org. Electron. **10** 1473-1477
[3] Servaites D.J, Yeganeh S, Marks T.J and Ratner M.A, 2010 Adv. Funct. Mater. **20** 97-104
[4] Wang J.C, Weng W.T, Tsai M.Y, Lee M.K, Horng S.F, Perng T.P, Yu C.C and Meng H.F, 2010 J.Mater. Chem. **20** 862-866
[5] Oh H, Krantz J, Litzov I, Pinna T and Brabec C.J, 2011 Sol. Energy Mater. Sol. Cells **95** 2194-2199
[6] Kawano K, Pacios R, Poplavskyy D, Nelson J, Bradley D and Durrant J.R, 2006 Sol. Energy Mater. Sol. Cells **90** 3520-3530
[7] Reese M.O, White M.S, Rumbles G, Ginley D.S and Shaheen S.E, 2008 Appl. Phys. Lett. **92** 053307/1-053307/3
[8] Paci B, Generosi A, Albertini V.R, Perfetti P, Firon M, Leroy J and Sentein C, 2005 Appl. Phys. Lett. **87** 194110-194110-3
[9] de Jong M.P, van Ijzendoorn L.J and de Voigt M.J.A, 2000 Appl. Phys. Lett. **77** 1212-1214
[10] Grossiord N, Kroon J.M, Andriessen R and Blom P.W.M, 2012 Org. Electron **13** 432-456

Computational studies of the bulk cobalt pentlandite (Co_9S_8): Validation of the potential model

M.A. Mehlape[1], **P.E. Ngoepe**[1] and **S.C. Parker**[2]

[1]Materials Modelling Centre, School of Physical and Mineral Sciences, University of Limpopo, South Africa, Private Bag, X1106, SOVENGA, 0727
[2]Computational Solid State Chemistry, University of Bath, Claverton Down, Bath, Avon, UK, BA2 7AY.

Email:mofuti.mehlape@ul.ac.za

Abstract. We use the density functional theory to study the cobalt pentlandite mineral (Co_9S_8). We investigate various forms of the cobalt pentlandite, Co_9S_8, at different temperatures, using classical atomistic simulation methods with the support of electronic structure calculations. The first interatomic potentials of Co_9S_8 based on the Born model, were derived with input data such as structure and elastic properties from experiments and electronic structure calculations respectively. The interatomic potentials were validated by running energy minimization and molecular dynamics calculations. The structure and elastic properties corresponded well with those determined by electronic structure methods. The calculations further reproduced the complex high temperature transformation to high form pentlandite and the melting of Co_9S_8; as deduced from the crystal structure and radial distribution functions.

1. Introduction

Pentlandites, $(Fe,Ni,Co)_9S_8$, are important nickel and cobalt sulphide minerals in economic deposits where it occurs with pyrrohotite, chalcopyrite and pyrite in mafic and ultramafic igneous rocks [1]. Furthermore, pentlandite minerals play an important role in the production of cleaner fuels with low or ultra-low sulphur content that require a continuous improvement of catalytic materials used in the refinement industry. In addition to supplying base metals, pentlandite compounds occur as solid solutions, in Merenksy reef, and intergrowths in UG2 reefs, with precious metal compounds, where the former occur in larger quantities [2]. In order to extract the precious metals from the ores effectively it is necessary to study and understand structural, including surface properties, of pentlandites in detail. Notwithstanding their significance in mineralogy, previous experimental studies on pentlandites are not as abundant as those of pyrites and metal oxide minerals, and computational modelling investigations are also very scarce. We present the first classical interatomic potential model [3] of Co_9S_8, and its validation, since the compound is easier to handle than $(Fe, Ni)_9S_8$, owing to its cubic symmetry. Such potentials render structural studies of surfaces and nanoparticles, with large number of atoms, and their variation with temperature more amenable.

2.1. Cobalt Pentlandite, Co_9S_8 structure

The conventional unit cell of the cobalt pentlandite has the formula $Co_{36}S_{32}$ and contains a cubic close-packed arrangement of sulphide ions containing 64 tetrahedral holes and 32 octahedral holes. Of the 64 tetrahedral holes, 32 are occupied by Co^{2+} ions, these being distributed through the lattice in groups of eight which lie at the corners of sub-cubes of edge length 0.250 nm. Of the 32 octahedral holes, 28 are pseudo-octahedral, distorted, and empty, whereas four are truly octahedral and each contains a Co atom in a formally zero oxidation state. Thus the solid attains the overall stoichiometry Co_9S_8 [4]. Figure 1 shows the conventional unit cell of Co_9S_8. The Co_9S_8 has a space group *Fm3m*.

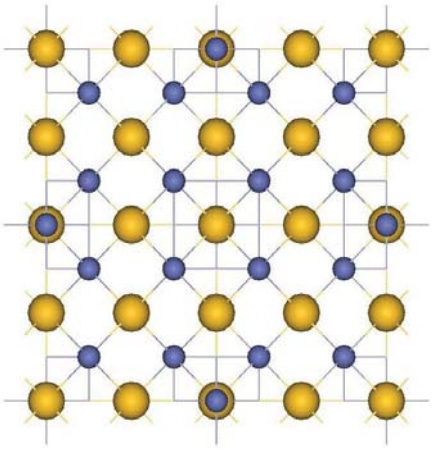

Figure 1: Conventional unit cell of cobalt pentlandite structure (Co_9S_8). Blue and yellow spheres represent cobalt (Co) and sulphur (S) atoms respectively.

2. Methodology

The VASP code [5] was used to calculate the elastic properties of Co_9S_8 (used as the existing data, for derivation of the interatomic potentials). Interatomic potentials of Co_9S_8 were derived by GULP [6] code and together with DLPOLY [7] molecular dynamics (MD) simulations were performed. The Born ionic model [8] was used and parameters were derived for short range interactions represented by the Buckingham potential, Morse potential and three body terms:

Buckingham Potential

In the Buckingham potential, the repulsive term is replaced by an exponential term and potential takes the form

$$U(r_{ij}) = A_{ij} * \exp^{-r_{ij}/\rho_{ij}} - \frac{C_{ij}}{r_{ij}^6} \quad (1)$$

where A_{ij} and ρ_{ij} are parameters that represent the ion size and hardness, respectively, while C_{ij} describe the attractive interaction and r_{ij} is the distance between ion i and ion j. The first term is known as the Born-Mayer potential and the attraction term (second term) was later added to form the Buckingham potential. Very often, for the cation-anion interactions, the attractive term is ignored due to the very small contribution of this term to the short-range potential, or, alternatively, the interaction is subsumed into the A and ρ parameters.

Morse Potential

The Morse potential is used to model the interactions between covalently bonded atoms and has the form

$$U(r_{ij}) = A_{ij} * \left(1 - \exp^{-B_{ij}*(r_{ij}-r_0)}\right)^2 - A_{ij} \quad (2)$$

where A_{ij} is the bond dissociation energy, r_0 is the equilibrium bond distance, and B_{ij} is a function of the slope of the potential energy well. The Coulombic interactions between covalently bonded atoms are often partially or totally ignored as the Morse potential already contains the attractive component of the interaction between neighbours.

Three-Body Potential

A further component of the interactions of covalent species is the bond-bending term, which is added to take into account the energy penalty for deviations from the equilibrium value. Hence, this potential describes the directionality of the bonds and has a simple harmonic form:

$$U(\theta_{ijk}) = \frac{1}{2} k_{ijk} (\theta_{ijk} - \theta_0)^2 \quad (3)$$

where k_{ijk} is the three-body force constant, θ_0 is equilibrium angle and θ_{ijk} is the angle between two interatomic vectors $i - j$ and $j - k$.

3. Results and Discussions

The properties, i.e. lattice parameters and elastic properties to validate the derived potential model of Co_9S_8 are discussed and also molecular dynamics simulation of bulk Co_9S_8 at high temperatures is discussed.

3.1. Validation of Potential Model of Co_9S_8

The accuracy of the derived interatomic potentials was checked by comparing the known experimental and calculated data. To validate our potential models we start by showing the properties that where obtained from our derived potentials i.e., lattice parameters and elastic properties. The lattice parameter obtained using energy minimisation code GULP is in good agreement with those from the literature as shown in Table 1.

Table 1. Comparison of the lattice parameter of Co_9S_8, obtained from the derived interatomic potentials, with the other calculated and experimental values.

Method	a (**Å**)
GULP (This work)	9.806
VASP (PW-GGA)(This Work)	9.811
*TB-LMTO[a]	9.918
Extended Huckel Type Band Calculations[b]	9.927
EXPERIMENTAL[c]	9.928

[a][10], [b][11], [c][9]
*Tight-binding linear-muffin-tin-orbital

Table 2 shows a comparison of the elastic properties of Co_9S_8 we calculated using DFT methods (VASP code) and those calculated from our derived interatomic potentials employing the GULP code; experimental elastic constants are currently not available for Co_9S_8. The elastic constants from the interatomic potentials are in good agreement with those from DFT calculations, together with the various moduli of elasticity, i.e. the bulk, shear, elasticity moduli and Poisson's ratio. In addition, the Co_9S_8 phase has elastic constants that satisfy the generalized elastic stability criteria for cubic crystals [12], [13];

$$(C_{11} - C_{12})/3 > 0, C_{11} + 2C_{12} > 0, C_{44} > 0 \quad (4)$$

The bulk modulus *B*, shear modulus *G* and elastic modulus *E* of the cubic Co_9S_8 phase were deduced according to the following formulae [14], [15], [16], [17];

$$B = \frac{1}{3}(C_{11} + 2C_{12}) \tag{5}$$

$$G = \frac{1}{5}(C_{11} - C_{12} + 3C_{44}) \tag{6}$$

$$E = \frac{(C_{11} - C_{12} + 3C_{44})(C_{11} + 2C_{12})}{2C_{11} + 3C_{12} + C_{44}} \tag{7}$$

Poisson ratio v is obtained from:

$$v = \frac{3B - E}{6B} \tag{8}$$

Table 2. Calculated elastic constants and moduli of the Co_9S_8 phase

Properties	VASP	GULP (Fitted)
C_{11}	223.8	214.3
C_{12}	80.3	82.3
C_{44}	71.3	70.0
Bulk Modulus, *B* (GPa)	128.1	126.3
Shear Modulus, *G* (GPa)	71.5	68.4
Elastic Modulus, *E* (GPa)	180.8	173.8
Poisson Ratio, v	0.26	0.27
Volume (A^3) *		947.6

*Experimental Volume is 978.56 $Å^3$ [9]

3.2. Molecular Dynamics Simulation of Co_9S_8

In order to demonstrate the phase changes of the Co_9S_8 structure using molecular dynamics, we superimposed the total radial distribution functions of Co_9S_8 bulk at different temperatures in Figure 2. The total magnified RDFs indicate that as the temperature increases, the peaks become broader and the number of peaks decreased. Furthermore, the total RDFs show that between 300 and 900 K, the second and third peaks (denoted by B and C, respectively) are well-defined and approach each other. However, at 1100 K the peaks coalesce, and the combined peak (denoted by D) remains in the same position at 1300 K. This is the temperature range where Co_9S_8 undergoes phase change from normal to high form pentlandite according to experimental work of Kitakaze & Sugaki [18]. They reckoned that the high form of cobalt pentlandite is stable up to 930°± 3 °C (1203 K ± 3 K) , where it breaks down to a mixture of cobalt monosulfide (Fe- and Ni-free end-member of monosulfide solid-solution) and liquid in an incongruent melting reaction. They finally observed that remnant cobalt monosulfide melts completely at 1069° ± 5 °C (1342 ± 5 K). Indeed our simulations (Figure 2) confirm the molten phase at 1500 K, since the height of the coalesced peak is reduced. At a higher temperature of 1900 K the height of the coalesced peak is further reduced showing a completely molten structure. The first peak of the RDF gives a radial distance of approximately 2.15 Å at 300 up to 900 K and 2.17 Å at 1100 K up to 1500 K. The radial distance is close to the experimental interatomic distance of Co-S on

the tetrahedral site which is 2.13 Å. The second and third peaks give approximately 3.45 Å and 3.97 Å, respectively at 300 K up to 900 K. At 1100 K up to 1500 K the second and third peaks combine to give one peak of approximately 3.61 Å. The radial distance is close to the EXAFS measurement interatomic distance of Co-Co on the tetrahedral site which is 3.54 Å [18]. Hence it may be deduced that the phase change from the normal to high form pentlandite is associated with the movement of Co on the tetrahedral sites. The ability of the interatomic potentials to reproduce the complex high temperature phase change of pentlandite and to elucidate atoms participating in such change demonstrates the robustness of the potentials.

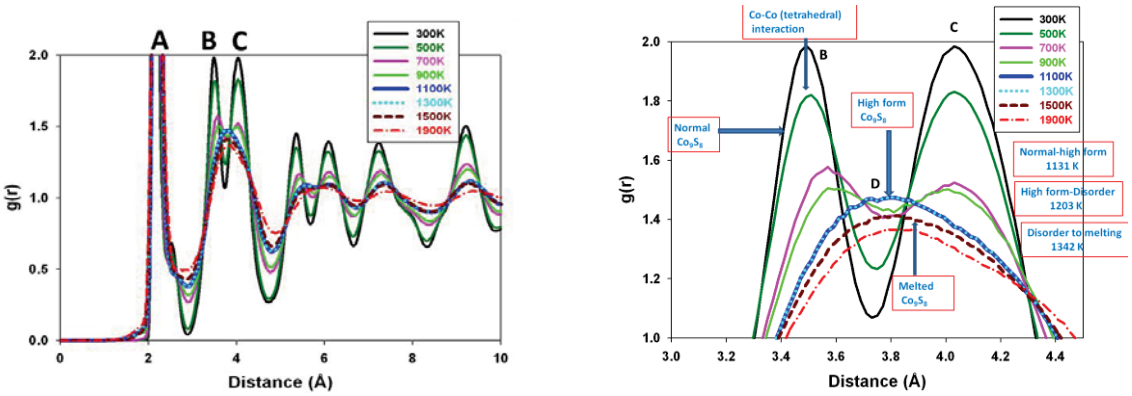

(a) (b)

Figure 2: The total radial distribution functions of the Co_9S_8 bulk structure at (a) different temperatures and (b) magnified RDFs showing the coalescing of the adjacent Co-Co tetrahedral peaks.

4. Conclusion

The derived interatomic potentials of Co_9S_8 were validated by the accurate determination of structure and elastic constants. The robustness of the interatomic potentials was further illustrated by their ability to reproduce complex high temperature transitions of the bulk Co_9S_8 which were observed experimentally. The change of radial distribution functions (especially the coalescing (coming together) of the adjacent Co-Co tetrahedral peaks) deduced from molecular dynamics studies, depicted the phase change from the normal to the high form Co pentlandite above 1100 K.

Acknowledgements

The computations were performed at the Materials Modelling Centre (MMC), University of Limpopo and at the Centre for High Performance Computing (CHPC). We also acknowledge the National Research Foundation (NRF) and Anglo Platinum for funding.

References

[1] Borodaev Y S, Bryzgalov I A, Mozgova N N and Uspenskaya T Y 2007 *Moscow Univ. Geol. Bull.* **62** 85-97

[2] Johan Z, Ohnenstetter M, Slansky E, Barron L M and Suppel D 1989 *Mineralogy and Petrology*, **40** 289-309

[3] Mehlape M A, 2013 *Computational Modelling Studies of Cobalt Pentlandite (Co_9S_8)*. (Ph Thesis, University of Limpopo)

[4] Hoodless R C, Moyes R B and Wells P B 2006 *Catalysis Today*, **114** 377–382

[5] Kresse G and Hafner J 1993 *Phys. Rev. B* **47** 558–561

[6] Gale J D 1997 *J. Chem Soc. Faraday Trans.* **93** 629

[7] Smith W and Forester T R 1996 *J. Mol. Graphics*, **14** 136-341

[8] Born M and Huang K 1954 *Dynamical Theory of Crystal Lattices 1st edition* (University Press: Oxford)

[9] Geller S 1962 *Acta Crystallogr*, **15** 1195-1198

[10] Chauke H R, Nguyen-Manh D, Ngoepe P E, Pettifor D G and Fries S G 2002 *Phys. Rev. B*,

66 155105-5
[11] Burdett J K and G J Miller 1987 *J. Amer. Chem. Soc.* **109** 4081-91
[12] Yu W, Wang N, Xiao X, Tang B, Peng L and Ding W 2009 *Solid State Sciences*, **11** 1400–07
[13] Dian-wu Z, Jin-shui L and Ping P 2011 *T. Nonferr. Metal. Soc.* **21** 2677−83
[14] Mehl M J, Osburn J E, Papaconstantopoulos D A and Klein B M 1990 *Phys. Rev. B: Condensed Matter*, **41** 10311−23
[15] Wang T, Chen P, Deng Y and Tang B, 2011 *Trans. of Nonferr. Metal Soc. of China*, **21** 388−394
[16] Screiber E, Anderson O L and Soga N, 1973 *Elastic constants and their measurement*, (McGraw Hill, New York)
[17] Benkabou F, Aourag H and Certier M, 2000 *Mater. Chem. Phys.* **66** 10–16
[18] Kitakaze A and Sugaki A 2004 *Can. Mineral*, **42** 17-42
[19] Bouwens S M A M, Van Veen J A R, Koningsberger D C, De Beer V H J, and Prins R, 1991 *J. Phys. Chem.* **95** 134-139

Luminescent properties of $Ca_5(PO_4)_3OH:Gd^{3+}$, Pr^{3+} phosphor powder

P.P. Mokoena[1], I.M. Nagpure[1], Vinay Kumar[1.2], H.C. Swart[1] and O.M Ntwaeaborwa[1]

[1] Department of Physics, University of the Free State, Bloemfontein, ZA9300, South Africa
[2] School of Physics, Shri Mata Vaishno Devi University, Katra (J&K)-182320, INDIA

E-mail: ntwaeab@ufs.ac.za

Abstract. Hydroxylapatite ($Ca_5(PO_4)_3(OH)$) is a well-known bioceramic material for medical application. It is biocompatible meaning that it has the ability to form chemical bonds with living tissues. Phosphate based inorganic compounds doped with rare earth ions form an important family of phosphors for solid state lighting applications [1]. In this study, we prepared (using co-precipitation method) and investigated the structure, morphology, and photoluminescent properties of ($Ca_5(PO_4)_3(OH)$) co-doped with gadolinium (Gd^{3+}) and praseodymium (Pr^{3+}). The X-ray diffraction (XRD) patterns show a hexagonal phase of $Ca_5(PO_4)_3(OH)$ consistent with the standard JCPDS data file No 73-0293. The XRD peaks were sharp and intense suggesting that the phosphor was highly crystalline. The scanning electron microscopic images show that the powders consist of an agglomeration of spherical particles. The photoluminescent spectrum of $Ca_5(PO_4)_3(OH):Gd^{3+},Pr^{3+}$ phosphor exhibit a narrow emission peak at 313 nm due to the $^6P_{7/2}\rightarrow{}^8S_{7/2}$ transition of the Gd^{3+} ion, and this emission was enhanced by Pr^{3+} co-doping. The photoluminescent properties of the $Ca_5(PO_4)_3(OH):Gd^{3+},Pr^{3+}$ phosphor are evaluated for application in phototherapy lamps.

Introduction

Hydroxylapatite is one of the three occurring mineral forms of apatite (calcium-phosphate mineral). These minerals are flourapatite ($Ca_5(PO_4)_3F$), chlorapatite ($Ca_5(PO_4)_3Cl$ and hydroxylapatite ($Ca_5(PO_4)_3OH$) [2]. Hydroxylapatite has been found to be an attractive new functional material used mainly in medical applications because of its biocompatibility. Today, it is also used as a host for rare-earth elements to prepare phosphors that can be used, among other things, in phototherapy lamps for treatment of different skin diseases and general lighting applications. The dopant Gd^{3+} has been used as a luminescent activator in hydroxylapatite hosts to produce ultraviolet radiation (UVR), specifically in the ultraviolet B (UVB) region of the electromagnetic wave spectrum. In addition, up-conversion emission of Gd^{3+} has also been reported which shows Gd^{3+} emission peaks in the range of ~280 - 320 nm. These spectral characteristics suggest that Gd^{3+} can have a wide range of UV applications. In this study, the enhancement of this UVB emission by co-doping with Pr^{3+} is demonstrated. The enhanced UVB emission will be useful in prolonging the life span of phototherapy lamps used in treatment of various skin diseases.

Experimental

1 Synthesis

$Ca_5(PO_4)_3(OH):Gd^{3+},Pr^{3+}$ phosphor was synthesized by the reaction of diammonium hydrogen phosphate ($(NH_4)_2HPO_4$), sodium hydroxide (NaOH) and calcium nitrate tetrahydrate ($Ca(NO_3)_34H_2O$) in distilled water. In a typical preparation, 100 ml of 0.4M ($(NH_4)_2HPO_4$) solution with pH= 6.5, 100 ml of 0.1M (NaOH) solution with pH = 13.5, and 100 ml of 0.6M ($Ca(NO_3)_34H_2O$), and 2M $Pr(NO_3)_36H_2O$ and 10M $Gd(NO_3)_3{\cdot}5H_2O$ solutions, both at pH = 7.3, were prepared and all the combined solutions were stirred vigorously at room temperature. Throughout the mixing process the pH of the system was maintained at pH = 6.5, and after adding 0.1M NaOH the pH of the solution increased to 10.8 and the white precipitate was formed. The precipitate was stirred for 12 hours at room temperature, was washed with distilled water and then with ethanol to increase the dispersion characteristics, and was finally dried at 80 °C for 24 hours. The dried powder was ground by using a mortar and pestle and calcined at 900 °C for 2 hours. $Ca_5(PO_4)_3(OH):Gd^{3+},Pr^{3+}$ powder phosphors with different concentrations of Gd^{3+} and Pr^{3+} were prepared.

2 Characterization

The crystalline structure was analyzed by X-ray Diffraction (XRD), using Bruker AXS D8 Advance diffractometer and the samples were irradiated with Cukα radiation (λ = 1.5406 Å). The crystallite size (D) was calculated from XRD peaks using Scherrer equation:

$$D = 0.89\lambda / \beta \cos\theta \qquad (1)$$

where λ is the wavelength of the used Cu Kα radiation, β is the full width at the maximum of the $Ca_5(PO_4)_3(OH):Gd^{3+},Pr^{3+}$ line and θ is the diffraction angle. The particle morphology was analyzed using Scanning Electron microscope (SEM). The photoluminescent (PL) was used to determine the luminescent properties of the samples in air at room temperature.

Results and discussion

Figure 1 (a) shows the XRD pattern of $Ca_5(PO_4)_3(OH):Gd^{3+},Pr^{3+}$ phosphor powder. The samples were all annealed at 900 °C in air. The diffraction peaks from $Ca_5(PO_4)_3(OH):Gd^{3+},Pr^{3+}$ are consistent with the hexagonal phase of $Ca_5(PO_4)_3$ referenced in the standard JCPDS Card Number 73-0293. The narrow and sharp diffraction peaks suggest that our materials were highly crystalline. Figure 1 (b) shows the XRD patterns of $Ca_5(PO_4)_3(OH):Gd^{3+},Pr^{3+}$ phosphor powders calcined at 600, 700, 800, 900 and 1000 °C for 2 hours. The spectra show that the crystallinity of the powder was improved with an increasing temperature. The strongest peaks that were used to estimate the crystallite size by Scherrer's equation were (2θ = 25.95°, 31.89°, 46.77°, and 49.55°). The average crystallite size of the phosphor powders calcined at the different temperatures was in the range of ~22 - 65 nm.

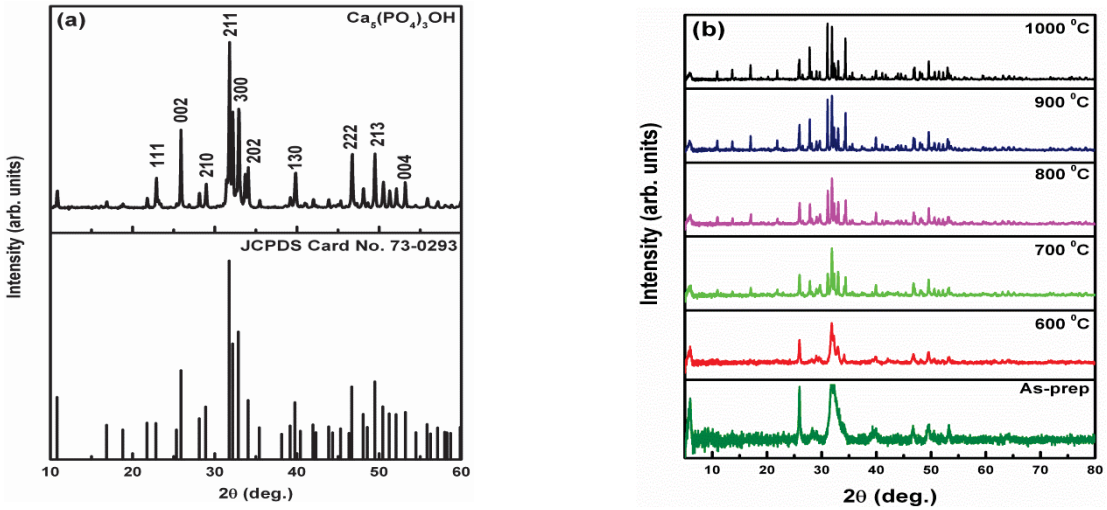

Figure 1 (a) XRD patterns of $Ca_5(PO_4)_3(OH)$ powder calcined at 900 °C (and standard JCPDS Card No. 73-0293), and (b) $Ca_5(PO_4)_3(OH):Gd^{3+},Pr^{3+}$ powders calcined at different temperatures.

Figure 2 (a) shows the SEM image of $Ca_5(PO_4)_3(OH):Gd^{3+},Pr^{3+}$ powder calcined at 900 °C for 2 hours in air. The image shows that the particles are agglomerated together with isolated particles appearing spherical in shape. A qualitative analysis of the chemical composition performed by EDS confirmed all the elements (Ca, P, O, Gd^{3+} and Pr^{3+}) as shown in figure 2 (b).

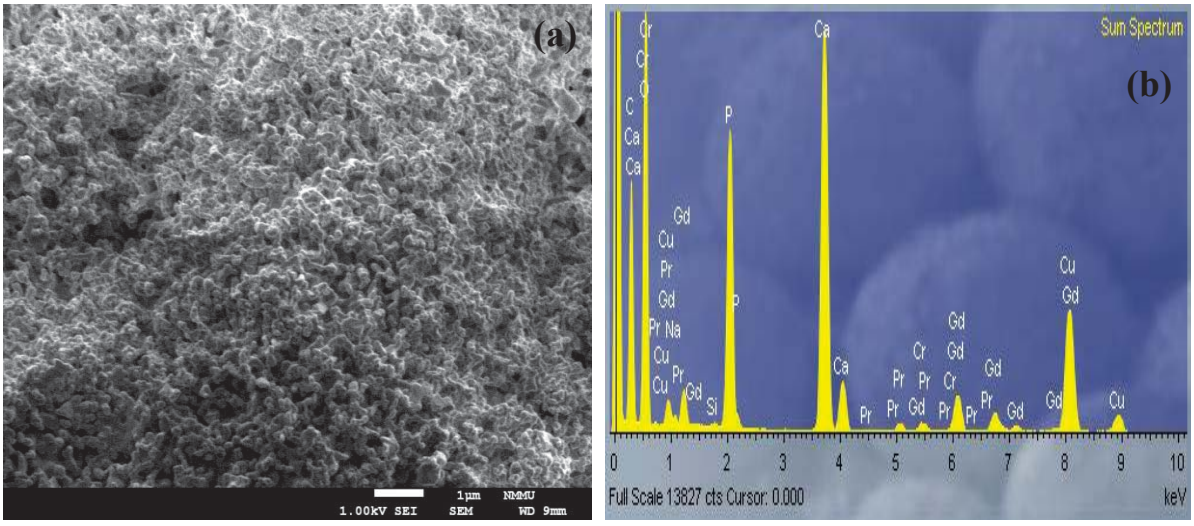

Figure 2 (a) SEM images and (b) EDS spectrum of $Ca_5(PO_4)_3(OH):Gd^{3+},Pr^{3+}$ phosphor powder.

Figure 3 (a) shows the optical absorption spectra of pure $Ca_5(PO_4)_3(OH)$, $Ca_5(PO_4)_3(OH):Gd^{3+}$, $Ca_5(PO_4)_3(OH):Pr^{3+}$ and $Ca_5(PO_4)_3(OH):Gd^{3+},Pr^{3+}$ powders. The host has a strong absorption bands with main absorption at 207 nm and minor absorption at 300 nm. The $Ca_5(PO_4)_3(OH):Gd^{3+}$ follow the same trend as that of the host. The peaks at 207 nm and 300 nm are respectively assigned to band to band absorption and intrinsic defects in the material [6, 7]. $Ca_5(PO_4)_3(OH):Pr^{3+}$ and $Ca_5(PO_4)_3(OH):Gd^{3+},Pr^{3+}$ systems shows two absorption bands at 446, 471, 483 nm assigned to $^3H_4 \rightarrow {}^3P_{j\ (j\ =\ 0,\ 1,\ 2)}$ and 593 nm assigned to $^3H_4 \rightarrow {}^1D_2$ transitions of Pr^{3+} [8,9]. The inset on

$Ca_5(PO_4)_3(OH):Pr^{3+}$ system show the enlargement of the absorption bands at range of 445 to 630 nm. Figure 3 (b) shows the plot of $(\alpha h\upsilon)^2$ vs photon energy ($h\upsilon$), where α is the absorption coefficient. The optical band gap was determined by extrapolating the linear portion of the curve or tail [10] and the estimated value of the band gap energy was found to be 5.2 eV.

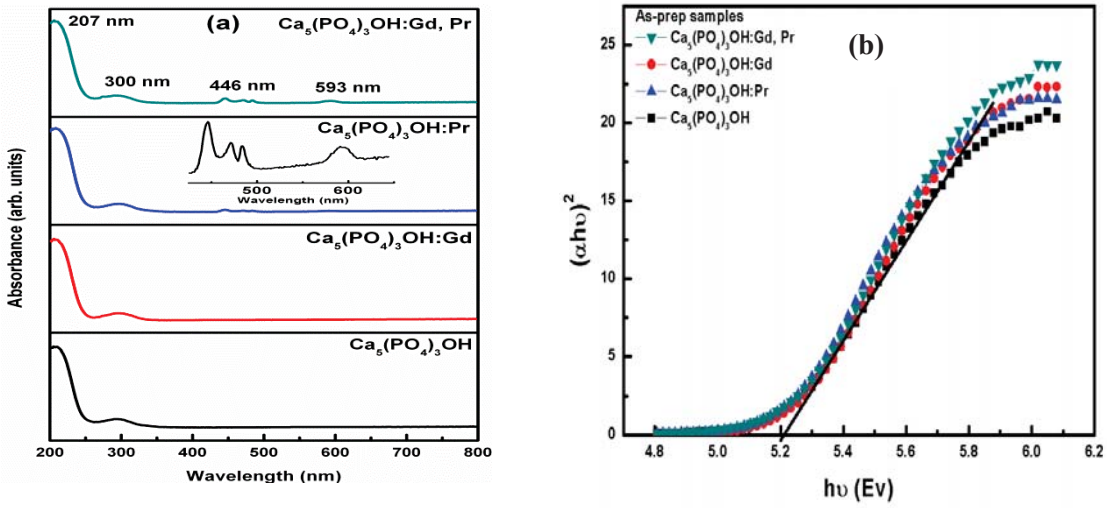

Figure 3: (a) Optical absorption spectra and (b) $(\alpha h\upsilon)^2$ vs photon energy ($h\upsilon$) plot of $Ca_5(PO_4)_3(OH):Gd^{3+},Pr^{3+}$

Figure 4 (a) shows the PL (i) excitation and (ii) emission spectra of $Ca_5(PO_4)_3OH$:Gd, Pr^{3+} calcined at 900 °C. The excitation peaks at 222 nm and 274 nm are attributed to host absorption and $^8S_{7/2}\rightarrow{}^6I_j$ transition of Gd^{3+} respectively [11, 12]. The PL emission of $Ca_5(PO_4)_3OH:Gd^{3+},Pr^{3+}$ consists of narrow band emission at 313 nm corresponding to $^6P_{7/2}\rightarrow{}^8S_{7/2}$ transition of Gd^{3+} [13]. The incorporation of Pr^{3+} was shown to improve the host absorption at 222 nm and this in turn improved the 313 nm emission of the Gd^{3+}. The mechanism by which Pr^{3+} enhances the host absorption is not known yet, but this study is in progress and the mechanism will be reported in our future publications. The energy absorbed by the host is transferred to Gd^{3+} which inturn enhances the UVB emission at 313 nm. The inset of figure 4 (a) shows that the maximum PL intensity was obtained when concentrations of Gd^{3+} and Pr^{3+} were 10 and 2 mol% respectively, suggesting that the excitation energy from the host to Gd^{3+} was transferred efficiently at this combination. Figure 4 (b) shows the emission and excitation spectra of $Ca_5(PO_4)_3OH:Gd^{3+},Pr^{3+}$ calcined at different temperatures (600 - 1000 °C). The PL intensity increased with an increasing temperature. All the peaks (excitation and emission) are at the same positions as those shown in figure 4 (a) suggesting that calcining at different temperatures did not affect the excitation and radiative transition of the $Ca_5(PO_4)_3OH:Gd^{3+},Pr^{3+}$.

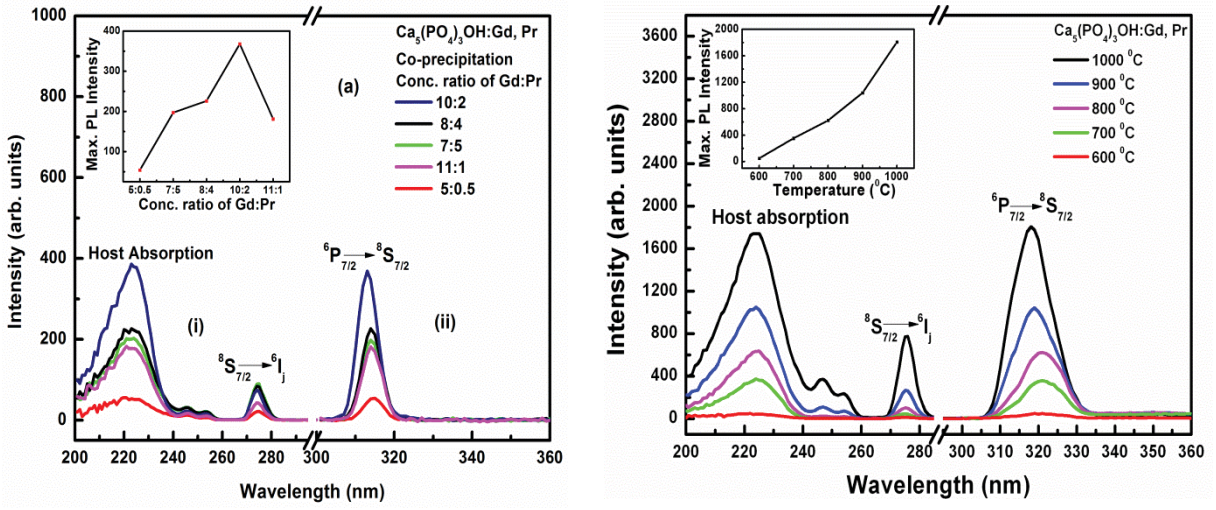

Figure 4. (a) PL excitation and emission spectra of $Ca_5(PO_4)_3OH:Gd^{3+},Pr^{3+}$ and (b) calcined at different temperatures.

Conclusion

In summary, $Ca_5(PO_4)_3(OH):Gd^{3+},Pr^3$ phosphor was successfully synthesized via the co-precipitation method. The $Ca_5(PO_4)_3(OH):Gd^{3+}$system exhibited a narrowband UVB emission at 313 nm. This emission was enhanced by co-doping with Pr^{3+} and also by calcining at different temperatures.

Acknowledgement

The project is financially support by the South African National Research Foundation (NRF), the rental pool programme of the council for scientific and industrial research (CSIR)'s national laser centre (NLC), the South African Research Chairs Initiative of the Department of Science and Technology and National Research Foundation of South Africa, and the cluster program of the University of the Free State.

References

[1] Shinde KN, Dhoble SJ, 2010, Advanced *Material letters*, **1(3)**, 254-258
[2] http://skywalker.cochise.edu/wellerr/students/apatite/project.htm[2012/04/12]
[3] Nakashima K, Takami M, Ohta M, Yasue T, Yamauchi J, 2005*, Journal of Luminescence*, **111**, 113-120
[4] Yin Y, Hong G, 2006*, Journal of Nanoparticle Research*, **8**, 755-760
[5] Bahman M, Behzad M, Nayereh A, 2011*, Processing and Applications of Ceramic*, **5 [4]**, 193-198
[6] Okamoto S, Uchino R, Kobayashi K, Yamamoto H, 2009*, Journal of Applied Physics*, **106**, 013522
[7] Chen L, Zhiguo S, Jianbei Q, Zhengwen Y, Xue Y, Dacheng Z, Zhaoyi Y, Rongfei W, Yuanyuan X, Yuechan C, 2012, *Journal of Luminescence*, **132**, 1807-1811
[8] Yu-Chun Li, Yen-Hwei Chang, Yee-Shin Chang, Yi-Jing Lin, Chih-Hao Laing, 2007*, Journal of Physical Chemistry C*, **111**, 10682-10688
[9] Sreenivasulu M, Rao AS, 2001, *Journal of Material Science letters*, **20**, 737-740
[10] Pereira PFS, de Moura AP, Nogueira IC, Lima MVS, Longo E, de Sousa Filho PC, Serra OA, Nassar EJ, Rosa ILV, 2012, *Journal of Alloys and Compounds*, **526**, 11-21

[11] Feldmann C, Justel T, Ronda CR, Wiechert DU, 2001, *Journal of Luminescence*, **92**, 245-254
[12] Han B, Liang H, Su Q, Huang Y, Gao Z, Tao Y, 2012, *Applied Physics B Laser and Optics*, **100**, 865-869
[13] Tian Z, Liang H, Han B, Su Q, Tao Y, Zhang G, Fu Y, 2008, *Journal of Physical Chemistry C*, **112**, 12524-12529

Magnetic properties of the $(Cr_{100-x}Al_x)_{99}V_1$ alloy system

B Muchono[1,2], C J Sheppard[1], A R E Prinsloo[1] and H L Alberts[1]

[1] Physics Department, University of Johannesburg, P.O. Box 524, Auckland Park, Johannesburg 2006, South Africa
[2] Applied Physics Department, NUST, Box AC939, Ascot, Bulawayo, Zimbabwe

E-mail address: alettap@uj.ac.za

Abstract. Electrical resistivity (ρ), Seebeck coefficient (S) and magnetic susceptibility (χ) measurements as a function of temperature on the $(Cr_{100-x}Al_x)_{99}V_1$ alloy system, with $0 < x < 7$ are reported. Néel temperatures (T_N) obtained from all these measurements decrease with Al concentration, disappearing near $x \approx 1.5$, again reappearing for $x > 4.0$. $\rho(T)$ and $S(T)$ for samples with $x \geq 6.1$ show weak anomalies making the determination of T_N difficult. However, these anomalies are sharply defined in $\chi(T)$, proving that it is an important tool in probing antiferromagnetic in this system. The present results show that the addition of just 1 at.% V to the $Cr_{100-x}Al_x$ alloy system suppresses antiferromagnetism in the concentration range $1.5 \leq x \leq 4.0$. This behaviour is similar to that observed for the $(Cr_{100-x}Al_x)_{95}Mo_5$ alloy system.

1. Introduction

Cr and its dilute alloys are itinerant electron spin density wave antiferromagnetic materials [1]. The influence of Al in the Cr matrix is rather unique amongst Cr alloys in that increasing the Al content does not continuously decrease the Néel transition temperature T_N [1] as expected from the two-band theory [2]. However, T_N decreases sharply, reaches a minimum value of approximately 100 K at a critical concentration $x_c \approx 2$ at.% Al, where after it increases sharply on further addition of the Al content [1, 3]. The critical concentration lies at a deep minimum on the $Cr_{100-x}Al_x$ magnetic phase diagram. The critical concentration separates the incommensurate spin-density-wave (ISDW) phase for which $x \leq x_c$, the commensurate spin-density-wave (CSDW) phase for which $x \geq x_c$ and the paramagnetic (P) phase for which $T > T_N$ [1, 3, 4]. The interesting magnetic properties of this system were previously explored by the addition of 5 at.% Mo to form a $(Cr_{100-x}Al_x)_{95}Mo_5$ alloy system [5]. Antiferromagnetism (AFM) in this system was suppressed to below 4 K in the range $2 \leq x \leq 5$ [5]. Alloying with Mo suppresses AFM in Cr and its alloys through electron hole pair breaking effects due to electron scattering and through a delocalization of the 3-d bands of Cr by the 4-d bands of Mo [1]. For comparison, the present study investigates the magnetic properties of the $Cr_{100-x}Al_x$ system further through the addition of V. This reduces the AFM in Cr alloys through a mechanism different to that associated with Mo by reducing the electron-to-atom (e/a) ratio [1].

2. Experimental

Polycrystalline $(Cr_{100-x}Al_x)_{99}V_1$ alloys in the range $0 \leq x \leq 7$ were prepared by repeated arc melting in a purified argon atmosphere. The starting materials were Cr, Al and V of nominal purity 99.999%, 99.999% and 99.98%, respectively. The alloys were separately sealed into quartz ampoules filled with ultra-high purity argon and annealed at 1300 K for 72 hours after which they were quenched into iced water. Elemental composition analysis done using scanning electron microscopy and electron

microprobe showed that the alloys were of good homogeneity. Spark erosion techniques were used to cut, shape and polish the samples into desired dimensions for each experimental set-up. The Quantum Design Physical Property Measurement System (PPMS) was used to measure the electrical resistivity (ρ) and Seebeck coefficient (S) during cooling and heating runs, respectively, in the temperature range 2 K ≤ T ≤ 390 K. The Quantum Design Magnetic Property Measurement System (MPMS) was used to measure the susceptibility (χ) in the temperature range 2 K ≤ T ≤ 390 K. The samples were zero field cooled to 2 K and measurements were taken on warming in a magnetic field of 100 Oe.

3. Results and discussion

Figure 1 shows representative examples of the temperature dependence of the electrical resistivity, $\rho(T)$, for the $(Cr_{100-x}Al_x)_{99}V_1$ alloy system. Well defined resistivity anomalies, in the form of a 'hump', are observed in figure 1(a) and (b) in the vicinity of T_N at the P-ISDW phase transition for alloys with x < 1.5. These resistivity anomalies are ascribed to a reduction of charge carrier density during AFM ordering when the nested parts of the Fermi surface (FS) annihilate on cooling through T_N. The annihilation of the FS induces SDW energy gaps at the Fermi energy, causing an increase in the electrical resistivity just below T_N [1]. T_N shown in figures 1(a) and (b) was taken at the temperature of the sharp minimum in the $(d\rho/dT)$ vs. T curve as is usually done for Cr alloys [1]. No anomalous $\rho(T)$-behaviour was observed for alloys in the concentration range 1.5 ≤ x ≤ 4.7 as shown by the typical example in figure 1(c). For these alloys, $\rho(T)$ is closely linear down to about 100 K, typical of what is expected for a paramagnetic Cr alloy [1]. The absence of $\rho(T)$-anomalies like that in figures 1(a) and (b) indicates paramagnetisn in this concentration range down to the lowest temperature of the

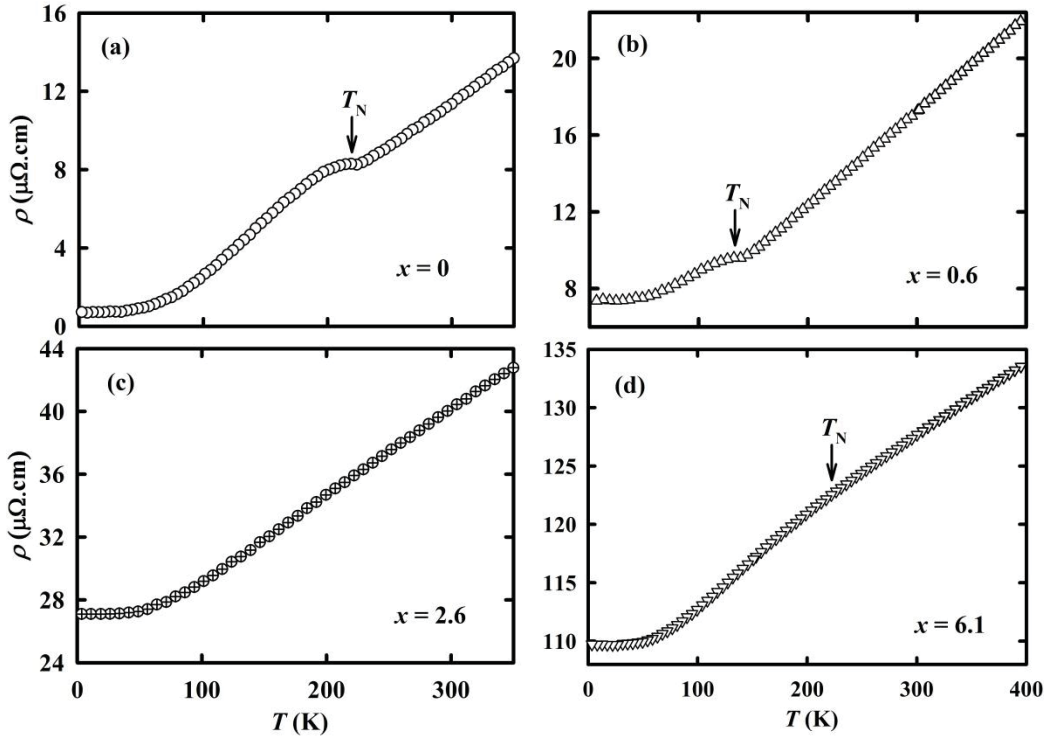

Figure 1: Representative examples of the temperature dependence of electrical resistivity, $\rho(T)$, of the $(Cr_{100-x}Al_x)_{99}V_1$ alloy system with (a) x = 0, (b) x = 0.6, (c) x = 2.6 and (d) x = 6.1. The arrows in panels (a) and (b) indicate the positions of T_N obtained from the minimum of the $(d\rho/dT)$ vs. T curves. T_N shown in panel (d) is obtained from Seebeck coefficient and magnetic susceptibility measurements of figures 2 and 3, respectively. The experimental error in ρ is approximately 5% originating from measurement of the sample dimensions. Note the different temperature scales.

measurements. For alloys with $x > 4.7$ $\rho(T)$ behave distinctly different from that observed for the previous two concentration ranges. A typical example is shown in figure 1(d) for $x = 6.1$ which, together with the $x = 7.0$ alloy, are expected to be CSDW AFM alloys. These two alloys show $\rho(T)$-behaviour that is characterized by a broad but weak anomaly in the form of a break in $d\rho/dT$ at a temperature marked "T_N" in the example of figure 1(d). This value of T_N corresponds very well with that obtained from Seebeck coefficient and magnetic susceptibility measurements of figures 2(d) and 3(b), respectively. A similar correspondence is obtained for T_N of the $x = 7.0$ alloy. It is unknown why T_N obtained from figures 2(d) and 3(b) correspond well with the break in $d\rho/dT$ for these two alloys, particularly since one would expect similar T_N-anomalies on $\rho(T)$ curves for both the ISDW and CSDW alloys. The downturn in $\rho(T)$ just below T_N for the CSDW alloys, instead of the expected upturn as for the ISDW alloys (figures 1(a) and (b)), is unexpected. Enhanced $\rho(T)$-anomalies, similar in form to that for the ISDW alloys, are rather expected for the P-CSDW T_N-anomaly, since the CSDW state is expected be more stable than the ISDW state [1]. Weak CSDW magnetic anomalies in $\rho(T)$ at T_N were previously also reported in the $Cr_{100-x}Al_x$ [6] and $(Cr_{100-x}Al_x)_{95}Mo_5$ [5, 7] alloy systems.

In some cases where the $\rho(T)$ magnetic anomalies are weak, Seebeck coefficient (S) measurements as a function of temperature provide a more sensitive method for locating T_N. Changes in the relaxation time τ of the itinerant charge carriers at the FS during AFM ordering is the dominant factor driving the enhanced anomaly observed in the $S(T)$ measurements [8].

The contribution to the Seebeck coefficient by electron diffusion is given by [1, 8]:

$$S = \frac{\pi^2 {k_B}^2 T}{3e}\left(\frac{\partial ln\Sigma}{\partial E} + \frac{\partial \bar{l}}{\partial E}\right)_{E_F}, \quad (1)$$

where Σ is the remaining FS area after annihilation due to electron-hole condensation and $\bar{l} = v\tau$ is the weighted average mean free path over Σ, v is the velocity of charge carriers at the remaining FS (Σ), and τ is the relaxation time. The two terms in equation (1) incorporating Σ and $\bar{l}$, are very sensitively affected on SDW formation in Cr and its alloys [8]. Σ is in many cases sensitive to the energy E, but for T just below T_N, where a 'hump' is observed in $\rho(T)$, the second term in equation (1) can dominate when the electron scattering may be largely determined by $\bar{l}$. At low temperatures a plot of S/T versus T^2 should then vary linearly [1, 8]:

$$S = aT + bT^3, \quad (2)$$

since both phonon and magnon drag in these itinerant electron AFM materials contribute T^3-terms to S at low temperatures [1, 8].

Previously investigated Cr alloys [1] all show $S(T)$ behaviour in the form of a relatively large 'dome' at $T < T_N$, compared to the small hump observed in $\rho(T)$. Trego *et al.* [8] discussed this behaviour in terms of a model in which the dominant effect is the decrease in the scattering rate of electrons by phonons when the AFM phase is entered on decreasing temperature. As indicated by equation. (1), S is determined by the energy dependence of both Σ and $\bar{l}$. The second term of equation (1) dominates [8] giving a net positive contribution to S at temperatures below T_N.

Figure 2 shows the temperature dependence of the Seebeck coefficient $S(T)$ for the $(Cr_{100-x}Al_x)_{99}V_1$ alloy system. Large anomalies in the form of a 'dome' are observed around the same region where the $\rho(T)$ curves showed a 'hump' for the alloys with $x < 1.5$ as indicated in figures 2(a) and (b). This 'dome' is as a result of a transition from P-ISDW phase as the alloys are cooled through T_N. The anomalies are small for alloys in the concentration range $1.5 \leq x \leq 4.7$ as shown in figure 2(b) and (c) (note the different scale on the S-axes of panels (b), (c) and (d) compared to that in panel (a)). These alloys show paramagnetic behaviour in the $\rho(T)$ measurements. The slight residue of a 'dome' observed in the $S(T)$ curves of the paramagnetic samples are at present not well understood, but was also observed in other Cr alloys [1, 8]. A noticeable and relatively sharp upturn is however present in $S(T)$ at temperatures larger than 150 K for x =1.5 in figure 2(b), compared to the behaviour observed for $x = 2.6$, 4.0 and 4.7. The electrical resistivity and magnetic susceptibility measurements of figures 2(c) and 3(a), respectively, nevertheless indicate paramagnetic behavior down to 2 K in the $x = 1.5$

alloy. Prominent anomalies reappear for alloys with $x > 4.7$ shown in figure 2(d). The magnetic anomalies observed in the $S(T)$ measurements are explained by Trego *et al.* [8] to result from the additional energy gaps that are formed during the annihilation of the nested parts of the FS. The energy gaps reduce the density of final states to which an electron can be scattered to, thereby increasing the mean free path as well as τ. The increase in the mean free path dominates the decrease in the FS area resulting in a positive magnetic contribution to $S(T)$ on cooling through T_N [8], explaining the 'domes' observed in figures 2(a) and (d). The magnetic anomalies observed in the $S(T)$ measurements of this alloy series are, as expected, better enhanced than those observed in the $\rho(T)$ measurements. The arrows in figure 2 indicate the positions of T_N values obtained from (dS/dT) vs. T curves. These values of T_N compare very well with those obtained from $\rho(T)$ measurements on assuming that T_N for $x = 6.1$ and 7.0 is taken at the temperature of the break in $d\rho/dT$, as in figure 1(d). This indicates that $\rho(T)$ and $S(T)$ measurements complement each other.

The study of magnetic properties of the $(Cr_{100-x}Al_x)_{99}V_1$ alloy system was extended to $\chi(T)$ measurements which give an indication of the density of states at the FS. Figure 3 shows the $\chi(T)$ curves for alloys with (a) $x \leq 2.6$ and (b) $x \geq 4.0$. The broken lines in figure 3 represent a back extrapolation from the paramagnetic phase at $T > T_N$. The T_N values indicated by arrows were obtained from the point where the $\chi(T)$ curve deviates from the broken line. Clear anomalies in the form of a downturn on cooling are observed in the vicinity of T_N for the alloys with $x = 0$, 0.6, 6.1 and 7.0, similarly to the behaviour usually observed for Cr alloys below T_N. The downturn in $\chi(T)$ on cooling through T_N is ascribed to a decrease in the density of states at the Fermi surface when the nested parts of the electron and hole Fermi sheets are annihilated. The decrease in the density of states is accompanied by a decrease in the itinerant electron concentration responsible for magnetism.

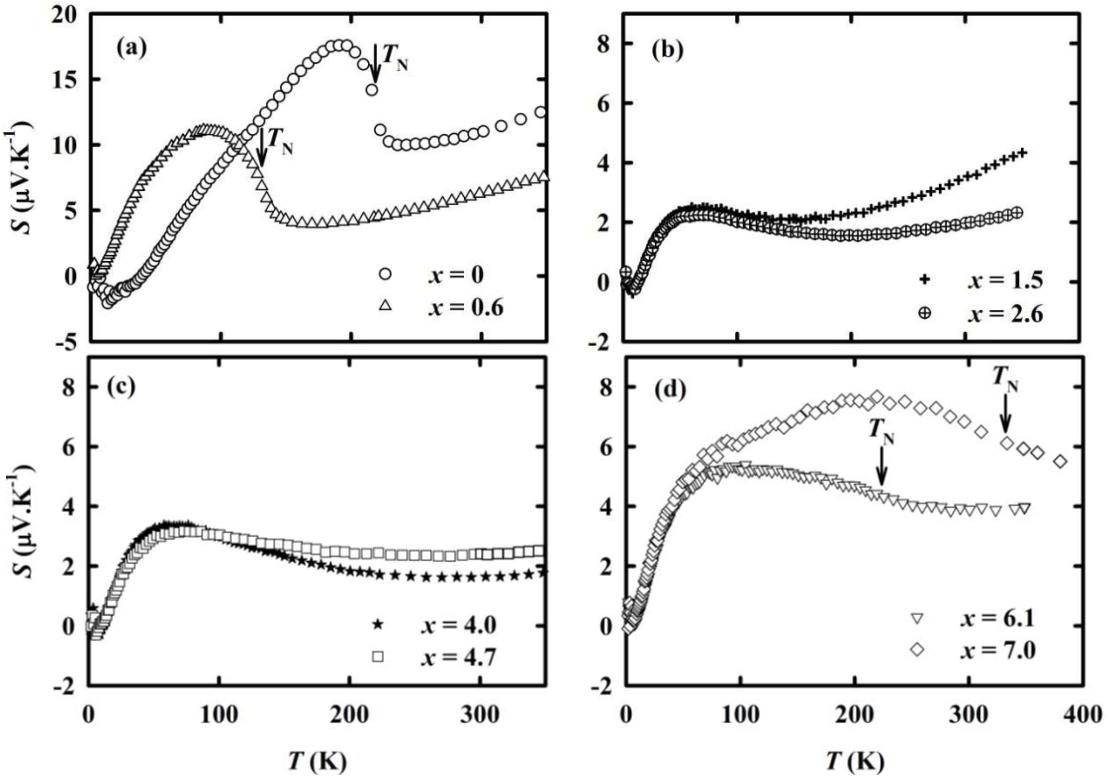

Figure 2: The temperature dependence of the Seebeck coefficient, $S(T)$, of the $(Cr_{100-x}Al_x)_{99}V_1$ alloy system with (a) $x = 0$ (○) and 0.6 (△), (b) $x = 1.5$ (+) and 2.6 (⊕), (c) $x = 4$ (★) and 4.7 (□) and (d) $x = 6.1$ (▽) and 7 (◊). The arrows indicate the positions of T_N obtained from the minimum of the (dS/dT) vs. T curves. Note the different temperature scales.

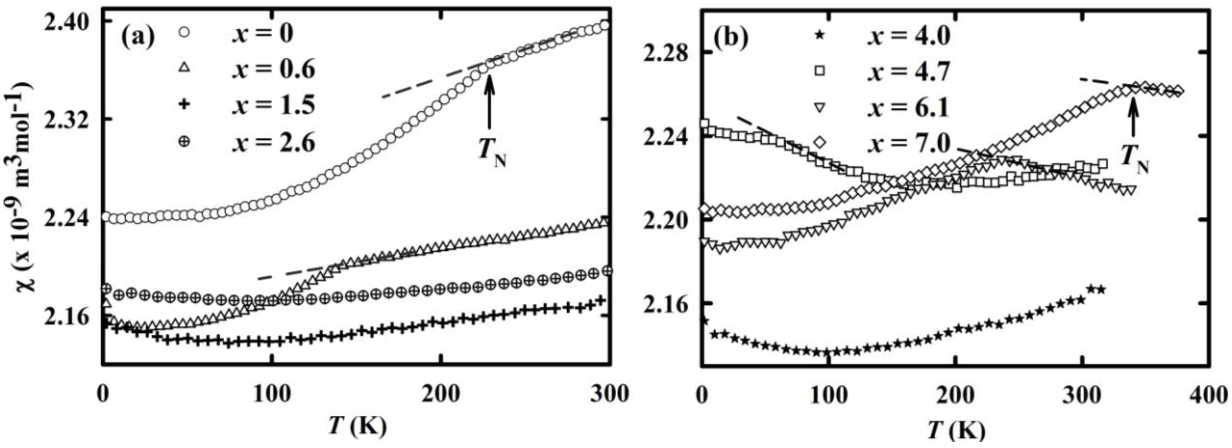

Figure 3: The temperature dependence of the magnetic susceptibility, $\chi(T)$, of the $(Cr_{100-x}Al_x)_{99}V_1$ alloy system with (a) $x = 0$ (○), 0.6 (△), $x = 1.5$ (+) and 2.6 (⊕) and, (b) $x = 4$ (★), 4.7 (□), $x = 6.1$ (▽) and 7 (◊). The experimental error in χ is approximately 0.1% emanating from measurement of the sample masses. Note the different scales in panels (a) and (b).

It is noted that the alloy with $x = 4.7$ of figure 3(b) depicts an anomaly in the form of a rather prominent upturn below a temperature of about 150 K, compared to the behaviour of alloys with $x = 1.5$, 2.6 and 4.0, despite the observation of paramagnetic behaviour in $\rho(T)$ for $x = 4$. This is taken as indication of a weak SDW AFM component for $x = 4.7$, with T_N estimated at approximately 70 K, taken at the point where the $\chi(T)$ curve deviates from the broken line. The anomalies observed in the $\chi(T)$ measurements for samples with $x > 4.7$ are better defined than those observed in the $\rho(T)$ and $S(T)$ curves. It is observed in figure 3(a) that χ increases almost linearly with temperature at $T > T_N$ for the ISDW alloys with $x < 1.5$. This is in contrast with the two $x = 6.1$ and 7.0 CSDW alloys that each depicts a downturn at $T > T_N$ and a peak in $\chi(T)$ at T_N, as is clear in figure 3(b). $\chi(T)$ peaks, followed by a broad minimum above the peak, were previously also observed by Sousa *et al*. [9] in the $Cr_{100-x}Al_x$ alloy system for CSDW alloys with $x = 2.23$ and 2.83. de Oliveira *et al*. [10] furthermore reported $\chi(T)$ peaks at T_N also in the $Cr_{100-y}V_y$ alloy system for alloys with $y \leq 0.67$. The peaks were attributed to a local SDW that is formed around the V atoms, resulting in Curie-Weiss paramagnetism above T_N [10]. This might also be the case in the present $(Cr_{100-x}Al_x)_{99}V_1$ alloy system. The minimum near 150 K in $\chi(T)$ for $x = 4.7$ of figure 3(b) is then considered as a precursor to a possible peak at T_N that is not fully realised down to 2 K in this alloy. Alloys with $x = 1.5$, 2.6 and 4.0 in figure 3 did not show anomalous behaviour associated with a magnetic transition and can be taken to be paramagnetic at all temperatures down to 2 K.

Figure 4 shows the magnetic phase diagram obtained from $\rho(T)$, $S(T)$ and $\chi(T)$ measurements on the $(Cr_{100-x}Al_x)_{99}V_1$ alloy system. It is observed that T_N decreases with an increase in Al content and is completely suppressed to below 2 K around 1.5 at.% Al. Antiferromagnetism reappears above about 4.0 at.% Al. Addition of just 1 at.% V completely suppresses antiferromagnetism in the $Cr_{100-x}Al_x$ alloy system in the concentration range $1.5 \lesssim x \lesssim 4.0$. The results indicate a phase transition from ISDW to P around 1.5 at.% Al and a P to CSDW transition around 4.0 at.% Al on increasing the Al content at 2 K.

The addition of V decreases the strength of AFM in the $Cr_{100-x}Al_x$ through a reduction of the itinerant electron concentration in the alloy system [1], while Mo suppresses AFM utilizing a different mechanism, through electron hole pair breaking effects due to electron scattering and a delocalization of the 3-d bands in Cr on introducing the 4-d bands of Mo [1]. Although the mechanisms of the suppression of AFM is different for V and Mo, it is interesting to note that the effect of 1 at.% V to the

$Cr_{100-x}Al_x$ alloy system is almost similar to that of 5 at.% Mo that suppresses AFM in the concentration range $2 \leq x \leq 5$ [5, 7]

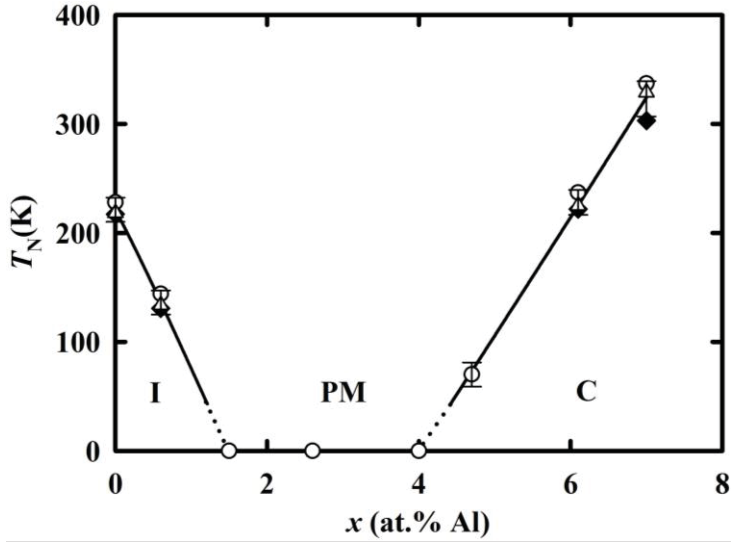

Figure 4: $(Cr_{100-x}Al_x)_{99}V_1$ alloy system in the range $0 \leq x \leq 7.0$ obtained from electrical resistivity (△), Seebeck coefficient (♦) and magnetic susceptibility (○) measurements. I, PM and C denotes incommensurate spin-density-wave, paramagnetic and commensurate spin-density-wave phases, respectively. The lines are guides to the eye through the data points. Error bars indicate the experimental errors in the determination of T_N

4. Conclusion

Electrical resistivity, Seebeck coefficient and magnetic susceptibility studies on the $(Cr_{100-x}Al_x)_{99}V_1$ showed that AFM in the alloy system is completely suppressed to below 2 K in the concentration range $1.5 \lesssim x \lesssim 4.0$. The results indicate an ISDW-P phase transition around 1.5 at.% Al and a P-CSDW phase transition around 4.0 at.% Al. The magnetic anomalies observed in the magnetic susceptibility measurements of the present study pin-point T_N in general more precisely than in the electrical resistivity and Seebeck coefficient measurements. $\chi(T)$ measurements therefore provide a useful tool in probing magnetic properties in this alloy system. Furthermore, the peak in the $\chi(T)$ measurements for alloys with $x > 4.7$ suggest the presence of a local magnetic moment component in $\chi(T)$ of the present $Cr_{100-x}Al_x)_{99}V_1$ alloy system, similar to that previously reported for $Cr_{100-x}Al$ and $Cr_{100-y}V_y$ alloys. The magnetic properties of the present alloy system mirrors that of the $(Cr_{100-x}Al_x)_{95}Mo_5$ system that suppresses AFM in the concentration range $2 \leq x \leq 5$.

References

[1] Fawcett E, Alberts H L, Galkin V Y, Noakes D R and Yakhmi J V 1994 *Rev. Mod. Phys*. **66** 25
[2] Lomer W M 1962 *Proc. Phys. Soc. (London)* **80** 489
[3] Baran A, Alberts H L, Strydom A M, and du Plessis P de V 1992 *Phys. Rev*. *B* **45** 10473
[4] Alberts H L, Prinsloo A R E and Strydom A M 2010 *J. of Magn*. *Magn*. *Mater*. **322 1092**
[5] Smit P and Alberts H L 1986 *J. Phys. F* **16** L191
[6] Alberts H L and Burger S J 1978 *Solid State Commun*. **28** 771.
[7] Muchono B, Prinsloo A R E, Sheppard C J, Alberts H L and Strydom A M *Proc. SAIP2011* 220
[8] Trego A L and Mackintosh A R 1968 *Phys. Rev*. **166** 495
[9] Sousa J B, Amado M M, Pinto R P, Pinheiro M F, Braga M E, Moreira J M, Hedman L E, Åström H U, Khlaif L, Walker P, Garton G and Hukin D 1980 *J .Phys. F: Metal Phys*. **10** 2535
[10] de Oliveira A J A, Ortiz W A, de Lima, O F and de Camargo P C 1997 *J. Appl. Phys*. **81** 4209

Low-energy electronic structure of the itinerant metamagnet $Sr_3Ru_2O_7$

A.S. Ngankeu, E. Carleschi and B.P. Doyle
Department of Physics, University of Johannesburg, P.O. Box 524 Auckland Park 2006, Johannesburg, South Africa

E-mail: ecarleschi@uj.ac.za

Abstract. We have investigated the low-energy electronic structure of $Sr_3Ru_2O_7$ single crystals via synchrotron-based angle resolved photoemission spectroscopy measurements performed at 1 K, focusing in particular on the band dispersion in the vicinity of the Γ and X points in the first Brillouin zone. Our results show the existence of two strongly renormalised bands - one centred around each high-symmetry point - attributed to Ru 4*d* states, whose heavy quasiparticles are located within the first 6.5 meV from the Fermi level, and show a remarkably sharp line width (about 6 meV). Such flat bands give rise to van Hove singularities in the near-Fermi-energy region whose energy scales are compatible with theoretical models for the appearance of itinerant metamagnetism in this system.

1. Introduction

The discovery of the unconventional spin triplet superconductivity in the single layer ruthenate Sr_2RuO_4 [1] attracted interest to the Ruddlesden-Popper (RP) series of strontium ruthenates $Sr_{n+1}Ru_nO_{3n+1}$. This family of metallic compounds turned out to exhibit remarkably different physical properties tuned by the number n of RuO_2 octahedra layers in the unit cell, ranging from superconductivity ($n = 1$), through anisotropic metamagnetic ordering ($n = 2, 3$) [2, 3, 4, 5], to itinerant electron ferromagnetism [2, 3, 4, 5] ($n > 3$). The contribution of the Sr states is non-negligible [6], with the electronic structure of the series being dominated by the RuO_2 octahedra layers. In particular, as Ru always appears to be in an oxidation state +4, the low energy electronic properties of ruthenates are determined by the electrons in the Ru t_{2g} manifold consisting of the nearly degenerate d_{xy}, d_{yz} and d_{zx} orbitals, which strongly hybridise with O $2p$ states [6].

In this study we focus only on the second member of the RP series, $Sr_3Ru_2O_7$. The ground state of $Sr_3Ru_2O_7$ is a paramagnetic Fermi liquid very close to a ferromagnetic instability at zero field [7]. The value of its electronic specific heat is $\gamma = 110$ mJ/(Ru mol K^2), which is among the largest in any oxide indicating strong electronic correlations [8]. This metal exhibits anisotropic itinerant metamagnetism with critical fields ranging from 5.5 T (for H $\parallel$ ab plane) to 7.7 T (for H $\parallel$ c-axis) [5]. This metamagnetic transition ends in a quantum critical point [5, 9, 10] and it is accompanied by the formation of a novel ordered quantum phase known as a "nematic phase" [11, 12] with broken rotational symmetry [11] and heavy d-electron masses [13].

A lot of effort has been so far devoted into understanding the nature of the microscopic origin of metamagnetism in $Sr_3Ru_2O_7$ and has presented a significant challenge within condensed

matter physics [14, 15, 16]. The underlying idea compatible with the Stoner model is that metamagnetism is caused by the presence of narrow peaks in the electronic density of states (called van Hove singularities, vHS) in the vicinity of the Fermi energy level E_F [14]. Such vHS can be found in regions of the reciprocal space where the gradient of the electronic bands is zero, i.e. where the bands are flat or show a saddle point in the dispersion. According to the above-mentioned model, the application of an external magnetic field would cause the vHS corresponding to spin up and spin down electrons into opposite directions, and one of these would be brought closer to the Fermi level - and even on the opposite side of it - producing a discontinuous transition in the magnetisation known under the name of metamagnetism [17].

In this study, we report detailed angle resolved photoemission spectroscopy (ARPES) measurements of $Sr_3Ru_2O_7$ around the high symmetry points X and Γ in the first Brillouin zone, reporting direct evidence of flat Ru 4*d* bands close to the Fermi energy, giving rise to vHS located within a few meV below E_F, the energy scale relevant for metamagnetism. Our results for the band dispersion around the X point are in agreement with that reported by Tamai and coworkers [18]. Finally, the line shape of the quasiparticle peaks can be described within the "peak-dip-hump" model, showing a fingerprint of strong electronic correlations in this system.

2. Experimental Method

$Sr_3Ru_2O_7$ single crystals were grown by the floating zone technique with Ru self-flux in the Department of Physics at the University of Salerno (Italy) [19]. Samples were characterized by means of X-ray diffraction, resistivity, energy dispersive microscopy and electron backscattering diffraction, confirming the phase purity and the high quality of the crystals. ARPES experiments were carried out at the 1^3 end-station installed at the beamline UE112-lowE-PGM-b of the synchrotron BESSY II in Berlin (Germany) using a Scienta R4000 electron energy analyser, which allowed us to simultaneously measure many energy distribution curves (EDC) in an angular range of 28°. Samples were cleaved *in situ* on the manipulator of the experimental chamber at 40 K, and then cooled down to the measurement temperature of 1 K (temperature that was kept constant throughout the experiment). The spectra presented here were measured with photon energies of 20 eV and 25 eV and with various incident photon polarisations. The overall energy and angular resolutions were $\sim$ 5 meV (as confirmed by the broadening of the Fermi level) and 0.15°, respectively.

3. Results and Discussion

Panels (a) and (b) in Figure 1 show the band dispersion of $Sr_3Ru_2O_7$ acquired around the *X* point with horizontally and vertically polarised light (HP and VP, respectively). The position of the dispersing quasiparticle peak as a function of $k_{||}$ has been determined by fitting the experimental EDC with a Gaussian line shape, and it has been plotted in Figure 1 (c) for four different light polarisations. From this plot it can be seen that the dispersion of the quasiparticle peak is very narrow and it is confined within a bandwidth of $\sim$ 2.5 meV for all polarisations, in a binding energy range that goes from 3 to 6.8 meV, and that the central part of the band centred around the X point is basically flat, i.e. it does not show any dispersion at all, and it is centred at an average binding energy of 5 meV. Such a flat band gives rise to a very high DOS below E_F, compatible with the presence of a vHS located within a few meV of the Fermi energy.

Further information regarding the symmetry of this vHS can be obtained by comparing the results obtained with HP and VP. In fact, changing the light polarisation in an ARPES experiment is an established methodology that allows to take advantage of the effect of the photoemission (PE) matrix elements associated to a specific electronic band. This fact results in the enhancement or suppression of the PE intensity from the band, from which one can gain information about the symmetry of those states. According to the experimental geometry exploited in this work, the electric field of vertically polarised light lays entirely in the *ab* plane of

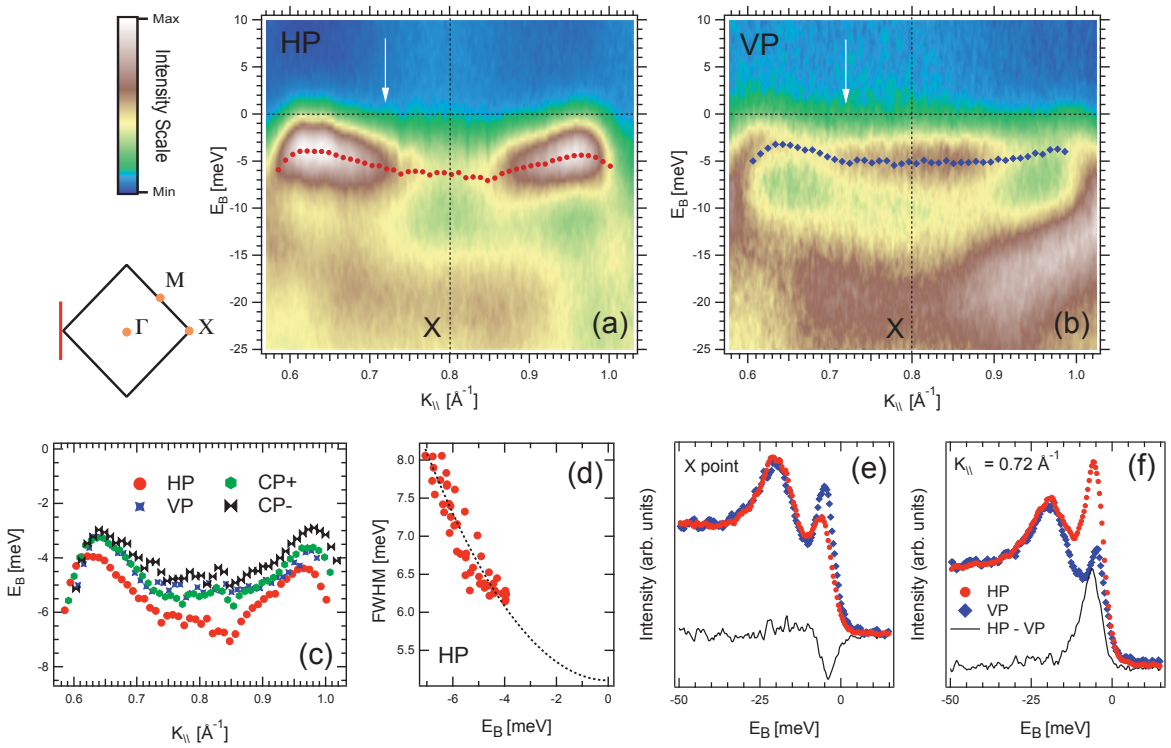

Figure 1. Panels (a) and (b): ARPES two-dimensional cuts acquired in the vicinity of E_F around the X point. These were taken along the direction indicated in the sketch of the first Brillouin zone and acquired at a temperature of 1 K and a photon energy hν = 20 eV with horizontal (HP) and vertical (VP) polarisation, respectively. White and blue colours correspond to high and low photoemission intensity, respectively, as indicated by the colour intensity scale. The fitted binding energy versus momentum curves (markers) have been plotted on top of the bands. (c) Momentum dependence of the quasiparticle peak binding energy fitted from momentum-energy cuts at different polarisations. The peak positions are found by fitting the energy distribution curves (EDCs) taken from (a) and (b) with a Gaussian function (the momentum-energy cuts for circular polarisations are not shown in this work). (d) Binding energy dependence of the full-width half-maximimum (FWHM) of the quasiparticle peak for the momentum-energy cut acquired shown in (a). The obtained experimental FWHMs are well fitted with a parabolic function (dashed black line), which is a fingerprint of Fermi liquid behaviour of this heavy quasiparticle in $Sr_3Ru_2O_7$ [20]. Panels (e) and (f): Comparison of HP and VP EDCs extracted from (a) and (b) at the X point and at $k_{||} = 0.72\,\text{Å}^{-1}$ (indicated by white arrows in (a) and (b)). The difference between HP and VP spectra is also shown in black.

the sample, while for horizontally polarised light it is almost completely parallel to the c axis of the sample. We can therefore conclude that, because of the dipole selection rules, VP enhances in-plane states while HP enhances out-of-plane states. The effect of PE matrix elements is evident in our data in panels (a) and (b) of Figure 1. The same band has an enhanced intensity in its central non-dispersing part (centred around the X point) in VP, while the use of HP seems to favour the emission from the dispersing wings of the band approaching E_F. This suggests that the non-dispersing part of the band has a majority in-plane character, while the dispersing part of the band has a majority out-of-plane character. This is also reflected in Figure 1 (e) and (f) where the difference between the EDCs in HP and VP shows how VP enhances the PE intensity close to E_F around the X point while it suppresses the intensity away from X. The in-plane character of the vHS close to the X point is in agreement with the theoretical models cited in the introduction [14, 15, 16] according to which the vHS close to the X point has d_{xy} orbital character [18].

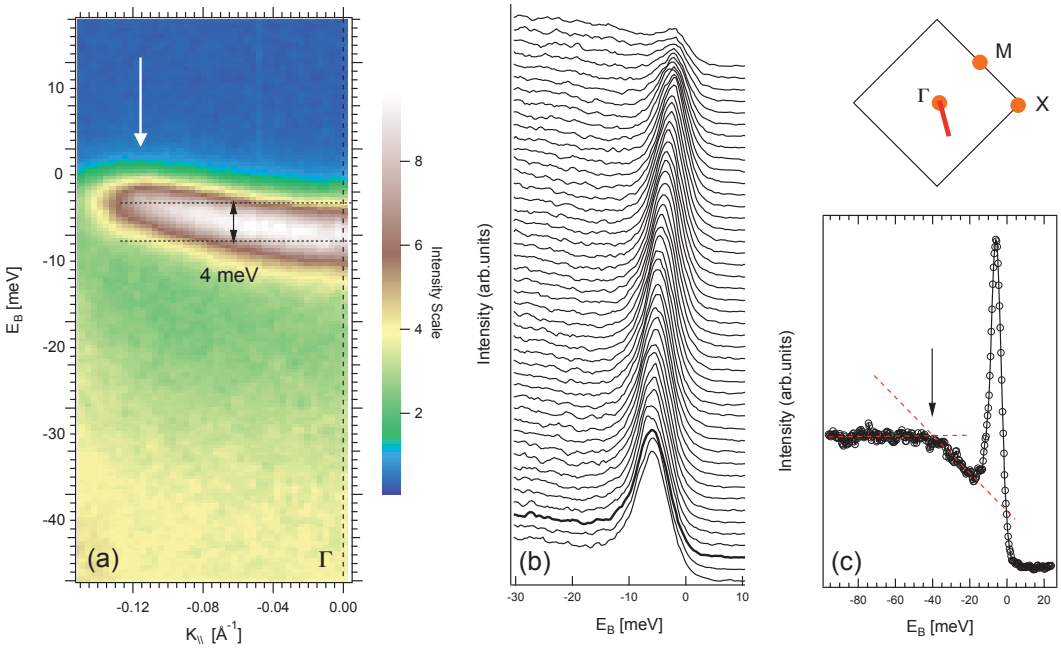

Figure 2. (a) ARPES two-dimensional cut acquired at a temperature of 1 K and a photon energy $h\nu = 25$ eV with left circularly polarised light in the vicinity of E_F around the Γ point. The red line in the schematic representation of the Brillouin zone shows the direction along which the cut was measured. (b) Stack of the EDC spectra constituting the cut shown in (a). (c) EDC spectrum at the Γ point. The arrow indicates the position of the hump.

Another promising Fermi surface sheet in terms of vHS is the so-called δ electron pocket whose dispersion is centred around the Γ point. Figure 2 (a) and (b) show the experimental quasiparticle dispersion of this feature, from where it can be seen that its bandwidth is limited to ~ 4 meV. By integrating the spectral weight of the δ pocket in the relevant $k_{||}$ region, one can see that this feature gives rise to a vHS (inset in Figure 2 (a)) located at 2 meV from the Fermi level, again in an energy scale which is relevant to the formation of metamagnetism in $Sr_3Ru_2O_7$.

It is worth mentioning at this point that the bandwidth of the δ pocket is reduced by a factor 25 with respect to the bare band dispersion predicted by LDA calculations [21] due to strong correlation effects. Signatures of strong correlation effects are also evident in the line shape of the quasiparticle peak itself, as shown in Figure 2 (c) for the Γ point EDC, where some of the spectral weight of the coherent quasiparticle has been pushed to higher binding energies to form the characteristic 'peak-dip-hump' line shape of correlated systems. Such a line shape was observed for the first time in high-T_c superconductors [22, 23] and then in other correlated systems [24], and there is agreement of it being due to the interaction between electrons and a sharp collective mode, which alters the shape of the self energy resulting in the appearance of an incoherent peak. Following Campuzano *et al.* [23], the position of the hump is located where the spectrum changes slope as highlighted by the intersecting straight lines in (c). The hump is located 34 meV below the Fermi level. Further investigation on the dispersion and the origin of the hump are beyond the scope of this work.

In conclusion, we have presented low-temperature electronic structure data for $Sr_3Ru_2O_7$, revealing the presence of heavy quasiparticles associated to two very flat bands centred around the X and Γ point in the first Brillouin zone. Such bands give rise to vHS in the close vicinity of

the Fermi level, which can be interpreted as responsible for the appearance of metamagnetism in this system.

Acknowledgements
The authors would like to thank R. Fittipaldi and A. Vecchione for providing the single crystals for this study, M. Cuoco for theoretical support and V.B. Zabolotnyy, I. Vobornik, M. Unnikrishnan and S. Borisenko for participating in the experiment. The Faculty of Science of the University of Johannesburg is also acknowledged for providing travel funding.

References
[1] Y. Maeno *et al. Nature* **372**, 532 (1994).
[2] G. Cao *et al. Phys. Rev. B* **68**, 174409 (2003).
[3] R. Gupta *et al. Phys. Rev. Lett.* **96**, 067004 (2006).
[4] Y. J. Jo *et al. Phys. Rev. B* **75**, 094413 (2007).
[5] R. S. Perry *et al. Phys. Rev. Lett.* **86**, 2661 (2001).
[6] M. Malvestuto *et al. Phys. Rev. B* **83**, 165121 (2011).
[7] S. I. Ikeda *et al. Phys. Rev. B* **62**, R6090 (2000).
[8] R. S. Perry *et al. J. Phys. Soc. of Japan* **74**, 1270 (2005).
[9] S. A. Grigera *et al. Science* **294**, 329 (2001).
[10] S. A. Grigera *et al. Science* **306**, 1154 (2004).
[11] R. A. Borzi *et al. Science* **315**, 214 (2007).
[12] J. F. Mercure *et al. Phys. Rev. Lett.* **103**, 176401 (2009).
[13] J. Lee *et al. Nature Physics* **5**, 800 (2009).
[14] B. Binz and M. Sigrist *Europhys. Lett.* **65**, 816 (2004).
[15] S. Raghu *et al. Phys. Rev. B* **79**, 214402 (2009).
[16] C. Honerkamp *Phys. Rev. B* **72**, 115103 (2005).
[17] E. P. Wohlfarth and P. Rhodes. *Philos. Mag.* **7** 1817, (1962).
[18] A. Tamai *et al. Phys. Rev. Lett.* **101**, 026407 (2008).
[19] R. Fittipaldi, PhD thesis, University of Salerno (2006).
[20] A. A Kordyuk and S. V. Borisenko arXiV:cond-mat/0510218v2.
[21] M.P. Allen *et al.* arXiv:1210.8382v1.
[22] M. R. Normal *et al. Phys. Rev. Lett.* **79**, 3506 (1997).
[23] J. C. Campuzano *et al. Phys. Rev. Lett.* **83**, 3709 (1999).
[24] V. Brouet *et al. Phys. Rev. B* **76**, 100403(R) (2007).

Effects of different TiO_2 phases on the luminescence of $CaTiO_3:Pr^{3+}$

Noto LL*, Pitale SS, Ntwaeaborwa OM, Terblans JJ, Yagoub MYA and Swart HC*

Physics Department, University of the Free State, P. O. Box 339, Bloemfontein, 9300, South Africa

*Corresponding author: NotoLL@ufs.ac.za or SwartHC@ufs.ac.za

Abstract. $CaTiO_3$ is widely used in the ceramic industry, and when it is doped with Pr^{3+} it glows with a single red emission at a wavelength of 613 nm. The red emission is attributed to the $^1D_2 \rightarrow ^3H_4$ radiative transition of Pr^{3+} upon ultraviolet (UV) or electron beam irradiation. The compound was prepared by using rutile and anatase polymorphs of TiO_2 to investigate their effects on the luminescence properties. X-ray diffraction patterns of $CaTiO_3:Pr^{3+}$ phosphor prepared with rutile polymorph show that the phosphor was successfully synthesized without any additional phases, whereas the patterns for the phosphor prepared with anatase polymorph show unreacted TiO_2 phases. The unreacted phases resulted in lowered luminescence intensity of the phosphor prepared with the anatase TiO_2. The chemical stability of the phosphor was also investigated by exposing it to a prolonged electron beam irradiation.

Keywords:$CaTiO_3$: Pr^{3+} red emission, long afterglow phosphor

1. Introduction

The intentervalence charge transfer mechanism is known to be the reason behind the single red emission of Pr^{3+} doped $CaTiO_3$ at room temperature. The phenomenon is attributed to complete depopulation of the $^3P_0$ level carriers by populating the $^1D_2$ state. However so, the intensity of the single red emission peak from $^1D_2 \rightarrow ^3H_4$ transition is highly dependent on energy transfer from the host to the luminescent centers of Pr^{3+}[1,2]. $CaTiO_3$, which is an orthorhombic perovskite, is known to exhibit good dielectric properties. The symmetry of this compound is temperature dependant and it changes from orthorhombic to tetragonal under different temperature exposure [3,4,5,6]. Solid state reaction is the main route to prepare this compound by directly firing the TiO_2 and $CaCO_3$/CaO as initial reagents at temperatures above 1000 ^oC [6]. The final compound can have different quantities of the different types of defects such as line defects, point defects, and vacancies. These are a result of slight changes in the preparation procedures such as heating rate, cooling rate and the rate of the chemical reaction. Different chemical reaction rates may also be introduced by different reagent phases. All these parameters may influence the properties of the final

compound, which may in return affect energy transfer from the host to the luminescent centers of Pr^{3+} because of many non-radiative centers that may be introduced in the material [7,8,9]. TiO_2 that is used as a reagent to fabricate $CaTiO_3$ itself exists in different modifications, such as the rutile, anatase and the brookite polymorphs [10,11]. The three polymorphs have similar crystal structures made of TiO_6 octahedrons that differ from each other with size and distortion at different temperatures and pressure [10]. The octahedrons link to each other through corners and edges, and there are two links for rutile, three links for brookite and four links for anatase [10]. The increase in the number of links has an effect of increased distortion and reduced volume to the octahedrons. At higher temperatures the factor of distortion increases the most for anatase and remains unchanged for rutile. This leads to rutile being the most chemically and physically stable polymorph of TiO_2 [10]]. The paper presents the effects of preparing $CaTiO_3$:Pr^{3+} phosphor using rutile and anatase polymorphs of TiO_2, to the luminescence intensity at different temperatures. The chemical stability of the phosphor is also investigated by probing its surface with a prolonged electron beam, and the effects to Cathodoluminescence (CL) emission were monitored.

2. Experimental

$CaTiO_3$ compound doped with 0.2 mol % of Pr^{3+} was prepared by stochiometrically reacting $CaCO_3$ with TiO_2 rutile and TiO_2 anatase in separate experimental setups. $PrCl_3$ was also stochiometrically incorporated into each of the two prepared $CaTiO_3$ products to introduce Pr^{3+} ions as activator ions for luminescence. Solid state chemical reaction was used to prepare these materials at different temperatures (1100 to 1500°C). The phosphors were analyzed using X-ray diffraction (XRD) (Bruker Advance D8) to identity the phases that are present in each compound, and scanning electron microscopy (SEM) (Shimadzu SSX-550, Kyoto, Japan) for the surface morphology. Photoluminescence (PL) spectroscopy (Varian – Carry Eclipse fluorescence spectrometer) was used to identify the absorption regions from the excitation spectra and luminescence from the emission spectra of the $CaTiO_3$:Pr^{3+} phosphor. The electron beam of an AES PHI 549 with 2 keV energy and 10 μA current was used to probe the surface of the phosphor and the cathodoluminescence (CL) spectrometer (Ocean optics inc. PC2000) was used to monitor the CL emission.

3. Results

$CaTiO_3$:Pr^{3+} XRD patterns are presented for compounds prepared by using rutile (figure 1(a)) and anatase (figure 1(b)) TiO_2polymorphs, which were sintered at different temperatures as indicated. TheXRD pattern of $CaTiO_3$ prepared with the rutile TiO_2 shows single phase formation when compared to the standard (JCPDS card no. 22-0153). On the contrary the XRD pattern of $CaTiO_3$ prepared with the anatase TiO_2 shows additional phases (marked by *) when compared to the standard (JCPDS card no. 22-0153), which match with those of TiO_2. The presence of the additional phases is attributed to the unreacted TiO_2. The peaks of the phosphor prepared using rutile polymorph are broader than those of the phosphor prepared using anatase polymorph, and this is correlated with the size effect. The effect may be attributed to particles of the phosphor of the sample prepared by the earlier polymorph being smaller than the latter polymorph of TiO_2[12]. The existence of TiO_2 in different polymorphs, rutile, anatase and brookite, gives it the unique ability to react with a particular material to fabricate a product with different properties. The properties referred to are: different quantities of Ti^{3+} and Ti^{4+} point defects, oxygen vacancies, line defects, different electronic structures, and different chemical and physical stability [8,13,14,16].Anatase TiO_2 has a greater quantity of point defects and oxygen vacancies compared to the

rutile TiO_2 due to its much more distorted nature, and this leads to it forming products that have much more point defects [10,14,16].The greater chemical stability of the rutile polymorph allows it to react more effectively than the anatase, and form products with a greater chemical stability [14,15]. Hence $CaTiO_3$ prepared using a rutile TiO_2 exists as a single phase as opposed to that prepared using anatase TiO_2, which has additional phases (figure 1(b)).

The surface morphology of the two $CaTiO_3$ phases prepared at 1300 ^oC using rutile TiO_2 phase (figure 2(a)) and anatase TiO_2 phase (figure 2(b)) showed approximately the same crystal shapes. They both had particles of different sizes and shapes. The particles for both SEM images are agglomerated because the high temperature (1300 ^oC) involved for the preparation of $CaTiO_3$ compounds.

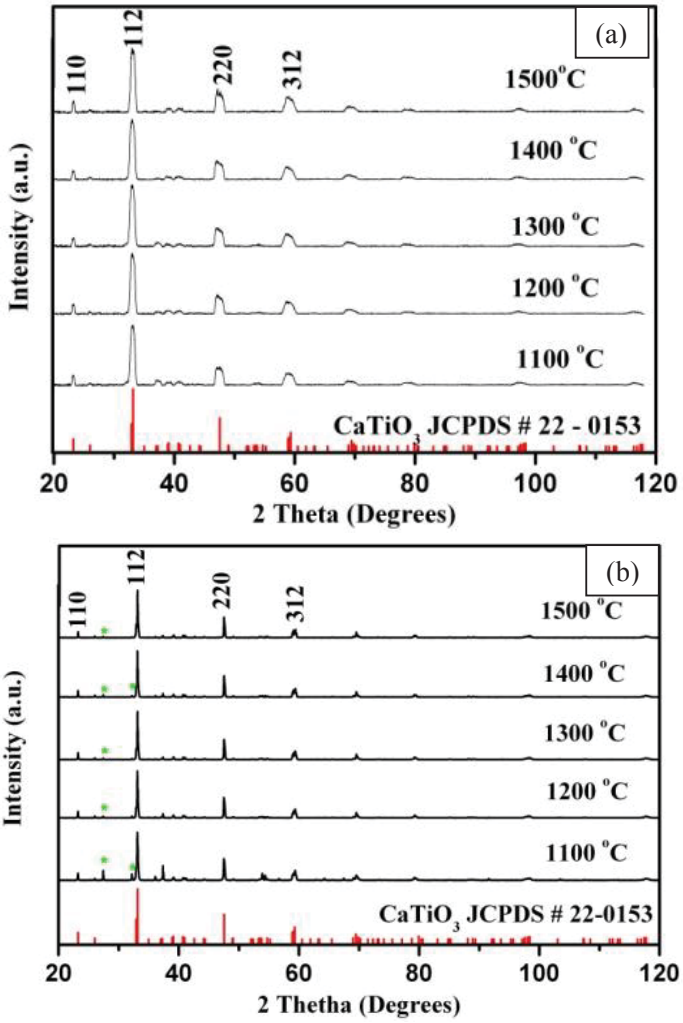

Figure 1: The XRD patterns of $CaTiO_3$ compounds prepared using different TiO_2 phases; rutile (a) and anatase (b) phases.

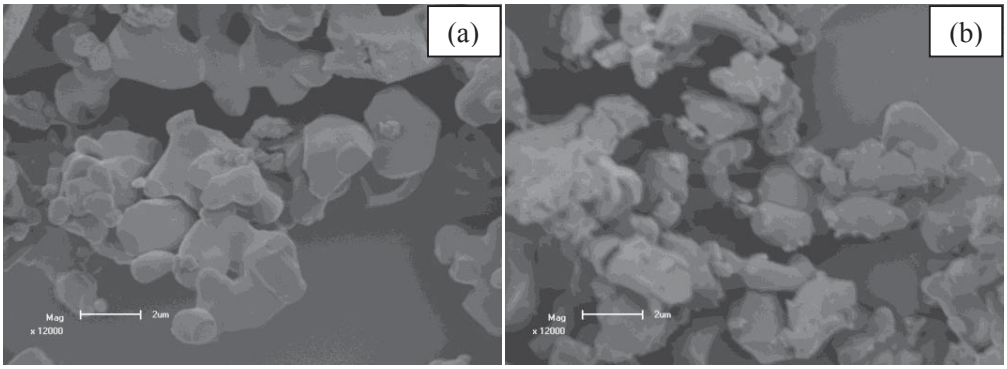

Figure 2: SEM images showing the surface morphology of $CaTiO_3$ prepared using rutile (a) and anatase (b) TiO_2 phases.

Perovskite materials are reported to be stable at temperatures above 1000 ^oC, and solid state reaction has so far been the famous route to prepare these materials [6]. However, recent reports have also shown chemical routes for their preparation [4,16]. The spectra in figure 3(a) show the PL excitation and emission of the $CaTiO_3:Pr^{3+}$(0.2 mol %) prepared by anatase and rutile TiO_2 polymorphs at 1200 ^oC. According to the excitation spectra, the two compounds can best be excited using a 330 nm wavelength source to excite electrons from the valence band to the conduction band, or excite them from the 4f level to the 4f5d level. The intensity of the $^1D_2 - {}^3H_4$ emission of $CaTiO_3$ prepared using rutile TiO_2 is more intense than that of the one prepared using the anatase TiO_2 phase. This outcome is attributed to the difference in phase purity of the two $CaTiO_3$ compounds, as evidenced in their XRD patterns (figure 1). The additional phases present in the $CaTiO_3:Pr^{3+}$ phosphor prepared with anatase TiO_2 introduce luminescent quenching centers that promote non-radiative relaxation to the excited carriers [17]. Figure 3(b) presents the comparison of the PL intensity of $CaTiO_3:Pr^{3+}$(0.2 mol %) phosphor at different preparation temperatures. PL intensity increases as a result of improved crystallinity of the material and it is at its maximum for the sample prepared at 1200 ^oC for the anatase prepared phosphor and 1300 ^oC for the rutile prepared phosphor. The decrement is attributed to increased point defects that act a quenching centers with an increase in temperature [17,18,19]. The energy required to produce defects in the material, is proportional to the temperature as modeled using the Arrhenius equation. This leads to the concentration of the defects to increase exponentially as temperature is increased [20].

The chemical stability of the compounds was investigated by probing the surface of the phosphor with a prolonged electron beam of 2 keV energy and 10 μA current *in-situ*. From the spectra, the CL emission of the $CaTiO_3:Pr^{3+}$ phosphor prepared using the rutile TiO_2 phase is stable compared to that prepared using the anatase phase. The CL emission of the anatase TiO_2 phase dropped with 60 %, until 2000 $C.cm^{-2}$ electron doses, before it stabilized.

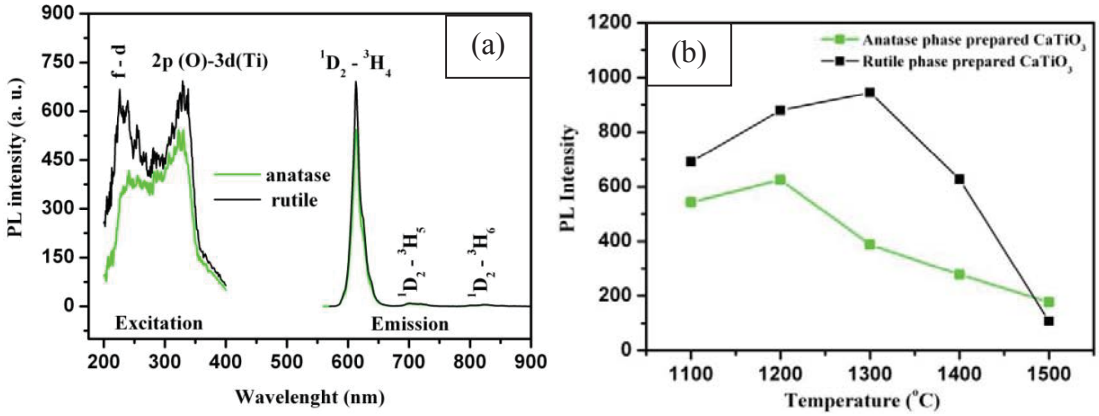

Figure 3: The excitation and PL emission spectra of $CaTiO_3$ at 1200 ^{o}C and the maximum PL intensity at different temperatures (b).

Oxide phosphors are known to be chemically stable materials, and are good candidates for fabricating television screens. This is because of their CL intensity that resists degradation under prolonged electron beam irradiation [21,22]. According to the ESSCR mechanism, CL degradation is a result of surface chemical changes which occur to non-chemically stable surfaces [23]. The CL intensity of $CaTiO_3$:Pr^{3+} (0.2 mol %) prepared using the rutile TiO_2 shows stability against prolonged electron beam, as opposed to that prepared by the anatase phase. This may be attributed to the $CaTiO_3$ prepared using the rutile TiO_2 being more chemically stable compared to that prepared using the anatase TiO_2 [11]. The surface of the compound with a higher chemical stability tends to resist dissociation by an electron beam more than the compound with a lesser chemical stability [22]. The surface dissociation follows the ESSCR mechanism proposed by Swart et al [23]. A 4 eV shift in the AES spectra (not shown) was, however, measured during the degradation of the anatase phase leading to band bending in which the excited electrons and holes are separated before recombination leading to a lower CL intensity. Similar surface charging occurs during electron bombardment of aged ZnS:Ag,Cl phosphor due to the formation of a non-conductive ZnO surface layer [24]. Noto et al. [25] also measured the formation of CaO and CaO_x as well as TiO_2/Ti_2O_3 non-luminescent species on the surface of (anatase phase) $CaTiO_3$:Pr^{3+}.

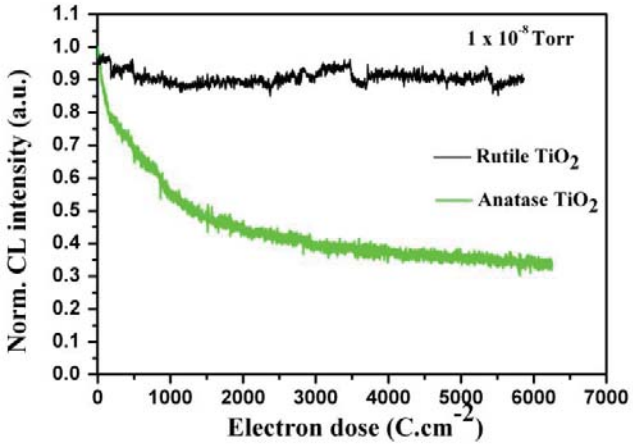

Figure 4: Cathodoluminescence of $CaTiO_3$:Pr^{3+} under prolonged electron exposure.

4. Conclusion

$CaTiO_3:Pr^{3+}$ (0.2 mol %) was prepared using two different polymorphs of TiO_2, the anatase and the rutile that is more chemically and physically stable. The phosphor glowed with a single red emission of 613 nm wavelength from the $^1D_2 \rightarrow {}^3H_4$ radiative transition at room temperature, due to complete quenching of the blue emission by the intervalence charge transfer. The rutile TiO_2 was effective in preparing phase pure $CaTiO_3:Pr^{3+}$ (0.2 mol %) phosphor at different temperatures as evidenced from the XRD. This effect led to samples prepared with rutile at different temperatures to have higher luminescence intensity. The surface of the phosphor prepared with the rutile TiO_2 was discovered to be more stable against prolonged electron beam irradiation.

Acknowledgement

This work is based on the research supported by the South African Research Chairs Initiative of the Department of Science and Technology and National Research Foundation of South Africa, and the University of Free State Cluster program for financial support.

References

[1] Boutinaud P, Sarakha L, Cavalli E, Bettinelli M, Dorenbos P and Mahiou R, 2009 J.Phys. D: Appl. Phys. **42** 045106.
[2] Diallo PT, Jeanlouis K, Boutinaud P, Mahiou R and Cousseins JC, 2001 J. Alloys and Compd. **218** 323.
[3] Cockayne E and Burton BP, 2000 Phys. Rev. B **63** 3735.
[4] Chen SYD and Tang W, 2007 J. Alloys and Compd. **441** 327.
[5] Johnson M and Lemmens P, 2008 J. Phys. Condens. Matter **20** 264001.
[6] Steele B, Burns AD, Chernatynskiy A, Grimes RW and Phillpot SR, 2010 J. Mater. Sci. **45** 168.
[7] Tang W and Chen D, 2009 Mater. Res. Bull. **44** 836.
[8] Zhang X, Zhang J, Chen X, Lu S and Wong XJ, 2007 J. Lumin. **122** 958.
[9] Boutinaud P, Pinel E, Dubois M, Vink AP and Mahiou R, 2005 J. Lumin. **111** 69.
[10] Meagher EP and Lager GA, 1979 Can. Mineral. **17** 77.
[11] Weber J, Lavrov E and Herklotz F, 2012 Physica B **407** 1456.
[12] Mohd RJ, Kok SW, Norliza H, Nurul AKA, 2012 Int. J. Electrochem. Sci. **7** 4942
[13] Ricci PC, Casu A, Salis M, Corpino R and Anedda A, 2010 J. Phys. Chem. C **114** 14441.
[14] Cho E, Han S, Ahn HS, Lee KR, Kim SK and Hwang CS, 2006 Phys. Rev. B **73** 193202.
[15] Scepanovicy M, Grujic-Brojcin M, Miric M, Dohcevic-Mitrovic Z and Popovic ZV, 2009 Acta Phys. Pol. A **116** 603.
[16] Park KH and Kim HG, 2011 J. Korean Phys. Soc. **56**(2) 648.
[17] Deren PJ, Pazik R, Strek W, Boutinaud P, Mahiou R, 2008 J. Alloys and Compd. **451** 595.
[18] Erdei S, Rodriguez NM, White FW, Ravichandran D and Cross LE, 1998 J. Mater. Chem. **8**(1) 99.
[19] Zhang J, Liang H and Su Q, 2009 J. Phys. D: Appl. Phys. **42** 105110.

[20] Askeland DR, Fulay PP, Wright VJ, The science and engineering of materials, 2010, 6th ed., Cengage learning Inc. USA, p115.
[21] Pitale SS, Kumar V, Nagpure IM, Ntwaeaborwa OM, Coetzee E and Swart HC, 2011 J. Appl. Phys. **109** 013105.
[22] Kumar V, Mishra V, Pitale SS, Nagpure IM, Coetzee E, Ntwaeaborwa OM, Terblans JJ and Swart HC, 2010 J. Appl. Phys. **107** 123533.
[23] Swart HC, Sebastian JS, Trottier TA, Jones SL and Holloway PH, 1996 J. Vac. Sci. Technol. **14**(3) 1697.
[24] Swart HC, Greeff AP, Holloway PH and Berning GLP, 1999 Appl. Surf. Sci. **140** 63.
[25] Noto LL, Pitale SS, Terblans JJ, Ntwaeaborwa OM and Swart HC, 2012 Physica B: Physics of Condensed Matter **407(10)** 1517.

Structural and magnetic properties of $Mg_xSr_xMn_xCo_{1-3x}Fe_2O_4$ nanoparticle ferrites

Nadir SE. Osman, Thomas Moyo and Hafiz M I Abdallah

School of Chemistry and Physics, University of KwaZulu-Natal, Westville campus, P/Bag X5400, Durban 4000, South Africa

Osmann@ukzn.ac.za

Abstract: A series of $Mg_xSr_xMn_xCo_{1-3x}Fe_2O_4$ nanoferrites (with x =0, 0.1, 0.2, 0.3, 1/3) were synthesized by glycol-thermal technique. X-ray diffraction (XRD) patterns of the as-prepared samples show single-phase cubic spinel structure. The average crystallite sizes, lattice parameters, XRD densities and porosities were estimated from XRD data. The average crystallite sizes were found in range of 7.5 to 9 nm. Mössbauer spectroscopy measurements were performed in order to investigate the magnetic order of the materials and the distribution of Fe^{3+} ions in the tetrahedral and octahedral sites. Room temperature magnetic measurements of the series were studied using a vibrating sample magnetometer. The results show that the values of the coercive fields and saturation magnetizations which increase with increase in Co content from 15 Oe and 56.51 emu/g for x=0.3 to 114 Oe and 76.61 emu/g for x= 0.1 respectively. Significant correlations between magnetizations and coercive fields are observed. A significant change in properties is observed for the $Mg_xSr_xMn_xCo_{1-3x}Fe_2O_4$ compound. These results are contrasted with low temperature measurements from 2 K to 300 K and magnetic fields to 5 Tesla.

Keywords: *Glycol-thermal, Nanoferrite; Spin-freezing; superparamagnetism, exchange-interaction*

1. Introduction

Nanoparticles have special magnetic and electrical properties that are significantly different from their corresponding bulk materials [1, 2]. Reduction in the scale of the bulk materials to less than 100 nm can produce materials that exhibit exceptional properties such as superparamagnetic relaxation phenomena and spin-canted structure due to surface effects [3]. Magnetic nanoparticles have been attracting considerable interest because of a variety of possible applications [4-5]. Therefore understanding the magnetic properties of nanoscale particles is a central issue in magnetic materials. Ferrites and related compounds have been found to be suitable for many applications such as making cores for audio frequency, high frequency transformers, coils, chokes, permanent magnets, magneto-optical displays, microwave absorbers and guides in gas sensors [6-7]. Spinel nanoferrites are amongst materials with interesting optical, magnetic and electrical properties [8]. By changing the divalent elements in the tetrahedral sites of the spinel, the magnetic properties can be tuned. $CoFe_2O_4$ ferrite is known for its good magnetostriction properties, magneto-crystalline anisotropy and moderate saturation magnetization. These features make $CoFe_2O_4$ an interesting system study. Abdallah *et al* [9]

reported enhanced magnetic properties of a sample $Mn_{0.3}Co_{0.7}Fe_2O_4$ by Mg and Sr substitutions. The results showed significant changes in the magnetic properties compared to the initial parent material. Jigajeni *et al* [10] have also reported that $Mn_{0.2}Mg_{0.3}Co_{0.7}Fe_{1.8}O_4$ is a good candidate for magnetoelectric applications because of favorable values of resistivity, saturation magnetization and coercive field. We have therefore extended these studies by performing simultaneous substitutions of Co by Mg, Sr and Mn in $CoFe_2O_4$ for a series of samples with equal atomic proportions of substituting elements. The intention is to investigate any structural and magnetic changes due to the symmetry in the stoichiometry of the substituting elements.

2. Experimental details

$Mg_xSr_xMn_xCo_{1-3x}Fe_2O_4$ (x = 0, 0.1, 0.2, 0.3, 0.33) nanoferrites were synthesized by the glycol-thermal method in a Watlow series model PARR 4843 stirred pressure reactor. The starting materials were high purity $CoCl_2.6H_2O$, $Fe_2Cl_3.6H_2O$, $MnCl_2.4H_2O$, $MgCl_2.6H_2O$ and $SrCl_2.6H_2O$. Full details of the synthesis method used in the present case have been reported elsewhere [11]. The phase and structural characterization of the samples were obtained by a Phillips X-ray diffractometer (XRD) type PW1710 using CoKα radiation. The average crystallite size was calculated from the most intense (311) XRD peak. The morphology of nanoparticle was investigated by high-resolution transmission electron microscopy (HRTEM) (type: Jeol_JEM-1010). The microstructures of samples were investigated by high-resolution scanning electron microscope (HRSEM). ^{57}Fe Mössbauer spectra were obtained by a conventional spectrometer using a ^{57}Co source sealed in Rh matrix and vibrated at constant acceleration. Magnetic measurements were performed at room temperature using a LakeShore model 735 vibrating sample magnetometer (VSM). A mini cryogen free measurement system was used to perform low temperature magnetization measurements from 2 to 300 K.

3. Results and discussion

Figure 1 shows the X-ray diffraction patterns of the as-prepared samples of $Mg_xSr_xMn_xCo_{1-3x}Fe_2O_4$ series. The patterns indicate that single phase spinel structures were formed and no impurity peaks were observed. All the patterns are in match with the standard patterns of spinel ferrite. The average grain sizes were calculated using the Scherrer equation $D = 0.9\lambda/(\beta\cos\theta)$, where β is the full-width at half-maximum of the most intense (311) XRD peak [12].

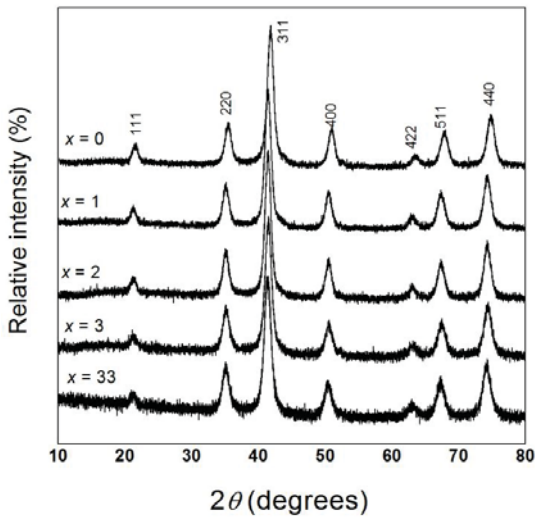

Fig. 1. X-ray patterns for the as-prepared samples of $Mg_xSr_xMn_xCo1\text{-}3_xFe_2O_4$ nanoparticle ferrites.

The lattice parameter *a,* was calculated using Bragg's law and equation $a=d(h^2+k^2+l^2)^{1/2}$ where d is the inter-planar spacing [13]. The XRD densities ρ_{XRD} were calculated using the formula $\rho_{XRD} = 8M_0/N_A a^3$ where M_o is the molecular weight and N_A is the Avogadro's number. The calculated lattice parameters a, crystallite sizes D, X-ray densities ρ_{XRD}, are presented in Table 1.The lattice parameter of the sample for x = 0 was found to be similar to a reported value [14]. However, there is no significant changes in the lattice parameters after substitution of Co except for the sample at x = 0.33 which shows a relatively high lattice parameter value. The XRD density values are observed to decrease with decreasing Co content.

The microstructure and the surface morphology were studied by means of HRTEM and HRSEM respectively. Figure 2 shows typical HRTEM micrographs showing uniform and nearly spherical nanoparticles with some agglomeration. Agglomeration can enhance the magnetic interaction between the nanoparticles [15]. The boundaries between the crystallites can also be clearly observed. The values of the crystallite sizes estimated from the images are also given in table 1 and appear to be consistent with the estimates from the XRD data. Figure 3 shows the HRSEM surface morphology of the as-prepared $Mg_xSr_xMn_xCo_{1-3x}Fe_2O_4$ which also support the observation from HRTEM.
Figure 4 shows room-temperature Mössbauer spectra for the as-prepared $Mg_xSr_xMn_xCo_{1-3x}Fe_2O_4$ samples at 300 K. Two sextets were used to fit the Mössbauer data and an additional one was required for the sample at $x = 0.1$ in order to obtain a better fit to the data. This additional sextet is attributed to the presence of Fe^{3+} in the grain boundaries [17].

Table 1: The lattice parameters (a), crystallite sizes (D), X-ray densities (ρ_{XRD}) of the series $Mg_xSr_xMn_xCo_{1-3x}Fe_2O_4$.

x	a (Å) ±0.003	D_{XRD} (nm) ±0.01	D_{HRTEM} (nm) ±1.69	ρ_{XRD} (g/cm^3) ±0.001
0.0	8.380	8.27	8.55	5.296
0.1	8.387	7.91	8.33	5.261
0.2	8.387	8.34	8.66	5.237
0.3	8.379	7.28	7.42	5.230
0.33	8.395	7.20	7.83	5.182

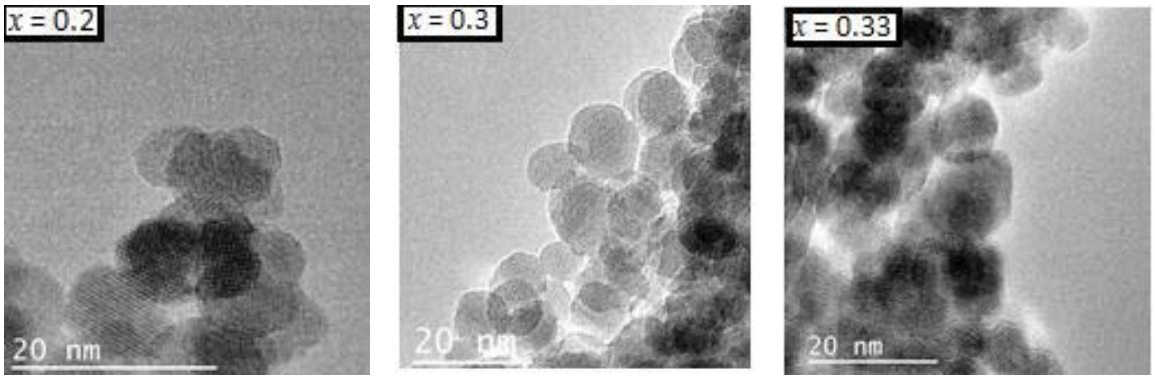

Figure 2. HRTEM images for the as-prepared $Mg_xSr_xMn_xCo_{1-3x}Fe_2O_4$samples.

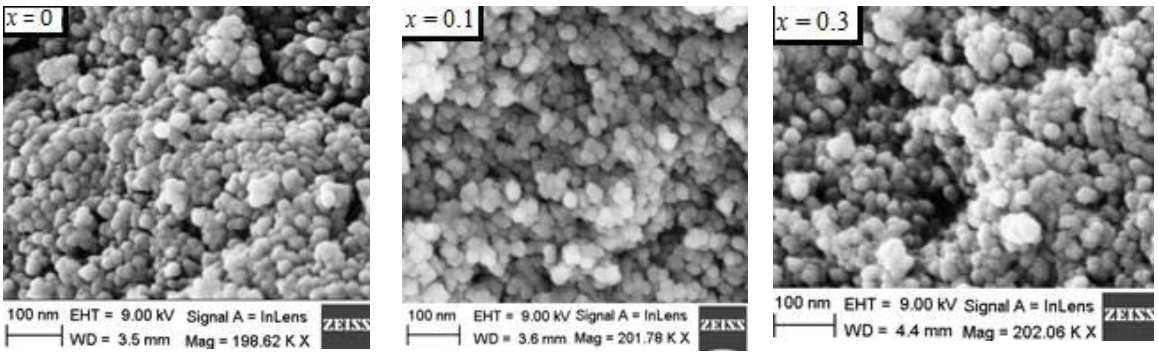

Figure 3. HRSEM micrographs for the as-prepared $Mg_xSr_xMn_xCo_{1-3x}Fe_2O_4$ samples.

The results of the hyperfine parameters are presented in table 2. Larger values of hyperfine fields are assigned to the B-sites [9, 17]. A decrease in hyperfine fields is observed which is associated with the reduction of Co content in the samples for $x > 0.1$. The isomer shift values are associated with Fe^{3+} ions [18] and show no significant changes with composition.

Figure 5 shows the hysteresis loops of the as-prepared $Mg_xSr_xMn_xCo_{1-3x}Fe_2O_4$ measured at an applied field of about 14 kOe at 300 K. Slightly substituting Co by Mg, Sr and Mn atoms significantly increases the value of the magnetization from 32.79 emu/g to 76.61 emu/g for x=0.1. There after the magnetization decreases with increasing x to 32.87 emu/g when x = 0.33. However, more reliable trends in coercive fields and magnetization need to be deduced for $H >> 14$ kOe. Room temperature magnetic properties can be understood in term of cations distribution [8] based on superexchange interaction between A and B sites. The increases in the saturation magnetization can be attributed to the magnetic moments of 5 μ_B Mg or Mn with the addition of Mn favoring more negative exchange interactions. The result show the coercivity decreases proportionally with the increase in x reflecting the decline in the Co atoms which are associated with high uniaxial anisotropy [19]. Table 3 also shows magnetic parameters deduced from magnetization measurements at room temperature. The magnetic moments can be deduced from saturation magnetizations [20].

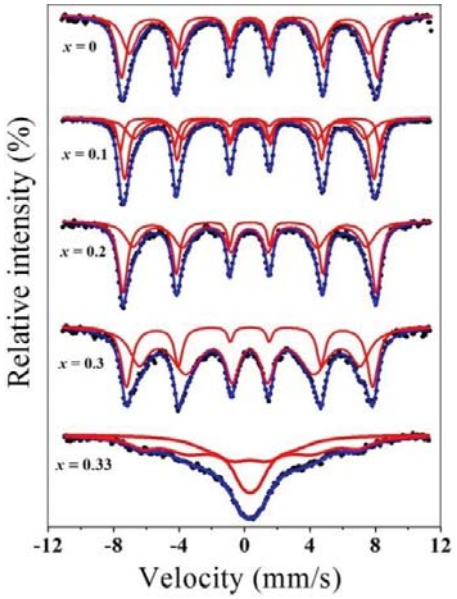

Figure 4. Mössbauer spectra for the as-prepared $Mg_xSr_xMn_xCo_{1-3x}Fe_2O_4$ samples at 300 K.

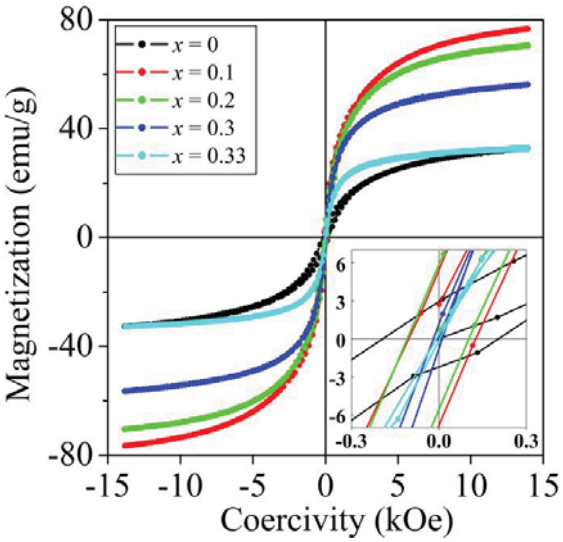

Figure 5. Room temperature hysteresis loop of $Mg_xSr_xMn_xCo_{1-3x}Fe_2O_4$ as-prepared. The inset shows magnified view of $M - H$ curves.

Table 2. Isomer shifts (δ), hyperfine magnetic fields (H), line widths (Γ) and Fe^{3+} fraction population (f) on A- and B- sites for the as-obtained $Mg_xSr_xMn_xCo_{1-3x}Fe_2O_4$ samples.

x	δ (mm/s)		H (kOe)			Γ (mm/s)		f (%)	
	δ_A	δ_B	H_A	H_B	H_{3rd}	Γ_A	Γ_B	f_A	f_B
	±0.03	±0.04	±9	±4	±7	±0.09	±0.08	±3	±7
0	0.31	0.31	453	485	-	0.32	0.24	50	50
0.1	0.30	0.34	473	493	439	0.26	0.21	41	24
0.2	0.31	0.31	442	480	-	0.42	0.17	49	51
0.3	0.32	0.32	419	467	-	0.55	0.21	70	30
0.33	0.38	0.34	161	409	-	0.94	1.35	47	53

The values of M_R/M_S indicate the hysteresis loop squareness [15], which can be a guide to how the nanoparticles could be used in different applications. It is also observed that the highest squareness value is observed when $x = 0.2$.

Low temperature magnetic measurements at a maximum applied field of 50 kOe were performed which can provide more reliable trends in the current series of compounds. M - H curves in figure 6 reveal some distortion of the hysteresis loops at 2 K for the samples at $x = 0.1$ and $x = 0.2$. We suggest this distortion to be due to the decoupling between the hard and soft magnetic phases. Upadhyay *et al* [21] have explained similar hysteresis loop behavior in terms of freezing of disordered spins. No distortions of the loops are observed for the samples at $x = 0$, 0.3, 0.33. The magnetization does not saturate even in fields of 50 kOe. Figure 7 shows the variation of the coercivity and the magnetization with the temperature. Both parameters are sensitive to temperature change and the effect of spin freezing [9]. Significant increases in coercive fields with temperature are observed for samples with $x = 0.1$, 0.2 and 0.3. The highest coercive field is obtained for $x = 0.1$ and the least for $x = 0.3$. The samples corresponding to $x = 0$ and 0.33 do not show significant changes in coercive fields at low temperatures.

Table 3. Magnetic parameters of $Mg_xSr_xMn_xCo_{1-3x}Fe_2O_4$ measured at 300 K.

x	H_c (Oe)	M_S (emu/g)	M_R (emu/g)	M_R/M_S	n_B (μ_B)
0.0	198.15	32.79	2.59	0.078	2.37
0.1	114.92	76.61	6.14	0.077	3.18
0.2	105.61	70.56	5.73	0.081	2.94
0.3	15.34	56.51	0.97	0.017	2.34
0.33	5.89	32.87	0.24	0.007	1.36

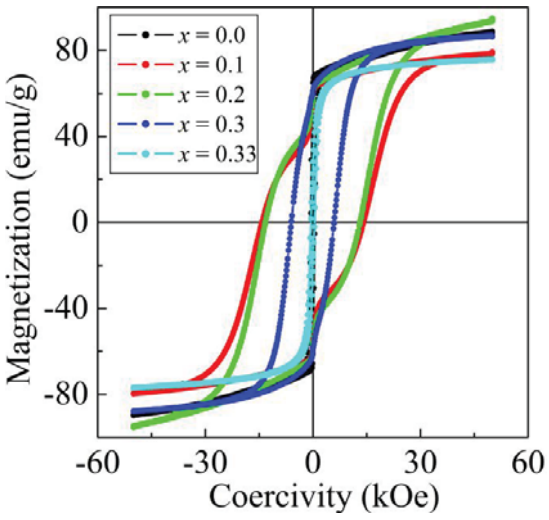

Figure 6. $H - M$ loops for $Mg_xSr_xMn_xCo_{1-3x}Fe_2O_4$ as-prepared measured at 2 K.

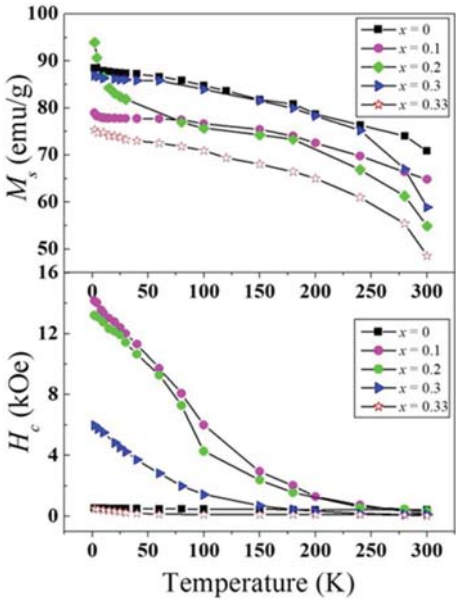

Figure 7. Variations of coercivity and saturation magnetization as function of measuring temperature for the as-prepared samples of $Mg_xSr_xMn_xCo_{1-3x}Fe_2O_4$.

4. Conclusions

$Mg_xSr_xMn_xCo_{1-3x}Fe_2O_4$ series have been successfully synthesized using glycol-thermal technique. XRD patterns indicated the formation of single phase spinel crystallites which are nearly spherical in shaped with sizes from about 7.5 to 8.5 nm. Hence simultaneous substitution of Co by Mg, Mn and Sr was achieved. Low temperature measurements show interesting trends in the magnetization and coercive fields. The samples with the highest and least Co content (x =0 and x = 0.33) show the least sensitivity to changes in coercive fields and magnetization at low temperatures. Significant enhancement of the coercive fields are obtained for $0.1 \leq x \leq 0.3$.

Acknowledgments

The authors would like to thank the National Research Foundation (NRF) of South Africa for equipment grants and Sudan University of Science and Technology for the study leave (NSEO).

References

[1] Pankhurst A, Connolly J, Jones S K, Dobson J 2003 *J. Phys. D: Appl. Phys.* **36** R167
[2] Kodama R H 1999 *J. Magn. Magn. Mater.* 359
[3] Didukh P, Greneche J M, lawska-Waniewska A S, Fannin P C, Casas L 2002 *J. Magn. Magn. Mater.* **242** 61
[4] Mornet S, Vasseir S, Grasset F, Duguet E 2004 *J. Mater. Chem.* **14** 216
[5] Lin X M, Samia A C S 2006 *J. Magn. Magn. Mater.* **305** 100
[6] Blasse G 1964 *Philips Research Reports Suppl.* **3** 96
[7] Nejati K, Zabihi R 2012 *Chem. Cent. J.* **6** 23
[8] Ashiq M, Saleem S, Malana M, Ur-Rehman A 2009 *J. AlloysComp.* **486** 640
[9] Abdallah H M I, Moyo T 2013 *J. Alloys Comp.* **562** 156
[10] Jigajeni S, Kulkarni S R, Kolekar Y, Kulkarni S B, Joshi P 2010 *J. Alloys Comp.* **402** 492
[11] Abdallah H.M.I, Moyo T, Msomi J.Z 2011 *J Supercond Nov Magn* **24** 673.
[12] Naseri M G, Saion E B, Ahangar H A, Hashim M, Shaari A H 2011 *J. Magn. Magn. Mater.* **323** 1745
[13] Kittel C 2005 *Introduction to Solid State Physics*, 5th edition, John Wiley & Sons pp. 302–304
[14] Dascalu G, Popescu T, Feder M, Caltun O F 2013 *J Magn. Magn. Mater.* **333** 69
[15] Aslibeiki B, Kameli P, Salamati H, Eshraghi M, Tahmasebi T 2010 *J. Magn. Magn. Mater.* **322** 2929
[16] Maaz K, Mumtaz A, Hasanain S K, Ceylan A 2007 *J. Magn. Magn. Mater.* **308** 289
[17] Manova E, Kunev B, Paneva D, Mitov I, Petrov L, Estournes C, D'Orleans C, Rehspringer J, Kurmoo M 2004 *Chem. Mater.* **16** 5689
[18] Jing J, Zhao F, Yang X, Gonser U 1990 *Hyperfine Interaction* **54** 571
[19] Chakrabarti S, Mandal S K, Chaudhuri S 2005 *Nanotechnology***16** 506
[20] Kambale R C, Shaikh P A, Kamble S S, Kolekar Y D 2009 *J. Alloys Comp.* **478** 599
[21] Papaefthymiou G C, Ahmed S R, Kofinas S 2005 *Rev. Adv. Mater. Sci.* **10** 306

Magnetic properties of epitaxial Cr/$Cr_{99.65}Ru_{0.35}$ heterostructures

A.R.E. Prinsloo[1], C.J. Sheppard[1], A.M. Venter[2], E.E. Fullerton[3], B.S. Jacobs[1] and K. C. Rule[4]

[1]Department of Physics, University of Johannesburg, PO Box 524, Auckland Park, 2006
[2]Research and Development Division, Necsa Limited, P.O. Box 582, Pretoria 0001, South Africa
[3]Center for Magnetic Recording Research, University of California, San Diego, 9500 Gilman Dr., La Jolla, CA 92093-0401, USA
[4]Bragg Institute, ANSTO, Locked Bag 2001, Kirrawee DC NSW 2232, Australia

Author e-mail address: alettap@uj.ac.za

Abstract. We investigate the magnetic properties of the Cr/$Cr_{99.65}Ru_{0.35}$ hetero-structures, with 10 nm $Cr_{99.65}Ru_{0.35}$ layers and the Cr layer thickness fixed at 10 and 50 nm. Previous resistivity measurements probed the dimensionality effects in epitaxial and polycrystalline $Cr_{100-x}Ru_x$ alloy thin films, as well as on epitaxial Cr/$Cr_{99.65}Ru_{0.35}$ heterostructures. These results suggested proximity induced magnetism in the Cr layers with thickness less than 30 nm. In the present investigation the magnetic properties are directly studied through exploratory neutron diffraction measurements. The temperature dependence of the neutron results indicates the existence of the paramagnetic phase, as well as commensurate and incommensurate spin-density-wave phases in these hetero-structures. Present results therefore confirm key characteristics of the magnetic ordering in these layers.

1. Introduction

Bulk Cr is an itinerant electron antiferromagnetic material that forms an incommensurate (I) spin-density-wave (SDW) phase below its Néel temperature T_N = 311 K [1]. Cr and Cr alloys with their SDW antiferromagnetism, exhibit a richness of magnetic phenomena that have attracted considerable interest for many years [1].

Substantial focus has in recent years been placed on the investigation of magnetic properties in thin films and hetero-structures of Cr and Cr alloys, which have revealed fascinating properties not observed in bulk materials [2, 3]. These properties include the mediating role of Cr thin films in exchange coupled super lattices and in giant magneto-resistive (GMR) materials [4]. In order to broaden this knowledge, a previous contribution reported on dimensionality effects in epitaxial and polycrystalline $Cr_{100-x}Ru_x$ alloy monolayer thin films, as well as on epitaxial Cr/$Cr_{99.65}Ru_{0.35}$ hetero-structures [5]. The choice of this alloy system was based on the interesting behaviour seen in the bulk $Cr_{100-x}Ru_x$ alloy system, where a commensurate (C) SDW phase is induced at a critical concentration $x_L \approx 0.2$ and temperature T_L = 331 K. Outstanding magnetic properties, such as exceptionally large concentration and pressure derivatives of T_N and peculiar magneto-elastic properties have been studied extensively in CSDW $Cr_{100-x}Ru_x$ bulk alloys and single crystals containing x = 0.3 [1].

Extending Cr-Ru alloy studies to include thin films and hetero-structures will explore the role of dimensionality and microstructure effects on the properties of this alloy system and further probe proximity effects in a purely itinerant magnetic system. Previous resistance studies [5] on Cr-Ru thin films and $Cr/Cr_{99.65}Ru_{0.35}$ hetero-structures showed interesting properties that also suggested proximity induced magnetism in the Cr layers with thickness less than 30 nm. In order to fully understand the behaviour of the SDW of Cr in these hetero-structure configurations, neutron diffraction studies on the $Cr/Cr_{99.65}Ru_{0.35}$ hetero-structures are required, following the same approach as was previously used for Cr/Cr-Mn super lattices in which pinning and temperature hysteresis of the Cr SDW order with temperature was observed [2].

In this paper the results of exploratory neutron diffraction studies done on the $Cr/Cr_{99.65}Ru_{0.35}$ hetero-structures are discussed and possible future measurements are proposed.

2. Experimental

$Cr/Cr_{99.65}Ru_{0.35}$ hetero-structures were grown using DC magnetron sputtering onto MgO(100) substrates. A 10 nm Cr buffer layer was first deposited at 800 °C, where after the hetero-structures were deposited at a lower temperature of 400 °C to avoid inter-diffusion between the layers. The $Cr_{99.65}Ru_{0.35}$ layers were co-sputtered from elemental sources maintaining a 10 nm layer thicknesses for both samples. For the two samples of this study the Cr inter-layer separation thicknesses (t_{Cr}) are fixed at 10 and 50 nm. All samples were prepared with a total thickness of approximately 700 nm. The concentrations and thicknesses of the various layers in the hetero-structures were confirmed using Rutherford Back Scattering (RBS) technique, while the film crystallographic structure was characterized using X-ray diffraction (XRD). Magnetic phenomena were studied by electrical resistance (R) measurements, using a standard DC four-probe method, to determine the Néel transition temperatures (T_N). Magnetic properties were directly probed with neutron diffraction investigations on the Taipan triple-axis spectrometer at ANSTO (Australia) to determine the magnetic structure as a function of temperature. By utilizing the triple-axis instrument in elastic mode a very low background contribution could be attained, providing a sensitive probe notwithstanding the small volume of material available to scatter from and associated magnetic moments in the $Cr/Cr_{99.65}Ru_{0.35}$ hetero-structures.

3. Results

Figure 1 shows the RBS spectrum for a typical Cr/CrRu multilayer. As an example [Cr(20 nm)/Cr-Ru(5 nm)]$_n$ hetero-structure sample's RBS spectrum (black line) is shown, where the number of repeats n = 8. From this figure it is noted that the top four layers are better resolved than the bottom four layers. The simulated spectrum (red line) shows eight clear peaks, thus indicating that minimal diffusion of Ru occurred between the various layers. Further RBS spectra obtained with the sample tilted at different angles with reference to the beam reveals some roughness in the layers.

In Figure 2 the XRD results are shown for the two different $Cr/Cr_{99.65}Ru_{0.35}$ heterostructures. The results indicate that both the samples had epitaxial crystallite orientations with preferred growth directions [200]. The lattice parameter of the two structures rendered values of 0.28873 and 0.28869 nm for the t_{Cr} = 10 nm and t_{Cr} = 50 nm samples respectively. The full-width at half-maximum (FWHM) of the Bragg peaks was used to determine the length scale over which the films are structurally coherent (in growth direction) [6] by applying the Debye-Scherer formula and neglecting instrumental resolution contributions. The crystal coherence lengths for both structures are similar, approximately 255 nm. The mosaic spread determined from the FWHM of rocking curves [6] were determined to be 0.55° and 0.61° respectively for t_{Cr} = 10 nm and 50 nm. Comparisons of in-plane and normal XRD scans indicate a normal plane strain of approximately 0.4%, that can be attributed to sample-substrate mismatch.

The Néel temperatures (T_N) of the films were determined from anomalies observed in electrical resistance (R) measurements as a function of temperature (T). The measured $R - T$ curves for the two $Cr/Cr_{99.65}Ru_{0.35}$ hetero-structures are shown in Figure 3 (a) and (b). Since only weak anomalies were

observed, T_N values were taken at the inflection point on the $R - T$ curves by considering the dR/dT versus T curves and taking T_N as the temperature of the minimum on each curve as shown in the insets of Figures 3 (a) and (b). The T_N values for the hetero-structures with t_{Cr} fixed at 10 nm and 50 nm were found to be 393 ± 4 K and 298 ± 3 K, respectively.

Previous research has shown that neutron diffraction investigations are well suited to determine the nature of the SDW ordering and to locate T_N in Cr and Cr alloys [7, 8, 9]. The presence of magnetic satellites at the (1±δ, 0, 0) position confirms the presence of the incommensurate (I) SDW, while the absence of these satellites with only a central peak confirms that the sample is in the CSDW phase [1].

The neutron diffraction investigations on the hetero-structures were technically challenging in that the sample orientations had to be very specific with reference to the instrumental geometry to enable observation of the magnetic scattering from the Cr multilayers. The approach followed was to firstly orientate the MgO(100) single crystal substrates taking cognisance that the orientations of the magnetic coatings would be 45° rotated in the vertical plane due to the epitaxial orientation of Cr to MgO(100).

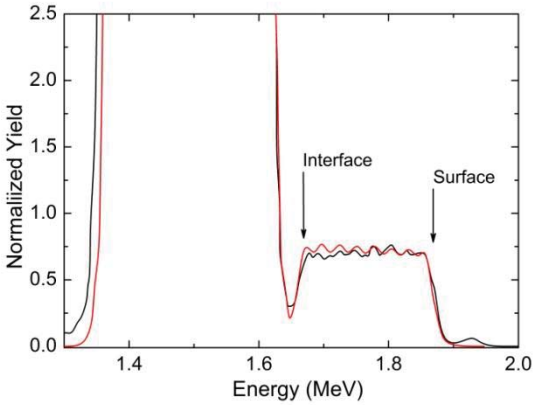

Figure 1: The RBS spectrum for a typical [Cr/Cr-Ru]$_n$ hetero-structure sample in which n = 8. The black line shows the measured spectrum for the sample and the red line the simulated spectrum.

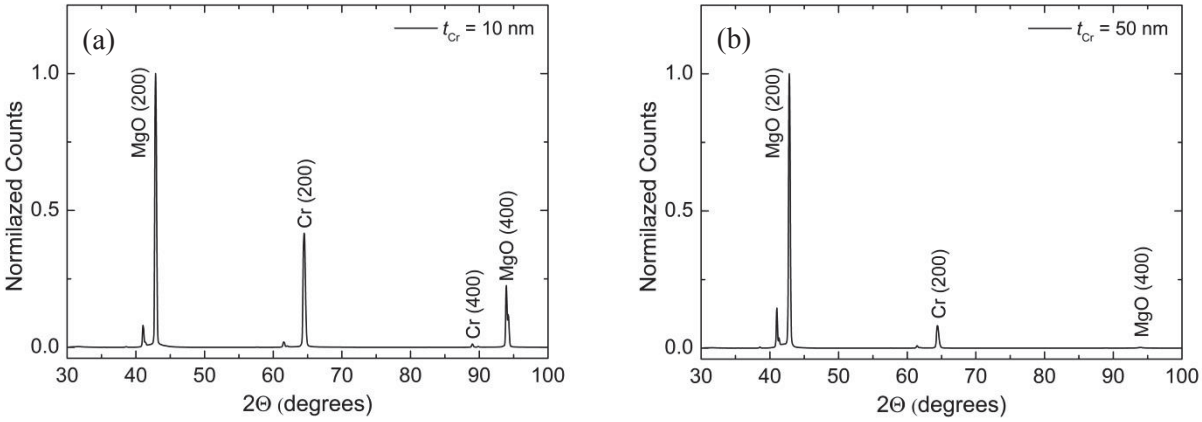

Figure 2: θ-2θ XRD scans (Bragg-Brentano geometry) in which the scattering vector is maintained normal to the plane of the film, for the Cr/$Cr_{99.65}Ru_{0.35}$ hetero-structures prepared on MgO(100) substrates with t_{Cr}: (a) 10 nm; and (b) 50 nm. The two unlabelled reflections at approximately 41° are possibly due to Cu K_β reflection of the MgO(200) peak.

The correlation geometries between the substrate and coating orientations are indicated in Figure 4. Substrate reflections are indicated in black, Cr/Cr-Ru coating reflections in blue and the magnetic reflections in red. A correlation matrix that links the crystal and laboratory systems (UB matrix) was setup from the orientation optimised single crystal reflections. This was then used to explore the reflections of the Cr coating based on the corrected lattice parameter and crystalline reflections (020), (111) and (101) indicated in blue. After optimisation, the magnetic (001) reciprocal lattice position was explored in the reciprocal lattice direction ql, by performing (0, 0, z) scans. The scans were done between $0.8 \leq z \leq 1.2$ in steps of 0.002. The intensity at the (001) position could be purely of magnetic origin due to the structure factor of the bcc crystalline structure of the Cr/Cr-Ru. Taking cognisance that the coatings were typically 700 nm in thickness, prolonged data acquisition times had to be employed for good counting statistics to identify the diffraction signals.

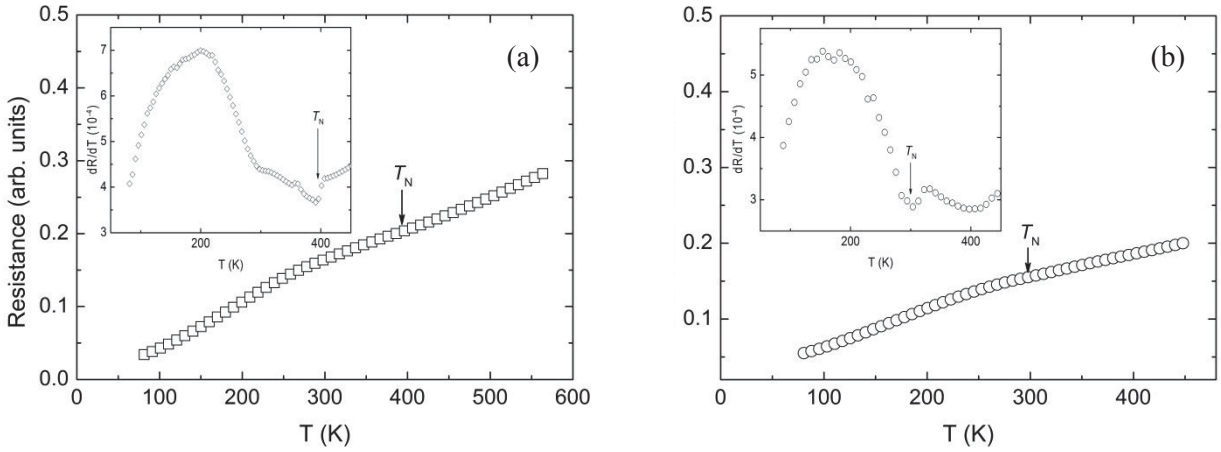

Figure 3: Resistance (R) versus temperature (T) graphs for $Cr/Cr_{99.65}Ru_{0.35}$ hetero-structures prepared on MgO(100) substrates with t_{Cr}: (a) 10nm; and (b) 50 nm. The insets show dR/dT versus T for each sample with the temperature of the minimum taken as the Néel temperature (T_N).

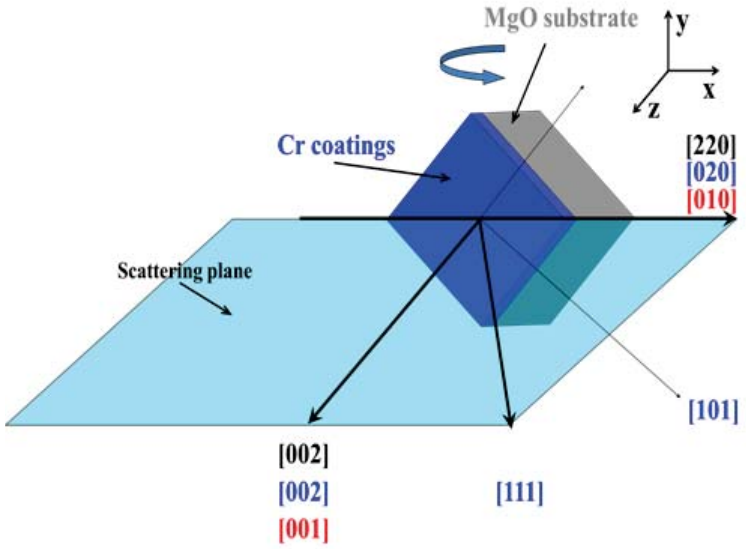

Figure 4: Sample orientation and expected reflections. Substrate reflections are indicated in black, Cr-Ru coating reflections in blue and the magnetic reflections in red.

Results from ql reciprocal-lattice scans of the (0,0,1-δ) regions of the $Cr/Cr_{99.65}Ru_{0.35}$ hetero-structures prepared on MgO(100) substrates with t_{Cr} = 10 nm and 50 nm are shown in Figures 5 and 6, respectively. Reciprocal-lattice scans of the t_{Cr} = 10 nm hetero-structure were taken at constant T in the sequence 300 K, 200 K, 130 K and 450 K, i.e. respectively below and above the expected Néel temperature (from the resistance measurements expected to be just above room temperature) and to search for possible magnetic phase transformations below T_N. The scan at 450 K clearly demonstrates the absence of magnetic ordering, i.e. sample is in the paramagnetic state. The peak at ql ≈ 0.92 showed no temperature dependence and is assumed to originate from higher-order wavelength contamination from the MgO(100) substrate that, notwithstanding (2 × 5cm) PG beam filters employed, remained intense compared to the intensity of the magnetic peaks. For all the temperatures lower than 300 K diffraction peaks of magnetic origin are observed. The temperature dependences of ql scans clearly revealed the presence of an ISDW phase below 200 K, and a CSDW phase at room temperature (300 K), with the Néel transition taking place between the room temperature and 450 K measurements. A weak peak is observed at ql = 1.05 in the 300 K data, but this is attributed to the effect of a sloping background. It is thus concluded that a CSDW-ISDW phase transition takes place between 300 K and 200 K. The period of the ISDW phase does not seem to display temperature dependence. This may be expected if the SDW wavelength is constrained by the periodicity of the layers and therefore will not show any T dependence.

Results for the $Cr/Cr_{99.65}Ru_{0.35}$ hetero-structure with t_{Cr} = 50 nm, shown in Figure 6, rendered much weaker magnetic ordering with the peaks of magnetic origin being only slightly higher than background. The background is in this case at least 5 times higher compared to the other sample. Conclusions drawn from the results are that the Néel transition occurs close to 300 K, since the magnetic ordering at 300 K is weakly commensurate, with an ISDW-to-CSDW phase transition taking place between 200 K and 300 K. In contrast to the sample with t_{Cr} = 10 nm the period of the ISDW phase seem to display a temperature dependence in this hetero-structure.

4. Conclusions

Exploratory neutron data resulting from this investigation support the conclusions made from resistance data, indicating that the T_N values for the hetero-structures with t_{Cr} fixed at 10 nm and 50 nm can be fixed at 393 ± 4 K and 298 ± 3 K, respectively. Most interesting, it is noted that from the neutron data it is evident that both samples show ISDW-CSDW phase transitions. These were not detected in resistivity measurements and needs to be investigated in more detail.

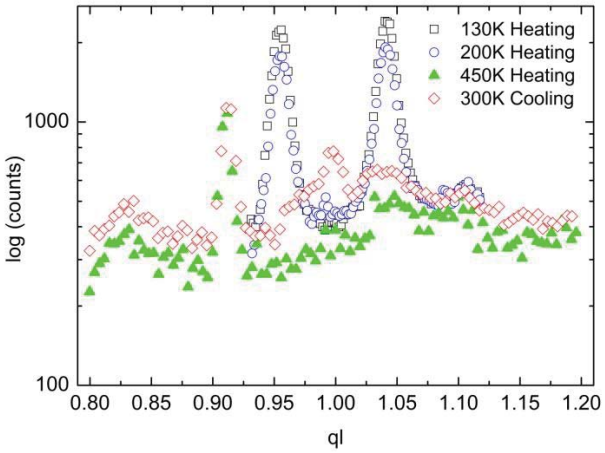

Figure 5: Reciprocal ql lattice scans of the (100) position of sample $Cr/Cr_{99.65}Ru_{0.35}$ hetero-structure with t_{Cr} = 10 nm taken at various constant temperatures.

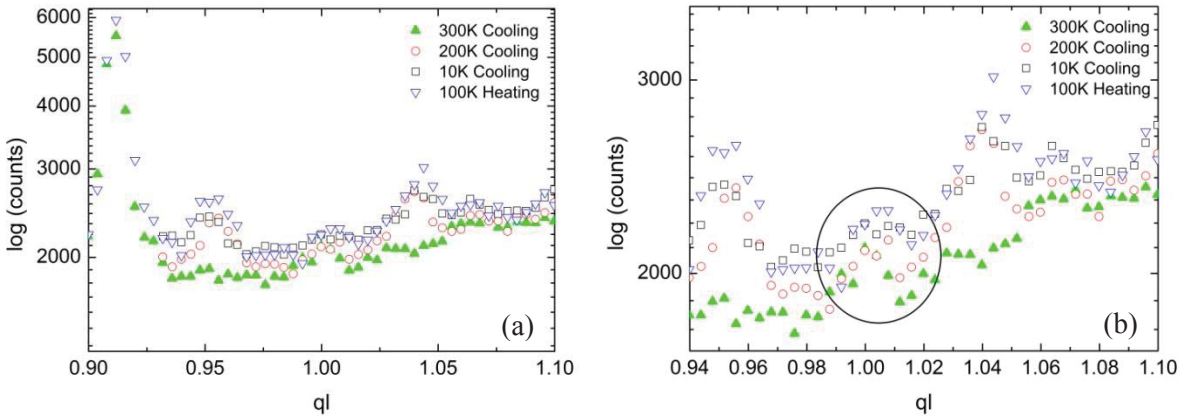

Figure 6: Reciprocal ql lattice scans of the (100) region in sample $Cr/Cr_{99.65}Ru_{0.35}$ hetero-structures with t_{Cr} = 50 nm taken at various constant temperatures. Figure (a) shows the wide ql range employed (searching for higher order resonance magnetic peaks), while figure (b) shows the region of the primary magnetic reflections close to the (100) position. The weak central peak indicative of the CSDW phase, is emphasized.

The present results indicate that it is feasible to measure the magnetic ordering in Cr multilayer systems with the Taipan instrument at ANSTO and will pave the way for further studies on the sample series. Investigation of both samples warrant further research in order to better characterize the magnetic ordering by measurements at a number of additional temperatures. Furthermore, in considering the present results, it is clear that better data quality can be obtained by employing at least double the measurement times for sample with t_{Cr} = 10 nm, especially close to the Néel transition. At least four times longer data acquisition times is required for the sample with t_{Cr} = 50 nm, in conjunction with attempting to reduce the background. In addition special care needs to be taken to reduce the higher-order wavelength contamination of the beam, as well as improving the non-flat background.

Future neutron diffraction work on the $Cr/Cr_{99.65}Ru_{0.35}$ hetero-structures also needs to include scanning along other reciprocal lattice directions – specifically exploring the qk orientation. This should render results in line with that obtained for the Cr/Cr-Mn system [2] in which pinning of the Cr SDW was observed and confirmed through neutron diffraction studies.

Acknowledgements

Financial support from the SA NRF (Grant Nos. 80928 and 80631) is acknowledged. ANSTO is acknowledged for the neutron diffraction beam time awarded.

References

[1] Fawcett E., Alberts H.L., Galkin V. Yu, Noakes D.R., Yakhmi J.V. 1994 *Rev. Mod. Phys.* **66** 25
[2] Fullerton E.E., Robertson J.L., Prinsloo A.E.R., Alberts H.L., Bader S.D. 2003 *Phys. Rev. Lett.* **91** 237201
[3] Kummamuru R.K., Soh Y.A. 2008 *Nature* **452** 859
[4] Zabel H.J. 1999 *J. Phys.: Condens. Matter* **11** 9303
[5] Prinsloo A.R.E., Derrett H.A., Hellwig O., Fullerton E.E., Alberts H.L., van den Berg N. 2010 *J. Magn. Magn. Mat.* **322** 1126
[6] Mattson J.E., Fullerton E.E., Sowers C.H., Bader S.D. 1995 *J. Vac. Sci. Technol.* **A 13**(2) 276
[7] Baran A., Alberts H.L., Strydom A.M. and du Plessis P. de V. 1992 *Phys. Rev.* **B 45** 10473
[8] Bacon G.E. 1961 *Acta. Cryst.* **14** 823
[9] Koehler W.C., Moon R.M., Trego A.L. and Mackintosh A.R. 1966 *Phys. Rev.* **151** 405

White cathodoluminescence from $Zn_{0.3}Mg_{0.7}Al_2O_4:Tb^{3+},Eu^{3+}$.

S K K Shaat, H C Swart and O M Ntwaebborwa[1]

Department of Physics, University of the Free State, Bloemfontein, ZA9300, South Africa.

E-mail: ntwaeab@ufs.ac.za

Abstract. In this study, a white cathodoluminescence was generated from $Zn_{0.3}Mg_{0.7}Al_2O_4:Tb^{3+};Eu^{3+}$ prepared by combustion route using urea as a fuel metal and nitrates as precursors. The XRD diffraction patterns from the samples showed phases associated with cubic structures of $ZnAl_2O_4$ and $MgAl_2O_4$ referenced in the standard JCPDS file No. 75-1796. The particle morphology of the $Zn_{0.3}Mg_{0.7}Al_2O_4:Tb^{3+};Eu^{3+}$ showed different irregular shape. White cathodoluminescence with the CIE coordinates (x = 0.343, y = 0.323) was observed when the phosphor was excited by a low voltage (2 keV) electron beam in vacuum. This was a result of the simultaneous emission of blue and green emissions from Tb^{3+} and red emission from Eu^{3+}. This phosphor is evaluated for possible applications in white LEDs. .

1. Introduction

Nowadays, researchers are working to prepare and develop white light emitting phosphors that can be used in solid state lighting applications such as flat panel displays (FPD), phosphor lamps and light emitting diodes (LEDs). The white colour is the combination of the primary colours namely blue, green and red. It is, however, not easy to have one phosphor to emit these three colours simultaneously. Traditionally, the production of white light in LEDs can be achieved by two routes. These are by combining yellow phosphor such as YAG:Ce^{3+} with a lnGaN-based blue diode and by combining a UV chip with a three converter system of red, green and blue phosphors. The problems with these are poor rendition and high thermal quenching of the yellow phosphor and reabsorption of the blue emission by the red or green phosphor in the three converter system [1]. To overcome these problems, a new generation of single host phosphors prepared mostly by doping alkali earth aluminates with divalent alkali earth and/or trivalent rare-earth ions has been developed. Alkali earth aluminates are chemically stable, environmentally friendly [2], and they can be easily produced cost-effectively. For example, a white emission from a tunable $Mg_3Al_2O_5Cl_2:Ce^{3+},Eu^{2+}$ phosphor based on energy transfer from Ce^{3+} to Eu^{2+} by a down-conversion process was reported by Song et al [1], while Shaat et al [3] generated white light from $Ca_xSr_{(1-x)}Al_2O_4:Tb^{3+};Eu^{3+}$ phosphor. In this study combustion method was used to prepare $Zn_{0.3}Mg_{0.7}Al_2O_4:Tb^{3+};Eu^{3+}$ to produce white cathodoluminescence. The structure, morphology, cathodoluminescent properties of this were examined, and are reported

2. Experimental

2.1. Sample Preparation.

A combustion method was used to prepare Tb^{3+} and Eu^{3+} single and co-doped $Zn_{0.3}Mg_{0.7}Al_2O_4$ nanophosphor. The metal nitrates of $Zn(NO_3)_2.4H_2O$ $Mg(NO_3)_2.6H_2O$, $Al(NO_3)_3.9H_2O$, $Tb(NO_3)_3.6H_2O$, $Eu(NO_3)_3.5H_2O$ and urea CON_2H_4 of AR grade purchased from Merck, South Africa

were used as starting materials (precursors) and were used as obtained without further purification. The distilled water used to dissolve the precursors with vigorous stirring at 50°C for 0.3 hr until the solution became clear. The resulting solution was transferred to a muffle furnace maintained at 450 ± 10% ^{o}C. The transparent solution started to boil and underwent dehydration, followed by decomposition and escaping of large amounts of gases (nitrogen, ammonia and oxides of carbon). White foamy and voluminous ash was produced after an occurrence of spontaneous ignition and the reaction underwent smouldering combustion with enormous swelling. The combustion reaction was completed in ~5 minutes. The product was cooled to room temperature and the ashes were ground gently info fine powders. The powders were characterized without any further post-preparation treatment. The crystalline structure of $Zn_{0.3}Mg_{0.7}Al_2O_4$:Tb^{3+};Eu^{3+} was analysed by Bruker D8 ADVANCE powder diffractometer with Cu Kα radiation, λ=1.5406 Å. The SEM data were collected by JEOL-JSM 7500 Scanning Electron microscope operated at 30 kV and 50 pA. The CL emission spectra were measured for using a beam of 2 kV electrons as excitation source. All measurements were carried out at room temperature.

3. Analysis and results discussion

3.1. Structural analysis.

$MgAl_2O_4$ and $ZnAl_2O_4$ materials belong to a close-pakced spinel cubic structure with O^7_h ($Fd3^-m$) space group symmetry [4-10]. The general chemical formula for spinel structure is given by the following formula (*)

$$(X_{1-s}Y_s)_{Tet.}(X_sY_{2-s})_{Oct.}O_4 \qquad (*)$$

where *X* and *Y* are the cations with valence number (2+) and (3+), respectively, and the concentration of *X* and *Y* that fill the tetrahedral site ( )$_{\text{Tet.}}$, and octahedral site { }$_{\text{Oct.}}$ is much equal to or less than 1. The normal spinel is obtained when $s = 0$ (i.e XY_2O_4) with eight formula units per cubic unit cell [9], otherwise we have intermediate or distorted spinel. Therefore, according to the formula (*) the divalent ions Mg^{2+} and/or Zn^{2+} can be distributed into tetrahedral site and octahedral site, and the same for Al^{3+}. This is in agreement with the network connection of $MgAl_2O_4$ shown in figure 1 [11]. It appears in the given structure that there are two positions for Mg^{2+} and Al^{3+} i.e. (Mg1 and Al2) and (Mg2 and Al1). It looks like that there is no effect or change when Zn^{2+} ions are added to the $MgAl_2O_4$ by small amount because the Mg^{2+} (ionic radius = 0.051 nm) and Zn^{2+} (ionic radius = 0.074 nm) have almost the same ionic radii [12], and have the same valency. Therefore, Zn^{2+} can occupy the two different sites of Mg^{2+} with ease. In addition, Tb^{3+} (ionic radius = 0.106 nm), and Eu^{3+} (ionic radius = 0.109 nm) ions can replace cations Al^{3+} (ionic radius = 0.053 A^{o}) and/or Mg^{2+}, and/or Zn^{2+} [12], or they can stay on the surface of the host lattice, the latter possibility is more appropriate because the ionic radii of the dopants are larger than those of the cations [13]. Figure 2 presents the XRD patterns of $Zn_{0.3}Mg_{0.7}Al_2O_4$:Tb^{3+} 0.6 mol%,Eu^{3+} 0.4 mol%. The pattern is consistent with the standard cubic structure of $MgAl_2O_4$ referenced in JCPDS file No. 75-1796. This indicates that, a pure single phase spinel cubic structure of $Zn_{0.3}Mg_{0.7}Al_2O_4$:Tb^{3+},Eu^{3+} was crystallized. This is due to the fact that both $MgAl_2O_4$ and $ZnAl_2O_4$ have the same cubic spinel structure, and have the same diffraction peaks. The average particle size estimated using the Debye-Scherrer formula was ~22 nm. The lattice parameters of $Zng_{0.3}Mg_{0.7}Al_2O_4$:Tb^{3+},Eu^{3+} were calculated, and are given in table 1, and they compare very well with the standard parameters referenced in JCPDS file No. 75-1796.

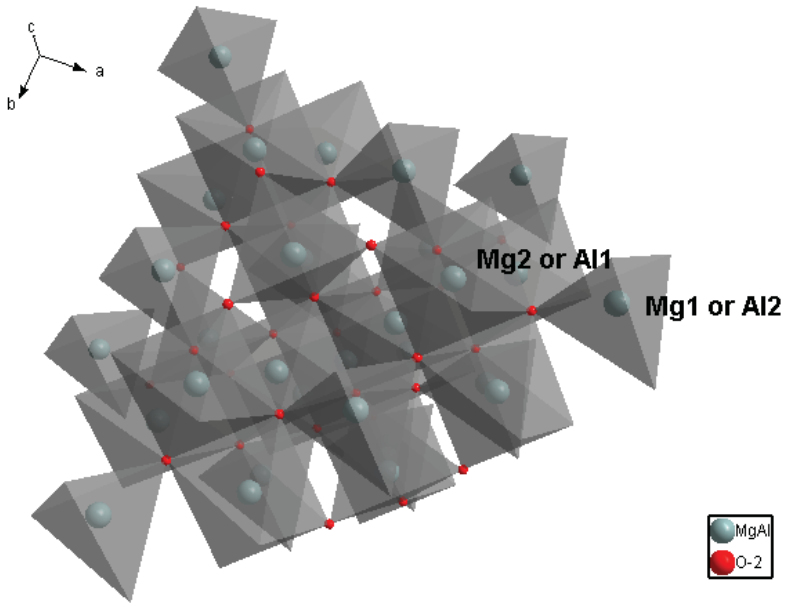

Figure 1. The connection of network of atoms in $MgAl_2O_4$ [11].

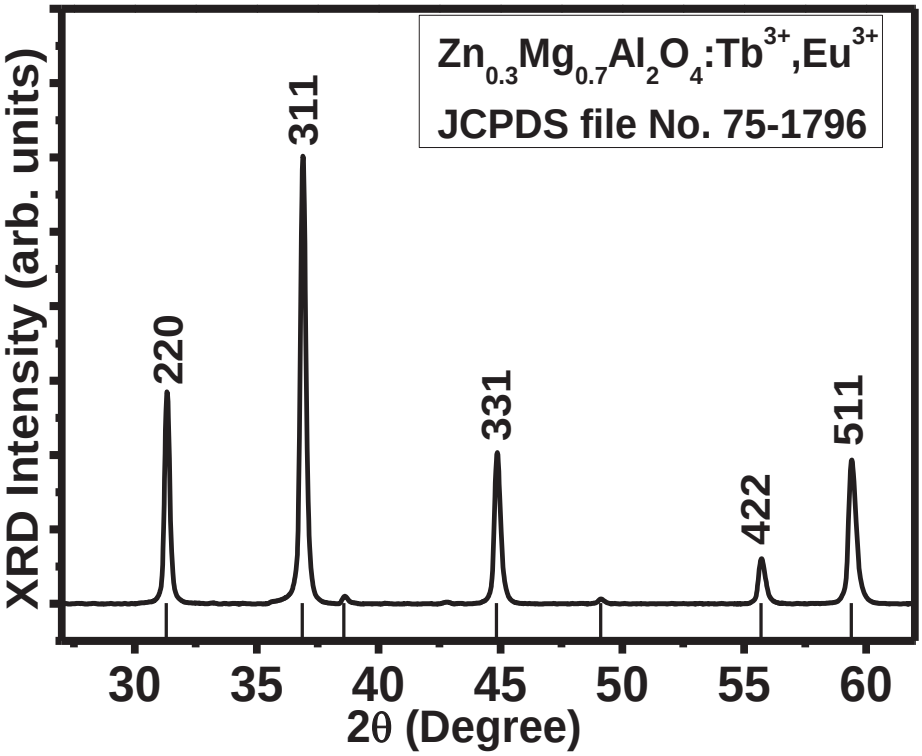

Figure 2. XRD patterns of $Zn_{0.3}Mg_{0.7}Al_2O_4:Tb^{3+},Eu^{3+}$.

Table 1. Lattice parameters of $Zn_{0.3}Mg_{0.7}Al_2O_4:Tb^{3+},Eu^{3+}$.

	Lattice constants			Angles		
	a	b	c	α	Γ	β
$Zn_{0.3}Mg_{0.7}Al_2O_4:Tb^{3+},Eu^{3+}$.	8.07A^o	8.07A^o	8.07A^o	90^o	90^o	90^o
JCPDS file No. 75-1796.	8.70A^o	8.70A^o	8.70A^o	90^o	90^o	90^o

3.2. Morphology study

The particle morphology of the $Zn_{0.3}Mg_{0.7}Al_2O_4:Tb^{3+},Eu^{3+}$ powders are shown in figure 3. The well-known semicontinuous folded dense platelet like morphology was observed, and there were also voids resulting from evolution, and escape of large amount of gases during the combustion process. Notice that the platelets were encrusted with smaller spherical particles.

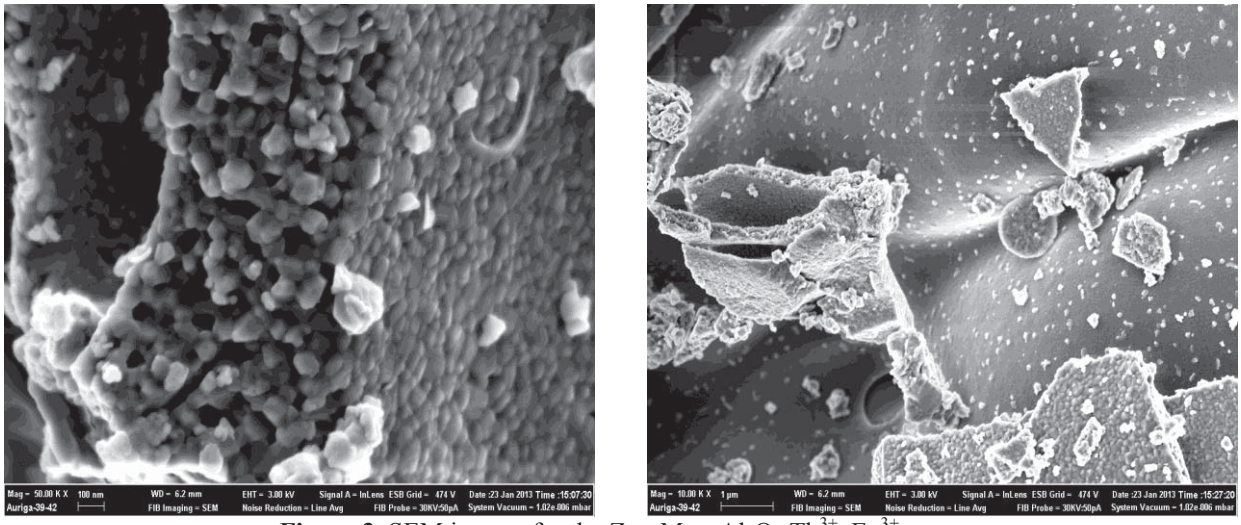

Figure 3. SEM images for the $Zn_{0.3}Mg_{0.7}Al_2O_4:Tb^{3+},Eu^{3+}$.

3.3. Cathodoluminescence study.

Figure 4 shows the cathodoluminescence (CL) emission spectrum of the $Zn_{0.3}Mg_{0.7}Al_2O_4:Tb^{3+},Eu^{3+}$ recorded when the phosphor was bombarded with low-voltage electron beam at 2 kV. As shown in figure 4, the CL spectrum consists of blue, green, and red emission arising from Tb^{3+} and Eu^{3+} transitions. The blue emissions at 381, 418, and 438 nm are ascribed to $^5D_3 \rightarrow {}^7F_J$ (J=6,5,4,3,2,1, and 0) transition of Tb^{3+}, green emission at 473, 491, and 547 nm are attributed to $^5D_4 \rightarrow {}^7F_J$ (J=6,5,4,3,2,1, and 0) transition of Tb^{3+} [14], and red emissions at 594, 619, 655, and 705 nm are ascribed to $^5D_0 \rightarrow {}^7F_J$ (J=0,1,2,3,4,5, and 6) transition of Eu^{3+} [14]. Among the Eu^{3+} transitions, the most intense emission peak at 619 nm, corresponding to $^5D_0 \rightarrow {}^7F_2$, usually occurs through the electric dipole transition (EDT), while the $^5D_0 \rightarrow {}^7F_1$ band at 594 nm is the magnetic dipole transition (MDT) [13]. The intensity of this transition increased with decreasing local symmetry of the Eu^{3+} ion [15]. The CL emission spectra of $Zn_{0.3}Mg_{0.7}Al_2O_4:Tb^{3+},Eu^{3+}$ suggest that there is no energy transfer between Tb^{3+} and Eu^{3+} since the blue, green and red emissions occurred simultaneously. Figure 5 shows the calculated CIE-1931 chromaticity coordinates diagram of white emissions from $Zn_{0.3}Mg_{0.7}Al_2O_4:Tb^{3+},Eu^{3+}$ obtained by CL excitation. The chromaticity coordinates of the white light are x = 0.342, y = 0.323, and are very close to the chromaticity coordinates of standard white light (x = 0.333, y = 0.333) [16].

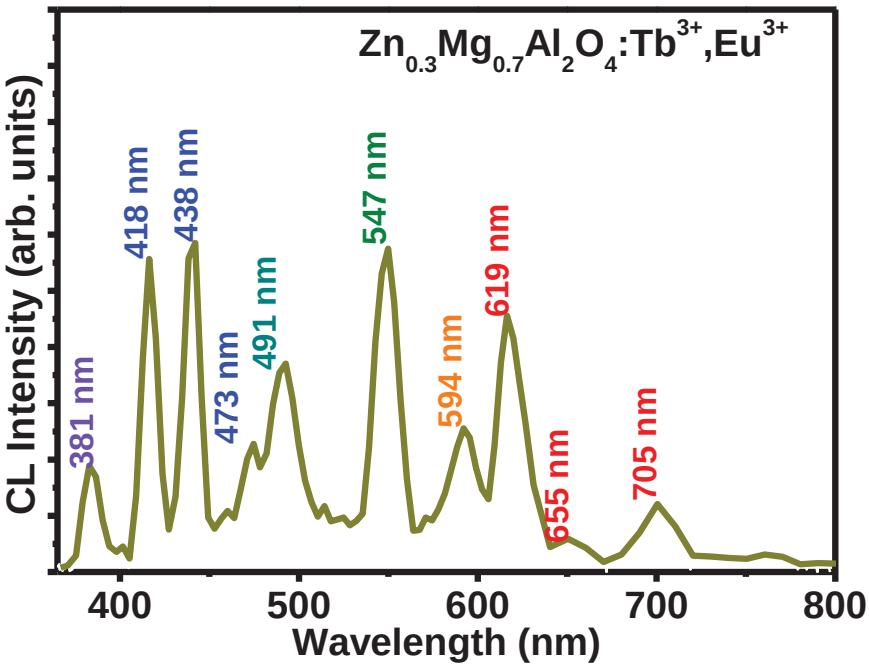

Figure 4. CL emission spectra of $Zn_{0.3}Mg_{0.7}Al_2O_4:Tb^{3+},Eu^{3+}$.

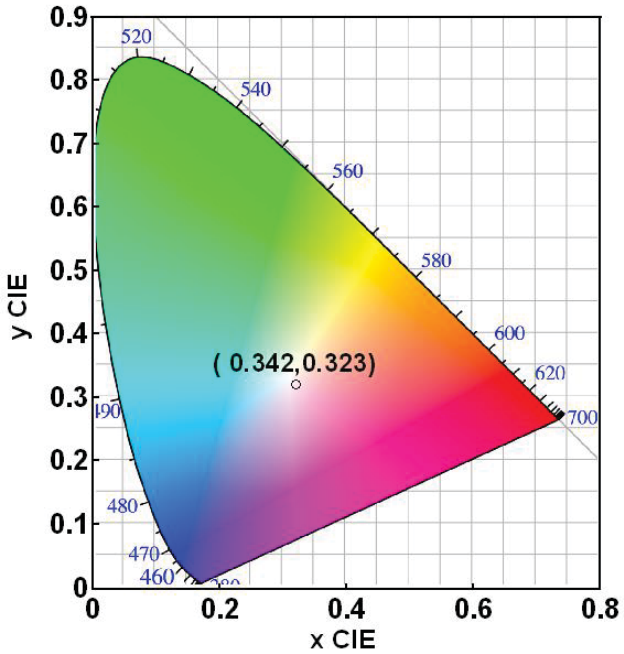

Figure 5. The CIE diagram showing coordinates of $Zn_{0.3}Mg_{0.7}Al_2O_4$: Tb^{3+},Eu^{3+}.

4. Conclusion

White cathodoluminescence was observed from $Zn_{0.3}Mg_{0.7}Al_2O_4:Tb^{3+},Eu^{3+}$. The structure resembles a single phase cubic structure referenced in JCPDS file No. 75-1796. The white generated light was the result of the combination of blue and green narrow line emission from Tb^{3+} and the red emission from Eu^{3+}. This phosphor holds good prospects for application in solid state lighting.

Acknowledgement
The authors would like to acknowledge the financial support from the cluster funds of the University of the Free State, the South African National Research Foundation (NRF), the South African National Laser centre (NLC), and the South African Research Chairs Initiative of the Department of Science and Technology and National Research Foundation of South Africa.

References

[1] Song Y H, Jia G, Yang M, Huang Y J, Youand H P and Zhang H 2009 *J Appl Phys. Lett.* **94** 091902
[2] Mothudi B M, Ntwaeaborwa O M, Pitale S S and Swart H C 2010 *J Alloys Compd.* **508** 262
[3] Shaat S K K, Swart H C and Ntwaeaborwa O M 2012 *Opt. Mater. Express* **7** 962
[4] Hernandez-Perez C D, Garcıa-Hipolito M, Alvarez-Perez M A, Alvarez-Fregoso O, Ramos-Brito F and Falcony C 2010 *Phys. Status Solidi* A **207** 417
[5] Miron I, Enache C, Vasile M and Grozescu I 2012 *Phys. Scr.* **T149** 014064
[6] Zawrah M F, Hamaad H and Meky S 2007 *Ceramics International* **33** 969
[7] Wiglusz R J, Grzyb T, Lis S and Strek W 2010 *J Lumin* **130** 434
[8] Sanjeev M, Bhushan D, Alagu R E, Morea S P, Gundu T K and Khera R K 2008 *J Lumin* **128** 1673
[9] Nakagawaa H, Ebisua K, Zhanga M and Kitaura M 2003 *J Lumin* **102** 590
[10] Yutaka F, Hiroaki T, Kazuhiro I, Shigetomo Y, Shiori M, Masanobu S, Kouichirou T, Yutaka K and Eiichi H 2008 *J Lumin* **128** 282
[11] Diamond, Version 3.0d, 1997–2005 Copyright© Crystal Impact GbR, Bonn, Germany
[12] Magnesium, [online], Available from http://www.webelements.com/magnesium/ [Accessed at 22 Feb 2013]
[13] Xiang Y C and Chao M 2010 *Optical Materials* **32** 415.
[14] Dongling G, Guogang L, Mengmeng S, Chong P, Yang Z, Ziyong C and Jun L 2012 *Dalton Trans*. **41** 3078
[15] Yufeng C, Songhua Z, Fei L, Fan L and Yiwang C 2011 *J Lumin* **131** 701
[16] Fan S, Yu C, He D, Wang X and Hu L 2012 Opt. Mater. Express **2(6)** 765

Characterization of epitaxial Cr thin films

CJ Sheppard[1], ARE Prinsloo[1], PR Fernando[1], ZP Mudau[1], AM Venter[2] and EE Fullerton[3]

[1]Department of Physics, University of Johannesburg, PO Box 524, Auckland Park, 2006
[2]Research and Development Division, Necsa Limited, P.O. Box 582, Pretoria 0001, South Africa
[3]Center for Magnetic Recording Research, University of California, San Diego, 9500 Gilman Dr., La Jolla, CA 92093-0401, USA

Author e-mail address: alettap@uj.ac.za

Abstract. Thin films and heterostructures of Cr and Cr alloys show fascinating properties that is not observed in the bulk material and research into their magnetic properties gives insight into dimensionality effects in these materials. This paper reports on the characterization of Cr thin films on MgO(100), MgO(110) and fused silica substrates, of thicknesses 20nm to 320nm. X-ray diffraction (XRD) results showed good epitaxial growth for films prepared on the single-crystalline MgO substrates, with Cr(002) and Cr(211), whilst those prepared on the polycrystalline fused silica were polycrystalline. The mosaicity and coherence length were determined from the XRD results. Standard four-point probe measurements were performed to obtain the resistance (R) of the films as function of temperature (T) the anomaly in the $\rho(T)$ curves was used to determine the Néel temperature (T_N). T_N versus thickness (t) graphs for the various substrates show the behaviour expected for the samples prepared on MgO(110) and fused silica substrates, but rather unique behaviour is seen in this curve for samples prepared on MgO(100). This might be attributed to internal strain effects in these thin films.

1. Introduction

Cr and Cr alloy systems exhibit a large variety of antiferromagnetic properties and constitute a class of systems that undergoes magnetic phase transitions associated with the extent of nesting between the hole and conduction bands of the Fermi surface [1, 2]. The interest in the properties of these materials originates from their spin-density-wave (SDW) state which is directly linked to the nested Fermi surface and which contributes to nearly all the magnetic properties of Cr [1, 2].

Bulk Cr is an itinerant antiferromagnet that forms an incommensurate (I) SDW below its Néel temperature (T_N) of 311 K. The ISDW is characterized by a temperature dependent wave-vector **Q** determined by the nesting of the Fermi surface along the ⟨001⟩-directions [2]. The ISDW period varies from 78 Å at T_N to 60 Å at 10 K. This bulk behaviour is easily perturbed by strain or impurities that can alter T_N, the spin directions, the ISDW period, or drive the magnetic order to be commensurate with the lattice, resulting in a commensurate (C) SDW phase [1, 2]. In view of this, previous research in this field therefore suggests that once the fundamental role of the SDW in the properties in these materials is understood, the alloy can be tailored to give physical properties that can be useful in practical applications [1, 3].

Taking this into consideration, significant research interest exits in the physical properties of dilute Cr alloys, specifically in their role as spacer layers in magnetic multilayer thin film structures [3-7]. Results obtained have revealed fascinating properties not previously observed in bulk materials, including giant magnetoresistance [3-8]. Since specific magnetic properties can be tailored and designed in artificially structured materials this makes them useful for practical applications. The magnetic ordering of Cr near surfaces, or in thin layers have also rendered interesting fundamental problems [3-7]. Thus the study of SDW effects of Cr and its alloys when confined in thin films and multilayer structures provides a fascinating experimental test bed and such studies will contribute valuable information on dimensionality effects on the behaviour of Cr and Cr alloys.

This project is aiming to link the magnetic properties of Cr and Cr alloy thin films with stress and strain in these films, this paper reports on the magnetic properties of epitaxial and polycrystalline Cr thin films.

2. Experimental

The Cr films were prepared using DC magnetron sputtering at 800°C from an elemental source onto single-crystal MgO(100), MgO(110) and polycrystalline fused silica substrates. This renders epitaxial and polycrystalline Cr thin films, respectively. Films were prepared in a thickness series with thickness (t) varying between 20 and 320 nm. Each film structure was characterized using X-ray diffraction (XRD) techniques. Electrical resistance measurements, using standard DC four-probe methods, were employed to determine the Néel transition temperatures (T_N) for these films.

3. Results

Figures 1(a), (b) and (c) show representative XRD results for the Cr thin films prepared on MgO(100) with t = 40 nm, MgO(110) with t = 40 nm and polycrystalline fused silica substrates with t = 320 nm, respectively. The results indicate that the samples prepared on the MgO(100) and MgO(110) are indeed epitaxial exhibiting a single crystallographic orientation, with the Cr layers showing preferred growth directions of (100) and (211), as is indicated in figure 1(a) and (b). Samples prepared on polycrystalline fused silica substrates did not deposit with preferred growth orientation, but show a polycrystalline crystalline structure, as is seen in figure 1(c).

XRD results from the thin films prepared on MgO(100) and MgO(110) substrates enabled determination of the lattice parameters, the coherence length (length scales over which the films are structurally coherent [9] along the growth direction, analyzed from the full-width at half-maximum (FWHM) of the Bragg peaks in conjunction with the Debye-Scherrer formula after removing the instrumental resolution) and the mosaic spread obtained from the FWHM of the rocking curves [9]. Assessment of the results summarized in Table 1 reveals that for the films on the MgO(100) the mosaicity decreases and the coherence length increases slightly with thickness. Samples prepared on the MgO(110) show no clear general trend in the mosaicity though the coherence length increase slightly as function of Cr thickness. This indicates a general trend of improved crystallite alignment with film thickness [7, 9]. It is also noted that for the 320 nm Cr samples on both the MgO(100) and MgO(110) substrates, the mosaicity and coherence length have weaker correlation compared to the 160 nm thick film.

The Néel temperatures (T_N) of the films were determined from anomalies observed in electrical resistance (R) measurements as a function of temperature (T). Representative examples of measured R – T curves are shown in figures 2(a), (c) and (d) for films with t = 160 nm on the MgO(100) substrate, t = 40 nm on MgO(110) and t = 80 nm on polycrystalline fused silica, respectively. Anomalies in the form of humps are observed in the R – T curves of the samples prepared on the MgO(100) and MgO(110) substrates. This behaviour is associated with the formation of the SDW on entering the antiferromagnetic phase on cooling through the Néel temperature (T_N) [1]. The sudden increase in resistivity on cooling through T_N finds its origin in the nesting of electron and hole Fermi surfaces [1].

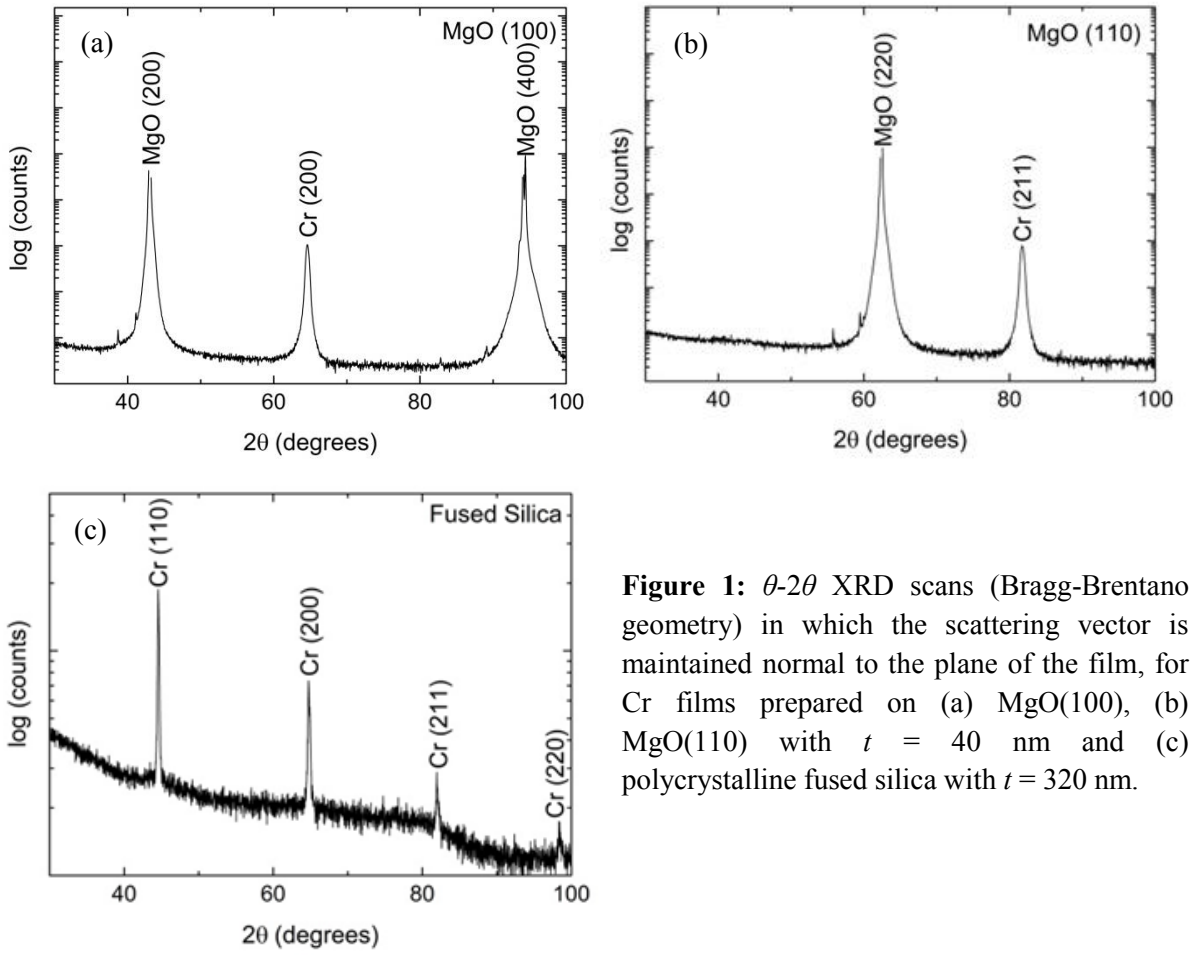

Figure 1: θ-2θ XRD scans (Bragg-Brentano geometry) in which the scattering vector is maintained normal to the plane of the film, for Cr films prepared on (a) MgO(100), (b) MgO(110) with t = 40 nm and (c) polycrystalline fused silica with t = 320 nm.

	MgO(100)				MgO(110)			
t **(nm)**	***a*** **(Å)**	**FWHM (200)**	T_{coh} **(nm)**	**Mosaic (200)**	***a*** **(Å)**	**FWHM (211)**	T_{coh} **(nm)**	**Mosaic (211)**
20	2.890	1.71°	11	1.71°				
40	2.886	0.79°	21	0.80°	2.885	0.58°	19	0.58°
80	2.886	0.81°	20	0.82°	2.890	0.84°	18	0.84°
160	2.886	0.40°	26	0.40°	2.890	0.34°	34	0.34°
320	2.888	0.50°	25	0.51°	2.889	0.57°	22	0.57°

Table 1: The measured out-of-plane full-width at half-maximum (FWHM) XRD parameters of the selected Bragg peak and the mosaic spread of this peak, for epitaxial Cr films of thickness t prepared at 800°C on MgO(100) and MgO(110) substrates, respectively. The coherence length, T_{coh}, was calculated using the Debye-Scherrer equation after removing the resolution of the instrument.

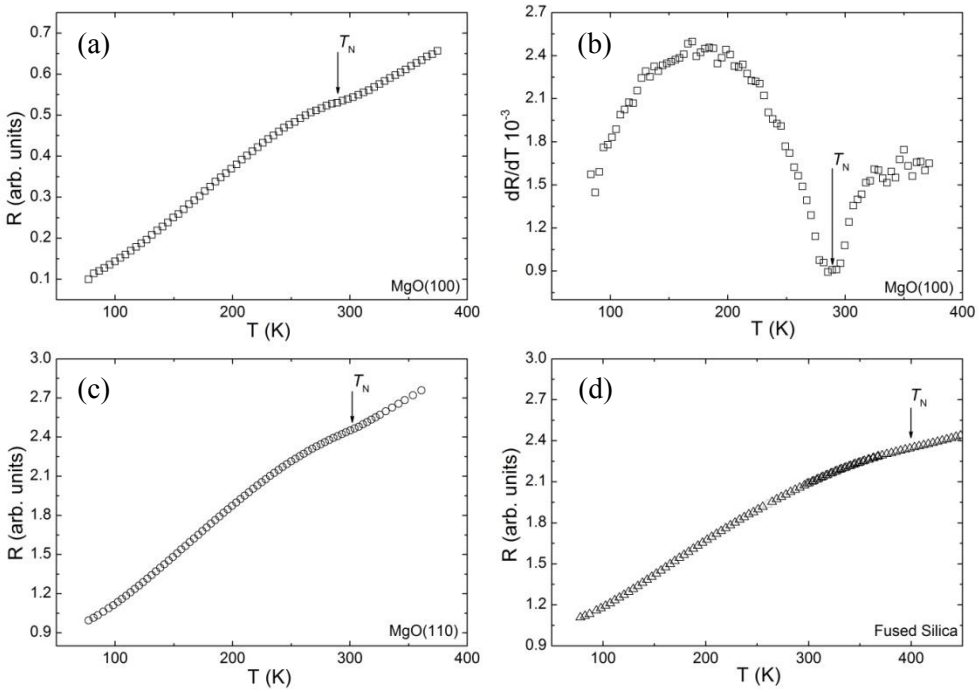

Figure 2: Resistance (R) versus temperature (T) graphs for Cr thin films prepared on the substrates: (a) MgO(100) with t = 160 nm measured along [100], (c) MgO(110) with t = 40 nm and (d) polycrystalline fused silica with t = 80 nm. Figure (b) shows dR/dT versus T for the sample prepared on the MgO(100) with t = 160 nm. The temperature associated with the minimum in the dR/dT versus T curves was taken as the Néel temperature (T_N) as indicated by the arrows in all the curves.

This leads to a reduction in the number of charge carriers available for conduction resulting in an increase in resistivity just below T_N [1]. In general the samples prepared on the quartz shows much weaker anomalies at T_N, as is evident from the example shown in figure 2(d). This is attributed to the higher disorder that exists in these structures with them not being epitaxial [7].

The Néel temperature for Cr alloys can be defined either as the temperature of the minimum in $R(T)$ accompanying the magnetic phase transition, or the inflection point in $R(T)$ curve [1]. As the anomalies associated with the magnetic transitions in these samples were relatively weak, it was decided to refer to the second definition and T_N was determined by considering the dR/dT versus T curves and T_N taken as the temperature associated with the minima on these curves. This is one of the accepted methods generally used for the determination of T_N in Cr based thin films [9]. An example of this is shown in the figure 2(b) for the t = 160 nm sample on MgO(100). It should however be mentioned that extrinsic morphology contributions that dramatically change the resistance, may bias obtained T_N values to some extend [8].

The variation in T_N as function of layer thickness, t, in the Cr thickness series is shown in figure 3 for the three substrates used. For the epitaxial films prepared on MgO(100), shown in figure 3(a), we observe an initial sharp decrease in T_N starting at a value of 320 K for the thinnest sample, to level off at a value of approximately 285 K for a sample of thickness 320 nm. Comparison with the literature

reveals contrasting behaviours. Considering the resistivity versus temperature data of Kummamuru *et al.* [7] (see their figure 1(c)) for their Cr thickness series, also prepared on MgO(100), with 17.5 nm ≤ t ≤ 350 nm, the values for T_N value also decreased with increasing thickness, whereas Mattson *et al.*[9] observed T_N to increase from approximately 230 K approaching the bulk value at a thickness of approximately 300 nm.

For the epitaxial films prepared on MgO(110), a general increase in T_N approaching the bulk value for Cr is observed for increased thickness, as reported by [4, 9]. For this series the values for T_N is generally lower than that observed for layers prepared on MgO(100), starting at $T_N \approx 230$ K for the thinnest sample, reaching a maximum value of 298 K at t = 80 nm, where after T_N tends to level off at approximately 270 K for $t \geq 160$ nm.

The T_N values obtained for the polycrystalline Cr thin films, deposited on the fused silica substrates are much higher compared to the epitaxial Cr films on MgO(100) and MgO(110) substrates, with $T_N \approx$ 360 K for the samples with $t < 80$ nm and increasing to $T_N \approx 460$ K for the sample with t = 320 nm. This behaviour corresponds to that observed in Cr-Ru thin films prepared on polycrystalline fused silica [8]. The high T_N for t = 320 nm is unexpected and cannot be explained. However, as was pointed out by Prinsloo *et al.* [8], it incidentally corresponds with T_N = 475 K for the CSDW-P Néel transition induced in bulk Cr through stresses associated with cold working [2].

Previous studies [10] on polycrystalline Cr films, grown on Corning glass substrates, also showed significant increases in T_N values by up to 60 K above the observed bulk value of 311 K [1] for samples with $t \leq 30$ nm. This was ascribed to tensile stresses in the films that arose, in part, from the grain boundaries [11, 12]. It is then possible that the polycrystalline films with a high density of grain boundaries may behave like a cold-worked sample, resulting in a high temperature CSDW-P transition for the Cr film on fused silica [12], whereas the epitaxial films will have different internal stresses [8].

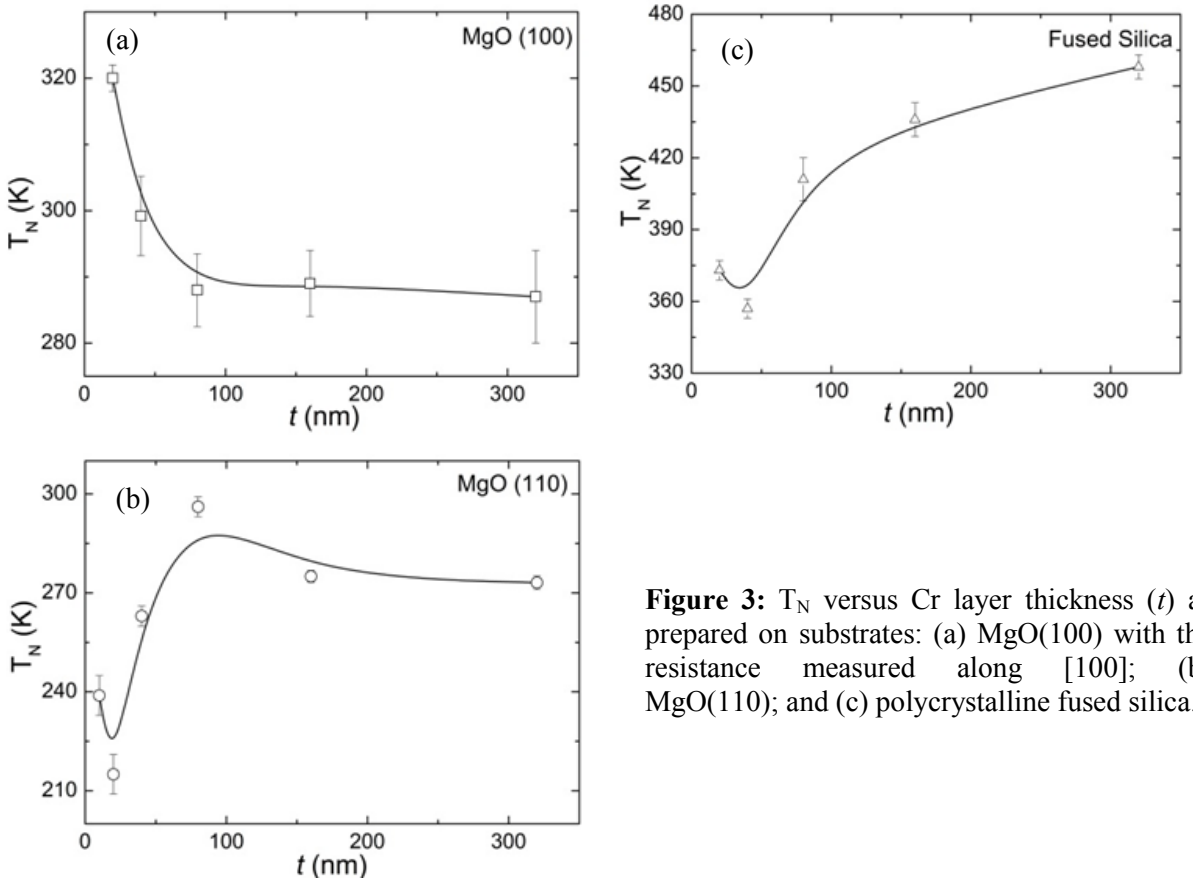

Figure 3: T_N versus Cr layer thickness (t) as prepared on substrates: (a) MgO(100) with the resistance measured along [100]; (b) MgO(110); and (c) polycrystalline fused silica.

4. Conclusions

The XRD characterization of Cr thin films prepared on MgO(100), MgO(110) and fused silica substrates, with thicknesses 20 nm to 320 nm, was used to determine the mosaicity and coherence length (along the growth direction) of the thin films. The results in general indicate a slight improvement in the layer quality with increase in sample thickness. T_N versus t graphs for the various substrates show an increase in magnetic transition temperature values with increase in thickness for the samples prepared on MgO(110) and fused silica substrates, whereas the opposite is observed for the MgO(100) samples. The relatively high T_N values obtained for the polycrystalline samples might be attributed to the presence of internal tensile stresses in the films that arise, in part, from the grain boundaries [11, 12].

The differences in the $T_N - t$ behaviour of the epitaxial films prepared on the MgO(100) and MgO(110) substrates, as well as the high T_N values obtained for the polycrystalline samples warrants further investigation. As an extension of the present study, stress and strain analyses on these samples are planned to gain insight into these characteristics.

Acknowledgements

Financial support from the SA NRF (Grant Nos. 80928 and 80631) is acknowledged.

References

[1] Fawcett E, Alberts HL, Galkin VY, Noakes DR and Yakhmi JV 1994 *Rev. Mod. Phys.* **66** 25
[2] Fawcett E 1988 *Rev. Mod. Phys.* **60** 209
[3] Zabel H 1999 *J. Phys. Condens. Matter* **11** 9303
[4] Pierce DT, Unguris J, Celotta RJ and Stiles MD 1999 *J. Magn. Magn. Mater.* **200** 209
[5] Fishman RS 2001 *J. Phys. Condens. Matter* **13** R235
[6] Fullerton EE, Robertson JL, Prinsloo ARE, Alberts HL and Bader SD 2003 *Phys. Rev. Lett.* **91**(23) 237201
[7] Kummamuru RK and Soh YA 2008 *Nature* **452** 859
[8] Prinsloo ARE, Derrett HA, Hellwig O, Fullerton EE, Alberts HL and Van den Berg N 2010 *J. Magn. Magn. Mat.* **322** 1126
[9] Mattson JE, Fullerton EE, Sowers CH and Bader SD 1995 *J. Vac. Sci. Technol. A* **13**(2) 276
[10] Lourens JAJ, Arajs S, Helbig HF, Cherlet L and Mehanna EA 1988 *J. Appl. Phys.* **63**(8) 4282
[11] Windischmann H 1992 *Crit. Rev. in Solid State and Mat. Sci.* **17** 547
[12] Boekelheide Z, Helgren E and Hellman F 2007 *Phys. Rev. B* **76** 224429

Spectrally selective doped zinc and aluminium oxide thin films prepared by spray pyrolysis for solar energy applications

P C Simpemba[1,2], K Chinyama[1],J Simfukwe[1] and N R Mlyuka[3]

[1]The Copperbelt University, School of Mathematics and Natural Sciences, Department of Physics, P.O. Box 21692, 10101 Kitwe, Zambia.
[2]School of Physics, University of Witwatersrand, Private Bag 3, Wits, 2050, South Africa.
[3]The University of Dar es Salaam, Faculty of Sciences, Physics Department, P. O. Box 35063,Dar es Salaam, Tanzania.

E-mail: pcs200800@gmail.com

Abstract. Metal oxide thin films have been used in thin film solar cells and other solar energy applications for many years. The concern has been to improve their physical, electrical and optical properties in order to increase their efficiency and lower their production costs. Zinc oxide doped with aluminium (ZnO:Al) and aluminium oxide doped with zinc (Al_2O_3:Zn) thin films have been produced by a spray pyrolysis process onto standard microscope glass slides at different substrate temperatures and for different solution concentrations, spray times and pressure. The main objective was to produce single, double and triple layer thin films and characterized them for their optical, electrical and structural properties. The spectral selectiveness of these oxide thin films and their applicability in producing efficient solar cells has been investigated. Optical measurements have been performed in spectrophotometers in the visible-to-near infrared (NIR-VIS) and infrared (IR) ranges. Structural characterization has been performed using an Atomic Force Microscope and a Tencor Alpha Step IQ Profiler. A four-point resistance square probe was used for electrical characterization. The transmittance, reflectance, thickness and the film resistance have been experimentally obtained. The solar transmittance of 88 % has been achieved for Al-doped zinc oxide (ZnO:Al) films whereas 71.94 % has been obtained for Zn-doped aluminium oxide (Al_2O_3:Zn). The film thicknesses fall in the range 0.14 μm to 87.7 μm. The wavelength-dependent refractive index of the films has been evaluated from reflectance and transmittance measurements. The refractive indices ranged from 1.28 to 2.0 for the probed wavelength range. The properties of these thin films have been modelled using the Bruggemann and Maxwell-Garnett effective medium theories. The film resistivity values of 2.43 x $10^{-4}\,\Omega$ m to11.80 x $10^{-4}\,\Omega$ m have been achieved. These film properties have been related to applications in thin film solar cells.

Key words: spectrally selective, spray pyrolysis, thin film, characterization.

1. Introduction

The utilization of solar technologies requires the development of materials that can be used to make this source of energy cheap and reliable. One such need involves the development of transparent conducting solid thin films that are spectrally selective. Spectral selectiveness is an important property in solar cells because the spectrum of interest for this application is restricted to the visible and near

infrared regions and so the unwanted wavelength regions must be selectively rejected. This research focuses on producing mutually doped transparent conducting thin films of zinc and aluminium oxides which are characterized and modelled for efficient solar energy applications in thin film solar cells and other solar energy systems. Thin film solar cells are a good choice in terms of the device design and fabrication process and offer an interesting alternative to p-n junction silicon based photovoltaic devices. The choice of zinc and aluminium oxides was based on the fact that they are readily available and can be obtained cheaply as opposed to the previously used indium tin oxide which is expensive and rarely available [1, 2].

A thin film solar cell is comprised of several layers of different thin film materials. It is typical that a cell is made up of a substrate, a transparent conducting oxide (TCO), a window layer, an absorber layer and a metal contact layer all of which have different physical, chemical, optical and electronic properties. Individual properties of the cell components each affect the overall performance of the cell. With this in mind, it is important to understand the behaviour of these solar cell components. Transparent conducting oxides (TCOs) are generally n-type semiconductor metal oxides which exhibit high transmittance of the visible (VIS) and near infrared (NIR) radiation and have high conductivity for efficient charge carrier transport when used as thin film electrodes or contacts in solar cells. It is important that TCOs have high transparency in the solar region and high electrical conductivity because enough light must be allowed to pass through them onto the absorbing layer

2. The Experimental Methodology

Zinc chloride ($ZnCl_2$) doped with a trace of aluminium chloride hexahydrate ($AlCl_3.6H_2O$) were dissolved in distilled water, forming aqueous solutions of different concentrations and doping levels. A little hydrochloric acid was added to the solution to prevent precipitation to hydroxide. In a similar manner, $AlCl_3.6H_2O$ aqueous solutions doped with zinc were prepared. A locally constructed pneumatic spray pyrolysis set up was used to prepare the oxide coatings. The process starts with production of small droplets of the precursor solution in the atomizer by way of a carrier gas pumped from a gas cylinder at controlled pressure by a system of pressure gauges. These droplets of the spray solution are transported by the carrier gas through a diffusion tube into the reaction chamber and onto a heated substrate where they immediately evaporate leaving a solid thin film [3]. In this particular setup the carrier gas used was nitrogen (N_2).

Prior to spraying, the substrates were cleaned in acetone and dried. Different films were obtained for different spray parameters. Optimization of film properties was achieved by varying substrate temperature, solution concentration, carrier gas pressure, doping levels, and spray times and multi-laying of films. Optical characterization in the ultraviolet, visible and infrared (UV/VIS/IR) were conducted using the Perkin Elmer Lambda 19 spectrophotometer and Perkin Elmer Spectrum BX FT-IR system. Electrical characterization was conducted using a four-point resistance probe whereas the surface and thickness characterization were done using an atomic force microscope and a Tencor Alpha Step profiler respectively.

3. Results and discussion

The temperature in the oven and that of the substrate were monitored with a calibrated chromium-nickel thermocouple.

3.1 Film thickness

The thickness of a thin film depends much on the growth parameters and conditions. Different thicknesses were obtained for films grown using different growth parameters such as spray time, pressure, concentration of precursor solution and to some extent, substrate temperature. It was observed that more concentrated solutions gave thicker films as compared to less concentrated ones under the same conditions.

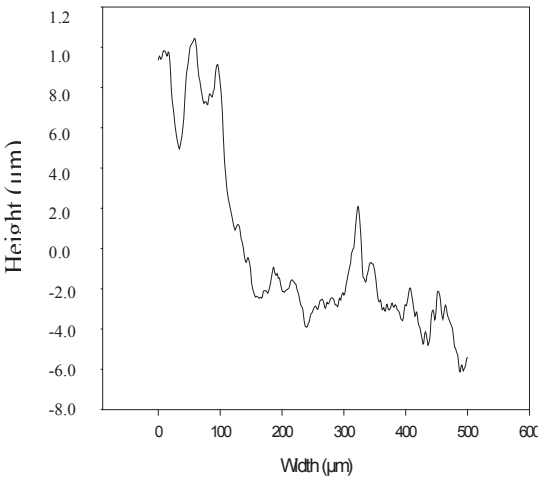

Figure 1. Thickness profile of single layer ZnO thin film.

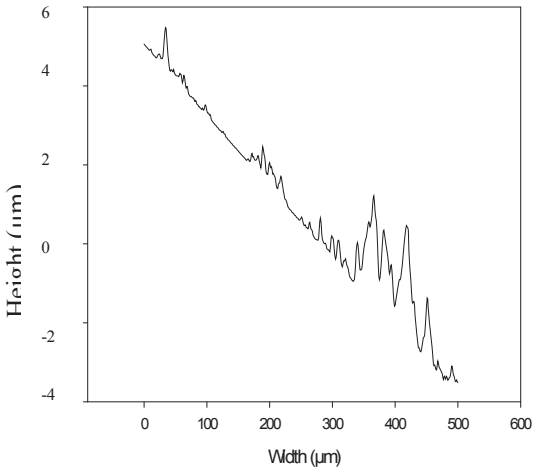

Figure 2. Thickness profile double layer aluminium oxide thin film.

The interesting result was that the edges of the thin film resulting from spray pyrolysis tend not to give a step ending but rather steadily reduce in height from the top to the surface of the substrate as seen from figure 1 and figure 2. In the two figures above, the vertical represents the thickness of the thin film whereas the horizontal represents the width of the profiled film section. In spray pyrolysis process, you obtain non-distinct edges but rather a steady decrease in thickness towards the edge. Thicknesses ranging from 0.14 µm to 87.7 µm have been achieved in this research. It has been noted that time of spray had the greatest influence on the thickness of the resulting coating film.

3.2 Transmittance and reflectance

A UV transmittance cut-off appears to take effect at wavelength near 325 nm. This coincides with a UV transmittance cut-off for a pure clean glass substrate. Similarly, infrared attenuation was observed at wavelength 2700 nm and at 4100 nm where the transmittance falls steadily to zero. Figure 4 compares the cut-off transmittance for the uncoated substrate and two substrates coated with ZnO and Al_2O_3. It was generally observed that ZnO films allow more of the incidence beam to be transmitted as compared to the aluminium films, transmitting nearly as much as the uncoated substrate. The highest transmittance was achieved for ZnO doped with aluminium. The average solar transmittance was 88.03 % for ZnO and 71.94 % for Al_2O_3.

The achieved transmittance of 88.02 per cent for ZnO films grown using spray pyrolysis method means that the thin films are suitable for use as window layers for heterojunction solar cells. It means that more light is admitted to improve the performance of the solar cell. We suggest that the use of these coatings would improve the efficiency of solar cells sufficiently.

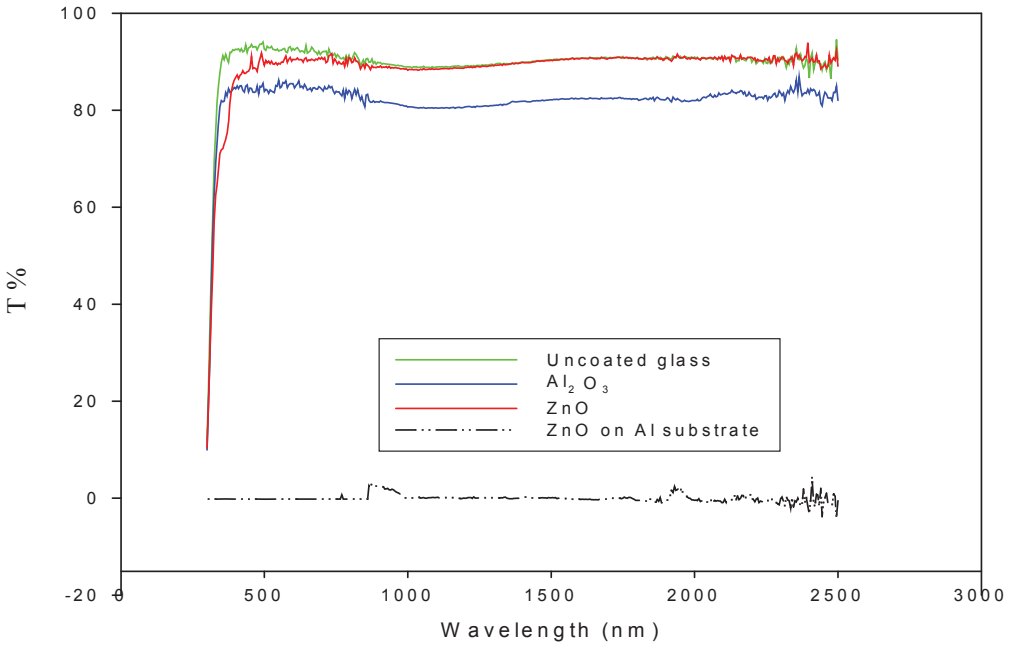

Figure 3. Comparative transmittance curves for aluminium and zinc oxides thin films UV-VIS-NIR grown under same conditions.

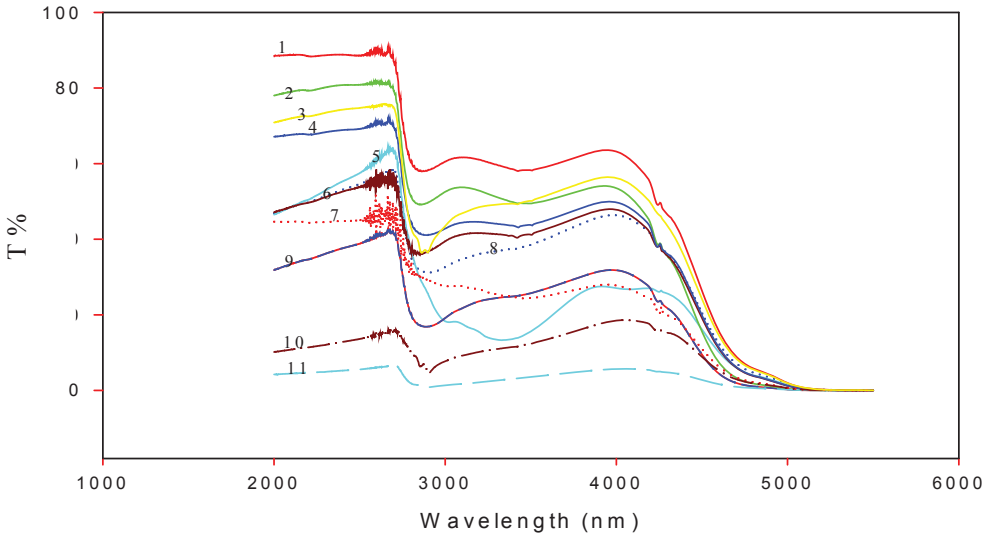

Figure 4. Comparative transmittance curves for aluminium and zinc oxides thin films in NIR region for thin films grown under same conditions.

Figure 5 shows how the transmittance of the different thin film coatings compares in the infrared. The curve labelled 1 is for the uncoated glass substrate, curves 2 to 7 represent the transmittance of the ZnO thin films, giving a trend of reduced transmittance with film thickness. Similarly the curves 8 to 10 represent transmittance curves for Al_2O_3 thin films. The transmittance for ZnO films is higher compared to the Al_2O_3 thin films.

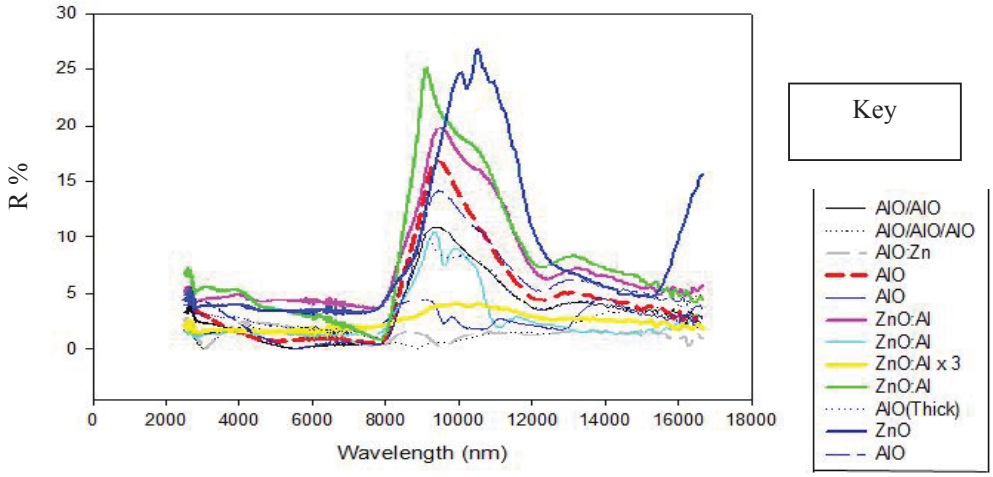

Figure 5. Transmittance curves in the IR region for different ZnO and Al_2O_3 films.

3.3 Surface characterization

The analysis with AFM revealed interesting structures of the film coatings. We present here the features of each of the samples with main emphasis being set on surface roughness, surface cross-section and particle size and distribution. The AFM micrograph presented below reveals the surface structure of the ZnO:Al thin film. The analysis indicated that the mean roughness for this particular coating was 14.11 nm. Figure 7 shows the surface roughness of the thin film and figure 8 is a surface profile of a section from figure 7. We associate the surface roughness to the effect this has on transmittance. It is expected that a rough surface tends to scatter the incident radiation resulting into poor solar energy yield for a solar thin film. The smoothness of the film is improved by coating the substrate with double or more layers.

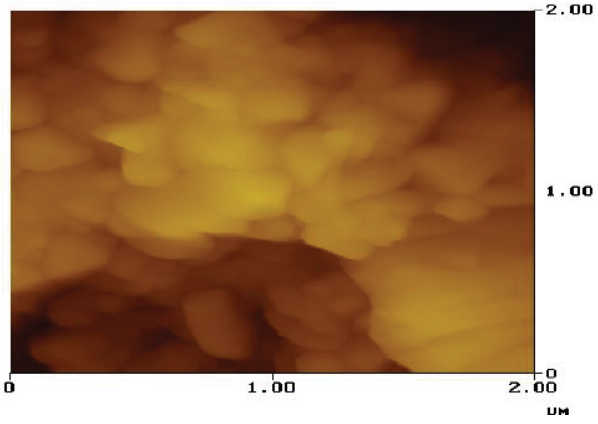

Figure 7. Surface roughness of 3.6 μ m thick ZnO:Al film deposited at 290 ^{o}C.

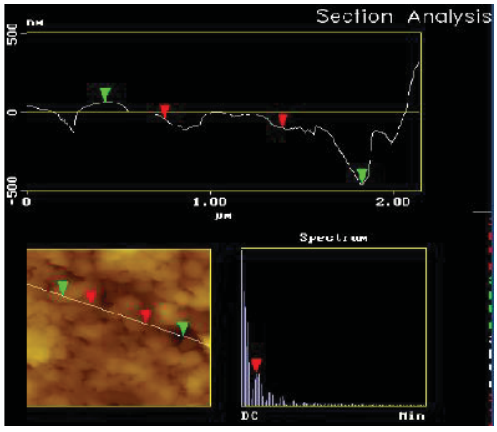

Figure 8. Section analysis of 3.6 μ m thick ZnO:Al film deposited at 290 ^{o}C.

3.4 Modelling the experimental results

This section examines experimentally derived results and uses them into theoretical models that help us to fully understand these properties and how they fit into the theoretical expectations. The average refractive indices for the two wavelength regions were obtained from reflectance equation for normal incidence and presented in table 1.

$$R = (n-1)^2 (n+1)^{-2} \quad (1)$$

Knowing the refractive index of the material is useful in the fabrication of thin film solar cells as this determines the reflectance or transmittance of solar radiation from or into a solar panel in a given wavelength range.

Table 1. Wavelength-dependent refractive indices of selected thin films.

Spectrum	Average refractive index		
	ZnO	ZnO:Al	Al_2O_3
VIS-NIR	1.80	1.96	2.00
FIR	1.28	1.53	1.30

The resistivity of ZnO:Al thin film was on average 0.29 Ωm whereas that for Al_2O_3 was 0.58 Ωm. These values were obtained by applying the theory presented by Hirunlabh [4]. They are on the higher side of most reported values which are of order $10^{-4}\,\Omega$m. Reflectance and transmittance values have been used to calculate the absorption coefficients. The result for doped ZnO with thickness 1.2 μm was 662.6 and the highest value rising to 239 000. The absorption coefficient has an inversely relation to the thickness of the coating but is also greatly influenced by both transmittance and reflectance values. Effective dielectric permeability of the thin films were modelled using the Maxwell-Garnett effective medium theory (MGET) and Bruggemann effective medium theory (BEMT) [5] to yield values in the range 5 to 6.1 for the MGET and 4.4 to 8.5 for the BEMT.

4. Conclusion

This Study has utilized a simple and cheap process of fabricating spectrally selective thin solid films by way of spray pyrolysis process. Process parameters were easy to control with a chance to coat large surfaces. Characterization for solid film parameters was successfully conducted on the samples. Optical and micro-structural properties were determined both experimentally and theoretically. An average solar transmittance of 88 % was obtained for doped zinc oxide and 71.9 % for aluminium oxide films. In the infrared region, reflectance peaks were observed in the wavelength range 8 μm to 13 μm. Maxwell-Garnett and Bruggemann effective medium theories were applied to obtain effective dielectric permeability of the coatings. The Maxwell-Garnett EMT produced dielectric permeability range of 5 to 6.1 and the Bruggemann approximation yielded the permeability range 4.4 to 8.5. These values indicate that doping ZnO with aluminium raises it dielectric permeability and also raises the refractive index.

Acknowledgements

We give special thanks to the Copperbelt University, the International Science Program (Sweden), the University of Zambia and the University of Dar es Salaam.

References

[1] Simpemba P C 2012 MSc. Diss. *University of Zambia*, Lusaka, Zambia.
[2] Chopra K L, Paulson P D and Dutta V 2004 *Prog. Photovolt: Res. Appl*. **12** 69-92.
[3] Perednis D and Gaucker L J, *2005 J. Electroceramics* **14**, 103-11.
[4] Hirunlabh J, Suthateeranet S, Kirtikara K and Pynn R D 1998 *Thamasat Int. J. Sc. and Tech.* **3 2** 10-20.
[5] Berthier S 1994 *J. de Phys. InT. de France*. **4**, 303-18.

Synthesis and Characterization of $CaB_4O_7:Eu^{3+}$ nano-phosphors prepared using Solution - Combustion Method

Sithole TM*, Dejene BF, Koao LF

Department of Physics, University of the Free State (Qwaqwa), Private Bag x 13, Phuthaditjhaba, 9866

sitholetm@qwa.ufs.ac.za

Abstract. Calcium borate ($CaB_4O_7:Eu^{3+}$) phosphors with different Ca:B molar ratio and holding Eu concentration constant have been synthesized by a solution combustion method at initial reaction temperature of 500^0C for 15 minutes. The morphology, structure and luminescence properties of the synthesized nanostructures were investigated using X-ray diffraction (XRD), Scanning Electron Microscopy (SEM) and Photoluminescence (PL) spectroscopy. The XRD spectra of all the as prepared samples show monoclinic phase. SEM micrograph show that the surface aspect are nanorod like for low Ca:B mole ratios but the grains become flake-like as the Ca:B molar ratio increased, giving rise to the increase in particle size resulting from agglomeration. PL results analysis showed that as the excitation wavelength increases the luminescence intensity also increases. The PL excitation spectra display broad spectra with a maximum at around 250 nm and narrow lines at around 396 nm. The PL result also shows that the luminescence intensity of these emission spectra increased with increase in Ca: B molar ratios. The narrow emission lines between 590-688 nm are due to transitions Eu^{3+}.

1. Introduction

In the last two decades, a burst of research activities has been devoted to nanomaterials. It has attracted many works in various fields from material science to biotechnologies and genetics [1–3]. Borates with non-centrosymmetric crystal structure are among the most frequently used nonlinear optical materials [4]. Phosphor nanocrystals are exceptionally promising materials in many fields of technology including photonics, luminescent displays, fluorescent lamps, lasers, cathodoluminescence, and biotechnology [5]. Europium ion (Eu^{3+}) is widely used as a luminescent center in a number of phosphors for the exhibited characteristic red emission mainly corresponding to its $^5D_0 \rightarrow ^7F_2$ transition [6,7]. In the luminescence study of $CaB_4O_7:Eu^{3+}$ nano-phosphors, the Eu^{3+} ion plays an important role as a luminescent probe. Borates doped with trivalent europium ions have excellent efficiencies and appropriate absorption Bands [6]. A great deal of work has been done on Eu^{3+} activation of these hosts [8]. Solution combustion is a well-known method for synthesis of rare earth activated insulating materials at low temperatures (350-500^0C) and very short times (<10 minutes). Wet chemical methods such as sol-gel [9, 10] and polymerized-complex [11] have been used to synthesis CaB_3O_7:Eu red phosphor. Although these methods have more control on size, structure and morphology, conventional solid reaction shows higher luminescence intensity [12]. Combustion synthesis offers many potential advantages over conventional techniques of synthesis, including relatively simple equipment, shorter processing time, lower energy requirement and higher purity [13]. The initial combustion process used the conventional furnace as heating system. This method was accidentally discovered in 1988 in Prof. Patil's lab in India [14].

In this paper, red phosphor $CaB_4O_7:Eu^{3+}$ have been successfully synthesized at 500^0C by combustion reaction. The effects of urea, boric acid and europium concentration on structural, morphology and Luminescence of $CaB_4O_7:Eu^{3+}$ were studied in detail.

2. Experimental

$Ca_4O_7:Eu^{3+}$ phosphor powders were prepared by a solutions combustion method. All the reagents were of analytical purity, and were used without further purification. In a typical procedure, three glass beaker were used with the same content of $Eu(NO_3)_3.5H_2O$, (H_3BO_3), $NH_3(ON)H_2$, NH_4NO_3 and mixed with different amount of $Ca(NO_3)_2$. In each glass beaker 15 ml of deionized water was added and the above solutions were stirred for 20 minutes in a 250 ml beaker at room temperature vigorous until everything has dissolved. The solution was later transferred into a crucible, and then the crucible was introduced into a furnace maintained at 500^0C. The solution under-went dehydration followed by decomposition with the evolution of large amounts of gases. The mixture then froths and swells forming foam, which ruptures with a flame and glows to incandescence. During the incandescence the foam further swells to the capacity of the container. The entire combustion process was over in less than 15 min. The crystal structures of the samples were determined with a Bruker D8 Advance X-ray diffractometer with CuK_α (1.5418 Å). The morphologies of the phosphor were characterized with scanning electron microscopy (SEM, Shimadzu SSX-550 Super scan). The Photo luminescent spectra were obtained by using a spectrum analyzer (Varian carry eclipse fluorescence). Emission and excitation spectra were recorded using a spectral slit width of 5 nm.

3. Results and discussion

3.1 Structure and morphology

Fig. 1 shows XRD patterns of CaB_4O_7: Eu^{3+} samples synthesized with different Ca:B molar ratio and Eu ions concentrations. Fig. 1(a) the XRD patterns of the samples are in good agreement with the reference database JCPDS card 83-2025, confirming the composition of the sample to be CaB_4O_7. The obtained product has a monoclinic lattice with the lattice parameters a= 12.34, b= 9.50, c= 7.850. Fig. 1(b) it also shows the monoclinic structure with the single phase. The results also showed that varying the Eu% does not affect the crystal structure of the phosphor. Moreover, the increase of the Eu concentration promotes urea decomposition and causes the more rapid ignition of the mixture, which provides higher temperatures for the reaction [14].

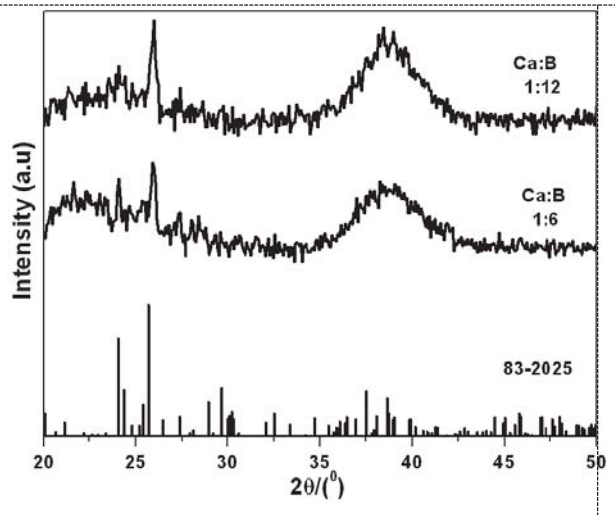

Figure 1. (a) X-ray diffraction patterns of CaB_4O_7 phosphors for various Ca:B mole ratio.

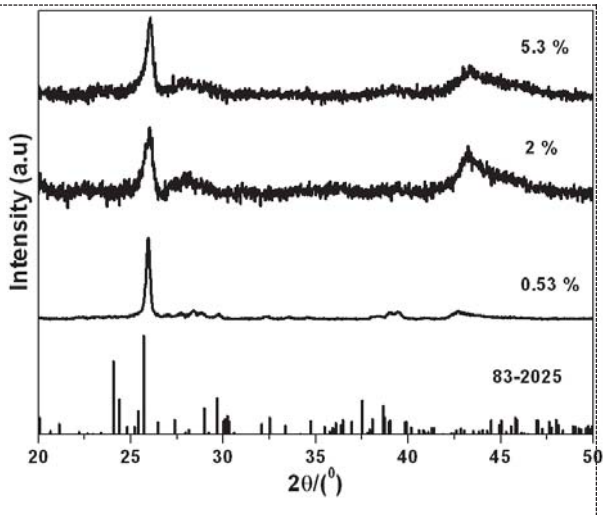

Figure 1. (b) X-ray diffraction patterns of CaB_4O_7 for different Eu concentrations.

Fig. 2 shows the SEM images of sample obtained for different Ca:B molar regular structured with well-developed edges as can be seen form Fig. 2(a and b). Eu ions concentration from Fig. 2(c and d) sows plate-like particles. Fig. 2(a,b) the SEM images of the $CaB_4O_7:Eu^{3+}$ powder also reveals nanorod like, agglomerated, porous for low Ca:B molar ratio but the grains become regular structured with well developed edges as the Ca:B molar ratio increased, giving rise to the increase in particle size. As for Fig. 2(c,d) the SEM images shows the plate-like structure with very narrow edges for low Eu concentration but as the Eu concentration increases it reveals mixed plate-like structure and irregular nanoparticles superimposed on them. It was reported that the flame temperature is responsible for agglomeration [15] and the evolution of large amount gaseous products during combustion produces highly porous voluminous powders [16]. When the ignition of the metal nitrate solution with nitrogen-based fuel starts, localization of the heat on the particle boundaries results in a semi-sintered morphology of particles [17]. In the literature, the observed particle size differences/ microstructure of oxides prepared by solution combustion technique using various fuels is usually explained based on the differences in the number of moles of gases liberated during the reaction.

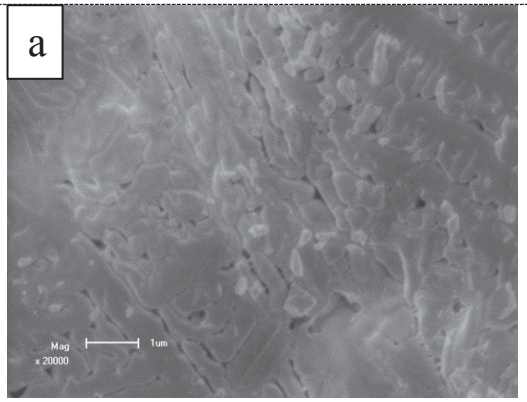

Figure 2. (a) SEM image of $CaB_4O_7:Eu^{3+}$ Ca:B 1:6 mole ratio sample.

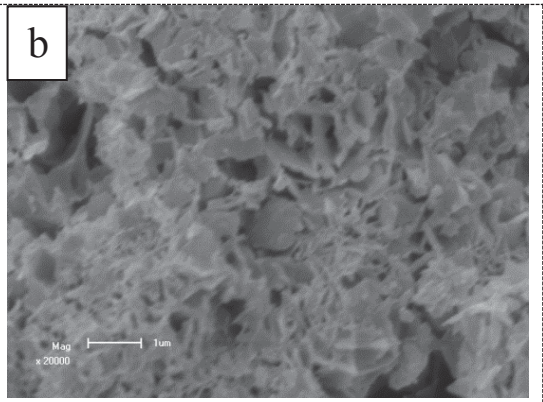

Figure 2. (b) A typical SEM image of samples with 1:12 Ca:B mole ratio sample.

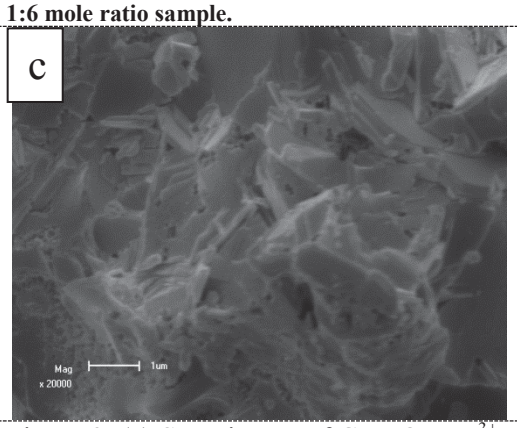

Figure 2. (c) SEM image of CaB_4O_7: Eu^{3+} samples with 0.53% Eu concentration.

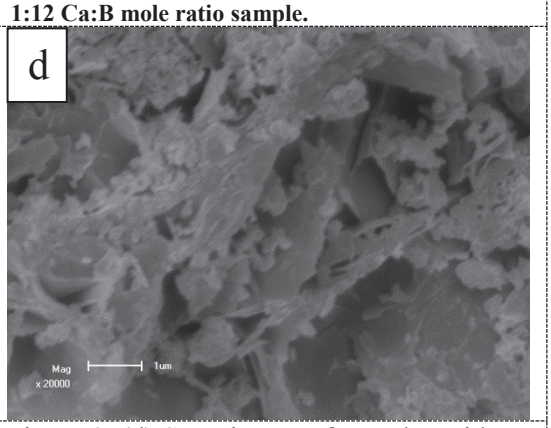

Figure 2. (d) SEM image of samples with 5.3% Eu concentration.

3.2 Photoluminescence characteristics

The excitation and emission spectra $CaB_4O_7:Eu^{3+}$ phosphors are shown in Fig. 3. From Fig. 3(a) the excitation spectra of the $CaB_4O_7:Eu^{3+}$ phosphor shows 3 bands from 200-400 nm. The excitation spectra by monitoring $^5D_0 \rightarrow {}^7F_2$ emission of Eu^{3+} in CaB_4O_7 can be divided into two regions: the broad excitation band in 220–300 nm regions originates from the charge-transfer transition of the Eu^{3+}–O^{2-} bond (CTB) [18]. The other sharp lines can be assigned, respectively, to the transitions between the ground level $^7F_0$ and the excited levels ^5H_J, $^5D_4$, ^5G_J, $^5L_6$ [19]. The most intense of f-f transitions is $^7F_0 \rightarrow {}^5L_0$ band (396 nm). The increase of the amount of the Ca: B molar ratios results in rise of the intensities of both CT and f-f bands. The emission spectra from Fig. 3(a) consist of transitions from $^5D_0$ level of Eu^{3+} ions to lower level of $^7F_4$ (680-700 nm), $^7F_3$ (648-659 nm), $^7F_2$ (608-633 nm), $^7F_1$ (583-603 nm) and the ground state $^7F_0$ (568-580 nm). The $^5D_0$-$^7F_2$ band is observed to be the most intense one (with the maximum at 614 nm) for all Ca: B molar ratios. This $^5D_0 \rightarrow {}^7F_2$ band also possesses a high intensity as a result, summary emission color is red.

Similarly from Fig. 3(b) similar results were observed with the variation of the Eu concentration. Under the excitation of CTB at 240 nm, it can be seen that the red emission lines at 614 nm originating from the electric dipole transition $^5D_0 \rightarrow {}^7F_2$ is the dominant luminescence in the spectrum. Sharp red emission indicates that CaB_4O_7: Eu^{3+} is suitable for display phosphors.

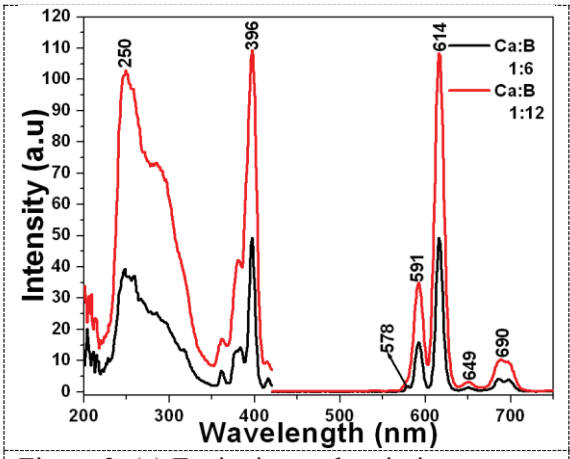

Figure 3. (a) Excitation and emission spectra of CaBxOy for various Ca:B mol ratio excited at 396 nm.

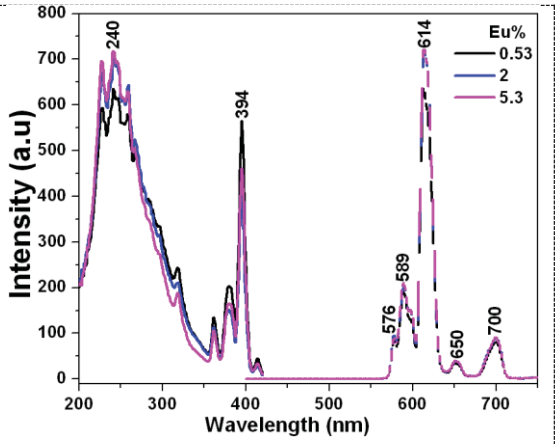

Figure 3. (b) Excitation and emission spectra of CaBxOy at different Eu concentration excited at 240 nm.

4. Conclusion

The $CaB_4O_7:Eu^{3+}$ phosphors with Ca:B molar ratio and Eu ions concentration have been successfully synthesized by the solution-combustion at furnace temperature of 500^0C. XRD analysis of phosphor shows a monoclinic phase. The SEM pictures of the $CaB_4O_7:Eu^{3+}$ powder reveals nanorod like, agglomerated, porous for Ca:B molar ratio but the grains become flake-like as the Ca:B molar ratio increased, giving rise to the increase in particle size. PL results shows the excitation spectra by monitoring $^5D_0 \rightarrow {}^7F_2$ emission of Eu^{3+} in CaB_4O_7, can be divided into two regions. The luminescent intensity of the $CaB_4O_7:Eu^{3+}$ phosphor increase with increase in both the Ca:B molar ratio and Eu ions concentration.

Acknowledgment
The authors send gratitude to the National Research Foundation (NRF) for funding the project and the University of Free State Physics (Physics department) for the research techniques used in this study.

References

[1] Fonseca A, Franco N, Alves E, Barradas N.P, Leitão JP, Sobolev N.A, Banhart DF, Prestinge H, Ulyanov VV, Nikiforov AI, 2004 *Nucl. Instrum. Methods Phys. Res* **241** 454–458.

[2] Freitas MLL, Silva LP, Azevedo RB, Garcia VAP, Lacava LM, Grisólia CK, Lucci CM, Morais PC, da Silva MF, Buske N, et al. 2002 *J. Magn. Magn. Mater* **252** 396–398.

[3] Kerman K, Morita Y, Takamura Y, Tamiya E, 2005 *Anal. Bioanal. Chem.* **381** 1114–1121.

[4] Becker P, 1998 *Adv. Mater*.**10** 979-991.

[5] Yang P, Gai S, Liu Y, Wang W, Li C, Lin J, 2011 *Inorg Chem* **50** 2182–2190.

[6] Wang L S, Lin J,Quan Z W, 2004 *J. Rare Earths* **22(1)** 91–100.

[7] Wang Y H, EndoTadashi, He L, Wu CF. 2004 *J Cryst Growth* **268** 568–574.

[8] Veith M, Mathur S, Kareiva A, Jilavi M, Zimmer M, Huch V. 1999 *J Mater Chem* **9** 3069–79.

[10] Matos M G, Pereira P F S, Calefi P S, Ciuffi K J, Nassar E, 2009 *J. Lumin* **129** 1120-1124.

[11] H. Kim, S. M. Park, J. Park, K. H. D. Park, K. Sohn, J. T. Park, 2002 *J. Electrochem* Soc. **149** 183-187.

[12] Chen Y, Wang J, Gong M, Su Q, 2007 *J. Solid State Chem* **180** 1165-1170.

[13] Ekambaram S, Patil K C, Maaza M, 2005 *J. Alloys Compd* **393** 81-92.

[14] Kingsley J J, Pederson L R, 1993 *Mat. Res. Soc. Symp. Proc.* **296** 361–366.

[15] Pederson L R, Maupin G D, Weber W J, McCready D J, Stephens R W, 1991 *Mater. Lett.* **10 (9)** 437–443.

[16] Wey C, Powell E A, Jagoda J I, 1984 *Combustion Science and Technology* **41** 193-200.

[17] Lenka R K, Mahata T, Sinha P K, Tyagi A K, 2008 *J. Alloys and Compds* **466** 326-332.

[18] Mahakhode J G, Dhoble S J, Joshi C P, Moharil S V, 2009 *J. Alloy. Compd* **438** 293-297.

[19] Jesus F A A D, Silva R S, Hermandes A, Macedo Z S, 2009 *J. Eur Ceram Sos* **29** 125-130.

The effect of chemical pressure on the ferromagnetic ordering of CeTX compounds

B M Sondezi, T Nemakhavhani and A M Strydom

Physics Department, University of Johannesburg, P.O. Box 524, Auckland Park, South Africa.

E-mail: bmsondezi@uj.ac.za

Abstract.

The transport and thermodynamic properties of CeTX (T = Au, Cu; X = Ge, Si) compounds have been studied. These well-ordered hexagonal compounds have shown ferromagnetic ordering anomalies in magnetic susceptibility, electrical resistivity and specific heat measurements at the ferromagnetic transition temperature $T_{\rm C}$, (10 K, 10 K and 15 K for CeAuGe, CeCuGe and CeCuSi, respectively). The location of magnetic ordering has been observed to be unstable under the influence of applied magnetic field, where the ferromagnetic ordering has been observed to shift upwards in temperature. However, the application of chemical pressure (dilution of Ce ions by non-magnetic isostructural La atoms) as observed from physical properties as well as magnetic properties measurements revealed a continuous tuning of $T_{\rm C}$ resulting in the ferromagnetic ordering temperature approaching 0 K as La content is increased. The calculation of the effective magnetic moment for small La content was observed to be 2.54 $\mu_{\rm B}$/mol of Ce, which is in agreement with the value of the full magnetic moment for Ce^{3+} ion. Powder x-ray diffraction (XRD) characterization of the dilution compounds indicated that the compounds retained their hexagonal crystal structure belonging to space group number 186 ($Ce_{1-x}La_x$)AuGe and 194 for ($Ce_{1-x}La_x$)CuGe and ($Ce_{1-x}La_x$)CuSi where the (0 0 0) Ce-site is partially substituted by La atoms. Rietveld refinement profile indicated that the lattice parameters a and c and the volume V of the dilution compounds increased with an increase in La content. This work presents the first results of the effect of isostructural substitution of Ce with La (($Ce_{1-x}La_x$)AuGe and ($Ce_{1-x}La_x$)CuGe. Measurements of magnetic susceptibility and specific heat for the dilution compounds gave the first evidence of tuning the ferromagnetic ordering temperature $T_{\rm C}$ to lower temperatures with the increase of La content in the compound.

1. Introduction

The study on quantum phase transitions (QPT) in local-moment systems has been mostly focussed on antiferromagnetic (AFM) systems. From the studies done on QPT, heavy fermion intermetallic compounds containing Ce, Yb, or U have been found to have unusual low temperature properties that appear to violate the dynamics of the Fermi-liquid (FL) metallic ground state paradigm [1]. These non Fermi liquid (NFL) materials exhibit weak power-law or logarithmic temperature dependences in various physical properties such as magnetic susceptibility, specific heat [2], and electrical resistivity at very low temperatures. NFL state then can be linked magnetic instability that arises at $T = 0$. Classical phase transition at nonzero temperatures, are driven by temperature as a control parameter with thermal fluctuations, a quantum phase transition is driven by a control parameter other than temperature, that is, external pressure, doping, or magnetic field at absolute zero, with quantum-mechanical

fluctuations. Such a control parameter tunes a system at the zero-temperature boundary from an ordered ground state towards a nonordered state crossing a quantum critical point [2].

The proximity of the suppressed magnetic phase transitions to the maximum T_C values, as well as more direct evidence of the instability of transition suggests the importance of magnetism, most likely, localized magnetism. A search into this phenomemon has been going on in condensed matter physics, particulary a search of quantum criticality in ferromagnetic compounds. It has been established from the previous studies that in compounds CeAuGe and CeCuGe, Ce carries a local moment with compounds ordering ferromagnetically at about 10 K, for CeAuGe [3] and CeCuGe [4], respectively. It is worth mentioning that these magnetic orders manifest anomalies in magnetic susceptibility, electrical resistivity and specific heat at T_C. In this work we present the first results of the effect of an isostructural substitution of Ce occupation site with La on the transition temperature T_C.

2. Experimental Procedure

Selected polycrystalline samples, $(Ce_{0.5}La_{0.5})AuGe$ and $(Ce_{0.7}La_{0.3})CuGe$ compounds were prepared by arc-melting stoichiometric quantities of the elements (purities in wt.%) Ce and La (4N), Cu (4N5), Ge and Si (6N) under-pressure in an ultra-high purity argon gas. The $(Ce_{0.7}La_{0.3})CuGe$ was subsequently annealed in an evacuated quartz tube at 800^0C for two weeks. This was followed by sample characterization through powder x-ray diffraction (XRD) and Rietveld refinement profile using General Structure Analysis Software (GSAS). The temperature dependent specific heat measurements of the compounds were performed using Physical Properties Measurement System (PPMS) from Quantum Design (QD) in San Diego. These measurements were performed in temperatures between 300 K and 1.9 K . Magnetic properties were measured using Magnetic Properties Measurement System (MPMS) in small applied magnetic field of 0.005 T ($(Ce_{0.5}La_{0.5})AuGe$) and 0.01 T for ($(Ce_{0.7}La_{0.3})CuGe$) between 395 K and 1.9 K.

3. Results

CeAuGe and CeCuGe are equiatomic intermetallic compounds confirmed to crystallize in a hexagonal crystal structure. The ordered ternary phase of CeAuGe crystallizes in the NdPtSb-type structure with the space group $P6_3/mc$ (number 186) (CeAuGe) and ZrBeSi-type structure with space group $P6_3/mmc$ (number 194) (CeCuGe). The unit cell is characterised by an elongated c-axis (almost double the length of the a-axis). The dilution compounds of the respective compounds were found to exhibit similar crystal structure and they remained as equiatomic compounds. As displayed in figure 1 the atomic arrangement of atoms in the unit cell show Ce atoms arranged in flat planes perpendicular to c-axis which are well separated by slightly puckered Au-Ge [3].

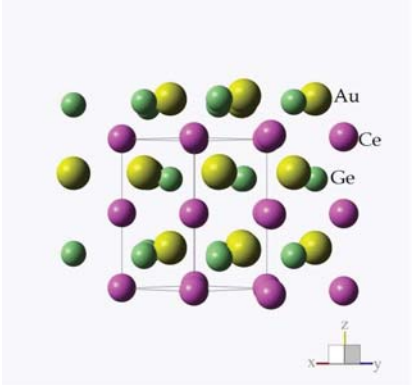

Figure 1. Crystal structure of CeAuGe, with slightly puckered -AuGe layer sandwiched between the Ce-layers.

Powder x-ray diffraction (XRD) recorded using Cu K_α radiation of wavelength $\lambda = 1.5406$Å confirmed the formation of single phase $(Ce_{0.5}La_{0.5})AuGe$ and $(Ce_{0.7}La_{0.3})CuGe$. The results of the Rietveld refinement are shown in figure 2. The refinable parameters in each compounds were instrument offset, the data background, unit cell parameters as well as full width half maximum (FWHM) of the peaks. It was observed that the lattice parameters (a, c) of these measured dilution compounds increased as the La element substituted some percentage of Ce-site. Table 1 lists the results output of Rietveld refinement profile of the CeAuGe, $(Ce_{0.5}La_{0.5})AuGe$, CeCuGe and $Ce_{0.7}La_{0.3}CuGe$ compounds. The observed lattice paramaters a, c and the volume V of the respective dilutions increase with the increase of La in the compound. More dilution compounds to complete the series of this study are in progress to conclusively determine the trend of the lattice parameters and the volume of the unit cell. This increase in the lattice parameters is ascribed to the change in the atomic dimensions of the rare earth site, as La partly replaces Ce.

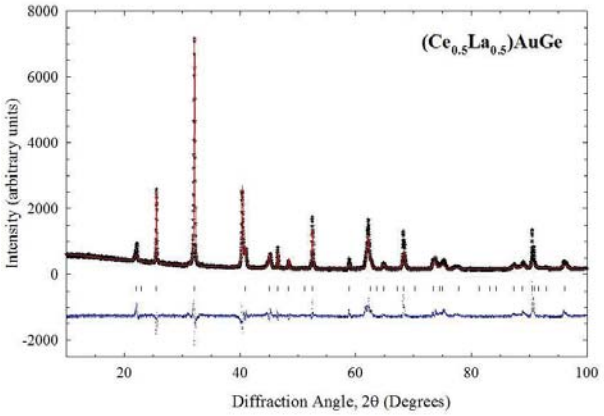

Figure 2. Experimental powder XRD data of $(Ce_{0.5}La_{0.5})AuGe$ (black symbols), Rietveld refinement fit (solid red line), difference curve (blue line) and the expected Bragg positions (pink vertical markers).

Table 1. The table of lattice parameters of $(Ce_{0.5}La_{0.5})AuGe$ and $Ce_{0.7}La_{0.3}CuGe$ as obtained from Rietveld Refinement fit.

	a(Å)	c(Å)	V(Å^3)
CeAuGe	4.4569(1)	7.9105(1)	136.078(1)
$(Ce_{0.5}La_{0.5})AuGe$	4.4598(1)	8.047(5)	136.611(2)
CeCuGe	4.299(5)	7.952(2)	127.252(3)
$(Ce_{0.7}La_{0.3})CuGe$	4.3175(5)	7.96(2)	128.5(5)

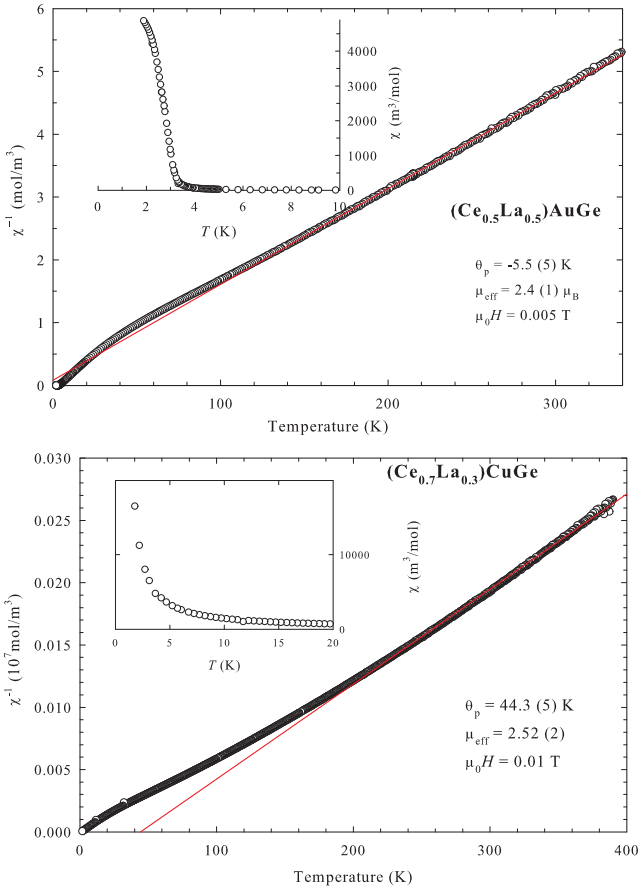

Figure 3. Temperature dependent inverse susceptibility of $(Ce_{0.5}La_{0.5})AuGe$ (top) and $(Ce_{0.7}La_{0.3})CuGe$ (bottom) where the insets show the low temperature data of magnetic susceptibility revealing long range ordering can be associated with ordering temperature.

Temperature dependent inverse susceptibility $\chi^{-1}(T)$ measured in the field-cooled (FC) mode in the temperature range between 350 K - 2 K (as there was no anomalous behaviour was expected above 350 K) and $\mu_0 H = 0.005$ T ($(Ce_{0.5}La_{0.5})AuGe$) and between 395 K - 2 K for $Ce_{0.7}La_{0.3}CuGe$ in constant applied magnetic field of 0.01 T is shown in figure 3. High temperature data ($T > 200$ K), is observed to follow the Curie-Weiss behaviour, and was fitted according to Curie-Weiss law:

$$\chi^{-1}(T) = \frac{3k_B(T - \theta_p)}{N_A \mu_{eff}^2}. \quad (1)$$

The fit yielded the paramagnetic Curie-Weiss temperature, θ_p = -5.5(1) K for $(Ce_{0.5}La_{0.5})AuGe$, which is an indication that the net interactions in the paramagnetic region of this compound are antiferromagnetic, despite the ferromagnetic ground state exhibited by this compound. An effective magnetic moment $\mu_{eff} = 2.41(1)\ \mu_B$ per Ce atom was calculated. This effective magnetic moment value is close to the theoretical value of $\mu_{eff} = 2.54\ \mu_B$. In the temperature region, $15\,K \leq T \leq 160\,K$ there is a deviation from Curie-Weiss behaviour. This deviation is attributed to the presence of crystal electric field effects (CEF) in this compound. In this regard, Ce in a hexagonal structure having a point symmetry of $\bar{3}$m, the ground state J-multiplet splits into

three doublets [5], which are mainly $|\pm M_J\rangle$ states where $|\pm M_J\rangle = \pm\frac{1}{2}$, $\pm\frac{3}{2}$ or $\pm\frac{5}{2}$ [6]. Within the framework of ionic model, the ground state of a configuration of Ce corresponds to $J = \frac{5}{2}$ ($L = 3, S = \frac{1}{2}$) and $g_J = \frac{6}{7}$. The insets on the top left corners of the figure 3, are the magnetic susceptibility data, exhibited to reveal the low temperature data. The long-range divergence is observed at about 3 K (from top inset), this could be associated with ferromagnetic ordering temperature T_C in this compound. From the inset in the bottom figure, the data diverges beyond our measuring temperature range, and this observation allows measurements to even lower temperatures (below 2 K). The fitted paramagnetic Curie-Weiss temperature, $\theta_p = 44.3(5)$ K for $(Ce_{0.7}La_{0.3})CuGe$ and the calculated effective magnetic moment $\mu_{eff} = 2.52(2)$ μ_B, were obtained, where μ_{eff} is in close agreement with the expected value for free Ce^{3+} ion [5] was obtained.

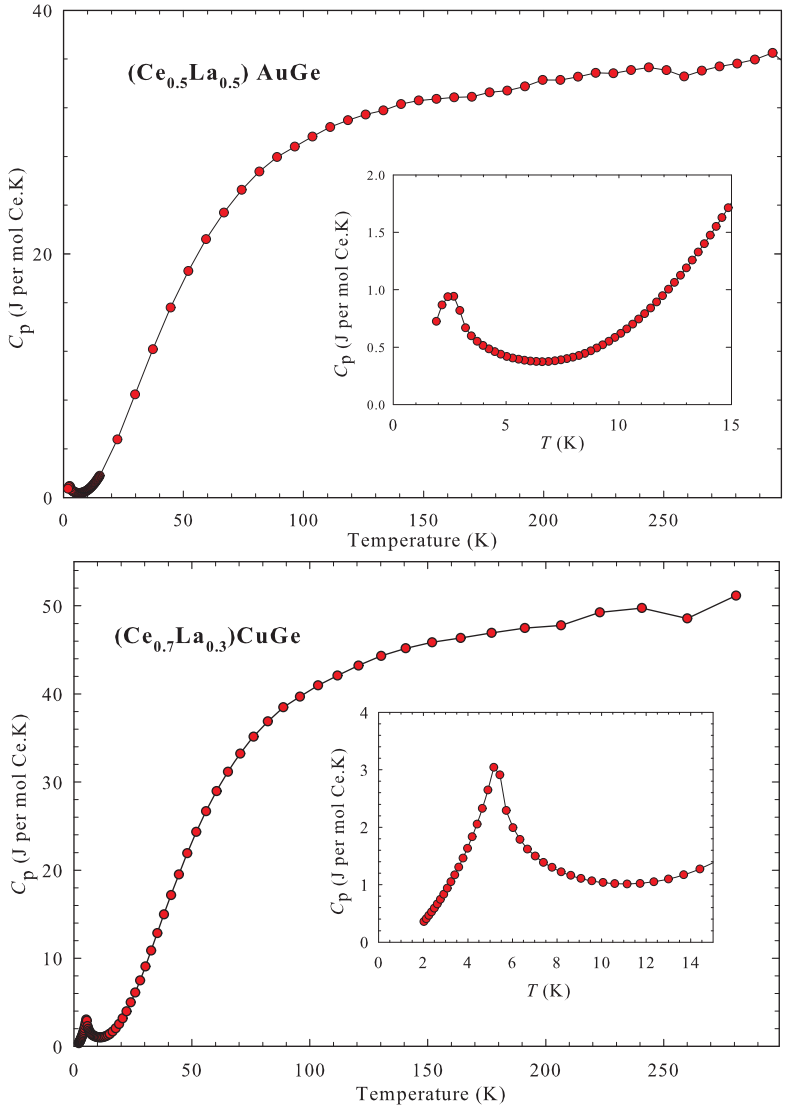

Figure 4. Specific heat of $(Ce_{0.5}La_{0.5})AuGe$ (top) and $(Ce_{0.7}La_{0.3})CuGe$ (bottom) where the insets show the low temperature data revealing a λ-type anomaly which can be associated with ordering temperature.

The specific heat data of the ternary CeAuGe has been confirmed to be at $T_C = 10$ K [3, 7] and that of CeCuGe was confirmed to be $T_C = 10$ K as well [4, 8]. The ordering temperatures are characterised by a λ-type anomaly in these data and are indicated by arrows in the inset of figure 4. The λ-type ordering temperature of the dilution compound $(Ce_{0.5}La_{0.5})AuGe$ is $T_C = 3$ K as taken from the maximum slope of the anomaly; whilst the ordering temperature of $(Ce_{0.7}La_{0.3})CuGe$ was observed at about $T_C = 5$ K. As the temperature increases beyond the ordering temperature, firstly there is an observable decrease in specific which is followed by a monotonous increase in the C_p data to maximum temperature, 300 K. This shift to lower temperatures as a result of chemical pressure which is achieved by the dilution of the Ce-moment, is contrary to the results obtained when the magnetic field is applied to equiatomic ternary compounds [4, 7, 9].

4. Conclusion

The isostructural substitution of Ce ions with La ions resulted in the shifting of lattice parameters as obtained from Rietveld refinement profile. The dilution compounds proved to retain similar structures as their ternary compounds. Magnetic susceptibility and specific heat measurements provided evidence of the tuning of ferromagnetic ordering towards lower temperatures. These results provide an opportunity to further investigate the possibility of NFL behaviour in these series of compounds.

Acknowledgements

B M Sondezi acknowledges financial assistance provided by the National Research Foundation (NRF) of South Africa grant number 282700, as well as the support provided by University Research Council (URC), UJ Science Faculty and Physics Department. A M Strydom thanks the SA-NRF grant number 78832.

References

[1] Maple M B, 1994 *J. Low Temp. Phys.* **95** 225
[2] Stewart G R, 2001 *Rev. Mod. Phys.* **56** 755
[3] Pöttgen R, Borrmann H and Kremer R K, 1996 *J. Magn. Magn. Mater.* **152** 196
[4] Yang F, Kuang J P, Li J, Bruck E, Nakotte H, de Boer F R, Wu X, Li Z and Wang Y, 1991 *J. Appl. Phys.* **69** 4705
[5] Kittel C, 1996 *Introduction to Solid States Physics* (John Wiley and Sons.)
[6] Gignoux D, Schmitt D and Zerguine M, 1986 *Solid State Commun.* **58** 559
[7] Mhlungu B M and Strydom A M, 2008 *Physica B: Condens. Mat.* **403** 862
[8] Sondezi-Mhlungu B M, Adroja D T, Strydom A M, Paschen S and Goremychkin E A, 2009 *Physica B* **404** 3032
[9] Sondezi-Mhlungu B M, Adroja D T, Strydom A M, W Kockelmann and Goremychkin E A 2010 *J. of Phys.: Confer. Series* **200** 012190

The determination of critical behaviour of ferromagnetic CeCuGe using magnetocaloric effect

B M Sondezi, J L Snyman and A M Strydom

Physics Department, University of Johannesburg, P.O. Box 524, Auckland Park, 2006, South Africa

E-mail: bmsondezi@uj.ac.za

Abstract. Critical behaviour of magnetic systems associated with a second order phase transition is of general interest in condensed matter physics as a useful tool to study universal behaviour across a wide range of magnetic systems. Typically a specific universality class is characterized by a set of critical exponents which determine the type of divergences occurring in thermo-magnetic quantities as the phase transition temperature is approached. Here we present results obtained from specific heat and magnetization measurements of CeCuGe. Isothermal magnetization of hexagonal, highly crystallographic ordered CeCuGe was measured across the paramagnetic to ferromagnetic phase transition in order to study resulting critical phenomena. From the analyses of the magnetization data, T_C was confirmed using the Arrot-plot technique. The critical exponents, β, γ and δ obtained from fits of the spontaneous magnetization, magnetic susceptibility and isothermal magnetization revealed that the system behaves as a mean field ferromagnet. An independent analysis of the critical behaviour is presented in terms of the magnetocaloric effect (MCE) and shows good agreement with the results derived from Arrot-plots analysis.

1. Introduction

The magnetocaloric effect describes the *reversible* heating or cooling of a magnetic system by changing the applied magnetic field to which a sample is exposed [1]. The effect has its origin in the change of magnetic configurational entropy induced by a changing applied magnetic field which is compensated for (under isentropic conditions) by a corresponding change in entropy in the non-magnetic sub-system (typically the crystalline lattice). Over the last two decades increasing attention has been paid to the magnetocaloric effect (MCE) in a variety of magnetic compounds due to the discovery of the so called 'giant' magnetocaloric effect in $Gd_5Si_2Ge_2$ [2]. Much of these recent efforts have been directed at finding suitable materials for use as room temperature magnetic refrigerants as an energy efficient alternative to gas-compression refrigeration cycles. The increasing scientific importance attributed to the MCE as a result of these studies established several protocols by which the MCE may be used as a fundamental probe into the magnetic state of a particular material in addition to more 'traditional' characterisation methods such as magnetometry and calorimetry. One such protocol is the determination of the universality class of a material through its magnetocaloric effect [3].

The feasibility of this protocol has been well established in literature for a group of soft, amorphous ferromagnetic materials [4]. However, experimental investigations into the applicability of this method to a broader family of magnetic systems are still incomplete. One

particular family of systems amenable to the study of this protocol is the class of Ce-based ferromagnetic systems in which strong hybridisation effects between the Ce^{3+} $4f$-electrons and the conduction band electrons are absent [5]. It is noted (on purely phenomenological grounds) in ref.[5] that this class of systems seem to establish ferromagnetic order preferentially through long range exchange interactions, implying that these compounds should belong to the same universality class containing model mean-field ferromagnets. Within this context the ternary intermetallic compound CeCuGe has been chosen for the current study, as is motivated next.

CeCuGe crystallizes in a hexagonal structure type belonging to the AlB_2 family [6]. The ordered ternary phase crystallizes in the ZrBeSi-type structure with space group $P6_3/mmc$ (number 194) and is characterised by a unit cell elongated in the direction of the c-axis (the latter almost double the length of the a-axis. The atomic arrangement of CeCuGe in the unit cell is described as Ce-ions arranged in flat planes perpendicular to c-axis which are well separated by Cu-Ge layers [6]. In this crystal structure the Ce-site has $\bar{3}$m point symmetry [7], which profoundly affects the ground state of the Ce^{3+} $4f$-electrons responsible for magnetic ordering through the crystalline electric field (CEF) interaction. An analysis of the specific heat of CeCuGe revealed the presence of a Schottky anomaly resulting from the upliftment of the 6-fold degenerate free $4f$-electron multiplet by the CEF into a level dispensation of lower degeneracy [8]. The Schottky contribution to the specific heat could be parameterized by an energy separation of $\Delta_1/k_{\rm B} = 140$ K and $\Delta_2/k_{\rm B} = 205$ K separating two excited doublets from a doublet $4f$-electron groundstate [9]. It has been established that a transition to a ferromagnetically ordered state in CeCuGe occurs at $T_{\rm C} = 10$ K [10]. This has been verified with independent measurements of the specific heat ($C_{\rm p}$) [9] where a prominent λ-type anomaly is observed at the transition temperature. The field dependence of the latter is consistent with ferromagnetic order.

For ferromagnetic systems it is expected that the magnetisation $M(T)$ and susceptibility $\chi(T)$ obey scaling laws $M \sim t^{\beta}$ and $\chi(T) \sim t^{-\gamma}$ (where t denotes a reduced temperature scale) in the vicinity of $T = T_C$ and in zero applied field, with $\beta = 0.5$ and $\gamma = 1$ for mean field systems [11]. Empirically it is known that in the critical temperature region ferromagnetic systems obey the Arrot-Noakes equation of state [12]

$$H^{1/\gamma} = a(T - T_C)M^{1/\gamma} + bM^{1/\gamma+1/\beta} \tag{1}$$

which allows for the determination of β and γ from Arrot plots [12]. The critical exponents determined from this analysis for CeCuGe yielded $\beta = 0.637(1)$ K, $\gamma = 0.962(2)$ K and the calculated $\delta = 2.509(1)$ K [13], suggesting that CeCuGe belongs to a class of mean field ferromagnets. The mean-field nature of this system implies that CeCuGe is a prime candidate compound with which to study the applicability of the above mentioned MCE protocol [3] outside of the narrow family of amorphous ferromagnets hereto investigated in literature. For this protocol to apply, the critical exponent characterising the field dependence of the MCE must correspond to that expected for a mean field ferromagnetic system.

2. Experimental procedure and sample characterisation

A polycrystalline CeCuGe sample was prepared in an arc furnace under ultra-high purity argon atmosphere. Stoichiometric amounts of the elements (purities in wt. %) Ce (99.99), Cu (99.995) and Ge (99.9999) were used. The ingots were remelted several times to promote homogeneity.

Powder x-ray diffraction (XRD) recorded using Cu K_α radiation of wavelength $\lambda = 1.5406$Å confirmed the formation of single phase CeCuGe. The measured data were fitted against the theoretical parameters [14] of the ZrBeSi-type structure. A Rietveld refinement profile according to the ZrBeSi-type structure (space group $P6_3/mmc$, number 194) was performed with calculated lattice parameters $a = 4.2987(8)$ Å and $c = 7.952(2)$ Å showing good correspondence with values previously reported in literature [14, 15]. The refinable parameters

were instrument offset, the data background, unit cell parameters as well as full width half maximum (FWHM) of the peaks.

A SQUID magnetometer (Magnetic Properties Measurement System, Quantum Design, San Diego) was used to obtain the magnetization data used for the Arrot-plot analysis. The heat capacity option of a Physical Properties Measurement System (Quantum Design, San Diego) was used to obtain the specific heat of CeCuGe, from which the MCE is subsequently determined.

3. Results and discussion

Critical exponents in the vicinity of the Curie temperature were determined by Arrot plots technique [12]. These results were presented in our earlier reports [13], and are briefly summarised below. Magnetization data was plotted in the form M^2 vs $\mu_0 H/M$. The spontaneous magnetization $M_{\rm s}(T,0)$ values were computed from y-intercept of this graph, and inverse initial susceptibility $\chi_0^{-1}(T)$ values were computed from the x-intercept. The values of these intercepts were determined for a number of magnetic isotherms around $T = T_{\rm C}$. The T dependence of the intercepts were then fitted according to the expressions [16]:

$$Y(T) = -M_s \left(\frac{\partial M_s}{\partial T}\right)^{-1} = -\frac{T - T_C}{\beta}, \tag{2}$$

$$X(T) = \chi_0^{-1} \left(\frac{\partial \chi}{\partial T}\right)^{-1} = \frac{T - T_C}{\gamma}, \tag{3}$$

where β and γ are fitting parameters and $T_{\rm C}$ is determined by the requirement that the associated isotherm is linear in $\mu_0 H/M$ and passes through the origin. The range of the applied magnetic field used in this analysis is 0 to 2 T, and the results are shown in figure 1.

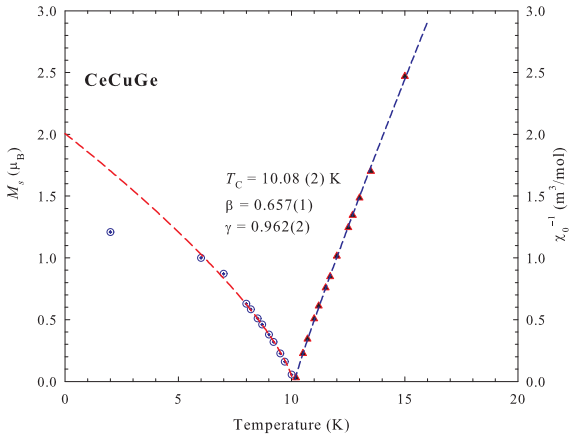

Figure 1. Spontaneous magnetization vs temperature (left hand axis),and initial susceptibility vs temperature (right hand axis).

The magnetocaloric effect is typically described in terms of two functions. The first is the change in entropy $\Delta S_{\Delta H}(T)$ resulting from an isothermal magnetisation process, increasing the applied field from an initial value H_i by an amount ΔH. For the values of $\Delta S_{\Delta H}(T)$ shown below an initial field of zero has been used throughout, implying that $\Delta H = H_f$. The second function describing the MCE is the change in temperature $\Delta T_{\Delta H}(T_i)$ resulting from a demagnetisation process achieved by decreasing the applied magnetic field while the sample is completely isolated from its surroundings. Here T_i denotes the temperature of the sample before demagnetisation. For the values of $\Delta T_{\Delta H}(T_i)$ shown below the final value of the applied magnetic field is zero throughout. As discussed above, $\Delta T_{\Delta H}(T_i) = T_i - T_f$ where T_i and T_f are determined by the isentropic condition $S(H_f, T_f) = S(H_i, T_i)$. Both $\Delta S_{\Delta H}(T)$ and $\Delta T_{\Delta H}(T_i)$ calculated for

CeCuGe are shown in figure 2. In order to contextualise these results, $\Delta T_{\Delta H}(T_i)$ calculated for a spin-1/2 mean field ferromagnet is shown in figure 3. From the figure it can be seen that the points where $\Delta T_{\Delta H}(T_i)$ is maximum traces out a straight line $T_i = T - T_C$ for the model system. This behaviour is putatively ascribed to the limitation placed on short range magnetic correlations inherent to the mean field model: in the classic mean field limit (see for example ref.[11]) the critical region is assumed to be infinitely small in temperetare and no short range correlations exist immediately above $T = T_C$. Similar behaviour is also observed for $\Delta T_{\Delta H}(T_i)$ calculated for CeCuGe, consistent with CeCuGe being a mean field ferromagnet.

According to the protocol established in ref.[3], the maximum values of $|\Delta S_{\Delta H}(T)|$ are expected to show scaling behaviour with the applied field so that:

$$|\Delta S_{\Delta H}(T)| \sim H_f^n, \tag{4}$$

n is derivable from the critical exponents β, γ and δ (see again ref.[3]) and is expected to have a value $n = 2/3$ for mean field systems. The scaling behaviour of $|\Delta S_{\Delta H}(T)|$ is also shown in figure 3. To a good approximation, the expected scaling law is satisfied up to $H_f = 90$ kOe and the value of $n = 0.62$ is derived by fitting the data in figure 3 by fitting the data to the behaviour expected from equation (5).

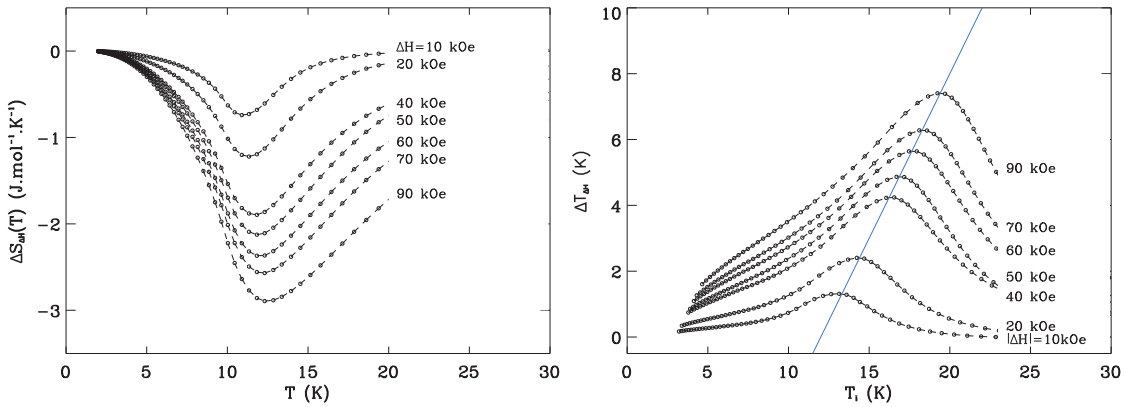

Figure 2. The isothermal change in entropy $\Delta S_{\Delta H}(T)$ (left) and the adiabatic change in temperature $\Delta T_{\Delta H}(T_i)$ (right) for CeCuGe as calculated from the specific heat data reported in [17]. The straight line in the right panel shows the locus $T_i = T - T_C^*$.

4. Conclusion

The protocol established by Franco *et al.* [3] by which the universality class of a system may be determined from an analysis of the magnetocaloric effect promises a powerful, yet simple technique by which critical behaviour in a magnetically ordered system may be characterised. This has been done with great success for a family of amorphous soft ferromagnets [18]. Here this protocol is applied to a completely different system, CeCuGe, forming part of a larger group of Ce-based ferromagnets [13]. Within the latter group mean field ferromagnetism is expected to predominate [5], and from an analysis of magnetisation data it could indeed be shown that CeCuGe is a mean field ferromagnet. Our analysis of the MCE in CeCuGe shows that both the peak values of the adiabatic temperature change $\Delta T_{\Delta H}(T_i)$ and the isothermal change in entropy $|\Delta S_{\Delta H}(T)|$ follow trends expected for, firstly a mean field ferromagnet, and secondly from the more general theory developed by Franco *et al* [3]. Specifically, the value of n, characterising the field dependence of the maximum values of $|\Delta S_{\Delta H}(T)|$ is found to be 0.62, close to $n = 2/3$

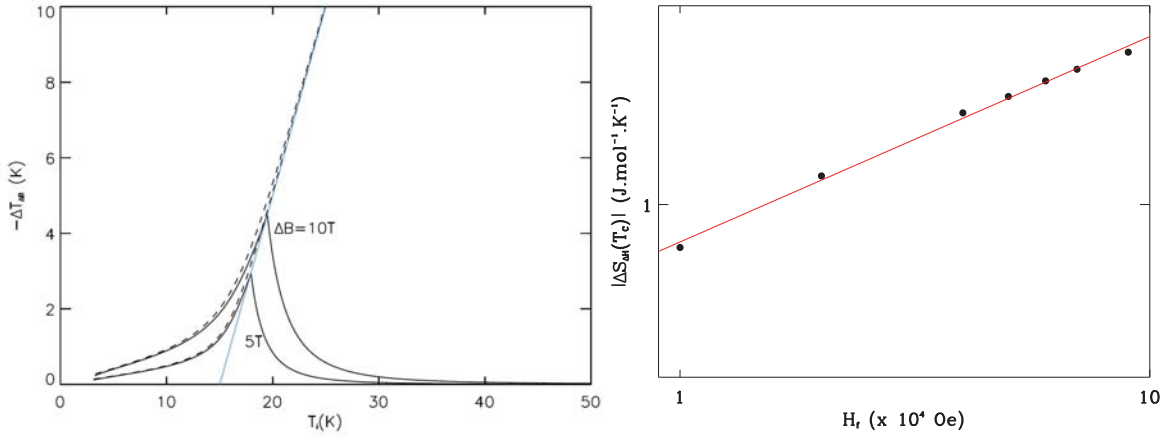

Figure 3. Left: $\Delta T_{\Delta H}(T_i)$ calculated for a spin-1/2 mean field ferromagnet. Dashed lines show asymptotic behaviour in the limit where the lattice contribution to the system entropy is negligible. The solid blue line is described by $T_i = T - T_C$. Right: The behaviour of $|\Delta S_{\Delta H}(T)|$ with applied magnetic field. The solid line shows the best fit of the scaling relationship $|\Delta S_{\Delta H}(T)| \sim H_f^n$ with $n = 0.62$.

expected for a mean field ferromagnet. In this analysis we implicitly assume that the exchange interaction responsible for ferromagnetism in CeCuGe is isotropic, and that in the vicinity of the Curie temperature anisotropy effects play a role secondary to critical fluctuations. This assumption is at least partially justified by the absence of strong anisotropy effects in the MCE (as was observed in polycrystalline $PrNiGe_2$ [19]) and by the fact that, although anisotropy effects result in different signatures in the MCE and magnetisation data, the critical exponents derived from both methods show close agreement. It is however hoped that a future study of a single crystal sample of CeCuGe will illuminate the validity of this assumption.

Acknowledgements

B M Sondezi acknowledges financial assistance provided by the National Research Foundation (NRF) of South Africa grant number 282700, as well as the support provided by university research council (URC), UJ Science Faculty and Physics Department. A M Strydom thanks the SA-NRF grant number 78832.

References

[1] Warburg E 1881 *Ann. Phys.* **13** 141
[2] Pecharsky V K and Gschneidner, Jr K A 1997 *Phys. Rev. Lett.* **78** 4494
[3] Franco V, Blazquez J S and Conde A, 2006 *Appl. Phys. Lett.* **89** 222512
[4] Franco V, Conde A, Romero-Enrique J M and Blazquez J S 2008 *J. Phys.: Condens. Matter* **20** 285207
[5] Sereni J G and Kappler J G 1991 *Physica B* **171** 166
[6] Iandelli A, 1983 *J. Less-Common Met.* **90** 121
[7] Gignoux D, Schmitt D and Zerguine M, 1986 *Solid State Commun.* **58** 559
[8] Kittel C, 1996 *Introduction to Solid States Physics* (John Wiley and Sons.)
[9] Sondezi-Mhlungu B M, Adroja D T, Strydom A M, Paschen S and Goremychkin E A, 2009 *Physica B* **404** 3032
[10] Yang F, Kuang J P, Li J, Bruck E, Nakotte H, de Boer F R, Wu X, Li Z and Wang Y, 1991 *J. Appl. Phys.* **69** 4705
[11] Kadanoff L P, Götze W, Hamblen D, Hecht R, Lewis E A S, Palciauskas V V, Rayl M, Swift J, Aspnes D and Kane J 1967 *Rev. Mod. Phys.* **39** 395
[12] Arrot A and Noakes J E 1967 *Phys. Rev. Lett.* **19** 786

[13] Sondezi-Mhlungu B M and Strydom A M 2011 *SAIP Confer. Proc.* **1** 324
[14] Chevalier B, Pasturel M, Bobet J L, Weill F, Decourt R and Etourneau I, 2004 *J. Solid State Chem.* **177** 752
[15] Oner Y, Kamer O, Ross J H, Lue C S and Kuo Y K 2005 *Solid State Commun.* **136** 533
[16] Mohan C V, Seeger M, Kronmuller H, Murugaraj P and Maier J, 1998 *J. Magn. Magn. Mater.* **183** 348
[17] Sondezi-Mhlungu B M, Adroja D T, Strydom A M, W Kockelmann and Goremychkin E A 2010 *J. of Phys.: Confer. Series* **200** 012190
[18] Franco V, Caballero-Flores R, Conde A, Knipling K E and Willard M A 2011 *J. Appl. Phys.* **109** 07A905
[19] Snyman J L and Strydom A M 2013 *J. Appl. Phys.* **113** 17E135

Blue luminescence from Bi doped $MgAl_2O_4$ prepared by the combustion method

W A I Tabaza, H C Swart and R E Kroon

Department of Physics, University of the Free State, IB51, P. O. Box 339, Bloemfontein, 9300, South Africa

E-mail: KroonRE@ufs.ac.za

Abstract. Magnesium aluminate ($MgAl_2O_4$) has received special attention as a technologically important material because of its attractive properties, such as mechanical strength, chemical inertness, a wideband gap, relatively low density, high melting point, high thermal shock resistance, low thermal expansion coefficient, resistance to neutron irradiation and low dielectric loss. It has also been used as a phosphor host activated by a variety of transition metal and lanthanide ions. As an alternative to such ions, luminescence can often be obtained from the ns^2 type ions such as Tl^+, Pb^{2+}, Bi^{3+} and Sb^{3+}. For Bi^{3+} the luminescence is attributed to the electron transition between the $6s^2$ ground state and the $6s^16p^1$ excited states. A simple combustion method was employed for the preparation of Bi doped $MgAl_2O_4$ nanocrystals using metal nitrates as precursors and urea as a fuel in a preheated furnace at 520˚C. The samples thus obtained were characterized by x-ray diffraction, UV-visible spectroscopy, scanning electron microscopy and photoluminescence spectroscopy. For an excitation wavelength of 335 nm, the Bi^{3+} doped $MgAl_2O_4$ produced a blue emission band centred near 400 nm, indicating that Bi^{3+} ions were successfully incorporated in the lattice. Maximum blue emission was obtained for the sample doped with 0.5 mol% Bi. The results indicate that doping $MgAl_2O_4$ with Bi ions may be an attractive alternative to doping it with Ce ions, which give broad blue-green luminescence in this host but requires reducing at a high temperature (1400˚C) to convert non-luminescent Ce^{4+} ions to the luminescent Ce^{3+} charge state.

1. Introduction

Phosphor materials are widely applied in lighting, displays, lasers and scintillators, and it is necessary that the phosphor host exhibits good optical, mechanical and thermal properties. Magnesium aluminate ($MgAl_2O_4$), corresponding to the mineral spinel, is considered to be an optically inert medium and its chemical and thermal stability increases its attractiveness as a host for luminescent ions [1]. Rare-earth ions are often used as activators for phosphor materials, especially in the trivalent charge state where luminescence is generally due to f–f electron transitions [2,3]. However, metallic impurities with an outer ns^2 configuration ground state such as Tl^+, Pb^{2+}, Bi^{3+} and Sb^{3+} ions may also be excellent luminescence activators [4]. Bi atoms have an electronic configuration $[Xe]4f^{14}5d^{10}6s^2p^3$ and Bi^{3+} ions, with outermost $6s^2$ electrons, have been widely used as activators for various host materials including oxides, phosphates, aluminates and borates [5]. The $6s^2$ ground state has a single energy level $^1S_0$ while the $6s^16p^1$ excited configuration has energy levels $^3P_0$, $^3P_1$, $^3P_2$ and $^1P_1$ in order of increasing energy. Electron transitions between the $^1S_0$ ground state and the ^3P_J levels are spin forbidden, but optical absorption can occur to the high energy $^1P_1$ level. However, spin-orbit coupling between the

$^1P_1$ and $^3P_1$ levels makes the lower energy transitions $^1S_0 \leftrightarrow {}^3P_1$ possible and the luminescence from Bi^{3+} activated phosphors is usually attributed to this transition. In some materials the $^1P_1 \rightarrow {}^1S_0$ emission is also observed [6]. The outer electron orbitals of Bi^{3+} are not shielded (as in the case of the 4f energy levels of trivalent lanthanide ions) so the broad luminescence band shows a strong dependence on the composition and crystal structure of the host lattice and the emission wavelength is tuneable from the ultraviolet, through blue to green [7].

Spinel powders have been prepared by solid-state reaction [2], precipitation [8], hydrothermal synthesis [3] and sol-gel synthesis [9]. Alternatively, synthesis via the combustion method [10] occurs via a highly exothermic redox reaction between metal nitrates and an organic fuel and this technique can produce a homogenous product in a short amount of time without using expensive high temperature furnaces. This method has been used to prepare novel $MgAl_2O_4$:Bi nanocrystalline phosphor powders in order to study their optical properties.

2. Experimental

$MgAl_2O_4$ was prepared by combustion synthesis using magnesium nitrate $Mg(NO_3)_2.6H_2O$ and aluminium nitrate $Al(NO_3)_3.9H_2O$ as precursors and urea CH_4N_2O as the fuel according to the reaction

$$3Mg(NO_3)_2 + 6Al(NO_3)_3 + 20\ CH_4N_2O \rightarrow 3MgAl_2O_4 + 32N_2 + 20CO_2 + 40H_2O$$

where the waters of crystallization of the nitrates have been omitted for simplicity. Either 5 or 10 mmol of aluminium nitrate was added to stoichiometric amounts of the other reactants in about 3 or 6 ml of distilled water, which was stirred vigorously for 30 min to obtain a homogeneous transparent solution. The transparent solution of reagents was transferred into a porcelain crucible which was placed in a muffle furnace maintained at 520˚C. Within a few minutes the water boiled off and the sample ignited as the exothermic combustion reaction occurred, giving off copious quantities of gas and heating the material to well above the furnace temperature. After the reaction the foamy white product was removed from the furnace and, after cooling to room temperature, it was crushed into powder using a pestle and mortar. Doping of samples with Bi ions was achieved by replacing an appropriate amount of aluminium nitrate with the same amount of bismuth nitrate $Bi(NO_3)_3.5H_2O$. In spinel the Al^{3+} ions occupying octahedral sites and the Mg^{2+} ions in tetrahedral sites are both small (effective ionic radii of 53 and 58.5 pm respectively [11]) compared to 6-coordinated Bi^{3+} ions (103 pm [12]). Although the Mg^{2+} ion is the larger of the two, the Al^{3+} ion has the same valence as Bi^{3+} and occupies the octahedral site with higher coordination number (6). From these considerations it appears that Bi^{3+} ions would not easily substitute the host cations, nor if it did which site it would prefer. However, lanthanide ions are also large and since it has been suggested that Eu^{3+} ions occupy the Al^{3+} ions sites in spinel [13], that is the assumption made here. However, it has also been reported that Eu^{3+} ions may occupy the Mg^{2+} sites in spinel [14].

X-ray diffraction (XRD) measurements were made using a Bruker D8 Advance diffractometer (40 kV, 40 mA) with Cu Kα x-rays (154.06 pm). Scanning electron microscope (SEM) images of the particle morphology were obtained using a Shimadzu SSX-550 instrument. Diffuse reflection spectra were measured using a Lambda 950 UV–Vis spectrophotometer (with spectralon as a reference material) and photoluminescence (PL) properties were measured using a Cary-Eclipse fluorescence spectrophotometer and a 325 nm He-Cd laser.

3. Results and discussion

3.1. Structure

The XRD pattern of pure $MgAl_2O_4$ shown in figure 1 matches the standard JCPDS card no. 74-1132 well. The main peak of the cubic structure, corresponding to the crystal plane with Miller indices {311}, is centred at $2\theta = 36.86^{\circ}$.

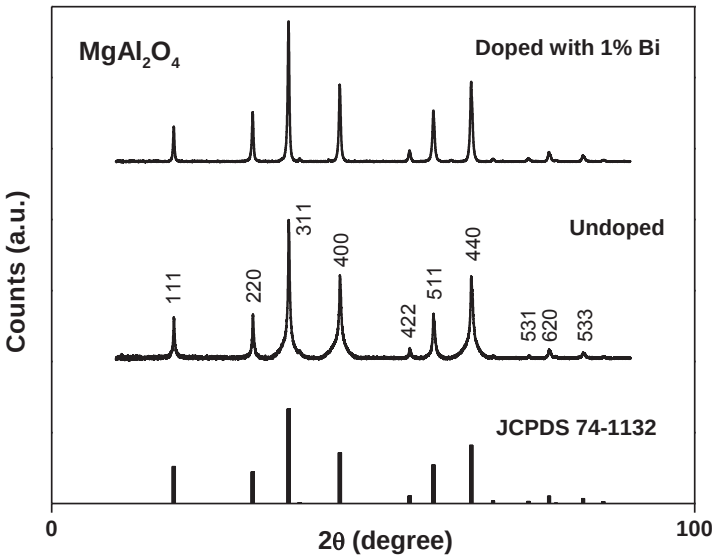

Figure 1. X-ray diffraction patterns of $MgAl_2O_4$ prepared by the combustion method, pure and doped with Bi.

The peaks are not Gaussian in shape, but are superimposed on a broad base (amorphous halo), indicating that the material between the crystallites is in a disordered state. For the sample doped with 1 mol% Bi no extra peaks are observed, nor was a shift of the peak positions detected. However, the peaks are now sharper, so the addition of a small amount of Bi has produced samples with better crystallinity. Bismuth oxide has a much lower melting point (817˚C) compared to Mg and Al oxides (> 2000˚C). Since the temperature during synthesis is estimated to be near 1500˚C [15], the addition of Bi may act like a flux, thereby improving the crystallinity. The average crystallite size D was estimated from the full-width at half-maximum β of the diffraction peaks at angle θ by using the Scherrer equation $D = \frac{0.9\lambda}{\beta \cos\theta}$ where λ is the x-ray wavelength and was about 25 nm for both the pure and doped samples. This value is approximate only, considering the non-Gaussian peak shape for the undoped sample and possible impurity or strain broadening of the peaks in the doped sample.

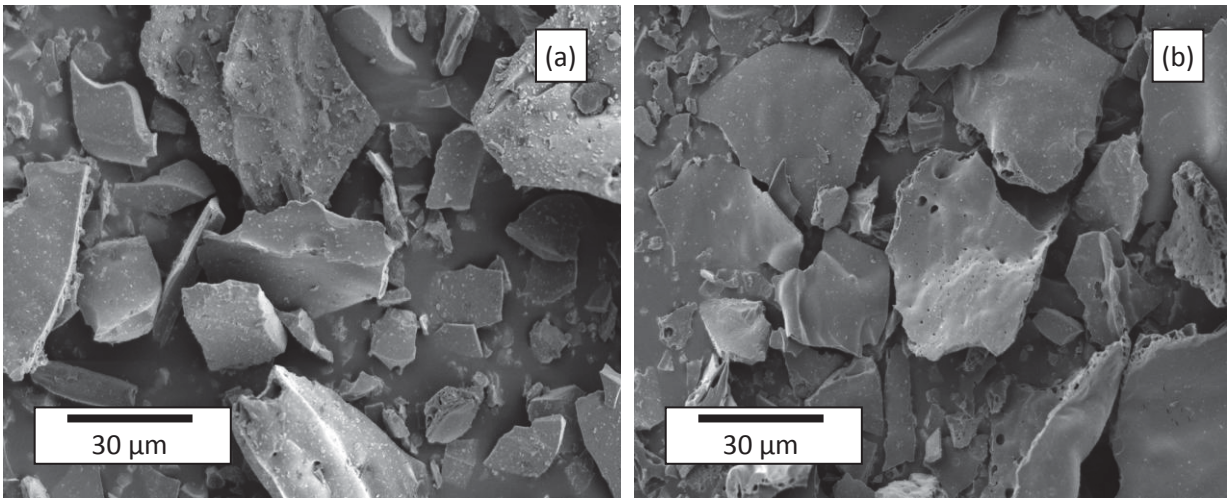

Figure 2. SEM images of $MgAl_2O_4$ powders obtained by the combustion method (a) undoped and (b) doped with 0.5 mol% Bi.

The SEM image in figure 2(a) shows the morphology of the undoped $MgAl_2O_4$ particles produced with the combustion process after grinding the foamy product with a mortar and pestle. The particle size varies up to several tens of microns and depends on the amount of grinding, but it is evident that

large flat, plate-like particles occur. This is characteristic of material made by combustion synthesis due to the large amount of gas that evolves during the reaction. The variation in thickness of the plates is due to the non-uniform distribution of temperature and mass flow in the combustion flame. Figure 2(b) shows that the sample doped with 0.5 mol% Bi, which has a similar morphology as the undoped sample. These SEM images show several pores in the particles which are formed by the escaping gases during the combustion reaction. These particles are much larger than the crystallite size estimated from the XRD results, indicating that the particles consist of smaller crystallites.

3.2. Optical properties

UV-Vis diffuse reflection spectroscopy was used to study the absorption characteristics of $MgAl_2O_4$ and the effects of Bi dopant measured with the Lambda 950 UV–Vis spectrophotometer at room temperature. Figure 3(a) compares the diffuse reflectance spectra of the different samples. For the undoped host (as-prepared) the reflectance remains high even for very short wavelengths, and the host only begins to absorb below 300 nm. The reflectivity R can be transformed into a value proportional to the absorption using the Kubelka-Munk function $K = (1 - R)^2/(2R)$, and the Tauc plot of $(Khv)^n$ against hv (with $n = 2$, applicable for a direct bandgap material) is given in Figure 3(b), from which the optical bandgap is estimated to be about 5.85 eV. When 1 mol% Bi is incorporated in the as-prepared material the reflectance spectrum changes dramatically, with absorption occurring at much longer wavelengths.

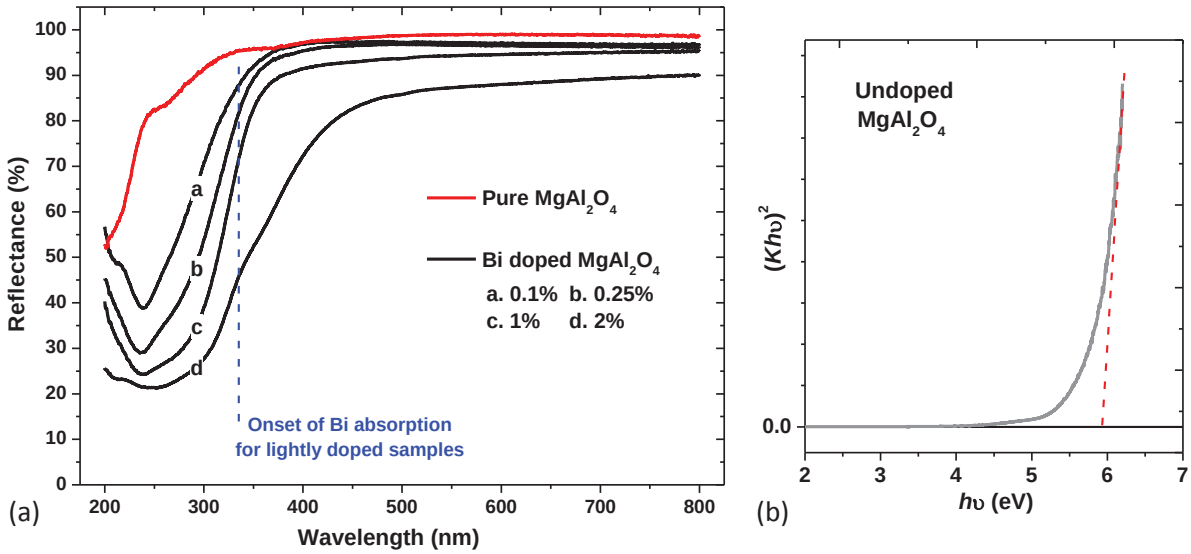

Figure 3. (a) Diffuse reflectance spectra of $MgAl_2O_4$ samples. (b) Estimate of the direct optical bandgap of undoped $MgAl_2O_4$ host using Kubelka-Munk function.

Figure 4(a) shows the PL excitation and emission spectra (for excitation with the xenon lamp at 335 nm) for the $MgAl_2O_4$:Bi (0.5 mol%) measured with the Cary-Eclipse fluorescence spectrophotometer, as well as the emission spectrum obtained when the sample is excited at 325 nm by a He-Cd laser. A single broad band of blue fluorescence emission was observed centred near 400 nm, which has an optimal excitation wavelength of 335 nm. This excitation wavelength corresponds to the onset of absorption in Bi doped $MgAl_2O_4$ samples as seen in Figure 3(a). The excitation and emission are attributed to $^1S_0 \leftrightarrow {}^3P_1$ transitions of Bi^{3+} ions, with a Stokes shift of 0.60 eV. For comparison, in Bi doped Y_2O_3 two emission bands occur at 410 and 520 nm with Stokes shifts of 0.31 and 1.24 eV respectively, which are attributed to Bi^{3+} ions in two different host lattice sites [5]. The single emission band in our results (figure 4(a)) indicates that only one site occurs for Bi^{3+} ions in spinel. Shoulders on both the low and high wavelength sides of the emission peak observed using the Cary-Eclipse (but not the laser PL system) require further study. Figure 4(b) shows that the luminescence intensity is a

maximum for a Bi^{3+} doping concentration of 0.5 mol%. Above that concentration the luminescence intensity decreases. While such an effect is often attributed to concentration quenching, the optimal concentration is rather low. Instead, it is suggested that the large size of the Bi^{3+} ions limits the amount of Bi that can be successfully incorporated into the host and that excess amounts of dopant leads to defects or quenching centres which then limit the luminescence intensity.

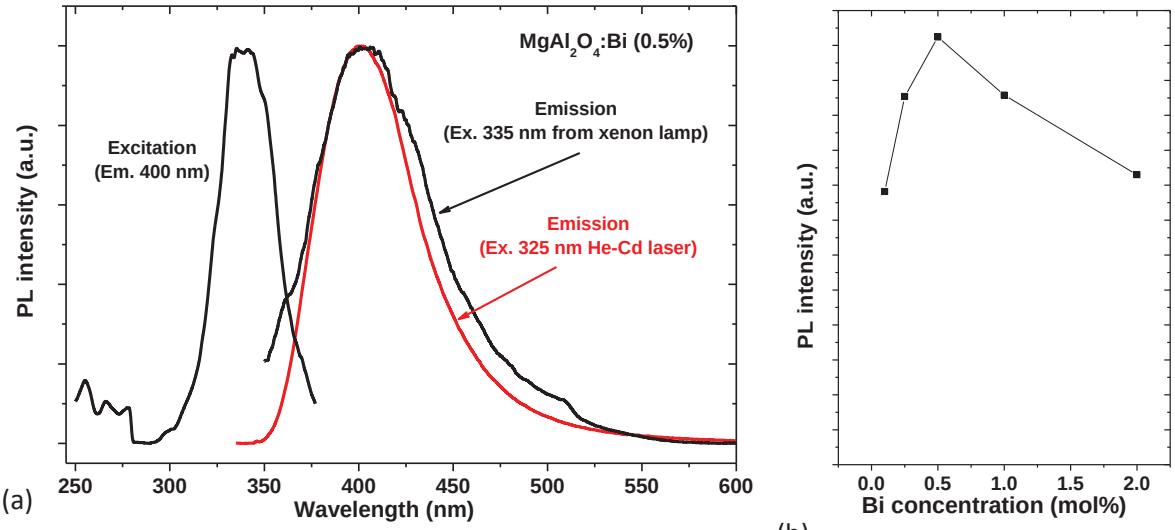

Figure 4. (a) Room temperature luminescence spectra of $MgAl_2C^{(b)}{}^{3+}$ (0.5 mol%) measured with the Cary-Eclipse fluorescence spectrophotometer (using a xenon lamp) as well emission when excited by a He-Cd laser. (b) Luminescence peak intensity as a function of Bi doping concentration measured with the Cary-Eclipse fluorescence spectrophotometer for excitation wavelength of 335 nm.

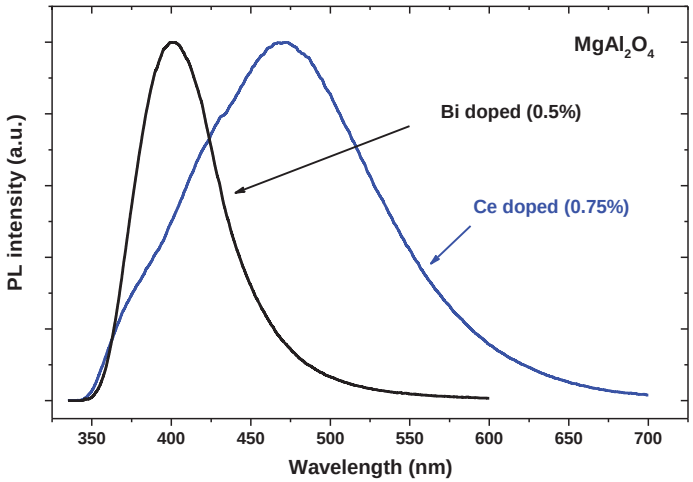

Figure 5. Comparison of the normalized emission spectra for Bi and Ce doped $MgAl_2O_4$, both excited with a He-Cd laser at 325 nm.

Figure 5 compares the PL emission spectra of Bi (0.5 mol%) and Ce (0.75 mol%) doped $MgAl_2O_4$, both excited by a He-Cd laser at 325 nm. The fluorescence of the Ce doped sample is a broad band centred near 470 nm and is attributed to the transition of electrons that have been excited to the 5d level returning to the $^2F_{7/2}$ and $^2F_{5/2}$ states of the 4f level, although the peaks corresponding to the two final states are not resolved. Ce is often used as a sensitizer for Tb ions in many phosphor hosts because it can be excited efficiently and also transfer energy to Tb as a result of an overlap of its emission spectrum with the f-f excitation bands of Tb. The Tb f-f excitation bands occur in almost the same position independent of the host, beginning near 380 nm and extending to shorter wavelengths.

This region is better overlapped by the Bi emission spectrum, suggesting that Bi may act as a good sensitizer for Tb. In addition, the Bi doped sample is more easily prepared, since it does not require annealing. The Ce doped sample had to be annealed in a reducing atmosphere of 4% H_2 in Ar at 1400˚C for 2 h in order to convert non-luminescent Ce^{4+} ions to trivalent Ce^{3+} ions before emission was obtained. Bi therefore seems a strong candidate to replace Ce in Ce,Tb co-doped samples, and co-doping spinel with Bi and Tb will therefore be the focus of future work.

4. Conclusion

Nanocrystalline Bi doped $MgAl_2O_4$ has been successfully synthesized by the combustion method. A broad band of blue fluorescence emission centred at 400 nm was observed for excitation at 335 nm, which is attributed to the $^3P_1 \rightarrow {}^1S_0$ transition of Bi^{3+} ions. The emission intensity was measured as a function of Bi doping concentration, with the maximum occurring for 0.5 mol% of Bi doping. The results indicate that doping $MgAl_2O_4$ with Bi ions may be an attractive alternative to doping it with Ce ions, which give broad blue-green luminescence in this host but requires reducing at a high temperature (1400˚C) to convert non-luminescent Ce^{4+} ions to the luminescent Ce^{3+} charge state. The emission of Bi also suggests that it may be act as a good sensitizer for Tb ions in $MgAl_2O_4$.

Acknowledgments

The authors thank H. Grobler at the University of the Free State Centre for Microscopy for assisting with SEM measurements. The financial support of the South African National Research Foundation, the Faculty of Natural and Agricultural Sciences of the University of the Free State and SARChI (Solid State Luminescent and Advance Materials) is acknowledged.

References

[1] Lim J H, Kim B N, Kim Y, Kang S, Xie R J, Chong I S, Morita K, Yoshida H and Hiraga K 2013 Appl. Phys. Lett. **102** 031104 (4 pages)
[2] Omkaram I, Seeta G and Buddhudu S 2008 J. Phys. Chem. Solids **69** 2066–2069
[3] Chen X, Ma C and Bao S 2010 Solid State Sci. **12** 857–863
[4] Yen W M, Shionoya S and Yamamoto H 2007 *Phosphor Handbook 2nd Ed.* (CRC Press, Boca Raton) p. 155
[5] Jacobsohn L G, Blair M W, Tornga S C, Brown L O, Bennett B L and Muenchausen R E 2008 J. Appl. Phys. **104** 124303 (7 pages)
[6] Porter-Chapman Y, Bourret-Courchesne E and Derenzo S E 2008 J. Lumin. **128** 87–91
[7] Fukada H, Konagai M, Ueda K, Miyata T and Minami T 2009 Thin Solid Films **517** 6054–6057
[8] Alvar E N, Rezaei M and Alvar H 2010 Powder Technol. **198** 275–278
[9] Xiaolin Z, Haijun Z, Yongjie Y and Zhanjie L 2004 Mater. Sci. Eng. A **379** 112–118
[10] Ianoş R and Lazău R 2009 Mater. Chem. Phys. **115** 645–648
[11] O'Neal H St C and Navrotsky A 1983 Am. Mineral. **68** 181–194
[12] Huang X Y, Ji X H and Zhang Q Y 2011 J. Am. Ceram. Soc. **94** 833–837
[13] Singh V, Haque M M and Kim D 2007 Bull. Korean Chem. Soc. **28(12)** 2477–2480
[14] Wiglusz R J, Grzyb T, Lis S and Strek W 2010 J. Lumin. **130** 434–441
[15] Patil, K C, Hegde, M S, Ratan, T and Aruna, S T 2008 *Chemistry of Combustion Synthesis, Properties and Applications Nanocrystalline Oxide Materials* (New Jersey, World Scientific) p. 45

Photoluminescent properties of $Sr_2SiO_4:Tb^{3+},Eu^{3+}$ phosphor

M A Tshabalala, H C Swart, O M Ntwaeaborwa
Department of Physics, University of the Free State, PO Box 339
Bloemfontein, ZA9300, South Africa

E-mail: ntwaeab@ufs.ac.za

Abstract. Terbium (Tb^{3+}) and europium (Eu^{3+}) co-doped strontium silicate ($Sr_2SiO_4:Tb^{3+}$, Eu^{3+}) phosphor was prepared via solid state reaction and its structure, particle morphology and photoluminescent properties were investigated. The X-ray diffraction patterns show phases associated with monoclinic (β-Sr_2SiO_4) and orthorhombic (α'-Sr_2SiO_4) structures of strontium silicate. Scanning electron microscopy images showed agglomerated particles with irregular shapes, encrusted with nanorods. The Tb^{3+} single doped Sr_2SiO_4 gave predominantly green emission at 546 nm ascribed to the $^5D_4$ - $^7F_5$ transition of Tb^{3+} while the Eu^{3+} single doped Sr_2SiO_4 gave a predominantly red emission at 616 nm ascribed to the $^5D_0$ - $^7F_2$ transition of Eu^{3+}. The Tb^{3+} - Eu^{3+} co-doped system gave simultaneous emission of blue, green and red with the green emission dominating the blue and the red. We speculate that the blue, green and red emissions can be balanced to get white emission by using a single excitation wavelength where the excitation spectra of these emissions overlap provided the right concentration ratio of Tb^{3+}:Eu^{3+} is used.

1. Introduction

Solid state host materials have attracted extensive attention because of their diverse applications in lighting. Strontium silicate (Sr_2SiO_4) is one of the examples of the solid state materials used as a host for rare-earth ions to prepare light emitting materials or phosphors. It has stable crystal structure, good mechanical strength and high thermal stability provided by the tetrahedral silicate $(SiO_4)^{2-}$ group [1]. Currently, rare earths orthosilicate based phosphors are being developed and investigated for application in white LEDs (Light emitting diodes) due to their high durability against high power, high temperature, and the packaging resins. The luminescent properties of many silicate phosphors such as $Sr_2SiO_4:Eu^{2+}$ (λ_{em} = 490 - 580 nm), $Mg_2SiO_4:Mn^{2+}$ (λ_{em} = 680 nm), $Ba_2SiO_4:Eu^{2+}$ (λ_{em} = 500 nm), $Ca_2SiO_4:Eu^{2+}$ (λ_{em} = 490 nm), $Zn_2SiO_4:Mn^{2+}$ (λ_{em} = 524 nm), and $Zn_2SiO_4:Tb^{3+}$ (λ_{em} = 545 nm) have been studied because of their ability to be efficiently excited by blue and ultraviolet (UV) lights [2-7]. Kim et. al investigated the white LEDs where a blue LED was combined with a yellow YAG:Ce phosphor which can be applied as a color-tunable phosphor for green or greenish white light emitting diode based on ultraviolet chip/phosphor technology [8]. Although YAG exhibits high luminescence efficiency and chemical stability, the combination of blue chip and YAG showed a lower color rendering index due to the lack of red color contribution [9, 10]. To get an excellent color index it is necessary to develop a single host phosphor that can absorb in the UV region and emit blue, green and red light simultaneously whose combination gives white light. The primary objective of this study was to develop such phosphor for LEDs by co-doping a single host (Sr_2SiO_4) with Tb^{3+} and Eu^{3+}.

When two kinds of rare-earths are co-doped into a single host material one of them sometimes acts as a sensitizer and the other acts as an activator for excitation energy transfer after photoexcitation. Examples such as $LaPO_4$: Tb, Ce phosphors where Ce^{3+} ions are efficient sensitizers to Tb^{3+} emission has been reported [11]. In this paper, we studied the structural and photoluminescent properties of $Sr_2SiO_4:Tb^{3+}:Eu^{3+}$ phosphor and we observed simultaneous emission of blue and green from Tb^{3+}, and red from Eu^{3+} when the phosphor was excited at different wavelengths using a monochromatized xenon lamp.

Preparation and Characterization Techniques

$Sr_2SiO_4:Eu^{3+}$, Tb^{3+} phosphors were prepared at a temperature of 1000 °C using solid state reaction process. The starting materials used in the preparation process were $SrCO_3$, SiO_2 and Eu_2O_3 and Tb_4O_7 which were weighed stoichiometrically and mixed thoroughly using a mortar and pestle. The concentrations of Eu^{3+} and Tb^{3+} were 0.5 mol% of Sr^{2+} ions in the Sr_2SiO_4 lattice. The mixture was sintered at 1000 °C for 3 hrs in air. The crystal structure and particle morphology were analyzed by an Advanced D8 Bruker powder X-ray diffractometer (XRD) and a Shimadzu Superscan ZU SSX-550 scanning electron microscope (SEM). The room temperature photoluminescence (PL) excitation spectra and PL emission were recorded from the Cary Eclipse fluorescence spectrophotometer using a monochromatized xenon lamp as the excitation source.

2. Results and discussion

2.1. Structure and morphology

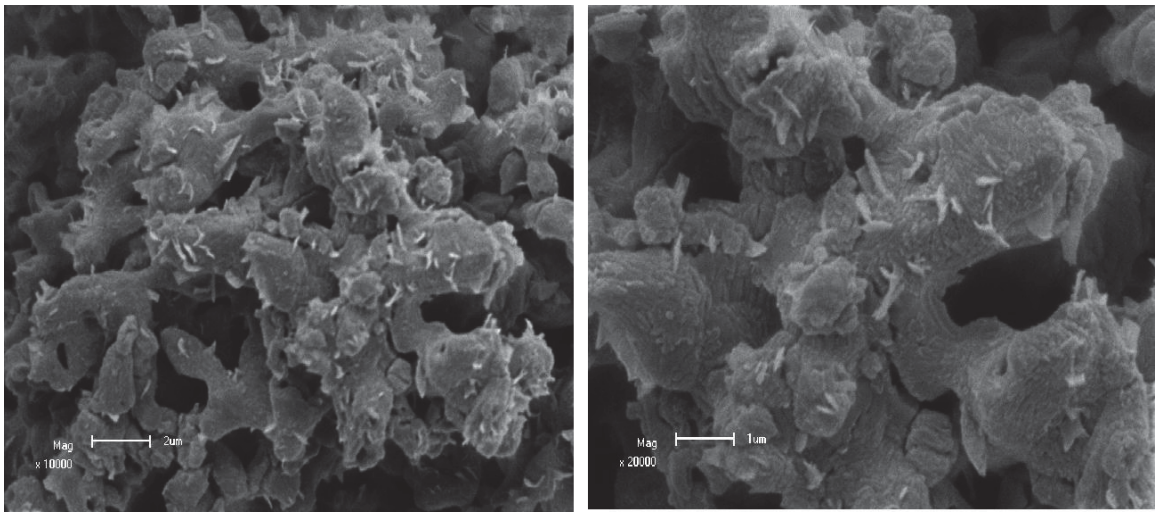

Figure 1. SEM micrographs of $Sr_2SiO_4:Tb^{3+}:Eu^{3+}$ at different magnifications.

It is known that the luminescence characteristics of phosphor particles depend on the morphology of the particles such as size, shape size distribution and defects. Figure 1 shows the SEM images of $Sr_2SiO_4:Tb^{3+}:Eu^{3+}$ with different magnification. The images show an agglomeration of irregular particles, which are encrusted with nanorods. The agglomeration of these particles is a result of overlapping of small particles.

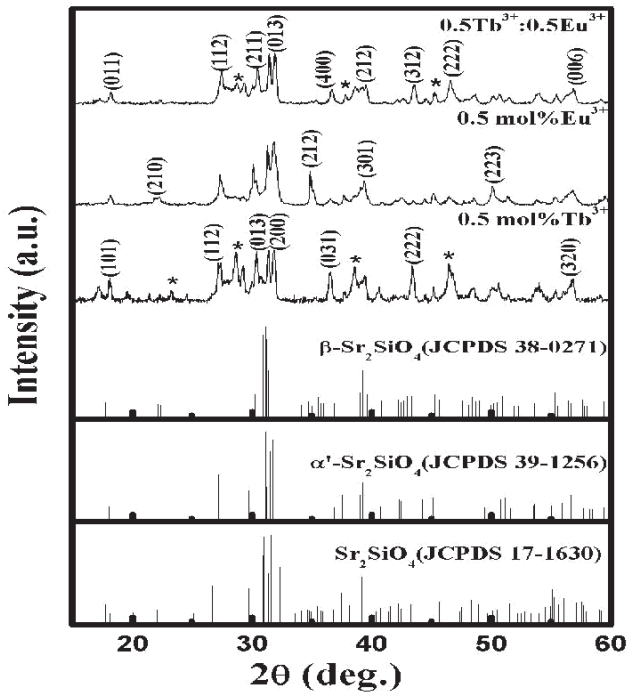

Figure 2. XRD spectra of $Sr_2SiO_4:Eu^{3+}$, $Sr_2SiO_4:Tb^{3+}$ and $Sr_2SiO_4:Eu^{3+}$, Tb^{3+} phosphors.

Figure 2 shows the XRD patterns of $Sr_2SiO_4:Eu^{3+}$, $Sr_2SiO_4:Tb^{3+}$ and $Sr_2SiO_4:Tb^{3+}:Eu^{3+}$ (Eu^{3+} and Tb^{3+} were 0.5mol %) phosphors. It has previously been reported that the crystal structures of α'-Sr_2SiO_4 and β- Sr_2SiO_4 are very similar, and the XRD peaks are therefore also similar in the JCPDS cards of both phases, and both structures can co-exist [12]. The α' and β phases are the two modifications of Sr_2SiO_4, and the phase transition between low temperature β phase and high temperature α' phase, whereas α' phase can also be stabilized at room temperature by substituting more Eu (0.1≥) or small amounts of Sr^{2+} [13]. As seen from Figure 2, $Sr_2SiO_4:Tb^{3+}$ is consistent with the standard JCPDS card no. 76-1630, while the $Sr_2SiO_4:Eu^{3+}$ agrees with the pure phase of α'-Sr_2SiO_4 (JCPDS card no. 39-1256). On the other hand, $Sr_2SiO_4:Tb^{3+}:Eu^{3+}$ agrees with the standard diffraction data of both α'-Sr_2SiO_4 (JCPDS card no. 39-1256) and β-Sr_2SiO_4 (JCPDS card no. 38-0271), so it can be concluded that the co-doped phosphor sample is a mixture of orthorhombic α'-$Sr_2SiO_4:Tb^{3+}:Eu^{3+}$ and monoclinic β-$Sr_2SiO_4:Tb^{3+}:Eu^{3+}$. There were secondary phases marked with asterisks (*), which may be due to the un-reacted $SrCO_3$ (JCPDS card no. 05-0418) and SiO_2 (JCPDS card no. 85-0462). These extra peaks indicate that the reaction of raw materials was not complete.

2.2. Photoluminescence analysis

Figure 3 illustrates the photoluminescent excitation (PLE) and (PL) emission spectra of $Sr_2SiO_4:Tb^{3+}$. The excitation spectrum was recorded when monitoring the green emission at 546 nm and the excitation peak at 227 nm is assigned to the f-f transitions of Tb^{3+}. The PL spectrum consists of one major emission peak at 546 nm which is assigned to the $^5D_4$ - $^7F_5$ transition of Tb^{3+}, the second major

emission at 382 (violet) and minor emissions at 415 nm (blue) and 435 nm (bluish-green) are due to $^5D_3$ - ^7F_J (J = 6, 5, 4) transitions of Tb^{3+}. Additional minor emissions at 490, 585 and 621 nm are due

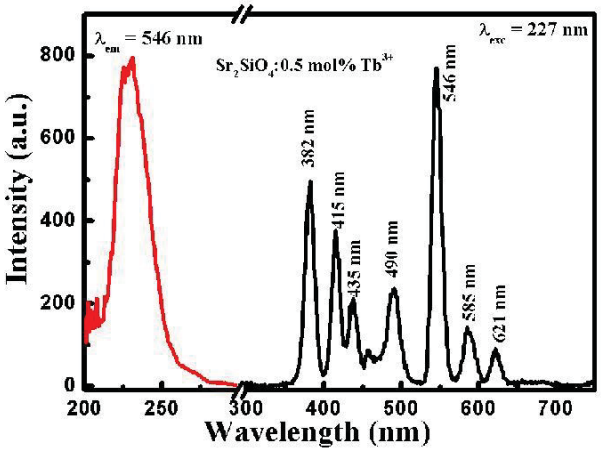

Figure 3. PLE and PL emission spectra of $Sr_2SiO_4:Tb^{3+}$ excited at 227 nm.

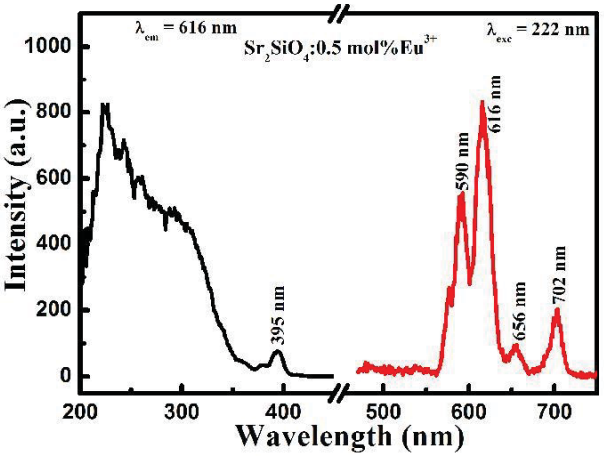

Figure 4. PLE and PL emission spectra of $Sr_2SiO_4:Eu^{3+}$ excited at 222 nm.

to $^5D_4$ - ^7F_J (J = 6, 4, 3) transitions of Tb^{3+}. Figure 4 shows the PLE and PL emission spectra of the $Sr_2SiO_4:Eu^{3+}$ phosphor. The excitation spectrum is asymmetrical with sharp peaks protruding from the broad excitation band extending from 200 - 400 nm [14]. The broad spectrum is due to $Eu^{3+} \rightarrow O^{2-}$ charge transfer states while the protruding sharp peaks are due to f→f transitions of Eu^{3+}. The PL spectra shows major red emission at 616 nm corresponding to $^5D_0$ - $^7F_2$ transition of Eu^{3+}, and a few minor peaks at 590, 656, and 702 nm assigned to the $^5D_0$ - ^7F_J (J = 1, 3, 4) transitions of Eu^{3+}.

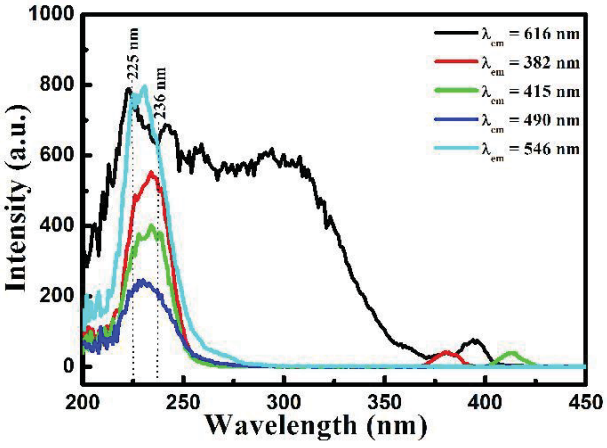

Figure 5. PLE spectra of $Sr_2SiO_4:Tb^{3+}:Eu^{3+}$ phosphor.

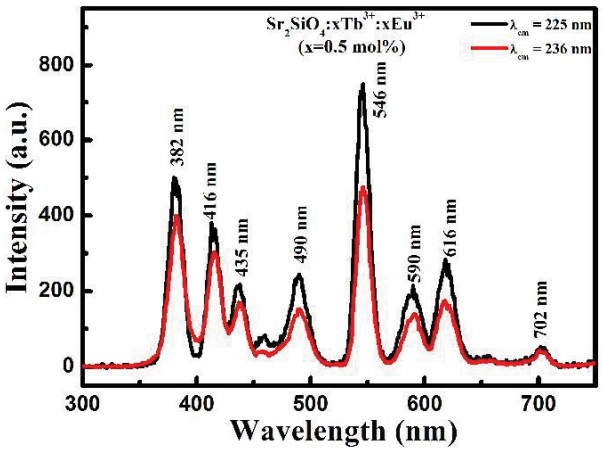

Figure 6. PL emission spectra of $Sr_2SiO_4:Tb^{3+}:Eu^{3+}$ phosphor.

Figure 5 and 6 shows respectively the PLE and PL spectra of $Sr_2SiO_4:Tb^{3+}$, Eu^{3+} (Eu^{3+} and Tb^{3+} were 0.5 mol %) phosphor. The PLE spectra were recorded when monitoring emission peaks at 382, 415, 546 nm coming from Tb^{3+} and 616 nm coming from Eu^{3+}. There were other weak excitation peaks located at 380, 394 and 413 nm when monitoring the peaks at 382, 616 and 415 nm which are related to the intra-4f

transitions of Eu^{3+} ions in the host lattice, which can be assigned to $^7F_0$-$^5G_2$, $^7F_0$-$^5L_6$ and $^7F_0$-$^5D_2$ transitions. The PL spectra where recorded when exciting the phosphor at 225 and 236 nm, which are the wavelengths where the Tb^{3+} and Eu^{3+} excitations are overlapping as shown in the figure. The reason for choosing these wavelengths was to find common wavelengths that can lead to simultaneous emission of blue and green emission from Tb^{3+} and red emission from Eu^{3+} as previously observed by Shaat et al [15]. For both excitations, the blue, green and red emissions from Tb^{3+} and Eu^{3+} were observed. However, the spectrum is dominated successively by the green and violet- blue emissions from Tb^{3+} when exciting at 225 nm and when exciting at 236 nm, the green emission is reduced considerably but the red emission from Eu^{3+} is still less intense than the green and violet-blue emissions from Tb^{3+}. The reason why Tb^{3+} emission are more intense especially when exciting at 225 nm is because of the fact that this excitation is in the same location as the f→f transitions of Tb^{3+} at 227 nm as observed in figure 3, and therefore it makes sense to have the green emission dominating other emissions. Although we could not get a balance of blue, green and red emission to get white light, these preliminary data serve as a good platform to help us get white emission in our future experiments. We believe that by getting a good balance of the concentration of Tb^{3+} and Eu^{3+} will improve the blue emission from Tb^{3+} and the red emission from Eu^{3+}. This study is in progress and we are optimistic about producing a single host phosphor that can be excited in the UV region and give white emission that can be used in LEDs.

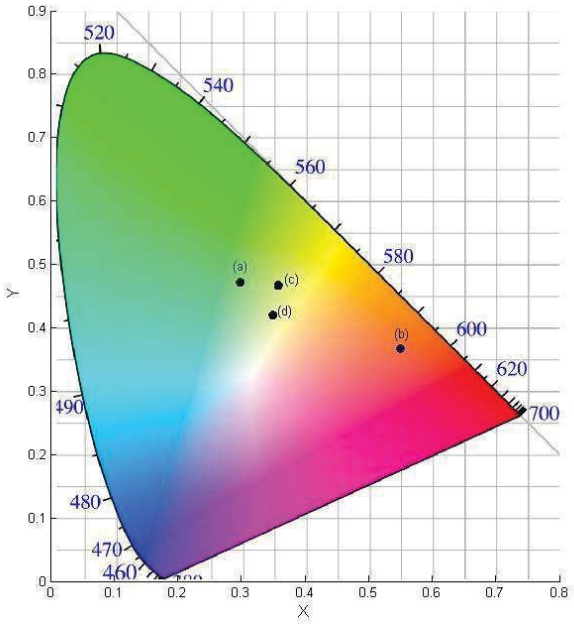

Figure 7. The CIE diagram showing coordinates of (a) Sr_2SiO_4:Tb^{3+}, (b) Sr_2SiO_4:Eu^{3+} and (c) Sr_2SiO_4:Tb^{3+}:Eu^{3+} (λ_{exc} = 225 nm) and (d) Sr_2SiO_4:Tb^{3+}:Eu^{3+} (λ_{exc} = 236 nm) phosphors.

To evaluate the material performance on color luminescent emission, Commission International de l'Eclairage France (CIE) x-y color coordinates diagram was used. Figure 7 showed the CIE coordinates of the Sr_2SiO_4:Tb^{3+},Eu^{3+} phosphor at different excitation wavelengths 225 and 236 nm which was found to be (c) x = 0.375, y = 0.446 and (d) x = 0.369, y = 0.424. The Figure also shows the chromaticity coordinates of (a) green Sr_2SiO_4:Tb^{3+} and (b) red Sr_2SiO_4:Eu^{3+}.

3. Conclusion

The phosphors $Sr_2SiO_4:Eu^{3+}$, $Sr_2SiO_4:Tb^{3+}$ and $Sr_2SiO_4:Tb^{3+}:Eu^{3+}$ were successfully synthesized by solid-state reaction technique. The particles were agglomerated and have irregular shapes. The structures of the materials showed phases associated with monoclinic (β-Sr_2SiO_4) and orthorhombic (α'-Sr_2SiO_4) structures of Sr_2SiO_4 with secondary peaks suggesting that some of the precursors did not react completely. Although the presently studied $Sr_2SiO_4:Tb^{3+}:Eu^{3+}$ did not give white emission that can be used in white LED, the study serves as a good platform to developing such phosphor in our future experiments.

Acknowledgement

The authors would like to thank the cluster programme of the University of the Free State and the South African National Research Foundation (NRF) and the South African national laser centre (NLC) for financial support. This work is based on the research supported by the South African Research Chairs Initiative of the Department of Science and Technology and National Research Foundation of South Africa.

References

[1] Naik Y P, Mohapatra M, Dahale N D, Seshagiri T K, Natarajan V, Godbole S V, 2009 *Journal of Luminescence* **129** 1225 - 1229
[2] Barry T L, 1968 *Journal of Electrochemical Society* **115** 1181 - 1184
[3] Poort S H M, Janssen W, Blasse G, 1997 *Journal of Alloys and Compounds* **260** 93 - 97
[4] Z T Kang, Y Liu, B K Wagner, R Gilstrap, M Liu, C J Summers, 2006 *Journal of Luminescence* **121** 595 - 600
[5] Kim J S, Park Y H, Kim S M, Choi J C, Park H L, 2005 *Solid State Communications* **133** 445 - 448
[6] Huang H, Yan B, 2006 *Applied Surface Science* **252** 2967 - 2972
[7] Kim J S, Jeon P E, Park Y H, Choi J C, Park H L, 2004 *Applied Physics Letters* **85** 3696 - 369
[8] Kim J S, Jeon P E, Choi J C, Park H L, 2005 *Solid state Communications* **133** 187 - 190
[9] Nag A, Kutty T R N, 2004 *Journal of Materials Chemistry* **14** 1598 - 1604
[10] Qiao Y, Zhang X, Ye X, Chen Y, Guo H, 2009 *Journal of Rare Earths* **27** 323 - 326
[11] Bourcet J C. Fong F K, 1974 *Journal of Chemical Physics* **60** 34 - 39
[12] Yanmin Q, Xinbo Z, Xiao Y, Yan C, Hai G, 2009 *Journal Rare Earths* **27(2)** 323 - 326
[13] Hu Y, Zhuang W, Hao J, Huang X, He H, 2012 *Open Journal of Inorganic Chemistry* **2** 6 - 11
[14] Li Y C, Chang Y H, Lin Y F, Chang Y S, Y-J Lin, 2007 *Journal of Alloys and Compounds* **439** 367 - 375
[15] Shaat S K K, Swart H C, Ntwaeaborwa O M, 2012 *Optical Materials Express* **2** 962 - 968

Effect of annealing on undoped and Ce, Dy, Eu, Ni-doped ZnO properties synthesized by sol-gel method.

J. Ungula, and F.B. Dejene

Department of Physics, University of the Free State (Qwaqwa), Private Bag x 13, Phuthaditjhaba, 9866

*Corresponding author e-mail address:dejenebf@qwa.ufs.ac.za

Abstract. In this study, undoped and Ce, Dy, Eu, and Ni-doped zinc oxide (ZnO) was prepared by sol-gel method from zinc acetate, metal nitrates and sodium hydroxide with water and ethanol as solvents and the effects of annealing temperature were investigated. The XRD measurements showed that the synthesized ZnO nanoparticles had the pure wurtzite structure. It is found that with annealing the crystallinity improved and the particle size increases while the band gap energy of the materials decreases. The reflectance spectra of the products show that the percentage absorption in visible range increases with annealing temperature. The SEM micrograph of ZnO revealed that the surface morphology dependents on both the dopant used and annealing temperature. Furthermore, PL spectra showed strong, broad and intense emission in visible region for Ce-doped ZnO samples while other dopants suppressed this green emission.

1. Introduction

In the last decade, ZnO has received much attention in view of optoelectronic device applications in the ultraviolet and the visible ranges due to its prominent properties, such as wide band gap (3.37 eV) and high exciton binding energy (60 meV) [1–3]. ZnO is also used in polycrystalline form for facial powder, piezoelectric devices, varistors, phosphors, and transparent conducting oxide films [3]. Besides the UV light-emitting properties, visible luminescence in a range of 400—700 nm for ZnO, was also studied widely because of the potential application in low-voltage field emissive display [4]. On the other hand, the intrinsic properties of ZnO have also been improved by controlling their preparation conditions [5–7]. Doping with selective elements offers an effective method to enhance and control the electrical and optical properties of ZnO nanostructures, which is crucial for its practical application. It is also suggested that annealing at temperatures between 500℃ and 700℃ leads to an improvement in the crystalline quality (due to the higher UV/DLE intensity ratio compared to the as grown sample). It is expected that at these temperatures, the energy supplied by annealing is sufficient to remove any surface adsorbed impurities and so it becomes energetically favorable for atoms to move into proper sites, leading to an improvement in the crystal quality [8]. In this report the effect of the annealing temperature on the particle size, morphology and photo-luminescence (PL) properties of the synthesized undoped and Ce, Dy, Eu, Ni-doped ZnO nanoparticles were investigated systematically.

2. Experimental

Zinc acetate reacted with sodium hydroxide in a molar ratio of 0.02mol to 0.08mol where the mixture of water and ethanol were used as solvent. For the production of pure ZnO nanostructures solution of NaOH was titrated against Zinc acetate dehydrate slowly and stirred vigorously for 2 hours, and then kept in a cabinet for some hours to form gel-like solution. This was rinsed using heptane and ethanol

mixture, filtered and dried in oven for 1 hour. The dried sample was separated into two portions. The first portion was left to dry further at room temperature and the second portion annealed for 1 hour at 600℃ in a furnace (air atmosphere). For the production of doped ZnO nanoparticles, it was performed by adding acetates of Ce, Eu, Dy and Ni to Zinc acetate dehydrate. The mixture so formed was treated through the same procedure for pure ZnO to obtain both the annealed and as prepared samples of the nanoparticles. The molar ratio of dopants to zinc was kept constant at 2%.The structure of ZnO nanoparticles was characterized by XRD on Bruker D8 X-ray diffractometer using Cu Kα radiation (λ=1.5406 Å) in the 2θ range from 20° to 80°.The surface morphology was studied with a SEM using a Shimadzu model SSX-550 superscan Scanning Electron Microscope. PL measurement was performed on a Cary Eclipse fluorescence spectrophotometer; model LS-55 with a built-in 150W xenon flash lamp as the excitation source and a grating to select a suitable excitation wavelength.

3. Results and discussion

3.1 SEM Analysis

SEM micrographs for annealed and variously doped ZnO nanoparticles are shown in the figure 1. Clearly the powders are in the form of agglomerates with non-uniform shapes and sizes caused by the difference in type of dopants. The SEM observation revealed nanorods and nanoparticles of ZnO depending on the dopant used. For calcinations, the particles showed increment in size, because at higher calcinations temperature the particles agglomerate to produce larger particles in size. It was also observed that the sizes of ZnO nanoparticles became bigger with annealing. In Figure 1 (a), Ce-doped ZnO shows relatively larger nanorods

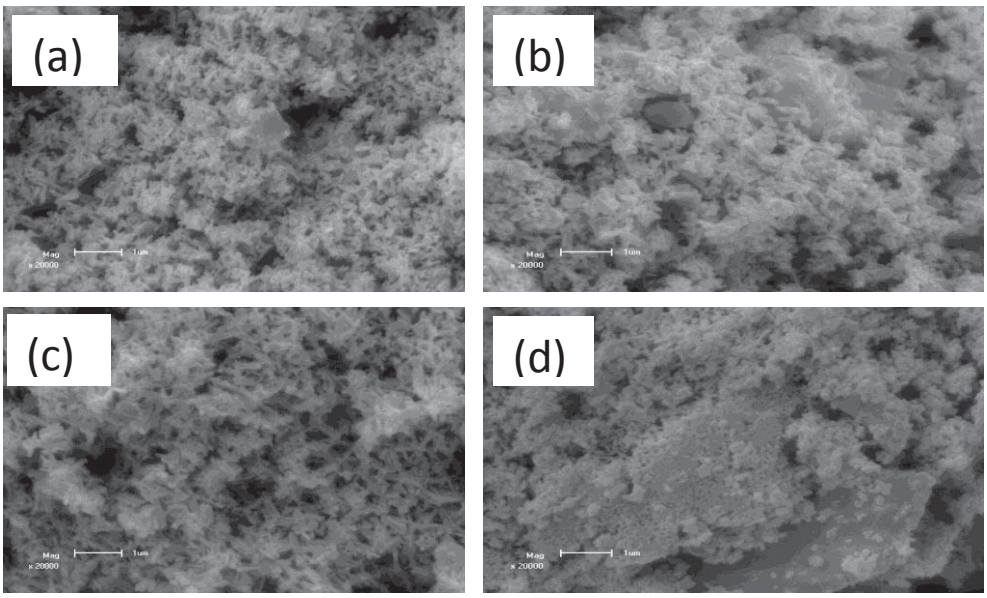

Figure 1: SEM images of annealed (a) Ce-doped ZnO (b) Eu-doped ZnO (c) Dy-doped ZnO (d) Ni-doped ZnO nanostructures.

3.2 XRD Analysis

The information about the crystal structure and the shape of ZnO nanostructures were obtained from XRD measurements. Figures 2 and 3 show that the diverse morphologies observed by SEM and the presence of the doping species do not seem to have an influence on the crystalline phase of the different samples. As revealed by XRD analysis, all ZnO nanostructures, either undoped or doped,

show the typical hexagonal wurtzite structure (with respect to the standard card-JCPDS No. 36-1451), and the sharp diffraction peaks indicate the formation of highly crystalline nanostructures. It was found that with annealing the crystallinity of the samples improved and particle sizes increase as shown by the increased intensity of peaks and narrowing of peak widths, respectively according to Fig. 2(a), while decreased peak intensity and broadening of peak width was observed for unannealed samples as shown in Fig 2(b). The crystallite size of as-prepared doped ZnO nanoparticles calculated using the Debye Scherer formula are in the range of 31.3 - 38 nm, while that of the annealed ZnO nanoparticles are in the range 31.4 - 39.1 nm. There is no substantial increase in grain size after annealing for 1 hour at 600°C. Apparently, the annealing time is too short to cause an appreciable increase in the grain size. The improvement of crystallinity after annealing may be due to defect healing and removal of adsorbed impurities as is stated earlier. This proves that the temperature has a slight impact on the crystalline size of ZnO nanoparticles as increase in annealing temperature enhances the kinetic energy of the reaction system, and subsequently increases the number of particle collusions. The increase in particle collusion decreases time to reach a stable size. According to aggregation theory time to reach a stable size is inversely proportional to particle size [9]. Therefore the particle size increases with annealing temperature.

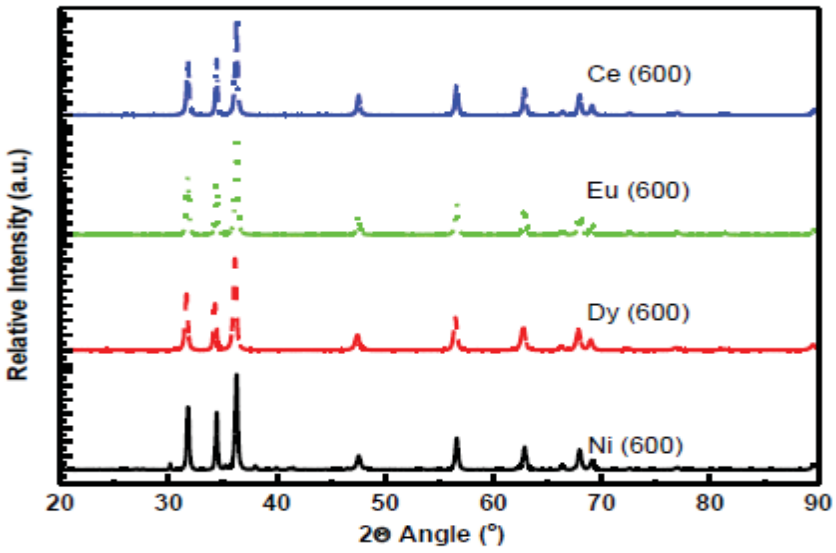

Figure 2 (a): XRD spectra of annealed doped ZnO nanoparticles

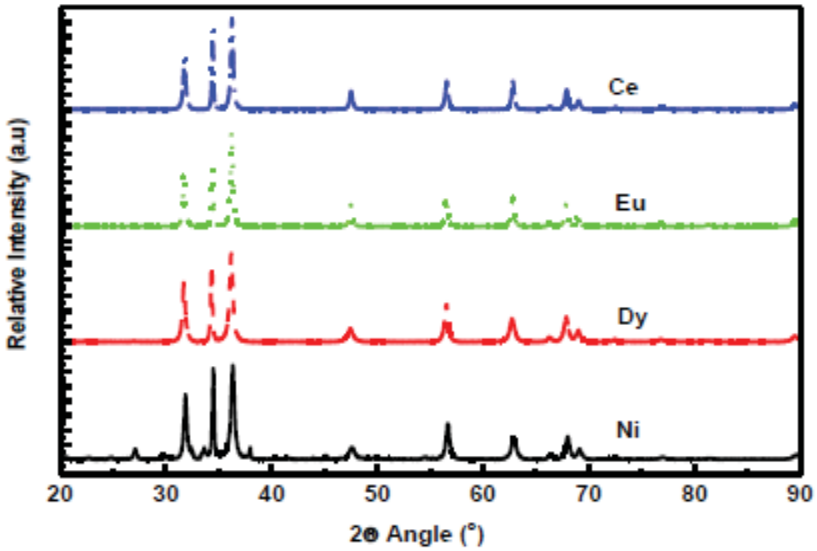

Figure 2 (b): XRD spectra of unannealed doped ZnO nanoparticles

3.3 Photoluminescence

Figure 3 shows the PL measurements recorded with excitation wavelength set at 364 nm. The undoped ZnO sample exhibits a weaker emission band at 380 nm and a broad intense band at around 560 nm in the UV and visible region, respectively. The near-band-edge (NBE) emission in the UV region is attributed to the recombination of free excitons, while the broad green emission is believed to be related to deep levels caused by intrinsic defects such as oxygen vacancies, Zn interstitials, or their complexes [10, 11]. The intrinsic luminescence spectrum of ZnO may vary slightly from sample to sample depending on the syntheses and processing conditions, but it always occurs in the green region of the spectrum. Emission of Eu-doped ZnO demonstrates a broad emission band at 554 nm in the visible range due Eu^{2+} as a result of the *f-d* transition [12]. A weaker emission appearing at ~618 nm is ascribed to the Eu^{3+} emission. The PL emission of Ce^{3+}-doped ZnO depicts broad emissions in the visible region. Two luminescence bands contribute to this two broad band with the maximum at 504 and 538 nm. It is well known that the emission from Ce^{3+} is either in the UV or visible region, consisting typically of two main luminescent centres [13] which corresponds to the transitions from the lowest ^{5}d1 crystal field component ($^2D_{3/2}$) to the two components ($^2F_{5/2}$ and $^2F_{7/2}$) of the 4f ground state. The PL emission spectra from ZnO:Ce^{3+} is very similar to that of ZnO but with slight blue shift. Evidently, the positions and intensities of the PL peaks were both affected by annealing temperature as the intensity of emission peaks of the undoped and doped-ZnO nanoparticles increase with annealing temperature. This shift of band-gap energy was believed to originate from the change of tensile stress because of lattice distortion. Similarly, the visible luminescence of ZnO nanoparticles increases with annealing. No emission bands were observed for Dy and Ni-doped ZnO samples.

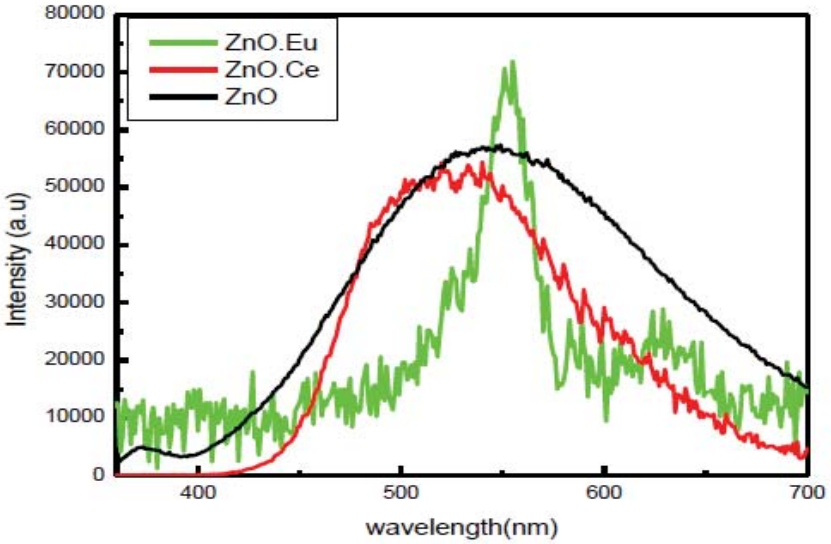

Figure 3: PL of undoped ZnO, Ce and Eu-doped ZnO nanoparticles

3.4 Optical properties

The absorption of the ZnO was obtained using the UV-Visible spectra. In general, absorption spectra probe the crystallite internal molecular orbital and provide information concerning size and particle composition [9]. Figure 4(a) shows the optical reflectance spectra of doped ZnO nanostructures. The UV measurements depict a slight shift in absorption edge confirming the changes in particle sizes. The energy band gap of these materials was estimated using the Kubelka-Munk function emission function [10] for direct transitions. The band gap energy of the ZnO nanostructures prepared with different types of dopant was found to vary between 2.9 and 3.1 eV as shown in Figure 4(b). The estimated band gap energy is lower than that of bulk ZnO (3.37 eV). This band gap reduction may be due to surface defects density of the synthesised undoped and doped ZnO nanostructures [14]. The absorption in the visible region changed with the changes in types of dopant. Ni-doped ZnO was seen to absorb the largest percentage of excitation energy, while Eu-doped ZnO absorbs the least.

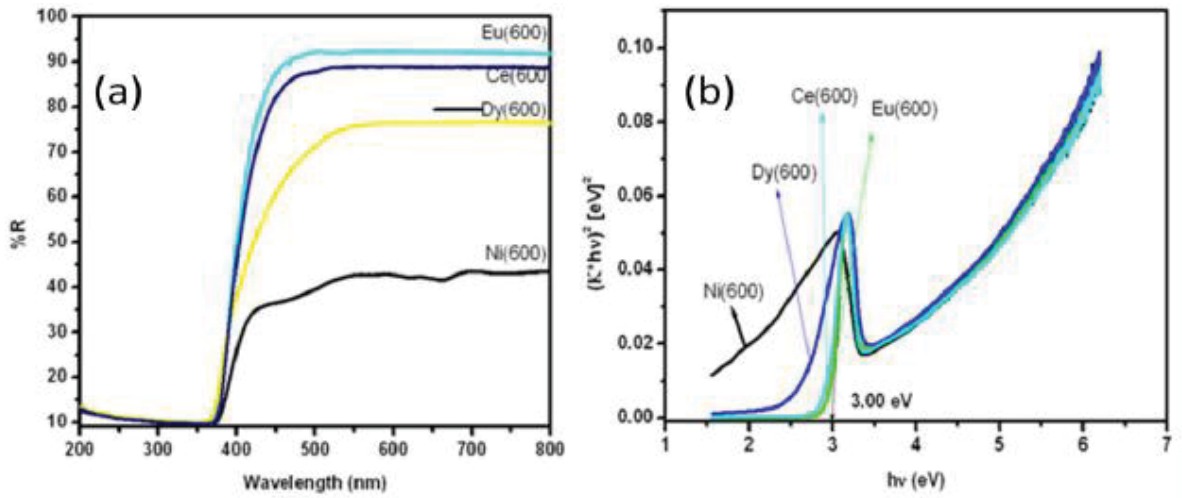

Figure 4: (a) Uv-Vis reflectance and (b) band gap energy spectra of annealed Ce, Dy, Eu and Ni-doped ZnO nanoparticles

4. Conclusion

In summary, the presented data suggest optical-structural correlations in nanosized undoped and doped ZnO materials in terms of crystallinity, defects, and quantum confinement. These properties were revealed by the XRD, SEM, UV-Vis and PL measurements. The incorporation of dopants can influence the morphology of ZnO nanostructures due to defect formation and, consequently, the intensity of the light emission. The effect of post-growth annealing on the structural properties of the nanostructures was determined to lead to an improvement in the crystalline quality. The strong UV and weak green bands emission imply a good optical quality. These results show a great promise for the application of annealed and doped ZnO nanoparticles with low expense and good quantities of electronic and optical properties.

Acknowledgements

Financial support from the National Research Foundation (NRF) of the government of South Africa and the services of the research equipment of University of Free State, Physics department used in this study are gratefully acknowledged by the authors.

References

[1] Liu Y, Yang J H, Guan Q F, Yang L L, Zhang Y J, Wang Y X, Feng B, Cao J, Liu X Y, Yang Y T, Wei M B, 2009 *J. Alloys Compd*., **486** 835.
[2] Wang D Y, Zhou J, Liu G Z, 2009 *J. Alloys Compd.*, **481** 802.
[3] Reynolds D C, Look D C, Jogai B and Morkoç H, 1997 *Solid State Commun.* **101** 643
[4] Leverenz V W, An Introduction to Luminescence of Solids, Dover, New York, 1968.
[5] Xiong G, Wilkinson J, Mischuck B, Tuzemen S, Ucer K B and Williams R T , 202 *Appl. Phys. Lett.* **80** 1195
[6] Ma Y, Du G T, Yang S R, Li Z T, B. Zhao J, Yang X T, Yang T P, Zhang Y T and Liu D, 2004 *J. Appl. Phys.* **95** 6268
[7] Oh M-S, Kim S-H and Seong T-Y, 2005 *Appl. Phys. Lett.* **87** 103
[8] Tan S T, Sun X W, Zhang X H, Chua S J, Chen B J, Teo C C, 2006 *J. Appl. Phys.* **100** 033502
[9] Chandrasekhar S,1943 Rev. Mod. Phys. **15** 1
[10] Ahn C H, Kim Y Y, Kim D C, Mohanta S, K, Cho H K 2009 *J. Appl. Phys.* **105** 013502
[11] J. Lee, A.J. Easteal, U. Pal, D. Bhattacharyy, 2009 *Current Applied Physics*, **9** 792–796.
[12] Bhargava, R N, Chhabra V, Som T, Ekimov A, Taskar, N. *Phys.* **2002** *Status Solidi B* **229** 897
[13] Koao L F, Swart H C, Coetsee E, Biggs M M, Dejene F B, 2009 *Physica B*, **404** 4499 –4503.
[14] Z. Wang, H. Zhang, L. Zhang, J. Yuan, C. Wang, 2003 *Nanotechnology* **14** 11.

A preliminary study of Thermoluminescence of beta-irradiated $SrAl_2O_4:Eu^{2+}$, Dy^{3+} phosphors

AH Wako[1], BF Dejene[1] and HC Swart[2]
[1]Department of Physics, University of the Free State (QwaQwa Campus), Private Bag X13,Phuthaditjhaba, 9866, South Africa
[2]Physics Department, University of the Free State, PO Box 339, Bloemfontein, 9300, South Africa

E-mail: wakoah@qwa.ufs.ac.za

Abstract. Eu^{2+} doped and Dy^{3+} co-doped strontium aluminate ($SrAl_2O_4:Eu^{2+},Dy^{3+}$) phosphors were synthesized by the solution - combustion technique at 500 ^oC using urea as a reducer, a widely known method for preparing nano sized phosphors. $Sr(NO_3)_2$, $Al(NO_3)_3.9H_2O$, CH_4N_2O, $Eu(NO_3)_3.5H_2O$ and $Dy(NO_3)_3$ were used as raw materials for the preparation of the $SrAl_2O_4$ (RE: Eu, Dy) precursor. The thermoluminescence (TL) properties of beta (β) irradiated $SrAl_2O_4:Eu^{2+},Dy^{3+}$ have been studied. The electron-trapping properties in terms of TL glow curves are discussed in detail. The TL intensity was recorded for different beta doses at different heating rates. The influence of repeated measurements on the same sample on peak temperature and TL intensity was also investigated. Different kinetic parameters like activation energy and frequency factor are calculated for different TL glow curves. We have also calculated the trap depth with the variable heating method.

1. Introduction

When an insulator, a semiconductor or a phosphor with deep traps is exposed to ionizing radiation for a while at rather low temperatures, it absorbs energy from the radiation and the (deep trap) defects become excited. When the temperature of the material is raised, it shows an increased after-glow called thermally stimulated luminescence (TSL) due to the recombination of electrons thermally reactivated from the deep traps where the energy is converted to luminescence and released in the form of visible light. This phenomenon is known as thermoluminescence (TL) [1]. The heat only acts as a stimulant whereas the ionizing radiation plays the role of an exciting agent. During the process of irradiating a material with α-rays, β-rays, UV-rays, χ-rays, or γ-rays, part of the irradiation energy is used to transfer electrons to traps [2]. Some of these trapped electrons locate themselves at a depth (E) below the conduction band. The trap levels or centers play a significant role in energy storage for persistent photoluminescent and thermoluminescent phosphors. This radiation energy stored in the form of trapped electrons is released by raising the temperature of the material and the released energy is converted to luminescence. This trapping process followed by the release of the stored energy in thermoluminescent materials is widely applied in radiology such as in ionizing radiation dosimeters. All phosphorescent materials may have a minimum threshold temperature for release of previously stored energy; but many have a minimum triggering temperature below normal temperatures and are not normally thought of as thermoluminescent materials [3]. Cooling a TL material and reheating it

does not make it emit light. It should first be exposed to radiation and then heated for it to emit light again. The storage capacity of a TL material makes it, in principle, suitable for dosimetric applications [4]. Materials that exhibit TSL include glasses, ceramics, plastics and some organic solids.
In order to obtain information about the luminescence process of phosphors and to apply them in various fields, knowledge of defects or traps and their location in the band gap of these materials is very important. TL measurement is a very important and convenient method of investigating and providing information concerning the nature of traps and trapping levels in crystals. The glow curve which is a representation of the temperature dependence of the emission intensity is a good means to measure the trap depth (i.e., the activation energy of traps) [5]. During TL measurements the irradiating source is cut off and the thermally stimulated luminescence recorded while gradually increasing the temperature. Various parameters of the trapping process such as activation energy (E_T), amount of trap (n), trapping rate, etc, are then deduced by analysing the shape and position of the obtained TL glow curve [6]. When a TL glow curve having several overlapping peaks is obtained, deconvolution is carried out in order to isolate one of the glow peaks from the others to enable the calculation of these parameters. The term "peak shape method" is reserved in the TL literature for such methods, although there are other methods for finding E_T which are also based on the glow-peak shape (i.e. curve fitting methods) [7, 8]. The work by Chen [9] is a reference point in the derivation of the peak shape methods.
$SrAl_2O_4:Eu^{2+},Dy^{3+}$ has been studied by many researchers for its use as luminescent material. Nevertheless, there are few reports dealing with its use as a TL material. In this study we report on preliminary results on the TL behaviour of the as-prepared $SrAl_2O_4:Eu^{2+},Dy^{3+}$ synthesised by solution-combustion method at an initiating temperature of 500 ^oC to find out its suitability in various TL applications. In particular this study is concerned with the dosimetric analysis of the $SrAl_2O_4:Eu^{2+},Dy^{3+}$ TL glow curves such as the dose response. Also kinetic analyses were carried out using variable heating rate method to study the energy levels and the discrete trapping and recombination centres within the phosphor material.

2. Experimental

2.1. Synthesis

The $SrAl_2O_4:Eu^{2+},Dy^{3+}$ phosphor was synthesized using the solution - combustion method. The starting raw materials used in the experiment included various proportions of analytical pure grade Sr $(NO_3)_2$, $Al(NO_3)_3.9H_2O$, $Eu(NO_3)_3.5H_2O$, $Dy(NO_3)_3$, and urea $(CO(NH_2)_2)$. The raw materials were weighed according to the chemical composition of $SrAl_2O_4:Eu^{2+},Dy^{3+}$, dissolved in 10 ml of de-ionized water and thoroughly mixed using a magnetic stirrer for 15 minutes without heating to obtain a uniform saturated aqueous solution.
The solutions were then poured into China crucibles and placed one at a time in a muffle furnace pre-heated to 500 ^0C. The mixture ignited and a fast, self-sustaining combustion reaction took place. At first, the solution boiled losing all the water in the form of steam followed by decomposition letting off large amounts of gases (oxides of carbon, nitrogen and ammonia). The mixture then frothed and swelled enormously forming foam, then spontaneous ignition and smouldering occurred which gradually led to an explosion which ruptured the foam with a flame that glowed to incandescence. The product of combustion was a voluminous white $SrAl_2O_4:Eu^{2+},Dy^{3+}$ foam. The foam was taken out of the muffle furnace, cooled then milled resulting in a dry, and usually crystalline, fine white oxide powders. The whole combustion process took about 5 minutes. The powders were stored in transparent glass sample bottles for characterization.

2.2. Characterization

TL measurements were made on the $SrAl_2O_4:Eu^{2+},Dy^{3+}$ phosphor. The samples were prepared into discs of 5 mm in diameter and 1 mm thick. A β-source based on the ^{90}Sr isotope was used for TL excitation prior to heating. The radiation dose rate at the location of the samples was 10.75 Gy per minute. TL measurements were taken in a nitrogen atmosphere using a Risø model TL/OSL-DA-20 Luminescence Reader. The TL was detected by an Electron Tubes Ltd model 9235QB photomultiplier through a BG-39 band-pass filter (transmission band 340–620 nm FWHM). Samples were heated from 30 to 200 ^0C at various heating rates and after various radiation doses.

3. Results and Discussions

3.1. Dose response

To check the dose dependence effect on the peak positions, the samples were irradiated with doses from 26 to 185 Gy and the TL measured at a constant linear heating rate of 5 $^0C\ s^{-1}$. Figure 1 shows the effect of dose variation on TL intensity with different irradiation doses. The position of the peak temperature, T_{max}, is observed to shift towards higher temperatures from 86-95 ^0C while the TL intensity increased with increased radiation dosage levels.

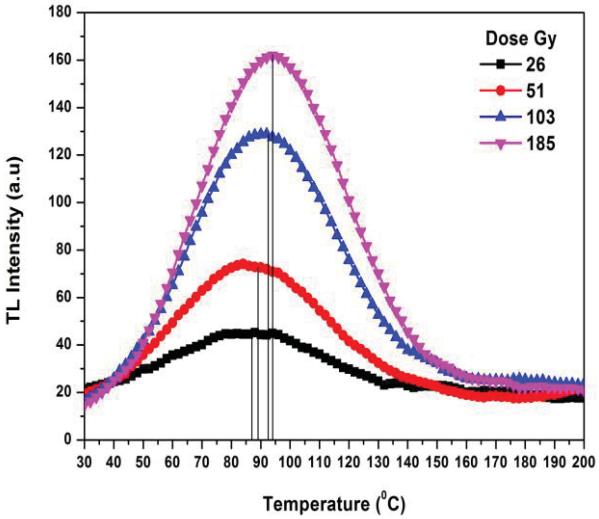

Figure 1. TL glow curves of $SrAl_2O_4:Eu^{2+},Dy^{3+}$ phosphor showing effect of irradiation doses on TL intensity.

From figure 2 (a) it can clearly be seen that the peak intensities increase linearly with a slope of 1.0 with higher doses. The glow curve intensity (I) during heating has been found to be proportional to the concentration n_o of the trapped charge carriers [10]. The increase in TL intensity with increase of absorbed radiation dose can be attributed to the increase in the number of electrons in the excited state, and hence recombination, with increasing radiation dose. In TL theory [8], the peak temperatures (T_{max}) of glow peaks are expected to be influenced only by changes in the heating rate, but the contrary is seen in figure 2(b) which shows an exponential dependence. This might also be attributed to the population of the trap centers and luminescence centers. The higher concentration of defects that generate non-radiative states within the band gap could be responsible for decrease in the T_{max} rate of change which tends to saturation with increased doses. More measurements, however, are needed at other doses to make a final conclusion.

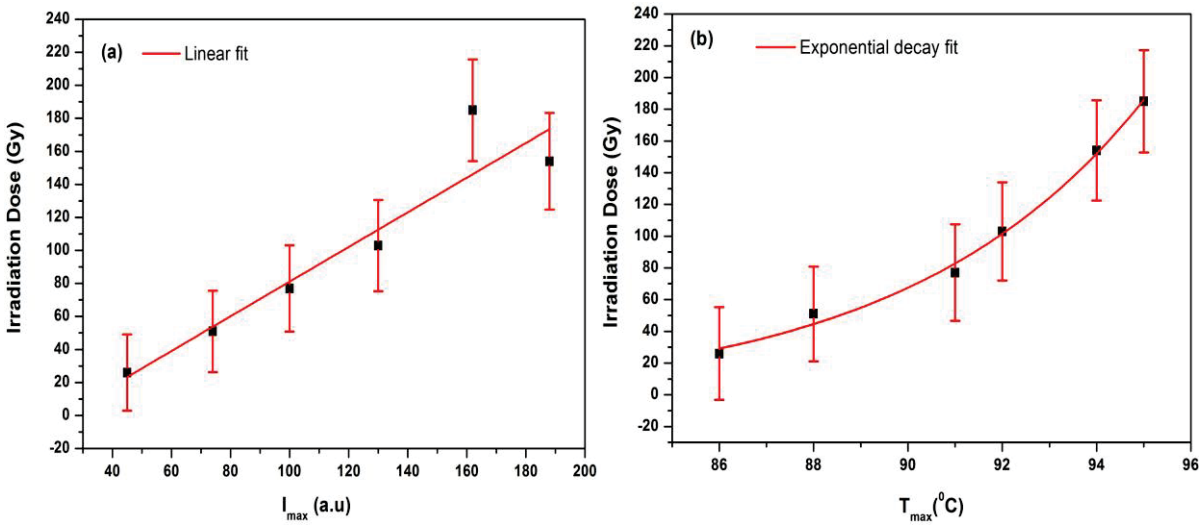

Figure 2 Effect of irradiation doses on **(a)** I_{max} and **(b)** T_{max} peaks of the TL glow curve of the $SrAl_2O_4:Eu^{2+},Dy^{3+}$ phosphor.

3.2. Variable heating rates

This method was used to determine the kinetic parameters in this investigation. The behaviour of the glow curve was monitored as the heating rate increased from 1 $^0Cs^{-1}$ to 5 $^0Cs^{-1}$. The glow curves of figure 3(a) shows the effect of these heating rates. The peak temperatures (T_{max}) of the glow curves are seen to shift to the higher temperature side from 72 to 82 ^{0}C with increased heating rate. This shift of T_{max} is associated with a deeper trap depth [11]. Glow curve peaks at higher temperature are as a result of deeper traps which have higher activation energy E_T. Hence, larger heat energy is required to free charge carriers from the deep traps.

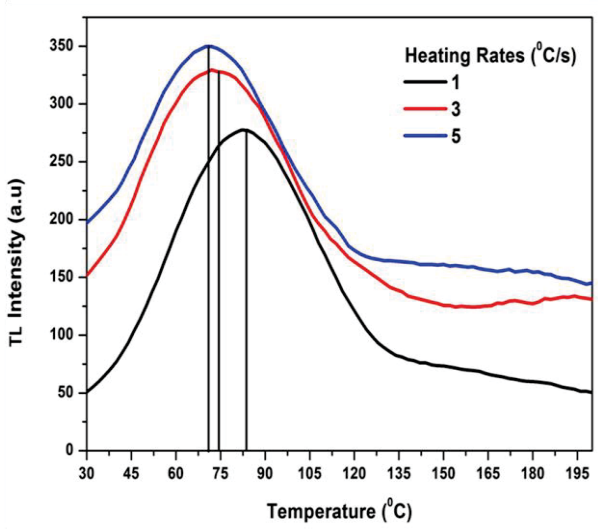

Figure 3. Effect of heating rate on TL intensity and Temperature of $SrAl_2O_4:Eu^{2+},Dy^{3+}$ phosphor.

The trap depths were calculated by the Hoogenstraaten method, which relates the TL peak temperature and heating rate [12]. The depth of each trap was determined using the following equation:

$$\ln\left(\frac{T_m^2}{\beta}\right) = \left(\frac{E}{k}\right)\frac{1}{T_m} + \ln\left(\frac{E}{sk}\right) \quad (1)$$

where β is the heating rate, T_m is the peak temperature (T_{max}) of the glow curve, E is the trap depth, k is the Boltzmann constant, and s is a frequency factor or "escape frequency" of the trapped charge carriers. A plot of $\ln\left(\frac{T_m^2}{\beta}\right)$ versus $\frac{1}{T_m}$ gives a linear relation with slope $\left(\frac{E}{k}\right)$ as shown in figure 4. The solid line through the data points gives the line of best fit for equation (1). Hence it is possible to obtain the trap depth or thermal activation energy (E_T) from the slope of the straight line. In this investigation, the frequency factor (s) is found to be 5×10^6 s^{-1} and the trap depth due to Dy^{3+} ion substitution is 0.89 ± 0.01 eV, which agrees with the theoretical value reported and shows a positive correlation between the trapping depth and the 4f-5d transition energy of Dy^{3+} [12,13,14]. The mechanism of electron trapping by rare earth ions can be explained using the model by Dorenbos [12]. The Eu^{2+} ($4f^7$) and Dy^{2+} ground energy states are 3.2 eV and 0.9 eV respectively, below the bottom of the conduction band. On exposure to electrons of sufficient energy from β-irradiation, the electron from Eu^{2+} absorbs the radiation and gets optically excited moving from the ground state to the excited just below the conduction band. When the material is thermally activated through the TL process, the 5d electron is excited to the conduction band forming Eu^{3+}. The electron is then trapped by Dy^{3+} to form Dy^{2+} [16]. The energy difference between the lowest 5d state and the bottom of the conduction band is 0.017 eV [12].

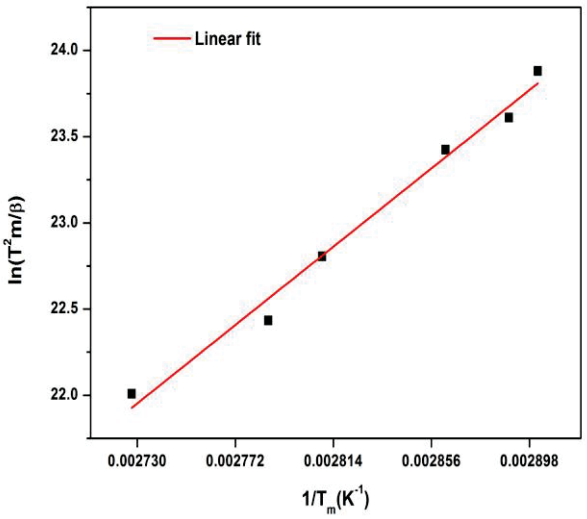

Figure 4. A plot of $\ln\left(\frac{T_m^2}{\beta}\right)$ versus $\frac{1}{T_m}$

Dorenbo's model [12] shows that the ground state of Dy^{2+} is located 0.9 eV below the bottom of the conduction band, which gives a value close to the trap depth of about 1 eV derived from TL studies by Yamamoto and Matsuzawa [17] and Nag and Kutty [18]. The trapped electron is thermally released

and recombines with Eu^{3+} yielding the 5d–4f emission of Eu^{2+}. Or in other words the Eu^{3+} ion releases a hole into the valence band reducing to the divalent Eu^{2+} state again becoming a source of electrons for the surrounding traps thus forming a cycle of continuous excitation. This explains the slow saturation and slow thermal release that brings about the persistent luminescence in phosphors.

4. Conclusions

$SrAl_2O_4:Eu^{2+},Dy^{3+}$ phosphor was synthesized using the solution - combustion method. Samples were heated from 30 to 200 ^{0}C at various heating rates and irradiation doses. The total TL signal and glow curve peaks show increase with dose of the incident β - radiation and temperature (T_{max}). The position of the peak temperature (T_{max}) shifts towards higher temperatures with increased radiation dosage levels. At higher doses the rate of change of peak temperature (T_{max}) seem to reduce, which could be due to higher concentration of defects that generate non-radiative states within the band gap. The peak TL intensity (I_{max}) of the glow curves decreased while the peak temperatures (T_{max}) are seen to shift to the higher temperature side with increase in heating rate. This might be attributed to the filling of the trap centers. For higher peak temperatures the trap depths are deep. The calculated value of activation energy was 0.89 ± 0.01 eV.

Acknowledgments

This work is based on the research supported by the South African Research Chairs Initiative of the Department of Science and Technology, the National Research Foundation of South Africa, University of the Free State Cluster Fund and Rhodes University Physics departments. Also the services of the research equipment of University of Free State and Rhodes University Physics departments used in this study are gratefully acknowledged by the authors.

References

[1] McKeever SWS 1988 *Thermoluminescence of Solids* (Cambridge University Press)
[2] Nameeta B, Bisen D P, Kher R S and Khokhar M S K 2009 *Physics Procedia* **2 (2)** 431
[3] Luminescence online available from http://www.uvminerals.org/ luminese.htm.
[4] Bos A J J 2007 *Rad. Meas.* **41** 45
[5] Basuna S, Imbuschb G F, Jiac D D, Yenc W M 2003 *J. Lumin*. **104** 283
[6] Chen R, Kirsh Y 1981 *Pergamon Press* 167
[7] Chen R, McKeever SWS 1997 *Theory of Thermoluminescence and Related Phenomena* (World Scientific, Singapore)
[8] Chen R 1969 *J. Appl. Phys*. **40** 570
[9] Randall J T, Wilkins M H F 1945 *P. Roy. Soc. Lond.* A **184** 365
[10] Xingdong L, Minjuan Z, Renqin W 2008 *J.Wuhan Univ. of Technology-Mater. Sci. Ed.* **23** 654
[11] Kojima Y, Aoyagi K, Yasue T 2006 *J. Soc. Inorg. Mater. Japan* **13** 228
[12] Dorenbos P 2005 *J. Elect.Chem. Soc.* **7** 152
[13] Nakazawa E, Murazaki Y and Saito S 2006 *J. Appl. Phys.* **100** 113113
[14] Arellano T O, Meléndrez R, Montero P M, Castañeda B, Chernov V, Yen W M and Barboza F M 2008 *J. Lumin.* **128** 173
[15] Bos A J J, Duijvenvoorde R M V, Kolk E V, Drozdowski W and Dorenbos P 2011 *J. Lumin.* **131** 1465
[16] Yamamoto H and Matsuzawa T 1997 *J. Lumin.* **287** 72-74
[17] Nag A and Kutty T R N 2004 *Mater. Res. Bull.* **39** 331
[18] McKeever SWS 1985 *Thermoluminescence of Solids* (Cambridge University Press)

The electrical transport properties of bulk nitrogen doped carbon microspheres

W P Wright[1,2], V D Marsicano[1,2], J M Keartland[1,2], R M Erasmus[1,2], S Dube[2,3] and N J Coville[2,3]

[1] School of Physics, University of the Witwatersrand, P.O. Wits, 2050 Johannesburg, South Africa

[2] DST/NRF Centre of Excellence in Strong Materials, P.O. Wits, 2050 Johannesburg, South Africa

[3] Molecular Sciences Institute and School of Chemistry, University of the Witwatersrand, P.O. Wits, 2050 Johannesburg, South Africa

E-mail: keartland@psi.phys.wits.ac.za

Abstract. Bulk nitrogen-doped carbon microspheres was synthesised using a horizontal chemical vapour deposition reactor (h-CVD). The sample was characterized using scanning electron microscopy (SEM), Raman spectroscopy and electron paramagnetic resonance (EPR) spectroscopy. Characterization showed spherical graphitic carbon microparticles with nitrogen incorporation in the lattice structure, and diameters ranging from 2.6 μm to 750 nm. EPR spectroscopy was also used as a non-destructive technique to measure the percentage of substitutional nitrogen present in the sample. This was determined to be 3.4 %. Electrical transport measurements were performed on the sample and resistance measurements show clear semiconducting behaviour from room temperature down to 10 K. The IV characteristics display curves with increasing non-linearity as temperature decreases. An anomaly is present in the IV characteristics at 300 K. A number of models were used to explain the data and the one providing the best fit is fluctuation induced tunneling. The model provides a satisfactory description of the data for both the IV characteristics and the resistance measurements.

1. Introduction

Since the discovery of carbon nanotubes (CNT) in 1991 [1], carbon nanomaterials have received intense and ongoing interest. In recent years another novel carbon allotrope has received much attention, the carbon microsphere (CMS). This attention is in no small part due to their unique physical properties, including great structural stability which has prompted their usage as a strengthening additive in materials such as rubber. Other uses for CMSs are as a gas storage material [2] and as anode materials in Lithium-Ion batteries [3].

The synthesis of CMSs using the chemical vapour deposition (CVD) technique has been widely reported in the literature [4], [5], [6]. Samples have been synthesised using a wide variety of furnace parameters, gas flow rates and precursors in an attempt to obtain a set of optimal growth conditions. The CVD technique is advantageous because a catalyst is not required. This ensures high sample purity and ease of synthesis and characterization of doped samples of CMSs. Doping can be achieved by allowing a dopant containing additive to flow in the reactor along with the carbon source.

Previously it has been shown that the doping of CNTs with nitrogen leads to n-type semiconducting behaviour [7] whereas doping with boron leads to p-type semiconducting behaviour [8]. The synthesis and physical properties of boron doped CMSs have been described previously [9]. Electrical transport measurements show that undoped CMSs conduct via Mott Variable Range Hopping, the boron doped samples adhered to this model of conduction only at temperatures higher than 170 K and exhibited a much lower conductivity than the undoped sample. This reduction in conductivity has been attributed to charge localization. It has also been shown that CMSs exhibit a Curie type paramagnetism that has been attributed to their characteristic architecture [10].

In this paper we detail the synthesis process of a sample of nitrogen doped CMSs using the CVD technique. The sample was then characterized using Scanning Electron Microscopy, Raman and Electron Paramagnetic Resonance (EPR) spectroscopy. EPR spectroscopy was also used to determine the nitrogen content of the sample. Temperature dependent resistance measurements and IV characteristics were performed on the sample, to explore the underlying conduction mechanism at work in the sample.

2. Synthesis

Samples were synthesized in a horizontal CVD reactor via the pyrolysis of acetylene. The acetylene was introduced into the reactor by using argon as a carrier gas. Reactants were introduced after the furnace was allowed to reach a temperature of 850 °C and was set to a flow rate of 100ml/min. The source of nitrogen dopant, acetonitrile, was then allowed to flow with the carrier gas. The reaction was left to run for 2 hours. Other runs were performed where the temperature was increased to 900 °C. Once the reaction was complete, samples were collected from the quartz boat in the centre of the reactor and from the lining of the quartz tube forming the interior of the reactor. The sample used in the remainder of this research was collected from the middle of the quartz tube. The other samples collected, 5 in total, would be used to determine the nitrogen content of the spheres.

3. Characterization

3.1. Scanning Electron Microscopy

Figure 1 shows the election microscope images that were taken of the sample with a Topcon SM510 Scanning Electron Microscope. At lower magnifications of approximately 500× (Figure 1a), larger agglomerates of particles can clearly be seen. The particels have a tendency to chain together forming long chains and groups of particles. Higher magnification images of approximately 5000× (Figure 1b) clearly show the spherical shape of the constituent particles. Analysis of the sizes of the particles across different sites in the sample show a large distribution in measured diameters for the spheres. The largest measured sphere diameters are approximately 2.6 μm. The smallest measured sphere diameters are approximately 750 nm.

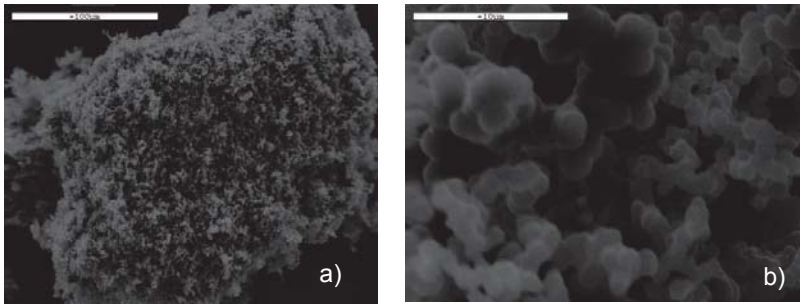

Figure 1. SEM images of the sample: a) 500× b) 5000×

3.2. Raman Spectroscopy

Raman spectroscopy measurements were performed using 514 nm and 647 nm laser light sources. Major peaks were observed at 1381 cm^{-1} and 1595 cm^{-1} with a minor peak at approximately 1200 cm^{-1}.The two dominant spectral lines, known as the D and G bands, indicate the presence of a graphitic carbon structure [11]. Full details are provided elsewhere.

3.3. Electron Paramagnetic Resonance Spectroscopy

The EPR spectrum for the nitrogen-doped carbon spheres was acquired using a Bruker ESP 300E spectrometer in continuous wave mode. The observed spectra are characteristic of non-graphitic carbon materials [12]. The resonance signal is slightly Dysonian indicating the presence of conduction electrons [13].

A novel technique was developed to determine the nitrogen concentration of the sample using the EPR spectra. Spectra of a set of carbon spheres produced with similar conditions but with different nitrogen concentrations were collected. These provide a rudimentary calibration curve for the spectrometer. When applied to this calibration curve the sample showed a nitrogen concentration of 3.4 % with an error of 0.7 %. The errors are large due to the small size of the sample used and the difficulties associated with spin-concentration EPR experiments. Details of the EPR characterization of this sample, and others, will be provided elsewhere.

4. Electrical Transport Measurements

Four-probe resistance measurements were performed on the sample over the temperature range of 300 K to 10 K. The CMS powder was compacted into a sample holding cell using a hand press. Electrical contact was made with the sample through 2 nickel needles acting as pressure contacts. Low temperature measurements were performed using an Oxford continuous flow cryostat. An accurate measure of the sample temperature was obtained using a carbon glass resistance thermometer mounted near the sample at the base of the cryostat.

Variable temperature IV characteristics were measured using a home-built digital variable power supply. This power supply was constructed using a conventional laboratory desktop 30 V DC power supply and an ATMEL ATmega328 microcontroller loaded with the Arduino open source development platform boot loader. This power supply could provide voltages from 0 V-30 V in steps of 500 mV for high bias measurements. The sample for the IV characteristics measurements was prepared in the same way, and the same apparatus was used in these experiments.

4.1. Resistance Measurements

Three different models were used to try account for the data obtained from the resistance. Mott variable range hopping (Mott VRH), where electrons traverse the material by hopping from different localized impurity states; Efros-Shklovskii variable range hopping (ES VRH), where a Coulomb gap forms as the density of states vanishes at the Fermi level; and fluctuation induced tunnelling (FIT), where the material is modelled as a series of metallic regions with small barriers separating them. Electrons are able to either travel over the barriers at higher temperatures, or tunnel through them at lower temperatures. This mechanism is important in describing conduction across junctions between CNTs. These models were chosen as they have found success in modelling the resistance and resistivity data obtained for a wide variety of both bulk and individual examples of nanostructures. Some examples include CNT mats, both doped [14] and pristine [15] and conducting polymer nanofibers [16].

Both Mott VRH and ES VRH can be described by an equation of the form:

$$R(T) = R_0 e^{\left(\frac{T_0}{T}\right)^{\frac{1}{d+1}}} \tag{1}$$

where T_0 is the characteristic temperature, d is the dimensionality of the system and in the case of 3 dimensions, Mott VRH is given by $d = 3$ and, in the case of ES VRH, is given by $d = 1$. R_0 is a constant which contains information regarding the localization length in the case of ES VRH and information regarding the density of states at the Fermi level in the case of Mott VRH.

The FIT model can be described by an equation of the form:

$$R(T) = \beta e^{\left(\frac{T_b}{T_s+T}\right)} \tag{2}$$

where β is a weak function of temperature that contains information regarding the barrier height and other properties of the network structure of connecting microparticles. It can be taken as a constant compared to the temperature dependence of the exponential. T_s is the temperature above which thermal fluctuations become a competing factor. T_b is a much more complicated quantity which is dependent on the barrier shape and height and is affected by the local electric field and the image force. It relates to the temperature below which tunnelling through the potential barriers is the dominant conduction mechanism.

Figure 2 shows each of the above equations fitted to the resistance data obtained for the sample. Figure 2a shows the Mott VRH equation fit, Figure 2b shows the ES VRH equation fit and Figure 2c shows the FIT equation fit. It can clearly be seen that the FIT model describes the data the most accurately. By analysing the parameters of the fit, we are able to extract the values of T_b, T_s and β. These values are given in Table 1 along with their associated errors. The

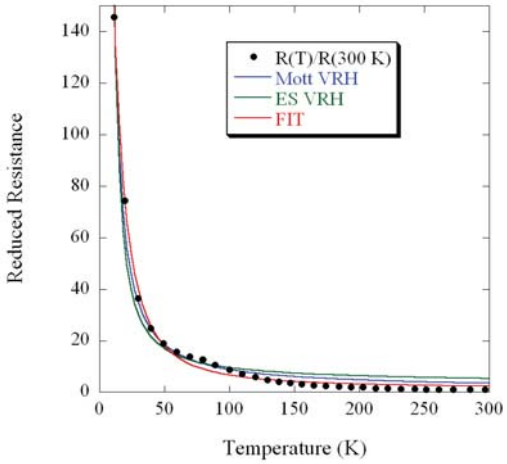

Figure 2. Model fits to resistance data. Clear semiconducting behaviour can be seen. While all 3 models provide a credible description of the data, it is clear that fluctuation induced tunneling provides the best.

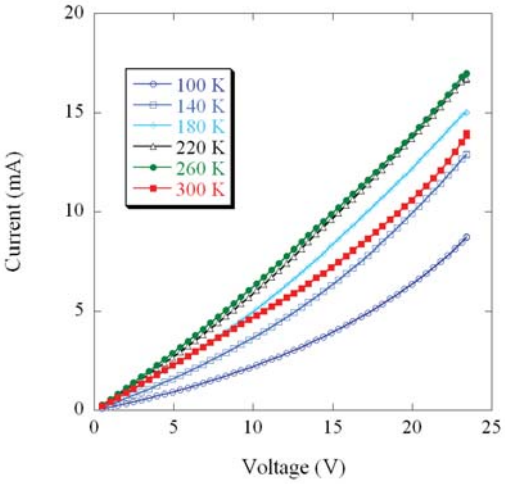

Figure 3. Fluctuation induced tunneling model fit to variable temperature IV characteristics. A Clear increase in non-linearity of the curves can be seen with decreasing temperature providing further evidence of fluctuation induced tunneling being the dominant conduction mechanism.

values obtained are consistent with those found in the literature [14], [17], [18]. The uncertainties in the values for T_s and T_b are quite large and it has been hypothesized that this can be attributed to the wide variety of type and number of junctions between interconnecting microparticles [14]. The spherical nature of the microparticles increases the potential for different kinds of contacts between the microparticles. In the experiments described here, the temperatures studied did

Table 1. Parameters extracted from the FIT model fit to the resistance data

T_b	T_s	β
250 ± 30	40 ± 4	1.2 ± 0.2

Table 2. Parameters extracted from the FIT model fit to the IV characteristics

	100 K	140 K	180 K	220 K	260 K	300 K
G_0 (in mS)	0.15	0.26	0.41	0.51	0.55	0.55
V_0 (in V)	26	26	35	37	51	−67
h	0.001	0.114	0.245	0.36	0.36	0.87

not approach the value of T_s. This indicates that thermal fluctuations play a significant role in allowing electrons to traverse the barriers between metallic regions. The T_b values are higher than those obtained for Nitrogen doped CNTs [14] which is indicative of a higher barrier height between conducting regions.

4.2. IV Characteristics

The temperature range investigated was between 300 K and 100 K in steps of 40 K. The voltage range over which readings were taken was between 0 V and 24 V at each temperature step. In the temperature range of 260 K to 100 K a clear trend can be seen in terms of the linearity of the IV characteristics. At higher temperatures the linear component dominates. As the temperature is decreased, the IV characteristics become more and more nonlinear. This trend provides further evidence that fluctuation induced tunnelling is the dominate mechanism for electrical transport in this temperature range. The behaviour of linearly dominated IV characteristics at higher temperatures is indicative of carriers being assisted by thermal fluctuations to travel over the potential barriers. The behaviour of nonlinear dominated IV characteristics at lower temperatures and an increase in nonlinearity as temperature is decreased is indicative of the carriers not having enough thermal energy to surmount the potential barriers and they tunnel through them.

Using the expression modified by Kaiser [16], the IV characteristics of a system where fluctuation induced tunnelling is the dominant transport mechanism is given by:

$$G = \frac{I}{V} = G_0 \frac{e^{\left(\frac{V}{V_0}\right)}}{1 + h\left(e^{\frac{V}{V_0}} - 1\right)} \tag{3}$$

where G_0 is the temperature dependent low field conductance, h is the parameter which governs the slowing of exponential increase at higher field values and V_0, which has a strong dependence on the potential barrier height, is the voltage scaling factor. In order to achieve the desired behaviour, $h < 1$.

Figure 3 shows the fits of the above equation to the IV data over the entire temperature range. The parameters of the fits are given in Table 2. In the temperature range 100 K to 260 K, the model fits the data very well and the parameters obtained correspond well with and follow the same trend as those seen in the literature [19]. The correspondence between the

resistance data and the IV characteristics of the sample in this temperature range gives a strong indication that fluctuation induced tunnelling is indeed the dominant conduction mechanism for this sample. However IV curve at 300 K is atypical. It already has a nonlinear component to it and when an attempt was made to fit the model to the data, a poor fit was obtained when compared to the other temperatures and non-physical parameters were extracted. This leads us to believe that another mechanism is competing with FIT at temperatures comparable to 300 K. High temperature measurements would be useful in exploring the reasons for this behaviour.

5. Conclusion

A sample of nitrogen-doped CMSs were synthesised using the CVD technique. The samples were characterized using electron microscopy confirming the spherical nature of the nanomaterials. Raman spectroscopy confirmed the graphitic nature of the samples, and EPR spectroscopy measurements indicated that nitrogen is incorporated into the lattice as a substitutional impurity. Electrical transport measurements were performed on the sample and it was found from the resistance measurements that the sample conducts via fluctuation induced tunnelling in the temperature range of 300 K to 10 K. The model fit parameters corresponded to those found in the literature. The IV characteristics measurements of the sample confirmed that fluctuation induced tunnelling is the dominant conduction mechanism in the temperature range 260 K to 100 K. An anomaly was discovered in the 300 K IV curve. Higher temperature experiments will allow us to investigate this effect.

References

[1] Iijima S 1991 *Lett. Nature.* **354** 56
[2] Wu C, Zhu X, Ye L, Yang C, Hu S, Lei L and Xie Y 2006 *Inorg. Chem.* **45**
[3] Wang Y, Su F, Wood C, Lee J and Zhao X 2008 *Ind. Eng. Chem. Research.* **47** 2294–300
[4] Wang Z and Yin J 1998 *Chem. Phys. Lett.* **289** 189–192
[5] Mehraban Z, Farzaneh F and Dadmehr V 2009 *Mat. Lett.* **63** 1653–1655
[6] Miao J, Hwang D, Narasimhulu K, Lin P, Chen Y, Lin S and Hwang L 2004 *Carbon.* **42** 813–822
[7] Ewels C and Glerup M 2005 *J. Nanosci. and Nanotech.* **5** 1345–1363
[8] Mondal K, Strydom A, Erasmus R, Keartland J and Coville N 2008 *Mat. Chem. and Phys.* **111** 386–390
[9] Mondal K, Strydom A, Tetana Z, Mhlanga S, Witcomb M, Havel J, R R E and Coville N 2009 *Mat. Chem. and Phys.* **114** 973–977
[10] Calderon-Moreno J, Labarta A, Batlle X, Pradell T, Crespo D and Binh V 2007 *Chem. Phys. Lett.* **447** 295–299
[11] Tuinstra F 1970 *J. Chem. Phys.* **53** 1126
[12] Mrozowski S 1979 *Carbon.* **17** 227–236
[13] Dyson F 1958 *Phys. Rev.* **98** 349–359
[14] Barnes T, Blackburn J, Lagemaat J, Coutts T, and Heben M 2008 *ACS. Nano.* **2** 1968–1976
[15] Bekyarova E, Itkis M, Cabrera N, Zhao B, Yu A, Gao J and Haddon R 2005 *J. Amer. Chem. Soc.* **127** 5990–5995
[16] Kaiser A, Rogers S and Park Y 2004 *Mole. Crys. Liq. Crys.* **415** 115–124
[17] Sheng P 1980 *Phys. Rev. B* **21** 2180–2195
[18] Shiraishi M and Ata M 2002 *Synth. Metal.* **128** 235–239
[19] Long Y, Yin Z, Li M, Gu C, Duvail J, Jin A and Wan M 2009 *Chinese. Phys. B* **18** 2514–2522

Luminescent properties of Pr^{3+} doped SrF_2 prepared by different synthesis techniques

MYA Yagoub, HC Swart, LL Noto and E Coetsee

Department of Physics, University of the Free State, PO Box 339, Bloemfontein, ZA9300, South Africa.

Corresponding author's e-mail address: CoetseeE@ufs.ac.za

Abstract. Pr^{3+} doped Strontium fluoride (SrF_2) was prepared by hydrothermal and combustion methods. X-ray diffraction patterns indicated that the samples were completely crystallized with a pure face-centred cubic (space group: Fm3m) structure. Both SrF_2:Pr^{3+} samples exhibit blue-red emission centred at 488 nm under a 439 nm excitation wavelength (λ_{exc}) at room temperature. The emission intensity of Pr^{3+} was found to be dependent on the synthesis procedure. The blue–red emission decreased with an increase in the Pr^{3+} concentration. This was attributed to the $[^3P_0, {}^3H_4] \rightarrow [^3H_6, {}^1D_2]$ and $[^1D_2, {}^3H_4] \rightarrow [^1G_4, {}^3F_{3,4}]$ cross-relaxation process that resulted from the smaller average interionic distances between the dopant ions.

1. Introduction

Pr^{3+} is an interesting ion because it has multiple transitions that allow for detailed studies of both radiative and non-radiative mechanisms. Pr^{3+} doped materials have been extensively investigated due to its potential use in a variety of applications [1, 2, 3, 4, 5]. For phosphor applications, the 4f – 4f transitions are the most relevant, especially the $^1D_2 \rightarrow {}^3H_4$ in red emission from Pr^{3+} doped oxide materials [6, 7]. Fluoride based luminescent materials are also prominent amongst other candidates because they have lesser energy losses due to the non-radiative relaxation processes [8]. Different synthesis methods have been invented to prepare nanostructured fluoride materials that can be used as efficient luminescent materials [9, 10].

Recently, the Pr^{3+} ion is found to be a promising ion in the lanthanide-based luminescent materials for quantum cutting, which can be used to enhance solar cell efficiency [1, 11]. The choice of a host material with lower vibrational energy, which can minimize the non-radiative transition, is very important for the quantum cutting procedure. Strontium fluoride (SrF_2) has a very small cut-off phonon energy (~ 350 cm^{-1}) and it was found to be a good host for the quantum cutting application [9]. The hydrothermal method is the most successful synthesis technique for the SrF_2 powders [12, 13, 14].

The SrF_2:Pr^{3+} system has been investigated by several researchers [5, 15, 16] and the majority reported the photon emission cascade and energy transfer mechanism in SrF_2 doped with Pr^{3+} ions

(with the main focus on the $4f^n - 4f^{n-1}5d$ emission). The 4f – 4f transitions have also been studied, but most of these results have been devoted to the red emission from Pr^{3+} doped oxide materials [6, 7, 17]. However, the application of Pr^{3+} in solar cells also requires knowledge of the 4f – 4f transitions. Hence, the information on 4f – 4f transitions are paramount important.

On the other hand, it has been shown that the probability of the multi-phonon relaxation between $^3P_0$ and $^1D_2$ levels of Pr^{3+} significantly decreases as the phonon energy of the host decreased [18]. It has also been observed that the emission intensity of the $^3P_0$ state of Pr^{3+} doped host with a small phonon energy decreased with increasing the Pr^{3+} concentration, which was attributed to the cross-relaxation process [18, 19, 20, 21]. This behaviour normally occurs at the smaller average interionic distances between the Pr^{3+} ions.

Herein, the luminescent properties of Pr^{3+} doped SrF_2 phosphor powders prepared by using both the hydrothermal and combustion methods are reported. In addition, the cross-relaxation mechanism from the $^3P_0$ level is also discussed.

2. Experimental

For the hydrothermal synthesis, analytical grade of $Sr(NO_3)_2$, $Pr(NO_3)_3.6H_2O$, NH_4F, sodium oleate, oleic acid and ethanol were used without further purification. For a typical synthesis of $SrF_2:Pr^{3+}$, ethanol, sodium oleate and oleic acid were added simultaneously to an aqueous solution containing $Sr(NO_3)_2$ and $Pr(NO_3)_3.6H_2O$**.** After 10 min of stirring the milky colloidal solution was transferred to 125 ml autoclave lined with teflon and heated at 180 ^{0}C for 24 h. The product was collected by centrifugal and washed with water and ethanol. Finally, the product was dried for 24 h in an oven at 80 ^{0}C.

In combustion synthesis, an aqueous solution of NH_4F was added drop wise to a mixture of $Sr(NO_3)_2$, $Pr(NO_3)_3.6H_2O$ and urea, which was used as fuel. The milky solution was collected after thoroughly stirring. Then, the obtained solution was transferred into a porcelain crucible and placed in a furnace at 500 ^{0}C until the ignition occurred. Finally, the as-prepared powder was sintered for 2 h at 700 ^{0}C. The phosphors were characterized by X-ray diffraction (Bruker Advance D8) to identify the crystalline structure of the powder. The luminescence spectra from $SrF_2:Pr^{3+}$ phosphors were collected using Photoluminescence (PL) spectroscopy (Cary Eclipse fluorescence spectrophotometer).

3. Results and Discussion

The XRD patterns of the $SrF_2:Pr^{3+}$ of both synthesis methods (hydrothermal and combustion) as well as the standard data for SrF_2 (card No. 00-086-2418) are shown in figure 1. The sharp and strong diffraction peaks indicate that the sample powder is fully crystallized (face-centred cubic with space group: Fm3m). Doping of 0.1 mol% of Pr^{3+} causes a slight shift to a higher angle with comparison to the standard data (figure 1). This can be attributed to the radius difference between Pr^{3+} (0.099 nm) and Sr^{2+} (0.126 nm) ions, which confirms that Pr^{3+} ions are incorporated into the SrF_2 lattice. The sintering temperature of the as-prepared hydrothermal sample caused a slight variation in the XRD intensities. The reason might be that the orientation growth of the particles occurs in certain directions. The calculated SrF_2 lattice parameters are (5.7744 ± 0.0054) Å and (5.764 ± 0.0025) Å for the samples prepared by the combustion and hydrothermal methods, respectively, indicating a small reduction in the unit cell in the hydrothermal method case.

The estimated particle sizes were calculated by using the diffraction peaks and Scherrer's equation [22]. These were found to be approximately 38 nm and 56 nm for samples prepared by hydrothermal and combustion methods, respectively. This shows that the hydrothermal method produces smaller particle size.

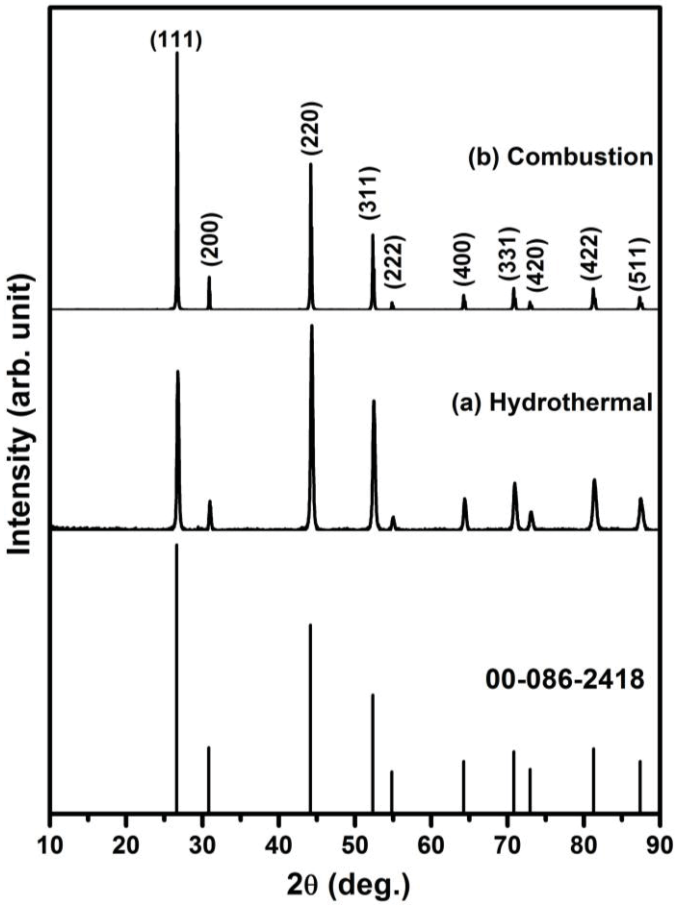

Figure1. XRD pattern of $SrF_2:Pr^{3+}$ 0.1 mol% samples of both methods (a) hydrothermal and (b) combustion.

Figure 2(a), (b) and (c) show the excitation and emission spectra of the SrF_2 doped with different concentration of Pr^{3+} ions that were prepared by the combustion and the hydrothermal methods. Upon 439 nm excitation (into the $^1I_6$ and ^3P_j, j = 0, 1, 2), depopulation from the $^1I_6$ and $^3P_{1,2}$ energy bands occurs to the metastable $^3P_0$ energy band. Both samples exhibit blue–red emission from the $^3P_0$ level. There are at least six luminescent bands that correspond to relaxation from the $^3P_0$ emission energy band. These six bands are centered at 488, 524, 605, 638, 715 and 730 nm, which are assigned to the $^3P_0 \rightarrow {}^3H_4$, $^3P_0 \rightarrow {}^3H_5$, $^3P_0 \rightarrow {}^3H_6$, $^3P_0 \rightarrow {}^3F_2$, $^3P_0 \rightarrow {}^3F_3$ and $^3P_0 \rightarrow {}^3F_4$ transitions, respectively [11]. The band with weak intensity at around 690 nm is assigned to the $^1D_2 \rightarrow {}^3H_5$ transition. This demonstrates that the dominant transition is the $^3P_0$ transition. There is also a small peak marked with (**S**) around 879 nm (figure 1(b) and (c)), which is assigned to the second order observation of the excitation wavelength. This band has been previously assigned to the $^3P_0 \rightarrow {}^1G_4$ transitions [11], but in this work, we observed that its position changes with the excitation wavelength, which is exactly twice of the excitation wavelength (λ_{exc}). The second order observation of the Pr^{3+} system has also been previously reported on Pr^{3+} doped YF_3 [2].

Figure 2(d) shows the Commission Internationale de I'Eclairage (CIE) coordinates plot for the $SrF_2:Pr^{3+}$ phosphor prepared by (A) the hydrothermal (0.4 mol%) and (B) the combustion techniques with 0.2 mol% of the dopant. The corresponding coordinates are at (X = 0.25, Y = 0.45) and (X = 0.30, Y = 0.40), respectively. This shows that the cyan color for the hydrothermal method is removed in the Pr^{3+} emission during the combustion method. This can be ascribed to the emission intensity difference between these two methods.

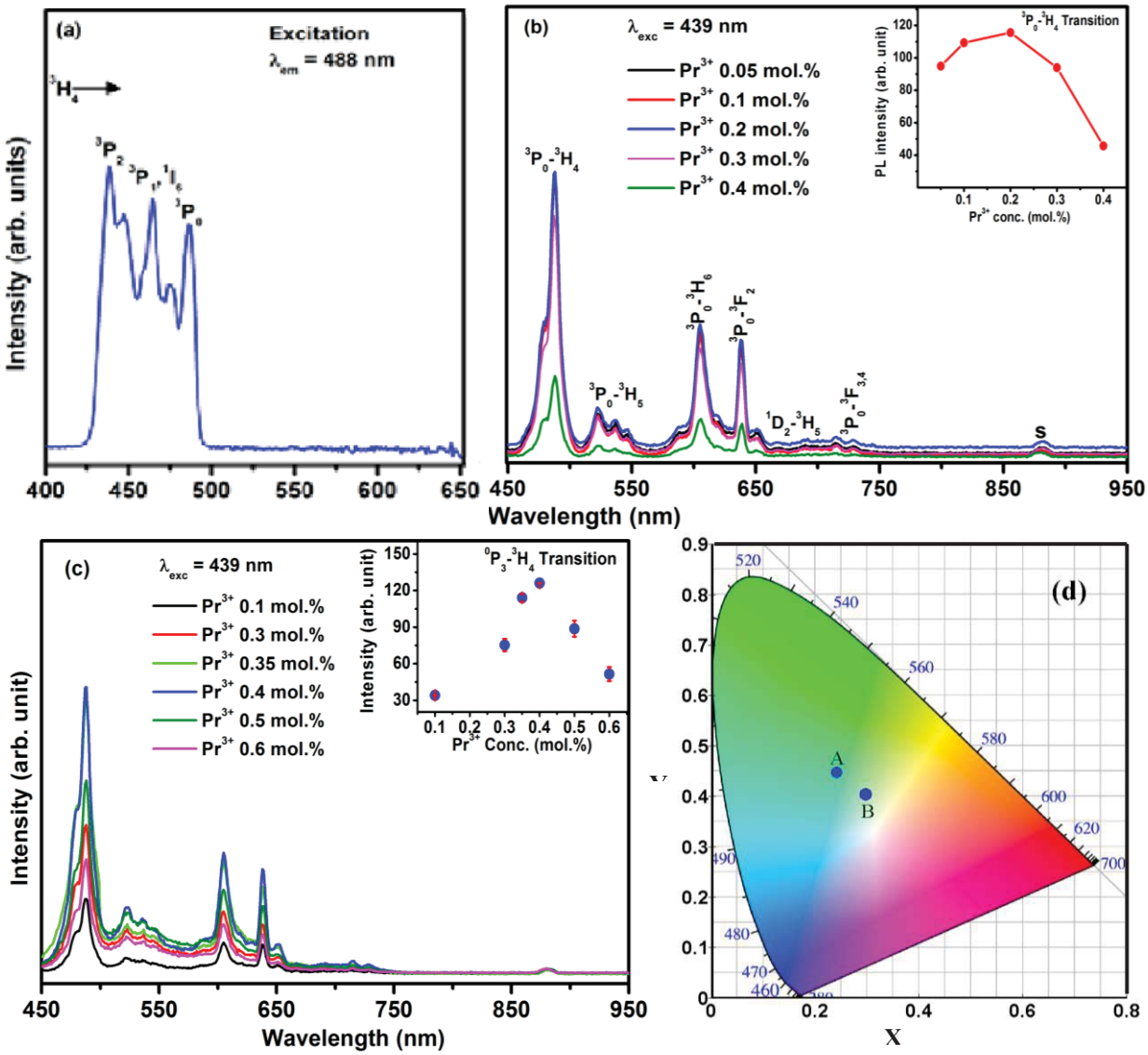

Figure 2. Excitation and emission spectra of $SrF_2:Pr^{3+}$ at different synthesis methods; (a) excitation spectrum, (b) emission spectrum for combustion method, (c) emission spectrum for hydrothermal method and (d) CIE chromaticity diagram for the $SrF_2:Pr^{3+}$ under λ_{exc} = 439 nm ((A) hydrothermal (X = 0.25, Y = 0.45) and (B) combustion (X = 0.30, Y = 0.40)). The inset graphs in (b) and (c) show the variation of the Pr^{3+} emission intensity as a function of the Pr^{3+} concentration.

The inset graphs in figure 2 show the $^3P_0 \rightarrow {}^3H_4$ emission intensity variation as a function of Pr^{3+} concentration. It is worth mentioning that all the samples were carefully synthesized and measured under the same condition for each preparation method so that the Pr^{3+} ion emission intensity can be compared. In the combustion method, the PL intensity of the $^3P_0$ emission increased from 0.05 to 0.2 mol% Pr^{3+}concentration, whereas in the hydrothermal method it increased from 0.1 to 0.4 mol% Pr^{3+} concentrations. It then started to decrease systematically as the Pr^{3+} concentration increased (figure 2). A comparison of the $^3P_0 \rightarrow {}^3H_4$ emission intensity in both methods shows the hydrothermal synthesis has a higher optimal concentration, which demonstrates that the hydrothermal synthesis gives rise to higher absorption strength. This difference in the intensity optimization can be associated to the dissimilarity of the synthesis procedure, which confirms that the emission intensity is strongly

dependent on the synthesis procedure [11]. The recent solid state synthesis of SrF_2:Pr^{3+} reported that the optimal concentration of Pr^{3+} was found to be 0.1 mol% [11]. However, the increase in the PL intensity reflects the increase of the luminescent centers of Pr^{3+} with increasing the Pr^{3+} concentration [17], whereas, the decrease in the $^3P_0 \rightarrow {}^3H_4$ emission intensity indicates the quenching of the luminescence intensity. In fact, the quenching of $^3P_0$ emission intensity can occur through three different processes: (1) relaxation by multi-phonon emission to the $^1D_2$ level, (2) cross-relaxation between Pr^{3+} pairs and (3) energy transfer to the killer sites [20, 23], where the latter two rely on the Pr^{3+} concentration in the host lattice. As it was mentioned earlier, the probability of the multi-phonon process significantly reduces as the phonon energy of the host decreases [18]. However, the energy difference between $^3P_0$ and $^1D_2$ is around 3500 cm^{-1} and the energy cut-off of the SrF_2 is about 350 cm^{-1}, therefore, ten phonons are required to bridge the energy gap. Hence, the multi-phonon relaxation processes for the $^3P_0$ and $^1D_2$ levels can be considered negligible. Therefore, the $^3P_0$ emission quenching might occur due to the cross-relaxation mechanism between the Pr^{3+} pairs. This kind of non-radiative mechanism depends on the distance that separates the neighboring Pr^{3+} ions.

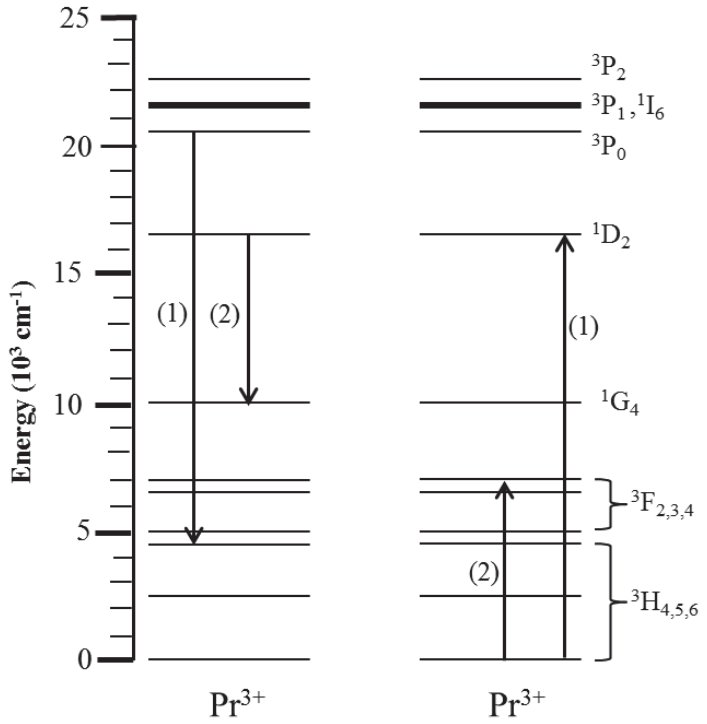

Figure 3. Schematic diagram showing a possible cross-relaxation mechanism.

A possible cross-relaxation mechanism that may occur in the Pr^{3+} ions is schematically shown in figure 3. The $[^3P_0,{}^3H_4] \rightarrow [^3H_6,{}^1D_2]$ cross-relaxation process is already suggested for similar system such as Pr^{3+}-doped yttrium aluminum garnet (YAG) and gadolinium gallium garnet (GGG) [18, 24]. The $^1D_2$ level can be populated, which in turn could be easily depopulated via the $[^1D_2, {}^3H_4] \rightarrow [^1G_4, {}^3F_{3,4}]$ pathway [18]. Hence, one can conclude that the weak peak around 690 nm is a result of $[^3P_0, {}^3H_4] \rightarrow [^3H_6,{}^1D_2]$ cross-relaxation process. The decrease in the emission intensity of Pr^{3+} doped materials has been reported by various researchers [19, 20, 21]. Chen et al. [25] reported that an increase in $^3P_0$ and $^1D_2$ emission intensity was observed with increasing the Pr^{3+} concentration up to 0.3 mol %. The total fluorescence quenching was observed for the $^1D_2$ state at 10 mol% [25]. R. Naccache et al. [18] found that the average Pr^{3+}– Pr^{3+} distance in GGG crystalline samples dramatically decreased as the Pr^{3+} concentration increased. Consequently, the cross-relaxation process

is more likely to occur in the most concentrated nano-crystals. Such information could be important for the optimization of the Pr^{3+} concentration in nano-crystalline materials for certain applications.

4. Conclusion

The SrF_2: Pr^{3+} powder was prepared by hydrothermal and combustion methods. The XRD patterns showed strong and sharp diffraction peaks for both samples, which indicate that the powders were completely crystallize with a pure face-centred cubic (space group: Fm3m) structure. In comparison between these two methods, the calculated particle sizes showed smaller particles for the hydrothermal technique. It was found that both sample**s** exhibit blue–red emission under 439 nm from 4f – 4f excitation at 425 to 500 nm. It was also showed that the $^3P_0 \rightarrow {}^3H_4$ emission intensity quenching might be due to the cross-relaxation process.

5. Acknowledgment

This work is based on the research supported by the South African Research Chairs Initiative of the Department of Science and Technology and National Research Foundation of South Africa. The University of the Free State Cluster program for financial support.

References

[1] Van der Ende B M, Aarts L and Meijerink A 2009 *Phys. Chem. Phys. Chem.* **11** 11081.
[2] Srivastava A and Duclos S J 1997 *Chem. Phys. Lett.* **275** 453.
[3] Gusowski M A, Swart H C, Karlsson L S and Trzebiatowska M -G 2012 *Nanoscale* **4** 541.
[4] Voloshin A I, Navaleev N M and Kazakov V P 2001 *J. Lumin.* **93** 199.
[5] Kristianpoller N, Weiss D and Chen R 2004 *Radiat. Meas.* **38** 719.
[6] Boutinaud P, Dubois M, Vink A P and Mahiou R 2005 *J. Lumin.* **111** 69.
[7] Deren P J, Pazik R, Strek W, Boutinaud Ph and Mahiou R 2008 *J. Alloys Comp.* **451** 595.
[8] Murakami T and Tanabe S 2007 *J. Ceram. Soc. Jap.* **115** [10] 605.
[9] Rakov N, Guimaraes R B Franceschini D F and Maciel G S 2012 *Mater. Chem. Phys.* **135** 317.
[10] Fedorov P P, Luginina A A, Kuznetsov S V and Osiko V V 2011 *J. Fluorine Chem.* **132** 1012.
[11] Van der Ende B M, Aarts L and Meijerink A 2009 *Adv. Mater.* **21** 3037.
[12] Peng J , Hou S, Liu X, Feng J, Yu X, Xing Y and Su Z 2012 *Mater. Res. Bull*. **47** 328.
[13] Sun J, Xian J and Du H 2012 *Appl. Surf. Sci.* **257** 3592.
[14] Zhang C, Hou S, Chai R, Cheng Z, Xu Z, Li Ch, Huang L and Lin J 2010 *J. Phys. Chem.* C **114** 6928.
[15] Radzhabov E 2009 *J. Lumin.* **129** 1581.
[16] Shendrik R and Radzhabov E 2012 *IEEE Trans. Nucl. Sci.* **9499** 1.
[17] Noto L L, Pitale S S, Gusowki M A, Terblans J J, Ntwaeaborwa O M and Swart H C 2013 *Powder Technol.* **237** 141.
[18] Naccache R, Vetrone F, Speghnini A, Bettinelli M and Capobianco J A 2008 *J. Phys. Chem.* C **112** 7750.
[19] Balda R, Fernandez J, Ocariz I S, Voda M and Garcia A J 1999 *Phys. Rev.* B **59** 9972.
[20] Chen Q J, Zhang W J, Huang X Y, Dong G P, Peng M Y and Zhang Q Y 2012 *J. Alloys Comp.* **513** 139.
[21] Collins J, Geen M, Bettinelli M and Di Bartolo B 2012 *J. Lumin.* **132** 2626.
[22] Oprea C, Ciupina V and Prodan G 2008 *Rom. J. Phys.* **53** 223.
[23] Domega C D, Meijerink A and Blasse G 1995 *J. Phys. Chem. Solids* **56** 673.
[24] Wu X, Dennis W M and Yen W M 1994 *Phys. Rev*. B **50**(10) 6589.
[25] Chen H, Lian R, Yin M, Lou L, Zhang W, Xia S and Krupa J -C 2001 *J. Phys.: Condens. Matter* **13** 1151.

Effect of annealing on the structure of $Y_3(Al,Ga)_5O_{12}$:Tb thin films grown by PLD

A. Yousif [1,2], H.C. Swart[1], O.M. Ntwaeaborwa

[1]Department of Physics, University of the Free State, P.O. Box 339, Bloemfontein, ZA 9300, South Africa
[2]Department of Physics, Faculty of Education, University of Khartoum, P.O. Box 321, 11115, Omdurman, Sudan.

Corresponding Author: *swarthc@ufs.ac.za*

Abstract. $Y_3(Al,Ga)_5O_{12}$:Tb thin films were grown in an O_2 working atmosphere on Si (100) substrates using the pulsed laser deposition technique. The influence of different annealing times on the optical, morphological and the structural properties of the films, was investigated. Atomic force microscopy showed an increase in grain size with an increase in annealing time. The photoluminecent (PL) emission spectrum presented similar characteristics for all different annealing times, and the emissions are described by the well-known $^5D_4$–^7F_J (J=6, 5, 4, 3…) transitions of the Tb^{3+} ion. The main PL emission peak was due to the $^5D_4 \rightarrow {}^7F_5$ transition of Tb^{3+} and was measured at a wavelength of 544 nm with minor peaks at 489 nm ($^5D_4 \rightarrow {}^7F_6$), 561 nm ($^5D_4 \rightarrow {}^7F_4$) and 625 nm ($^5D_4 \rightarrow {}^7F_3$). A new excitation band located at around 200 nm was observed from all the annealed films which pointed to a change in the chemical environment, owing to the fact that, the 5d level depends strongly on the nature of the host due to a greater radial extension of the 5d orbital. A shift in the peak position to lower diffraction angles with increased annealing time was also observed in the X-ray diffraction results compared to the pattern of the $Y_3(Al,Ga)_5O_{12}$:Tb powder and other thin films.

1. Introduction

Luminescent materials have received technological interest worldwide for a broad range of everyday applications. Among them, Yttrium aluminium garnet material (YAG) activated with Tb^{3+} is one of the most heavy-duty phosphors which are widely used in display applications [1-3]. The brightness and saturation characteristics were improved by the replacement of a portion of Al with Ga in the YAG host to improve the saturation characteristics at higher electron beam density excitations [4,5]. On the other hand, this partial replacement of Al with Ga slightly increased the deterioration of luminescence efficiency under electron bombardment [1]. However, $Y_3(Al,Ga)_5O_{12}$:Tb phosphor powder, showed very good cathodoluminescent (CL) stability, during prolonged electron bombardment [2]. Most phosphor materials consist of multi-components and their luminescence efficiency is largely affected by the right stoichiometry and growth mode. One of the most important things in the deposition of a phosphor thin film is the stoichiometric transfer of target material to the substrate [6]. It is well known that the pulsed laser deposition (PLD) technique can produce a wide variety of complex compounds with controlled composition and properties. In this study, PLD $Y_3(Al,Ga)_5O_{12}$:Tb thin films were grown with a set of fixed processing conditions. Thermal

processing was used to improve the crystal quality and to decrease the amount of structural defects in the films. It is well known that, during the annealing process, dislocations, and other structural defects move in the material and adsorption/decomposition may occur at the surface, thus the structure and the stoichiometric ratio of the material may change [6]. As reported in the literature [3], the interdiffusion of atomic species between the Si substrate and $Y_3(Al,Ga)_5O_{12}$:Tb thin films were observed for post annealing at higher temperatures, which has an impact on the film's optical properties. A. Yousif *et. al.* [7] reported that annealing improved the photoluminescence (PL) intensities as well as the crystallinity of the $Y_3(Al,Ga)_5O_{12}$:Tb films, but changes in the surface topography were observed after the annealing process, which showed spherically grains covered with an inhomogeneous distribution of Ga on the surface relative to the bulk distribution of the deposited film. Another study on the annealing effect on the $Y_3(Al,Ga)_5O_{12}$:Tb film [8], showed that stress and aggravated cracking occurred during annealing, which left regions enriched with Si after annealing at the higher temperatures. In this work, we report on the effect of different annealing times on the optical, morphological and the structural properties of the $Y_3(Al,Ga)_5O_{12}$:Tb film annealed at 800 ^oC.

2. Experiment

The Si (100) wafers used as substrates were first cleaned as described elsewhere [3, 7]. The PLD technique was used for the preparation of the films. The deposition chamber was evacuated to a base pressure of 1.3×10^{-5} mbar and then backfilled with O_2 to a pressure of 5.3×10^{-2} mbar. The $Y_3(Al,Ga)_5O_{12}$:Tb target was ablated in the O_2 working atmosphere using a 266 nm Nd:YAG pulsed laser. The laser frequency, number of pulses, fluency, substrate temperature and target-to-substrate distance were fixed at 10 Hz, 20000, 0.767 J/cm^2, 300 ^oC and 4.5 cm, respectively. Some of the deposited thin films were annealed for 1 and 2 hrs at 800 ^oC in air. $Y_3(Al_x,Ga_y)_5O_{12}$:Tb was also synthesized by using an urea-nitrate solution combustion synthesis technique. $Y(NO_3)_3.4H_2O$, CON_2H_4 and $Ga(NO_3)_3.5H_2O$ were used as starting materials, which were dissolved in diluted water during stirring and heating to obtain a mixing aqueous homogenous precursor solution. The solution was placed in a furnace preheated at 500 °C. After the combustion process was completed, the obtained solid precursors were then ground and fired at 900 °C for 2 h in air to produce the final samples. X-ray diffraction (XRD) analysis was carried out using a Bruker AXS D8ADVANCE X-ray diffractometer. The PL properties of the films were measured using a Cary eclipse spectrophotometer at room temperature. The surface topography was examined using a Shimadzu SPM-9600 atomic force microscope (AFM).

3. Results and discussion

Figure 1(a) shows the XRD patterns of the powder, the as-deposited and the annealed $Y_3(Al,Ga)_5O_{12}$:Tb thin films. A small (420) diffraction peak at the same position for the powder was observed for the as-deposited film. The annealed films shows three diffraction peaks at 29.3^o, 32.7 ^{o}, and 35.9^o which correspond to the (400), (420) and (422) crystalline planes[2], respectively. Furthermore, an increase in the annealing time resulted in an increase in the intensity of the (420) diffraction peak as shown in Figure 1(a). Which clearly indicates that the crystallinity of the $Y_3(Al,Ga)_5O_{12}$:Tb film was enhanced with an increase in the annealing time. The estimated average crystallite size of the $Y_3(Al,Ga)_5O_{12}$:Tb was obtained by using Scherrer's equation [9] and was found to be ~ 23 nm and ~25 nm for the 1 and 2 hrs annealed films, respectively. Furthermore, a slight shift in the peak position to a lower diffraction angle was observed for the annealed films compared with the $Y_3(Al,Ga)_5O_{12}$:Tb commercial powder. Figure 1(b) represents the XRD patterns for the commercial and synthesised $Y_3(Al_x,Ga_y)O_{12}$:Tb powder with different Ga concentrations, which show a shift of the peaks to lower diffraction angles with an increase in the Ga concentration. This is due to the fact that the ionic radius of Ga^{3+}(0.062 nm) is larger than the ionic radius of Al^{3+} (0.053 nm) [10]. Therefore with an increase in Ga concentration a change in the host lattice is expected. Figure 2 demonstrates the effect of the Ga concentration on the lattice parameter, showing the host site with

a=12.27 Å, 12.16 Å and 12.06 Å for $Y_3Ga_5O_{12}$ [11], $Y_3Al_{2.1},Ga_{2.9}O_{12}$ [12] and $Y_3Al_{3.97},Ga_{1.03}O_{12}$, [13] respectively. As a result of an increase in the Ga concentration, the inter-planar spacing will increase and a shift towards lower angles in the diffraction peak will be observed as pointed out by Bragg's law. It can be concluded that the shift towards the lower diffraction angles in the XRD patterns of the annealed films probably indicating that the films are enriched with Ga compared with the as prepared film. The Auger electron spectroscopy elemental mapping of films showed some inhomogeneous distribution of Ga on the surface of the deposited films, indicating that some areas of the films were enriched with Ga [7]. Ga with a very low melting point of 29.76 ^oC, maybe transferred as agglomerated clusters during the PLD process and with annealing treatment, started to interact with the rest of materials to form structures that are enriched with Ga.

Figure 3(a-c) shows the AFM micrographs of the surface of the as-deposited and annealed $Y_3(Al,Ga)_5O_{12}$:Tb thin films. The regions evaluated show that the surface layer was uniform and the substrate was well covered with particles. The as-deposited films consist of a granular structure of grains with various grain sizes. Annealing at 800°C for 1 and 2 hrs induced changes in the root mean square (RMS) roughness and the surface topography. The RMS roughness changed from 16 nm to 21 and 30 nm respectively. The surface topography shows larger grain sizes compared with the as prepared film, due the fact that, grain growth takes place by diffusion when the temperature is high enough and/or the heat treatment time is long enough [14].

Figure 4(a) shows the excitation and emission spectra, for the as prepared Tb^{3+} in $Y_3(Al_x,Ga_y)_5O_{12}$ host with different Ga and Al concentrations. The emission lines were obtained for the excitation wavelength of 260, 267 and 272 nm for $Y_3Ga_5O_{12}$:Tb, $Y_3Al_3Ga_2O_{12}$:Tb and $Y_3Al_5O_{12}$:Tb respectively. Four main PL bands for both green and blue emission are clearly resolved which are associated with the f–f internal orbital transitions of Tb^{3+} ions. They are attributed to the well-known $^5D_4$–^7F_J (J=6, 5, 4, 3…) and $^5D_3$–^7F_J (J=6, 5, 4, 3…) transitions of the Tb^{3+} ions [2, 3], which present similar characteristics for the Tb in $Y_3(Al_x,Ga_y)_5O_{12}$ with different Al and Ga concentration. This is due to the fact that, the lanthanide elements (rare earth) have a partially filled inner $4f^n$ shell surrounded by completely filled outer $5s^2$ and $5p^6$ orbitals which shielded the sharp 4f-4f line emissions of the Tb^{3+} from the anionic environment. Therefore they are relatively independent of the host material and are determined by the energy transition between the 4f states only. On the other hand, the energy of the 5d levels depends strongly on the nature of the host due to a greater radial extension of the 5d orbital which can be seen in the excitation bands of as prepared powder with different Al and Ga concentrations.

Mayolet et al.[15] studied the $4f^75d$ configuration in $Y_3(Al_x,Ga_y)_5O_{12}$:Tb and they concluded that there are five excitation band energies (E_1, E_2, E_3, E_4 and E_5) which clearly depend strongly on different concentrations of Ga. Figures 5(b-d) are the excitation bands changes for different concentrations of Ga, as redrawn from Ref. [15]. Their results may be summarized as follows:

1. For a high Al composition: the E_l, E_2, E_3 and E_4, excitation bands, correspond to the excitation of the $4f^75d$ states of Tb^{3+} whereas, E_5 is hidden by the inter-band transition E_g in the host.
2. For a high Ga composition: E_l, E_2, $E_{3,4}$ (E_3, E_4 collapse) and E_5 (shoulder) correspond to the excitation of a $4f^8 \rightarrow 4f^75d$ transition of Tb^{3+} ions.

If the peak positions, as determined from the excitation spectra, are known for the different excitation bands, it may be used to explain the appearance of the new excitation band at 200 nm for the annealed films compared to as prepared film in Figure 5 (a), as indication that the annealed films were enriched with Ga. Figure 4(e) shows the E_5 excitation spectra of the $Y_3(Al_x,Ga_y)_5O_{12}$:Tb with different concentration of Ga as indicated, which clearly confirms the above statements.

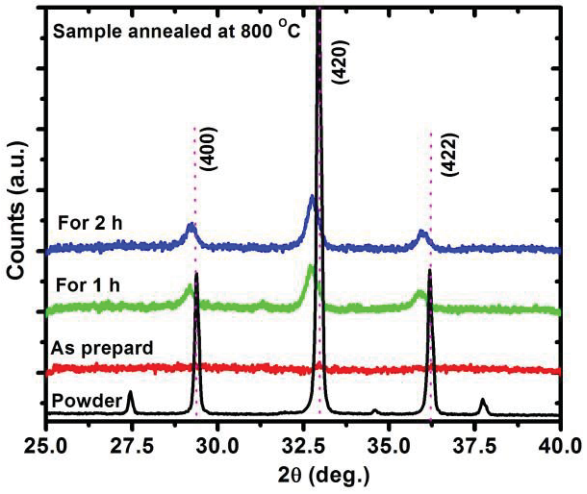

Figure 1 (a) XRD patterns of the $Y_3(Al,Ga)_5O_{12}$:Tb phosphor powder, and $Y_3(Al,Ga)_5O_{12}$:Tb films as prepared and annealed at 800 °C.

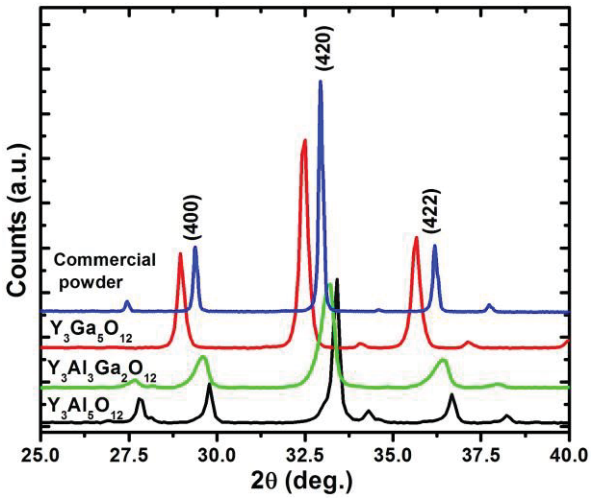

Figure 1 (b) XRD patterns of the commercial and prepared $Y_3(Al_x,Ga_y)O_{12}$:Tb powder, showing the change in the peak position with different Ga concentrations.

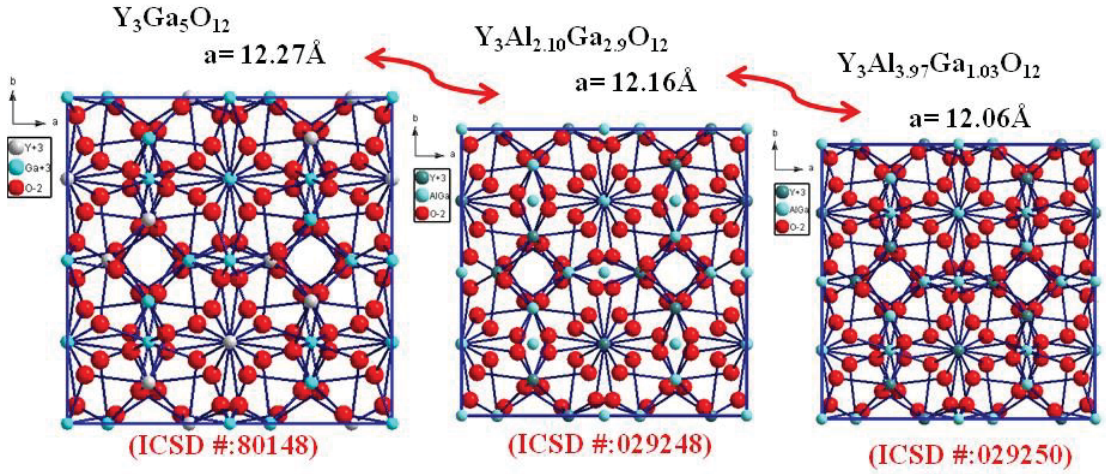

Figure 2 Change in lattice parameter of the garnet crystal structure with different Ga concentrations.

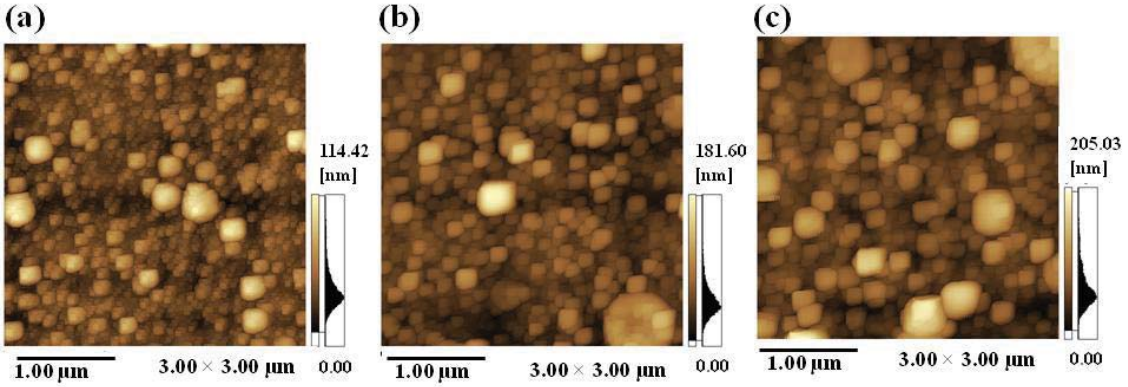

Figure 3 AFM images of the surface of the $Y_3(Al, Ga)_5O_{12}$:Tb films (a) as prepared and annealed at 800 °C for (b) 1 h and (c) 2 h.

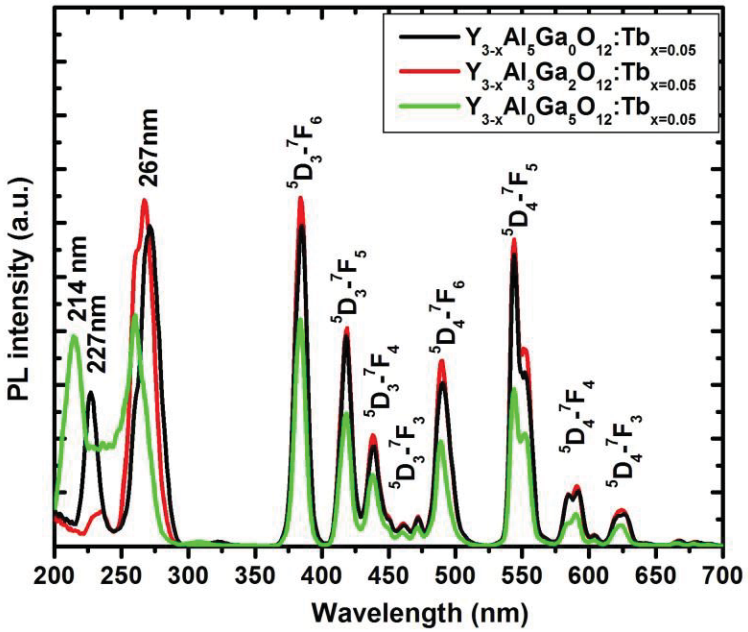

Figure 4 PL excitation and emission of the prepared $Y_{3-x}(Al_x, Ga_y)_5O_{12}$:$Tb_{x=0.05}$ powder with different Ga concentration.

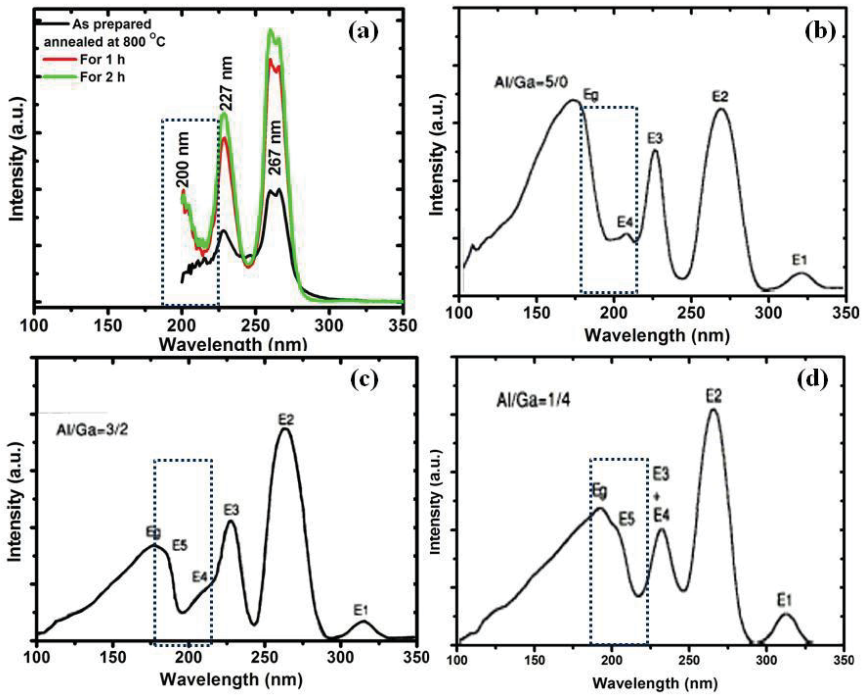

Figure 4 (a) PL excitationof the $Y_3(Al, Ga)_5O_{12}$:Tb films as prepared and annealed at 800 °C for 1 h and 2 h. **(b)- (d)** PL excitation of the $Y_3(Al, Ga)_5O_{12}$:Tb powder with different Ga concentration.

4. Conclusion

The influence of different annealing time on the optical and structural properties was observed as a new excitation band located at 200 nm and a shift in the diffraction peak position to lower diffraction angles, respectively. Both of them were attributed to an increase in the Ga concentration of the annealed films. An increase in the grain size with an increase in annealing time was also observed from the film morphology.

Acknowledgment

This work is financial supported by the African Laser Center (ALC) and it is based on the research supported by the South African Research Chairs Initiative of the Department of Science and Technology and National Research Foundation of South Africa as well as the University of the Free State Cluster program. We would like to thank the National Laser Center for allowing us to use their PLD system.

References

[1] O. Katsutoshi, A. Tomohiko, K. Tsuneo, 1990 *J. Appl. Phys.* **29** 103.
[2] A. Yousif, H.C. Swart, O.M. Ntwaeaborwa, 2012 *Appl. Surf. Sci.* **258** 6495.
[3] A. Yousif, H.C. Swart, O.M. Ntwaeaborwa, E. Coetsee,2013 *Appl. Surf. Sci.* **270** 331.
[4] H. Matsukiyo, H. Toyama, Y. Ueharab, H. Yamamotoc, 1997 *J. Lumin.* **229** 72.
[5] Q. Li, F. Qiu, J. Zhang, X. Pu, X. Liu, W. Zhang, 2009 *J. Alloys and Comp.* **474** 441.
[6] L.P. Peng, L. Fang, X.F. Yang, Y.J. Li, Q.L. Huang, F. Wu, C.Y. Kong, 2009 *J. Alloys and Comp.* **484** 575.
[7] A. Yousif, H.C. Swart, O.M. Ntwaeaborwa, 2013 *J. Lumin* **143** 201
[8] A. Yousif, H.C. Swart, O.M. Ntwaeaborwa, *Physica B*, in press.
[9] P. Y. Jia, J. Lin, X. M. Han, M. Yu, 2005 *Thin Solid Films* **483** 122.
[10] Rachael Hansel, Steve Allison, Greg Walker, 2008 *J. Materials Research Society* **K 06-06** 107.
[11] A Nakatsuka, S. Yoshiasa, S. Takeno, 1995 *Acta Crystallogr. Sec. B: Structural Science*, **51** 737.
[12] M. Marezio, J. P. Remeika, P. D. Deernier, 1968 *Acta Crystallogr., Sec. B* **24** 1670.
[13] Marezio, M., Remeika,J.P., 1968 *Acta Crystallogr., Sec.B* **24** 1670.
[14] F. X. Gil, D. Rodriguez and J. A. Planell, 1995 *J. Scripta Metallurgica et Materialia* **33** 1361.
[15] A. Mayolet, W. Zhang, E. Simoni, J.C. Krupa, P. Martin, 1995 *J. Optical Materials* **4** 757.

Division B – Nuclear, Particle and Radiation Physics

Investigations beyond the standard model

G Amar

National Institute for Theoretical Physics, School of Physics, University of the Witwatersrand, South Africa

E-mail: gilad.amar@cern.ch

Abstract. The LHeC, a possible addition to the LHC, allows for electron beams within the LHC. In this report new possibilities for investigating physics beyond the Standard Model with the LHeC are explored. An investigation of anomalous Higgs couplings in electron and positron collisions is presented, with promising results for detection of beyond Standard Model physics using the LHeC.

1. Feasibility study for beyond Standard Model research

The LHeC is a proposed project investigating the possibility of extending the collision types and energies at the LHC. The idea for achieving a wider range of collision possibilities is realized by colliding an electron beam from a new accelerator with the already existent proton beam of the LHC. Preliminary studies indicate that a luminosity of 10^{33} cm^{-2}s^{-1} would be possible, with a centre of mass energy beyond 1 TeV [1].

There are a number of proposed designs for the LHeC layout. The rst is a new electron ring on top of the current proton ring in the LHC tunnel, this yields the largest luminosities of the considered designs. Such an electron accelerator based inside the LHC tunnel can conceivably produce an electron beam of 50 GeV and a luminosity of 5×10^{33} cm^{-2}s^{-1} which corresponds to an integrated luminosity of order 100fb^{-1}. Alternatively, a linear accelerator can be used instead. The advantages of such a design include the construction of the LHeC to be largely separate from the existing LHC site, reducing complexity and cost, and larger electron beam energies are a possibility [2]. Energies up to 150 GeV are in consideration, with the design largely limited by cost. In contrast with the electron ring design, the linear accelerator may provide an electron beam of 150 GeV , a luminosity of 5×10^{32} cm^{-2}s^{-1} and an integrated luminosity of order 10fb^{1}. Of course, in either case, there is the added possibility of using a lead ion beam instead of protons further increasing the range of possible collision types and energies. In the example of the electron-ring LHeC, 2.7 TeV per nucleon is likely with a luminosity of 10^{31} cm^{-2}s^{-1}.

Physics programs stand to gain a lot from the LHeC. For example, the largely unexplored Standard Model (SM) processes which have prohibitively small cross-sections with the current LHC set-up can now be studied. These include the production of a light Higgs and a single top-quark. Undiscovered particles and new physics on distance scales below 10^{19}m are more sensitive to being probed. Promising channels include lepton-quark bound states, super-symmetric electrons and excited leptons. The determination of nucleon structure with greater precisionis now a possibility, xing the poor knowledge of gluon density and d/u quark ratio. In addition, more precise measurements of the SM electroweak and strong parameters can be made. Using

heavy-ion beams instead of protons opens the door to further measurement of the deep inelastic structure of nuclei which would be a welcome change from the previous lepton-nucleon scattering experiments which relied on xed target nucleons. Measurements of this kind would be four orders of magnitude larger beyond the accessible kinematic range of prior experiments.

1.1. Investigating Beyond the SM

Symmetry breaking is transmitted from the scalar sector to the gauge sector by having gauge boson-scalar couplings from the assignment of non-trivial gauge quantum numbers to the scalar fields in the theory. The precise couplings of the SM Higgs to the heavy electroweak gauge bosons $W^{\pm}$ and Z come out as

$$L_{int} = -gM_W \left(W_\mu W^\mu + \frac{1}{2cos\theta_W} Z_\mu Z^\mu \right) H. \tag{1}$$

The constants g, M_W and θ_W are all accurately measured, this vertex being fully determined in the SM. In confirming that the SM mechanism for breaking electroweak symmetry is the correct one, independent measurement of these vertices is required. In addition to these vertices requiring copious amounts of Higgs production for convincing statistical results, these vertices are also sensitive to Beyond Standard Model (BSM) physics. The $H(k)W^+(p)W^-(q)$ vertex can be parametrised in the following form [3]

$$i\Gamma^{\mu\nu}(p,q)\epsilon_m u(p)\epsilon^*_\nu(q). \tag{2}$$

Deviations from the SM form of $\Gamma_{SM}(p,q) = gM_W g$ would indicate the presence of BSM physics. These BSM deviations can be specified using the following formula

$$\Gamma^{BSM}_{\mu\nu}(p,q) = \frac{g}{M_W}[\lambda(p.qg_{\mu\nu} - p_\nu q_\mu) + \lambda'\epsilon_{\mu\nu\rho\sigma}p^\rho q^\sigma] \tag{3}$$

where λ and λ' are the effective strengths for the anomalous CP-conserving and CP-violating operators respectively. Whilst the CP properties are difficult to measure directly, they can be known if the couplings λ and λ' can be determined with good precision and accuracy.

1.2. Computational Research

The computational research in this paper will analyse the $e^+ + e^- \rightarrow h + \nu + \overline{\nu}$ process and see if there are any BSM physics involved. MadGraph 1.5.9, a program used to do Monte Carlo simulations allowing the user to calculate cross sections and to obtain unweighted events, was installed [4]. FeynRules is a Mathematica package that allows the calculation of Feynman rules in momentum space for any QFT physics model [5]. The minimal information to describe the new model including BSM higgs couplings is contained in the model-file. This information is then used to calculate the Feynman rules associated with the Lagrangian. The Feynman rules generated are then implemented into MadGraph. The number of events to be simulated were set to 100000. The programming framework ROOT was used to generate histograms. ROOT is a system environment and set of libraries developed by CERN designed specifically for particle physics data analysis [6]. Simulated event data is stored in .lhe files. The Les Houches Events (LHE) file format is an agreement between Monte Carlo event generators and theorists to define Matrix Element level event listings in a common language [7]. Adding the Pythia extension to MadGraph allows MadGraph to store the events, usually in a .lhe extension in .root files [8]. The different format being more easily used within the ROOT framework. All events utilise what is known as a Monte Carlo Numbering Scheme. This convention facilitates communication between event generators, detectors and analysis packages.

1.3. Results and Analysis

There are two channels in which the process $e^+ + e^- \rightarrow h + \nu_e + \overline{\nu}_e$ can occur. An S-channel is the joining of colliding particles into an intermediate particle that eventually splits into other particles. A T-channel is where two colliding particles interact via the emission of an intermediate particle from one of them. The S-channel features the production of the neutrinos through the decay of a Z boson.

$$e^+ + e^- \rightarrow z \rightarrow h + \nu_e + \overline{\nu}_e. \tag{4}$$

This means that the simulated events for the production of the Higgs and two neutrinos must come from the production of a Z boson that decays. In contrast the T-channel features the production of the Higgs and neutrino pair through vector boson fusion.

$$e^+ + e^- \rightarrow h + \nu_e + \overline{\nu}_e \backslash Z. \tag{5}$$

The '$\backslash Z$ denotes that processes contributing to the final state resulting from the decay of the Z boson are excluded. In understanding what contributions to the complete process are made from the two channels it is possible to learn how to distinguish between the sources of the data that are accrued by the detector.

Having run simulations of the two channels separately histograms were plotted for a beam energy of 125 GeV . At the centre of mass (COM) energy of 250 GeV, five different simulations were done. All differed on the strength of the factors λ and λ' using values of ± 1. For all the histograms that follow, the SM plot is in black for convenience of easy distinction from the coloured, or BSM, physics. λ equal to one and negative one are red and green respectively. λ' equal to one and negative one are purple and blue respectively.

Two histogram plots were selected for their useful insights and strikingly apparent differences between the physics models. Those selected are of the Higgs angle phi (azimuthal angle distribution w.r.t. the reaction plane defined by the incident particles) and a two-dimensional histogram showing the correspondence between theta (angle between colission product and incident beam) and momentum of the Higgs [9]. Histograms featuring properties of the emitted neutrinos were omitted as they, whilst showing appreciable differences, are near impossible to investigate with the detectors of the LHC. The S-channel features a Gaussian distribution centred

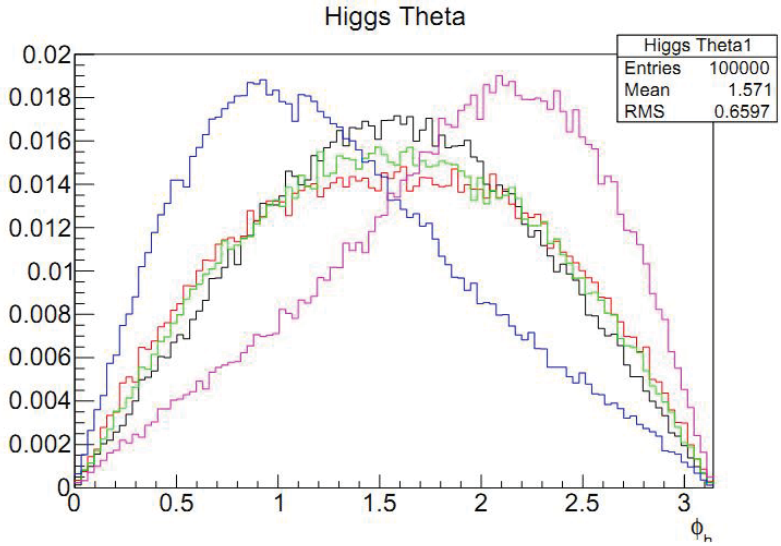

Figure 1. Higgs theta distribution from the S-channel at COM energy of 250 GeV.

around 61 GeV . This makes for easy separation of the two channels by merely excluding all

measurements of the Higgs momentum in near the peak. A quick glance at the Higgs theta distribution shows that the $\lambda = \pm 1$ processes differ slightly to the SM prediction, however the $\lambda' = \pm 1$ processes introduce a strong asymmetry about the line $\theta = \frac{\pi}{2}$ which can be used to determine if the true value of λ is non-zero. The two-dimensional histogram highlights the spike in momentum-theta phase space for the S-channel.

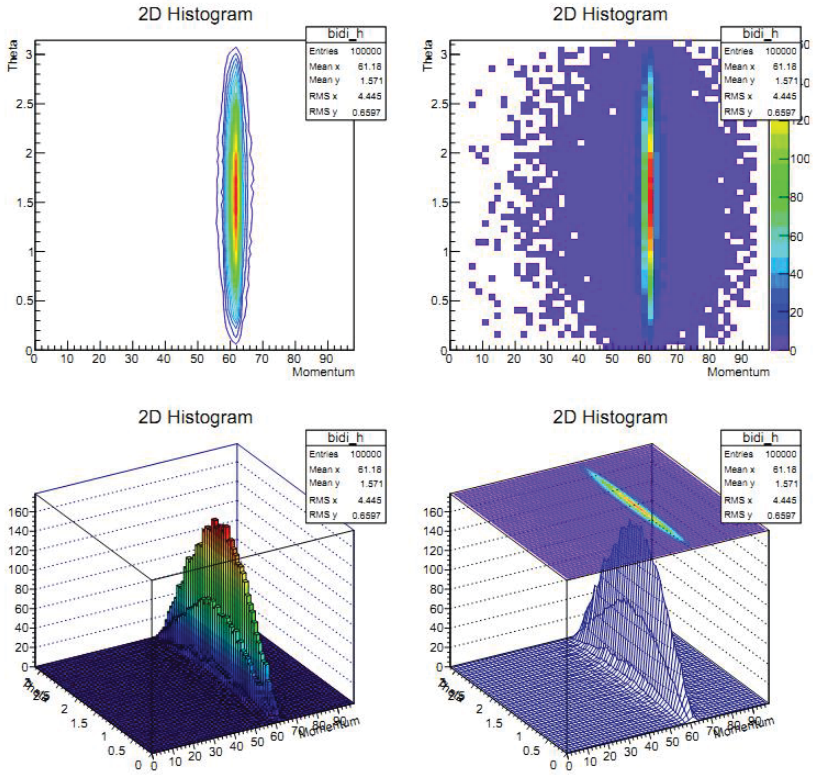

Figure 2. Two-dimensional histogram showing the correlation of the S-channel Higgs momentum and theta at COM energy 250 GeV.

In contrast with the S-channel, it can be seen that the T-channel Higgs momentum has a wide range of accessible values. So in excluding the peak of the S-channel it is quite possible to explore the T-channel and any variations from the SM. Compared to the S-channel, we see all the BSM parameters do affect the T-channel Higgs theta distribution, but unfortunately no asymmetry about $\frac{\pi}{2}$ which can be exploited as in the case of the S-channel. It is apparent in the T-channel that there is a much more widely distributed momentum and theta correlation that that of the S-Channel. As you can see, what makes for a very effective separation of the signal from the background is that the S-channel features a very strong peak of the Higgs momentum at a certain energy. In cutting out the momentum window it is not so simple as excluding a particular range of detected events without considering the specifics of the detector. The momentum of the the Higgs particle cannot be measured directly as it decays very rapidly. Primarily decaying to a $b\bar{b}$ quark pair, each producing a jet of particles, it is the measured momentum of these jets that tells us about the momentum of the initial Higgs boson. The resolution of the initial energy of the b quark has been found to be $\frac{60\%}{\sqrt{E}}$, the resolution of the Higgs momentum, the sum of the two b-jets is then given by $\sqrt{2}\frac{60\%}{\sqrt{E}}$. In excluding a two sigma E window on either side of the peak we ensure that 95% of the events within the range are cut out, however there will be a

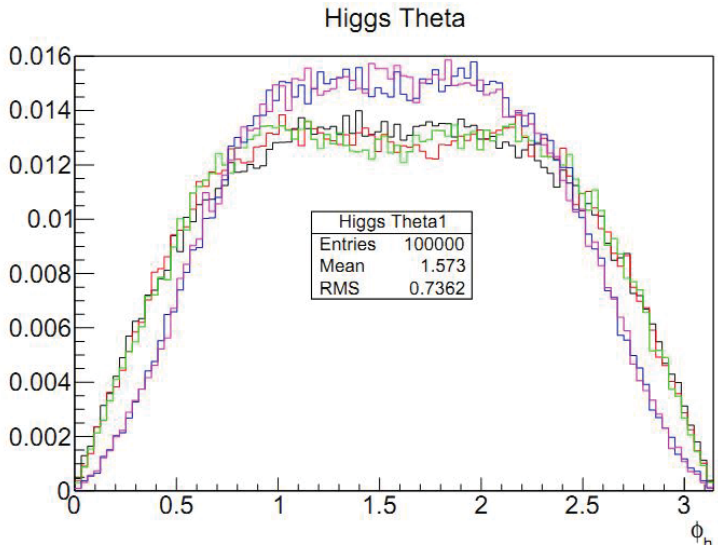

Figure 3. Higgs theta distribution from the T-channel at COM energy of 250 GeV.

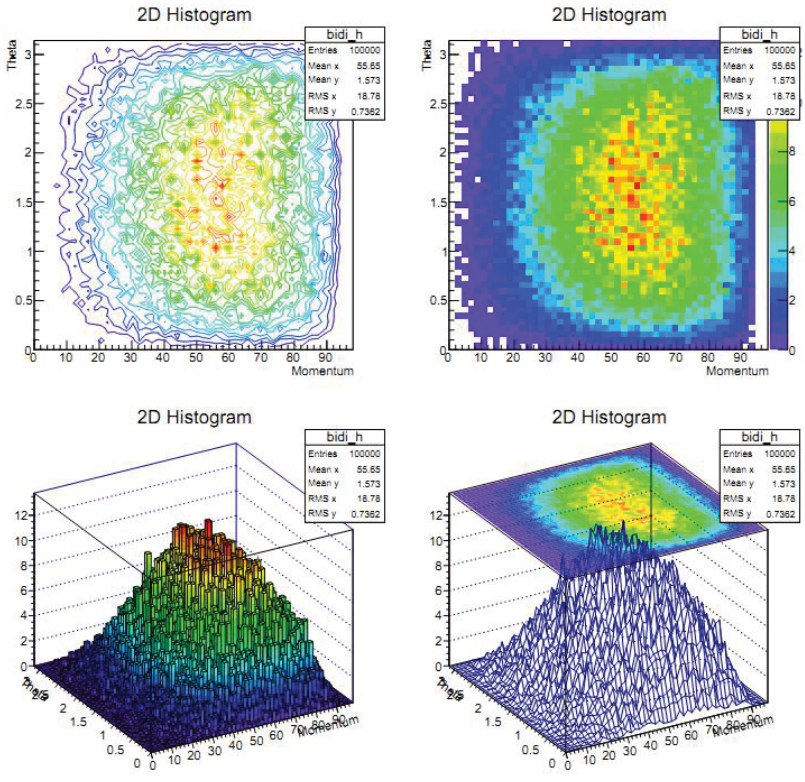

Figure 4. Two dimensional histogram showing the correlation of the T-channel Higgs momentum and theta at COM energy 250 GeV.

5% migration of some events that were within the window, being detected as having been from without.

The cross-sections are given from the outcome of the MadGraph run. Such output will have

to be modified by the cuts we imposed and other considerations. In all the simulations the output state was declared to involve an electron and anti-electron neutrino pair. However the lepton universality allows for end-states involving tau and muon neutrino pairs also, as such the MadGraph given cross-section needs to be multiplied by three. The cuts on the allowed momentum too will affect the cross-section. The fraction of events that survive the cut, times the cross-section signifies the cross-section for the process. Finally, the Higgs to $b\bar{b}$ branching ratio of 57.7% must also be considered. This simply means that the cross-section must be multiplied by 0.577.

1.4. Prospects for the future

Many avenues of further research still remain. Using results derived from Wilks and Wald, confidence intervals on the model parameters can be obtained, accounting for systematic uncertainties in test procedures. In this way the results of the experiment, especially the two-dimensional distributions, can be used to determine the values of λ and λ' even possibly finding them to be complex valued which was not explored in this paper. As with any simulation, higher order corrections may be explored, increasing accuracy at the cost of CPU time. Higher order corrections would be the inclusion of more Feynman diagrams and the multiple decay paths of the Higgs. The study was almost entirely focused on the parton-level, a more comprehensive and involved study would include the Higgs decay and hadronization of the resultant jets. Finally, it should not be said that all criterion useful for evaluating the BSM parameters were discovered. For instance, the asymmetry in Higgs theta distribution as a result of λ' values may be exploited to further increase the accuracy obtained from the two dimensional distributions.

2. Conclusion

In conclusion, it is seen that the existence of BSM physics parameters can make a signicant and detectable dierence to Higgs production. A useful ratio was discovered to test dierences from the SM and with further statistical based work can be expanded to determine BSM parameters and their respective condence intervals. The construction of the LHeC would go a long way toward studying BSM physics in a signicantly less convoluted way than the LHC alone could.

Acknowledgments

Acknowledgments The research in this paper was conducted as part of a internship for the National Institute of Theoretical Physics (NITheP) under the supervision of Dr. Alan Cornell. I sincerely appreciate Dr. Cornell and my co-supervisor, Prof. Bruce Mellado for their valuable insight and guidance. I am indebted to Kirtimaan Mohan for introducing me to Madgraph and providing me with his FeynRules. Finally I wish to thank NITheP, in particular to Renè Kotzè for having organized the internship.

References

[1] O. Bruening and M. Klein, Mod. Phys. Lett. A **28**, no. 16, 1330011 (2013) [arXiv:1305.2090 [physics.acc-ph]].
[2] P. Newman, Nucl. Phys. Proc. Suppl. **191**, 307 (2009) [arXiv:0902.2292 [hep-ex]].
[3] A. Djouadi, R. M. Godbole, B. Mellado and K. Mohan, Physics Letters B **723**, , pp. 307 (2013) [arXiv:1301.4965 [hep-ph]].
[4] http://madgraph.phys.ucl.ac.be/
[5] N. D. Christensen and C. Duhr, Comput. Phys. Commun. **180**, 1614 (2009) [arXiv:0806.4194 [hep-ph]].
[6] http://root.cern.ch/drupal/
[7] J. Alwall, A. Ballestrero, P. Bartalini, S. Belov, E. Boos, A. Buckley, J. M. Butterworth and L. Dudko *et al.*, Comput. Phys. Commun. **176**, 300 (2007) [hep-ph/0609017].
[8] https://pythia6.hepforge.org/
[9] A. R. Baden, Int. J. Mod. Phys. A **13**, 1817 (1998).

Challenges in the simulations of the iThemba LABS segmented clover detector

T. D. Bucher[1], S. P. Noncolela[1, 2], E. A. Lawrie[1], O. Shirinda[1], J. L. Easton[1, 2]

1. iThemba LABS, National Research Foundation, P. O. Box 722, 7129, Somerset West, South Africa.

2. University of Western Cape, Private Bag X17,7535, Bellville, South Africa.

Abstract. The Multi Geometry Simulation (MGS) code was employed to simulate the response of the iThemba LABS segmented clover detector for an arbitrary γ-ray interaction within its Ge crystals. The results from these simulations showing that the detector is sensitive to the position of the γ-ray interaction are topic of another paper. Here, the focus is on the challenges experienced during the simulations and on the progress made so far in obtaining realistic pulse shapes with the MGS code. Taking into account all the data, the way forward is outlined.

1. Introduction

A large volume n-type HPGe detector dedicated for γ-ray measurements is usually constructed in closed-ended coaxial geometry [1]. In this configuration, one electrode, the p^+ contact, is fabricated at the outer surface of the cylindrical crystal and another electrode, the n^+ contact, is located at the inner surface of the central hole. These contacts are made through the diffusion of a lithium layer on the inner surface and by boron ion implantation on the outer surface of the detector. The p-n junction of this coaxial detector is located at the outer surface of the detector and when the positive high voltage (reverse biased) is applied to the n^+ contact, the depletion region expand from the p^+ contact inwards, see figure 1.

When the detector if fully depleted, the potential throughout the coaxial type detector is given by the Poisson equation in cylindrical coordinates,

$$\frac{d^2\Phi}{dr^2} + \frac{1}{r}\frac{d\Phi}{dr} = -\frac{\rho}{\epsilon_0}$$

where ρ is the net charge density, and ϵ_0 is the dielectric constant for the material. This equation can be solved by letting the potential difference equal to the applied voltage. The electric field can be described using,

$$-E(r) = -\frac{\rho}{2\epsilon_0}r + \frac{V + (\rho/4\epsilon_0)(r_2^2 - r_1^2)}{r\ln(r_2/r_1)}$$

where r_1 and r_2 are the inner and outer radii of the coaxial detector. The depletion region is the sensitive region of the detector. Therefore, when charge carriers are created in this region they will be swept by the applied electric field to their contacts. The depth of the depletion region, d, can be calculated using the Poisson equation and the voltage required to deplete the detector, V_d, is determined by setting $E(r_1)=0$,

$$V_d = \frac{\rho}{2\epsilon_0}\left[r_1^2 \ln\frac{r_2}{r_1} - \frac{1}{2}(r_2^2 - r_1^2)\right].$$

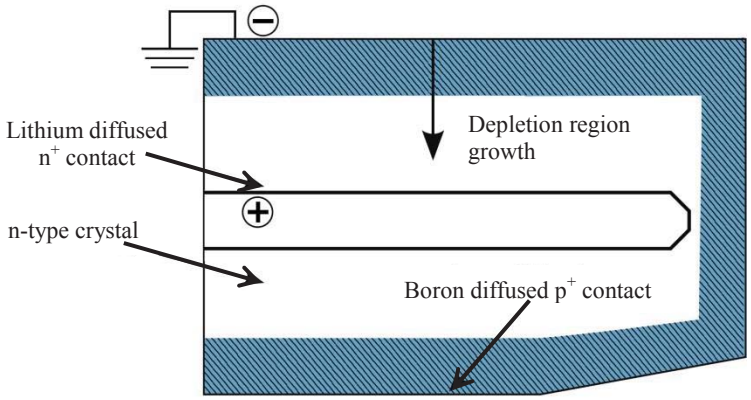

Figure 1: Depletion region expand from the p-n junction at the outer electrode when the positive high voltage (reverse biased) is applied to the inner electrode.

2. iThemba LABS segmented clover detector

The iThemba LABS segmented clover detector, manufactured by Canberra, France [2], consists of four n-type HPGe crystals. The crystals dimensions are: a diameter of 60 mm (before tapering) and a length of 90 mm. Each crystal is electrically segmented into 8 contacts on the outer surface, with depth segmentation at 35 mm. This results in a total of 36 electronic channels of which 32 are associated with the outer contacts and 4 with the inner core contacts of the detector.

During γ-ray interaction, all segments and inner core contacts produce signals with specific pulse shapes. These pulse shapes carry information about the position (x,y,z) where a γ-ray interacted within the Ge crystal. To make use of this position sensitivity of the detector, a database of simulated pulses for various γ-ray interaction positions is needed.

3. Detector simulation

In June 2012, a free access electric field simulation code called Multi Geometry Simulation (MGS) [3] was acquired. It can derive the pulse shape response at the contacts of a segmented HPGe detector. In order for MGS to produce these pulse shapes, it calculates: electric potential surfaces by solving the Poisson equation, electric fields, drift velocities for electrons and holes in the electric field, and lastly weighting potential which is a coupling between the charge carriers and electrodes.

The first simulation of crystal A of the iThemba LABS segmented clover detector yielded the pulse shapes on all its contacts and they looked reasonable. The simulation involved a detailed description of the geometry of the detector, default linear parameterization of the crystal impurities. Most surprisingly, however, it was observed that the simulated depletion region was growing from the inside outwards, which is incorrect for an n-type detector with positive bias applied on the inner core electrode. These results are illustrated on figure 2.

When a positive high voltage of 1000V was applied, the undepleted region (shown in blue) remained large (see figure 2(a)). But even when the biased voltage was increased to 2250V which is higher than the depletion voltage of this crystal as measured by the manufacturer, the simulation yielded some undepleted spots at the corners (see figure 2(b)). To reach complete depletion of the crystal in these simulations a biased voltage higher than 3000V (which is the suggested operational voltage), was needed. The problem was discussed with the MGS code's developer, Mr P. Medina. Nevertheless for a long time it looked as if MGS simply not designed to describe correctly the depletion voltage. While the work on this was in progress, other improvements in the MGS simulations were made.

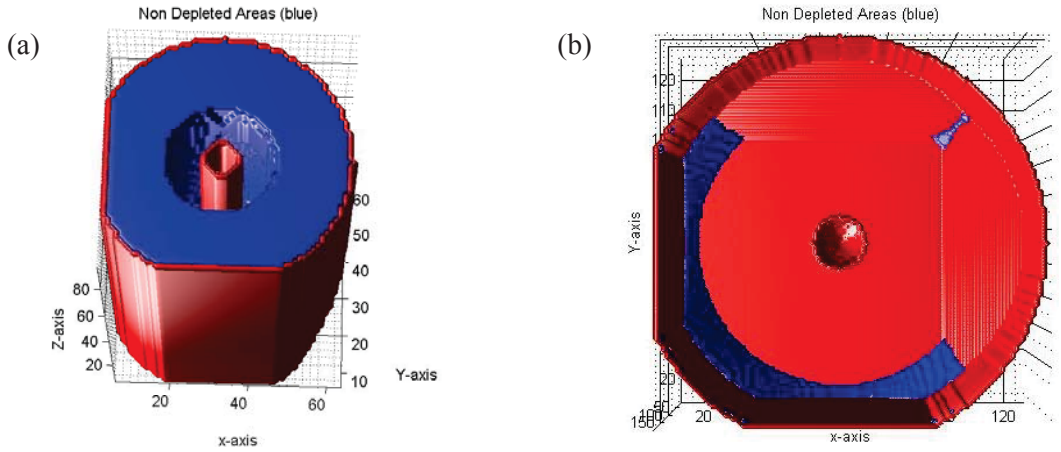

Figure 2. MGS simulations of the depletion region for crystal A. (a) At an applied voltage of 1000V. (b) At an applied voltage of 2250V. The depletion voltage, as given by the manufacture, is 2000V.

Simulation progress

In the MGS code, the impurity concentration profile of the crystal was assumed to be liner function along the depth of the detector. This was because the manufacturer supplied all detectors with impurity concentration values at front and back of the crystals only.

During a research visit to Canberra Lingosheim in June 2012 there was an opportunity to discuss directly with the manufacturer of the detector some remaining issues. During this visit detailed impurity concentration profiles for the crystals of the iThemba LABS segmented clover detector was obtained. The actual impurity profile for crystal A is shown in figure 3. This profile was then implemented in the MGS code.

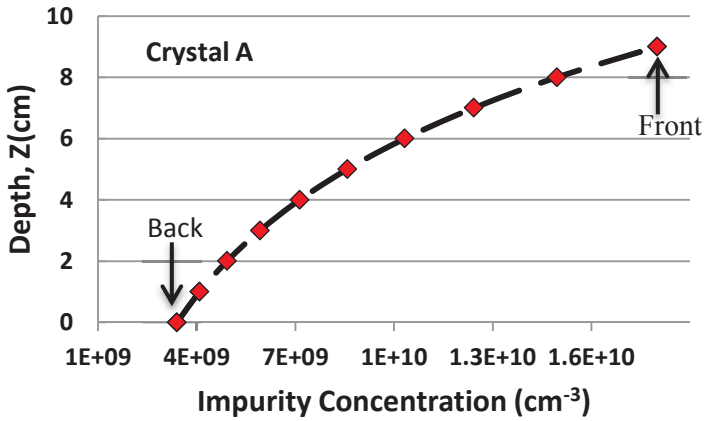

Figure 3. An exponential profile of the impurity concentration provided by the manufacturer with higher impurities at the front and lower at the back of the crystal.

At this stage minor changes were also made in the geometry of the crystal, to implement the exact shape and the outside segmentation. The current simulated geometry of crystal A is shown in figure 5.

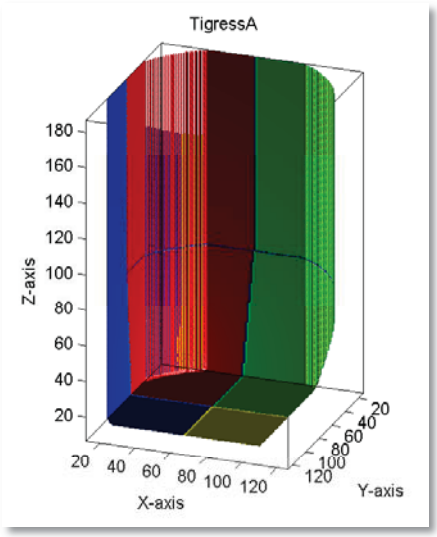

Figure 5. MGS simulations of the crystal geometry with front vertical segmentation at an angle as designed by the manufacturer.

Most bothering, however, was the problem with the depletion voltage. It was finally understood, that the code was not able to describe the actual structure of a semiconductor, but the p-n junction of an n-type detector was defined simply through the features of an electric field. That required special definition of the field and net charge density. After then input was corrected, and taking account the other improvements in the simulations, the depletion of the detector was reproduced well. Figure 6 illustrate these results. At the applied biased of 500 V, the depletion region starts growing from outside inwards, see figure 6(a). At the applied biased of 1500 V, a small part of undepleted region remains near the front part of the core electrode see figure 6(b) since the impurity concentration is higher at the front than at the back. Furthermore it was found that crystal A is completely depleted at a voltage of 2000V, see figure 6(c), which matches the depletion voltage given by the manufacture.

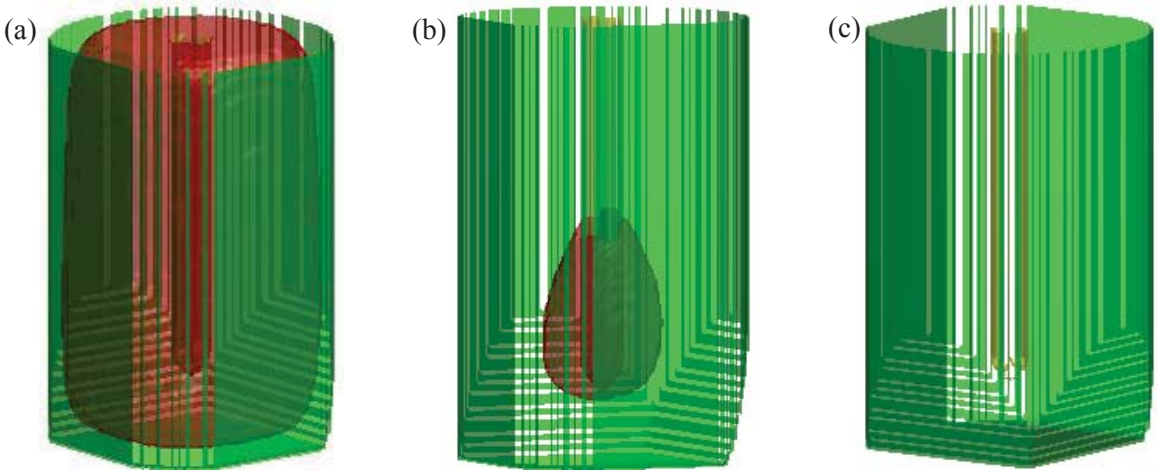

Figure 6. MGS simulations of the depletion region as a function of the applied voltage; undepleted region is shown in red. (a) At 500 V, small depletion region near the surface is observed; the depletion is growing from outward inside. (b) At 1500V, undepleted region remains near the front end of the core electrode. (c) A complete depletion of the crystal at a depletion voltage of 2000V.

4. Additional simulations

The initial difficulties to simulate the depletion region with the MGS code prompted us to look for alternative software. In June 2013, another free access code called AGATA Detector Library (ADL) [4] was acquired from France. This code is specially developed to simulate pulse shapes for AGATA [5] detectors. The implementation of the geometry of the segmented clover, see figure 7, and the changes in the code making it able to deal with an exponential impurity concentration profile were challenging. Nevertheless, the first preliminary ADL simulations of the iThemba LABS segmented clover detector were completed and are shown in figure 8 (b).

The pulses end when the charge carriers are fully collected. Different end-points of the pulses are easily observed in the MGS simulations, see figure 8(a), while the ADL pulses are artificially extended at a constant value corresponding to the full charge. The comparison of the pulse shapes of the MGS and ADL codes for various γ-ray interaction positions shows very similar results. Fine tuning of the parameters of both codes is in progress. Most importantly the parameterisation of the electron and holes drift velocities in made in a different way in the two codes. Thus it is unclear whether the charge mobility is exactly the same in both codes. Instead to try to adjust drift velocities in the two codes to one another, we plan to measure the experimental pulses, and to make the necessary corrections based on them.

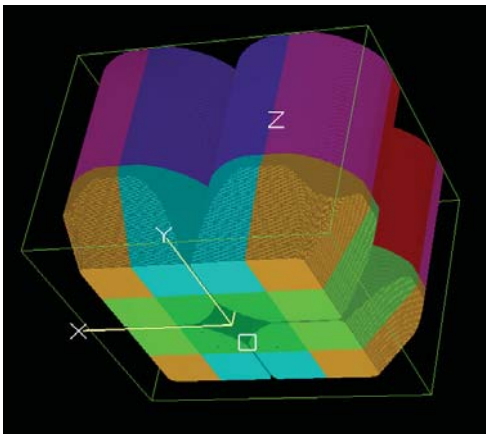

Figure 7. ADL simulations of the four iThemba LABS segmented crystals.

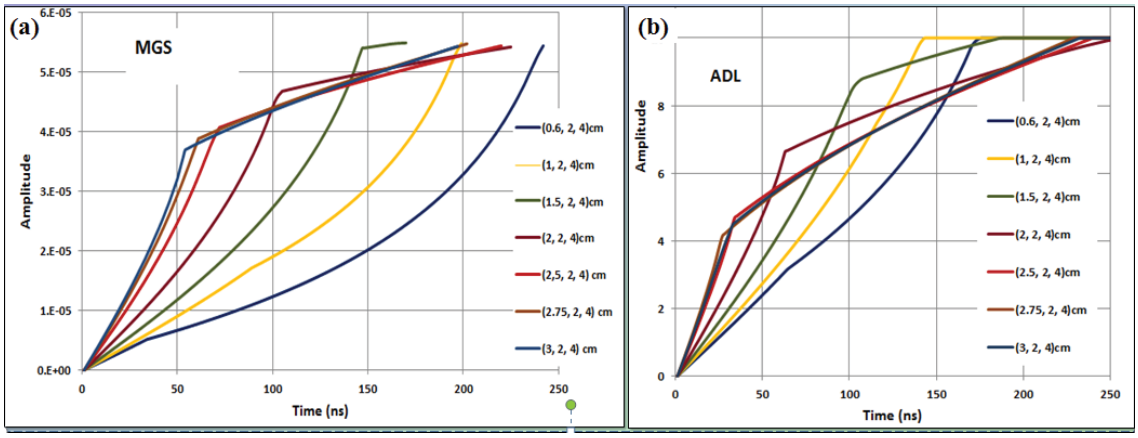

Figure 8. The charge pulse shapes on the inner contacts simulated with the MGS (a) and ADL (b) codes for crystal A, and before the preamplifier response function is implemented. The simulations were performed for various interaction positions with different x, but same y and, z.

5. Summary

Simulation of the pulses on the 9 electrodes of crystal A of the iThemba LABS segmented clover detector was completed with two software codes, MGS and ADL. The progress so far proved that the task of performing realistic simulations is challenging and requires high precision with numerous details. Next step will be to convolute the simulated charge pulses from the two codes with the response function of the preamplifier and the remaining electronics. Most important will be to compare the simulated pulses with a set of measured ones. For such a measurement precise determination of the positions of the interaction points inside the detector is needed. In addition the electronic cross-talk has to be determined. Preparations for such measurements are in progress.

6. References

[1] Knoll G. F., Radiation Detection and Measurements, Chapter 12, Fourth Edition, John Wiley & Sons, 2010.

[2] Canberra France: http://www.canberra.com/fr/#2.

[3] Medina P, et. al., Proceedings of the 21st IEEE Instrumentation and Measurement Technology (IEEE Cat. No.04CH37510), pages 1828–1832, 2004.

[4] ADL, http://www.ikp.uni-koeln.de/research/agata/index.php?show=download

[5] AGATA, official website </http://www-w2k.gsi.de/agata>.

Lifetime measurements in the transitional nucleus ^{150}Sm

[1]S. P. Bvumbi, [1]S. H. Connell, [2]J. F. Sharpey-Scafer, [3]S. M. Mullins, [3]R. A. Bark, [3]E. A. Lawrie, [3]J. J. Lawrie, [1]P. L. Masiteng, [3,4]S. S. Ntshangase and [2,3]O. Shirinda

[1]University of Johannesburg, Department of Physics, P. O. Box 524, Auckland Park 2006, South Africa
[2]University of the Western Cape, South Africa
[3]iThemba LABS, South Africa
[4]University of Zululand, South Africa

E-mail: suzanb@uj.ac.za

Abstract. Weakly populated band structures have been established in the nucleus ^{150}Sm at low to medium spins following the ^{136}Xe(^{18}O, 4n)^{150}Sm fusion evaporation reaction at 75 MeV. The band built on the second 0^+ state has been established. Lifetime measurements have been performed by the Doppler Shift Attenuation method in the positive-parity S-band. Experimental transition strengths B(E2) together with angular-intensity ratios and linear polarization were measured. The preliminary results support the strong collective interpretation.

1. Introduction

The nucleus $^{150}_{62}$Sm$_{88}$ lies in a transitional region where nuclear collectivity rapidly changes from vibrational to rotational motion [1]. This is reflected in the rapid change in the experimental $\frac{E(4^+)}{E(2^+)}$ energy ratios between $N = 86$ and $N = 96$ nuclei for isotopes with $Z \sim 64$, as shown in Fig 1. The $\frac{E(4^+)}{E(2^+)}$ ratios of 2.00, 2.50 and 3.33 are expected for pure vibrational, γ-soft and rotational, respectively. The ratio $\frac{E(4^+)}{E(2^+)}$ for ^{150}Sm is $\sim$ 2.32 approaching 2.50, the value expected for a γ-soft rotor [2]. The structure of the nucleus ^{150}Sm is very complex and extracting lifetimes is a useful approach because this gives information on the reduced electromagnetic transition rates which are very sensitive to the intrinsic structure of the excited states. From these measurements, information on the deformation of the different collective structures in a deformed nucleus may be obtained.

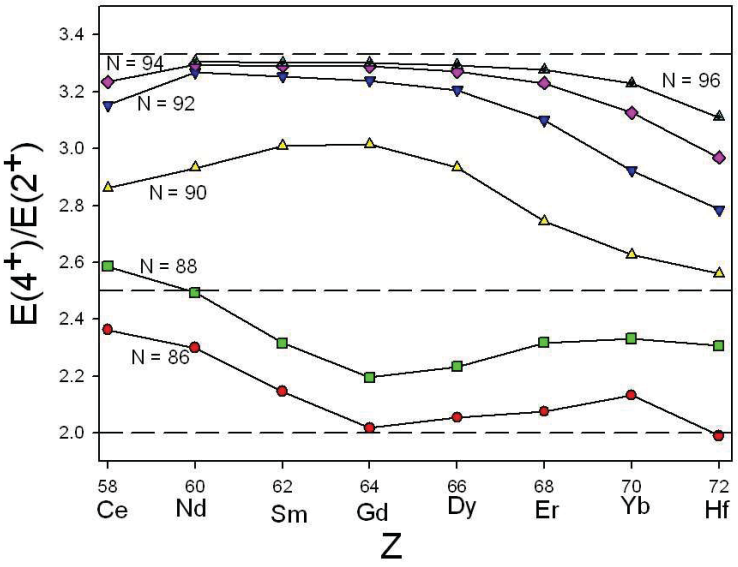

Figure 1. $\frac{E(4^+)}{E(2^+)}$ energy-ratio systematics for even-even nuclei as a function of atomic number Z. The horizontal dashed lines represent limits expected for pure vibrational (2.00), rotational (3.33), and γ-soft (2.50) behaviour.

2. Experimental details and Results

The high spin states of the nucleus ^{150}Sm were populated using the ^{136}Xe(^{18}O, 4n)^{150}Sm fusion evaporation reaction. It was studied at iThemba LABS, using the AFRODITE spectrometer array equiped with 9 clover HPGe detectors in BGO shields. An ^{18}O beam energy of 75 MeV was used to bombard $\sim$5 mg.cm^{-2} of frozen ^{136}Xe target, backed by a 1 mg.cm^{-2} layer of ^{197}Au. A total of $\sim 5 \times 10^8$ events was accumulated over 3 days of beam time. The trigger condition was such that two Compton-suppressed HPGe detectors fired in prompt time coincidence. The data was unfolded into a two-dimensional matrix which was analyzed using Radware [3]. The decay scheme obtained from our data is shown in Fig. 2. In order to extract lifetimes in the excited levels in ^{150}Sm we used the doppler shift attenuation method (DSAM) [4]. This method senses the lifetime of the nuclear level by careful modelling of the velocity dependent doppler shift of the emitted photon. The recoiling nucleus slows down on a time scale that correlates with different velocity distributions for different nuclear level lifetimes. It requires a good knowledge of the material in which the recoiling nucleus comes to rest. The analysis is further assisted by viewing the recoiling nucleus from several different angles, (forward, perpendicular and backward with respect to the average recoil directions), as this allows a more robust modelling of the DSAM lineshapes.

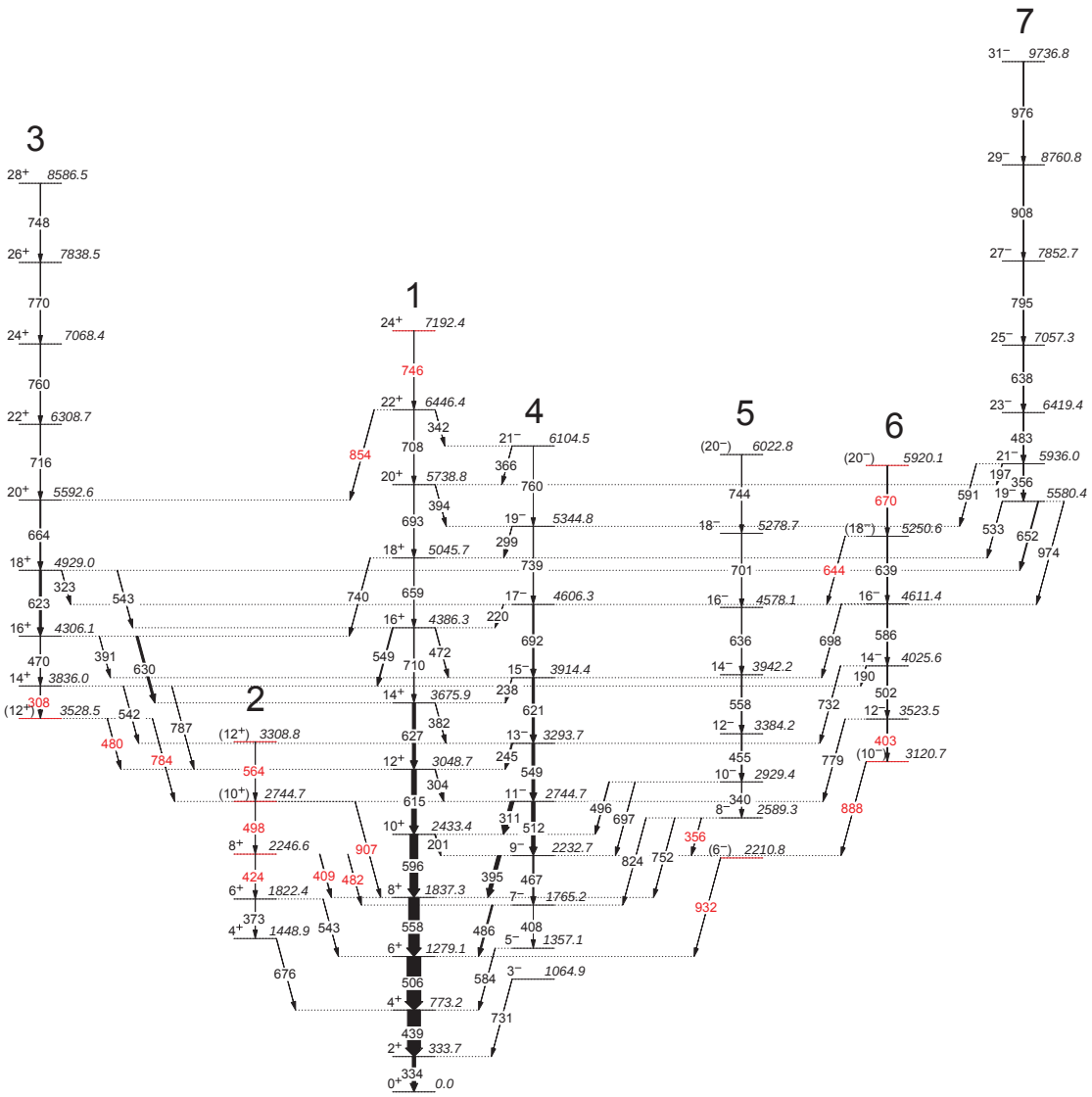

Figure 2. The new level scheme for ^{150}Sm obtained from our ^{136}Xe(^{18}O, 4n)^{150}Sm reaction with new levels and γ-rays in red. The levels with spin and parity in parentheses represent levels whose spins and parities could not be determined due to lack of statistics.

2.1. New levels in ^{150}Sm

The new levels observed in this work are shown in Fig. 2. Three weakly populated bands 2, 5 and 6 have been observed in ^{150}Sm. Previously, states up to 6^+ were observed in band 2 and the current work has observed three additional levels from 8^+ to (12^+). Levels in bands 5 and 6 are reported in the nuclear data base, however their origins cannot be traced and previous studies done by [5] did not observe this states, we therefore consider them new observations. Two new states have been added in band 6, making its band-head to be at energy 3120.7 keV with spin-parity (10^-). Band 6 decays only to the lowest-negative parity band via a series of $\triangle I = 1$ transitions. Bands 2 and 5 decay to the ground-state band via a series of $\triangle I = 0$ transitions. Recently band 2 has been reported by [6] to have $\triangle I = 1$ decays to the lowest-negative parity

band 4. In order for us to make firm spin and parity assignments to the transitions in the level scheme, angular-correlation measurements [7] using the directional correlation from oriented states (DCO) and linear polarization anisotropy [8] techniques were used.

2.2. Lifetime measurements

The lifetime measurements we made were more complicated due to the imperfect knowledge of the target thickness and absence of forwards (45°) spectra. Xenon targets gradually sublimate under irradiation and without knowledge of the exact target thickness distribution during the experiment DSAM measurements are less precise. There are further complications due to complex spectra arising from some contamination, we illustrate this in Fig. 3. Our statistics allowed us to make measurements for lifetimes of the 20^+ and 22^+ states of band 3. The recoil stopping times in solid Xe and Au differ by a factor of four. At 3 mg/cm^2 of Xe, recoils are stopped mainly in the target with low stopping power, while at 1 mg/cm^2 they are stopped mainly in the Au backing with high stopping power. Correspondingly, for the 664 keV lineshape analysis, the difference in lifetime obtained is very large. Peaks in ^{150}Sm are strongly contaminated by other known lines or unknown background peaks, and as a result only a lifetime limit can be obtained. Similarly for the 716 keV transition, this peak is contaminated by two known lines, the 710 keV and 708 keV transitions in the ground state band 1. The lifetimes we obtain are different as well, however, the uncertainty could be removed if 45° spectra were measured. When the lifetime of an excited state is known, its experimental strength B(E2) can be evaluated as [9],

$$B(E2) = \frac{0.05659}{t_{\frac{1}{2}}(E2)(E_\gamma)^5}(eb)^2, \tag{1}$$

where $t_{\frac{1}{2}}$ is the half-life of the E2 transition and E_γ is the energy of the E2 transition. With estimates of the thickness target we obtained limits of 0.45 ps and 1.3 ps for the 716 keV transition de-exciting the 22^+ level of band 3, and limits of 1.15 ps and 2 ps for the 664 keV transition de-exciting the 20^+ level in the same band, see Fig. 5 and Fig. 4. With these lifetimes estimates we get B(E2) values of 0.668 (eb)^2 and 0.231 (eb)^2 for the 716 keV transition respectively, and for the 664 keV transition we get B(E2) values of 0.398 (eb)^2 and 0.219 (eb)^2 respectively. The B(E2) values of the 716 keV and 664 keV transitions differ by a factor of three due to the different lifetimes. The estimates of the target thickness were made using Monte Carlo simulation codes COMPA, GAMMA, and SHAPE [4].

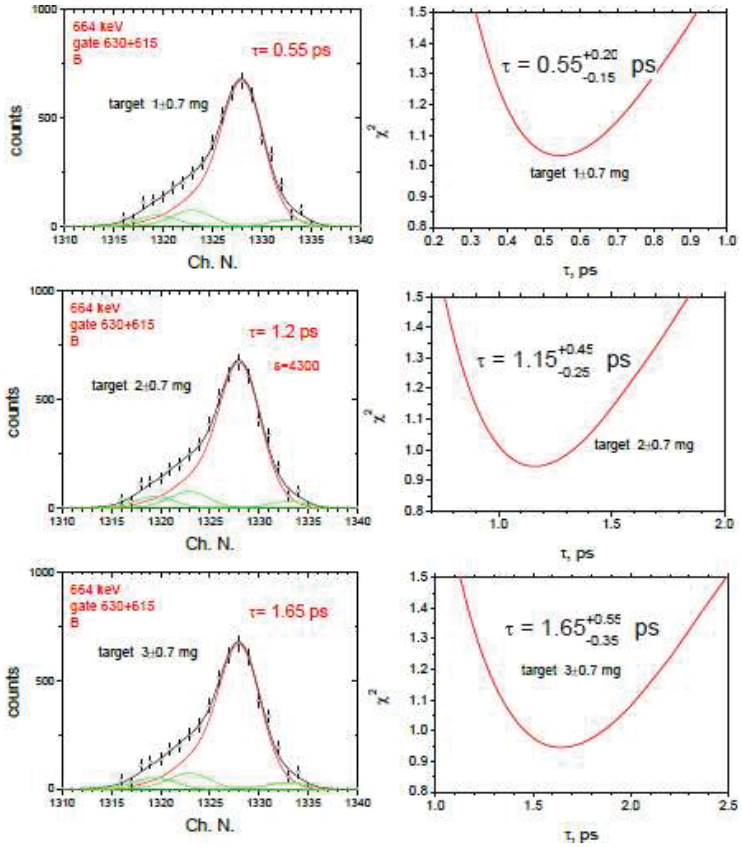

Figure 3. Lineshape analysis of the 664 keV peak and illustration of target thickness control during the experiment. The target thickness is evaluated by the lineshape observed.

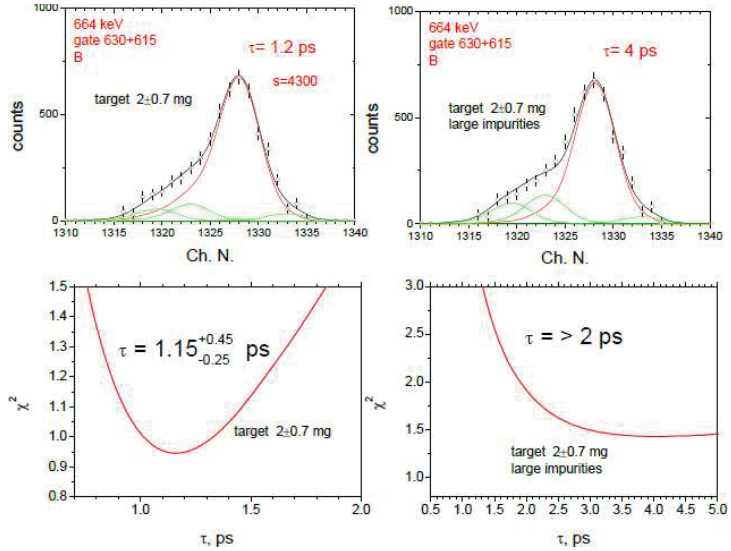

Figure 4. The lineshape analysis of the 664 keV transition from the 20^+ state of band 3 at 135° and the obtained lifetimes.

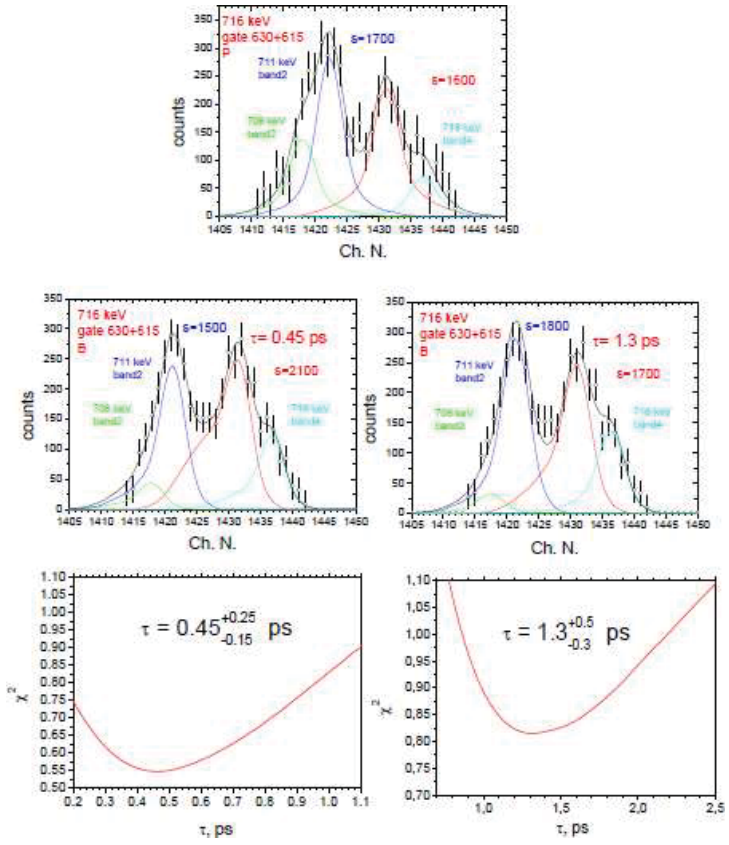

Figure 5. The lineshape analysis of the 716 keV transition from the 22^+ state of band 3 at 135° and the obtained lifetimes.

3. Discussion

The lowest levels of band 2 were originally associated with a $K^\pi = 0^+$ β-vibrational band [10]. However the low excitation energy of the 0^+ band-head has lead to the questioning of this interpretation by [11]. In this reference they are interpreted as a second vacuum (0_2^+) coexisting with the first 0_1^+ ground state vacuum caused by configuration-dependent pairing. The transition strengths B(E2) values that we obtained show that these structures are indeed collective and are deformed. This is confirmed by comparing them with the B(E2) values (1.35 e^2b^2, 1.35 e^2b^2 and 1.67 e^2b^2) of the excited 2_1^+ state in the isotones ^{150}Sm, ^{148}Nd and ^{152}Gd respectively, these are very comparable [12].

4. Conclusion

The high spin measurements with AFRODITE have led to the discovery of new non-yrast structures and allowed lifetime estimates to be made in the nucleus ^{150}Sm. The 0_2^+ band has been established to a spin-parity of 12^+. Additionally, experimental lifetimes for the 20^+ and 22^+ states of the S-band 3 have been measured following the target thickness estimates. The preliminary lifetime measurements enabled the B(E2) values to be calculated. This analysis supported the more strongly collective interpretation of these states. This work support further measurements where in order to have a best fit for lifetime, relative target thickness should be evaluated every shift together with registration of the average beam current during the experiment, and 45° spectra should also be collected in order to minimize the uncertainty in the measurements.

4.1. Acknowledgments
We would like to thank all our many colleagues in the AFRODITE group and students for their participation in the experiment and for the allocation of beam time at iThemba LABS.

References

[1] Casten, R. F. and Zamfir, N. V., Phys. Rev. Lett. **47**, 1433 (1981).
[2] R. F. Casten and P. Von Brentano and K. Heyde and P. Van Isacker and J. Jolie, Nucl. Phys. A **439**, 289 (1985).
[3] D. C. Radford, Nucl. Instr.Methods Phys. Res. Sect. A **306**, 297 (1995).
[4] Srebrny and Ch. Droste and T. Morek and K. Starosta and A. A. Wasilewski and A. A. Pasternak *et al.*, Nucl. Phys. A **683**, 21 (2001).
[5] W. Urban and J. C. Barcela and J. Nyberg, ACTA. Phys. Pol. **32**, 2527 (2001).
[6] S.P. Bvumbi, J. F. Sharpey-Schafer, P. M. Jones, S. M. Mullins *et al.*, Phys. Rev. C **87**, 044333 (2013).
[7] K. S. Krane and R. M. Steffen and R. M. Wheeler, Nucl. Data Tables A **11**, 351 (1973).
[8] P. J. Twin, Nucl. Instr. Methods **106**, 481 (1973).
[9] K. E. G. Löbner and M. Vetter and V. Hönig, Nucl. Data Tables, **47**, 495 (1970).
[10] P. A. Aguer and C. F. Liang and J. Libert and P. Paris and A. Peghaire and A. Charvet and R. Duffait and G. Marguier, Nucl. Phys. A **252**, 293 (1975).
[11] J. F. Sharpey-Schafer and S. M. Mullins and R. A. Bark and J. Kau and F. Komati and E. A. Lawrie and J. J. Lawrie and T. E. Madiba and P. Maine and A. Minkova and S. T. H. Murray and N. J. Ncapayi and P. A. Vymers, Eur. Phys. J. A **47**, 5 (2011).
[12] S. Raman and C. W. Nestor JR. and P. Tikkanen, Atm. Data. and Nucl. Data. Tables **78**, 1-128 (2001).

Using the Higgs as a portal to the "hidden sector"

Elizabeth Castaneda-Miranda
University of Johannesburg, Johannesburg, South Africa
E-mail: elizabeth.castaneda.miranda@cern.ch

Abstract. The ATLAS and CMS experiments at the Large Hadron Collider at CERN provide an opportunity for studying the physics of the Standard Model (SM) and beyond. In particular, one may search the so called "hidden sector" for a possible new neutral boson which could be revealed by the study of the decay of the recently discovered Higgs-like boson or alternatively any other as yet undiscovered Higgs boson. After the LHC successfully concluded a three years running period, the ATLAS and CMS experiments presented their recent results in Moriond conference with 25 fb^{-1} of integrated luminosity recorded. We present a phenomenology study on $H \to Z'Z' \to 4l$ using the recent results from the ATLAS and CMS experiments. The aim of this work is interpreting the experimental results using the HAHM as a benchmark model and presenting the compatibility of the model with these results with the SM.

1. Introduction

In the summer of the 2012, the ATLAS and CMS collaborations announced the discovery of a new particle, compatible with Higgs boson [1, 2]. However, we lack strong evidence for the Higgs decaying into fermions ($H \to \tau\tau$ and $H \to bb$) which is important to probe the SM Higgs boson hypothesis (see the latest published results from ATLAS and CMS in the $H \to \tau\tau$ search [3, 4] and in the $H \to bb$ search [5, 6]). Furthermore a precise measurement of the properties of this "new boson" is needed: spin, CP-states, mass, signal strength.

The signal strength is the first quantity which has been measured experimentally. It is defined as the ratio between the observed rate and the SM predicted rate ($\mu = \sigma_{obs}/\sigma_{SM}$). This quantity is the one leading to the observation claim. The current experimental results show that μ is close to 1 [7, 8], but an interesting case would be if μ becomes significantly different to 1, as then it would require an extention of the SM.

For these reasons the theories describing physics beyond the Standard Model (BSM) attempt to re-interpret the experimental results. One of these BSM theories is the "Hidden Abelian Higgs Model" (HAHM) [9, 10].

The HAHM model introduces two extra physical states which serve as the main routes to find evidence for the HAHM at the LHC:

- the existence of a new gauge boson Z' (lighter than the Z boson) that couples to SM states according to the strength of the kinematic mixing parameter;
- the existence of two CP-even Higgs boson mass eigenstates, both of which couple to SM states by virtue of the mixing of the HAHM Higgs boson with the SM Higgs boson.

The search for $H \to Z'Z' \to 4l$ is an interesting decay channel which is compatible with one of the main decay channels ($H \to ZZ^{(*)} \to 4l$) used in the discovery of the Higgs and is also motivated by the HAHM model.

The present study investigates how the rate of the observed $4l-$events is changed assuming Wells *et al*. model (HAHM) instead of the SM.

2. Hidden Abelian Higgs Model (HAHM)

The HAHM is one of the representative cases of a Hidden World, where "hidden" means a collection of particles that are not from the SM, that are not charged under the SM gauge groups, and that do not couple via gauge interactions to SM particles.

To explore this "hidden sector", two SM operators that are gauge-invariant can be exploited: the hypercharged field strength tensor $B_{\mu\nu}$ and the Higgs modulus squared $|H_{SM}|^2$. These two operators can couple to the "hidden sector" in a relevant way (dimension≤ 4).

Then, with both SM operators ($B_{\mu\nu}$ and $|H_{SM}|^2$) and extra $U(1)_X$ factor in addition to the SM gauge group with a complex Higgs boson Φ_H that breaks the symmetry upon condensation, the HAHM is defined.

2.1. Model parameters

The description of the parameters of the model are presented in references [9, 10]. Three of these parameters are considered to be free: the mass of the Higgs boson (M_H), the mass of the new gauge boson ($M_{Z'}$) and the mixing angle between the SM and the Hidden Higgs sectors (θ_h). For convenience, we will use the sine-square of the mixing angle ($\sin^2\theta_h \equiv s_h^2$) and then also define the cosine-square of the mixing angle ($\cos^2\theta_h \equiv c_h^2$). The SM limit is when there is no mixing (i.e. $\theta = 0$, which is equivalent to $\chi^2 = 1$ [10]).

2.2. Couplings

2.2.1. Higgs couplings In this model, the Higgs boson is coupled to SM particles in the same way as is with the SM Higgs with the following features:

- it introduces an extra new gauge boson in the allowed decays ($H \to Z'Z'$ and $H \to ZZ'$);
- the $H \to ZZ^*$ couplings are non-trivially modified with respect to SM;
- the Higgs production by gluon fusion is supressed by a factor c_h^2.

Here we consider only $H \to ZZ^*$ and $H \to Z'Z'$ decays. The $H \to ZZ'$ decay is suppressed to first order.

2.2.2. Coupling to SM fermions The gauge bosons Z and Z' are coupled to SM fermions. To the first order, the $Z \to l^+l^-$ coupling in the HAHM is the same as in the SM, and we consider that the new gauge boson Z' decays only to leptons with a very small width, however with a 100% branching fraction.

3. Experimental results from ATLAS and CMS in the $H \to ZZ^{(*)} \to 4l$

For this study, we assume that the new boson observed by the ATLAS and CMS experiments [1, 2] is a Higgs boson. Here we used the recent experiment results given by ATLAS and CMS [7, 8].

3.1. Higgs boson mass and signal strength

Although the ATLAS and CMS experiments measure a different mass for the new boson (difference of 2 GeV) [7, 8], in this study we assume that the Higgs boson has a mass of 126 GeV.

Table 1 shows the signal strength μ which is the ratio of the cross-section observed with respect to the SM expectation and its uncertainty σ_μ, these values correspond to the $4l$ channel only.

Table 1. The recent experimental results by ATLAS [7] and CMS [8] experiments.

Experiment	μ	σ_μ
ATLAS	1.66	$^{0.45}_{-0.38}$
CMS	0.93	$^{0.26}_{-0.23}$

3.2. Experimental selection criteria

The selection criteria for the analyses of both the ATLAS and the CMS experiments are based on selecting events with 4 leptons and forming leptons pairs. The invariant mass of one of the leptons-pairs (m_{12}) is close to the mass of the SM Z boson and the another leptons-pair (m_{34}) is considered for the off-shell Z boson. The selection criteria on these quantities considered by the ATLAS and CMS experiments is shown in Table 2.

Table 2. Selection criteria over m_{12} and m_{34} by ATLAS [7] and CMS [8] experiments for m_{4l} about 126 GeV.

Experiment	m_{12}	m_{34}
ATLAS	> 50 GeV	> 17.5 GeV
CMS	> 40 GeV	> 12.0 GeV

Since the kinematics of the leptons from $H \to Z'Z' \to 4l$ events are similar to the ones from $H \to ZZ^* \to 4l$, we will assume that all the efficiencies and acceptance are unchanged.

In order to have a consistent approach with both experiments and avoid boundary effects, we will consider two cases:

- in the case of the $H \to Z'Z'$ events with 20 GeV $< M_{Z'} <$ 35 GeV the H can not be detected by the experiment, because the applied cuts exclude this case;
- in the case of the $H \to Z'Z'$ events with 55 GeV $< M_{Z'} <$ 80 GeV the H can be detected by the experiment, because this case is compatible with the applied cuts.

Because of the cuts on m_{12} and on m_{34}, the cases with $M_{Z'} <$ 20 GeV and 35 GeV $< M_{Z'} <$ 55 GeV are not considered. We also don't consider the case where the Z' boson is havier than the Z boson.

4. Constraints on HAHM parameters

We obtain limits on the hidden sector parameters by calculating the event rate predicted by HAHM, compared to the SM, and by checking the compatibility with the experimental results. According to the HAHM, the hidden width depends on the three free parameters: M_H, $M_{Z'}$ and s_h^2. We will present the results in the $(M_{Z'}, s_h^2)$ plane where the mass of the Higgs boson is fixed to 126 GeV.

4.1. Method

Considering only gluon fusion, which is a dominant production mode at the LHC, we compute the expected production rate of the $H \to 4l$ events using Equation 1:

$$\frac{\sigma_{HAHM}}{\sigma_{SM}} = \frac{\sigma_{HAHM}(gg \to H) \times BR_{HAHM}(H \to 4l)}{\sigma_{SM}(gg \to H) \times BR_{SM}(H \to 4l)} \quad (1)$$

where the denominator is given by the SM values which depends only on the SM Higgs mass. The term $BR_{SM}(H \to 4l)$ involves only the $H \to ZZ^* \to 4l$ events, and therefore is a constant of the SM (since the mass of the Z boson is known). In the numerator, the values comes from the HAHM model and depends on the free parameters (M_H, $M_{Z'}$ and s_h^2). The cross-section term depends on the Higgs mass and the mixing angle.

The term $BR_{HAHM}(H \to 4l)$ can be decomposed into three components:

$$\begin{aligned} BR_{HAHM}(H \to 4l) &= BR_{HAHM}(H \to ZZ^* \to 4l) + BR_{HAHM}(H \to Z'Z' \to 4l) \\ &+ BR_{HAHM}(H \to ZZ' \to 4l) \end{aligned}$$

We also assume the universal suppression in Equation 1:

$$\frac{\sigma_{HAHM}}{\sigma_{SM}} = c_h^2 = (1 - s_h^2) \quad (2)$$

We compare the quantity obtained by Equation 1 in the $(M_{Z'}, s_h^2)$ plane, with the measured value of the production rate divided by the SM prediction (μ), this approach was used in reference [11]. The reason we chose to look specifically at the Z' mass, is because we want to place ourselves in the case of Hidden particles decaying into SM fermions which can be detectable by the experiments.

As we mentioned before, the $H \to Z'Z' \to 4l$ events are considered as detected if $M_{Z'} > 55$ GeV, and as not detected if $M_{Z'} < 35$ GeV. Therefore, the formulas that are used to evaluate the rate of events in the HAHM model, where the branching fraction from $H \to ZZ' \to 4l$ is neglected, are:

$$\frac{\sigma_{HAHM}}{\sigma_{SM}} = \begin{cases} (1 - s_h^2) \times \frac{BR_{HAHM}(H \to ZZ^*)}{BR_{SM}(H \to ZZ^*)}, & \text{if } M_{Z'} < 35 \text{ GeV}. \\ (1 - s_h^2) \times \frac{BR_{HAHM}(H \to ZZ^*)[BR_{SM}(Z \to 2l)]^2 + BR_{HAHM}(H \to Z'Z')}{BR_{SM}(H \to ZZ^*)[BR_{SM}(Z \to 2l)]^2} & \text{if } M_{Z'} > 55 \text{ GeV}. \end{cases} \quad (3)$$

Here we have used that the branching franction $Z' \to l^+l^-$ is 100%. Given the experimental selection criteria that we used, an immediate consequence in the first case ($M_{Z'} < 35$ GeV), was that the ratio is always less than 1 since the branching fractions in the HAHM model are lower than the SM, this means, the HAHM model, for lower Z' mass predicts less events than the SM. On the other hand, for the second case ($M_{Z'} > 55$ GeV), the ratio can be either larger or smaller than 1.

4.2. Results

The results are presented in two cases: low-mass Z' (20 GeV $< M_{Z'} <$ 35 GeV) and high-mass Z' (55 GeV $< M_{Z'} <$ 80 GeV). We show the distribution of the $\frac{\sigma_{HAHM}}{\sigma_{SM}}$ in the $(M_{Z'}, s_h^2)$ plane, and we superimpose the contour corresponding to the experimental results (ATLAS and/or CMS) for μ, and also the 68% and 95% C.L. The values used are presented in Table 1.

4.2.1. Low-mass Z' case: (20 GeV $< M_{Z'} <$ 35 GeV) This is the region where the $M_{Z'}$ does not pass the experimental cuts, and where we used the first case of Equation 3. Figure 1 shows the distribution of $\frac{\sigma_{HAHM}}{\sigma_{SM}}$ in the $(M_{Z'}, s_h^2)$ plane, with the μ contour is the solid line, with the 68% C.L. (dashed line) and with 95% C.L. (dot-dashed line) contours.

From Figure 1, the left plot shows only the 95% C.L. contours. This is because the value of μ for ATLAS is larger than 1, while the HAHM predicts less events than the SM. Therefore, the yellow region is compatible with ATLAS results at 95% C.L. For the CMS case where μ is lower than 1, we can see that the HAHM results are compatible with CMS results at 68% C.L. (see the green region from the plot on the right from Figure 1).

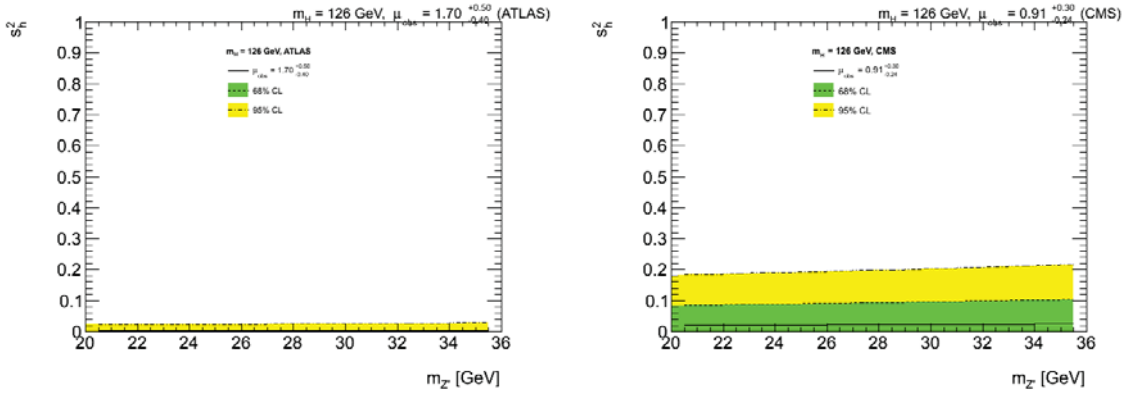

Figure 1. Low-mass Z' case. The plots show the distribution of $\frac{\sigma_{HAHM}}{\sigma_{SM}}$ in the $(M_{Z'}, s_h^2)$ plane and the 68% and 95% C.L. contours for HAHM using the experimental results from (a) ATLAS and from (b) CMS. The HAHM model is almost excluded by ATLAS (a) with $\mu > 1$.

4.2.2. High-mass Z' case: (55 GeV < $M_{Z'}$ < 80 GeV) The high mass region between (35 GeV, 55 GeV) is excluded as well, because of the experimental analysis cuts applied. Then, we used the second case of Equation 3. Figure 2 shows the the distribution of $\frac{\sigma_{HAHM}}{\sigma_{SM}}$ in the $(M_{Z'}, s_h^2)$ plane for high-mass Z' case.

As we mentioned before, for the high-mass Z' case, the $\frac{\sigma_{HAHM}}{\sigma_{SM}}$ ratio can be smaller or larger than 1, therefore more contours are visible. The green and yellow regions are part of the parameter space that is compatible with the experimental results at 68% C.L. and 95% C.L. respectively. We can see from Figure 2 that a large region is allowed: the region for $M_{Z'}$ below 63 GeV and the s_h^2 between to 0/1. Indeed for $M_{Z'} < 63$ GeV $\sim M_H/2$ and small or large mixing angle, the $H \to Z'Z'$ decay with two on-shell bosons is kinematically allowed whereas the $H \to ZZ^*$ 3-body decay is somewhat suppressed. Accordingly the expected number of $4l-$events will significantly increase. We should consider that the branching fraction of $Z' \to 2l$ has been taken as 100% which overestimated the expected number of evens with the HAHM model.

For $M_{Z'} > 63$ GeV $\sim M_H/2$ the $H \to Z'Z'$ 3-body decay is suppressed compared with the $H \to ZZ^*$ 3-body decay, and so we are in the SM case. Most of the parameter space is compatible with the experimental results at 95% C.L.

5. Conclusions

The HAHM model is not yet excluded experimentally by the ATLAS and the CMS experiments. We have performed a phenomenology study on the $H \to Z'Z' \to 4l$ using the HAHM model as a benchmark model to extract limits on the model in the $(M_{Z'}, s_h^2)$ parameter space from the recent experimental results from these experiments.

In this study we show that the measured event rate is compatible with a large part of the HAHM parameter space (see section 4.2.2 and Figure 2), therefore the model is still compatible with the experimental results and with the SM.

Since the search for $H \to Z'Z' \to 4l$ is compatible with the $H \to ZZ^* \to 4l$, we expect the experimental results soon from this search using the HAHM as a benchmark model to complement this study.

References

[1] The ATLAS Collaboration 2012, *Phys. Lett. B*, **716** 1-29

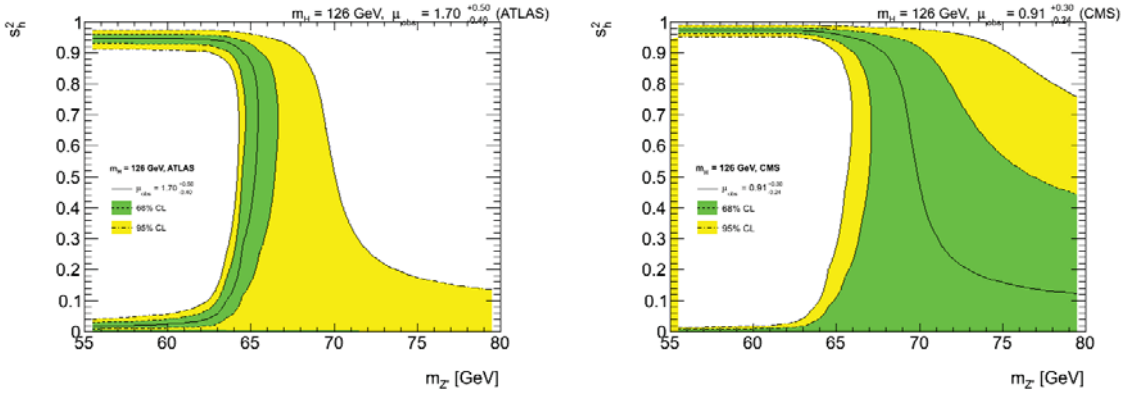

Figure 2. High-mass Z' case. The plots show the distribution of $\frac{\sigma_{HAHM}}{\sigma_{SM}}$ in the $(M_{Z'}, s_h^2)$ plane and the 68% and 95% C.L. contours for HAHM using the experimental results from (a) ATLAS and from (b) CMS. In the $M_{Z'} = 63$ GeV a transition of the s_h^2 it can be seen. For $M_{Z'} < 63$ GeV the $H \to Z'Z'$ is more favored while $M_{Z'} > 63$ GeV, $H \to Z'Z'$ is suppresed conpared with $H \to ZZ^*$, so it is SM-like.

[2] The CMS Collaboration 2012, *Phys. Lett. B*, **716** 30-61
[3] The ATLAS Collaboration 2013, *ATLAS-CONF-2013-108*
[4] The CMS Collaboration 2013, *arXiv:1401.5041*
[5] The ATLAS Collaboration 2013, *ATLAS-CONF-2013-079*
[6] The CMS Collaboration 2013, *arXiv:1310.3687*
[7] The ATLAS Collaboration 2013, *arXiv:1406.3827*
[8] The CMS Collaboration 2013, *arXiv:1312.5353*
[9] Wells J D 2008, How to Find a Hidden World at the Large Hadron Collider, *Preprint arXiv:0803.1243*
[10] Gopalakrishna S, Jung S and Wells J D 2008, *Phys. Rev. D*, **78** 055002
[11] Bock S, Lafaye R, Plehn T, Rauch M, Zerwas D and Zerwas P 2010, *Phys. Lett. B*, **694** 44-53

Re-mobilization of uranium and thorium from sediments contaminated by naturally occurring radioactive material (NORM) through leaching by acid mine drainage (AMD).

Faanhof A[1], Shongwe NS[2] and Connell, SH[2]

[1] North-West University, Private Bag X2046, Mmabatho 2735, South Africa.
[2] Department of Physics, University of Johannesburg P.O. Box 524, Auckland Park, 2006, South Africa

*Corresponding author: E-mail: shongwens@yahoo.com

Abstract. The potential re-mobilization of uranium and thorium from sediments contaminated with NORM wastes from decades of gold mining and the possible radiological environmental issues associated with the recent increase of acid mine drainage (AMD) in one of the major gold mining areas in South Africa has been studied through simple leaching experiments with simulated AMD. The K_d values of uranium and thorium predict the rapidity and reversibility between the dissolved (C_w, $Bq.\ell^{-1}$) and the adsorbed (C_s, $Bq.kg^{-1}$) phases. In principle one would expect uranium to be more mobile than thorium and accordingly uranium may be remobilized to the liquid phase while thorium is expected to stay in the solid phase. However, uranium appears to be concentrated in the insoluble fraction of the sediments and accordingly will not be mobilized by AMD, while thorium may be homogeneously distributed (adsorbed) between the soluble and insoluble fractions of the sediments. From the K_d values it is expected that thorium contained in the soluble fraction of the sediments will quickly be adsorbed in the insoluble fraction of the sediments and accordingly will not become part of the water body.

1. Introduction

Due to excessive gold mining activities in the Witwatersrand basin heavy metals, radioactive minerals and other potentially harmful chemicals have found their way into the rivers and wetlands in the gold mining areas enhancing the radioactivity of the environment. Plants that die in the riverine system contribute to the formation of sediments, together with run-off from land and slimes-dams and through deposition of airborne dust. From a radiological point of view there are three sources of contaminants emanating from the decay chains of ^{238}U, ^{235}U and ^{232}Th. This study concentrated on uranium and thorium only. Instrumental neutron activation analysis (INAA) and inductively coupled plasma mass spectrometry (ICP-MS) were used in the analysis of the sediments and leachates.

2. AMD Formation and Nuclide Mobility

Acid mine drainage (AMD) is one of the proceeds associated with the oxidation of pyrite (iron sulphide, FeS_2) in the gold ores **[1].** AMD can basically be regarded as the ground/surface water contaminated with sulphuric acid at pH=4.

The degree of radionuclide sorption on the solid phase is quantified by the solid-liquid distribution coefficient (K_d). The K_d-values are used when assessing the overall mobility and likely residence times of the radionuclides in soils **[2].** The K_d-value (ℓ/kg^{-1}) is based on the hypothesis of a reversible and rapid equilibrium between the dissolved (C_w, $Bq.\ell^{-1}$) and the adsorbed (C_s, $Bq.kg^{-1}$) (solid) phases of radionuclide as shown in Equation 1:

$$\mathbf{K_d} = \frac{C_s}{C_w} \quad (1)$$

For solid sources, like ores of uranium and thorium, the mobility in the sediments depends on solubility and dissolution (leaching) **[3]**. Concentration variations are induced by local differences in sediment mineralogy and properties leading to interactions such as adsorption to clay or by physical selection processes like settling of a contaminant at the inside of a river bed due to velocity differences **[4].**

2.1 Uranium

The aqueous uranyl (VI) ion (UO_2^{2+}) is very mobile and through its mobility it can be distributed over larger areas **[5].** The adsorption of uranium is low at pH values less than 3, increases with increasing pH and reaches a plateau between pH 5 and 8 while for higher pH adsorption decreases again **[4].**Typical values for K_d ($\ell.kg^{-1}$) of uranium are 35 (sand), 400 (organic material) and 1600 (clay) in **[6]** and agrees with those in **[2].**

2.2 Thorium

In an aqueous environment thorium exists as Th (IV) and its mobility is limited by the formation of its insoluble hydroxide $Th(OH)_4$ **[4].** Thorium has a strong affinity towards suspended particles, and once mobile it will be rapidly re-adsorbed to become immobile.

Table 1 provides some of the adsorption coefficients of NORM nuclides to a number of matrices.

Table 1. Partition coefficient, K_d of some of the NORM nuclides of interest in soils ($\ell.kg^{-1}$) **[2].**

Nuclide	Sand	Loam	Clay	Organic
Ac	450	1500	7400	5400
Bi	120	400	670	1500
Pa	540	1800	2700	6600
Pb	270	16000	540	22000
Po	150	400	2700	6600
Ra	490	36000	9000	2400
Th	3000	3300	5400	89000
U	33	12	1500	400

3. Materials and Methods

3.1 Study location/area

Figure 1. Locality of Wonderfonteinspruit catchment.

The measurements were conducted on twenty-one (21) selected samples from a batch of 250 samples collected in a previous study on the Mooi-river sediments from the Wonderfontein catchment. The samples selected were distributed through the catchment area. Samples with high uranium and thorium concentrations were selected to ensure adequate sensitivity of the analysis techniques applied. The leaching experiments were done at the Radioanalytical laboratories of Necsa. INAA was also done at Necsa, while the ICP-MS analyses were partly done at Necsa as well as at the University of Johannesburg.

3.2 Summary of the experimental design

The chosen sediment samples were analyzed prior to leaching both by ICP-MS and INAA. Thereafter, a 25 gram portion of the sediments were leached in 150 mℓ of a diluted sulphuric acid (pH=4) for 24 hours using a magnetic stirrer, stirring at such a speed that sediments were equally distributed along the water column, simulating the potential remobilization of naturally occurring radionuclides after heavy flooding of the catchment area with the AMD contaminated water. At the end of 24 hour leaching it was assumed that a near constant K_d value resulted for the dissolved elements in each sample. The samples were filtered and the leachates were stored in polyethylene bottles for analysis by ICP-MS. The leached sediments were washed three times with distilled water to remove any remaining acid and analyzed for uranium and thorium using both INAA and ICP-MS.

4. Results and Discussion

4.1 *Quality control*

In a previous study **[8]** the same sediments were analysed for a suite of toxic elements including uranium and thorium. These data were used to assure some quality control on the current results. The

two sets of data indicate that the uranium and thorium concentration ratios are close to 1 (1.12 ± 0.29 for uranium and 1.24 ± 0.25 for thorium) for most samples except for one, which gives an indication that "hot" particles can lead to substantial discrepancies and that the samples are not entirely homogeneous at the mass of 300 mg as used for INAA.

4.2 Uranium and thorium leaching from the sediments

The average concentrations of uranium and thorium in the sediments before and after leaching with AMD based on INAA results are given in table 2.

Table 2. Uranium and thorium leaching as observed through INAA.

Sediment mass (g)			**Uranium mass (mg)**			**Thorium mass (mg)**		
Prior to	After	Loss (%)	Prior to	After	Loss (%)	Prior to	After	Loss (%)
25.0	20.22	19.1	3.25±0.11	3.28±0.15	-0.88	0.289±0.08	0.235±0.08	18.8

It can be seen from table 2 that after doing mass corrections there is on average no decrease in the uranium mass. This is confirmed by the low uranium content of the leachates as shown in table 3. In general the simulated AMD has apparently not leached U from the sediments into the leachate. The U recovered in the leachate from table 3 is $9.01\mu g$. This indicates the insolubility of the uranium containing mineral as shown by a K_d value for U (see table 1), and accordingly to the conclusion that uranium is adsorbed to insoluble clay particles and/or part of insoluble particles originating from effluents from the mining industries released to the surface water and/or run-off or wind-blown residues from tailings dams.

The AMD modelling indicates that potential remobilization of uranium nuclides after heavy flooding of the catchment area in real life samples may not exist.

From table 2 one can see that on average the thorium content in the sediments decreased by about 18.8%. This coincides well with the observed average relative reduction of the mass of the sediments upon leaching with the simulated AMD of 19.1%. Accordingly, in spite of the high K_d values for thorium for a majority of materials one may come to the conclusion that thorium also forms part of the soluble fraction of the sediments and as such may be partly remobilized by AMD. However, looking at the ICP-MS results in table 3 one observes almost no thorium recovery in the leachate.

From this one can conclude that part of the thorium that was remobilized as a result of dissolution of the soluble part of the sediments did not remain in the leachate but was again strongly adsorbed to most likely the wall of the containers the leachate was stored in or to the filter used in the filtration process. This is a strong indication that thorium once remobilized will be rapidly re-adsorbed to the residual sediments and that potential remobilization of thorium after heavy flooding of the catchment area in real life samples may not exist.

Table 3. Uranium and thorium concentrations in the leachates by ICP-MS.

Sediment mass (g)			Uranium mass (mg)			Thorium mass (mg)		
Prior to	After	Loss (%)	Prior to	Leachate	Loss (%)	Prior to	Leachate	Loss (%)
25.0	20.22	19.1	3.246±0.11	0.009	0.288	0.289±0.08	9.2×10^{-6}	0.003

5. Conclusion

The current study suggests that at a pH of 4, uranium is not readily desorbed being part of the insoluble matrix when exposed to acid mine drainage, while thorium will be initially remobilized as part of the soluble fraction of the sediments, but will most likely be re-adsorbed to the remaining sediments. Actual samples in the catchment areas influenced by AMD should be collected to confirm our results.

The potential remobilization of other nuclides from the NORM-series nuclides should also be investigated in follow-up work.

Acknowledgements

The author would like to acknowledge the National Research Foundation, Necsa and the University of Johannesburg for financial support. We are also grateful to the staff at SPECTRAU at the University of Johannesburg.

References

[1] Diale PP, Mkhize SL, Muzenda E and Zimba J 2011 The sequestration of heavy metals contaminating the Wonderfonteinspruit catchment area using natural zeolite. *WASET* **74:**766—72.

[2] International Atomic Energy Agency (IAEA) 2010 *Handbook of Parameter Values for the Prediction of Radionuclide Transfer in Terrestrial and Freshwater Environments.* Technical Reports Series No. 472.

[3] Battacharyya, DK 1998 Issues in the disposal of waste containing NORM. *Appl. Radiat & Isot* **49**:215—26.

[4] van der Graaf ER, Koomans RL, Limburg J and Vries K 2007 In situ radiometric mapping as a proxy of sediment contamination: Assessment of the underlying geochemical and physical principles. *J. Appl. Radiat and Isot* **65**:619—633.

[5] International Atomic Energy Agency (IAEA) 1997 *Environmental Impact Assessment for Uranium Mine, Mill and In situ Leach Projects*, IAEA – TECDOC-979, Vienna.

[6] Environmental Protection Agency (EPA) 1999 *Understanding Variation in Partition Coefficients, K_d, values for Cadmium, cesium, Chromium, Lead, Plutonium, Radon, Strontium, Thorium, Tritium (3H) and Uranium.* EPA Report 402-R-99-004B, United States. EPA, Office of Air and Radiation, USA.

[7] International Atomic Energy Agency 2007 Modeling the transfer of Radionuclides from Naturally Occurring Radioactive Material. Report of the NORM Working Group of (Environmental Modeling for Radiation Safety) Theme 3.

[8] Ramatlhape II 2009 *Analysis of Naturally Occurring Radioactive Material and Radio-cesium in sediments from the Wonderfonteinspruit Catchment Area in the North-West Province and Mosses from Minsk Using Gamma Spectroscopy and Gas Flow Proportional Counting.* Dissertation, Radiation Science & Technology, Northwest University.

Cytogenetic analysis of ^{60}Co γ-radiation-induced chromosome damage and simulations using the Geant4 Monte Carlo toolkit

H Fourie[1], R T Newman[1], J P Slabbert[2] and P Beukes[2]

[1]Department of Physics, Stellenbosch University, P. Bag X1, Matieland, Stellenbosch 7602, South Africa

[2] iThemba LABS, National Research Foundation, P.O. Box 722, 7129 Somerset West, South Africa

E-mail: fourieh@sun.ac.za

Abstract. The study involves the determination and quantization of radiation damage on a cellular level and the replication of this energy deposition using the Geant4 Monte Carlo toolkit, developed for particle transportation simulations at CERN. The detection of micronuclei in binucleated cells was used to analyse the effects of the radiation. Results from micronucleus assays of rat brain endothelial and Chinese hamster ovary cells that have been irradiated with gamma rays, produced by a Co-60 teletherapy unit at iThemba LABS, are presented. Linear-quadratic dose response curves were determined for both cell lines. The simulated results of the Co-60 setup, irradiation and other relevant features offered by the Geant4 toolkit are also discussed. Finally, prospective microdosimetric studies and simulations of damage caused by DNA-incorporated I-123 will be mentioned.

1. Introduction

A standard method used to determine the combined effects of ionizing radiation-induced damage and repair is cytogenetic analysis (or analysis of chromosomes). Chromosomal aberrations resulting from non- or misrepaired radiation-induced double strand breaks can be detected using this method.

The cytokinesis-block micronucleus (CBMN) cytome assay is one such cytogenetic method [1]. After *in vitro* irradiation, cells are blocked from performing cytokinesis (the division of cytoplasm and cell membrane) by the addition of cytochalasin-B (cyt-B). Cyt-B is an inhibitor of actin polymerization required for the formation of the microfilament ring that constricts the cytoplasm between the daughter nuclei during cytokinesis [2]. Since nuclei can still divide, after one division, cells will consequently appear as binucleated (BN) cells. DNA damage events are scored specifically in once-divided BN cells and include micronuclei (MNi).

MNi, possibly resultant from the radiation damage, are small extranuclear bodies detected around these BN cells. MNi are formed from acentric chromosome fragments and whole chromosomes that lag behind in anaphase and are left outside the daughter nuclei in telophase [3]. Additionally, ionizing radiations are more effective on cells which have a greater reproductive activity [4]. Therefore MNi provide a convenient and reliable index of both chromosome breakage and loss; and as the number of radiation-induced MNi is strongly correlated with radiation dose and quality, the CBMN assay is an appropriate test for biological dosimetry and the assessment of intrinsic radiosensitivity [5], [6]. Although the CBMN assay is generally applied on lymphocytes, micronuclei can be detected in all types of cells, as long as they are capable of division.

The knowledge of absorbed dose is required for evaluation of observed radiobiological effects and to predict or compare the effectiveness of different radiations. Due to small cellular dimensions direct dose measurement is virtually impossible [7]. According to the stochastic character of all interaction processes, a large number of pathways exist by which energy may be deposited. Because these energy exchanges are random processes, the Monte Carlo technique is an appropriate tool for their simulation; as well as a feasible method to obtain correct dose values under considerations of all irradiation aspects like geometry and activity distributions [8].

Geant4 is an open source Monte Carlo toolkit, based on object orientated programming rules using the C++ language, which provides functions for simulating the passage and interactions of particles through matter [9]. The main advantage of this toolkit is its openness to modification and extensions. The code is freely downloadable from the Geant4 web site as well as detailed descriptions of the toolkit design and the physical fundamentals may be found in the "Geant4 User's Guide for Application Developers" and the "Physics Reference Manual" [10].

In this study, CBMN assays were used to analyze the effects of γ-radiation from a ^{60}Co source on rat brain endothelial (bEND5) and Chinese hamster ovary (CHO-K1) cells. Dose-response curves were then determined for both cell lines. These linear-quadratic equations will be used as reference curves in future work concerning the relative biological effectiveness of Auger electrons from DNA-incorporated ^{123}I.

Geant4 was used to simulate the experimental setup and the decay of a ^{60}Co source and to determine the energy deposition in a certain volume. From these simulations, an equation relating activity to dose rate was determined. The predicted dose rate was then compared to the measured value. This basic simulation was done to determine the accuracy and reliability of Geant4 for future work regarding the simulation of energy depositions due to Auger electrons from the full decay of ^{123}I (incorporated into the anatomy of a cell).

2. Experimental procedure

2.1. Biological experiments

2.1.1. Cell preparation and irradiation

The samples were individually irradiated using a ^{60}Co teletherapy unit (Eldorado 76, Atomic Energy of Canada Ltd.) at iThemba LABS-NRF, Somerset West. The irradiation setup consisted of a field size of 30 × 30 cm^2 and a source-to-surface distance (SSD) of 75.6 *cm*. A 6 *mm* thick Perspex sheet was placed at 75 *cm* to act as build-up material and insure electronic equilibrium. A 4.9 *cm* slab of Perspex was placed 3.5 *cm* from the build-up to aid in dose deposition due to backscatter. On 5 June 2013 the dose rate of the ^{60}Co unit was 0.49 *Gy/min*, measured according to the International Commission on Radiation Units and Measurements protocol. According to accompanying documentation, the teletherapy unit had an activity of 48.4 *TBq* on that date.

The bEND5 cells were allowed to grow to confluence; incubated at 37°C in a humidified atmosphere of CO_2. On the day of irradiation, the cells were trypsinized from the culture flasks. A hemocytometer was used to obtain a cell count of approximately 3×10^5 cells/*ml*. Cell culture medium (RPMI 1640) was added to the cell mixture as needed in order to obtain the required concentration. Tubes were labeled according to the planned exposure values (namely 0 – 4 *Gy* in 0.5 *Gy* increments, hence 9 dose values). Into each of these tubes, concentrated cell mixture and medium were added. The tubes were then individually irradiated using the ^{60}Co unit. After the irradiation, the contents of each tube were divided into 2 wells of a 6-well plate, labeled A and B with their corresponding dose value, culminating in 18 separate samples. To block cytokinesis, 3.76 *μl* of Cyt-B was added to each well. The cells were then stored in an incubator at 37°C overnight (approximately 20 – 24 hours). After incubation, the cells were harvested by trypsinization, treated with a hypotonic solution of 75 *mM* KCl, fixed once with a 4/1/5 methanol/acetic acid/Ringer's solution mixture and stored overnight at

4°C. On the day of slide preparation, the cells were fixed three times with a 4/1 methanol/acetic acid as described previously by Vandersickel, et al. [11]

In a similar procedure, the CHO-K1 cells were harvested after incubation by trypsinazation. A cell count of approximately 1.5×10^5 cells/*ml* was obtained. Nine small Petri dishes (35 *mm*) were labeled according to the exposed dose; each containing a 22 *mm* glass cover slip. Into each of these dishes, 0.2 *ml* of CHO-K1 cells and medium were added, and then individually irradiated. Similarly, Cyt-B was added after irradiation, and the cells were incubated for approximately 24 hours. Afterwards, the supernatants were removed, the seeded cells treated with a hypotonic solution of 75 *mM* KCl and fixed once with a 1/3 methanol/acetic acid solution. Supernatants were then removed; the cover slips were allowed to air dry and then stored at room temperature until slide preparation.

2.1.2. Slide preparation and MN scoring

Duplicate slides were prepared for each bEND5 cell culture. The supernatants of each tube was removed and retained for storage. Forty *µl* of the cells were dropped on each of the 2 clean slides and air dried. The supernatants were replaced with the remaining cells in the tube for refrigerated storage. Finally, the slides have labels A1, A2, B1, and B2 for each exposure value, resulting in 36 slides in total. The resulting DNA damage due to the radiation was quantified by numerating the number of MNi per BN cell. Two drops of DAPI Vectashield were added to each slide to stain the nuclei. The slides were then each covered with a cover slip and allowed to dry. A semi-automatic counting method was implemented using the Msearch Module of the Metafer 4 automated imaging system [12]. This was done for all 36 slides. To analyse the obtained results, the number of MNi per BN cell was averaged over the 4 samples (A1, A2, B1, and B2) of each exposure value and then normalized to per 1000 BN cells. This value was then plotted against the dose and a linear-quadratic curve was fitted to the data points (using the MATLAB v 7.6 analysis package). Once the intrinsic MNi of the cell culture has been subtracted (obtained from the 0 *Gy* sample), the curve has the form:

$$y = \alpha \cdot D + \beta \cdot D^2$$

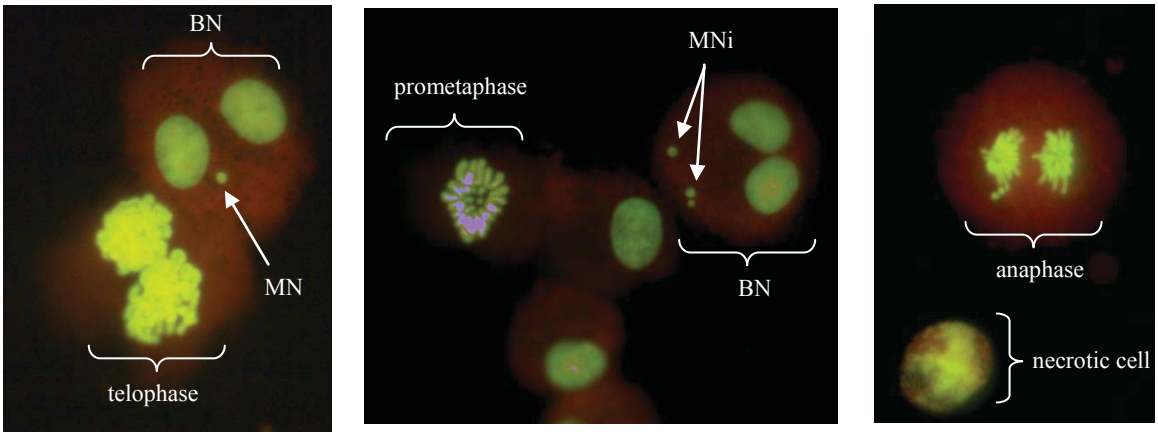

Figure 1. CHO-K1 stained with Acridine Orange. The cytoplasm emits an orange/red colour whereas the nuclei are a yellow / bright green colour. Pictured are some cells in varying phases of mitosis.

A working solution of Acridine Orange stain was made by adding 0.5 *ml* Acridine Orange solution to 45 *ml* buffer solution (pH 6.8). For each of the CHO-K1 cover slips: the cover slip was immersed in the working solution of Acridine Orange for 1 min. The cover slip was then rinsed with distilled water. Finally, the cover slip was immersed in the buffer solution (pH 6.8) for 1 min to de-stain. A drop of buffer solution was placed on a clean microscope slide and the cover slip was carefully mounted upside-down, avoiding any bubble formation. The edges of the cover slip were sealed with Cutex to prevent the drying of the slide. The MNi per BN cell were then counted, using ZEISS Axio Scope A1 and FITC filter (see figure 1), up to 200 cells. This was done for each of the 9 dose points. As

previously, the number of MNi per BN cell was normalized to per 1000 BN cells; plotted against the exposed dose and had a linear-quadratic curve fit to the data points.

2.2. Monte Carlo simulations

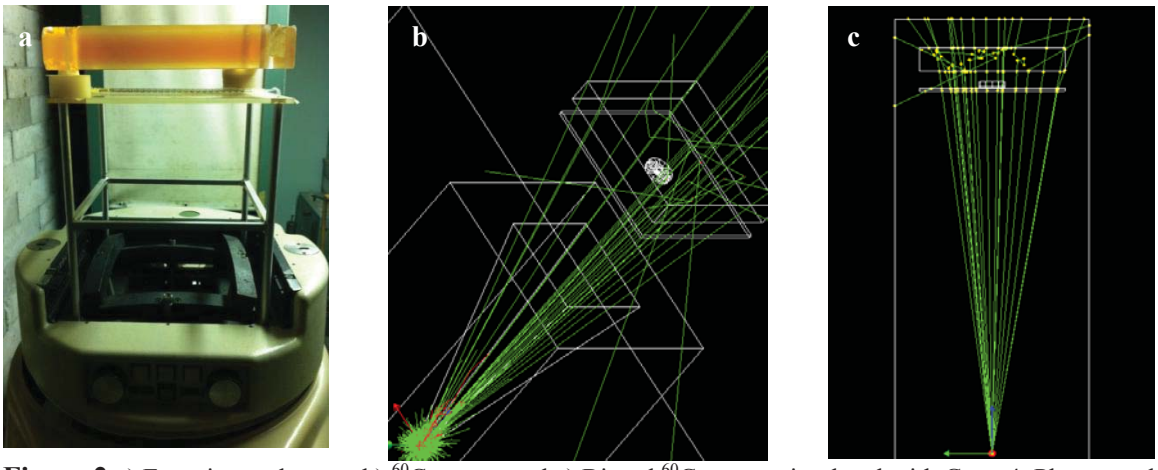

Figure 2.a) Experimental setup. b) ^{60}Co setup and c) Biased ^{60}Co setup simulated with Geant4. Photon and electron tracks are shown in green and red, respectively.

Geant4.9.6 and Microsoft Visual C++ 2010 Express was used on a Windows 7, Intel Core2 Duo @ 2x2 GHz, 3 GB RAM platform to reproduce the experimental setup. In a world geometry filled with air at standard temperature and pressure, a Perspex build-up was placed at 75 *cm* from the source, and a slab of Perspex was placed 79.1 *cm* from the source to act as backscatter material. The source was placed at the origin and a volume of water (r = 2.65 *cm*, h = 4 *mm*, ρ = 1 *g/cm*^{3}) was placed at 75.6 *cm*. A certain activity (*Bq* = disintegrations/sec) of source material was simulated and the energy deposited per second, in the investigated volume, was measured. This energy deposition rate was then converted to an absorbed dose (*Gy* = *J/kg*) rate. Two different simulations were constructed: a full, isotropic decay of a ^{60}Co source, and an energy- and directionally biased simulation. In both the RanecuEngine randomizing engine was used [13]. The experimental and simulated setups can be seen in figure 2. Simulations were run up to 10 *MBq*.

In the "^{60}Co setup", a ^{224}U housing with a 10x10 cm^2 square-aperture was placed around the origin, to produce a 30x30 cm^2 collimated field at 75 cm. In this simulation, the ^{60}Co nuclei were allowed to isotropically β^- -decay to their ^{60}Ni ground state, producing all of the documented particles and their spectrum of energies. In the physics list, the interaction processes were individually set for each type of particle (e.g. gammas can undergo the Photoelectric effect, Compton scattering, gamma conversion leading to pair-production).

In the "Biased ^{60}Co setup", the production of a 1.173 and 1.332 MeV pair of γ-rays was considered as one decay. These photons were produced within an 11.2° angle in the forward direction. The built-in QBBC reference physics list was used to govern the particle interaction processes in this simulation [14].

3. Results and Discussion

3.1. Biological results

From figure 3 we can see that the bEND5 cells are vastly more radiosensitive than the CHO-K1 cells, also indicated by the larger α-value in table 1. For bEND5 cells we see that points above 2.5 *Gy* reach a plateau, indicating that the cells have been saturated by the radiation. The limited number of cells on each slide also limit the number of MNi/BN cells. The linear-quadratic trend is present in both cell lines, as it should. The values for each dose point will differ when compared to values available in literature, as they are dependent on the specific cell line and the scoring method used [15].

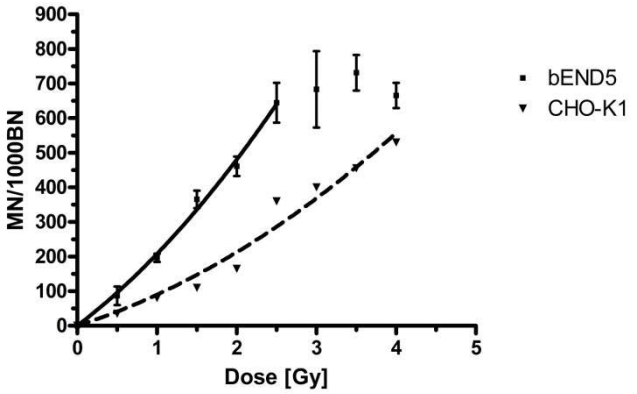

Figure 3. Number of micronuclei per 1000 bi-nucleated cells versus dose and the resulting dose-response curve.

Table 1. ^{60}Co radiation dose response parameters for MN frequencies.

Cell line	α (Gy^{-1})	β (Gy^{-2})
bEND5	175.0 ± 31.8	32.5 ± 15.1
CHO-K1	73.2 ± 22.3	16.48 ± 6.8

3.2. Monte Carlo results

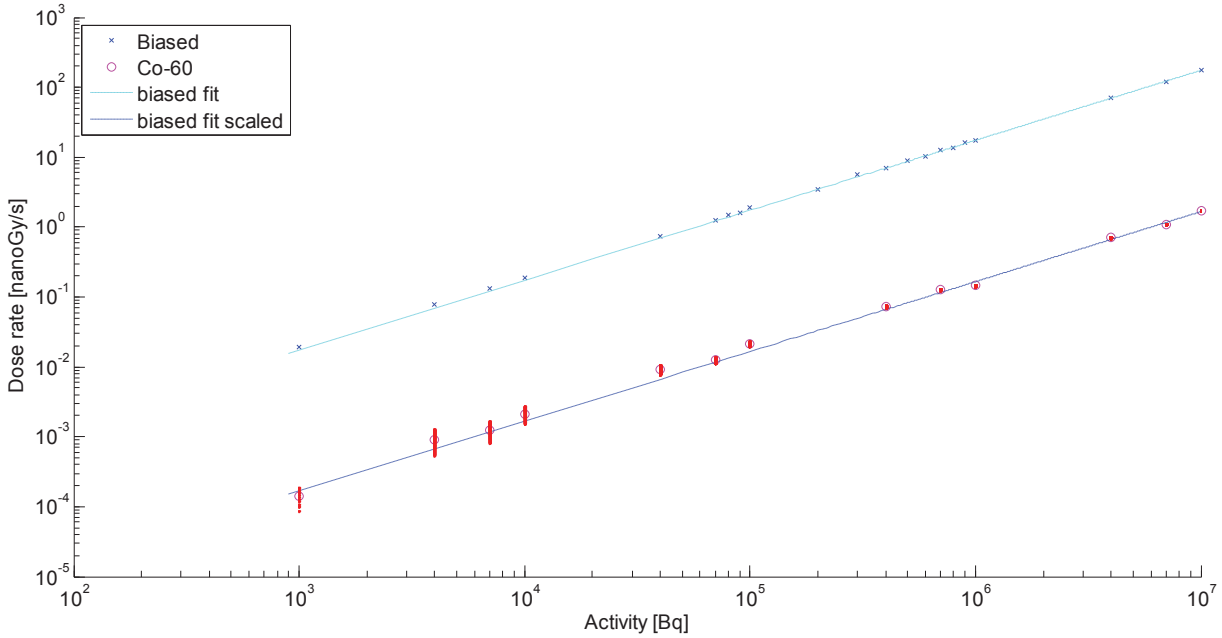

Figure 4. Dose rate (nGy/s) as a function of activity (Bq) for the biased and ^{60}Co simulations.

The fitted curves of the biased (scaled to compensate for the decreased solid angle) and ^{60}Co simulated data points are given by the following respective two equations, with dose rate in *nGy/s* and activity in *Bq*:

$$\dot{D} = \frac{0.1197}{4\pi}(174.2 \times 10^{-7}) \cdot A \quad (1)$$

$$\dot{D} = (1.663 \times 10^{-7}) \cdot A \quad (2)$$

The 95% confidence interval for the above dose rates can be obtained by multiplying $\dot{D}$ with 0.3%. Given in table 2 are the comparisons between the measured dose rate and those predicted by (1) and (2) when working with the documented activity (48.4 *TBq*) of the therapy unit's source; as well as the percentage difference between the measured and predicted value.

Table 2. Comparison of measured and simulated dose rate and difference between measured and simulated values.

	Dose rate (mGy/s)	% difference
Measured value	8.16	0
(1) Biased simulation	8.03 ± 0.03	1.6 ∓ 0.3
(2) ^{60}Co-simulation	8.05 ± 0.03	1.4 ∓ 0.3

4. Conclusion

Deviations in the CHO-K1 dose points exists, since only one slide per dose point was analyzed (due to time constraints) as well as human errors during the counting procedure (e.g. some count higher / lower than others). The α- and β-parameter values will be used in future studies regarding the relative biological effectiveness of Auger electrons from DNA-incorporated ^{123}I for these same cell lines.

The Monte Carlo simulations give the most accurate results when the decay of the source is simulated as comprehensively as possible; this however leads to an increase in computational time (213 *min* for a 10 *MBq* ^{60}Co-source). Overall, Geant4 produces results with an accuracy of at least 98%. This benchmarks the reliability of Geant4 for future work.

Acknowledgements

This work was supported by the National Research Foundation of SA and Stellenbosch University.

References

[1] Fenech M 2007 Cytokinesis-block micronucleus cytome assay *Nat. Prot*. **2**(5) 1084-104.
[2] Cayman Chemical 2013 *Cytochalasin B*
[3] Norppa H and Falck G 2003 What do human micronuclei contain? *Mutag*. **18**(3) 221-33.
[4] Bergonié J and Tribondeau L 1959 Interpretation of some results of radiotherapy and an attempt at determining a logical technique of treatment *Rad. Res*. **11**(4) 587-88.
[5] Vral A, Verhaegen F, Thierens H and De Ridder L 1994 Micronuclei induced by fast neutrons versus Co-60 gamma-rays in human peripheral blood lymphocytes *Int. J. Rad. B*. **65** 321-28.
[6] Vral A, Thierens H, Baeyens A and de Ridder L 2002 The micronucleus and g2-phase assays for human blood lymphocytes as biomarkers of individual sensitivity to ionizing radiation: limitations imposed by intraindividual variability *Rad. Res*. **157**(4) 472-77.
[7] Freudenberg R, Wendisch M and Kotzerke J 2011 Geant4 simulations for cellular dosimetry in nuclear medicine Z. *Med. Phys*. **21** 281-9.
[8] Ftacnikova S and Bohm R 2009 Monte-Carlo calculations of energy deposition on cellular, multi-cellular and organ level for Auger emitters *Rad. Prot. Dos*. **2**(4) 279-88.
[9] Agostinelli S, et al. 2003 Geant4 - a simulation toolkit. *Nuc. Instr. Meth. Phys. Res.* A **506**(3) 250 - 303.
[10] Geant4. [Online]. Available from: www.geant4.org.
[11] Vandersickel V, Mancini M, Slabbert J, Marras E, Thierens H, Perletti G and Vral A 2010 The radiosensitizing effect of Ku70/80 knockdown in MCF10A cells irradiated with X-rays and p(66)+Be(40) neutrons. *Rad. Onc.* **5** 30.
[12] Varga D, Johannes T, Jainta S, Schwarz-Boeger U, Kiechle M, Garcia B and Vogel W 2004 An automated scoring procedure for the micronucleus test by image analysis *Mutag*. **19** 391-7.
[13] Geant4 Collaboration 2012 *Geant4 User's Guide for Application Developers*
[14] Ivantchenko A, Ivanchenko V, Molina J and Incerti S 2012 Geant4 hadronic physics for space radiation environment *Int. J. Rad. Bio*. **88**(1) 171-5.
[15] Slabbert J, Theron T, Serafin A, Jones D, Böhm L and Schmitt G 1996 Radiosensitivity variation in human tumor cell lines exposed in vitro to p(66)/Be neutrons or Co-60 γ-rays *Strahlenth. Onk.* **172** (10) 567-72.

Research progress of the inclusion of tau-leptons in the Higgs to four lepton decay channel with the ATLAS detector

Guillermo Nicolas Hamity

University of the Witwatersrand, 1 Jan Smuts Avenue, Johannesburg, South Africa 2000

E-mail: guillermo.nicolas.hamity@cern.ch

Abstract. The Standard Model, SM, Higgs boson to four lepton (either electrons or muons) decay channel has good signal to background ratio and can be used to reconstruct the Higgs boson invariant mass with a good resolution over an intermediate mass range Higgs boson. This makes the four lepton channel one the most relevant channels to study at the Large Hadron Collider, where a Higgs boson has been discovered with a mass of approximately 125 GeV. Although the Higgs boson to four lepton decay channel played an important role in this discovery, the decay leptons considered excluded tau leptons in the final state. Reasons for this lie in the hard-to-detect hadronic or leptonic tau decays. A study which includes tau leptons in the four lepton decay channel is beneficial to completing the picture of the Higgs boson search, particularly in the statistically limited vector-boson-fusion production mode. The implementation of tau decay to this channel is discussed.

1. Introduction

The unification of electroweak theory at the end of the 1960's and the later unification of the electroweak theory and quantum chromodynamics (QCD) lead to what is known today as the Standard Model (SM) of fundamental interactions [1]. The model's predictions of fundamental particle masses, widths and branching ratios are being experimentally matched with astonishing precision. The last piece of the puzzle for the SM is the discovery of the predicted Higgs boson, which is a product of spontaneous symmetry breaking in the SM [2, 3, 4]. The precise mass of the Higgs boson is not precisely predicted by the SM and the search for this elusive particle was performed at the Large Hadron Collider (LHC [5]) which is currently operational at CERN. The two experiments which shed light on this matter are the ATLAS [6] and CMS [7] experiments at the LHC. In July 2012 both ATLAS and CMS independently announced the discovery of a Higgs-like particle with a mass of around 125 GeV[8, 9]. By mid-March 2013 the experiments had confirmed that this particle is in fact a Higgs particle [10]. The LHC now aims to measure the properties of this Higgs boson and continue the quest of searching for hints of new physics. More research needs to be performed in order to tell whether this Higgs boson is in fact the SM Higgs boson, or if it is rather a Higgs boson from one of the more exotic theories, e.g. the Minimal Supersymmetric Standard Model (MSSM)[11]. This paper will introduce the concepts needed in order to expand on the signal sensitive four lepton decay channel (which was used extensively in the Higgs boson discovery) by including tau leptons, with the goal of ultimately including the tau decay into this channel to improve the Higgs boson's statistics.

Table 1. Cross sections are given for the center of mass energies $\sqrt{s} = 7$, 8 TeV in pb for the leading Higgs boson production mechanisms at $m_H = 125$ GeV.

CME	ggF	VBF	WH	ZH	$t\bar{t}H$
$\sqrt{s} = 7$ TeV	15.3%	1.22%	0.57%	0.32%	0.09%
$\sqrt{s} = 8$ TeV	19.5%	1.58%	0.7%	0.39%	0.13%

2. The Discovery of a Higgs boson

The gauge theories from which the SM arises describe infinite range forces, i.e. massless mediators, such as photons and gluons. However, the weak force mediators, the Z^0 and $W^{\pm}$, are massive particles. Moreover, in the unperturbed theory, fermions are massless. The mechanism which gives rise to the introduction of masses was developed by R. Brout, F. Englert, G. Guralnik, C. R. Hagen, T. Kibble and P. Higgs [2, 3, 4]. The mechanism is a spontaneous symmetry breaking phenomena which introduces a new field with a corresponding scalar particle called the Higgs boson. In the current SM formulation the Higgs boson is an isospin doublet. The precise mass of the Higgs boson is however not predicted by the model and must be determined experimentally. If a Higgs boson exists, it will be produced by means of high energy proton collisions, like the ones performed at the LHC. The leading production mechanisms of the SM Higgs boson are: gluon-gluon fusion (ggF), Vector Boson Fusion (VBF), associated production with weak bosons (WH and ZH) and associated production with top quarks ($t\bar{t}H$). Table 1 displays the cross sections of the leading production mechanisms wrt. the center of mass energies reached at the LHC in the 2011 (7 TeV) and 2012-2013 (8 TeV) data collection periods.

The ATLAS detector is used to reconstruct the particles produced in the proton collision. The decay channels and branching ratios of a SM Higgs boson depends on the mass of the Higgs. Figure 1 shows the predicted SM Higgs branching ratios as a function of the Higgs boson mass m_H.

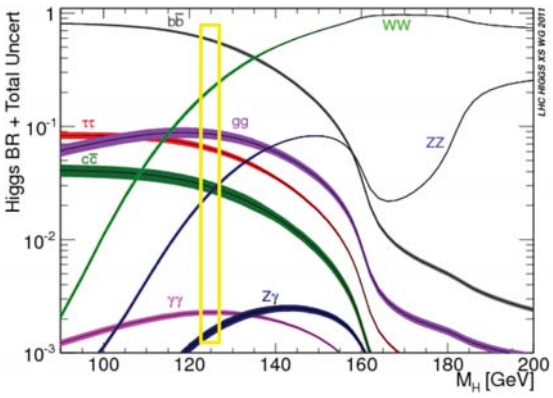

Figure 1. The SM Higgs branching ratios as a function of the Higgs boson mass m_H. The branching ratios of a Higgs boson of m_H at approximately 125 GeV is highlighted.

The SM Higgs boson will decay according to the branching ratios predicted. It is therefore important to test as many decay channels as possible, in order to compare experimentally measured branching ratios to the predicted ones.

In 2012 a Higgs particle was found at the LHC with a mass of around 125 GeV [8, 9]. The primary channels used by ATLAS in the discovery where the $H \to ZZ^{(*)} \to 4\ell$ ($\ell = e$, μ) and $H \to \gamma\gamma$. Figure 2 shows the distribution of the invariant mass of selected candidates compared

to background expectation of the 4ℓ and $\gamma\gamma$ experiments at ATLAS. Both experiments show a significant deviation from the background expectation at approximately 125 GeV which lead to the Higgs boson discovery.

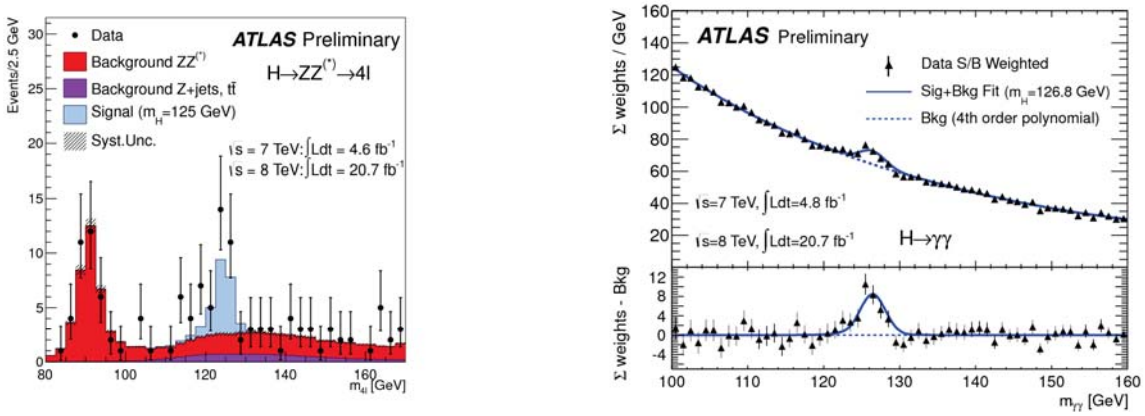

Figure 2. The distribution of the four-lepton (left) [12], and di-photon (right) invariant mass [8] for the selected candidates compared to the background expectation for the combined $\sqrt{s} = 8$ TeV and $\sqrt{s} = 7$ TeV data sets.

3. Higgs to $ZZ^{(*)}$ to four lepton decay channel

The four lepton analysis will be introduced in this section, along with some of the lepton identification and selection criteria that where used [12]. This will lay a foundation for expanding the four lepton channel to include tau leptons.

The $H \to ZZ^{(*)} \to 4\ell$ ($\ell = e$, μ) decay mode has four final states: 4μ,$4e$,$2\mu2e$ and $2e2\mu$. The $2\mu2e$ and $2e2\mu$ states differ by flavour of pair closest to the Z mass. There are very few processes that decay to four leptons and hence this four lepton channel yields a good signal over background ratio. The only irreducible background to the four lepton channel comes from non-resonant ZZ production. There are also small background contributions from Z+jets and $t\bar{t}$ production.

In order to probe this channel, efficient reconstruction of electrons and muons was performed. Single- and di-lepton triggers where used to trigger events of interest (efficiency of $> 97\%$ for μ and 100% for e). Electron reconstruction required that electron candidates have energy depositions in the calorimeter associated with tracks in the inner detector (ID). Tracks had to be refitted with a Gaussian-Sum Filter in order to compensate for Bremsstrahlung energy loss (energy of a charged particle lost due to acceleration). To be consistent with electromagnetic showers, calorimeter showers had to meet certain identification criteria. The electron transverse momentum, p_{T}, can then be reconstructed from the energy depositions in the calorimeter and the track direction at the interaction point.

Muon candidates consist of ID tracks associated with complete or partial tracks in the muon spectrometer (MS). For complete MS tracks, ID and MS momentum measurements are combined to reconstruct the muon p_{T}. In the forward region of the detector (direction close to the beam pipe) tracks are reconstructed using MS tracks only, since this area lies outside the range of the ID. There is also a lack of MS coverage in the very central region of the detector (perpendicular to beam pipe from the interaction point). Here, tracks with ID and calorimeter measurements with $p_T > 15$ GeV are identified as muons.

In order to reconstruct the four lepton events, the analysis must search for two same-flavour opposite-sign lepton pairs in each event (quadruplet). Requirements are imposed on the impact parameter in order to reject muons from cosmic rays. Kinematic selection criteria are imposed on the electrons (muons). This includes rejecting electrons (muons) with transverse energy $E_T < 7$ GeV ($p_T < 6$ GeV) as well as minimum p_T requirements on each lepton of the quadruplet. The invariant mass of each of the di-lepton pairs is now reconstructed. The di-lepton pair with invariant mass closest to the Z mass ($m_Z \approx 91.2$ GeV) is known as the leading lepton pair, Z_1, while the other di-lepton pair is known as the sub-leading pair, Z_2. Only one quadruplet is chosen per event, corresponding to the quadruplet with m_{Z_1} and m_{Z_2} closest to m_Z. The reconstructed di-lepton masses must satisfy $50 < m_{Z_1} < 106$ GeV and $m_{min} < m_{Z_2} < 115$ GeV, where m_{min} is dependant on the total four lepton invariant mass, $m_{4\ell}$. Separation criteria on the lepton tracks are implemented. A requirement that all possible di-lepton combinations in a quadruplet have an invariant mass greater that 5 GeV removes any background from $J/\psi \to \ell\ell$. Further impact parameter and track- and calorimeter-based isolation requirements are applied to leptons in order to reduce Z+jets and $t\bar{t}$ backgrounds. Finally the four lepton invariant mass $m_{4\ell}$ is reconstructed.

Background and Higgs signal samples are produced using Monte Carlo (MC) simulations. MC samples, as well as data from the experiment, are passed throughout the analysis. As seen in figure 2, the invariant mass is reconstructed for the background and Higgs signal and compared to the data from the experiment. The data matches the MC predictions with a $m_H = 125$ GeV Higgs signal.

4. Including tau leptons in the analysis

Tau leptons where not included in the initial four lepton analysis since the tau lepton decays are difficult to identify from background processes. Furthermore, tau lepton decays contain neutrinos, which makes the reconstruction of the invariant masses non-trivial. In order to expand on the four lepton channel by including the tau leptons, one needs an efficient way to reconstruct these tau leptons, and ultimately reconstruct the Higgs boson's invariant mass. In this section I will outline the difficulties in doing this, and point to some possible solutions to these challenges.

The lifetime of a τ-lepton is not long enough to allow for its direct measurement in the detector. This forces us to have to reconstruct tau leptons from it's decay products. Tau leptons undergo either hadronic (τ_h) or leptonic (τ_l) decay. The reconstruction of τ-leptons is usually understood as a reconstruction of the hadronic decay modes, since it is difficult to distinguish leptonic modes from primary electrons and muons [13]. However, in reference [14], $Z \to \tau_h\tau_\ell$ events where reconstructed by identifying electrons (muons) with $E_T > 24$ GeV ($p_T > 20$ GeV) as τ_ℓ. This type of selection criteria, where energetic leptons are identified as taus, could possibly be used to include τ_ℓ in the four lepton analysis.

Tau leptons will undergo leptonic decay at a rate of approximately 17.41% for muons and 19.58% for electrons. Leptonic τ-decay occurs in the $\tau \to \ell\,\bar{\nu}_\ell\nu_\tau$ and $\tau \to \ell\,\bar{\nu}_\ell\nu_\tau\gamma$ channels, where $\ell = e$ or μ[15]. Hadronic τ-lepton decay occurs at a rate of 64.8% and has a characteristic 1-prong (one charged π) or 3-prong (three charged π) signature. The prong number refers to the number of charged particle tracks found from the same vertex in the detector. Hadronic τ-lepton decays, with one charged π, occur in the channels $\tau \to \pi^\pm\upsilon$ (22.4%) and $\tau \to n\pi^0\pi^\pm\upsilon$ (73.5%), while decays with three charged π occur as $\tau \to 3\pi^\pm\upsilon$ (61.6%) and $\tau \to n\pi^0 3\pi^\pm\upsilon$ (33.7%) [13]. The 1- and 3-prong channels are therefore dominated by $\pi^\pm$ and π^0 plus a small percent of $K^\pm$ detected by the same techniques used to detect pions. Hadronic τ-leptons can be distin-

guished from QCD jets by 1- or 3-track multiplicity in narrow cones deposited in the hadronic calorimeter. Furteremore, we expect to be able to supress most background to hadronic tau decay by considering in particular the VBF production mechanism. This particular mechanism has a very good signal to background ratio, and is easily identified by two signature quark-jets produced in the forward and backward regions of the detector. Although the cross section of the VBF mechanism is quite poor, the increase in the CME at the LHC will improve statistics considerably in this channel.

Since hadronic tau decay is the more trivial of the tau decay modes to identify, the analysis considered will look at the case where one $Z \rightarrow \tau_h\tau_h$ and the other $Z \rightarrow \ell\ell$ ($\ell = e, \mu$). A preliminary tau reconstruction has been use to reconstruct hadronic taus: tau candidates must have good calorimeter or calorimeter and track hits; a requirement is made on their pseudorapidity, η (a measure of the angle from the beam direction), such that the crack region of the detector is not considered; and tau kinematics require the candidates to have $p_T > 20$ GeV and $\eta < 2.47$. The event selection will be similar to the four lepton case, except that we require quadruplets with one opposite charge tau pair, and one opposite charge same flavour lepton pair. One should note that without specifically identifying τ_ℓ, this analysis will probe $ZZ \rightarrow \tau_h\tau_h\tau_\ell\tau_\ell$ and $ZZ \rightarrow \tau_h\tau_\ell\tau_h\tau_\ell$ decay modes as well. Efficient kinematic selection criteria will have to be identified in order to identify τ_ℓ, as explained before. The inclusion of an efficient τ_ℓ identification will also allow for the inclusion of $3\tau_h\tau_\ell$ and $\tau_h 3\tau_\ell$ final states into the analysis. The Missing Mass Calculator algorithm [16] is the last piece of the puzzle, allowing efficient tau lepton invariant mass reconstruction.

5. Results and Conclusion

Including tau leptons in the four lepton Higgs boson channel has been identified as a viable way to increase statistics on the newly discovered Higgs boson, particularly since the channel has a good signal to background ratio in the VBF production process. The inclusion of this channel will become particularly important when the LHC re-opens in 2015 at a higher CME and we have attained an increase in statistics. Identification of hadronic and leptonic taus is noted to

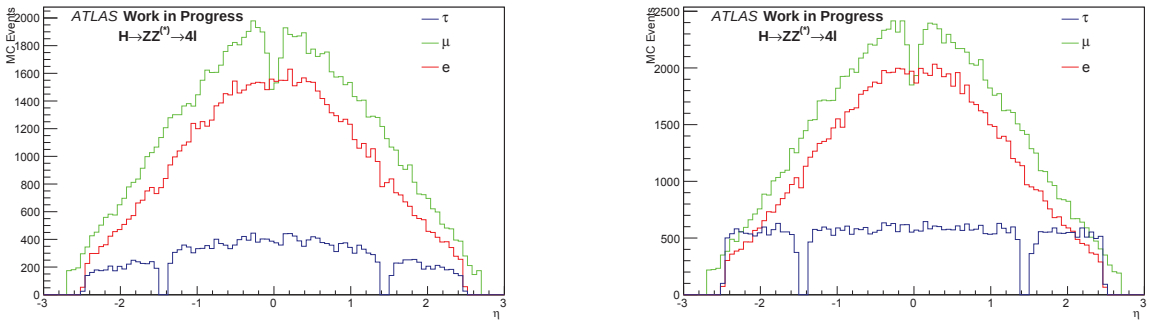

Figure 3. Histogram showing the pseudorapidity of reconstructed leptons of ggF (left) and VBF (right) Monte Carlo Higgs signal ($m_H = 125$ GeV) events.

be of primary importance in this analysis. At present the only channel that is being considered is the $H \rightarrow Z \rightarrow \tau_h\tau_h\ell\ell$ ($\ell = e, \mu$), for the sake of triviality. The preliminary hadronic tau selection criteria considered has performed inefficiently. Figure 3 shows η plots of the number of MC events (Higgs signal of $m_H = 125$ GeV) that pass electron, muon and tau selection. The

tau statistics are low and the selection criteria will have to be re-evaluated in order to optimize the selection. The dip around $\eta = 0$ in the muon plot is due to the lack of MS coverage in the very central region discussed before. The lack of events in the tau plot at around $|\eta| = 1.5$ is due to explicitly removing tau candidates in the detector crack region. Once the hadronic tau selection has been optimized, focus will be aimed at reconstructing the tau masses, as well as identifying τ_ℓ, there by incorporating non trivial decay modes.

References

[1] Bettini A 2008 *Introduction to Elementary Particle Physics* (New York: Cambridge University Press)
[2] Higgs P W 1964 Broken symmetries and the masses of gauge bosons *Phys. Rev. Lett.* **13** 508
[3] Guralnik G S, Hagen C R and Kibble T 1964 Global conservation laws and massless particles *Phys. Rev. Lett.* **13** 585
[4] Englert F and Brout R 1964 Broken symmetry and the mass of gauge vector mesons *Phys. Rev. Lett.* **13** 321
[5] Evans L and Bryant P 2008 LHC Machine *J . Instrum.* **3** S08001
[6] The ATLAS Collaboration (Aad G *et al.*) 2008 The ATLAS experiment at the CERN Large Hadron Collider *J. Instrum.* **3** S08003
[7] The CMS Collaboration 2008 The CMS experiment at the CERN LHC *J. Instrum.* **3** S08004
[8] The ATLAS Collaboration 2012 Observation of a new particle in the search for the standard model Higs boson with the ATLAS detector at the LHC *Phys.Lett. B* **716** 1-29
[9] The CMS Collaboration 2012 Observation of a new boson with mass near 125 GeV in pp collisions at $\sqrt{s} = 7$ and 8 TeV *J. High Energy Phys.* JHEP06(2013)081
[10] The ATLAS Collaboration 2013 *Combined coupling measurements of the Higgs-like boson with the ATLAS detector using up to 25 fb*$^{-1}$ *of proton-proton collision data* ATLAS-CONF-2013-034
[11] Arbeya A,Battagliac M,Djouadic A and Mahmoudic F 2012 The Higgs sector of the phenomenological MSSM in the light of the Higgs boson discovery *J. High Energy Phys.* JHEP09(2012)107
[12] The ATLAS Collaboration 2013 *Updated results and measurements of properties of the new Higgs-like particle in the four lepton decay channel with the ATLAS detector* ATL-PHYS-SLIDE-2013-097
[13] The ATLAS Collaboration 2008 *Expected Performance of the ATLAS Experiment: Detector, Trigger and Physics* arXiv:0901.0512v4 [hep-ex]
[14] The ATLAS Collaboration 2013 *Identification of Hadronic Decays of Tau Leptons in 2012 Data* ATLAS-CONF-2012-142
[15] Particle Data Group (J. Beringer et al.) 2012 Particle Physics Booklet *Phys. Rev.* **D86**
[16] Elagin A, Murat P, Pranko A and Safonov A 2011 A new mass reconstruction technique for resonances decaying to $\tau\tau$ *Nucl. Instrum. Methods Phys. Res. Sect. A* **654** 481-9

Validation of a passive beam Monte Carlo model for measuring prompt gamma rays during proton radiotherapy

[1]**Jeyasingam Jeyasugiththan,** [1]**Stephen Peterson,** [2]**Jaime Nieto Camero and** [2]**Julyan Symons**

[1]Department of Physics, University of Cape Town, Rondebosch, 7701, South Africa
[2]Medical Radiation Division, iThemba L.A.B.S., Faure, 7131, South Africa

E-mail: jeyasugiththan@yahoo.com

Abstract. In proton beam radiotherapy, secondary gamma rays are produced by proton-nuclei inelastic collisions within the treatment volume. A Monte-Carlo model of the iThemba proton treatment nozzle was developed using the Geant4 toolkit to detect these secondary or prompt gamma rays, which could be used for on-line treatment verification. The passive beam proton treatment facility at iThemba Labs in Cape Town, South Africa was studied in detail and all the nozzle components that interact with the proton beam were built and positioned in the model at the locations specified by the manufacturer. NaI detectors with different dimensions were modeled and standard gamma emitting sources in the energy range from 0.661 to 4.438 MeV were used to determine the detector response. The simulated treatment nozzle was validated against depth dose and lateral profiles in a water phantom for different therapeutic proton ranges. The position of the graphite double wedge energy degrader was calibrated within the model. Range uncertainties due to secondary production energy threshold were measured in detail. Our Geant4 treatment nozzle model is in good agreement with measurements and has the ability to produce depth dose profiles and lateral profiles for different proton ranges. Lastly simulations to detect prompt-gammas produced in a water phantom were performed and will be validated with future experimental measurements

1. Introduction

Protons have a finite range in material compared to the exponential attenuation of photons. This difference has been used to develop proton radiation therapy, where proton therapy has exhibited significant dose control and tissue sparing compared to traditional photon therapy. These properties of protons also require a more precise delivery of the radiation, which is hindered by the absence of primary particles exiting the patient for verification purposes. One option is to use secondary radiation for dose verification purposes, like prompt gammas produced by proton-nuclei inelastic collisions [1]. This work is developing a Monte Carlo model of the proton beam line at iThemba Labs in order to validate on-going prompt-gamma measurements.

2. Geant4 passive beam line model

In the passive beam proton therapy treatment technique, an accelerated mono-energetic proton beam is directed into a treatment nozzle where a single or double beam scattering method is

used to broaden the proton beam uniformly in the lateral direction by placing high-Z scattering plates into the beam path. The beam can also be spread out along the beam direction to form a spread out Bragg peak (SOBP) with the use of a range modulator wheel. In addition, there is a set of collimators in place to spare the patent and electronics from excess scattered radiation by the beam-line elements. Our passive beam line model is built using the Geant4 [2] Monte Carlo (v9.6) code. Geant4 is an object oriented and open source C++ toolkit used to simulate particles travelling through a medium, and has been used to compute proton treatment nozzle by many researchers [3], [4].

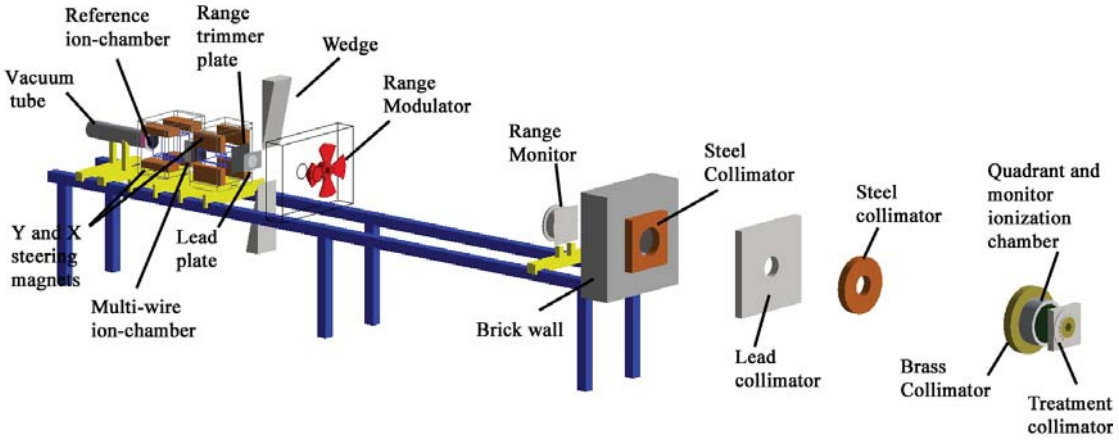

Figure 1: Geant4 Monte Carlo model of the proton passive beam line at iThemba Labs.

The entire Monte Carlo beam model is shown in the Figure 1, including all elements that directly interact with the beam. The vacuum chamber is the first element in the treatment nozzle. The reference ionization chamber which was placed next to the vacuum tube acts as the first scatterer. The lead plate or graphite double wedge degrader is the second scatterer (see Figure 2(a)). The double wedges are mounted back to back on a drive mechanism that allows them to slide up and down parallel to each other in opposite directions. Therefore the thickness of the double wedge energy degrader at the beam axis varies in order to produce different proton ranges at the isocenter. The maximum range (R_{50}), measured at the 50% distal edge of the Bragg peak, that can be produced using the wedges is 220 mm. The R_{50} range for the open position of the wedges (shooting through the lead plate) is 240 mm. The range monitor which is a vacuum chamber that consists of a multi-layer Faraday cup (MLFC), a brass occluding rod and a steel scattering plate is responsible for producing the lateral dose profile. Figure 2(b) illustrates the distribution of energy deposited by the proton beam within the range monitor. Protons traveling through the occluding rod are completely stopped in order to produce a uniform lateral dose distribution.

Geant4 provides a complete physics process model for electromagnetic and hadronic interactions that can be modified at the user's convenience. In this study, we adapted the physics model using G4VModularPhysicsList class that allows the definition of all the pre-packaged Reference physics lists. We have chosen the recommended QGSP_BIC_EMY reference physics list, validated for proton and ion beam radiotherapy [5]. The accuracy of particle tracking depends on two factors: RangeCut(energy threshold) and StepMax(maximum step size). In our beam line model, the particle step size of 0.01 mm was set inside the water phantom and the remaining regions. The step limit of 0.01 mm is good enough to ensure adequate energy deposit within each detector slice and smaller than thickness of the slice. The range cut was set to

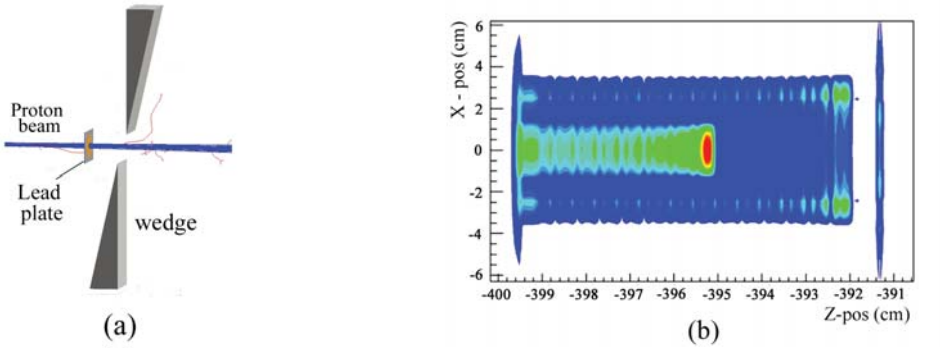

Figure 2: *(a) The double wedge energy degrader and lead plate system (b) Distribution of energy deposited within the range monitor.*

0.01 mm, which is translated into an equivalent minimum energy threshold for each type of the simulated particles. The primary particles were generated using Geant4 General Particle Source package(GPS).

3. Validation of passive beam Monte Carlo model

In order to validate the Geant4 model of the proton beam line, it must be able to replicate the dose profiles used for the treatment of patients, specifically the depth dose and lateral dose profiles. The iThemba proton beam line is calibrated before every treatment by measuring the range of the beam, measured at the 50% distal falloff position in water (R_{50}). Range trimmer plates are added or removed from the beam to adjust for variations in the beam until the 50% distal position is at 24 cm. For the Monte Carlo model, instead of working backwards from a 24 cm range, we must start with a detailed description of the incoming beam of protons. The expected proton energy exiting the vacuum window into the treatment room is 199.78 MeV, but this value was adjusted to 201.36 MeV in order for our simulations to line up with the measured values.

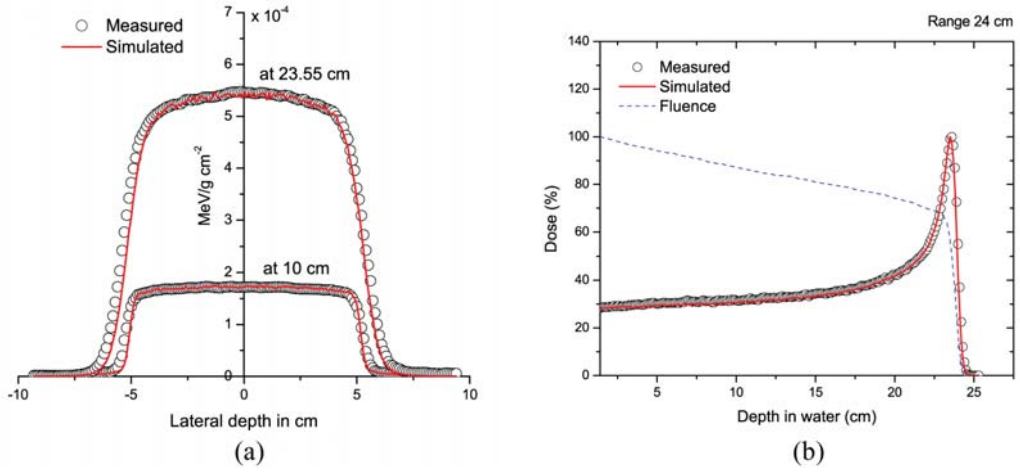

Figure 3: *Comparison of measured and simulated data using adjusted beam energy (a) lateral dose profile at the depth of 10 cm and 23.55 cm and (b) Bragg peak.*

Measured depth dose and lateral dose data were used to validate the beam line model. The simulation measurements were performed in a voxelized region created within the water phantom using the ROGeomtry classes. The volume of each cubic voxel is 0.01 cm^3, which is equal to the effective volume of the ionization chamber typically used at iThemba Labs for the beam calibration. The energy deposited by both primary protons and secondary radiation in each voxel was collected at the end of each run. Figure 3(b) is comparing the simulated Bragg curve with adjusted energy (201.36 MeV) normalized to the 100% dose level while Figure 3(a) is comparing the lateral dose profile at 10 cm and 23.55 cm (at the Bragg peak). The agreement between the simulated and measured data is within 0.3%.

3.1. Validation of double wedge degrader

For ranges less than 24 cm, the double wedge degrader is used to reduce the energy of the beam. The vertical wedge position (WP) of the double wedge degrader was calibrated against different proton ranges within the model. The following relationship was obtained by linear fitting the data as shown in the Figure 4(a).

$$WP(mm) = \frac{Range - a}{b} \tag{1}$$

where a and b are constants ($a = 9.39337 \pm 0.00238$ cm and $b = 0.74359 \pm 0.00025$). Figure 4(b) shows the comparison of simulations against experimental results for different proton ranges in water. The agreement between the simulated and measured data for different wedge positions is within 0.5% for proton ranges between 22 and 5 cm.

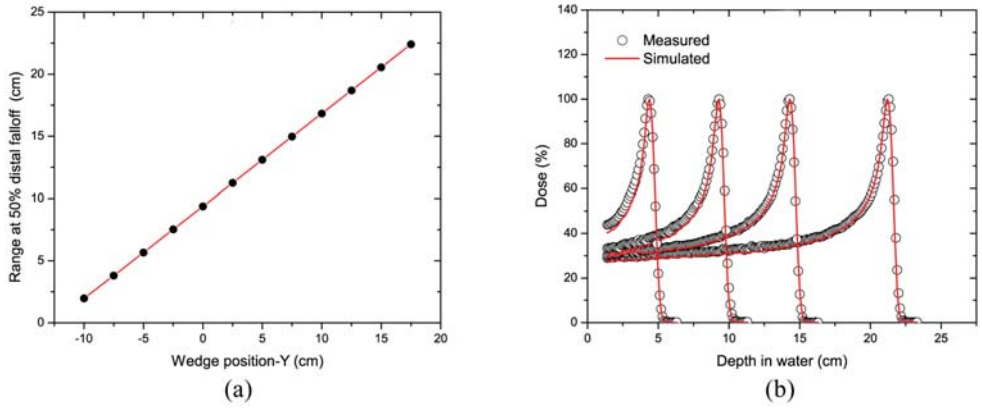

Figure 4: (a) Proton range as a function of wedge position and (b) comparison of relative dose profile with measurement for 22.73, 14.75, 9.7 and 4.72 cm ranges.

3.2. Effect of the mean excitation energy

In Geant4, the continuous energy loss per step in a track is based on restricted stopping power calculated using the Bethe-Bloch formula. In the Bethe-Bloch equation, the energy deposition per unit length is strongly dependent on both density and mean excitation energy[1] (MEE) of the target material. Moreover, the mean excitation energy can be approximated by $MEE = (10$

[1] also called mean ionization potential

eV)Z, where Z is the atomic number of the material. The ICRU-recommended MEE value for water is 75 ± 3 eV [6]. The uncertainty on the MEE value can not be ignored because other authors have reported slightly different values: 80 ± 2 eV [7] measured relative to Al using Bragg curves, 81.8 eV [8] which was used to produced stopping power tables, 77 eV [9] obtained by matching the measured Bragg peaks of carbon-ion and 78.4 ± 1.0 eV [10] which was determined from the proton beam ranges in water. Furthermore, a 0.8 - 1.2% [10] variation in the stopping powers was reported to have the same impact on the absorbed dose for MEE values between 75 and 80 eV in the energy range of 10 - 250 MeV. Andreo(2009) studied the variation of the Bragg peak with different mean excitation energy of water and the composition of organs and tissue for pencil beam of protons and carbon [11].

Table 1 : A summary of calculated $R_{50\%}$ values corresponding to different MEE of water for proton of 240 mm range. Measured value is 240.1 mm ($^{m}R_{50\%}$).

IEnergy (eV)	$^{IE}R_{50\%}$ (mm)	$^{m}\Delta R_{50\%}$ (mm)	$^{s}\Delta R_{50\%}$ (mm)	%
67	232.86	7.2	-3.2	-1.3
70	234.05	6.0	-2.0	-0.8
72	234.86	5.2	-1.2	-0.5
73	235.24	4.9	-0.8	-0.3
75	236.04	4.1	0	0
77	236.82	3.3	0.8	0.3
78	237.19	2.9	1.2	0.5
80	237.85	2.2	2.0	0.8
81	238.27	1.8	2.2	0.9
83	238.99	1.1	2.95	1.2
84	239.33	0.8	3.3	1.4
86	240.03	0.1	4.0	1.7
90	241.40	-0.3	5.4	2.3

$^{m}\Delta R_{50\%} = {}^{m}R_{50\%} - {}^{IE}R_{50\%}$
$^{s}\Delta R_{50\%} = {}^{IE}R_{50\%} - {}^{75}R_{50\%}$

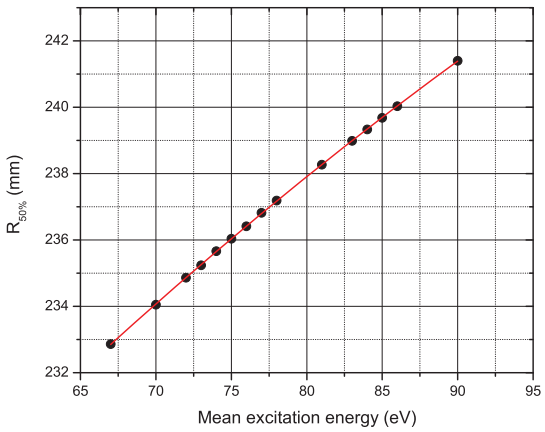

Figure 5: *Range as a function of mean excitation energy of the water.*

Table 1 summarizes the simulated proton ranges for different MEE values. The calculated ranges were then compared to the measured proton range of 240.1 mm. Protons starting with an initial energy of 199.78 MeV lose energy along the beam line in both the scatterers as well as the energy degrader. The mean proton energy exiting the final patient collimator and reaching the target was measured to be 188.6 MeV or producing an equivalent range of 23.5 cm (0.4% from the expected value of 24 cm). As shown in figure 5, the appropriate MEE value to produce a 24 cm range (with a 199.78 MeV starting proton energy) is 85.9 eV. This MEE value fell outside of the expected range of values discussed above, so the ICRU-recommended value of 75 eV was used and a readjustment to the proton beam of 1.58 MeV was used to compensate for the lower MEE value. The corrected beam energy was 201.36 MeV.

4. Validation of NaI detector

The detector response function is essential to generate the actual detector spectral responses of the prompt gamma in the Geant4 Monte Carlo simulation. The ideal mono-energetic gamma ray spectrum is a sharp line at the energy of the incident gamma (E) as shown in Figure 6(a), but due to statistical fluctuations in the number of electron-ion pairs produced by the photo-electron and Doppler broadening during the proton-nuclei collisions, the actual gamma ray spectrum has a Gaussian shape as shown in Figure 6(a).

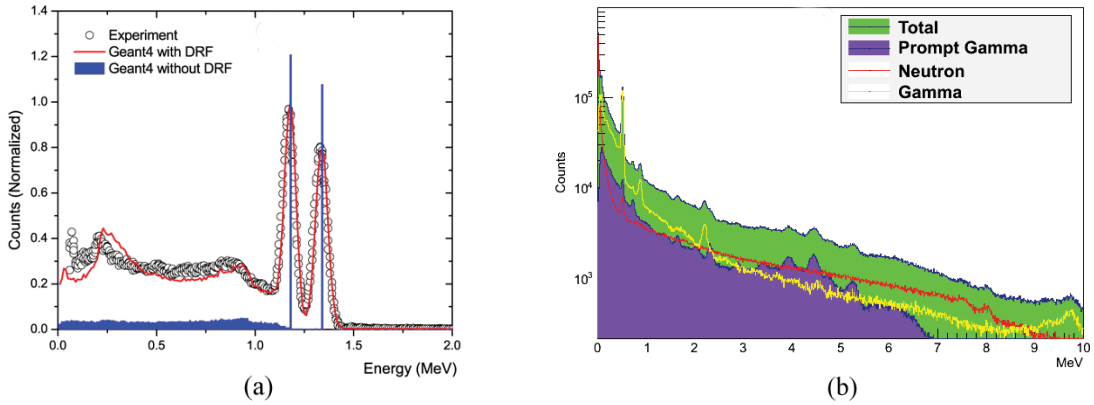

Figure 6: (a) Comparison of measured ^{60}Co spectra and simulated ^{60}Co spectra with and without the detector response function of a 3 x 3 inch NaI detector. (b) Simulated prompt gamma spectrum measured in water by a 3 x 3 inch NaI detector.

Each detector has a unique response to these factors, thus producing slightly different energy resolution values. The parameter FWHM (full width of the photo peak at half its maximum) measures the detector energy resolution. A higher resolution detector has a smaller value of FWHM. If the shape of the photo peak is a standard Gaussian shape, the FWHM is given by

$$FWHM = \sigma\sqrt{8ln2} \tag{2}$$

The standard deviation σ of the Gaussian shape depends on the energy of the detected gamma ray. This relationship $\sigma = xE^y$ was reported as a good choice to determine the detector response because of its simplicity [12], where E is the incident particle energy. The parameters x and y were determined by measured the energy resolution of the specific detector to be used for the prompt gamma measurements. Standard gamma emitting sources with an energy range from 0.661 to 4.438 MeV were used for the detector resolution calibration. The detector response was then validated against the measured energy spectra of different radioactive sources. The comparison between simulation (with and without detector response) and experimental energy spectra of ^{60}Co point source for 3 x 3 inch NaI detector is shown in the Figure 6(a). The Geant4 generated detector response agree with experiment well in the photo peak and Compton edge energy regions. The differences in the lower energy region could be due to the contribution of scattered gamma rays from surrounding objects that were not modeled in the simulation.

5. Validation for prompt gamma measurements

Although the prompt gamma measurements are on-going, these validation simulations have been used as a preliminary expectation of results and to assist in the set-up of the experimental measurements. Simulations were carried out to detect prompt-gammas produced in the water phantom by a 24-cm proton beam. The simulated prompt-gamma spectra (shown in Figure 6(b)) shows the various peaks for ^{12}C, ^{14}N and ^{16}O at 0.73, 1.02, 1.98, 2.31, 2.74 and 4.44 MeV. In addition, a strong 0.511 MeV gamma peak produced by positron annihilation was observed. The single and double escape peaks of the 4.44 MeV gamma-ray from ^{12}C are clearly seen within the energy range between 3.0 and 5.0 MeV. Once the experimental data measuring the prompt gammas have been completed, these simulations will be updated to reflect the actual detector set-up as well as any other changes required to ensure the Geant4 model mimics the measured results.

6. Conclusion

Our Geant4 treatment nozzle model is in good agreement with treatment-relevant measurements and has the ability to produce depth dose and lateral profiles at different proton ranges. Moreover, the model has produced promising prompt gamma results that are currently being pursued with measurements at iThemba Labs. The physics model for prompt gamma emission will be validated against the experimental results and energy spectra will then be compared with measured data.

Acknowledgments

The authors would also like to thank the Center for High Performance Computing (CHPC), CSIR Campus, 15 Lower Hope St., Rosebank, Cape Town, in South Africa for providing them access to their clusters and resources.

References

[1] Polf J C, Peterson S, Ciangaru G, Gillin M and Beddar S 2009a *Phys. Med. Biol.* **54** 731
[2] Agostinelli S, Allison J, Amako K and Apostolakis J 2003 *Nucl. Instrum. Methods Phys. Res.* **A 506** 250–303
[3] Parodi K, Paganetti H, Shih H A, Michaud S, Loeffler J S, Delaney T F, Liebsch N J, Munzenrider J E, Fischman A J, Knopf A and Bortfeld T 2007 *Int J Radiat Oncol Biol Phys.* **68** 920–934
[4] Peterson S W, Polf J, Bues M, Ciangaru G, Archambault L, Beddar S and Smith A 2009 *Phys. Med. Biol* **54** 3217–3229
[5] Cirrone G A P, Cuttone G, Mazzaglia S E, Romano F, Sardina D, Agodi C, Attili A, Blancato A A, Napoli M D, Rosa F D, Kaitaniemi P, Marchett F, Petrovic I, Ristic-Fira A, Shin J, Tarnavsky N, Tropea S and Zacharatou C 2011 *Progress in nuclear science and technology* **2** 207–212
[6] ICRU 1993 Stopping powers and ranges for protons and alpha particles International Commission on Radiation Units and Measurements,Bethesda, MD ICRU Report 49
[7] Bichsel H and Hiraoka T 1992 *Nucl. Instrum. Methods Phys. Res. B* **66** 345–51
[8] Janni J F 1982 *At. Data Nucl. Data Tables* **27** 147–529
[9] Krmer M, Jkel O, Haberer T, Kraft G, Schardt D and Weber U 2000 *Phys. Med. Biol* **45** 3299–3317
[10] Kumazakia Y, Akagib T, Yanoua T, Suga D, Hishikawa Y and Teshimac T 2007 *Radiat. Meas.* **42** 1683–91
[11] Andreo P 2009 *Phys. Med. Biol* **54** N205–N215
[12] Wang J, Wang Z, Peeples J, Yu H and Gardner R P 2012 *Applied Radiation and Isotopes* **70** 1166–74

Aspects of the structure of heavy carbon isotopes

S Karataglidis[1,2], K Amos[2,1], J P Svenne[3], L Canton[4], P R Fraser[4,2], and D van der Knijff[2]

[1] Department of Physics, University of Johannesburg, P.O. Box 524 Auckland Park, 2006, South Africa
[2] School of Physics, University of Melbourne, Victoria 3010, Australia
[3] Department of Physics and Astronomy, University of Manitoba, and Winnipeg Institute for Theoretical Physics, Winnipeg, Manitoba, Canada R3T 2N2
[4] Istituto Nazionale di Fisica Nucleare, Sezione di Padova, Padova I-35131, Italia

E-mail: [1]stevenka@uj.ac.za

Abstract. A multi-channel algebraic scattering (MCAS) method has been used to obtain spectra of a number of light-mass nuclei, which are treated as a two-cluster system, in these cases a nucleon plus nucleus. The MCAS method gives both sub-threshold and resonance states of the nuclei in question. To date, collective models have been used to specify the interactions between the nucleon and low-lying states of the nucleus that form the compound. For the case of the carbon isotopes, these studies have been complemented by sufficiently complex and complete shell-model calculations. Comparisons with the shell model results provide new insights into the validity of those from MCAS.

1. Introduction

In a recent article [1] we presented results from a study of the structures of ^{17}C and ^{17}Na that used a coupled-channel method with collective-model interactions between a neutron/proton and a select set of states of the core nucleus, ^{16}C/^{16}Ne. A multi-channel algebraic scattering (MCAS) method was used, as has previously been applied to a number of other systems. For example, in the cases of ^{15}C and ^{15}F, modelled as n+^{16}C and p+^{16}O respectively [2], it was shown to have predictive power. In [2], the two resonances in ^{15}F known at the time were well-reproduced, and further narrow resonances at higher energy were predicted. Resonances in the relevant energy regime were later observed in experiments by Mukha *et al.* [3, 4]. Fortune [5] criticised our mass-17 results based upon results of a simplified $0\hbar\omega$ shell model in which three neutrons are considered in the *sd* shell outside of an inert closed core of ^{14}C. Comparisons of results of that structure model with those found using MCAS were used as presumptive proof of "flaws" with the MCAS approach. Basically, those were the number and spin-parities found using MCAS and of the resonance widths so determined. However, those problems ascribed to MCAS were refuted in a recent article [6].

By way of addressing these issues in a broader context, we present a study of the spectra of the isotopes $^{12-19}$C using no-core, complete (as far as possible) multi-$\hbar\omega$ shell models with a fixed set of two-nucleon potentials. The objective is not to attain spectral energies that best agree with experimentally known ones; it is already known that there are discrepancies such as inversion of some low-lying states [7]. Rather we seek to find what are the orbit occupancies in the states and what connections there are to one and two neutron removal from each state of an

isotope with the low-lying states of a core system. For this objective, the consistent shell model approach serves. In that regard, this extends our earlier work which concentrated on ^{17}C and ^{19}C [8].

2. MCAS

While the MCAS method has been published elsewhere [9], to which we refer the reader for full details, we present a brief summary as a guide. The method is a means of solving the coupled-channel Lippmann-Schwinger (LS) equations describing a two-cluster system, which, for the present purpose, is given by a nucleon coupled to an even-mass nucleus. It is based on a collective-model description of the target (core) nucleus to specify the matrix of interaction potentials defining the coupled-channel problem. Nothing is assumed of the spectrum of target states. Sturmians are used to specify the matrix of potentials; a finite set of ~ 30 are needed to ensure convergence. In order to treat the problem of Pauli-exclusion, whereby the coupling of a nucleon to a filled orbit in the target is prohibited, we use orthogonalising pseudo-potentials (OPP's) with weights of 10^6 MeV to ensure those sturmians are orthogonal to any nucleon orbit that is full. Smaller weights are used to account for partially-filled orbits. (A summary of both may be found in Refs. [6, 2].)

With those sturmians and OPPs set, the matrix of potentials is re-expressed as a sum of separable potentials in momentum space as input to the LS equations. Solutions of the coupled equations may be found for both bound (negative energy, with respect to the particle emission threshold in the compound nucleus) and scattering (positive energy) states. Energies and widths are found of the states in the compound nucleus, assuming that the channels specified are only those of a nucleon coupled to a nucleus, in which case the widths so obtained correspond to nucleon-emission only.

3. Shell-model considerations

The shell model we consider for the carbon isotopes is that specified in the $(0+2)\hbar\omega$ model specified within the *spsdpf* basis. That model space is complete in $\hbar\omega$ for ^{12,14}C while for $^{16-18}$C the model space is truncated by necessity. The truncation, for the $(0+2)\hbar\omega$ calculations, is the exclusion of the $0g1d2s$ shell; a shell required for a complete evaluation of $1p-1h$ excitations by $2\hbar\omega$ from the *sd* shell. For ^{15}C, the presence of the single nucleon outside the $0p$-shell requires that the ground state and positive parity excited states be calculated in a $(1+3)\hbar\omega$ model space, for which the truncation on the basis is more severe with regards to the $3\hbar\omega$ components. All calculations have been made using the OXBASH code [10] with two interactions: the WBP interaction of Warburton and Brown [11] and the MK3W interaction [12] for comparison.

The ground states of ^{12,14}C so obtained illustrate the importance of the $2\hbar\omega$ components. Using the WBP interaction, we find

$$\begin{aligned} \left|^{12}\mathrm{C}\right\rangle &= 87.0\%\,|0\hbar\omega\rangle + 13.0\%\,|2\hbar\omega\rangle \\ \left|^{14}\mathrm{C}\right\rangle &= 84.9\%\,|0\hbar\omega\rangle + 15.1\%\,|2\hbar\omega\rangle\,. \end{aligned} \tag{1}$$

(The results using the MK3W interaction show $\sim 20\%$ admixture of the $2\hbar\omega$ components in both nuclei.) The ground state of ^{15}C is

$$\begin{aligned} \left|\tfrac{1}{2}^+;\tfrac{3}{2}\right\rangle_1 &= 78.1\%\,|1\hbar\omega\rangle + 21.9\%\,|3\hbar\omega\rangle \ \text{(MK3W)}, \\ &= 84.5\%\,|1\hbar\omega\rangle + 15.5\%\,|3\hbar\omega\rangle \ \text{(WBP)}. \end{aligned} \tag{2}$$

The negative parity states in ^{15}C come from the $(2+4)\hbar\omega$ model space, with the dominant contributions ($\sim 85\%$) being $2\hbar\omega$ in character, consistent with the heavier isotopes, which are purely $2\hbar\omega$ in character.

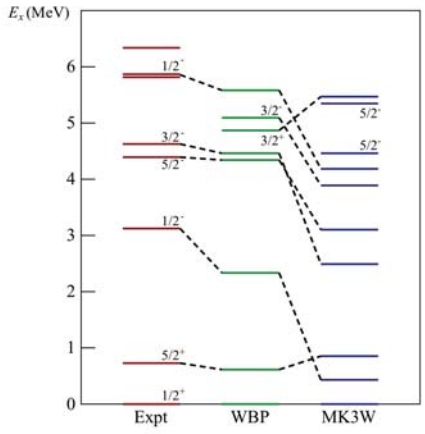

Figure 1. Spectrum of ^{15}C as obtained from our shell model. The data are from [13].

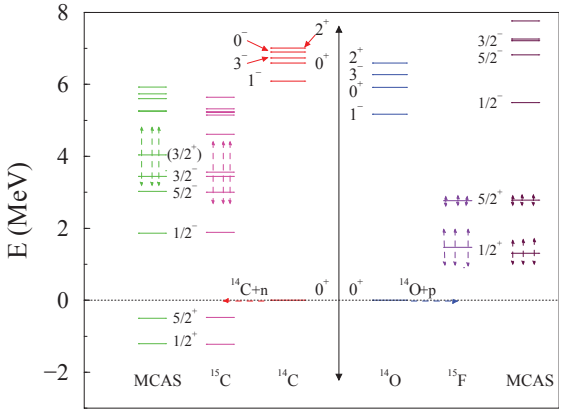

Figure 2. The mass-15 spectrum obtained from MCAS [2].

Table 1. $B(E2\uparrow)$ values, in units of $e^2\text{fm}^4$, for even-mass isotopes. Energies are in MeV, and the polarisation charge is in units of e.

Nucleus	E_x (exp.)	$B(E2)$ (exp.)	$B(E2)$		e_{pol}	
			MK3W	WBP	MK3W	WBP
^{12}C	4.43	40(3)	30.54	16.03	0.07	0.28
^{14}C	7.01	19(3)	25.30	17.66	–	0.04
^{16}C	1.77	3.1(6)	4.44	1.76	–	0.05
^{18}C	1.59	4.3(1.0)	3.33	2.52	0.02	0.05

An assumption often made in using a minimal (packed) model of the isotopes, particularly for mass-15 and higher, which have neutron occupation in the *sd* shell, is that the six proton play little or no role in defining the low-excitation spectrum. However, the six protons in these models are not passive: components of states, even the ground states, have admixtures of protons divided at least between the two $0p$ orbits. Then, as two protons in the $0p_{3/2}$ orbit can couple giving angular momentum values of 0 and 2, adding the latter to the angular momenta allowable with, for example, three $0d_{5/2}$ neutrons results in combinations with angular momenta ranging from $1/2^+$ to $13/2^+$ inclusive.

The spectrum of ^{15}C, as obtained from our shell-model calculation, is shown in Fig. 1, while Fig. 2 shows the spectrum obtained for mass-15 from MCAS [2]. It is clear that both the shell model and MCAS reproduce the experimental spectrum for ^{15}C quite well; the latter assuming a neutron coupled to low lying states in ^{14}C.

Another observable that is quite sensitive to details of the nuclear structure are the $B(E2)$ values. Table 1 shows the $B(E2)$ values for the even isotopes between ^{12}C and ^{18}C. Most of the data were taken from [14] and supplemented with data on ^{16}C from [15, 16] and on ^{18}C from [17]. Apart from the WBP result for ^{12}C, the required polarisation charges are all less than $0.1e$ reflecting that, for this observable, the wave functions from both models are quite good. For ^{14}C and ^{16}C the $B(E2)$ values from the MK3W are higher than the measured values. A polarisation charge cannot correct for that model; a smaller oscillator length may lead to agreement with

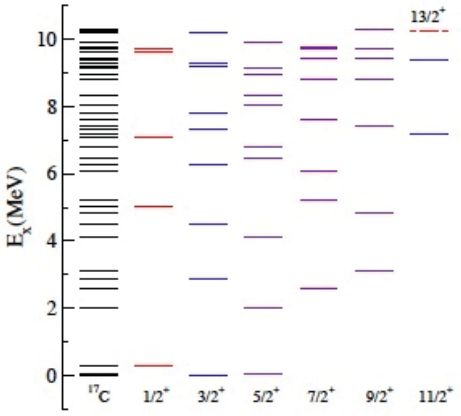

Figure 3. Low-excitation spectrum of ^{17}C as obtained from the shell model.

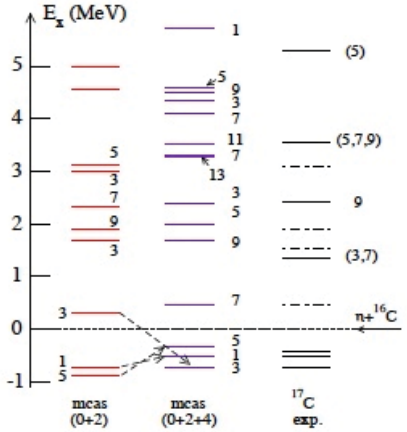

Figure 4. As for Fig. 3 but as obtained from MCAS using coupling of the neutron to the 0^+ and 2^+ as well as coupling to 0^+, 2^+, and 4^+ states in ^{16}C.

data.

Figs. 3 and 4 show the spectrum of ^{17}C as obtained by the shell model and MCAS, respectively. (The spins shown therein are $2J$. The MCAS calculation was obtained by assuming the coupling of a neutron to the low-lying states $(0^+, 2^+, 4^+)$ states in ^{16}C. The two approaches reproduce reasonably well the experimental spectrum. Fortune [5] finds that the underlying structures of the states obtained in MCAS are different to those obtained in the shell model. Yet the shell model studies therein [5] are simple $0\hbar\omega$ models which indicate a large $1s_{1/2}$ component, which is missing in MCAS. That is true, but not obvious: the mixing of the $1s_{1/2}$ orbit is there, but its contribution is part of the whole mixing due to the channel-coupling. This aspect of a small $1s_{1/2}$ component is also found by our shell model. The spectroscopic factors for the addition of a neutron to states in ^{16}C forming the compound ^{17}C ground state indicate a dominant $0d_{5/2}$ component when capture to the 0^+, 2^+, and 4^+ states in ^{16}C are taken collectively. A dominant $1s_{1/2}$ component is only present for coupling to the 0^+ state in ^{16}C.

4. Conclusions

The neutron-rich isotopes of carbon have been described using both a large-scale shell model and also MCAS. The results between the two schemes indicate that the collectivity inherent in MCAS may indicate admixtures of higher $\hbar\omega$ components are necessary in any shell-model description. This also negates any simplistic description of the carbon isotopes based on limited-basis $0\hbar\omega$ shell models.

Acknowledgments

SK acknowledges support of the National Research Foundation. JPS acknowledges supports from the Natural Sciences and Engineering Council of Canada (NSERC). PRF acknowledges funds from the Dipartimento di Fisica a Astronomia dell'Università di Padova and the PRIN research project 2009TWL3MX.

References

[1] Amos K, Canton L, Fraser P R, Karataglidis S, Svenne J P and van der Knijff D 2012 *Nucl. Phys.* **A879** 132

[2] Canton L, Pisent G, Svenne J P, Amos K and Karataglidis S 2006 *Phys. Rev. Lett.* **96** 072502
[3] Mukha I *et al.* 2009 *Phys. Rev. C* **79** 061301
[4] Mukha I *et al.* 2010 *Phys. Rev. C* **82** 054315
[5] Fortune H T 2012 *Nucl. Phys.* **A890** 25 and references cited therein
[6] Amos K, Canton L, Fraser P R, Karataglidis S, Svenne J P and van der Knijff D 2013 *Nucl. Phys.* **A912** 7
[7] Karataglidis S, Halse P and Amos K 1995 *Phys. Rev. C* **51** 2494
[8] Karataglidis S, Amos K, Fraser P, Canton L and Svenne J P 2008 *Nucl. Phys.* **A813** 235
[9] Amos K, Canton L, Pisent G, Svenne J P and van der Knijff D 2003 *Nucl. Phys.* **A728** 65
[10] OXBASH-MSU (the Oxford-Buenos-Aries-Michigan State University shell model code). A. Etchegoyen, W.D.M. Rae, and N.S. Godwin (MSU version by B.A. Brown, 1986); B.A. Brown, A. Etchegoyen, and W.D.M. Rae, MSUCL Report Number 524 (1986)
[11] Warburton E K and Brown B A 1992 *Phys. Rev. C* **46** 923
[12] Warburton E K and Millener D J 1989 *Phys. Rev. C* **39** 1120
[13] Tilley D R, Kelley J H, Godwin J L, Millener D J, Purcell J E, Sheu C G and Weller H R 2004 *Nucl. Phys.* **A745** 155
[14] TUNL Nuclear Data Evaluation, http://www.tunl.duke.edu/nucldata/index.shtml
[15] Imai N *et al.* 2004 *Phys. Rev. Lett.* **92** 062501
[16] Elekes Z *et al.* 2005 *Phys. Lett. B* **614** 174
[17] Ong H J *et al.* 2007 arXiv: nucl-ex/0711.4062

Determination of ^{235}U in the context of interference with ^{226}Ra for the study of the disequilibrium in the ^{238}U decay series

T N Khumalo[1,2], J Watterson[2,3], A Kwelilanga[2], S Connell[1]
[1]Departmant of Physics, University of Johannesburg P.O. Box 524 Auckland Park 2006, South Africa
[2]Environmental Radiation Laboratory, iThemba LABS (Gauteng), P.O. Box 7129, Somerset West, South Africa
[3]School of Physics, University of the Witwatersrand, Johannesburg

E-mail: thokozanik74@gmail.com, john.watterson@wits.ac.za, kwelilanga@tlabs.ac.za, shconnell@uj.ac.za

Abstract. The compound peak from ^{235}U and ^{226}Ra at 186 keV has been used to study methods for the de-convolution of complex peaks in gamma-ray spectroscopy and hence to determine the state of radioactive equilibrium of geological and environmental materials. A uranium reference material known to be in equilibrium has been analysed by gamma-ray spectroscopy, using a broad energy, HPGe detector (BEGE by Canberra Electronics) with the sample in a Marinelli beaker geometry. The compound peak at 186 keV has been studied in detail. The energies of the ^{226}Ra and ^{235}U lines that contribute to this peak are accurately known from published data. Although these two lines are separated by only 0.5 keV it has been shown that it is possible to obtain reliable values for the two peak intensities by using this detector together with appropriate data manipulation strategies. The FWHM of the detector and its variation with energy were determined experimentally to reduce the free parameters in the fit; a least squares fit of a sum of the two Gaussians superimposed on a second degree polynomial background was then performed on the $^{235}U/^{226}Ra$ 186 keV compound peak using the MIGRAD minimizer in ROOT (an object oriented C++ data analysis platform developed at CERN). The free parameters in the fit were the heights of the two Gaussians and the background model parameters. A numerical method for determining the intensity of ^{235}U and hence its concentration in an environmental sample, independent of ^{226}Ra / ^{222}Rn equilibrium state has been established and the chi squared surface has been studied to determine the errors in the important intensity parameters and to compare these values with the case where the FWHM and peak positions are also free parameters.

1. Introduction

The accurate determination of ^{235}U in the environment is of great importance. Not only in the commercial exploration for uranium, but also in the assessment of the risk of radiation exposure due to naturally occurring radioactive material (NORM) [1,2] as well as many other applications.

Natural uranium is mainly composed of ^{238}U and ^{235}U with abundances of 99.27 % and 0.72 % respectively [3]; therefore the ratio of ^{238}U to ^{235}U in the environment is expected to be very close to 136.14 and accurate determination of ^{235}U can be used to deduce the total amount of uranium in a typical environmental sample. Any alteration of this ratio in the environment is due to human intervention, or as a remote possibility, to a natural nuclear process such as the Oklo reactor in Gabon, Africa.

In many gamma-ray spectroscopy procedures secular equilibrium in the uranium decay series is assumed. Uranium (^{235}U and ^{238}U) decay through these series to stable isotopes of lead. Many of these decays emit characteristic gamma-rays. Gamma-ray spectroscopy is a nuclear analytical technique that utilizes these emitted gamma-rays. It is non-destructive and makes use of the penetrating nature of gamma-rays emitted by specific isotopes to identify the isotopes present in a sample, as well as their concentrations. In most gamma-ray methods for NORM the peaks from the decay of ^{214}Pb and ^{214}Bi are used to infer the activity of ^{226}Ra [4,5]. These isotopes (of lead and bismuth) follow the gaseous ^{222}Rn, the daughter of ^{226}Ra, in the uranium decay series. It is relatively easy (through tight sealing of sample counting containers) to compensate for the problem of radon escape so that, after ingrowth, these peaks are a direct measure of the ^{226}Ra content of the samples. However, the equilibrium between radium and uranium can be strongly affected by a number of geological processes. Because of the constant ratio between ^{235}U and ^{238}U in nature, as mentioned above, the 185.715 keV peak from ^{235}U can be used as a measure of the uranium content. In order to do this with good accuracy, it must be de-convoluted together with the 186.211 keV peak from ^{226}Ra. A BEGe HPGe detector is widely used for monitoring environmental radioactivity because of its good resolution [5,6]; in spite of this good resolution, it still fails to resolve these peaks, making extraction of vital information in this peak difficult. Procedures for determining ^{226}Ra from the ^{222}Rn daughters after ingrowth, followed by subtraction to determine ^{235}U from the compound peak can introduce errors. Therefore a direct method for ^{235}U determination is required.

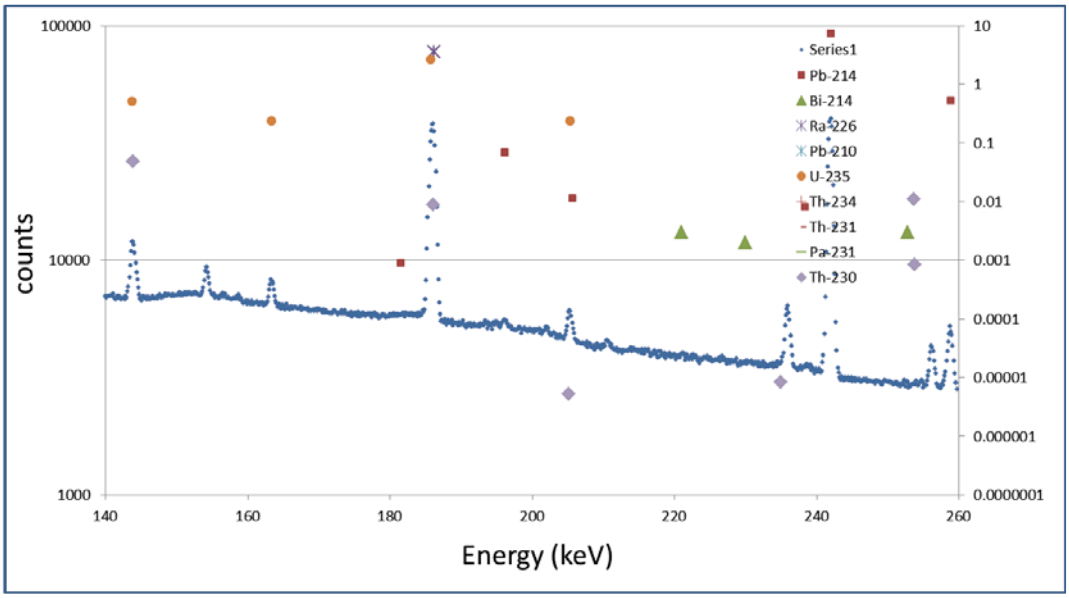

Figure 1. The 140-360 keV region of a gamma-ray spectrum from reference material (IAEA U1GX) containing uranium in equilibrium with its daughters. The relative intensities of the lines are shown using the logarithmic scale on the right.

2. Extraction of peak intensities from uranium decay

The gamma-ray spectra from the uranium (and thorium) decay series are complex (see Figure 1). Certain of the peaks are well resolved and it is relatively straightforward to extract their intensities. On the other hand, many of the peaks do overlap, even using the best available high-purity germanium detectors and the extraction of the relevant intensities is much more challenging. In this work we focus on the extraction of the ^{235}U and ^{226}Ra peak intensities from the compound peak at 186 keV. The energies of the gamma lines are 185.715 keV from ^{235}U and 186.211 keV from ^{226}Ra [5]. These lines are only 0.496 keV apart and their relative intensity for a specimen in equilibrium is 0.7490:1. Their

separation is significantly less than the resolution, expressed as the full-width at half maximum (FWHM), of modern high purity germanium (HPGe) detectors. The extraction of the individual intensities from this peak is therefore an important and interesting example in the analysis of compound peaks. The techniques developed can be used in a number of other applications as well, in optically stimulated luminescence dating, for example. The de-convolution of compound peaks depends on the application of peak fitting methods, particularly least squares or maximum likelihood techniques. Where the FWHM or the peak positions are included in the fit the method is essentially non-linear whereas if these are known, a linear method can be used. The important parameters to extract from the procedure are the peak intensities and the fitting procedure should therefore minimise the errors in these quantities. This is a somewhat different problem from that of just obtaining the *best fit* to the data itself. These outcomes are closely related but they are not the same. For example if the FWHM values and the peak positions can be established independently, that will both increase the number of degrees of freedom per estimated parameter and also allow the use of a linear LSSQ method with an exact algebraic solution instead of a numerical solution based on the minimum in the chi-squared surface. The effect of this on the errors, both systematic and statistical, in the peak intensity parameters will be studied in the present work. In this approach the model used to describe the reality of the gamma-spectrum in the peak region is crucial. It must describe both the peak shape and the background shape accurately but with a minimum of estimated parameters. In our initial studies we have chosen to describe the peak shape by a simple Gaussian and the background by a second degree polynomial. So the initial model fitted was (Note FWHM = 2.3548 sigma):

$$N_i = aE_i^2 + bE_i + c + d\frac{2.355}{F_{235}\sqrt{2\pi}}\exp\left(\frac{-\left(E_i - E_{235}\right)^2}{2\left(F_{235}/2.355\right)^2}\right) + f\frac{2.355}{F_{226}\sqrt{2\pi}}\exp\left(\frac{-\left(E_i - E_{226}\right)^2}{2\left(F_{226}/2.355\right)^2}\right)$$

where i is the channel number for the gamma-ray spectrum in the region to be fitted, E_i is the energy equivalent of channel i and typically $170 < E_i < 195$ keV

N_i is the number of counts in channel i.
F_{235} is the FWHM of the ^{235}U peak;
F_{226} is the FWHM of the ^{226}Ra peak and these are essentially the same;
E_{235} is the energy of the ^{235}U peak;
E_{226} is the energy of the ^{226}Ra peak;
a, b, c, d and f are free parameters in the fit.
d and f are the intensities of the two peaks and the errors in these parameters are to be minimised.

The peak positions were determined by an accurate calibration over the energy region of interest and fixed for the fit while the FWHM's were determined by using an experimental determination with a standard source and an interpolation for the variation with energy and also fixed for the fit.
The shapes of the 185.715 keV peak from ^{235}U and 186.211 peak from ^{226}Ra (as well of course as their intensities) can depend on the structure of the particular detector as well as the counting geometry. These experimental details are given in the next section. The fitting method chosen uses the CERN system ROOT [9]. This makes use of the MIGRAD algorithm, implemented in the MINUIT function optimization system [9].

3. Experimental

3.1. Sample Preparation and Counting Geometry

Sample preparation and the choice of counting geometry are of great importance in the counting of environmental radioactive samples [10]. In this study, a sealed Marinelli beaker was used as a sample container (see Figure 2, which shows a schematic of the counting geometry used in this study). Counting in a Marinelli beaker increases the efficiency; and reduces counting times for low activity

samples [10]. Sealing is important if it is intended to determine ^{238}U from the radon daughters. Thefore sealing of the Marinelli beaker is not relevant to the deconvolution method developed in this study. The sample mass was obtained and the typical

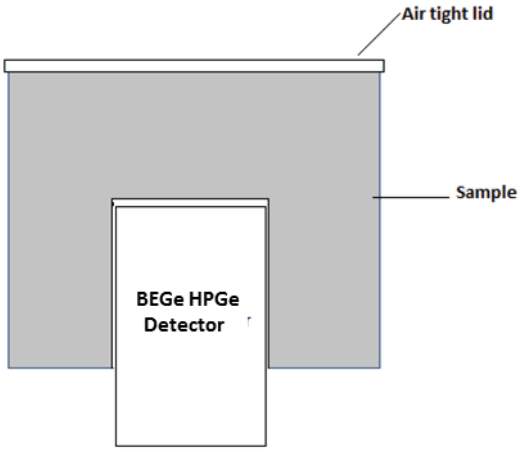

Figure 2. A schematic of the counting geometry

counting period was 24 hours in order to minimise the statistical uncertainty.

3.2. Gamma-ray spectroscopy

A BEGe HPGe with crystal diameter and thickness of 61.1 mm and 21.2 mm, respectively, was used in this study. The canning material of the detector is made of carbon composite material. . The accompanying electronics consisted of analog to digital converter (ADC), signal amplification systems (preamplifier and amplifier) and a Canberra DSA-1000 digital signal processing (DSP) system interfaced to a multichannel analyzer (MCA). The use of a DSA-1000 system with its greatly increased peak gain stability of a factor of two or three times better than past generation analog systems is of great importance in this approach.

3.3. Energy calibration

Energy calibration uses standard sources such as ^{60}Co and ^{137}Cs with well known transition energies to establish the equivalent energy of each channel. A least squares fit of a polynomial function of second degree is often used [11]. In this work the peak positions must be very accurately known and a two stage procedure was adopted. An initial energy calibration utilised standard sources such as ^{60}Co and ^{137}Cs with well known transition energies together with a first degree polynomial.

This was refined in a second stage procedure using peaks from ^{214}Pb and ^{214}Bi present in the sample spectrum to obtain a highly accurate energy calibration over the region of interest.

3.4. FWHM and efficiency calibration

The variation of the full energy peak efficiency and the variation of the FWHM for the detector with energy were determined using a standard multi-isotope source from Eckert and Ziegler Isotope Products. The same source was used to determine the variation in the resolution as a function of energy. These results were all obtained for the specific counting geometry shown in Figure 2.

4. Data analysis

The raw data (counts vs channel numbers) were then read into the C++ programme for further analysis. The C++ program has been written to read in the data and implement the routine MIGRAD

in the ROOT platform. Since the region of interest is the 186 keV ^{235}U/^{226}Ra compound peak, the C++ procedure read data in the range $130keV \le E_i \le 200keV$. To initiate the quest of finding the best parameters for the fit function, the user is prompted to supply the FWHM for the detector and then

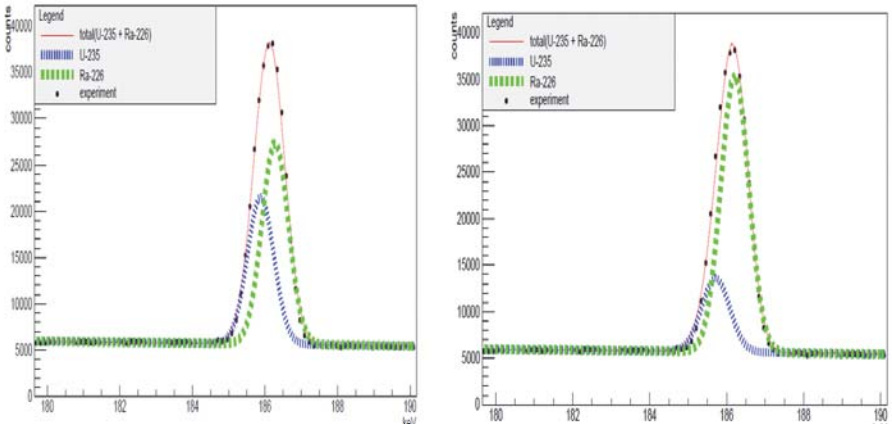

Figure 3. Data points together with fit of two Gaussians plus background using ROOT. Sample IAEA U1GX reference material in equilibrium; detector: BEGe. (a) With an energy calibration slope of 0. 12553 keV per channel and (b) with a calibration slope of 0. 12531 keV per channel; FWHM 0.85 keV in both cases.

MIGRAD iterates, scanning the chi-square surface until a convergence criterion is satisfied, thereby printing out the best fit parameters as well as the associated errors. Experimental data was then plotted together with the theoretical prediction.

5. Results and discussion

Values for the centroids of the ^{235}U and ^{226}Ra are known from published data to be 185.715 keV and 186.211 keV, respectively [12]. Initial results were used to test the sensitivity of the reduced parameter

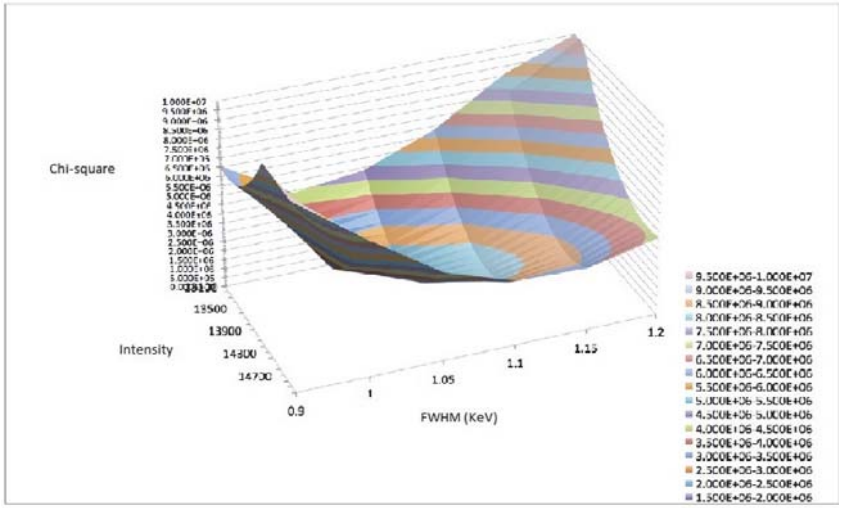

Figure 4. Chi-squared surface for co-axial detector illustrating how the surface varies with changes in the FWHM and the intensity of the ^{235}U peak. The value of the intensity at the minimum is a sensitive function of the value of the FWHM.

approach to the energy calibration. Figure 3b shows the results obtained from the de-convolution of the compound 186 keV peak in the spectrum from the IAEA uranium standard using a slope of

0.12531 keV per channel for the energy calibration. With this value the best fit predicts an intensity that is close to the theoretical value of 0.749:1 for a sample in equilibrium. As is shown in Figure 3a, a slope of 0.12553 keV per channel gave a ratio that is much too small for the ^{235}U peak intensity. A common FWHM of 0.85 keV was used to obtain these results. These results demonstrate the need for a very high degree of accuracy in the energies of the transitions as well as the energy calibration when the reduced parameter approach is used.

To investigate the sensitivity of the parameters (intensities) to the choice of FWHM, chi-square was plotted against the peak intensity and the FWHM. Figure 4 shows the resulting chi-square surface and it is observed that a small change (of about 0.05 keV) in the FWHM results in a large variation in the local minimum of the chi-square surface.

6. Conclusion

This de-convolution method for a compound peak without the peak position as a free parameter requires a highly accurate energy calibration in the peak region. If this is not the case then there can be large errors in the peak intensities found even at the minimum chi squared value. The results show that the energy calibration slope should be accurate to at least four significant figures in the case of the compound 186 keV peak.

The chi-squared variation and thus the errors in the determination of the important intensity parameters are also sensitive to variations in the FWHM and this parameter must also be known with a high degree of accuracy for the linear least squares method to be successfully applied. If these two requirements can be met then the positions and widths of the peaks can be fixed and do not have to be used as parameters in the fit. This greatly reduces the statistical error. Further work will be carried out to assess the accuracy of this method for the simultaneous determination of the amounts of ^{235}U and ^{226}Ra and the use of this technique to assess the degree of disequilibrium in geological and environmental samples as well as to areas such as optically stimulated luminescence dating.

References

[1] T Santawamaitre, D Malain, et al 2011 Study of natural radioactivity in riverbank soils along the Chao Phraya river basin in Thailand *Nucl. Instr. Meth. Phys. Res. A* **652** 920-924

[2] H. Florou, G. Trabidou, G. Nicolaou 2007 An assessment of the external radiological impact in in areas of Greece with elevated natural radioactivity *J. Environ. Radioac.* **93** 74-83

[3] Krane K S 1988 *Introductory Nuclear Physics* (New Jersey: John Wiley & Sons)

[4] K Ravisanker, K Vanasndari, et al 2012 Measurement of natural radioactivity in building materials of Namakkal, Tamil Nadu, India using gamma-ray spectrometry *Appl. Radiat. Isot.* **70** 699-704

[5] Ma Los Arcos, Menno Blaauw, et al 2005 The IAEA test spectra for low level gamma-ray spectrometry software *Nucl. Instr. Meth. Phys. Res. A* **536** 189-195

[6] S A Saqan, M K Kullab and A M Ismail 2001 Radionuclides in hot mineral spring waters in Jordan *J. Environ. Radioac.* **52** 99-107

[7] Glenn F Knoll 2000 *Radiation Detection and Measurement*. John Wiley & Sons

[8] S. Hurtado, M. Garcia-Leon, R. Garcia-Tenorio 2006. A revision of energy and calibration method for Ge detectors. *Nuclear Instruments and Methods in Physics Research A* **564** 295-299

[9] F. James 1975. MINUIT-A System for Minimization and Analysis of the Parameter Errors and Correlations .*Computer Physics Communications* **10** 343-367

[10] Guogang Jia, Jing Jia 2012 Determination of radium isotopes in environmental samples by gamma spectrometry, liquid scintillation counting and alpha spectrometry: a review ofanalytical methodology *J. Environ. Radioac* **106** 98-119

[11] Fabien Courtine, e al 2014 Calibration of a germanium well-detector using ^{60}Co: The effects of the angular correlation of the two gamma rays emitted in cascade, quantified with Monte Carlo simulations *Rad. Mea.* **61 78-82**

[12] www.nndc.bnl.gov/nudat2

Developing gamma-ray tracking with a segmented Ge detector

E A Lawrie[1], T D Bucher[1], J L Easton[1,2], S P Noncolela[1,2] and O Shirinda[1]

[1] iThemba LABS, National Research Foundation, P.O. Box 722, 7129 Somerset West, South Africa
[2] University of the Western Cape, Private Bag X17, 7535 Bellville, South Africa

E-mail: elena@tlabs.ac.za

Abstract. Basic techniques that make it possible to trace the gamma-ray interactions inside a segmented Ge detector and reconstruct the gamma-ray trajectory are discussed. The process of developing gamma-ray tracking in general and the plans for establishing the position sensitivity of the iThemba LABS segmented clover detector are outlined.

1. The idea about developing gamma-ray tracking

Some fifteen years ago the most powerful gamma-ray arrays, GAMMASPHERE and EUROBALL, were delivering plenty of gamma-spectroscopic data with the aid of which many new phenomena in nuclear structure were discovered. These powerful arrays consisting of Compton-suppressed gamma-ray detectors covered a solid angle of 4π, with a total photopeak efficiency of about 9% for a gamma-ray with energy of 1.3MeV. Nevertheless the question whether we can improve even further the resolving power of the gamma-ray arrays was discussed.

The GAMMASPHERE and EUROBALL arrays consisted of a large number of HpGe detectors, each surrounded by a Compton-suppression shield made of scintillator detectors. The Ge crystals covered only about 50% of the 4π solid angle. The Compton-suppression shield is used to veto the gamma-rays that Compton scatter outside the Ge crystal after depositing part of their energy, and thus they contribute to an unwanted Compton background. The BGO shield then improves substantially the Compton background and therefore the resolving power of the array. But one can consider whether the performance of the array may not be enhanced by replacing the scintillators with Ge crystals, making in that way a full 4π ball made entirely of Ge crystals. In this case, when a gamma-ray scatters from one Ge crystal to a neighbouring one, instead of rejecting the event, we can measure all deposited energies and sum them to recover the total energy of the incident gamma-ray.

In order to implement this idea there is one problem that needs to be solved. Assume that two Ge crystals were hit, and the deposited gamma-ray energies were E_1 and E_2. One needs to determine whether these two hits were caused by one gamma-ray with a total energy of $E = E_1+E_2$, that scattered between the two crystals, or whether they were two independent gamma-rays with energies of E_1 and E_2 respectively. It is obvious that in the latter case the two energies should not be summed.

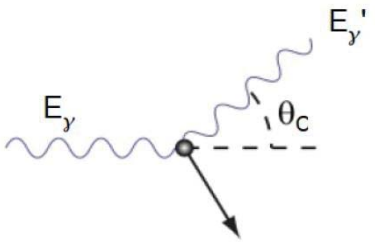

Figure 1. Diagram showing Compton scattering of a gamma-ray.

In fact one can easily distinguish a Compton scattering event by testing whether the deposited energies E_1 and E_2, and the scattering angle θ_C (see figure 1) obey the Compton scattering formula:

$$\cos \theta_C = 1 + 0.511(1/E\gamma - 1/E\gamma')$$

where the deposited energies are $E_1 = E_\gamma - E_\gamma'$ and $E_2 = E_\gamma'$

In order to test that equation we need to measure not only the energies, but also the scattering angle θ_C. Therefore the detectors need to have an extra capability, that is to be able to measure the position at which the gamma-ray interaction occurred.

The latest developments in gamma-ray detector technology made it possible to construct such detectors. These detectors are made of segmented Ge crystals and are a new generation of gamma-spectroscopy detectors. They have one central electrode where a high voltage with positive polarity is applied, while the outside electrode (covering the whole outside surface of the detector) is segmented and electrically connected to ground. For example the segmented Ge crystal used in the AGATA and GRETA arrays (shown in figure 2), is segmented in 6 x 6 = 36 segments. In comparison another segmented Ge detector, a TIGRESS detector, is also shown in figure 2 and has a 4 x 2 = 8 segmentation per Ge crystal.

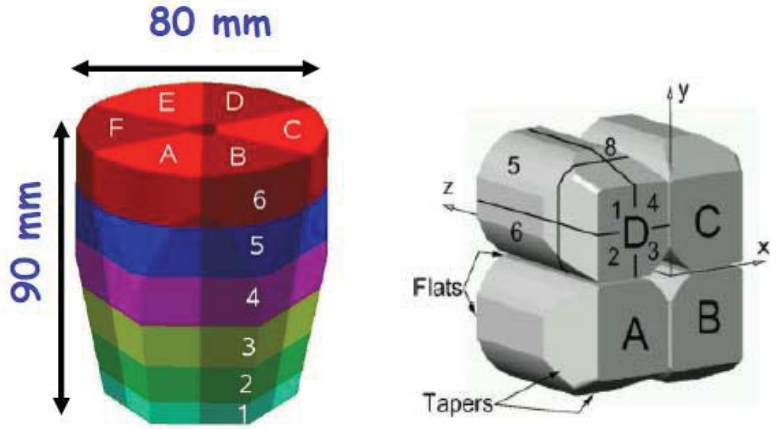

Figure 2. Left: An AGATA/GRETA Ge crystal, segmented in 6 x 6 fold. Right: TIGRESS detector with a segmentation of 4 x 2 = 8 fold per crystal.

When a gamma-ray interacts inside the detector, it creates charges. These charges move towards the electrodes creating electric currents. The signals observed on the electrodes represent such currents and have shapes that are indicative of the mobility of the electron and hole charge carriers, and also of where (i.e. how far from the electrode) the charges were created. A few examples for shapes of the signals created at different positions are illustrated in figure 3.

The signals shown in figure 3 are measured for a TIGRESS detector. Three interaction points are illustrated as black, red and blue dots. The corresponding average signals (amplitude of the signal as a function of time) on the three outside electrodes C1, C2 and C4, and for the three interaction points are shown in the figure. The interaction points plotted in red and black are situated at the same radius with respect to the core electrode, so they are at approximately the same distance from the electrode C1.

That is why the black and the red signals on the electrode C1 have approximately the same shapes. The signal for the blue interaction point however shows a distinctly different shape, because this point lies at a different radius.

The amplitudes of the induced signals on the neighbouring electrodes C2 and C4, can be used to determine how close each interaction point is to these electrodes. For instance the signals measured at electrode C2 indicate that the blue and the red interaction points are lying at approximately similar distance from the electrode C2, while the black interaction point is closer, because this signal has a larger amplitude. In a similar way we can deduce that the red interaction point is closer to electrode C4 than the black and the blue interaction points because the signal from the red interaction position has a larger amplitude.

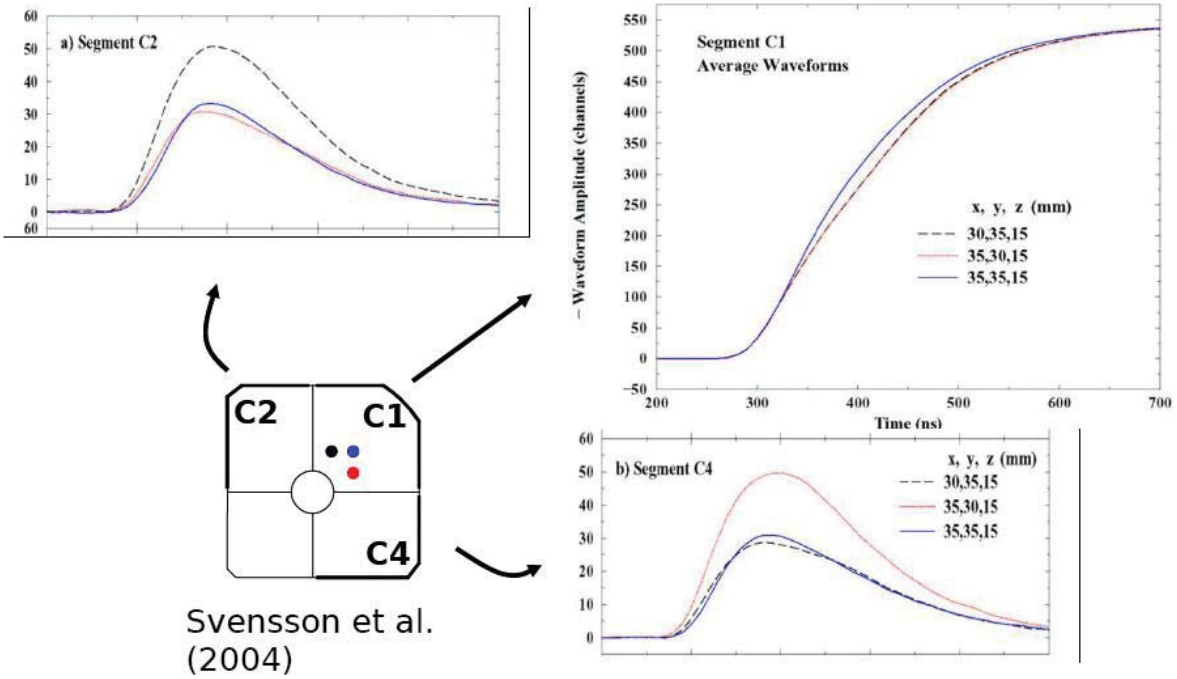

Figure 3. Average amplitudes of the signals as a function of time measured for a TIGRESS detector for three different interaction positions, shown with black, red and blue. From [1].

In fact the set of signals measured at all electrodes is unique for each interaction point. It is also different for different type of detectors, as well as for different detectors with the same geometry. That is because the shape of the signals depends not only on the geometry of the detector, but also on the high voltage, on the features of the Ge crystal such as impurity concentrations, crystal orientation, etc., and on the specific characteristics of the particular preamplifier.

To utilize the position sensitivity of a segmented Ge detector we have to create a data base containing sets of pulses that characterize every possible interaction position in the volume of the detector. Then an experimentally measured set of pulses associated with certain gamma-ray interaction point can be compared with the data base. The best match will then determine the exact position of the gamma-ray interaction within a few millimetres.

Once the interaction positions associated with a gamma ray are deduced, the gamma-ray trajectory needs to be recovered by determining the correct order of the set of gamma-ray interaction points. This is usually done by applying a tracking algorithm that checks which ordering of the interaction points satisfies the Compton scattering formula.

New gamma ray arrays, able to implement this gamma-ray tracking technique have been designed, such as AGATA and GRETA. They have typical efficiency of about 43% for 1.3 MeV gamma rays,

and resolving power of 2-3 orders of magnitude larger than the GAMMASPHERE and EUROBALL arrays [2]. Smaller versions of these arrays, called AGATA demonstrator and GRETINA are already in operation.

2. Advantages of gamma-ray tracking

Gamma-ray tracking was suggested and developed as a necessary technique to build a 4π array of Ge detectors. However the gamma-ray tracking has other additional advantages. Successful gamma-ray tracking leads to:
(i) efficient add-back, i.e. recovering the total energy of a Compton-scattered gamma-ray,
(ii) efficient rejection of the Compton background, better than what can be achieved with a typical Compton-suppression shield,
(iii) precise measurement of the position for the first interaction point of the gamma-ray inside the detector. This offers unprecedented accuracy and precision for several experimental techniques, such as: lifetime measurements using Doppler effects, correction of Doppler shifts for gamma-rays emitted by nuclei in flight (that improves substantially the energy resolution and the resolving power of the detector), angular distribution measurements which can yield precisely measured mixing ratios and g-factors, etc.,
(iv) precise measurement of the position for the second interaction point of the gamma-ray inside the detector. This offers unprecedented precision for linear polarization measurements and allows establishing the electric or magnetic nature of the gamma ray.
The gamma-ray tracking is a challenging new technique that cannot be performed with 100% efficiency. The number of successfully tracked gamma-rays depends strongly on the properties of the segmented Ge detector, and also on the features of the emitted gamma-rays.

3. Developing gamma-ray tracking with the iThemba LABS segmented clover detector

The iThemba LABS segmented clover detector is a detector with TIGRESS geometry – it consists of 4 Ge crystals, each 8-fold segmented, as shown in figure 2. Each crystal has a diameter of 60 mm before shaping and a length of 90 mm. It is designed to be placed at 14.5 cm or 11 cm from the target and is complemented by a Compton-suppression shield. Simulations yield efficiency of 0.63% and 1% for a 1.3 MeV gamma ray at these two distances [3].

The major interest in the iThemba LABS segmented clover detector lies with its position sensitivity. The wish is to use this detector for applications requiring extreme precision in the measured position of the first and second interaction points. To develop the gamma-ray tracking capacity of this detector the following major steps are planned:
(i) Simulations of the geometry, electric field, movements of the charge carriers and finally the shape of the pulses on the 36 contacts of the segmented clover detector. Creating a data base with characteristic pulses for each interaction position.
(ii) Experimental verification of the simulations by measuring the pulses observed at several different well-defined interaction positions inside the iThemba LABS segmented clover detector.
(iii) Developing a procedure to compare the experimentally measured pulses with the pulses in the data base and extracting the best match to determine the position of the gamma-ray interaction.
(iv) Based on the established interaction positions the full gamma-ray track inside the detector will be reconstructed, yielding in particular the first and the second interaction points.

The development of gamma-ray tracking with the iThemba LABS segmented detector is under way. Results obtained so far from the simulations of the detector are discussed in the presentations given by S. P. Noncolela and T.D. Bucher. The experimental measurements of the performance of the segmented detector are discussed in the presentations of J.L. Easton and O. Shirinda. It is anticipated that once the gamma-ray tracking capacity of this detector is developed, it will be used as a new-generation gamma-ray detector for carrying out new types of nuclear structure experiments. As soon as the position resolution of the segmented clover is established, and its performance as a tracking detector is well understood, details of such experiments can be devised for optimal results.

4. Acknowledgement
The financial support from NRF for purchasing the segmented clover detector is gratefully acknowledged.

References
[1] Svensson C E *et al.*, 2005 *Nucl. Instum. and Methods* A **540** 348-360
[2] Akkoyun S *et al.*, 2012 *Nucl. Instum. and Methods* A **668** 26-58
[3] Shumaker M A *et al.*, 2007 *Nucl. Instum. and Methods* A **570** 437-445

^{194}Tl as the first example revealing chiral symmetry breaking in a pair of four-quasiparticle bands

P.L. Masiteng[1,2,3,*], E.A. Lawrie[1], T.M. Ramashidzha[1,2], R.A. Bark[1], B.G. Carlsson[4], J.J. Lawrie[1], R. Lindsay[2], F. Komati[1,5], J. Kau[1,5], P. Maine[1,2], S.M. Maliage[1,2], I. Matamba[6], S.M. Mullins[1], S.H.T. Murray[1], K.P. Mutshena[1,6], A.A. Pasternak[7], I. Ragnarsson[4], D.G. Roux[2], J.F. Sharpey-Schafer[1,2], O. Shirinda[1,2], P.A. Vymers[1,2]

[1] iThemba LABS, National Research Foundation, P.O. Box 722, 7129 Somerset West, South Africa
[2] University of the Western Cape, Private Bag X17, 7535 Bellville, South Africa
[3] University of Johannesburg, P.O. Box 524, 2006 Auckland Park, South Africa
[4] Division of Mathematical Physics, LTH, Lund University, SE-221 00 Lund, Sweden
[5] University of North West, Private Bag X2046, 2735 Mmabatho, South Africa
[6] University of Venda for Science and Technology, Thohoyandou, South Africa
[7] A.F. Ioffe Physical-Technical Institute, 194021 St.-Petersburg, Russia

E-mail: *plmasiteng@uj.ac.za

Abstract. A study of ^{194}Tl has revealed the presence of two strongly coupled negative-parity rotational bands up to the 24^- and 23^- states, respectively. These two bands are associated with the two-quasiparticle configuration at lower spins and the four-quasiparticle configuration at higher spins. The two 4-quasiparticle bands show exceptionally close near-degeneracy in the excitation energies. The relative excitation energies of these 4-quasiparticle bands were compared to the relative excitation energies of the best known chiral candidates with close near-degeneracy. This is one of the best cases of near degeneracy in partner bands observed to date, probably resulting from a chiral geometry in the angular momentum space. It is also the first pair of 4-quasiparticle bands associated with chiral symmetry.

1. Introduction

The manifestation of chirality in atomic nuclei, originally suggested in Ref. [1] and vigorously investigated over the past few years from both the experimental and theoretical standpoint, continues to be the subject of intense discussion. Subsequent to the observation of chiral doublet bands in $N = 75$ isotones [2], candidate chiral bands have been reported in more than 21 nuclei in $A \sim$80, 100, 130, 190 mass regions.

Nuclear chirality depends on a delicate balance between the collective core with a triaxial mass distribution and a single particle degree of freedom associated with a triaxial mass distribution and a single particle degree of freedom associated with the valence proton and neutron. An energy minimizing mechanism among the core and the valence nucleons results in a mutually perpendicular coupling of their respective angular momenta forming either a left- or right-handed system in the nuclear body-fixed frame. The intrinsic chirality then is seen in the laboratory frame, which is free of handedness, as a doubling of energy levels with the same spin and parity.

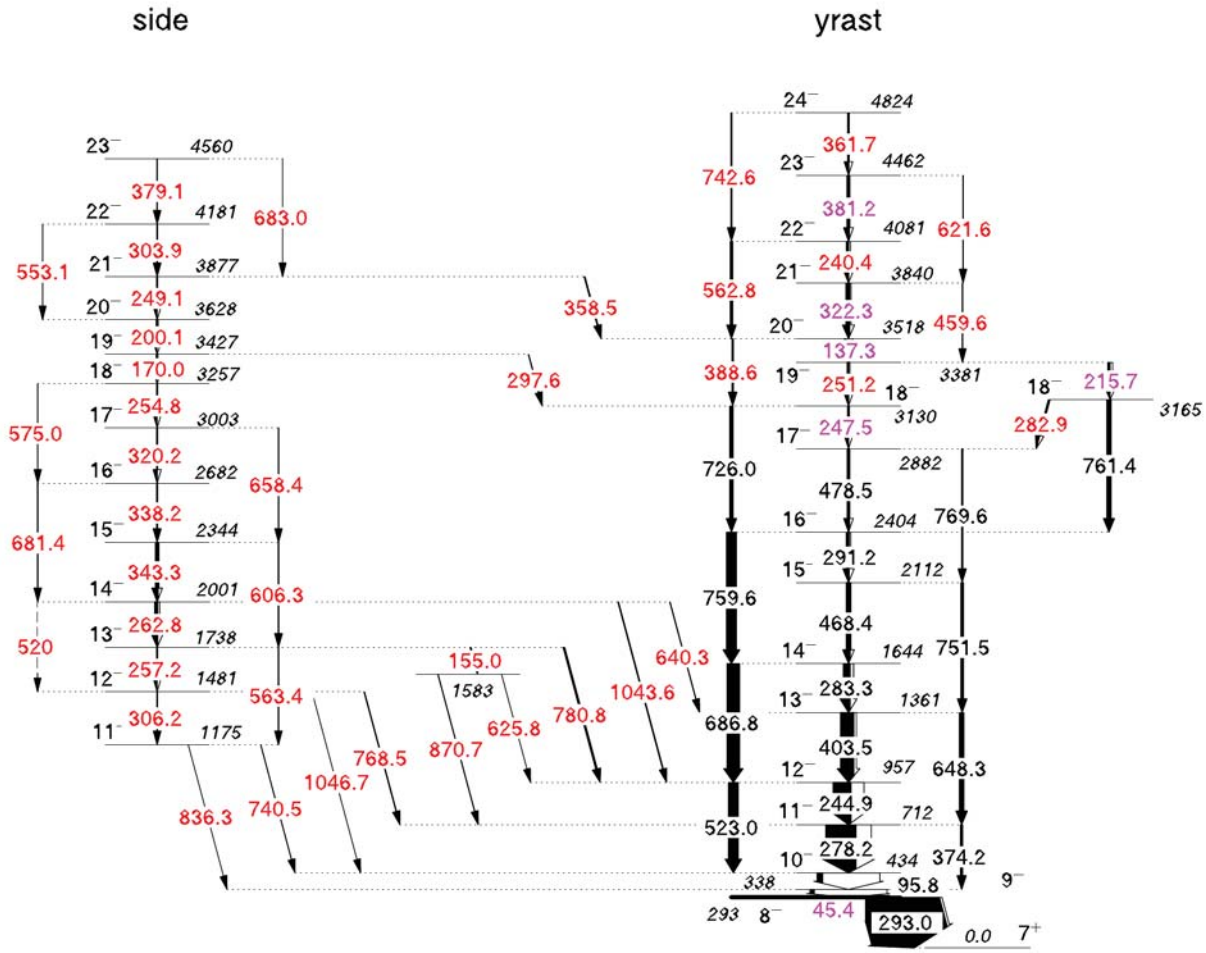

Figure 1. Partial level scheme showing the near-degenerate pair of rotational bands in ^{194}Tl. The uncertainties in the measured γ-ray energies are typically about 0.3 keV for most transitions, but increase to 0.5 keV for weak and doublet transitions.

Despite many discoveries reported on possible chiral partner bands, degenerate band structures are yet to be discovered, instant the currently known chiral candidates show similar properties rather than degeneracy. The best known nearly degenerate band structures were reported in odd-A ^{135}Nd [3], ^{126,128}Cs [4, 5], ^{104}Rh [6] and recently in ^{194}Tl [7]. In the present report we discuss a candidate chiral band structure found in ^{194}Tl and compare the observed degeneracies in the four nuclei ^{135}Nd , ^{128}Cs and ^{104}Rh.

2. Experimental method and Data analysis

High-spin states in ^{194}Tl were populated using the ^{18}O(^{181}Ta, 5n) reaction at 93 and 91 MeV beam energies. The beam provided by the separator sector cyclotron (SSC) of the iThemba LABS impinged upon a self-supporting stack of two (and three) 0.5 mg/cm^2 target foils. The emitted γ rays were detected by the AFRODITE γ-ray spectrometer [8, 9], which comprised of 8 Compton-suppressed clover detectors and 6 LEPS detectors with the trigger logic set to accept events when at least two γ rays were detected in coincidence in the clover detector. The data were sorted into matrices and spectra and RadWare software package [10] was employed for analyses.

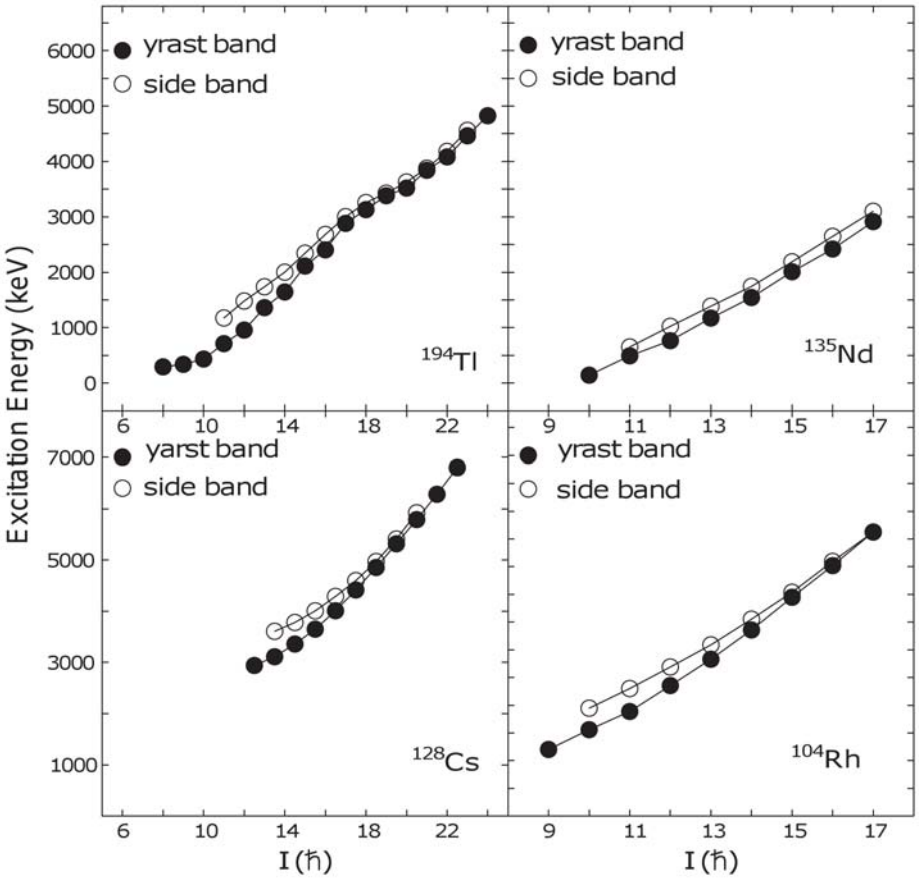

Figure 2. Comparison of the excitation energy vs spin plots of the best known close near-degenerate chiral candidate bands in ^{194}Tl, ^{128}Cs, ^{135}Nd and ^{104}Rh.

In order to determine the spins and parities of the new transitions angular distribution ratios, R_{AD}, and linear polarization anisotropies were measured, respectively. The previously known level schemes [11, 12] were revised and considerably extended. More than 130 new transitions were observed and placed in five rotational bands, three of which are observed for the first time. In this report we show the two bands which exhibit close-near-degeneracy, see Figure 1. Detailed experimental method and data analysis procedure for this experiment can be found in [7].

3. Results and Discussion

The properties of the partner bands in ^{194}Tl were evaluated with respect to the suggested fingerprints of chiral doublet bands such as: degeneracy in the excitation energies, moments of inertia, $B(M1)$ and $B(E2)$ reduced transition probabilities, and showed good similarities [7]. The remarkable feature of these two 4-quasiparticle $\pi h_{9/2} \otimes \nu i^{-3}_{13/2}$ bands is the exceptionally good near-degeneracy observed in a long spin range.

Figure 2 presents the excitation energy as a function of spin for the partner bands in ^{194}Tl and in the previously known examples of partner bands with best near degeneracy, the two-quasiparticle $\pi h_{11/2} \otimes \nu h^{-1}_{11/2}$ bands in ^{126,128}Cs (the near-degeneracy in ^{126}Cs is very similar to that in ^{128}Cs) and $\pi g^{-1}_{9/2} \otimes \nu h_{11/2}$ bands in ^{104}Rh, and the three-quasiparticle $\pi h^{2}_{11/2} \otimes \nu h^{-1}_{11/2}$ bands in ^{135}Nd. The ^{194}Tl pair of four-quasiparticle bands maintain a constant relative energy

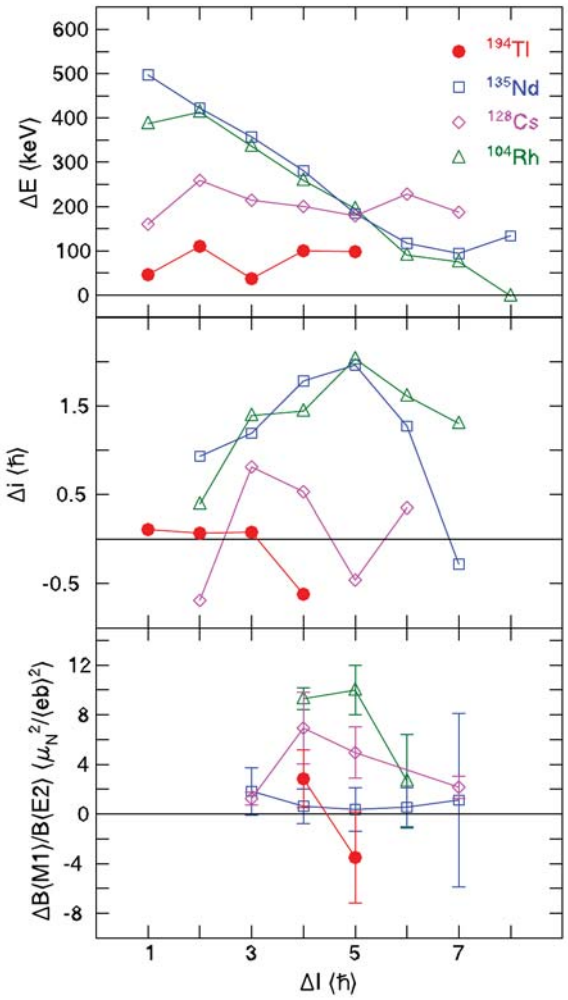

Figure 3. The difference in the excitation energies ΔE, alignments Δi, and ratios of the reduced transition probabilities $\Delta B(M1)/B(E2)$, as a function of spin ΔI with respect to the band head spin, for the 4-quasiparticle bands in ^{194}Tl, 3-quasiparticle bands in ^{135}Nd, and 2-quasiparticle bands in ^{128}Cs. The alignments are calculated with reference parameters of $J_0 = 8\ \hbar^2$/MeV and $J_1 = 40\ \hbar^4$/MeV^3 for ^{135}Nd, and $J_0 = 16\ \hbar^2$/MeV and $J_1 = 33\ \hbar^4$/MeV^3 for ^{128}Cs. Experimental data for ^{135}Nd and ^{128}Cs are taken from [3, 13] and [5], respectively.

separation of about 110 keV within the whole observed spin range of I = 19-23 and achieve a value as small as 37 keV at $I = 21$. The relative excitation energies of the levels in the ^{126,128}Cs partner bands remain approximately constant at $\Delta E \sim 200$ keV over the whole observed spin ranges of I = 11-22 and I = 11-17, respectively while the relative excitation energy in the close near-degenerate bands of ^{135}Nd is not constant but decreases from $\Delta E = 497$ keV at $I = 22/2$ and reaches a value of $\Delta E = 94$ keV at $I = 39/2$ and a subsequent increasing trend is then observed. In the case of ^{104}Rh these partner bands also show a decreasing trend of the relative excitation energy from $\Delta E = 413$ keV at $I = 11$, to an almost completely vanishing value of ΔE = -1 keV at $I = 17$.

The exceptional near-degeneracy of this pair of bands in ^{194}Tl is further illustrated in Figure 3 in which the differences in the excitation energies ΔE=E_{side}-E_{yrast}, alignments Δi=i_{side} − i_{yrast}, and ratios of reduced transition probabilities $\Delta B(M1)/B(E2)$=$B(M1)/B(E2)_{side}$ −

$B(M1)/B(E2)_{yrast}$ for the four-quasiparticle bands in ^{194}Tl and the partner bands in ^{104}Rh, ^{135}Nd, ^{128}Cs are shown. The spin $\Delta I{=}I - I_0$ is with respect to the band head spin I_0 of 9, 10, 25/2, and 18 are adopted for ^{104}Rh, ^{128}Cs, ^{135}Nd and ^{194}Tl, respectively.

In summary, the relative excitation energy of a pair of negative-parity bands observed in ^{194}Tl was compared to the relative excitation energies of the chiral candidates with best known close near-degeneracy. This comparison shows that near-degeneracy in the 4-quasipartcle bands in ^{194}Tl is possibly the best found to date.

Acknowledgments

We would like to thank the crew of the iThemba LABS separated sector cyclotron for the delivery of the oxygen beam. This work is based upon research supported by the National Research Foundation, South Africa with grants GUN 65581 and 76632, and by a South Africa - Russian Federation bilateral agreement with a grant GUN 75248.

4. References

[1] Frauendorf S and Jie Meng 1997 *Nucl. Phys.* **A617** 131.
[2] Starosta K *et al.* 2001 *Phys. Rev. Lett.* **86** 971.
[3] Zhu S *et al.* 2003 *Phys. Rev. Lett.* **91** 132501.
[4] Wang S, Liu Y, Komatsubara T, Ma T Y, Zhang Y, 2006 Phys. Rev. C **74** 017302.
[5] Koike T, Starosta K, Chiara C J, Fossan D B, LaFosse D R, 2003 Phys. Rev. C **67** 044319.
[6] Vaman C, Fossan D B, Koike T, Starosta K, Lee I Y, Macchiavelli 2004 *Phys. Rev. Lett.* **92** 032501.
[7] Masiteng P L *et al.* 2013 Phys. Lett. B **719** 83-88.
[8] Newman R T*et al.* 1998 Balkan Phys. Lett. **Special Issue** 182.
[9] Sharpey-Schafer J F 2004 Nucl. Phys. News **12** 5.
[10] Radford D C 1995 Nucl. Instrum. Methods Phys. Res. A **361** 297.
[11] Kreiner A J 1979 Phys. Rev. C **20** 2205.
[12] Pai H *et al.* 2012 Phys. Rev. C **85** 064313.
[13] S. Mukhopadhyay *et al.* 2007 Phys. Rev. Lett. **99** 172501.

The Discovery of a Higgs Boson at the LHC

Bruce Mellado

University of the Witwatersrand, 1 Jan Smuts Avenue, Johannesburg 2000, South Africa

E-mail: bruce.mellado@wits.ac.za

Abstract. The Standard Model, SM, of electro-weak and strong interactions successfully describes collider data. However, weak bosons, quarks and leptons are massive. The mechanism of spontaneous electro-weak symmetry breaking is introduced in the SM in order to reconcile weak boson and fermion masses with gauge invariance of the theory. In its minimal expression this mechanism leads to a new physical state, a scalar boson, usually referred to as the Higgs boson. The ATLAS and CMS collaborations at the Large Hadron Collider have observed a new particle consistent with a scalar boson and with a mass of about 125 GeV.

1. Introduction

In the Standard Model, SM, of electro-weak, EW, and strong interactions, there are four types of gauge vector bosons (gluon, photon, W and Z) and twelve types of fermions (six quarks and six leptons) [1, 2, 3, 4]. These particles have been observed experimentally. At present, all the data obtained from the many experiments in particle physics are in agreement with the Standard Model. In the Standard Model, there is one particle, the Higgs boson, that is responsible for giving masses to all the elementary particles [5, 6, 7, 8]. In this sense, the Higgs particle occupies a unique position.

In July 2012 the ATLAS and CMS experiments reported the discovery of a boson, a Higgs-like particle with a mass $m_H \approx 125$ GeV based on the data accumulated during 2011 and part of 2012 periods [9, 10]. The Tevatron experiments have reported an excess of events consistent with this observation in the decay to bottom and anti-bottom quarks [11]. It is also relevant to note that no additional Higgs bosons with couplings as in the Standard Model have been observed in the range of $m_H < 600$ GeV.

2. Production and Decays

For the calculation of the particle production cross sections in proton-proton collision it is necessary to briefly discuss the factorization theorem. The production of particle can be viewed as the result of the scattering of partons of the incoming hadrons. It can be shown that the production cross section of a process Y, $\sigma(AB \to Y + X)$, where A and B pertain to the incoming protons and X refers to the proton remnants that do not participate in the production of process Y, can be obtained from [12, 13]:

$$\sigma(AB \to Y + X) = \sum_{a,b} \int dx_a dx_b f(x_a, \mu_F^2) f(x_b, \mu_F^2) \times \frac{d\hat{\sigma}_{ab\to Y}(x_a, x_b, \mu_R^2)}{dx_a dx_b}. \quad (1)$$

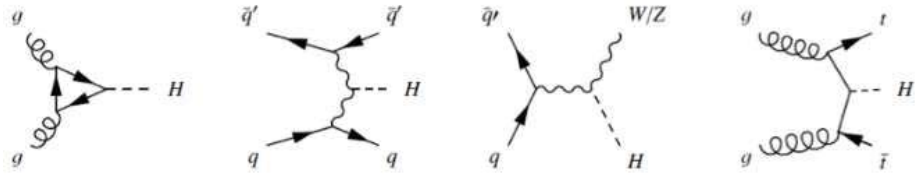

Figure 1. Leading Order Feynmann diagrams for the dominant processes involving the production of a SM Higgs boson at the LHC. From left to right: gluon-gluon fusion, Vector Boson Fusion, associated production with weak bosons and associated production with top quarks.

Table 1. Summary of QCD and EW higher order corrections currently available for the leading production mechanisms of the SM Higgs boson. Cross sections (from Ref. [14]) are given for $\sqrt{s} = 7, 8$ TeV in pb for $m_H = 125$ GeV, including the corresponding theory uncertainties.

	ggF	VBF	WH	ZH	$t\bar{t}H$
QCD	NNLO+NNLL	NNLO	NNLO		NLO
EW	NLO	NLO	NLO		LO
$\sigma(7$ TeV$)$	$15.32^{+14.7\%}_{-14.9\%}$	$1.222^{+2.8\%}_{-2.4\%}$	$0.5729^{+3.7\%}_{-4.3\%}$	$0.3158^{+4.9\%}_{-5.1\%}$	$0.0863^{+11.8\%}_{-17.8\%}$
$\sigma(8$ TeV$)$	$19.52^{+14.7\%}_{-14.7\%}$	$1.578^{+2.8\%}_{-3.0\%}$	$0.6966^{+3.7\%}_{-4.1\%}$	$0.3943^{+5.1\%}_{-5.0\%}$	$0.1302^{+11.6\%}_{-17.1\%}$

Here the subscripts a and b refer to partons (quarks and gluons) of protons A and B, respectively. Parton density functions, pdfs, are denoted with $f(x)$ where $x = x_a, x_b$ and x_a (x_b) is the fraction of the proton A (B) carried by parton a (b). At LO the proton pdfs can be interpreted as the probability of finding a parton with the fraction x of the momentum of the proton. The factorization scale, μ_F is viewed as the scale that disentangles long-distance (non-perturbative) and short-distance (perturbative) strong interactions. The pdfs are considered to be universal long-distance functions that are extracted from the data, primarily from deep inelastic scattering. The partonic cross section, $\hat{\sigma}_{ab\to Y}$, is calculable with perturbative QCD. Because the cross section is known to a finite number of orders in perturbation a residual dependence of the cross section due to the choice of scales needs to be taken into account as a theoretical uncertainty in the prediction. Scale-driven variations of the cross section are typically calculated by taking the largest variations by changing the renormalization and factorization scales by factors of two. This includes variations of both scales in the directions and all other combinations that for which the ratio of the scales is not larger than a factor of two. Uncertainties related to pdfs are also taken into account.

The Standard Model Higgs boson is produced at the LHC via several mechanisms. These are determined by the way the Higgs boson couples to SM particles. Figure 1 displays the LO Feynmann diagrams of the leading production mechanisms in proton-proton collisions. From left to right Fig. 1 displays the diagrams for gluon-gluon fusion, ggF, vector boson fusion, VBF, associated production with weak bosons and associated production with top quarks.

Figure 2 shows the production cross sections for the different Higgs boson production mechanisms, as outlined in Fig. 1. Cross sections are reported as a function of the Higgs boson mass and for the center of mass energy of $\sqrt{s} = 7$ TeV. The leading production mechanism is ggF, constituting about 90% of the total production cross section. This is to a large extent due to the large gluon flux at the LHC.

Table 1 displays the order up to which the radiative higher order EW and QCD radiative

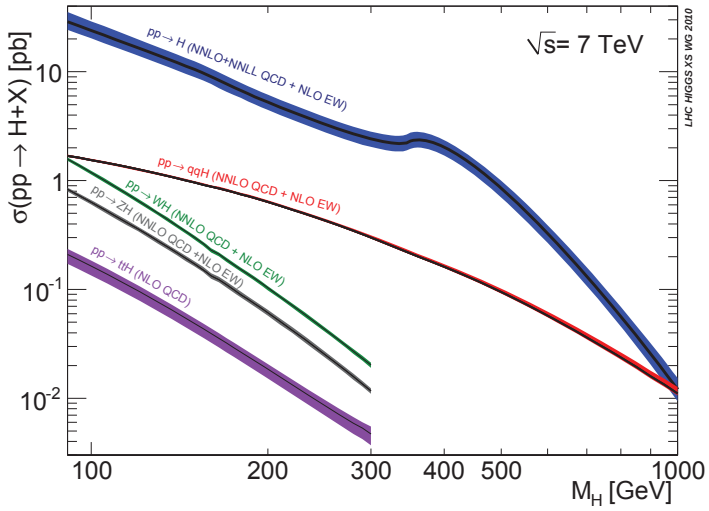

Figure 2. Standard Model Higgs boson production cross sections (in pb) for proton-proton collisions at $\sqrt{s} = 7$ TeV center of mass energy as a function of m_H (from Ref. [14]). The bands correspond to the current status of the theoretical errors.

corrections are calculated for the different production mechanisms. The values of the cross sections used by the experiments for $m_H = 125$ GeV are also given.

Figure 3 shows the branching ratios of the SM Higgs boson to different decay products. Branching ratios in Fig. 3 are given as a function of the Higgs boson mass. The plot on the left in Fig. 3 display the branching ratios in the range $90 < m_H < 200$ GeV, the region of particular interest, given the electro-weak fits. The final states most suitable for discovery at the LHC vary depending on the branching ratios, which are a function of the Higgs boson mass, and the relevant backgrounds. For $m_H < 2m_W$ the dominant decay mode is through $b\bar{b}$ with $B_b = 0.577^{+3.2\%}_{-3.3\%}$ for $m_H = 125$ GeV. The $\gamma\gamma$ final state has a small branching fraction, $(2.28 \times 10^{-3})^{+5.0\%}_{-4.8\%}$ for $m_H = 125$ GeV, but excellent γ/jet separation and γ energy resolution help to make this a very significant channel. The $H \to \tau\tau$ decay is accessible if the Higgs boson is produced in association with jets. Table 2 displays branching fractions of the SM Higgs boson with $m_H = 125$ GeV into different decays.

If the Higgs boson mass is large enough to make the WW and ZZ modes kinematically accessible, the $H \to WW^{(*)}$ final-states are powerful over a very large mass range (WW accounts for ~95% of the branching fraction at $m_H \sim 160$ GeV), as is the $H \to ZZ^{(*)} \to 4\ell$ final state– the latter of which is commonly referred to as the "Golden Mode" as with four leptons in the final state the signal is easy to trigger on and allows for full reconstruction of the Higgs boson mass. For SM Higgs boson masses close to $2m_{top}$, the channel $H \to t\bar{t}$ opens up (see the right plot in Fig. 3), thus reducing the branching fraction of $H \to ZZ, WW$. Due to the very large cross section for the production of non-resonant $t\bar{t}$ pairs, the inclusive search for the SM Higgs boson with $H \to t\bar{t}$ is not considered feasible.

3. Results

In this section the results of the combination of the expectation and observation of the discovery channels discussed above are summarized. Results are presented in terms of upper exclusion limits and p-values. This is performed for the individual discovery channels and/or their combination, when available.

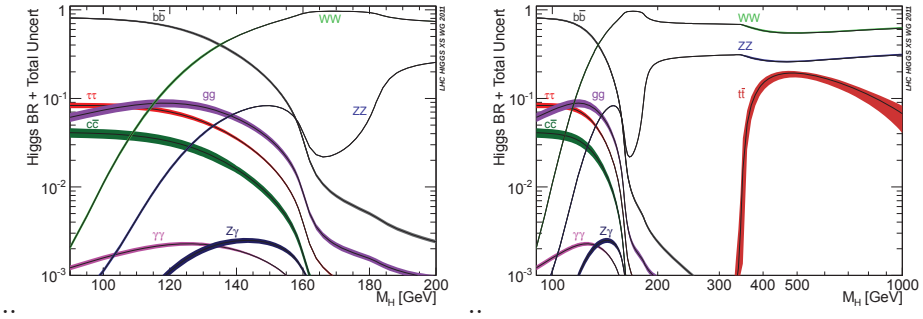

Figure 3. Branching fractions of the Standard Model Higgs boson to different decay products as a function of the mass (from Ref. [15]). The plot on the left and the right correspond to two different mass ranges.

Table 2. Branching ratios for the SM Higgs boson with $m_H = 125$ GeV (from Ref [15]). The errors correspond to current level of theory uncertainties and are expressed in terms of fractional deviations in %. The total width is given in MeV.

B_b	B_τ	B_μ	B_c	B_g
$0.577^{+3.2\%}_{-3.3\%}$	$0.0632^{+5.7\%}_{-5.7\%}$	$(2.2\times10^{-4})^{+6.0\%}_{-5.9\%}$	$0.0291^{+12.2\%}_{-12.2\%}$	$0.0857^{+10.2\%}_{-10.0\%}$
B_γ	$B_{Z\gamma}$	B_W	B_Z	Γ_H[MeV]
$(2.28\times10^{-3})^{+5.0\%}_{-4.8\%}$	$(2.28\times10^{-3})^{+9.0\%}_{-8.8\%}$	$^{+4.3\%}_{-4.2\%}$	$2.64^{+4.3\%}_{-4.2\%}$	$4.07^{+4.0\%}_{-3.9\%}$

Figure 4 shows the combination results presented by the CMS collaboration. The upper left plot corresponds to the exclusion limits in terms of the CL_s values in the mass range $110 < m_H < 145$ GeV. The dashed line shows the median of the background-only expectation while the green and yellow bands correspond to the 68% and 95% CL bands, respectively. The solid curve shows the experimentally observed upper exclusion limit. As a result of the strong excess observed in the data the observed exclusion limit for $m_H \approx 125$ GeV lies significantly above the median and outside the 95% CL bands. The regions where $CL_s < \alpha$ are excluded with at least $(1-\alpha)$ CL. The horizontal lines correspond to the 95% and 99% and 99.9% CL values. The upper right plot shows the expected p-values for a SM Higgs boson signal in the mass range and decay modes specified above and their combination. For $m_H \approx 125$ GeV CMS reports the $H \to ZZ^{(*)} \to 4\ell$ channel to be the most sensitive, closely followed by the di-photon search. The expected p-value for $m_H \approx 125$ GeV falls below the $5\,\sigma$ mark. CMS reports an observed local p-value at the $5\,\sigma$ level with an expected p-value of $5.8\,\sigma$ for $m_H = 125$ GeV. The global observed p-value is $4.5-4.6\,\sigma$, depending on the mass range considered for the evaluation of the trials factor. The lower right plot shows the compatibility of the location of the excess in the $\sqrt{s} = 7$ TeV and $\sqrt{s} = 8$ TeV data samples.

Figure 5 displays the combination results presented by the ATLAS collaboration. The upper plots correspond to CL_s in the entire range of the search, $110 < m_H < 600$ GeV. The solid and dashed lines correspond to the observed and expected CL_s. Dashed horizontal lines indicate the 95% and 99% CL values. Similar discussion as in the case of CMS results for $m_H \approx 125$ GeV apply here. It is worth noting that no significant excess is seen for m_H hypotheses outside the $m_H \approx 125$ GeV region. This translates into exclusions on the existence of another neutral Higgs boson with SM couplings with at least 95% and 99% in a wide range of masses. These results are expressed in terms of 95% CL upper limit exclusions on the signal strength in the

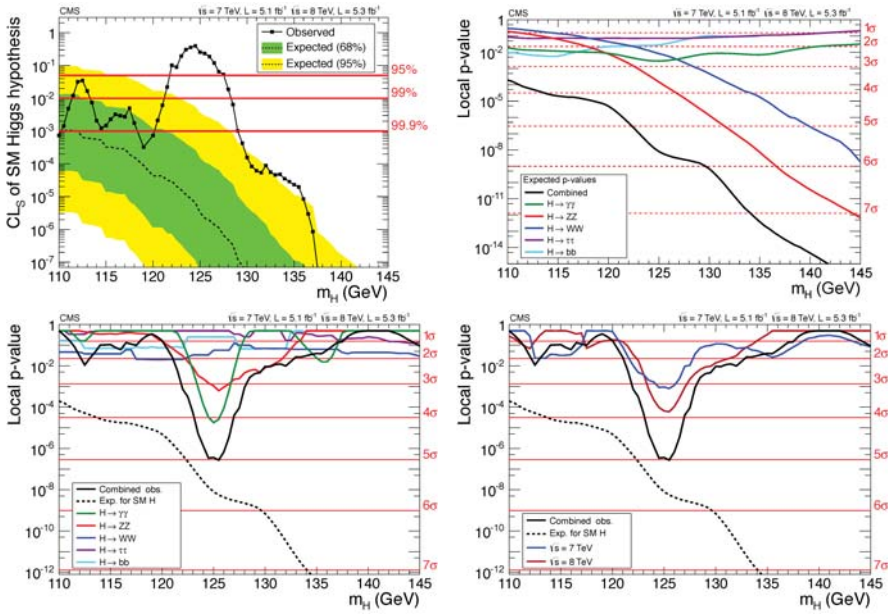

Figure 4. Results of the statistical combination of the various searches for the Higgs boson by the CMS experiment as a function of the m_H (from Ref. [10]). The upper left plot shows the combined CL_s for the SM Higgs boson hypothesis. The upper right and the lower left plots display the expected and observed local p-values of the individual search channels and their combination, respectively The lower right plot exhibits the observed local p-values for the $\sqrt{s} = 7$ TeV and $\sqrt{s} = 8$ TeV data sets separately. See text for more details.

upper right plot. The solid and dashed lines correspond to the observed and the median of the background-only expectation, respectively. The green and yellow bands correspond to the 65% and 95% CL bands, respectively. The solid and dashed lines in the lower left plot shows the combined observed and expected local p-values in a range $110 < m_H < 150$ GeV, respectively. The blue band corresponds to the 68% CL band. ATLAS reports an excess of $5.9\,\sigma$ with an expected local p-value of $4.9\,\sigma$ for $m_H = 126.5$ GeV. The global p-value becomes $5.3\,\sigma$ when considering the range $110 < m_H < 150$ GeV. The lower right plot shows the breakdown of the contribution from each individual channel. The dashed and solid lines correspond to the expected and observed p-values. In the region of the excess the most sensitive channel is the $H \to ZZ^{(*)} \to 4\ell$ decay closely followed by the $H \to WW^{(*)} \to \ell\nu\ell\nu$ and $H \to \gamma\gamma$ channels.

In summary, both the ATLAS and CMS collaborations independently observe a strong excess of the order of $5\,\sigma$ or more in a similar mass range around 125 GeV. The existence of additional bosons with SM couplings to other known particles is excluded with at least a 95% CL in the range $110 < m_H < 600$ GeV barring a narrow region around $m_H \approx 125$ GeV by both collaborations independently. Preliminary analyses on data samples collected during the second half of 2012 at $\sqrt{s} = 8$ TeV report the persistence of excess of events in the data in the range of $m_H \approx 125$ GeV consistent with that reported in Refs. [9, 10].

4. Conclusions

At present, all the data obtained from the many experiments in particle physics are in agreement with the Standard Model. In the Standard Model, there is one particle, the Higgs boson, that is responsible for giving masses to all the elementary particles. The ATLAS and CMS experiments

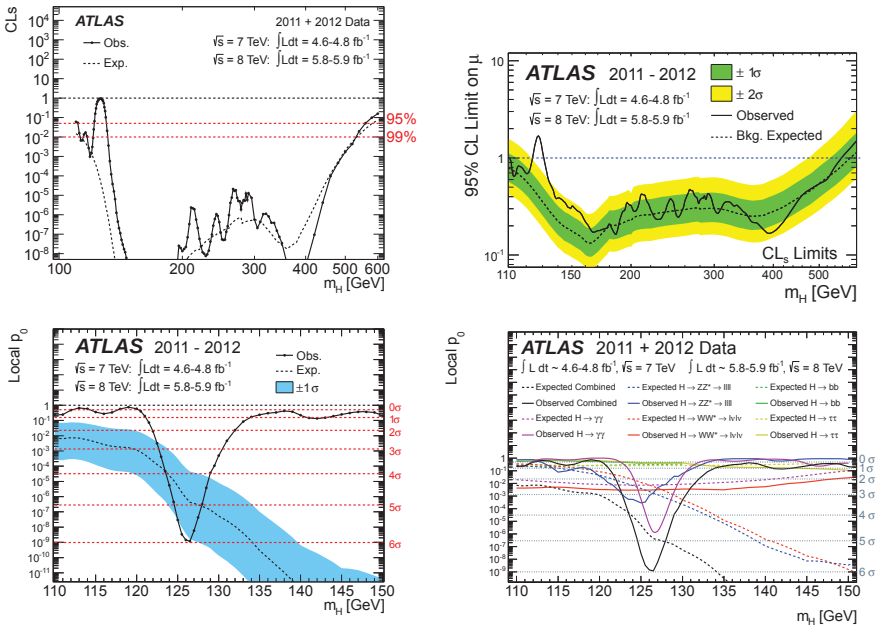

Figure 5. Results of the statistical combination of the various searches for the Higgs boson by the ATLAS experiment as a function of m_H (from Ref. [9]). The upper left and right plots plot display the CL_s for the SM Higgs boson hypothesis and 95% CL upper limit exclusion on the signal strength in the entire range of the SM Higgs boson search, respectively. The lower left plot shows the combined expected and observed the local p-values. The lower right plot displays the breakdown of the expected and observed p-values for the different channels. See text for more details.

at the Large Hadron Collider have declared the discovery of a Higgs boson with a mass around 125 GeV, as the result of the combination of several decay channels.

References

[1] S. Glashow, *Nucl.Phys.* **22**, 579 (1961).
[2] S. Weinberg, *Phys.Rev.Lett.* **19**, 1264 (1967).
[3] A. Salam, Proceedings to the eigth nobel symposium, may 1968, ed: N. svartholm (wiley, 1968) 357.
[4] S. Glashow, J. Iliopoulos and L. Maiani, *Phys.Rev.* **D2**, 1285 (1970).
[5] F. Englert and R. Brout, *Phys.Rev.Lett.* **13**, 321 (1964).
[6] P. W. Higgs, *Phys.Lett.* **12**, 132 (1964).
[7] P. W. Higgs, *Phys.Rev.Lett.* **13**, 508 (1964).
[8] G. Guralnik, C. Hagen and T. Kibble, *Phys.Rev.Lett.* **13**, 585 (1964).
[9] ATLAS Collaboration Collaboration (G. Aad *et al.*), *Phys.Lett.* **B716**, 1 (2012).
[10] CMS Collaboration Collaboration (S. Chatrchyan *et al.*), *Phys.Lett.* **B716**, 30 (2012).
[11] CDF Collaboration, D0 Collaboration Collaboration (T. Aaltonen *et al.*), *Phys.Rev.Lett.* **109**, 071804 (2012).
[12] J. C. Collins and D. E. Soper, *Ann.Rev.Nucl.Part.Sci.* **37**, 383 (1987).
[13] J. M. Campbell, J. Huston and W. Stirling, *Rept.Prog.Phys.* **70**, 89 (2007).
[14] LHC Higgs Cross Section Working Group, S. Dittmaier, C. Mariotti, G. Passarino and R. Tanaka (Eds.), *CERN-2011-002* (CERN, Geneva, 2011).
[15] LHC Higgs Cross Section Working Group, S. Dittmaier, C. Mariotti, G. Passarino and R. Tanaka (Eds.), *CERN-2012-002* (CERN, Geneva, 2012).

Search for invisible anomalous Higgs boson decay with the ATLAS detector at the LHC

German Carrillo Montoya and Itumeleng Molefi on behalf of the ATLAS Collaboration

University of the Witwatersrand, 1 Jan Smuts Avenue, Johannesburg, South Africa, 2000

E-mail: g.carrillo.montoya@cern.ch

Abstract. A direct search for evidence of decays to invisible particles of a Higgs boson at the Large Hadron Collider (LHC) is presented. This search is performed for a Standard Model-like Higgs boson produced in association with a Z boson and having a mass between $m_H = 115$ GeV and $m_H = 300$ GeV. The results are interpreted to place limits on the branching fraction to invisible particles of the newly discovered boson with mass near 125 GeV. Assuming that this is the Standard Model Higgs boson, its decay to invisible particles is not measurable, but could have a large contribution from the decay to the dark matter particles, for example. In addition, limits are set on any neutral Higgs-like particle, produced in association with a Z boson and decaying predominantly to invisible particles.

No deviation from the Standard Model expectation is observed in the search, which uses 4.7 fb^{-1} of 7 TeV pp collision data and 13.0 fb^{-1} of 8 TeV pp collision data collected by the ATLAS experiment at the LHC. Assuming the ZH production rate for a 125 GeV Standard Model Higgs boson, limits are set on the invisible branching fraction at 95% condence level. The observed exclusion is for branching fractions greater than 65%, and the expected limit is 84%.

1. Introduction

Some extensions to the Standard Model (SM) allow a Higgs boson [1-3] to decay to stable or long-lived particles that interact with the Higgs boson, but have only weak interactions with other elementary particles. The results obtained so far in the search for the SM Higgs boson do not exclude the possibility of a sizeable branching ratio to invisible particles for the SM Higgs boson candidate at $m_H \sim 125$ GeV [4,5]. Combined LEP results [6] have excluded an invisibly decaying Higgs boson for $m_H < 114.4$ GeV under the assumption that such a Higgs boson is produced in association with a Z boson at the rate expected for a SM Higgs boson and that it decays predominantly to invisible particles. A further Higgs-like boson decaying predominantly to invisible particles is not excluded for $m_H > 115$ GeV. This note presents a search for decays to invisible particles for a narrow scalar boson produced in association with a Z boson with the same cross section as the SM Higgs boson and having a mass between 115 and 300 GeV. The results are also interpreted in terms of the 125 GeV Higgs boson candidate, where the ZH production cross section is taken to be that predicted for a SM Higgs boson.

2. Signal Analysis and Analysis Overview

The signal process searched for is the associated production of ZH. The Higgs boson is assumed to decay to invisible particles. The Z boson decaying into electrons or muons is considered for this analysis. The SM ZH cross section for $m_H = 125$ GeV is 316 fb at $\sqrt{s} = 7$ TeV and 394 fb at $\sqrt{s} = 8$ TeV [7,8]. It is calculated at NLO [9] and at NNLO [10] in QCD, and NLO EW radiative corrections [11] are applied. Including the requirement that the Z boson decays to e, μ, or τ reduces these cross sections to 31.9 fb and 39.8 fb respectively. A very small SM contribution to the $ZH \to ll+$ inv. nal state arises when the Higgs boson decays to four neutrinos via two Z bosons. The predicted cross section of this process for $m_H = 125$ GeV is 3.4×10^2 fb at $\sqrt{s} =$ 7 TeV and 4.2×10^2 fb at $\sqrt{s} = 8$ TeV. The present search is not sensitive to this particular process although it is part of the signal, but instead searches for enhancements of the invisible decay fraction due to physics beyond the Standard Model (BSM).

The POWHEG [12] interfaced with HERWIG++ [13] Monte Carlo (MC) generator is used to simulate the signal. In the simulation the associated produced Z boson is forced to decay to e, μ, or τ. The invisible decay of the Higgs boson is simulated by forcing the Higgs boson to decay to two Z bosons, which are then forced to decay to neutrinos. For most distributions shown in this note the signal simulation is normalised assuming the SM ZH production rate and a 100% branching fraction of the Higgs boson to invisible particles. Signal samples are generated at Higgs boson masses of 115, 120, 125, 130, 150, 200, and 300 GeV.

This analysis searches for an excess of events over the SM contribution in the dilepton + large missing transverse energy (E_T^{miss}) final states. The processes that contribute to the SM expectation are as follows. The $ZZ \to ll\nu\nu$; this is an irreducible background and contributes approximately 70% of the total background. The $WZ \to l\nu ll$, where the W decay lepton is not identified either by failing lepton identification or by being outside the kinematical selections. The WZ background contributes approximately 20% of the total background. The $WW \to l\nu l\nu$ events, where the leptons mimic a Z boson. This background constitute approximately 5% of the total background. The top quark events ($t\bar{t}$ and Wt) where the leptons mimic a Z boson are considerably reduced by applying a jet veto. These contribute approximately 2% of the background. The $Z \to ll$ events are largely reduced by requiring large E_T^{miss}. Additional cuts are also applied to further suppress this background. The remaining background contributes approximately 1% to the total background. The $W \to l\nu$ and dijet events can fake the signal if one or two jets are reconstructed as leptons. These backgrounds are approximately 1% of the total. The $H \to ZZ^{(*)} \to ll\nu\nu$, for a 125 GeV SM Higgs boson, would produce a E_T^{miss} that falls below the cut. Thus, this process is considered negligible. And finally the $H \to WW^{(*)} \to l\nu l\nu$, for a 125 GeV SM Higgs boson, would have a dilepton mass that falls outside the Z peak and is thus also considered to be negligible.

3. Data and Monte Carlo Samples

This search uses 4.7 fb^{-1} of data recorded in 2011 at a centre of mass energy of 7 TeV and 13.0 fb^{-1} of data recorded in 2012 at a centre of mass energy of 8 TeV. Events are selected using a combination of triggers that select single electrons or muons or a pair of electrons or muons. The trigger efficiency, for signal events passing the full selection cuts described below, is nearly 100% in both data periods in the electron channel, and approximately 95% and 94% in the 2011 and 2012 periods respectively in the muon channel. The data are required to have been recorded during stable beam conditions and during nominal detector performance and data readout conditions.

Background processes are modelled using tree level and NLO MC generators. Table 1 above summarises the Monte Carlo (MC) simulation used to estimate the backgrounds.

Background	Generator	Cross Section	MC Statistics
ZZ	HERWIG	6.49 pb (7 TeV)	50k
$Z \to ll$	SHERPA	0.38 pd (8 TeV, m_{ll}-filtered)	400k
$WZ \to l\nu ll$	HERWIG	17.9 pb (7 TeV)	100k
WZ	SHERPA	2.51 pb (8 TeV, m_{ll}-filtered)	590k
$H \to ZZ^{(*)} \to ll\nu\nu$	POWHEG	16.3 fb (7 TeV)	50k
	POWHEG	20.8 fb (8 TeV)	50k
$H \to WW^{(*)} \to l\nu l\nu$	POWHEG	374.7 fb (7 TeV)	50k, 30k
	POWHEG	478.5 fb (8 TeV)	500k, 500k

Table 1: The MC simulation samples used to estimate the ZZ, WZ background, and yields of the Standard Model Higgs boson processes sharing the same final state. For the MC statistics of the $H \to WW^{(*)} \to l\nu l\nu$ boson samples, the first number indicates the statistics of the gluon-gluon fusion samples, whereas the second indicates the statistics of vector-boson fusion samples.

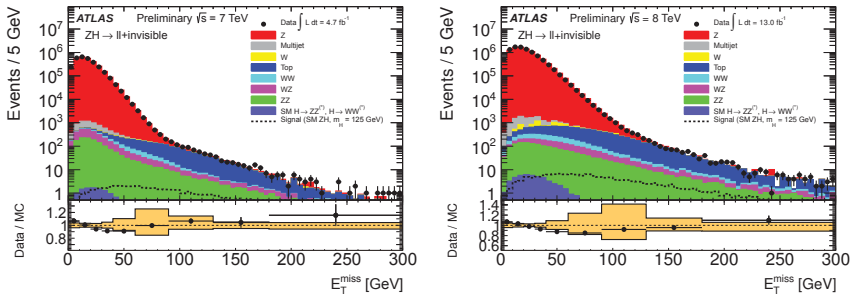

(a) (a) (b) (b)

Figure 1: E_T^{miss} distributions after the dilepton mass requirement from the 2011 (a) and 2012 (b) data. The observed data are represented by the black dots and the histograms represent the background predictions from the MC samples listed in Section 3. The signal hypothesis is shown by the dotted line and assumes the SM ZH production rate for a Higgs boson with $m_H = 125$ GeV and a 100% invisible branching fraction. The insets at the bottom of the figures show the ratio of the data to the combined background expectations as well as a band corresponding to the combined systematic uncertainties.

4. Event Selection

Events are selected using a combination of triggers that select single electrons or muons or a pair of electrons or muons as mentioned in Section 3. Only well identified leptons are selected to ensure that leptons from non-collision events like cosmic rays are rejected. As a result, muon are required to be picked up in the Inner-Detector and the Muon-Spectrometer while electrons must have tight electromagnetic shower-shape requirements. Lepton pairs are required to be of the same flavour and must be oppositely charged. These leptons must further be compatible with decay from a Z boson. One of these compatibility requirements, for example, is that the events must have $E_T^{miss} > 90$ GeV. Events with three leptons need to be vetoed. A full jet veto is also required to sort out events with fake a missing transverse energy. There is also a series of requirements to ensure that the E_T^{miss} is genuine. That is, it is not produced by leptons or jets that are missmeasured.

Figure 1 shows the E_T^{miss} distributions after the dilepton mass requirement. The data agree with the MC within the uncertainty error bands.

Process	Estimation method	Uncertainty (%)	
		2011	2012
ZH Signal	MC	7	6
ZZ	MC	11	10
WZ	MC	12	14
WW	MC	14	not used
Top quark	MC	90	not used
Top quark, WW and $Z \to \tau\tau$	$e\mu$ CR	not used	4
Z	ABCD method	56	51
W + jets, multijet	Matrix method	15	22

Table 2: Summary of the systematic uncertainties on each background and on the signal yield. The method used to estimate the backgrounds and the associated sources of systematic uncertainties are given and the total systematic uncertainties for each data taking period are given.

5. Systematic Uncertainties

Systematic uncertainties on the signal mode, the ZZ and WZ backgrounds as well as the WW and top quark backgrounds (for the 2011 data taking period) are estimated from MC samples. Uncertainties in the backgrounds are either measured from data or based on normalisation to data in control regions. The luminosity uncertainty (1.8% for 2011 and 3.6% for 2012) is derived using the same method as source [14]. Lepton trigger and identification efficiencies as well as energy scale and resolution uncertainties are derived from high statistics Z samples. These contribute typically 1.0-1.5% to the overall selection uncertainty. Jet energy scale and resolution uncertainties (which contribute 3-6% uncertainty to the final event selection) are derived using a combination of techniques that use dijet, photon + jet, and Z+ jet events [15]. Both the uncertainties on the leptons and the jets are propogated to the E_T^{miss} calculation and an additional uncertainty on E_T^{miss}, related to the pile-up simulation, contribute a 1-2% uncertainty on the final even selection in signal and backgrounds estimated from the MC simulation.

Uncertainties on the ZH production cross section are derived from the variations of the QCD scale, α_s and PDF variations [7,8]. These combine to give an uncertainty of 4.9-5.1% on the cross section for the SM Higgs boson having a mass between 115 and 300 GeV. This analysis is sensitive to the transverse momentum of the Higgs boson the E_T^{miss} and uncertainties in the p_T boost of the Higgs boson can affect the signal yield. An additional systematic uncertainty of 1.9% is applied to the normalization and differentioal uncertainties as a function of the transverse momentum of the Higgs boson is considered as shape systematics [16,17].

The object and theoretical uncertainties are considered as correlated between the 2011 and 2012 data and between the signals and all the backgrounds estimated from the MC simulation. The systematic uncertainties in the data-driven methods are also assumed to be correlated between the two datasets while the luminosity uncertainty is considered to be uncorrelated. Since different methods are used for the background estimation between the 2011 and 2012 datasets, the uncertainties for the WW and the top quark backgrounds are considered to be uncorrelated between the two datasets.

The systematic uncertainties are summarised in Table 2.

6. Results

Table 3 summarises the expected contributions from each background source and observed number of data events. Figure 2 shows the final E_T^{miss} distributions with the observed data and expected backgrounds for both the 2011 and 2012 data taking periods. No excess is observed

Data Period	2011 (7 TeV)	2012 (8 TeV)
ZZ	$23.5 \pm 0.8 \pm 2.5$	$56.5 \pm 1.2 \pm 5.7$
WZ	$6.2 \pm 0.4 \pm 0.7$	$13.9 \pm 1.2 \pm 2.1$
WW	$1.1 \pm 0.2 \pm 0.2$	used $e\mu$ data-driven
Top quark	$0.4 \pm 0.1 \pm 0.4$	used $e\mu$ data-driven
$e\mu$ data-driven	used MC	$4.9 \pm 0.9 \pm 0.2$
Z	$0.16 \pm 0.13 \pm 0.09$	$1.4 \pm 0.4 \pm 0.7$
W + jets, multijet	$1.3 \pm 0.3 \pm 0.2$	$1.4 \pm 0.4 \pm 0.3$
Total BG	$32.7 \pm 1.0 \pm 2.6$	$78.0 \pm 2.0 \pm 6.5$
Observed	27	71

Table 3: Observed number of events and expected contributions from each background source separated into the 2011 and 2012 data taking periods. Associated uncertainties with the background predictions are presented with statistical uncertainties first followed by the systematic errors.

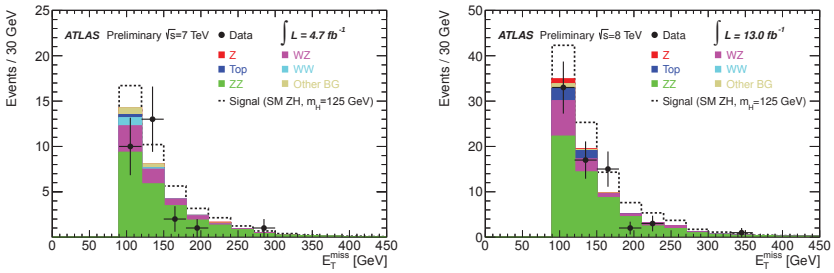

(a) (a) (b) (b)

Figure 2: Distribution of E_T^{miss} for signal events in the 2011 (a) and 2012 (b) data taking periods. The observed data is indicated by the black points and the histograms represent the background predictions. The dashed line indicates the prediction from the signal model and is stacked on the background prediction. The signal model assumes a SM Higgs boson with a mass of 125 GeV and a 100% branching fraction to invisible particles.

over the SM expectation and limits are set for two scenarios. The first scenario explores the possibility that the recently discovered Higgs boson with $m_H \sim 125$ GeV has a non-negligible branching ratio to invisible particles while the second considers the possibility of a Higgs-like boson in a range of masses from 115 GeV to 300 GeV with a significant branching fraction to invisible particles.

The limits are computed from a maximum likelihood fit to the E_T^{miss} distribution following the CL_S modified frequentist formalism with profile-likelihood test statistics [18,19].

Figure 3 shows the interpretation of the first scenario. Assuming a ZH production rate for a 125 GeV SM Higgs boson, limits are set on the invisible branching fraction at 95% CL. The observed exclusion is for branching fractions greater that 65% and the expected limit is 84%.

For the second scenario limits are set considering only the hypothesis of a single invisibly decaying Higgs-like boson. The limits do not consider possible multiple Higgs boson candidates all having non-negligible invisible branching fractions. Figure 4 shows 95% CL limits on the ZH production cross section multiplied by the invisible branching fraction of such a Higgs boson in the mass range 115-300 GeV for the considered data taking periods, as well as the limit achieved from the combination of both periods. Again, no excess is observed over the mass range.

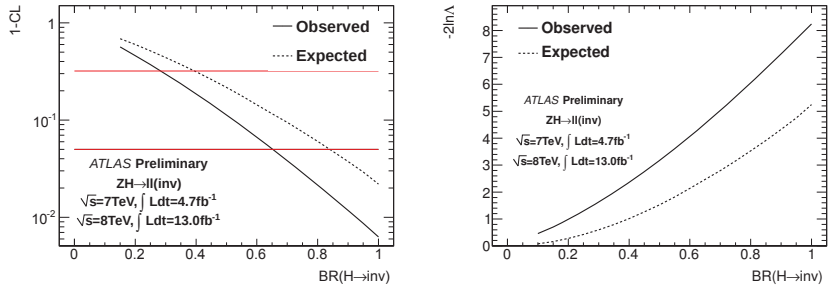

(a) (a) (b) (b)

Figure 3: Confidence level (CL) (a) and profile likelihood (b) scanned against BR($H \to$ invisible) for the SM Higgs boson with $m_H \sim 125$ GeV. The dashed line shows the expected values and the solid line indicates the observed values. The red lines in (a) indicate the 68% and 95% CL.

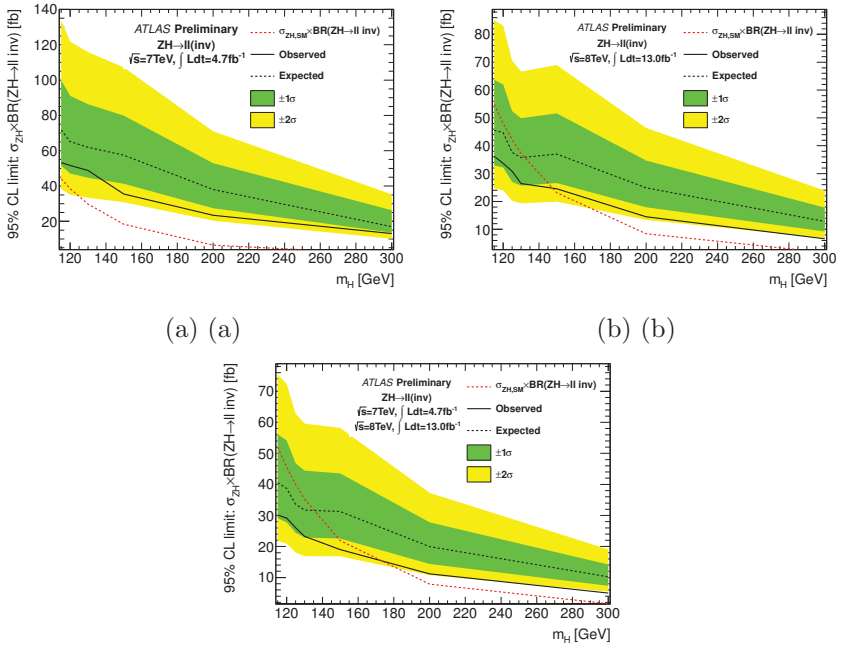

(a) (a) (b) (b)

(c) (c)

Figure 4: 95% CL limits on the cross section times branching fraction of a Higgs-like boson decaying to invisible particles for the 2011 (a) and 2012 (b) data taking periods and a combination of both periods (c). Dashed lines show the background only expected limits and solid lines show the observed limit.

7. Conclusion

A direct search for evidence of the invisible decays of a Higgs boson at the LHC has been performed. While the invisible branching fraction for a SM Higgs boson is too small to be accessible, this measurement is sensitive to enhancements of the invisible branching fraction such as from decays to dark matter particles. After the full selection, 27 events are observed compared to a SM expectation of 32.7 $\pm$ 1.0 (stat.) $\pm$ 2.76 (syst.) background events in 4.7 fb^{-1} of data taken at $\sqrt{s} = 7$ TeV during the 2011 run and 71 events are observed compared to an expected 78.0 $\pm$ 2.0 (stat.) $\pm$ 6.5 (syst.) background events in 13.0 fb^{-1} of data taken at $\sqrt{s} = 8$ TeV during part of the 2012 run. No significant excess over the expected background is observed and limits are set on the allowed invisible branching fraction of the recently observed 125 GeV Higgs boson candidate. Assuming the ZH production rate for a 125 GeV SM Higgs boson, limits are set on the invisible branching fraction at 95% CL. The observed exclusion is for branching fractions greater than 65% and the expected limit is 84%. Limits are also set on the cross section times invisible branching fraction of a possible additional Higgs-like boson over the mass range 115-300 GeV. No excess is observed over the mass range.

8. References

[1] F. Englert and R. Brout, *Broken symmetry and the mass of gauge vector mesons*, Phys. Rev. Lett. 13, (1964) 321323.

[2] P. W. Higgs, *Broken symmetries and the masses of gauge bosons*, Phys. Rev. Lett. 13, (1964) 508509.

[3] G. Guralnik, C. Hagen, and T. Kibble, *Global conservation laws and massless particles*, Phys.Rev. Lett. 13, (1964) 585587.

[4] ATLAS Collaboration, *Observation of a new particle in the search for the Standard Model Higgs boson with the ATLAS detector at the LHC*, Phys. Lett. B716, (2012) 129, arXiv:1207.7214 [hep-ex].

[5] CMS Collaboration, *Observation of a new boson at a mass of 125 GeV with the CMS experiment at the LHC*, Phys. Lett. B716, (2012) 3061, arXiv:1207.7235 [hep-ex].

[6] LEP Higgs Working Group, *Searches for Invisible Higgs bosons: Preliminary combined results using LEP data collected at energies up to 209 GeV*, Phys. Lett. B716, LHWG Note 2001-06 (2001), arXiv:hep-ex/0107032.

[7] LHC Higgs Cross Section Working Group, S. Dittmaier, C. Mariotti, G. Passarino, and R. Tanaka (Eds.), *Handbook of LHC Higgs Cross Sections: 1. Inclusive Observables*, CERN-2011-002 (CERN, Geneva, 2011), arXiv:1101.0593 [hep-ph].

[8] LHC Higgs Cross Section Working Group, S. Dittmaier, C. Mariotti, G. Passarino, and R. Tanaka (Eds.), *Handbook of LHC Higgs Cross Sections: 2. Dierential Distributions*, CERN-2012-002 (CERN, Geneva, 2012), arXiv:1201.3084 [hep-ph].

[9] T. Han and S. Willenbrock, *QCD correction to the $pp \to WH$ and ZH total cross-sections*, Phys. Lett. B273 (1991) 167172.

[10] O. Brein, A. Djouadi, and R. Harlander, *NNLO QCD corrections to the Higgs-strahlung processes at hadron colliders*, Phys. Lett. B579 (2004) 149156, arXiv:hep-ph/0307206 [hep-ph].

[11] M. Ciccolini, S. Dittmaier, and M. Kramer, *Electroweak radiative corrections to associated WH and ZH production at hadron colliders*, Phys. Rev. D68 (2003) 073003, arXiv:hep-ph/0306234 [hep-ph].

[12] S. Frixione, P. Nason and C. Oleari, *Matching NLO QCD computations with Parton Shower simulations: the POWHEG method*, JHEP 0711 (2007) 070, arXiv:0709.2092 [hep-ph]

[13] M. Bahr, S. Gieseke, M. A. Gigg, D. Grellscheid, K. Hamilton, O. Latunde-Dada, S. Platzer, P. Richardson, M. H. Seymour, A. Sherstnev, J. Tully, and B. R. Webber, *Herwig++ Physics and Manual*, Eur. Phys. J. C 58 (2008) 639707, arXiv:0803.0883 [hep-ph].

[14] ATLAS Collaboration, *Improved luminosity determination in pp collisions at $\sqrt{s} = 7$ TeV using the ATLAS Detector at the LHC*, CERN-PH-EP-2013-026 (2013), arXiv:1302.4393 [hep-ex].

[15] ATLAS Collaboration, *Jet energy scale and its systematic uncertainty in proton-proton collisions at $\sqrt{s} = 7$ TeV with ATLAS 2011 data*, ATLAS-CONF-2013-004 (2013), https://cds.cern.ch/record/1509552.

[16] M. Ciccolini, A. Denner and S. Dittmaier, *Strong and electroweak corrections to the production of Higgs +2 jets via weak interactions at the LHC*, Phys. Rev. Lett. 99 (2007) 161803, arXiv:0707.0381 [hep-ph].

[17] ATLAS Collaboration, *Search for the Standard Model Higgs boson produced in association with a vector boson and decaying to bottom quarks with the ATLAS detector*, ATLAS-CONF-2012-161 (2012), https://cds.cern.ch/record/1493625.

[18] A.L. Read, *Presentation of search results: The CLs technique*, Phys. G 28 (2002) 26932704.

[19] G. Cowan, K. Cranmer, E. Gross, O. Vitells, *Asymptotic formulae for likelihood-based tests of new physics*, Eur. Phys. J. C 71 (2011) 1554.

Search for chirality in ^{193}Tl

J Ndayishimye[1,2], E A Lawrie[1], J L Easton[1,3], R A Bark[1], S B Bvumbi[1,6], T S Dinoko[1,3], P M Jones[1], A Kamblawe[1,2], E Khaleel[1,2], N Y Kheswa[1], J J Lawrie[1], S N T Majola[1,5], P L Masiteng[1,3,6], D Negi[1], J N Orce[3], P Papka[2,1], A A Pasternak[4], J F Sharpey-Schafer[3], O Shirinda[1], M A Stankiewicz[1,5], M Wiedeking[1], S M Wyngaardt[2]

[1] iThemba LABS, National Research Foundation, P.O. Box 722, 7129 Somerset West, South Africa

[2] University of Stellenbosch, P.O. Box 1529, Stellenbosch 7599, South Africa

[3] University of the Western Cape, Private Bag X17, 7535 Bellville, South Africa

[4] Cyclotron Laboratory, A.F. Ioffe Physical Technical Institute 194021, St. Petersburg, Russia

[5] University of Cape Town, Private Bag, 7701, Rondebosch, South Africa

[6] University of Johannesburg, P.O. Box 524, 2006 Auckland Park, South Africa

Abstract. A search for chiral bands in ^{193}Tl is under way using the ^{160}Gd(^{37}Cl,4n) reaction. Analysis of the level scheme and the spin and parity assignments is in progress. The previous level scheme of ^{193}T is modified and extended. Most importantly three rotational bands, that could be involved in a possible chiral structure are identified.

1. Introduction

Chirality refers to an object that is not identical to its mirror image. In this case the original and its image have different handedness, like our two hands. In the nuclear domain, chiral symmetry is defined in the angular momentum space. It was introduced by S. Frauendorf and J. Meng [1]. A nuclear chiral system can be built in a triaxially deformed nucleus if its total angular momentum has large projections along all three nuclear axes. For instance in an odd-odd nucleus the total angular momentum might be a sum of three nearly orthogonal angular momenta, those of the odd proton, the odd neutron, and the collective rotation of the core. These nearly-perpendicular angular momenta can then be oriented in a left-handed or a right-handed system ensuring that the nucleus exhibits chiral symmetry. The rotational angular momentum of triaxial nuclear core favours alignment along the intermediate nuclear axis. To form a chiral system the odd proton and the odd neutron should have a particle and a hole nature respectively, which ensures that their angular momenta favour alignments along the short and long nuclear axes respectively. In the laboratory reference frame, a chiral structure is exhibited by the observation of a doublet $\Delta I=1$ bands with the same parity and levels with similar excitation energy for the same spins [1, 2].

So far, candidate chiral doublet bands have been proposed in a number of odd-odd and odd-A nuclei [3]. Some of them were discovered in experiments done at iThemba LABS (A~80, A~100, A~130 and A~190) and (A~80). Moreover a new region of possible chiral symmetry in the heavier Tl isotopes was suggested at iThemba LABS. A candidate chiral pair was suggested in ^{198}Tl [4, 5] and perhaps the best chiral symmetry to date was found in ^{194}Tl [6]. Thus ^{193}Tl as a neighbour of ^{194}Tl is likely to be a very good chiral candidate.

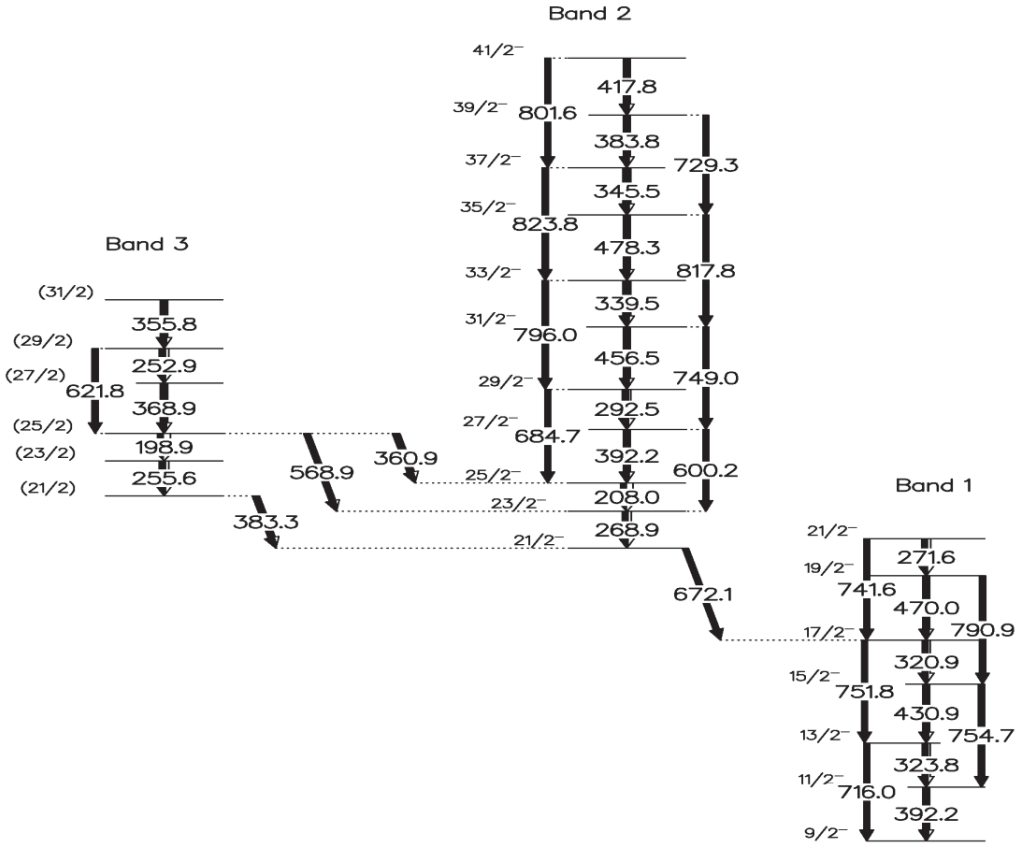

Figure 1: Partial revel scheme of ^{193}Tl [taken from 7].

Previous investigations in ^{193}Tl found a negative parity band (Band 2 in Figure 1) which is built on a $\pi h_{9/2} \times \nu i_{13/2}^2$ configuration [7]. The proton lies at the bottom of the $h_{9/2}$ shell and thus have predominantly a particle nature, while the neutrons occupy orbitals near the top of the $i_{13/2}^2$ shell and thus have predominantly hole nature. Therefore this configuration is suitable for a chiral symmetry system. Furthermore a weak band (Band 3 in Figure 1) with uncertain spin and parity assignments was also observed [7]. This weak band could be a chiral partner to Band 2. The question whether this band has the same parity as Band 2, and thus can be its chiral partner remained unsolved. We performed an experiment to extend the level scheme of ^{193}Tl and to determine the spin and parity of this weaker band. In addition measurements of the lifetimes of the levels of ^{193}Tl using the DSAM technique are planned.

2. Experimental methods and data analysis

Gamma spectroscopy studies of ^{193}Tl were performed using the ^{160}Gd(^{37}Cl,4n) reaction at 167 MeV, with a thin target of ~1.5mg/cm^2 and the 9 clovers of the AFRODITE array placed at 90^0 and 135^0 with respect to the beam direction. Two weekends of beam time were awarded for this thin target experiment. The trigger condition required at least two clovers firing in coincidence. The data were gainmatched and sorted into matrices which were used for construction of the ^{193}Tl level scheme based on coincidence relationships.

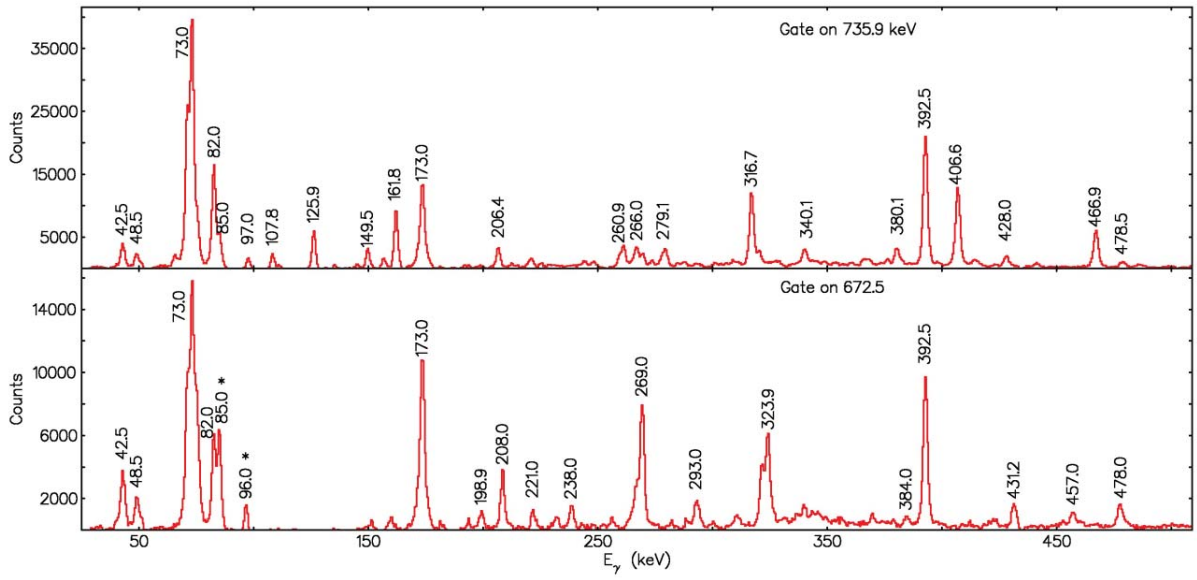

Figure 2: Two gated spectra showing the transitions in ^{193}Tl. The gamma rays that belong to Band 4 are observed in the spectrum gated on the 735.9 keV transition, while the spectrum gated on the 672.5 keV transition shows the gamma rays in Bands 2, 3 and 5. Star signs show the two low energy transitions (85.0 keV and 96.0 keV) which are placed at the band crossing region between Band 1 and Band 2.

3. Results and discussion

The experiment was optimized for lifetime measurements by choosing a reaction producing the ^{193}Tl nuclei at high recoil velocity. However, this reaction has a relatively low cross-section of about 30 mb. The data obtained in the thin target experiment was not sufficient to determine the spin and parity assignments of Band 3.

Nevertheless several modifications and extension of the previously proposed level scheme [7] were made. For instance two low energy transitions were added at the band crossing region between Band 1 and Band 2, thus changing the spin of the yrast chiral candidate band (Band 2) by 2ħ. The low energy 85.0 keV γ–ray which overlaps with the X-rays, can be clearly identified in the spectrum gated on the 672.5 keV transition, where a clear enhancement of the X-ray peak at 85.0 keV is observed in comparison with this peak in the spectrum gated in the 735.9 keV transition (see Figure 2). The gated spectra also show a new 96 keV transition in coincidence with the 672.5 keV transition. There is a 97 keV transition previously placed in coincidence with the 735.9 keV transition. We confirm this coincidence relationship, see Figure 2, but modify the placement of the 97 keV transition, because it is also in coincidence with both 406.6 keV and 466.9 keV transitions, in contrast to its previous placement in anti-coincidence with the 406.6 transition.

Many other modifications and some extension of the previous level scheme were performed in this work. Most importantly the placement of one band, now called Band 5 (see Figure 3) was revised. This band was previously placed above the 735.9 keV transition, but we found that it feeds the levels above the 672.5 gamma ray. This band is of particular interest, because it could play an important role in the chirality scenario. Concerning Band 3, none of the previously proposed linking transitions could be identified. The total level scheme of ^{193}Tl constructed so far is shown in Figure 3.

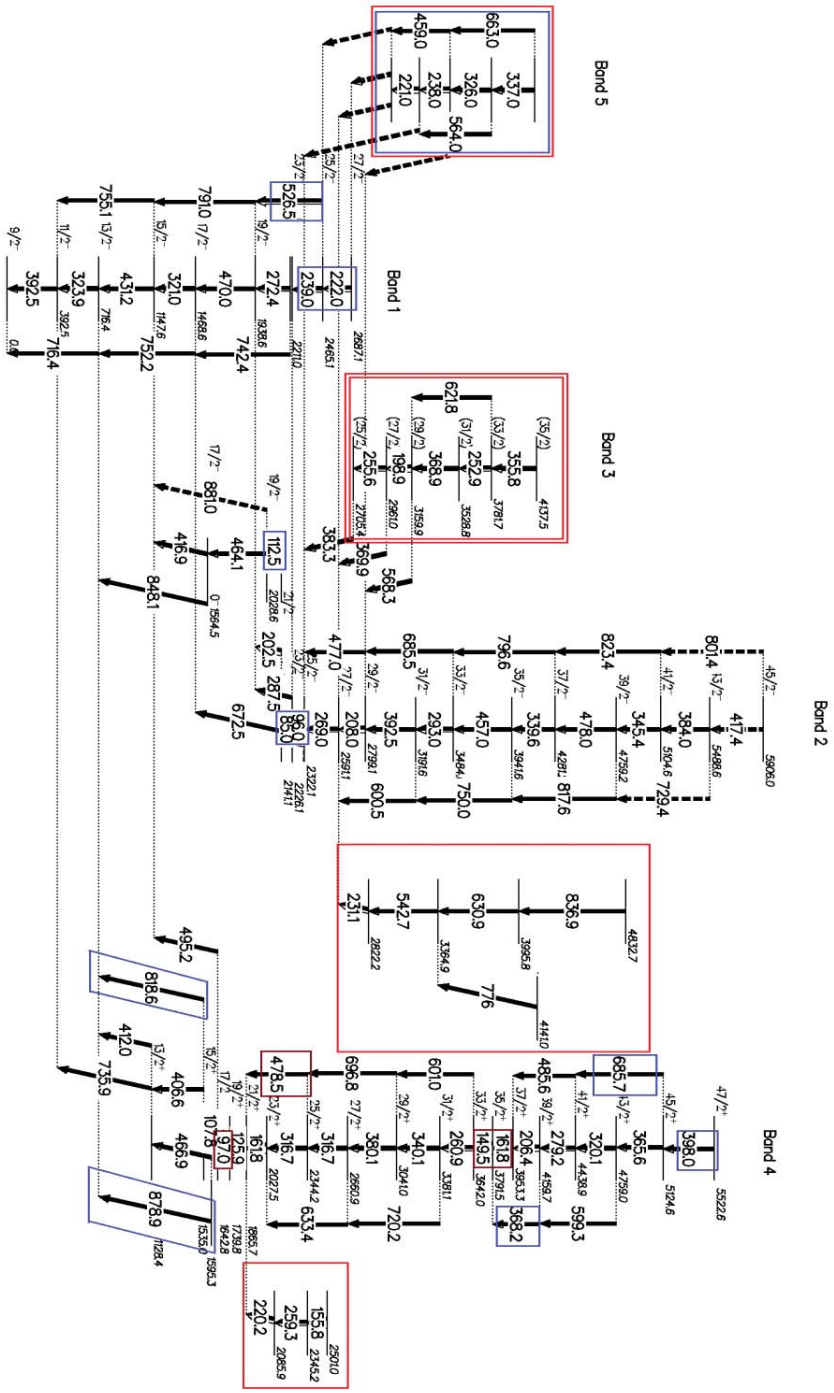

Figure 3: The level scheme of ^{193}Tl as constructed in this work. New transitions are shown in blues rectangles. Maroon rectangles show the transitions with revised placement. The two structures inside red rectangles are still under investigation. Bands 3 and 5, bounded by double rectangles are possibly part of a chiral structure, together with the previously observed Band 2. Band 5 is not yet linked.

Although some important modifications and an extension of the level scheme were performed, the data did not allow us to solve the question about the presence of chiral structure in this nucleus. More experimental data is needed. A proposal to use a new reaction with much larger cross section for the production of ^{193}Tl was submitted and approved. We anticipate that a new much larger data set will be collected soon.

References

[1] S. Frauendorf and J. Meng, Nucl. Phys. A617, (1997) 131
[2] S. Frauendorf, Reviews of Mod. Phys. 73 (2001) 463
[3] T. Koike et al., Nucl. Phys. A. 834 (2010) 36C)
[4] E.A. Lawrie et al., Phys. Rev. C 78, 021305(R) (2008)
[5] E.A. Lawrie et al., Eur. Phys. J. A 45, (2010) 39
[6] P.L Masiteng et al., Phys. Lett. B719 (2013) 83-88
[7] W. Reviol et al., Nucl. Phys. A548 (1992) 331

Emissions of Trace Elements from Motor Vehicles Monitored by Active Biomonitoring: a tunnel study in the Western Cape, South Africa using ICP-MS and neutron activation

Ndlovu NB[1,3], Frontasyeva MV [2], Newman RT [1], Maleka PP [3]

[1]Physics Department, Stellenboch University, Merensky Building, Merriman Ave., Matieland, 7602, Stellenbosch, Republic of South Africa.
[2] Sector of Neutron Activation Analysis and Applied Research, Division of Nuclear Physics, Frank Laboratory of Neutron Physics, Joint Institute for Nuclear Research, Dubna, 141980, Str. Joliot-Curie, 6 Moscow Region, Russian Federation
[3]iThemba LABS, Somerset West, Republic of South Africa

E-mail: nbndlovu@sun.ac.za

Abstract. Application of mosses and lichens as biomonitors, analyzed by nuclear and related techniques, has been extensively used to provide information about air quality. These plants possess efficient accumulation capacity for many air pollutants from atmospheric deposition. Studying air pollution with plants, instead of the commercial air filters is a simple, low-cost, effective method to estimate levels of air pollutants and their impact on humans and animals. A steady global increase of the use of active biomonitoring, whereby biomonitors are collected from relatively pristine habitats and transplanted to different environments, is due to scarcity or total absence of native biomonitors in certain environments e.g. large cities with heavy technogenic load and industrial regions as well as in arid areas. Biomonitoring of trace elements resulting from road traffic, specifically from tunnels, has not yet received adequate attention in the research world. In our pilot study in the Western Cape, moss and lichen species were deployed inside Huguenot tunnel and the results are presented in this work. Samples were analysed by the multi-elemental Inductively-Coupled Mass Spectrometry (ICP-MS). Moreover, samples will later be subjected to the non-destructive instrumental epithermal neutron activation analysis (ENAA), thus facilitating an intercomparison of results obtained by ENAA and ICP-MS.

1. Introduction

Air quality assessment is one of the necessary procedures implemented by countries in order to manage their air quality. This is because air pollution is a serious environmental health problem. Anthropogenic pollutants produced by industrialization, urban growth and vehicle emissions are major causes of atmospheric pollution [1] Biomonitoring of air pollution, whereby mosses and lichens are used as biomonitors, is a widely used technique world-wide although it has not yet been fully utilized in South Africa. Evaluating air pollution using this method is considerably simpler and cheaper than using ordinary aerosol filters [2]. Biomonitoring may generally be defined as the use of biological material to acquire information about the condition of the environment. Due to the absence of a root system in mosses and lichens, these organisms predominantly rely on the environment to which they

are exposed to for their nutrient uptake and they possess high capacities of retaining many ions [3, 4]. Hence they were found suitable to monitor atmospheric deposition of heavy metals and other trace elements, either by *in situ* (passive biomonitoring) or by the use of transplants (active biomonitoring) [5, 6]. Active biomonitoring is an alternative and a valuable tool of evaluating air pollution levels in large cities with heavy technogenic load and industrial regions as well as in arid areas where mosses of lichen do not grow [2]. However, active biomonitoring of trace elements emitted by vehicles, especially using biomonitors in tunnels, has not yet received adequate attention in the research world [7]. Here we report first (preliminary) results of element concentrations measured inside Huguenot tunnel using lichen and moss. Two bags of lichen species; *Usnea subfloridana* and *Parmotrema perlatum*, were deployed next to each other to study their effectiveness in the uptake of a series of trace elements from air inside the tunnel over a defined time period. In addition, two bags with a mixture of two moss species (*Leptodon smithii* and *Pterogonium gracile*) were deployed and used to investigate the uptake rate of trace elements from vehicle emissions by using biomonitors. Lichen and moss samples were analysed using the multi-elemental analytical technique, Inductively-Coupled Mass Spectrometry (ICP-MS), and the results are presented here. At a later stage, these samples will be analysed using the non-destructive instrumental epithermal neutron activation analysis (ENAA) method at the IBR-2 pulsed fast reactor of Frank Laboratory of Neutron Physics (FLNP) - Joint Institute for Nuclear Research (JINR), Dubna, Russia. This will facilitate an intercomparison of results obtained by ENAA and ICP-MS.

2. Materials and Methods

2.1. Study Area

This study was conducted inside the Huguenot tunnel, a toll tunnel near Cape Town in the Western Cape Province, South Africa (SA). The tunnel is 3.9 kilometres long. It is an extension of the national road (N1) through the Du Toitskloof mountains that separate Paarl from Worcester (Figure 1). Huguenot tunnel is maintained by a subsidiary of the Murray & Roberts construction company called Tolcon. It currently provides one lane of traffic in each direction. At least 12 000 vehicles; including both light and heavy-duty vehicles using both diesel and petrol, pass through the tunnel daily.

The samples were deployed at the first vehicle cross cutting (VCC1), which is about 1 km from the western entrance (in the direction Cape Town to Worcester) of the tunnel.

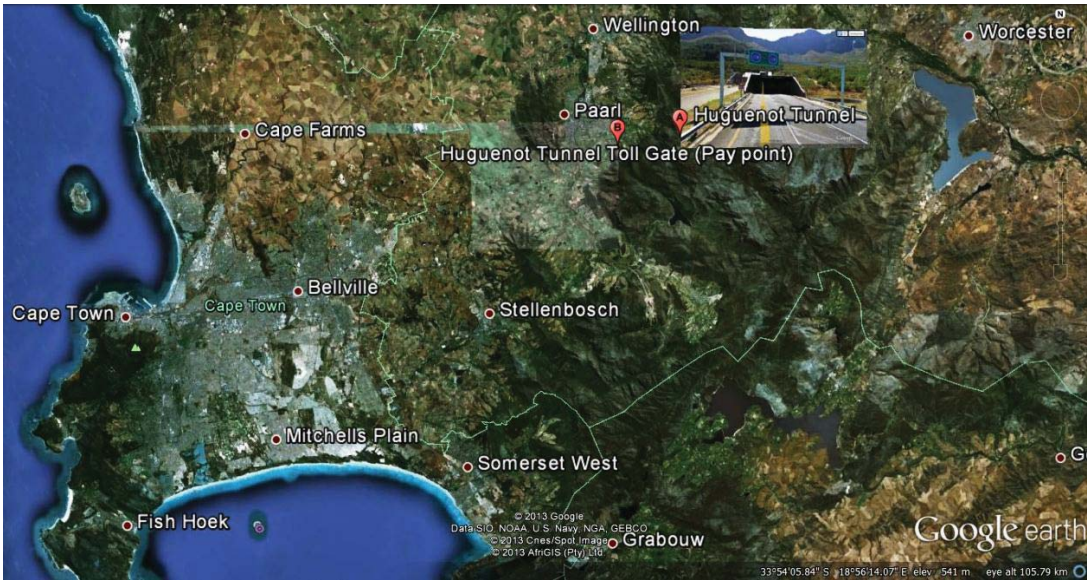

Figure 1. Google earth map of the Western Cape showing location of Huguenot tunnel.

2.2. Preparation of Lichen and Moss Bags and their Exposure

Lichens and mosses were collected from a pristine area (mountainous area near Montagu) in the Western Cape. In the laboratory, lichen and moss species were not washed but cleaned from foreign plant material and soil particles. About 3 g dry-weight of lichens and mosses was loosely packed in a 10×10 cm^2 nylon mesh bags, with 1 mm mesh size. The lichen and moss bags were deployed on a railing attached to the wall of the tunnel, about 4 m above the ground. Table 1 below shows a summary of exposure and collection dates for our lichen and moss bags.

Table 1. Exposure and collection dates for our lichen and moss bags.

Date	Lichens		Mosses	
5-April-2013	Both bags exposed			
17-April-2013		Both bags collected	Both bags exposed	
24-April-2013				1st bag collected
5-May-2013				2nd bag collected

Lichen bags were both exposed on 5th of April 2013, prior to moss bags, and were both collected on the 17th of April 2013 (12 days exposure time). Moss bags were both exposed on the 17th of April 2013. The first one was collected on the 24th of April 2013 (7 days exposure time) and the second one was collected on the 5th of May 2013 (19 days exposure time).

2.3. Sample preparations and measurements for ICP-MS method

To determine the initial (background) concentrations of trace elements in the biomonitors, 2 replicates of non-exposed samples for each biomonitor were analysed by ICP-MS before being exposed in the tunnel. After exposure, lichens and mosses were removed from the nylon mesh bags and manually homogenized. Concentrations of a series of trace elements in them were determined by ICP-MS method. ICP-MS measurements were performed at the Central Analytical Facilities (CAF), Stellenbosch University, Stellenbosch, South Africa, using an Agilent 7700x ICP-MS with Octupole Reaction System.

Samples were dried at 40 °C in a laboratory oven for 3 days. After the drying process, samples were milled in IKA A10 analytical mill. About 0.3 g of each sample was weighed and transferred into a microwave vessel and about 10 ml HNO_3 was added into each vessel. Samples were left to stand open for 20 minutes to predigest before the vessels were sealed and commencing with the microwave heating process. About 40 g of deionised water was weighed and added in a sample bottle that was cleaned in 1% HNO_3 and then added to the digest sample in the microwave vessel to make up 50 ml. Samples were stirred in the microwave vessel, transferred to the sample bottle and then subjected to the ICP-MS.

3. Results and Discussion

The amounts of trace elements found in lichens and mosses after exposure in the tunnel were compared with the initial values that were measured from the unexposed samples. In order to evaluate the accumulated content of trace elements, concentration of each element measured before exposure ($C_{initial}$) was subtracted from the one measured after exposure ($C_{exposed}$);

$$C_{final} = C_{\exp osed} - C_{initial}$$

Comparing the results of elemental concentrations obtained in three tunnel studies from; Lisbon (Portugal) traffic tunnel, Laaer Berg tunnel in Vienna, Austria and highway tunnel in Houston (USA), the following elements Zn, V, Ba, Cr, Pb, Ni, Cd, As, Cu, and Sb were identified and linked to

vehicular emissions inside traffic tunnels while Fe was mostly associated with road dust [7, 8, 9, 10]. Hence in this study, the relative high concentrations of Fe were excluded for further discussions. Furthermore, those authors agree on Zn, Ba, Cr and Cu as the major marker elements for vehicle emissions inside traffic tunnels.

In addition, using various species of biomonitors, in this study their accumulation rates were investigated. The mean concentrations of Zn, Ba, Cu, Pb and Fe increased after exposure (of 12 days) for *Usnea subfloridana (lichen) and* the mixture of *Leptodon smithii* and *Pterogonium gracile (both mosses)* but not for the *Parmotrema perlatum species (lichen).* This trend did not occur in the case of V, Ni, and Cr. This includes a decrease in concentrations of V, Ni, and Cr in both lichen species (see Table 1 and Figures 1 and 2). Results for Cd, As and Sb were also excluded due to their relatively low concentration levels.

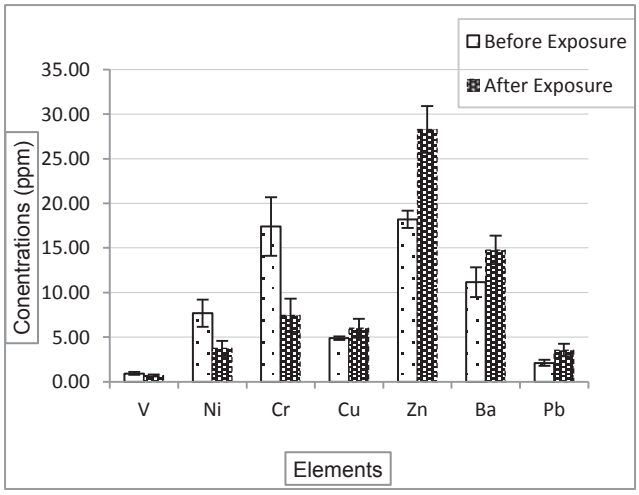

Figure 2. Figure showing accumulation of elements in *Usnea subfloridana* after 12 days of exposure.

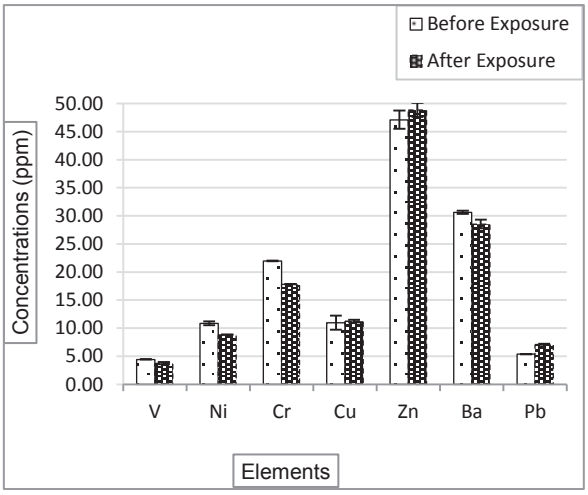

Figure 3. Figure showing accumulation of elements in *Parmotrema perlatum* after 12 days of exposure.

For both species, concentrations of V, Ni, and Cr are higher before exposure than after exposure. For *Usnea subfloridana*, there is a slight increase observed in concentrations of Cu, Ba, Pb while a large increase is found in Zn. For *Parmotrema perlatum*, the differences in concentrations for Cu, Zn, Ba and Pb are within uncertainties. In a study by Gailey and Lloyd in 1986, specifically looking at "The Effects of Length of Exposure on Metal Concentrations", they stated that some trace elements (more especially heavy metals) entrapped by biomonitors can be leached/volatilized out of the nylon net of the suspended bag and this will lead to a decrease in the contents of some trace elements in biomonitors. This usually happens when biomonitors are still trying to adjust under toxic conditions of the new environment in which they have been trans-located to. However, once they reach equilibrium with the new environment, then they accumulate metals most efficiently. Moreover, the leaching of those metals is likely to also occur when biomonitors approach their saturation level [11]. Therefore, the decrease in concentrations of V, Ni, Cu observed in our results in both lichen species, as well as of Ba in *Parmotrema perlatum,* is likely to be caused by leaching. That means 12 days exposure time was not enough for our lichens to reach equilibrium with the harsh conditions inside the tunnel. Zn and Pb were accumulated in both species, i.e. their mean concentrations increased within 12 days period of exposure. However, *Usnea subfloridana* shows extra effectiveness in absorbing and accumulating Zn.

In figure 4, we observe an increase in average concentration levels as the exposure time increases for the elements shown.

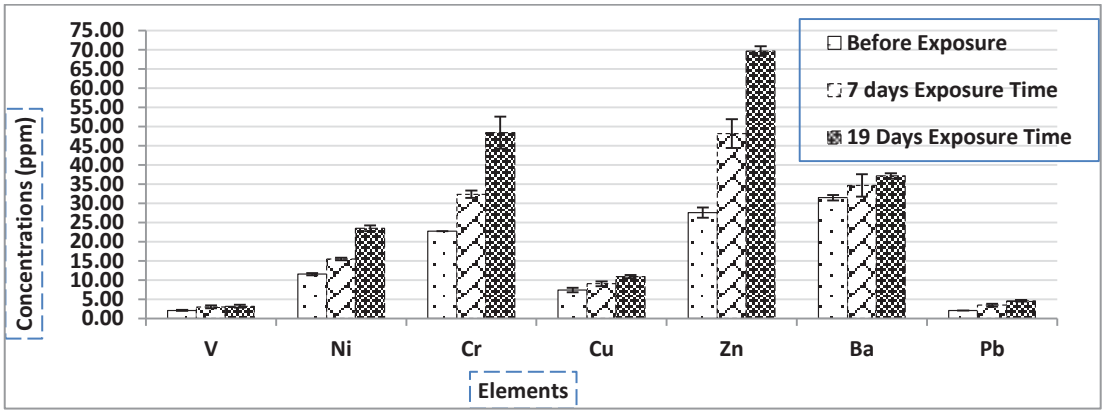

Figure 4. Figure showing accumulation of elements in a mixture of two moss species *(Leptodon smithii and Pterogonium gracile)* over different exposure times.

Most of biomonitoring investigative work has always been done using mosses as they are regarded as analogues of air filters. This is due to their well-known exceptional ability to absorb, accumulate and retain heavy metals through wet and dry atmospheric deposition [2, 7]. In this study, the moss species also behaved in similar manner. In this respect, we can deduce that the increase in the elemental content in the exposed mosses is directly proportional to the length of exposure even for our shortest length of exposure (i.e. 7 days).

In Figure 5 we show results of cluster analysis (CA) for indicators of road traffic emissions in tunnels, presenting three clusters. Our results are consistent with the results from fairly comparable studies [7, 8, 9, 10].

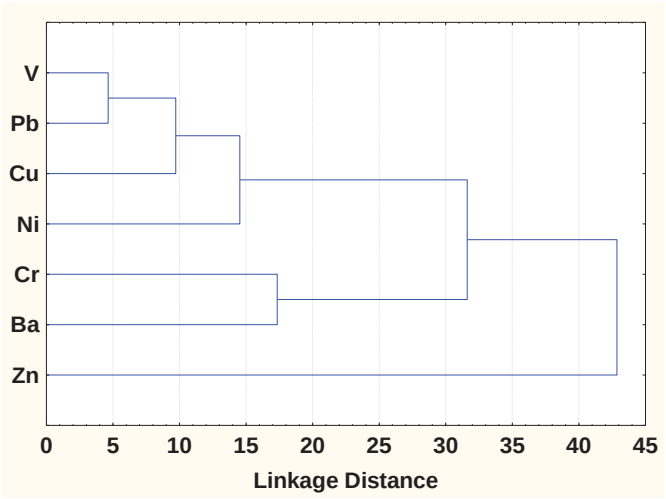

Figure 5. Dendrogram resulting from hierarchical cluster analysis of trace elements associated with road traffic emissions.

Variables (V, Pb, Cu and Ni) contained in the first cluster are linked to different road traffic related source; road dust containing traffic related particles, auto exhausts, oil combustion, as well as brake and tire wear. The second cluster with Cr and Ba represents diesel fuel and tire wear. The third cluster also represents a number of traffic related sources; auto exhausts, motor oil, as well as break and tire wear. The fact that all groups are connected at a certain distance demonstrates that all the main sources

of those elements are emissions from motor vehicles. According to [12], the application of multivariate statistical analysis (e.g. cluster analysis) to datasets assists in revealing the character and the origin of pollution sources within a particular study area.

4. Summary and Conclusion

Our results show *Usnea subfloridana* to be more efficient in accumulating trace elements from vehicle emission in tunnels, compared to the other lichen species *Parmotrema perlatum*. Lichens are likely to initially undergo leaching of trace elements when exposed to unfavourable conditions like tunnels. Thus, a longer exposure time is essential for them to reach equilibrium with their new environment before they can appropriately accumulate trace elements. All determined elements associated with vehicle emissions in tunnels were considerably accumulated by mosses even after a short exposure time of 7 days, which is 5 days shorter than that of lichens. Hence biomonitoring with mosses is generally ideal. The outcomes of this study demonstrate mosses to be more efficient than lichens in monitoring road traffic emission even under enhanced polluted conditions of a traffic tunnel. Cluster analysis of our results for the considered elements confirms the linkage of those trace to emissions from vehicles.

ACKNOWLEDGEMENTS

This work is part of the research supported by the National Research Foundation. The authors are grateful to the National Research Foundation (South Africa) for a grant under the South Africa – JINR programme to partly fund this project.

Moreover, the authors express appreciation to the Western Cape Nature Conservation Board for granting them permission to collect samples for this project (related to permit No. AAA008-00104-0028).

The authors are also thankful to the South African National Roads Agency Ltd (SANRAL) and Murray & Roberts Construction (Pty) Ltd for the permission to conduct this study in Huguenot tunnel; especially for the assistance from Eric Eksteen, Christo Van der Linde, and Leonard Louw.

References

[1] Aničić M 2009 Environ. Pollut. 157, 673-679
[2] Frontasyeva MV 2011 Phys. Part. Nuclei 42(2), 332-378
[3] Markert B, Wuenschmann S, Fraenzle S, Wappelhorst O and Weckertl V 2008 *Int. J. Environ. and Pollut.* **32**(4), 486-498
[4] Steinnes E, Berg T and Uggerud HT 2011 *Sci. Total Environ.* **412-413**, 351–358
[5] Steinnes E 1993 *Kluwer Acad. Publ.* **25** 87-97
[6] Steinnes E 1984 *Fresen J. Anal. Chem.* **317**, 350
[7] Zechmeister HG, Dullinger S, Hohenwallner D, Riss A, Hanus-Illnar A and Scharf S 2006 Environ. Sci. Pollut. Res. 13(6), 398 – 405
[8] Chellam S, Kulkarni P and Fraser MP 2005 *J. Air & Waste Manage*. **55,** 60–72
[9] Almeida-Silva M, Canha N, Freitas MC, Dung HM and Dionísio I 2011 *Appl. Radiat. Isotopes* **69,** 1586–1591
[10] Aničić M, Tasić M, Frontasyeva MV, Tomašević M, Rajšić S, Mijić Z and Popović A 2009 *Environ. Pollut.* **157**, 673-679
[11] Gailey FAY and Lloyd OL1 1986 *Environ. Pollut.* (Series B) **12**, 61-74
[12] Frontasyeva MV 2009 *Ovidius Univ. Annals Chem.* **20 (1)**, 11-18

Measuring the performance of the iThemba LABS segmented clover detector

O Shirinda[1,3], J L Easton[1,2], E A Lawrie[1], T D Bucher[1] and S P Noncolela[1,2]

[1] iThemba LABS, National Research Foundation, P.O. Box 722, 7129 Somerset West, South Africa
[2] University of the Western Cape, Private Bag X17, 7525 Bellville, South Africa
[3] obed@tlabs.ac.za

Abstract. The iThemba LABS segmented clover detector, capable of performing gamma-ray tracking, was characterised. The measured energy resolutions (FWHM) of this detector at 121 keV and 1332 keV are < 1.4 keV and < 2.2 keV respectively for the inner-core contacts. The photo-peak efficiency in direct and add-back modes were measured at four different distances. The detector preamplifiers are fast enough to enable time variations larger than 40 ns to be distinguished, which is sufficient for measuring variations in the signal rise time of ~200 ns for the iThemba LABS segmented clover detector.

1. Introduction

Large volume high-purity germanium (HPGe) detectors are commonly used in applications (such as gamma-ray spectroscopy) that require good energy resolution and high detection efficiency. iThemba LABS recently bought a new state of the art segmented clover detector. The new detector contains four cylindrical HPGe crystals (see figure 1) housed in a common vacuum cryostat and held at temperature of around 75 K by a metal cooling structure that extends back into a dewar of liquid nitrogen. This detector has 32 outer contacts. These are in addition to the four inner-core contacts, and so the total number of electrical signals from the detector is thirty-six. The principal reason for this segmentation is to provide information about the three-dimensional localization of gamma-ray interactions within the detector. Charge sensitive preamplifiers allow all thirty-six electrical signals to be read out, providing precise energy information from the core contact and signals for position localization from the outer contacts. Due to its segmentation, the detector can be used not just as a standard clover detector, but also in a gamma-ray tracking mode. Therefore measurement for the performance of this detector is very important prior to developing γ-ray tracking. In this work results obtained from tests which include measuring the energy resolutions (FWHM) for each crystal and for the outside electrodes at different rates, measuring rise and decay times and efficiency at different source-to-detector distance are presented. Measurements were carried out mainly by means of Pixie-4 digital electronics.

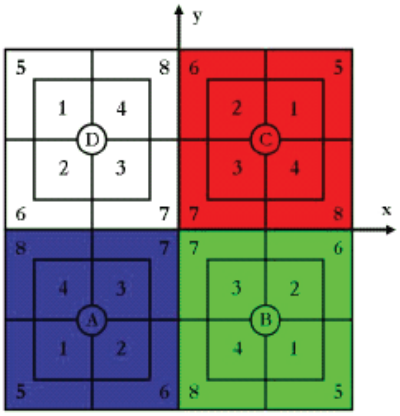

Figure 1. Schematic drawing of the iThemba LABS segmented detector layout. The colours of the crystals, corresponding to labels A through D, are Blue, Green, Red, and White.

2. Experimental measurements and results

2.1. Preamplifier response measurements

The preamplifier represents an interface between the detector and the signal processing electronics. Its basic function is to amplify and shape the small signal from the detector and to transfer it to the electronic chain with the least degradation. Typically, charge sensitive preamplifiers are used for Ge detectors. In a charge sensitive preamplifier, the charge carried by the incoming pulse is first integrated on a capacitor and then removed by a slow discharge through a resistive feedback network. This produces a pulse with a fast leading edge (rise time), corresponding to the charge collection time in the detector, and a slow exponential decay (fall time). In order to preserve as well as possible the information carried in the signal leading edge, a very fast, low noise, low power consumption and stable preamplifier is required. To obtain a fast response, i.e. a signal with short rise time, a large bandwidth (BW) preamplifier is required.

The preamplifier response of the detector was measured by injecting a 5 ns rise time square wave into the test input of each crystal, and measuring the rise time and decay constant τ of the subsequent core signal. The rise time was measured as the time the pulse takes to grow from 10% to 90% of its final amplitude using a Tektronix DPO3054 digital oscilloscope (500 MHz, 2.5 GS/s). The shapes of the injected and preamplifier output signals are shown in figures 2(a)-(d) and figures 3(a)-(d).

Several different decay time constants τ are being used:

(i) The decay time constant τ : is equal to the time at 37% (1/e) of the pulse amplitude.

(ii) 50% time constant $t_{1/2}$: is equal to the time at 50% of the pulse amplitude. It is related to τ by $\tau = t_{1/2}/\ln 2$.

(iii) 90% - 10% time constant $t_{90\% - 10\%}$: is equal to the time taken by the pulse to fall from 90% to 10% of its amplitude. It is related to τ by $\tau = t_{90\%-10\%}/\ln 9$.

All core contacts exhibit good rise times and decay constants, falling well below 44 ns and 52.5 μs respectively (see table 1). It can then be concluded that the detector preamplifiers are fast enough to enable time variations larger than 40 ns to be distinguished. This time resolution is sufficient for measuring variations in the signal rise time, which for the iThemba LABS segmented clover detector is of the order of 200 ns. Note that the shape of the signal observed from crystal C shows some oscillations (see figure 2(c)). When the signal oscillates, the settling time is an issue in addition to the

amounts of over/under shoots. Thus the performance of the preamplifier of crystal C raises a concern, and is under further investigations[1].

Table 1. Rise times and decay time constants τ for the iThemba LABS segmented clover detector. The value marked with * is measured when ignoring the oscillation of the signal.

	Injected 5 ns square pulse	
Crystal	**Rise time (ns)**	**Decay constant τ (µs)**
A	42.6	49.9
B	42.2	49.9
C	33.0*	50.5
D	43.8	51.7

(a) Crystal A

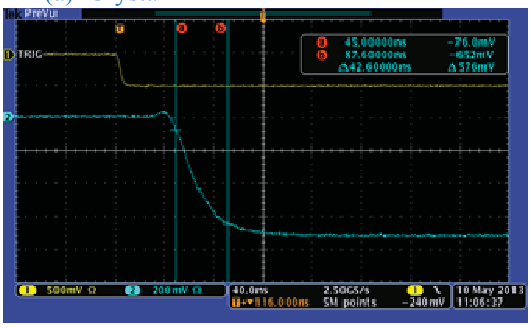

(b) Crystal B

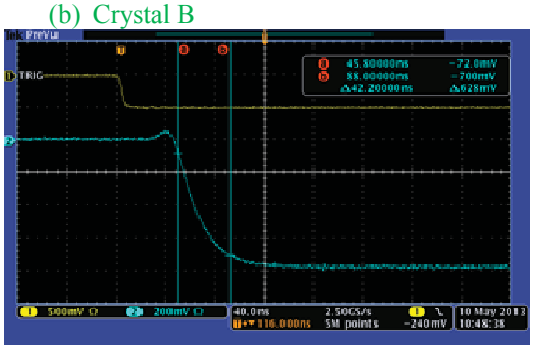

(c) Crystal C

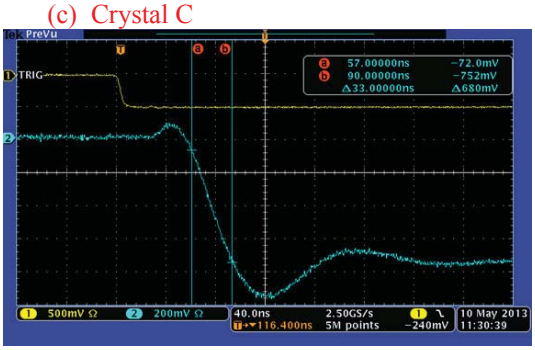

(d) Crystal D

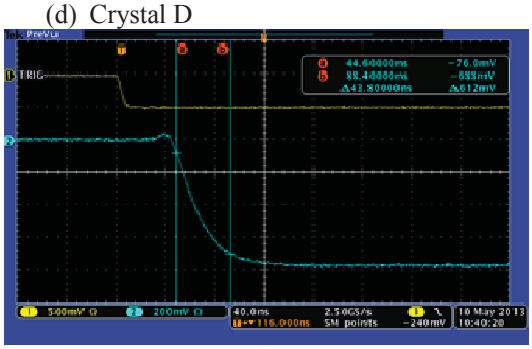

Figure 2(a)-(d). Rise times of each full volume signal from iThemba LABS segmented clover detector, resulting from an injected 5 ns rise time square pulse.

2.2. Energy resolution and efficiency measurement

Detector energy resolution is a quantity that reflects the capability of a detector to distinguish between two close-lying energy peaks in a spectrum. According to the Institute of Electrical and Electronics Engineers (IEEE) standard [1], the energy resolution for a Ge detector is defined by the full width at half maximum (FWHM) of the photo-peak at 1332 keV from a ^{60}Co source.

[1] While the article was in the process of reviewing the issue was resolved by increasing the bandwidth of the preamplifier of the test input on crystal C.

The detector efficiency reflects the probability that a photon (or a particle) emitted from a source will be detected in a radiation detector. Furthermore, the detector efficiency depends not only on the type of the radiation but also on the energy of the incident radiation and the geometry of the detector. It is convenient to divide the detector efficiency into three types.

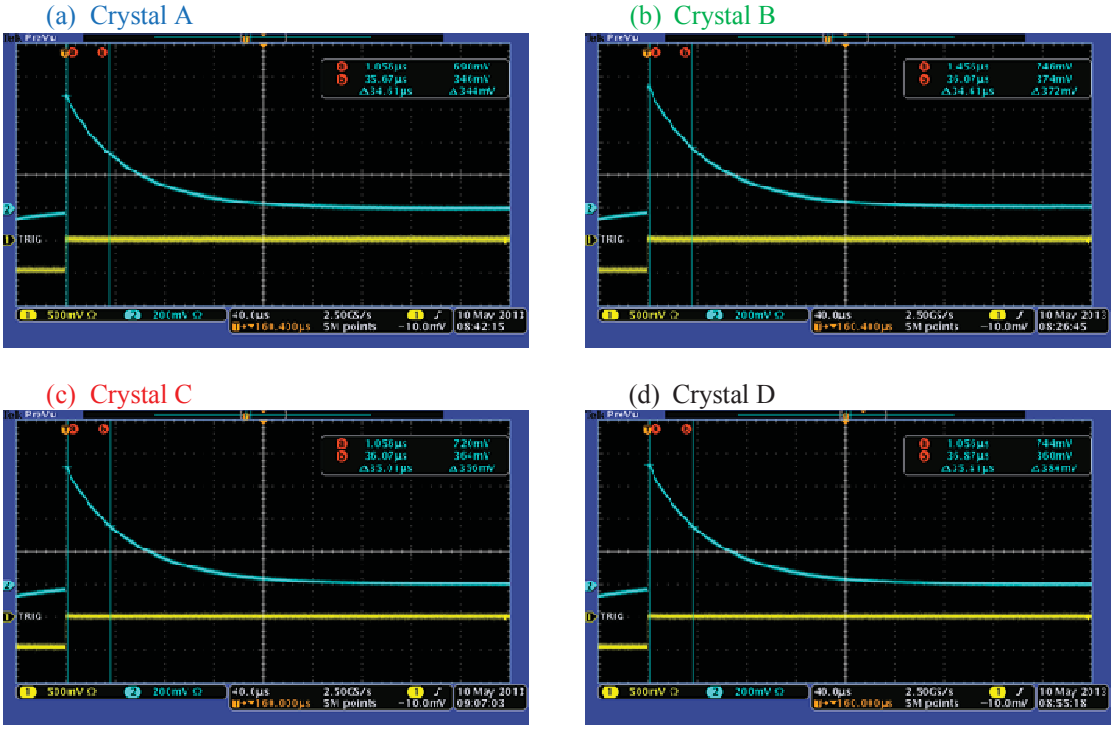

Figure 3(a)-(d). Decay time constant τ of each full volume signal from iThemba LABS segmented clover detector, resulting from an injected 5 ns rise time square pulse.

(i) The absolute efficiency ϵ_{abs} is defined as the number of registered particles divided by the total number of particles emitted by the source in all directions, and it is therefore influenced by the detector and source geometry.

(ii) The intrinsic efficiency ϵ_{int} is defined as the number of registered particles divided by the number of particles incident on the detector. It depends on the detector material, the type of radiation, the energy as well as the geometry of the detector. The absolute efficiency is related to the intrinsic efficiency via the geometrical factor, η. This coefficient reflects the geometrical configuration of the detector and the source and their mutual positions.

(iii) The relative efficiency ϵ_{rel} is the efficiency of a germanium detector relative to a NaI(Tl) crystal, 76 mm in diameter and 76 mm in length, measured at 25 cm from the source. This is the absolute efficiency ϵ_{abs} divided by 1.244×10^{-3}.

In this work the absolute efficiency was measured.

Our measurements were performed while the detector was in direct and add-back modes. In direct mode each of the four n-type coaxial HPGe crystals (A, B, C and D) comprising the segmented clover detector was considered as an independent detector. In this mode each individual crystal measures separately the γ-ray energy absorbed.

In add-back mode, the four separate n-type coaxial HPGe crystals (A, B, C and D) comprising the segmented clover detector are considered as a composite detector. In the add-back mode, the crystals work together and sum up all the detected energies in each crystal on an event-by-event basis. This technique is very important for increasing the photo-peak efficiency, because if a γ-ray is detected in one crystal and Compton scatters to another crystal where it also gets detected, the energy deposited in the first crystal should be added to the energy deposited in the second crystal to recover the total energy.

Five different radioactive standard sources, ^{152}Eu, ^{133}Ba, ^{60}Co, ^{137}Cs and ^{241}Am emitting γ-rays of different energies were used. Sources were placed at distances of 11 cm, 14.5 cm, 19.6 cm and 22.5 cm in front of the Ge crystals. Source activities were approximately 10 μCi for ^{152}Eu, ^{60}Co and ^{137}Cs; 10.72 μCi for ^{133}Ba, and 12.36 μCi for ^{241}Am. The data were collected for 15 minutes per measurement and recorded with Pixie-4 digital electronics.

2.2.1. *Energy resolution.* The energy resolutions (FWHM) of the iThemba LABS segmented clover detector in direct mode are shown in figure 4. The specification is FWHM ≤ 1.35 keV and FWHM ≤ 2.35 keV at 121 keV and 1332 keV respectively for the cores; and FWHM ≤ 3.00 keV and FWHM ≤ 3.50 keV at 121 keV and 1332 keV respectively for the segments [2]. We found that in add-back mode the width of the peaks are slightly larger than in direct mode. In direct mode some of the measured FWHM for the core and segments at 121 keV and 1332 keV γ-ray are slightly larger than the guaranteed values given by the manufacture, see figure 4. We also found that changing the position between the detector and the source has little impact on the FWHM of the detector.

2.2.2. *Efficiency*. Figure 5 shows the measured absolute photo-peak efficiencies for the detector in direct (left) and in add-back (right) modes. In direct mode all the crystals have a similar absolute efficiency. At low γ-ray energies the photo-peak efficiency in the direct mode is higher than the efficiency in add-back mode due to coincidence summing. It needs to be underlined that apparently the coincidence summing has significant effect also for such low gamma-multiplicity sources as ^{152}Eu and ^{133}Ba. The photo-peak efficiency at higher γ-ray energies shows an enhancement in add-back mode over the sum of the photo-peak efficiencies of all four crystals in direct mode. The photo-peak efficiency in add-back mode increases with γ-ray energy due to the increased contribution of Compton scattering. The add-back factor is a measure of the enhancement in the add-back photo-peak energy efficiency of a γ-ray, and is defined as the ratio of the photo-peak detection efficiency in the add-back mode divided by that in the direct mode. Short source-to-detector distance results in an increase of the photo-peak efficiency, but is strongly affected by the coincidence summing effects and increase in the dead time. One can note that the measured efficiency (dashed) at d = 11 cm is much lower than the one (dash-dotted curve) obtained from the efficiency at d = 22.5 cm after normalization with a geometrical factor for d = 11 cm. This shows that considerable efficiency is lost due to these effects. The evaluation of the impact of these two effects is in progress.

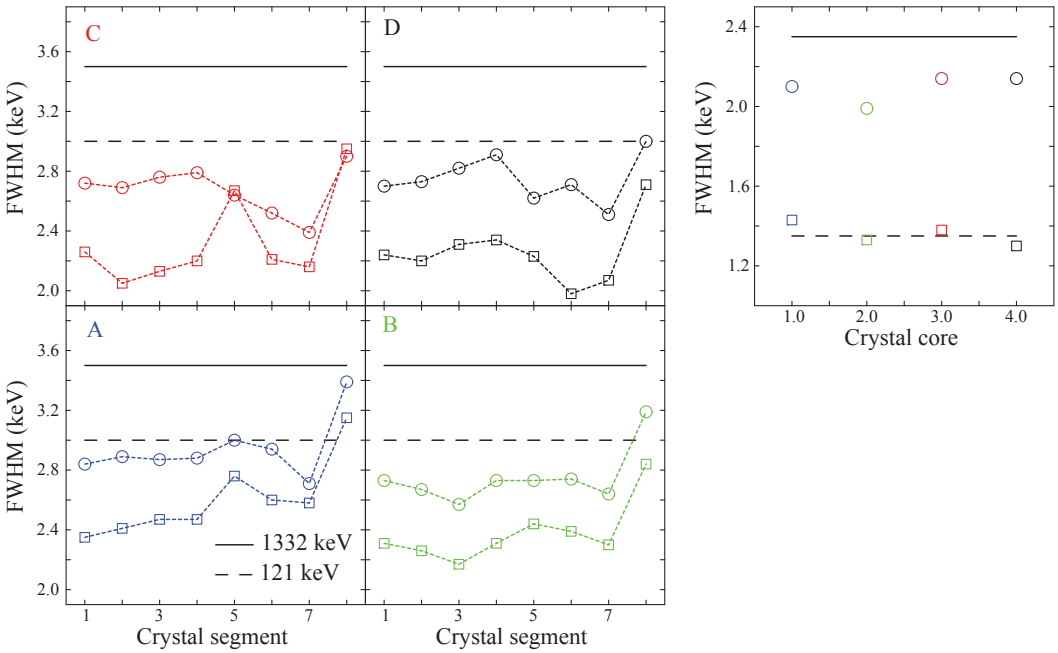

Figure 4. Measured energy resolutions (FWHM) of iThemba LABS segmented clover detector for a 121 keV (squares) and 1332 keV (circles) photo-peaks from ^{152}Eu and ^{60}Co respectively. Solid and dashed lines correspond to the manufacturer guaranteed values of FWHM for 1332 keV and 121 keV respectively.

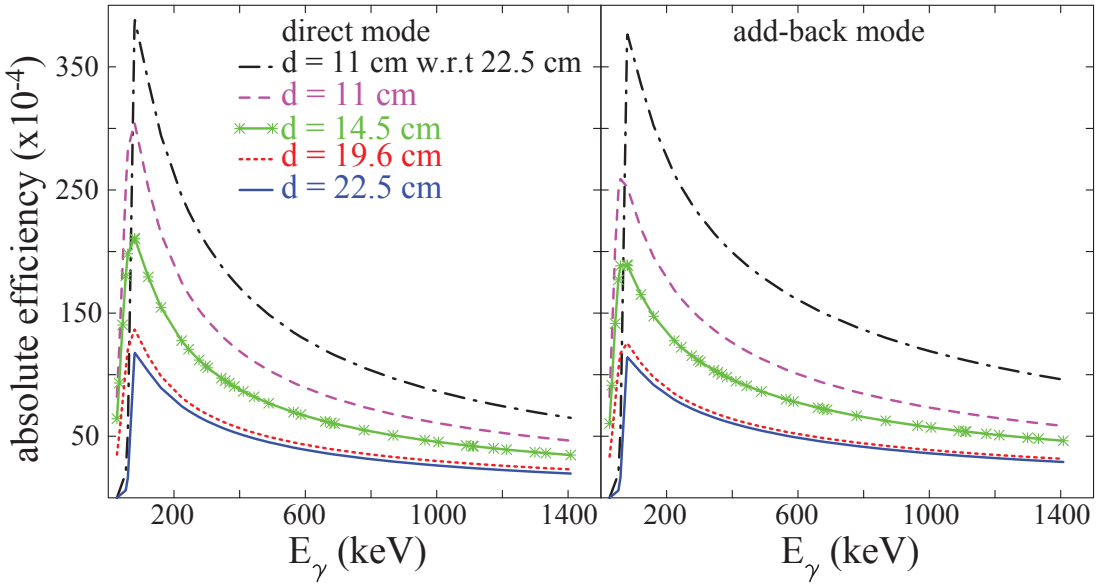

Figure 5. Measured absolute efficiencies in direct (left) and add-back (right) modes for the iThemba LABS segmented clover detector. The absolute efficiency for the dash-dotted curve was obtained from the absolute efficiency at d = 22.5 cm after normalization with a geometrical factor for a distance of d = 11 cm.

3. Summary

The iThemba LABS segmented clover detector characteristics such as energy resolution and absolute efficiencies in direct and add-back modes were measured. The measured FWHM values are consistent with the values given by the manufacturer. At low γ-ray energies the photo-peak efficiency in the direct mode is higher than the one in add-back mode. For higher γ-ray energies the values for the photo-peak efficiency show an enhancement in add-back mode over the efficiencies in the direct mode. Short source-to-detector positions exhibit effects of the coincidence summing. We also found that the detector preamplifiers are fast enough to enable time variations larger than 40 ns to be distinguished. This time resolution is sufficient for measuring variations in the signal rise time, which for the iThemba LABS segmented clover detector is of order of 200 ns.

References

[1] 325-1996-IEEE standard test procedures for germanium gamma-ray getectors 1997
[2] Canberra iThemba clover 4x60x90 seg32 user's manual s/n: 21 2010

Division C – Photonics

The Impact of Low Intensity Laser Irradiation on Lung Cancer Stem Cell Viability and Proliferation

A. Crous and H. Abrahamse
Laser Research Centre, University of Johannesburg, P.O. Box 17011, Doornfontein, Johannesburg, 2028, South Africa

Email: habrahamse@uj.ac.za

Abstract. *Background*: Cancer stem cells or tumour initiating cells are cells that have been attributed to metastatic drive and tumour genesis. These cells contribute to cancer recurrence, metastasis, aggressiveness and resistance to therapy. Laser irradiation has been shown to have a diverse range of clinical applications including wound healing and photo dynamic therapy (PDT). Middle infrared (MIR) radiation has shown to inhibit cellular proliferation and induce morphological changes to the cytoskeletal dynamics of A549 lung cancer cells. Recent studies done using Low Intensity Laser Irradiation (LILI) using visible red light with a wavelength of 636 nm and fluence between 5- 15 J/cm^2 on adipose derived stem cells (ADSCs) which are adult mesenchymal stem cells (MSCs), have shown to have an increase in proliferation, viability and differentiation into smooth muscle cells. The effects of LILI on cancer stem cells have yet to be elucidated. *Methodology:* Isolated A549 lung cancer stem cells were exposed to a wavelength of 636 nm and a fluence of 5 or 10 J/cm^2, where after cellular responses were monitored after several time intervals to evaluate proliferation and viability with the view to establish the wavelength and fluence at which LILI causes an effect on proliferation and viability after a specific incubation time. *Discussion*: This study assists in the understanding of the effects of LILI on isolated lung cancer stem cells by evaluating the results produced and comparing the different effects of different laser parameters on these cells.

1. Introduction

Lung cancer is a leading threat of cancer-related deaths world-wide [1]. Contributing factors include the deficiency in treatment modalities, local recurrence and systemic metastasis. Advancements in these areas are likely to improve overall outcome. Lung cancer is represented by tumour formation consisting of atypical cells; the cancer is then classified according to the cell types it consists of [2]. Research confirmed that these tumours also contain a subpopulation of cells, thought to drive tumour genesis, called cancer stem cells (CSCs) or tumour initiating cells (TICs) displaying stem like properties such as rapid proliferation, are clonal in origin and can self-renew [3]. These CSCs are partly held responsible for therapeutic resistance of cancer as it is said to regenerate the tumour after treatment [4,5]. This information poses the strategy to target CSCs with different treatment options [5]. Current cancer treatment strategies include Low Intensity Laser Irradiation (LILI) in conjunction with a photosensitiser called photodynamic therapy (PDT).

LILI is a technique that uses optical waves at a specific wavelength and no heat is produced [6]. LILI has been shown to promote viability and proliferation in various types of stem cells, especially in the red to near infrared spectrum (600-700 nm). This is most likely due to the mitochondrial respiratory chain components being able to absorb light at this wavelength resulting in the increase of reactive oxygen species (ROS), and adenosine triphosphate (ATP) or cyclic adenosine monophosphate (cAMP), and initiating a signalling cascade which promotes cellular proliferation and cytoprotection [7]. In previous LILI studies conducted using diabetic induced human skin fibroblast cells (WS1) at wavelengths of 632.8, 830 and 1064 nm at 5 and 16 J/cm^2 showed both a dose and wavelength dependent response, showing that cells respond best using visible red irradiation at a fluence of 5 J/cm^2 and a

wavelength of 632.8 nm [8]. Similar results were obtained in a study using adipose derived stem cells (ADSCs), both studies indicating that higher fluences such as 10 -16 J/cm^2 induced cell damage and decrease cell viability and proliferation [8,9].

In this study cells were characterised using cell surface marker CD133+ (prominin-1), which is a five-transmembrane glycoprotein and one of the most frequently demonstrated markers for CSCs in multiple organs/tissues including the lung [10,11]. Cells were treated with LILI using visible red light at a wavelength of 636 nm and fluences of 5 or 10 J/cm^2 to identify the dosage levels at which the cells indicate a response in cell proliferation and viability.

2. Materials and Methods

Characterisation: Isolated A549 CSCs were characterised using fluorescent microscopy and cell surface marker CD 133+. CaCo2 cells were used as a positive control and SKUT-1 as a negative control. *Culture:* The isolated cells were seeded into 3.4 cm^2 diameter culture dishes and incubated over night to allow cells to attach. Cell cultures were irradiated once in the dark from the top with a 636 nm diode with a fluence of, 5 or 10 J/cm^2. Non-irradiated cells used as a control were treated similar to irradiated cells, without the irradiation. Post-irradiation, cultures were incubated for 24, 48 and 72 hours. Post-incubation cells were trypsinysed for detachment and re-suspended in 1 ml complete medium. All tests were performed on different populations (n=4) of cells for each sample group and each biochemical assay was performed in duplicate [9]. *Cell viability:* All cell populations were treated with CellTiter-Glo® and ATP luminescence was recorded using a spectrophotometer measuring the ATP present in each sample. *Cell proliferation:* All samples were treated with 10% alamarBlue® where absorbance was measured quantitatively using an excitation wavelength of 560 nm and emission wavelength of 590 nm. Statistical significant differences between groups were indicated as $p<0.05$ (*), $p<0.01$ (**) and $p<0.001$(***) and considered as 95 percent confidence interval for the population mean.

3. Results

To characterise the isolated stem cells, they were labelled with a lung CSC marker CD133$^+$ as indicated by Figure 1.

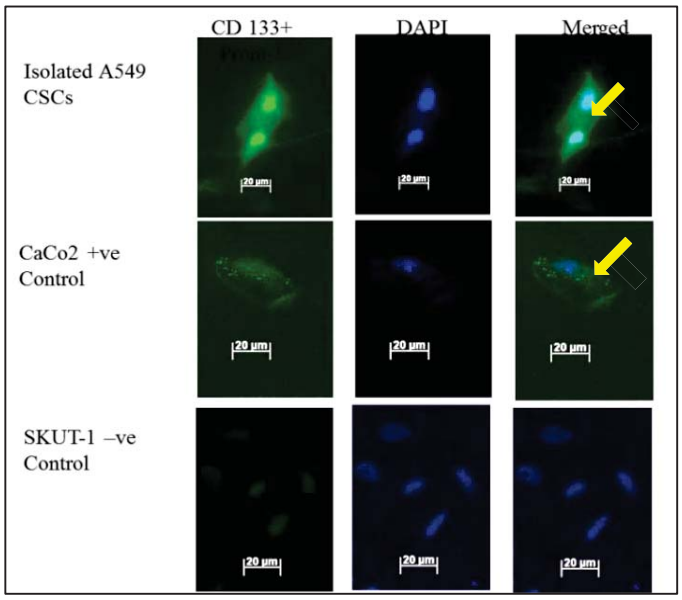

Figure 1: Characterisation of isolated A549 CSCs. 1^0 unconjugated antibody CD133$^+$ and 2^0 FITC conjugated antibody staining the cell surface green and DAPI staining the nucleus blue. Results indicate A549 CSCs and CaCo2 are both positive for CD 133, whereas SKUT-1 is negative.

CaCo2 cells were used as the positive control cell line and SKUT-1 the negative control. Positive results were indicated by green fluorescence and a counterstain of DAPI, making the cell nucleus fluoresce blue. Negative results only indicated the blue fluorescence.

Cell viability was determined by ATP luminescence (Fig 2.), showing an increase in viability as time elapses from 24 to 72 h. A similar trend is seen with proliferation (Fig.3) when Alamar blue is read as an absorbance value and an increase is seen in all samples measured over a period of time.

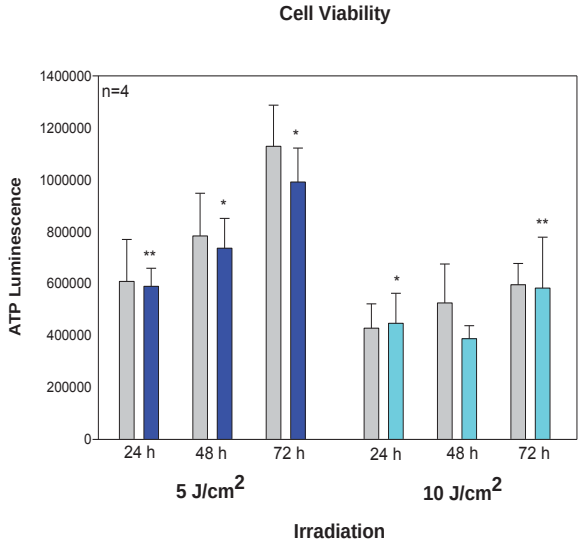

Figure 2: Increase in ATP luminescence is seen in all the samples as time elapses from 24- 72h. No significant change was observed with irradiation when comparing 5 J/cm^2 to 10 J/cm^2. Statistical significant differences were expressed as p<0.05 (*), p<0.01 (**) and p<0.001(***). All samples were compared to their control groups. Experiments were repeated four times (n=4).

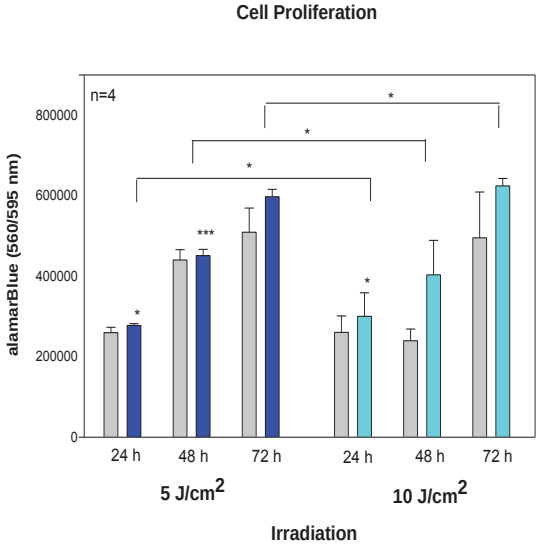

Figure 3: Irradiated samples all show a momentous increase in proliferation over a period of time. All samples are compared to their control counterparts as a statistical difference of p<0.05 (*), p<0.01 (**) and p<0.001(***). Statistical significant differences in time intervals when comparing 5 J/cm^2 to 10 J/cm^2 irradiation are indicated as p<0.05 (*) for 24h, 48h and 72h. Experiments were repeated four times (n=4).

4. Discussion and Conclusion

Fluorescence microscopy reveals that the isolated lung A549 CSCs were positive for the CD133 antigen used to characterise lung CSCs as well as the CaCo2 cells used as a positive control. This work concurs with research published in previous studies [10,11]. The negative results obtained for the SKUT-1 smooth muscle cells used as a negative control correlates with previous studies done [12]. These results obtained indicate that the isolated cells were CSCs.

An increase was observed in both ATP viability and alamarBlue® proliferation in the isolated A549 human lung CSCs. The rise in ATP level correlates with the increase in proliferation of the CSCs. Both the increase in viability and proliferation using a fluence of 5 J/cm^2 and wavelength of 636nm can be attributed to photobiostimulation which has a positive effect on cells at that specific dose and wavelength. This increase in cellular viability and proliferation can be made due to intracellular chromophores absorbing the light, activating the cells' electron transport chain, having an increased

effect on ATP production [13]. These effects have also been demonstrated in previous studies conducted on diabetic induced WS1 and ADSCs [8,9]. There was no significant decrease observed when comparing irradiation at 5 J/cm^2 and 10 J/cm^2. Results indicated yet another increase in viability and proliferation over time when irradiating the CSCs at 10 J/cm^2. These findings are contradictory to those observed in previous studies showing a decline in cellular proliferation and viability when using fluences between 10 and 16 J/cm^2 on ADSCs [9]. This effect can be attributed to CSCs sharing essential capabilities similar to those found in normal stem cells. These include self-renewal and differentiation potential; other CSC characteristics also include resistance to cell death as compared to normal cell death rates and failure of current treatment methodologies such as chemo and radiation therapy that should reduce proliferation potential [14]. The results obtained indicate both a dose and wavelength dependent response on cells treated. A higher fluence of irradiation should be considered when wanting the desired effect of decreasing cell viability and proliferation of CSCs. It should be considered that current studies being conducted using a fluence of 20 J/cm^2 should demonstrate to be an effective inducer of CSC death.

References

[1] Kang H-W, Crawford M, Fabbri M, Nuovo G, Garofalo M (2013) A Mathematical Model for MicroRNA in Lung Cancer *PLoS ONE* **8**(1): e53663. doi:10.1371/journal.pone.0053663

[2] Lung cancer, Columbia Electronic Encyclopedia, 6th Edition, Feb2013 MasterFILE Premier, EBSCOhost: www.ebscohost.com.ujlink.uj.ac.za accessed on 23 May 2013.

[3] Baiguera S, Kaiathur M and Macchiarini P (2011) Cancer Stem Cells in Lung and Pleural Malignancies CML *Lung Cancer* **4**(3):69-78.

[4] Lu B, Chiou S, Deutsch E and Loric A (2011) Cancer Stem Cells *J Oncol* Article ID 269437, doi:10.1155/2011/269437

[5] Michael H (2009) Cancer Stem Cells: A Guide for Skeptics *J Cell Biochem* **106**:745–749.

[6] Yazdani SO, Golestaneh AF, Shafiee A, Hafizi M, Omrani HAG and Soleimani M (2011) Effects of low level laser therapy on proliferation and neurotrophic factor gene expression of human schwann cells in vitro *J. Photochem. Photobiol., B* **107**(2012) 9–13.

[7] Gao X and Xing D (2009) Molecular mechanisms of cell proliferation induced by low power laser irradiation *J Biomed Sci* **16**(4): doi: 10.1186/1423-0127-16-4

[8] Houreld NN and Abrahamse H (2008) Laser light influences cellular viability and proliferation in diabetic-wounded fibroblast cells in a dose- and wavelength-dependent manner *Lasers Med Sci* **23**(1): 11-18.

[9] Mvula B and Abrahamse H (2013) The role of adipose derived stem cells, smooth muscle cells and low intensity laser irradiation (LILI) in tissue engineering and regenerative medicine *Cent Eur J Biol* **8**(4):331-336.

[10] Xiaodan W, Hong C and Xiangdong W (2012) Can lung cancer stem cells be targeted for therapies? *Cancer Treat Rev* doi:10.1016/j.ctrv.2012.02.013

[11] Pine SR, Marshall B and Varticovski L (2008) Lung cancer stem cells *Dis Markers* **24**(2008):257–266.

[12] Schwartz JD, Dumler F, Hafron JM, Wilson GD, Wolforth SC, Rooney MT, Li W and Zhang PL (2013) CD133 Staining Detects Acute Kidney Injury and Differentiates Clear Cell Papillary Renal Cell Carcinoma from Other Renal Tumors *ISRN Biomarkers*, available from: http://dx.doi.org/10.1155/2013/353598

[13] Wan-Ping H, Jeh-Jeng W, Chia-Li Y, Cheng-Che EL, Gow-Shing C and Hsin-Su Y (2007) Helium–Neon Laser Irradiation Stimulates Cell Proliferation Through Photostimulatory Effects in Mitochondria *J Invest Dermatol* **127**: 2048–2057.

[14] Croker AK and Allan AL (2008) Cancer Stem Cells: Implications for the Progression and Treatment of Metastatic Disease *J Cell Mol Med* **12**:374–390.

Cold atoms at the University of KwaZulu-Natal

M. Gumede[1], S. Dlamini[1], M. J. Morrissey[1] and F. Petruccione[1,2]

[1] Quantum Research Group, School of Chemistry & Physics, University of KwaZulu-Natal, Westville, Durban, South Africa.
[2] National Institute for Theoretical Physics, School of Chemistry & Physics, University of KwaZulu-Natal, Westville, Durban, South Africa.

E-mail: Petruccione@ukzn.ac.za

Abstract. The focus of this paper is based on the current experimental setup of a magneto-optical trap by the Quantum Research Group at University of KwaZulu-Natal (UKZN). In particular, presented are the details of the ultra-high vacuum system, optical system, and magnetic field generation that are implemented in the cold atom experiment. In addition to this, a fluorescence imaging system is described which can be used to determine the characteristics of the atom cloud.

1. Introduction

The concept of laser cooling was introduced in 1975 [1] and has since become an important part of experimental physics. These principles were utilised by Chu *et al*. in 1985 with the first creation of optical molasses, where atoms were cooled to a temperature of 240 μK using the radiation pressure of counter-propagating laser beams [2]. In the same year Migdall *et at*. expanded upon this idea even further where the laser-cooled atoms were trapped using a spherical quadrupole magnetic field at a temperature of 17 mK [3]. In 1987 Raab *et al* combined these two techniques of laser cooling and magnetic trapping to create a magneto-optical trap (MOT) [4]. This technique implied laser cooling to provide a velocity dependent force on the atoms reducing its temperature. The addition of the magnetic field, in combination with the circular polarisation of the beams, created a position dependent force allowing the cold atoms to be trapped in space.

The MOT has now become a standard tool by which to create a sample of cold atoms. Since its initial creation, cold atoms in a MOT have found applications in high precision metrology [5], atomic and molecular physics [6, 7], atom optics [8] as well as many other fields of research. The advancement of the cold atom and related fields has also lead to the creation of the first Bose-Einstein condensate (BEC) [9]. This has facilitated researchers to study the quantum mechanical nature of atoms on a macroscopic scale. It is the aim of the Quantum Research Group to develop Africa's first BEC experiment. However, the first step in achieving such a feat is to create a large number of laser-cooled atoms from which the BEC can be formed. Presented in this paper is the experimental setup that is currently implemented at UKZN for the creation of this cold atom reservoir. At a later stage techniques such as the compressed MOT and magnetic trapping will be implemented to increase the density of the atom cloud whereas techniques such as molasses and RF evaporative cooling will be implemented to reduce its temperature.

2. Experimental Setup

Cold atom physics is a multidisciplinary topic and therefore involves a wide range of experimental equipment; ultra-high vacuum (UHV) technology, laser frequency stabilisation, imaging systems, magnetic field coils, computer control system as well as the associated state-of-the-art electronics. Presented in this section will be the experimental setup currently at UKZN for the development of a cold atom experiment.

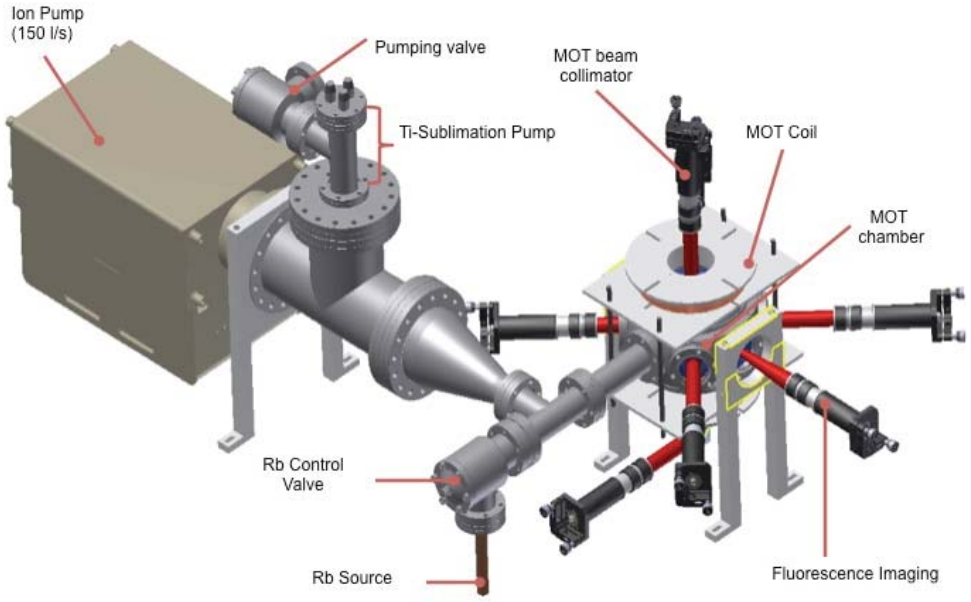

Figure 1: Illustration of the complete MOT system including the vacuum, magnetic coils and beam alignment systems.

2.1. Vacuum System

Although it is possible to achieve cold atoms in a MOT with a pressure of 10^{-6} mbar, the performance of the experiment in terms of steady state number of atoms, lifetime, and density, is dramatically limited by the atomic collision rate with the thermal background vapour. It is thus desirable to achieve an UHV system with a base pressure of ~10^{-9} mbar which allows the isolation of the atom cloud from the surrounding environment. The current vacuum system at UKZN is illustrated in Figure 1, along with other experimental components, and is based upon the industrial standard ConFlat (C.F.) flange technology for ultrahigh vacuum. The MOT chamber is a stainless steel octagonal chamber with seven 2.75" C.F. viewports around the octagonal surfaces and two 6" C.F. viewports on the top and bottom faces for optical access of laser beams.

In order to create the required vacuum pressure, a turbo-molecular pump (TMP), which is backed up by a scroll pump (Agilent Technologies, TPS Compact), is attached to the pumping valve. The scroll pump is initially used alone to decrease the pressure to approximately $2\text{x}10^{-2}$ mbar. The TMP is then initiated and a pressure of ~$1\text{x}10^{-7}$ mbar is achieved within a few hours. This is the limit of the TMP and therefore to decrease the pressure even further a bakeout procedure is used. This is where the entire vacuum system is slowly heated to ~300 ºC causing the internal contaminants to evaporate and be removed via the TMP. This temperature is maintained for approximately two days after which time the temperature is decreased slowly. At approximately 120 °C the pumping port is closed and both the TMP and the scroll pumps are switched off. The ion pump is switched on and thus the entire vacuum system is being pumped solely by the ion pump. Using this technique a base pressure of $2\text{x}10^{-9}$ mbar has been achieved.

The Rb dispenser comes in the form of a vacuum-sealed capsule which contains 1 mg of rubidium. The capsule is housed in a copper tube which is squeezed once the UHV environment is created thus breaking the capsule and exposing the rubidium to the vacuum environment. Due to the UHV, the rubidium metal constantly evaporates and thus the Rb vapour pressure can be controlled by varying the position of the control valve. The titanium sublimation pump is used after some period of time to decrease the base pressure if it has increased due to continuous diffusion of rubidium into the system.

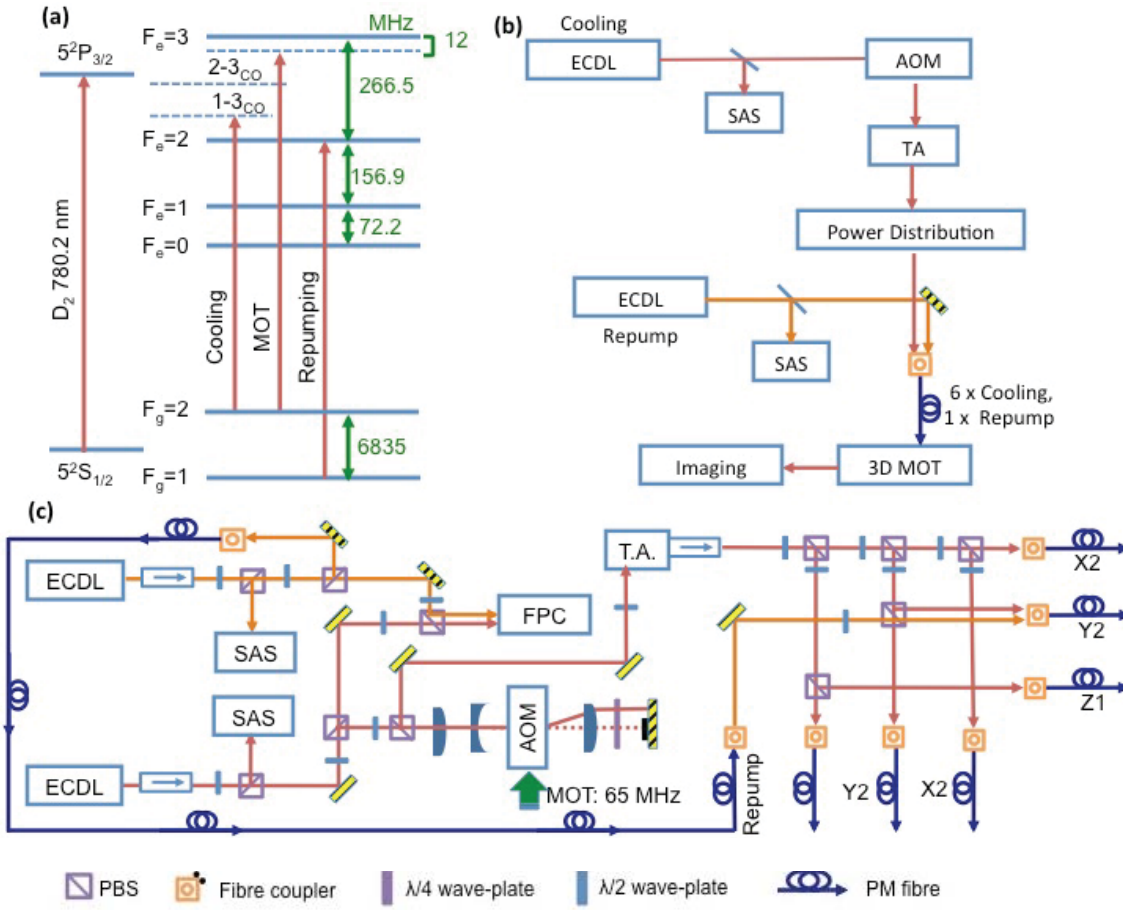

Figure 2: (a) The hyperfine structure of ^{87}Rb with all the necessary optical transitions used for the MOT and corresponding frequencies shown. (b) A block diagram showing an overview of the laser system layout. (c) Full schematic of laser system.

2.2. Laser System

Figure 2(a) shows the hyperfine structure of the $5^2S_{1/2} \rightarrow 5^2P_{3/2}$ ^{87}Rb transition as well as the required laser frequencies necessary to create a MOT. The closed $F_g = 2 \rightarrow F_e = 3$ transition is used as the cooling cycle. However, due to inaccuracies in the degree of circular polarisation in the cooling beam, a small percentage of atoms can decay down to $F_g = 1$ ground state. Once the atoms are in this atomic state, they are out of resonance with the cooling cycle and thus will no longer be cooled. To prevent this from occurring a second repumping laser is used to excite the atom to the $F_e = 2$ state from where it can decay to the $F_g = 2$ state and rejoin the cooling cycle. Therefore two separate extended cavity diode lasers (ECDL) are used to generate these frequencies (MOGLabs, ECD001). The ECDL configuration provides an output with a reduced linewidth and improved control of the laser at the expense of a slightly reduced output power. A schematic overview of the laser system can be seen in

Figure 2(b) and a more detailed version is illustrated in Figure 2(c). A small portion of the cooling laser output power (1 mW) is sent to a Doppler-free saturated absorption spectroscopy (SAS) setup [10] where it is locked to the $F_g = 2 \rightarrow F_e = (1\text{-}3)$ crossover transition. The majority of the laser power is passed through an acousto-optical modulator (AOM) (InterAction Corp, ATM Series) in a double pass configuration [11] shifting the frequency by a total of 120 MHz. The resultant laser frequency (labelled "MOT" in Figure 2(a)) is thus 12 MHz red-detuned from the cooling transition which compensates for the Doppler shift experienced in the atoms frame of reference. Approximately 15 mW of this laser beam is then injected into a tapered amplifier (TA) (Sacher Lasertechnik) creating an output power of up to 2 W. This power is split into the six cooling beams using a series of half wave-plates and polarisation beam splitters (PBS) as can be seen in Figure 2(c). These are coupled to polarisation maintaining (PM) optical fibres (Thorlabs, P3-780PM-FC-5) and sent directly to the vacuum chamber. By adjusting the half wave-plates the powers coupled to each fibre can be varied. The repumping frequency is provided by a separate ECDL laser locked directly to the $F_g = 1 \rightarrow F_e = 2$ repumping transition using a Doppler-free SAS setup. The repumping power is also coupled to one of the MOT fibres and thus coproprogates with this beam. A small portion of both the cooling and repumping beams are sent to a Fabry-Perot cavity (FPC) for analysis of their relative frequencies and laser locking status.

2.3 Magnetic Field Generation

The MOT operates with a spherical quadrupole magnetic field created by a pair of coils in anti-Helmholtz configuration where the current through the individual coils flow in opposite directions as shown in Figure 3(a). The magnetic field, B, along the axial direction can be determined using the Biot-Savart law:

$$B = \frac{\mu_0 NIa}{2}\left(\frac{1}{\left[1+(r_{coil}-x)\right]^{3/2}} - \frac{1}{\left[1+(r_{coil}+x)\right]^{3/2}}\right) \quad (1)$$

where r_{coil} is half the separation of the coils, a is the average radius of the coils, N is the number of loops per coil, I is the current passed through the coils and x represents the distance from the field point to the geometrical centre of the coils. The coils have a diameter of 125 mm, 700 loops of enameled wire of 1 mm diameter and are separated by a distance of 137 mm from centre-to-centre. Figure 3(b) shows the calculated magnetic field along the axial direction for each individual coil (green and blue) as well as the resultant magnetic field created by the coil pair (red) for an applied current of 1A. This creates an axial gradient of 10.7 (Gauss/cm)/A and a gradient of half this value along both of the radial axes. Figure 3(c) shows the contour plot of the spherical quadrupole field at the centre of the coils. The elongation of the contour plot along in the y-axis is due to the fact that its magnitude of the magnetic field gradient is half of that in the x-axis.

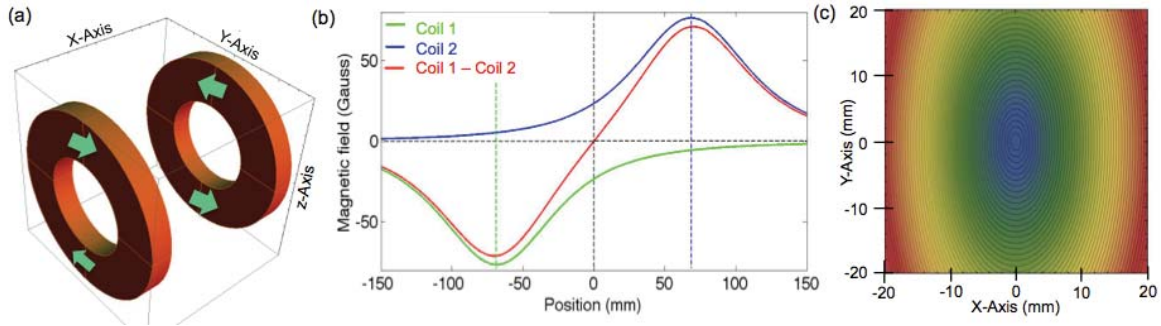

Figure 3: (a) MOT coils in anti-Helmholtz configuration. (b) Magnetic field generated by the MOT coils for a current of 1 A (c) contour plot of the spherical quadrupole field created by the MOT coils.

2.4 The Magneto-Optical Trap

The laser light is transported from the laser setup to the vacuum chamber via PM fibre as explained in Section 2.3. On exiting the fibre the beam freely expands and is subsequently collimated to a diameter of ~25 mm as is illustrated in figure 4. The circular polarisation is set with the aid of a quarter wave-plate. Three of the expanded beams are aligned mutually orthogonal to each other through the viewports of the MOT chamber. The three remaining laser beams are aligned to counter-propagate against these beams with orthogonal circular polarisations. Each beam is operated with a central intensity of approximately 3 mW/cm^2. The magnetic coils are place on the top and bottom view ports with the geometrical centre of the coils overlapping with the beam intersection. During normal operation of the MOT, the coils will generate an axial gradient of between 10 – 15 Gauss/cm.

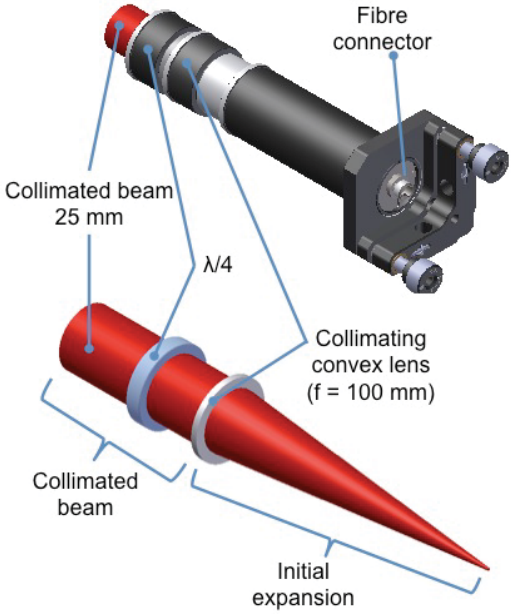

Figure 4: Expansion of the MOT beams

3. Fluorescence Imaging

In order to determine the parameters and characteristic of the cold atom cloud a fluorescence imaging system will be implemented. This is where the spontaneous emission from atoms within the MOT is focused onto the detection device. This is illustrated in Figure 5 where the fluorescence from laser cooled atoms is captured by a collimating lens and subsequently focused on to the detection device which will either be a CCD camera or a photodiode (PD). When the fluorescence is captured and focused onto a PD, the intensity of fluorescence is being directly measured. This is directly proportional to the number of trapped atoms and thus the real-time number of atoms in the MOT can be determined. This number of atoms, *N*, can be determined by:

$$N = \frac{4\pi P}{\Omega_{\mathrm{Im}} R_{sc}} \tag{2}$$

where P is the power falling onto the PD and Rsc is the scattering rate which depends on experimental parameters such as laser power and detuning of the cooling laser beams. The solid angle $\Omega_{\mathrm{Im}} = \pi D_{lens}^2 / 4 d_{\mathrm{Im}}^2$ is the angle subtended by the collimating lens of the imaging system where d_{Im} is the distance between the MOT and the first lens and D_{lens} is the diameter of the first lens. This

detection device also allows the detection of dynamic properties such as the loading time as well as lifetime. By measuring such characteristics, the MOT experimental parameter such as magnetic field gradient, laser power and detuning can be adjusted to optimise the performance of the atom cloud.

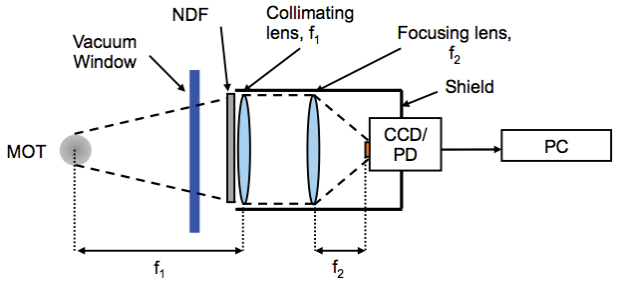

Figure 5: Fluorescence imaging apparatus used for the analysis of cold atom in a MOT.

When the cold atom fluorescence is focussed onto a CCD camera an image of the atom cloud can be taken. Through the analysis of this image a 2-D density profile can be determined. By applying Gaussian fits to the intensity profile of the image, the size and shape of the cloud is acquired.

4. Conclusion and Outlook

Presented here is the design and implementation of the cold atom setup in UKZN. The experiment is broken up into three different sections; the vacuum chamber, laser system and magnetic field generation. The details of each section are described as well as how they are combined to create a cold atom experiment.

The overall goal of the experiment is to create Africa's first Bose-Einstein condensation experiment. The cold atom experiment described here is a first step in creating this ultra-cold quantum gas. This will allow researcher to study the quantum mechanical nature of atoms and develop quantum technologies for future quantum information science.

5. Acknowledgements

We would like to acknowledge and thank the National Institute for Theoretical Physics as well as the CSIR National Laser Centre and the Department of Science and Technology for valuable financial support. We would also like to thank Enoch Chekure for technical and electronic support.

6. References

[1] Hänsch T W and Schawlow A L 1975 *Cooling of gases by laser radiation* Opt. Comm. **13,** 68.
[2] Chu S, Hollberg L, Bjorkholm J E, Cable A and Ashkin A 1985 *Three- dimensional viscous confinement and cooling of atoms by resonance radiation pressure* Phys. Rev. Lett. **55,** 48.
[3] Migdall L, Prodan J V, Phillips W D, Bergeman T H and Metcalf H J 1985 *First observation of magnetically trapped neutral atoms* Phys. Rev. Lett. **54,** 2596.
[4] Raab E L, Prentiss M, Cable A, Chu S and Pritchard D E 1987 *Trapping of neutral sodium atoms with radiation pressure* Phys. Rev. Lett. **59,** 2631.
[5] Udem T, Holtzwarth R and Hänsch T W 2002 *Optical frequency metrology*", Nature **416,** 233.
[6] Sesko D W, Walker T G and Wieman C E 1990 *Behaviour of neutral atoms in a spontaneous force trap* J. Opt. Soc. Am. B. **8,** 946.
[7] Donley E A, Claussen N R, Thompson S T and Wieman C E 2002 *Atom- molecule coherence in a Bose-Einstein condensate* Nature **417,** 529.
[8] Hughes I G, Barton P A, Roach T M, Boshier M G and Hinds E A 1997 *Atom optics with magnetic surfaces: I. storage of cold atoms in a curved 'floppy disk 1997* J. Phys. B: At. Mol.

Opt. Phys. **30,** 647.
[9] Anderson M H, Ensher J R, Andrews M R, Wieman C E and Cornell E A *Observation of Bose-Einstein condensation in a dilute atomic vapour* Science **269,** 198
[10] MacAdam K B, Steinbach A and Wieman C E 1992 *A narrow-band tunable diode laser system with grating feedback, and a saturated absorption spectroscopy for Cs and Rb* Am. J. Phys. **60,** 1098.
[11] Donley W A, Heavner T P, Levi F, Tataw M O, and Jefferts S R 2005 *Double-pass acousto-optic modulator system* Rev. Sci. Instrum. **76**, 063112.

Low Intensity Laser Irradiation (LILI) in Combination with Growth Factors in a Co-culture System Supports the Differentiation of Mesenchymal Stem Cells

B Mvula and H Abrahamse[1]
Laser Research Centre, Faculty of Health Sciences, University of Johannesburg, P.O. Box 17011, Doornfontein 2028, Johannesburg, South Africa

E-mail: habrahamse@uj.ac.za

Abstract. Mesenchymal stem cells have the capacity to differentiate into a variety of cell types that could potentially be used in tissue engineering and regenerative medicine. Low intensity laser irradiation (LILI) has been shown to have positive effects on different cell types, including a significant increase in cell viability and proliferation. Growth factors such as retinoic acid (RA) and transforming growth factor β1 (TGFβ1) have been shown to play important roles in the differentiation of cells. The aim of this study was to investigate whether LILI in combination with growth factors could induce the differentiation of adipose derived stem cells (ADSCs) co-cultured with smooth muscle cells (SMCs). The study used primary and continuous ADSC cell lines and a SMC line (SKUT-1). Cells were co-cultured at a ratio of 1:1, with and without growth factors and then exposed to LILI at 5 J/cm^2 using a 636 nm diode laser. The cellular morphology, viability and proliferation of the co-cultures were assessed over a period of 24h. The expression of the cell specific markers was monitored over the same period of time. Cell viability and proliferation increased significantly in the co-cultured groups that were exposed to laser alone, as well as in combination with growth factors. Furthermore, there was a significant decrease in the expression of stem cell markers in the ADSCs over time. The results indicate that LILI in combination with growth factors not only increases the viability and proliferation of co-cultured cells but also decreases the expression of ADSC stem cell markers. This could indicate the possible differentiation of ADSCs into SMCs.

1. Introduction

Mesenchymal stem cells have the capability of self-renewal and differentiation. They have a high capacity for proliferation [1]. Adipose derived stem cells (ADSCs) are mesenychmal stem cells that are easily isolated in large numbers and have the ability to differentiate into several lineages [2]. Studies have shown that ADSCs could be differentiated into smooth muscle cells (SMCs) [3] and neuron cells [2]. So far studies have indicated that ADSCs co-cultured with adipocytes could not differentiate into adipocytes [4] while ADSCs co-cultured with melanocytes, increased melanocyte proliferation and migration [5].

SMCs play a vital role in angiogenesis and vasculogenesis during development of the embryos [6] and are active components of intestinal, urinary, cardiovascular and reproductive systems. These cells have been differentiated from mesenchymal stem cells in the presence of growth factors [7]. SMCs are known to play a role in diseases like asthma, hypertension, cancer and arteriosclerosis [8].

[1]To whom any correspondence should be addressed

Low Intensity Laser Irradiation (LILI) has been shown to have positive effects such as increased viability and proliferation on different types of cells including ADSCs. It has had effects on these cells in combination with the growth factors as well [9, 10].

In rats, LILI promotes recovery from disuse muscle atrophy with satellite cell proliferation and angiogenesis [11]. Recent studies have also shown that LILI increased human periodontal ligament cell line at 670 nm [12]. It has also been recently found out that LILI up-regulates the genes involved in the electron transport chain in human fibroblast cells [13].

Growth factors have been shown to have an influence on cell differentiation, maturation, proliferation and apoptosis [14, 15]. Retinoic acid (RA) has been found to mediate neuronal differentiation from human embryonic stem cells [16]. Transforming Growth factor-Beta1 (TGF-β1) promotes smooth muscle differentiation of genes in fibroblasts of rats [17]. It has been shown to act as a key physiological factor in maintaining the stem cell reserve by up-modulating CD34 [18]. Studies involving another growth factor, TGF-β3, found that it could promote cartilage formation of ADSCs in a culture system [19].

This study aimed at investigating whether LILI in combination with growth factors could induce the differentiation of ADSCs co-cultured with SMCs. The success of the study could be beneficial in regenerative medicine and tissue engineering.

2. Materials and Methods

Primary and continuous ADSCs and a SMC cell line were used in this study. The cells were cultured individually to semi-confluency (ADSCs) and confluency (SMCs) and then co-cultured directly into 3.4 cm^2 diameter dishes in a ratio of 1:1. Growth factors (RA and TGF-β1) were added at concentration of 0.1 μM and 1 ng/ml respectively. The cells were then exposed to LILI at 5 J/cm^2 using a diode laser (National Laser Centre) with a wavelength of 636 nm. Six groups were established; co-cultured (CC - control group), co-cultured and LILI (CC+LILI), co-cultured and RA (CC+RA), co-cultured, RA and LILI (CC+RA+LILI), co-cultured and TGF-β1 (CC+ TGF-β1) and then co-cultured, TGF-β1and LILI (CC+ TGF-β1+LILI).

Cellular morphology was assessed using light inverted and fluorescence microscopy. Trypan blue and adenosine triphosphate (ATP) assays were used to assess cellular viability. Cell proliferation was analysed using optical density (OD) assay and flow cytometry assessed the expression of the markers CD29 (β1-Integrin) and CD90 (Thy-1) for ADSCs and heavy myosin chain for the SMCs. Statistically, the study used sigma plot 11.0. Significant differences between groups for viability, proliferation and expression of the markers were indicated by *$P \geq 0.05$, **$P \geq 0.001$and ***$P \geq 0.0005$.

3. Results

3.1 Cell morphology

Both types of cells were stained with CFDA-SE for morphological analysis. There was no difference in the morphology of ADSCs and SMCs (figure 1).

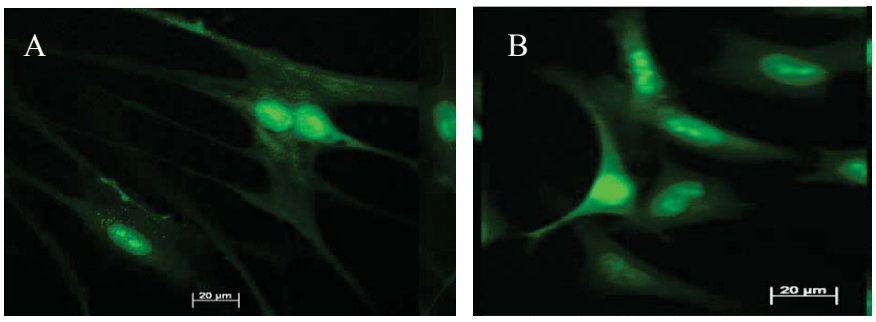

Figure 1: Showing the morphology of A - ADSCs and B - SKUT-1.Cells (SMCs) stained by carboxyfluorescein diacetate succinimidyl ester (CFDA-SE), a dye that stains the cytoplasm (green) and nucleus (bright green).

3.2 Cell viability and proliferation

ATP luminescence and trypan blue assays were used to analyse cell viability while OD assay was used for proliferation. There was an increase in cell viability and proliferation in cells that were co-cultured and irradiated as compared to cells that were co-cultured and with added growth factors. The co-cultured cells that were added with the growth factors and irradiated, increased in viability and proliferation as compared to those that were only co-cultured and with added growth factors (table 1, figure 2 and 3).

Table 1. Trypan blue assay showing percentage viability of the co-cultured cells. The black stars*indicate significant decrease in viability percentage of the co-cultures as compared to the control group (CC) while the black hash# indicate the significant increase.

Time Post Irradiation	CC	CC +LILI	CC + RA	CC+ RA + LILI	CC + TGF-β1	CC + TGF-β1 +LILI
24 h	74.5	72.8	66.3*	68.2	65.4*	71#

The co-cultures that were added with the growth factors (CC + RA and CC + TGF-β1) showed significant decreases in percentage viability as compared to the control group (CC) while the group that was co-cultured with added growth factor, TGF-β1 and irradiated (CC + TGF-β1 +LILI) showed a significant increase in percentage viability as compared to its control (CC + TGF-β1).

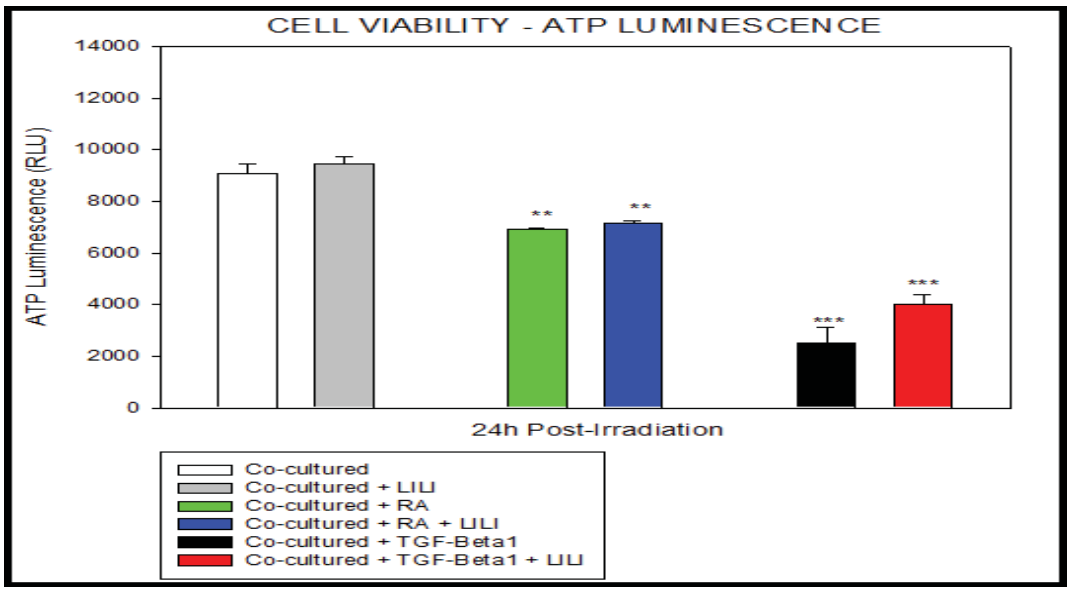

Figure 2: Cell viability as analysed by ATP luminescence at 24h after irradiation for the different six groups. There was an increase in viability in cells that were co-cultured and irradiated while a decrease was observed in groups that had growth factors. However there was an increase in viability in cells that had growth factors and irradiated as compared to those that had growth factors only.

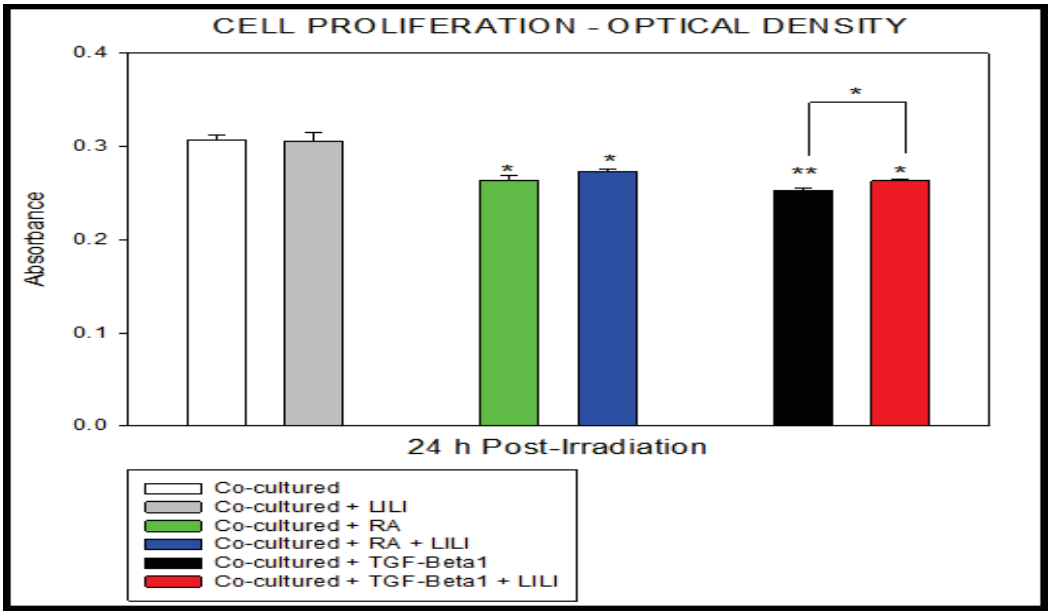

Figure 3: OD results showing cell proliferation at 24h after irradiation for the different six groups. There was a significant .decrease in proliferation in groups with added growth factors as compared to the control groups at 24 h.

3.3 Expression of the markers

Expression of the ADSCs markers showed a decrease in cells that were co-cultured with added growth factors and irradiated (figure 4) while there was an increase in expression of the SMC marker (figure 5) and the increase was more in cells that were co-cultured, with added growth factors and irradiated cells.

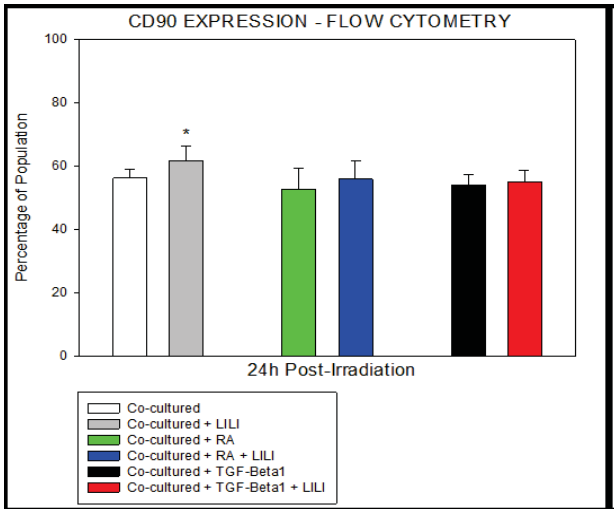

Figure 4: There was a decrease in the expression CD90, an ADSCs marker over the period of 24h in co-cultures with added growth factors though the decrease was not significant. But there was a significant increase in the expression of CD90 in

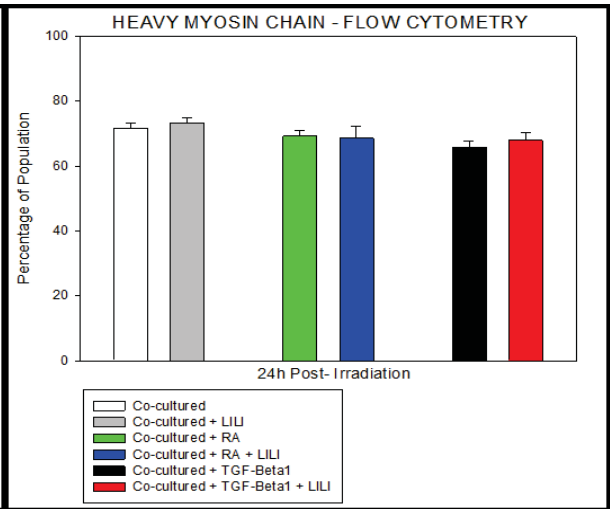

Figure 5: Heavy myosin chain, an SMC marker decreased in the co-cultures that were added with the growth factors but the decrease was not significant as shown in the figure above over the period of 24h.

4. Discussion and Conclusion

The findings in this study agree with those from other studies which found that LILI could increase viability and proliferation of cells [3, 9, 10]. Growth factors such as RA and TGF-β have been used to induce differentiation in previous studies [16]. TGF-β1 has been used in the differentiation of human mesenchymal stem cells into osteoblasts and adipocytes [20]. Recent studies used TGF-β to induce differentiation of smooth muscle cells from human embryonic stem cells [21]. Chen and Lechleider [22] in their study, induced the differentiation of a neural crest stem cell line into smooth muscle cells with TGF-β. The current study found out that there was a decrease in the expression of the ADSC markers in the co-cultures with added growth factors. However, more investigations are required to prove that this could indicate a possible differentiation of ADSCs to SMCs. If this is achieved, the co-culture system with LILI and growth factors can be a promising method in research for treatment applications in tissue engineering and regenerative medicine.

References

[1] Pittenger M F *et al* 1999 *Sci* **284** 143-147
[2] Huang T, He D, Kleiner G and Kuluz J 2007 *J Spinal Cord Med* **30** S35-S40
[3] De Villiers J A, Houreld N N and Abrahamse H 2011 *Stem Cell Rev Rep* **7(4)** 869-882
[4] Song K, Li W, Wang H, Wang Ha, Liu T, Ning R and Wang L 2012 *Appl Biochem Biotechnol* **167** 2381-2387
[5] Kim J Y, Park C D, Lee J H, Lee C H, Do B R and Lee AY 2012 **92(1)** 16-23 Acta Derm Venereol
[6] Carmeliet P 2000 *Nat Med* **6** 389-395
[7] Rodriguez L V, Alfonso Z, Zhang R, Leung J, Wu B and Ignarro L J 2006 *PNAS* **103(32)** 12167-12172
[8] Sinha S *et al* 2006 *Stem Cells* **24** 1678-1688
[9] Mvula B, Mathope T, Moore T and Abrahamse H 2008 *Lasers Med Sci* **23(3)** 277-282
[10] Mvula B, Moore T and Abrahamse H 2010 *Lasers Med Sci* **25** 33-39
[11] Nakano J, Kataoka H, Sakamoto J, Origuchi T, Okita M and Yoshimura T 2009 *Exp Physiol* **94(5)** 1005-1015
[12] Huang T, Liu S, Chen C, Shie M and Kao C 2013 *Photomed Laser Surg* **31(2)** 72-77
[13] Masha R, Houreld N N and Abrahamse H 2013 *Photomed Laser Surg* **31(2)** 47-53
[14] Asson-Batres M A, Smith W B and Clark G 2009 *J Nutr* **139** 1067-1072
[15] Baharvand H, Mehrjardi N Z, Hatami M, Kiani S, Rao M and Haghighi M M 2007 *Int J Dev Biol* **51** 371-378
[16] Tong P D and Andrews P W 2010 **80(1)** 20-30
[17] Kennard S, Liu H and Lilly B 2007 *J Biol Chem* **283(3)** 1324-1333
[18] Batard P, Monier M, Fortunel N, Ducos K, Sansilvestri-Morel P, Phan P, Hatzfeld A and Hatzfeld J A 2000 *J Cell Sci* **113** 383-390
[19] Hashemibeni B, Razavi S, Esfandiary E, Karbasi S, Mardani M and Nasresfahani M 2008 *J Basic Med Sci* **11(1)** 10-17
[20] Mimura *et al* 2011 *Int J Dev Biol* **55** 181-187
[21] Guo X, Stice S L, Boyd N L and Chen S Y 2012 *Am J Pysiol Cell Physiol* **304** C289-C298
[22] Chen S and Lechleider R J 2004 *Circ Res* **94** 1195-1202

Design and evaluation of a low-cost Photovoltaic system with semi-diffuse structured aluminium reflectors

Joseph Simfukwe *[1], Kaumba G. Chinyama [1], Prospery Simpemba [1], Sylvester Hatwaambo[2],

[1]Copperbelt University, Department of Physics, Box 22692, Kitwe, 10101, Zambia.

[2]University of Zambia, Department of Physics, Box 32379, Lusaka, 10101, Zambia.

* Corresponding Author: Tel: +260 955 958573
Email: josephsimfukwe@yahoo.com

Abstract: The current energy production from fossil fuels and nuclear materials has environmental drawbacks. These drawbacks include the creation of nuclear waste, and the pollution associated with fossil fuels which lead to global warming and climate change. It is apparent that an alternative and sustainable source of energy must be found. A potential solution to this problem is solar electricity. Currently, solar panels are expensive and hence un-economical for most buyers**.** The use of solar concentrators creates a potential for less expensive electricity because concentrators raise the amount of incident radiation over a relatively small area of the absorber. The reduction in cost is achieved by reducing the module area and the use of low-cost reflectors. However, specular reflectors cause high concentrated heating and form hot spots on the solar module cells. These hot spots are a result of uneven concentration of radiation. The overall effect is the reduced fill-factor and overall efficiency of the system. In this paper, we report an alternative solution to the problem of non-even illumination by using locally available low-cost semi-diffuse reflector with four different groove orientations scribed on it so as to scatter the radiation flux onto the module. The groove orientations were plain sheet (NG), horizontal grooves (HG), vertical grooves (VG), and the crisscross groove (CG) orientations. Our results show that the locally purchased semi-diffuse aluminium structure can be used as a booster reflector compared with the commercial high specular reflector.

Key words: Semi-diffuse, specular, fill-factor, non-even illumination, low-concentration

1. Introduction

The costs of solar panels compared to the amount of power they produce make their purchase un-economical for most end-users**.** The use of solar concentrators create a potential for producing less expensive electricity by replacing expensive solar cell area with inexpensive optical materials such as plastic refractors or metal reflectors[1, 2]. In this paper we address two of the problems faced with concentrating photovoltaic systems namely; non-even illumination and use of expensive lenses and specular materials as reflectors by designing, constructing and evaluating a low concentrator system, using locally available low-cost semi-diffuse aluminium structure reflector with four different groove

orientations scribed on it to improve on the fill-factor (FF) of the module for low cost electricity. A solar module with a high fill-factor is able to produce high power for a longer period of time. Therefore, by improving the FF of the module we are increasing both the power output and the durability of the module [3].

2. Experimental details

2.1 Design and construction of the compound parabolic concentrator (CPC)

We first designed the Compound Parabolic concentrator (CPC) using the standard polar co-ordinate system proposed by Winston [4, 5]. The coordinates of the parabola were generated from equations (1) and (2), where a is the half width of the exit aperture of the CPC, θ is the acceptance half angle of the CPC, $f = a(1+\sin\theta)$ is the focal length of the CPC and ϕ is the angle subtended by axis of the parabola and the absorber normal. The value of a which is the half width of the exit aperture was determined after deciding on the size of the solar module string to be used after which the acceptance half angle θ of the CPC was decided while ϕ varied from 5° to 107° in our case. The determined values of a and θ in this case were (a=5cm and θ=15°).The x and y co-ordinates generated form equations (1) and (2) were then plotted on the graph paper to design the CPC which was later constructed. Figure 1 shows the CPC designed (a) and the actual constructed Compound Parabolic Concentrator (b) used for the current-voltage (I-V) measurements.

$$x = \frac{2f\sin(\phi-\theta)}{1-\cos\phi} - a \tag{1}$$

$$y = \frac{2f\cos(\phi-\theta)}{1-\cos\phi} \tag{2}$$

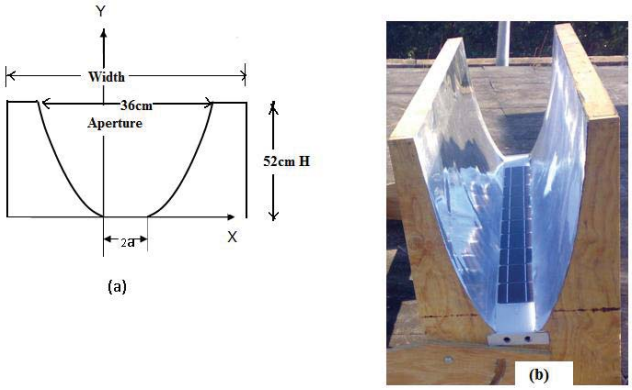

Figure 1: Shows the CPC design from polar co-ordinates into the X-Y co-ordinates system (a) and the actual compound parabolic concentrator constructed (b).

2.2 Spectral reflectance of structured aluminium

An ideal reflector material for solar electricity production should have a relatively high reflectance in visible and ultra violet regions of the solar spectrum and to maintain this relative high reflectance for the entire life of the solar system [6]. In this experiment we used one reflector material (semi-diffuse aluminium structures), but with four different orientations of the grooves namely; plain (NG) (no grooves), horizontal grooves (HG) vertical grooves (VG) and criss-cross groove (CG) orientations as shown in figure 2. The groove sizes ranged between 2mm to 3mm. Our aim was to determine which of these four orientations was able to provide uniform illumination and a better fill-factor improvement using the named reflector .The optical properties of this reflector material were obtained from the Perkin Elmer spectrophotometer lambda 19. The total integrated reflectance (TIR) was calculated from equation (3). The TIR gives the overall reflectance of the material the property that shows how much flux the material is able to scatter.

$$R_s = \frac{\sum_{305nm}^{2450nm} R(\lambda)G(\lambda)\Delta\lambda}{\sum_{305nm}^{2450nm} G(\lambda)\Delta\lambda} \qquad (3)$$

where $R(\lambda)$ is the wavelength-dependent spectral property of a material, such as responsivity, transmittance, reflectance, absorptance while $G(\lambda)$ represents the solar spectral irradiance, and, R_s ,is the mean value of the property $R(\lambda)$.

The reflectance $R(\lambda)$ of the reflecting samples were measured using the Perkin Elmer Lambda 19 Spectrophotometer fitted with an integrating sphere. These values had to be normalized by making reference to the standard solar spectral irradiance $G(\lambda)$ and the total integrated reflectance was then calculated from equation (3) for each reflecting material.

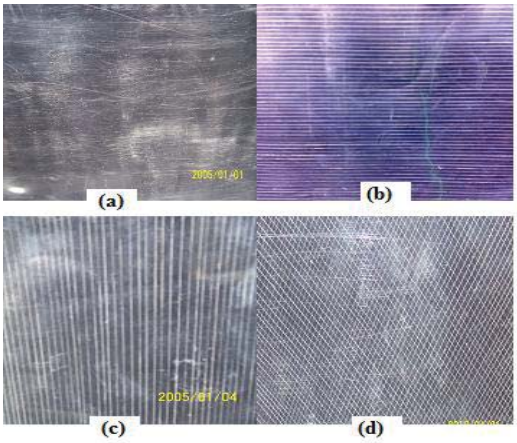

Figure 2 showing the four different orientations of the grooves on the semi-diffuse structured aluminium: (a) plain sheet (NG) (b) horizontal grooves (HG) (c) vertical grooves (VG) and (d) criss-cross grooves (CG)

2.3 Current-voltage (I-V) curve measurements.

The current and voltage generated by the module under concentration was measured using the current-voltage tracker instrument obtained from Vattenfall Utveckling in Sweden. For each reflector material, short-circuit current *Isc*, open-circuit voltage V_{oc}, power maximum P_m, maximum current I_m, and the maximum voltage V_m were extracted from each I-V curve. The fill-factor (FF) was evaluated from equation (4).

$$FF = \frac{I_m.V_m}{I_{sc}.V_{oc}} = \frac{P_m}{I_{sc}.V_{oc}}. \quad (4)$$

The reference fill-factor measurement was done by taking the I-V curve reading when the module was outside the concentrator. All measurements were done at normal angle of incidence (0^o), i.e when the irradiance was perpendicular to the plane of the module when placed outside the concentrator or inside the concentrator. Hence, all the calculated fill-factors were compared from the reference fill-factor.

3. Results

3.1 The Total Integrated Reflectance(TIR) Results

Table 1*:* Shows the total integrated reflectance (TIR) for the four types of reflector materials.

Orientation	Total Integrated Reflectance (TIR)
NG	**89%**
HG	**85%**
VG	**82%**
CG	**88%**

From Table 1, it is observed that the plain sheet (NG) had the highest value of TIR of 89% followed by the criss-cross grooves (CG) orientations with 88%, the horizontal grooves (HG) orientation was the third highest with 85% while the vertical orientations of the grooves on the aluminium structure was the least with 82%, as calculated from equation (4). The error is less than 1% in the reflectance.

3.2 Fill-factor comparison at normal incidence (0°)

The results for the fill-factor comparison revealed that the criss-cross grooves (CG) gave the highest fill-factor followed by the horizontal grooves (HG) and then the vertical grooves (VG). The plain sheet had the least fill-factor. The results also show that the drop in the fill-factor from the reference for the criss-cross grooves and the horizontal grooves orientations was about 3%, while that of the vertical grooves (VG) and the plain sheet was 8% and 12% respectively. The better results of fill-factor for the criss-cross grooves and the horizontal grooves can be attributed to the fact that, the orientation of the grooves in this manner provided evenly scattering of the solar flux on the module thereby reducing the

hot spot formation and causing an even distribution of current within the solar cell . On the other hand, the reduced fill-factor for the plain sheet and the vertical grooves can be expalined in terms of the non-uniform irradiance leading to non even distribution of current within the solar cell. This causes hot-spot formation that leads to the overall degradation of the module.

3.3 Power comparison at 0° (normal)

Figure 4 shows the comparison of power at 0º with VG and NG giving the highest power output, but these are a result of high currents which cause hot spots and an overall reduction in the performance of the module. Hot-spot heating occurs when a large number of series connected cells cause a large reverse bias across the shaded cell, leading to large dissipation of power in the poor cell. Essentially the entire generating capacity of all the good cells is dissipated in the poor cell. The enormous power dissipation occurring in a small area results in local overheating, or "hot-spots", which in turn leads to destructive effects, such as cell or glass cracking, melting of solder or degradation of the solar cell [3].

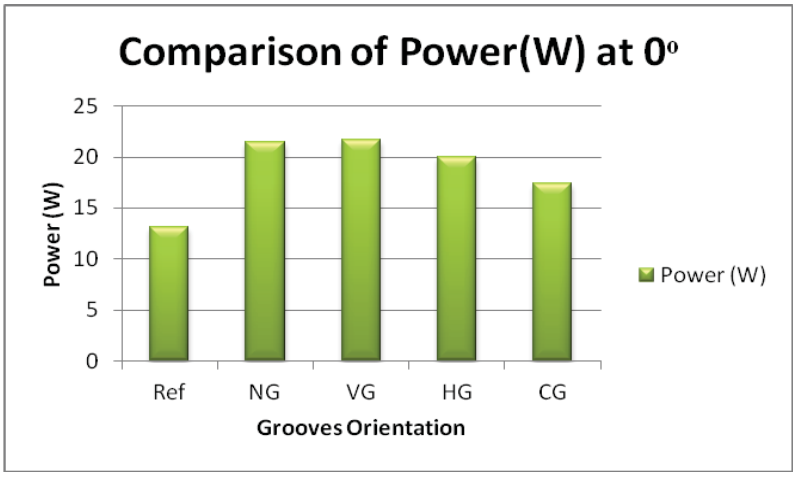

Figure 4: Bar charts showing comparison of the power for the four different grooves orientations and the reference (Ref) (without concentration).

4. Discussion and Conclusions

The performance of the CPC constructed using the locally available materials has been analyzed and the results show that the locally purchased semi-diffuse aluminium structure can be used as a booster reflector in low cost photovoltaic system. The results also show that the criss-cross groove and the horizontal groove orientations were found to be the best orientations for the fill-factor improvement since they had only a 3% drop in fill-factor from the reference. The two orientations were able to scatter the solar flux evenly across the solar cell module. It is the even scattering that causes uniform distibution of currents within the solar cell thus reducing the hot spot formation. However, between the two orientations we would recommend the horizontal grooves(HG) because it is less costly when making the grooves but it gives a better fill-factor as much as that of the criss-cross grooves. The horizontal grooves

also gave a higher power increase of 52% compared to 33% for the criss-cross grooves. We further point out that our results compare well with similar works done by Hatwaambo et al, [2] on Rolled Aluminium, Miro, and Aluminium Foil.

Acknowledgements

My deep and heartfelt appreciation to Dr. Hatwaambo Silvester under whose guidance, patience, and genuine criticism, this work was successfully done. I am also indebted to the Solar Energy Materials (SEM) Project in the Department of Physics at the University of Zambia (UNZA) in conjunction with the International Science Programme (ISP) of the Uppsala University in Sweden for granting me a scholarship. Many thanks to the Copperbelt University (CBU) management for sponsoring my trip to attend SAIP 2013 where this paper was presented.

References

[1] Hatwaambo S 2008 et al, *Angular Characterization of low concentrating PV-CPC Using low-cost reflectors, Solar Energy Materials & Solar Cells* Vol. **92**, 1347-51.(Elsevier).

[2] Hatwaambo S, Hakansson H, Roos A and Karlson B 2009 , *Mitigating the non-uniform illumination in low concentrating CPCs using structured reflectors, Solar Energy Materials & Solar Cells* Vol. **93**,2022-24 (Elsevier).

[3] http://pvcdrom.pveducation.org/MODULE/Hotspot.htm

[4] Welford W T and Winston R 1989 *High Collection Non-imaging Optics*,(Academic Press).

[5] Winston R, Miñano J C and Benitez P 2005 *Non-imaging Optics* (Elsevier Academic Press).

[6] Brogren M 2004 *Optical Efficiency of Low –Concentrating Solar Energy Systems with Parabolic Reflectors* (PhD. Thesis, Uppsala University, Sweden)

Division D1 - Astrophysics

Dust in the Radio Galaxy and Merger Remnant NGC 1316 (Fornax A)

B D Asabere[1], C Horellou[2], H Winkler[1], T Jarrett[3] and L Leeuw[4]

[1] Department of Physics, University of Johannesburg, P.O. Box 524, 2006, Auckland Park, Johannesburg, South Africa

[2] Department of Earth and Space Sciences, Chalmers University of Technology, Onsala Space Observatory, SE-439 92 Onsala, Sweden

[3] Department of Astronomy, University of Cape Town, Private Bag X3, Rondebosch 7701, South Africa

[4] Department of Interdisciplinary Research, University of South Africa, Pretoria, South Africa

E-mail: bd.asabere@gmail.com

Abstract. We present dust maps of NGC 1316 (Fornax A), a well-studied early-type galaxy located in the outskirts of the Fornax cluster. We used the Large APEX BOlometer CAmera (LABOCA), operating at 870 μm with an angular resolution of 19.″5 on the Atacama Pathfinder EXperiment (APEX) 12 m submillimeter telescope in Chile and the Wide-field Infrared Survey Explorer (*WISE*). *WISE* observes in four mid-infrared bands centered at 3.4, 4.6, 12 and 22 μm with angular resolutions ranging from 6 to 12″. The *WISE* and LABOCA maps reveal emission from dust in the central 2′ of NGC 1316. The disturbed optical morphology with many shells and loops, the complex distribution of molecular gas and our dust maps are evidences of past merger activity or gas accretion in the galaxy. Combining the LABOCA flux measurement with existing mid- and far-infrared measurements, we estimate the temperature of the cold (∼20 K) and warm (∼55 K) dust components in the galaxy. This study will be extended to other southern radio galaxies and merger remnants. Those galaxies are good targets for future observations at higher angular resolution and sensitivity with *ALMA* to probe the interaction of the radio jets with the dusty molecular gas near active galactic nuclei.

1. Introduction

Dust is ubiquitous in the interstellar medium (ISM) of galaxies but it constitutes only about 1% of the total mass of the ISM. Notwithstanding, dust plays an important role in galaxies: it is a tracer of star formation and stellar evolution, and contributes to the evolution of galaxies [1, 2]. Interstellar dust grains span a wide range of sizes (∼0.001 - 0.25 μm) and temperatures (∼20 - 200 K). Dust causes extinction of starlight: it dims and reddens the galaxy light at ultraviolet (UV) and optical wavelengths, but re-radiates about 90% of the absorbed galaxy energy into the infrared and submillimeter wavebands. Interstellar dust can thus be observed in different galactic environments by mapping the re-radiated emission at mid-infrared, far-infrared and submillimeter wavelengths [3, 4].

Contrary to the belief that early-type galaxies are "red and dead" with little interstellar medium and star formation [5, 6], recent studies have revealed that more than 30% of nearby early-type galaxies are rich in molecular clouds, gas and dust [7, 8] due to past merger events that contribute to interstellar and nuclear activities.

NGC 1316 (Fornax A, PKS 0320-37, Arp 154) is a peculiar dusty early-type radio galaxy located in the outskirts of the Fornax cluster; roughly 2 Mpc from the core of the cluster and at an adopted distance of 21.0 Mpc [9]. It is one of the two most luminous galaxies in the Fornax cluster and the third most powerful nearby radio source besides Centaurus A and Virgo A. It has a pair of radio lobes lying outside the optical galaxy [10] and a two-sided radio jet in the central 30″ [11]. The galaxy has a disturbed outer morphology with numerous loops, ripples, tidal tails and shells [12, 13, 14]. Spectroscopy of the brightest globular clusters suggests that a major merger took place about 3 Gyr ago [15]. Other studies [13, 16] peg a merger event about 0.5 Gyr ago. The abundance of molecular gas and the different kinematics of the stars and the gas [17, 18] support the idea of a recent merger with a companion gas-rich galaxy.

NGC 1316 displays prominent dust patches in the central 2′.4 x 2′.4, with an inner dust lane of about 2′ oriented along the apparent optical minor axis at a position angle of $\sim 140°$ [19, 20]. Massive dust-heating stars are being formed in the galaxy [21]. The amount of dust estimated from optical extinction measurement is $\sim 2.13 \times 10^5 M_\odot$, that from *IRAS* total flux densities is $2.11 \times 10^6 M_\odot$ and the estimate from the integrated flux densities at *Spitzer/MIPS* is $3.2 \times 10^6 M_\odot$ [22, 23]. CO emission has been detected in two regions ($\sim 30''$ southeast and $\sim 45''$ northwest) of the nucleus, with corresponding molecular hydrogen masses of $0.9 \times 10^8 M_\odot$ and $2.2 \times 10^8 M_\odot$ respectively [17]. X-ray observations in the energy range 0.3 - 8.0 keV have revealed a low-luminosity AGN ($L_X \sim 5.0 \times 10^{39} erg\ s^{-1}$) [24, 25, 26]. AGN feedback may inhibit star formation [27]. NGC 1316 is therefore a self-contained laboratory for studying galaxy formation and evolution, gas settling toward equilibrium after a merger activity, and feedback from AGN on the star-forming ISM.

2. Observations and Data Processing

NGC 1316 was observed in June 2012 for 8 hours and 10 minutes with LABOCA [28], a bolometer camera operating on the APEX 12 m submillimeter telescope [29] at 5105 m elevation in the Atacama desert in Chile, one of the driest places on Earth. LABOCA observes in the continuum at a central wavelength of 870 μm (345 GHz) in total-power scanning observing mode. The angular resolution is 19.″5 and the field of view is 11.′4. Its passband has a full width half maximum of about 60 GHz ($\sim$150 μm) to match the corresponding atmospheric window. The version 2.12-2 of `Crush-2` [30] was used to reduce the data and produced the full and detailed map of the dust. `Crush-2` a is comprehensive bolometric data reduction utility and imaging software package for ground-based telescopes. Iteratively, `Crush-2` removed correlated noise from the raw data in the digitized time-streams, identified and flagged problematic data pixels and provided clean and independent bolometer signals in the individual ($\sim$70) scans, which were then co-added to produce the final maps. The flux measurement, signal-to-noise ratio and the root-mean-square analyses and estimations were all done with `Crush-2`.

WISE (Wide-field Infrared Survey Explorer: [31]) is a space infrared telescope that mapped the whole sky in four mid-infrared bands at central wavelengths of 3.4, 4.6, 12 and 22 μm labeled $W1$ to $W4$. The angular resolutions are 6.1, 6.4, 6.5 and 12″ respectively [32]. The *WISE* All-sky Data Products and Atlas Images are archived by the NASA IPAC (Infrared Processing and Analysis Center) in the IRSA (Infra-Red Science Archive). However, reduced drizzled and cleaned *WISE* images of NGC 1316 in the four bands were used for the study (see [32, 33]). The `ellipse` task in the IRAF (Image Reduction and Analysis Facility) isophote package was used to extract the flux information in the respective *WISE* bands following the guidelines provided in the *WISE* Explanatory Supplement [33, 34].

3. Results and Discussion

As one moves to longer wavelengths ($\lambda > 2$ μm), stars contribute less and less to the observed emission, and the ISM dust component begins to dominate. The $W1$ and $W2$ bands (3.4 and 4.6 μm) are nearly extinction-free bands that are mostly sensitive to the evolved stellar population: the Rayleigh-Jeans part of the black-body emission of cool stars ($T > 2000$ K). The emission in $W3$ is dominated by polycyclic aromatic hydrocarbons (PAHs) at 11.3 μm and warm continuum dust emission from small grains. The $W4$ band (22 μm) is more sensitive to the warm dust emission, which comes from photon-dominated regions (or ultraviolet radiation fields) in the ambient ISM. LABOCA, at 870 μm, is sensitive to cold dust that tends to dominate the bolometric luminosity in star-forming galaxies.

3.1. Flux measurements

The measured fluxes are given in Table 1. The values measured in the four *WISE* bands are comparable to those measured in the respective Spitzer bands (at 3.6, 4.5, 8 and 24 μm; see [20]) for our chosen elliptical apertures. The *WISE* flux measurements were obtained by performing elliptical aperture photometry with the `ellipse` task in the IRAF isophote package to get the total counts in each band (in data number (DN) units) after background subtractions, and applied the respective band corrections [31, 33]. The associated errors were estimated from the corresponding uncertainty maps [34]. The measured flux in each *WISE* band came from an ellipse centered on the image (with position coordinates (03h 22m 41.7s, -37° 12′ 30″)). Both the ellipticities and position angles were held constant during the elliptical isophotal fittings (see Table 1). The LABOCA flux was estimated in a circular aperture of about 2′.

3.2. Dust maps

We used the software `Galfit` [35] to identify the stellar component. We perform a two-dimensional fit of the superposition of a Sérsic model, a point-source and sky background to the $W1$ image, following the same method as [20] in their analysis of *Spitzer* images. We then fixed all the parameters of the Sérsic model from the $W1$ fit except the amplitude and center, and did a fit to the $W3$ image (see Figure 1a). The $W3$ dust map of the galaxy, shown in Figure 1b, was obtained by subtracting the Sérsic model (identified as the stellar contribution) and the sky component. LABOCA dust contour map is shown in Figure 2. The images in Figures 1 and 2 were generated using the `kvis` image display and manipulation program [1].

3.3. Spectral energy distribution

We did a fit to published mid-infrared flux measurements and to our LABOCA submillimeter measurement, to model the SED of NGC 1316, as shown in Figure 3. We modeled the dust emission as the superposition of two modified black-body components, at different temperatures,

$$S_\nu = A_w \lambda^{-\beta_w} B_\nu(T_w) + A_c \lambda^{-\beta_c} B_\nu(T_c) \quad (1)$$

where β_w and β_c are the dust emissivity indices for the respective warm (T_w) and cold (T_c) temperature components. We fixed the emissivity indices to 2. $B_\nu(T)$ is the Planck function at the temperature of interest, A_w and A_c are amplitudes [36]. The inferred temperature values are $T_w = 55.0 \pm 4.2$ K and $T_c = 21.7 \pm 1.3$ K, in agreement with previous estimates [36].

[1] http://www.atnf.csiro.au/computing/software/karma

Table 1: Flux measurements. The first column lists the four *WISE* bands and LABOCA with their corresponding central wavelengths in parenthesis. In the elliptical isophotal fits, fluxes were measured within ellipses with *semi-major axes (SMA)* lengths shown in column 2 at position angle of 34.7° for the *WISE* bands. The LABOCA flux was estimated in a circular aperture of about 2′. The axis ratios listed in column 3 were derived by dividing the semi-minor axis by the semi-major axis lengths. The effective radii in columns 4 were also obtained from the isophotal fits with the `ellipse` task in the isophote package of IRAF. The total counts in each elliptical aperture were converted into integrated fluxes, given in column 5, after extended aperture corrections [33, 34].

Band	SMA (arcsec)	Axis ratio	Effective radius (arcsec)	Flux density (Jy)
W1 (3.4 μm)	766.6	0.645	103.3	2.870±0.031
W2 (4.6 μm)	586.8	0.645	94.5	1.501±0.016
W3 (12 μm)	187.9	0.645	60.5	0.451±0.005
W4 (22 μm)	101.6	0.645	39.4	0.342±0.004
LABOCA (870 μm)	-	-	-	0.113±0.015

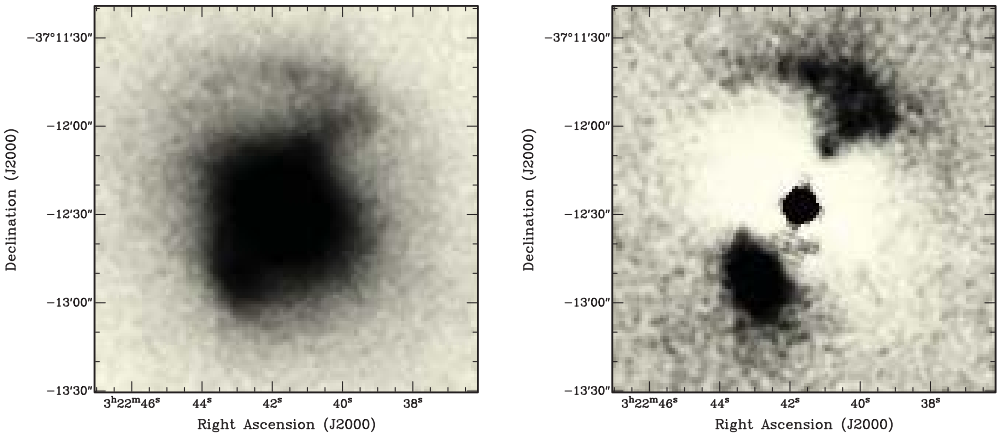

(a) W3 (12 μm) image

(b) $W3$ dust map

Figure 1: *(a)* W3 (12 μm) map of NGC 1316 and *(b)* the $W3$ dust map of the galaxy obtained after subtraction of the stellar component modeled as a Sérsic model and sky component. The northern dusty "arc" and the southern dust concentration seen in the *HST* and in the *Spitzer* images [20] are apparent.

4. Conclusion

We have presented an ongoing analysis of the dust emission in the galaxy NGC 1316 based on *WISE* and LABOCA measurements in the mid-infrared and the submillimeter wavelengths. The $W3$ dust map revealed in this study, represents the PAHs (at 11.3 μm) dust component of the galaxy, which is shown for the first time in this galaxy. The central region of the $W3$ dust map appears over-subtracted. Separation of the stellar component from the dust is crucial and will be refined. Recently, [37] presented LABOCA observations of NGC 1316. Our 870 μm flux

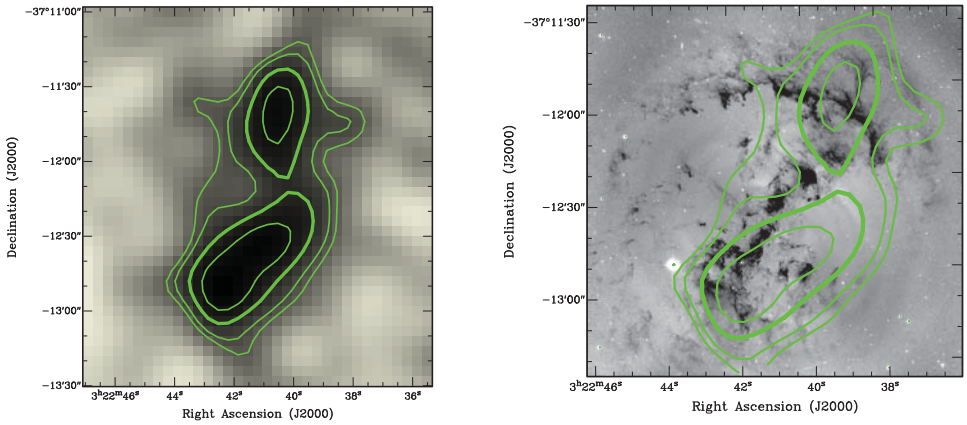

(a) LABOCA dust map (b) LABOCA dust map on *HST* image

Figure 2: *(a)* LABOCA 870 μm image of NGC 1316 in green contours overlaid on the greyscale image. The contours range from 3 to 6 times the noise level, which is equal to 2.5 mJy/beam. The angular resolution of the image is $28''$. Figure *(b)* the *HST* image in grey-scale and LABOCA image in green contours. The two peaks detected in the submillimeter map correspond roughly to the dust lanes seen in extinction in the HST image.

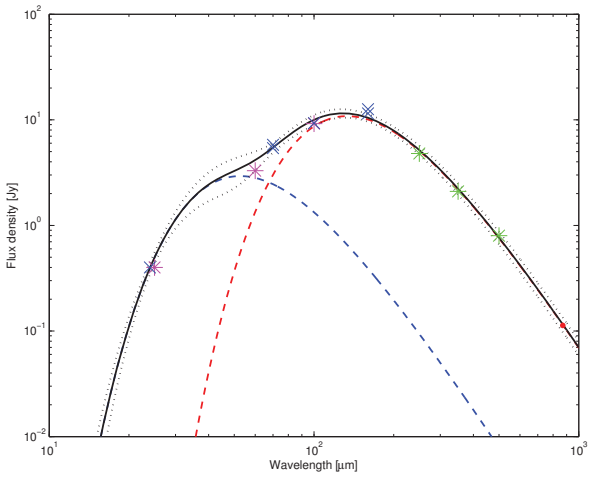

Figure 3: Mid-infrared to submm spectral energy distribution of NGC 1316. The points are the measurements listed in Table 2 of [36] and our LABOCA point shown in red. The magenta stars are from *IRAS*, the blue crosses from *Spitzer* (refer to [20]) and the green stars from *Herschel* (see [36]). The dashed lines show the best-fit models of the cold dust emission (in red) and the warm dust emission (in blue). The black solid line is the sum of the two, and the dotted lines show the 95% confidence interval. The emissivity index was fixed to 2 for both components.

measurement is lower than theirs but consistent within the error bars. A more detailed analysis of the *WISE* and LABOCA images will be presented in a forthcoming paper. NGC 1316 is a target of choice for future observations of the dust and molecular gas with *ALMA* to study their possible interaction with the inner radio jet.

5. Acknowledgements

We thank Zolt Levay and Paul Goudfrooij for making their *HST* image available to us.

References

[1] Spitzer L 1978 *Physical Processes in the Interstellar Medium* (New York: Wiley) pp 250–333
[2] Blain A W, Smail I, Ivison R J, Kneib J P and Frayer D T 2002 *Phys Reports* Issue 2 **369** 111–76
[3] Draine B T 2009 *Space Sci. Revs.* **143** 333–45
[4] Kennicutt R C *et al.* 2003 *Publ. Astron. Soc. Pac.* **115** 928–52
[5] Faber S M and Gallagher J S 1976 *Astrophysical J.* **204** 356
[6] 1 Thomas D, Maraston C, Bender R and Mendes de Oliveira C 2005 *Astrophysical J.* **621** 673–94
[7] Kuntschner H *et al.* 2010 *Mon. Not. R. Astron. Soc.* **408** 97–132
[8] Bureau M *et al.* 2011 *IAU Symposium Proceedings* **277** 55–8
[9] Blakeslee J P *et al.* 2009 *Astrophysical J.* **694** 556–72
[10] Ekers R D, Goss W M, Wellington K J, Bosma A, Smith R M and Schweizer F 1983 *A & A* **127** 361–65
[11] Geldzahler B J and Fomalont E B 1984 *Astronomical J.* **89** 1650–57
[12] Schweizer F and Seitzer 1988 *Astrophysical J.* **328** 88
[13] Schweizer F 1980 *Astrophysical J.* **237** 303–18
[14] Matthews T A, Morgan W W and Schmidt M 1964 *Astrophysical J.* **140** 35
[15] Goudfrooij P, Gilmore D, Whitmore B C and Schweizer F 2004 *Astrophysical J.* **613** 121
[16] Mackie G and Fabbiano G 1998 *Astrophysical J.* **115** 514
[17] Horellou C, Black J H, van Gorkom J H, Combes F, van der Hulst J M and Charmandaris V 2001 *A & A* **376** 837–52
[18] Bosma A, Smith R M and Wellington K J 1985 *Mon. Not. R. Astron. Soc.* **212** 301
[19] Grillmair C J, Forbes D A, Brodie J P and Elson R A W 1999 *Astronomical J.* **117** 167–80
[20] Lanz L, Jones C, Forman W R, Ashby M L N, Kraft R and Hickox R 2010 *Astrophysical J.* **721** 1702–13
[21] Temi P, Mathews W G and Brighenti F 2005 *Astrophysical J.* **622** 235–43
[22] Dale D A *et al.* 2007 *A & A* **655** 863–84
[23] Draine B T *et al.* 2007 *Astrophysical J.* **663** 866–94
[24] Kim D W and Fabbiano G 2003 *Astrophysical J.* **586** 826
[25] Feigelson E D, Laurent-Muehleisen S A, Kollgaard R I and Fomalont E B 1995 *Astrophy. J. Lett.* **449** 149
[26] Fabbiano G, Kim D W and Trinchieri G 1992 *Astrophysical J. Suppl. Ser.* **80** 531–644
[27] Hopkins P F and Quataert E 2010 *Mon. Not. R. Astron. Soc.* **407** 1529
[28] Siringo G *et al.* 2009 *A & A* D **497** 945–62
[29] Güsten R, Nyman L A, Schilke P, Menten K, Cesarsky C and Booth R 2006 *A & A* **497** 13
[30] Kovács A 2008 *SPIE Proc.* **7020** 45K
[31] Wright E L *et al.* 2010 *Astronomical J.* **140** 1868–81
[32] Jarrett T H*et al.* 2012 *Astronomical J.* **144** 68
[33] Jarrett T H*et al.* 2013 *Astronomical J.* **145** 1–34
[34] Cutri R M *et al.* 2012 *WISE All-Sky Data Release Products Explanatory Supplement* **2012wise.rept.**
[35] Peng C Y, Ho L C, Impey C D, and Rix H 2002 *Astronomical J.* **124** 226
[36] Galametz M *et al.* 2012 *Mon. Not. R. Astron. Soc.* **425** 763
[37] Galametz M *et al.* 2014 *Mon. Not. R. Astron. Soc.* **439** 2542

Implementation of an offset-dipole magnetic field in a pulsar modelling code

M Breed[1], C Venter[1], A K Harding[2] and T J Johnson[3]

[1] Centre for Space Research, North-West University, Potchefstroom Campus, Private Bag X6001, Potchefstroom, 2520, South Africa

[2] Astrophysics Science Division, NASA Goddard Space Flight Center, Greenbelt, MD 20771, USA

[3] National Research Council Research Associate, National Academy of Sciences, Washington, DC 20001, resident at Naval Research Laboratory, Washington, DC 20375, USA

E-mail: 20574266@nwu.ac.za

Abstract. The light curves of γ-ray pulsars detected by the *Fermi* Large Area Telescope show great variety in profile shape and position relative to their radio profiles. Such diversity hints at distinct underlying magnetospheric and/or emission geometries for the individual pulsars. We implemented an offset-dipole magnetic field in an existing geometric pulsar modelling code which already includes static and retarded vacuum dipole fields. In our model, this offset is characterised by a parameter ϵ (with $\epsilon = 0$ corresponding to the static dipole case). We constructed sky maps and light curves for several pulsar parameters and magnetic fields, studying the effect of an offset dipole on the resulting light curves. A standard two-pole caustic emission geometry was used. As an application, we compared our model light curves with *Fermi* data for the bright Vela pulsar.

1. Introduction

The first pulsar was discovered in 1967 by Bell and Hewish [1]. Pulsars are identified as compact neutron stars, formed in supernova explosions, that rotate at tremendous rates, and their magnetospheres contain strong electric, magnetic, and gravitational fields [2]. Pulsars emit radiation across the electromagnetic spectrum, including radio, optical, X-ray, and γ-rays [3]. We focus on γ-ray pulsars, specifically the Vela pulsar, which is the brightest persistent GeV source in the γ-ray sky. The Vela pulsar was detected [4] by the *Fermi* Large Area Telescope (LAT) [5], a γ-ray telescope that was launched in June 2008. *Fermi* LAT measures γ-rays in the energy range between 20 MeV and 300 GeV. The second *Fermi* pulsar catalogue [6] discussing the properties of 117 γ-ray pulsars has recently been released. The observed light curves are diverse, and detailed geometric modelling of the radio and γ-ray light curves may therefore provide constraints on the magnetospheric and emission characteristics. In this paper, we discuss the implementation of an offset-dipole magnetic field in a geometric code, and compare some representative light curves with those observed from Vela.

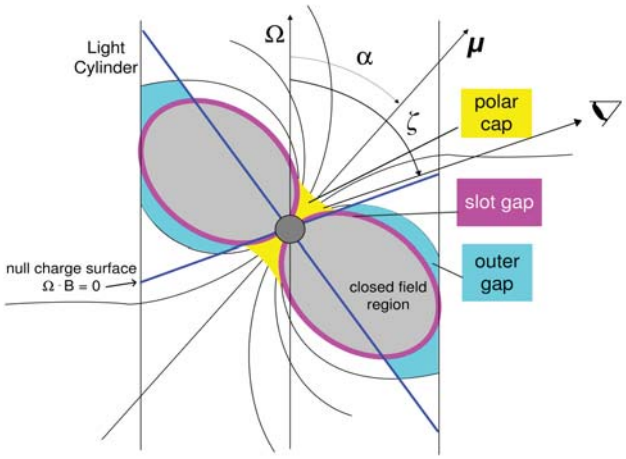

Figure 1. A schematic representation of geometric pulsar models. The PC model extends from $R_{\rm NS}$ (neutron star radius) up to low altitudes above the surface (yellow region). The TPC emission region (curved magenta lines) extends from $R_{\rm NS}$ up to $R_{\rm LC} = c/\Omega$ (light cylinder radius), and the OG region (cyan regions) from above the null charge surface (blue lines) to $R_{\rm LC}$. Adapted from [12]. See text for definition of symbols.

2. Model

2.1. Emission gap geometry

Several models have been used to model γ-ray emission from pulsars. These include the two-pole caustic (TPC) [7] (the slot gap (SG) [8] model may be its physical representation), outer gap (OG) [9, 10] and polar cap (PC) model [11]. Consider the ($\boldsymbol{\Omega}$, $\boldsymbol{\mu}$) plane, with $\boldsymbol{\mu}$ (the magnetic moment) inclined by an angle α with respect to the rotation axis $\boldsymbol{\Omega}$ (the angular velocity). The observer's viewing angle ζ is the angle between the observer's line of sight and the rotation axis. A 'gap region' is defined as the region where particle acceleration and emission take place. The emissivity of γ-ray photons within this gap region is assumed to be uniform in the corotating frame (for the TPC and OG models) and the γ-rays are expected to be emitted tangentially to the local magnetic field in this frame [13], which means that the assumed magnetic field geometry is very important with respect to the predicted light curves. The gap region for the TPC model extends from the surface of the neutron star along the entire length of the last closed magnetic field lines, up to the light cylinder (where the corotation speed equals the speed of light), as indicated by the magenta region in Figure 1. For the OG model, the gap region extends from the null-charge surface, where the Goldreich-Julian charge density $\rho_{\rm GJ} = 0$ [14], to the light cylinder, as indicated by the cyan region. The PC gap (yellow region) extends from the neutron star surface to the low-altitude pair formation front, where the E-field is screened by pairs formed via single-photon pair production. In what follows, we will focus on the TPC model.

2.2. Magnetic field structure

Several magnetospheric structures have been studied, including the static dipole field [15], the retarded dipole field [16] (a rotating vacuum magnetosphere which can in principle accelerate particles but do not contain any charges or currents) and the force-free field [17] (being filled with charges and currents, but unable to accelerate particles, since the E-field is screened everywhere). A more realistic pulsar magnetosphere [18] would be one that is intermediate between the vacuum retarded and the force-free fields.

The main focus of this paper is on the offset-dipole B-field. Retardation of the B-field and asymmetric currents may cause small distortions in the B-field structure, shifting the polar caps by small amounts and different directions. In the 'symmetric case', in the corotating magnetic

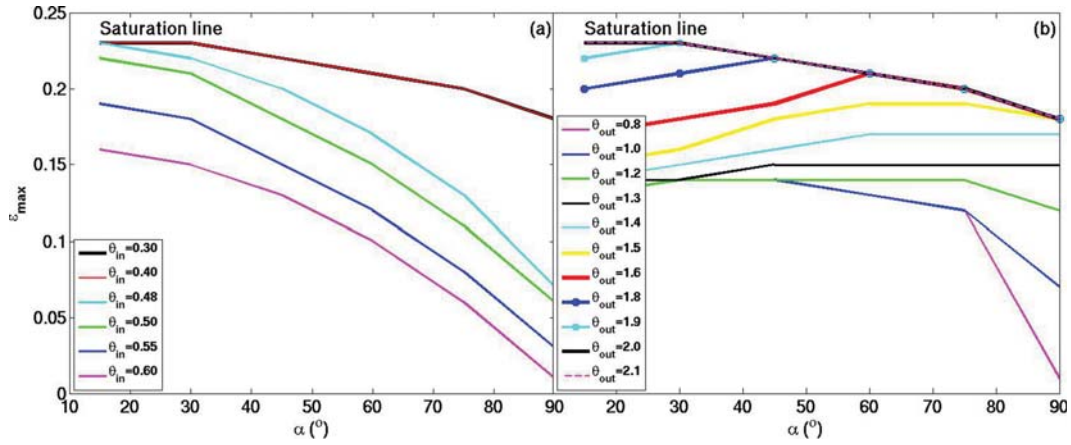

Figure 2. A plot of $\epsilon_{\max}$ as a function of α. In panel (a) each line corresponds to a different value of $\theta_{\rm in}$ for a constant value of $\theta_{\rm out} = 2.0$ (both in units of polar cap angle $\theta_{\rm PC} \approx \sqrt{R_{\rm NS}/R_{\rm LC}}$). For values smaller than $\theta_{\rm in} = 0.40$, $\epsilon_{\max}$ becomes saturated, and for larger $\theta_{\rm in}$, $\epsilon_{\max}$ decreases significantly. In panel (b) each line corresponds to a different value of $\theta_{\rm out}$ for a constant value of $\theta_{\rm in} = 0.3$, where $\epsilon_{\max}$ becomes saturated at $\theta_{\rm out} = 2.0$, and as $\theta_{\rm out}$ decreases, $\epsilon_{\max}$ also decreases.

frame (where $\hat{\mathbf{z}}' \parallel \boldsymbol{\mu}$), the offset-dipole B-field in spherical coordinates is given by [19]

$$\mathbf{B}'(r', \theta', \phi') = \frac{\mu}{r'^3}\left[\cos\theta'\hat{\mathbf{r}}' + \frac{1}{2}(1+a)\sin\theta'\hat{\boldsymbol{\theta}}' - \epsilon\sin\theta'\cos\theta'\sin(\phi'-\phi_0)\hat{\boldsymbol{\phi}}'\right], \tag{1}$$

where $\mu = B_0 R_{\rm NS}/2$ is the magnetic moment, B_0 the surface B-field strength at the magnetic pole, $R_{\rm NS}$ the stellar radius, ϕ_0 the magnetic azimuthal angle defining the plane in which the offset occurs, and

$$a = \epsilon\cos(\phi' - \phi_0). \tag{2}$$

The magnitude of the offset is characterised by a parameter ϵ, which represents a shift of the polar cap from the magnetic axis, with $\epsilon = 0$ corresponding to the static-dipole case.

3. Implementation of the offset-dipole B-field in the code

3.1. Transformation of B-field

We start with a B-field defined in the magnetic frame ($\hat{\mathbf{z}}' \parallel \boldsymbol{\mu}$), specified using spherical coordinates

$$\mathbf{B}'(r', \theta', \phi') = B'_r(r', \theta', \phi')\hat{\mathbf{r}}' + B'_\theta(r', \theta', \phi')\hat{\boldsymbol{\theta}}' + B'_\phi(r', \theta', \phi')\hat{\boldsymbol{\phi}}'. \tag{3}$$

(We choose $\phi' = 0$ in the direction toward $\boldsymbol{\Omega}$). We transform this to a Cartesian coordinate system:

$$\mathbf{B}'(x', y', z') = B'_x(x', y', z')\hat{\mathbf{x}}' + B'_y(x', y', z')\hat{\mathbf{y}}' + B'_z(x', y', z')\hat{\mathbf{z}}'. \tag{4}$$

This is done using expressions that specify spherical unit vectors and coordinates in terms of Cartesian coordinates (see, e.g., [15]). Next, we rotate both the B-field components and the associated Cartesian frame (or equivalently, the position vector) through an angle $-\alpha$, thereby transforming the B-field from the magnetic frame to the rotational frame ($\hat{\mathbf{z}} \parallel \boldsymbol{\Omega}$):

$$\mathbf{B}(x, y, z) = B_x(x, y, z)\hat{\mathbf{x}} + B_y(x, y, z)\hat{\mathbf{y}} + B_z(x, y, z)\hat{\mathbf{z}}. \tag{5}$$

After initial implementation of the offset-dipole field in the geometric code we discovered that we could solve the polar cap rim (for details, see [13]) only for small values of ϵ. We improved

the range of ϵ by changing the parameters $\theta_{\rm in}$ and $\theta_{\rm out}$, which delimit a bracket in colatitude thought to contain the last open field line (tangent to $R_{\rm LC}$). Figure 2 indicates the progressively larger range of ϵ that we were able to use upon decreasing $\theta_{\rm in}$ and increasing $\theta_{\rm out}$.

3.2. The offset-dipole E-field

It is important to take the accelerating E-field into account (in a physical model) when such expressions are available, since this will modulate the emissivity in the gap (as opposed to geometric models where we just assume constant emissivity in the corotating frame). The low-altitude E-field in the offset-dipole magnetosphere, for the SG model, is given by

$$E_{\parallel,\rm low} \approx -3\mathcal{E}_0\nu_{\rm SG}x^a\left\{\frac{\kappa}{\eta^4}e_{1\rm A}\cos\alpha+\frac{1}{4}\frac{\theta_0^{1+a}}{\eta}\left[e_{2\rm A}\cos\phi'+\frac{1}{4}\epsilon\kappa e_{3\rm A}(2\cos\phi_0-\cos(2\phi'-\phi_0))\right]\sin\alpha\right\}(1-\xi_*^2), \tag{6}$$

where the symbols have the same meaning as in [20]. Here

$$e_{1\rm A}=1+\frac{a}{3}(\eta^3-1);\quad e_{2\rm A}=(1+3a)\eta^{(1+a)/2}-2a;\quad e_{3\rm A}=\frac{5-3a}{\eta^{(5-a)/2}}+2a. \tag{7}$$

We approximate the high-altitude SG E-field by [20]

$$E_{\parallel,\rm high} \approx -\frac{3}{8}\left(\frac{\Omega R}{c}\right)^3\frac{B_0}{f(1)}\nu_{\rm SG}x^a\left\{\left[1+\frac{1}{3}\kappa\left(5-\frac{8}{\eta_c^3}\right)+2\frac{\eta}{\eta_{\rm LC}}\right]\cos\alpha+\frac{3}{2}\theta_0 H(1)\sin\alpha\cos\phi'\right\}(1-\xi_*^2), \tag{8}$$

and the general E-field valid from $R_{\rm NS}$ to $R_{\rm LC}$ by

$$E_{\parallel,\rm SG}\simeq E_{\parallel,\rm low}\exp\left(\frac{-(\eta-1)}{(\eta_c-1)}\right)+E_{\parallel,\rm high}, \tag{9}$$

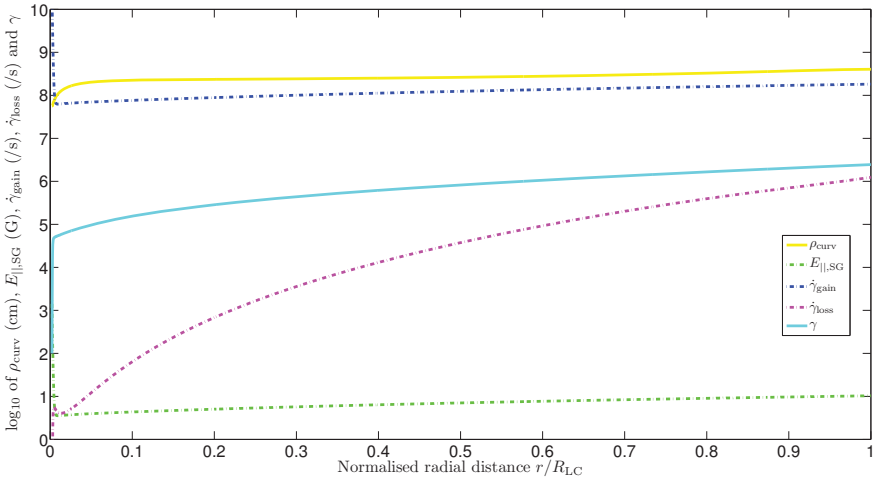

Figure 3. Plot of $\log_{10}$ of curvature radius $\rho_{\rm curv}$ (solid yellow line), general $E_{\parallel,\rm SG}$-field (dash-dotted green line), gain (acceleration) rate $\dot{\gamma}_{\rm gain}$ (dash-dotted dark blue line), loss rate $\dot{\gamma}_{\rm loss}$ (dash-dotted pink line), and the Lorentz factor γ (solid light blue line) as a function of normalised radial distance $r/R_{\rm LC}$. We used $P=0.0893$ s, $B_0=1.05\times10^{13}$ G (corrected for general relativistic effects), $I=0.4MR_{\rm NS}^2=1.14\times10^{45}$ g cm^2, $\phi'=1.60$ radians (at the stellar surface), $\xi_*=0$, and $\eta_c=1.4$.

where $\eta_c = r_c/R_{\rm NS}$ is the critical scaled radius where the high-altitude and low-altitude E-field solutions are matched (see, e.g., equation [59] of [20]).

4. Results

4.1. Solution of particle equation of motion

Using equation (9) we next solve the particle transport equation (taking only curvature radiation losses into account)

$$\dot{\gamma} = \dot{\gamma}_{\rm gain} + \dot{\gamma}_{\rm loss} = \frac{eE_{\parallel,\rm SG}}{mc} - \frac{2e^2\gamma^4}{3\rho^2_{\rm curv}mc}, \tag{10}$$

to obtain the particle Lorentz factor $\gamma(\eta, \phi', \xi_*)$ with $\eta = r/R_{\rm LC}$ the normalised radial distance, and ξ_* a normalised colatitudinal angle which is $\xi_* = 0$ at the middle of the SG and $\xi_* = 1$ at the boundaries [8]. Radiation reaction occurs when the energy gain balances the losses, and $\dot{\gamma} = 0$. In Figure 3 we plot the $\log_{10}$ of curvature radius $\rho_{\rm curv}$, general E-field $E_{\parallel,\rm SG}$, gain rate $\dot{\gamma}_{\rm gain}$, loss rate $\dot{\gamma}_{\rm loss}$, and particle Lorentz factor γ as a function of η. We can see that the radiation reaction limit is not reached in this case, due to the relatively low SG E-field. The Lorentz factor is initially set to $\gamma = 100$ and rapidly rises until it nearly reaches $\gamma \sim 10^6$. For different choices of ϕ' and ξ_*, the E-field may be even lower and γ may not even exceed $\sim 10^5$, leading to negligible curvature radiation losses along those field lines. On 'unfavourably curved' field lines ($\phi' \approx \pi$), the E-field may even change sign at higher altitudes. This may cause oscillation of particles and very low values of γ, and such field lines should be ignored when constructing phaseplots.

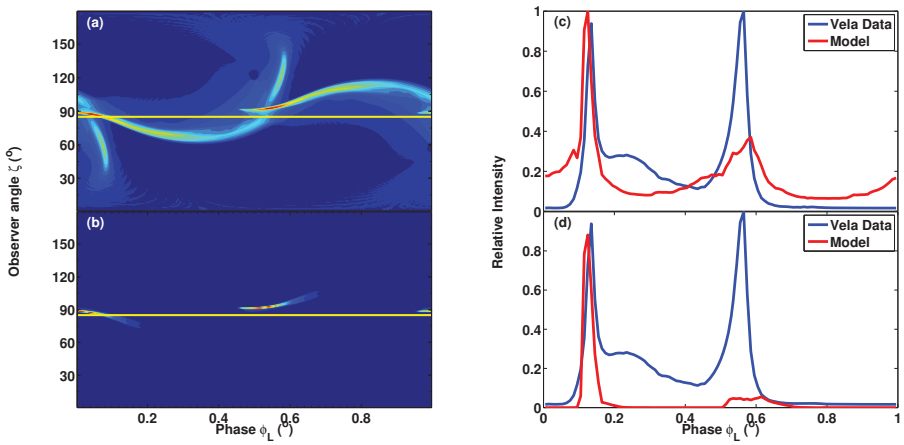

Figure 4. Phaseplots and light curves for the offset-dipole field. Panels (a) and (b) illustrate the emission per solid angle versus ζ and $\phi_{\rm L}$ for $\alpha = 60°$ and panels (c) and (d) their corresponding light curves for $\zeta = 85°$ (indicated by the solid yellow lines). The solid blue line denotes the observed Vela profile (e.g., [6]) and the solid red line our model profile. Panel (a) and (c) are for the case of constant emissivity, whereas panel (b) and (d) are for the case when using the offset-dipole E-field and solving for γ. We assumed $\epsilon = 0.2$, a gap width of 5% of the polar cap angle, and $R_{\rm max} = 1.2R_{\rm LC}$ for an SG model.

4.2. Phaseplots and light curves

In Figure 4, we show the phaseplots (emission per solid angle versus ζ and observer phase $\phi_{\rm L}$) and the corresponding light curves (i.e., cuts along constant ζ) for the offset-dipole B-field and TPC model. The dark circle in panel (a) is the non-emitting polar cap, and the sharp, bright regions are the emission caustics, where radiation is bunched in phase due to relativistic effects. The caustic structure is qualitatively different between the two cases (constant emissivity vs. solution of γ using $E_{\parallel}$), leading to differences in the resulting light curves. The caustics seem wider and more pronounced in the constant-emissivity case. The blue lines in panel (c) and (d) are the measured Vela profiles [6], while the red lines are the predicted light curves. Note that the latter are merely representative, and still fail to adequately reproduce the second large peak of the measured profile.

5. Conclusions and future work

We have studied the effect of implementing the offset-dipole B-field on γ-ray light curves for the TPC geometry. We observe that the polar cap is indeed offset compared to the case of the static dipole (not shown Figure 4) when assuming a constant emissivity. However, when including an E-field and solving for γ, we see that the resulting phaseplot becomes qualitatively different, given the fact that γ only becomes large enough to yield significant curvature radiation at large altitudes. Furthermore, we do not attain the radiation-reaction limit, due to a relatively low E-field. In future, we want to solve for η_c on each field line, instead of using a constant value where we match E-field solutions. Lastly, we want to produce light curves for several model parameters and search for a best-fit profile, thereby constraining Vela's low-altitude magnetic structure and system geometry.

Acknowledgments

This work is supported by the South African National Research Foundation (NRF). AKH acknowledges the support from the NASA Astrophysics Theory Program. CV, TJJ, and AKH acknowledge support from the *Fermi* Guest Investigator Program.

References

[1] Hewish A *et al.* 1968 *Nature* **217** 709–13
[2] Abdo A A *et al.* 2010 *ApJS* **187** 460–94
[3] Becker W, Gil J A and Rudak B 2007 *Highlights of Astronomy* **14** 109–38
[4] Abdo A A *et al.* 2009 *ApJ* **696** 1084–93
[5] Atwood W B *et al.* 2009 *ApJ* **697** 1071–102
[6] Abdo A A *et al.* 2013 *ApJS* **208** 17–76
[7] Dyks J and Rudak B 2003 *ApJ* **598** 1201–6
[8] Muslimov A G and Harding A K 2003 *ApJ* **588** 430–40
[9] Cheng K S, Ho C and Ruderman M 1986, *ApJ* **300** 500–39
[10] Romani R W 1996 *ApJ* **470** 469–78
[11] Daugherty J K and Harding A K 1996 *ApJ* **458** 278–92
[12] Harding A K 2004 *22nd Texas Symp. on Relativistic Astrophysics* ed P Chen, E Bloom *et al.* p 40
[13] Dyks J, Harding A K and Rudak B 2004 *ApJ* **606** 1125–42
[14] Goldreich P and Julian W H 1969 *ApJ* **157** 869–80
[15] Griffiths D J 1995 *Introduction to Electrodynamics* (San Francisco: Pearson Benjamin Cummings)
[16] Deutsch A J 1955 *Annales d'Astrophysique* **18** 1–10
[17] Contopoulos I, Kazanas D and Fendt C 1999 *ApJ* **511** 351–8
[18] Kalapotharakos C, Kazanas D, Harding A and Contopoulos I 2012 *ApJ* **749** 1–15
[19] Harding A K and Muslimov A G 2011 *ApJ* **743** 181–96
[20] Muslimov A G and Harding A K 2004 *ApJ* **606** 1143–53

Investigating Brightest Cluster Galaxies: kinematics with SALT

S. I. Loubser

Centre for Space Research, North-West University, Potchefstroom 2520, South Africa

E-mail: Ilani.Loubser@nwu.ac.za

Abstract. We present detailed, high spatial and spectral resolution, longslit observations of four active central cluster galaxies (CCGs) in cooling flow clusters (Abell 0085, 0133, 0644 and Ophiuchus). Our sample consists of CCGs with Hα filaments, and have existing data from the X-ray to radio wavelength regimes available. Here, we add the detailed optical data over a broad wavelength range to probe the kinematics of the stars. This, combined with the other multiwavelength data, will form a complete view of the different phases (hot and cold gas and stars) and how they interact in the processes of star formation and feedback detected in central galaxies in cooling flow clusters, as well as the influence of the host cluster.

1. Introduction

The most massive of early-type galaxies – central cluster galaxies (CCGs) – are special. They have extremely high luminosities, diffuse and extended structures, and dominant central locations in clusters. They are believed to be sites of very interesting evolutionary phenomena (e.g. dynamical friction, galactic cannibalism, cooling flows), and may well require there to have been a special process of formation. These processes will leave different imprints in the dynamical properties, the detailed chemical abundances, and the star formation histories of these galaxies, which can be studied using high-quality spectroscopy (Loubser et al. 2008; 2009).

Cooling-flow clusters are common in the local Universe and CCGs are often found at the centres of these systems. If the central cluster density is high enough, and the cooling time of the hot intracluster medium is significantly shorter than the Hubble time (Edge, Stewart & Fabian 1992), intracluster gas could condense and form stars at the bottom of the potential well. The lack of widespread detection of iron lines expected from cluster gas cooling in *XMM-Newton* observations of cool-core clusters contradicted the model that stars are formed in cooling flows (this is sometimes referred to as the "cooling flow problem"). However, previous studies have reported several examples of ongoing star formation in CCGs, in particular those hosted by cooling-flow clusters (Crawford et al. 1999; Loubser et al. 2009).

The central cluster galaxies often host radio-loud AGN, which may account for the necessary heating to counteract radiative cooling (Von der Linden et al. 2007). Thus, CCGs lie at the interface where it is crucial to understand the role of feedback and gas accretion in star formation and also in galaxy and cluster evolution. Within these cooling-flow CCGs, cool molecular clouds, warm ionized hydrogen, and the cooling intracluster medium are related. A complete view of the star formation process necessarily incorporates the stars with the gas and an understanding

of the processes by which these phases interact, and therefore, requires information from several wavelength regimes.

We proposed long-slit observations of the stellar populations in active CCGs in cooling-flow clusters. We have selected a sample with confirmed extended H-alpha emission, and with near-infrared (2MASS), ultraviolet (GALEX), X-ray data (Chandra), and in some cases VLA 1.4 GHz fluxes, already available (McDonald et al. 2010).

2. Sample

We have chosen our sample of active central cluster galaxies from the Hα imaging presented in McDonald et al. (2010), who in turn, selected their sample from White, Jones & Forman (1997). McDonald et al. (2010) enforced the cuts: $\delta < +35\,\mathrm{deg}$ and $0.025 < z < 0.092$, after which they selected 23 clusters to cover the full range of properties, from very rich clusters with high cooling rates to low-density clusters with small cooling flows. Their classical cooling rates range from 6.3 – 431 $\mathrm{M}_{\odot}\ \mathrm{yr}^{-1}$ which means that while covering a large range in properties, their sample consisted of only cooling flow clusters. From their 23 cooling flow clusters, we selected all the clusters with clearly detected Hα in their centres (albeit filamentary, extended or nuclear emission). In addition, all of these central galaxies have optical imaging, near-IR (2MASS) and UV (Galex data) available. Thereafter, we selected all the central galaxies with detailed X-ray (Chandra) data, as well as VLA 1.4 GHz fluxes, available. This resulted in a sub-sample of 10 galaxies. We observed four of these galaxies with the GMOS IFU (as presented in Loubser & Soechting 2013), and we observed four of these galaxies with the SALT Robert Stobie Spectrograph (RSS). The latter four galaxies are in the redshift range z $0.028 - -0.071$, and were observed with exposure times in the order of 10000 seconds. Their kinematic results will be described here.

3. Observations and data reduction

The data were obtained with the RSS on the SALT telescope between October 2011 and October 2012 (during two observing semesters and on 24 different nights during dark time). The rest wavelength of interest is 4860 – 6731 Å (redshifted to 5000 – 7300 Å). To achieve this, and to avoid losing essential emission lines in the ccd gaps, the pg0900 grating was used with 1.2" slit at a carefully selected central wavelength setting. In addition to the targets, the necessary flat-fields and arcs frames were also observed at regular intervals, as well as spectrophotometric standard stars for flux calibration. The basic reductions were performed with the PySALT: SALT science pipeline, whilst further reductions were done in IRAF (see Loubser in preparation).

The galaxy and associated error spectra were binned in the spatial direction to ensure a minimum S/N of 30 per Å in the Hβ region of the spectrum for measurements as a function of radius. A S/N ratio of 30 per bin was chosen to resolve the optimal number of possible points, whilst still having acceptable errors on the measurements. Thus, the spatial cross-sections are broader with increasing radius from the centre of the galaxy. In all the profiles plotted here (Figures 1 and 2), the values of the measurements are plotted at the luminosity-weighted centres of the spatial bins used to derive the kinematics (radial velocity and velocity dispersion). The effective half-light radius was calculated as $a_{\mathrm{e}} = \frac{r_{\mathrm{e}}(1-\epsilon)}{1-\epsilon\ |cos(|PA-MA|)|}$, with ϵ the ellipticity (data from NED), r_{e} the radius containing half the light of the galaxy (computed from the 2MASS K-band 20th magnitude arcsec^{-2} isophotal radius as described in Loubser et al. 2008), PA the slit position axis, and MA the major axis. These parameters are showed in Table 1.

Table 1. Properties of the CCGs. The PA is given as deg E of N. The half-light radii (r_e) were calculated from the 2MASS catalogue. The last column lists the fraction of the effective half-light radii spanned by the radial profiles measured in this work.

Object	Slit PA (degrees)	Major Axis MA (degrees)	r_e (arcsec)	ϵ	a_e (arcsec)	Fraction times a_e
ESO541-013	197	17	10.63	0.40	10.63	0.87
MCG-02-02-086	149	149	12.10	0.22	12.10	0.71
PGC023233	193	35	6.45	0.14	6.37	0.92
2MASXJ17122774-2322108	135	145	20.06	0.28	19.94	0.16

4. Kinematic measurements

To accurately measure the features of the CCG spectra, we use a combination of the PPXF (Cappellari & Emsellem 2004) and GANDALF (Sarzi et al. 2006) routines[1]. Gandalf version 1.5 was used as it enables a reddening correction to be performed, and it encorporates errors. This code treats the emission lines as additional Gaussian templates, and solves linearly at each step for their amplitudes and the optimal combination of stellar templates, which are convolved by the best stellar line-of-sight velocity distribution. The stellar continuum and emission lines are fitted simultaneously. All 985 stars of the MILES stellar library (Sánchez-Blázquez et al. 2006) were used as stellar templates to automatically include α-enhancement in the derived optimal template. After the kinematics are fixed, a Gaussian template is constructed for each emission line at each iteration, and the best linear combination of both stellar and emission-line templates (with positive weights) is determined. We have adapted the gandalf code to apply it to the SALT data with a longer wavelength range. None of the four active CCGs contained measureable emission lines despite being surrounded by ionised nebulae in cooling flow clusters. The GANDALF code was used to measure the spatially resolved velocity and velocity dispersion of the absorption spectra. Our slit placement avoided the ionised gas. The spatially resolved velocity and velocity dispersion gradients are shown in Figures 1 and 2. In all the spatially resolved profiles plotted here, the values of the parameters are plotted at the luminosity-weighted centres of the spatial bins used to derive the parameters. The kinematic properties investigated here (rotation and incidence of velocity substructure) seem normal compared with their ordinary giant elliptical counterparts. Despite the small sample size, we already detect variety in the kinematical properties of these galaxies.

5. Summary

We have used SALT to derive the rotational velocity and velocity dispersion profiles for 4 active central cluster galaxies in cooling flow clusters. Despite the undeniably special nature of BCGs due to their extreme morphological properties and locations, the kinematic properties investigated here (rotation and incidence of velocity substructure) seem normal compared with their ordinary giant elliptical counterparts. Despite the small sample size, we already detect variety in the kinematical properties of these galaxies which is unusual given the homogeneous morphological appearance and similar environments of these galaxies.

We will be adding the detailed stellar population analysis, and place the derived information from the optical spectra in context with multiwavelength data over the full spectrum in a future

[1] We make use of the corresponding PPXF and GANDALF IDL (Interactive Data Language) codes which can be retrieved at http:/www.leidenuniv.nl/sauron/.

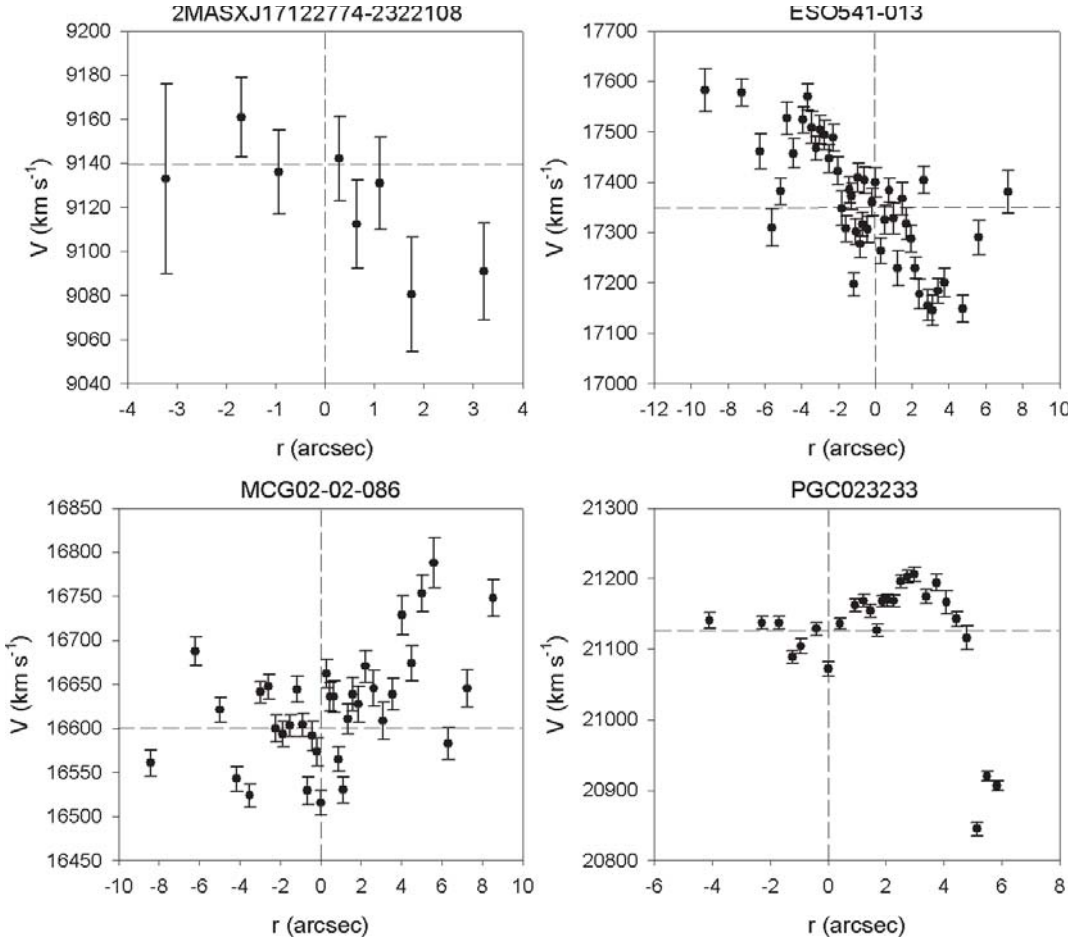

Figure 1. Velocities of the four BCGs. From left to right, top to bottom: 2MASXJ17122774-2322108, ESO541-013, MCG02-02-086, PGC023233.

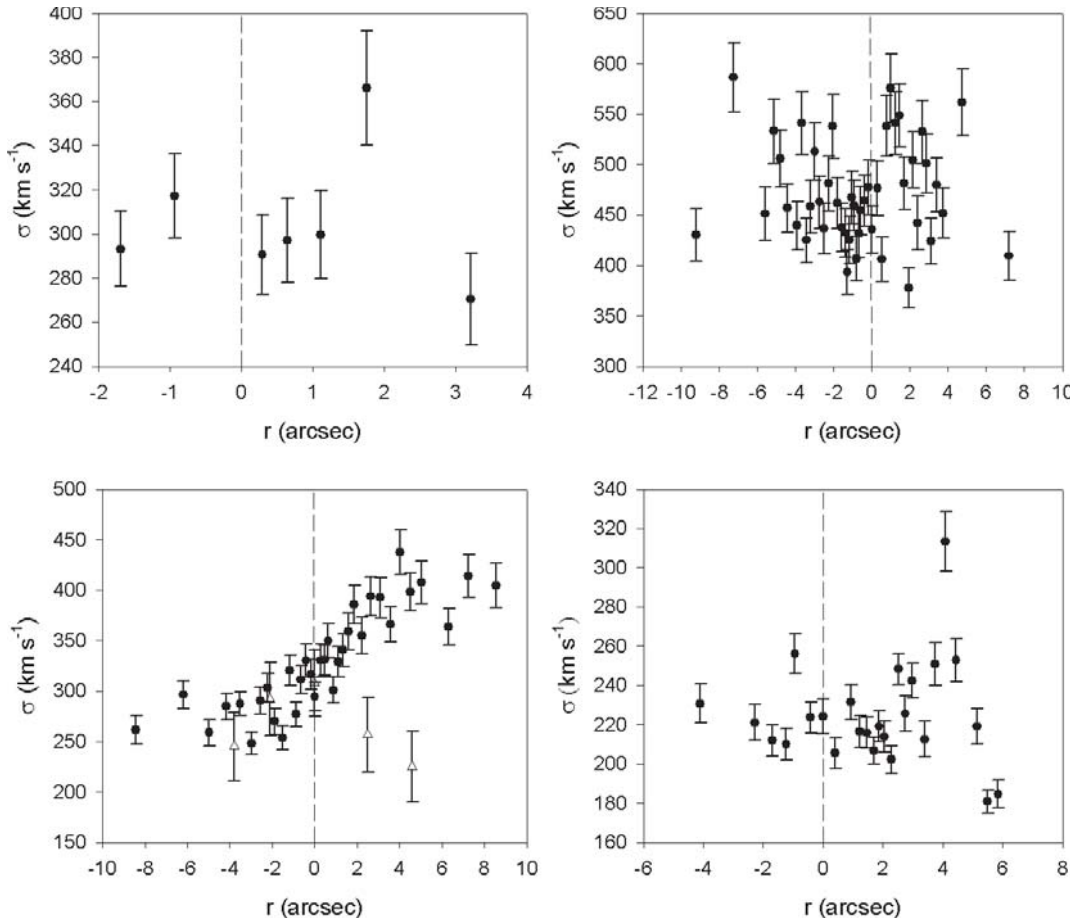

Figure 2. Velocity dispersion of the four BCGs. From left to right, top to bottom: 2MASXJ17122774-2322108, ESO541-013, MCG02-02-086, PGC023233. The empty triangles in MCG02-02-086 is data from Fisher et al. (1995) also taken along the major axis and shown here as comparison.

paper (Loubser, in preparation), to explain the diverse nature of these galaxies.

6. Acknowledgments

SIL is financially supported by the South African National Research Foundation.

7. References

[1] Cappellari M and Emsellem E 2004 *PASP.* **116** 138
[2] Crawford C S, Allen S W, Ebeling H, Edge A C, Fabian A C 1999 *MNRAS.* **306** 857
[3] Edge A C, Stewart G C, Fabian A C 1992 *MNRAS.* **258** 177
[4] Edwards L O V, Hudson M J, Balogh M L, Smith R J 2007 *MNRAS.* **379** 100
[5] Fisher D, Illingworth G, Franx M 1995 *ApJ.* **438** 539
[6] Loubser S I, Sansom A E, Sánchez-Blázquez P, Soechting I K, Bromage G 2008 *MNRAS.* **391** 1009
[7] Loubser S I, Sánchez-Blázquez P, Sansom A E, Soechting I K 2009 *MNRAS.* **398** 133
[8] Loubser S I and Soechting I K 2013 *MNRAS.* **431** 2933
[9] McDonald M, Veilleux S, Rupke D S N, Mushotzky R 2010 *ApJ.* **721** 1262
[10] Sánchez-Blázquez P et al. 2006 *MNRAS* **371** 703
[11] Sarzi M et al. 2006 *MNRAS.* **366** 1151
[12] Von der Linden A, Best P N, Kauffmann G, White S D M 2007 *MNRAS.* **379** 867
[13] White D A, Jones C, Forman W 1997 *MNRAS* **292** 419

Recent Results on the Spatially Resolved Molecular Gas Star Formation Law from CARMA Survey Toward Infrared-bright Nearby Galaxies (STING)

Nurur Rahman[1,†], Alberto D. Bolatto[2], and the STING[‡] Collaboration

[1]Department of Physics, University of Johannesburg, Auckland Park Campus, Johannesburg 2006, South Africa.
[2]Department of Astronomy, University of Maryland, College Park, MD, USA.
†South Africa SKA Fellow.
‡The STING is a collaboration of radio astronomers from USA, Canada, Germany, and South Africa.

E-mail: nrahman@uj.ac.za; nurur@yahoo.com

Abstract. The functional relationship between star formation rate surface density and molecular gas surface density in galaxies is commonly known as the star formation law. Observational determinations of this law require taking into account a number of factors. The extinction, contributions from non star-forming populations affect many measures of star formation, the treatment of the diffuse emission, and the statistical methodologies employed all have impacts on the precise relation between gas and star formation. Using CARMA STING data-set, a 3mm (CO J = 1-0) survey of nearby galaxies, we recently investigate the relationship at the sub-kpc level.

We find that the precise observational constraint on the linear or non-linear functional form of the relationship requires an accurate estimate of the fraction of the diffuse emission. Our results show that the treatment of the diffuse emission has significant impact on the intrinsic scatter in the Schmidt-Kennicutt type star formation law. The scatter varies substantially with the choice of the star formation tracer used. For example, the mid-infrared non-linear 24 μm star formation tracer shows the tightest correlation with the molecular gas content whereas (azimuthally averaged) extinction corrected Hα as a star formation tracer appears to be the noisiest. By measuring the relationship in the bright, high molecular gas surface density ($\Sigma_{\rm H_2}\sim$20 M$_\odot$ pc^{-2}) regions of the disks to minimize the contribution from diffuse extended emission and using 24 μm emission as a tracer of star formation, we find an approximately linear relation between molecular gas and star formation rate surface density with a molecular gas depletion time $\sim$2.30 Gyr.

1. Introduction

Stars form within molecular clouds. However, the processes responsible for converting molecular gas into stars in various galactic environments are still poorly understood. Observations find that the star formation rate (SFR) and the gas content in galaxies are related by, $\Sigma_{\rm SFR} = {\rm A}\ \Sigma^{\rm N}_{\rm gas}$, where $\Sigma_{\rm SFR}$ and $\Sigma_{\rm gas}$ are the star formation rate surface density and the gas (atomic and molecular) surface density, respectively; and A is the normalization constant representing the

efficiency of the processes ([1], [2], [3], [4], [5]). This relationship between gas and SFR surface densities is commonly referred to as the Schmidt-Kennicutt star formation (SF) law.

Spatially resolved SF law studies, whether it is a rigorous case study or a meticulous investigation of a sample, frequently reach dissimilar conclusions on the value of the exponent in the relation above when relating *molecular gas* to SFR (hereafter we express the exponent as N_{mol} to represent the molecular gas SF law). These studies provide a spread in the value of the power law index ranging from $N_{mol} \sim 0.8 - 1.5$ ([6], [7], and references therein). Whether the local SF law is linear or non-linear has implications for the dominant SF mechanisms as well as for modeling efforts. The range in the index of the SF law observed within and among galaxies may be intrinsic and contain valuable astrophysical information, or be entirely attributable to the different choices of gas and SFR tracers, methodologies for internal extinction correction, differences in the CO-to-H_2 conversion, or the range of spatial scales probed.

To explore the impact of various methodological aspects related to the local SF law we recently make two comprehensive analyses of the SF law using high resolution ($3'' - 5''$) STING[1] CO $J = 1 - 0$ data procured from Combined Array for Research in Millimeter Astronomy (CARMA) interferometer observations. Our results are presented in [6] and [7]. Rahman *et al* 2011 [6] is a pilot project which centers on 1) the use of different SFR tracers and the scatter associated with those tracers, 2) the role of the diffuse emission (DE), a component of the integrated disk emission which is not necessarily related to the star-forming regions, and 3) the role of fitting methodologies and data sampling strategies in determining the functional form of the SF law. The insights obtain from this work leads us to further investigate the local SF at high (molecular gas) surface brightness regions for the STING sample galaxies [7]. In this report we underline the key results obtained from these studies.

2. Data

The sample is composed of 23 northern ($\delta > -20°$), moderately inclined ($i < 75°$), and nearby galaxies (within 45 Mpc) which are taken from the *IRAS* Revised Bright Galaxy Survey (RBGS; [8]). These galaxies have been carefully selected to have uniform coverage in stellar mass ($\sim 10^{8.1} - 10^{11.5}$ $M_\odot$), SF activities ($\sim 0.05 - 12.30$ $M_\odot$ Gyr^{-1} pc^{-2}), and morphological types.

We use CO $J = 1 - 0$ spectral cube to produce integrated CO intensity maps. We apply a conversion factor, $X_{CO} = 2.0 \times 10^{20}$ $cm^2/(K\ km\ s^{-1})$, to convert intensity maps to molecular gas column density maps. To construct SFR tracer maps for the sample we use 24 μm images from the Multi-band Imaging Photometers (MIPS; [9]) instrument on board the *Spitzer Space Telescope*. The calibrated mid-infrared images are obtained from the *Spitzer* Heritage Archive. The FUV and Hα images of NGC 4254 are obtained from *GALEX* Nearby Galaxies Survey [10] and *Spitzer* Infrared Nearby Galaxies Survey [11]. The spatial resolution of our studies is limited by the point spread function of the 24 μm map, which has a FWHM of $6''$. This angular resolution covers a range of physical scales in the sample ($\sim$160-1250 pc) for varying physical distances of individual galaxies ($\sim$5.5-43.1 Mpc). Higher resolution images were Gaussian-convolved to have the same image resolution and pixel sampling.

Construction of various data products such as molecular gas surface density (Σ_{H_2}) map, SFR surface density (Σ_{SFR}) map and the associated error maps as well as data sampling and fitting strategies are described in detail in [6]. We use unsharp masking to model and remove the DE from the SFR tracer maps. However, unlike [6] which uses combined CO data (both single dish and interferometer), in this report we use only CARMA data to obtain molecular hydrogen. Since interferometric observation filters out extended emission, the CO data does not warrant the need to remove the DE.

[1] PI: A. D. Bolatto, University of Maryland, MD, USA; http://www.astro.umd.edu/∼bolatto/STING/

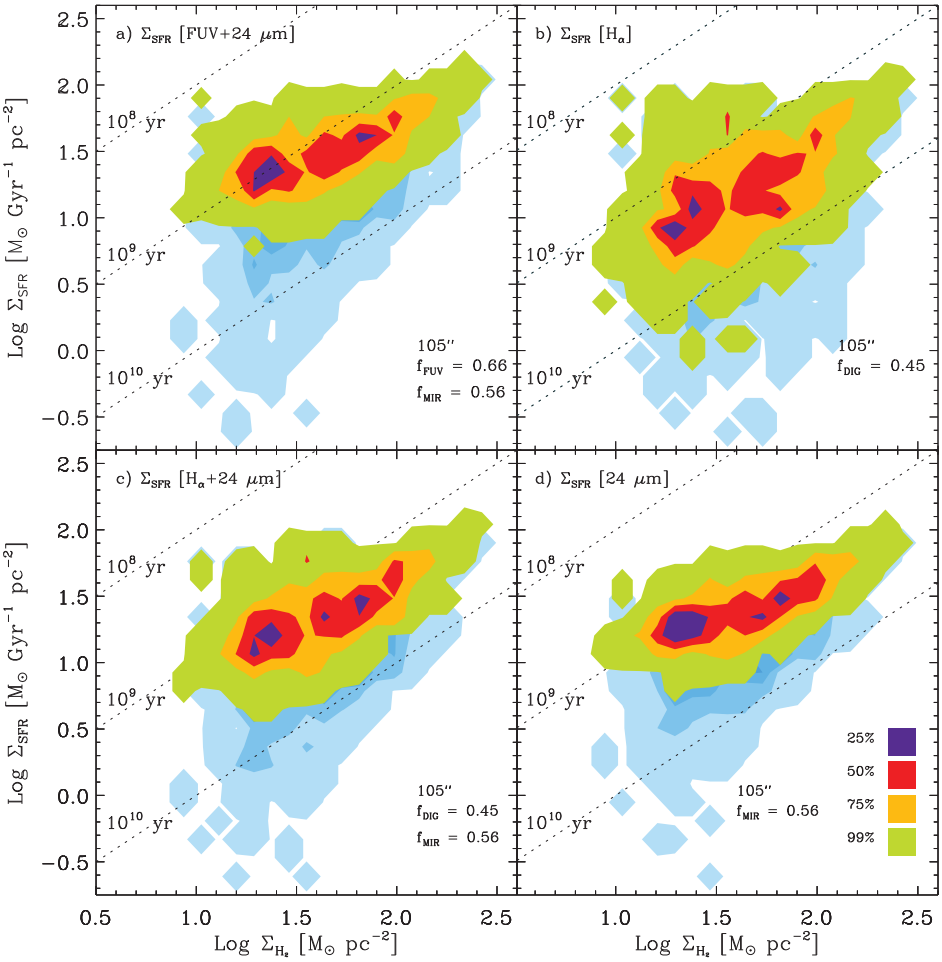

Figure 1. Pixel analysis of the observed $\Sigma_{\rm SFR}$ - $\Sigma_{\rm H_2}$ relationship for NGC 4254 at 6″ resolution using four different SFR tracers (NGC 4254 a STING member galaxy). The figure shows the relationship when no DE is subtracted from the total emission of the SFR tracer (green-brown-red-blue contours) and at one particular filter scale of unsharp masking (blue contours) to highlight the significance of the subtraction of DE in the SF law. The contours are placed at 90%, 75%, 50%, and 25% of the maximum frequency. The diagonal dotted lines represent constant star formation efficiency (ϵ) where ϵ ∼100%, 10%, and 1% correspond to gas depletion time scale, $\tau_{\rm dep}$=0.1, 1.0, and 10 Gyr. The 1σ sensitivity limit of $\Sigma_{\rm H_2}$ map is ∼5.3 $M_\odot$ pc^{-2} which is derived from CARMA CO $J = 1 - 0$ observation. NGC 4254 is a normal star-forming spiral located at a kinematic distance of 16.6 Mpc. The 6″ angular scale corresponds to a physical length of ∼480 pc in the disk of the galaxy. It is apparent that the subtraction of the DE affects the low surface density regions and hence the functional form of the $\Sigma_{\rm SFR}$ - $\Sigma_{\rm H_2}$ relationship. It is also obvious that $\Sigma_{\rm H\alpha}$ shows the largest scatter among all SFR tracers.

3. Results and Analyses

3.1. NGC 4254: A Detailed Case Study

In Rahman *et al* 2011 [6] we exploit multi-wavelength data-set of NGC 4254 to conduct a thorough investigation of the impact of various methodological features in determining the

functional form of the SF law. The available data facilitates a detailed analysis using four different SFR tracer maps including FUV and 24 μm, extinction corrected Hα, observed Hα and 24 μm, and only 24 μm. We construct these maps following the prescriptions provided by [12], [13], and [14]. The variety of indicators is critical in appraising the robustness of the $\Sigma_{\rm SFR}$ - $\Sigma_{\rm H_2}$ relationship against the treatment of the DE. The details of different data samplings, various fitting considerations, and the technique to remove the DE can be found in [6].

Figure 1 underscores the results obtained from the pixel sampling and the OLS bisector fitting method only. In this figure a direct relation between the slope of the SF law and the magnitude of the DE subtracted in the pixel analysis is conspicuous: *subtraction of higher diffuse fraction corresponds to a steeper power-law index*. Compared to other sampling methods, this trend is *only* observed in the pixel analysis which contains the low surface brightness regions. Since the DE is proportionally more important in fainter regions, its subtraction increases scatter in the gas-SFR relation mostly at low surface densities. As a result, removing the DE steepens the SF law. It is also evident that the scatter in the SF law is substantially lower when no DE is subtracted from the total emission of the SFR tracers.

Among all SFR tracers, mid-infrared 24 μm displays the tightest correlation with the molecular gas ($\sigma\sim$0.2 dex from the OLS fitting). This is likely due to a combination of two effects: 1) the times scales for GMC dissipation by massive star formation and 24 μm emission are essentially the same, and 2) by its nature, this SFR tracer does not need to be corrected by extinction. The extinction-corrected $\Sigma_{\rm H\alpha}$ shows the largest scatter ($\sigma\sim$0.5 dex). This bearing is persistent regardless of the level of the unsharp masking applied to remove the DE. This is due to the fact that the extinction correction is azimuthally averaged, and it does a poor job at correcting any one position although it yields the correct result in a statistical sense.

3.2. The Sample

Rahman *et al* 2012 [7] examines $\Sigma_{\rm SFR}$ - $\Sigma_{\rm H_2}$ relation for 14 STING galaxies (including NGC 4254) by setting $\Sigma_{\rm H_2} > 20$ M$_\odot$ pc^{-2}. This threshold is chosen to ensure that: 1) the signal-to-noise is good, 2) interferometric deconvolution issues are minimized, 3) the potential contribution by the DE is less problematic, and 4) we focus on regions dominated by molecular gas. The selection of galaxies is based on secured CO $J = 1 - 0$ detection, availability of data at other wavelengths, and the $\Sigma_{\rm H_2}$ threshold mentioned above. In this subset, the molecular gas and star surface densities span a wide range, $\Sigma_{\rm H_2}\sim$20-1000 M$_\odot$ pc^{-2} and $\Sigma_{\rm SFR}\sim$4-570 M$_\odot$ Gyr^{-1} pc^{-2}. The stellar mass M$_*$ ranges in between $\sim 10^{9.7} - 10^{11.5}$ M$_\odot$.

The left panel of Figure 2 highlights spatially resolved pixel analysis for the STING sample. A simple correlation test shows that the points in this diagram are strongly correlated. We find a Pearson correlation coefficient r$\sim$0.7. The OLS bisector method yields a power-law index N$_{\rm mol}$ $\sim$1.1$\pm$0.1 where the error is derived from bootstrapping. This is an intriguing result. Despite the fact that these measurements are coming from wide variety of galactic environments and galaxy properties, the result suggests that the ensemble of points yields an approximately linear SF law. The right panel of Figure 2 shows molecular gas depletion time as a function of molecular gas surface density. The construction of the means and the error bars did not include the data points from NGC 772 and NGC 3147 (see [7] for detail explanation). It is clear from this diagram that the H$_2$ depletion time has at most a very weak dependence on $\Sigma_{\rm H_2}$. A small correlation coefficient (r$\sim$0.2) suggests that $\tau_{\rm dep}$ is mostly uniform across the disk.

The uniformity of $\tau_{\rm dep}$ over a wide range of $\Sigma_{\rm H_2}$ is most naturally explained as a consequence of the approximate constancy of the depletion time for molecular gas in GMCs. Indeed the observations of Local Group galaxies suggest that the properties GMCs are fairly uniform ([16], [17], [18]). In this scenario a linear SF law follows naturally, where the $\Sigma_{\rm SFR}$ - $\Sigma_{\rm H_2}$ relation arises from the number of GMCs filling the beam ([14], [15]). A linear molecular gas SF law is consistent with the scenario in which GMCs turn their masses into stars at an approximately

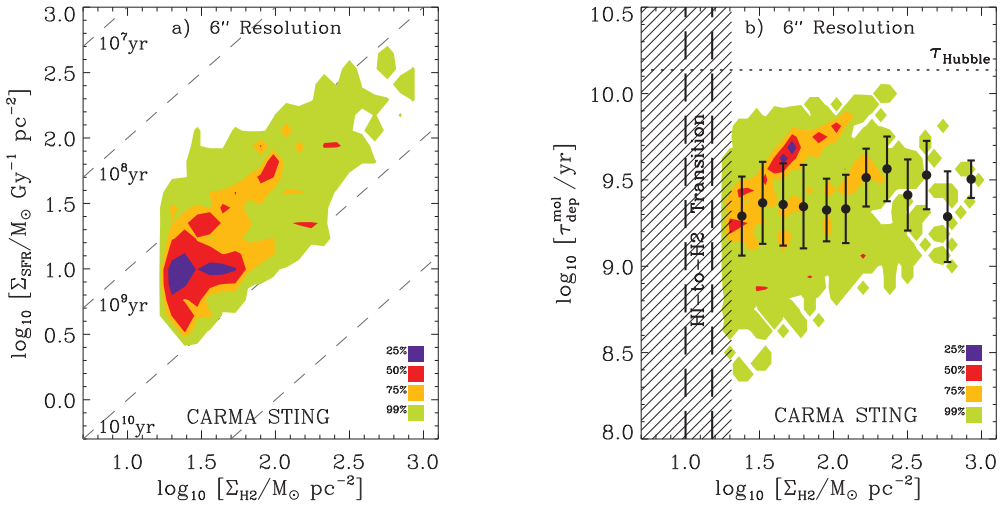

Figure 2. Panel a: Pixel analysis of the observed Σ_{SFR} - Σ_{H_2} relationship at 6″ resolution 14 CARMA STING galaxies (the original sample contains 23 galaxies). The panel shows a smoothed two-dimensional distribution where each point is weighted by the inverse of the total number of points of the contributing galaxy (all galaxies are equally important in the distribution, irrespective of the number of points they contribute). The contours of the smoothed distribution enclose 99%, 75%, 50% and 25% of the total. The diagonal dashed lines represent τ_{dep} as in Fig. 1. **Panel b:** Molecular gas depletion time (τ_{dep}) versus Σ_{H_2} at 6″ resolution for the same galaxies shown in panel a. The horizontal dotted line represents the Hubble time, and the filled circles and associated error bars in black represent the median and 1σ dispersion in Σ_{H_2} bins. The gray hatch illustrates the region where $\Sigma_{H_2} < 20$ M$_\odot$ pc^{-2} which we remove from our analysis. Observational studies suggest that HI-to-H_2 phase transition occurs around Σ_{H_2} ~10-15 M$_\odot$ pc^{-2} and the nature of the (total) gas-SFR surface density relation changes dramatically around this range [13]. By sampling high Σ_{H_2} regions, $\Sigma_{H_2} > 20$ M$_\odot$ pc^{-2}, we, therefore, investigate the SF law in the molecular region of a galaxy disk [7].

constant rate, irrespective of their environmental parameters [19].

4. Summary and Conclusions

It is important to note that the different choices of SFR tracers and spatial scales mean sampling different SF histories and different time scales in a galaxy. It is also possible that these differences correspond to a spectrum of physical SF mechanisms present in a wide range of environments. Using CARMA STING data-set we analyze the relationship between the SFR and molecular gas surface densities at the sub-kpc level to explore how the functional form of the SF law depends on the treatment of various data sampling. We also critically examine how different fitting techniques influence the outcome. In particular, we probe in-depth the contribution of the DE in various SFR tracers and its consequences on the spatially resolved SF law.

We find that a precise observational constraint on the linear or non-linear functional form of the relationship requires an accurate estimate of the fraction of the DE. Our results show that the treatment of the DE has notable impact on the intrinsic scatter in the canonical SF law. The scatter varies substantially with the choice of the SF tracer used. For example, the non-linear 24 μm star formation tracer shows the tightest correlation with the molecular

gas content whereas (azimuthally averaged) extinction corrected Hα as a tracer appears to be the noisiest. By measuring the relationship in the bright, high molecular gas surface density ($\Sigma_{H_2} \sim$ 20 $M_\odot$ pc^{-2}) regions of the disks to minimize the contribution from diffuse extended emission and using 24 μm emission as a tracer of SF, we find an approximately linear relation between molecular gas and star formation rate surface density with a molecular gas depletion time $\sim$2.30 Gyr.

Acknowledgments
NR acknowledges support from the South Africa Square Kilometer Array (SKA) Postdoctoral Fellowship program. The authors thank SINGS and GALEX NGS teams for their excellent data set. This work has made use of the NASA/IPAC Extragalactic Database (NED) which is operated by the JPL/Caltech, under contract with NASA. Support for CARMA construction was derived from the Gordon and Betty Moore Foundation, the Eileen and Kenneth Norris Foundation, the Caltech Associates, the states of California, Illinois, and Maryland, and the NSF. Funding for ongoing CARMA development and operations are supported by NSF and CARMA partner universities.

5. References

[1] Schmidt M 1959 *ApJ* **129** 243
[2] Schmidt M 1963 *ApJ* **137** 758
[3] Sanduleak N 1969 *AJ* **74** 47
[4] Hartwick F D A 1971 *ApJ* **163** 431
[5] Kennicutt R C Jr 1989 *ApJ* **344** 685
[6] Rahman N, Bolatto A D, Wong T, *et al* 2012 *ApJ* **730** 72
[7] Rahman N, Bolatto A D, Xue R, *et al* 2011 *ApJ* **745** 183
[8] Sanders D B, Mazzarella J M, Kim D C, Surace J A, and Soifer B T 2003 *AJ* **126** 1607
[9] Rieke G H, *et al* 2004 *ApJs* **154** 25
[10] Gil de Paz A, *et al* 2007 *ApJS* **173** 185
[11] Kennicutt R C Jr *et al* 2003 *PASP* **115** 928
[12] Calzetti D, *et al* 2007 *ApJ* **666** 870
[13] Kennicutt R C Jr *et al* 2007 *ApJ* **671** 333
[14] Bigiel F, Leroy, A, Walter F *et al* 2008 *AJ* **136** 2846
[15] Komugi S, Sofue Y, Nakanishi H, Onodera S, and Egusa F 2005 *PASJ* **57** 733
[16] Blitz L, Fukui Y, Kawamura A, *et al* 2007 *ProtoStars and Planets* vol V, ed B Reipurth, D Jewitt, *et al* (Tucson: University of Arizone Press) p 81
[17] Bolatto A D, Leroy A K, Rosolosky E, Walter F and Blitz L 2008, *ApJ* **686** 948
[18] Fukui Y and Kamagura A 2010 *Annu. Rev. Astron. Astrophys.* **48**, 547
[19] Krumholz M R and McKee C F 2005 *ApJ* **630** 250

SDSS J120011-020452: Unusual I Zw 1 object or a nearby BAL Seyfert?

Nurur Rahman†, Hartmut Winkler

Department of Physics, University of Johannesburg, PO Box 524, 2006 Auckland, Johannesburg, South Africa.
†South Africa SKA Fellow.

E-mail: nrahman@uj.ac.za

Abstract. Emission line diagnostics in active galactic nuclei (AGN) provide vital clues about the physical conditions of gas accountable for the emission emanating from the central region. We typically identify a region of narrow-line formation that normally includes oxygen, nitrogen, sulfur, and other forbidden lines. In some objects (Type 1 Seyferts) we in addition detect broad Balmer lines, helium lines and, in some instances, emission features attributed to Fe II. During a search for AGN in the Sloan Digital Sky Survey (SDSS), we discovered a spectrum of SDSS J120011-020452, a z∼0.091 Seyfert galaxy that displays some unusual features. The narrow forbidden lines are all but absent (with only [O II] very barely visible), the Fe II spectrum is prominent and Na I absorption is clearly detected. In these respects, the object resembles the usually much more distant "broad absorption line" quasars (BAL) with strong Fe II lines (e.g., IRAS 07598+6508). The emission lines are in addition comparatively narrow, which makes this object an interesting hybrid between the BAL Seyferts and the class of AGN referred to as "narrow line Seyfert 1" galaxies (NLS1) with weak forbidden lines (e.g., I Zw 1 objects). We perform spectral line fitting on the SDSS data and compare line ratios in an attempt to shed light on the nature of the nuclear region of this interesting object. We discuss the limitations of the available data, and conclude that a better signal to noise (S/N) spectrum would allow us to determine the relative strengths of any other forbidden lines in the spectrum, get better profiles of the absorption features and better define the Fe II spectrum. We use this to motivate for follow-up observations using the the South African Large Telescope (SALT) Robert Stobie Spectrograph (RSS) in the upcoming round of proposals.

1. Introduction

Type 1 Seyfert galaxies have broad H I, He I, and He II emission lines with full-width at half-maximum (FWHM) of the order 1-5 $\times 10^3$ km/sec and typically oxygen, nitrogen and sulfur forbidden lines with FWHM of about 5 $\times 10^2$ km/sec. The spectra of Seyfert galaxies are virtually always characterized by prominent [O III] $\lambda\lambda$4959, 5007 lines. Many Seyfert 1 galaxies also show broadened permitted (and sometimes even forbidden) Fe II emission lines which overlap in two broad 'bands' near λ4570 and λ5250 [1]. The Narrow Line Seyfert 1 (NLS1) galaxies are a sub-class of Seyferts in which broad H I and He emission lines are relatively narrow (FWHM $<$ 2000 km/sec). These objects also have strong Fe II emission, but their [O III] emission tends to be weak compared to other Seyferts ([2], [3], [4], [5], [6]). Broad absorption line (BAL) quasars are yet another, normally luminous, class of objects with spectra that may be broadly classified as Seyfert 1. Characteristic features of the BAL systems are the absorption features of Mg II

λ2798, He I λ3889 and Na I $\lambda\lambda$5889, 5895 lines. Markarian 231 and IRAS 07598+6508 are two well-known examples of comparatively nearby BAL systems ([6], [7], [8]).

During a search for AGN in the Sloan Digital Sky Survey (SDSS) archive [9], we noticed the spectrum of SDSS J120011-020452, which displays some unusual features. In the spectrum the forbidden lines are narrow and weak. Only [O II] $\lambda\lambda$3726, 3729 evident, but the feature at the approximate position of [O III] λ5007 is in fact one of the Fe II lines. The Fe II spectrum is clearly prominent, and furthermore the Balmer and Fe II line widths are small (as found in NLS1). In that respect the spectrum matches that of the well known I Zw 1 [6], which is also the prototype of a sub-class of NLS1 with strong iron features named after it. However, unlike in typical I Zw 1 objects, Na I absorption is clearly detected in SDSS J120011-020452. These uncommon characteristics suggests that the subject of this study is a rare hybrid whose spectrum encompasses attributes present in I Zw 1 type objects on the one hand and BAL AGN on the other. In this report we provide a preliminary analysis of the SDSS data on the basis of which we will justify the need to obtain higher quality spectra of this object using the SALT.

2. Data Analysis

We examined a multi-wavelength image of SDSS J120011-020452 displayed on the SDSS website (Fig. 1) as well as the spectrum (Fig. 2) of the source, also from the SDSS archive [9]. The estimated redshift (z $\sim$ 0.0911) puts the source at $\sim$412 Mpc away (based on the SDSS-adopted parameters). This implies a host galaxy disk size of $\sim$10 kpc. The u, g, r, i, and z magnitudes of the source are given as $19.63 \pm 0.03, 18.20 \pm 0.01$, $17.42 \pm 0.01, 16.80 \pm 0.01$,and 16.52 ± 0.01, respectively [9]. The parameters fitted to the emission or absorption lines and the continuum are provided by the SDSS data reduction pipeline and we use these estimates. The lines are fitted with Gaussian profiles.

The continuum-subtracted spectrum shows moderately broad Balmer lines (Fig. 3). The peaks flux densities of Hα, Hβ, Hγ, Hδ lines are 436, 92, 23, and 9 $\times 10^{-17}$ erg cm^{-2} s^{-1} Å^{-1}, respectively, and the FWHM of these lines are 1189, 1436, 1198, and 640 km/sec. A significantly lower FWHM of Hδ line (factor of 2) compared to other Balmer lines can be attributed to poor S/N. The Hϵ line is barely visible. The Balmer line ratio Hα/Hβ $\sim$ 4.7 suggests presence of reddening in the emission line region. This is supported by the presence of the absorption. The He I λ5875, λ6678, λ7065 lines are present in the spectrum albeit weakly. For these lines we find He I/Hβ $\sim 0.11 - 0.16$. With the exception of the previously mentioned [O II] λ3727,λ3729 line, [S II] λ6716, λ6731 also shows up weakly, but all other spectral features can be attributed to Fe II. Despite the poor S/N, we tried to estimate the forbidden line peak flux densities and widths. We find these to be 10-20 $\times 10^{-17}$ erg cm^{-2} s^{-1} Å^{-1} and FWHM $\sim$ 200-300 km/sec.

An interesting property of this spectrum is the absorption of the Na I λ5889, λ5895 doublets. The equivalent width of this absorption feature is $\sim$ 3 Å, strength Na I D/Hβ $\sim$ 0.12, and the FWHM corresponds to an outflow velocity $\sim$385 km/sec. The prevalence of both narrow and broad Fe II emission lines from ultra-violet to near-infrared is a characteristic of type I Seyfert galaxies. The spectrum of SDSS J120011-020452 clearly shows signatures of Fe II λ4570 and λ5250 multiplet. The peak ratio between these lines and Hβ is $\sim$ 0.12. In Fig. 4 we identify several Fe II emission lines present in the λ4570 multiplet using the narrow and broad Fe II emission template provided by [4].

3. Discussions

In contrast to the previously discovered and earlier mentioned BAL AGN, SDSS J120011-020452 has narrower and thus more sharply defined emission features. Its spectrum therefore presents the opportunity to identify and fit blended lines with an accuracy otherwise not possible in the more nearby BAL AGN.

To gain insight about the properties of the central emitting regions, and especially to determine the nature of the narrow-line forming gas clouds, we need high quality spectra with better S/N. In order to achieve this we are planning to make a follow-up observation of this object using the SALT RSS. A better S/N spectrum could 1) determine the relative strengths of any other forbidden lines in the spectrum (in the SDSS spectrum we only see extremely weak [O II] and [S II], 2) get better profiles of the absorption features (which are visible even in the SDSS spectrum), 3) enable us to better define the FeII spectrum, and 4) apply improved fits to the data to be consistent with the emission line diagnostics studies in the literature. The planned further study is likely to offer a unique insight into the nature of BAL AGN weak narrow-line regions and the formation of the absorption bands.

Acknowledgments
NR acknowledges support from South Africa Square Kilometer Array (SKA) Postdoctoral Fellowship program. Funding for the SDSS and SDSS-II has been provided by the Alfred P. Sloan Foundation, the Participating Institutions, the National Science Foundation, the U.S. Department of Energy, the National Aeronautics and Space Administration, the Japanese Monbukagakusho, the Max Planck Society, and the Higher Education Funding Council for England. The SDSS Web Site is http://www.sdss.org. The SDSS is managed by the Astrophysical Research Consortium for the Participating Institutions. The Participating Institutions are the American Museum of Natural History, Astrophysical Institute Potsdam, University of Basel, University of Cambridge, Case Western Reserve University, University of Chicago, Drexel University, Fermilab, the Institute for Advanced Study, the Japan Participation Group, Johns Hopkins University, the Joint Institute for Nuclear Astrophysics, the Kavli Institute for Particle Astrophysics and Cosmology, the Korean Scientist Group, the Chinese Academy of Sciences (LAMOST), Los Alamos National Laboratory, the Max- Planck-Institute for Astronomy (MPIA), the Max-Planck- Institute for Astrophysics (MPA), New Mexico State University, Ohio State University, University of Pittsburgh, University of Portsmouth, Princeton University, the United States Naval Observatory, and the University of Washington.

4. References

[1] Osterbrock D E and Ferland G J 2006 *Astrophysics of Gaseous Nebulae and Active Galactic Nuclie* Second edition (California : University Science Books)
[2] Osterbrock D E and Pogge R W 1985 *ApJ* **297** 166
[3] Boroson T A and Green R F 1992 *APJS* **80** 109
[4] Véron-Chetty M-P, Joly M and Véron P 2004 *A&A* **417** 515
[5] Véron-Chetty M-P, Joly M, Véron P *et al* 2006 *A&A* **451** 851
[6] Véron-Chetty M-P, Véron P, Jolly M and Kollatschny W 2007 *A&A* **475** 487
[7] Boroson T A, Meyers K A, Morris, S L and Persson S E 1991 *ApJ* **370** L19
[8] Lipari S, Colina L and Macchetto F 1994 *ApJ* **427** 174
[9] Abazajian K, Adelman JJ, Agueros M, *et al* 2003 *Astron. J.* **126** 2081

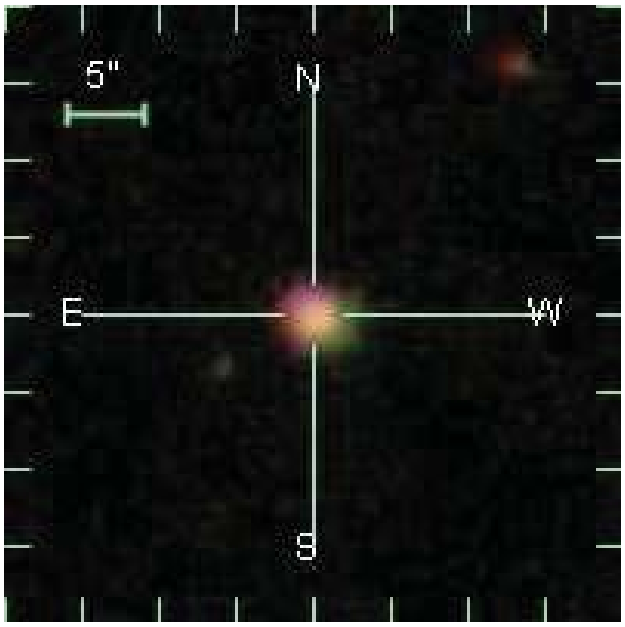

Figure 1. The SDSS multi-wavelength image of the source SDSS J120011-020452. The field-of-view is $\approx 40" \times 40"$.

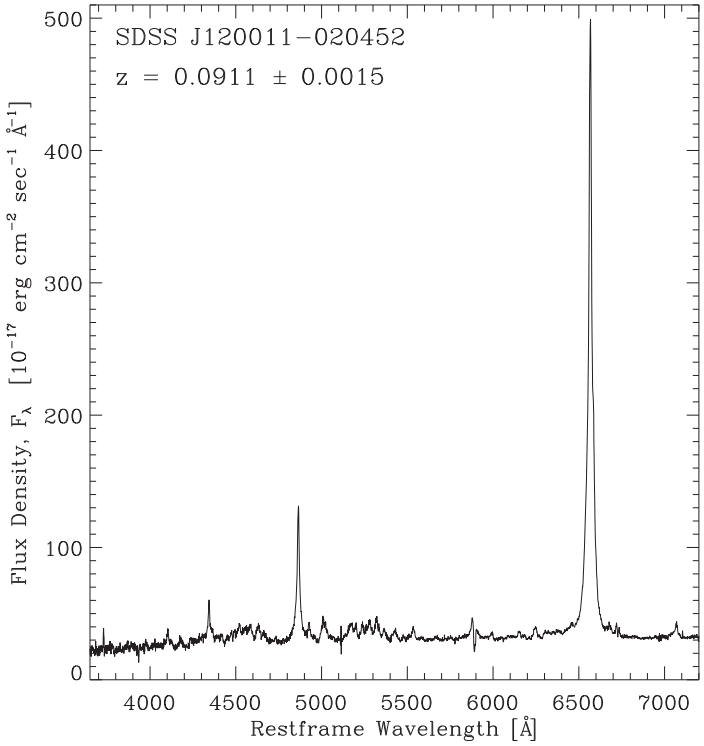

Figure 2. The rest-frame optical spectrum of the source containing both continuum and line fluxes.

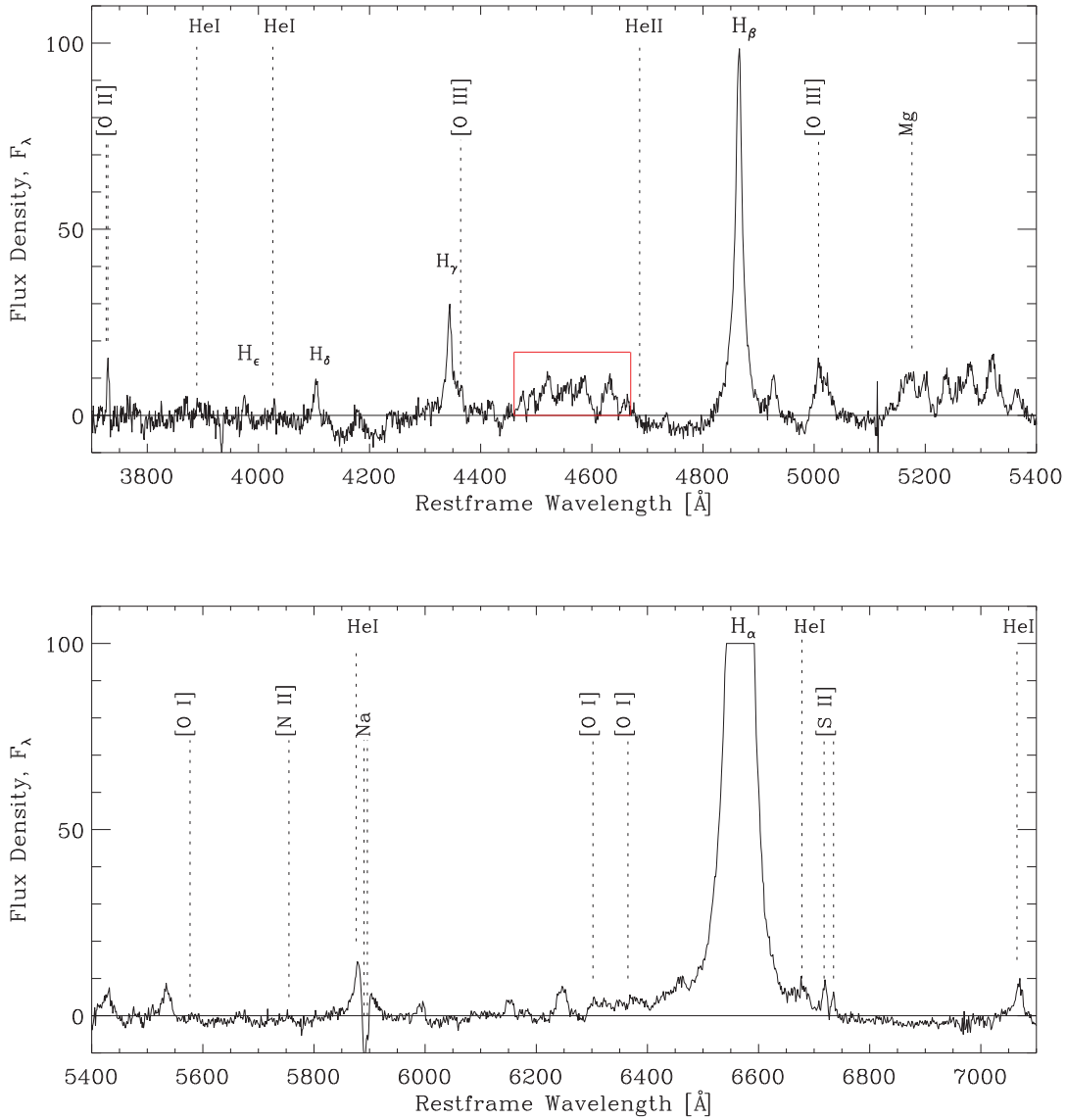

Figure 3. The emission and absorption lines in the continuum subtracted rest-frame spectrum of the source. The box highlights part of the spectrum containing both permitted and forbidden lines of Fe II λ4570 multiplet. The flux density is in unit of 10^{-17} erg cm^{-2} s^{-1} Å^{-1}.

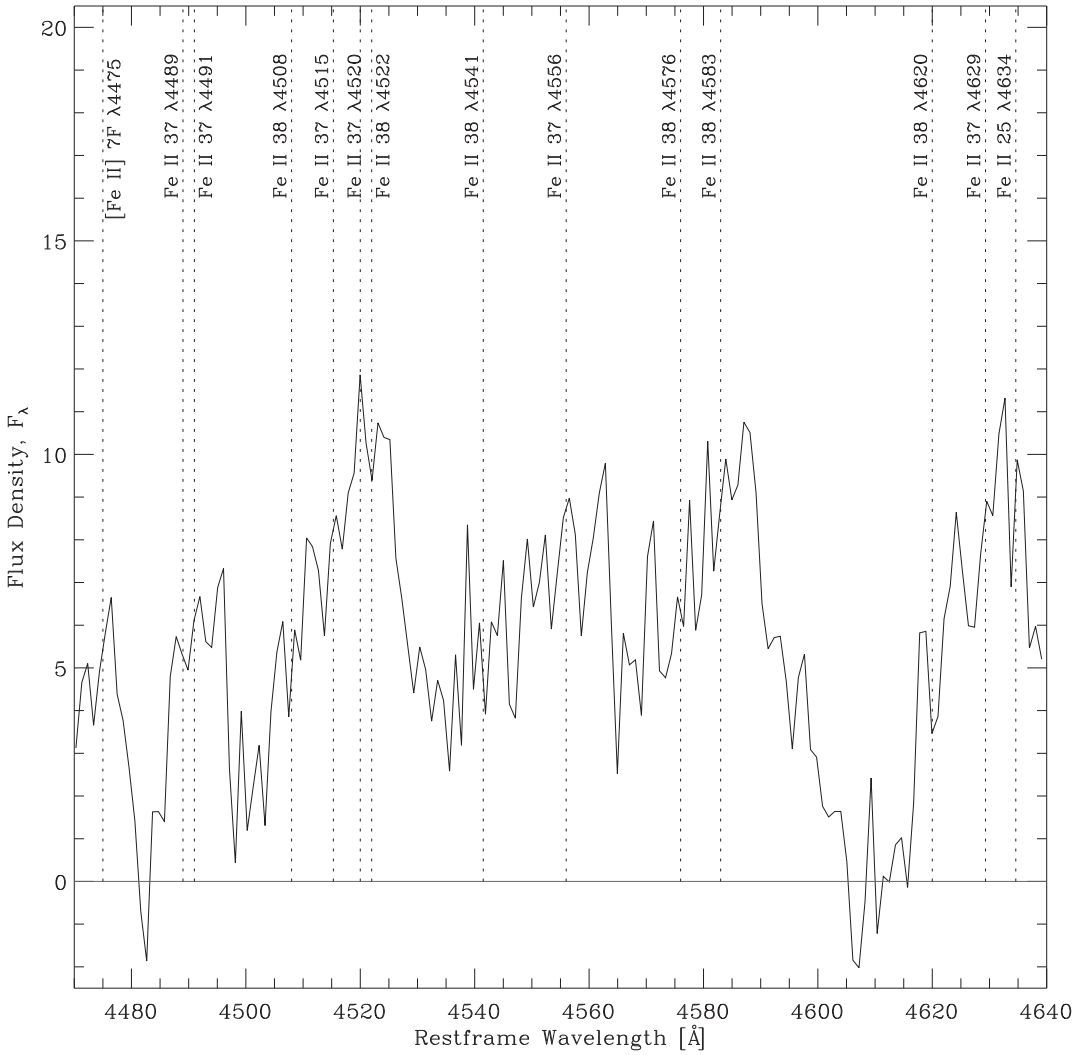

Figure 4. The region within the box in Fig. 3 is enlarged and several Fe II emission lines are identified using the template provided by [4]. The flux density is in unit of 10^{-17} erg cm^{-2} s^{-1} Å^{-1}.

Galaxy peculiar velocities in the Zone of Avoidance

K Said, R C Kraan-Korteweg and T H Jarrett

Astrophysics, Cosmology and Gravity Centre (ACGC), Department of Astronomy, University of Cape Town, Private Bag X3, Rondebosch 7701, South Africa.

E-mail: khaled@ast.uct.ac.za, kraan@ast.uct.ac.za, jarrett@ast.uct.ac.za

Abstract. Dust extinction and stellar confusion of the Milky Way hinder the detection of galaxies at low Galactic latitude, creating the so-called Zone of Avoidance (ZoA). This has hampered our understanding of the local dynamics, cosmic flow fields and the origin of the Cosmic Microwave Background dipole. The ZoA ($|b| \leq 5^\circ$) is also excluded from the "whole-sky" Two Micron All-Sky Survey (2MASS) Redshift Survey (2MRS) and 2MASS Tully-Fisher Survey (2MTF). The latter aims to provide distances and peculiar velocities for all bright inclined 2MASS galaxies with $K_s^o \leq 11\overset{\text{m}}{.}25$. Correspondingly, knowledge about the density distribution in the ZoA remains limited to statistical interpolations. To improve on this bias we pursued two different surveys to fill in the southern and northern ZoA. These data will allow a direct measurement of galaxy peculiar velocities. In this paper we will present a newly derived optimized Tully-Fisher (TF) relation that allow accurate measures of galaxy distances and peculiar velocities for dust-obscured galaxies. We discuss further corrections for magnitudes and biases and present some preliminary results on flow fields in the southern ZoA.

1. Introduction

Galaxies are not uniformly distributed in space. They instead tend to accumulate in over-dense regions such as clusters, walls and filaments, which surround low-dense regions called voids. To fully understand the dynamics of the Local Group (LG), cosmic flow fields, and the origin of the observed dipole in the Cosmic Microwave Background (CMB), we need to trace this Large-Scale-Structure (LSS) through all-sky surveys, not only with galaxy positions, but also their velocities [1, 2]. Velocities of galaxies can be decomposed into two components: a recession velocity due to the uniform expansion of the universe and a peculiar velocity caused by density inhomogeneities. The peculiar velocity (its radial component) is measured as the difference between the observed recession velocity of a galaxy and its Hubble velocity. Because they arise as a result of gravity, peculiar velocities can be used as tracers of the matter distribution, both luminous and dark.

Separation of these two components requires a distance indicator. Since the discovery of the empirical Tully-Fisher relation (TF; [3]), it has been widely used as the distance indicator in peculiar velocity surveys. The Two Micron All-Sky (2MASS; [4]) Tully-Fisher Survey (2MTF; [5]) intends to provide a complete Tully-Fisher analysis (i.e. distances and peculiar velocities) of all bright inclined spirals in the 2MASS Redshift Survey (2MRS; [6]). Although the use of a Near InfraRed (NIR) TF analysis will reduce the impact of dust extinction of the Milky Way because it suffers less from extinction, the Zone of Avoidance (ZoA) is not sampled in the 2MTF ($|b| < 5^\circ$; $|b| < 8^\circ$ for $|l| < 30^\circ$). For cosmological applications, different methods have been employed to interpolate across this part of the sky e.g. [7, 8]. This may be valid for the conspicuous features that cross the ZoA, such as the Great Attractor (GA), Perseus-Pisces

Supercluster, Puppis Cluster or the Local Void. However, more recent ZoA surveys reveal large-scale structures that were not anticipated. Blind HI surveys in the southern ZoA [9, 10] have opened an elegant way to fill in this gap. These kind of surveys do not suffer from foreground extinction. We aim to use these data to determine reliable peculiar velocities for the galaxies in the ZoA which are excluded from the 2MRS and the 2MTF. The 2MTF thus supplemented with our data will result, for the first time, in a complete all-sky peculiar velocity survey.

This paper is organized as follows. In Section 2 we discuss the data from both the southern and northern ZoA. Section 3 provides a recipe on how to derive peculiar velocities for field galaxies in the ZoA. A preliminary flow field for a subsample of the southern ZoA is presented in Section 4.

2. Data in the ZoA

The extent of the Zone of Avoidance is different in various wavebands. While in the optical and the NIR the major problems are dust extinction and stellar confusion, systematic HI surveys do not suffer from these effects. Therefore, two independent observing programmes have been started to obtain HI observations for galaxies in both the southern and the northern ZoA.

2.1. HI Parkes Deep ZoA Survey

The HI Parkes Deep Zone of Avoidance Survey (HIZoA) is a blind HI survey of the southern ZoA ($|b| \leq 5°$; Dec $< +15°$), conducted on the 64 m Parkes radio telescope [12, 13, 14]. The survey covers the whole southern ZoA visible from Parkes out to 12700 km/s, and resulted in about 900 detected galaxies with rms $\sim$ 6mJy/beam. We have performed an imaging NIR J, H, K_s bands follow-up survey of all HIZoA-galaxies with the InfraRed Survey Facilty (IRSF) on the 1.4m telescope at Sutherland, South Africa [15].

2.2. 2MASX Redshift ZoA

In 2009, Kraan-Korteweg and collaborators started an observing programme to obtain HI redshifts for all bright galaxies in the 2MASS Extended Source Catalog (2MASX) [16] with $K_s^o < 11.25$ mag in the ZoA ($|b| < 10°$) which do not have any previous redshift determinations. The Nançay Radio Telescope (NRT) in France and the Parkes radio telescope in Australia have been used to cover the entire ZoA. Over a thousand galaxies without previous redshifts have been observed with the NRT (Dec $> -38°$), resulting in more than 250 detected galaxies [11]. Parkes observations started in 2013 and 74 galaxies without previous redshifts have been observed to date.

3. Methodology

The Tully-Fisher relation is a correlation between rotational velocities and absolute magnitudes of spiral galaxies. The rotational velocity is extracted directly from the HI spectral data, and the apparent magnitude is measured from the imaging data. Deriving peculiar velocities from the TF relation, requires the calibration of a global TF relation from a sample of galaxies with known distances. The peculiar velocity is defined as the difference in the Hubble velocity according to the TF distance and the observed velocity from its redshift.

3.1. Tully-Fisher template relation in J, H, and K_s bands

The TF calibration sample should be unbiased. Although the galaxies of the template sample lie far from the Galactic Plane, their photometric and spectroscopic data should be treated in the same way as any peculiar velocity sample to which it will be applied. The currently most elaborate and extensive NIR TF calibration in J, H, and K_s bands [5] of 888 galaxies is based on the total magnitude as the closest proxy to total mass. However, 2MASS does not trace

the lower surface brightness features very well. This is particularly severe in areas of high dust extinction and stellar density. We therefore prefer to work with isophotal magnitudes which should not be affected by those effects.

To demonstrate this, we construct a comparison between two different surveys, the 2MASX [16] and the IRSF galaxy Catalog [15]. The depth of the IRSF survey (10 min exposure time) and four times higher spatial resolution ($0\farcs45$/pix) results in a 2 mag deeper survey compared to 2MASX. We select a subsample of 66 galaxies, observed in both 2MASX and the IRSF Catalog and compare their total extrapolated magnitudes and isophotal magnitudes (measured in an elliptical aperture defined at the $K_s = 20$ mag arcsec^{-2}).

Figure 1 displays the offsets between 2MASX and IRSF, $\Delta m = m(\mathrm{2MASS}) - m(\mathrm{IRSF})$, for both total and isophotal magnitude in the J, H, and K_s bands. The deeper observations with high optical resolution prove that the 2MASX total magnitudes have large scatter and are on average underestimated. Note that such systematic offsets produce artificial flow in the analysis of peculiar velocities. This effect completely disappears when we use isophotal magnitudes.

This result confirms that it is imperative to use the isophotal magnitude for $|b| < 5^\circ$, or any other region of high dust obscuration. Using isophotal magnitudes on the other hand can equally well be applied in dust and star-free areas of the sky, hence allow real whole-sky coverage.

We therefore re-calibrated the NIR J, H, K_s bands TF relation following the exact same steps and procedures as outlined in [5], but for isophotal magnitudes and including Galactic extinction correction according to [17].

3.2. Peculiar velocity in the ZoA

To test our newly calibrated TF relation we used a preliminary sample in the ZoA based on a subsample of HIZoA galaxies with $v_{hel} = 6000$ km/s that have bona-fide counterparts in the IRSF catalogue. We consider here only 120 galaxies with high-fidelity photometric and spectroscopic parameters, after applying additional restrictions on inclination (i) and linewidth (W). All photometric and spectroscopic data were corrected to be consistent with the TF template relation. We confirm that the isophotal magnitudes lead to a significant decrease in the TF scatter and reduce the overall offset (systematic flow) compared to total magnitudes.

4. Early results

The majority of the derived peculiar velocities for the 120 bright, inclined spiral galaxies lie within $|v_{pec}| \leq 1000$ km/s, with the largest outliers out to $|v_{pec}| \leq 2500$ km/s. The latter seem to originate from fairly face-on or low mass galaxies. We used these peculiar velocities to construct a flow-field map in the ZoA (Figure 2). This map is obtained by interpolating the peculiar velocities across the Galactic longitude and the recession velocity. Each dot in the map is a galaxy colour-coded by its measured peculiar velocity. The black star presents the centre of the GA [18]. The map clearly shows the infall into the GA.

The selection of galaxies with $v_{obs} \leq 6000$ km/s limits our ability to quantify the backside infall toward the GA, and the infall into the much more remote Shapley Concentration (SC). To improve on the GA infall signal we started to extend our sample to $v_{obs} \leq 9000$ km/s in 2012. For even larger redshifts the sample becomes very sparse and the errors on measured peculiar velocities become comparable to the peculiar velocities themselves. The peculiar velocity error is calculated by combining the absolute magnitude error, velocity width error, and the intrinsic scatter in TF-template relation in a quadratic form. Most of the galaxies have errors of a few hundred km/s, which is a typical value for most methods available today.

For a first interpretation of the resulting data, we compare our peculiar velocities with a GA model proposed by Faber & Burstein [19]. The model describes the influence of the GA $v_{pec,A} = v_A(r_A/d_A)[(d_A^2 + c_A^2)/(r_A^2 + c_A^2)]^{(n_A+1)/2}$, where v_{pec} is the predicted peculiar velocity, r_A is the distance of a galaxy from the infall centre, d_A is the distance of the infall centre

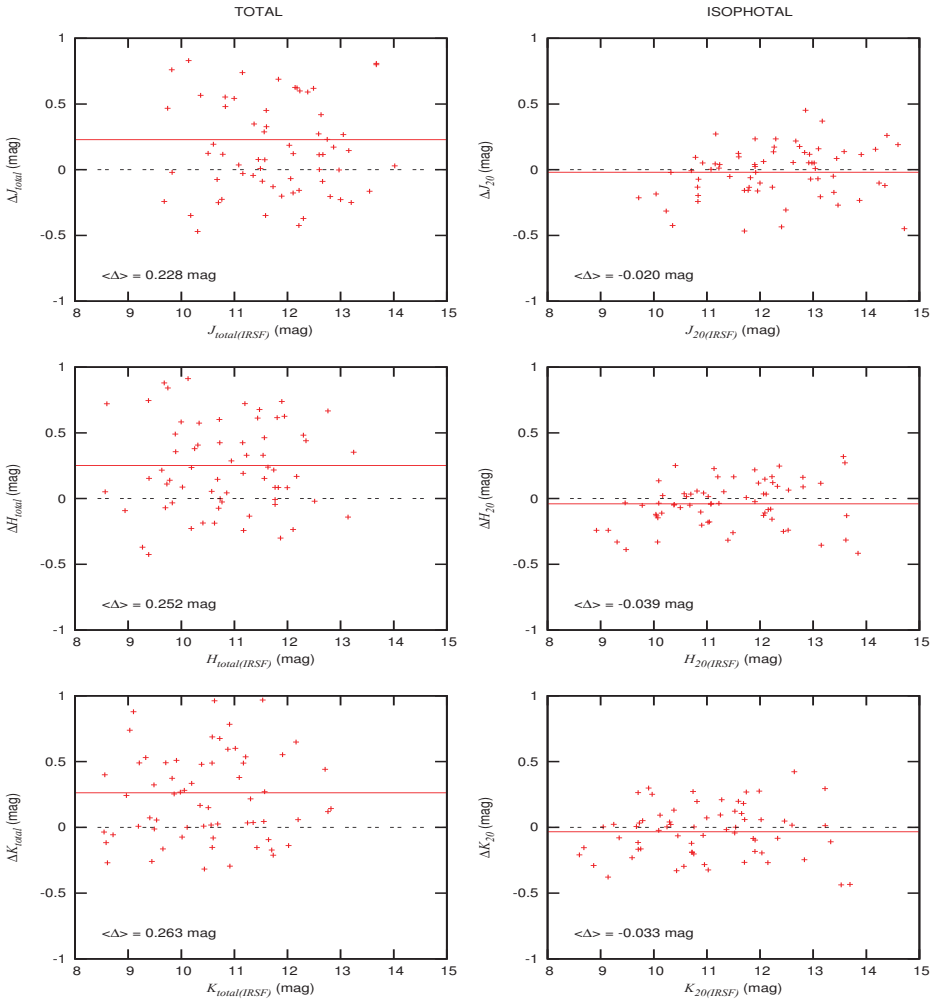

Figure 1: Comparison of 2MASS and IRSF photometry of ZoA galaxies. The left panels display the total magnitudes and the right panels display the isophotal magnitudes with J, H, and K_s band arranged from top to bottom. In all panels, solid red lines mark the mean of the difference, and the dashed black lines is the zero-line. The mean difference is given in the bottom left corner of each plot.

from the Local Group, v_A is the peculiar velocity generated by the GA at the position of the LG, and c_A is the core radius of the centre of the GA. We adopted the values of parameters given in [20], $n_A = 1.7$, $v_A = 535$ km/s and $c_A = 1430$ km/s. For d_A we used 4844 km/s, following [18]. To compare the single GA model to our data, we restricted our sample to the most accurate subsample using only the galaxies with $\log W > 2.3$ and $i < 0.5$ in the GA region ($290° < l < 350°$; $|b| \leq 5°$). Figure 3 depicts the data with the GA model. The shaded area presents our observational limit of $v_{obs} \leq 6000$ km/s. While the errors of the peculiar velocities increase with distance (as expected), the peculiar velocities seem to follow the shape of the early GA model quite well (although no quantitative analysis has been done as yet).

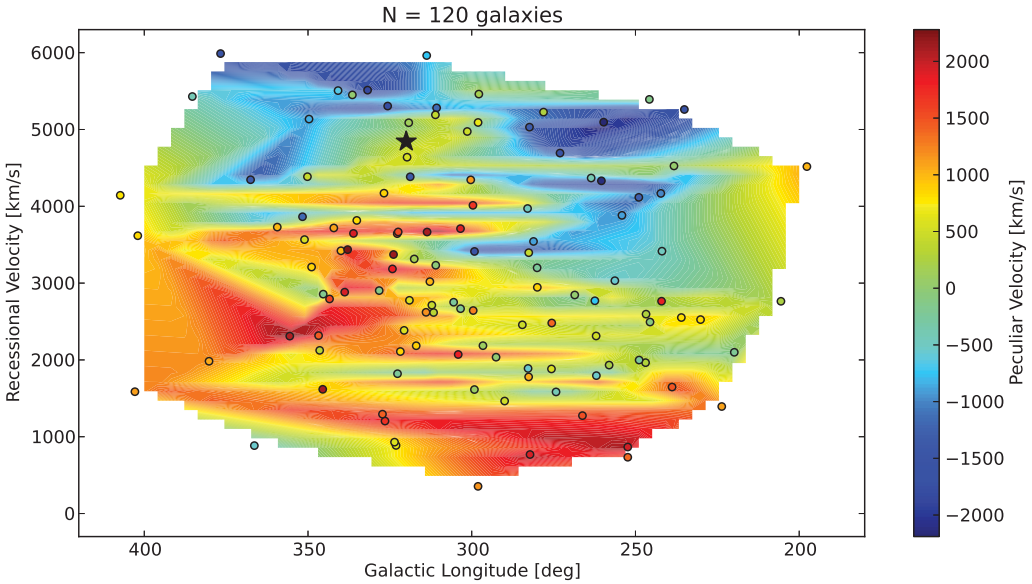

Figure 2: Peculiar velocity map of galaxies with recession velocities below 6000 km/s and -2500 km/s $< v_{pec} <$ 2500 km/s, obtained by interpolating the peculiar velocities across the Galactic longitude and recession velocity. All galaxies with $\log W > 1.8$ are used here. Individual galaxies are colour-coded by their derived peculiar velocities (in km/s). The centre of the GA is plotted as a large black star.

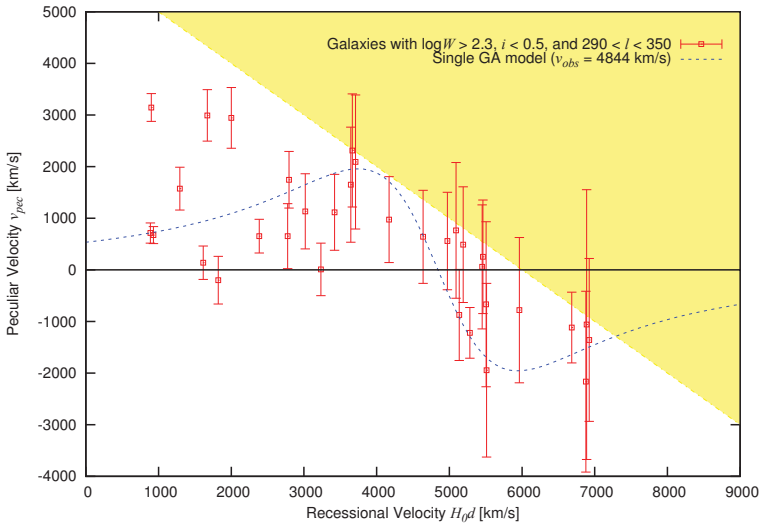

Figure 3: Peculiar velocity as a function of recessional velocity for a subsample of galaxies with $\log W > 2.3$, $i < 0.5$ in the region $290° < l < 350°$. The dotted curve presents the GA model. The error bars reflect the peculiar velocity errors. The deviation of some points from the curve probably due to selection effects.

5. Conclusions

We have shown that a peculiar velocity analysis in the ZoA is feasible if a NIR isophotal TF relation is applied. This new tool and new data provide a powerful tool to trace the matter distribution in the ZoA. Our preliminary (yet incomplete) data with $v_{hel} \leq 6000$ km/s show clear infall into the GA. The data set has since been extended to include all the HI galaxies in the southern ZoA within $v_{obs} \leq 9000$ km/s. This will enable us to test multi-attractor models,

such as GA plus the Shapley Concentration. Combining our data with that from 2MTF will lead to a complete all-sky peculiar velocity survey.

Acknowledgements
This work is based upon research supported by the South African National Research Foundation and Department of Science and Technology. The authors thank Wendy Williams for communicating her data in the ZoA. KS is very grateful to Dr. Maciej Bilicki for his reading and comments on the paper. We acknowledge the HIZOA survey team for early access to the data. This publication makes use of data products from the Two Micron All Sky Survey, which is a joint project of the University of Massachusetts and the Infrared Processing and Analysis Center, funded by the National Aeronautics and Space Administration and the National Science Foundation.

References
[1] Kraan-Korteweg, R.C., & Lahav, O. 2000, A&ARv 10, 211
[2] Loeb, A. & Narayan, R. 2008, MNRAS, 386, 2221
[3] Tully, R. B., & Fisher, J. R. 1977, A&A, 54, 661
[4] Skrutskie, M. F., Cutri, R. M., Stiening, R., et al. 2006, AJ, 131, 1163
[5] Masters, K. L., Springob, C. M., & Huchra, J. P. 2008, AJ, 135, 1738
[6] Huchra, J. P., Macri, L. M., Masters, K. L., et al. 2012, ApJS, 199, 26
[7] Lahav, O., Fisher, K. B., Hoffman, Y., Scharf, C. A., & Zaroubi, S. 1994, ApJ, 423, L93
[8] Kolatt, T., Dekel, A., & Lahav, O. 1995, MNRAS, 275, 797
[9] Henning, P. A., Staveley-Smith, L., Ekers, R., et al. 2000, AJ, 119 2686
[10] Kraan-Korteweg, R. C., Staveley-Smith, L., Donley, J., Koribalski, B., & Henning, P. A. 2005, in IAU Symposium, Vol. 216, Maps of the Cosmos, ed. M. Colless, L. Staveley-Smith, & R. A. Stathakis, 203
[11] Ramatsoku, M. 2012, MSc thesis, University of Cape Town
[12] Kraan-Korteweg, R. C. 2005, RvMA, 18, 48
[13] Donley, J. L. et al. 2005, AJ, 129, 220
[14] Shafi, N. 2008, MSc thesis, University of Cape Town
[15] Williams W.L., Woudt P.A. & Kraan-Korteweg R.C. 2011, Ten years of Infrared Survey Facility and the Future, eds. T. Nagayama, S. Sato, and K. Wakamatsu, 98 (arXiv:1107.1096)
[16] Jarrett T. H., Chester T., Cutri R., et al. 2000, AJ, 119, 2498
[17] Riad, I. F., Kraan-Korteweg, R. C., & Woudt, P. A. 2010, MNRAS, 401, 924
[18] Woudt, P. A., Kraan-Korteweg, R. C., & Fairall, A. P. 1999, A&A, 352, 39
[19] Faber, S. M. & Burstein, D. 1988, Motions of galaxies in the neighborhood of the local group, ed. Rubin, V. C. & Coyne, G. V., 115-167
[20] Burstein D., 1990, Rep. Prog. Phys., 53, 421

Modelling the γ-ray and radio light curves of the double pulsar system

A S Seyffert[1], C Venter[1], A K Harding[2] and T J Johnson[3,4]

[1] Centre for Space Research, North-West University, Potchefstroom Campus, Private Bag X6001, Potchefstroom 2520, South Africa

[2] Astrophysics Science Division, NASA Goddard Space Flight Center, Greenbelt, MD 20771, USA

[3] National Research Council Research Associate, National Academy of Sciences, Washington, DC 20001

[4] High-Energy Space Environment Branch, Naval Research Laboratory, Washington, DC 20375, USA

E-mail: 20126999@nwu.ac.za

Abstract. Guillemot et al. recently reported the discovery of γ-ray pulsations from the 22.7 ms pulsar (pulsar A) in the famous double pulsar system J0737−3039A/B. The γ-ray light curve of pulsar A exhibits two peaks separated by approximately half a rotation, and these are non-coincident with the observed radio and X-ray peaks. This suggests that the γ-ray emission originates in a part of the magnetosphere distinct from where the radio and X-ray radiation is generated. Thus far, three different methods have been applied to constrain the viewing geometry of pulsar A (the inclination angle between its magnetic and rotation axes, and the observer angle): geometric modelling of the radio and γ-ray light curves, modelling of the position angle sweep in phase seen in the radio polarisation data, and independent studies of the time evolution of the radio pulse profile of pulsar A. These three independent, complementary methods have yielded consistent results: pulsar A's rotation axis is likely perpendicular to the orbital plane of the binary system, and its magnetic axis close to lying in the orbital plane (making this pulsar an orthogonal rotator). The observer is furthermore observing emission close to the magnetic axis. Thus far, however, current models could not reproduce all the characteristics of the radio and γ-ray light curves, specifically the large radio-to-γ phase lag. In this paper we discuss some preliminary modelling attempts to address this problem, and offer ideas on how the light curve fits may be improved by adapting the standard geometric models in order to reproduce the profile peak positions more accurately.

1. Introduction

Using the Parkes multibeam receiver Burgay et al. reported the discovery of a 22 ms pulsar, PSR J0737−3039A, in a close binary system. The derived orbital parameters implied that the system consists of two neutron stars [1]. The short orbital period (roughly 2.4 hr) coupled with the high orbital eccentricity (0.88) made this system the most rapidly merging neutron star binary yet discovered, with the eventual merger predicted to occur in approximately 85 Myr. This discovery was soon followed by the discovery of radio pulsations from pulsar A's binary companion, PSR J0737−3039B, with a pulsation period of 2.8 s [2]. The fact that both stars are observed as radio pulsars made this system the first of its kind and allowed very sensitive,

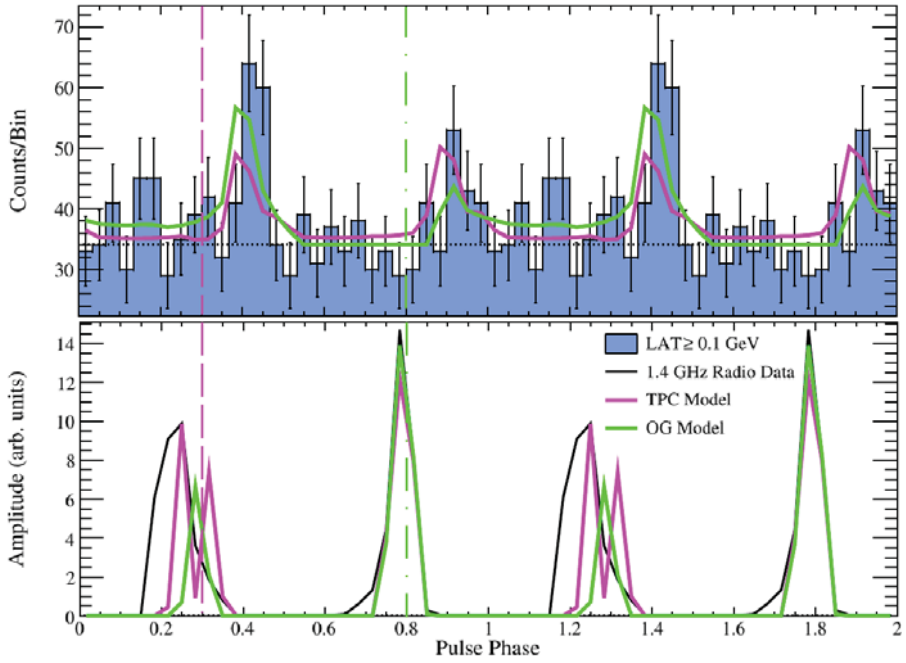

Figure 1: The phase-averaged observed radio (bottom; black; rebinned) and γ-ray (top; histogram) LCs for PSR J0737−3039A with best-fit solutions for the OG (green) and TPC (pink) geometric models. The horisontal dotted line on the γ-ray LC shows the estimated background level associated with PSR J0737−3039A. The vertical dashed and dash-dotted lines indicate the point in phase where the observer's line of sight is in the plane defined by the magnetic and rotation axes of the pulsar (the fiducial plane) for the the best-fit OG and TPC model LCs respectively [4]. The geometric parameters associated with these best-fit LCs are listed in Table 1.

and famous, confirmation of the predictions of Einstein's General Relativity using high precision measurements of the orbital motions of the two stars [3].

The discovery of pulsed γ-ray radiation from the millisecond pulsar PSR J0737−3039A [4] further added to the value of this system as there are relatively few pulsars with periods and period derivatives (with respect to time) similar to those of PSR J0737−3039A. PSR J0737−3039A is the first mildly recycled millisecond pulsar observed to emit in γ-rays.

2. Constraining the Geometry of PSR J0737−3039A

The first constraint on the viewing geometry of PSR J0737−3039A that can be obtained from the γ-ray and radio light curves (LCs) is that the two radio peaks are most likely associated with opposite magnetic poles as they are separated by about half a rotation in phase. This means that the inclination angle α between the magnetic and rotation axes of this pulsar is most likely close to 90°. Furthermore, the large radio-to-γ phase lag suggests that the radio and γ-ray radiation are produced in different regions of the magnetosphere. This large radio-to-γ phase lag is, however, very troublesome when trying to reproduce these LCs through standard model simulations.

Figure 1 shows the radio and γ-ray LCs observed for PSR J0737−3039A at 1.4 GHz and $\geqslant$0.1 GeV respectively. Both LCs display a widely-spaced two-peak structure. Note that two rotations of the pulsar are shown in the interest of clarity. Two sets of best-fit LC solutions are also shown. These were obtained using the outer gap (OG [5, 6]; green) and two-pole caustic

(TPC [7]; pink) geometric models for the γ-ray emission alongside a semi-empirical conal model [8] for the radio emission [4]. As can be seen in the bottom panel, the biggest difficulty when trying to fit the observed LCs is reproducing the large radio-to-γ phase lag, with the leading radio peak in the predicted LCs still lying too close to the trailing peak.

In addition to the radio and γ-ray LCs there are also high quality radio polarisation data available for PSR J0737−3039A with which the viewing geometry can be constrained. Fitting these data using a modified rotating vector model [9] yields a geometry consistent with the one found using the geometric models, with PSR J0737−3039A being an almost orthogonal rotator (see Table 1).

The last estimate of the geometric parameters to mention here is the one obtained by Ferdman et al., who studied six years of radio observations of PSR J0737−3039A [10]. By modelling the time-varying pulse widths they were able to constrain the geometry of PSR J0737−3039A. The results of their study agree very well with the results of the other two approaches discussed above (see Table 1).

3. Improving the geometric fits

The good agreement between the results yielded by the three independent approaches increases our confidence in the identification of PSR J0737−3039A as an orthogonal rotator, but simultaneously poses a challenge to the geometric models employed. Neither geometric γ-ray model (OG or TPC) is able to reproduce the large radio-to-γ phase lag when coupled with the conal radio model. A refinement of the current models is clearly necessary, and we have made some attempts to rectify the problem.

The first alternative model invoked a low-altitude slot gap geometry for the radio emission (see [11] for the original slot gap model), coupled with the usual TPC model for the γ-rays. This geometry is proposed in the context of a radio cone producing radio peaks that lead the caustic γ-ray peaks. The profiles produced by this model still could not reproduce the radio-to-γ phase lag satisfactorily, even though the LC shapes were reasonable. Figure 2 shows fits obtained using this alternative model.

The second alternative model considered, instead, a conal structure for both the radio and γ-ray emitting regions, with the γ-ray region lying *lower* than the radio region. This configuration was motivated by the idea that the radio may indeed have a dominating leading peak, with the γ-ray LC leading the radio LC. It was however found that it is not possible to reproduce both the radio and γ-ray profile shapes simultaneously within the context of this model, leading us to abandon this scenario.

Table 1: The geometric parameters of PSR J0737−3039A as determined by three independent methods.

Method	α (°)	ζ (°)	Ref.
Geometric LC modelling (TPC)	80^{+9}_{-3}	86^{+2}_{-14}	[4]
Geometric LC modelling (OG)	88^{+1}_{-17}	74^{+14}_{-4}	[4]
Polarisation data fitting	$98.8^{+8}_{-1.5}$	$95.8^{+13.2}_{-4.3}$	[9]
Radio width analysis	$90.2^{+16.3}_{-16.2}$	$90.8^{+0.27}_{-0.46}$	[10]

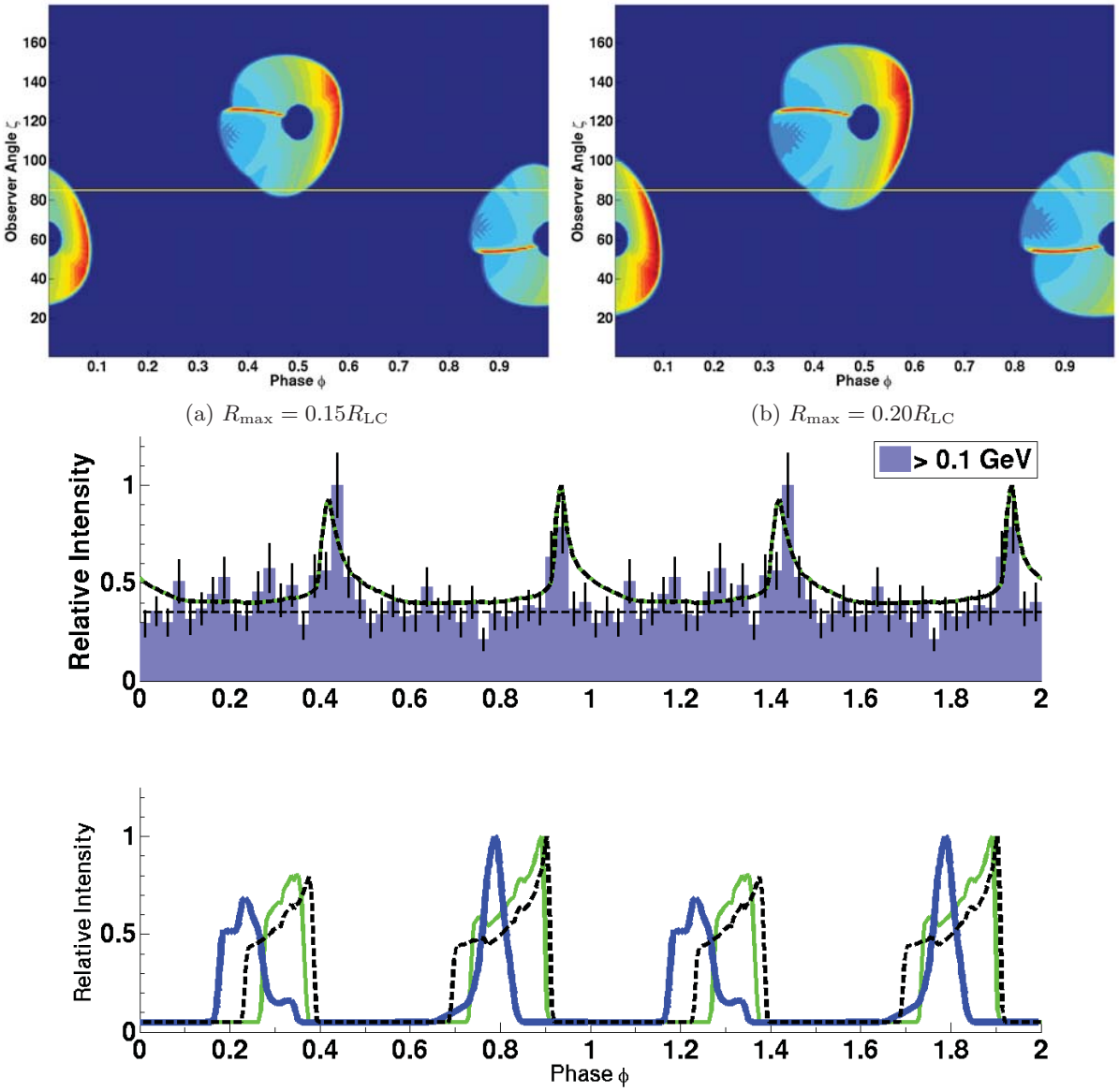

Figure 2: Best-fit LC solutions obtained using the first alternative model discussed in Section 3. For our fits we used the observed γ-ray LC weighted by the spectrum (histogram in the middle panel) and the 1.4 GHz radio LC (solid blue line in the lowest panel). The coloured plots at the top are radio intensity maps (or phaseplots) plotting relative intensity per solid angle as a function of rotational phase ϕ and observer angle ζ (the angle between the observer's line of sight and the rotation axis). The best-fit LCs are obtained from these phaseplots by cutting along lines of constant ζ (the yellow horisontal lines shown). The green radio LCs (obtained from phaseplot *(a)*) correspond to an emission gap extending from the pulsar's surface to a radius $R_{\rm max} = 0.15R_{\rm LC}$, where $R_{\rm LC}$ is the radius of the light cylinder (where the corotation speed is c), and the black dashed radio LC (obtained from phaseplot *(b)*) corresponds to a gap extending from the pulsar's surface to $R_{\rm max} = 0.20R_{\rm LC}$. In both cases the large radio-to-γ phase lag cannot be reproduced. For illustration, we used $\alpha = 60°$ and $\zeta = 85°$.

4. Future work

The fits obtained using the preliminary alternative models discussed in Section 3 may not be satisfactory, but they do point to interesting avenues of model refinement, e.g., the investigation of non-uniform emissivities, such as patchy or one-sided radio cones, or non-aligned radio and γ-ray cones. The fact that these LCs are hard to fit using the established geometric models, coupled with the unique characteristics of the system within which PSR J0737−3039A finds itself, suggests that there may be some form of interaction between the two pulsars, perhaps through their pulsar winds. Such an interaction may be observable through changes in the γ-ray LCs at the orbital period, but thus far no such periodic phenomenon has been observed. It may also be the case that the pulsar wind eminating from PSR J0737−3039B, and specifically the currents it constitutes, interacts with the magnetosphere of PSR J0737−3039A. This would mean that the structure of PSR J0737−3039A's magnetosphere may be different from what it would be if it was not a member of a binary pulsar system. Such a perturbed magnetosphere structure would mean that the geometry of the emitting regions may also be different. Such perturbations are currently not included in the geometric models employed thus far, and an investigation into how these two pulsars interact may lead to valuable refinements to the current geometric models.

Acknowledgments

ASS and CV are supported by the South African National Research Foundation. AKH acknowledges support from the NASA Astrophysics Theory Program. CV, TJJ, and AKH acknowledge support from the *Fermi* Guest Investigator Program. The *Fermi* LAT Collaboration acknowledges support from a number of agencies and institutes for both development and the operation of the LAT as well as scientific data analysis. These include NASA and DOE in the United States, CEA/Irfu and IN2P3/CNRS in France, ASI and INFN in Italy, MEXT, KEK, and JAXA in Japan, and the K. A. Wallenberg Foundation, the Swedish Research Council, and the National Space Board in Sweden. Additional support from INAF in Italy and CNES in France for science analysis during the operations phase is also gratefully acknowledged.

References

[1] Burgay M et al. 2003 *Nature* **426** 531–3
[2] Lyne A G et al. 2004 *Science* **303** 1153–7
[3] Kramer M 2006 *Science* **314** 97–102
[4] Guillemot L et al. 2013 *Astrophys. J.* **768** 169–77
[5] Cheng K S, Ho C and Ruderman M 1986 *Astrophys. J.* **300** 500–22
[6] Cheng K S, Ho C and Ruderman M 1986 *Astrophys. J.* **300** 522–39
[7] Dyks J and Rudak B 2003 *Astrophys. J.* **598** 1201–6
[8] Story S A, Gonthier P L and Harding A K *Astrophys. J.* **671** 713–26
[9] Craig H A and Romani R W 2012 *Astrophys. J.* **755** 137–44
[10] Ferdman R D et al. 2013 *Astrophys. J.* **767** 85–95
[11] Arons J 1983 *Astrophys. J.* **266** 215–41

Modelling the light curves of *Fermi* LAT millisecond pulsars

C Venter[1], T J Johnson[2,3], A K Harding[4] and J E Grove[2]

[1] Centre for Space Research, North-West University, Potchefstroom Campus, Private Bag X6001, Potchefstroom 2520, South Africa
[2] High-Energy Space Environment Branch, Naval Research Laboratory, Washington, DC 20375, USA
[3] National Research Council Research Associate, National Academy of Sciences, Washington, DC 20001
[4] Astrophysics Science Division, NASA Goddard Space Flight Center, Greenbelt, MD 20771, USA

Abstract. We modelled the radio and γ-ray light curves of millisecond pulsars using outer gap, two-pole caustic, low-altitude slot gap, and pair-starved polar cap geometric models, combined with a semi-empirical conal radio model. We find that no model fits all cases, with the outer gap and two-pole caustic models providing best fits for comparable numbers of millisecond pulsar light curves. We find a broad distribution of best-fit inclination angles as well as a clustering at large observer angles. The outer gap model furthermore seems to require relatively larger inclination angles, while the two-pole caustic model hints at an inverse trend between inclination angle and pulsar spin-down luminosity.

1. Introduction: why millisecond pulsars are special

There are 40 millisecond pulsars (MSPs) in the second pulsar catalogue (2PC) [1] of the *Fermi* Large Area Telescope (LAT) [2]. These represented roughly a third of the then-known γ-ray pulsar population[1]. Their uniqueness is related to their relatively small magnetospheres. This is due to their small periods P, which determine their so-called light cylinder radius ($R_{\rm LC} = Pc/2\pi$) where the corotation speed equals the speed of light, acting as a boundary characterising the magnetospheric size. These smaller magnetospheres may result in radio emission originating at higher altitudes (and at larger corotation speeds, where relativistic aberration is enhanced), and covering larger solid angles than in the case of their younger counterparts [3]. In turn, this may lead to radio beams that are detectable at relatively larger impact angles $\beta = \zeta - \alpha$, with α the inclination angle and ζ the observer angle, both being measured with respect to the rotation axis. MSPs therefore offer unique opportunities for studying pulsar emission geometries over a larger region in phase space than non-recycled, radio-loud γ-ray pulsars. In this context, it is interesting to note that all observed γ-ray MSPs are radio-loud. This is in contrast to non-recycled pulsars. Given their much longer and more violent evolutionary history, including spin-up via accretion [4], MSP magnetic fields may be more complex than those of younger pulsars. This may in part explain why their pulse profiles are more intricate and diverse. For

[1] The newest MSP fraction is now in excess of 40%. See https://confluence.slac.stanford.edu/display/GLAMCOG/Public+List+of+LAT-Detected+Gamma-Ray+Pulsars

example, MSPs were found to exhibit three classes of light curves (LCs) – those where the radio leads the γ-ray profile, those where these are aligned, and those where the radio profile trails the γ-ray profile, termed 'Class I', 'Class II', and 'Class III' respectively. See [5]. In contrast, the radio leads the γ-ray profiles in the bulk of young pulsars (making them 'Class I'), and only the Crab shows phase alignment of radio and γ-ray profiles ('Class II'). Lastly, MSPs generally seem to be more massive than their younger counterparts [6] due to accretion of matter from their companion stars, which may enhance general relativistic effects such as frame dragging [7]. This may lead to increased electric fields which accelerate primary charges near the polar cap.

2. Geometric modelling and light curve fitting

We modelled the MSP radio and γ-ray LCs using standard emission geometries, including the outer gap (OG) [8], two-pole caustic (TPC) [9], altitude-limited OG and TPC (alOG, alTPC) [5], low-altitude slot gap (laSG) [5], and pair-starved polar cap (PSPC) [10] geometric models. All these geometric models have physical counterparts[2] based on different electrodynamical assumptions of the acceleration. The latter lead to different locations and extents of acceleration regions (or 'gaps') within the magnetosphere, associated with high-energy emitting regions. We combined these γ-ray geometries with a semi-empirical conal radio model [11, 12], but used a core component when indicated by polarimetry (e.g., when sense changing of circular polarisation is observed). Our models assume the retarded vacuum dipole magnetic field [13] as the basic magnetospheric geometry, and correct for aberration and time-of-flight delays of emitted photons [14], while assuming a constant emissivity in the corotating frame for all except the laSG and PSPC models. After collecting the emission (per solid angle) of a particular simulated pulsar in a 2D skymap (ζ vs. phase) for a fixed value of α, we constructed LCs (by making constant-ζ cuts) on a grid of model parameters, and then used a maximum likelihood approach to obtain best joint radio / γ-ray LC fits for each 2PC MSP using *Fermi* LAT and radio LC data. Lastly, we estimated errors on the model parameters using either one- or two-dimensional likelihood profiles. More details may be found elsewhere [5, 15, 16].

3. Results: tentative trends

3.1. Towards a hybrid geometry?

We find that no model can universally fit all MSP LCs. The OG and TPC models perform best, providing best fits for 83% of the LCs ($\sim$ 40% each). The TPC geometry better fits LCs with significant off-peak γ-ray emission, while OG models prefer LCs with little or no off-peak emission. There are 28 Class I MSPs, 16 being best fitted by the TPC, and 12 by OG geometry. There are 6 Class II MSPs, 1 of which is best fitted by the alTPC model, 4 by the alOG model, and 1 by the laSG model. Lastly, the 6 Class III MSPs are best fitted exclusively by the PSPC model. The above implies that a "mix" of models may be needed to fit all observed profiles, pointing to some hybrid model that incorporates features of the different models studied so far. Alternatively, a new geometry may be needed which may provide greater richness in terms of potential LCs it can produce, e.g., mimicking TPC LCs in some cases and OG LCs in other.

3.2. Pulsar geometry and visibility constraints

From our best fits of MSP LCs, we find a broad distribution of α (Figure 1). This may argue against the idea [17] of spin-axis alignment with age, as the latter would imply a preference for smaller values of α for MSPs. This is in contrast with modelling results obtained for non-recycled γ-ray pulsars [18], where generally the best-fit $\alpha > 40^\circ$ (and young radio-loud pulsars have small β). The large range in α for MSPs partly reflects their wider radio beams and smaller magnetospheres which allow both the radio and γ-ray beams to be visible over a larger region of

[2] Technically, the PSPC model *is* the actual physical model in this case.

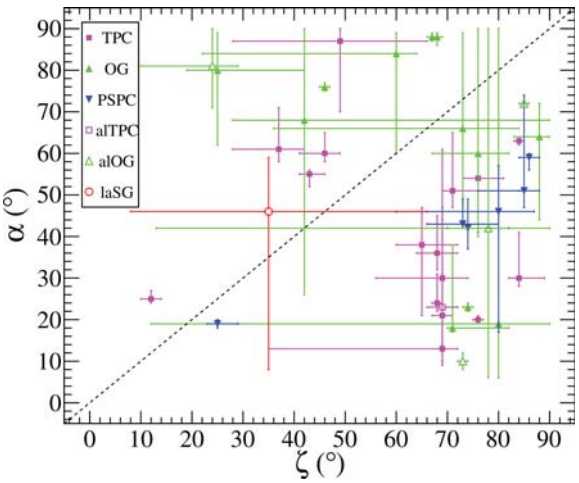

Figure 1. Best-fit α vs. ζ. Different symbols distinguish different emission geometries.

phase space than is the case for longer-period pulsars. While there may be younger pulsars with small α and large ζ, their narrow radio beams may be missed due to an unfavourable observing geometry (i.e., large β). They will be radio-quiet γ-ray pulsars, if indeed γ-ray pulsations may be identified via, e.g., a blind periodic search [19] (see Figure 7 of [18]). The angle α for such pulsars may therefore be very uncertain, if pulsations are indeed found. Otherwise, these sources must be considered unidentified. The smaller range in α (and β) may thus be indicative of this selection effect. For the MSPs, on the other hand, a relatively larger range of β is allowed, restricting the number of radio-quiet MSPs to very few. Indeed, there are no radio-quiet MSPs in the 2PC, while half of the young γ-ray pulsars are radio-quiet.

There seems to be a 'zone of avoidance' along $\alpha = \zeta$. This was not expected *a priori* in terms of the possible α and ζ that MSPs may assume. While it would be interesting to see if this region is filled as more MSPs are discovered, this effect may point to some necessary refinement of our assumed radio emission geometry (i.e., one where profiles with lower multiplicities may be produced, even at $\alpha \approx \zeta$). Figure 1 furthermore indicates a clustering at large ζ, corresponding to the fact that it is generally the bright caustic emission (at large ζ, near the spin equator) that is sampled by the observer to form the γ-ray profile peaks. A preference of ζ close to 90° is also expected if pulsar spin axes are distributed randomly with respect to the Earth line of sight (in which case ζ should follow a $\sin\zeta$ distribution). The relatively larger α for the OG (vs. the TPC model) is connected to visibility – the OG model is simply not visible when α is too small, due to the fact that it does not produce any emission below the null charge surface[3] as in the case of the TPC model. In the PSPC case, the majority of best-fit α values lie in the range $40° - 60°$, giving optimal off-peak emission levels and radio peak multiplicities. Interestingly, all currently modelled Class III MSPs (using the PSPC model) have $\zeta > \alpha$.

3.3. An evolutionary trend?

Figure 2 indicates the best-fit α vs. spin-down power $\dot{E}$. The TPC model best-fit results hint at an inverse trend between α and $\log_{10}\dot{E}$ for Class I MSPs (the Pearson correlation coefficient is -0.47 and the chance probability is 1.3×10^{-2}). At larger $\dot{E} \propto P^{-3}$, we have smaller P, so that smaller values of α seem to be associated with shorter-period pulsars in this case. If we accept that ζ is generally large (Section 3.2), these results may imply a larger impact angle β for these

[3] Defined by the condition $\rho_{\rm GJ} = 0$, where $\rho_{\rm GJ}$ is the Goldreich-Julian charge density [20].

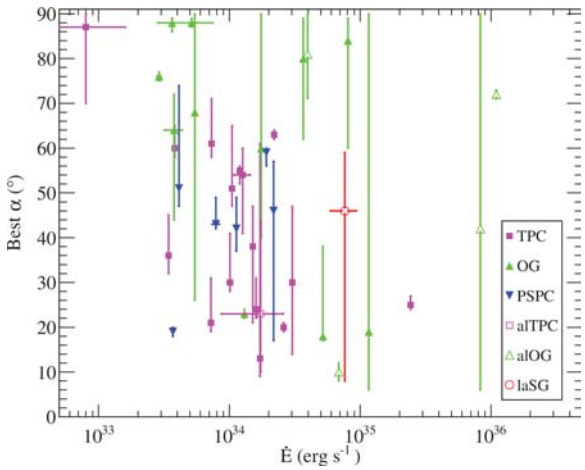

Figure 2. Plot of best-fit α vs. $\dot{E}$.

pulsars. This corresponds to the fact that the TPC is indeed visible for larger values of β when compared with the OG model, since it includes low-altitude emission that is not present in the OG geometry. Furthermore, since all MSPs in this plot are radio-loud, we expect that the radio beams of high-$\dot{E}$ MSPs will generally be at higher altitudes. These would therefore be wider, allowing one to probe smaller α. Lower-$\dot{E}$ MSPs may not be visible in radio if their narrower radio beams are pointing away from the observer and so may not be easily identified as γ-ray pulsars. On the other hand, there may be hints of an underlying evolution of α toward the equator with age (smaller values of $\dot{E}$). A population synthesis approach would be necessary to disentangle the effects of visibility and obliquity evolution. In any case, noting the presence of outliers and points with large uncertainties, this observed trend should be regarded with caution.

3.4. Caustic radio emission

In the case of Class II MSPs, we find that the radio emission may be caustic in nature (i.e., emission originating at different altitudes in the magnetosphere being bunched in phase by relativistic effects; see [21]), since radio and γ-ray profiles are phase-aligned, implying a common origin of the emission. Radio emission would therefore originate at higher altitudes. This is in contrast with the usual low-altitude conal emission found in the Class I and Class III MSPs [5], and should be expected to be associated with depolarisation and rapid position angle swings, since the emission from a large range of altitudes and magnetic field orientations is compressed into a narrow phase interval when forming the bright peaks [14]. Although the radio emission altitudes cannot be well constrained by current statistics, we do find that the radio and γ-ray emission regions typically have significant overlap, while the radio is generally more limited in altitude and originates higher up than the γ-rays.

3.5. Tapping the power source – luminosity and beaming

The γ-ray luminosity L_γ is a very important intrinsic parameter characterising how rotational energy is converted into γ-ray emission. This is estimated from the observed γ-ray energy flux G using $L_\gamma = 4\pi f_\Omega G d^2$ (e.g., [22]), where f_Ω is the beaming correction factor which accounts for the fact that emission is not beamed isotropically. We can estimate f_Ω from the emission pattern implied by the model by comparing the total emitted pattern to the one observed at a particular ζ for given α. Our fits indicate that $f_\Omega < 1$ in most cases. We are thus typically sampling emission that is above the average emission level. Conversely, for PSPC

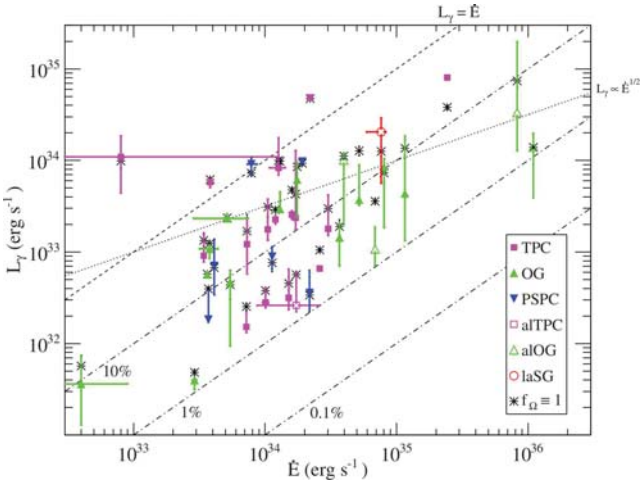

Figure 3. Plot of L_γ vs. $\dot{E}$. Black stars indicate values where $f_\Omega = 1$ was assumed. The dashed and dash-dotted lines show efficiencies of 0.1%, 1%, 10%, and 100%. The dotted line indicates $L_\gamma \propto \dot{E}^{0.5}$ with arbitrary normalisation.

best-fit profiles, we have $f_\Omega > 1$ in most cases, since we are missing the brightest part of the emission concentrated at low altitudes near the polar caps. The evolution of L_γ with $\dot{E}$ is very important, as this characterises the regime in which energy conversion takes place. It is expected that younger pulsars find themselves in a screened-potential regime, characterised by a relation $L_\gamma \propto I_{\rm PC} \propto \dot{E}^{1/2}$ (where $I_{\rm PC}$ is the polar cap current, and the polar cap potential $V_{\rm PC}$ is roughly constant in this case), while older pulsars operate in a rather more pair-starved regime where conversion of emitted γ-rays into electron-positron pairs is inefficient, and $L_\gamma \propto V_{\rm PC} I_{\rm PC} \propto \dot{E}$ [23]. We find that L_γ roughly follows a linear trend with $\dot{E}$ for the MSPs, which is consistent with this expectation (Figure 3). Lastly, we observe a clustering around a γ-ray efficiency of $L_\gamma/\dot{E} = 10\%$.

3.6. Discriminating between the different LC classes

Figure 4 shows the positions of the modelled MSPs on a period-period-derivative ($P\dot{P}$) diagram, with the different classes differentiated by different symbols as described in the legend. Grey dots are radio MSPs with no detection in 2PC. Contours of constant magnetic field $B_{\rm LC}$ at the light cylinder are indicated by dashed lines, while constant-$\dot{E}$ contours are indicated by dot-dashed lines, assuming dipole spin-down and a canonical moment of inertia of $I = 10^{45}$ g cm^2. We see no clear differentiation of MSP LC classes according to the usual pulsar variables such as P, $\dot{P}$, $\dot{E}$, or $B_{\rm LC}$, although it seems that Class II MSPs favour lower values of P, and Class III MSPs scatter about low values of $B_{\rm LC}$.

4. Conclusion

We described our attempt to model the LCs of all MSPs that appear in *Fermi* LAT's 2PC. We noted some tentative trends (e.g., a broad distribution in α, clustering at large ζ, and a linear relation between $\log_{10} L_\gamma$ vs. $\log_{10} \dot{E}$), which may strengthen as more data are accumulated. A new hybrid model may be needed to unify the different older models and reasonably reproduce all existing LCs. Different LCs classes are not easily distinguished based on canonical pulsar variables alone, but may rather be a reflection of the complex electrodynamical environment of the pulsar. We intend to next study the effects of new magnetic field geometries (e.g. [24, 25, 26]) and more complex higher-altitude radio emission patterns on the predicted MSP LCs.

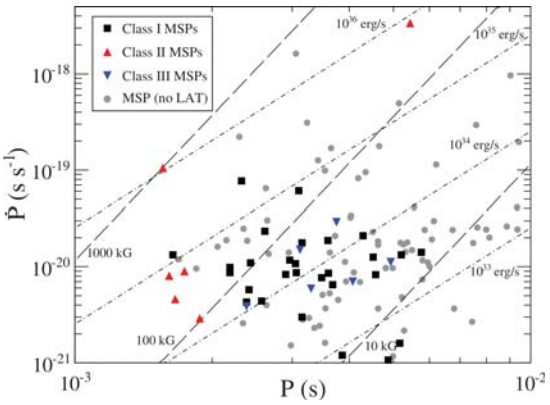

Figure 4. The $P\dot{P}$ diagram indicating different MSP LC classes. Contours of constant $\dot{E}$ and $B_{\rm LC}$ are also shown.

Acknowledgments

CV is supported by the South African National Research Foundation. AKH acknowledges support from the NASA Astrophysics Theory Program. CV, TJJ, and AKH acknowledge support from the *Fermi* Guest Investigator Program. The *Fermi* LAT Collaboration acknowledges support from a number of agencies and institutes for both development and the operation of the LAT as well as scientific data analysis. These include NASA and DOE in the United States, CEA/Irfu and IN2P3/CNRS in France, ASI and INFN in Italy, MEXT, KEK, and JAXA in Japan, and the K. A. Wallenberg Foundation, the Swedish Research Council and the National Space Board in Sweden. Additional support from INAF in Italy and CNES in France for science analysis during the operations phase is also gratefully acknowledged.

References

[1] Abdo A A *et al.* 2013 *ApJS* **208** 17–75
[2] Atwood W B *et al.* 2009 *ApJ* **697** 1071–102
[3] Ravi V, Manchester R N and Hobbs G 2010 *ApJL* **716** L85–9
[4] Alpar M A, Cheng A F, Ruderman M A and Shaham J 1982 *Nature* **300** 728–30
[5] Venter C, Johnson T J and Harding A K 2012 *ApJ* **744** 34–55
[6] Lattimer J M 2012 *AIP Conf. Ser.* vol 1484, ed S Kubono *et al.* pp 319–26
[7] Muslimov A G and Tsygan A I 1992 *MNRAS* **255** 61–70
[8] Cheng K S, Ho C and Ruderman M 1986 *ApJ* **300** 500–21
[9] Dyks J and Rudak B 2003 *ApJ* **598** 1201–6
[10] Harding A K, Usov V V and Muslimov A G 2005 *ApJ* **622** 531–43
[11] Kijak J and Gil J 2003 *A&A* **397** 969–72
[12] Story S A, Gonthier P L and Harding A K 2007 *ApJ* **671** 713–26
[13] Deutsch A J 1955 *Ann. d'Astrophys.* **18** 1–10
[14] Dyks J, Harding A K and Rudak B 2004 *ApJ*, 606, 1125–42
[15] Venter C, Harding A K and Guillemot L 2009 *ApJ* **707** 800–22
[16] Johnson T J *et al.* 2014 *ApJS* **213** 6–59
[17] Young M D T *et al.* 2010 *MNRAS* **402** 1317–29
[18] Pierbattista M *et al.* 2014 *ApJ*, in press.
[19] Saz Parkinson P M *et al.* 2010 *ApJ* **725** 571–84
[20] Goldreich P and Julian W H 1969 *ApJ* **157** 869–80
[21] Morini M 1983 *MNRAS* **202** 495–510
[22] Watters K P, Romani R W, Weltevrede P and Johnston S 2009 *ApJ* **695** 1289–301
[23] Harding A K, Muslimov A G and Zhang B 2002 *ApJ* **576** 366–75
[24] Harding A K and Muslimov A G 2011 *ApJ* **743** 181–96
[25] Breed M, Venter C, Johnson T J and Harding A K 2013, these proceedings
[26] Kalapotharakos C, Harding A K, Kazanas D and Contopoulos I 2012 *ApJL* **754** L1–5

Line, LINER, linest - from micro-AGN to ultra-luminous LINERs. One and the same?

Hartmut Winkler
Department of Physics, University of Johannesburg, PO Box 524, 2006 Auckland Park, Johannesburg, South Africa

E-mail: hwinkler@uj.ac.za

Abstract. This paper compares the optical spectra of a wide range of galaxies categorised as members of the Low Ionisation Nuclear Emission Region (LINER) class of active galactic nuclei (AGN). LINERs are defined by emission spectra with relatively faint high ionisation lines (compared to other AGN classes). The gas emission luminosity ranges from the weak flux emanating from some nearby galactic nuclei all the way to extremely luminous radio galaxies, where the line emission can completely dominate the host galaxy starlight component. In this study I analyse the Sloane Digital Sky Survey optical spectra of 15 LINERS identified in the course of the preparation of the new edition of the ZORROASTER AGN catalogue, spanning the largest possible luminosity range. I compare relative emission line strengths, focusing on uncommonly analysed ratios such as those involving [N I], line widths, profiles and even the spectral features of the host galaxy stellar continuum. The study identifies possible luminosity-dependent trends in the spectral properties of the studied objects. Possible reasons are presented to rationalise these trends, and the paper concludes with a discussion regarding the uniformity of the LINER class.

1. Introduction

The second version of the ZORROASTER[1] online catalogue of optical spectra of active galactic nuclei (AGN), to be released in October 2013, will now include numerous narrow-line objects. In particular, the update contains a significant number of entries meeting the general criteria of a class of AGN referred to as LINER (Low Ionisation Nuclear Emission-line Region).

The LINER class was originally suggested by Heckman [1], and its main characteristics are the comparatively strong spectral lines corresponding to low ionisation features such as [O I] and [N I]. Conversely, the high excitation [O III] lines are much weaker than found in most other types of AGN (e.g. Seyferts and starburst galaxies).

It is not clear that LINERs constitute a homogeneous class of objects. Various mechanisms have been suggested to explain the general features of the optical spectra, including i) photoionisation by an accretion disk surrounding a black hole (as in Seyfert galaxies), ii) photoionisation by stars (as in starburst galaxies) and iii) shock heated gas (as in some radio galaxies) [2,3,4]. None of these models have been completely discounted for all objects associated with this classification. It should hence be considered that several classes of AGN share similar spectral features, but are in fact quite disparate types of objects with very different physical characteristics.

[1] http://www.uj.ac.za/EN/Faculties/science/departments/physics/

It has become common to use line ratios as the defining parameter to distinguish LINERs from alternative AGN classes. In particular, two-dimensional logarithmic plots of one line ratio versus another offer a convenient systematic tool to automatically assign activity classes to large samples of galaxies [5,6]. However, by failing to carefully consider the peculiarities and full details of individual objects, this procedure is prone to misclassifications.

The line ratio based classification scheme also does not consider the wide range observed in LINER luminosities. It is well established that a lot of the otherwise unremarkable nuclei of nearby galaxies exhibit faint LINER emission spectra [7]. But highly luminous AGN like Arp 102B are also viewed as part of this class [8]. The luminosity dependence of LINER spectra is not properly established.

This paper investigates the spectra of 15 objects that satisfy the general LINER classification requirements according to the original definition [1], and explores possible line ratio vs. luminosity correlations. Their coordinates, redshifts and common names (where applicable) are listed in table 1.

Table 1. LINERs studied in this paper.

RA(2000)	Dec(2000)	z	common name
02h45m27.5s	+00°54′52″	0.0244	Mkn 1052
03h16m54.9s	–00°02′31″	0.0232	Mkn 1074
03h19m48.1s	+41°30′42″	0.0176	NGC 1275
09h22m05.2s	+00°09′03″	0.0694	
09h33m46.1s	+10°09′09″	0.0108	NGC 2911
09h39m17.2s	+36°33′44″	0.0197	
09h43m19.2s	+36°14′52″	0.0221	NGC 2965
09h50m50.2s	+09°52′37″	0.0512	
10h01m31.2s	+46°59′46″	0.0860	
12h15m00.8s	+05°00′51″	0.0782	
15h08m42.8s	+03°33′10″	0.0549	
15h24m12.6s	+08°32′40″	0.0371	
15h26m06.2s	+41°40′14″	0.0083	NGC 5929
16h52m58.9s	+02°24′03″	0.0245	NGC 6240
21h25m12.5s	–07°13′30″	0.0639	

2. Spectral data analysis

2.1. Archival spectra

For the majority of objects analysed here, electronic spectra are available in the Sloan Digital Sky Survey (SDSS) database [9]. These cover the entire optical range, and successive data point in the spectrum corresponds to adjacent channels of wavelength intervals of $\Delta(\log \lambda) = 0.0001$. In addition to the SDSS objects, two well-studied AGN with LINER features (NGC 1275 and NGC 6240) were included in the sample as well. Archival spectra of these were also available in electronic form [10,11], and were converted into the SDSS format. All spectra are displayed in figure 1.

2.2. Bands

The 2013 version of the ZORROASTER database is set to include total fluxes for selected bands consisting of 11 adjacent channels. These are strategically chosen to include all the major emission

features in AGN, including the following: [O II] 3727 Å, [O III] 5007 Å, [N II] 5198 Å, [O I] 6300 Å, [N II] 6584 Å and [S II] 6728 Å. Further bands are defined on either side of these lines, allowing continuum subtraction. In that way the line flux can be estimated in a crude but robust manner that makes no specific assumptions regarding line widths and profiles.

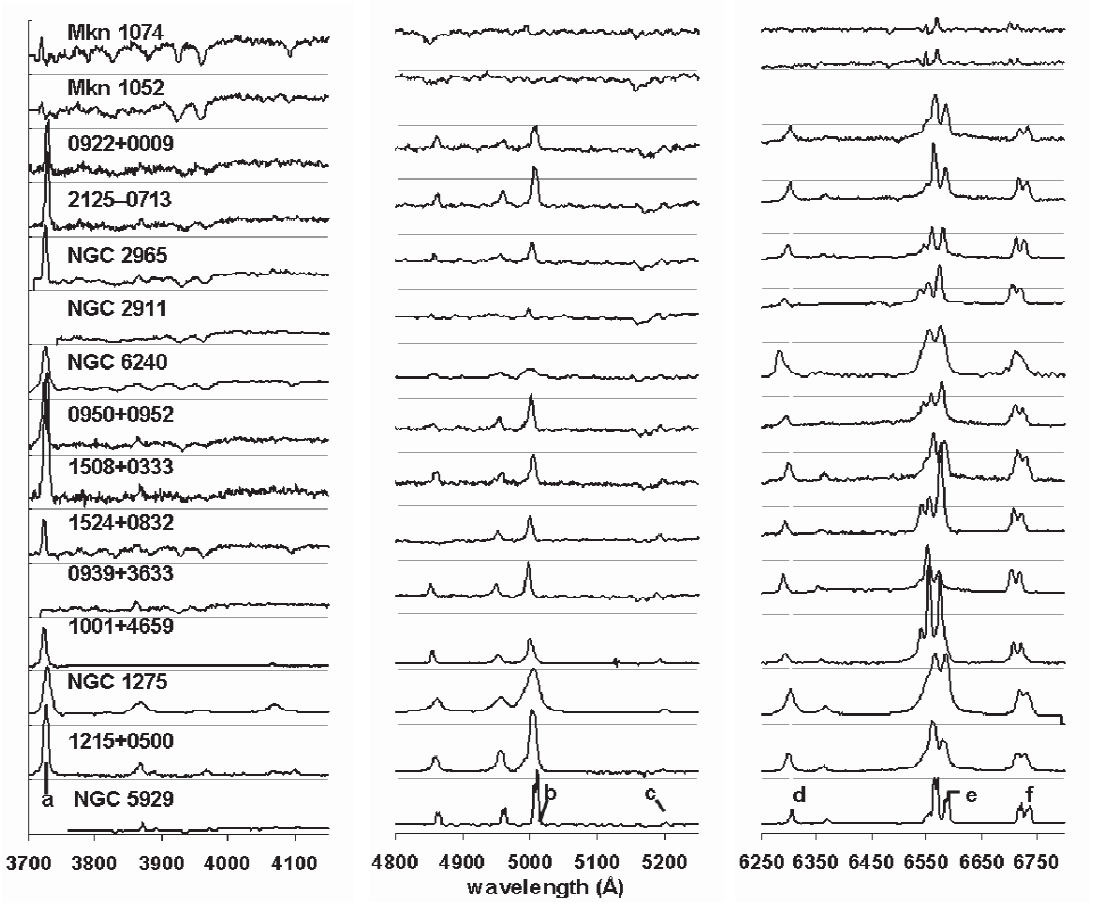

Figure 1. Sections of the redshift corrected spectra of the LINERs investigated in this study including the emission lines utilised in this study, whose positions are marked as follows: a - [O II] 3727 Å, b - [O III] 5007 Å, c - [N I] 5198 Å, d - [O I] 6300 Å, e - [N II] 6584 Å, f - [S II] 6725 Å.

3. Results

The comparative emission line region luminosity L was parameterised through multiplication of the continuum-subtracted band fluxes by z^2. The second column of table 2 gives the values of log L (plus an arbitrary constant) for the band flux corresponding to [N II] 6584 Å. The remaining columns of table 2 quantify the ratio of the continuum-corrected band fluxes of the earlier mentioned lines representative of [N I], [N II], [O I], [O II] and [S II] relative to [O III] 5007 Å. These are presented in the form

$$R([x]/[y]) = \log\left(f([x])/f([y])\right).$$

A variety of plots were constructed to test the interdependence between line ratios and the emission line region luminosity for the different elements and states of ionisation. In each case $R([x]/[y])$ was plotted against log L for the combinations listed in table 3. The respective slopes and degrees of correlation (in terms of the standard correlation coefficient squared) obtained are given in that table.

Table 2. Relative distance corrected luminosity of the emission line region (determined from [N II] 6583 Å) and line ratios (given as R([x]/[O III]). Due to the weakness and resultant unreliability of its measured line strengths, the results for Mkn 1052 are not included here.

Name	log L([N II]) + C	R([N I]/ [O III])	R([N II]/ [O III])	R([O I]/ [O III])	R([O II]/ [O III])	R([S II]/ [O III])
Mkn 1074	0.38		0.33	–0.16	0.43	0.38
NGC 1275	2.08	–1.08	0.09	–0.22	–0.10	0.12
SDSS 0922+0009	1.73		0.30	–0.09	0.23	0.08
NGC 2911	1.31	–0.56	1.07	0.08		0.83
SDSS 0939+3633	1.27	–1.47	–0.07	–0.22		0.20
NGC 2965	1.26		0.27	–0.05	0.43	0.40
SDSS 0950+0952	1.83	–1.07	0.31	–0.41	0.23	0.22
SDSS 1001+4659	2.78	–0.86	0.58	–0.35	0.08	0.22
SDSS 1215+0500	2.43	–1.41	–0.30	–0.48	–0.10	–0.18
SDSS 1508+0333	1.60		0.32	–0.04	0.62	0.47
SDSS 1524+0832	1.76	–0.81	0.46	–0.23	0.08	0.37
NGC 5929	1.27	–1.40	–0.09	–0.52		–0.02
NGC 6240	1.78	–0.73	0.84	0.20	0.51	0.70
SDSS 2125–0713	1.69	–1.25	0.01	–0.26	0.16	0.11

Table 3. Correlation tests for the line ratio vs. line luminosity graphs. The entries correspond to the slope and (in brackets) R^2 correlation parameter. Bold entries correspond to the strongest correlations, significant at the 95% level.

	R([N II]/ [N I])	R([O II]/ [O I])	R([N I]/ [O III])	R([N II]/ [O III])	R([O I]/ [O III])	R([O II]/ [O III])	R([S II]/ [O III])
log L([N I])	–0.162 (0.326)	–0.033 (0.009)	–0.063 (0.013)	–0.226 (0.086)	–0.176 (0.193)	–0.339 (**0.539**)	–0.285 (0.283)
log L([N II])	–0.108 (0.109)	–0.105 (0.157)	+0.055 (0.008)	–0.039 (0.004)	–0.107 (0.088)	–0.239 (**0.368**)	–0.162 (0.117)
log L([O I])	–0.202 (**0.465**)	–0.122 (0.205)	–0.226 (0.157)	–0.265 (0.184)	–0.132 (0.147)	–0.256 (**0.413**)	–0.268 (**0.345**)
log L([O II])	–0.168 (0.222)	–0.060 (0.041)	–0.370 (**0.448**)	–0.226 (0.176)	–0.171 (0.239)	–0.230 (0.278)	–0.253 (0.349)
log L([S II])	–0.210 (0.349)	–0.106 (0.133)	–0.174 (0.064)	–0.212 (0.093)	–0.150 (0.150)	–0.265 (**0.378**)	–0.244 (0.226)

Examples of some of these plots are shown in figures 2 and 3.

4. Discussion

Even a cursory visual inspection of the spectra displayed in figure 1 reveals peculiar characteristics for practically every one of the objects analysed, even though they are ostensibly all of the same AGN class. Mkn 1074 has a continuum with comparatively deep hydrogen absorption features, indicating a relatively high proportion of early type stars. Both Markarian objects only have very weak emission features. SDSS 1001+4659 appears to have narrow starburst-like peaks superimposed on some

emission lines, while several other objects (e.g. the well-known NGC 1275) display unusually wide forbidden lines. The [O I] line strengths in some objects (e.g. NGC 6240) are far greater than elsewhere (e.g. NGC 2911).

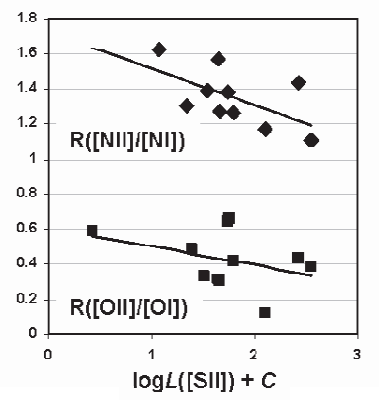

Figure 2. Plot of some line ratios vs. the [S II] emission line region luminosities

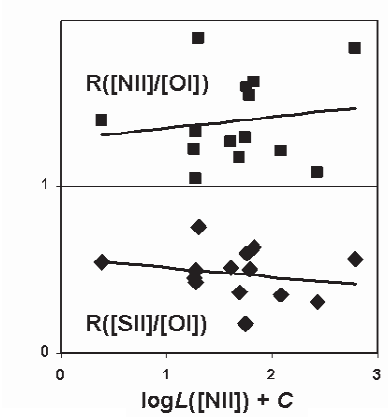

Figure 3. Plot of some line ratios vs. the [N II] emission line region luminosities.

The fact that there seems to be a dependence of the line ratios on luminosity is not entirely surprising, as both the plotted parameters depend on the strength and spectral distribution of the excitational radiation and element abundances. It is however notable that some ratios, for example *R*([O II]/[O III]) and *R*([S II]/[O III]), correlate far better with luminosities than, say, R([O II]/[O I]). Also, the [O I] region luminosity is usually much better correlated with the line ratios than the [N II] region luminosity.

The complete lack of correlation in particular cases such as those illustrated in figure 3 suggests that these may be indicative of intrinsically different line forming mechanisms in some of the objects plotted here. These may paradoxically be optimal for differentiating between different sub-classes of LINERs undergoing distinct physical processes.

5. Conclusion

The study confirms that what we collectively refer to as LINERs are likely to be an inhomogeneous group of AGN, generated by a variety of very disparate processes. Specific plots of line ratios versus emission line region luminosities show promise of differentiating between the various types of objects. The achievement of this will however require the analysis of a vastly larger sample of LINERs, something that will soon be possible due to the imminent expansion of the ZORROASTER database.

Acknowledgments

This paper utilized data from the Sloan Digital Sky Survey (SDSS). Funding for the SDSS and SDSS-II has been provided by the Alfred P. Sloan Foundation, the Participating Institutions, the National Science Foundation, the U.S. Department of Energy, the National Aeronautics and Space Administration, the Japanese Monbukagakusho, the Max Planck Society, and the Higher Education Funding Council for England. The SDSS Web Site is http://www.sdss.org/.

The SDSS is managed by the Astrophysical Research Consortium for the Participating Institutions. The Participating Institutions are the American Museum of Natural History, Astrophysical Institute Potsdam, University of Basel, University of Cambridge, Case Western Reserve University, University of Chicago, Drexel University, Fermilab, the Institute for Advanced Study, the Japan Participation Group, Johns Hopkins University, the Joint Institute for Nuclear Astrophysics, the Kavli Institute for Particle Astrophysics and Cosmology, the Korean Scientist Group, the Chinese Academy of Sciences

(LAMOST), Los Alamos National Laboratory, the Max-Planck-Institute for Astronomy (MPIA), the Max-Planck-Institute for Astrophysics (MPA), New Mexico State University, Ohio State University, University of Pittsburgh, University of Portsmouth, Princeton University, the United States Naval Observatory, and the University of Washington.

References

[1] Heckman T M 1980 *Astron. & Astrophys.* **87** 152
[2] Ho L C, Filippenko A V and Sargent W L W 1993 *Astrophys. J.* **417** 63
[3] Filippenko A V 2003 LINERs and their physical mechanisms *ASP Conf. Series* **290** 369
[4] Dopita M A and Sutherland R S 1995 *Astrophys. J.* **455** 468
[5] Veilleux S and Osterbrock D E 1987 *Astrophys. J. Suppl.* **63** 295
[6] Kewley L J, Groves B, Kauffmann G and Heckman T 2006 *Monthly Notices Roy. Astron. Soc.* **372** 961
[7] Ho L C, Filippenko A V and Sargent W L W 1997 *Astrophys. J. Suppl.* **112** 312
[8] Halpern J P, Eracleous M, Filippenko A V and Chen K 1996 *Astrophys. J.* **464** 704
[9] Abazajian K, Adelman J, Agueros M, et al. 2003 *Astron. J.* **126** 2081
[10] Kennicutt R C 1992 *Astrophys. J. Suppl.* **79** 255
[11] Moustakas J and Kennicutt R C 2006 *Astrophys. J. Suppl.* **164** 81

Division D2 – Space Science

Evaluation of the NeQuick model in Southern mid-latitudes using South African co-located GPS and Ionosonde data

S M Ahoua[1,2], P J Cilliers[1], O K Obrou[2] and J B Habarulema[1]

[1] South African National Space Agency (SANSA) Space Science Directorate, P O Box 32 Hermanus, 7200, South Africa.

[2] Laboratoire de Physique de L'Atmosphère, Université F.H.B de Cocody, 22 BP 582 Abidjan 22, Côte d'Ivoire.

Abstract. This work investigates the performance of the NeQuick model in southern mid-latitudes. The NeQuick is used among others for the European Geostationary Navigation Overlay Service (EGNOS), developed to supplement the GNSSs systems by reporting on the reliability and accuracy of the positioning data. It is used by recommendation the International Telecommunication Union-Radiocommunication Sector (ITU-R), to compute the estimated total electron content (TEC) along the ray path of the signal from satellite to the GNSS receiver. The performance of the NeQuick is evaluated after it is adapted to the local conditions by ingesting the foF2 and M(3000)F2 recorded by the means of the Ionosonde at Hermanus (34.40°S; 19.20°E, South Africa). It is then used to compute a theoretical TEC above Hermanus and compared to the observed TEC derived from the co-located GPS receiver which belongs to the TrigNet network. To evaluate the model under different geomagnetic activity states we select three days each of quiet and magnetically disturbed days according to different solar activity indicators. It has been noticed that the ionosonde parameters allowed the model to get rid of the geomagnetic condition obstacle with RMSs almost similar for quiet and disturbed days. The NeQuick is significantly better for periods of minimum and moderate solar activity while it shows a large discrepancy during epochs of high solar activity.

1. Introduction

The accuracy of the position and time information provided by the Global Navigation Satellite Systems (GNSSs) is affected by several factors such as the troposphere, multipath and the ionosphere which is the most significant factor (See table 1). The satellite signal undergoes a time delay due to free electrons of the ionosphere. The effect of the delay on the pseudo-range computing can be minimized by using dual frequency signals (L1 and L2). For Single Frequency (SF) receivers, which still represent 75% of the market, the errors in positioning can reach 100 m under conditions of severe ionospheric disturbances. Single Frequency receivers rely on models such as the Klobuchar model, which is incorporated in the receivers, to compute the ionosphere total electron content (TEC) and then allows one to reduce the effect of the ionospheric delay. For Galileo SF receivers the NeQuick model

has been chosen for the ionospheric effect correction [1]. Several studies have been done to evaluate and improve the NeQuick model [1][2][3]. For these studies the following variables which affect the characteristics of the ionosphere have been considered: solar activity, geomagnetic activity, latitude, and time of day. This paper presents the assessment of the accuracy of the NeQuick model for the Southern mid-latitudes. It follows the method used in the study carried out by [4] who used co-located GPS and Ionosonde data in Europe (Northern mid-latitudes). We have adapted the NeQuick to the local conditions by ingesting "ionosonde parameters" recorded at Hermanus (34.4^0S; 19.2^0E, South Africa). The modified NeQuick is then used to compute a theoretical TEC above Hermanus and this TEC value is compared with the observed TEC derived from the co-located GPS receiver. The study reported here extends the work of [4] by also considering magnetically quiet and disturbed days in order to improve the ionospheric correction related to geomagnetic activity level. We selected three days corresponding to Minimum, Moderate and Maximum solar activity for each geomagnetic activity level.

Table 1. Typical contributions to the position error from various elements in GNSS systems [5].

Factor of error	Typical error
Ephemeris	2.1 m
Satellite Clock	2.1 m
Ionosphere	4.0 m
Troposphere	0.7 m
Multipath	1.4 m
Receiver	0.5 m

2. NeQuick

NeQuick is known as a quick-run model in computing the electron density and the TEC by numerical integration. It is considered suitable for trans-ionospheric applications [1]. This model has been developed at the Aeronomy and Radiopropagation Laboratory of the Abdus Salam International Centre for Theoretical Physics (ICTP) - Trieste, Italy and at the Institute for Geophysics, Astrophysics and Meteorology (IGAM) of the University of Graz, Austria. The NeQuick model calculates the ionospheric electron density profile by relying on three anchor points: E, F1 (if present) and F2 which represents the peaks of the different ionosphere layers. The anchor points are defined by providing the ionosonde parameters foE, foF1, foF2 and M(3000)F2. These parameters are computed by default by built in models but can also be provided to the model by ingesting observed data (See figure 1). The NeQuick model runs in Fortran code and computes the electron density by one to three "Epstein layers". The shape of an Epstein layer is given by the following function [4]:

$$N_L(h) = 4\mathrm{N}_{\max}\frac{\exp\left(\frac{\mathrm{h}-\mathrm{h}_{\max}}{\mathrm{B}_L}\right)}{\left[1+\exp\left(\frac{\mathrm{h}-\mathrm{h}_{\max}}{\mathrm{B}_L}\right)\right]^2} \quad (1)$$

where, B_L is the thickness parameter of the layer L.

The inputs to the NeQuick model are the geographic position, the time and the solar index (F10.7 or R12). The latest version of the model is NeQuick 2. For this study the NeQuick 1 version was used

since this version is being assessed by the European Space Agency (ESA). More details about the NeQuick model can be found in the work of [1]. NeQuick was implemented in the Global Ionospheric Scintillation Model (GISM) to calculate the background ionosphere. In Australia, it has been used in a simulation toolkit for a future GNSS in development. IRI -2007 uses NeQuick for the description of topside parameters. The most important use of the NeQuick model is its adoption by ESA for ionospheric delay correction in Galileo Single Frequency receivers The NeQuick in Galileo SF (future European GNSS) will be driven by an "effective ionization level" Az defined as follows:

$$Az(\mu) = a_0 + a_1\mu + a_2\mu \quad (2)$$

where μ is the modified dip latitude (MODIP) [5]. The coefficients a_0, a_1 and a_2 are broadcast by EGNOS to the GNSS receivers and allows Az calculation at any wanted location. For the European Geostationary Navigation Overlay Service (EGNOS) developed to supplement the GNSSs systems, those coefficients are broadcast in band L1 (1575.42 MHz), and then Az is used as input by NeQuick instead of the solar flux F10.7 to compute the TEC. The ionosphere time delay in L1 can be determined as follows:

$$dt = \left(\frac{K \bullet TEC}{f^2}\right) \quad (3)$$

Where dt is the time delay in s, f the signal frequency in MHz, $K=1.34.10^{-3}$ $m^2s^{-1}TECu^{-1}$ and TEC is the Total Electron Content along the ray path expressed in TEC units (TECu) (1 $TECu=1x10^{16}$ electrons/m^2) .

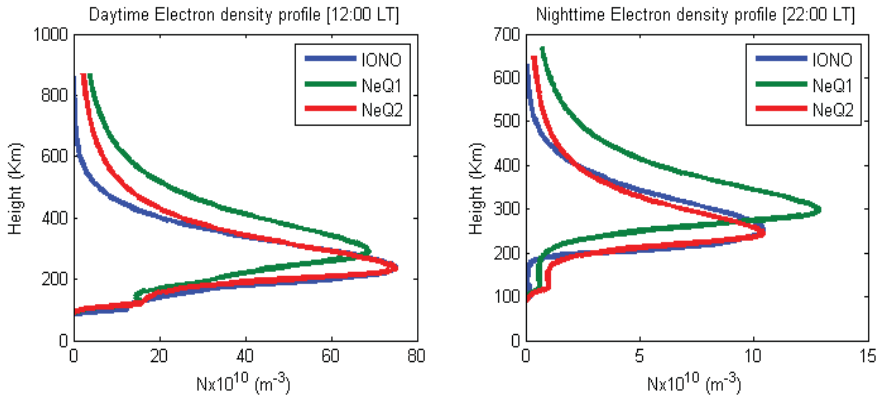

Figure 1: Evaluation of the NeQuick1 before (NeQ1) and after (NeQ2) ingestion of foF2 and M(3000)F2 recorded at the Hermanus Ionosonde station (IONO) for daytime and nighttime cases. NeQ2 presents a better match with the ionosonde observations (IONO).

3. Data and Processing

TEC NeQuick1 was used to obtain vertical TEC (NeQ TEC) above Hermanus after ingesting the foF2 and M(3000)F2 recorded by the means of Ionosonde at Hermanus (34.40°S; 19.20°E). The Hermanus Ionosonde, the fourth of the South African Network has been in operation since July 2008 so our study is limited from this year. This station consists of one transmitter and four receiver antennas and a DPS-4D Digisonde from the University of Massachusetts Lowell Center for Atmospheric Research (UMLCAR). The NeQ-TEC computed for each hour of the selected days has then been compared to the observed TEC (GPS TEC) derived from co-located GPS receiver which belongs to the TrigNet

network (http://www.trignet.co.za). The GPS data are stored in Receiver Independent Exchange format (RINEX) and the TEC values are determined by using the Gopi v2.2 software free available on internet. In our limited years of study (from 2008 to 2013), the monthly solar flux F10.7 varies from 68 to 153 solar flux units (s.f.u.), thus the months have been classified in different solar epochs according to this range. Using the Dst (Disturbance Storm-Time) index available on the internet (http://wdc.kugi.kyoto-u.ac.jp), we have chosen for each selected month one quiet day (Dst≈0nT) and one disturbed day (Dst <-50nT).

4. Results and Discussion

The results of this investigation are shown in figure 2 in which each row consists of two days of the selected month according to the solar activity. Figure 2 reveals that in general the magnetic activity level does not affect on the accuracy of NeQuick. For instance, the modelled TEC is closer to the observed TEC on day 4 (disturbed day) than on day 3 (quiet day). The discrepancies between the model and the GPS data are highest in the month of highest solar activity. NeQ TEC does not present a peak contrary to the other epochs where the peak appears near mid day. In the same month, the influence of the magnetic activity level is brought to light by a totally different behaviour of the two models for TEC as shown on day 6. The largest difference occurs during the main phase of the geomagnetic storm and tends to disappear with the recovery phase 18:00 UT (20:00 LT) to midnight. The contribution of this study is clearly demonstrated by Figure 3 which shows the difference between the GPS TEC and NeQ TEC (TECdiff). For the months of minimum and moderate solar flux, ΔTEC (GPS TEC-NeQuick TEC) remains below 6 TECu while it reaches 14 TECu during the epoch of

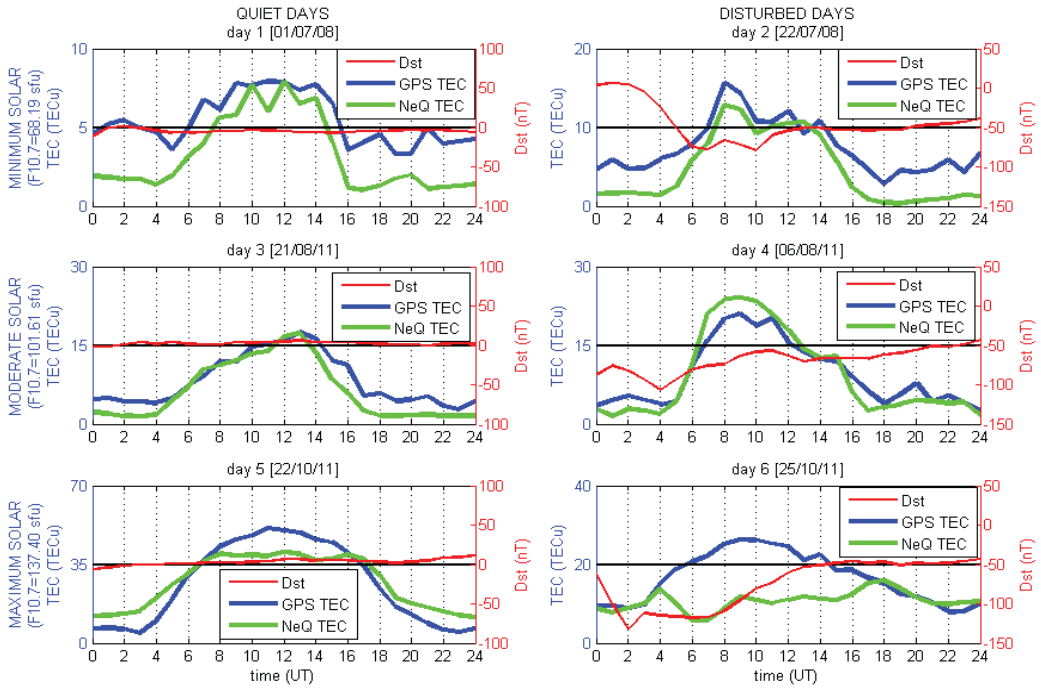

Figure 2: Comparison between the NeQuick TEC (NeQ TEC) and the GPS TEC above Hermanus for three different solar activity levels. The different solar activity levels are expressed by the F10.7 value (top: 68.19 sfu; middle: 101.61 sfu; bottom: 137.40 sfu) and by the geomagnetic activity by Dst (left=Dst≈0, right=Dst < −50 nT). The selected days are mentioned on top of every box

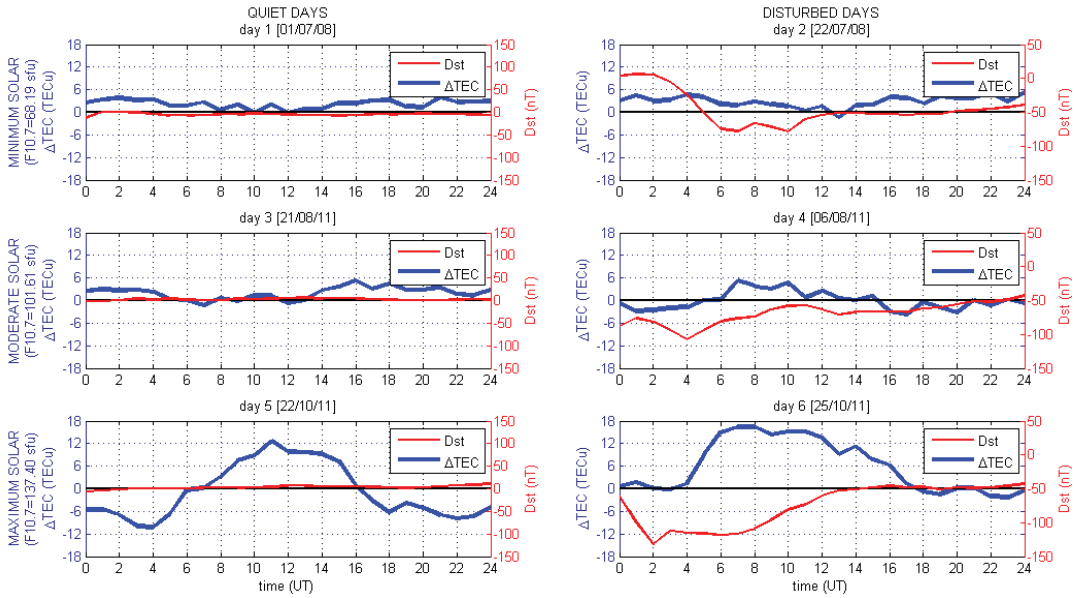

Figure 3: The difference between the GPS TEC and NeQuick TEC. The parameters of the panels are the same as in Figure 2.

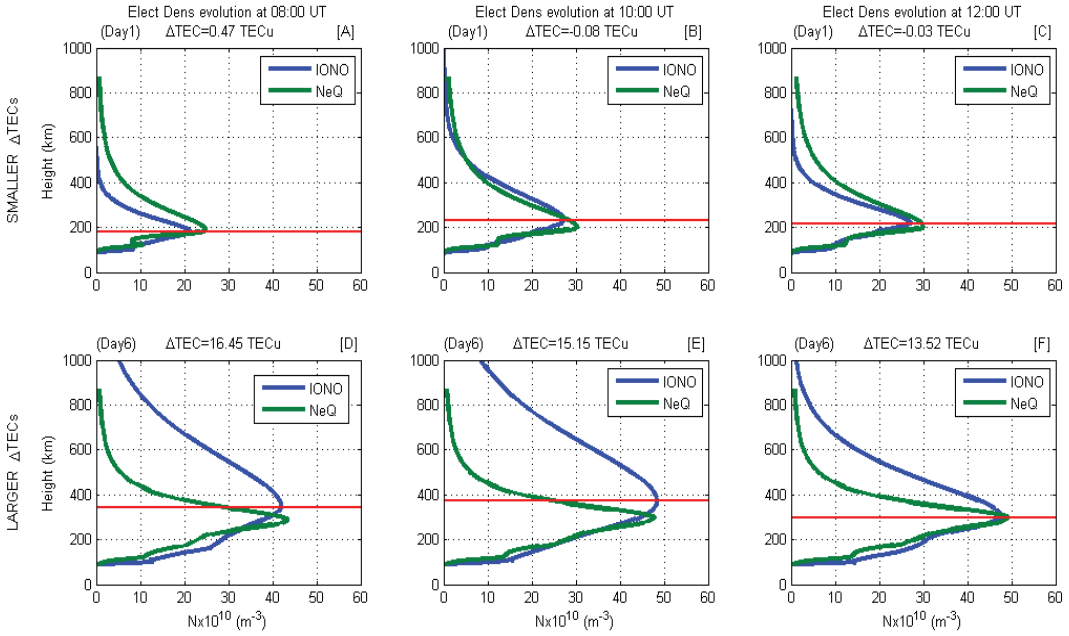

Figure 4: Comparison between the electron density profiles from the NeQuick model (NeQ) and from ionosonde data (IONO). The top and bottom set of 3 panels are for different times of respectively day 1 and day 6 of Figure 2. ΔTEC is given at the top of each panel. The F2 peak height hmF2 is indicated by the red line

maximum solar activity. Day 4, which is a geomagnetically disturbed day, nevertheless presents the smallest RMS difference (2.40 TECu) versus 2.45 and 2.52 TECu respectively for day 1 and 3, two

quiet days. Since the TEC is proportional to the peak electron density, we have also analysed the electron density profile provided by NeQuick. Seeing that GPS data does not provide the electron density directly (electron density can be obtained by a method of inversion) the electron density provided by the ionosonde was used for comparison with the NeQuick TEC (See Figure 4). Several studies like [6] have shown the strong correlation between GPS TEC and Ionosonde TEC. As seen in figure 3, the absolute value of ΔTEC is remains above 12 TECu from 06:00 to 12:00 UT on day 6 and below 2 TECu on day 1 at the same time-interval. Thus, three selected hours of this interval (08:00 UT, 10:00 UT and 12:00 UT) of those days have been used for this study. The results are shown in figure 4. These plots reveal that the lager ΔTECs are recorded when the F2 layer peak (hmF2) is higher than 300 km and the smaller ΔTECs are recorded when hmF2 is below 210 km. So, though F2 peak position in term of height (hmF2) and density (NmF2) is the "same" for the NeQuick and the ionosonde (figure 4F), ΔTEC (13.52 TECu) is large than the one shows on figure 4B (ΔTEC=0.08 TECu)

5. Conclusions

In this paper, we presented the assessment of the accuracy of NeQuick 1 or ITU-R over Hermanus, South Africa (34.40°S; 19.20°E). It has been found that NeQuick exhibits a weakness during a period where the solar flux is high with the difference between NeQuick TEC and Ionosonde TEC reaching 14 TECu. The lack of influence of the geomagnetic activity during the months of minimum and moderate solar activity has also been observed. The divergence between the model and the observation is a function of the F2 peak height hmF2, so during the hours and the days where the hmF2 is above 300 km, the model accuracy is worse. This study is a prelude to a further study on the evaluation of the models used by the GNSSs Single frequency (L1-only) receivers to reduce the ionospheric effect on GNSS position accuracy for the Southern mid-latitudes. It may provide useful information to advise users in this region on the choice of their GNSS equipment.

References

[1] Radicella S M 2009 The NeQuick model genesis, uses and evolution. *Ann. Geophys.* **52** 417-22

[2] Leitinger R, Zhang M-L and Radicella S M 2005 An improved bottomside for the ionospheric electron density model NeQuick. *Ann. Geophys.* **48** 525-34

[3] Nava B, Radicella S M and Azpiolicueta F 2011 Data Ingestion into NeQuick 2 *Radio Science* **46**. RS0D17 doi;10.1029/2010RS004635

[4] Bidaine B and Warnant R 2010 Assessment of the NeQuick model at mid-latitudes using GNSS TEC and ionosonde data *Adv. Space Res.* **45**, 1122–28

[5] Arbesser-Rastburg B. The Galileo single frequency ionospheric correction algorithm 3rd European Space Weather Week, Brussels, November 2006, Available on http://sidc.be/esww3/presentations/Session4/Arbesser.pdf

[6] McKinnell L-A, Opperman B D L and Cilliers P J 2007 GPS TEC and ionosonde TEC over Grahamstown, South Africa: First comparisons *Adv. Space Res.* **39**. 816-20

Extraction of surface impedance from magnetotelluric data

Sfundo Khanyile and Pierre Cilliers

South African National Space Agency Space Science, Hermanus 7200, Western Cape

Email: pjcilliers@sansa.org.za

Abstract. This paper presents the analysis of South African magnetotelluric (MT) data in the time domain. And the time domain is converted to frequency-domain for the purpose of extracting representative values of surface impedance. The surface impedance is used in the derivation of geo-electric fields produced by rapid variations in the geomagnetic field, as occurs during geomagnetic storms. The magnetotelluric method uses the spectra of associated time varying horizontal electric and magnetic fields at the Earth's surface to determine the frequency-dependent impedance tensor and equivalent surface impedance. The theory of operation of MT devices will be presented, as well as the typical MT data obtained from Hermanus, Vaalputs and Middelpos sites. The various steps in the analysis are aimed at reducing noise and outliers. In the time domain, a Hanning window is used to select data from successive periods during a day, while reducing the end effect (Gibbs' phenomenon) by tapering the series towards the start and ends of each selected time period. The spectral transformation is performed by means of a fast Fourier transformation (FFT). Spectral bands are selected by binning in the frequency-domain. Typical results and challenges in performing this analysis will be presented.

1. Introduction

The magnetotelluric (MT) method is based on measuring time variations of horizontal components of the electric and magnetic fields at the surface of the Earth [8]. The time invariant quantity called MT impedance tensor is the response of the Earth to electromagnetic induction and carries information about the conductivity distribution of the subsurface [7] & [9]. The electromagnetic fields can be produced by ionospheric, magnetospheric or atmospheric events [8]. At the surface, the plane waves induce current flows in the Earth which give rise to a secondary field [3].

The horizontal electric and magnetic fields are measured at Earth's surface, and they vary with time. In the frequency domain, the electromagnetic fields are assumed to be linearly related by the impedance tensor as given in equation 1[3]; [4] & [7],

$$\begin{pmatrix} E_x(\omega) \\ E_y(\omega) \end{pmatrix} = \frac{1}{\mu} \begin{pmatrix} Z_{xx}(\omega) Z_{xy}(\omega) \\ Z_{yx}(\omega) Z_{yy}(\omega) \end{pmatrix} \begin{pmatrix} B_x(\omega) \\ B_y(\omega) \end{pmatrix} \tag{1}$$

where B_x and B_y are the magnetic fields in nT, E_y and E_x are the electric fields in $mVkm^{-1}$ and $Z_{ij}(i, j = x, y)$ the components of the impedance tensor Z in Ω. The components of the impedance tensor are called polarizations, the E-B polarizations refer to the xy-yx tensor components [3].

The procedure that will be employed in this paper is called the spectral analysis method, which is similar to the Fourier transform. The reason why the Fourier transform is chosen is that the energy at

any interval of the Fourier power spectrum is directly related to the energy in the same frequency interval for the signal source.

2. Processing algorithm

In this paper, the MT data were collected using the LEMI 417 instruments from three recording stations (Hermanus, Middelpos & Vaalputs sites). This instrument records five horizontal magnetotelluric components $\left(b_x, b_y, b_z, e_x \ \& \ e_y\right)$ as time series of which the spectra lie in the range between 1 Hz and 1 mHz. Data from three above sites are analysed in this paper with their geographic and geomagnetic locations of the stations as listed in table 1.

Table 1. Geographic and geomagnetic co-ordinates of the stations

Stations	Latitude ($^{\circ}S$)	Longitude ($^{\circ}E$)	Altitude (m)
Hermanus	34°.25'45.01''	19°.13'32.94''	26
Middelpos	31°.54'36.14''	20°.14'05.25''	1135
Vaalputs	30°.09'14.01''	18°.31'73.27''	1023

To reduce the bias of spectral estimation from the time series, a Hanning window was introduced and applied to the MT data. A Fourier transform of all the MT horizontal components was carried out and the Fourier coefficients were obtained. Likewise, Fourier transforms were combined into non smoothed auto and cross spectral. For further reading or details on the cross spectral see the paper by [6]. In order to analyse MT data, the robust estimate was adopted. Equation 1 was rewritten in terms of auto- and cross spectral densities:

$$\mu E_x B_x^{\ *} = Z_{xx} B_x B_x^{\ *} + Z_{xy} B_y B_x^{\ *} \tag{2}$$

$$\mu E_x B_y^{\ *} = Z_{xx} B_x B_y^{\ *} + Z_{xy} B_y B_y^{\ *} \tag{3}$$

$$\mu E_y B_x^{\ *} = Z_{yx} B_x B_x^{\ *} + Z_{yy} B_y B_x^{\ *} \tag{4}$$

$$\mu E_y B_y^{\ *} = Z_{yx} B_x B_y^{\ *} + Z_{yy} B_y B_y^{\ *} \tag{5}$$

where $E_x B_x^{\ *}$ denotes smoothed spectral densities. It is known that the smoothing procedure leads to the least squares solution that is biased by the uncorrelated noise in input channels B_x and B_y, the statistics used allow the data to be contaminated by such noise without bias to the estimator e.g. the $Z_{xy}(\omega)$ component of the impedance tensor is estimated as

$$Z_{xy}(\omega) = \frac{\mu E_x B_y^{\ *} B_x B_x^{\ *} - \mu E_x B_x^{\ *} B_x B_y^{\ *}}{B_x B_x^{\ *} B_y B_y^{\ *} - B_x B_y^{\ *} B_y B_x^{\ *}} \tag{6}$$

The same procedure was used to derive other impedance tensor components ($Z_{yx}(\omega)$, $Z_{xx}(\omega)$ & $Z_{yy}(\omega)$).

Using equation 6 and assuming that the Earth is homogenous and isotropic [1] & [9], then $Z_{xx}(\omega) = Z_{yy}(\omega) = 0$, and $Z_{xy}(\omega) = Z_{yx}(\omega)$, and the apparent resistivity and phase impedance of the Earth can be expressed in the frequency domain as

$$\rho_{xy}(\omega) = \frac{\left|Z_{xy}(\omega)\right|^2}{\omega\mu} \tag{7}$$

$$\phi_{xy} = \tan^{-1}\left(\frac{\mathrm{Im}\left(Z_{xy}(\omega)\right)}{\mathrm{Re}\left(Z_{xy}(\omega)\right)}\right) \tag{8}$$

where ω is the angular frequency and Im & Re indicate the imaginary and real parts, respectively. The same method was used to derive other resistivity and phase impedance components ($\rho_{yx}(\omega)$, $\rho_{xx}(\omega)$ & $\rho_{yy}(\omega)$ and $\phi_{yx}(\omega)$, $\phi_{xx}(\omega)$ & $\phi_{yy}(\omega)$), respectivily.

3. Results and discussion

The MT data were collected at three stations, Hermanus, Middelpos and Vaalputs. For each of the sites, the raw time series recorded at 1 s interval were reprocessed using the robust method [6] based on the least squares solution. It involves creating a time series by sampling a signal at equal intervals of time. These segments are cosine tapered prior to the Fourier transforms. The Fourier coefficients are corrected for the influence of the instrument response functions and subsequently they are divided into sub-bands centred around frequencies that are equally distributed on a logarithmic scale. For each of these sub-bands and electromagnetic field components, smoothed autospectra and cross-spectra are computed. The final response function estimates are derived by stacking the single event spectra from all frequency bands using the iterative robust algorithm described in [4]. For further understanding about the method read also a paper by [6]. In this study, remote reference processing was no considered. For details about the remote reference method refer to [4].

Figure 1 shows the apparent resistivity (a,b) and phase (c,d) of both off diagonal components of the impedance tensor at the Middelpos station plotted as a function of period (period=1/frequency). The different lines represent data on different days in all three stations. In Fig. 1, the apparent resistivity (a,b) and phase impedance (c,d) plots appear variable from day to day around periods less than 100 s. For good data a small day to day variability is expected such as documented in [10].

Figure 2 shows the apparent resistivity (a,b) and phase (c,d) of both off diagonal components at the Vaalputs station. In Fig. 2, the apparent resistivity (a,b) and phase impedance (c,d) plots have a high day-to-day variability; no conclusions can be made because of the noise at these sites.

Figure 3 shows the apparent resistivity (a,b) and phase (c,d) of both off diagonal components at the Hermanus station. In Fig. 3, the apparent resistivity (a,b) and phase impedance (c,d) plots have a high day-to-day variability . Of the three sites where MT data were collected, Middelpos seems to provide the lowest variability. According to [5] the robust processing method should reduce the variability in the data at any site. However, in Figs 2-3 no improvement is seen using the robust processing technique and averaging over a long period should be done to reduce what seems to be noise in these sites. An article by [2] indicated that a comparison of techniques for magnetotelluric response function estimation could be used to reduce noise in these sites.

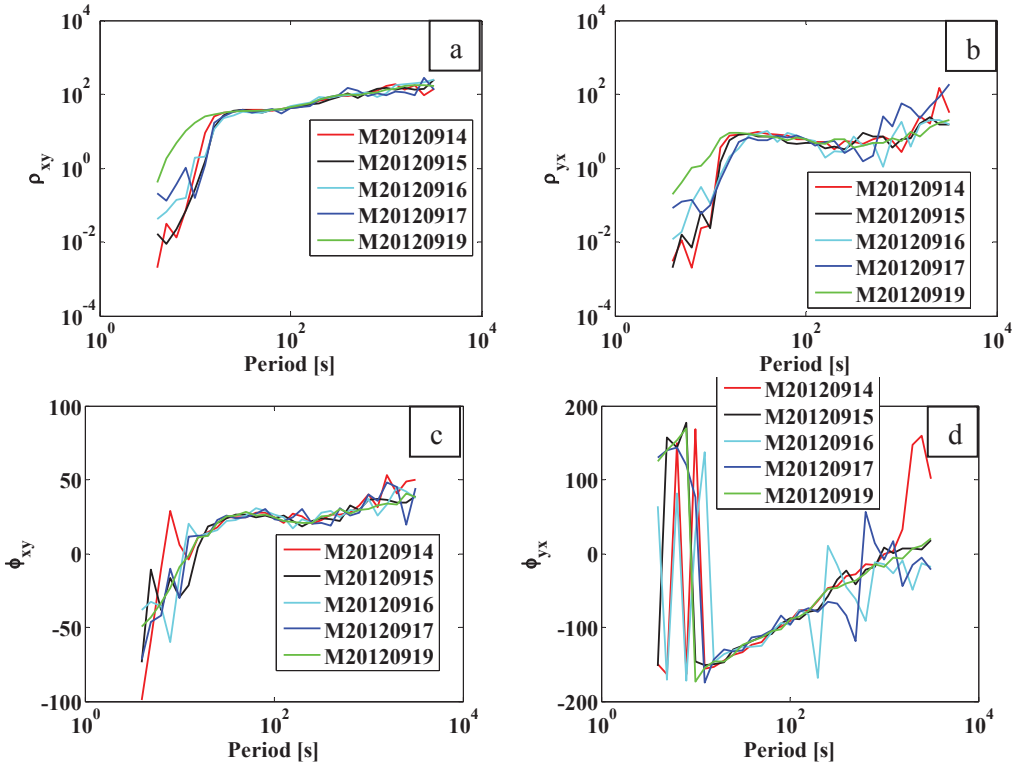

Figure 1. The solid lines show the estimates of the off-diagonal elements of the apparent resistivity using robust processing for five subsequent days. Apparent resistivity (a,b) and impedance phase (c,d) as function of periods at Middelpos site. The similarity of the ρ_{xy} and ρ_{yx} values indicate a fairly isotropic ground resistivity at Middelpos in the frequency range corresponding to periods of 10 to 100 s

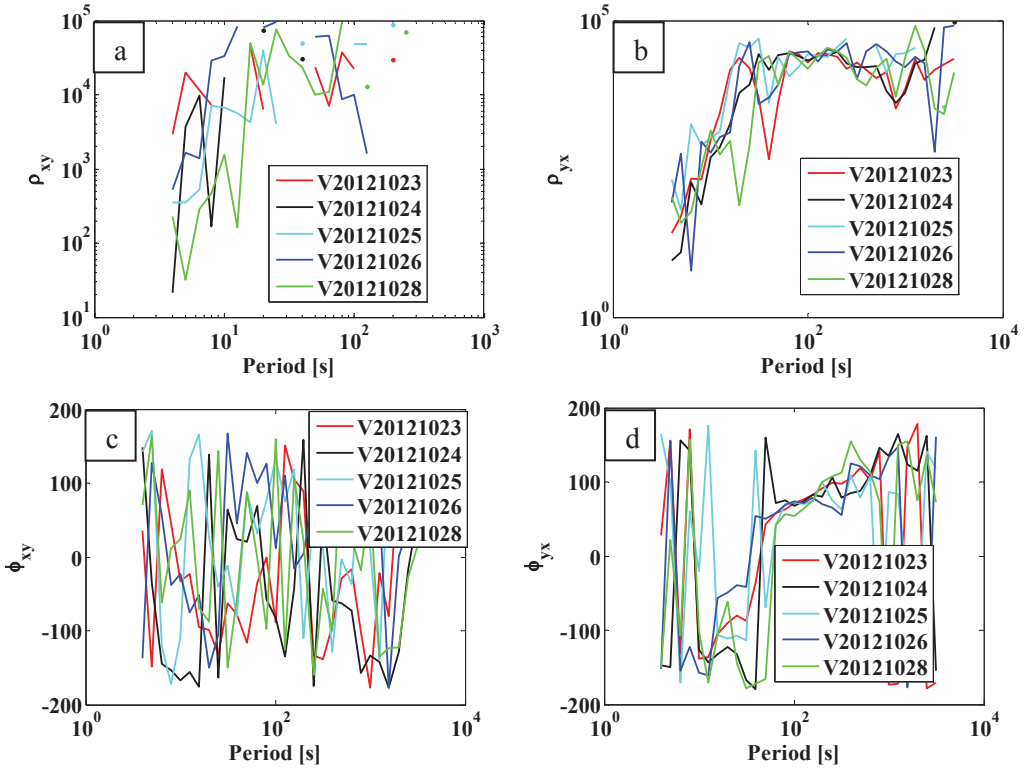

Figure 2. Same parameters as in Fig.1, but at Vaalputs site. The large day-to-day variability indicates that there is a source of noise at this site which reduces the consistency of the data.

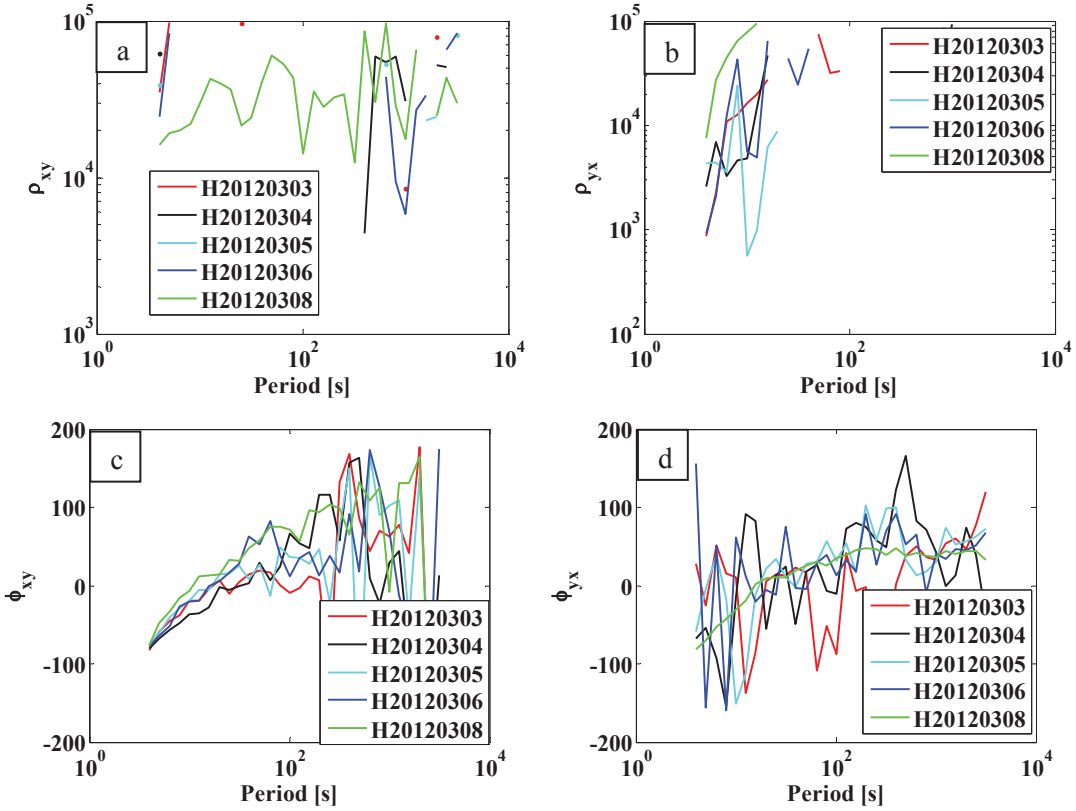

Figure 3. Same parameters as in Fig.1, but at Hermanus site. The variability of the Hermanus data is similar to that at Vaalputs, and much higher that at Middelpos.

4. Conclusions

In this paper, we present for the first time MT data from three recently deployed MT instruments in South Africa. The typical day-to-day variability of the off-diagonal components of the apparent resistivity is demonstrated. The results also show the variability from site to site, with the Middelpos site showing the least day-to-day variability and the closest correspondence to previous MT measurements in Southern Africa [10]. Typically, most observed electromagnetic field components are contaminated to some extent with noise. In order to retrieve unbiased estimates of the apparent resistivity and surface impedance, long recording times are required to ensure that sufficient data are available for processing through long-duration averaging. Further analysis of the data from these sites are required to determine their usefulness for the estimation of geomagnetically induced currents.

References

[1] Hermance J F, 1973 Processing of magnetotelluric data, *Physics of the Earth and Planetary interiors*, **7** 349-364

[2] Jones A G, Chave A D, Egbert G, Auld D and Barh K, 1989 A comparison of techniques for magnetotelluric response function estimation, *Geophys. J. int.,* **94,** 201-214

[3] Chant I J and Hastie L M, 1992 Time frequency analysis of magnetotelluric data, *Geophys. J. int.,* **111,** 399-413

[4] Ritter O, Junge A and Dawes G J K, 1998 New equipment and processing for magnetotelluric remote reference observations, *Geophys. J. int,* **132,** 535-548

[5] Muller A, 2000 A new method to compensate for bias in magnetotellurics, *Geophys. J. int*., **142**, 257-269

[6] Smirnov M Y, 2003 Magnetotelluric data processing with a robust statistical procedure having a high breakdown point, *Geophys. J. int*., **152**, 1-7

[7] Chave A D and Thompson D J, 2004 Bounded influence magnetotelluric response function, *Geophys. J. int*., **157**, 988-1006

[8] Weckmann U, Magunia A, and Ritter O, 2005 Effective noise separation for magnetotelluric single site data processing using a frequency domain selection scheme, *Geophys. J. Int*. **161**, 635-652

[9] Khoza D, Jones A G, Muller M R, Evans R L, Webb S J and Miensopust M, 2012 Tectonic model of the Limpopo belt, *Precambrian research*, **226**, 143-156

[10] Weckmann, U., O. Ritter, A. Jung, T. Branch, and M. de Wit (2007), Magnetotelluric measurements across the Beattie magnetic anomaly and the Southern Cape Conductive Belt, South Africa, J. Geophys. Res., 112, B05416, doi:10.1029/2005JB003975.

Methods of measuring and modelling geomagnetically induced currents (GIC) in a power line.

E Matandirotya[1,2,3], P J Cilliers[1,2] and R R van Zyl[2,3]

[1]Cape Peninsula University of Technology, Bellvile, South Africa
[2]South African National Space Agency(SANSA): Space Science , Hermanus, South Africa
[3]French South African Institute of Technology (F'SATI), Bellville, South Africa

E-mail: esiziba@sansa.org.za,electdom@gmail.com

Abstract. The implementation of proposed techniques for measuring and modelling geomagnetically induced currents (GIC) in power lines are discussed in this paper. GIC are currents in grounded conductors driven by an electric field produced by time varying magnetic fields linked to magnetospheric-ionospheric currents. These currents are enhanced by adverse space weather events such as magnetic storms and can cause overheating and permanent damage to high voltage transformers in power systems. Measurements of GIC are done on the neutral to ground connections of transformers in some substations. There is a need to know the magnitude and direction of the GIC flowing on the power lines connected to the transformers. Direct measurements of GIC on the lines are not feasible due to the low frequencies of these currents which make current measurements using current transformers (CTs) impractical. Two methods are proposed to study the characteristics of GIC in power lines. The differential magnetic measurement (DMM) technique is an indirect method to calculate the GIC flowing in the power line. With the DMM method, low frequency GIC current in the power line is estimated from the difference between magnetic recordings made directly underneath the power line and at some distance away, where the natural geomagnetic field is still approximately the same as under the power line. An analysis of the spectrum of GIC, the DMM technique, and preliminary results are presented. Finite element (FE) modelling with COMSOL-Multiphysics software is implemented so that the nature of the return currents flowing on the power lines and the Earth's surface can be analysed. In order to develop the FE-model, historical geomagnetic data recorded at Hermanus and Earth conductivity values derived from literature are used as the modelling inputs to the FE model. Preliminary results of current density distributions obtained by means of FE modelling are also presented.

1. Introduction

Geomagnetically induced currents (GIC) are a major concern when grounded conductors are considered. GIC are an end product of adverse "space weather". The propagation of the solar winds from the Sun to the Earth results in the interaction of the solar winds with the Earth's magnetosphere. During this interaction the current system in the magnetosphere-ionosphere coupled region is enhanced. Such current enhancement in the region yields geomagnetic disturbances such as geomagnetic storms. During a geomagnetic storm, time varying geomagnetic field on and beneath the Earth's surface are induced [1]. The geomagnetic field induces a geo-electric field and thus voltage differences are set between points on the surface of the Earth. The Earth has its own conductivity profile i.e. there will be spatial distribution of

the current flow in the Earth. These currents which arise due to the voltage differences between the ends of a grounded conductor can produce damage in the system attached to that conductor. The extent of damage depends on the particular system configuration [2].

Power systems, gas pipe lines, railway lines and telephone lines are technologies where the occurrence of these GIC has been noted and reported in [3, 4]. The focus of this paper is on power lines. With the daily dependence of human society on electricity, understanding the effects of GIC on power system has been at the center of GIC research. The aim is to improve the understanding of GIC in order to facilitate the management and mitigation of the impact of damages caused by the GIC on power systems. The presence of GIC in the power network initiates transformer saturations. Such saturations result in the increase of the excitation currents and disruption of the normal behavior of the transformers [5]. The overall damage may be observed as transformer heating, relay tripping and at worst case, a black out like the Hydro-Quebec 1989 incident [6].

GIC are currently measured in substations at the neutral to ground connections. Figure 1 shows typical GIC data recorded at the Grassridge substation (4-6 April 2010). A Fast Fourier Transform (FFT) performed on the data set indicates that GIC are low frequency currents with most of the energy in the GIC below 0.2 mHz. Figure 2 shows the amplitude spectrum of the Grassridge GIC data.

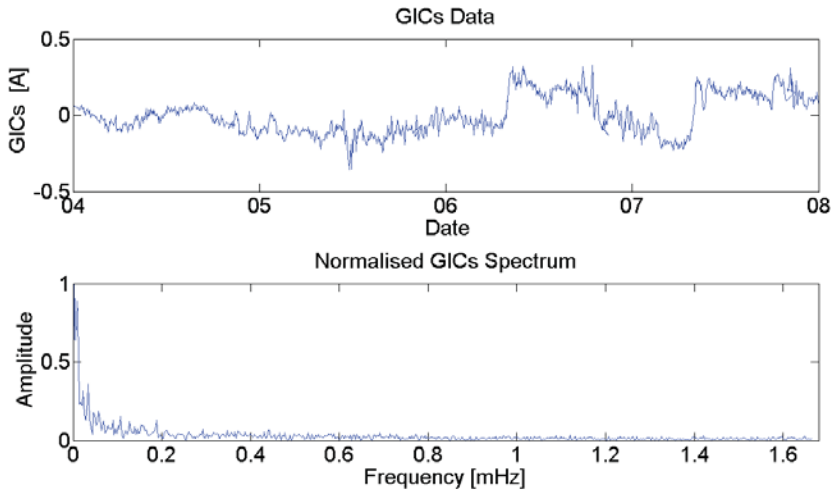

Figure 1. GIC data recorded during on 4-6 April 2010 at the Grassridge substation

However, there is need to know the magnitude of GIC flowing into the transformer. The power lines are the feeders of transformers so it makes sense to measure the GIC in the power lines for an overall comprehension of GIC flowing into the transformers. The paper discusses the approach proposed to achieve the GIC measurements on power lines. Due to the impracticality of direct GIC measurement using current transformers (CT), an indirect method is proposed. This method will be referred to as differential magnetic measurement (DMM) technique and it involves the use of two fluxgate magnetometers. This technique has been applied in the measurement of GIC in a 400 kV line in the Finland network and gas pipelines (since 1990s) [7].

At this point it is worth noting that the proposed measurements are to be done in a mid-latitude region. Unlike high latitude regions, mid and low latitude regions were believed to be less prone to GIC. However, mid- latitude regions such as Australia, Brazil, China, Spain, and South Africa have invested in measurements, recording, modelling GIC in the networks since a link between power grid mal-operation and adverse space weather events was established, see [8, 9, 10, 11, 12].

2. Differential magnetic measurements

The differential magnetic measurements technique will be implemented as an indirect way of measuring GIC on power lines. The technique comprises of simultaneous recordings by means of two identical magnetometers. The measurement concept assumes that one magnetometer under the power lines will measure both the natural Earth magnetic field and the magnetic field induced by GIC in the power line. The general set up is as shown in Figure 2, while Figure 3 illustrates the necessary components. The second magnetometer, placed at a distance from the first will measure the natural geomagnetic field only. The calculated difference between the measured fields will then be the contribution of the quasi-DC current flowing on the power lines. The GIC in the power lines can be inferred from the difference between the magnetic field measured under the power line and at some distance from the power line.

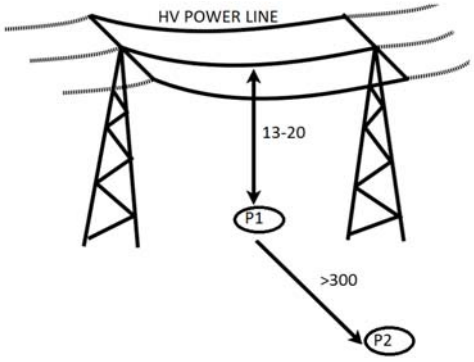

Figure 2. The magnetometer set-up for differential magnetometers

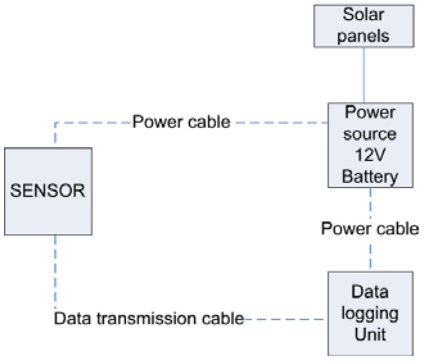

Figure 3. Components essential for the DMM technique

2.1. Site identification and environment

When selecting a site for GIC measurements, certain aspects need to be considered so as to enhance accuracy of the DMM and validity of the measured results.

- While very little or nothing can be done about the natural occurring field variations, an area with minimal man-made magnetic disturbances should be considered. This is to avoid magnetic interference from the man-made influence.
- It should also be possible to have a comparison of the GIC measured on the power lines as well as those from the transformer neutrals fed by the same power lines. GIC cannot be measured on some transformer neutrals as series capacitors are installed on the network [5]. The capacitors block the flow of GIC into the transformers and hence protect the network. The selected site should be a power line which terminates in non dc compensated substation.
- There should be minimum or negligible natural spatial variation of the geomagnetic field at the magnetometer placement positions. A set of measurements need to be carried out to validate this condition. Using magnetic field data measured in a quiet day (when there are no geo-magnetic disturbances), the spectral analysis through Fourier transforms can be used to infer the spatial uniformity of the geomagnetic field at the measurement positions. In this case similar frequency spectra will imply uniformity.
- Using historically measured GIC data from the South African power grid, a range of expected geomagnetic field can be calculated. If the estimated source current for a measured magnetic field difference is the less than 1 % of the corresponding recorded GIC, the variation will be deemed negligible.

2.2. DMM technique preliminary results

The trial run of the technique was to test if the selected magnetometer and control instruments could operate under the power line. The anticipated challenge was the sensor saturation due to the 50 Hz component of the magnetic field. A setup was done under a power line connected to a non dc compensated substation which also complied with the listed conditions. The location is on a farm near Botriver were there is limited man made magnetic interference. Figure 4 illustrates the first set of measurements at the selected site. The variations shown in Figure 4 shows us that the magnetometer did not saturate in the vicinity of the power lines.

The recorded field variations were compared with recorded magnetic data from Hermanus (Botriver is $\sim$ 50 km from Hermanus). The Hermanus magnetic data recorded at the same time as at Botriver was extracted from the daily magnetic data. Though the x-component of the magnetic field variations exhibit a similar trend, the y- and the z- component are not. At this stage considering that this was a pre-test to test the equipment it sufficed to prove that the saturation of the instruments did not occur and that the 50 Hz component did not appear in the measured data. Longer period recordings will hence be done when high memory data loggers are available. Such data will also aid in the validation of the spatial uniformity of the geomagnetic field at the measurement site.

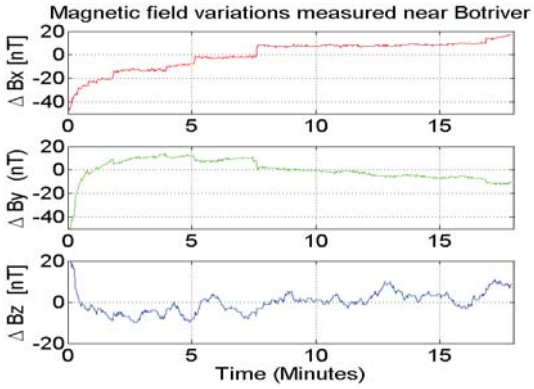

Figure 4. Magnetic field variations recorded at the chosen measurement site near Botriver

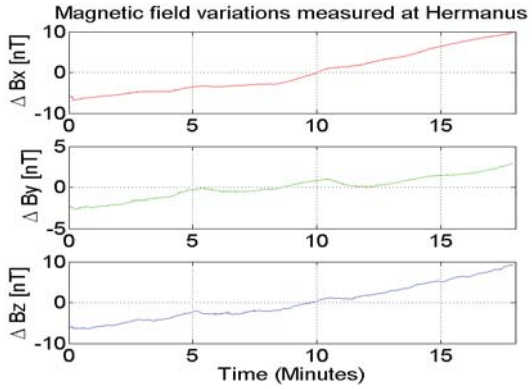

Figure 5. Magnetic field variations recorded at Hermanus

3. Finite element modelling with Comsol-Multiphysics

To enhance the understanding the depth, direction and spatial distribution of the return currents during a geomagnetic storm, a 3D finite element (FE) modelling is also proposed. The FE is introduced to address complexities posed by the Earth's geometry. COMSOL-Multiphysics FE Software is proposed to handle the FE modelling. FE modelling approximates a solution to a complex problem. The solution from an FE model may not be "exact" but it closely approximate a desired solution when analytical techniques are difficult to implement. Understanding the characteristics of GIC will aid in the comprehension of the nature of the return currents flowing in the power lines.

Modelling GIC involves two steps. The first step involves the determining the horizontal electric field at the Earth's surface during the rapid geomagnetic variations during the storm. At this stage, the system configuration does not play a role in the characteristics of the induced field. A set of Maxwell's equation linking the magnetic and the electric field are the basis of the solution in this stage of modelling. To accomplish this level of modelling, the Earth's conductivity and the measured geomagnetic field variations or the magnetospheric-ionospheric currents are regarded the crucial modelling inputs. The second stage of modelling involves

calculating the GIC on a particular network. Various network parameters play a significant role on the magnitude of the GIC estimates. This means that, this stage of modelling can not be generalised but will differ with network configuration.

To test the application of the software to achieve the broader objective of modelling the characteristics of GIC in the power lines, certain validation tests have to be performed on the software. This begins with validation of the inputs such as the time varying magnetic field. This include comparing the results obtained from the simulations with solutions with theoretical results. Measured data are available from Hermanus. The data can be used to test designed simulation setup.

4. FE Preliminary results

A $20 \times 20 \times 1$ km block of conductivity ($\sigma = 0.001 S/m$) , permittivity ($\epsilon = 1 F/m$) , and relative permeability ($\mu_r = 1$), was built in the software. In this exercise, a plane wave was assumed and its -x component was used as the input in the model. A time varying magnetic field shown Figure 6, was applied on the surface of this block in the -x direction. The computation done was such that the magnitude of the induced current and electric field in the block can be simulated. The aim is to further expand the computation so that the spatial direction and depth of the currents can be simulated for an N layered Earth model.

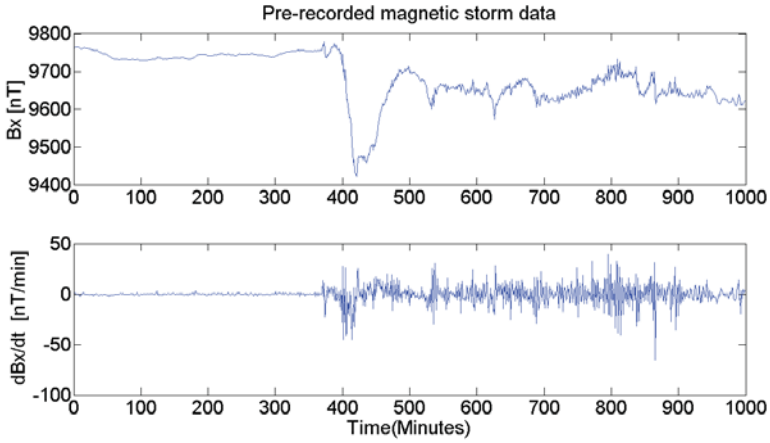

Figure 6. Pre-recorded magnetic data and corresponding dB/dt used as input in the model

From the results shown Figures 7 and 8, it can be noted that, the computed software results agree with ohm's law that relates current density and Electric field. Mathematically the law is represented as $J = \sigma E$ where J is the current density and E is the electric field. The constant of proportionality is the conductivity of the material which in this case is 0.001 S/m and is evident in the the two figures.

5. Conclusion

At this stage of the research, no significant results concerning the characteristics of GIC on power lines have been drawn. For the DMM technique, a permanent setup is under design to have longer period magnetic variations recordings. The longer the period of data recording the better will be the understanding of the variations at the site. Data from the Hermanus will be used for reference when analysing the data measured at the Botriver site.

Concerning the finite element modelling, the different geometry setups are currently being studied and designed so that sensible results can be drawn from the simulations. The software package has so far proved to be suitable for the proposed study. COMSOL Multiphysics offers

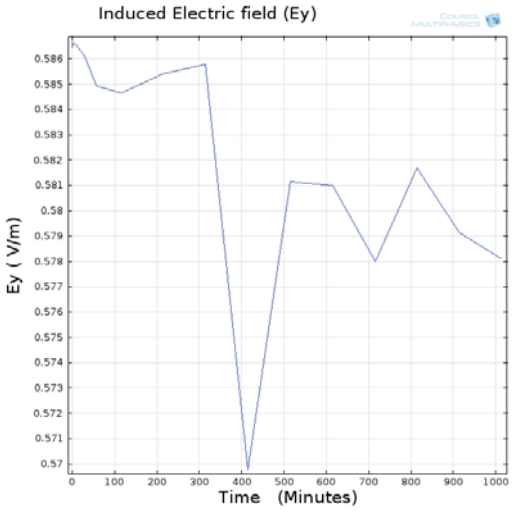

Figure 7. Electric Field strength induced within the block due to magnetic field variation

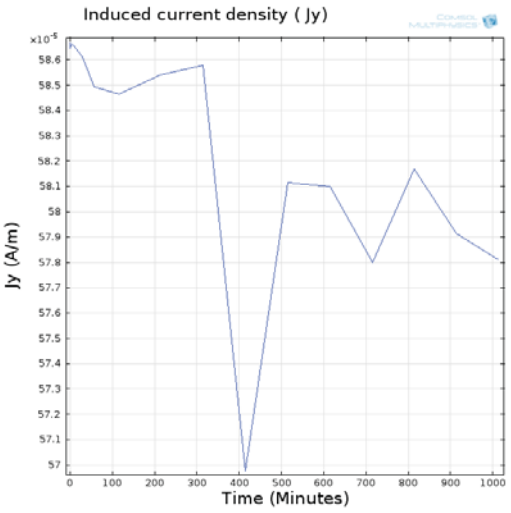

Figure 8. Induced current density within the block due to magnetic field variation

the platform to simulate electric and magnetic field at the same time. This is achieved through the AC/DC module.

Acknowledgments

The material and financial support for the research is provided by South African National Space Agency (SANSA), Space Science Directorate and the French South African Institute of Technology (F'SATI).

References

[1] Koskinen H, Transknen E, Prijola R, Pulkkinen A, Dyer C, Rodgers D, Cannon P, Mandeville J and Boscher D 2001 *ESA space weather study* **2**
[2] Pirjola R 2000 *IEEE, Transactions on Plasma Science.* **28** 1867–1873
[3] Boteler D H, Prijola R and Nevanlinna H 1998 *Advances in Space Research* **22** 17–27
[4] Gummow R A 2002 *Journal of Atmospheric and Solar-Terrestrial Physics* **64** 1755–1764
[5] Molinski T S 2000 *Astrophysics and Solar Terrestial Physics* **64** 1765–1778
[6] Czech M P, Charo S, Hynk H and Dutel A 1989 (San Francisco, California) pp 36–60
[7] Viljanen A T, Pirjola R J, Pajunpaa R and Pulkkinen A A 2009 (Saint-Petersburg,Russia) pp 227–230 june 16-19, 2009.
[8] Marshall R A, Gorniak H, van der Walt T, Waters C L, Sciffer M D, Miller M, Dalzell M, Daly T, Pouferis G, Hesse G and Wilkinson P J 2012 *Space Weather*
[9] Trivedi N B, Vitorello I, W Kabata, Padilha A, Bologna M S, de Padua M B, A P Soares, G S Luz, de A Pinto F, Pirjola R and Viljanen A 2007 *Space Weather* **5** 1–10
[10] Liu C, Liu L, Pirjola R J and Wang Z 2009 *Space Weather* **7**
[11] Torta J M, Serrano L, Regué R J, Sánchez A M and Roldán E 2012 *Space Weather* **10** 1–11
[12] Koen J 2002 *Geomagnetically Induced Currents in the Southern African Transmission Network* Ph.D. thesis University of Cape Town Cape Town, South Africa

Tomographic imaging of the ionospheric structure and disturbances in the East-Central Africa region

M Mutale[1], P Sibanda[1],

[1]Department of Physics, School of Natural Sciences, University of Zambia, Great East Road Campus, P.O Box 32379, Lusaka 10101, Zambia

E-mail: mubela.m@gmail.com

Abstract. Knowledge of the ionospheric electron density distribution and its fluctuations are essential for models such as the International Reference Ionosphere (IRI) for predicting ionospheric characteristics for radio wave propagation and for other applications such as satellite tracking and navigation. The Global Navigation Satellite Systems (GNSS), such as the Global Positioning System (GPS), can be used to determine the Total Electron Content (TEC) in the ionosphere. TEC is an important characteristic of the Earth's ionosphere that carries information on time and position variability of the ionosphere and has proved to be useful as a sensor of ionospheric climatology. However, such satellite to ground-based receiver measurements can only produce information about the density in the form of path-integrated snap-shots of the TEC. The challenge is to decompose its integral properly in the different values of electron density (Ne) in order to generate the distribution of the Ne with altitude. In this study, we use tomographic reconstruction techniques to successfully reconstruct altitudinal structure of the ionosphere from TEC data. Using the data from the recently installed Africa Array GPS stations in the central-Southern Africa region, we calculate three-hour average Ne profiles over this wide region using ionospheric tomography. The advantage of tomographic ionospheric Ne profiles is that they provide information of the Ne distribution up to global positioning system (GPS) orbiting altitude (with the coordination of space-based GPS tomographic profiles), and can be incorporated into the next generation of the IRI model. Since it uses real measurement data, tomographic average Ne profiles describe the ionosphere during quiet and disturbed periods.

1. Introduction

Because of the wide application of the ionosphere in space science, knowledge of the ionospheric vertical electron density (Ne) distribution is essential. Several factors affect the vertical distribution of the Ne, for example, solar activity such as flares and coronal mass ejections often produce large variations in the particle and electromagnetic radiation incident upon the earth. Such variations can, in turn, lead to disturbances of the magnetosphere. Such disturbances tend to generate large disturbances in ionospheric density distribution, total electron content (TEC), and the ionospheric current system. These ionospheric disturbances have important terrestrial consequences such as disrupting satellite communications and interrupting the flow of electrical energy over power grids. Furthermore, irregularly structured ionospheric regions can cause diffraction and scattering of trans-ionospheric radio signals. When received at an antenna, these signals present random temporal fluctuations in both amplitude and phase. This is known as ionospheric scintillation. Ionospheric scintillation may cause

problems such as signal power fading, phase cycle slips, receiver loss of lock, etc., and degrade the quality of satellite navigation systems.

It is therefore necessary to obtain knowledge of the ionosphere as this is a natural resource for radio wave propagation. Knowledge of the ionospheric variations is essential in other aspects such as for error correction of Global Positioning System (GPS) applications, over the horizon radar, navigation, surveying, geodesy, and simplification of scientific research for Sun-Earth physicists.

Ionospheric tomography, proposed by Austen et al. (1986), has developed from initial modelling studies to be a viable technique for monitoring ionospheric Ne profiles. The first experimental results were presented by Andreeva et al. (1990), while Pryse and Kersley (1992) presented the first observation in which a tomographic Ne profile was verified by incoherent scatter radar (ISR). Several experimental campaigns have been conducted since then (e.g., Raymund et al., 1993; Foster et al., 1994; Kunitake et al., 1995; Mitchell et al., 1997; Yin et al., 2004; Yizengaw et al., 2004, and the references therein). These studies have extensively validated the performance of tomographic reconstruction technique in providing accurate Ne profiles of the ionosphere. However, all of these experimental campaigns were focused on extracting instantaneous or a few minute average Ne profiles using ground-based tomographic reconstruction of the slant total electron content (STEC). Therefore, tomography was not used to make average Ne profiles.

Although ionospheric tomography has been introduced to provide broad spatial coverage of ionospheric density profiles, most previous tomographic campaigns were focused on determining instantaneous Ne profiles. Currently, there are not sufficient densities of ionosonde or ISR facilities to make routine regional or global ionospheric Ne profiles. Therefore, global ionospheric models are used to "fill in" gaps in data coverage.

Currently, there are several models that provide a monthly mean value of ionospheric Ne distributions over an extended region of latitudes. Among these ionospheric models is the international reference ionosphere model which is one of the most widely used. However, calculating the average Ne over an extended region of latitude from real measurements has been restricted to areas where ground-based ionosonde and ISR facilities are located. Therefore, average Ne profiles in areas where those instruments are not available are needed to develop and test model Ne profiles.

This study uses a technique that can be used to calculate average Ne profiles over a wide area of coverage, using total electron content measurements from ground-based GPS receivers. The advantage of using GPS-TEC for such applications is they have a relatively low cost of installation and therefore there are dense networks of GPS receivers. The global distribution of GPS receivers is much denser than ionosondes and ISR. In this study we apply the tomographic reconstruction technique using GPS-TEC to calculate 3-hour average Ne profiles over a wide region within the central African region and show how the ionospheric electron density distribution varies with geomagnetic activity.

2. Data and method

The GPS constellation currently consists of 29 satellites orbiting at ~55^{o} inclination in six distinct orbital planes and at ~20,200km altitude. Each satellite broadcasts two L-band signals at frequencies f_1=1.57542 GHz and f_2=1.2276 GHz. Owing to the dispersive nature of the ionosphere, dual frequency GPS measurements can provide integral information about the ionosphere and plasmasphere by computing the differential phases of the code and carrier phase measurements recorded at the ground-based GPS receivers (Klobuchar, 1996). Also, Mannucci et al. (1998) developed a method of calculating TEC from these GPS observables.

For this study we use the algebraic reconstruction technique (ART) to invert the GPS STEC into two-dimensional (altitude and latitude) average density profiles.

With this we observe how the ionosphere behaves at different levels of geomagnetic disturbance. The level of geomagnetic disturbance is quantified by the Kp index. The scale of Kp index ranges from 0 to 9, with Kp = 0 indicating no geomagnetic disturbance and Kp = 9 indicating extreme geomagnetic disturbance. Three hour averaged TEC values are used to derive tomographic images for two levels of geomagnetic activity, relatively quiet (with kp<2) and relatively disturbed (with kp>5).

The density values for individual pixels are then obtained from all STECs traversed through each pixel. This provides an averaged two dimensional description of the ionospheric Ne distribution. The images show how the level of geomagnetic activity as indicated by the Kp index affects the structure of the ionosphere.

The effectiveness of tomographic reconstruction depends on the distribution of the measurements. The International GNSS service (IGS) and the Africa Reference Frame (AFREF) and the Africa Array Networks have been set up and tomography has become a viable technique for ionospheric investigation in the African sector. Other GPS receiver networks have been set up in other locations such as the recently installed GPS stations is Zambia. These have created a relatively dense network for ionospheric tomography.

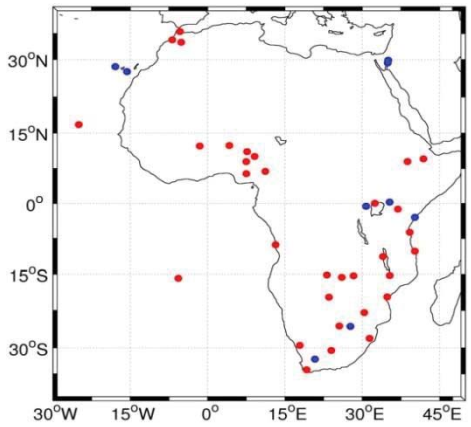

Figure1. Africa GNSS reference receiver stations

The results presented in this paper are obtained from measurements made during experimental campaigns using GPS stations in the East-Central African region.

Table 1: Geographical locations of the GPS stations being used in this study

Country	GPS station name	Latitude	Longitude
Zambia	Zamb	-15.42	+28.31
Zambia	Mong	-15.25	+23.15
Zambia	Tezi	-15.73	+26.02
Malawi	Mzuz	-11.43	+34.01
Kenya	Maua	-19.90	+23.53
Congo	Ulub	-11.63	+27.48
Tanzania	Dodm	-6.19	+35.75
	Zomb	-15.38	+35.33

3. Results

Although we have presented the 3-hour models for only two days, we have extensively analysed several case studies with similar respective levels of geomagnetic activities. Figure 2 presents results for a relatively "quiet day". The figure shows a gradual increase in ionization with very little disturbance in the structure of the ionization. On the other hand the "disturbed day" on Figure 3

although showing similar evolution in ionization has a lot more structure. Using the colour code, in figure 2a it can be seen that the level of ionization is very low at midnight as expected. The level of ionisation stays low for the rest of the night time hours because ionisation is mainly caused by solar radiation incident upon the earth which is not present at this time. The opposite is seen in the day time images (e.g. figure 2f and figure 3d) where the level of ionisation begins to increase with time. More so, the altitude over which there is ionization becomes wider. This is because the F1 and F2 layers become one layer at night and split into two during the day. Structure and density of the F region depend on the time of day and the zenith angle of the sun. Ionization density of the F1 layer depends on the zenith angle of the sun. The low ionization at night is also because the D layer is a daytime layer and therefore disappears at night. This layer accounts for the extension of the ionosphere to lower altitudes in the daytime images as well as the reduction during the night time images.

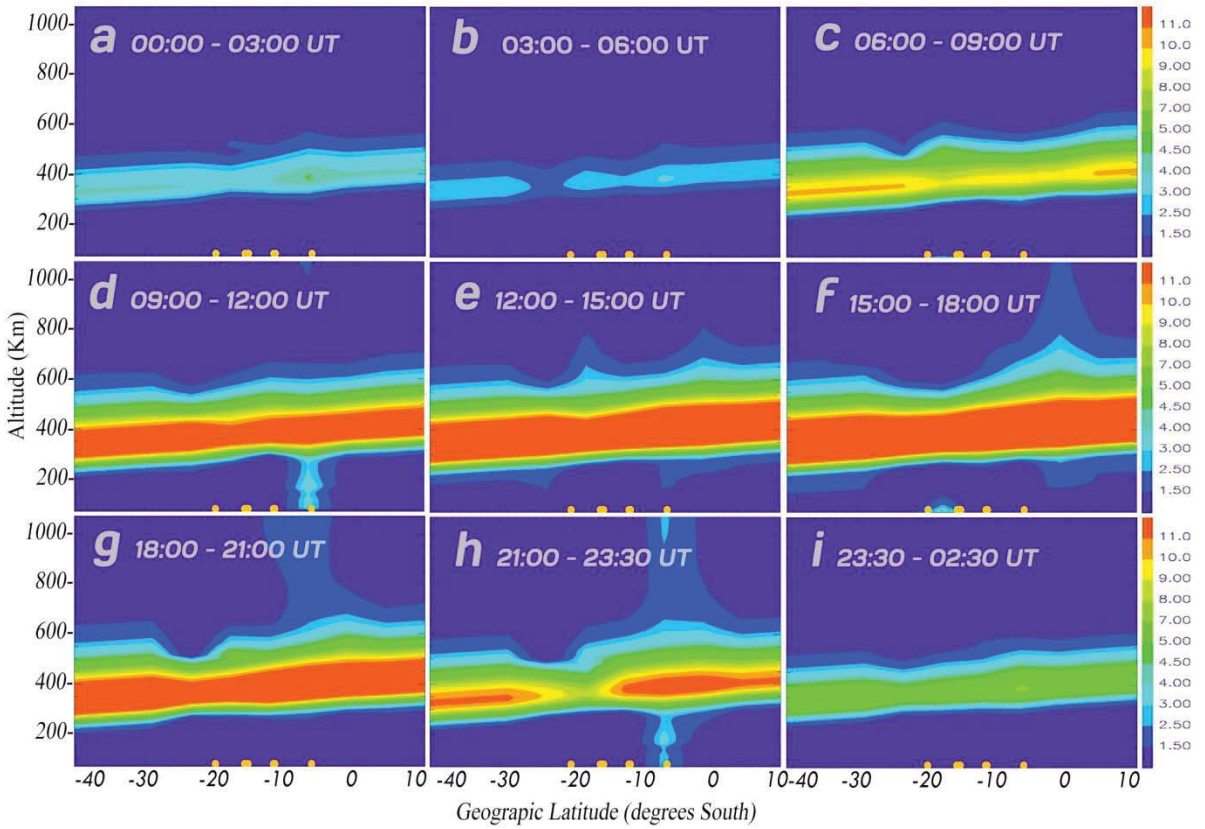

Figure 2. image of ionization on February 18 (Quiet day), showing the ionization on a graph of altitude against latitude. The right hand color code scale shows the electron density from 1.5 X10^5 el/cm^3 to 11 x 10^5el/cm^3. Each image is formed by taking all the TEC in a single 3-hour period averaging it to form the single image. The evolution shows selected images from midnight to midnight.

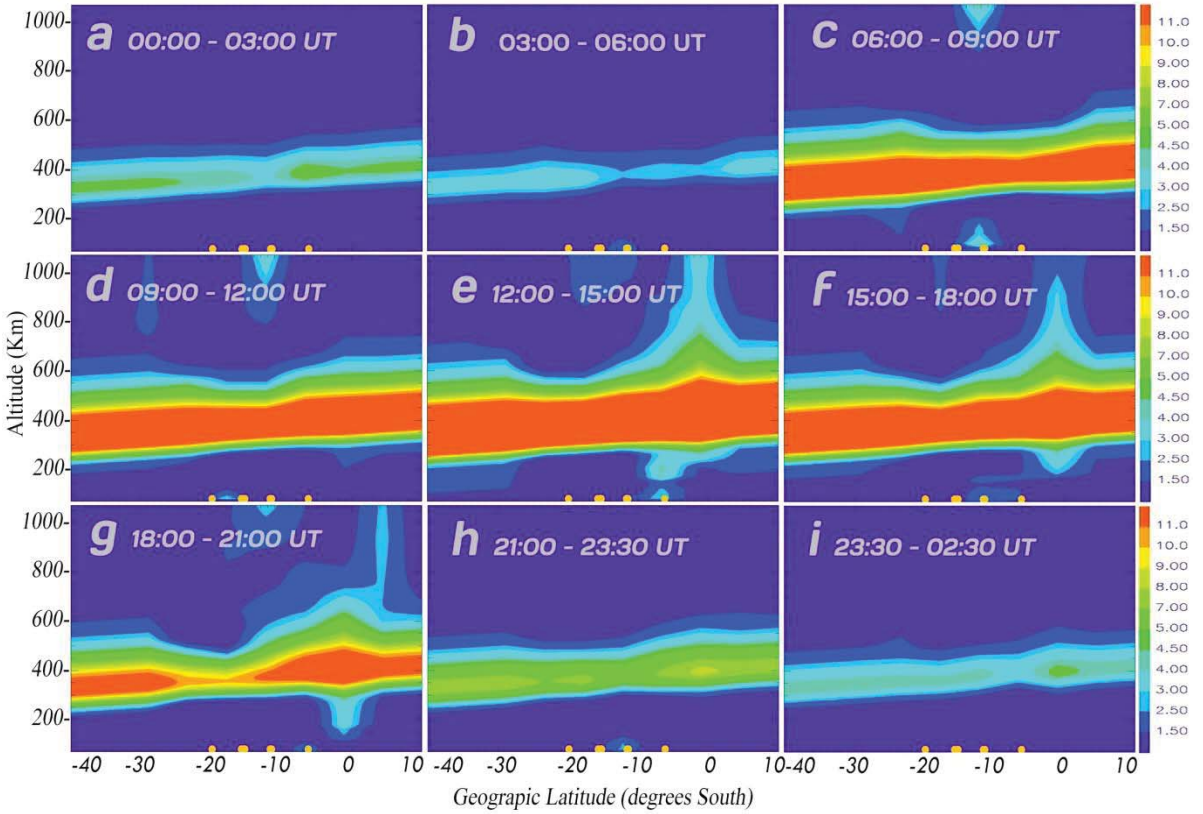

Figure 3. images showing the ionisation on March 9 (Disturbed day) – The images show how the evolution of ionisation due to diurnal changes occurs and how the ionisation levels are affected by geomagnetic disturbance. These are selected images showing the evolution from midnight to midnight. The left hand scale shows the altitude while the bottom scale shows latitude from equator going south. The right hand scale is a color coding for the electron density from 1.5 X 10^5el/cm^3 to 11 x 10^5el/cm^3.

At low latitudes the largest electron densities are found in peaks on either side of the magnetic equator; this is a feature known as the equatorial anomaly (figure 2c and 3a). The peak ionospheric concentrations do not occur on the equator, as might be expected from the maximum in solar ionizing radiation, but instead are displaced on either side. This anomaly occurs irrespective of day or season. The main driving force for the establishment of the equatorial anomaly (Fejar, 1991; Mikhailov et al, 1994) is the east west electric field, which is westward during night-time. Therefore, the corresponding resultant **E**×**B** motion is downward. This is opposite of that required to produce the anomaly; so such vertically extended density features would not normally be present at night.

Large scale structure such as the mid latitude trough (figures 2.h and 3.g), as well as a rise in ionization at the latitude 15^{o}S geomagnetic in both the quiet and disturbed times are also present. Clearly the ionization during the disturbed period is a lot more evident and structured than the quiet period in day time as well as at night.

4. Conclusion

Although tomographically reconstructed density profiles have been extensively validated for the case of instantaneous Ne profiles and documented in for example, Raymund et al., 1993; Foster et al .,1994; Kunitake et al., 1997; Yin et al., 2004; Yizengaw et al., 2004, and the references therein, the tomographic profiles presented in this paper describe the averaged behaviour of the ionosphere. This knowledge is important to single-frequency GPS users who depend on ionospheric models to achieve

optimal positioning accuracy because the ionospheric signal delay is the largest error source for positioning and navigation. Tomography provides Ne profiles at specific epoch owing to the fact that it uses calculated GPS-TEC. Though TEC is just an integrated parameter, ionospheric tomographic reconstruction routine using algebraic reconstruction enables us to decorelate this into the vertical distribution of the electron density profile thereby providing more information required for HF radio propagation. Other than that the technique used in this study shows how the level of geomagnetic activity affects the structure of the ionosphere. This is especially important for the topside ionosphere since current models have to rely on density profiles obtained from the sparsely located ground-based instruments that provide mainly bottom side Ne profiles to infer information about the topside ionosphere. The tomographic Ne profiles, which describe Ne distribution from ground to the GPS satellite altitude, can be used for the next generation of IRI models, enabling them to model the topside ionosphere more accurately. As long as dense arrays of GPS receivers are available, tomographic imaging can be used to augment sparsely located ground based instruments, such as ionosonde and incoherent scatter radar.

Acknowledgements
My gratitude goes to the University of Zambia for hosting this research. Also this research was supported by the Natural Science and Technological Council of Zambia NSTC. Thanks are due to the UNAVCO for the GPS data

References

[1] Andreeva E S, Galinov A V, Kunitsyn V E, Mel'nichenko Yu A, Tereshchenko E D, Filimonov M V and Chernykov S M 1990 *Journal of Experimematal and Theoretical Physics letter* **52**, 145 – 148.
[2] Austen J R, Fmake S J and Liu C H, 1986 In: Tauriainen A (Ed.), Radio Beacon Constributions to The Study of Ionization and Dynamics of The Ionosphere and to Corrections to Geodesy and Technical Workshop. *Ouluensis Universitas, Oulu, Finland*. 25-35.
[3] Bilitza D 2001 International reference ionosphere 2000 *Radio Science.* **36** 261-275.
[4] Fejer B G 1991 *Journal of Atmospheric and Terrestrial Physics*. **53** 677-693.
[5] Foster J C, Buonsanto M J, Klobuchar J A, Holt J M, Fougere P, Pakula W A, Raymund T D, Kuntisyn V E, Andreeva E S, Tereschenko E D and Kudukon B Z 1994 *International Journal of Imaging System and Technology*. **5** 148-159.
[6] Klobuchar J A 1996 Ionospheric effects on GPS. In: Parkinson B W and Spilker J J. (Eds). Global Positioning System: Theory And Application, vol. 1. *American Institute of Aeronautics and Astronautics INC.*
[7] Kunitake M, Ohtaka K, Maruyama T, Tokumaru M, Morioka A and Watanabe S 1995 *Annales Geophysicae,* **13** 1303-1310.
[8] Mikhailov A V, Förster M and Skoblin M G 1994 *Annales Geophysicae.* **12** 226-231.
[9] Pryse S E, Kersley L, 1992 *Journal of Atmospheric and Terrestrial Physics* **54** 1007-1012.
[10] Raymund T D, Pryse S E, Kersley L, Heaton J A T 1993 *Radio Science* **28** 811-818.
[11] Yisengaw E, Dyson P L, Essex E A and Moldwin M B 2005a *Annales Geophysicae* **23** 707-721.

Study of the geomagnetic field over southern Africa applying harmonic splines technique on CHAMP satellite data

E. Nahayo[1], P. B. Kotzé[1] and H. McCreadie[2]

[1] South African National Space Agency (SANSA) Space Science, PO Box 32, Hermanus, South Africa

[2] University of KwaZulu-Natal, Private Bag X54001, Durban, South Africa

E-mail: enahayo@sansa.org.za, pkotze@sansa.org.za and mccreadie@ukzn.ac.za

Abstract. The monitoring of the Earth's magnetic field time variation requires a continuous recording of geomagnetic data with a good spatial coverage of the area of study. In the southern Africa, ground recording stations are limited and the use of satellite data is needed for the studies where high spatial and temporal resolution data is required. The study of the fast time variation of geomagnetic field in the southern Africa region was conducted applying the harmonic splines technique on CHAMP satellite data that has been recorded between 2001 and 2005. The derived core field model, the Southern Africa Core Field Model (SACFM-1), was evaluated using the ground-based data and the International Geomagnetic Reference Field model (IGRF-11). The results of this study suggest that the southern Africa regional model can be improved combining the satellite data and ground data.

1. Introduction

The geomagnetic field changes on different space and time scales. The core field represents the dominant part of the Earth's magnetic field and its variation over time scales of decades to centuries is referred to as secular variation. This study focuses on southern Africa that is situated in the region where the most rapid decrease of field intensity is observed at the Earth's surface stretching across southern Africa and south Atlantic Ocean [1]. This coincides with a region known as the South Atlantic Anomaly where the field is already very weak compared to other locations at the same latitude.

In this region, the ground recording stations are limited and the use of satellite data is needed for the studies where high spatial and temporal resolution data is required. The attempt to study the time variation of geomagnetic field in this region using the harmonic splines technique was done previously using only the ground-based data [2]. In this paper, the results of the use of harmonic splines technique on CHAMP satellite data recorded between 2001 and 2005 were evaluated using the ground based data and the global IGRF-11 model [3].

2. Method

The use of the harmonic splines technique was first introduced by [4] for global magnetic field modelling, but it is as well suitable for regional modelling. The core field model is derived over southern Africa using harmonic splines. The harmonic spline functions satisfy Laplace's

equations, therefore allowing a potential field approach combining the individual components in a physical meaningful way [5].

According to [2] and [6], the Earth's magnetic field can be written as:

$$B(\vartheta,\varphi,r) = -\bigtriangledown\left\{\sum_j \alpha_j^r F_j^{Lr}(\vartheta,\varphi,r) + \sum_j \alpha_j^\vartheta F_j^{L\vartheta}(\vartheta,\varphi,r) + \sum_j \alpha_j^\varphi F_j^{L\varphi}(\vartheta,\varphi,r)\right\}, \quad (1)$$

where the functions $F_j^{Lr}(\vartheta,\varphi,r)$, $F_j^{L\vartheta}(\vartheta,\varphi,r)$ and $F_j^{L\varphi}(\vartheta,\varphi,r)$ are defined as follows:

$$F_j^{Lr} = a\sum_{l,m}^{L} f_l(l+1)\left[\left(\frac{a}{r_j}\right)^{l+2} Y_l^m(\vartheta_j,\varphi_j)\right]\left(\frac{a}{r}\right)^{l+1} Y_l^m(\vartheta,\varphi), \quad (2)$$

$$F_j^{L\vartheta} = a\sum_{l,m}^{L} f_l\left[\left(\frac{a}{r_j}\right)^{l+2} \partial_\vartheta Y_l^m(\vartheta_j,\varphi_j)\right]\left(\frac{a}{r}\right)^{l+1} Y_l^m(\vartheta,\varphi), \quad (3)$$

$$F_j^{L\varphi} = a\sum_{l,m}^{L} f_l\left[\left(\frac{a}{r_j}\right)^{l+2} \frac{\partial\varphi}{sin\vartheta_j} Y_l^m(\vartheta_j,\varphi_j)\right]\left(\frac{a}{r}\right)^{l+1} Y_l^m(\vartheta,\varphi), \quad (4)$$

where $\sum_{l,m}^{L}$ denotes the double sum $\sum_{l=1}^{L}\sum_{m=-l}^{l}$, ϑ, φ and r are the geocentric colatitude, longitude and radius, a is the Earth's reference radius (6371.2 km), $Y_l^m(\vartheta,\varphi)$ are the usual Schmidt semi-normalised spherical harmonic functions of degree l and order m, L is the maximum degree of expansion of internal sources and $f_l = \frac{2l+1}{4\Pi(l+1)^4 l^2}$. The parameter f_l imposes smooth characteristics on the derived field model.

Equation (1) is time independent, it defines a linear system of equations where α_j^r, α_j^ϑ and α_j^φ are unknowns. This linear system is square and can be solved directly. For time representation, we expand each of the coefficients α_j^r, α_j^ϑ and α_j^φ on a basis of B-splines. The maximum degree of expansion of internal sources was set to 20. This degree is small enough to reveal mostly the field contributions from the core. For the time representation, order four B-splines with spline knots spaced at 1 year intervals between 2001.0 and 2006.0 are used.

3. Data selection and processing

The CHAMP satellite data was recorded between 300 km and 450 km of altitude. The quiet night data recorded between 2001 and 2005 were selected over the southern Africa region covering the area between 10°S and 38°S in latitude and 10°E and 38°E in longitude. Only quiet time data corresponding to a Dst index between -20 nT and +20 nT measured during the local times between 18:00 - 07:00 were considered.

The model input data were obtained by creating 225 data bins of 0.2°×0.2° on a grid of 2° of latitude and 2° of longitude. The middle point of the bin was considered to be the data center and consequently 225 data centers were created (fig. 1). The data values recorded in the same bin at the same epoch (within 37 days, e.g. 2003.2) were averaged to get a single data value at the data center (6687 different data values of X, Y and Z over 5 years between 2001 and 2005 were obtained). In this process, it was possible to get a number of data values recorded at different epochs and altitudes at the same data center for the period of 2001 - 2005.

The comparative evaluation of SACFM-1 with the global model IGRF-11 was performed using data recorded at geomagnetic repeat stations (CRA, GAR, MES, OKA, UND, MAU and SEV) and geomagnetic observatories (HER, HBK and TSU) over the same time period between 2001 and 2005 (Table 1). These 10 reference points were selected

Table 1. Geodetic coordinates of 10 points used in the comparative evaluation of the developed models.

Station	Latitude (°)	Longitude (°)	Altitude (m)
Cradock (CRA)	-32.2	25.6	847
Garies (GAR)	-30.6	18.0	229
Messina (MES)	-22.4	30.1	484
Okaukuejo (OKA)	-19.2	15.9	1039
Underberg (UND)	-29.8	29.5	1530
Maun (MAU)	-20.0	23.4	907
Severn (SEV)	-26.6	22.9	890
Hermanus (HER)	-34.4	19.2	26
Hartebeesthoek (HBK)	-25.9	27.7	1555
Tsumeb (TSU)	-19.2	17.6	1273

based on the availability of data at geomagnetic repeat stations (also available at http://www.geomag.bgs.ac.uk/data_service/data/home.html) and geomagnetic observatories (also available at http://www.intermagnet.org) in the southern Africa region. The secular variation at the repeat station was determined by means of the procedure given by Newitt et al. [7].

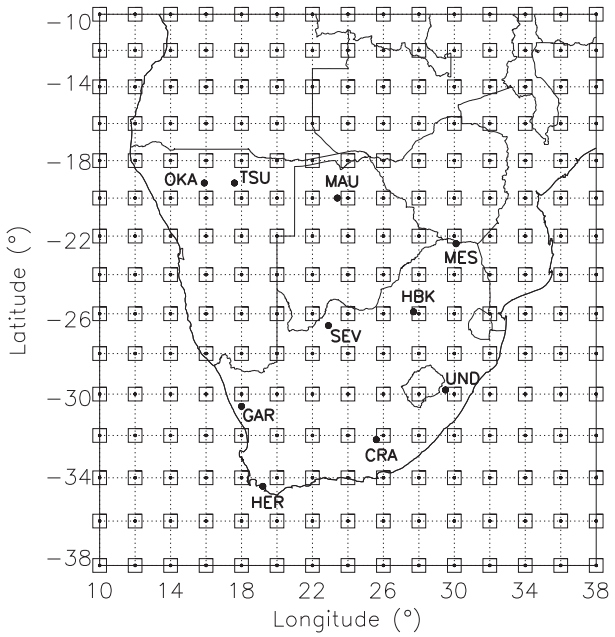

Figure 1. The data bins (0.2°×0.2°) used for generating input data (represented by square shapes), the middle of each data bin represents a data center (not all data centers have data points for every year). The black big dots represent the reference ground points used to evaluate the developed model.

4. Data modelling results

4.1. Main field models

Using 225 centers and 6687 different data values of X, Y and Z over 5 years between 2001 and 2005, the root mean square (RMS) values of the difference between observed and model values were 13.7 nT, 8.6 nT and 6.9 nT for X, Y and Z components respectively.

The presented results of the main field models were obtained by predicting the geomagnetic field at 225 points at 1 km altitude. To validate the SACFM-1, the only 2003.5 epoch main field values and 2003.0 epoch secular variation values for H, D and Z field components and total field intensity F are compared with the ground based data and the global IGRF-11 model. The comparison of two models is presented in fig. 2 and Table 2. The latter presents the comparison of 2 models using the ground data. The SACFM-1 and IGRF-11 performances in D and F are very close. But, there is a poor performance of the SACFM-1 model in H and Z components. The RMS values of the differences between SACFM-1 and ground data are 148.4 nT and 102.9 nT for H and Z components, respectively.

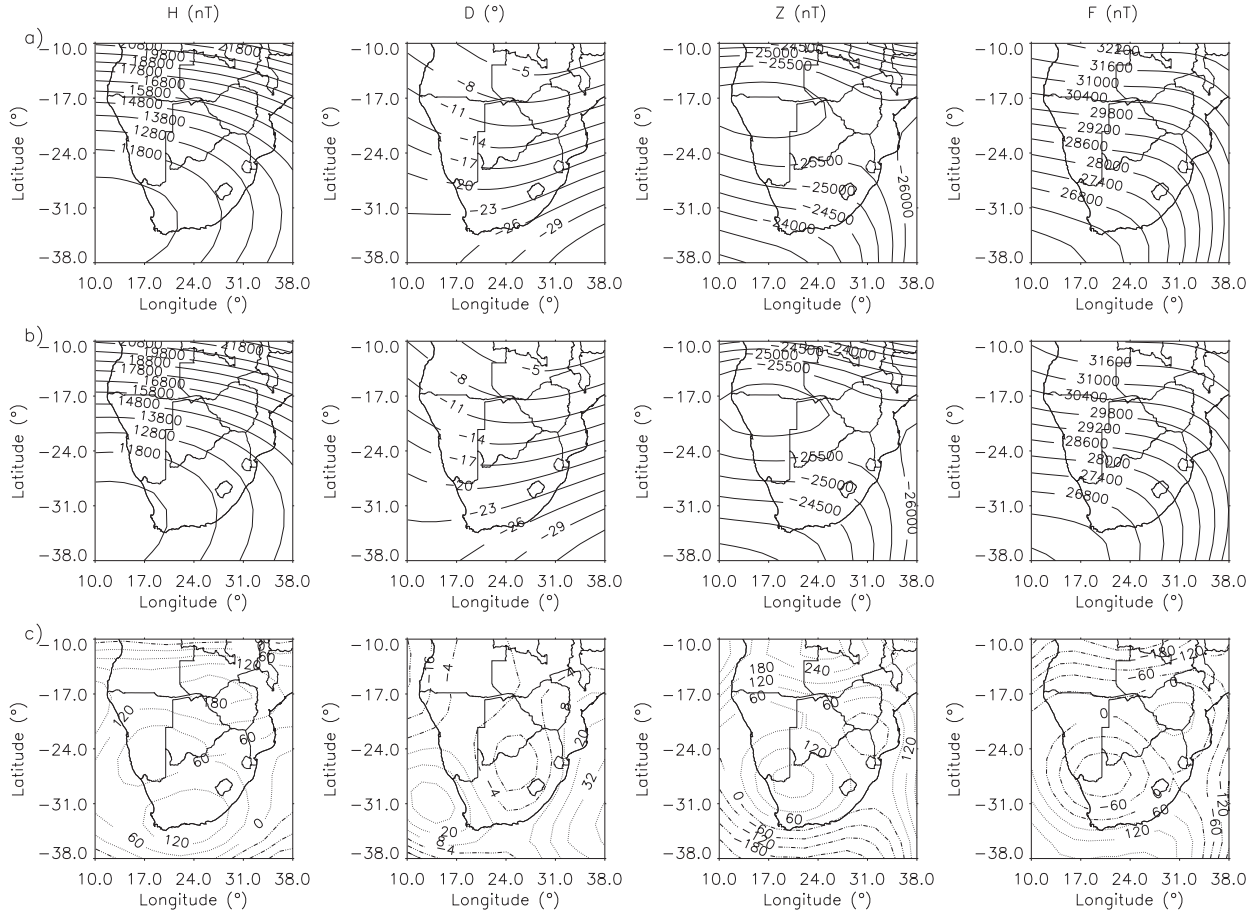

Figure 2. The comparison between (a) SACFM-1 (first row) and (b) IGRF-11 (second raw) models for H, D, Z and F (from left to right) at 1 km of altitude for epoch 2003.5. The third raw (c) represents the difference between the main field models of SACFM-1 and IGRF-11 for H, D (min), Z and F (from left to right).

Table 2. The RMS values of the differences between the SACFM-1 and IGRF-11 main field models and ground data at 10 reference points for epoch 2003.5.

Field component	SACFM-1 - Ground data	IGRF-11 - Ground data
D (min of arc)	29.6	29.3
H (nT)	148.4	77.7
Z (nT)	102.9	66.9
F (nT)	74.3	68.6

4.2. Secular variation models

The results of the secular variation models for H, D, Z and F are presented in fig. 3 and the comparison of these 2 models using the ground data is illustrated in Table 3. The SACFM-1 performs better than the global IGRF-11 model in H and Z components and there is a close performance of two models in the D component and the total intensity F.

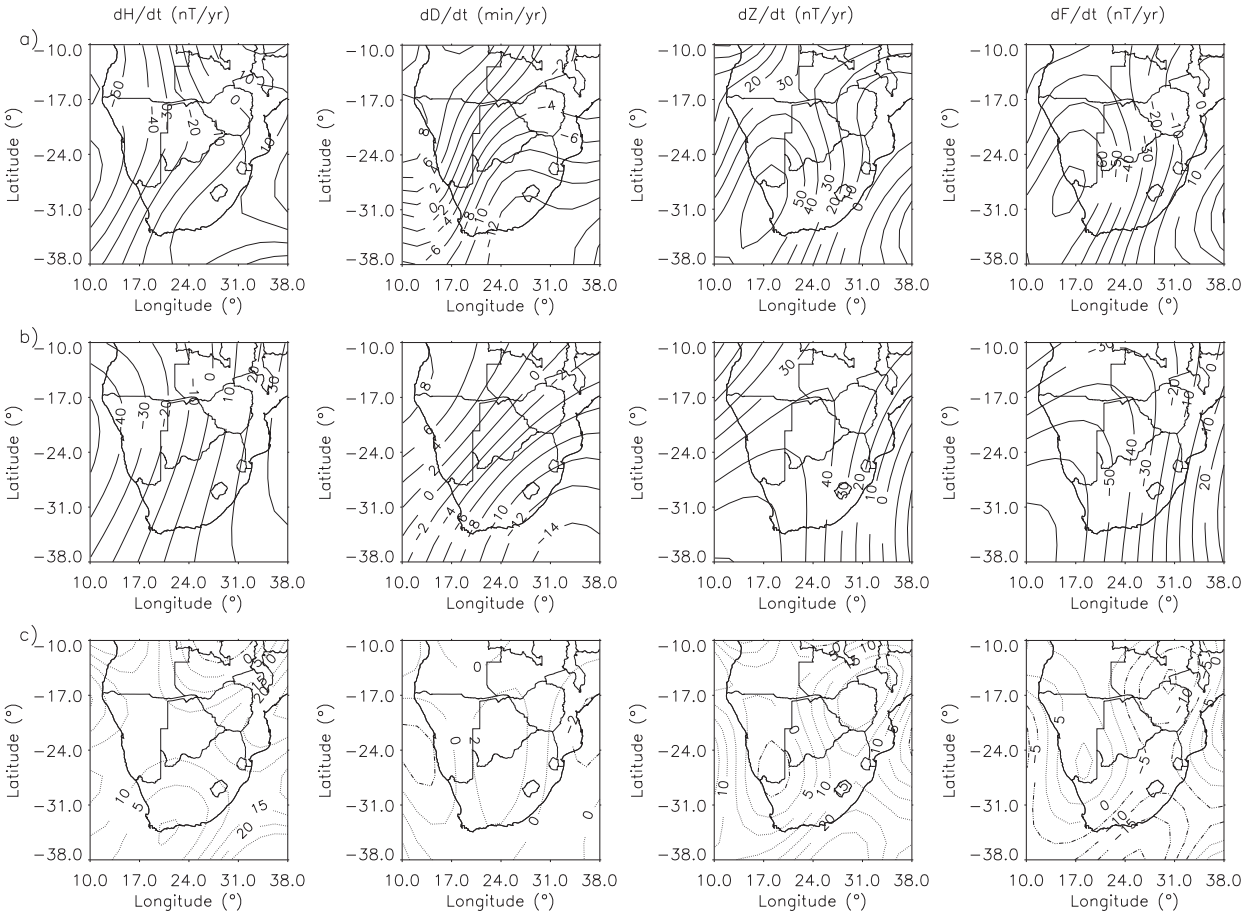

Figure 3. The comparison between (a) SACFM-1 (first row) and (b) IGRF-11 (second row) models for secular variation of H, D, Z and F (from left to right) at 1 km of altitude for epoch 2003.0. The third raw (c) represents the difference between the secular variation models of SACFM-1 and IGRF-11 for H, D , Z and F (from left to right).

Table 3. The RMS values of the differences between the SACFM-1 and IGRF-11 secular variation models and ground data at 10 reference points for epoch 2003.0.

Field component	SACFM-1 - Ground data	IGRF-11 - Ground data
dD/dt (min/yr)	1.7	1.3
dH/dt (nT/yr)	8.1	9.4
dZ/dt (nT/yr)	8.2	10.6
dF/dt (nT/yr)	6.1	6.4

5. Discussion and conclusion

The study of time variation of geomagnetic field was conducted applying the harmonic splines technique on CHAMP satellite data recorded between 2001 and 2005. Using the ground data measured at the 10 reference points, the developed regional model, SACFM-1, was compared with the global IGRF-11 model. For the secular variation models, the results presented in Table 3 show that SACFM-1 performs better than IGRF-11 in the H and Z components. In addition, both models SACFM-1 and IGRF-11 have a very similar performance in the D component and the total field intensity F.

The poor performance in H and Z components for main field models can be partially attributed to the external field contamination in satellite data and a poor data coverage. One would suggest that the model can be improved by reconsidering the data selection criteria or removing the unwanted contribution of external field from data. Furthermore, the increase of data centers to get a good data coverage would improve the model performance. The use of ground data together with satellite data should be considered, this would result in a regional model that can perform better than the global models and allowing the study of rapid variation of geomagnetic field in southern Africa.

Acknowledgments

The support of the CHAMP mission by the German Aerospace Center (DLR) and the Federal Ministry of Education and Research are gratefully acknowledged.

References

[1] Nahayo E and Kotze P B 2012 Polynomial modelling of CHAMP satellite data to investigate rapid secular variation fluctuations over southern Africa during 2003 and 2004 *Earth Planets Space* **64** 525-603

[2] Geese A, Hayn M, Mandea M and Lesur V 2009 Regional Modelling of the Southern African Geomagnetic Field using Harmonic Splines *Geophys. J. Int.* **200** 1-16

[3] Finlay C C, Maus S, Beggan C D, Bondar T N, Chambodut A, Chernova T A, Chulliat A, Golovkov V P, Hamilton B, Hamoudi M, Holme R, Hulot G, Kuang W, Langlais B, Lesur V, Lowes F J, Lühr H, Macmillan S, Mandea M, McLean S, Manoj C, Menvielle M, Michaelis I, Olsen N, Rauberg J, Rother M, Sabaka T J, Tangborn A, TØffner-Clausen L, Thébault E, Thomson A W P, Wardinski I, Wei Z and Zvereva T I 2010 International Geomagnetic Reference Field *Geophys. J. Int.* **183** 1216-1230

[4] Shure L, Parker R L and Backus G E 1982 Harmonic splines for geomagnetic modelling *Physics of the Earth and Planetary Interiors* **28** 215-229

[5] Geese A, Korte M, Kotzé P and Lesur V 2011 Southern African geomagnetic secular variation from 2005 to 2009 *South African Journal of Geology* **114** 515-524

[6] Lesur V 2006 Introducing localised constraints in global geomagnetic field modelling *Earth Planets Space* **58** 477-483

[7] Newitt L R, Barton C E and Bitterly J 1996 Guide for Magnetic Repeat Station Surveys *International Association of Geomagnetism and Aeronomy*

Inversion of geomagnetic fields to derive ionospheric currents that drive geomagnetically induced currents.

J S de Villiers[1] **and P J Cilliers**[1]

[1]Space Science Directorate, South African National Space Agency, PO Box 32, Hermanus, 7200

E-mail: Jdevilliers@sansa.co.za

Abstract. Start your abstract here This research focusses on the inversion of geomagnetic field measurement to obtain source currents in the ionosphere. The ionospheric currents during a geomagnetic storm induce geo-electric fields, which in turn create geomagnetically induced currents (GICs) in power lines. These GICs may cause damage to grounded power transformers. The ultimate aim is to develop a system for predicting the ionospheric source currents from solar event data and use the link between the source currents and GICs to provide advance warning to power utilities. Line currents running East-West along given latitude are postulated to exist at a certain height above the Earth's surface. This physical arrangement expresses the fields on the ground in terms of the magnetic north and down component, and the electric east component. Ionospheric currents are modelled by inverting Fourier integrals of elementary geomagnetic fields using the Levenberg-Marquardt technique. The output parameters of the model are the current strength, height and latitude of the ionospheric current system. A conductivity structure with ten layers from Loxton, South Africa, based on the Layered-Earth model, is used to obtain the complex skin depth at a given angular frequency. The paper will present inversion results based on the Loxton structure and simulated geomagnetic fields. Model parameters can be obtained to within 2% of synthetic values. This technique has applications for modelling the currents of electrojets at the equator and auroral regions, as well as currents in the magnetosphere.

1. Introduction

Solar events, such as coronal mass ejections, that become geo-effective, creates disturbances within the Earth's magnetosphere giving rise to geo-magnetic storms and substorms. These events affect the ionospheric current systems (an example setup is given in figure 1(a)) and create fluctuations in the electric and magnetic fields on the ground. Rapid changes in the geomagnetic field generate geomagnetically induced currents (GICs) in power lines (figure 1(b)). The GICs has the potential of causing the transformers to fail, with subsequent consequences of a blackout to the general public, who are increasingly reliant on electrical power generation for their everyday operations and living.

Therefore, it is of interest to both academics and power utility operators that a warning system be developed that can predict GICs as and when an event occurs on the sun. Due to the complexities involved in such a solar-terrestrial interaction and the tremendous challenges facing such a project, we consider as a first step the inversion of the geomagnetic field observations to obtain ionospheric source currents. From these source currents we estimate the induced geo-electric fields as measured at any location of interest and the electric fields responsible for GICs in power grids on the ground.

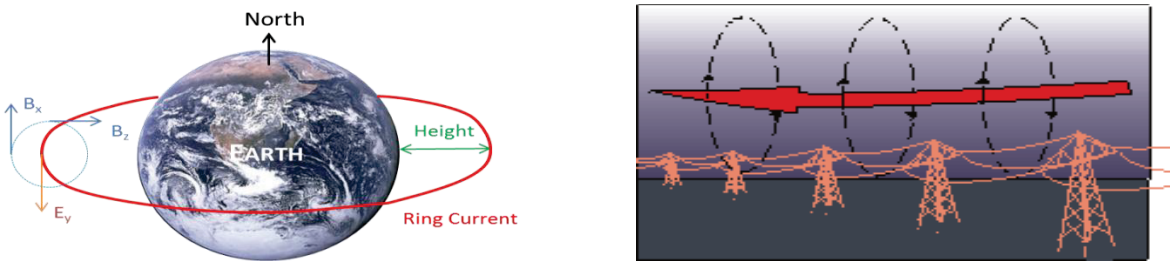

Figure 1(a): Ring current system around the Earth. **(b):** Power-lines through which GICs can be generated by fluctuations in the magnetic and electric fields.

2. Theory

2.1. Magneto-telluric Background

For a line current running in an East/West y-direction at latitude $x = 0$ and a height $z = -h$ above the Earth with a strength I, as shown in Figure 1a, the only non-zero component of the electric field is E_y (eastward). This field is determined from a diffusion equation $\nabla^2 E_y = i\sigma\omega\mu\, E_y$ in the plane-earth model [1]. The σ is the conductivity, ω is the angular frequency. The solution has both incident and reflected terms.

The magnetic field components are computed by taking the curl of this diffusion equation and using Maxwell's equations. The only non-zero components are then B_x and B_z. To relate these elementary fields to that of a line current, one must take Fourier integrals of the components and from any standard integral table, such as [2], the final form solutions of these expressions are obtained.

$$B_x(x,z) = \frac{I\mu}{2\pi}\left(\frac{h}{h^2+x^2} + \frac{h+2p}{(h+2p)^2+x^2}\right), \tag{2.1}$$

$$B_z(x,z) = -\frac{I\mu}{2\pi}\left(\frac{x}{h^2+x^2} - \frac{x}{(h+2p)^2+x^2}\right), \tag{2.2}$$

$$E_y(x,z) = -i\omega\frac{I\mu}{2\pi}\ln\left(\frac{(h+2p)^2+x^2}{h^2+x^2}\right)^{1/2}. \tag{2.3}$$

The skin depth $p(\omega)$ is related to the part reflected from the Earth's surface [3]. This paper diverges from [4] by studying only line current systems and replacing x with $x' = x - x_o$. This allows one to deal with the case where the current isn't vertically above the observation location, by choosing the latitude x_o of the system to be other than $x = 0$.

The complex skin depth $p(\omega)$ is computed by using a layered-earth model. The appendix of [5] describes a general approach to determine the complex surface impedance, $Z = -E_y/H_x$, from the 1D ground conductivity structure of a given location. The half-space impedance is $Z_{N+1} = K_{N+1}$. The

remaining layer impedances are calculated from a recursion relation, starting at the bottom and working all the way up to the top (that is for $n = N, \dots, 1$):

$$Z_n = K_n \frac{Z_{n+1} - K_n \tanh \lambda_n h_n}{K_n - Z_{n+1} \tanh \lambda_n h_n} \tag{2.4}$$

where $K_n = \frac{i\omega\mu_n}{\gamma_n} = \frac{(i\omega\mu_n)^{1/2}}{(\sigma_n + i\omega\varepsilon_n)^{1/2}}$ and $\gamma_n = (i\omega\mu_n)^{1/2}(\sigma_n + i\omega\varepsilon_n)^{1/2}$.

Each layer n has a thickness h_n and uniform conductivity σ_n. Once the surface impedance $Z = Z_1$ is found; it is used in the equation for the complex skin depth $p = Z/i\omega\mu_0$. In this study the permitivities is all set to $\varepsilon_n = \varepsilon_0$ and permeabilities to $\mu_n = \mu_0$.

2.2. Inversion theory

Usually we have a data set (fields) $\vec{d}$ and a model set (current, etc.) $\vec{m}$ related to each other by an operation $\boldsymbol{G}$ through the relation $\vec{d} = \boldsymbol{G}(\vec{m})$**.** We only have available the observations $\vec{d}$. The process has to be inverted for $\vec{m} = \boldsymbol{G^{-1}}(\vec{d})$ that requires optimisation techniques and an objective function**.** The optimisation is in general a non-linear least-squares fit, usually of the L_2 norm. The linear form is $\vec{m} = \boldsymbol{G^{-1}}\vec{d}$ in which case $\boldsymbol{G}$ is a matrix. In this study the Levenberg-Marquardt method were applied to this problem. This is summarized in table 1.

Table 1: Summary of the optimization setup.

Setup component	Description
The data set:	Magnetic field measurements.
The model parameters:	h = Height, x_0 = Latitude, I = Current.
The objective function:	The real and imaginary parts of magnetic field components $B_x(\omega)$, $B_z(\omega)$ and given frequency ω.
The technique:	Levenberg-Marquardt.
Derivatives	Automatically determined (Forward finite-difference).
Constraints:	None.
The performance outputs:	Iterations done, Function counts and values, Sum-of-squares residual norm, Optimality, Any messages, errors or warnings.

3. Methodology

Before optimisation can be done on determining current systems in the ionosphere, reference data were obtained against which the inversion can be tested. This was done in a forward problem using ideal current system, with given parameters and determining the fields under the current system.

Plots of impedances and skin depths and of the fields were made with respect to angular frequency in order to study its behaviour in the frequency domain. The skin depth p, or equivalently the surface impedance Z, are dependent on the frequency ω and the structure thicknesses h_i and conductivities σ_i, and therefore cannot be regarded as a model parameter. There are N levels where the $(N+1)^{\text{th}}$ level is actually the remaining half-space in plane-earth geometry with conductivity σ_{N+1} and infinite thickness.

In the optimisation the output parameter set $[I, h, x_0]$ was chosen, while keeping the structure set $[h_i, \sigma_i], i = 1, \dots, N$ plus σ_{N+1} fixed. From the field final forms, it is clear that the current strength is a linear model parameter, leading to a linear least-square inversion problem when only this parameter is adjusted for. While the placement of the height and latitude position in those field expressions turns the inversion problem into a non-linear least-squares fit.

All standard deviations are based on the Gaussian statistics of inversion theory [6]. Inversion parameter standard deviations are calculated from the Sum-of-Squares (SS) standard deviation using the Jacobian J_o of the objective function $\boldsymbol{G_i}(\vec{m}) = f(x_i; \vec{m})$ of the inversion.

A co-variance matrix is formed

$$\Sigma_\lambda = s_{SS}\left[{J_o}^T J_o\right]^{-1} \tag{3.1}$$

where the SS standard deviation is

$$s_{SS} = N^{-1} \sum_i^N {r_i}^2. \tag{3.2}$$

and the residuals is

$$r_i = d_i - \boldsymbol{G_i}(\vec{m}), \tag{3.3}$$

The variance for the parameters can then be obtained from the diagonal elements of Σ_λ. The square roots of the diagonal elements are then the parameter standard deviations.

4. Results

The 1D ground resistivity structure of Loxton, South Africa (coordinates 31^0 28' 47"S, 22^0 20' 49"E), for 10 layers is as follows: thicknesses [25,25,100,100,50,110,110,150,230,100] km, resistivities [630,10,20,30,55,40,13,4.3,2.5,0.9] Ωm. For a fixed frequency and skin depth plots of the fields vs latitude will also be shown (figure 2).

The surface impedance is $Z(\tau) = 389.7 + 976.0i$ μΩ and skin depth is $p(\tau) = 37.08 - 14.81i$ km at a fixed angular period of $\tau = 5$ minutes, or angular frequency $\omega = \frac{2\pi}{\tau} = 0.0209$ Hz. Then, using these values, one inverts the magnetic fields to obtain the best fit to the output model parameters of a line current system. The fields were first synthesised in the forward problem and a random function scaled at 10 nT added for noise before the inversion was done. The parameter values to target for were: height $h = 100$ km, latitude $x_o = 0$ km, and current strength $I = 10^6$ A. Also, the current and height were initialised at 10% above and latitude at 100 km to the north of their respective target values.

Table 2: Results from the inversion.

Model parameters	Full	Distance case 1	Distance case 1
Current $\boldsymbol{I}$ *[kA]*	$(990 \pm 2.016) \times 10^3$	$(990 \pm 2.083) \times 10^3$	$(998 \pm 2.349) \times 10^3$
Height $\boldsymbol{h}$ *[km]*	295.000 ± 0.977	295.000 ± 1.010	Fixed.
Latitude $\boldsymbol{x_o}$ *[km]*	1.620 ± 0.972	Fixed.	1.590 ± 1.144

The parameter values of the inversion are given in table 2. These three scenarios shows that all parameters stop within 1% below the values targeted for after they were initialised at 10% above the same values. This shows that the height of the current system remains the same in the first 2 cases. The latitude decreases in the last case. The current is closer to its target value. Rerunning the inversion with both distance parameters fixed leaves only the current to vary. The current obtained is $I = 10^6$ A (its target value) with a standard deviation of $\pm 3.6 \times 10^3$ A. This is even better than its fitted value in the full inversion.

In moving from the full inversion to fixing any to all parameters except one, the standard deviations among the fitted parameters are redistributing and increasing among the parameters left to vary. This is because the inversion is dealing with the same input magnetic data with errors inherent within them and displayed by their residuals. These errors are then propagated to the variances of the output parameters fitted for. So when one starts removing (fixing) a parameter from the inversion, the standard deviations of the fitting parameters that remain are expanded.

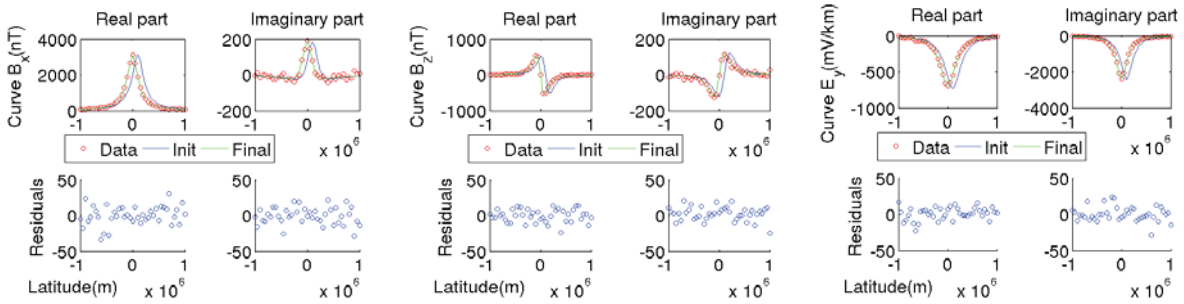

Figure2(a): Magnetic north [x-] (fitted); **(b):** Magnetic down [z-] (fitted); **(c):** Electric east [y-] (estimated).

5. Conclusions

The field plots against latitude for the chosen fixed frequency in the table, shows the expected results postulated in the forward problem. The synthetic data were used in inversion as a simulation to recover the targeted parameter values. However, due to errors introduced by a random function, the output parameters were within 1% of the given values.

As can be seen from the residual plots, the values from the fitted magnetic fields are smaller and more randomly distributed around zero. The residuals of the electric field being estimated show a similar behaviour to that for the magnetic field. This indicated that the electric field is accurate to within the error given. In practice insufficient electric field ground measurements are available. Thus, the electric field has to be excluded from the inversion procedure and can only be estimated.

These results show great promise for further investigations of current systems that are affected by events from the sun. Figure 3 shows an example of a magnetogram of the closest magnetic station to Loxton: i.e. Hermanus (latitude: 34.425°S, longitude: 19.225°E) for 31st May and 1st June 2013. The plot shows evidence of a short magnetic storm. In later investigations these real data will be Fourier analysed and then inverted in frequency space to obtain the total current strengths of multiple systems in equatorial and auroral regions within the ionosphere as well as in the magnetosphere. The approach may also apply to power lines as a current system above the ground.

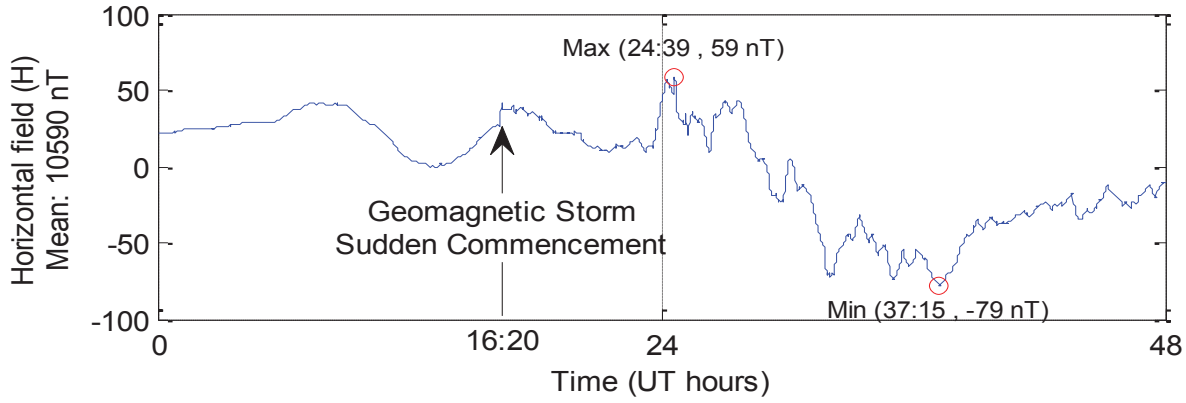

Figure 3: Magnetogram of Hermanus for 31st May and 1st June 2013.

Acknowledgements

The results presented in this poster rely on the data collected at SANSA Space Science Directorate (formerly the Hermanus Magnetic Observatory). We thank the South African National Space Agency (SANSA) for supporting its operation and INTERMAGNET for promoting high standards magnetic observatory practice (www.intermagnet.org).

References

[1] Hermance J and Peltier W 1970 Magnetotelluric fields of a line current. *J. Geophys. Res.* **75** 3351-6.

[2] Gradshteyn I and Ryzhik I 1965 *Table of integrals, Series and Products* (New York: Academic Press)

[3] Boteler D and Pirjola R 1998 The complex-image method for calculating the electric and magnetic fields produced at the surface of the Earth by the auroral electrojet. *Geophys. J. Int.* **132** 31-40.

[4] Boteler D, Pirjola R and Trichtchenko L 2000 On calculating the electrical and magnetic fields produced in technological systems at the Earth's surface by a "wide" electrojet *J. Atm. Solar-Terr. Phys.* **62** 1311-5.

[5] Wait J R 1980 Electromagnetic surface impedance for a layered earth for excitation *Radio Sci.* **15(1)** 129-34.

[6] Clifford A A 1973 *Multivariate error analysis: a handbook of error propagation and calculation in many-parameter systems* (Wiley and Sons)

[7] Evans R L, Jones A G, Garcia X, Muller M, Hamilton M, Evans S, Fourie C J S, Spratt J, Webb S, Jelsma H and Hutchins D 2011 Electrical lithosphere beneath the Kaapvaal craton, Southern Africa *J. Geophys Res.* **116** B04105.

Division E – Physics Education

University students' performance in different types of exam questions informs on their problem solving skills as well as studying ability

C Albers, D Clerk and D Naidoo

School of Physics, University of the Witwatersrand, Private Bag 3, WITS 2050

E-mail: claudia.albers@wits.ac.za

Abstract. An evaluation of students' performance in different questions in an exam at the end of a first year Physics major course, at the University of the Witwatersrand, in terms of the different skills required to answer each question, leads to insight into their level of problem solving and studying skills. Student performance, in a Physics I major test and a Physics II major test, both at the end of the first semester, is also evaluated. The students in the evaluations found questions that were new and required more intuitive, or lateral and logical type thinking, the most difficult to answer. The students, surprisingly, also found some questions that required the memorization of material only, also difficult to answer. Problems that only required a routine operation, or plugging into an equation, seen many times before, were perceived by the students as the easiest type of question to answer. These results also inform on the type of learning and studying the students have been acclimatised to due to the type of instruction received prior to entering university.

1. Introduction

Problem solving is a central component of learning and doing physics. Physicists need to use problem solving techniques in order to advance the current knowledge of physics. The strategies applied by trained physicists are however usually quite different from those of physics university students. Trained physicists use qualitative techniques [1], such as diagrams and physical principles to solve problems. Students lack these skills; they have difficulty connecting different aspects of a problem and in using the information available to solve the problems. A problem solver transforms into an expert problem solver through experience, that is, he transforms into a physics problem solver who has the ability to intuitively know what principles to apply and how to apply them [2].

Any instructor therefore attempts to encourage students to 'think like a physicist' [1]. This usually means that students are encouraged to draw diagrams and to apply the principles, such as Newton's second law, or conservation of energy, to different problems where appropriate. Specific problem solving instruction, however, has been demonstrated to actually make physical concepts less understandable to students [3]. This is because when students see a specific method for solving a problem they seem to see steps that follow one after the other rather than the broader principles that need to be applied to this type of problem. It is therefore only when students are faced with a problem of the same type but yet different from the one for which they have seen the solution that they begin to realize that it is principles that have to be applied and not a specific set of steps that is always the same for a certain set of problems.

Thus, if a physics instructor has any hope of teaching students how to think like a physicist it is imperative that new problems that require the different skills, needed to eventually 'think like a physicist', are set before them. The research presented here looks at how students perform when faced with such problems in exam and test conditions. Problems set for a test or exam requires different skills, namely:

1. Book-work knowledge: This includes definitions, laws and principles that are specifically taught to the students.
2. Intuitive thinking: This is the ability to make logical connections that are not immediately obvious, between different given information.
3. Routine operation skills: This includes the mathematical techniques needed to manipulate equations in order to solve for the desired physical quantity. It also includes the insertion of number values into equations.
4. New problem thinking: Here in the absence of a solution that could have been memorized, the problem solver has to create his own solution, using his knowledge of the physical principles involved in the specific problem, and his knowledge of how these principles should be applied.

Trained physicists, who work at the frontier of physics, also need to have bookwork knowledge, need to use intuitive thinking, and need to be able to use routine operations, even though these may be a lot more complex than those encountered by students.

2. Method

Questions in the Physics I major 2012 November exam at the University of the Witwatersrand were evaluated in terms of skills listed above, namely: Bookwork knowledge (BW), intuitive thinking (INT), routine operation skills (RO) and new problem thinking (NP). Thereafter students' performance in the different questions was analysed using a spreadsheet previously designed by Clerk, Naidoo and Shrivastava [4]. The same process was repeated with the Physics I major class test in May 2013 and with the second Physics II major Classical Mechanics class test.

In addition, a questionnaire, shown in Figure 1, was designed and given to the Physics I major students after completion of the May class test.

Physics Test questionnaire

Date: 24 May 2013 Student Number:
……

Test: Physics I Major class test 2 written on 20 May 2013
Look through the test and decide which three questions were the most difficult and place them in order below:

Most difficult question: …….
Second most difficult question: ……
Third most difficult question: ……

Now consider the question you found to be the most difficult and select one of the following:
I found the question difficult because: (tick one of the following)
A: I did not study the relevant sections of the course properly so I had no idea what to do
B: I studied the relevant sections of the course but I did not know how to start solving the problem
C: I knew what principles to apply in order to solve the problem but did not quite know how to use them in this case.
D: I managed to solve the second part of the question but not the first because there was something about the application involved in solving the problem that I did not understand
E: Other, write down your own explanation below:
……
…

Figure 1: Questionnaire given to Physics I major students after their second class test in 2013. The questionnaire offered the students an opportunity to declare which of the four questions they found the most difficult and to give an explanation using the four different suggested options and/or one open-ended last option.

The open-ended option was designed to allow students to provide more insight into their difficulties when faced with the test questions.

3. Results

The results obtained from the analysis of the 2012 November exam appears in Table 1. The first two rows in the table show the question number and parts in each question. The third row shows marks assigned to each question. The total number of marks in the paper was 100 and the number of students who wrote was 182. The average mark obtained by the students for each question part is shown in row 3 as a percentage (%). Rows 4 to 8 show the different skills required by each question as determined by the lecturer. A rating of 0 for some skill means that the question does not require that skill, and a rating of 5 means that the question only requires that specific skill. For example, question 1 has a rating of 2 out of 5 for bookwork (BW) knowledge, 2 out of 5 for routine operation (RO) skill and the degree of novelty of the problem is rated as 1 out of 5.

Student performance for questions 9a and b is extremely good. These questions were rated as being routine operation questions, thus showing that these are the types of questions that students find to be the easiest. The question with the lowest student performance is question 3, where the average performance is only 17%, and this question is rated highly, 4 out of 5, for new problem type thinking skills. Surprisingly, questions that require only bookwork knowledge, questions 5a, 14a and 14b, also show a relatively low performance average, namely, 38%, 51% and 31%, respectively. This suggests that the students have difficulty with this type of question as well but not as much as with the problems that require a lot of new problem thinking. The question that requires the greatest degree of intuitive (INT) thinking is question 13b in which students also performed badly, achieving an average performance of 18%. This question was rated relatively high by the lecturer, with a 2, for new problem (NP) thinking skills required, so this may have contributed to the students' low performance. Question 10 also has a rating of 2 for NP thinking skills and a rating of 1 for INT thinking skills but the average performance for that question is higher at 52%, which demonstrates that the degree of intuitive thinking required by the question plays an important role in students' performance.

Table 1: Student performance in the November 2012 Physics I major exam.

Number		1	2		3	4	5	6	7		8		9				10	11		12		13		14	
Part			a	b					a	b	a	b	a	b	c	d		a	b	a	b	a	b	a	b
Out of:		7	6	3	6	7	10	7	4	3	5	2	1	2	2	2	6	5	5	4	4	3	2	2	2
Average %		79	75	44	17	82	85	69	51	58	38	53	91	93	77	50	52	38	42	74	39	67	18	51	31
Type:	BW	2	2	2	1	0	2	2	1	2	5	2	0	0	0	0	1	5	1	0	0	0	0	5	5
	INT	0	0	0	0	0	0	0	0	0	0	0	0	0	0	0	1	0	0	0	0	0	2	0	0
	RO	2	3	3	0	3	3	3	1	2	0	0	5	5	5	5	1	0	1	3	2	2	1	0	0
	NP	1	0	0	4	2	0	0	3	1	0	3	0	0	0	0	2	0	3	2	3	3	2	0	0

The analysis of the results from the second Physics I major class test, which was written in May 2013, is shown in Table 2. This test was written by 323 students and the total number of marks for the test was 50. The table has been populated in a similar manner as Table 1 with an additional row included that defines one more type of thinking, namely: complexity. Complexity, here, is referring to the complexity of the mathematical manipulations required to derive a final answer. The numbers assigned for complexity show that all the questions were of about the same complexity except for question 3. The total rating for the other types of questions, BW, INT, RO and NP, is still 5, but the rating given to complexity (CO) is in addition to that.

Table 2 shows that students performed the best in question 3, with an average mark of 61%, so complexity did not seem to present much difficulty for them. This question was rated by the lecturer to have some degree of routine operation skill. From Table 1, we have already found that the students find this type of skill requirement in a problem the easiest to deal with. The NP rating for this question is zero. The questions showing the least average performance are 2b, 1b and 1a which have a significant element of novelty with a new problem (NP) rating of 3. Therefore the NP thinking skill seems to be the one that leads to the lowest average performance from the students.

Table 2: Student performance in the second Physics I major class test written in May 2013.

Number		1		2		3	4
Part		a	b	a	b		
Out of:		8	8	4	4	12	14
Average %		32	28	55	19	61	44
Type:	BW	1	1	1	1	1	1
	INT	1	1	2	1	1	2
	RO	0	0	0	0	2	0
	NP	3	3	2	3	1	2
	CO	1	1	1	1	2	1

The third test to be analysed, in the same manner as the Physics I major November 2012 exam and the Physics I major May 2013 class test, was the second Classical Mechanics test given to Physics II major students. The test comprised of 44 marks and 46 students wrote it. The results of the analysis are shown in Table 3 below.

Table 3: Physics II major student performance in the Classical Mechanics May 2013 class test.

Number		1				2		
Part		ai	aii	b	c	ai	aii	b
Out of:		2	2	3	15	7	12	3
Average %		40	50	67	22	30	20	33
Type:	BW	5	2	5	4	2	3	5
	INT	0	3	0	0	3	2	0
	RO	0	0	0	0	0	0	0
	NP	0	0	0	1	0	0	0
	CO	0	0	0	3	0	2	1

From Table 3, we see that at second year level, the complexity in questions seems to play a role in the students' performance on that question, which was not easily visible at first year level. Questions 1ai, aii and b are rated with zero complexity (CO), whilst question 2b is rated as having low complexity. Question 2b was actually a first year level question so it was rated with 1 for CO. Questions 2aii and 1c have the highest complexity and the students performed the worst in those two questions. It is however also worth noting that question 1c was the only question to require a level of new problem type thinking and question 2aii required some intuitive thinking as well as having a relatively high complexity rating, namely 2. So NP thinking skills and INT thinking also play a role in the student performance.

Table 4: Percentage of Physics I major students choosing a category describing the reason for difficulty encountered with the questions in the May 2013 class test.

Category	Percentage
A: I did not study the relevant sections of the course properly so I had no idea what to do.	6.6
B: I studied the relevant sections of the course but I did not know how to start solving the problem.	34
C: I knew what principles to apply in order to solve the problem but did not quite know how to use them in this case.	44.3
D: I managed to solve the second part of the question but not the first because there was something about the application involved in solving the problem that I did not understand.	5.7
E: Other	9.4

The results from the questionnaire are summarized below. There were four questions in the test and 111 students chose to complete the questionnaire about the test. The number of students choosing each option in the questionnaire was added up and divided by the number of students who completed the questionnaire in order to obtain percentages for each available option. The percentage of students who thought that question 4 was the most difficult question was 51%. In addition 35% of the students

indicated question 1 was the most difficult question, 37% responded that question 1 was the second most difficult question and 36% suggested that question 2 was the second most difficult question. So question 4 was thought by these students to be the most difficult, with question 1 being the second most difficult. This is a little surprising as the students performed better in question 4 than in question 1, as seen from Table 2.

The reasons students chose for finding a question difficult are shown in Table 4. By far the most popular category was C: I knew what principles to apply in order to solve the problem but did not quite know how to use them in this case.

Table 5 shows the categories that emerged from the open ended option E in the questionnaire. The different categories appear in the left column and an example of the type of response given appears in the right column.

Table 5: Categories emerging from the open-ended option in the questionnaire, with examples of student responses.

Category	**Student response example**
E1: I knew what principles to apply but did not study or practice this section well enough	*"I didn't practice enough for this section so I struggled to apply the theory of statics."*
E2: I knew what principles to apply but I did not have enough time.	*"It is because I had not enough time to answer the question."*
E3: There was not enough information in the data sheet	"*I am not sure if the data sheet had enough data."*
E4: I knew what to do but got stuck somewhere whilst solving	*"I knew what to apply and the problem was I got 2gl instead of 3gl and I couldn't manage to get 3gl and I didn't understand where 3gl came from."*
E5: There was something about the question I missed	*"I knew what I had to do, I applied the principles but there was a trick in the degrees that I didn't see. That led to me failing to answer the question."*
E6: I did not understand the wording of the question	*"I did not understand the statement of the question."*

The category attracting the most responses was E4: I knew what to do but got stuck somewhere whilst solving.

4. Discussion and Conclusion

The analysis of the Physics I major November exam 2012 and the Physics I major May class test summarized in Tables 1 and 2, show that students perform the worst on questions that require new problem type of thinking and best in problems that mainly require the routine operation type skill. The complexity required in the solution of the problem does not seem to play a role at first year level but does at the second year level, as indicated in the results appearing in Table 3.

The different open ended categories, E1 to E6, as shown in Table 5, are very interesting, the most popular was E4: *I knew what to do but got stuck somewhere whilst solving, with four responses reflecting this idea*. Since even trained physicists get stuck now and then we cannot use it to reflect on the degree of expertise of the students. But all the other categories are significant and reflect the problems encountered by students who have not learnt the concepts and principles they needed to learn in order to become expert enough to answer problems that are novel, namely they recognise they needed to practice the application of the principles more often (E1). The lack of expertise or practice may also lead to the students being slow in the application of the principles to the problem at hand and so run out of time (E2). Another problem is that they may expect the data sheet to supply all the equations they may need (E3) whilst they are actually supposed to memorize a few simple things or be

able to derive them, again showing that the student failed to reach the expert level of skill required, and may still want physics to be a routine operation exercise. Other symptoms of lack of expert level skill is not understanding the question (E6) or missing something when reading it (E5).

Other results obtained from the questionnaire are the main reasons for finding a question difficult and therefore underperforming in that particular question. As seen from Table 4, 44% of the students chose category C: I knew what principles to apply in order to solve the problem but did not quite know how to use them in this case, as their reason for finding a question difficult. This shows that the vast majority of the students knew which principles were to be used in solving the problem but not exactly how to apply them. The natural question to then ask is why? Why did they have this difficulty? Now let us look at the question in May 2013 class test that they found the most difficult, namely question 4, which is shown below:

A uniform rod of weight *W* hangs from the ceiling via two ropes connected to each end, as shown in the figure below. The rope connected to point *B* makes an angle of 60° with the ceiling. The rod makes an angle of 30° with the horizontal direction.

(a) Show that the tension in the rope at *B* is given by

$$T_B = \frac{\sqrt{3}}{4}W$$

(b) Find the angle θ that the rope, connected to point *A*, makes with the ceiling.

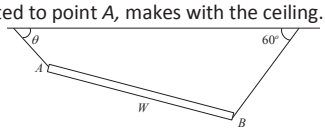

Note: $\sin 30^o = \cos 60^o = \frac{1}{2}$ and $\cos 30^o = \sin 60^o = \frac{\sqrt{3}}{2}$

This question is a standard first year statics problem, but what made it so difficult for the students? The students had seen a similar problem with a rod and strings at both ends in a tutorial problem but in that particular tutorial problem the rod had been horizontal. In the test question above, the rod is not horizontal. The students had however seen a problem from a previous test where the bar had not been horizontal but there was a hinge instead of a string at one end. The two diagrams used in the problems students had seen appear in Figure 2. So the combination of the non-horizontal rod with the two strings was enough to make this particular problem a novel problem to the students. Consequently many of them were not able to apply the required principles. This shows that many students (51%) had not reached the expert level of skill required to deal with a standard but novel question. These students had learnt solutions to the problems as a set of steps to follow and not as principles that can be applied to different problems.

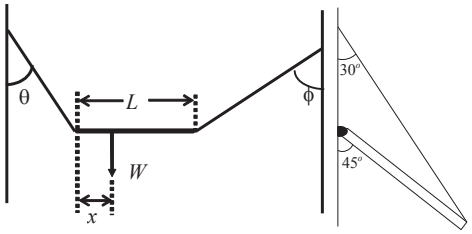

Figure 2: Diagrams used in the problems students had seen prior to the test.

References

[1] A. Van Heuvelen, "Learning to think like a physicist: A review of research-based instructional strategies," Am. J. Phys. **59**, 891-897 (1991).

[2] A. S. Dhillon, "Individual differences within problem-solving strategies used in physics," Sci. Ed. **82**, 379-405 (1998).

[3] P. Hewitt, *Conceptual physics: The high school physics program* (Addison-Wesley, Menlo Park, CA, 1992).

[4] D Clerk, D Naidoo & S Shrivastava, Contrasts between student and examiner perceptions of the nature of assessment tasks, *56th Annual Conference of the South African Institute of Physics.* (2011).

Correlation between mathematics proficiency and performance in a first-year physics course

E. Carleschi and B.S. Jacobs

Department of Physics, University of Johannesburg, P.O. Box 524, Auckland Park 2006, Johannesburg, South Africa

E-mail: ecarleschi@uj.ac.za

Abstract. We report here on the results of a mathematics entry test given to the 2013 intake of first year students enrolled for first year introductory physics course (non-major) in the faculties of Science and Health Sciences at the University of Johannesburg. The test was designed to assess the background knowledge and mathematical skills deemed to be necessary for the students to successfully undertake an algebra-based first year physics course. The topics covered in the test were based on the grade 11 and grade 12 mathematics syllabi and the use of calculators was prohibited. On comparison of the results of this test with the matric marks for mathematics, it has become apparent that the latter is inflated and reflects neither the real skills nor the success rate of students at university level. This is reflected on the macroscopic level in the comparison between the class average of the test (42%) and the class average of the matric mathematics marks (65%). The mathematics entry test also revealed the inability of students to solve simple numerical calculations, inability that can be attributed to the use of calculators from an early age. A strong correlation between the lack of basic mathematics skills and the performance of students in our first year physics course has been found. Finally, Grade 12 physical science marks, on which the admission to university is based, are proved to be inflated when compared with the performance of students in first year physics.

1. Introduction

Mathematics is the language of physics and is aptly chosen for its simplicity and accuracy. The association between mathematics and physics is embedded in the minds of science students from a young age. Counting was one of the first scientific inventions of primitive man [1]. Physics is quite simply the study of physical nature and mathematics is one of the oldest scientific tools and so there is an inherent relation between the two. The laws, theories and principles of physics translate into equations, the resolution of which resides in mathematics. According to Gross [2], mathematics and physics have had the longest union and the most fruitful exchanges.

The study of mathematical transition from the secondary to the tertiary level of education is reflected in recent literature [3, 4]. Questionnaires and quizzes are often a means to gauge the students preparedness for tertiary study. Jennings [3] attributed the decline in mathematical proficiency of students to two main factors - altering entry requirements of universities by dropping prerequisites to attract more students and the diverse cultural and educational backgrounds that the students have. Regardless of the cause, the effects of this are far reaching. Mathematical aptitude is a non-negotiable pre-requisite for problem solving in physics. Redish [5] explains how to use mathematics to describe a physical system related to

problem solving. Firstly, in tackling the problem or describing the physical system, the ability *to get the physics right* is crucial. Students must be able to decide and focus on just the vital parts of the information given and discard the rest. The next step is creating a mathematical model. This requires knowledge of the mathematical operations and structures that are available and applicable to the problem at hand. Once the mathematical model is set up, it needs to be processed: in other words, the equation needs to be solved. This is followed by interpretation and evaluation. The last two steps are perhaps the most crucial as students need to be able to judge whether their results describe the physical system or whether their mathematical modelling step needs to be revisited.

The auxiliary physics course at the University of Johannesburg is offered in the first year of the three and four year bachelors degrees of life sciences and health sciences, respectively. This course is algebra based and requires an average of at least 50% in matric mathematics and physical sciences (PS). Despite having marks in mathematics and PS well above the required minimum (the average matric mathematics and PS marks for this group are 65% and 66%, respectively), the performance of the students in the mathematics entry test and the subsequent physics tests has been poor. This paper aims to suggest a correlation between mathematical aptitude and performance in physics.

2. Method

We have compiled the results of a mathematics entry test that was given to 103 first year students of the 2013 intake in an introductory physics course (non-major) in the Faculties of Science and Health Sciences at the University of Johannesburg. The two authors of this paper are the lecturers of this course. Here we report and analyse the results only for those students who wrote the National Senior Certificate examinations at the end of 2012, and enrolled at University at the beginning of 2013 (103, as stated above). Such students have therefore attempted to pass physics for the first time in 2013 (i.e. repeating students and senior students are excluded from this analysis). The test was given to the students at the beginning of the second week of the first term. This was deliberately done in order to discard the influence of notions acquired at the university on the results of the study. The topics of the test were communicated to the students during the first lecture of term, i.e. six days before the test was written. The test was set out of 86 marks, it had a duration of 1 hour and 50 minutes and the use of calculators was prohibited. The test was constituted by six sets of questions based on the current South African grade 11 and grade 12 syllabi. In particular:

- Question 2 (17 marks): factorization and simplification of fractions (hereafter Q2);
- Question 3 (11 marks): addition of fractions (Q3);
- Question 4 (9 marks): exponents (zero and negative exponents, fractional exponents) (Q4);
- Question 5 (29 marks): linear, quadratic and logarithmic equations (Q5);
- Question 6 (14 marks): simultaneous solving of sets of two quadratic equations (Q6).

Problems used to compile the test were taken from the textbooks in Refs. [6, 7]. Moreover, students were asked to solve six simple calculations (including powers and roots) without a calculator (question 1 for 6 marks, hereafter Q1). Given the relevance of this particular question in the following part of the paper, we considered worthwhile to reproduce Q1 in detail [8]: a) 8×17; b) $(10^7)^2$; c) $(0.2)^3$; d) $\sqrt{0.01}$; e) $25 \times 13 + 13^2$; f) $2^6 + 7 - 36 \times 24$.

The mathematics test marks (MTM) were thoroughly analysed against the performance of the students in the theory part of the course at the end of the semester, i.e. end of May 2013, reflected in the theory mark (TM) (calculated considering 80% from two semester tests and the rest from minor assessments, i.e. discarding the performance in the practical part of the course). Many studies have in fact shown how the proficiency in mathematics is positively correlated to their performance in university first year physics courses [9]. In particular, the linear correlation between the mathematics test marks (X) and the theory marks (Y) was evaluated by means of

the Pearson product-moment correlation coefficient r [10], defined as

$$r = \frac{\sum_{i=1}^{n}(X_i - \overline{X})(Y_i - \overline{Y})}{\sqrt{\sum_{i=1}^{n}(X_i - \overline{X})^2}\sqrt{\sum_{i=1}^{n}(Y_i - \overline{Y})^2}} \quad (1)$$

where (X_i, Y_i) represent the paired data for each student, $\overline{X} = \frac{1}{n}\sum_{i=1}^{n} X_i$ and $\overline{Y} = \frac{1}{n}\sum_{i=1}^{n} Y_i$ represent the mean values of X and Y respectively, and $n = 103$ in the present study. The Pearson coefficient is commonly used in statistical analysis in order to measure the linear correlation between two sets of data.

3. Results and Discussion

Table 1 reports the analysis of the performance of the students for the overall test and for each of the six questions. In particular, the average, the lowest and highest marks are reported together with the Pearson coefficient r calculated against the TM. A class average of 42% reveals an overall poor performance of the students in this assessment. Interestingly, the mathematics test marks has a good degree of correlation with the TM, represented by a coefficient r of 0.47. Such correlation can be seen in the plot of the TM versus the mathematics test marks in Figure 1 (a). As a minimum TM of 40% is required in order for students to write the examination, the

	Class Average Mark	Lowest Mark	Highest mark	r
Test	42%	12%	74%	**0.47**
Q1	2.6 marks	0 marks	6 marks	**0.48**
Q2	36%	0%	82%	0.37
Q3	35%	0%	100%	0.26
Q4	32%	0%	100%	0.09
Q5	41%	14%	83%	0.34
Q6	61%	0%	100%	0.34

Table 1. Average mark, lowest mark, highest mark and Pearson coefficient r (measured against the semester mark of the students) for the overall mathematics test and for each of the six individual questions.

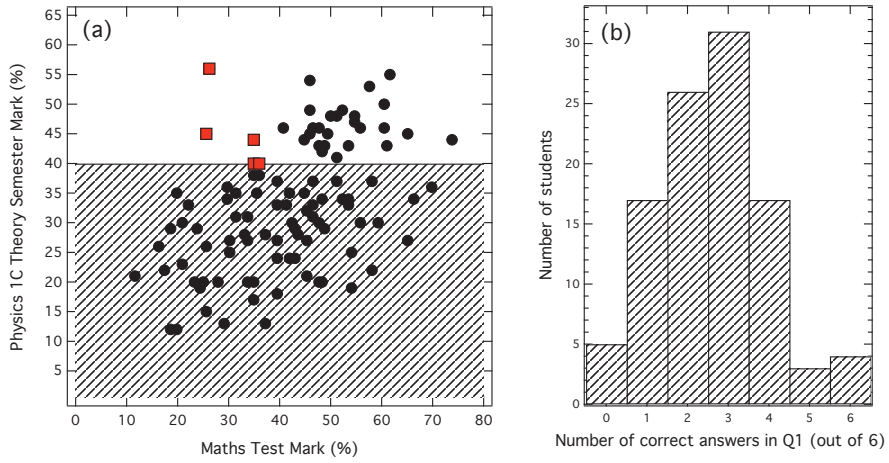

Figure 1. (a) Plot of the theory marks versus the mathematics marks for Physics 1C students. (b) Histogram of the performance of the students in Q1.

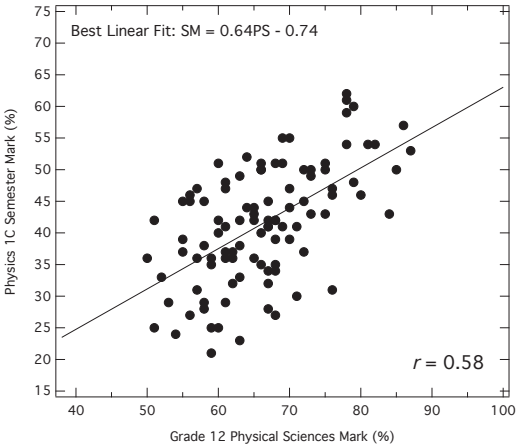

Figure 2. Plot of the Physics 1C semester marks (SM) versus the Grade 12 PS marks. The straight line represents the best fit to the data.

shaded region in the plot serves to highlight those students who did not gain exam entrance. It can therefore be seen that, apart from 5 students highlighted with red squares, no student with a maths test mark below 40% achieved a physics SM of 40%, i.e. had a performance during the semester enough to grant him/her access to examination. This indicates that this test can be used to predict, to a certain extent, the success of students in this physics course. The above seems to be a necessary condition, but not a sufficient one, as some of the students with marks above 40% in the maths test still did not qualify for the examination.

Looking at the performance in each question, it is interesting to note that the r coefficients for Q2 to Q6 are low, showing a poor correlation between the performance in these questions and the TM. In particular, the coefficient r for Q4 is very close to zero. This is attributed to the fact that this question assessed the background knowledge in exponents, a less relevant topic as far as problem solving of algebra-based physics problems is concerned. On the other side, the correlation between the marks scored in Q1 and the TM is higher than the one for the other questions, and it is as good as the correlation of the maths test itself ($r = 0.48$). This result is particularly interesting if we consider that this question was meant to assess the capability to perform simple calculations without the use of a calculator, and the background knowledge required to do so is meant to be acquired long before Grades 11 and 12. This finding suggests that the assessment of such basic skills is as good to predict the students' performance in first year physics as the assessment of the background knowledge of those topics widely used in solving problems in an algebra-based physics course, such as quadratic equations and the algebra of fractions. Taken together, the fact that Q2 to Q6 show poor correlation with the physics performance seems to indicate that students are taught to memorise solving methods without the understanding of the basic rules. This is reflected in the struggle to apply the same rules when different symbols are used, i.e. physical symbols instead of the habitual x, y, z or a, b, c.

It is worth noting that, as reported in the histogram in Figure 1 (b), only 4 students out of 103 were able to score full marks for Q1. This is particularly worrying when we consider that the typical mistakes derived from the lack of knowledge of multiplication and division priorities in solving the numerical expressions, lack of knowledge of the rules in exponents and above all the lack of knowledge of the meaning of a square root and powers. Below are examples of the common misconceptions we dealt with this year:

Example 1: $\sqrt{v_f^2 - v_i^2} = v_f - v_i$

Example 2: $\frac{v_i^2+v_f^2}{v_i+v_f} = v_i + v_f$

Example 3: $F = mg\sin\theta - \mu_k mg\cos\theta$, giving - after dividing by μ_k on both sides: $F = mg\frac{\sin\theta}{\mu_k} - mg\cos\theta$

Finally, we have analysed the correlation between the Physics 1C final semester marks (calculated by adding 70% of the TM to 30% of the final practical mark) and the Grade 12 marks in PS, as shown in Figure 2. The Pearson correlation coefficient between these two sets of data is good ($r = 0.58$), showing that the matric marks can be used to predict students performance in first year physics, with a degree of uncertainty given by the fact that our data show that school marks have been considerablly inflated. In fact, the best linear fit to the data in Figure 2 is described by the following equation: $SM = 0.64PS - 0.74$, where SM represents the first year physics semester mark and PS the Grade 12 PS mark.

4. Concluding remarks

Our rigorous analysis has led us to conclude that the underlying problem leading to pitiable throughput is poor understanding in basic mathematics. Solving physics problems, a bulk portion of all physics assessments, is close to impossible with a shaky foundation in mathematics and will lead to an undesired collapse.

Our results suggest that, in order to improve the course throughput in first year physics courses, universities should not base students admission uniquely on Grade 12 marks, but also on admission tests aimed at assessing the real background knowledge of matriculants. Alternatively, any interventions implemented at the university level should firstly concentrate on the basic mathematical skills discussed in this paper, rather than on physical principles.

References

[1] G.S. Bhatia, *Physics and the limits of human thought* (Essay).

[2] D.J. Gross, *Proc. Natl. Acad. Sci.* **85** 8371 (1988).

[3] M. Jennings. *Issues in bridging between senior secondary and first year university mathematics* (Essay).

[4] A. Kajander and M. Lovric, *Int. J. Mat. Edu. in Sci. and Tech.* **36** 149 (2005).

[5] E.F. Redish, *Problem solving and the use of maths in physics courses*, in Conference Proceedings - World view on physics education in 2005: focusing on change, Delhi, August 2005.

[6] P. Laridon (coordinating author) et al., *Classroom Mathematics: Grade 11 (Learner's book)*, Sandton: Heinemann (2006); P. Laridon (coordinating author) et al., *Classroom Mathematics: Grade 12 (Learner's book)*, Sandton: Heinemann (2007).

[7] K.P. Doyle, *Mathematics for Matriculants*, Juta and Company Limited (1982).

[8] The reader may request a soft copy of the question paper by directly emailing the corresponding author.

[9] T. Hudson and W.R. McIntire, Am. J. Phys. **45**, 470 (1977); T. Hudson and D. Liberman, Am. J. Phys. **50**, 1117 (1982), and citing articles.

[10] J.K. Sharma, Fundamentals of business statistics, Pearson Education India (2010).

Physics foundation program: Implications for second year mainstream physics module.

Paul Molefe and Buyisiwe M Sondezi

Physics Department, University of Johannesburg, P.O. Box 524, Auckland Park, South Africa.

E-mail: pmolefe@uj.ac.za

Abstract. There has been much concern about the universities physics department low third year enrolment. Physics as basic science plays a fundamental role in underpinning technolgical development. The national importance of physics in fulfilling its essential role in the economic development of the country and the Africa continent, allied to the general demand of physicists, makes the discipline an indisputable scare skill (CHE, 2013) The physics departments offer physics as service modules to health sciences and engineering faculties, this results to physics department not enroling physics major students. This low enrolment has placed universities under considerable pressure to in particular increase physics major students. In order to incresase physics major enrolments, the duration of the three-year undergraduate physics program at the University of Johannesburg (UJ) was elevated to four years in order to make provision for additional tuition. This study examines the impact of physics first-year accelerated program on students' academic performance on their first encounter with physics mainstream curriculum from first year through to first semester of their second year at UJ by providing a comparative analysis of the performance of students from foundation program and their counterparts in the mainstream curriculum.

1. Introduction

Universities and higher education institutions are increasingly becoming aware of the importance and significance of the transition from high school to first year undergraduate study. Literature on the transition from high school to university suggest that strong academic background, achievement of good grades, and academic motivation are needed for students to persist in their engineering and physics majors [1]. Besterfield-Scare *et al*, [2] has seen the first year as critical for both academic and retention of Science, Engineering and Technology (SET) students. This trend has also been widely observed within South African universities.

An increasing number of students pursuing studies in SET and a relatively low first semester completion rates by students entering first year university studies is widely observed in South Africa (SA). At UJ the first semester of the first year of study is one of the major factors for early drop-out from university, since a pass in this semester is the pre-requisite to enroll for second semester. After the transformation of the education system over the past few years there has been significant changes in the throughput of the students in their first year of university studies. A closer look into the investigation of the number of SET graduates produced by South African universities was undertaken with the intention of identifying problem areas experienced by students as they enter universities. Amongst the identified challenges observed were the huge gap between the school and post school education. This has placed universities under considerable

pressure to in particular adapt undergraduate physics curricula in order to provide adequate mathematics foundation required to navigate the physics curricula. Foundation Provision Program (FPP) was conceptualized [3] to develop the foundation competencies necessary for students to embark on successful first year studies and beyond. It is important to note that for students to proceed to the second year level of physics, they must pass physics 1 (PHY1) which is comprised of physics 1A and physics 1B modules. At UJ, the two groups of students are chosen, the mainstream (3 year program) students complete their PHY1A in a semester whilst the extended (four year program) complete their PHY1A in three semesters. It must be mentioned that these groups are chosen based on their NSC APS scores (Four year 50-59% and three year >60).

It is known that strong academic background, achievement of good grade, and academic motivation are needed for students to persist in their science studies. It is realized that if physics educators are to respond to country's call for an increased number of SET graduates, a large portion of that increase is likely to come from a more diverse range of students, including women, as well as students with lower entry-level qualifications in mathematics and physical science. It is also realized that while these students may initially struggle academically, they may well have the potential and motivation to make a significant contribution to the SET profession, provided appropriate academic and social support systems, remedial and "catch-up" courses are provided. It was previously reported by Sondezi-Mhlungu *et al*,[3], that students show great improvement in their performance after the introduction of FFP. This has resulted in researchers now being interested in these students particularly in their second semester of second year mainstream performance. Some of these students proceed to join their counter parts in first year mainstream in second semester of their second year of their academic year. At this level of study, they are taught electricity, magnetism, light and optics topics in the same class with mainstream students. The study aims to investigate how this FPP group of students continues to perform and merge the expected capabilities of their counterparts in mainstream and beyond their first year level of university studies.

1.1. Definition of phrases and terms

- **Semester Mark**: Contribution of all the assessment marks obtained by a students in one semester. This mark is comprised of all assessments undertaken in a semester, that is, the combination of class tests, tutorial tests, homeworks and practical mark.
- **Average Module Mark**: Final mark obtained after the contribution of the semester mark and the exam mark.
- **Module Pass Rate**: This is the percentage obtained by considering the number of students who participated in a given examination. The total number of students passing the exam over the number of students allowed to write the exam gives a pass rate of that particular group.
- **Throughput**: This is the percentage of the number of students who passed the module over the total number of students who enrolled for the course at the beginning of the year.
- **Final Results**: The average of the semester mark and the exam mark.

2. Methodology

The performance of mainstream students was looked at against the performance of extended degree program students by looking at two different sets of data which was taken over two years (from 2011 to 2012 academic year). The data collected in 2012 for mainstream students were the data of the students who registered in the same academic year whereby they undertook physics 1A in the first semester and proceeded to physics 1B in their second semester of their first year university experience. Physics 1A extended data collected in 2011 and 2012 were taken from

the students that registered for physics 1E/2E and 3E, after completing physics 1A extended in their first semester of their second year university experience. Table 1 lists the statistics of this data.

Table 1. The table showing the statistics of the students collected over the years 2011 and 2012.

	2011	2012
PHY1A1E	448	
PHY1A2E	267	
PHY1A3E		195
PHY1A		419
PHY1B		198
PHY1BEX		90

The data collected in the 2012 academic year were the data for the students that came from first year extended program (which lasted for three semesters) and those that came from the first year mainstream degree program. These students were taught in the same class in the second semester of 2012. The final results (average of the semester and examination marks, the pass rate and the throughput) of the respective groups were analysed and reported. For easy data handling, all presented data was converted into percentages.

3. Results and Discussion

Figure 1 shows the histogram of the final marks performances of physics 1A1E, 2E, 3E and 1A for academic year 2011 and 2012, respectively. The histograms show both the results obtained from students belonging to extended as well as those from mainstream degree program.

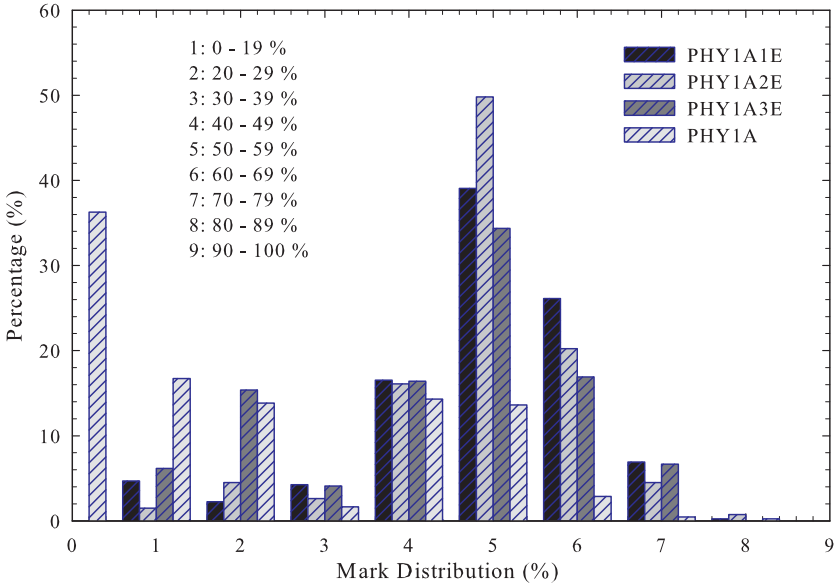

Figure 1. : Percentages (number of students) vs mark distribution (%) of PHY1A1E, 2E in 2011 and PHY3E, PHY1A mainstream in 2012 final marks performance.

The observed feature of these histograms is the high percentage of the students passing the extended module(s) (obtaining $> 50\%$). It must be mentioned that these modules were taught in different classes over different time periods (mainstream taught over a semester and extended program taught over three semesters). It is evident from the graphs that a number of extended students obtained a subminimum pass mark over their three semesters in all modules. These are evidenced by the overall performance of more than 70% final mark results as observed from the accumulative percentage frequencies of the student numbers. The encouraging feature is the less percentage ($< 25\%$, as observed from the histogram) of students who could not achieve the minimum requirement (50%) to pass the module. It is observed that the bulk of PHY1A students failed to obtain the minimum requirement (50%) to pass the module; this is despite their high APS score from NSC.

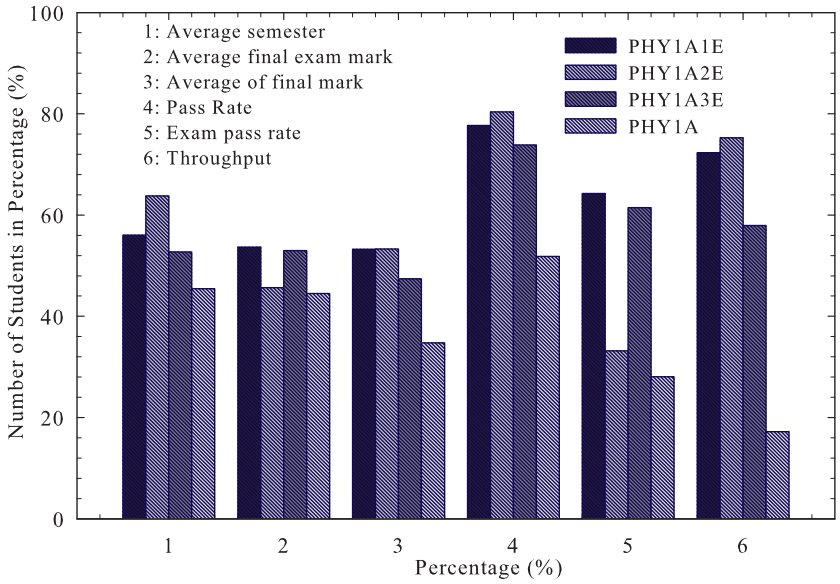

Figure 2. Distribution of students' marks in percentages of the total contribution towards students' promotion, for 2010, 2011 and 2012, respectively.

Similar analysis for the same categories of students for the 2011 and 2012 final marks performances are presented in figure 2. The meaning of the terms indicated in insert carry the same meaning as defined in our work [4]. The focus of this analysis will be on average of final mark and the throughput of the respective groups. It is observed that the average of final mark of PHY1A1E, PHY1A2E and PHY1A3E are 53%, 53% and 47%, respectively whilst the final mark of PHY1A is 30%. The respective throughputs of the groups are 72%, 75% and 58% for PHY1A1E, PHY1A2E and PHY1A3E, respectively, whilst the throughput of PHY1A is 17%. The results seem very different but the total or overall extended throughput is calculated to be 25%. This was calculated from the total students that wrote the extended degree program over the total registered students at the beginning of the extended degree program. We need to indicate that low overall throughput of extended program result from many factors, e.g. students not qualifying to obtain the prerequisite to continue in the extended degree program. We observed a student enrolment decline in each extended module which reflected this overall reduced throughput. The difference in the throughputs of these results can be ascribed to the time spent on teaching physics content which improved the understanding of the content better which translated into the enhanced pass rate and throughput result for the extended group.

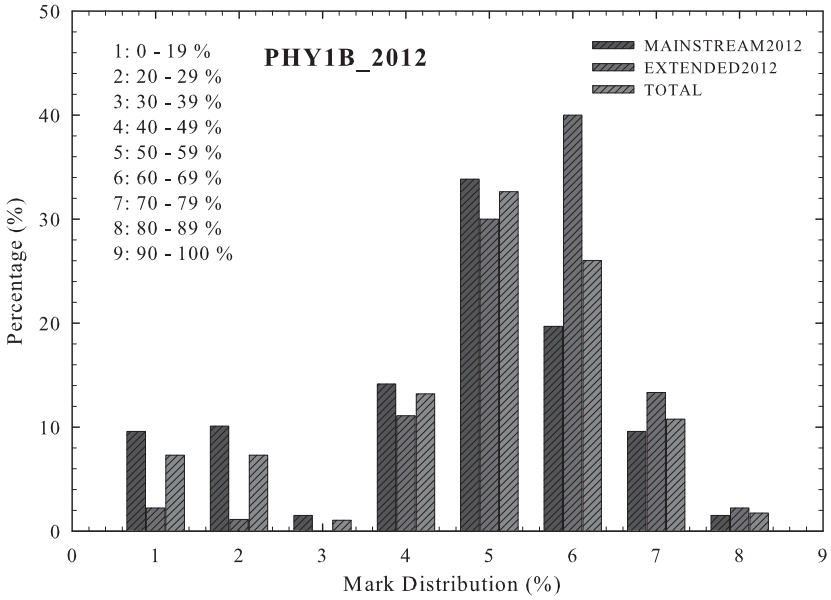

Figure 3. Performances of mainstream (in the second semester) and extended degree (in the fourth semester) students in the PHY1B module in 2012.

Figure 3 represents the histogram of the PHY1B group. This group is comprised of the students that did their first year PHY1A over three semesters (as outlined in the method above) and those that did their PHY1A in the first semester of 2012. The histograms of final marks performances of individual groups are compared to the total obtained from combined groups. The percentage of students who passed the module (>50%) for mainstream students is 65%; whilst the percentage of students who passed the module from extended program is 86%. However, the combined results yield a drop in the average marks of the class. In overall, the bulk of the students are passing the module.

4. Conclusion

The results of the investigation in this regard seem to suggest that students from the extended degree program appeared to have gained a somewhat adequate knowledge, understanding and confidence. This was shown by the 21% performance difference observed above their counterparts from mainstream in PHY1B module. This improved performance could be attributed to physics foundation modules that help students to simulate concepts thoroughly. In addition, the observed impact of the extended degree program on the confidence of students in coping with the mainstream module has also been acknowledged by the lecturers of these respective modules. The results obtained from this study are an indication that the extended degree program has contributed immensely in producing competent students who would perform well in their level 2 physics studies. We recommend that the students with APS scores of 6 be enrolled in a four year degree program as this can enhance the overall first year throughput and increase the number of third year and honours students.

5. Acknowledgements

The authors acknowledge the assistance from the department of physics at UJ.

6. References

[1] Smaill C, Godfrey E and Rowe G B, 2008 *Proc. American Society for Engineering Education Annual Conference* **1** 752

[2] Besterfield-Scare M, Atman C J and Shuman L J, 1997 *Journal of Engineering Education* **86** 139

[3] Sondezi-Mhlungu B M and Molefe P, 2011 *56th Annual Conference of South African Institute of Physics Proceedings* **1** 637

[4] Sondezi-Mhlungu B M and Molefe P, *57th Annual Conference of South African Institute of Physics Proceedings* **1**

Is there a gap between the high school curriculum and first year university experience?

Buyisiwe M Sondezi and Paul Molefe

Physics Department, University of Johannesburg, P.O. Box 524, Auckland Park, South Africa.

E-mail: bmsondezi@uj.ac.za

Abstract. The transition of high school curriculum from the previous Senior Certificate Examination (SCE) (which offered both Higher Grade (HG) and Standard Grade (SG)) to National Curriculum Statement (NCS) (subjects offered at one level) yielded in a number of learners who pass their National Senior Certificate (NSC) with the minimum admission point score (APS). However, the expected knowledge and understanding of the content of the subject matter is rather contrary. This has been a recent observation experienced by first year physics lecturers at University of Johannesburg (UJ). One area of difficulty for the first year students is the basic understanding of vectors. A study performed previously indicated that some intervention(s) were necessary in an endeavor to improve vector concepts' understanding. A study performed indicated that most of the students treated this section in their NCS level, yet the application of the knowledge to their first year physics and to the related concepts was still problematic for most students.

1. Introduction

The researchers' study [1] prompted a need to engage on a short term, short scale investigation of students understanding of vectors. In this study, we examined the implications of time factor in teaching vector sections. These time factors were looked at against times spent in treating these sections as stipulated by the National Curriculum Statement(NCS) for physical science. In this search, it was observed that the curriculum contains and provides enough topics to manage the first year mechanics course at university. The Further Education and Training (FET) physical science revealed that, vector related sections are taught only in four hours as stipulated in Physical science Curriculum and Assessment Policy Statement (CAPS) [2]. The vector section is taught in grade 11 academic year within the first quarter and momentum is taught in second quarter of their grade 12 studies where thirteen hours are spent on this section.

We further examined the ability of students to determine and use qualitatively the magnitude and direction of the vector from knowledge of drawing a free-body diagram at first year level at UJ. The use of vector components concepts to draw free-body diagrams are basics to most mechanics problems. The lecturers in the first year extended programme spent more time in teaching the vector related concepts. The students were encouraged to be actively involved in drawing free-body diagrams and the addition of vectors. It was intended to emphasize to students that the vector nature of forces, fields, and kinematics quantities requires that students have a good grasp of basic vector concepts if they are to be successful in mastering introductory level physics [3]. Student learning is our primary criterion for determining teaching effectiveness. Lectures were taught in an interactive manner and the use of their own experience in applications

of vector knowledge. Questions related to this section and beyond, were treated in lectures and during the tutorial sessions.

It was observed that some students struggled with drawing vector diagrams. In an attempt to address this challenge,more active learning was encouraged during tutorial sessions, by insisting that before the problem could be attempted, a free-body diagram be presented to the tutor for verification. These sessions at UJ take place every second week for each tutorial group and are managed in conjunction with two senior student tutors in each session. Despite most students' being exposed to drawing of free-body diagrams, still misconceptions and difficulties related to vectors were observed. This study suggests that instructors in introductory physics course must give explicit consideration to students' conception development in the learning of vectors.

The objective of this study was to examine the ability of students to draw free-body diagrams and interpret them in relation to the given problem and be able to manipulate basic mathematics and to successfully solve the problem. The questions were designed to measure students' knowledge on basic level of vectors; they contained the drawing of the free-body diagrams, addition of vectors algebraically and graphically, expressing vectors in terms of magnitude and direction using trigonometric functions to calculate the direction of the vectors.

2. Methodology

Initially, a questionnaire was given to 192 students, where the focus was on three questions listed in the table 1. Only 138 out of those 192 students responded to the physics skills test (PST). The general physics skills test of 20 multiple choice questions was also given to students at the end of the course, to check if the students gained the basic knowledge of vectors and are able to apply to fundamental mechanics topics. Five questions out of the 20 multiple choice questions were designed to measure students' knowledge of basic level of vectors. These questions were based on kinematics, addition of vectors algebraically, expressing vectors in terms of magnitude and direction. Further similar questions including problem solving questions were given to students through the course and were finally given a familiar question in their mod-year examination, to determine whether conceptual understanding was gained. About 161 out of 192 students qualified to write these mid-year physics exam. The specific question to be studied in the examination was marked by one lecturer and was moderated by the other lecturer teaching the module and an internal examiner from the physics department. The above mentioned question was intended to examine if students could draw the correct free-body diagram, add vectors and to calculate the acceleration of the system.

3. Results and Discussion

After the assessment of CAPS and the establishment of what the students have learnt in high school; added to the 12 hours of formal lecturing and 9 hours of tutorial sessions the understanding of students on vector topic was tested. The questionnaire responses of the students listed in the table, gave hope that the students will be performing well in this topic. In their responses, 15% indicated that there was nothing to be unlearnt, leaving a large percentage of students who had to unlearn some concepts.

3.1. Survey Questions

- **Q1**: Are there any areas of PHY1A1E in which you had to unlearn concepts you had previously learnt at high school? **Yes/No**.
  If so, please specify the concept(s).
- **Q2**: Are there any areas of PHY1A1E which assumed knowledge of concepts that you had not previously met? **Yes/No**.
  If so, mention those areas.

- **Q3**: Are there any areas of PHY1A1E that repeated material that you had already thoroughly mastered at high school? **Yes/No**.
  If so, please elaborate.

In the response of Q2, it is indicated that 21% of students have previously learnt something on vectors, implying that they were not coming across these topic for the first time. This is a further positive result, expected to yield better pass rate and throughputs. This is further supported by the response of Q3, where it is portrayed that 41% were repeating the material. These were further positive indicators about the group of students we had. Closer look at Q2 and Q3, point to the same conclusion, which could be summarised as; 62% in our group of students have seen and treated some vector related problems in their high school curriculum.

Table 1. A table listing the specific questions and responses of the survey taken after the lecturing of vector section.

Question	Responses (%)
Q1	15
Q2	21
Q3	41

The analysis of the four year physics first semester results of 2013 at UJ is presented below. These results were carefully looked at considering the academic background of the students. After the presentation of the section on vectors for the duration mentioned, the understanding of the concept was tested. Figure 1 shows the accompanying diagram of the question on the left hand side of the histogram and responses of the question are also outlined. The question, the codes and responses of the options from which the students had to choose from are listed in table 2.

Question 1: A small box X is moving on a horizontal frictional surface towards a stationary heavier box Y. After the boxes collide they rebound off each other. Some heat is generated during this collision. Which of the following must be true after the collision?
Below are the options from which the students had to choose from for the above given question in figure 1.

- **1**: The speed of X is zero and Y moves to the right.
- **2**: X moves to the left and Y moves to the right.
- **3**: Both X and Y move to the right.
- **4**: X moves to the left and Y remains stationary.
- **5**: We need more information to determine which box moves after the collision, and in which direction they move.
- **6**: I do not know the answer because I do not understand the Physics in this question.
- **7**: I do not know the answer because I do not understand some of the words used in this question.
- **8**: Unanswered.

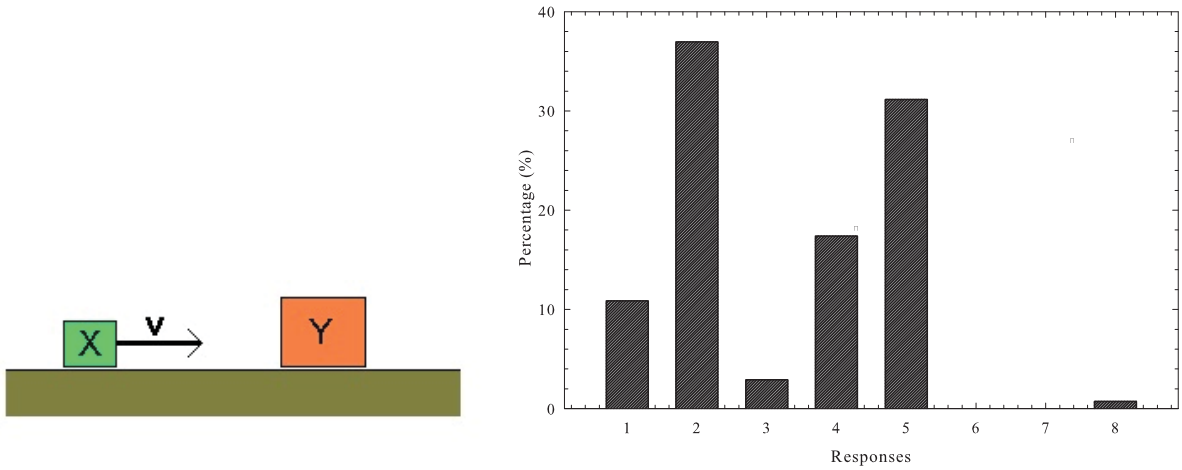

Figure 1. Left: A diagram used in clarifying question 1 and the histogram (Right) presenting the data of the number of students in percentage form, against students' responses, *the momentum problem.*

It is observed that most students chose option 2 followed by the response from option 5. Most students (about 37%) believe that the small box X will move to the left while the big box Y will move to the right. It is clear that these students have an idea of momentum concepts, but they still struggle to read the question carefully to get all relevant information needed to solve the problem. The realities of the differences in masses, the velocities, including the fact that the big box Y is initially stationary were not considered. It is evident that the students did not consider that the surface is frictional. It is only 30% of the students who managed to observe that more information is needed to successfully solve the problem. It is also very interesting to learn how students respond to the problem of an inclined plane.

Question 2: A box is placed on a frictionless incline (see diagram). Which arrow best describes the direction of the force of reaction exerted by the incline to the box?

A number of vector components are involved in the system, whether the system is stationary or will be in motion. It was also established that there is still a lot of misunderstanding on the use of words like "by", "to". The question asked had "B" or option "2" as the correct response. Only 28% of students gave the correct response. These students managed to understand that the question was referring to the ground as opposed to "slope" as implicated from the responses of students who chose "A" (1) and/or "D" (4).

Question 3: A block is held stationary in equilibrium against a rough vertical wall by a horizontal force (illustrated by the black arrow in the diagram). Which arrow in the right diagram best illustrates the direction of the frictional force acting on the block?

These responses bring an understanding that the students have less understanding of the use of vectors (lines and arrows) and their effect on the system. The lack of understanding in the use of lines and arrows in indicating what happens onto the system, poses a challenge in the way vectors should be presented to first year level students.

Another challenge was identified after the students' response of question 3, which is presented in figure 3. Although 40% of students managed to get the answer right, an equal number of

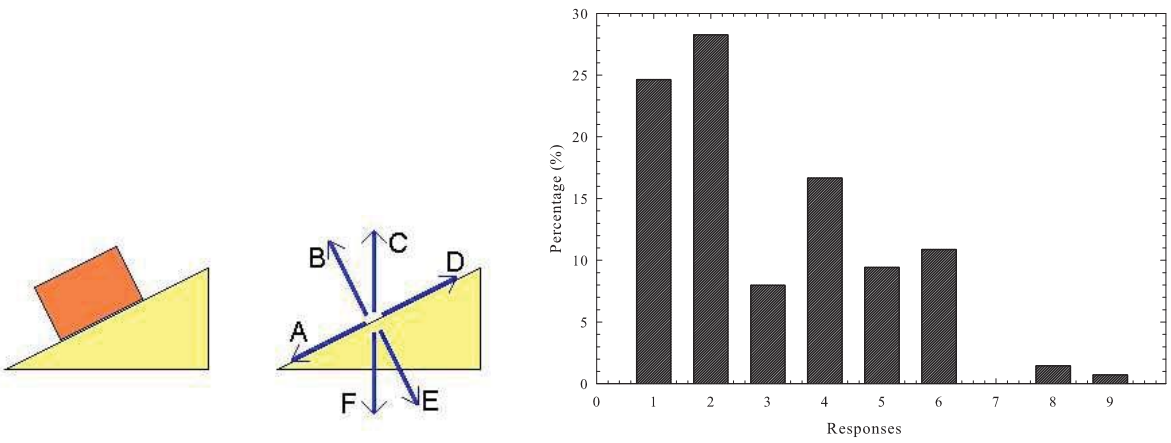

Figure 2. Left: A diagram used in clarifying question 2 and the histogram presenting the data of the number of students in percentage form, against students' responses, *the inclined problem.*

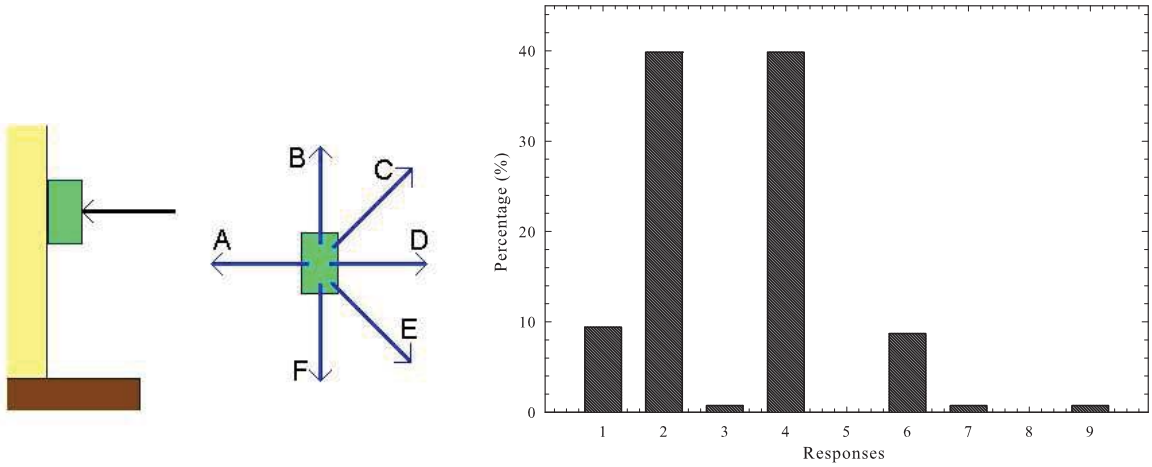

Figure 3. Left: A diagram used in clarifying question 3 and the histogram (right) presenting the data of the number of students in percentage form, against students' responses, *friction against the wall problem.*

students gave a response which eluded that the students are still mixing up concepts. This latter group of students' responses imply that the only opposing force or vector should be in the same dimension (axis) but in the opposite direction. In this assumption by the students, a number of conditions are ignored and hence the wrong conclusion is drawn. As mentioned above, tutorial sessions were actively employed as an intervention means after the outcome of the survey performed. As means of testing effectiveness of the intervention especially in this section, a specific vector question was later given to students as part of their mid-year exam. Figure 4 (left) shows the diagram used in this assessment where students were required to use their understanding of vectors addition as means of calculating the acceleration of the system. Figure 4 (right) shows the results obtained from that investigation. Only 20% of the students who wrote the exam, managed to get the question correct, that is, only 30 out of 161 students that wrote an exam. The histogram shows the distribution of their marks from the minimum

Table 2. A table listing the codes used in figure 2, 3 and 4.

Codes	Choices(Q 2)	Choices (Q 3)	Ranges of Figure 4 (%)
1	A	A	50-59
2	B	B	60-69
3	C	C	70-79
4	D	D	80-89
5	E	E	90-100
6	F	F	-
7	I don't know	I don't know	-
8	I don't understand	I don't understand	-
9	Unanswered	unanswered	-

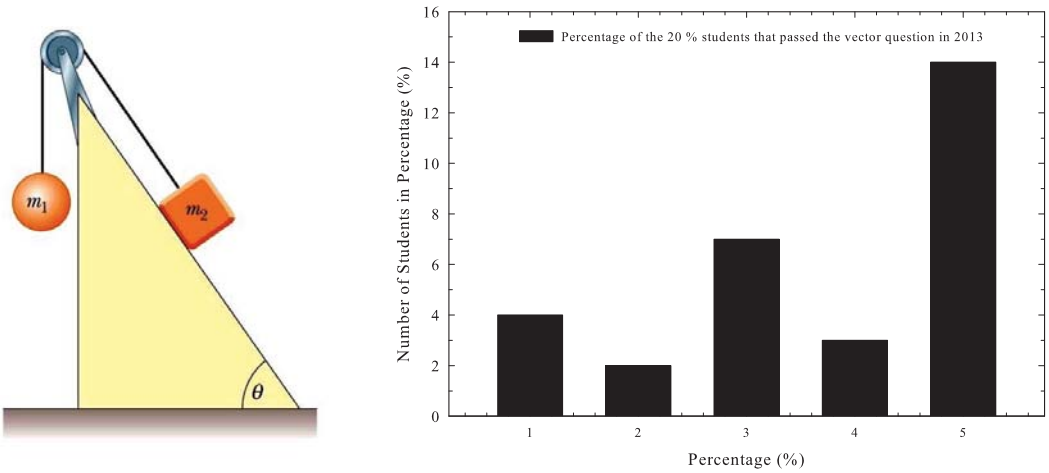

Figure 4. (Left) The question asked in the exam and (Right) The percentage of students who passed the vector problem as written in the first semester exam.

mark of 50% to the maximum of 100%. The fourth column in table 2 indicates these marks distributions. It is shown that in this percentage of students that passed, 14 of them got the maximum marks, and 7 of them got the marks between 70 and 80%.

4. Conclusion

The results of the investigation in this regard seem to suggest that students generally experience difficulty in vector-related problems. This is despite the fact that the basic concepts in this section have been introduced at high school level. Although this is expected to be advantageous and beneficial to the students, the contrary is observed. The students seem to assume that the concepts are familiar and as a result less attention is paid in the simulation of fundamental concepts related to this section. This was evidenced by the 20% performance obtained from the exam question. Further investigations are ongoing in trying to enhance the understanding of the vector-related fundamental concepts.

5. Acknowledgements
The authors acknowledge Prof. H Winkler's contribution and the department of physics at UJ.

References

[1] Molefe P and Sondezi-Mhlungu B M, *57th Annual Conference of South African Institute of Physics Proceedings* **1**
[2] Curriculum and Assessment Policy Statement, *Government Gazette*
[3] Knight R D, 1995 *The Physics Teacher* **33** 74

Division F – Applied Physics

Digital Signal Processing Algorithm for Signal Analysis and Performance Monitoring in an Optical Communication Link

T V Chabata, R R G Gamatham, H Y S Kourouma, E K Rotich Kipnoo, A W R Leitch and T B Gibbon

Physics Department, Optical Fibre Research Unit, Nelson Mandela Metropolitan University, P. O. Box 77000, Summerstrand, Port Elizabeth-6031, South Africa. Tel: +27 41-504-2141; Fax: +27 41-504-2573
Email: Tichakunda.Chabata@live.nmmu.ac.za

Abstract: - Digital signal processing (DSP) algorithm is proposed to analyse and monitor the performance of a digital optical communication link. In this paper, an efficient offline and flexible reprogrammable DSP algorithm is developed, to determine the bit error rate (BER) as a measure of performance of an optical communication system. The 10 Gbps optical signal transmitted over the fibre is received, sampled and reconstructed in the digital electrical domain. Further a DSP algorithm is implemented offline to normalise and quantise the signal before it is digitized into respective transmitted bits. The DSP technique is an indispensable technology for next generation ultra-fast optical fibre communication. The developed offline DSP algorithm has outstanding advantages such as guaranteed accuracy, perfect reproducibility and high reliability. The effectiveness of the proposed algorithm is quantitatively verified by measuring the BER for different transmissions.

1. Introduction

The ultimate goal of the optical signal transmission is to achieve the acceptably low bit-error rate (BER) between any two nodes in an optical network. Recently deployed optical fibre communication systems exploit intensity modulation and direct detection (IMDD) to transmit information [1]. The drive towards higher spectral efficiency in optical fibre systems has generated interest in digital signal processing (DSP). Digital signal processing technique encompasses computer science technology, communication science and mathematics in analysing a signal [2].

Recent advances in analogue-to-digital (A/D) conversion technology make it possible to use DSP techniques to demodulate high-speed optically modulated signals. Pairing DSP with IMDD, optical receivers have attracted attention recently due to increased CPU memory and clock speed. Nowadays it is possible to use a commercially available computer to handle the light wave data sequence.

This article describes the actual modulation and detection methods in order to explain how an optical receiver including offline processing works. DSP algorithms for signal reconstruction and the subsequent BER computations are done as a measure of performance of intensity modulated optical communication link. Reconstructing the signal involves filtering, sampling, normalising, quantising and digitizing the continuous signal into a discrete time signal. The back to back BER measurements are important in the determination of the receiver sensitivity at a set threshold error value.

2. Theory

An optical communication link comprises of a transmitter, transmission medium and a receiver. The main purpose of the optical receiver in terminating the light wave path is to convert the signal from

optical to electrical domain. The obtained electrical signal is then processed appropriately to recover the data being transmitted. The optical signal generated by the semiconductor laser has to be modulated by the information-bearing signal before being transmitted over the optical fibre. The mapping of the data onto the transmission signal is achieved by either directly modulating or externally modulating the bias current of semiconductor laser.

Through the external modulation process, one of the parameters of the continuous wave signal, used as a signal carrier, is varied in accordance with the information-bearing signal. A monochromatic electromagnetic wave is commonly used as a carrier, and its electrical field *E(t)* can be represented by

$$E(t) = pA\cos[\omega t + \varphi] \quad (1)$$

where parameters A, ω *and* φ are amplitude, frequency, and phase respectively. Parameter p denotes the polarization orientation [3]. Each of those parameters can be used to carry information, and the information-bearing signal can be either continuous wave or discrete.

In a digital optical communications, bit-error rate (BER), defined as the ratio of bits in error to total number of transmitted bit at the decision point, is commonly used as a figure of merit. In that sense, the receiver sensitivity is defined as the minimum required received optical power to keep BER below a given value [3].

3. Experimental setup

The experimental setup is shown in figure 1. A 1550 nm WDM laser signal is intensity modulated at 10.3 Gbps and transmitted through a single mode fibre.

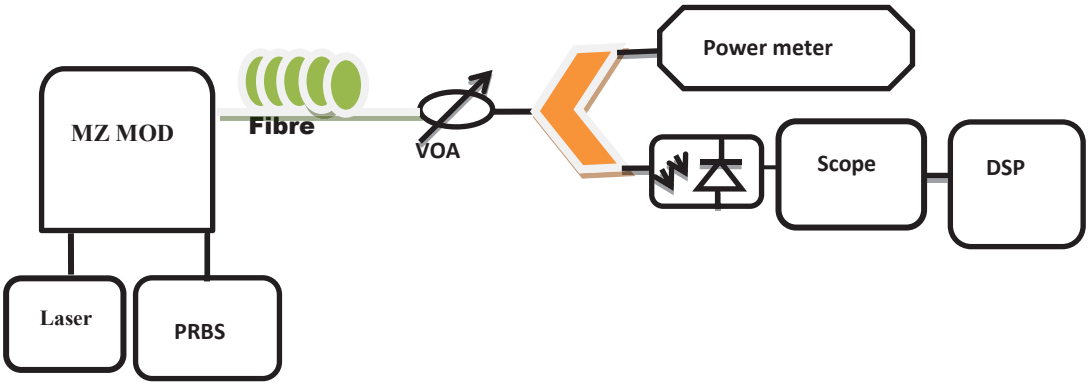

Figure 1: Experimental setup for transmitter and a single ended detection receiver [VOA- Variable optical attenuator, MZ- Mach-Zender]

A variable optical attenuator controls the power of the signal prior to detection and conversion to an electrical signal by the photodiode. The Agilent oscilloscope was used to acquire a measurement burst of the received transmitted data, which is then transferred to a computer for offline processing. The received continuous time signal is represented with a sequence of numbers representing the amplitude of the continuous time signal at a specific instant in time. The received electrical signal is processed offline using relevant DSP algorithm to determine the BER as the measure of performance of the optical fibre transmission link.

4. Results and Discussion

For intensity modulation, the receiver scheme comprises of a 3 dB coupler, a single photodiode, oscilloscope and the digital signal processing algorithm. A 2^7-1 pseudo random binary sequence (PRBS) bit pattern sequence is transmitted at 10.3 Gbps at different attenuation values for back to back transmission. The developed DSP algorithm comprises of four important parts. The function of the first part is to load the digital data saved in the sampling scope to an offline processing computer.

The second part normalises and digitizes the continuous signal into discrete bits. The third part generates the pseudo random binary sequence (PRBS) $(2^7\text{-}1)$ bit pattern and then compares it to the recovered data bits to determine the bit error rate. The fourth and last part of the algorithm plots the eye diagram.

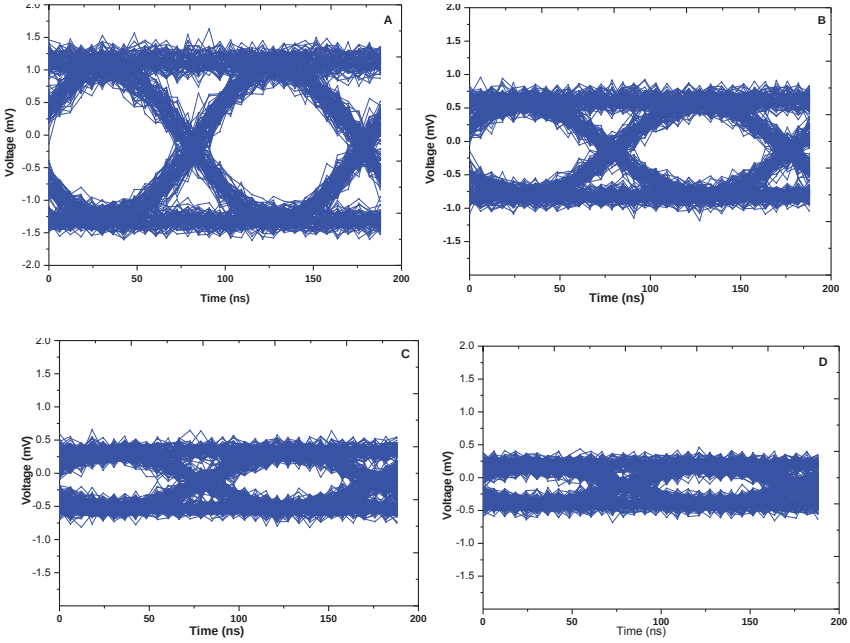

Figure 2: DSP Eye Diagram plots at different Power values

An eye diagram is a quick way of assessing the signal quality. Figure 2 A to D shows the eye diagram plots at different optical power values as indicated on figure 3 B. The eye closure suggests degradation in the signal quality due to attenuation. Information can be easily and reliably recovered from the free transmission eye diagram (figure 2 A) and very little or no information can be recovered from the closed eye diagram in figure 2 D.

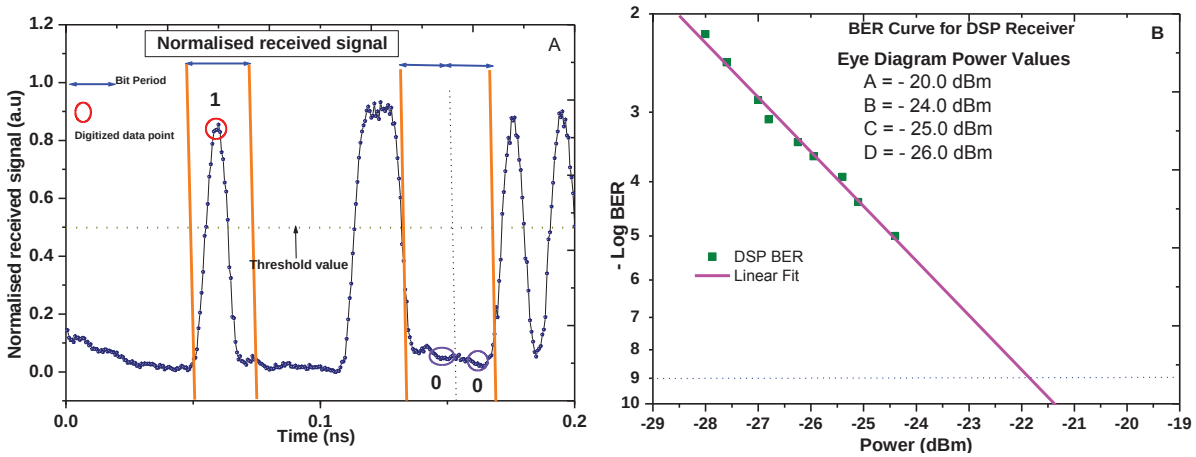

Figure 3: A. DSP normalised and digitized signal as captured from the digital storage oscilloscope
B. DSP back to back BER curves for different received optical powers.

Digital signal processing is the process of extracting useful information from an incoming signal. The received, loaded data is normalised to reduce the large data range to between zero and one for easy

and accurate computations. The algorithm sums up the first three bits from the middle of the bit period. The sum is compared to a set threshold to determine whether its logic value one or zero. Any value greater than the threshold value is assigned a logical value '1' and any value below the threshold is assigned a logical zero '0' as shown in Figure 3 A.

A total of 200 000 bits was used for the bit to bit comparison between the transmitted and received signals. Figure 3 B shows the back to back DSP bit error rate curves for different attenuation values. The extrapolated receiver sensitivity value of -21.8 dBm is obtained at a threshold BER value of 10^{-9}.

5. Conclusion

The developed DSP algorithm is an effective and efficient method to determine the BER, due to its cost, consistency, accuracy and reproducibility. Conclusively the developed DSP algorithm for signal reconstruction and subsequent BER calculation for intensity modulated and demodulated optical link was successfully implemented.In future DSP algorithms are going to be developed for advanced modulation formats to compensate for transmission impairments in the fibre.

6. Acknowledgement

This work is based on the research supported in part by the National Research Foundation of South Africa (Grant 84352). We are also grateful for research funding from: African Laser Centre ALC, CSIR, Telkom, Dartcom, Ingoma and THRIP.

References

[1] Liu C, Pan J, Detwiler T, Stark A, Hsueh Y, Chang G and Ralph S E 2013 Joint digital signal processing for superchannel coherent optical communication systems *Optics Express* Vol. **21** Issue 7 pp. 8342-8356

[2] Smith S W, 2009 The *Scientist and Engineer's Guide to Digital Signal Processing 2nd ed. (*California Technical Santiago California)

[3] Ivan D, William R and Bane V 2010 *Coding for Optical Channels* (Tucson Springer Science) pp 25 -28

[4] Gibbon T B, Yu X, and Monroy I T 2009 Photonic ultra-wideband 781.25-mb/s signal generation and transmission incorporating digital signal processing detection *IEEE Photonics Tech. Lett.* Vol. **21** No. 15 pp. 1060-1062.

[5] Gibbon T B, Yu X, and Monroy I T 2009 High-speed ultra-wideband wireless signals over fibre systems: Photonic generation and DSP detection *Proc. APMP* pp. J01

[6] Nakazawa M 2011 Ultrafast and high-spectral-density optical communications systems *Conf. Lasers and Electro-Optics CLEO* pp. 1-6

[7] Gilley J E 2003 Bit-Error-Rate Simulation Using Matlab Transcript International, Inc.

[8] Peracchi A, Corsini R and Ciaramella E 2012 Accurate BER Estimation for Coherent Optical Transmission Systems *ACP Technical Digest OSA*

[9] Agrawal G P. 2007 Nonlinear *Fibre optics* 4th *ed*. (Santiago California : Academic press)

[10] Rodes R, Cheng N, Jensen J B and Monroy I T 2012 10Gb/s Real –Time All VCSEL Low Complexity Coherent scheme for PONS *Proc. OFC/NFOEC Tech. Digest OSA*

Advancement of quantum communication through entanglement

Y. Ismail[1], A. Mirza[1], A. Forbes[1,2] and F. Petruccione[1,3]

[1]Quantum Research Group, University of KwaZulu-Natal, Private Bag X54001, Durban 4000
[2]CSIR-National Laser Centre, PO Box 365, Pretoria, 0001
[3]National Institute of Theoretical Physics, South Africa

205513117@stu.ukzn.ac.za

Abstract. Quantum communication exploits some of the fundamental features of the quantum world. One of the most advanced quantum information related application aspects at present is Quantum Key Distribution (QKD) which is a process that involves transmitting a secure key between two individuals. The most vital characteristic of such a method is that the secrecy of the generated key is guaranteed by the laws of nature. QKD systems, although capable of producing provably secure keys, must in themselves be trusted. Entanglement provides a basis for an additional layer of security. In this paper, we will outline an optical system used to generate entanglement. The aim of this paper is to characterise the entanglement system. The correlation of entangled pairs was quantified by measuring by the visibility of the rectilinear and diagonal bases. Within the system studied entanglement was verified by violation of the CHSH inequality which was determined to be 2.71 ± 0.03. Furthermore, we touch-on exploiting QKD together with entanglement to shape a quantum network.

1. Introduction

Quantum information science is based on the notion that the manipulation of information is governed only by the laws of physics. Hence, information can be characterized, quantified and processed as a physical entity using the basic properties of quantum mechanics by exploiting some of the fundamental features of the quantum world, i.e. the superposition principle and the Heisenberg uncertainty relation.

Quantum information encapsulates two major disciplines, quantum computing and quantum communication. Ultimately, the security of information lies in the development of quantum communication [1]. At present in classical computers, although capable of utilising mathematical algorithms to uphold the security of information, communication may be threatened by the rapid development of more powerful systems. It is feared that even the key distribution process of the one time pad, which is the most secure method of encryption to date, could reach a point where it could be rendered breakable.

The classical computer may store information as binary logic however with quantum computing it is possible to compute information as a superposition of bits of 0's and 1's known as qubits. While some classical algorithms require exponential processing time, the time frame for the corresponding quantum algorithms is reduced to polynomial time. [2].

Currently one of the inefficiencies experienced by quantum computers is invoking entanglement on demand however immense research is being carried out in this field to further develop this branch of technology. When this becomes a reality, it would be mandatory to consider quantum communication, in particular QKD, to maintain the security of information. Entanglement occurs when two particles interact physically and thereafter separate while maintaining some mutual correlations, the knowledge about one particle can be obtained by observing its entangled partner. The fact that this knowledge of the remote particle is obtained in the absence of any physical interaction with the particle, is significant. This is applicable to all sub-atomic particles such as photons, electrons and molecules.

In this paper we will give an overview of entanglement which will be discussed in Section 2. Section 3 deals with the key distribution process based on the successful implementation of an appropriate protocol. The realisation, generation and verification of entangled states will be dealt with in Section 4. The concluding remarks will be discussed in Section 5 and furthermore we will touch on the advancement of quantum communication through entanglement.

2. Entanglement

Entanglement is the core of quantum information science since it is applicable to the development of both quantum communication and quantum computing. Photons which are entangled are considered indistinguishable and are therefore represented as a single state. This means that there exists a strong mutual correlation between maximally entangled photon pairs independent of the distance between them. This condition implies that quantum entanglement contradicts the concept of locality [3]. A concrete test of the conflict between local realism and quantum mechanics was later verified [4] and consists of a set of inequalities which must be satisfied by any local and realistic theory. Furthermore, quantum mechanics predicts the violation of these so-called Bell's inequalities for measurements on specific quantum-entangled systems. An experimental realisation of the so called Bell's inequalities was later presented by Clauser, Horne, Shimony and Holt (CHSH), which demonstrated a classical argument that bounds the correlation of two particles [5].

Photons can be entangled via phase or polarisation. For the purpose of this study we will concentrate on a polarisation based entanglement source. A photon pair which is entangled via polarisation can be represented either by the rectilinear (horizontal and vertical) or the diagonal (± 45 degrees) basis denoted as:

$$|\psi\rangle = \frac{1}{\sqrt{2}}\left[|V\rangle_s|V\rangle_i + e^{i\phi}|H\rangle_s|H\rangle_i\right], \quad (1)$$

where $|V\rangle$ and $|H\rangle$ are the vertical and horizontal states respectively and s and i denote the signal and idler.

Prior to testing for entanglement by the violation of the CHSH inequality, a test of visibility is used to determine the correlation of the entangled photon pairs. The visibility is measured in both bases by considering the maximum and minimum coincidence according to the following condition:

$$V = \frac{C_{max} - C_{min}}{C_{max} + C_{min}}, \quad (2)$$

where V corresponds to the visibility for a given bases and C_{max} and C_{min} are the maximum and minimum coincidence rates respectively.

The verification of entanglement however, lies in the violation of the CHSH inequality which states that in local realistic theories the absolute value of a particular combination of correlations between two particles is bounded by 2, such that the violation is represented as follows:

$$S(\alpha, \alpha', \beta, \beta') = E[\alpha, \beta] - E[\alpha, \beta'] + E[\alpha', \beta] + E[\alpha', \beta'] \leq 2, \quad (3)$$

where α and α' and β and β' denotes the local measurement settings of the two observers, each receiving one of the particles. The normalised expectation value $E[\alpha, \beta]$ is given by:

$$E[\alpha, \beta] = \frac{C(\alpha,\beta) - C(\alpha_\perp,\beta) - C(\alpha,\beta_\perp) + C(\alpha_\perp,\beta_\perp)}{C(\alpha,\beta) + C(\alpha,\beta_\perp) + C(\alpha_\perp,\beta) + C(\alpha_\perp,\beta_\perp)}, \quad (4)$$

where $C(\alpha, \beta)$ denotes the coincidence count rate obtained for the combination of polariser settings and $\alpha_\perp$ and $\beta_\perp$ are the perpendicular polarisation orientations.

Quantum Key Distribution

QKD is a process of sharing a secure key between two authorised parties, the transmitter and the receiver. Communication between QKD systems, to date, has focused on phase-encoded fibre-based solutions. This is due to the ease of implementation. However of recent much investigation has focussed on free-space QKD solutions. This provides further versatility for quantum communication solutions. The key distribution process is achievable by manipulating the quantum state of polarisation of single photons to obtain a secure key. This process makes uses of two channels, a quantum channel in which the encoded single photons are transmitted to initiate a raw key and the classical channel which is used for the post-processing to determine a secure key. QKD is realised by the implementation of the appropriate protocol. There are mainly three types of QKD schemes. One is the prepare-and-measure scheme, such as BB84 [6] and B92 [7], the other are the entanglement based QKD, such as E91 [8] and BBM92 [9] and the continuous variable scheme [10]. For the purpose of this study the BB84, B92 and E91 will be discussed.

BB84

The BB84 protocol was the first QKD protocol. It was proposed by Bennet and Brassard [6]. This is a four state protocol which makes use of two non-orthogonal polarisation bases namely the rectilinear and the diagonal basis. Implementation of the BB84 protocol lies in the encoding of single photons with either the vertical, horizontal or the $\pm 45^o$ state of polarisation. The process entails transmitting a train of encoded single photons to the receiver. The receiver randomly chooses to measure each of the photons in the rectilinear or diagonal bases. This procedure is carried out on the quantum channel. The classical channel is used by the receiver to announce the basis used for each measurement. A sifted key is then produced from the combination of the quantum and classical communication. Single photons with a mismatch in the prepare and measure bases will be discarded. The remainder of the single photons are kept for the continuation of the post-processing procedure.

B92

This is a two-state protocol, similar to the BB84 protocol, except in this case instead of the measurement bases being announced on the classical channel during the post-processing, the detector that clicked is publicized. This protocol entails pre-assigning a bit value to each detector. The single

photons are transmitted as per the BB84 protocol. A classical channel is used to determine the sifted key from the raw key. The authorised parties would be able to distinguish the sifted key by the click of the detector. This process is less efficient than the BB84 protocol however there is greater secrecy during the post-processing of the single photons [7].

E91

The E91 protocol is also similar to the BB84 protocol except it makes use of entanglement. A pair of entangled photons is emitted from a single source such that one photon is directed towards the receiver while the other is sent to the transmitter. Both authorised parties will carry out a measurement independent of each other by randomly choosing between the rectilinear or the diagonal bases. Since these photons are entangled, if the receiver is the first carry out a measurement, the transmitter will automatically measure the anti-correlated state. By one of the authorised parties inverting their string of bits received, a raw key can be produced [8]. The post-processing is carried out as per the BB84 protocol from which a sifted key is obtained.

2. Generation of entangled photon pairs

Experimentally, one implementation of entangled photon pair is generated by a process known as spontaneous parametric down conversion (SPDC),whereby photons of an intense laser pump beam spontaneously are converted by a non-linear crystal into photons of lower frequency. The entangled photon pair that is generated is separated into a signal photon and an idler photon. During this process, the conservation of momentum and energy are obeyed such that the additive energy of the signal and idler is equal to the energy of the pump photon and similarly for the momentum.

A simple optical system scheme was engineered to generate single photon pairs within a polarisation based entanglement system. Within this scheme a UV laser (λ= 404 nm) with an output power of 20 mW was used to pump the nonlinear crystal. The most important component was the type-I Beta Barium Borate (BBO) crystal which is the optical element utilised to initiate the SPDC process. A half wave plate, cylindrical lens and birefringent crystal were used to compensate for additional alignment concerns within the system. Polarisers were placed in both arms to vary the bases (rectilinear or diagonal) and carry out measurements on the entangled photon pairs. Single photon detectors were used to measure the single photon counts, which are the measure of entanglement, used to determine the coincidence count rates. The optical system described is represented schematically and as constructed in the lab in Figure 1(a) and Figure 1(b) respectively. To determine if the system was entangled, a visibility test and the violation of the CHSH inequality were determined and will be discussed in the section that follows.

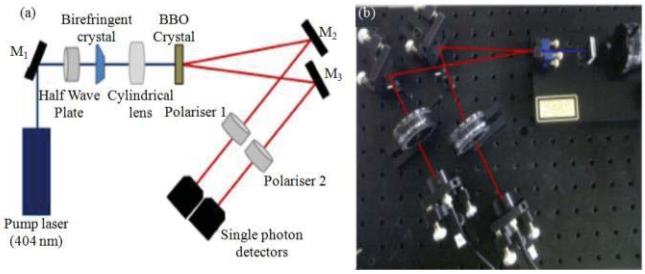

Figure 1: Optical system engineered to generate and verify entanglement: A schematic of an entanglement source (a) and as seen in the laboratory (b).

2.1. Verification of entanglement

The simplest test to verify entanglement of photon pairs would be to carry out a measurement of the correlation curves in two non-orthogonal complementary bases. This is accomplished by fixing the orientation α of one of the polarisers represented in Figure 1(a) and continuously varying the orientation of β of the other. The results obtained are illustrated in Figure 2 where α was set at 0° and 45° for the rectilinear and diagonal basis respectively.

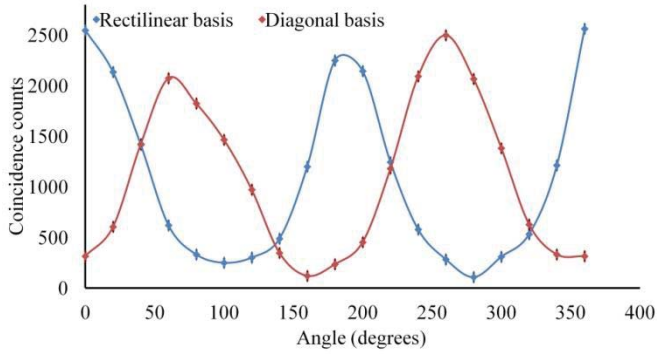

Figure 2: Plot representing the correlation of the rectilinear and diagonal bases.

The recorded coincidence count rates for the above chosen setting showed a $\cos^2(\alpha-\beta)$ dependence. To quantify the quality of the polarization correlations, the visibility, V, of the measured curve was directly estimated by Equation 2. From the above mentioned analysis the visibility in the horizontal/vertical and diagonal basis were determined to be 91.00 ± 0.76 % and 91.00 ± 0.82 % respectively.

To measure the violation of the CHSH inequality the coincidence counts were determined by varying the angles of the polarizer in both arms of the source. To test for the violation the following set of orientation are chosen, $\alpha = 0^{\circ}$, $\alpha' = 45^{\circ}$, $\beta = 22.5^{\circ}$ and $\beta' = 67.5^{\circ}$. Four separate experimental runs were conducted corresponding to the four terms $E[\alpha, \beta]$ in the definition of S expressed in Equation 3. Each of the terms, $E[\alpha, \beta]$, were calculated from four coincidence counts making it 16 count rates in total as represented in Table 1. The coincidence counts measured resulted in an S-value of 2.71 ±0.03, evaluated using Equation 3 and Equation 4, which indicated a violation of the CHSH inequality and hence verified entanglement.

Table 1: Data collected for the experimental runs to verify entanglement

Expectation value when α is 0 and β is 22.5 deg								
α	β	$\alpha_{\perp}$	$\beta_{\perp}$	C(α, β)	C($\alpha_{\perp}$, β)	C(α , $\beta_{\perp}$)	C($\alpha_{\perp}$, $\beta_{\perp}$)	E(α , β)
0	22.5	90	112.5	8557	1838	1886	8939	0.649
Expectation value when α' is 45 and β is 22.5 deg								
α'	β	$\alpha'_{\perp}$	$\beta_{\perp}$	C(α', β)	C($\alpha'_{\perp}$, β)	C(α', $\beta_{\perp}$)	C($\alpha'_{\perp}$, $\beta_{\perp}$)	E(α', β)
45	22.5	135	112.5	11296	2253	1041	10442	0.737
Expectation value when α is 0 and β' is 67.5 deg								
α	β'	$\alpha_{\perp}$	$\beta'_{\perp}$	C(α , β')	C($\alpha_{\perp}$, β')	C(α , $\beta'_{\perp}$)	C($\alpha_{\perp}$ $\beta'_{\perp}$)	E(α , β')
0	67.5	90	15.5	2950	10707	7238	1642	-0.592
Expectation value when α' is 45 and β' is 67.5 deg								
α'	β'	$\alpha'_{\perp}$	$\beta'_{\perp}$	C(α', β')	C($\alpha'_{\perp}$, β')	C(α', $\beta'_{\perp}$)	C($\alpha'_{\perp}$, $\beta'_{\perp}$)	E(α', β')
45	67.5	135	157.5	13180	1697	2070	11211	0.732

3. Concluding remarks

We have thus shown that it is possible to generate polarisation based entangled photon pairs and characterise them by measuring the visibility of the correlation curves of the rectilinear and diagonal bases. We also proved that our system is entangled since we were able to violate the CHSH inequality. Upon characterising the system, entanglement can be utilised for the advancement of QKD. This is due to the bond that entangled photons share. This instantaneous relationship is a platform for quantum teleportation experiments making QKD the optimal technology for the further development of quantum communication. It has already been shown that ground to ground communication is possible using entanglement [11], being able expand this technology to ground to satellite communication would hopefully result in creating a global quantum network.

References

[1] Buchmann B and Dahmen, eds. 2009 Post-Quantum Cryptography Springer,

[2] Rieffel E 2000 An Introduction to Quantum Computing for Non-Physicists arxiv:quant-ph/9809016v2

[3] Einstein A, Podolsky B and Rosen N 1935 Can Quantum-Mechanical Description of Physical Reality Be Considered Complete? Phys. Rev. vol.47 (10) 777–780

[4] Bell J S 1964 On the Einstein-Podolski-Rosen Paradox Physics (Long Island City, New York) 403-408

[5] Clauser J, Holt R, Horne M and Shimony A 1969 Proposed Experiment to Test Local Hidden-Variable Theories Phys. Rev. Lett. vol.23 (15) 880-884

[6] Bennett C H and Brassard G 1984 Quantum cryptography: public key distribution and coin tossing Proc. of IEEE International Conference on Computers, Systems and Signal Processing 175-179.

[7] Bennett C H 1992 Quantum cryptography using any two non-orthogonal states. Phys. Rev. Lett. 68 3121-3124

[8] Ekert A 1991 Quantum Cryptography Based on Bell's Theorem Phys. Rev. Lett. vol. 67 (6) 661-663

[9] Bennett C H, Brassard G and Mermaid N D 1992 Quantum Cryptography without Bell's Theorem Phys Rev. Lett. vol.68 (5) 557-559

[10] Grosshans F and Grangier P 2002 Phys. Rev. Lett. 88(5) 057902-1-4

[11] Ursin *et al* 2007 Entanglement-based quantum communication over 144km Nature vol. 3 481-486

Open-Source electronics for quantum key distribution

M.Mariola[1], A. Mirza[1] and F. Petruccione[1,2]

[1]University of KwaZulu-Natal, Westville Campus, Durban, South Africa,
[2]National Institute for Theoretical Physics, South Africa .

E-mail: mmspazio@libero.it

Abstract. Quantum cryptography is a coding system that allows us to exchange a secret key without the risk of eavesdropping. The cryptographic key is composed by a series of quantum states of single photons. Each quantum state is known now as quantum bit or qubit. Quantum cryptography exploits the Heisenberg's uncertainty principle, whereby after a measurement, the quantum state is necessarily changed from the original state. In order for the key exchange to takes place it is necessary that the transmitter and receiver are linked with a quantum channel. This link may be realized by fiber optics or free space. In free space the quantum state is represented as polarization. In free space the photon beam is subject to wandering, scintillation and attenuations by the atmospheric turbulence. In this article the design of a possible electronics system able to compensate for the atmospheric effects on the photon beam using open-source electronics is presented. These systems are useful in order to build prototypes and at low cost products.

1. Introduction

Cryptography is a way to secure the messages against the eavesdropper. The message is encrypted by a private key shared between the transmitter and receiver. The protocol currently used in modern communication is the RSA protocol [1]. This protocol is at best computationally secure. In the RSA protocol the private key is contained in a public key sent through the public channel. However, Shor's algorithm is the efficient way to calculate the private key given a quantum computer [2]. This is because one is able to calculate the private key in polynomial time and in that case the private key is not safe. Quantum cryptography permits one to share a private key while ensuring there is no eavesdropping in between the transmitter and receiver. By convention the transmitter is referred to as ALICE and the receiver is referred to as BOB, the eavesdropper is named EVE.

Quantum cryptography exploits the Heisenberg's uncertainty principle where the bits of the key are composed by the quantum states of single photons. If ALICE sends the single photon to BOB and EVE measures the quantum state of the photon, BOB will measure a different value from ALICE with a finite probability due to the Heisenberg's uncertainty principle. ALICE and BOB use a subset of the distributed photons to verify the validity of the photons sent. If the statistical outcome of the comparison illustrated a large variation ALICE and BOB know that there is an eavesdropper in the middle of the channel. The first protocol was invented by Bennet and Brassard in 1984 and this protocol is known as BB84 protocol [3]. In free space the quantum state is the polarization of the photon. The protocol uses two non-orthogonal polarization bases as shown in Table 1. ALICE randomly chooses the bases and sends the photons to BOB and BOB randomly chooses a basis to measure each photon. Through the public channel ALICE

Table 1. The polarization bases of the BB84 protocol.

BASE	0	1
+	↑	→
×	↗	↖

broadcasts to BOB the basis used to transmit each photon. ALICE and BOB also share the time stamp for the bits of the key. Since ALICE and BOB do not use a common basis all the time they exclude the bits where the bases chosen were not the same. Once this sifting procedure is complete, ALICE and BOB use a subset of the key to check if the measurement outcomes are coherent. If the error rate is above a security threshold it implies that EVE was between ALICE and BOB. ALICE will only send the encrypted message to BOB if she is sure that EVE has not eavesdropped on the key distribution process. The protocol is summarized in Table 2. Other

Table 2. ALICE sends each bit of the key using different polarization bases. BOB chooses randomly the bases to receive the bit from ALICE. The final key is composed by the bits sent and received with the same basis.

BOB	1	2	3	4	5	6	7	8	9
+	1		1	0			1		
×		0			0	1		0	0
ALICE									
+		0	1	0	0		1	1	
×	1					1			0
FINAL KEY			1	0		1	1		0

protocols such as B92 [4] exist for quantum key distribution(QKD). In free space the photon beam does not change in polarization however due to the turbulent atmospheric effects, the beam is subject to wandering and scintillations. If Alice occupies the stationary point and Bob is mounted on a vehicle it is necessary to design a tracking system and a system to collimate the polarizer of Alice and Bob. In this paper an electronic open-source solution is presented. Open-source electronics permits the build of low cost systems for prototyping and commercial systems.

2. Propagation of electromagnetic beam in atmosphere

Recent studies show the feasibility of quantum cryptography for long distances [5]. The synchronization between ALICE and BOB is necessary to ensure correct time stamping and gating by ALICE and BOB respectively. For the BB84 protocol it is necessary that BOB knows how many bits ALICE has sent. In free space a tracking and synchronization system is also required. The tracking system is composed of a coarse and fine alignment system. For coarse alignment, it is possible to exploit the radio channels used to transmit the encrypted message [6]. The coarse alignment is necessary when the relative positions of ALICE and BOB are not known. Fine alignment and synchronization between ALICE and BOB can be implemented through a laser beacon. The laser beacon unfortunately is also affected by wandering, scintillations and spread due to atmospheric turbulence. It is therefore necessary to know the characteristic of the channel and build a system able to follow the centroid of the laser beacon.

2.1. Beam spread and wandering

The atmospheric refractive index is not constant due to the local changes of the wind speed. The relation between the wind speed and the refractive index n is given by [7]

$$n_1(\vec{r},t) = n_1[\vec{r} - \vec{V}(\vec{r})t], \tag{1}$$

where $n_1(\vec{r},t)$ is the fluctuation of the refractive index, $\vec{r}$ is the vector of the spatial position,$\vec{V}$ is a local speed of the wind and t is the time. The refractive index is given by

$$n(\vec{r},t) = 1 + n_1(\vec{r},t). \tag{2}$$

To design the tracking system it is necessary to consider the beam wandering and reciprocal movements between ALICE and BOB. The tracking system is required to align the polarizers of ALICE and BOB. The effects of the turbulence on the polarization of the beam is negligible [7]. In the absence of turbulence the angular spread of the laser is in the order of λ/D where λ is the wavelength of the photon and D is the initial diameter of the laser beam. If the turbulent effect is small compared to the diameter of the laser beam, the beam is not deflected significantly, while if the turbulent effect is larger than the diameter of the laser beam, the beam is significantly deflected. According to Equation (1), the refractive index changes with time. If we compare pictures in different temporal steps it is possible observe the change in position of the laser spot. The single spots are inside a circle with average radius ρ_l as shows in the Figure 1. When the

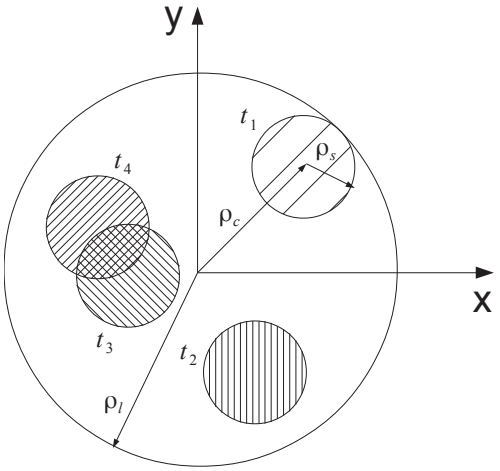

Figure 1. With time, the position of the laser spot changes. ρ_s is the spot of the laser, ρ_l is the average radius contained the single spots and ρ_c is the position of single spot at time t [7].

turbulence is greater the laser does not wander significantly hence multiple spots are received that are contained in circular area of radius ρ_l. The weighted average point of the spatial positioning of the laser beam is defined as the centroid. The tracking system must be able to follow the wandering of the centroid with respect to the inertial frame reference.

3. Open-Source electronics used for tracking systems

For the experiment and prototyping, open-source electronics is used. Analog signals from the sensor are captured by the micro-controller, ARDUINO UNO, which then provides a command to the actuators to move the mechanics of the tracking systems. The ARDUINO UNO micro-controller has six analog inputs, thirteen digital lines of input and output and is

easily programmable in C [8]. Arduino can be controlled through the USB port of a personal computer. This permits the use ARDUINO UNO in conjuction with RASPBERRY PI. RASPBERRY PI is an ARM based computer, the size of a credit card, and the operating system is linux [9]. The peculiarity of ARDUINO UNO and RASPBERRY PI is that they can be exploited to build an integrated system for prototyping a system at low-cost for quantum cryptography.

4. Tracking system

In this section the tracking system is described. The tracking system is used to compensate for the beam wandering and the relative movements between ALICE and BOB. The system aligns the polarizers of Alice and Bob.

4.1. Tracking system with PSD

The laser beacon is received by a telescope and the spot is concentrated on the position sensitive device (PSD) [10]. PSD is a plate of doped silicon that has four output terminals. The beacon spot activates the surface of the sensor and provides the position of the spot, as a function of the current values for each terminal. Using this current signature we are able to determine the position of the centroid as shows in the Figure 2. The automatic tracking control can be

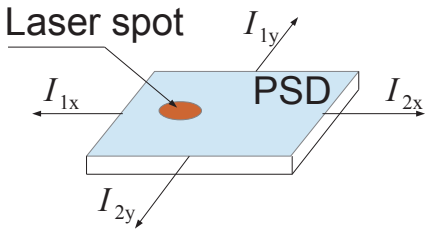

Figure 2. The laser is received by a PSD. When the laser spot changes from the central position the values of the current I_{1x}, I_{2x}, I_{1y} and I_{2y} change.

implemented using the open-source micro-controller ARDUINO UNO. The signal from the PSD is amplified and successively elaborated by the micro-controller. Micro-controller provides the measurement of the movement of the spot and at the same time it can control the power system able to move the mechanics for the tracking.

4.2. Tracking system using a camera

In the previous subsection the tracking system uses a PSD sensor to follow the spot. In the previous case the system is completely autonomous and it is not necessary to use a computer but it is not accurate. It is also possible to follow the laser spot using a camera. The spot of the laser is visualized with a camera, the position of the centroid can be computed and consequently the command can be sent to the electromechanical system of the tracking unit. The computer receives the images as a matrix of numbers. The dimension of the matrix depends on the number of pixels on the sensor of the camera. The color of the single pixel is represented by a number. When the spot is received from the camera, the computer acquires the position of the single pixel which corresponds to the color of the laser and computes the centroid position. The program was tested by SCILAB [11] and the result is shown in the Figure 3. The same algorithm proposed in SCILAB can be rewritten in phyton to be used in RASPBERRY PI. RASPBERRY PI and ARDUINO UNO permit one to have an integrable and autonomous system.

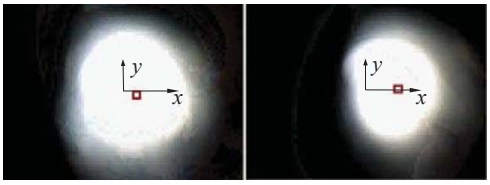

Figure 3. The red square follows the movement of the spot with respect the center of the camera indicated by the axes x, y. The same coordinates used to follow the centroid with the red square can be used to move the mechanics of the tracking system.

4.3. Polarization tracking systems

The effects of the turbulence on the polarization of the laser beam can be neglected since atmospheric turbulence does not effect polarization of the beam. If ALICE and BOB are two non stationary systems the relative position and the geometrical collimation of the polarizers will continuously change. BOB transmits a polarized laser beacon to ALICE who follows the polarization of the laser beacons using a sensor system. The system comprises of two polarizers where the polarization direction is tilted by 90 degrees as shown in the Figure 4. The reference

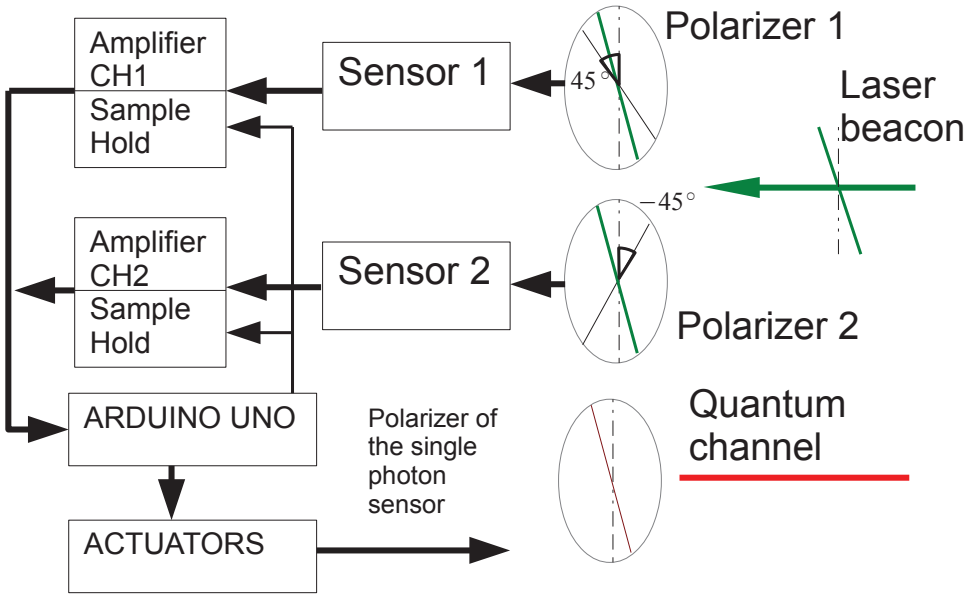

Figure 4. The figure shows the optical and electronic scheme to track the polarization of the laser beacon. If the laser beacon is received at a different angle with respect to the vertical, indicated by the dash line, the signals from polarizer 1 and polarizer 2 are different. By this difference the tracking system turns the optics until the signals from polarizer 1 and polarizer 2 are the same.

frame of the polarizers of ALICE are aligned with the vertical polarization of the incident laser beacon. If BOB is not aligned with the vertical polarization of the laser beacon, sensor 1 will measure a different value from sensor 2. The signals from the sensors are amplified and by ARDUINO UNO the analogical signals from the sensors are converted to digital signals and these are numerically compared. If the signal from the sensor 1 is higher than the signal from the sensor 2, as shows in the Figure 4, the system mechanically turns the instrument using the actuators in an anticlockwise direction. When the QKD units are correctly orientated, the

signal from sensor 1 and sensor 2 are identical and the tracking system locks this position of the polarizers. The state of polarization of the qubit is tilted with respect to the tracking polarizers of 45 and -45 degrees respectively.

5. Conclusion

The paper shows that in free space QKD it is necessary to have automatic control tracking system able to follow the relative movement of ALICE and BOB and to be able to align their orientation and hence, polarization. For a stationary unit, the turbulence affects the laser beam through wandering and spread. The prototyping of the tracking system can be made by open source electronics. The micro-controller and micro-computer mentioned in this paper permit one to build prototypes and low cost systems. The circuit of the ARDUINO UNO and RASPBERRY PI can be modified for our purposes with the advantage that it is possible to use the open-source software such as python for video processing and hardware control. Currently experiments are being undertaken in the laboratory but in the future this system will be tested for long distance QKD and for transmission between two non stationary points. The success of the experiment will encourage quantum cryptography for commercial users.

6. Acknowledgments

This work is based on research supported by the South African Research Chair Initiative of the Department of Science and Technology and National Research Foundation. M. Mariola would like to thank Professor Paolo Villoresi for a very useful research visit at the University of Padova.

reference

[1] [online] Dalla crittografia classica alla crittografia quantistica; http://www.philos.unifi.it/upload/sub/Seminari/Filosofia-Fisica/crittografia.pdf
[2] P. Shor, Polynomial-time algorithms for prime factorization and discrete log- arithms on a quantum computer, SIAM J.SCI.STATIST.COMPUT., vol. **26**, p. 1484, 1997.
[3] Bennett C and Brassard G 1984 *Quantum cryptography: public key distribution and coin tossing* Proc of IEEE International conference on computer systems and signal processing 175-179
[4] Bennet C 1992 Quantum cryptography using two nonorthogonal states *Phys. Rev. Lett.* **68** 3121-31247
[5] Ursin R et al.3 June 2007 *Entanglement-based quantum communication over 144 km* Nature physics **3** 481-486
[6] Mariola M Mirza F Petruccione 2011 *Quantum cryptography for satellite communications* Proc. South African Institute of Physics ISBN:978-1-86888-688-3 pp.403-408
[7] Ronald L. Fante 1979 *Electromagnetic beam propagation in turbulent media* proc. of IEEE, Vol. 63, NO.12 1669-1692
[8] [online] http://www.arduino.cc/
[9] [online] http://www.raspberrypi.org/
[10] [online] http://en.wikipedia.org/wiki/Position_sensitive_device
[11] [online] http://sivp.sourceforge.net/

An assessment of wind energy potential of the Amatole district in the Eastern Cape Province of South Africa

P Masukume[1], G Makaka[1] and D Tinarwo[2]
[1]University of Fort Hare, Department of Physics, P. Bag X1314, Alice 5700, South Africa.
[2]University of Venda, Department of Physics, P. Bag X5050, Thohoyando,0950, South Africa.

E-mail:pmasukume@gmail.com

Abstract: South Africa is heavily depended on fossil fuels for its energy needs and is the highest emitter of greenhouse gasses in Africa and 18th in the world. It is therefore imperative to shift to renewable energy sources for power production to mitigate the carbon emissions. The purpose of this paper is to investigate wind energy potential in the Amatole District in the Eastern Cape Province of South Africa. The Weibull density function was used to estimate the wind energy potential in this location. The Weibull parameters, k(shape parameter) and c(scale parameter) varied from 1.651 to 2.026 and 3.093 to 4.310 respectively. The study shows that at a hub height of 10m above the ground, the area has moderate wind energy potential for low speed decentralized wind energy systems. Therefore at this hub height it is not suitable for large scale wind energy production.

1. Introduction

South Africa's energy intensive economy depends greatly on fossil fuels for its energy needs, with almost 90% coal based electricity generation and is the highest emitter of green house gasses in Africa and 18th in the whole world (Olivier et al, 2012). However, South Africa is endowed with abundant unexploited renewable energy resources. Wind energy is one of the least exploited renewable energy sources. The use of wind energy can significantly reduce the combustion of fossil fuels and consequently limit the emission of Carbon dioxide (CO_2), a principal cause of enhanced green house effect.

For any power plant to generate electricity, it needs fuel, for a wind power plant, that fuel is wind. It is therefore imperative to have a thorough wind resource assessment to establish the wind energy potential of the site for successful planning and implementation(Anyanwu and Iwuagu, 1995, Celik et al, 2010, Islam et al, 2011). Estimates of wind resources are expressed in wind power classes ranging from 1 to 7, with each class representing a range of mean wind power density or equivalent mean wind speed at specified heights above the ground. A wind class table is shown in Table 1.

Measurements of wind speed distribution or frequency distribution are used for calculating the output of the wind energy in a particular site if available. If not, the wind speed distribution can be represented by other analytical distribution functions for the occurrence of the wind speed. One of these functions is the Weibull distribution function (named after the Swedish physicist Weibull, who applied it when studying material strength in tension and fatigue in the 1930s) (Ulgen and Hepbasli, 2002). Several researchers have used the Weibull distribution in wind energy potential assessment (Lun and Lam, 2000, Seguro and Lambart, 2000, Weisser,2003 and Zhou et al, 2006). This analytical distribution for fitting wind speed data is generally accepted as the standard approach.(Bansal et al,2002, Persaud et al, 1999). This approach has been adopted in this paper. This paper presents a wind energy potential assessment of the Amatole District in the Eastern Cape province using the Weibull distribution function.

Table 1. Classes of wind power density (Tong, 2010)

	10m		65 m	
Wind power class	Wind power density (W/m^2)	Mean wind speed (m/s)	Wind power Density (m/s)	Mean wind speed (m/s)
1	<100	<4.4	<200	<5.6
2	100-150	4.4-5.1	200-300	5.6-6.4
3	150-200	5.1-5.6	300-400	6.4-7.0
4	200-250	5.6-6.0	400-500	7.0-7.5
5	250-300	6.0-6.4	500-600	7.5-8.0
6	300-400	6.4-7.0	600-800	8.0-8.8
7	>400	>7.0	>800	>8.8

2. Methodology

2.1 Site and data collection

The wind assessment was done in the Amatole district in the Eastern Cape province of South Africa. The wind speed data in hourly time series format over a period of 3 years (2010-2012) was supplied by the South African Weather Service(SAWS). The data was measured at a meteorological weather station at Fort Beaufort. The measurements were taken at a standard height of 10 m above the ground. Table 2. Summarizes the station location.

Table 2. Location of Fort Beaufort.

Station	Duration (yrs)	Latitude	Longitude	Height above sea level (m)
Fort Beaufort	2010-2012	32.7880	26.6290	455

2.2 Weibull distribution function

The Weibull distribution function was used to analyze the wind speed data as alluded to in the previous section. The general form of the two-parameter Weibull probability density function is given by (Keyhani et al, 2010):

$$f(v)=\frac{k}{c}\left(\frac{v}{c}\right)^{k-1}\exp\left[-\left(\frac{v}{c}\right)^{k}\right] \quad (1)$$

where f(v), is the probability of observing speed v, k, is the dimensionless Weibull shape parameter and c, is the Weibull scale parameter.

The corresponding cumulative probability function of the Weibull distribution is given as (Akpinar and Akpinar,2004):

$$F(v)=1-\exp\left[-\left(\frac{v}{c}\right)^{k}\right] \quad (2)$$

The Weibull parameters, k and c, characterize the wind potential of the site under study. The scale parameter , c, indicates how "windy" the site under consideration is, where as the shape parameter, k, indicates how peaked the wind distribution is (ie, if the wind speed tend to be very close to a certain value, the distribution will have a high k value and is very peaked)

2.3 Parameter estimation

The Weibull parameters were estimated using the Maximum likelihood method. This method was

widely used by other researchers(Dike et al, 2011). The shape parameter k, and scale parameter c, are estimated by the following(Maatallah et al, 2012):

$$k = \left(\frac{\sum_{i=1}^{n} v_i^k \ln(v_i)}{\sum_{i=1}^{n} v_i^k} - \frac{\sum_{i=1}^{n} \ln(v_i)}{n} \right)^{-1} \quad (3)$$

$$c = \left(\frac{\sum_{i=1}^{n} (v_i)^k}{n} \right)^{\frac{1}{k}} \quad (4)$$

Where v_i *and n* are respectively the wind speed and the number of observed non zero wind speeds.

2.4 Meaningful wind speeds

There are basically two meaningful wind speeds for wind energy estimation when using the Weibull distribution function. These are the most probable wind speed, V_{mp}, and the wind speed carrying the maximum energy, V_{maxE}. The most probable wind speed denotes the most frequent wind speed for a given wind probability distribution and is expressed as(Jamil et al,1995):

$$V_{mp} = c\left(\frac{k-1}{k} \right)^{\frac{1}{k}} \quad (5)$$

The wind speed carrying the maximum energy represents the wind speed that carries the maximum amount of energy and is expressed as (Celik, 2004):

$$V_{\max E} = c\left(\frac{k+2}{k} \right)^{\frac{1}{k}} \quad (6)$$

2.5 Wind power density (WPD)

It is well known that the power of the wind that flows at a speed v, through a blade sweep area A increases as the cube of its velocity and is given by:

$$P_{(v)} = \frac{1}{2}\rho A V^3 \quad (7)$$

Wind power density(WPD), expressed in Watt per square metre (W/m^2), takes into account the frequency distribution of the wind speed and also depend on air density and the cube of the wind speed. Therefore WPD is generally considered a better indicator of the resource than wind speed. (Al-Nassar et al, 2005). Monthly or annual wind power density per unit area for a region, based on the Weibull probability density function, can be expressed as follows(Rumbayan and Nagasaka, 2011):

$$P_w = \frac{1}{2}\rho c^3 \Gamma\left(1 + \frac{3}{k}\right) \quad (8)$$

Where Γ, is the gamma function, ρ, is the air density which can be calculated as follows:

$$\rho = \frac{P}{RT} \quad (9)$$

P is the average pressure, T is the average temperature and R is the dry gas constant

2.6 Wind shear

Wind speed increases height with due to wind shear. Commercial wind turbines can have hub heights of 65 m or more. To estimate the wind velocity at this height in terms of the given data, a logarithmic formula was used and given as (Manwell et al, 2002):

$$V_{2\,(Z_2)} = V_{1(Z_1)}\,\frac{ln\left(\frac{Z_2}{Z_0}\right)}{ln\left(\frac{Z_1}{Z_0}\right)} \qquad (10)$$

Where Z_1 is the reference height, Z_0 is the roughness height of the terrain, Z_2 the desired height for which the velocity is to be determined and $V_{2\,(Z_2)}$ is the velocity at Z_2.

2.7 Goodness of fit

The Goodness of fit test were done using the Kilmogrov-Smirnov(KS) test, Anderson-Darling (AD) test and the Chi-squared(CH) test.

3. Results and discussion

3.1 Wind characteristics

The wind speed for a period of 3 years from 2010 to 2012 was analysed. Figure 1 shows the mean daily wind speeds values for 2010. It is clear from the diagram that the mean daily wind speed varies from 0.9 m/s to 7.5 m/s between April and September and 1.3 m/s to 5.6 m/s between October and March. It has been observed that the trend of this variation over the three years is similar. The mean monthly wind speeds vary between 2.3 m/s to 3.45 m/s. It has also been observed that all the months between October to January have mean monthly wind speeds over 3 m/s. The trend is the same for all the years under study. This indicate that this is the windiest time of the year. Figure 2 shows the mean monthly wind speed values for 2010.

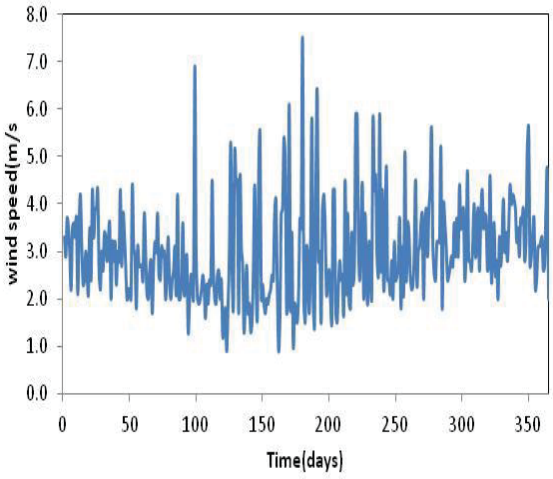

Figure 1. Mean daily wind speeds (2010)

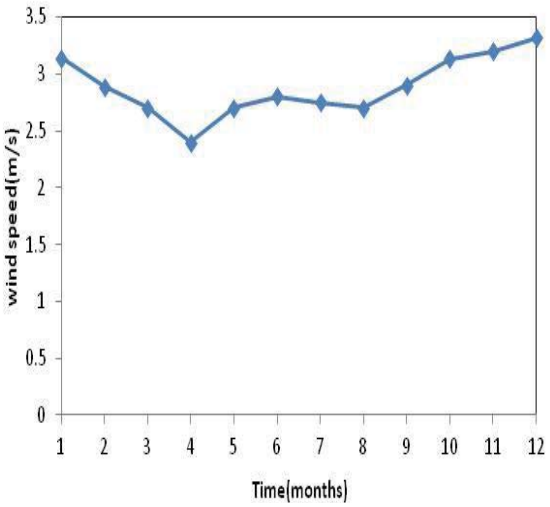

Figure 2. Mean monthly wind speeds (2010)

It is clear from the graph that the mean monthly wind speeds between October to January is well over 3 m/s. The month of April has the least mean monthly wind speed of 2.4 m/s in 2010. And the maximum of 3.32 m/s in December. A minimum of 2.22 m/s and 2.39 m/s were observed in March 2011 and 2012 respectively. It can be concluded that the months of March and April have the least wind speeds while December has the maximum wind speed over 3 m/s. The yearly mean wind speed can be obtained by averaging all the available wind speeds in the year. For this site, the yearly mean

wind speeds are less than 3 m/s. The yearly mean for 2010 is 2.92m/s while that for 2011 and 2012 is 2.72 m/s and 2.76 m/s respectively. The overall mean wind speed for the site under study is 2.80 m/s.

3.2 Weibull Distribution

The mean monthly Weibull parameters for the site , the scale parameter c and the shape parameter k, are shown in Table 5. The shape parameter k, has a smaller variation than the scale parameter c. k varied from 1.651 to 2.026 while c varied from 3.093 to 4.310 during the same period. K had the least value in December and its highest in March. In the same period c had the least value in March and it is the maximum in December. Figure 3 shows a histograms of the variation of the observed and the superimposed Weibull probability density function for the site under study. The graph is skewed to the right. The calculated values for skewness and excess kurtosis in Table 3, agrees with the nature of the graph. The excess kurtosis in the graph of figure 3 indicates that the peak of the graph is sharper than the normal distribution. The corresponding cumulative distribution function for the site is also shown in figure 4. The closeness of the graph to the observed data is a clear indication that the Weibull distribution fit the data. The results of the goodness of fit applied to the data are given in Table 4. All the p-values are above 0.05, indicating that the Weibull distribution fits the data.

Table 3. Descriptive statistics

Period	skewness	Excess kurtosis
2010-2012	0.56	-0.23

Table 4. Goodness of fit tests

Period	KS p-value	AD p-value	CS p-value
2010-2012	0.7311	0.9105	0.2121

Table 5. Descriptive statistics, meaning full velocities, Weibull parameters and wind power density

Month	V_m (m/s)	σ (m/s)	c (m/s)	k	V_{mp} (m/s)	V_{maxE} (m/s)	WPD (W/m^2)
Jan	3.052	1.971	4.130	1.691	2.433	6.553	70.841
Feb	2.770	1.825	3.490	1.863	2.309	5.162	37.543
Mar	2.443	1.614	3.093	2.026	2.211	4.341	23.797
Apr	2.431	1.763	3.097	1.830	2.010	4.636	26.813
May	2.493	1.856	3.103	1.742	1.901	4.813	28.806
Jun	2.951	2.231	3.597	1.656	2.056	5.802	48.281
Jul	2.667	1.864	3.267	1.811	2.096	4.926	31.897
Aug	2.531	2.217	3.630	1.730	2.204	5.660	46.551
Sep	2.913	2.013	3.557	1.780	2.237	5.430	42.108
Oct	3.128	1.962	4.016	1.757	2.487	6.189	61.676
Nov	3.107	1.944	4.216	1.733	2.566	6.565	72.754
Dec	3.114	1.950	4.310	1.651	2.453	6.970	83.469

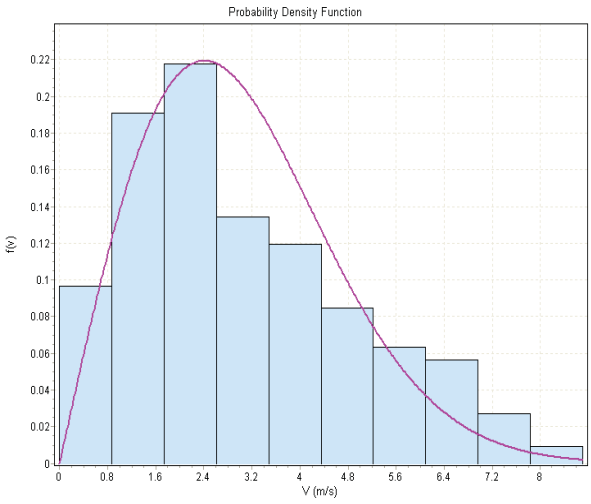

Figure 3. Histogram of observed and Weibull PDF simulation

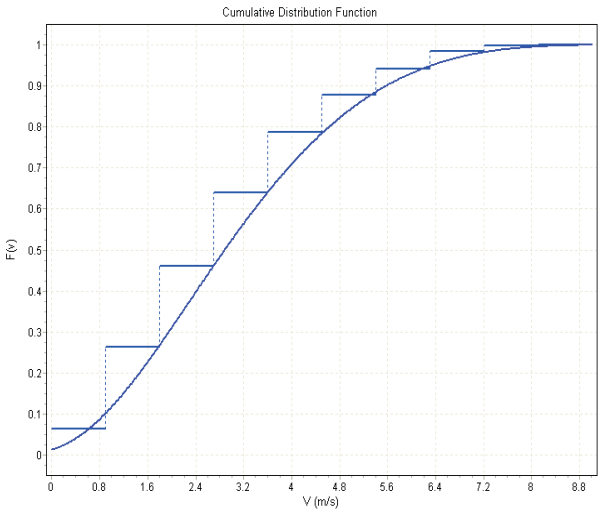

Figure 4. Cumulative probability function for the data

3.3 The Power density

The most probable wind speed V_{mp} , varied from 1.901 m/s to 2.566 m/s. In all cases it is observed that the most probable wind speed is less than the mean monthly wind speed but are quite close. The wind speed carrying the maximum energy varied from 4.341 m/s to 6.970 m/s. Unlike the most probable wind speed, the wind speed carrying the maximum energy is greater than the monthly mean and is almost twice as much. The wind power density varied from 23.797 W/m^2 to 83.469 W/m^2 . The lowest was in March and April. It was 23.797W/m^2 in March and 26.813W/m^2 in April. The period October to January produced the most wind power density, ranging from 61.676 W/m^2 to 83.469 W/m^2. The overall wind power density of the site is 47.878 W/m^2. This value is less than 100 W/m^2, therefore the WPD is in Class 1 according to the classification shown in Table 1.

3.4 Wind speed at hub height of 65m above the ground

Table 6 Values used to estimate $V_{2\,(Z_2)}$

Roughness height (Z_0) (m)	Reference height(Z_1) (m)	Z_2 (m)	$V_{1\,(Z_1)}$ (m/S)	$V_{2\,(Z_2)}$ (m/S)
0.25	10	65	3	4.5

The wind speed at a hub height of 65 m is 4.5 m/s and according to Table 1, the location is in Class 1. Class 2 wind speeds are not suitable for large scale wind development.

4. Conclusion

This paper assessed the wind energy potential of Amatole District. The average wind power density of the site at a hub height of 10 m is 47.878 W/m^2 and is in Class 1 according to the classification in Table 1.The estimated wind velocity at a hub height of 65 m is 4.5 m/s. According to the classification shown in Table 1, the wind speed is in Class1. Class 1 wind speeds are not suitable for large scale wind energy development. We therefore conclude that Amatole District has moderate wind energy potential for low speed decentralized wind energy systems, it is not suitable for large scale wind development.

Acknowledgements: Authors would like to acknowledge the South African Weather Service (SAWS)

References

[1] Akpinar E S, Akpinar S 2005 An assessment of seasonal analysis of wind energy characteristics and wind turbine characteristics. Energy Conversion and Management **46** :1848-1867

[2] Al-Nassar W, Alhajraf S, Al-Enizi A, Al-Awadhi L 2005 Potential wind power generation in the State of Kuwait. *Renew Energy **30**:2149–61*.

[3] Anyanwu E E, Iwuagwu C J 1995 Wind characteristics and energy potential for Oweri, Nigeria. *Renewable Energy **6** (2) 208-215*

[4] Bansal C, Bhatti T S, Kothari D P 2002 On some of the design aspects of wind energy conversion systems. *Energy Conversion Management 4**3** 2175-87*

[5] Çelik A N 2004 A statistical analysis of wind power density based on the Weibull and Rayleigh models at the southern region of Turkey. *Renewable Energy*, vol.29 **4** 593-604

[6] Celik A N, Makiwi A, Muneer T 2010 Critical evaluation of wind speed frequency distribution function. Journal of Renewble and Sustainable Energy **2** 1-18

[7] Dike V N, Chineke C T, Nwofor O K, Okoro U K 2011 Estimating wind energy potential in some coastal cities of the Niger Delta Region of Nigeria. *The Pacific Journal of Science and Technology. Vol. **12** Number 1*

[8] Islam M R, Saidur R, Rahim N A 2011 Assessment of wind energy potentiality at Kudat and Lubuan, Malaysia using Weibull distribution function. *Energy **36** 985-992*

[9] Jamil M, Parsa S, Majidi M 1995 Wind power statistics and evaluation of wind energy density. *Renewable Energy 1995;**6**:623–8.*

[10] Keyhani A, Ghasemi-Varnamkhasti M, Khanali M, Abbaszadeh 2010 *Energy **35** 188-201*

[11] Lun I Y F, Lam J C 2000 A study of Weibull parameters using long-term wind observations. Renewable energy **20** 145-53

[12] Maatallah T, Alimi E S, Damouni A W, Nasrallah S B 2012 Wind power assessment and evaluation of electricity generation in the Gulf of Tunis, Tunisia. *Sustainable Cities and Societies **6** 1-10*

[13] Manwell J F, MacGowan J G, Rogers A L 2002 Wind energy explained, theory design and application. John Wiley and sons Ltd

[14] Olivier J G J, Janssens-Maehout G, Peters J A H W 2012 Trends in Global CO_2 emissions 2012 Report. *The Hague:PBL Netherlands Environmental Assesment Agency; Ispara: Joint Research Centre*

[15] Persaud S, Flynn D, Fox B 1999 Potential for wind generation on the Guyana costal lands. *Renewable energy **18 (2):**175-87*

[16] Rumbayan M, Nagasaka K 2011 Assessment of wind energy potential in Indonesia using Weibull distribution function. *International Journal of Electrical and Power Engineering **5 (6):**229-23*.

[17] Seguro J V, Lambert T W 2000 Modern estimation of the parameters of the speed distribution in Saudi Arabia. Solar Energy, vol.**53** 473–9.

[18] Tong W 2010 Wind power generation and wind turbine design. Kollmorgen Corporation, USA.

[19] Ulgen K, HepbasliI A 2002 Determination of Weibull parameters for wind energy analysis of İzmir, Turkey. *International Journal of Energy Research., vol.**26** 495-506*

[20] Weisser D 2003 A wind energy analysis of Grenada: an estimation using the Weibull density function. *Renew Energy **28** 1803–12*

[21] Zhou W, Yang H, Fang Z, 2006 Wind power potential and characteristic analysis of the Pearl River Delta region, China. *Renewable Energy*, vol.**31** 739-5

Analyses of the spatial and spectral neutron distribution of various conceptual core designs with the aim of optimizing the SAFARI-1 research reactor

[1,2] **O. Oluwaleye, [2]R. H. Prinsloo, [2]B. A. Adetula, [1]S. H. Connell.**

[1]University of Johannesburg, Physics Department, cnr Kingsway Ave and University Rd, PO Box 524, Auckland Park, 2006, South Africa. [2]Radiation and Reactor Theory, Necsa, Building 1900, PO Box 582, Pretoria, South Africa.

E-mail: kunle335@gmail.com

Abstract. The SAFARI-1 research reactor at Pelindaba is a 45 year old 20 MW tank-in-pool type material testing reactor, and is expected to reach the end of its operating life between 2020 and 2030. The purpose of this study is to investigate various inhomogeneous neutron distributions within the core, arising from different core layouts of the SAFARI-1 reactor, which nonetheless still achieve efficiency in the operation for various design purposes, but with a lower power output. The spatial and energy neutron distribution is one of the most important parameters in the characterization of such an alternative core layout. This neutron distribution is a result of basic physics processes such as particle matter interactions, nuclear reactions, material properties, the effect of temperature and the time evolution of the system. A SAFARI-1 reference core, obtained through an equilibrium cycle calculation, is used to generate a set of safety and utilization targets against which alternative designs are measured. Alternative core layouts were developed by using a parametric study to determine the size and power level of potential candidate conceptual cores while adhering to the safety and utilization requirements. Results indicate that an alternative core with a power of 17 MW can achieve similar performance results as the current 20 MW SAFARI-1 design, by simply rearranging components in the core.

1. Introduction

The SAFARI-1 research reactor is at present (2014) the only research reactor in South Africa, utilized for both research and isotope production purposes. It utilizes a plate-type fuel element design, where the core is constructed from a lattice of fuel elements (and other components) sitting in a large pool of water. Control elements, reflector elements and irradiation channels further fill the lattice. The water serves as moderator and at the same time cools the reactor. Beam tubes are also present and stream leaking neutrons from the core to various instruments. The focus of this study is the steady-state neutron distribution within the highly heterogeneous and complex geometry of the SAFARI-1 reactor core described above. This information may be used to determine the neutron reaction rate with its surrounding material and thus estimate the depletion rate of the core fuel and modification to the core structure. For example, the total reaction rate, over some volume in the reactor and the whole energy range, for a given reaction type (k), in which a neutron-nuclear reaction occurs, can be defined in terms of the material

cross section (σ), the material atomic density (N) and the neutron scalar flux (φ) as:

$$R_t = \int \int \varphi(\vec{\mathbf{r}}, N) N(\vec{\mathbf{r}}) \sigma_t(\vec{\mathbf{r}}, E) d^3\vec{\mathbf{r}} dE. \quad (1)$$

In this work, these quantities (reaction rate, flux and material distribution) are resolved over a number of different potential core design concepts, in order to design an optimal core for the SAFARI-1 research reactor at Necsa. In this context, an optimal core is defined as the core geometry yielding a steady state spatial and spectral neutron flux distribution which satisfies all safety and utilization requirements throughout the operating cycle, but with a minimized power level.

2. Methodology

In this work, we proceed in three steps in order to obtain such an optimal core design. Firstly, we determine the metric for core evaluation in terms of a set of operating objectives and constraints. Secondly we determine the conceptual core characteristics for achieving the set objectives, and finally we extrapolate the conceptual core design to a detailed and realistic SAFARI-1 core layout.

2.1. Core evaluation metric

The metric for core evaluation is established by analyzing the set of defined SAFARI-1 operating objectives and investigating the sensitivity of these objectives to the reactor power level. These objectives and constraints, evaluated via numerical analyses with the OSCAR-4 code system, are defined as:

- power peaking factor: The power peaking factor is defined as the ratio of the maximum power density in a given localized region divided by the average power density in the reactor core [1]. In order to ensure that the fuel does not sustain damage, the local power density at the hottest part of the nuclear fuel should be estimated accurately.
- reactivity: The degree of change, in neutron multiplication in a nuclear reactor core, is evaluated by the reactivity in the core. The reactivity measures of interest consist of excess reactivity (additional reactivity at the beginning of cycle (BOC)), control bank worth (total absorbing capability of all the control rods), shut down margin (amount of negative reactivity available to counteract any initiating events).
- position dependent thermal flux: The thermal flux level, in a number of positions in the core, is critical to meet operating objectives. These include flux levels in general irradiation positions, in Mo-99 production positions and at the entry point of beam tubes (to support beam instruments for research purposes).
- fuel economy: The discharge mass, which is the amount of U-235 remaining in spent fuel elements, is a typical measure of fuel economy and should be minimized. It is of critical importance to operate the core in a way that minimize fuel usage, given the significant fuel cost. Generally, a reduction in power implies a reduction in fuel usage.

These set of performance and safety parameters, that are used to ensure the viability of any proposed core, are defined and expressed as a function of typical neutronic results available from the standard calculational tools used to model the SAFARI-1 reactor. Input from the reactor managers and clients are utilized to rank these objectives in terms of priority. In order to determine the set of reference values for these parameters, two approaches are followed.
Firstly, a set of existing SAFARI-1 operating cycles are analyzed in order to quantify the current SAFARI-1 performance. Although highly realistic, these set of reference values prove difficult to utilize for theoretical comparison, given the non-constant nature of the actual operating schedule

(due to unplanned outages or varying user requirements). Therefore, an idealized equilibrium core is also constructed, based on a typical, repeatable SAFARI-1 cycle and loading definition. It is, however, important that this equilibrium reference core performs within the range of actual operating performance parameters in order to use it as an acceptable reference for evaluating alternative proposed cores.

2.2. Conceptual core design

In the next phase, a parametric study is undertaken in order to determine the relationship between core size, core power level and core performance. Parameters that are investigated include minimum core size, minimum power level, the number of fuel elements and the minimum number of production facilities. In particular, we investigate the core size and power combinations which yield acceptable maximum power density and minimum isotope yield.
We employed the constraints of not enlarging the existing SAFARI-1 core, not changing the control rod positions and not adjusting the number of isotope irradiation positions in the core. The outcome of this phase of the study is the characterization of an allowable space spanned by the dimensions of core size and core power level.

2.3. Detailed core design

Once the boundaries of allowable core size and power are established, it remains to construct a realistic SAFARI-1 core layout which falls within these parameters. This process is based on existing core flexibility, SAFARI-1 loading constraints and established know-how in core design. It is reiterated that this is not a typical design process of a new reactor core, given that a number of limitations are placed by the existing SAFARI-1 plant and its capabilities and as such any benefit provided by a new core design has to be considered in conjunction with the nature and gravity of the changes required. In particular, changes which would require significant licensing adaptations might prove problematic.

3. Modelling Tools

Reactor calculation code systems, with associated automation procedures, are crucial in the prediction of these reactor safety and utilization parameters [2]. The OSCAR-4 code system, which is the dedicated code to model the SAFARI-1 reactor, is utilized as a modelling tool in this study. OSCAR-4 [3] solves for the neutron flux distribution within the reactor in a multi-step deterministic fashion. However, the neutron transport equation is solved in 2D on the scale of each reactor component in full heterogeneous detail in order to generate component averaged cross-sections and the neutron diffusion equation is then utilized (along with these averaged cross-sections) to calculate the flux distribution on the global 3D core level. The neutron transport and diffusion equations, which are solved in this two step process within the OSCAR-4 system, are given below. The neutron transport equation, solved for each core component, may be written as:

$$\frac{1}{\upsilon}\frac{\partial\phi}{\partial t} + \nabla\cdot\vec{J}(\vec{\mathbf{r}},E,t) + \Sigma_t(\vec{\mathbf{r}},E)\phi(\vec{\mathbf{r}},E,t) = \int_0^\infty dE'\Sigma_s(E'\rightarrow E,)\phi(\vec{\mathbf{r}},E',t) + S(\vec{\mathbf{r}},E,t). \quad (2)$$

Where, $\Sigma_s(E'\rightarrow E)$ represents the macroscopic differential scattering cross section, $\Sigma_t(\vec{\mathbf{r}},E)$ represents the total macroscopic cross section for all interactions, υ is equal to the neutron speed and $S(\vec{\mathbf{r}},E,t)$ represents the fission source and other source terms in Equation 2. ϕ is equal to the neutron flux, $\vec{J}$ is equal to the neutron current density and E is the neutron energy. The multi-group neutron diffusion equation is utilized to determine the 3D global core flux distribution. The numerical solution schemes surrounding these equations are implemented within the OSCAR-4 code system and additional discussions on these techniques may be found in [4].

4. Results and Discussion

In this section, we present results from each of the three steps in the methodology section above.

4.1. Definition of the reference core

As stated, both the actual SAFARI-1 operating cycles and an idealized equilibrium core model were utilized to determine the set of reference values for the safety and utilization objectives identified. Table 1 identified the set of objectives in column 1, lists the values of these objectives from an actual (and typical) SAFARI-1 operating cycle in column 2 and provides the corresponding values from the idealized equilibrium reference core in column 3. An equilibrium core is obtained when a particular fuel loading pattern is applied to a series of cycle calculations until core parameters, such as core reactivity, U-235 distribution and flux distribution converge from cycle-to-cycle. The loading pattern employed in this case is that the fuel with the highest mass is placed in a core position with a lower flux, in order to limit excessive power peaking in high power fuel assemblies. The convergence parameter used to determine when the equilibrium is reached is the end-of-cycle (EOC) k-eff. EOC k-eff values converge at the 30th cycle in the multi-cycle set and the equilibrium oscillates between an even cycle and odd cycle. This two-step equilibrium appears due to the loading of fresh control elements as one fresh control element is loaded only every second cycle. This is done to follow the typical approach employed at SAFARI-1.

Calculated results presented in Table 1 show that all the reference core safety and utilization parameters reasonably match those of the actual SAFARI-1 reactor operating cycle. With these results it can be concluded that this equilibrium core model is suitable for use as a reference core against which alternative core designs can be measured. This reference core was constructed by loading 3 fresh elements in a given cycle, and then loading 3 fresh fuels and one fresh control element in the following cycle. Considering ten operating cycles per year, this implies the usage of 30 fuel elements and 5 control elements per year.

4.2. Conceptual parametric study

Figure 1 demonstrates the results of the parametric study conducted to determine the acceptable range of core sizes and power levels. In order to evaluate the various cases, the reference SAFARI-1 core model was utilized as a basis (represents the intersection point of 20 MW with a core size of 29 fuel elements - 26 standard fuel and six followers counted as a half element each). This core model was then adapted in both power level and core size to evaluate all other combinations of these parameters. For a decreasing core size, fuel elements were systematically removed and replaced with water filler elements. For each core concept obtained, the values of power peaking and Mo-99 production were determined.

The Mo-99 yield and the power peaking factor values obtained from the neutronic evaluation of the proposed core concepts are listed in Tables 2 and 3. Based on results of all such core evaluations, an overlapping area bounded by the upper power level constraints of maximum power density and lower power level constraints of minimum isotope production was developed and is demarcated by area BCDG. We thus expect that any core within this demarcated area would yield, for the selected combination of power level and core size, a viable alternative to the current SAFARI-1 arrangement of 29 fuel elements at 20 MW.

The upper boundary of the allowable area is limited by line AC, which results from the maximum power density limitation. This line was obtained based on the current acceptable maximum power density in the SAFARI-1 core, utilizing the current cooling capacity. Line CD occurs due to the intention of reducing the current SAFARI-1 power and thus limiting the target power level to below 20 MW. Similarly, line DG occurs since the intention is to reduce the current SAFARI-1 core size. Line BG indicates the lower limit which retains an acceptable level of isotope production.

Table 1. Summary results of safety and utilization parameters

Parameters	SAFARI-1	Reference core	17 MW core	Limit
Calculated cycle length (days)	36.69	44.92	36.84	$>$ 29.96
Max Mo-99 yield	0.02 Ci	9.01 Ci	5.78	
Excess reactivity (\$)	7.97	10.06	8.23	
Control bank worth (\$)	29.49	32.22	37.72	$>$ 20.00
Shut-down margin (\$)	18.89	20.43	27.96	
Min individual RW (\$)	2.92	2.52	4.00	$>$ 2.00
Power peaking factor	3.32	3.41	2.27	$<$ 3.50
Peak power density (W/cm^3)	565.24	589.16	451.37	
Assembly with peak power ensity	B5	B5	C7	
BOC bank position (cm)	51.45	46.50	49.68	
EOC bank position (cm)	66.37	62.08	68.16	
Target plate worth (\$)	2.62	1.73	1.52	
BOC bank with target plate (cm)	46.05	42.88	47.88	$>$ 39.53
BOC equilibrium Xe bank (cm)	56.72	52.76	56.30	
Number of rigs in the core	7	7	7	
Silicon facility 1 fluxes (n/cm^2/s)	2.66	1.78	3.54	
Core box fast flux (n/cm^2/s)	1.69	0.97	2.40	
Max IPR1 flux (n/cm^2/s)	9.00	9.00	9.00	
Max IPR2 flux (n/cm^2/s)	7.86	7.17	8.83	
Beam tube 5 flux (n/cm^2/s)	1.82	1.86	1.92	
Beam tube 2 flux (n/cm^2/s)	6.30E10^{-15}	5.78E10^{-15}	6.43E10^{-15}	
Beam tube 1 flux (n/cm^2/s)	0.33	0.35	1.26	
Number of fuel	26	26	22	
Control rods	6	6	6	
Power level	20.00 MW	20.00 MW	17.00 MW	

Table 2. The power peaking factor in the reference core and the proposed core concepts

Core	power peaking factor
Reference core	3.41
17 MW core	2.72
16 MW core	3.20
15 MW core	3.18

Table 3. The molybdenum-99 yield in the reference core and the proposed core concepts

Position	17MW core % change in Mo-99 yield	16MW core % change in Mo-99 yield	15MW core % change in Mo-99 yield
Total Mo-99 yield	1.81	-7.85	-14.26
Max. Mo-99 yield	-2.86	-6.03	-11.91

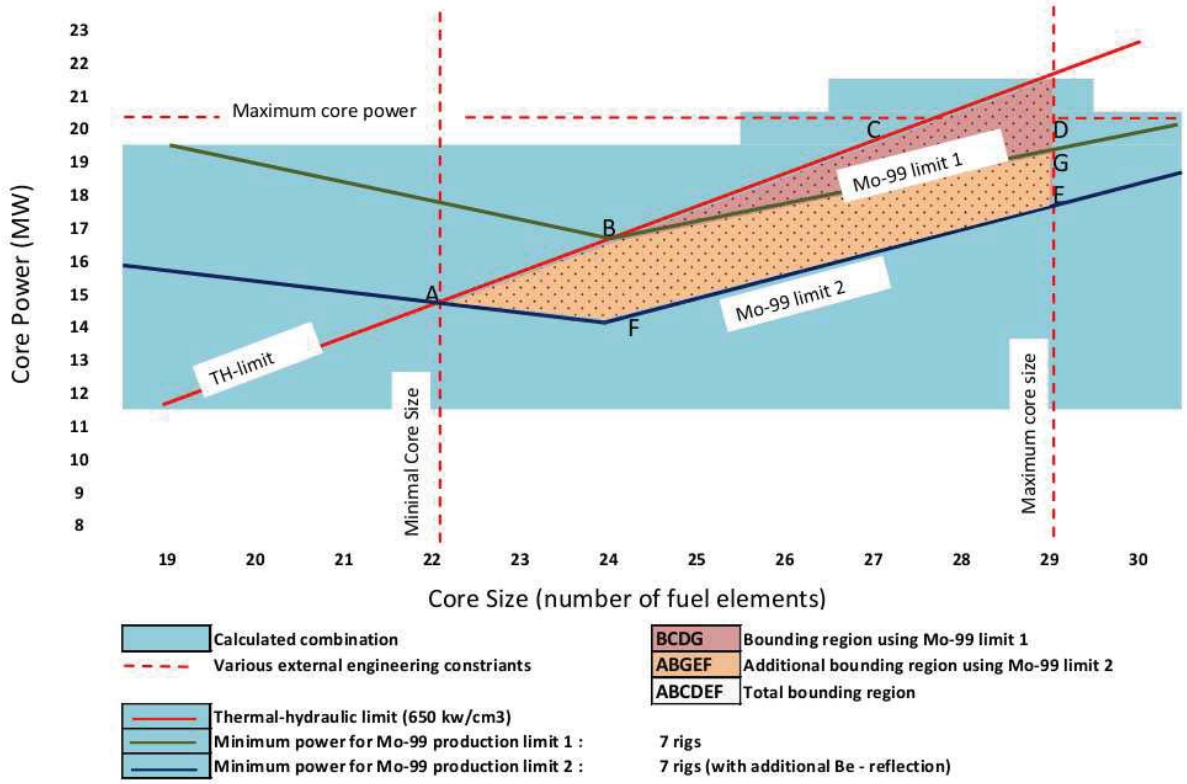

Figure 1. Result of Parametric study

Note further that a second, less restrictive, lower power limit in isotope production is possible if all excore positions are filled with Beryllium reflector elements. This limit, referred to in the graph as "+Reflection" allows even lower power cores to be potentially viable and enlarges the legal area to the space indicated by ABCDEF. This occurs because the additional Beryllium elements reduce leakage in the core and as such provides reactivity. This enlargement of the space does not require any significant core changes other than the cost of a number of additional Beryllium elements and is quite attractive.
To illustrate how this graph can be utilized, we now choose the intersection point of 17MW with 25 fuel elements as our first proposed core and consider it in the next section. As can be seen from the allowable area in the graph, 17 MW is quite a conservative choice and it might be possible to operate a 25 element core at around 15 MW. Nevertheless, as a first application of this study, we investigate the 17 MW core as a viable option with some margin.

4.3. Evaluation of proposed detailed core
From the result of the parametric study (Figure 1) a potential realistic core which can operate at 17 MW with 25 fuel assembly is selected and evaluated from the neutronic perspective. The layout of the SAFARI-1 core and the proposed core may be seen in Figure 2. It represents a 15 percent power reduction as compared to the current SAFARI-1 reactor operating power (20 MW). All parameters for this core are calculated and compared to the set limits and targets and is used to complete column 4 of Table 1. Note from the core layout that we have utilized the option of flooding the ex-core regions with beryllium elements in order to introduce some additional reactivity. Removed fuel elements, which facilitated the reduction of the number of

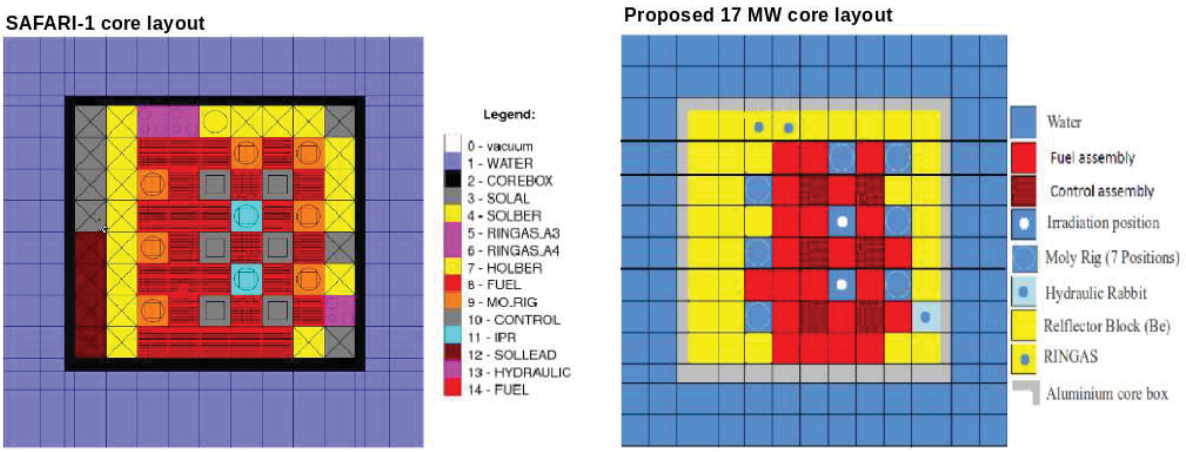

Figure 2. The Proposed 17 MW core layouts

fuel from 29 to 25, have also been filled with beryllium elements.
From the evaluation of this 17 MW core it can be seen that the reactivity, power density and production requirements all meet expectation, as is suggested by the preceding parametric study. It may be concluded that it is indeed possible to operate the SAFARI-1 reactor at a reduced power level, whilst maintaining the capabilities of the current core. Such a power decrease would save in fuel cost and potentially provide some life extension to the reactor.

5. Conclusion

The result present in Table 1 shown that an alternative core with a power of 17 MW can achieve similar performance as the current 20MW SAFARI-1 design, by simply rearranging components in the core. Additional power reduction may only be possible if more significant core design changes are allowed, but studies concerning such core concepts are still underway.

6. References

[1] Man Gyun Na, Dong Won Jung, Sun Ho Shin, Kibog Lee and Yoon Joon Lee October 2004 *Estimation of the Nuclear Power Peaking Factor Using In-core Sensor Signals* vol 36 Number 5 (Korean: Nuclear Society) pp 420–429

[2] Wagner F. S. 1982 *Global optimization method applied to the nuclear reactor core design* (Anderson Alvarenga de Moura Meneses Claudio do Nascimento Abreu Pereira) pp 441–456

[3] Prinsloo R. H., Moloko L., Stander G., Theron S., Tomasevic D. l., Reitsma F. and Mulle E. 2009 *OSCAR-4 Tutorial documentation* (NECSA Internal RRT document) (South Africa: South Africa Nuclear Energy corporation)

[4] Stander G., Prinsloo R. H., Muller E. and Tomasevic D. l. 2008 *OSCAR-4 Code System Application to the SAFARI-1 Reactor* (Proceedings of the International Conference on Reactor Physics, Nuclear Power, Interlaken, Switzerland, September 14-19).

Chromatic Dispersion Compensation for VCSEL Transmission for Applications such as Square Kilometre Array South Africa

E K Rotich Kipnoo, H Y S Kourouma, R R G Gamatham, A W R Leitch and T B Gibbon
Physics Department, Nelson Mandela Metropolitan University, P. O. Box 77000, Summerstrand South, Port Elizabeth-6031, South Africa
Email: Enoch.Rotich@live.nmmu.ac.za

Abstract-In addition to attenuation, optical fibre transmission suffers significant penalty from dispersion related effects. We theoretically and experimentally investigate the compensation of chromatic dispersion of 4.25 Gbps 1550 nm vertical cavity surface emitting laser (VCSEL) transmission using inverse dispersion fibre. Simulated results show that inverse dispersion fibre can compensate up to 3.7 dB on a 35 km ITU-T G.652 fibre. The residual dispersion penalties are small, thus effective compensation is achieved. In an experimental demonstration, a 25.4 km low water peak (LWP) fibre with a low negative dispersion value was found to improve the signal clarity when combined with a G.652 fibre. Inverse dispersion fibres cancel the cumulated dispersion in transmitting fibres, hence improving the VCSEL transmission significantly. This is a cost effective and simple chromatic dispersion mitigation technique, suitable for square kilometre array application as the transmission distances increase at different construction phases.

1. Introduction

Attenuation and dispersion in fibres are two factors that determine the distance information can be sent in an optical network. The two main types of dispersion in fibres are chromatic dispersion (CD) and polarization mode dispersion (PMD) [1]. With the modern fibres of low PMD values and the development in coherent transmission technologies [2], PMD which is a secondary effect has not been of a major concern. Vertical cavity surface emitting lasers (VCSELs) have shown a great potential in applications such as passive optical networks (PONs) [3,4]. This includes fibre to the home/curb/building/premise/node (FTTx) as well as wavelength division multiplexing (WDM) demanding applications. VCSELs are suitable for these applications because of low power consumption, wavelength tuneability, suitability for relatively short distance transmission, relatively low cost, high bandwidth, single mode operation within C-L bands and the convenience of direct modulation [5,6]. These VCSELs are however limited by the CD and chirp [4]. SKA South Africa is a big telescope project that is under construction. The construction is in different phases; KAT-7, MeerKAT, SKA 1 and SKA 2. KAT 7 consists of 7 dishes that are currently functional. The

MeerKAT phase will consist of 64 dishes and is currently under construction and will be completed in 2016. The number of dishes is expected to increase to about 3,000 extending out to about 3,000 km upon completion in 2025 [7]. This will constitute to 120 TB/s data for aggregation and processing. SKA distances between the individual dishes and the processing station for the various construction phases is expected to increase, for example, in the MeerKAT, the farthest dish is 12 km while in SKA 1, it will extend out to about 100 km from the central core. As the transmission distance increase, the effects of CD should be mitigated so as to boost the efficiency of the VCSEL and reduce the dispersion penalties. In this paper, we show the effect of chromatic dispersion compensation on the transmission performance of the 1550 nm VCSEL.

2. Theory

The inherent property of the fibre is responsible for the dispersion. Speed of light is dependent on the refractive index of the fibre. The refractive index therefore varies with wavelength. The different wavelengths in a light pulse will propagate with different group velocities, v_g in the fibre due to finite spectral widths of the signal thus resulting to group delay being dependent on the optical frequency, ω. This leads to spreading of pulse.

The group velocity is given by

$$v_g = \left(\frac{\partial \beta}{\partial \omega} \right)^{-1} \tag{1}$$

where v_g is the group velocity and β is the propagation constant. Different group velocities lead to group delay, T_G is given by

$$T_G = \frac{\partial \varphi}{\partial \omega} \tag{2}$$

where φ is the optical phase and ω is the optical frequency.

Differentiating T_G with respect to optical frequency, ω

$$\mathrm{D} = \frac{\partial^2 \varphi}{\partial \omega^2} \tag{3}$$

where D is the fibre dispersion.

Mathematically, D is the second order derivative of the optical phase with respect to the optical frequency as shown in equation (3). Second order dispersion parameter, β_2 describes the group-velocity dispersion (GVD), and is related to the dispersion parameter at the reference wavelength, λ as

$$\beta_2 = -\frac{\lambda^2}{2\pi c} D \tag{4}$$

Therefore dispersion, D in equation (3) can be rewritten as

$$D = \frac{\partial}{\partial \lambda} \left(\frac{1}{v_g} \right) = -\frac{2\pi c}{\lambda^2} \beta_2 \tag{5}$$

where v_g is group velocity, c is speed of light, β_2 is the group-velocity dispersion and λ is reference wavelength. Differentiating equation (5) with respect to wavelength, it yields the dispersion slope, S given by

$$S = \frac{\partial D}{\partial \lambda} = \frac{2\pi c}{\lambda^3}\beta_2 + \left(\frac{2\pi c}{\lambda^2}\right)^2 \beta_3 \qquad (6)$$

where S is the dispersion slope, β_2 is the group-velocity dispersion and β_3 is the third order dispersion parameter. At zero dispersion wavelength, β_2=0. So the dispersion slope is proportional to β_3 [3].

The broadening of the pulse limits the available bandwidth and transmission distance especially as the bit rates increase. Therefore to increase the transmission distance at increased bit rates some compensation is needed. Compensation approaches have been suggested [8, 9, 10,11,12], these are precompensation scheme that involve electronic chirp implementation on laser diode and modulator chirp, in-line compensation that make use of dispersion compensating fibre (DCF), fibre Bragg grating (FBG) and phase conjugation and lastly postcompensation scheme involving electronic equalization at the receiver.

Dispersion compensating fibre (DCF) is a fibre with large negative dispersion coefficient at 1550nm. It is used in optimizing 1550 nm transmission in a G.652 single mode fibre (SMF) [13]. The DCF is added to an existing SMF to cancel the dispersion. The length of the DCF required for compensation can be reduced by using fibres with very large negative dispersion coefficients [13]. Therefore, the higher the dispersion coefficient of the compensating fibre, the smaller the length. The relationship is given as

$$L_{DCF} \times D_{DCF} = -L_{SMF} \times D_{SMF} \qquad (7)$$

where L_{DCF} is the length of the DCF, L_{SMF} is the length of the SMF, D_{DCF} is the dispersion value of the DCF and D_{SMF} is dispersion value of the SMF.

The negative dispersion and dispersion slopes are achieved by doping the core of the compensating fibre. This makes it possible for the accumulated dispersion in transmission fibre over a wide range of wavelength [14]. The dispersion and dispersion slope of the DCF and transmitting fibre should be matched in order to compensate the accumulated dispersion effectively over all the wavelengths [15,16]. New design of DCF called inverse dispersion fibre (IDF) has been introduced [17]. It has high negative dispersion values depending on SMF to DCF length ratios and negative dispersion slope enabling dispersion and dispersion slope compensation [17,18]. This work presents the CD compensation using the IDF.

3. Research design

The experimental setup is as shown in figure 1. In this work, a 4.25 Gbps 1550 nm VCSEL was directly modulated and the signal transmitted over a SMF fibre. A large negative dispersion IDF of -54 ps/nm.km was used to cancel the cumulative dispersion introduced by G. 652 fibre at 1550 nm transmission. The dispersion for the standard SMF, G.652 was 17 ps/nm.km [19] and that of nonzero dispersion shifted fibre (NZDSF-), ITU-T G.655 was -2.8 ps/nm.km. A VOA was used to vary the input power on the photo detector as the BER measurements were performed. Different fibre lengths for G.652 fibre were also separately simulated and the BER obtained. The experimental validation with compensation was performed on a 36.9km (11.5 km G.652 fibre combined with 25.4 km Truewave submarine reduced slope (SRS)) fibre. This is compared to 11.5 km G.652 fibre transmission without compensation.

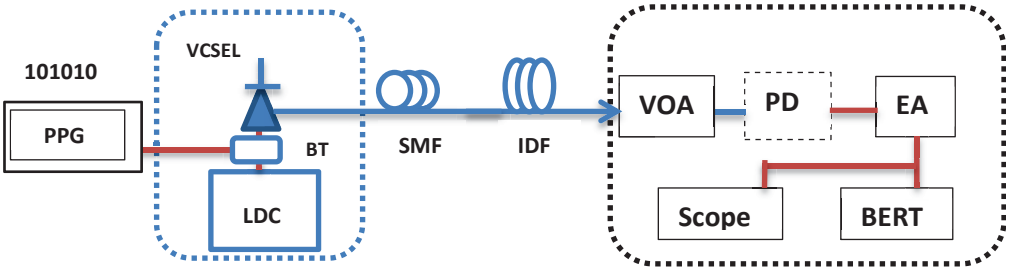

Figure 1: Setup for VCSEL transmission with CD compensation; PPG is pulse pattern generator, LDC is laser diode control, BT is a bias tee, SMF is single mode fibre, IDF is inverse dispersion fibre, VOA is variable optical attenuator, PD is photo detector, EA is electrical amplifier and BERT is bit error rate tester.

4. Results and Discussions

VCSEL are relatively low power devices. Figure 2 (a) shows the current power curve of the 4.25 Gbps 1550 nm VCSEL. The operating range is in mA with optimum performance at approximately 6 mA giving an output power of about 0.8 mW. The inset graph shows the wavelength tunability as the modulation current is varied from 2 mA to 9.9 mA. The signal wavelength is found to vary from 1545 nm to 1549.8 nm on tuning the modulation current. This is an advantage for applications such as wavelength division multiplexing (WDM) systems. Figure 2 (b) on the other hand shows the BER measurements for 1550 nm transmission on an ITU-T G.652 fibre. The error floor at acceptable BER threshold of 10^{-9} without CD compensation on an ITU-T G.652 fibre is about 35 km.

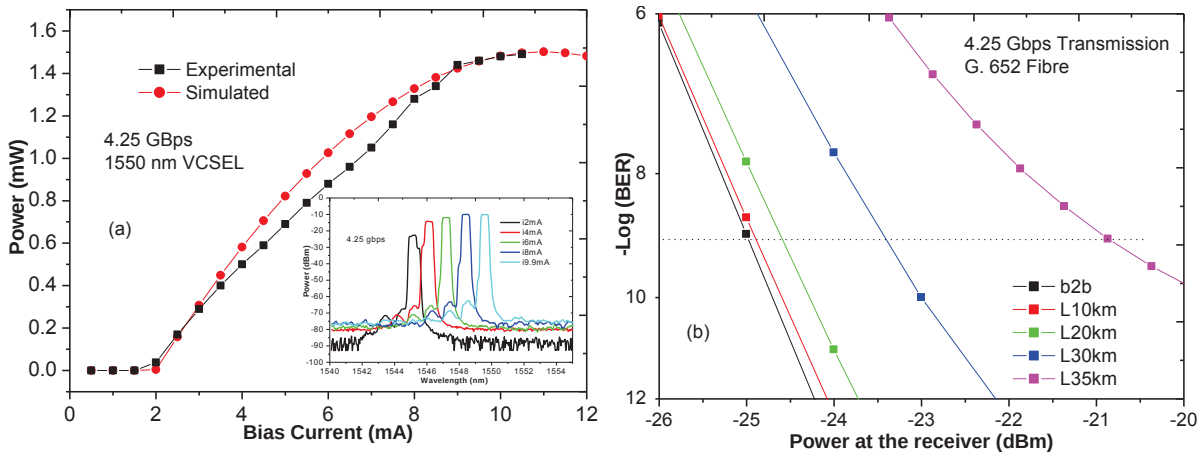

Figure 2: (a) 4.25 Gbps 1550 nm VCSEL characterization. Inset: wavelength tuneability on different bias currents (b) Simulated BER measurements on an ITU-T G.652 fibre without compensation.

Figure 3(a) presents the compensated case on a 35 km ITU-T G.652 SMF. In this transmission, 3.72 dB of power is compensated. A 10.4 km IDF fibre with dispersion value of -54 ps/nm.km was used. The dispersion slopes of SMF and IDF were 0.08 ps/nm^2.km and -0.18 ps/nm^2.km respectively. The IDF length is derived from equation (7), this relation is shown on the inset graph in figure 3(b). The power compensated is seen to increase with increase in the fibre length as shown in figure 3(b). This is due to cumulative dispersion effects in the fibre. With IDF, we are able to enhance the reach on a G.652 SMF using the 4.25 Gbps 1550 nm VCSEL with receiver sensitivity of about -24.5 dBm as shown experimentally in figure 4. In this regard, the transmission limitation is the attenuation which is about 0.3 dB/km on this G.652 fibre. This implies that with compensation, SKA phase 1 inner baselines (up to 50 km) clock transmission can be achieved using VCSELs. Figure 3 (a) shows that the residual dispersion is very small and amount to a penalty of about 0.4 dB over 35 km G.652 fibre, hence the compensation is efficiently attained.

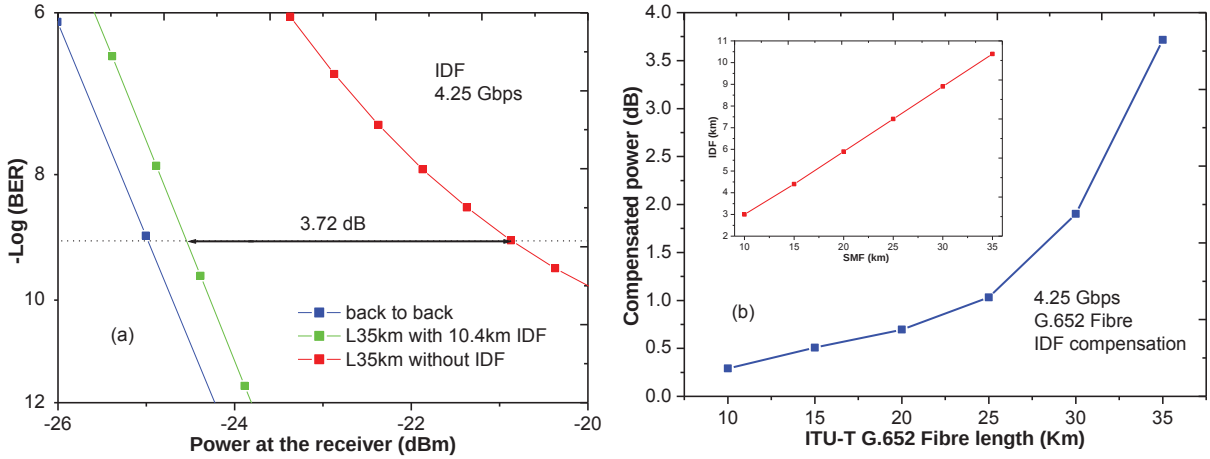

Figure 3: (a)Simulated BER curves showing compensated power in a 35 km G.652 with and without IDF compensation (b) Simulated compensated power with increasing fibre length in a 4.25 Gbps VCSEL. Inset: DCF and SMF relation.

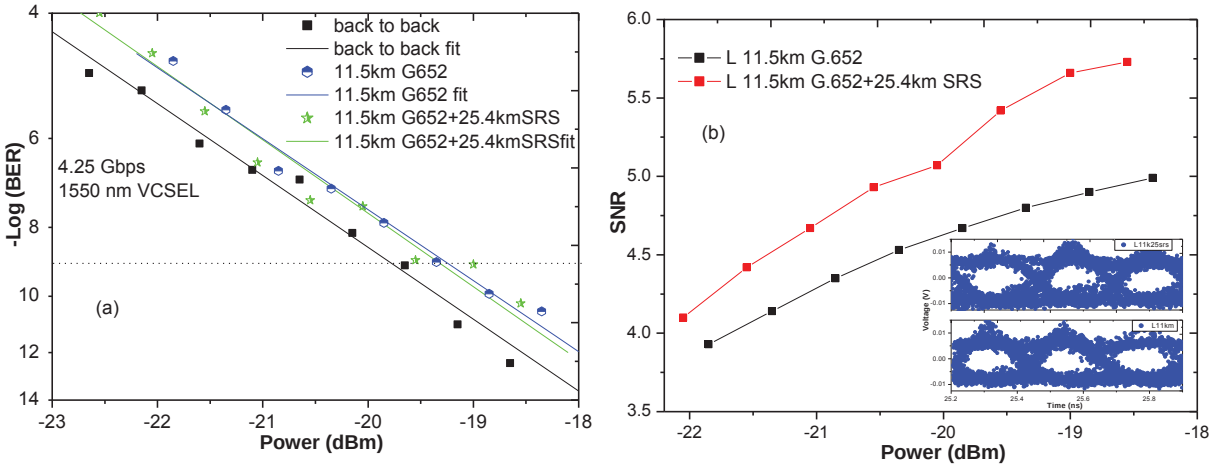

Figure 4: (a) Experimental BER estimation for 4.25 Gbps VCSEL transmission at 36.9 km (11.5 km G.652 combined with 25.4 km SRS fibre) and11.5 km G.652 fibre lengths. (b) Corresponding signal to noise ratios (SNR) Inset: Eye diagrams for 36.9 km and 11.5 km respectively.

In experimental investigation, non-return zero (NRZ) pseudorandom bit sequence (PRBS 2^7-1) was transmitted over 11.5 km G.652 and 36.9 km (a combination of 11.5 km G. 652 and 25.4 km SRS) fibres. An Avalanche photodiode (APD) receiver was used. The performance of the two fibres is shown in figure 4 (a) and (b).The penalties in both cases are less than 1dB. This is a relatively low penalty at this transmission rates. The quality factor (Q-factor) was used to estimate the BER. Details of using Q factor technique to estimate BER are given in [20]. Signal to noise ratio (SNR) of the signal is compared in figure 4 (b). We notice that in both cases, the eye is open. Considering transmission distance, the combined G.652 and SRS fibre (36.9 km) should have had reduced eye opening as compared to11.5 km G.652 fibre. The SRS fibre has low negative dispersion which cancels the dispersion thus improving the signal. This is observed on the signal strength as inferred from the SNR. However, the compensation in this case is not achieved fully because of low negative dispersion SRS fibre. IDFs have high negative dispersion values, therefore to cancel the dispersion of the transmitting fibres, short lengths are required. By combining the negative dispersion fibre with a positive dispersion one, we cancel the dispersive effects and eventually improving the signal clarity. This increases the VCSEL transmission distance without errors.

5. Conclusion

An inverse dispersion fibre is a promising dispersion management tool for VCSEL transmission. The use of IDF should solve the chromatic dispersion limitation in VCSELs by reducing the dispersion penalties and improving the quality of signal. A 3.72 dB compensated power has been achieved on a 35 km G.652 fibre. This has significantly improved the transmission distance of a 4.25 Gbps 1550 nm VCSEL attained without compensation. This should help in improving the VCSEL performance as well as the reach in applications such as access networks and SKA clock reference distribution.

Acknowledgement

This work is based on the research supported in part by the National Research Foundation (NRF) of South Africa (Grant 84352), Telkom, Dartcom, Ingoma, CSIR, THRIP, and Scholarship Funding from SKA/NRF.

References

[1] Goff D R 2003 *Fibre Optic Video Transmission 1st ed.*(Woburn Massachusetts)
[2] Infinera website 2012: www.infinera.com/pdfs/whitepapers/Infinera_Coherent_Tech.pdf, CA 94089 USA
[3] Kazovsky L, Cheng N, Shaw W, Gutierrez D and Wong S 2011 *Broadband Optical Access networks* (Hoboken New Jersey: Wiley)
[4] Gibbon T B, Prince K, Pham T T, Tatarczak A, Neumeyr C, Rönneberg E, Ortsiefer M 2011 VCSEL transmission at 10 Gb/s for 20 km single mode fibre WDM-PON without dispersion compensation or injection locking *Elsevier Opt. Fib. tech*. **17** pp 41-45
[5] Iga K 2000 Surface-emitting laser -its birth and generation of new optoelectronics field *IEEE J. Sel. Top. Quantum Electron*. vol. **6** pp 1201-1215
[6] Thienpont H and Danckaert J 2003 VCSELs and optical interconnects *SPIE Proc.* vol. **4942**
[7] Square kilometre array (SKA) website: http://www.ska.ac.za/index.php
[8] Zhang B, Zhao X, Christen L, Parekh D, Hofmann W, Wu M C, Amann M C, Chang-Hasnain C J, and Willner A E 2008 Adjustable chirp injection-locked 1.55-μm VCSELs for enhanced chromatic dispersion compensation at 10-Gbit/s*OFC/NFOEC* pp 1-3
[9] Aikawa K, Yoshida J, Saitoh S, Kudoh M and Suzuki K 2011 Dispersion compensating fibre module *Fujikura Technical review* pp 16-22
[10] Gumaste A and Antony T 2002 *DWDM Network Designs and Engineering Solutions* (Indianapolis, IN 46290 USA: Cisco Press) ISBN 1-58705-074-9
[11] He G S 2002 Optical phase conjugation: principles, techniques, and applications, *Prog. in Quant. Elect.* **26** pp 131–191
[12] Sano A, Miyamoto Y, KuwaharaS and Tobo H 2000 A 40 Gbps WDM transmission with SPM/XPM suppression through prechirping and dispersion management *J. of Lightw. Tech*. **18** issue 11 pp 1519-1527
[13] Agrawal G P 2001 *Nonlinear Fibre Optics 3rd Ed.* (San Diego: Academic)
[14] Grüner-Nielsen L, Wandel M, Kristensen P, Jorgensen C, Jorgensen L V, Edvold B, Pálsdóttir B, and Jakobsen D 2005 Dispersion-compensating fibres *J. of Lightw. Tech.* vol. **23** Issue 11 pp 3566-3579
[15] Goyal I C, Ghatak A K and Varshney R K 2002 Dispersion compensating fibres *proc. of 4th Int. Conf. on Transparent Optical Networks (ICTON)* Warsaw Poland
[16] Ramachandran S 2007 Fibre based dispersion compensation *OFC, Report 5* (New York USA: Springer) ISBN 978-0-387-40347-2 e-ISBN 978-0-387-48948-3
[17] Knudsen S N and Veng T 2000 Large effective area dispersion compensating fibre for cabled compensation of standard single mode fibre *Opt. Fib. Comm. Conf*. vol.**1** pp. 98-100
[18] Tokle T, Peucheret C and Jeppesen P 2004 System optimization of dispersion maps using new cabled dispersion compensating fibres *J. of Opt. Comm*. vol **25** Issue 2 pp 75–78
[19] International Telecommunication Union, ITU G-series 2009 Transmission systems and media, digital systems and networks; characteristics of a single mode fibre and cable
[20] Kaminow I P and Li T 2000 *Optical fibre telecommunications IV B* (San Diego: Academic) pp 172-177

Modelling and real time simulation of the instantaneous performance of residential air source heat pump water heater.

Stephen L. Tangwe, Michael Simon and Edson L. Meyer

Fort Hare Institute of Technology, University of Fort Hare, Alice, Eastern Cape, South Africa, Phone: +277406022086, Fax: +27 40 653 0665, e-mail: stangwe@ufh.ac.za

Abstract. Air source heat pump (ASHP) water heater extract low grade aero-thermal energy from the vicinity of the evaporator during vapour compression cycle in the production of sanitary hot water. The optimization of power and coefficient of performance (COP) of the system requires a detail and crucial investigation of compressor, condenser, evaporator, expansion valve and thermo physical properties of the refrigerant to ensure components are under steady state conditions for their optimal performance when the system is in operational heating up cycle mode. It is worth mentioning that this approach for optimizing system, is challenging and time consuming. Hence this paper appraises identifying primary and secondary predictors of the system performance and these variables were employed to develop a multiple linear regression model (OLS) of the power and COP. Since our goal was to develop a robust model, an optimization of the input variables was performed using constrained linear least square solver in the MATLAB optimization tool. Furthermore, a data acquisition system (DAS) was designed and built to measure ambient temperature, relative humidity, condenser, evaporator, inlet and outlet water temperatures of the ASHP. In addition, electrical power of the ASHP water heater and its water flow rate were also measured. The results showed that COP depends primarily on volume of water heated, temperature of the inlet and outlet water from the ASPH while the influence of ambient temperature and relative humidity were secondary. The predictors were ranked by weight importance using a function (relief) in the MATLAB statistical tool.

Air source heat pump (ASHP); Ordinary least square (OLS); Coefficient of performance (COP); Data acquisition system (DAS); Predictors weight ranking (ReliefF)

1. Introduction

The first heat pump water heater intended for mass production was designed and built by Calm in 1984 [1]. ASHP water heater is one of the heat pump types that operates on a vapour compression refrigerant cycle and has the capability of providing over two units of useful thermal energy just with one unit input of electrical energy when the system is in heating up cycle [2]. It is classified as a renewable device because it is capable of extracting majority of the waste thermal energy from the ambient as aero-thermal [3]. This special characteristic of heat pump that enables it to provide such a very high efficiency of 300% is called COP [4]. The instantaneous, seasonal or annual COP can be calculated using simulation with TRYSNY software package [5] and an analytic mathematical modeling correlating COP and temperature of solar assisted ASHP water heater [6]. The COP of ASHP water heater depends on various parameters including component design, heating load cycle, thermo-physical properties of refrigerant, ambient temperature, relative humidity and air speed through the duct space [7]. In this study, a multiple linear regression model for both the COP and power consumption was built using data obtained from seven heating up cycles (first hour heating rating condition) of a single phase 230 V, 1.2 kW SIRAC ASHP retrofitting a 200 liter hot water cylinder at different input cold water and ambient temperatures while the hot water temperature was set at 55^{o}C.

2. Materials and brief description

The DAS composed of two power track analyzers, power and energy meter, U30-NRC hobo data logger, two flow meters, 8 temperature sensors, UX120 hobo data logger, one ambient temperature and relative humidity sensor. The power track analyzers are power meters with an inbuilt data logger and were configured to log every one minute interval, the power consumption of the propeller axial fan connected to the rear end of the evaporator coils and the water circulation pump. The flow meters were connected to the water pipe supplying water into the inlet of ASHP and the other to the outlet hot water pipe delivering hot water to the building. The power and energy meter (T-VER-E50B2) was connected to the power cable of the ASHP water heater and measured the power consumption and power factor of the entire system. The temperature sensors were installed at the evaporator, suction line, discharge line, condenser inlet, condenser outlet, vicinity of the evaporator, inlet and outlet water pipes of the ASHP. The relative humidity and ambient temperature sensor measured relative humidity and the ambient temperature. All these sensors were connected to U30-NRC and UX120 hobo data loggers that were configured to be logging every one minute. These sensors carry an input pulse adapter attached to their connecting cables that convert the analogue signal to digital and hence reduces errors in the measurements. All the temperature sensors were well insulated to prevent reading from external interference. The relative humidity and ambient temperature sensor was enclosed by a solar radiation shield which prevented the sensor from damage by intense solar radiation and other climatic factors. The data stored in both the UX120 and U30-NRC was read out by hoboware pro software before it can be downloaded and exported for further analysis. The data were analyzed using the MATLAB software and based on the derived regression model for power and COP, a simulation was designed and built in the Simulink environment. Since the instantaneous power and COP were derived from an ordinary least square method, the results were optimized using constrained linear least square solver in the MATLAB optimization tool. Finally, predictors were ranked in importance of weight for both responses (power consumption and COP).

3. Data acquisition system and experimental setup

Figure 1 and 2 shows the combine installed heat pump water heater schematic block diagram layout of the setup and the DAS. The system was installed in a middle class home in Fort Bueafort, located in the Eastern Cape Province in South Africa. I (UX120) logged ASHP inlet water flow rate in counts (one count is equal to 3.7854 liters) and also the real energy in Wh, reactive energy in VARh and ampere hour in Ah are in the form of counts were 1 Wh and 1 VARh is equal to 1 count while 1 Ah is 100 counts. H and G (power track analyzers) measured the power consumed by fan and water circulation pump respectively. F (T-VER E50B2 power and energy meter) measured the power, energy and power factor of the ASHP water heater and the data are stored in J. The temperature sensors, flow meter to hot water outlet pipe from the tank, relative humidity and ambient temperature sensors are all housed by J (U30-NRC data logger). A is the compressor and on the suction and discharge lines were installed temperature sensors that measured temperatures of the refrigerant (R417A) at the aforementioned sides. B is the evaporator and the temperature sensors installed on the coils measured the evaporator temperature. E is the condenser and the two temperature sensors installed on either ends, measured the inlet and outlet temperature of the refrigerant in the condenser. C and D are the fan and capillary tube respectively. The temperature sensor in the pipe connected to ASHP with the flow meter measured water temperature into the inlet of the ASHP while the temperature sensor on the outlet pipe measured water temperature out from the ASHP. The storage tank served as a reservoir for hot water to be stored after attaining the set point temperature. There is also a strainer connected to the inlet water pipe into the ASHP, which helped to block debris from entering the unit and also a non-return gate valve at the outlet water pipe that stopped the exit water from flowing backward into the ASHP.

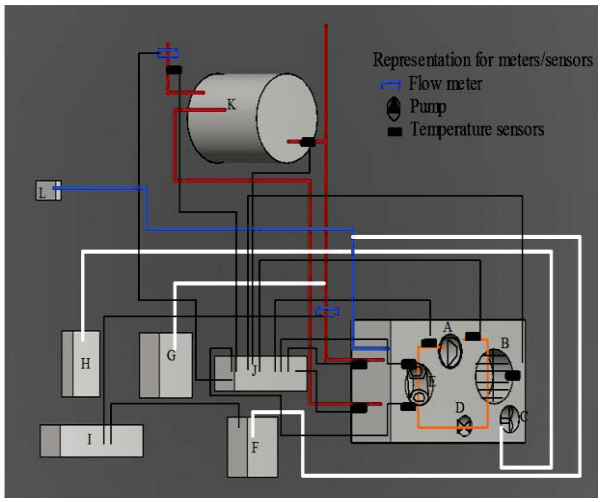

Figure 1: Schematic layout of setup

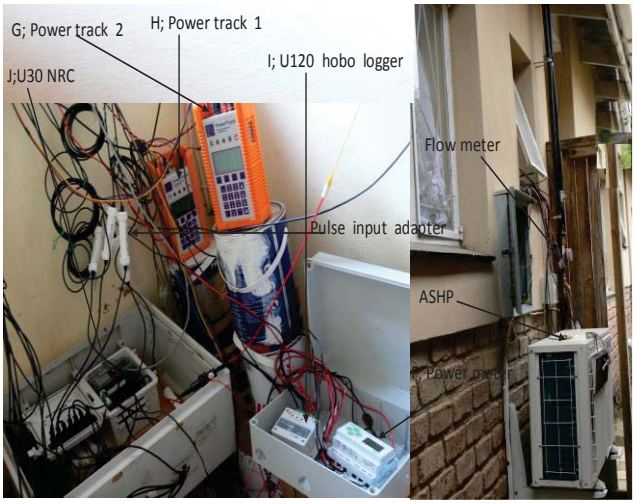

Figure 2: Shows system installs and DAS

3.1. Theory and determination of the multiple regression models

The data for the seven heating up cycles were integrated in a five minute interval. The measured power obtained from the power and energy meter and the calculated COP determined from the ratio of useful thermal energy output and the electrical energy input given in equation 1 below was considered as output for the model.

$$COP = \frac{mc(T_o - T_i)}{E_{in}} \quad (1)$$

The volume of water heated by ASHP (V_h), ASHP inlet water temperature (T_i), ASHP outlet water temperature (T_o) of the ASHP, the ambient temperature (Ta) and relative humidity (RH) were considered as input predictors. The m and c are the mass of water heated and specific heat capacity. The input power P_{in} and power factor (PF) is derived from the power and energy meter using the following formula given in equation 2 and 3 below.

$$p = \frac{Wh}{3600} \quad (2)$$

$$PF = \sqrt{\frac{(Wh)^2}{(Wh)^2 + (VARh)^2}} \quad (3)$$

A reliefF test was conducted to rank the input variables in order of importance of weights of the response [9]. The weight rank ranges from 1 to -1, 1 if the input variable has a strong correlation with the output and -1 if no correlation exist between the input and output. If the weight is positive the input variable is a primary factor for the output and if negative is a secondary factor. The rank weight for the power as depicted by the bar chart in figure 3 below showed that all five input variables were primary factor to the ASHP water heater power with outlet water temperature ranked the most important followed by volume of water heated and least is relative humidity. The rank weight for the COP show that the volume of water heated, ASHP inlet water and ASHP outlet water temperatures are primary factors while ambient temperature and relative humidity are secondary factors. The order of rank weight importance showed volume as most important and relative humidity as least as shown in figure 4 below.

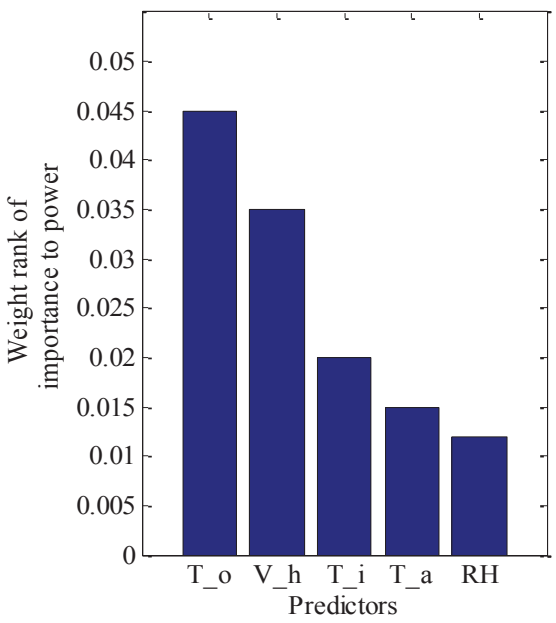

Figure 3: Predictors weight ranking to power

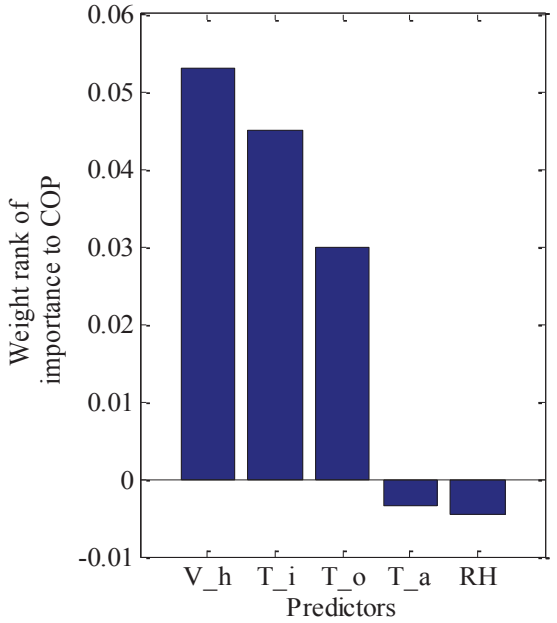

Figure 4: Predictors weight ranking to COP

3.1.1. Multiple regression model for the power consumption of ASHP water heater

The regression model of the power consumption of the ASHP water heater built from the above predictors is given by equation 4 below where $\omega_0, \omega_1, \omega_2, \omega_3, \omega_4$ and ω_5 are the scaling parameters and V_h, T_i, T_o, T_a and RH are input parameters [8].

$$p = \omega_0 + \omega_1 V_h + \omega_2 T_i + \omega_3 T_o + \omega_4 T_a + \omega_5 RH \quad (4)$$

The coefficients of the scaling parameters are given in table 1 below.

Table 1: Input parameters and scaling constants for the power multiple regression model

Predictor	Symbol	Scaling notation	Scaling factor	Output
Volume heated	V_h	ω_1	0.0054	Power (p)
ASHP inlet temp	T_i	ω_2	-0.0060	
ASHP outlet temp	T_o	ω_3	0.0201	
Ambient temp	T_a	ω_4	0.0081	
Relative humidity	RH	ω_5	0.0021	
Forcing Constant		ω_0	0.2196	

The scaling values predict that power consumption would increase with the increase in volume of water heated, ASHP outlet water temperature, ambient temperature and relative humidity. The power consumption is likely to increase if the initial cold water temperature is very low.

2.3.2. Multiple regression model for the COP of ASHP water heater

The regression model of the COP of the ASHP water heater built from the above predictors is given by equation 5 below where $\kappa_0, \kappa_1, \kappa_2, \kappa_3, \kappa_4$ and κ_5 are the scaling parameters and V_h, T_i, T_o, T_a and RH are input parameters.

$$COP = \kappa_0 + \kappa_1 V_h + \kappa_2 T_i + \kappa_3 T_o + \omega_4 T_a + \kappa_5 RH \quad (5)$$

The coefficients of the scaling parameters are given in table 2

Table 2: Input parameters and scaling constants for the COP multiple regression model

Predictor	Symbol	Scaling notation	Scaling factor	Output
Volume heated	V_h	κ_1	0.0448	COP
ASHP inlet temp	T_i	κ_2	-0.0164	
ASHP outlet temp	T_o	κ_3	-0.0542	
Ambient temp	T_a	κ_4	0.0703	
Relative humidity	RH	κ_5	0.0194	
Forcing Constant		κ_0	1.8669	

The scaling values predict that COP increased with increased in volume of water heated, ambient temperature and relative humidity. The COP is likely to increase if the cold water temperature is higher and hot water temperature reduced to a lower set point.

4. Results and discussion

4.1. Variation of temperature dependent input variables with COP

The profile of ASHP outlet water, ASHP inlet water and ambient temperatures (T_o, T_i and Ta) and COP for one typical heating up cycle (5 th cycle shown on table 4) was analyzed. This profile is divided into three zones A, B and C. At start time, corresponding to zone A, the thermal energy is zero and both T_o and T_i are equal. In zone B, ASHP inlet water is heated to set point temperature and as ambient temperature increases the COP also increase, although is not much significant as if the hot water temperature was at a lower set point temperature. The COP can also increase if the cold water is at a relatively high temperature. The COP again drops significantly at zone C since the power of an ASHP water heater is switched off in this zone, hence no further heating. This heating up cycle was completed in about 80 minutes with 15 minutes used at both zone A and C. The average COP for the cycle is over 3.2 due to the high average ambient temperature of 37^{o}C and cold water temperature of 24^{o}C. The COP is maximum when the difference in temperature between T_o and T_i is maximum. The profile of the air temperature in the vicinity of the evaporator shows a 4^{o}C difference with ambient temperature profile due to the shading effect occurring at the location of the installation of ASHP but there was no mean significant difference if either of the two was used in the power or COP modeled.

4.2. Variation of volume of heated water and relative humidity with system COP

The profile for the 5 th heating up cycle shows that the volume of water heated pattern was strongly in correlation to COP since is a primary factor. However, relative humidity is decreasing slowly insinuating COP will decrease theoretically. But it is not the case practically, as relative humidity is a secondary factor and least in the ranking by weight of importance to the COP. Furthermore, during this heating up cycle the initial cold water temperature was 24^{o}C which is in the range of cold water temperature of ASHP water heater to operate with maximum COP. Again, both the volume of water heated and ambient temperature were increasing and hence enhance COP. The zones A and C represent the performance phase without the flow of incoming cold water and the termination phase when the ASHP power is switched off.

4.3. Comparative analysis of input variables to the measured and modeled output

The table 4 below summaries the average input variable values for each of the heating up cycle and the actual (calc) and modeled responses they produce. The table 4 also shows that the ASHP water heater has the highest efficiency in the 5th heating up cycle where the total volume of heated water (V_T) and average power consumption are greatest. The initial cold water temperature for this heating up cycle is higher when compared to the rest of the heating up cycles. Despite the relative humidity is low when

compared to the heating up cycles 1,2,3,4 and 7, this is only a secondary factor and is least rank by weight of importance.

Table 4: Show a comparative analysis of the inputs and output both measured and modeled

Cycle No	Total V/L	mean T_i/°C	mean T_o/°C	mean T_a/°C	mean RH /%	mean Calc COP	mean Model COP	mean Calc p/kW	mean Model p/kW
1	246.1	19.1	52.1	15.7	76.5	1.80	1.85	1.37	1.35
2	234.7	20.4	51.4	16.4	69.4	1.76	1.70	1.35	1.37
3	253.6	19.4	52.3	12.8	79.6	1.64	1.67	1.35	1.34
4	488.3	24.6	56.1	37.9	23.5	3.28	3.30	1.48	1.46
5	529.9	26.7	55.8	39.7	19.1	3.41	3.43	1.51	1.51
6	454.2	24.7	55.4	40.3	17.3	3.14	3.04	1.47	1.46
7	355.8	23.3	53.4	27.9	57.9	2.82	2.64	1.44	1.44

5.0 Conclusion

The results from our research depict that the heating up cycle under the first hour heating mode with the best COP is also having the highest average power consumption, although is of no mean significant difference compared to the rest of the heating up cycles. The performance of ASHP water heaters with fan of constant speed can be accurately evaluated using a multiple linear regression model of power and COP correlating all the predictors. Furthermore, running an optimization using constrained linear least squares to test the efficiency from the objective function value can help improve accuracy of the data set used as predictors in the models. During the heating up cycles were all input variables are changing, the instantaneous or average COP is dominated by the primary factors drivers. Albeit, relative humidity and ambient temperature also affected performance but are secondary factors. Finally, it was deduced that the modeled power and COP are related to optimized power and COP by ± 0.01 and ± 0.04 respectively. The results also show that in all the seven heating up cycles, no predictors remain constant, but the COP value is dominated by primary factors.

References

[1] Calm, J.M. 1984. Heat Pump Water Heaters. Electric Power Research Institute (EPRI), Palo Alto

[2] Levins, W.P. 1982. Estimated Seasonal Performance of a Heat Pump Water Heater Including Effect of Effects of Climatic and In-House Location. Oak Ridge National Laboratory, Oak Ridge, TN.

[3] Marrison, G.L., Anderson, T. and Behnia M. (2004). Seasonal Performance Rating of Heat Pump Water Heaters. School of Mechanical and Manufacturing Engineering, University of New South Wales, Sydney, Australia. Energy Conservation and Management.76:147-152.

[4] De Swardt, C. and Meyer, J.P. The Performance of a Municipality Water Reticulation Ground-Source Reversible Heat Pump System Compared to an Air- Source System, South Africa's 10th International Air Conditioning, Refrigeration & Ventilation Congress, Gallagher Estate, Midrand, paper no: 16, 7 pages, 8 – 10 March 2000.

[5] Kline et al., 2000. TRNSYS 15 a Transient System Simulation Program. University of Wisconsin Solar Energy Laboratory Available from http.//sel.me.wisc.edu/TRNSYS/Default.htm.

[6] Marrison G.L. 1977. TRNSYS Extensions (TRNAUS). School of Mechanical and Manufacturing Engineering, University of New South Wales, Sydney, Australia. Report STEL/1 1997

[7] Itoe, S., Miura, N., Wang, K., 1999. Performance of Heat Pump using Direct Expansion Solar Collector. Solar Energy V65, 189-196

[8] Chatterjee, S and A.S. Hadi; Influential observations, High leverage points and outliers in linear regression Statististical science. Vol 1.1986, PP 379-416

[9] Robnik-Sikonja and Kononenko, L. (2003): Theoretical and empirical analysis of RELIEFF. Machine learning. pp 23-69

Elemental analysis of Kimberlite and associated Country Rock

Marius Tchonang[1], Martin Cook[1], Faan Bornman[2], Simon Connell[1] and Sergio Ballestrero[1]

[1] Physics Department, University of Johannesburg, PO Box 524 Auckland Park
[2] Multotec Process Equipment (Pty) Ltd

E-mail: mariust82@gmail.com

Abstract. The elemental analysis of kimberlite and country rock was performed as part of an ongoing study into the Mineral-PET online rock sorting technique. This is a technology proposed to locate high densities of carbon in kimberlite and country rock using the very well known medical physics technique called Positron Emission Tomography (PET). Carbon in kimberlite is not a natural positron emitter; one has to convert the naturally occurring carbon into a positron-emitting isotope. In this case it is done through the photo-nuclear transmutation reaction $^{12}\mathrm{C}(\gamma, n)^{11}\mathrm{C}$. We accomplish this reaction by irradiating the host rock using gamma rays with energies in the Giant Dipole Resonance (GDR) region. It is then important to determine the full inventory of radioisotopes produced in this process. The irradiation of kimberlite was performed using the 100 MeV electron microtron at Aarhus University in Denmark. In this paper, we first describe the experiment, and then perform an analysis of the data. This provides quantitative identification of the prompt, short, mid-term and even long-term radioactivity of irradiated kimberlite. This is necessary in order to assess more efficiently the radiation safety of the equipment and people working in the facility. A unique feature of this analysis in the unambiguous identification and quantification of each radioisotope formed by the two dimensional spectroscopy of the energy and the emission time of the signature gamma lines using time differential spectroscopy.

1. Introduction

The extraction of diamonds from excavated rocks has to date been an uneconomical process requiring lot of energy. In a typical diamond mine, the rocks are first coarse-crushed into pieces of about 10 to 15 cm diameter and then ultimately crushed into pieces of some few millimetres. It is then assumed that most of the diamonds will be liberated or exposed at the surface. Different techniques are then used to extract them [1]. This method is inefficient since only a small fraction of the rock contains diamond. Mineral-PET proposes a more economical method where, after the coarse crush, only diamond bearing rock could be further processed. A similar approach has been used in the well known medical Positron Emission Tomography (PET), but rather than introducing the positron emitter in the patient, it is produced within the host rock by irradiating it with a photon beam with energies in the Giant Dipole Resonance (GDR) region [2, 3]. It is important to determine the full inventory of radioisotopes produced in the irradiation process. The irradiation was performed using the 100 MeV electron microtron at Aarhus University in Denmark. Time differential gamma-ray spectroscopy is used to identify the peaks of the spectrum. The possible primary reactions in the host rock are (γ, n), (γ, p),

(γ, α), $(\gamma, 2n)$ and $(\gamma, n + p)$. The products of these reactions can interact with the host rock in many other secondary reactions. furthermore, we assess all the nuclides involved in the activation of kimberlite as the viability of the mineral-PET technique relies on this assessment. The time differential gamma-ray spectroscopy offers the advantage of allowing the identification of active isotopes based on both lifetime and energy, rather than only the energy, which is the only information available in normal gamma ray spectroscopy.

2. Experiment

The Aarhus 100 MeV electron Microtron irradiation system is used to irradiate a piece of kimberlite rock. This facility is equipped with an irradiation stage for the samples. The beam energy can be modified by the use of degraders. The electron current and irradiation time are measured. The electron and photon irradiation spectrum distribution is modelled with Monte Carlo transport calculations. The irradiation dose details can therefore be controlled, measured and modelled. In the example below the irradiation condition was 100 MeV electrons incident on a 2 mm stainless steel exit port.

A piece of Kimberlite rock is irradiated, keeping the sample in position in front of the beam exit point. The irradiation time was 1000 s for a dose of 5.25×10^{13}electrons/cm^2. Note that this is about 17 times the anticipated dose in the Mineral-PET facility[5]. After irradiation, a gamma spectroscopy system based on event-by-event acquisition implemented on a VME standard records time-stamped energy data for each event. The data is analyzed offline in a time differential manner, to provide both the gamma-line energy and lifetime. One detection run therefore yields complete information about both the energies and lifetimes of all isotopes present, allowing for unique isotope identification in most cases.

3. Data analysis and results

3.1. Method

The time-stamped energy data is collected for each event and a calibrated energy histogram is plotted. From figure 1, the different peaks corresponding to diverse energy lines present in the spectrum can easily be distinguished . The graph in figure 1 presents many peaks with the most visible ones being at 511 keV, 846 keV, 1271 keV, 1365 keV, 1432 keV, 1460 keV, 1730 keV, 2164 keV, 2241 keV and 2754 keV. A time differential energy spectrum of the irradiated kimberlite shows that the height of the peaks varies with time. Figure 2 shows the dominance of the 511 keV peak, and also some very short-lived peaks vanishing before 1000 s. One can also distinguish very long-lived peaks with the intensity remaining almost constant for a few hours. The data is time sliced with different time bin sizes depending on the number of events required to have a histogram representing the different peaks. The peaks are fitted with an asymmetric gaussian and the area under the fit for every time slice is calculated[4]. This yields the peak intensity (area) as a function of the time. The lifetime of each energy line as a function of the time can be extracted from the peak intensity for different time slices . These new data is fitted with an exponential decay. In the cases with interfering peaks, two components in the decay of the line were included. The energy of the line and the half-life yields an unambiguous isotope identification using a database of nuclide level schemes[6].

Figure 3 presents the histograms and the asymmetric gaussian fit for the 511 keV peak for different time slices. The histograms and the fits are stacked, remaining exactly at the position 511 keV. In figure 5, the peak tends to be moving which suggest the 845.8 keV might be a combination of two very close lines with the centres at 844 keV and 846 keV.

3.2. Results and discussion

The single decay fit of the 845.8 keV line shown in figure 5 gives a lifetime of 94 minutes with some discrepancies in the early and the latter part of the spectrum. This suggests a two

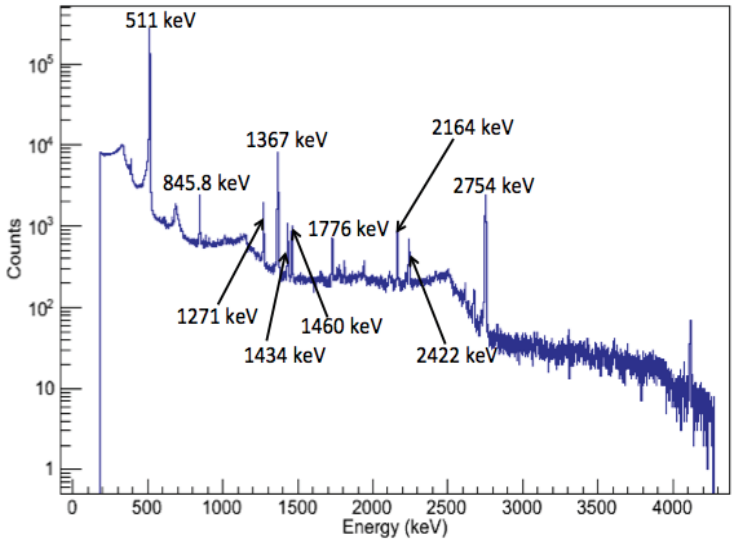

Figure 1. Calibrated energy spectrum with the dominance of the 511 keV PET line

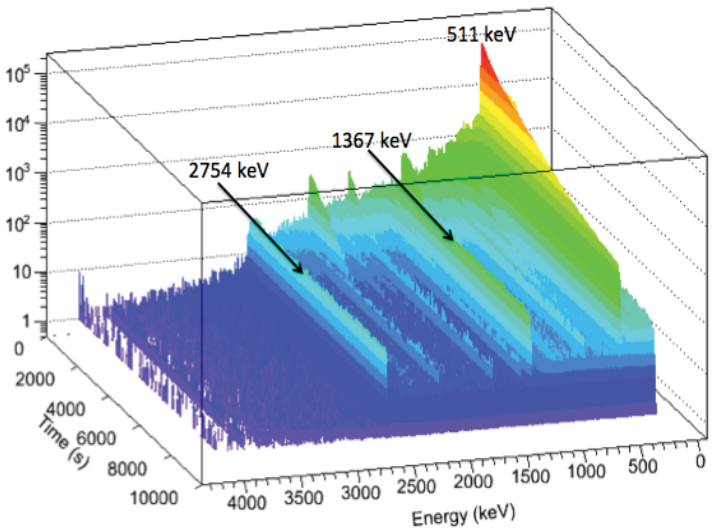

Figure 2. Time differential gamma spectroscopy for life-time determination for each gamma-line

component fit of the data. For the long-lived component of the fit, the possible candidates are ^{87}Kr with lifetime of 76.3 min 9 s and ^{56}Mn with a lifetime of 2.58 h. ^{87}Kr could come from neutron absorption on the natural ^{86}Kr but from the kimberlite composition, it is highly unlucky that krypton could be present in the environment[7]. ^{56}Mn is either from neutron capture on ^{55}Mn (abundance 100%) which is present in kimberlite or from (γ, p) and $(\gamma, n+p)$ reactions on different iron isotopes, also present in kimberlite. For the short-lived component, we fixed the long-lived one to ^{56}Mn and extracted a lifetime of 10 min for the unknown short-lived isotope. Figure 6 shows the two best candidates with lifetimes shorter and longer than 94 minutes, namely 56Mn with half-life 155 m and 27Mg with half-life 9.5 m. ^{27}Mg is probably from neutron capture

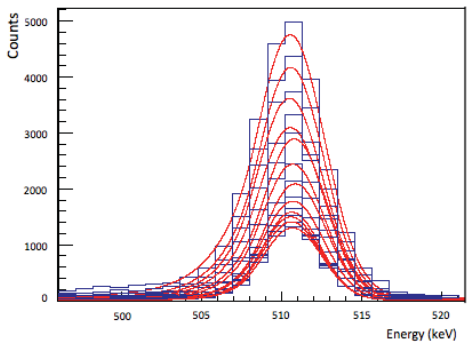

Figure 3. Single spectrum for the 511 keV gamma-line for consecutive time slices.

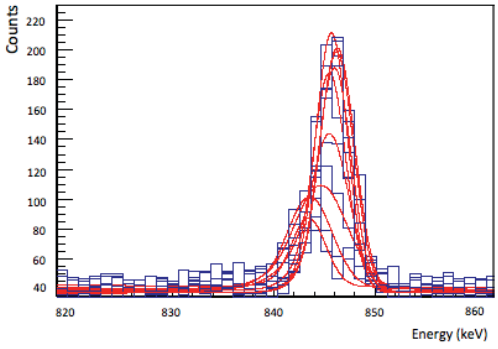

Figure 4. Single spectrum for the 845.8 keV gamma-line for consecutive time slices.

on stable ^{26}Mg or (n,p) reaction on ^{27}Al.

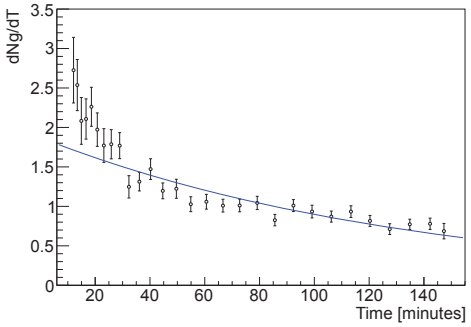

Figure 5. One decay best fit of the 845.8 keV signal with the fit missing the data after 100 min.

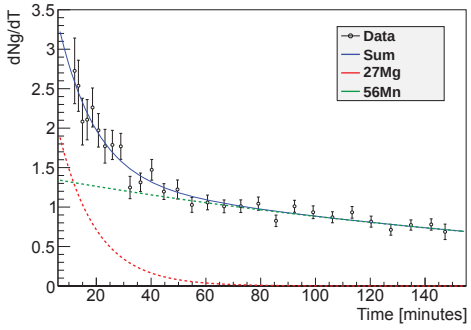

Figure 6. Lifetime spectrum of the 845.8 keV signal which is a sum of 2 decays: magnesium and manganese.

Similar procedure allows for the identification other lines and the results are presented in Table 1. There are many other small peaks which are most probably noise from adjacent intense ones. Some of these lines come from the same isotope but at different energy or even from a process known in gamma-ray spectroscopy as single or double escape peaks[8]. This is the case for the 1653 keV and 1143 keV respectively. We also have a peak at 2675 keV which comes from a single pile-up (2164 keV collected simultaneously with a 511 keV gamma ray).

Table 1. List of peaks with the parents, half-lives and possible processes leading to the isotopes or peaks.

Energy (keV)	Parents	Halflife	Process
511	^{11}C	20min23s	(γ,n) on ^{12}C
	^{15}O	2min2s	(γ,n) on ^{16}O
	^{13}N	10min	(γ,n) on ^{14}N
845.8	^{27}Mg	9min27s	n-capture on ^{26}Mg/(n,p) on ^{27}Al
	^{57}Mn	2h35min	(γ,p) on ^{57}Fe, (γ,n+p) on ^{58}Fe or n-capture on ^{55}Mn
1271	^{29}Al	6min40s	(γ,p) on ^{30}Si or (n,p) on ^{29}Si
1367	^{24}Na	15h	n-capture on ^{23}Na/(γ,p) on ^{25}Mg
1434	^{52m}Mn	21min7s	(p,n) on ^{52}Cr
1460	^{40}K	1,27 billion y	n-capture on ^{39}K
1776	^{29}Al	6min40s	(γ,p) on ^{30}Si or (n,p) on ^{29}Si
1809	^{56}Mn	2h35min	(γ,p) on ^{56}Fe or n-capture on ^{55}Mn
2164	^{38}K	7min56s	(γ,n) on ^{39}K
2422	^{29}Al	6min40s	(γ,p) on ^{30}Si or (n,p) on ^{29}Si
2754	^{24}Na	15h	n-capture on ^{23}Na / (γ,p) on ^{25}Mg

4. Conclusion

We irradiated a kimberlite sample using a 100 MeV electron beam to produce a bremsstrahlung radiation. Note that this energy is higher than the Mineral-PET energy, however this experiment gave a good idea of the different radioisotopes that would be produced during the activation process of Mineral-PET. We were able to unambiguously identify the contributors to the dominant gamma lines together with their lifetimes. A conclusive identification of some of the peaks could not be made because they were absorbed by noise. This is also the reason the lifetime spectra are taken after 10 min. The time taken to get the sample to the detectors and the initial period where the detectors are swamped were also taken into consideration. The use of the lifetime data can be seen here as a revolution in gamma-ray spectroscopy because without these data, many identifications would not have been possible. The next step in this analysis will be to identify all the remaining gamma lines, and based on the chemical composition of kimberlite use software like say FISPACT to inventory all the nuclear reactions that lead to the production of these radioisotopes.

References

[1] M. S. H.O.A. Meyer, Natural Diamond, Ch. 10 in Handbook of industrial diamonds and diamond films (CRC Press, 1988).
[2] G. Muehllehner and J. Karp, Phys. Med. Biol. 51, R117 (2006).
[3] G. C. Baldwin and G. S. Klaiber, Physical Review 711, 3 (1947).
[4] Medhat et al, PRAMANA– Journal of Physics, Vol. 65, No 2 August 2005, pp.245-258
[5] S. Ballestrero et al, CERN-Proceedings-2010-001: Proceedings of the 12th Varrenna Conference on Nuclear Reaction Mechanisms, July 2009.
[6] nucleardata.nuclear.lu.se/toi/radSearch.asp (last access on 17th July 2014)
[7] T.R. Mcgetchin, The American Mineralogist, Vol 55, September-October 1970
[8] Kenneth S. Krane, 1988. Introductory Nuclear physics. 1st ed. New York. John Wiley& Sons.

Pulse Delay Chromatic Dispersion Measurements in Single Mode Fibre

S Wassin, E K Rotich Kipnoo, R R G Gamatham, A W R Leitch and T B Gibbon
Physics Department, Nelson Mandela Metropolitan University, P. O. Box 77000, Summerstrand South, Port Elizabeth-6031, South Africa.

Email: Shukree.Wassin@live.nmmu.ac.za

Abstract. – In recent years, there has been a rising demand for high bandwidth in long haul fibres to assist with high-speed data transmission. Chromatic dispersion limits high-speed data transmission making it essential to perform chromatic dispersion measurements. Chromatic dispersion measurements play an important role during the manufacturing processes of the optical fibre, in characterizing the different types of optical fibre, when designing optical networks and in transmission penalty estimations. In this paper, a unique laboratory setup based on the pulse delay technique was used to characterize the chromatic dispersion in a single mode fibre. The chromatic dispersion of a 6.1 km long G.652 single mode fibre was measured within the 1550 nm to 1553 nm wavelength range. The dispersion values obtained were in the region of 15.3-20.0 ps/nm.km, which compares well with the theoretical values for the G.652 optical fibre.

1. Introduction

The transmission of data over long haul optical fibre cables at speeds of 40 Gbps or higher is an essential asset to the telecommunication industry as it is of valuable assistance to those making use of the Internet and its applications such as teleconferencing. Optic fibre does not only play a pivotal role in the telecommunication industry but it is also an important component in the field of medicine, where it is used in laparoscopic surgery and also in laser surgery. Other uses such as the transmitting of high power laser beams and fibre optic sensors also rely on optical fibre. However nonlinear effects, attenuation of the optical signal, polarization mode dispersion and chromatic dispersion can interfere with the high-speed data transmission. These effects are but a few detrimental factors that limit the optical fibre to perform at its peak. In this paper, chromatic dispersion is discussed and an accurate experimental method for measuring chromatic dispersion is described. This method is based on the pulse delay measurement technique. This type of measurement is important to be made as it provides a better understanding of the fibre and its characteristics when selecting the correct fibres for different network designs and during the manufacturing process of fibre.

2. Theory

Suppose an optical signal propagates along a fibre having a distinct pattern of 1's and 0's where a 1 will indicate the existence of light and a 0 indicates the lack of light as depicted in figure 1(b). The pulses denoted by a 1 can be regarded as a wavepacket consisting of several waves, where each has a distinct wavelength [1]. As it moves along the fibre some of these wavelengths will travel faster than others because of the inherent dependence of the refractive index on the wavelength. This results in

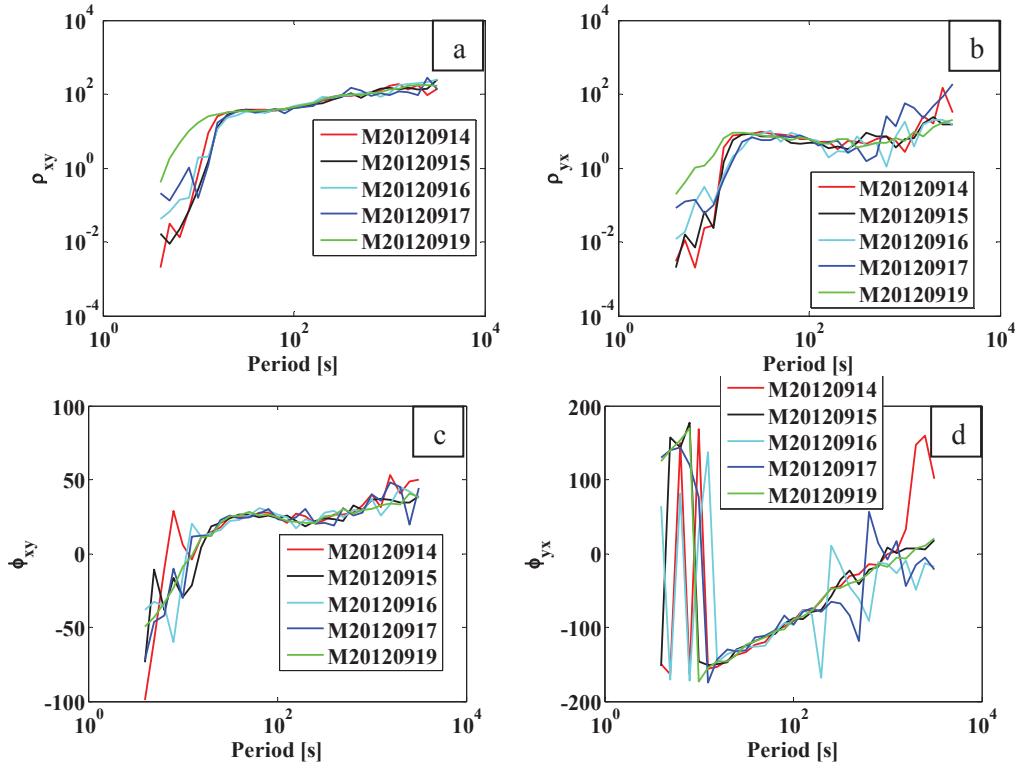

Figure 1. The solid lines show the estimates of the off-diagonal elements of the apparent resistivity using robust processing for five subsequent days. Apparent resistivity (a,b) and impedance phase (c,d) as function of periods at Middelpos site. The similarity of the ρ_{xy} and ρ_{yx} values indicate a fairly isotropic ground resistivity at Middelpos in the frequency range corresponding to periods of 10 to 100 s

given mode travelling through the fibre travels at different speeds depending on the wavelength of light. This occurs because the group velocity V_g of a particular mode is a function of the refractive index of the fibre [4]. Material dispersion is an intramodal form of dispersion. Waveguide dispersion arises because a single mode fibre confines 80 percent of the light to core and 20 percent of the light to the cladding. Because the light confined in the cladding travels faster than the light confined to the core, dispersion occurs within the fibre which gives rise to pulse spreading [4].

The pulse delay measurement technique, the phase shift measurement technique, the differential phase shift measurement technique and the interferometric measurement technique are the preferred methods adopted for measuring the chromatic dispersion [1,5,6]. The pulse delay method makes use of the time of flight approach, where the time delay between two pulsed light of different wavelengths are measured. This method requires the use of a broadband laser source with high peak power. The pulse delay measurement technique has the ability to resolve a 50 ps to 100 ps time delay between two successive pulses. This is the smallest time delay that can ne measured by this method, making it inadequate for characterizing optic fibre cables shorter than 0.5 km [7].

3. Experimental Procedure

This experiment was conducted in a laboratory environment where the chromatic dispersion was measured in 6.1 km of G.652 single mode fibre. The experimental measurement technique was uniquely designed and assembled using bench-top equipment and laboratory components. The technique is based on the pulse delay method and the setup is illustrated in the figure 3.

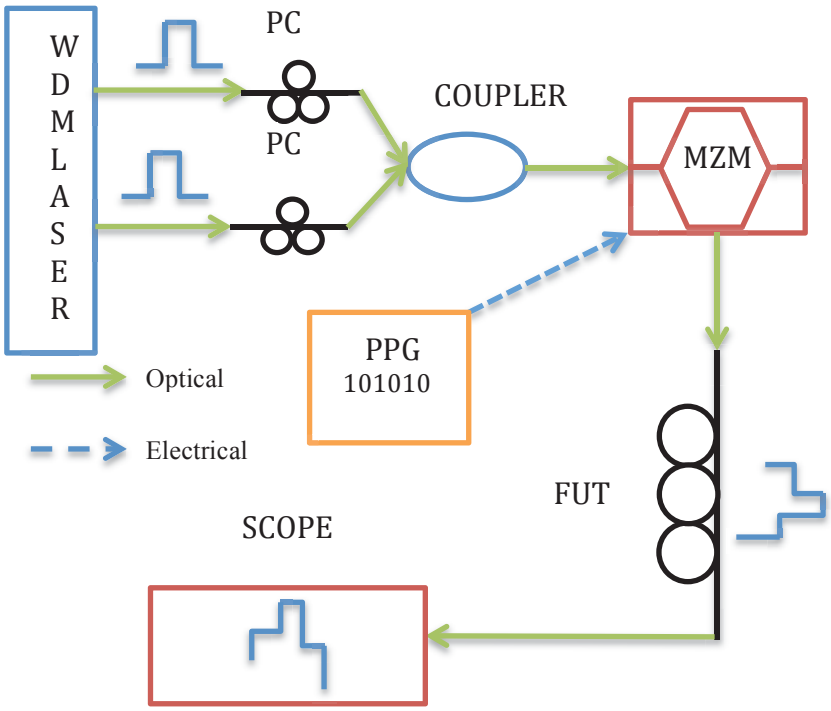

Figure 3. Schematic of the pulse delay setup.

An eight-channel wavelength division multiplexer (WDM) laser source, provided continuous light. A Mach-Zehnder modulator (MZM) modulates the intensity of the light, which generated the optical light pulses transmitted through the 6.1 km long G.652 single mode fibre. The pulse adopted a specific sequence of 1's and 0's set by a pulse pattern generator (PPG). The Mach-Zehnder modulator (MZM) is polarization sensitive. Hence manual polarization controllers were used to adjust the state of

polarization of the input signal. This was done in order to maximize the efficiency of the Mach-Zehnder modulator. The chromatic dispersion in the fibre under test (FUT) can then be determined as a function of wavelength from pattern collected on the oscilloscope as described below.

4. Results and Discussions

The question presented was, what actually happens as the two pulses of different wavelength travels through the fibre? Due to the difference in propagating speeds of the input pulses, the individual pulse combine to form a broadened and disfigured pulse as indicated in figure 4. The solid lines denote the delay experienced between the two pulses as a result of the different propagation speeds.

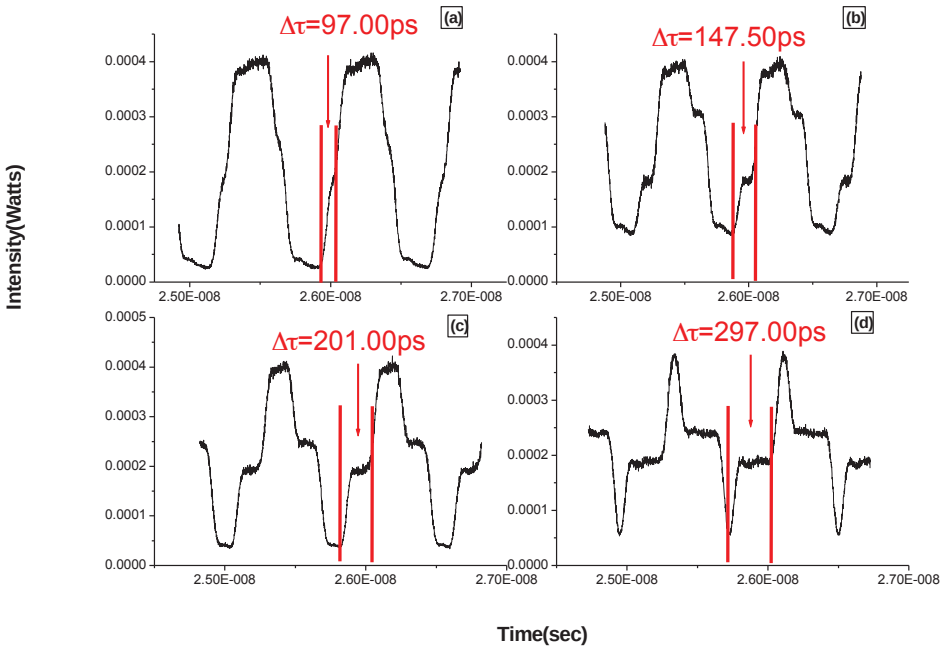

Figure 4. Typical pulse broadening displayed on the scope as a result of the dispersion. The broadening illustrated occurred at different wavelength spacing's of (a) 0.80 nm, (b) 1.33 nm, (c) 1.91 nm and (d) 2.84 nm respectively in the 6.1 km single mode fibre.

Figure 4 describes the progression of pulse broadening as the pulse propagates along the fibre at different wavelength spacing's. It is clear that as the wavelength spacing increases Δτ increase as well. This is a direct result of the difference in the propagation speeds between the two individual pulses. A larger wavelength spacing between to pulses implies that pulse 1 has a greater velocity than pulse 2, yielding a greater time delay between the two pulses. The resolution is limited by the challenge to distinguish the dispersion between two pulses with narrow wavelength spacing. It can be concluded that, material dispersion could be the primary form of dispersion due to the wavelength dependence on the refractive index being such a major contributing factor to the chromatic dispersion.

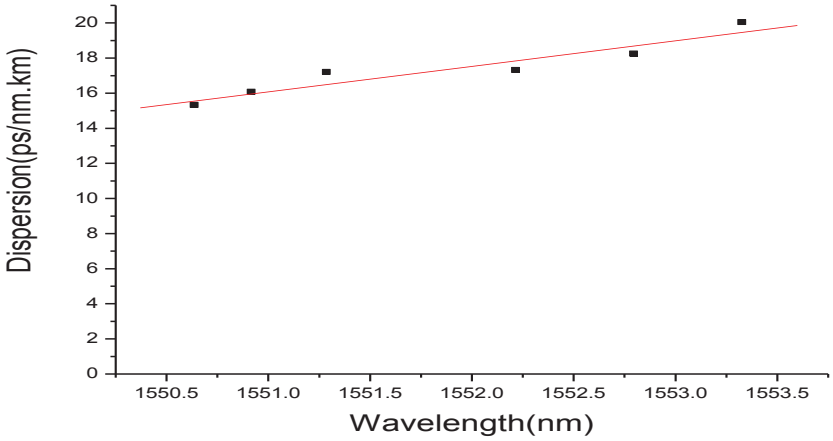

Figure 5. Dispersion curve for a 6.1 km G.652 single mode fibre measured using in a wavelength range of 1550 nm to 1553 nm.

From figure 4, it can be seen how pulse broadening increases the errors when distinguishing between 1's and 0's. The dispersion curve obtained for the wavelength range selected, 1550 nm to 1553 nm, in figure 5 is in close agreement with the theoretical dispersion curve displayed in figure 2 for the same wavelength range. A dispersion of 15.9 ps/nm.km to 20.0 ps/nm.km was measured, again this is in close agreement to the theoretical dispersion values. Table 1 displays the dispersion coefficients D obtained at their corresponding wavelength value in the 6.1 km single mode fibre. The experimental results obtained for the dispersion coefficients do not entirely agree with the theoretical standard of 17 ps/nm.km at the 1550 nm wavelength region found in the relevant literature. This can be related to the poor resolution displayed by the pulse delay method, however the measurement technique described above can be utilized for characterizing the chromatic dispersion in single mode fibres.

Table 1. Chromatic dispersion coefficients at their respective wavelengths.

Wavelength (nm)	Time Delay (ps)	Dispersion (ps/nm.km)
1553.33	97.5	20.0
1552.80	147.5	18.2
1552.22	201.0	17.3
1551.29	297.0	17.2
1550.92	313.5	16.0
1550.64	325.0	15.3

5. Conclusion

A method has been proposed for measuring the chromatic dispersion in a 6.1 km long G.652 single mode fibre. The dispersion coefficients obtained for the 1550 nm to the 1554 nm wavelength range is in agreement to those found in the relative literature. Furthermore, it is required that additional chromatic dispersion measurements be undertaken in lengths of fibre exceeding 6 km, in order for one

to see if the dispersion coefficient improves as well as the resolution. The measurement technique described above can be utilized for characterizing the chromatic dispersion in G.652 single mode fibre.

6. Acknowledgements
This work is based on the research supported in part by the National Research Foundation of South Africa (Grant 84352). We are also grateful for research funding from: African Laser Centre ALC, CSIR, Ingoma, Dartcom,NLC, THRIP and Telkom.

7. References
[1] Kaminow I and Tinhye L 2002 *Optical Fiber Telecommunications IVB Systems and Impairments* (USA: Academic Press) pp 214-216
[2] Tateda M, Shibata N, and S Seikai 1981 Inferometric Method for Chromatic Dispersion Measurement in a Single-Mode Optical Fibre *IEEE J. of Quant. Elect*. **QE-17(3)** 404-407
[3] Cisco White Paper 2008 *Fibre Types in Gigabit Optical Communication* (USA: Cisco Systems) pp 13-14
[4] Keiser G 2000 *Optical Fiber Communication 3rd Edition* (Singapore: Mcgraw-Hill Companies) p104
[5] Costa M,Mazzoni D,Puleo M and Vezzoni E 1982 Phase Shift Technique for the Measurement of Chromatic Dispersion in Optical Fibres Using LED's *IEEE J. Quant Elect*.**QE-18(10)**.pp1509-1515
[6] Chauvel, G. 2008. Dispersion in Optical Fibers.Japan.Anritsu Corporation. Available from: http://www.Ausoptic.com/Alltopic/Download/Disp_in_Opt_FibresPMD_CD [Accessed 21 February 2013].
[7] Cohen L G 1985 Comparison of Single-Mode Fiber Dispersion Measurement Techniques *J. Lightwave Techn.* **LT-3(5)** pp058-960

South African night sky brightness during high aerosol epochs

H Winkler[1,3], F van Wyk[2] and F Marang[2]
[1] Department of Physics, University of Johannesburg, PO Box 524, 2006 Auckland Park, Johannesburg, South Africa
[2] South African Astronomical Observatory, PO Box 9, 7935 Observatory, Cape Town, South Africa

E-mail: hwinkler@uj.ac.za

Abstract. Sky conditions in the remote, dry north-western interior of South Africa are now the subject of considerable interest in view of the imminent construction of numerous solar power plants in this area. Furthermore, the part of this region in which the core of the SKA is to be located (which includes SALT) has been declared an Astronomical Advantage Zone, for which sky brightness monitoring will now be mandatory. In this project we seek to characterise the sky brightness profile under a variety of atmospheric conditions. Key factors are of course the lunar phase and altitude, but in addition the sky brightness is also significantly affected by the atmospheric aerosol loading, as that influences light beam scattering. In this paper we chose to investigate the sky characteristics soon after the Mount Pinatubo volcanic eruption in 1991, which resulted in huge ash masses reaching the stratosphere (where they affected solar irradiance for several years). We re-reduced photometric sky measurements from the South African Astronomical Observatory archives (and originally obtained by us) in different wavelengths and in a variety of directions. We use this data explore relationships between the aerosol loading and the sky brightness in a range of conditions, including several post-Pinatubo phases and during the passage of biomass burning induced haze and dust clouds. We use this data to explore the impact of our findings on the applicability of light scattering models and light scatterer properties.

1. Introduction

The quantification and spectral shape of sky brightness in the north western interior of South Africa has become of great importance for two quite different disciplines.

On the one hand, a vast region incorporating the Sutherland site of the South African Astronomical Observatory (SAAO) as well as the nucleus of the future Square Kilometer Array (SKA) has been declared an astronomical reserve, where light pollution is now restricted by law, and where sky conditions will have to be monitored regularly [1]. In addition, optimal use and scheduling of the SAAO Sutherland facilities (especially for the South African Large Telescope – SALT) requires the best possible knowledge of the sky illumination under all plausible conditions, e.g. aerosol loading and lunar phase and position.

Secondly, the broad geographic region adjacent to the astronomy reserve has been identified as the optimal site for a considerable number of solar power plants [2]. The energy yield of such plants is amongst other factors a function of the atmospheric transparency and the angular illuminance profile

[3] To whom any correspondence should be addressed.

of the sky dome. In particular, the popular photovoltaic power generating method is (in addition to direct sunlight) also responsive to 'diffuse' irradiation (i.e. scattered skylight), and energy generation in this technology is furthermore critically dependent on the wavelength of the incoming photons.

While sky conditions in this region may during most days be considered as 'pristine', episodes of high aerosol concentration do occur periodically [3]. The bulk of these aerosols can be attributed to southern African biomass burning, local wind-induced dust production and occasional global-scale volcanic events.

The Mount Pinatubo volcanic eruption during the period immediately after 15 June 1991 resulted in the largest scale injection of aerosols into the stratosphere experienced in the 20th century [4]. After several weeks the effects of stratospheric mixing resulted in these aerosols becoming spread around the globe. They first became detected over South Africa on 9 August 1991. Their concentration peaked soon thereafter, before gradually decreasing and reaching pre-eruption levels towards the end of 1994 [5].

2. The data and its analysis

In the course of normal astronomical photometric work, the brightness of an object of interest is determined by measuring the number of photons recorded from a patch of sky including this object ("star plus sky"), and subtracting from this value the brightness of a nearby and equally large empty patch of sky ("sky").

Tens of thousands of such sky background measurements have been made over the past decades by the authors, under a large variety of conditions, but such readings are normally used purely for calibration purposes, and have not been utilised in any way thereafter. It will be shown here how this archival data can be used to gain significant insights about sky brightness.

2.1. Measurements

The data was obtained with the 0.5 m telescope at the South African Astronomical Observatory in Sutherland. The light beam is first directed through a circular aperture at the focal point and then through a colour filter. Photons passing through these are finally recorded by means of a photomultiplier.

The circular aperture prevents light from nearby sources entering the detector, and hence limits the recorded light to that emanating from the circular patch of sky defined by the aperture.

Measurements were done through the U, B, V, R and I filters commonly used in astronomical work. Their transmittances as a function of wavelength [6] are illustrated in figure 1.

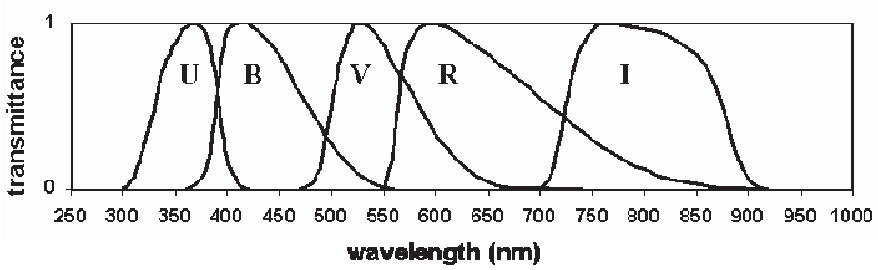

Figure 1. Relative transmittance of the colour filters used in this study.

2.2. Selection of nights for analysis

For this paper we have chosen to analyse some of the sky measurements made during the nights listed in table 1. These nights span a range of conditions encountered just prior to and soon after the

Pinatubo event. We also include an unrelated high-opacity episode to explore a different type of aerosol.

Table 1. Nights analysed in this study and the atmospheric conditions. The last five columns list the optical depth τ_λ at wavelengths representative of the colour filters used.

Night	Aerosol	moon	$\tau_{(366\ nm)}$	$\tau_{(438\ nm)}$	$\tau_{(545\ nm)}$	$\tau_{(641\ nm)}$	$\tau_{(798\ nm)}$
26-27 Jun 1991	low	yes	0.497	0.249	0.138	0.092	0.065
24-25 Jul 1991	low	yes	0.497	0.249	0.138	0.092	0.065
9-10 Aug 1991	low	no	0.539	0.272	0.152	0.106	0.070
24-25 Oct 1991	volcanic	yes	0.640	0.345	0.212	0.180	0.134
20-21 Jan 1992	volcanic	yes	0.562	0.313	0.184	0.143	0.120
18-19 Feb 1992	volcanic	yes	0.562	0.313	0.203	0.157	0.129
10-11 Oct 1992	volcanic/pyrogenic	yes	0.589	0.332	0.212	0.180	0.138
21-22 Mar 2000	aeolian or pyrogenic	yes	0.585	0.295	0.157	0.115	0.074

In addition to describing the aerosol and lunar characteristics, table 1 also lists the optical depth τ in each of the filter bands measured during the night in question. The optical depth is defined as

$$\tau = -(\ln T)/X \quad . \tag{1}$$

T refers to the atmospheric transmittance, and equals the fraction of the original light beam reaching ground level. The parameter *X* is referred to the relative airmass, and designates the path length of a beam of light from the external radiation source through the atmosphere relative to the zenith atmospheric thickness. We adopt the following approximation for the airmass (which were also used in previous similar studies [7,8]), in terms of the zenith angle ζ:

$$X = \left(1 - 0.96\sin^2\zeta\right)^{-0.5} \tag{2}$$

2.3. Flux calibration

For the chosen nights, the brightness measurements were calibrated through the observation of a large number of stars from the SAAO list of calibration standards [9]. During these nights the standard star observations were carried out at a wide range of zenith angles in order to minimise the errors in the optical depth value calculations.

3. The theory of sky brightness at night time

The luminance of the night sky is the combined contribution of a number of components:

- starlight (including the diffuse light of distant stars in the Milky Way and other galaxies).
- traces of evening or morning twilight.
- zodiacal light, which is caused by the reflection of sunlight by small solar system particles.
- airglow due to molecular transitions in the upper atmosphere, or other processes linked to atmospheric particles (auroral light, infrared thermal emission).
- light pollution in areas with ample artificial illumination sources.
- last, but not least, reflected moonlight, which can completely dominate the other contributions around the time of full moon [10].

The lunar brightness depends mainly on the angle Sun-Moon-Earth, but also on the Earth-lunar distance *D*. In particular, it needs to be considered that the lunar surface brightness is enhanced near

full moon due to two optical effects referred to as shadow hiding and coherent backscatter [11]. We adopted a formulation derived from Noll et al [8],

$$\log B_\lambda(\omega, D) = \log B_\lambda(0, D_{av}) - 0.4 \times \left(0.026|\omega| + 4 \times 10^{-9}\,\omega^4\right) - 2\log\left(D / D_{av}\right) \quad (3)$$

where B_λ is the lunar brightness in the filter band of wavelength λ, ω is the phase angle of the moon (in degrees, and equal to zero at full moon) and D_{av} is the average distance of the moon.

The brightness of a patch of sky σ due to the scattering of moonlight is a function not only of i) the lunar brightness, but also of ii) the lunar zenith angle and its corresponding lunar airmass X_m, iii) the sky patch zenith angle X_s, iv) the lunar and sky patch azimuths, v) the optical depth and vi) the appropriate atmospheric particle scattering function f [7,8].

The scattering function sums contributions f_R due to Rayleigh scattering by the smallest particles and f_M due to Mie scattering by larger aerosols. The Rayleigh contribution may be assumed to take the form

$$f_R(\psi) \propto \left(C_R + \cos^2\psi\right) \quad (4)$$

where ψ is the angular distance between the moon and the observed sky patch (i.e. a direct function of the zenith and azimuth angles) and where C_R is a constant known to be close to 1 (C_R = 1.06 was adopted in previous studies [7,8]). In these same studies the Mie contribution was assumed to take on a relationship of the form

$$f_M(\psi) \propto 10^{-\psi / C_M} \quad . \quad (5)$$

with C_M taken to be 40°. The inherent inadequacies of the above approach are evident by the fact that proportionality constants ranging by a factor of 10 have been adopted for the f_M expression in equation 5, and that the formulations do not consider any dependence on wavelength.

The true total scattering function can however also be determined empirically, by measuring the sky brightness σ at a variety of wavelengths for a wide range of lunar and sky patch positions, and then utilising the relationship

$$f_\lambda(\psi) \propto \sigma_\lambda(\psi, X_s) \times \left[B_\lambda \exp(-\tau_\lambda X_m)\left(1 - \exp(-\tau_\lambda X_s)\right)\right]^{-1}. \quad (6)$$

This procedure is adopted in this study. The locations of the Sun and Moon relative to the observing site can be determined to any desired accuracy. The freely available Solar and Moon Position Algorithm (SAMPA) used in this study calculates the solar and lunar coordinates to an accuracy of better than 10″ [12].

4. Results

After evaluating the measured sky brightness per unit solid angle (through division of the total flux by the area of the aperture), we used equation 6 to calculate the values of f_λ for every sky measurement. When taking the logarithm of this quantity and plotting all values against the corresponding lunar-sky patch separation angle ψ for each filter, we obtained a series of diagrams illustrated (for the U, V and I filters) in figure 2.

5. Discussion and conclusions

The graphs shown in figure 2 illustrate very clearly the shape and location of the scattering function $f(\psi)$, as well as the impact that wavelength and the presence of aerosols have on this. The increase in f with growing optical depth can partly be explained as a consequence of a strengthening Mie component, which primarily affects those parts of the diagram where ψ is small. That does however not account for the large discrepancies near $\psi \sim 90°$.

The visibly steeper nature of the plots for longer wavelength filters as opposed to what happens in the violet/UV diagram is also to be expected in view of the dominance of Rayleigh-scattered light in the blue part of the spectrum (even at night, blue photons dominate the radiation reflected off the atmosphere). The Mie fraction would thus be strongest at the longest wavelengths, explaining why the scattering function is considerably higher here for small ψ.

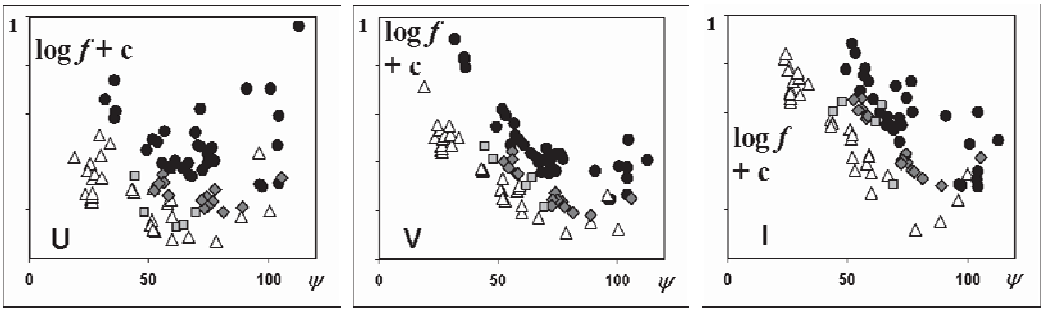

Figure 2. A comparison for the scattering function obtained in the U, V and I bands versus ψ (in degrees) under the following conditions: i) pre-Pinatubo (white triangles); ii) early (Oct. 1991-Feb. 1992) post-Pinatubo (black circles); iii) late (Oct. 1992) post-Pinatubo (grey diamonds); iv) later (2000) dust event (grey squares).

Figure 2 also confirms the presence of the Rayleigh scattering function component. As predicted by the Rayleigh model in equation 4, f reaches its minimum around $\psi = 90°$.

The discrepancy between the aerosol-free and aerosol-loaded curves is expected to be a consequence of the oversimplified assumptions that went into the derivation of equations by the previous studies [7]. A more sophisticated model formulation is required to adequately reproduce the interplay between attenuated moonlight and scattering events at various depths in the atmosphere. Such a model should also allow multiple scattering events.

Finally, the fact that the early post-Pinatubo plots are furthest removed from the 'low aerosol' curve (despite sharing similar opacity values with the plots associated with the later dates) indicates a probable dependence on the nature of the aerosols. It needs to be noted here that following volcanic eruptions the largest particles fall to the ground first due to their greater mass, while smaller particles stay airborne for considerably longer. This effect was also noted for the Pinatubo eruption [5]. It is projected that the planned systematic analysis of all available SAAO night sky data will be able to explore these and other questions in greater detail.

Acknowledgments

We thank successive Directors of the South African Astronomical Observatory for the generous allocation of observing time, and its numerous support staff for the good maintenance of the equipment. A special thanks to Di Cooper and Ramotholo Sefako for their assistance in the retrieval of archival data. Last, but not least, we thank Dave Kilkenny. Without his dedicated leadership of the SAAO photometry programme and his continual oversight of the quality control processes, this work would not have been possible.

References

[1] Jonas J L 2009 *Proc. Inst. Elec. Electron. Eng.* **97**, 8, 1522
[2] Fluri T P 2009 *Energy Policy* **37** 5075
[3] Formenti P, Winkler H, Fourie P, Piketh S, Makgopa B, Helas G and Andreae M O 2002 *Atmospheric Research* **62** 11

[4] McCormick M P, Thomason L W and Trepte C R 1995 *Nature* **373** 399
[5] Kilkenny D 1995 *The Observatory* **115** 25
[6] Bessell M and Murphy S 2012 *Publ. Astron. Soc. Pacific* **124** 140
[7] Krisciunas K and Schaefer B E 1991 *Publ. Astron. Soc. Pacific* **103** 1033
[8] Noll S, Kausch W, Barden M, Jones A M, Szyska C, Kimeswenger S and Vinther J 2012 *Astron. & Astrophys.* **543** A92
[9] Menzies J W, Cousins A W J, Banfield R and Laing J D 1989 *South African Astronomical Observatory Circulars* **13** 1
[10] Patat F 2003 *Astron. Astrophys.* **400** 1183
[11] Kieffer H H and Stone T C 2005 *Astron. J.* **129** 2887
[12] Reda I 2010 *Solar Eclipse Monitoring for Solar Energy Applications using the Solar and Moon Position Algorithms* NREL Report No. TP-3B0-47681

Division G – Theoretical and Computational Physics

A Review of Generalized and Unsharp Measurements

Humairah Bassa[1] **and Thomas Konrad**[1,2]

[1] School of Chemistry and Physics, University of KwaZulu-Natal, Durban 4000, South Africa
[2] National Institute of Theoretical Physics, Durban, South Africa

E-mail: konradt@ukzn.ac.za

Abstract. Unsharp measurements are a special class of generalized measurements whose experimental potential has not as yet been fully explored. Unlike the usual projective measurements which collapse the state of a quantum system into an eigenstate of the measured observable, unsharp measurements have a weaker influence on the state of the system. These types of measurements are advantageous when we need to gain information about a system but the disturbance must not exceed a certain level. It is therefore useful to study the set of unsharp measurements from first principles by reformulating the measurement postulate in terms of generalized measurements. The necessary requirements of an unsharp measurement are presented. A recent implementation scheme for unsharp measurements on trapped ions is reviewed.

1. Introduction

In 1932, John von Neumann [1] formulated a rigorous description of what happens to a quantum object when it is measured. The measurements he described are aptly named projective measurements since the measurement process projects the initial state of the system into an eigenstate of the measured observable. This eigenstate corresponds to the eigenvalue which was identical to the measurement outcome. For example, if we measured the energy of an atom in a projective measurement the outcome would be one of the quantized energies which are characteristic for that atom. As we can see these measurements are highly accurate since the measurement outcome is a definite and precise value which upon immediate repetition of the measurement would occur again. They are therefore also known as ideal or *sharp* measurements. However, the more accurate a measurement is, the greater is its disturbing influence on the measured system. We may sometimes require information about a quantum system but only a certain degree of disturbance may be acceptable. A possible example would be the real time estimation and monitoring of the Rabi oscillations of a single atom in a resonant driving field. Carrying out a sequence of projective measurements of the atomic energy would greatly disturb the system and in the continuum limit they would lead to the Quantum Zeno effect, i.e. they would freeze the dynamics of the system. An alternative are *unsharp* measurements which have a weaker influence on the state of the system but still convey some information about an associated ordinary observable, such as energy, position or spin. It has been shown that continuous unsharp measurement allows us to monitor the Rabi oscillations in the aforementioned case [2]. Remarkably, this is even possible in the presence of noise [3].

This article serves as a concise introduction to generalized and unsharp measurements and it is structured as follows. In Section 2, we reformulate the measurement postulate in terms

generalized measurements which is the set of all measurements possible within the limit of quantum mechanics. The special properties of unsharp measurements are reviewed in Section 3 while Section 4 presents an implementation scheme for unsharp measurements on a trapped ion. A short discussion is given in Section 5.

2. Generalizing the measurement postulate

The measurement postulate, as described by von Neumann, fully characterizes a projective or sharp measurement and can be phrased as follows:

The result of a projective measurement of an observable A on a system prepared in the state ρ_{in} will be one of the eigenvalues of the observable defined by, $A|a\rangle = a|a\rangle$. The probability of obtaining measurement result "a" reads

$$p(a, \rho_{\text{in}}) = \text{Tr}[P_a \rho_{\text{in}}] \quad \text{where} \quad P_a = |a\rangle\langle a|, \tag{1}$$

and the change of the state due to the measurement is given by

$$\rho_{\text{in}} \to \rho_{\text{out}} = \frac{1}{p(a, \rho_{\text{in}})} P_a \rho_{\text{in}} P_a^\dagger. \tag{2}$$

The eigenstates of the observable form a complete orthonormal set thus we have the completeness relation $\sum_a P_a = \mathbb{1}$.

Projective measurements, however, only represent a restricted set of allowed measurements in Quantum Mechanics. Furthermore, unsharp measurements often occur during the experimental realization of projective measurements of observables such as energy, position and spin. This is because projective measurements of these quantities are an idealization and do not take into account measurement error which may result in the actual measurement being unsharp.

A more general description of measurements was introduced to Quantum Theory in the 1970, cp. [4]. In this framework the statistics of any quantum mechanical measurement can be evaluated if the set of Effects, $\{E_a\}$, associated with the possible results, a, of the measurement as well as the state of the system immediately before the measurement, ρ_{in}, are known. The set of Effects forms a positive operator valued measure (POVM) [5] and each element E_a of the set corresponds to the event of "measuring a". Note that for projective measurements the Effects $\{E_a\}$ correspond to the projectors $\{P_a\}$. The probability for the result a to occur can be calculated as

$$p(a, \rho_{\text{in}}) = \text{Tr}[E_a \rho_{\text{in}}]. \tag{3}$$

Unlike for projective measurements, however, knowing the Effects is in general not enough to determine the state of the system after measurement; we further need to know the Kraus measurement operators M_k which make up the POVM elements E_a, i.e.

$$E_a = \sum_{k \in I_a} M_k^\dagger M_k \tag{4}$$

where I_a is an index set associated with the measurement result a. The change of the state due to the measurement is then given by

$$\rho_{\text{in}} \to \rho_{\text{out}} = \frac{1}{p(a, \rho_{\text{in}})} \sum_{k \in I_a} M_k \rho_{\text{in}} M_k^\dagger. \tag{5}$$

Generalized or POVM measurements play an important role in Quantum Theory since they allow us to investigate fundamental question such as the information gain and state disturbance trade-off. Furthermore they are useful in developing novel experimental schemes like the quantum optical measurement of the number of photons in a cavity or the measurement of the position of an atom in a standing light wave, cp. [5].

3. Unsharp measurements

A generalized measurement is called pure if to each measurement result a there corresponds exactly one Kraus operator M_a. This preserves the purity of states in the so-called selective regime of measurement; i.e. conditioned on a concrete measurement result, a pure state $|\psi\rangle$ is mapped in the course of a measurement onto a pure state: $|\psi\rangle \to \frac{M_a}{N}|\psi\rangle$ where $N \equiv \sqrt{\langle\psi|E_a|\psi\rangle}$ is the norm of the state which is the square of the probability to obtain the measurement result. The completeness relation then reads,

$$\sum_a M_a^\dagger M_a = \mathbb{1}. \tag{6}$$

A measurement is called unsharp if, in addition, not all the Effects $E_a = M_a^\dagger M_a$ are projectors but the Effects must be mutually commutating,

$$[E_a, E_b] := E_a E_b - E_b E_a = 0 \quad \text{for all measurement results } a, b. \tag{7}$$

This restriction is necessary because it allows one to distinguish which Effect was measured. An unsharp measurement thus has the same requirements as a projective measurement, except that not all the Effects are projectors. [1]

4. Scheme for implementing unsharp measurements

Now that the foundation has been laid, it is interesting to know how unsharp measurement can be implemented in a realistic experiment. Implementation schemes for unsharp measurements on trapped ions were recently demonstrated in [6]. We will briefly review one of these schemes here. The intricate details of the ion traps are neglected in order to keep the discussion focused and understandable.

One possible method for carrying out an unsharp measurement is through an ancilla system as shown in [6]. The basic idea is as follows. Conventional quantum logic operations for ion traps allow us to introduce weak entanglement (see below) between the target ion and an auxiliary ion. A projective measurement carried out on the auxiliary ion then leads to a realization of an unsharp measurement on the target ion.

We have two different species of ions trapped in the same ion trap so they share collective vibrational (or phonon) modes. One is the target ion which we prepare in a coherent superposition of its qubit levels

$$|\psi_t^{(0)}\rangle = c_1|g_t\rangle + c_2|e_t\rangle \tag{8}$$

where $|g_t\rangle$ and $|e_t\rangle$ are two hyperfine electronic ground levels and $|c_1|^2 + |c_2|^2 = 1$. We aim to measure the z component of its effective spin σ_z, unsharply. For this purpose we choose to implement two symmetric measurement operators

$$M_0 = \sqrt{p_0}|g_t\rangle\langle g_t| + \sqrt{1-p_0}|e_t\rangle\langle e_t|, \tag{9}$$

$$M_1 = \sqrt{1-p_0}|g_t\rangle\langle g_t| + \sqrt{p_0}|e_t\rangle\langle e_t|, \tag{10}$$

which satisfy the necessary requirements for an unsharp measurement mentioned in the preceding section. The target ion must also have a third metastable excited state $|r_t\rangle$, to assist with the unsharp measurement. The second ion is the auxiliary ion which is used for sympathetic cooling of the phonon modes as well as for implementing the unsharp measurement on the target ion. Since the ions are of different species, the laser used to manipulate one ion does not affect the other, thus the ions can be addressed independently.

[1] Please note, that we consider unsharp measurements to be pure, while in the literature unsharp measurements are just required to have commuting effects, cp. [5].

The state of the system of ions in the trap after the ground-state cooling on the auxiliary ion can be described by

$$|\psi\rangle = |\psi_t^{(0)}\rangle|\psi_a\rangle|0\rangle = (c_1|g_t\rangle + c_2|e_t\rangle)|\psi_a\rangle|0\rangle \tag{11}$$

where $|\psi_a\rangle$ is the state of the auxiliary ion and $|0\rangle$ is vibrational ground state of the ions (i.e. zero phonons). The measurement preparation proceeds by applying four laser pulses to the target ion. The first pulse is a carrier pulse on resonance with the transition $|g_t\rangle \rightarrow |r_t\rangle$ for the duration $t = (2/\Omega_1)\cos^{-1}(\sqrt{p_0})$ where Ω_1 is the Rabi frequency connecting $|g_t\rangle$ and $|r_t\rangle$, which results in the state,

$$|\psi_1\rangle = \Big[c_1\Big(\sqrt{p_0}|g_t\rangle + \sqrt{1-p_0}|r_t\rangle\Big) + c_2|e_t\rangle\Big]|\psi_a\rangle|0\rangle. \tag{12}$$

The second pulse is a red sideband pulse between $|g_t\rangle$ and $|r_t\rangle$, which induces the transitions $|r_t\rangle|n\rangle \rightarrow |g_t\rangle|n+1\rangle$ and $|g_t\rangle|n\rangle \rightarrow |r_t\rangle|n-1\rangle$ where n is the number of phonons. Hence the two-ion state becomes

$$|\psi_2\rangle = \Big[c_1|g_t\rangle\Big(\sqrt{p_0}|0\rangle + \sqrt{1-p_0}|1\rangle\Big) + c_2|e_t\rangle|0\rangle\Big]|\psi_a\rangle. \tag{13}$$

It is important to note that the component $|g_t\rangle|0\rangle$ is unaffected because the state $|r_t\rangle|-1\rangle$ does not exist. The third pulse is again a carrier pulse but this one is on resonance with the transition $|e_t\rangle \rightarrow |r_t\rangle$ for the duration $t = (2/\Omega_2)\cos^{-1}(\sqrt{1-p_0})$ where Ω_2 is the Rabi frequency connecting $|e_t\rangle$ and $|r_t\rangle$, which leads to the state,

$$|\psi_3\rangle = \Big[c_1|g_t\rangle\Big(\sqrt{p_0}|0\rangle + \sqrt{1-p_0}|1\rangle\Big) + c_2\Big(\sqrt{1-p_0}|e_t\rangle + \sqrt{p_0}|r_t\rangle\Big)|0\rangle\Big]|\psi_a\rangle. \tag{14}$$

Finally, a red sideband pulse between $|e_t\rangle$ and $|r_t\rangle$ yields,

$$|\psi_4\rangle = \Big[c_1|g_t\rangle\Big(\sqrt{p_0}|0\rangle + \sqrt{1-p_0}|1\rangle\Big) + c_2|e_t\rangle\Big(\sqrt{1-p_0}|0\rangle + \sqrt{p_0}|1\rangle\Big)\Big]|\psi_a\rangle, \tag{15}$$

$$= \Big[\Big(\sqrt{p_0}c_1|g_t\rangle + \sqrt{1-p_0}c_2|e_t\rangle\Big)|0\rangle + \Big(\sqrt{1-p_0}c_1|g_t\rangle + \sqrt{p_0}c_2|e_t\rangle\Big)|1\rangle\Big]|\psi_a\rangle. \tag{16}$$

Now, a projective measurement on the vibrational state in the basis $\{|0\rangle, |1\rangle\}$ results in the internal state of the target being either

$$\Big(\sqrt{p_0}c_1|g_t\rangle + \sqrt{1-p_0}c_2|e_t\rangle\Big) \tag{17}$$

or

$$\Big(\sqrt{1-p_0}c_1|g_t\rangle + \sqrt{p_0}c_2|e_t\rangle\Big). \tag{18}$$

The projection measurement of the vibrational state is accomplished through a Quantum Logic Spectroscopy measurement [7]. An unsharp measurement of σ_z is thus realized since this sequence is equivalent to applying the measurement operators of Eqs. (9) and (10) on the initial state of the target atom, i.e. Eq. (8).

5. Discussion

We introduced the concept of generalized measurements and reformulated the measurement postulate in terms of them. The properties of unsharp measurements where presented and an application of these measurements for a realistic experiment was demonstrated. Unsharp measurements are an appropriate means to obtain information about an observable under the constraint that the disturbance of a system must not exceed a certain level.

References

[1] von Neumann J *Mathematical Foundations of Quantum Mechanics* (Princeton: Princeton University Press) 1955

[2] Audretsch J, Konrad T and Scherer A 2001 *Phys. Rev.* A **63** 052102

[3] Konrad T and H Uys 2012 *Phys. Rev.* A **85** 012102

[4] Davies E B *Quantum Theory of Open Systems* (London: Academic Press) 1976

[5] Busch P, Grabowski M and Lathi J P *Operational Quantum Physics* (Heidelberg: Springer Verlag) 1995

[6] Choudhary S K, Konrad T and H Uys 2013 *Phys. Rev.* A **87** 012131

[7] Schmidt P, Rosenband T, Langer C, Itano W, Bergquist J and Wineland D 2005 *Science* **309** 749

Heavy Baryons with Strangeness

J. P. Blanckenberg

E-mail: jpblanck@sun.ac.za

H. Weigel

E-mail: weigel@sun.ac.za

Physics Department, Stellenbosch University, Matieland 7602, South Africa

Abstract. We apply the soliton description of baryons with a single heavy quark (charm or bottom). In this approach such baryons emerge as bound composites of a soliton of meson fields built from light quarks (up, down, strange) and a meson field that contains a heavy quark. We show that in this case the soliton must then be quantized as a diquark while the fermionic character arises from binding the heavy meson field. We are particularly interested in heavy baryons that have non-zero strangeness; in the quark model that corresponds to, say, up-strange-bottom (usb). Thus the flavor symmetry breaking among the light quarks must be fully incorporated when constructing diquark states. In the soliton model that symmetry breaking is parameterized by differences between the masses and decay constants of kaons and pions. Here we present computations of the diquark eigen-energies and eigen-functions that incorporates all orders of the light flavor symmetry breaking. We also compare these results to a leading order treatment of flavor symmetry breaking. The heavy meson couples according to the heavy spin-flavor symmetry to the chiral field that carries the soliton. In the background of the soliton the heavy meson field develop bound states. We compute the associated binding energies. These are the second major ingredient for our prediction of heavy quark baryons.

1. Introduction

There is some interest in the spectrum of baryons with a heavy quark. The light quark part of the model is formulated in terms of the chiral field U, which is a 3×3 matrix in the flavor space of *up*, *down* and *strange* quarks (q). The interactions of this field are dictated by chiral symmetry and its spontaneous breaking. In particular we consider the Skyrme model which has a soliton solution that describes baryons [1]. The heavy quark part is represented by a heavy meson field that has valence quark content *bottom* (or *charm*)–$\overline{q}$. The interactions of its heavy degrees of freedom are governed by the heavy quark effective theory (HQET) [2, 3] while the light degrees of freedom couple to U in a chirally invariant manner. Thus the model captures the major symmetries of QCD, the fundamental theory of strong interactions according to which hadrons form.

2. Skyrme Model

The model is defined by the action which is the sum of three contributions

$$\Gamma = \int d^4x \left[\mathcal{L}_{\rm SK} + \mathcal{L}_{\rm SB}\right] + \Gamma_{\rm WZ}\,. \tag{1}$$

The field variable is the chiral field U, a 3×3 matrix that is the non–linear representation of the pseudoscalar pions, kaons and η. (Mixing between η and η' is an interesting issue, but not important in the present context). The Skyrme model Lagrangian also contains chiral symmetry breaking

$$\mathcal{L}_{\rm SK} = \frac{f_\pi}{4}{\rm tr}\left(\partial_\mu U \partial^\mu U^\dagger\right) + \frac{1}{32e^2}{\rm tr}\left(\left[U^\dagger\partial_\mu U, U^\dagger \partial_\nu U\right]^2\right) + \frac{f_\pi^2 m_\pi^2 + 2f_K^2 m_K^2}{12}{\rm tr}\left(U + U^\dagger - 2\right)\,. \tag{2}$$

Flavor symmetry breaking is incorporated via

$$\mathcal{L}_{\rm SB} = \frac{f_\pi^2 m_\pi^2 - f_K^2 m_K^2}{2\sqrt{3}}{\rm tr}\left(\lambda_8 U\right) + \frac{f_K^2 - f_\pi^2}{12}{\rm tr}\left([1 - \sqrt{3}\lambda_8]U(\partial_\mu U)^\dagger \partial^\mu U\right) + {\rm h.c.}\,, \tag{3}$$

where h.c. stands for Hermitian conjugation and λ_a $(a = 1, \ldots, 8)$ are the eight Gell–Mann matrices. Finally, the anomaly is included as the Wess–Zumino term. It is an integral

$$\Gamma_{\rm WZ} = -\frac{iN_c}{240\pi^2}\int d^5x \epsilon^{\mu\nu\rho\sigma\tau}\,{\rm Tr}[\alpha_\mu\alpha_\nu\alpha_\rho\alpha_\sigma\alpha_\tau] \qquad (\alpha_\mu = U^\dagger\partial_\mu U) \tag{4}$$

over a five dimensional manifold whose boundary is Minkowski space. Here N_C is the number of colors in QCD. The Skyrme model is expected to be valid (at least) in the limit $N_C \to \infty$. For actual calculations we use, of course, $N_C = 3$.

The hedgehog is embedded

$$U(\vec{x}, t) = A(t){\rm exp}\left[i\hat{x}\cdot\vec{\lambda}F(r)\right]A^\dagger(t) \tag{5}$$

in $SU_F(3)$ with $\vec{\lambda} = (\lambda_1, \lambda_2, \lambda_3)$. Upon substitution this field configuration into the above defined action yields the Lagrange function (for $N_C = 3$)

$$L_{\rm Sk} = -E_{\rm cl} + \frac{1}{2}\alpha^2\sum_{i=1}^{3}\Omega_i^2 + \frac{1}{2}\beta^2\sum_{\alpha^4}^{7}\Omega_\alpha^2 - \frac{\sqrt{3}}{2}\Omega_8 - \frac{1}{2}\gamma_S\left[1 - D_{88}\right]\,. \tag{6}$$

The coefficients $E_{\rm cl}$,...,γ are functionals of the chiral angle $F(r)$. In particular application of the variational principle onto the classical energy $E_{\rm cl}$ determines $F(r)$ together with the boundary conditions $F(0) = \pi$ and $\lim_{r\to\infty}F(r) = 0$, suitable for baryon number one. The information on the collective coordinates $A \in SU(3)$ is parameterized via the angular velocities $A^\dagger\dot{A} = \frac{i}{2}\sum_{a=1}^{8}\Omega_a\lambda_a$ and the adjoint representation $D_{ab} = \frac{1}{2}{\rm tr}\left[\lambda_a A\lambda_b A^\dagger\right]$.

3. Coupling of Heavy Mesons

As indicated in the introduction, the heavy mesons couple to the light mesons (parameterized via the chiral field U) according to chiral symmetry while the interactions of the heavy degrees of freedom are governed by HQET. The latter requires to treat the pseudoscalar (P) and vector components (Q_μ) on equal footing. Note that these fields are three component arrays in $SU_F(3)$:

$$\begin{aligned}\mathcal{L}_H &= \left(D^\mu P\right)^\dagger D_\mu P - \frac{1}{2}\left(Q^{\mu\nu}\right)^\dagger Q_{\mu\nu} - P^\dagger M^2 P + Q^{\mu\dagger}M^{*2}Q_\mu \\ &\quad + 2iMd\left[P^\dagger p_\mu Q^\mu - Q_\mu^\dagger p^\mu P\right] - \frac{d}{2}\epsilon^{\alpha\beta\mu\nu}\left[Q_{\nu\alpha}^\dagger p_\mu Q_\beta + Q_\beta^\dagger p_\mu Q_{\nu\alpha}\right]\,,\end{aligned} \tag{7}$$

with $Q_{\mu\nu} = D_\mu Q_\nu - D_\nu Q_\mu$ and the covariant derivative is $D_\mu = \partial_\mu - iv_\mu$. Furthermore $M^2 = \mathrm{diag}(M^2, M^2, M_s^2)$ is the matrix containing the square heavy pseudoscalar meson masses. Likewise, M^{*2} stands for the heavy vector meson masses. HEQFT enforces the coefficients of the two last terms in Eq. (7) in the specific way they are presented. Lorentz and chiral invariance alone do not relate these two terms. The light (pseudo)vector currents are given by

$$p_\mu = \frac{i}{2}\left(\xi\partial_\mu\xi^\dagger - \xi^\dagger\partial_\mu\xi\right) \quad \text{and} \quad v_\mu = \frac{i}{2}\left(\xi\partial_\mu\xi^\dagger + \xi^\dagger\partial_\mu\xi\right), \tag{8}$$

where ξ is the root of the chiral field, *i.e.* $U = \xi\cdot\xi$. Substituting the soliton solution into these currents generates an attractive potential for the heavy mesons fields. The resulting binding energies will be central to the model prediction for the spectrum of the heavy baryons. The most strongly bound states are expected in the P–wave channel. The corresponding *ansätze* introduce four profile functions

$$\begin{aligned} P &= \frac{\mathrm{e}^{i\epsilon t}}{\sqrt{4\pi}}\Phi(r)A(t)\hat{x}\cdot\vec{\lambda}\chi\,, \qquad Q_0 = \frac{\mathrm{e}^{i\epsilon t}}{\sqrt{4\pi}}\Psi_0(r)A(t)\chi\,, \\ Q_i &= \frac{\mathrm{e}^{i\epsilon t}}{\sqrt{4\pi}}A(t)\left[i\Psi_1(r)\hat{x}_i + \frac{1}{2}\Psi_2(r)\epsilon_{ijk}\hat{x}_j\lambda_k\right]\chi\,, \end{aligned} \tag{9}$$

where $\chi = \begin{pmatrix} a_1 \\ a_2 \\ 0 \end{pmatrix}$ is a space independent spinor in flavor space. In the adiabatic approximation (A=const.) the field equations then turn into coupled ordinary differential equations for $\Phi(r)$ and $\Psi_{0,1,2}(r)$. We construct solutions with $|\epsilon| \leq M$ that decay exponentially as $r \to \infty$. This only occurs for discrete values ϵ_i which are the searched–for bound state energies. Finally the computed profile functions are normalized such that heavy meson field carries unit charge of the associated flavor[4]. The so constructed bound state contribute

$$L_{\mathrm{H}} = -\frac{1}{2}\gamma_B\left[1 - D_{88}\right] + \frac{\sqrt{3}}{6}|Q_H|\Omega_8 + \frac{1}{2}\chi_P\,\chi^\dagger\left[\sum_{i=1}^{3}\Omega_i\lambda_i\right]\chi + \ldots \tag{10}$$

to the collective coordinate Lagrangian. The symmetry breaking term is the integral

$$\gamma_B = \int dr r^2\left[\left(M_{B_s}^2 - M_B\right)\Phi(r)^2 + \left(M_{B_s}^{*2} - M_B^*\right)\left(\Psi_1(r)^2 + \frac{1}{2}\Psi_2(r)^2 - \Psi_0(r)^2\right)\right] \tag{11}$$

and Q_H is the charge of the heavy flavor.[1] Furthermore χ_P is the hyperfine splitting coefficient, which is also an integral over all profile functions [4]. The ellipsis indicate terms that are subleading in the combined $1/N_C$ and heavy flavor expansion.

The ansatz, Eq. (9) corresponds to ordinary positive parity baryons. Negative parity baryons can be described by

$$\begin{aligned} P^{(-)} &= \frac{\mathrm{e}^{i\epsilon t}}{\sqrt{4\pi}}\Phi(r)A(t)\chi\,, \qquad Q_0^{(-)} = \frac{\mathrm{e}^{i\epsilon t}}{\sqrt{4\pi}}\Psi_0(r)A(t)\hat{x}\cdot\vec{\lambda}\chi\,, \\ Q_i^{(-)} &= \frac{i\mathrm{e}^{i\epsilon t}}{\sqrt{4\pi}}A(t)\left[\Psi_1(r)\hat{x}\cdot\vec{\lambda}\,\hat{x}_i + \frac{1}{2}\Psi_2(r)r\vec{\lambda}\cdot(\partial_i\hat{r})\right]\chi\,. \end{aligned} \tag{12}$$

Though in this case the profile functions obey different differential equations leading to different energy eigenvalues ϵ_i and integral[2] γ_B, the form of the Lagrangian, Eq. (10) remains unchanged.

[1] That is, $Q_H = 1$ if the bound state is occupied but vanishes otherwise.

[2] Formally only the factor of Ψ_2^2 changes from $\frac{1}{2}$ to 2, but the radial functions differ significantly.

4. Quantization in $\mathbf{SU_F(3)}$

Quantization is performed canonically, *i.e.* canonical commutation relations are imposed for the collective coordinates and their conjugate momenta. This is equivalent to $SU(3)$ commutation relations for the (right) generators[1]

$$R_a = -\frac{\partial L}{\partial \Omega_a} \qquad [R_a, R_b] = -i f_{abc} R_c \,, \tag{13}$$

where $L = L_{\rm Sk} + L_{\rm H}$. The full wave–function of the heavy baryon is the product of the heavy meson bound state and the wave–function $\Psi(A)$. If it were not for flavor symmetry breaking (measured) by $\gamma = \gamma_S + \gamma_B$, these were $SU(3)$ D–functions. We include the effects of flavor symmetry breaking according to the Yabu–Ando method which goes beyond a perturbative expansion in γ[5]. Before doing so, we need to emphasize the most important consequence of the heavy meson bound state on the structure of $\Psi(A)$. The angular velocity Ω_8 only appears linearly in the Lagrangian. Hence

$$R_8 = \frac{\sqrt{3}}{2} - \frac{\sqrt{3}}{6} Q_H \tag{14}$$

is a constraint. Without the heavy meson bound state it requires $\Psi(A)$ to be a wave–function with half–integer spin. With the bound state $\Psi(A)$ must have integer spin, *i.e.* the soliton with spin J_s must be quantized as diquark in flavor space for $Q_H = \pm 1$[6].

The Yabu–Ando method requires to find the eigenvalues $\epsilon_{\rm SB}$ in

$$\left(\sum_{a=1}^{8} R_a^2 + \gamma \beta^2 \left[1 - D_{88} \right] \right) \Psi_{IJ_s}(A) = \epsilon_{\rm SB}(I, J_s) \Psi_{IJ_s}(A) \tag{15}$$

for a given set of soliton spin (J_s) and isospin (I) quantum numbers. Without flavor symmetry breaking the solutions to this eigenvalue equation are elements of a definite SU(3) multiplet. When the strangeness zero element of such a multiplet is uniquely identified by its isospin projection I_3, the soliton spin, J_s is uniquely given by the total isospin of that element.[3] The spin of the baryon is related to the soliton spin as $J = J_s \pm \frac{1}{2}$.

For a pertinent parameterization of collective coordinates in terms of SU(3) *Euler angles* the above eigenvalue equation reduces to ordinary differential equations for just a single angle, the so–called strangeness changing angle ν[5, 1]. Collecting pieces, the mass of a baryon is

$$M_B(I, J) = \text{const.} + \frac{J_s(J_s+1)}{2} \left(\frac{1}{\alpha^2} - \frac{1}{\beta^2} \right) - \frac{R_8^2}{2\beta^2} + \frac{\epsilon_{\rm SB}(I, J_s)}{2\beta^2} + \left| Q_{\rm H}\, \epsilon_i \right| . \tag{16}$$

The constant includes all contributions that are identical for all baryons, such as the classical energy. Also, we have omitted the hyperfine contribution (related to χ_P) because its role in flavor SU(3) is still under investigation. This will ultimately resolve the ambiguity between J and J_s. Without that, we observe a degeneracy between the $J = J_s \pm \frac{1}{2}$ baryons.

5. Results

In a first step we investigate the eigenvalue equation (15) in the relevant diquark channels. In the absence of flavor symmetry breaking ($\gamma = 0$) the eigenstates are pure $SU(3)$ representation and the lowest–lying diquarks are within the anti–triplet ($J_s = 0$) and the sextet ($J_s = 1$). Once symmetry breaking is included admixtures of higher dimensional representations occur. They can be perturbatively estimated as a power expansion in $\gamma\beta^2$[6] or by directly solving Eq. (15). We compare the results of both procedures in figure 1 as a function of the perturbation

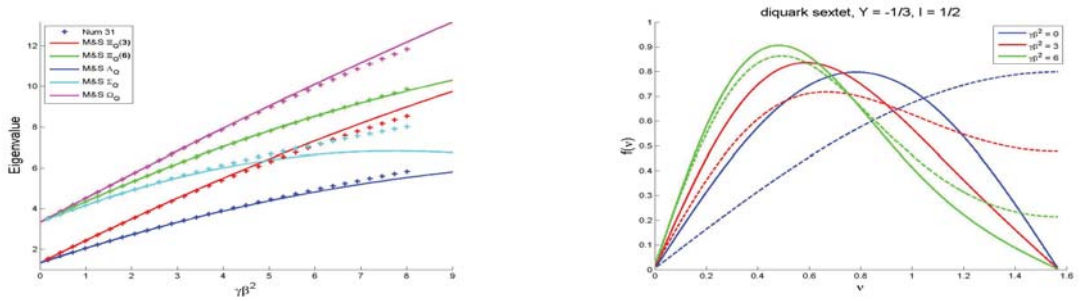

Figure 1. Comparison of second order perturbative (M & S[6]) and exact (numerical) solutions to Eq. (15).

Flavor	$\Delta\epsilon_B$(MeV)	Baryon	Δm (MeV)(exp)
B	257	Λ_b	293
C	285	Λ_c	306

Table 1. Mass differences between S and P-wave compared to mass differences between heavy baryons of opposite parity.

parameter. In case of the eigenvalues we present results for all interesting spin and isospin channels. For $\gamma\beta^2 \geq 6$ we observe sizeable deviations from the second order perturbation calculation. This requires to extend that calculation to third or even higher order. That would be cumbersome since the number of the required $SU(3)$ Glesch–Gordan coefficients is approximately proportional to the factorial of the order. On the other hand, the effort in numerically integrating Eq. (15) is independent of the value of $\gamma\beta^2$.[4] For the wave–functions we restrain ourselves to display the variation with the strangeness changing angle for $J_s = 1$, $I = \frac{1}{2}$ channel that involves two functions and would be a member of the sextet at zero symmetry breaking. As $\gamma\beta^2$ increases, the wave–functions get more pronounced at smaller values of the strangeness changing angle. This is to be expected because the probability to rotate into strangeness direction decreases with the mass of the strangeness carrying fields.

Of course, $\gamma\beta^2$ is not a parameter to be chosen. Rather, once the model parameters are fixed, it is a prediction as both factors are functionals of the chiral angle $F(r)$. The parameters entering the Skyrme model action, Eq. (1) are taken from meson properties as far as possible: $f_\pi = 93$MeV, $f_K = 1.22 f_\pi$, $m_\pi = 138$MeV and $m_K = 495$MeV. Though the Skyrme constant e could be related to pion–pion scattering, this does not give a sufficiently definite value and also other terms from the chiral expansion would contribute. Therefore we use $e \approx 5$ that reasonably reproduces the Δ–nucleon mass difference[1]. For the masses of the heavy mesons we take $M = 1865$MeV, $M^* = 2007$MeV, $M = 1969$MeV and $M = 2106$MeV in the charm sector or $M = 5279$MeV, $M^* = 5325$MeV, $M = 5367$MeV and $M = 5416$MeV in the bottom sector[8]. The coupling constant for the interaction between heavy and light mesons is estimated from heavy meson radiative decays $d \approx 0.53$[7].

The P and S channel bound states correspond to heavy baryons of opposite parities. Hence the differences should be compared to the mass difference of the observed $\Lambda_{c,b}$ with positive and negative parity. This comparison is shown in table 1 and yields satisfactory results.

Having not yet finalized the investigation of hyperfine splitting in the context of flavor $SU(3)$ we can only compare predictions for $J_s = 0$, as it unambiguously is associated with total spin

[3] This feature persists when flavor symmetry breaking is included.

[4] At very large values, the boundary solutions require some care.

I	P	Model	PDG
0	-	308	308
$\frac{1}{2}$	+	88	151
$\frac{1}{2}$	-	408	503

Table 2. Comparison of model predictions to experiment (PDG [8]) for mass differences of charmed baryons with respect to Λ_c. Note that the PDG has not determined the J^P quantum numbers but adopted them from the non–relativistic quark model.

$J = \frac{1}{2}$. For the charm sector this is shown in table 2. Our predictions are in the right ball park, though the mass difference between the Λ_c and the Ξ_c's is somewhat underestimated.

References

[1] H. Weigel, Lect. Notes Phys. **743** (2008) 1.
[2] A. V. Manohar, M. B. Wise, Camb. Monogr. Part. Phys. Nucl. Phys. Cosmol, **10** (2000) 1.
[3] D. Blaschke, M. A. Ivanov, M. A., T. Mannel, Lect. Notes Phys. **647** (2002) 1.
[4] J. Schechter, A. Subbaraman, S. Vaidya, H. Weigel, Nucl. Phys. A **590** (1995) 655 [Erratum-ibid. A **598** (1996) 583]; M. Harada, A. Qamar, F. Sannino, J. Schechter, H. Weigel, Nucl. Phys. A **625** (1997) 789.
[5] H. Yabu and K. Ando, Nucl. Phys. B **301** (1988) 601.
[6] A. Momen, J. Schechter and A. Subbaraman, Phys. Rev. D **49** (1994) 5970.
[7] P. Jain, A. Momen and J. Schechter, Int. J. Mod. Phys. A **10** (1995) 2467.
[8] J. Beringer *et al.* [Particle Data Group Collaboration], Phys. Rev. D **86** (2012) 010001.

Quantum measurements along accelerated world-lines

JM Hartman[1] , SH Connell[1] and F Petruccione[2]

1. University of Johannesburg , Johannesburg, South Africa
2. University of Kwa-Zulu Natal, South Africa

Abstract. In this research, we are working with a formalism for quantum measurements that takes special relativity into account. The ultimate goal is to modify this framework to work with more general space-times rather than just Minkowski space-time and determine how the metric would affect quantum entanglement by doing a calculation of Bell's Theorem in curved space-time. As a first step in that direction, in this paper, we calculate the case for quantum measurements along an accelerated world line by solving the Schwinger-Tomonaga equation.

1. Introduction

Most of modern physics can be described either within the framework of general relativity or within the framework of quantum mechanics. General relativity describes one of the four fundamental forces, gravitation, as a warpage of space-time whereas the other three, namely the electromagnetic, the strong and weak nuclear forces can be adequately described within the framework of quantum mechanics. However, combining general relativity with quantum mechanics in order to formulate a theory of quantum gravity has proven difficult. The ultimate goal of the current work is to modify a framework of relativistic quantum mechanics, though not full quantum field theory, such that it includes metrics other than the Minkowski metric as the space-time background. This relativistic framework was formulated by Breuer and Petruccione [1] [2]. The goal is also to determine what the effect of the space-time background, if any, is on the measurements of entangled particles.

This paper summarises the framework, both non-relativistic and relativistic. In the non-relativistic case, the framework is a statistical multi-particle formalism of quantum mechanics which is formulated in terms of probabilities and allows for interactions between different quantum particles. In the relativistic case, we work with the Schwinger-Tomonaga equation instead of the Schröedinger equation which, in this case, is a functional differential equation and the state-vectors are taken as functionals that take as input, space-like hypersurfaces in space-time. The ultimate goal of this research is to extend this special relativistic framework to work with curved space-time backgrounds and then find out what, if any, effect the metric itself has on the phenomenon of quantum entanglement. That means to work with more generalised space-time backgrounds rather than just Minkowski space-time.

2. Quantum Measurements

In an ideal measurement in quantum mechanics, if a property B with corresponding projection operator $E(B)$ is measured on a quantum statistical ensemble $\mathcal{E}$ described by density matrix ρ, then after the measurement, we find that the density matrix ρ' which describes the ensemble $\mathcal{E}'$ that consists of the systems for which the property B is found to be true is given by

$$\rho' = \frac{E(B)\rho E(B)}{\mathrm{tr}\{E(B)\rho E(B)\}}, \tag{1}$$

where the projection operator $E(B)$ is defined in terms of the spectral family of $\hat{R} = \int_{-\infty}^{\infty} r dE_r$ by $P_R(B) = \langle \psi | E(B) | \psi \rangle$ (see [1], pp 59-62). Equation (1) is called the von Neumann-Lüders projection postulate [3] [4]. The above describes the ideal measurement of the projection $E(B)$ derived from the spectral family of $\hat{R}$ but in practice one can only measure an approximation that involves the finite resolution of the detector. If we consider a measurement scheme which yields a set $\mathcal{M}$ of possible outcomes $m \in \mathcal{M}$, then the von Neumann-Lüders projection postulate (1) can be generalised as follows:

(i) The measurement outcome m represents a classical random number with probability distribution

$$P(m) = \mathrm{tr}\{F_m \rho\}, \tag{2}$$

where F_m is a positive operator, called the effect, which satisfies the normalisation condition

$$\sum_{m \in \mathcal{M}} F_m = I, \tag{3}$$

such that the probability $P(m)$ is also normalised as

$$\sum_{m \in \mathcal{M}} P(m) = 1. \tag{4}$$

(ii) In the case of a selective measurement, the sub-ensemble of the systems for which the outcome m has been found to be described by the density matrix

$$\rho'_m = P(m)^{-1} \Phi_m(\rho), \tag{5}$$

where $\Phi_m = \Phi_m(\rho)$ is a positive super-operator, called an operation, and it maps positive operators to positive operators. We also assume that the operation Φ_m obeys the condition

$$\mathrm{tr}\Phi_m(\rho) = \mathrm{tr}\{F_m \rho\}. \tag{6}$$

Equation (6) together with equation (2) yields the normalisation

$$\mathrm{tr}\rho'_m = P(m)^{-1} \mathrm{tr}\Phi_m(\rho) = 1. \tag{7}$$

(iii) The density matrix for the corresponding non-selective measurement is given by

$$\rho' = \sum_{m \in \mathcal{M}} P(m) \rho'_m = \sum_{m \in \mathcal{M}} \Phi_m(\rho), \tag{8}$$

which is normalised according to equations (6) and (3) as

$$\mathrm{tr}\rho' = \sum_{m \in \mathcal{M}} \mathrm{tr}\Phi_m(\rho) = \sum_{m \in \mathcal{M}} \mathrm{tr}\{F_m \rho\} = \mathrm{tr}\rho = 1. \tag{9}$$

An important measurement scheme which can be treated within the framework of the generalised theory of quantum measurements above is the concept of an indirect measurement. Instead of directly measuring the system, in an indirect measurement, we perform the measurement on what we will call a quantum probe that has interacted with the system at some point. The aim of the indirect measurement scheme we're going to describe here is to obtain

information on the state of the object that we want to measure by performing measurements on the probe ([1], pp 96). This indirect measurement scheme can be considered to be consisting of three elements. The three elements are the quantum system to be measured, called the quantum object and has a Hilbert space $\mathcal{H}_O$, the quantum probe with Hilbert space $\mathcal{H}_P$ and a classical apparatus by which a measurement is performed on the quantum probe following it's interaction with the quantum object. Thus for an ideal measurement, we have three requirements. The first requirement is that prior to the interaction, and at time $t = 0$, the probe is prepared in a well defined quantum state ρ_P while the quantum object is in a state ρ_O. The second requirement is that the the measurement takes place after the interaction is over. So, the interaction between the probe and object may start at time $t = 0$ and end at time $t = \tau > 0$ but the measurement may only take place after the interaction has ended. The third requirement is that the measurement on the probe by the classical apparatus can be described as an ideal measurement by the von Neumann-Lüders projection postulate described above.

At the initial time $t = 0$, the density matrix of the combined system consisting of both probe and object is given by the tensor product $\rho_O \otimes \rho_P$ in the total Hilbert space given by $\mathcal{H} = \mathcal{H}_O \otimes \mathcal{H}_P$. The Hamiltonian of the total system is given by

$$H(t) = H_O + H_P + H_I(t), \tag{10}$$

where H_O and H_P, describe the free evolution of the object and probe respectively. The $H_I(t)$ term describes the evolution due to the interaction between the object and the probe. Outside the interaction time interval, $[0, \tau]$, the term $H_I(t)$ vanishes. The time evolution over this time interval according to the Schröedinger equation

$$i\frac{d}{dt}\left|\psi(t)\right\rangle = H(t)\left|\psi(t)\right\rangle, \tag{11}$$

can be described by a unitary operator called the time-evolution operator. It is given by

$$U \equiv U(\tau, 0) = T_{\leftarrow} \exp\left[-i\int_0^\tau dt H(t)\right], \tag{12}$$

where $T_{\leftarrow}$ is the chronological time-ordering operator that order the products of time dependent operators from right to left, in the direction of the arrow with earlier times on the right and the later times on the left, and we have used units such that $\hbar = 1$. If we assume $\rho(0) = \rho_O \otimes \rho_P$ to be the initial density matrix, then in terms of the time-evolution operator, the density matrix at time τ is given by

$$\rho(\tau) = U(\rho_O \otimes \rho_P)U^\dagger. \tag{13}$$

If we now assume that at time τ, the classical apparatus measures a probe observable $\hat{R} = \sum_m r_m \left|\varphi_m\right\rangle\left\langle\varphi_m\right|$, then we can obtain the indirect measurement by applying the von Neumann-Lüders projection postulate to the measurement of the probe and then by introducing the spectral decomposition of the density matrix of the probe, $\rho_P = \sum_k p_k \left|\phi_k\right\rangle\left\langle\phi_k\right|$, we can derive a measurement operation on the quantum object of the form ([1], pp 97-99)

$$\Phi_m(\rho_O) = \sum_k \Omega_{mk}\rho_O\Omega_{mk}^\dagger, \tag{14}$$

where $\Omega_{mk} = \sqrt{p_k}\left\langle\varphi_m \mid U \mid \phi_k\right\rangle$. When using these operators, the effect is given by $F_m = \sum_k \Omega_{mk}^\dagger\Omega_{mk}$ and so both the operaation and effect has the form of the representation theorem (see equations 2.157 and 2.158 on page 89 of Breuer and Petruccione [1], pp 97-99).

3. Relativistic Quantum Mechanics

In the relativistic framework, everything is re-formulated in terms of four-vectors with a Minkowski background. Here the four-vector $x^\mu = (x^0, \vec{x})$ represents the space-time coordinates of an event x in Minkowski space-time and we use the symbol $\eta_{\mu\nu}$ to represent the Minkowski metric. The Interaction picture representation of the Schröedinger equation ([1], pp 112-115) is used with the Interaction Hamiltonian defined as $H_I = \int \mathcal{H}(t, \vec{x}) d^3x$, where $\mathcal{H}(t, \vec{x})$ is the Hamiltonian density. In a given fixed coordinate system, the vector $|\Psi(t)\rangle$ gives the state of a quantum mechanical system at each time $x^0 = t$ and so allows the evaluation of expectation values for all observables which are localised on the hypersurface $x^0 = t =$ constant in Minkowski space-time. In order to get a Lorentz invariant generalisation of this concept, consider a state vector associated with a three-dimensional space-like hypersurface σ which is defined as a manifold in Minkowski space that extends to infinity in all directions. Consider further that at each point $x \in \sigma$ on the hypersurface, there exists a unit, timelike normal vector $n^\mu(x)$ satisfying the normalisation $n_\mu(x)n^\mu(x) = 1, n^0(x) \geqslant 1$. The state vector then becomes a functional $|\Psi\rangle = |\Psi(\sigma)\rangle$ in the space of all such hypersurfaces. The same is true of the density matrix of the system which is given as the functional $\rho = \rho(\sigma)$. The generalisation of the Schröedinger equation in this relativistic framework is thus a functional differential equation and is given by the Schwinger-Tomonaga equation [5] [6] [7] [8], which is given by

$$\frac{\delta |\Psi(\sigma)\rangle}{\delta\sigma(x)} = -i\mathcal{H}(x) |\Psi(\sigma)\rangle . \tag{15}$$

In direct analogy to partial differential equations, the Schwinger-Tomonaga equation is subject to the integrability condition

$$\frac{\delta^2\rho(\sigma)}{\delta\sigma(x)\delta\sigma(y)} - \frac{\delta^2\rho(\sigma)}{\delta\sigma(y)\delta\sigma(x)} = [[\mathcal{H}(x), \mathcal{H}(y)], \rho(\sigma)] = 0, \tag{16}$$

where the points x and y are located on the same hyper surface σ. This integrability condition is a direct consequence of the requirement of the micro-causality of the Hamiltonian density which states that $\mathcal{H}(x)$ and $\mathcal{H}(y)$ must commute if x and y are space like separated, i.e $[\mathcal{H}(x), \mathcal{H}(y)] = 0$ for $(x - y)^2 < 0$. This integrability condition insures that the Schwinger-Tomonaga equation has a unique solution $\rho(\sigma)$ once one has chosen an appropriate initial density matrix $\rho(\sigma_0)$ for an initial hypersurface σ_0. This solution is normally given as

$$\rho(\sigma) = U(\sigma, \sigma_0)\rho(\sigma_0)U^\dagger(\sigma, \sigma_0), \tag{17}$$

where $U(\sigma, \sigma_0)$ is the generalisation of the unitary time-evolution operator given by

$$U(\sigma, \sigma_0) = T_\leftarrow \exp\left[-i \int_{\sigma_0}^{\sigma} d^4x \mathcal{H}(x)\right], \tag{18}$$

where $T_\leftarrow$ is the chronological time-ordering operator, as usual where the time-ordering is ordered by the hypersurfaces of the foliation from the initial hypersurface σ_0 on the right up to the hypersurface at time τ given by $\sigma(\tau)$ on the left.

A foliation of Minkowski space is defined as a smooth one-parameter family $\mathcal{F} = \{\sigma(\tau)\}$ of space like hypersurfaces $\sigma(\tau)$ with the property that each space-time point x is located on precisely one hypersurface of the family. A given foliation $\sigma(\tau)$ gives rise to a corresponding family of state vectors $|\Psi(\tau)\rangle = |\Psi(\sigma(\tau))\rangle$. The Schwinger-Tomonaga equation (15) can then be re-formulated as an integral equation

$$|\psi(\tau)\rangle = |\Psi(0)\rangle - i \int_{\sigma_0}^{\sigma(\tau)} d^4x \mathcal{H}(x) |\Psi(\sigma_x)\rangle , \tag{19}$$

where we have denoted $\sigma_x = \sigma(\tau)$ for exactly one parameter value τ.

The hypersurfaces $\sigma(\tau)$ of a foliation can be defined with the help of an implicit equation of the form $f(x,\tau) = 0$, where $f(x,\tau)$ is a smooth scalar function. With an appropriate normalisation of f, the unit normal vector can be assumed to be given by $n_\mu(x) = \frac{\partial f(x,\tau)}{\partial x^\mu}$. Consider two infinitesimally separated hypersurfaces corresponding to two parameter values τ and $\tau + d\tau$. Then $d\,|\Psi(\tau)\rangle = |\Psi(\tau + d\tau)\rangle - |\Psi(\tau)\rangle$, which according to equation (19) is therefore

$$d\,|\Psi(\tau)\rangle = -i \int_{\sigma(\tau)}^{\sigma(\tau+d\tau)} d^4x \mathcal{H}(x)\,|\Psi(\tau)\rangle\,. \tag{20}$$

The four-volume element d^4x can be re-written as $d^4x = d\sigma(x) \left| n_0 \frac{\partial x_0}{\partial \tau} \right| d\tau = d\sigma(x) \left| \frac{\partial f}{\partial \tau} \right| d\tau$. Substituting this into equation (20) and dividing both sides by $d\tau$, we get

$$\frac{d}{d\tau}\,|\Psi(\tau)\rangle = -i \int_{\sigma(\tau)} d\sigma(x) \left| \frac{\partial f}{\partial \tau} \right| \mathcal{H}(x)\,|\Psi(\tau)\rangle \equiv -iH(\tau)\,|\Psi(\tau)\rangle\,. \tag{21}$$

For a particular example, let's consider an observer O moving along a straight world line $y(\tau) = n\tau$ with constant velocity $\vec{v}$ such that $n = \frac{dy}{d\tau} = (\gamma, \gamma\vec{v})$, where $\gamma = \frac{1}{\sqrt{1-|\vec{v}|^2}}$. Here we can see that n is the four-velocity of O. Here, the parameter τ is the proper time of the observer O, or the time measured by a clock carried along the world line $y(\tau)$ by O. At each fixed value of τ, the time axis in the rest frame of observer O is in the direction of the unit vector n while the instantaneous three-space at τ is given by the flat, spacelike hypersurface $\sigma(\tau)$ which is orthogonal to n and contains the point $y(\tau)$. So, the function f is then defined as

$$f(x,\tau) \equiv n(x - y(\tau)) \equiv nx - \tau = 0. \tag{22}$$

We see that the hypersurface $\sigma(\tau)$ consists of all the space-time points x with which the observer O assigns the same time coordinate τ. Since $\left| \frac{\partial f}{\partial \tau} \right| = |-1| = 1$, equation (21) then becomes

$$\frac{d}{d\tau}\,|\Psi(\tau)\rangle = -i \int_{\sigma(\tau)} d\sigma(x) \mathcal{H}(x)\,|\Psi(\tau)\rangle \equiv -iH(\tau)\,|\Psi(\tau)\rangle\,. \tag{23}$$

In the coordinate system where the normal vector n coincides with the time axis, i.e $n^\mu = (1,0,0,0)$, then equation (23) becomes identical to the Schröedinger equation.

On the other hand, the term $\left| \frac{\partial f}{\partial \tau} \right| \neq 1$ in general, equation (23) only applies if the observer O travels along a straight world-line with constant four-velocity n.

As discussed in the Abstract, before we extend the formalism to the case of general space-times, the first step is to calculate the Schwinger-Tomonaga equation for uniformly accelerated world lines. If we allow for acceleration such that $n(\tau)$ varies in time, then we have to include a different value for $\left| \frac{\partial f}{\partial \tau} \right|$ in general. To take another example, let's consider the case of the observer O accelerating uniformly with respect to an observer O'. In other words, the reference frame of the observer O is such that there is a constant non-zero proper acceleration $\vec{a}$ as felt by observer O. If we again assume that the unit normal vector $n(\tau)$ is the four-velocity, then the four-acceleration is given by $a^\mu(\tau) = \frac{dn^\mu(\tau)}{d\tau}$. Now, since the four-velocity is always normalised as $n^\mu(\tau)n_\mu(\tau) = \eta_{\mu\nu}n^\mu(\tau)n^\nu(\tau) = 1$, we also have $\frac{d}{d\tau}(n_\mu(\tau)n^\mu(\tau)) = 2n_\mu(\tau)a^\mu(\tau) = 0$. Therefore any four-acceleration is orthogonal to the corresponding four-velocity at a given proper time τ, i.e. $a^\mu(\tau)n_\mu(\tau) = 0$ at all times τ. In the observer frame O, the unit normal vector n coincides with the time axis. Therefore the four-velocity of O is $n^\mu = (1,0,0,0)$ when measured with respect to it's own reference frame, while the four-acceleration is given by $a^\mu = (0,\vec{a})$.

Noting that the magnitude of the four-acceleration as measured in the observer frame O is $|(0,\vec{a})| = |\vec{a}| = a$, the only way to make sure that the acceleration of O remains uniform is to ensure that the magnitude of the four-acceleration remains constant at a. Using the fact that a^μ and n^μ are orthogonal, we obtain for the four-acceleration,

$$a^\mu(\tau) = (a\sinh(a\tau), \frac{a}{|\vec{a}|}\cosh(a\tau)\vec{a}), \tag{24}$$

and for the four-velocity,

$$n^\mu(\tau) = (\cosh(a\tau), |\vec{a}|^{-1}\sinh(a\tau)\vec{a}), \tag{25}$$

such that $a^\mu a_\mu = a^2(\sinh^2(a\tau) - \cosh^2(a\tau)) = -a^2$, $a^\mu n_\mu = 0$ and $n^\mu n_\mu = \cosh^2(a\tau) - \sinh^2(a\tau) = 1$. The observer therefore follows a hyperbolic world-line $y(\tau) = (a^{-1}\sinh(a\tau), a^{-1}|\vec{a}|^{-1}\cosh(a\tau)\vec{a})$ and the function f hypersurface is given by $f(x,\tau) \equiv n(\tau)(x - y(\tau)) = n(\tau)x = 0$. Therefore $\left|\frac{\partial f}{\partial \tau}\right| = |a^\mu(\tau)x_\mu|$ and so the Schwinger-Tomonaga equation (21) for the case of an accelerated world line now becomes

$$\frac{d}{d\tau}|\Psi(\tau)\rangle = -i\int_{\sigma(\tau)} d\sigma(x)\,|a^\mu(\tau)x_\mu|\,\mathcal{H}(x)\,|\Psi(\tau)\rangle\,. \tag{26}$$

4. Conclusion

The main part of this paper provides an overview of a framework for special relativistic quantum mechanics, although it is not full quantum field theory. It describes a statistical interpretation of non-relativistic quantum mechanics for multi-particle systems and then proceeds to use that interpretation to describe a theory of quantum measurement. The framework was then generalised to a framework for special relativistic quantum mechanics. This framework was initially formulated by Breuer and Petruccione [1].

The main part of this paper is devoted to the description of non-relativistic measurements. In addition, we have derived the relativistic evolution equation for a closed quantum system with respect to a reference frame moving at constant velocity and a reference frame with uniform acceleration. In future we will describe the projection measurements in a relativistic setting. Based on this and the description of unitary evolution, one could attempt a relativistic description of generalised measurements, all of which could be realised as indirect measurements. We will also try to derive Bell-state measurements within the framework before attempting to introduce more general metrics into the framework other than the Minkowski metric.

References

[1] Breuer H and Petruccione F 2007 *The Theory of Open Quantum Systems* (OUP Oxford) ISBN 9780199213900 URL `http://books.google.co.za/books?id=DkcJPwAACAAJ`

[2] Breuer H P and Petruccione F 1999 State vector reduction in relativistic quantum mechanics: An introduction *Lecture Notes in Physics, Berlin Springer Verlag* (*Lecture Notes in Physics, Berlin Springer Verlag* vol 526) ed Breuer H P and Petruccione F p 1

[3] von Neumann J 1996 *Mathematical Foundations of Quantum Mechanics* translation - from german ed (Princeton University Press) ISBN 0691028931 URL `http://www.amazon.com/exec/obidos/redirect?tag=citeulike07-20&path=ASIN/0691028931`

[4] Lüders G 2006 *Annalen der Physik* **518** 663–670 (*Preprint* `arXiv:quant-ph/0403007`)

[5] Tomonaga S 1946 *Progress of Theoretical Physics* **1** 27–42 URL `http://dx.doi.org/10.1143/ptp.1.27`

[6] Koba Z, Tati T and Tomonaga S 1947 *Progress of Theoretical Physics* **2** 101–116

[7] Schwinger J 1948 *Physical Review* **74** 1439–1461

[8] Schweber S S 2005 *An Introduction to Relativistic Quantum Field Theory* (Dover Publications) ISBN 0486442284 URL `http://www.amazon.com/exec/obidos/redirect?tag=citeulike07-20&path=ASIN/0486442284`

Concavity of energy surfaces

S Karataglidis[1] and B. G. Giraud[2]

[1] Department of Physics, University of Johannesburg, P.O. Box 524 Auckland Park, 2006, South Africa

[2] Institut de Physique Théorique, Centre d'Etudes Saclay, 91190 Gif-sur-Yvetta, France

E-mail: [1]stevenka@uj.ac.za

Abstract. The property of concavity in calculations of energy surfaces is developed and discussed, in reference to strict energy minimisation when collective coordinates are constrained. Such collective coordinates are actually subject to quantum fluctuations and these prevent, via tunnel effects, the probing of maxima and saddle points. A solution to the problem is developed. It allows to bypass the concavity syndrome and recover maxima and saddle points.

1. Introduction

For practical calculations in many-body physics, be they atomic, nuclear, molecular, or condensed matter, the concept of collective coordinates [1] has been of central importance. Its goal has been to generate models involving far fewer degrees of freedom than the true number, $3A$, as required for a proper, microscopic, description of a system of A particles. As is also often the case, the dynamics can be compressed into slow motions of a few collective degrees of freedom (B), while the other, faster, degrees of freedom are averaged out. Also, in the case of identical particles, such collective degrees of freedom may be represented as one-body operators: $B = \sum_{i=1}^{A} \beta(\mathbf{r}_i, \mathbf{p}_i, \sigma_i, \tau_i)$, where $\beta(\mathbf{r}_i, \mathbf{p}_i, \sigma_i,$ and τ_i refer to the individual particle i's position, momentum, spin, and, if necessary, isospin, respectively.

Once prescribed, such models lead to energy surfaces [2] of the system. Given the collective operator B with expectation value $b \equiv \langle B \rangle$, most collective models accept that there exists an energy function, $e(b)$, and an inertia parameter, $\mu(b)$, that drive the collective dynamics. Descriptions of such energy surfaces leads to terminology such as "saddles", "barriers", etc. [2, 3, 4].

Central to the prescription is the assumption that the energy function is a result of an energy *minimisation* under constraint. That is, while the system evolves through various values of b, it is accepted that the energy is tuned to achieve a (local) minimum. This aspect of finding the energy surface is central to many fields of physics. Consider a Hamiltonian, $H = \sum_i T_i + \sum_{i<j} V_{ij}$, where T and V denote the kinetic and potential energy operators. Given a trial set of density operators, $\mathcal{D}$, in many-body space and normalised by $\mathrm{Tr}\mathcal{D} = 1$, with Tr denoting the trace, the energy surface may be defined by

$$e(b) = \inf_{\mathcal{D} \Rightarrow b} \mathrm{Tr}\left\{H\mathcal{D}\right\}. \tag{1}$$

The constraint, $\mathcal{D} \Rightarrow b$, enforces $\mathrm{Tr}\left\{B\mathcal{D}\right\} = b$.

However, there are theories which do not use, *a priori*, energy minimisation for the "fast" degrees. Time-dependent Hartree-Fock (HF) trajectories [5], generalisations with pairing, adiabatic versions [6], often exhibit collective motions. Equations of motion [7] and/or a maximum decoupling [8] of "longitudinal" from "transverse" degrees of freedom, have also shown significant successes in the search for collective degrees. This has come at the cost, however, of imposing a one-body nature of both collective coordinates and momenta and accepting state-dependence of those operators. Such approaches define an energy surface once trajectories of wave functions in many-body spaces have been calculated. (They are not the subject of the present paper.) Herein, we focus on fixed operators constraining energy minimisation within a fixed basis for single-particle and many-body states.

To define properly am energy function $e(b)$ of the collective coordinate, one should first diagonalise B within the space defined by the many-body states. The resulting spectrum of B is assumed to be continuous, or at least have a high level density for the chose trial space. For each eigenvalue, b, one should then find the ground state energy eigenvalue $e(b)$, of the projection of H onto that eigensubspace labelled by b.

However, in practice, one settles for the diagonalisation of the constrained operator $\mathcal{H} = H - \lambda B$, where λ is a Lagrange multiplier, or, alternatively, for the minimisation of $\langle \mathcal{H} \rangle$. (This is not restricted to one constraint: one may add more constraints with suitable Lagrange multipliers defined.) B is assumed to have both lower and upper bounds, or, that the constrained Hamiltonian will always have a ground state. From that constrained Hamiltonian, one may obtain the free energy, $\varepsilon(\lambda) \equiv \langle \mathcal{H} \rangle$. The label b is no longer an eigenvalue but just an average value, as defined by the expectation value of B. A Legendre transform of $\langle \mathcal{H} \rangle$ then returns the energy surface $e(b)$, with b and λ forming a Legendre pair. Thus $d\varepsilon/d\lambda = -\mathrm{Tr}\{B\mathcal{D}\} = -b$ and $de/db = \lambda$. The problem lies when considering a constrained variation in a *quantum* system without additional precautions as: i) there is a link between strict minimisation and the curvature properties of $e(b)$; and ii) the usual interpretation of b as a well-defined coordinate for a collective model can be negated by non-negligible fluctuations (whatever the cause).

2. Theorem linking minimisation and concavity

Before proving the theorem, we must recall that with Hartree-Fock (HF) and Hartree-Bogoliubov (HB) approximations both concave and convex branches were obtained for $e(b)$ by replacing the constraint term, $-\lambda \langle B \rangle$, in $\langle \mathcal{H} \rangle$ by either $-\lambda' \langle B \rangle + \mu \langle B \rangle^2 /2$, [9], or $-C (\langle B \rangle - \mu)^2 /2$, [3, 4], with adjustable values of λ', C, and μ. However, both methods, while stabilizing the numerical procedure, amount to use an effective Lagrange multiplier, namely $\lambda_{\mathrm{eff}} = \lambda - \langle B \rangle \mu$ and $\lambda_{\mathrm{eff}} = C (\langle B \rangle - \mu)$, respectively. We shall, therefore, stick to the generic form, $H - \lambda B$, in the following.

Consider a solution branch $\mathcal{D}(\lambda)$, expanding up to second order, and assuming that the manifold of solutions is suitably analytic,

$$\mathcal{D}(\lambda + d\lambda) = \mathcal{D}(\lambda) + d\lambda(d\mathcal{D}/d\lambda) + (d\lambda^2/2)(d^2\mathcal{D}/d\lambda^2). \tag{2}$$

The stationarity and minimality of $\mathrm{Tr}\{\mathcal{H}\mathcal{D}\}$ with respect to any variation of $\mathcal{D}$, and in particular w.r.t. that variation, $\mathcal{D}(\lambda + d\lambda) - \mathcal{D}(\lambda)$, induce,

$$\begin{aligned} \mathrm{Tr}\{\mathcal{H} d\mathcal{D}/d\lambda\} &= 0, \\ \mathrm{Tr}\left\{\mathcal{H} d^2\mathcal{D}/d\lambda^2\right\} &\geq 0. \end{aligned} \tag{3}$$

The free energy ε is also stationary for $\mathcal{D}(\lambda + d\lambda)$, but the Hamiltonian is now $\mathcal{H}(\lambda) - B d\lambda$, and the derivative of the state is $d\mathcal{D}/d\lambda + d\lambda(d^2\mathcal{D}/d\lambda^2) + \mathcal{O}(d\lambda^2)$, hence,

$$\mathrm{Tr}\left\{(\mathcal{H} - B d\lambda)\left[d\mathcal{D}/d\lambda + d\lambda(d^2\mathcal{D}/d\lambda^2) + \mathcal{O}(d\lambda^2)\right]\right\} = 0. \tag{4}$$

The zeroth order of this, Eq. (4), is, $\mathrm{Tr}\{\mathcal{H}d\mathcal{D}/d\lambda\}$. It vanishes, because of the first of Eqs. (3). The first order, once divided by $d\lambda$, gives,

$$-\mathrm{Tr}\{Bd\mathcal{D}/d\lambda\} = -\mathrm{Tr}\left\{\mathcal{H}d^2\mathcal{D}/d\lambda^2\right\}. \tag{5}$$

The left-hand side of Eq. (5) is nothing but the the second derivative, $d^2\varepsilon/d\lambda^2$. The right-hand side is semi-negative-definite, because of the second of Eqs. (3). Hence, the plot of $\varepsilon(\lambda)$ is a convex curve and the plot of its Legendre transform, $e(b)$, is concave. (Other authors may have the opposite sign convention of the second derivative to define concavity versus convexity.) With our sign convention [10, 11], strict minimisation necessarily induces concavity, and any convex branch means that the "fast" degrees of freedom are not in a minimal energy.

It is important to note that this proof does not assume any specification of $\mathcal{D}(\lambda)$, whether it is constructed either from exact or approximate eigenstates of $\mathcal{H}$. Therefore strict minimisation can *only* return *concave* functions $e(b)$. Maxima are impossible. In the generalisation where several collective operators $B_1, \ldots, B_N$, are involved, concavity stills holds, so saddles are also excluded. Hence, only an absolute minimum is possible. (However, we shall show below how to overcome the paradox: by *keeping constant the fluctuations* of the collective coordinate(s), one can deviate from concavity, and more important, validate a constant quality of the representation provided by branches $\mathcal{D}(\lambda)$.)

Alternatively, let $\psi(\lambda)$ be the ground state of $\mathcal{H}$. (For the sake of simplicity, we assume that there is no degeneracy.) The corresponding eigenvalue, $\varepsilon(\lambda)$, is stationary with respect to variations of ψ, among which is the "online" variation, $d\lambda\,(d\psi/d\lambda)$, leading to the well-known first derivative, $d\varepsilon/d\lambda = -b \equiv -\langle\psi|B|\psi\rangle$. Consider the projectors $P = |\psi\rangle\langle\psi|$ and $Q = 1 - P$. Brillouin-Wigner theory yields the first derivative of ψ, *viz.*

$$\frac{d|\psi\rangle}{d\lambda} = -\frac{Q}{\varepsilon - Q\mathcal{H}Q}B|\psi\rangle. \tag{6}$$

This provides the second derivative of ε,

$$-\frac{db}{d\lambda} \equiv -\frac{d}{d\lambda}\langle\psi|B|\psi\rangle = 2\left\langle\psi\left|B\frac{Q}{\varepsilon - Q\mathcal{H}Q}B\right|\psi\right\rangle. \tag{7}$$

Since the operator $(\varepsilon - Q\mathcal{H}Q)$ is clearly negative-definite, the eigenvalue, ε, is a convex function of λ. It is trivial to prove that the same convexity holds for the ground state eigenvalue $\varepsilon(\lambda_1, \ldots, \lambda_N)$ if several constraints, $B_1, \ldots, B_N$, are used. If, moreover, a temperature T is introduced, the thermal state, $\mathcal{D} = \exp[-\mathcal{H}/T]/\mathrm{Tr}\exp[-\mathcal{H}/T]$, replaces the ground state projector, $|\psi(\lambda_1, \ldots, \lambda_N)\rangle\langle\psi(\lambda_1, \ldots, \lambda_N)|$, and the free energy, $\varepsilon(\lambda_1, \ldots, \lambda_N; T)$, also contains the entropy contribution, $-TS$, where $S = -\mathrm{Tr}\{\mathcal{D}\ln\mathcal{D}\}$. A proof of the convexity of the exact $\varepsilon(\lambda_1, \ldots, \lambda_N; T)$ is also easy [12].

At $T = 0$ the usual Legendre transform expresses the energy, $e \equiv \langle\psi|H|\psi\rangle$, in terms of the constraint value(s) rather than the Lagrange multiplier(s). For simplicity, consider one constraint only; the generalization to $N > 1$ is easy. Since $e \equiv \varepsilon + \lambda b$, then $de/db = \lambda$, a familiar result for conjugate variables. Furthermore, the second derivative, d^2e/db^2, reads, $d\lambda/db = 1/(db/d\lambda)$. From Eq. (7), the derivative, $db/d\lambda$, is positive-definite. Accordingly, e is a concave function of b. Now, if $T > 0$, the Legendre transform instead generates a reduced free energy, $\eta \equiv (e - TS)$, a concave function of the constraint value(s). An additional Legendre transform returns e alone, as a concave function of the constraint(s) and S.

Let b_- and b_+ be the lowest and highest eigenvalues of B. When λ runs from $-\infty$ to $+\infty$, then b spans the interval, $[b_-, b_+]$. There is no room for a junction with convex branches under technical modifications as used by [9, 3, 4]. For every exact diagonalization of $\mathcal{H}$, or

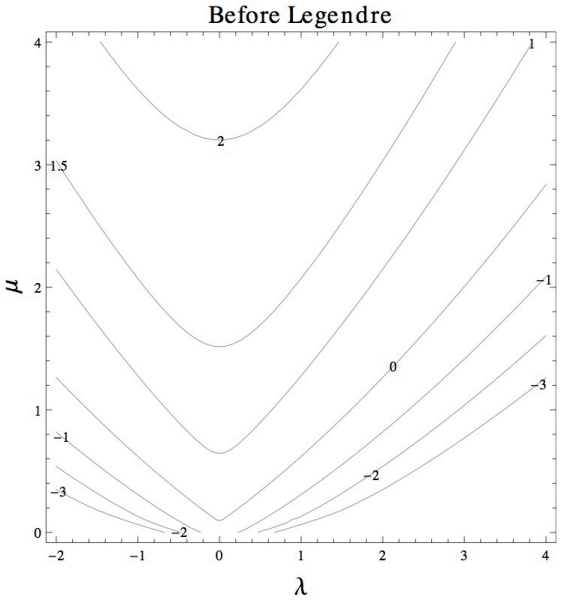

Figure 1. The convex contour plot of $\varepsilon(\lambda, \mu)$, for the model of Eq. (9).

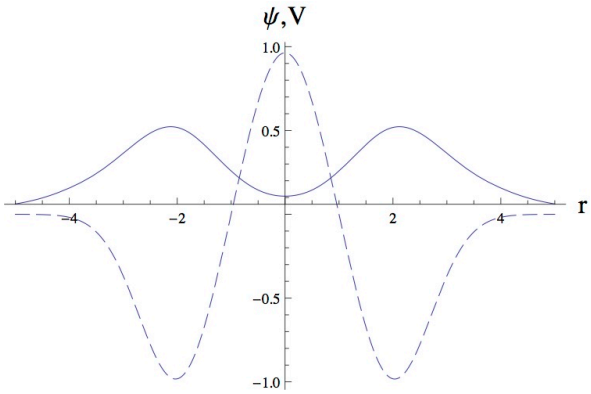

Figure 2. Ground state (solid line) when $\lambda = \mu = 0$, and potential (dashed line).

exact partition function, concavity sets a one-to-one mapping between b in this interval and λ. More generally, with exact calculations, there is a one-to-one mapping between the set of Lagrange multipliers, $\{\lambda_1, \ldots, \lambda_N\}$, and that of obtained values, $\{b_1, \ldots, b_N\}$, of the constraints. Concavity, *in the whole obtained domain of constraint values*, imposes a poor landscape: there is one valley only.

3. Results

With Q now denoting our generic constraint, we diagonlise $\mathcal{H} = H - \lambda Q$ accordingly, where the Lagrange multipler $\lambda \in (-\infty, \infty)$. This is equivalent to finding the roots of the equation $\mathcal{P}(\lambda, \varepsilon) \equiv \det(H - \lambda Q - \varepsilon) = 0$. We track of $\langle H \rangle$ and $\langle Q \rangle$, along the eigenstates of $\mathcal{H}$, *viz.*

$$\mathcal{Q}(\lambda, \varepsilon) \equiv \frac{\partial \mathcal{P}}{\partial \lambda} - \langle Q \rangle \frac{\partial \mathcal{P}}{\partial \varepsilon} = 0. \tag{8}$$

We replace ε in terms of $\langle H \rangle$, λ, and $\langle Q \rangle$, in $\mathcal{P}$ and $\mathcal{Q}$. By eliminating λ we obtain a resultant $\mathcal{R}(\langle H \rangle, \langle Q \rangle) = 0$. We plot $\langle H \rangle$ as a multi-valued function of $\langle Q \rangle$. (See Ref. [13] for details.)

Consider a model consisting of 11 (or 21) oscillators, where the Hamiltonian is

$$\begin{aligned} H &= \frac{P^2}{2} + V(r) \\ \mathcal{H} &= H - \lambda r + \mu r^2, \end{aligned} \tag{9}$$

which is a model with two constraints. Fig. 1, shows the (convex) contour plot of the lowest eigenvalue $\varepsilon(\lambda, \mu)$ of $\mathcal{H}$. Fig. 2 shows the ground state and potential energy of the model. If one allows for a fluctuation in r, denoted by Δr, as given in Fig. 3, one recovers the ground state energy landscape, Fig. 4, by subtracting the zero point energy. Figs. 5 and 6 show 3d plots of the energy as functions of constraints and of fluctuations, respectively. Concavity in the surface is clearly observed in Fig. 5, as is the shape of the potential in Fig. 6. Note that with increasing fluctuation the constraint is clearly lost.

4. Conclusions

There are problems in defining energy surfaces as a result of minimisations when constraints are subject to fluctuations. Controlling the effect of such fluctuations by second-order constraints is necessary to keep the quality of the energy across the landscape.

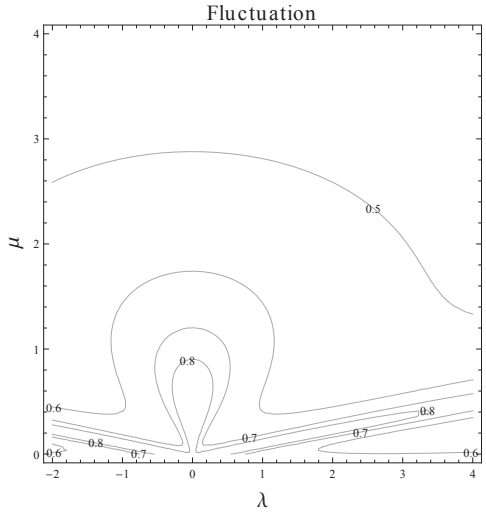

Figure 3. Contour plot of the fluctuation, Δr.

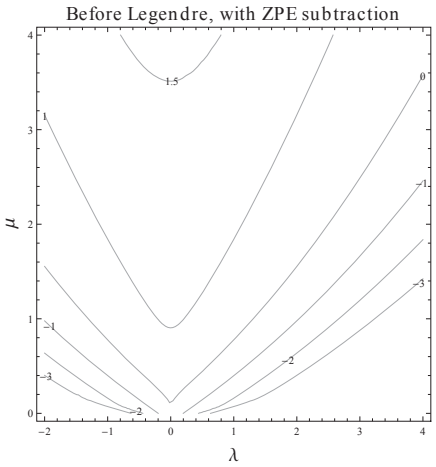

Figure 4. Contour of the ground state energy after subtraction of the zero point energy.

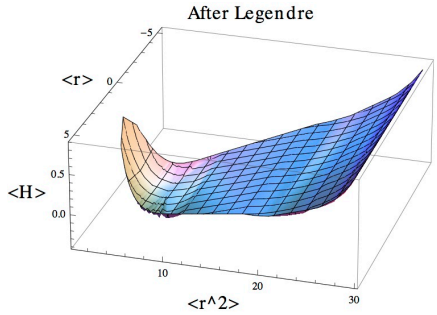

Figure 5. Constrained ground state as a function of $\langle r \rangle$ and r^2 .

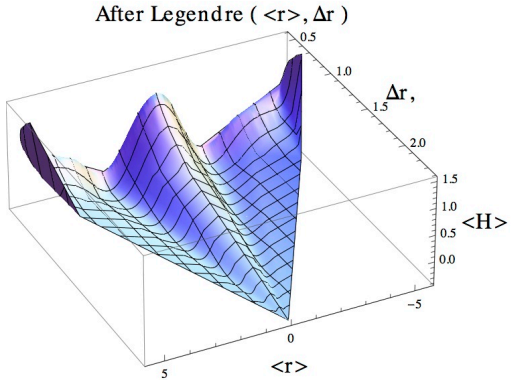

Figure 6. Same as Fig. 5, except as a function of $\langle r \rangle$ and Δr.

Acknowledgments

SK acknowledges support of the National Research Foundation of South Africa.

References

[1] Bohr A and Mottelsohn B 1998 *Nuclear Structure* (Singapore: World Scientific)
[2] Nix J R and Swiatecki W J 1964 *Nucl. Phys.* **71** 1
[3] Flocard H, Quentin P, Kerman A K and Vautherin D 1973 *Nucl. Phys.* **A203** 433
[4] Flocard H, Quentin P, Vautherin D, Veneroni M and Kerman A K 1974 *Nucl. Phys.* **A231** 176
[5] Bonche P 1976 *J. Physique* **C37** 5
[6] Villars F 1977 *Nucl. Phys.* **A285** 269
[7] Bulgac A, Klein A, Walet N R and Dang G D 1989 *Phys. Rev. C* **40** 945
[8] Matsuyanagi K, Matsuo M, Nakatsukasa T, Hinobara N and Sato K 2010 *J. Phys. G* **33** 064018
[9] Giraud B G, Tourneux J L and Wong S K M 1970 *Phys. Lett.* **32B** 23
[10] Barrett B R, Giraud B G, Jennings B K and Toberg N 2009 *Nucl. Phys.* **A828** 267
[11] Neergaard K, Pashkevich V V and Frauendorf S 1976 *Nucl. Phys.* **A262** 61
[12] Balian R 2007 *From microphysics to macrophysics: Methods and applications of Statistical Physics* (Berlin: Springer)
[13] Giraud B G and Karataglidis S 2011 *Phys. Lett.* **B703** 88

Tsallis entropy and quantum uncertainty in information measurement

Mhlambululi Mafu[1], **Francesco Petruccione** [1,2]

[1] Centre for Quantum Technology, School of Chemistry and Physics, University of KwaZulu-Natal, P/Bag X54001 Durban 4000, South Africa

[2] National Institute for Theoretical Physics (NITheP), KwaZulu-Natal, South Africa

E-mail: mafum@ukzn.ac.za, petruccione@ukzn.ac.za

Abstract. The Tsallis entropy defines an important generalization of the usual concept of entropy which depends on parameter α. Our goal is to establish a connection between the quantum uncertainty principle and the Tsallis entropy for single discrete observables. In particular, we show that there exist a generalized uncertainty bound reached in order to appropriately express the quantum uncertainty principle in terms of the Tsallis entropy. This kind of connection forms an initial important step towards finding an important application of this α-entropy in the area of quantum communication for which they have not been extensively investigated.

1. Introduction

Depending on the application, a number of entropic forms [1] and uncertainty relations [2, 3, 4] have been derived. Amongst entropies, the most important and greatly studied entropy that has even found major applications is the Shannon entropy [5]. Many generalizations or versions of the Shannon entropy have already been found and one of the generalizations is the Tsallis entropy [6]. The Tsallis entropy was introduced by Havrda and Charvát in 1967 [7] and later studied by Darcózy in 1970 [8], it was in 1988 when Tsallis [6] exploited its features and placed a physical meaning on this entropy. Therefore, this entropy is now known as the Tsallis entropy. Similar to the Shannon entropy, the Tsallis entropy has also found many interdisciplinary applications [9]. In particular, it has been established that the Tsallis and Shannon entropies can be connected by means of some transformation [9]. Therefore, this connection between these two entropies shows a possibility of interchangeability between these two entropies, however only up to some bound.

On the other hand, the first uncertainty relation to be derived was by Hirschman [10]. This uncertainty relation was a position-momentum relation which is based on the Shannon entropy. However, the Heisenberg uncertainty principle [11] forms one of the most developed results of quantum theory. In particular, Robertson showed that a product of two standard deviations of two discrete observables A and B measured in the quantum state $|\psi\rangle$ is bounded from below [12]. This can be expressed as $\triangle A \cdot \triangle B \geq \frac{1}{2}|\langle\psi|[A,B]|\psi\rangle|$. This result was improved by Deutsch in 1983 [13]. The improvement on Deutsch's work was conjectured by Kraus [14] and later proved by Maassen and Uffink [15]. However, it has also been observed that this Robertson's bound does not express all the features expected from an uncertainty relation if the observables A and B are finite [16].

Recently, the entropic uncertainty relations have found several applications especially in quantum information [17, 18]. We highlight that such applications in quantum information are based on properties of the Shannon entropy. However, the Tsallis entropy has not been utilized in such applications. A major difference exists between the Shannon and the Tsallis entropy, i.e., the Shannon entropy is additive for independent probability distributions while the Tsallis entropy is non-additive [19]. Therefore, this difference proves to be a challenge in trying to immediately connect the Tsallis entropy to these applications in quantum information. Despite this major difference in the non-additivity property for independent probability distributions of the Tsallis entropy, it is the object of this paper to explicitly show a bound based on Tsallis entropy and subsequently a possible extension of the application for Tsallis entropies to physical processes in quantum information specifically on quantum key distribution. Therefore, we establish a connection between the quantum uncertainty principle and the Tsallis entropy for single discrete observables. We also show an immediate application of the Tsallis entropy on how they can be useful in quantifying information in quantum key distribution.

2. Tsallis entropy

For a probability distribution, p_i, on a finite set, the Tsallis entropy, $S_\alpha(p_i)$ for order α is defined as [6]

$$S_\alpha(p_i) = -\sum_{i=1}^{n} p_i^\alpha \ln_\alpha p_i, \tag{1}$$

where $0 < \alpha < \infty$. The Tsallis entropy can also be expressed as $S_\alpha(p_i) = \frac{1}{1-\alpha}\left(\sum_i p_i^\alpha - 1\right)$. The α algorithm in Eq (1) is defined as $\ln_\alpha(x) = x^{1-\alpha} - 1/(1-\alpha)$ for any nonnegative real numbers α and x. At $\alpha = 1$, $S_\alpha(p_i)$ does not exist, therefore we use the L'Hopitals rule to show that the Tsallis entropy approaches the Shannon entropy as $\alpha \mapsto 1$, because the α logarithm uniformly converges to a natural logarithm as $\alpha \mapsto 1$ i.e., $\lim_{\alpha\mapsto 1} S_\alpha(p_i) = -\sum_i p_i \ln p_i$ which is the Shannon entropy [5]. In particular, there is also a close relationship between the Rényi entropy and the Tsallis entropy written as

$$H_\alpha(p_i) = \frac{1}{1-\alpha}\ln(1 + (1-\alpha)S_\alpha(p_i)). \tag{2}$$

where $H_\alpha(p_i)$ is the Rényi entropy. Among the property of these entropies, a major difference exists, the Shannon and Rényi entropies are derived to be additive whilst the Tsallis entropy is derived to be pseudo-additive for $\alpha \neq 1$ and is expressed as

$$S_\alpha(p_i, p_j) = S_\alpha(p_i) + S_\alpha(p_j) + (1-\alpha)S_\alpha(p_i)S_\alpha(p_j), \tag{3}$$

where p_i and p_j are distributions for independent random variables A and B respectively.

In order to arrive at our goal, we start by summarizing the result of Ref [13]. Of importance, Deutsch established that the generalized Heisenberg inequality does not properly express the quantum uncertainty principle except in the canonically conjugate observables. In general, he found that in order to properly quantify the quantum uncertainty principle, there exists an irreducible lower bound in the result of uncertainty of a measurement. This can be written quantitatively as

$$\mathcal{U}(\hat{A}, \hat{B}; \psi) \geq \mathcal{B}(\hat{A}, \hat{B}), \tag{4}$$

where $\mathcal{U}$ is the uncertainty in the measurement of $\hat{A}$ and $\hat{B}$ which are simultaneously prepared or measured observables, $|\psi\rangle$ is the outcome state and $\mathcal{B}$ is the irreducible lower bound as according to Ref [13]. The function $\mathcal{U}(\hat{A}, \hat{B})$ depends only on the state $|\psi\rangle$ and the sets $\{|a\rangle\}$ and $\{|b\rangle\}$ while $\mathcal{B}(\hat{A}, \hat{B})$ depends on the set $\{\langle a|b\rangle\}$ of the inner product of two eigenstates of A and B respectively.

Based on Ref [13], the most natural measure of uncertainty is the result of a measurement or preparation of a single discrete observable which can be expressed in the entropic form as

$$S_{\hat{A}}(|\psi\rangle) = -\sum_{a} |\langle a|\psi\rangle|^2 \ln |\langle a|\psi\rangle|^2. \tag{5}$$

We can recognize that the right hand side of Equation (5) is expressed in terms of the Shannon's entropy where, $p_i = |\langle a_i|\psi\rangle|^2$ and $p_j = |\langle b_j|\psi\rangle|^2$ are projectors of $|\psi\rangle$ on $\hat{A}$ and $\hat{B}$ respectively. It has been shown in Ref [14] that

$$\mathcal{U}(\hat{A}, \hat{B}; \psi) \geq 2 \ln \frac{1}{1+c}, \tag{6}$$

where $c = \max_{ij} |\langle a_i|b_j\rangle|$. As stated previously that this bound was later improved by Maassen and Uffink [15] for which they obtained

$$\mathcal{U}(\hat{A}, \hat{B}; \psi) \geq 2 \ln \frac{1}{c}, \tag{7}$$

by considering measurements from two mutually unbiased bases, therefore our aim to investigate whether the non-extensivity property of the Tsallis entropy will ever make a difference on the requirements of $\mathcal{B}$ instead of using the Shannon entropy. However, surprisingly, we reach a bound which can be expressed in a similar manner as in Ref [13].

We consider two observables $\hat{A}$ and $\hat{B}$ which are simultaneously measured or prepared and a state $|\psi\rangle$ which represents the outcome of a measurement or preparation. Therefore, for our scenario in order to find the bound on $\mathcal{B}(\hat{A}, \hat{B})$ we relate this function to the pseudo-additivity property of Tsallis entropy instead of using additivity of Shannon entropy and without loss of generality we write Equation (3) as

$$\mathcal{U}(\hat{A}, \hat{B}; \psi) = S_\alpha(\hat{A}; \psi) + S_\alpha(\hat{B}; \psi) + (1-\alpha) S_\alpha(\hat{A}; \psi) S_\alpha(\hat{B}; \psi). \tag{8}$$

Now we calculate the bound $\mathcal{U}$ by using the Tsallis entropy as an information measure by proceeding as follows

$$\begin{aligned}
\mathcal{U}(\hat{A}, \hat{B}; \psi) &= -\sum_a |\langle\psi|a\rangle|^{2\alpha} \ln_\alpha |\langle\psi|a\rangle|^2 - \sum_b |\langle\psi|b\rangle|^{2\alpha} \ln_\alpha |\langle\psi|b\rangle|^2 \\
&+ (1-\alpha) \sum_a |\langle\psi|a\rangle|^{2\alpha} \ln_\alpha |\langle\psi|a\rangle|^2 \sum_b |\langle\psi|b\rangle|^{2\alpha} \ln_\alpha |\langle\psi|b\rangle|^2 \\
&= -\sum_{ab} |\langle\psi|a\rangle|^{2\alpha} |\langle\psi|b\rangle|^{2\alpha} [(\ln_\alpha |\langle\psi|a\rangle|^2 + \ln |\langle\psi|b\rangle|^2) \\
&- (1-\alpha) \ln_\alpha |\langle\psi|a\rangle|^2 \ln_\alpha |\langle\psi|b\rangle|^2].
\end{aligned} \tag{9}$$

We can maximize the parenthesized quantity in Equation (9), by performing the following operations:

$$\begin{aligned}
\mathcal{U}(\hat{A}, \hat{B}; \psi) &= \max_{|\psi\rangle} |\langle\psi|a\rangle\langle b|\psi\rangle| \\
&\leq \max_{|\psi\rangle} | \left(\frac{|a\rangle\langle a| + |b\rangle\langle b|}{2} \right) |.
\end{aligned} \tag{10}$$

In the following analysis, we are going to restrict our attention to two vectors at a time. In order to calculate the maximum eigenvalue of the expression in Equation (10), we apply the following substitution

$$|a\rangle = \begin{pmatrix}1\\0\end{pmatrix}, \quad |b\rangle = \begin{pmatrix}\cos\theta e^{-i\alpha}\\ \sin\theta\end{pmatrix}$$

and arrive at an expression of the form

$$\begin{aligned}\left(\frac{|a\rangle\langle a| + |b\rangle\langle b|}{2}\right) &= \frac{1}{2}\begin{pmatrix}1 & 0\\ 0 & 0\end{pmatrix} + \frac{1}{2}\begin{pmatrix}\cos^2\theta & \cos\theta\sin\theta e^{-\alpha}\\ \sin\theta\cos\theta e^{-i\alpha} & \cos^2\theta\end{pmatrix}\\ &= \frac{\mathbb{1}}{2} + \frac{\sin\theta\cos\alpha}{2}X - \frac{\sin\theta\cos\theta\sin\alpha}{2}Y + \frac{\cos^2\theta}{2}Z, \end{aligned} \tag{11}$$

where X, Y and Z are the Pauli matrices.

Theorem: If we consider $M = a\mathbb{1} + bX + cY + dZ$ where $a, b, c, d \in \mathbb{R}^+$ where $m = a \pm \sqrt{b^2 + c^2 + d^2}$ are the eigenvalues of M.

Based on Equation (9) find that $a = \frac{1}{2}$, $b^2 = \frac{\sin^2\theta\cos^2\theta\cos^2\alpha}{4}$, $c^2 = \frac{\sin^2\theta\cos^2\theta\sin^2\alpha}{4}$ and $d^2 = \frac{\cos^4\theta}{4}$. By substitution and some few algebraic steps we arrive at the value of

$$m = \frac{1}{2} \pm \frac{\cos\theta}{2}. \tag{12}$$

The maximum eigenvalue of M i.e., $m_{\max} = (1 + \cos\theta)/2$ corresponds to $|\psi\rangle$ and occurs midway between $|a\rangle$ and $|b\rangle$. Therefore, we can express this as a function

$$\begin{aligned} f(a,b) = \mathcal{U}(\hat{A}, \hat{B}; \psi) &= -2\ln\left[\frac{1 + \langle a|b\rangle}{2}\right]\\ &= 2\ln\frac{2}{1 + \langle a|b\rangle}. \end{aligned} \tag{13}$$

Using the fact that $\sum_a |\langle\psi|a\rangle|^2 = 1$ and $\sum_b |\langle\psi|b\rangle|^2 = 1$, we can express

$$\begin{aligned}\sum_{a,b} |\langle\psi|a\rangle|^2 \cdot |\langle\psi|b\rangle|^2 \cdot f(a,b) &\geq \min_{a,b} f(a,b)\\ &\geq 2\ln\frac{2}{1 + \langle a|b\rangle}. \end{aligned} \tag{14}$$

3. Results

Considering that

$$\min\left[\frac{\ln 2}{1 + \langle a|b\rangle}\right] = \frac{\ln 2}{1 + \max|\langle a|b\rangle|}, \tag{15}$$

we can put everything together as

$$\mathcal{U}(\hat{A}, \hat{B}; \psi) = S_\alpha(\hat{A}; \psi) + S_\alpha(\hat{B}; \psi) + (1 - \alpha)S_\alpha(\hat{A}; \psi)S_\alpha(\hat{B}; \psi). \tag{16}$$

It is immediately seen that $\mathcal{U}(\hat{A}, \hat{B}; \psi) \geq 0$, with $\mathcal{U}(\hat{A}, \hat{B}; \psi) = 0$ if and only if $|\psi\rangle$ is a common eigenstate of $\hat{A}$ and $\hat{B}$. Besides this, $\mathcal{U}(\hat{A}, \hat{B}; \psi)$ is never greater than $(1 - N^{2(\alpha-1)})/1 - \alpha$, where N is the parenthesized quantity inside the square brackets in the equation below.

$$\mathcal{U}(\hat{A}, \hat{B}; \psi) \geq \frac{1}{1 - \alpha}\left[1 - \left(\frac{2}{1 + \max|\langle a|b\rangle|}\right)^{2(\alpha-1)}\right]. \tag{17}$$

If we take $c = \max_{ij}|\langle a_i|b_j\rangle|$, where $|a_i\rangle$ and $|b_j\rangle$ are the eigenvectors of $\hat{A}$ and $\hat{B}$ respectively, we obtain the bound

$$\mathcal{U}(\hat{A},\hat{B};\psi) \geq \frac{1}{1-\alpha}\left[1-\left(\frac{2}{1+c}\right)^{2(\alpha-1)}\right]. \tag{18}$$

However, by appealing to the Riesz's theorem [15, 20] in the region of $1/2 \leq \alpha \leq 1$, a better hence tighter bound is obtained which can be expressed as

$$\mathcal{U}(\hat{A},\hat{B};\psi) \geq \frac{1}{1-\alpha}\left[1-\left(\frac{1}{c}\right)^{2(\alpha-1)}\right]. \tag{19}$$

This result has the same form as shown in Ref [13]. This gives an irreducible lower bound (generalized uncertainty measure) of the uncertainty on the simultaneous measurement of observables when we use the Tsallis entropy to express the quantum uncertainty relation. Based on this connection, we can directly use this result as an information measure in quantum key distribution protocols where the two legitimate parties, Alice and Bob generate a secret key based on the measurements of the states which they receive. However, this communication takes place in the presence of an eavesdropper, Eve who tries to learn the information being communicated. The eavesdropper can perform any kind of attack on the communication channel but however is only limited by the laws of physics [21]. Provided the correlations are stronger between the measurements of the two legitimate parties, they can still generate a secret key. We therefore appeal to the result by Devetak and Winter [22]. This result quantifies the amount of extractable key, and is expressed as

$$K \geq H(X|E) - H(X|B), \tag{20}$$

where K is the final shared secret key, $H(X|E)$ is the amount of key that Alice can extract from a string X when given the uncertainty of the adversary about X, and $H(X|B)$ is the amount of information that Bob needs to correct his errors, using optimal error correction, given by his uncertainty about the shared string X. Therefore, without loss of generality we can simply re-write this lower bound in terms of Tsallis entropy as

$$K \geq \frac{1}{1-\alpha}\left[1-\left(\frac{1}{c}\right)^{2(\alpha-1)}\right] - S_\alpha(X|B) - S_\alpha(Y|B). \tag{21}$$

Suppose that Alice's measurements are represented by X and X' and Bob's measurements are represented by Y and Y', therefore in order to generate a secret key the two parties need to communicate the choice of their measurements to each other. Based on the property that measurements cannot decrease entropy [23] we can write

$$K \geq \frac{1}{1-\alpha}\left[1-\left(\frac{1}{c}\right)^{2(\alpha-1)}\right] - S_\alpha(X|X') - S_\alpha(Y|Y'). \tag{22}$$

By assuming symmetry i.e., $S_\alpha(X|X') = S_\alpha(Y|Y')$, this gives us a simple proof against collective attacks which was shown in Ref [24] for the BB84 protocol by using the Shannon entropy. The conditional Tsallis entropy is defined in the Appendix.

4. Conclusion

We have shown that the quantum uncertainty principle can be expressed in terms of the Tsallis entropy. We remark that this result preserves a form similar to the most important result which

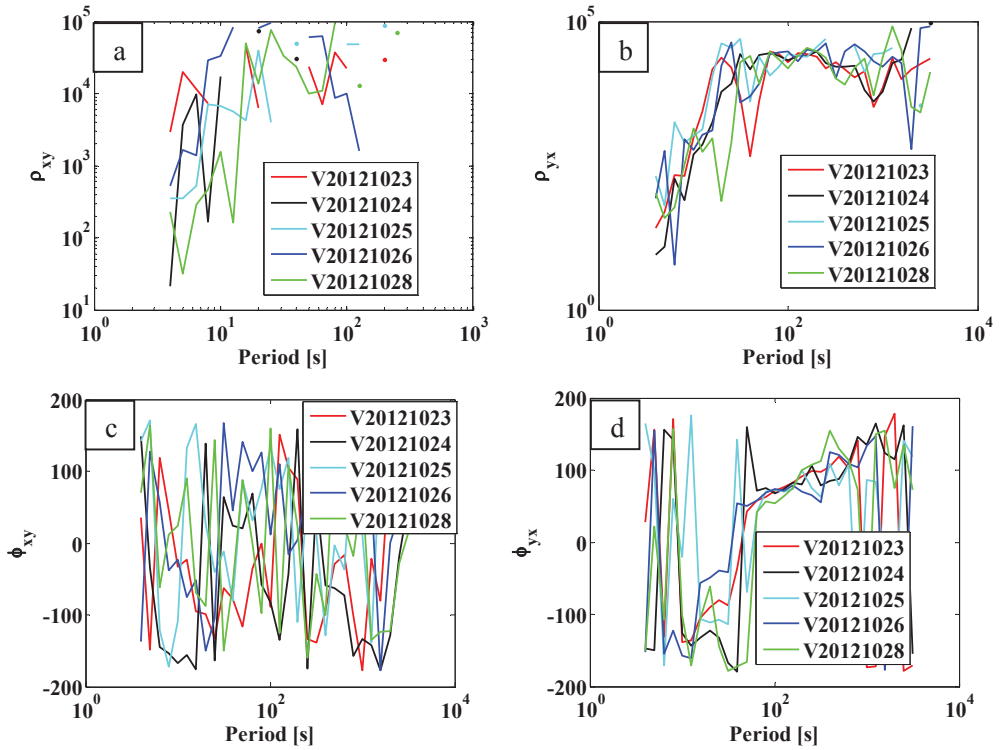

Figure 2. Same parameters as in Fig.1, but at Vaalputs site. The large day-to-day variability indicates that there is a source of noise at this site which reduces the consistency of the data.

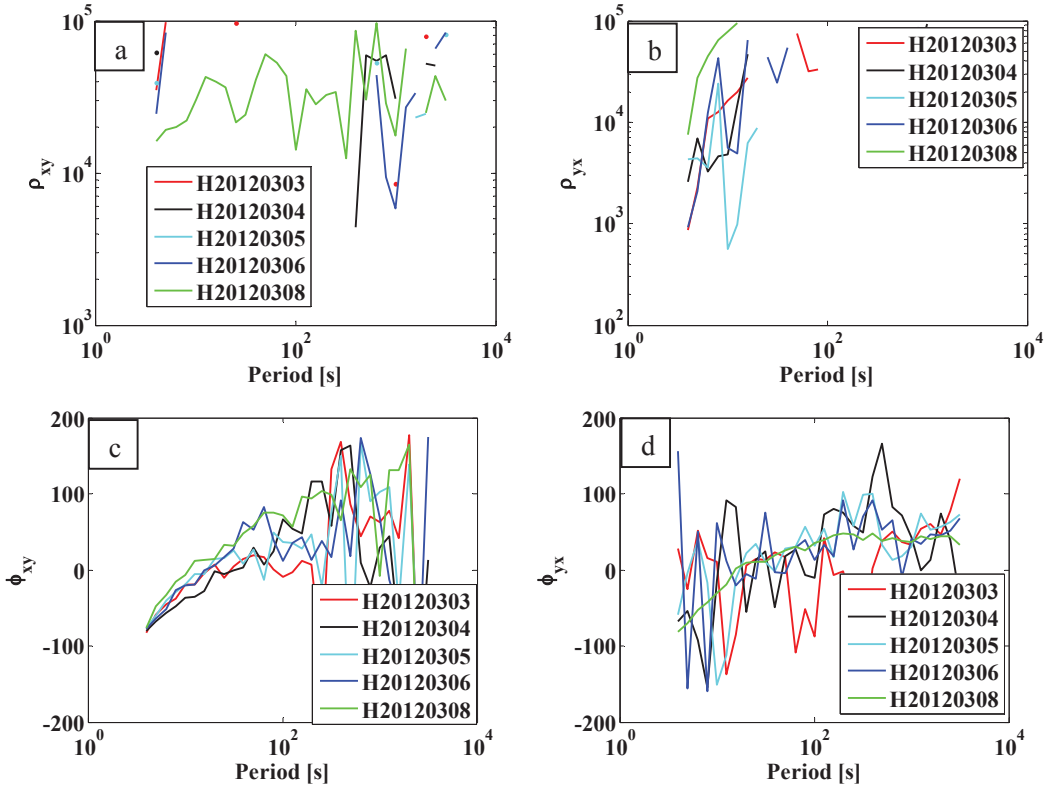

Figure 3. Same parameters as in Fig.1, but at Hermanus site. The variability of the Hermanus data is similar to that at Vaalputs, and much higher that at Middelpos.

Finite-size key in QKD protocols for Rényi entropies

Mhlambululi Mafu[1], Kevin Garapo[1] and Francesco Petruccione[1,2]

[1] Centre for Quantum Technology, School of Chemistry and Physics, University of KwaZulu-Natal, P/Bag X54001 Durban, South Africa

[2] National Institute for Theoretical Physics (NITheP), KwaZulu-Natal, South Africa

E-mail: 209526077@stu.ukzn.ac.za, 209523532@stu.ukzn.ac.za, petruccione@ukzn.ac.za

Abstract. A realistic quantum key distribution protocol necessarily runs with finite resources. This is in contrast to the existing quantum key distribution security proofs which are asymptotic in the sense that certain parameters are exceedingly large as compared to practical realistic values. In this paper, we derive bounds on the secret key rates for the B92 protocol (*Phys. Rev. Lett.* 68, 3121 (1992)) which includes a preprocessing step. The derivation for finite-size key is expressed as an optimization problem by using results of the uncertainty relations and the smooth Rényi entropies.

1. Introduction

Quantum Key Distribution (QKD) provides the only physically secure and proven method for the transmission of a secret key between two distant parties, Alice and Bob [1, 2]. The goal of QKD is to guarantee that the possible eavesdropper known as Eve, with access to the communication channel is unable to obtain useful information about the message [2]. Since the invention of the BB84 protocol [1] which forms the most studied protocol, various protocols have been invented. Some of the common protocols are E91 [3], B92 [4] and SARG04 [5]. Moreover, the unconditional security proofs of these protocols against various attacks have been realized. In addition, various QKD products ave been realized. The tools for the possible study of unconditional security in the finite-key regime for all discrete variable protocols are now available in [6, 7]. Many efforts have been done to improve the bounds on the secret key rates for finite amount of resources [8, 9, 10, 11, 12]. Recently, a technique of using the uncertainty relations for the smooth entropies has been realized [13]. This approach has proved to be elegant because instead of providing bounds for coherent attacks, it provides bounds also for the general kind of attacks. Moreover, the uncertainty relation has direct applications in quantum cryptography and also this generalizes the results for the Shannon or von Neumann entropy.

The security bounds for the BB84 and the six-state protocols have been calculated using the smooth min-entropies in Ref [7, 8]. The secret key rate for the six-state protocol via Rényi entropies has been presented in Ref [12]. In this paper, we present bounds on the achievable key length for the B92 protocol [4] which involves a preprocessing step by using the uncertainty relations [13] and the Rényi entropies [14].

2. The B92 QKD Protocol

The B92 protocol [4] resembles symmetry like the BB84 and the six-state protocol. In contrast to the BB84 protocol which uses four states, the B92 protocol utilizes two non-orthogonal states.

By encoding in the non-orthogonal states of the quantum system, it makes it neither possible for the eavesdropper to make an exact copy of the system nor to gain partial information about the system without disturbing it. Below we describe the steps taken in the execution of the B92 protocol.

State preparation. Alice sends one of the two non-orthogonal states which we denote by $|\psi_{\pm}\rangle$, to Bob. Bob chooses randomly to measure one of the two von Neumann measurements. The first measurement projects onto the basis $|\psi_{+}\rangle$ which consists of the vectors $\{|\psi_{-}\rangle, |\tilde{\psi}_{-}\rangle\}$, where $|\tilde{\psi}_{-}\rangle$ is orthogonal to $|\psi_{-}\rangle$. The second measurement similarly projects onto the basis $|\psi_{-}\rangle$ which consist of the vectors $\{|\psi_{+}\rangle, |\tilde{\psi}_{+}\rangle\}$, where $|\tilde{\psi}_{+}\rangle$ is orthogonal to $|\psi_{+}\rangle$. Then Bob announces an acceptance if he gets an outcome which corresponds to $|\tilde{\psi}_{\pm}\rangle$, otherwise both parties discard the values that they recorded.

Sifting and Measurement. Alice records the bit value 0 or 1 if she sends $|\psi_{+}\rangle$ or $|\psi_{-}\rangle$ and Bob records 0 or 1 if he obtains $|\tilde{\psi}_{-}\rangle$ or $|\tilde{\psi}_{+}\rangle$. Alice sends each quantum state with equal probability and Bob chooses randomly with equal probability between his two measurements.

Parameter estimation. The role of the parameter estimation step is to minimize the set of compatible states Γ, given m sample points. Let $\Gamma_{\varepsilon_{\mathrm{PE}}}$ be a set of states from which a key is extracted with non-negligible probability where $\varepsilon_{\mathrm{PE}}$ is the failure probability in the parameter estimation step (i.e., the parameter estimation passes although the raw key does not contain sufficient secret information). In particular, if the statistics λ_m are obtained by measuring m samples of ρ_{AB} (i.e., the entangled state shared by Alice and Bob) according to a POVM measurement with d possible outcomes and $\lambda_{\infty}(\rho_{AB})$ denotes the perfect statistics in the limit of infinitely measurements then for any state ρ_{AB} [6]

$$\Gamma_{\xi} := \{\rho_{AB} : ||\lambda_m - \lambda_{\infty}(\rho_{AB})||_1 \leq \xi\}, \tag{1}$$

where by the Law of Large numbers [7]

$$\xi := \sqrt{\frac{\ln(1/\varepsilon_{\mathrm{PE}}) + 2\ln(m+1)}{2m}}. \tag{2}$$

Error correction. The error correction step serves the purpose of correcting all the erroneously received bits and giving an estimate of the error rate. Alice and Bob hold correlated bits strings denoted as X^n and Y^n. The number of bits leaked during the classical communication to an eavesdropper is given by [6, 8]

$$L_{\mathrm{EC}} = f_{\mathrm{EC}} n h(Q) + \log_2(\frac{2}{\varepsilon_{\mathrm{EC}}}), \tag{3}$$

where f_{EC} is a constant larger than 1 (in practice $f \approx$1.05 - 1.2), $h(Q)$ is the binary Shannon entropy, Q is the QBER and $\varepsilon_{\mathrm{EC}}$ is the error probability in the error correction step.

Privacy amplification. The objective of this step is to minimize the quantity of correct information which the eavesdropper may have obtained about Alice's and Bob's raw key. Let Alice (X) and Bob (Y) hold a perfectly correlated bit string X^n on which Eve (E) might have some information. Alice chooses at random a function $\mathcal{F}$ from a two universal hash functions and sends a description of $\mathcal{F}$ to Bob. Then Alice and Bob compute their keys $S_A = \mathcal{F}(X^n)$ and $S_B = \mathcal{F}(\hat{X}^n)$. By using an important result in [15], it has been found that the achievable length

of the secret key rate that can be computed from X by the two universal hash function $\mathcal{F}$ can be expressed as

$$\ell = H_{\max}^{\bar{\varepsilon}}(X|E) - H_{\min}^{\bar{\varepsilon}}(X|Y) - 2\log_2(1/\varepsilon), \tag{4}$$

where $\bar{\varepsilon} = (\varepsilon/8)^2$ and ε quantifies the security of the final key.

3. Definitions

3.1. Rényi entropies

The Rényi entropies are a family of functions on probability distributions. They quantify the uncertainty or randomness of a system. The Rényi entropy of order α is defined as [14]

$$H_\alpha(X) = \frac{1}{1-\alpha}\log\sum_{x\in\mathcal{X}} P(x)^\alpha, \quad \alpha \in (0,1)\cup(1,\infty), \tag{5}$$

for which $H_\infty(\alpha\to\infty)$, $H_0(\alpha\to 0)$ and the Shannon entropy ($\alpha\to 1$) are defined as limits. For a finite-dimensional Hilbert space $\mathcal{H}$, we use $\mathcal{P}(\mathcal{H})$ to denote the set of positive semi-definite operators on $\mathcal{H}$. The set of normalized quantum states $\mathcal{S}(\mathcal{H}) := \{\rho \in \mathcal{P}(\mathcal{H}) : \mathrm{tr}\rho = 1\}$ and the set of sub-normalized states $\mathcal{S}_\leq(\mathcal{H}) := \{\rho \in \mathcal{P}(\mathcal{H}) : \mathrm{tr}\rho \leq 1\}$. We use indices to denote multi-partite Hilbert spaces for example, $\mathcal{H}_{AB} = \mathcal{H}_A \otimes \mathcal{H}_B$.

Definition 1. Let $\rho_{AB} \in S_\leq(\mathcal{H}_{AB})$ and $\sigma_B \in \mathcal{S}(\mathcal{H}_B)$, then the min-entropy of A conditioned on B of the state ρ_{AB} relative to σ_B is defined as [7]

$$H_{\min}(A|B)_{\rho|\sigma} := \max_\sigma \sup\{\lambda \in \mathbb{R} : \rho_{AB} \leq 2^{-\lambda}\mathbb{1}_A \otimes \sigma_B\}, \tag{6}$$

where the maximum is taken over the states $\sigma_B \in \mathcal{S}(\mathcal{H}_B)$. Furthermore, we define

$$H_{\min}(A|B)_\rho := \max_{\sigma_B\in\mathcal{S}(\mathcal{H}_B)} H_{\min}(A|B)_{\rho|\sigma}. \tag{7}$$

The min-entropy, $H_{\min}(A|B)_\rho$ is finite if and only if $\mathrm{supp}\{\rho_B\} \subseteq \mathrm{supp}\{\sigma_B\}$ and $-\infty$ otherwise. The max-entropy is its dual with regards to a purification ρ_{ABC} of ρ_{AB} on an auxiliary Hilbert space $\mathcal{H}_C$.

Definition 2. Let $\rho_{ABC} \in S_\leq(\mathcal{H}_{ABC})$ be pure, then the max-entropy of A conditioned on B of the state ρ_{AB} is defined as

$$H_{\max}(A|B)_\rho := -H_{\min}(A|C)_\rho. \tag{8}$$

The quantum entropies can be ordered as follows

$$H_{\min}(A|B)_\rho \leq H(A|B)_\rho \leq H_{\max}(A|B)_\rho. \tag{9}$$

In order to define smooth versions, we consider the set of states close to ρ in the following sense. For $\varepsilon > 0$, we define an ε-ball of states around $\rho \in \mathcal{S}(\mathcal{H})$ as

$$\mathcal{B}^\varepsilon(\rho) := \{\tilde{\rho} \in \mathcal{S}_\leq(\mathcal{H}) : C(\rho,\tilde{\rho}) \leq \varepsilon\}, \tag{10}$$

where $C(\rho,\tilde{\rho}) := \sqrt{1-F^2(\rho,\tilde{\rho})}$ is a distance measure (on normalized states) based on the fidelity $F(\rho,\tilde{\rho}) := \mathrm{tr}|\sqrt{\rho}\sqrt{\tilde{\rho}}|$. We use this choice of measure because it is invariant under purifications and is directly related to the trace distance for pure states. Smoothed versions of the min-entropy are then defined as:

$$\begin{aligned} H_{\min}^\varepsilon(A|B)_{\rho|\sigma} &:= \max_{\tilde{\rho}\in\mathcal{B}^\varepsilon(\rho_{AB})} H_{\min}(A|B)_{\tilde{\rho}|\sigma}, \\ H_{\min}^\varepsilon(A|B)_\rho &:= \max_{\tilde{\rho}\in\mathcal{B}^\varepsilon(\rho_{AB})} H_{\min}(A|B)_{\tilde{\rho}}, \end{aligned} \tag{11}$$

and similarly

$$H_{\max}^{\varepsilon}(A|B)_{\rho} := \min_{\tilde{\rho}\in\mathcal{B}^{\varepsilon}(\rho_{AB})} H_{\max}(A|B)_{\tilde{\rho}}. \tag{12}$$

The Rényi entropies with $\alpha > 1$ are close to the smooth min-entropy in the sense that

$$H_{\min}^{\varepsilon}(X) \geq H_{\alpha}(X) - \frac{1}{\alpha - 1}\log\frac{1}{\varepsilon}, \quad \alpha > 1, \tag{13}$$

while those with $\alpha < 1$ are close to the smooth max-entropy.

3.2. Bound on the secure key rate

According to [7], for any $\varepsilon \geq 0$, a final key S is said to be ε-secure with respect to an adversary Eve if the joint state ρ_{SE} satisfies

$$\min_{\rho_E} \frac{1}{2}||\rho_{SE} - \tau_S \otimes \rho_E||_1 \leq \varepsilon, \tag{14}$$

where $\rho_{SE} = \sum_{s\in\mathcal{S}} P_s(s)|s\rangle\langle s| \otimes \rho_E^s$ and $\{|s\rangle\}_{s\in\mathcal{S}}$ is an orthonormal basis of some Hilbert space $\mathcal{H}_s$. The parameter τ_S is the completely mixed state on the key space, ρ_E is the state held by an eavesdropper, and $||\cdot||_1$ is the trace distance. The parameter ε, represents the maximum failure probability in which an adversary may have gained some information on S, or it can be interpreted as the maximum failure probability in which the extracted key deviates from the ideal key. The secret key rate in the asymptotic regime is expressed as

$$\lim_{N\to\infty} r = S(X|E) - H(X|Y), \tag{15}$$

where $S(X|E)$ and $H(X|Y)$ are the conditional von Neumann and the Shannon entropies [8]. However, in the non-asymptotic regime this equation becomes invalid as we have a finite number of bits that Alice sends to Bob. In the non-asymptotic limit, the secret key rate is found to be [6]

$$r = \frac{n}{N}\left[\min_{\sigma_{\mathrm{XE}}\in\Gamma} H(X|E) + \triangle - L_{\mathrm{EC}}\right] + \frac{2}{N}\log_2(2\varepsilon_{\mathrm{PA}}), \tag{16}$$

where $\triangle = (2\log_2 d + 3)\sqrt{[\log_2(2/\bar{\varepsilon})]/n}$. The total security parameter, ε of a QKD scheme depends on the sum of probabilities of failures of the classical post-processing protocols which can be written as

$$\varepsilon = \bar{\varepsilon} + \varepsilon_{\mathrm{PA}} + \varepsilon_{\mathrm{EC}} + \varepsilon_{\mathrm{PE}}, \tag{17}$$

where $\bar{\varepsilon}$ denotes the error in the smooth min-entropy and $\varepsilon_{\mathrm{PA}}$ is the probability of error in the privacy amplification step.

In order to determine the length ℓ, of ε-secure key bits that can be generated by this protocol we use the following results on the uncertainty relation [13]. The amount of key that can be extracted from a string X is given by uncertainty of the adversary about X, measured in terms of the smooth Rényi entropies. The amount of information B needs to correct his errors, using optimal error correction is given by his uncertainty about A's string again measured in terms of the smooth Rényi entropies. Combining these two results we have [16]

$$H_{\min}^{\bar{\varepsilon}}(\mathbf{X}|E) + H_{\max}^{\bar{\varepsilon}}(\mathbf{Z}|B) \geq \log\frac{1}{c}, \tag{18}$$

where $\bar{\varepsilon} \geq 0$ is the smoothing parameter and c quantifies the 'incompatibility' between the measurements $\mathbf{Z} = Z^{\otimes n}$ and $\mathbf{X} = X^{\otimes n}$. It is defined as $c = -\max_{x,z}||\sqrt{M_X}\sqrt{N_Z}||_{\infty}^2$, where

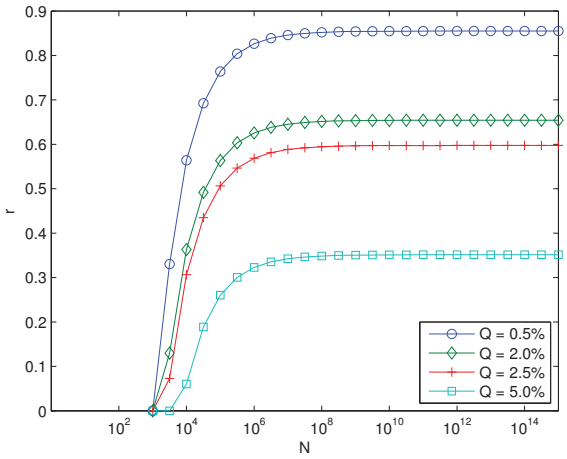

Figure 1. (Color online) Lower bound on the secret key fraction, r, for the finite B92 protocol as a function of the exchanged quantum signals N for bit errors Q= 0.5%, 2%, 2.5%, 5%. The maximum failure probability of the protocol is $\varepsilon = 10^{-5}$ and the failure probability of the error correction procedure is $\varepsilon_{\rm EC} = 10^{-10}$.

$\{M_X\}$ and $\{N_Z\}$ are POVM elements for preparing the state corresponding to **X** and **Z** basis respectively [16].

The definitions of the smooth min and max-entropies have been given above. The measure of uncertainty for Bob's measurement $H_{\max}$ can only increase under information processing such that

$$H^{\bar{\varepsilon}}_{\max}(\mathbf{Z}|B) \leq H^{\bar{\epsilon}}_{\max}(\mathbf{Z}|\mathbf{Z}'), \tag{19}$$

where the measurement $\mathbf{Z}' = Z'^{\otimes n}$ is made on Bob's system [17]. The protocol does not need to prescribe the actual measurements of **Z** and $\mathbf{Z}'$. However, based on the observed parameters we can replace the measurement on **X** and $\mathbf{X}'$ in this hypothetical protocol by highly correlated measurements **Z** and $\mathbf{Z}'$ respectively. This means that the uncertainty in $H^{\bar{\varepsilon}}_{\max}(\mathbf{Z}|\mathbf{Z})$ is small and holds for the following bound on the smooth max-entropy

$$H^{\bar{\varepsilon}}_{\max}(\mathbf{Z}|\mathbf{Z}') \leq nh(Q), \tag{20}$$

where Q is the QBER. This result follows the argument in [16].

3.3. Bound on the achievable key length

Let ρ_{XBE} be the state describing Alice's bit string X^n and Bob's string B^n as well as Eve's quantum information represented by ρ_{E^n}. Let $\bar{\varepsilon}, \varepsilon_{\rm PA} \geq 0$. If the length of the key is such that

$$\ell \leq \max_{\bar{\varepsilon},\varepsilon_{\rm PA}} \left(H_{\min}(\mathbf{X}|E)_{\rho_{XBE}} - 2\log\frac{1}{2\bar{\varepsilon}} - 2\log\frac{1}{2\varepsilon_{\rm PA}} \right), \tag{21}$$

then the protocol is $(2\bar{\varepsilon} + \varepsilon_{\rm PA})$-secure.

By using the data processing inequality [7] and the uncertainty relation in (18) we have

$$\begin{aligned} H^{\bar{\varepsilon}}_{\min}(\mathbf{X}|E') &\geq H^{\bar{\varepsilon}}_{\min}(\mathbf{X}|E) - {\rm leak}_{\rm EC} \\ &\geq nq - H^{\bar{\varepsilon}}_{\max}(\mathbf{Z}|\mathbf{Z}') - {\rm leak}_{\rm EC} \\ &\geq nq - \frac{(1-2\delta)\eta + 2\delta}{2}(\varepsilon - (1-\varepsilon)h(x)) \\ &- nh(Q) - {\rm leak}_{\rm EC}, \end{aligned} \tag{22}$$

4. Conclusions

In this paper, we present for the first time MT data from three recently deployed MT instruments in South Africa. The typical day-to-day variability of the off-diagonal components of the apparent resistivity is demonstrated. The results also show the variability from site to site, with the Middelpos site showing the least day-to-day variability and the closest correspondence to previous MT measurements in Southern Africa [10]. Typically, most observed electromagnetic field components are contaminated to some extent with noise. In order to retrieve unbiased estimates of the apparent resistivity and surface impedance, long recording times are required to ensure that sufficient data are available for processing through long-duration averaging. Further analysis of the data from these sites are required to determine their usefulness for the estimation of geomagnetically induced currents.

References

[1] Hermance J F, 1973 Processing of magnetotelluric data, *Physics of the Earth and Planetary interiors*, **7** 349-364

[2] Jones A G, Chave A D, Egbert G, Auld D and Barh K, 1989 A comparison of techniques for magnetotelluric response function estimation, *Geophys. J. int.,* **94,** 201-214

[3] Chant I J and Hastie L M, 1992 Time frequency analysis of magnetotelluric data, *Geophys. J. int.,* **111,** 399-413

[4] Ritter O, Junge A and Dawes G J K, 1998 New equipment and processing for magnetotelluric remote reference observations, *Geophys. J. int,* **132,** 535-548

[5] Muller A, 2000 A new method to compensate for bias in magnetotellurics, *Geophys. J. int*., **142**, 257-269

[6] Smirnov M Y, 2003 Magnetotelluric data processing with a robust statistical procedure having a high breakdown point, *Geophys. J. int*., **152**, 1-7

[7] Chave A D and Thompson D J, 2004 Bounded influence magnetotelluric response function, *Geophys. J. int*., **157**, 988-1006

[8] Weckmann U, Magunia A, and Ritter O, 2005 Effective noise separation for magnetotelluric single site data processing using a frequency domain selection scheme, *Geophys. J. Int*. **161**, 635-652

[9] Khoza D, Jones A G, Muller M R, Evans R L, Webb S J and Miensopust M, 2012 Tectonic model of the Limpopo belt, *Precambrian research*, **226**, 143-156

[10] Weckmann, U., O. Ritter, A. Jung, T. Branch, and M. de Wit (2007), Magnetotelluric measurements across the Beattie magnetic anomaly and the Southern Cape Conductive Belt, South Africa, J. Geophys. Res., 112, B05416, doi:10.1029/2005JB003975.